C55.612/2: 978

COLLECTED REPRINTS 1978

PENNSYLVANIA STATE UNIVERSITY
MAY 19 1980
DOCUMENTS COLLECTION

Wave Propagation Laboratory

NATIONAL OCEANIC AND ATMOSPHERIC ADMINISTRATION
Environmental Research Laboratories

February 1980

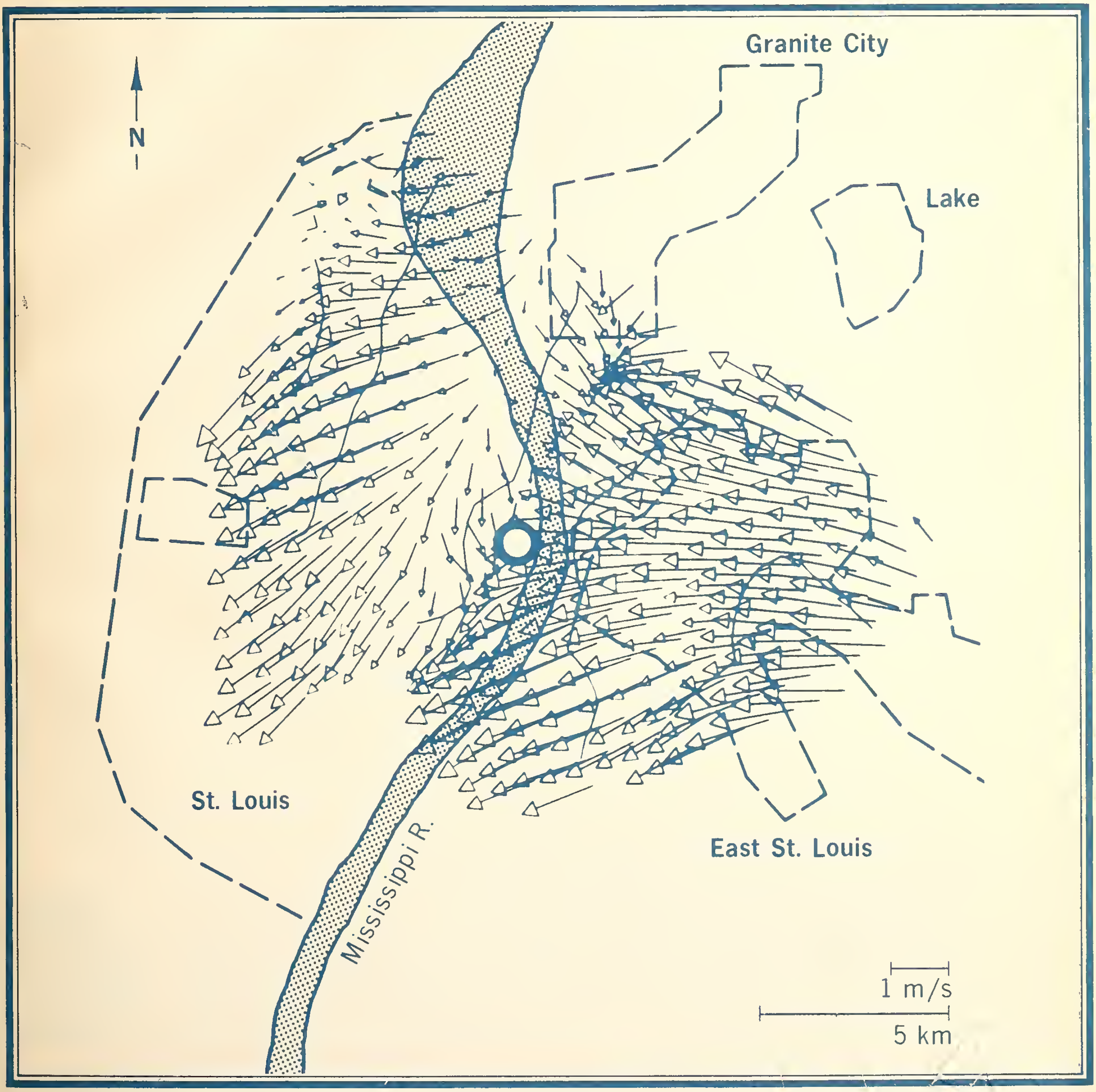

Cover figure—A high-resolution wind map near the surface in the dry mixed layer that was modified by the St. Louis urban heat island during METROMEX. The mean wind, 3 m/s from the northeast, has been removed, revealing a striking and persistent line of convergence originating at the heavily industrialized area just south of Granite City and extending across the central business district to the southwest. The map was produced by the transportable X-band dual-Doppler radar system developed at the Wave Propagation Laboratory. Details of the analysis are contained in the article by Kropfli and Kohn reprinted in this volume (page 465).

COLLECTED REPRINTS 1978

Wave Propagation Laboratory

February 1980

Boulder, Colorado

UNITED STATES
DEPARTMENT OF COMMERCE
Philip M. Klutznick, Secretary

NATIONAL OCEANIC AND
ATMOSPHERIC ADMINISTRATION
Richard A. Frank, Administrator

Environmental Research
Laboratories
Wilmot N. Hess, Director

U. S. Depository Copy

NOTICE

The Environmental Research Laboratories do not approve, recommend, or endorse any proprietary product or proprietary material mentioned in this publication. No reference shall be made to the Environmental Research Laboratories or to this publication furnished by the Environmental Research Laboratories in any advertising or sales promotion which would indicate or imply that the Environmental Research Laboratories approve, recommend, or endorse any proprietary product or proprietary material mentioned herein, or which has as its purpose an intent to cause directly or indirectly the advertised product to be used or purchased because of this Environmental Research Laboratories publication.

FOREWORD

The Wave Propagation Laboratory seeks to advance the nation's geophysical research and services through the creation and application of new remote measurement systems. Since no one technique is able to measure the full range of parameters required, the Laboratory has developed a wide range of active and passive optical, radio, and acoustic remote sensing systems. The new sensors typically have several important advantages over standard, in situ instruments; in particular, it is often possible to provide the researcher with one-, two-, or three-dimensional data sets that possess excellent continuity and resolution in both time and space. In many cases, these data sets are much richer than those available by other techniques, and are therefore able to provide new insights into atmospheric and oceanographic structure and processes.

The sixth volume of Collected Reprints comprises material published during the calendar year 1978. To avoid unnecessary duplication, only the abstracts of WPL/NOAA Technical Memoranda and Technical Reports are included.

To quite an extent, the field of remote sensing has grown up outside the atmospheric and oceanographic research communities which it seeks to serve. We have found that previous volumes of WPL Collected Reprints have helped fill the potential communication gap with our colleagues in these fields; we hope and expect that this will be true of this latest volume of WPL publications.

C Gordon Little

C. Gordon Little
Director
Wave Propagation Laboratory

SYNOPSIS OF CONTENTS

Page

Foreword iii

I. SURVEY, REVIEW AND PLANNING DOCUMENTS 1

II. MEASUREMENTS AND TESTS 125

III. REMOTE SENSING SYSTEMS AND INSTRUMENTS

A. Sensors Using Acoustic Techniques 166

B. Sensors Using Optical Techniques 201

C. Sensors Using Radio Techniques 250

D. Systems Which Combine Techniques 285

IV. GEOPHYSICAL STUDIES

A. Atmospheric Boundary Layer 315

B. Atmospheric and Oceanic Waves 385

C. Storms, Gusts and Shears 405

D. Clouds 439

E. Site Characterization 464

V. Wave Propagation Theory 473

VI. Data Interpretation and Analysis Techniques 628

Index to Authors 689

Contents

I. SURVEY, REVIEW AND PLANNING DOCUMENTS

Page

Barrick, D. E.: HF radio oceanography--a review. Boundary Layer Meteorology 13:23-43, 1978. 1

Beran, W. D. and C. G. Little (PROFS): A strategy to improve local weather services. Proceedings of the AMS/NWS Conference on Weather Forecasting and Analysis and Aviation Meteorology, Silver Spring, Maryland, 16-19 October, 228-233, 1978. 23

Brown, E. H. and F. F. Hall: Advances in atmospheric acoustics. Review of Geophysics and Space Physics 16:47-110, 1978. 29

Golden, J. H., C. F. Chappel, C. G. Little, A. H. Murphy, E. B. Burton, and E. W. Pearl: What should the NWS be doing to improve short-range weather forecasting? Bulletin of the American Meteorological Society 59:1334-1342, 1978. 93

Gossard, E. E.: The use of radar for studies of clouds. NOAA Technical Memorandum ERL WPL-39, 1978. (Abstract only). 102

Hogg, D. C.: Millimeter waves-propagation and application. Proceedings of the IEE International Conference on Antennas and Propagation, Part 2, London, 28-30 November, 110-113, 1978. 103

Hooke, W. H.: The Boulder Atmospheric Observatory. Proceedings of the Third U. S. National Conference on Wind Engineering Research, Wind Engineering Council and National Science Foundation, Gainsville, Florida, 26 February-1 March, 81-88, 1978. 107

Huffaker, R. M. (Editor): Feasibility study of satelliteborne lidar global wind monitoring system. NOAA Technical Memorandum ERL WPL-37, September, 1978. (Abstract only). 115

C. G. Little (Chairman) and D. W. Beran (Editor-in-Chief), PROFS PDP Panel: Program Development Plan for Prototype Regional Observing and Forecasting Service (PROFS), 1978. (Abstract only). 116

Westwater, E. R. and F. O. Guiraud: Ground-based passive microwave sensing of water vapor and cloud liquid. Fourth Symposium on Meteorological Observation and Instrumentation, American Meteorological Society, Denver, 10-14 April, 150-152, 1978. 117

Wyngaard, J. C.: Progress in research on turbulent flow. Preprint Volume; WMO Symposium on Boundary Layer Physics Applied to Specific Problems of Air Pollution, Norrkoping, Sweden, 39-43, 1978. 120

II. MEASUREMENTS AND TESTS

Chadwick, R. B., K. P. Moran, and G. E. Morrison: Measurements toward a C_n^2 climatology. Preprint Volume; 18th Radar Meteorology Conference, 100-103, American Meteorological Society, Atlanta, Georgia, 1978. 125

Chadwick, R. B., K. P. Moran, G. E. Morrison, and W. C. Campbell: Measurements showing the feasibility for radar detection of hazardous wind shear at airports. Final report AFGL-TR-78-0160, Air Force Geophysics Laboratory, Hanscom AFB, Massachusetts, 1978. (Abstract only). 129

Cohen, R. and W. H. Hooke: Neutral atmospheric motions manifested in radar echo Doppler shifts from two-stream irregularities in the equatorial electrojet. *Journal of Geophysical Research* 83:4791-4797, 1978. 130

Decker, M. T., E. R. Westwater, and F. O. Guiraud: Tests of microwave radiometric sensing of atmospheric temperature and water in the Gulf of Alaska. Fourth Symposium on Meteorological Observation and Instrumentation, 10-14 April, 148-149, American Meteorological Society, Denver, 1978. 137

Derr, V. E., G. M. Lerfald, and M. J. Post: Measures of inhomogeneity of aerosols. U. S. Army ASL-CR-78-8017-1, July, 1978. (Abstract only). 139

Haugen, D. A. and J. C. Kaimal: Measuring temperature structure parameter profiles with an acoustic sounder. *Journal of Applied Meteorology* 17:895-899, 1978. 140

Haugen, D. A. and J. C. Kaimal: Measuring C_T^2 profiles with acoustic sounders. Preprint Volume; Fourth Symposium on Meteorological Observation and Instrumentation, 278-280, American Meteorological Society, Denver, Colorado, 1978. 145

Neff, W. D.: Beamwidth effects on acoustic backscatter in the planetary boundary layer. *Journal of Applied Meteorology* 17:1514-1520, 1978. 148

Neff, W. D. and D. A. Haugen: Multi-beamwidth studies of excess acoustic attenuation. Preprint Volume; Fourth Symposium on Meteorological Observation and Instrumentation, 281-284, American Meteorological Society, Denver, Colorado, 1978. 155

Post, M. J.: Experimental measurements of atmospheric aerosol inhomogeneities. _Optics Letters_ 2:166-168, June, 1978. 159

Wyngaard, J. C., J. C. Kaimal, G. R. Ochs, R. J. Hill, and D. C. Sorensen: An optical heat flux experiment. Preprint Volume; Fourth Symposium on Meteorological Observations and Instrumentation, 10-14 April, 47-50, Denver, Colorado. Published by the American Meteorological Society, Boston, Massachusetts, 1978. 162

III. REMOTE SENSING SYSTEMS AND INSTRUMENTS

A. Sensors Using Acoustic Techniques

Bedard, A. J. and W. H. Hooke: The Dulles Airport pressure-sensor array for gust-front detection--system design and preliminary results. Preprint Volume; Fourth Symposium on Meteorological Observation and Instrumentation, 115-124, American Meteorological Society, Denver, Colorado, 1978. 166

Bedard, A. J. and T. T. Fujita: An omnidirectional, tilt insensitive, wind speed threshold detector. Preprint Volume; Fourth Symposium on Meteorological Observation and Instrumentation, 83-86, American Meteorological Society, Denver, Colorado, 1978. 176

Brown, E. H., C. G. Little, and W. M. Wright: Echosonde interferometer for atmospheric research. _Journal of the Acoustical Society of America_ 63:694-699, 1978. 180

Kaimal, J. C.: Sonic anemometer measurement of atmospheric turbulence. Proceedings of the Dynamic Flow Conference, 551-565, Baltimore, Maryland, 1978. 186

B. Sensors Using Optical Techniques

Derr, V. E.: Applications of lidar to atmospheric sensing. Proceedings of the International Conference on Lasers '78, 11-15 December, 40-47, Orlando, Florida, Society of Photo-Optical Instrumentation Engineers, 1978. 201

Earnshaw, K. B., Ting-i Wang, R. S. Lawrence, and R. G. Greunke: A feasibility study of identifying weather by laser forward scattering. _Journal of Applied Meteorology_ 17:1476-1481, 1978. 209

Lawrence, R. S., G. R. Ochs and S. F. Clifford: Applications of a laser-beam average wind sensor to pollution meteorology. Fourth Joint Conference on Sensing of Environmental Pollutants, 294, 1978. 215

Lerfald, G. M. and V. E. Derr. Experimental atmospheric extinction measurements at nine wavelengths between 0.3 and 10μm. Society of Photo-Optical Instrumentation Engineers 161: Optics Applied to Solar Energy IV, 109-113, November, 1978. 216

Ochs, G. R. and Ting-i Wang: Finite aperture optical scintillometer for profiling wind and Cn-squared. Applied Optics 17:3774-3778, 1978. 221

Schwiesow, R. L., M. J. Post, and V. E. Derr: Measurement by Doppler lidar of atmospheric velocities relevant to environmental monitoring. Proceedings of the Fourth Joint Conference on Sensing Environmental Pollutants, 403-406, 1978. 226

Wang, Ting-i: Optical remote sensing on turbulence and cross-wind. Science Monthly Tapei, Taiwan, the Republic of China 9:48-53, February, 1978. (In Chinese). (Abstract only). 230

Wang, Ting-i, K. B. Earnshaw, and R. S. Lawrence: A fast-response optical sensor for measuring rainfall rate and raindrop size distribution. Summaries of the 1978 International Symposium on Antennas and Propagation, 493-495, Paper C-9-4, Sendai, Japan, 29-31 August 1978. 231

Wang, Ting-i, K. B. Earnshaw, and R. S. Lawrence: Simplified optical path-averaged rain gauge. Applied Optics 17:384-390, 1978. 234

Wang, Ting-i and G. R. Ochs: An optical cross-wind profiler. Summaries of the 1978 International Symposium on Antennas and Propagation, 497-500, Paper C-9-5, 29-31 August, Sendai, Japan, 1978. 241

Wang, Ting-i, G. R. Ochs, and S. F. Clifford: A saturation-resistant optical scintillometer to measure Cn-squared . Journal of the Optical Society of America 68:334-338, 1978. 245

C. Sensors Using Radio Techniques

Decker, M. T., E. R. Westwater, and F. O Guiraud. Experimental evaluation of ground-based microwave radiometric sensing of atmospheric temperature and water vapor profiles. Journal of Applied Meteorology 17:1788-1795, 1978. 250

Fedor, L. S. and D. E. Barrick: Measurement of ocean wave heights with a satellite radar altimeter. EOS Transactions of the American Geophysical Union 59:843-847, 1978. 258

Gossard, E. E., R. B. Chadwick, K. P. Moran, R. G. Strauch, G. E. Morrison, and W. C. Campbell: Observation of winds in the clear air using an FM-CW Doppler radar. Radio Science 13:285-289, 1978. 263

Rufenach, C. L. and W. R. Alpers: Measurement of ocean wave heights using the GEOS 3 altimeter. Journal of Geophysical Research 83:5011-5018, 1978. 268

Westwater, E. R.: The accuracy of water vapor and cloud liquid determination by dual-frequency ground-based microwave radiometry. Radio Science 13:677-685, July-August, 1978. 276

D. Systems Which Combine Techniques

Hooke, W. H.: The implications of remote-sensing developments for air-pollution meteorology. Proceedings of the WMO Symposium on Boundary Layer Physics Applied to Specific Problems of Air Pollution, 19-23 June, 259-270, Norrkoping, Sweden, 1978. 285

Kaimal, J. C. NOAA instrumentation at the Boulder Atmospheric Observatory. Preprint Volume; Fourth Symposium on Meteorological Observation and Instrumentation, 35-40, American Meteorological Society, Denver, Colorado, 1978. 297

Lerfald, G. M. and V. E. Derr. Effects of weather and pollution on incident solar energy - basic measurements leading to computer models. Proceedings of the Fifth National Conference on Energy and the Environment, 335-338, American Institute of Chemical Engineers, 1978. 303

Post, M. J., R. L. Schwiesow, R. E. Cupp, D. A. Haugen, and J. T. Newman: A comparison of anemometer- and lidar-sensed wind velocity data. Journal of Applied Meteorology 17:1179-1181, August, 1978. 307

Westwater, E. R.: Improved determination of vertical temperature profiles of the atmosphere by a combination of radiometric and active ground-based sensors. Fourth Symposium on Meteorological Observation and Instrumentation, 10-14 April, 153-157, American Meteorological Society, Denver, 1978. 310

IV. GEOPHYSICAL STUDIES

A. Atmospheric Boundary Layer

Brost, R. A. and J. C. Wyngaard: A model study of the stably-stratified planetary boundary layer. Journal of Atmospheric Science 35:1427-1440, 1978. 315

Gaynor, J. E.: Anaylsis of the disturbed boundary layer during GATE using acoustic sounder data. Conference papers, 11th Technical Conference on Hurricanes and Tropical Meteorology, 242-246, Miami, Florida, 1978. 329

Gaynor, J. E.: Acoustic sounding in a moist tropical marine atmospheric boundary layer during GATE. Preprint Volume; Fourth Symposium on Meteorological Observation and Instrumentation, 410-414, Denver, Colorado, 1978. 334

Gaynor, J. E. and P. A. Mandics: Analysis of the tropical marine boundary layer during GATE using acoustic sounder data. Monthly Weather Review 106:223-232, 1978. 339

Hall, F. F., Jr.: Boundary layer climatologies from acoustic sounder investigations. Preprint Volume; Fourth Symposium on Meteorological Observations and Instrumentation, 330-332, 1978. 349

Kaimal, J. C.: Horizontal velocity spectra in an unstable surface layer. Journal of Atmospheric Science 35:18-24, 1978. 352

Moninger, W. R., A. S. Frisch, W. C. Campbell, and R. G. Strauch: Doppler radar measurements of plume dispersal and dissipation rates in the boundary layer. Preprint Volume; 18th Conference on Radar Meteorology, 49-54, Atlanta, Georgia, 1978. 359

Neff, W. D. and F. F. Hall: Acoustic remote sensing of the planetary boundary layer at the South Pole. Preprint Volume; Fourth Symposium on Meteorological Observation and Instrumentation, 357-361, Denver, Colorado, 1978. 365

Neff, W. D.: Boundary layer research at South Pole Station using acoustic remote sensing. The Antarctic Journal of the U.S. 13(4):179-181, 1978. 370

Wyngaard, J. C., W. T. Pennell, D. H. Lenschow and M. A. Le Mone: The temperature-humidity convariance budget in the convective boundary layer. Journal of Atmospheric Science 35:47-58, 1978. 373

B. Atmospheric and Oceanic Waves

Barrick, D. E., M. W. Evans, and B. L. Weber: Ocean surface currents mapped by radar. Proceedings of a Working Conference on Current Measurement, Technical Report DEL-SG-3-78, College of Marine Studies, University of Delaware. 59-65, 1978. 385

Bedard, A. J.: Infrasound originating near mountainous regions in Colorado. Journal of Applied Meteorology 17:1014-1022, 1978. 392

Lipa, Belinda: Inversion of second-order radar echoes from the sea. Journal of Geophysical Research 83(C2): 959-962, 1978. 401

C. Storms, Gusts and Shears

Bedard, A. J.: The Dulles International Airport windshear detection system - statistical results. Conference on the Atmospheric Environment of Aerospace Systems and Applied Meteorology, 57-66, American Meteorological Society, 1978. 405

Bedard, A. J. and M. J. Sanders, Jr.: Thunderstorm-related wind shear detected at Dulles International Airport using a Doppler acoustic/microwave radar, a monostatic sounder, and arrays of surface sensors. Proceedings of the Conference on Weather Forecasting and Analysis and Aviation Meteorology, 347-352, American Meteorological Society, Silver Springs, Maryland, 1978. 415

Dye, J. E., L. J. Miller, B. E. Martner, and Z. Levin: Growth and recirculation of precipitation in an evolving convective storm. Preprint Volume; Conference on Cloud Physics and Atmospheric Electricity, 528-533, Seattle, Washington, 1978. 421

Miller, L. J.: Horizontal airflow and precipitation fallspeed in a convective storm from triple Doppler radar measurements. Preprint Volume; 18th Radar Meteorology Conference, 207-211, American Meteorological Society, Atlanta, Georgia, 1978. 427

Moninger, W. R. and R. Carbone: Report on preliminary data from a multi-Doppler radar study of weather systems in and near the Sierra Nevada. Preprint Volume; Conference on Sierra Nevada Meteorology, 133-134, American Meteorological Society, 1978. 432

Strauch, R. G. and W. R. Moninger: Radar measurement of wind shear and wind profiles for air safety. Preprint Volume; 18th Radar Meteorology Conference, 432-436, Atlanta, Georgia, 1978. 434

D. Clouds

Danielson, K. S. and V. E. Derr: Phase detection of convective cloud hydrometers using lidar. Proceedings of Conference on Cloud Physics and Atmospheric Electricity, 2 August, 341-346, Seattle, Washington, 1978. 439

Lopez, R. E.: Internal structure and development processes of C-scale aggregates of cumulus clouds. Monthly Weather Review, 1488-1494, October, 1978. 445

Platt, C. M. R., N. L. Abshire, and G. T. McNice. Some microphysical properties of an ice cloud from lidar observation of horizontally oriented crystals. Journal of Applied Meteorology 17:1220-1224, August, 1978. 452

Platt, C. M. R.: Lidar backscatter from horizontal ice crystal plates. Journal of Applied Meteorology 17:482-488, April, 1978. 457

E. Site Characterization

Abshire, N. L., V. E. Derr, G. M. Lerfald, G. T. McNice, R. F. Pueschel, and C. C. Van Valin: Aerosol characterization at Colstrip, Montana, Spring and Fall, 1975. NOAA Technical Memorandum, ERL WPL-33, 1978. (Abstract only). 464

Kropfli, R. A. and N. M. Kohn: Persistent horizontal rolls in the urban mixed layer as revealed by dual Doppler radar. Journal of Applied Meteorology 17:669-676, 1978. 465

V. WAVE PROPAGATION THEORY

Brown, E. H.: Quantitative acoustic measurements of atmospheric turbulence. Preprint Volume; Fourth Symposium on Meteorological Observation and Instrumentation, 275-277, American Meteorological Society, Boston, Massachusetts, 1978. 473

Chimonas, G.: Packet-scale motions forced by nonlinearities in a wave system. Journal of Atmospheric Science 35:382-396, 1978. 476

Clifford, S. F. and D. E. Barrick: Remote sensing of the sea state by analysis of backscattered microwave phase fluctuations. IEEE Transactions on Antennas and Propagation AP-26:699-705, 1978. 491

Clifford, S. F., Ting-i Wang, and T. Priestley: Spot size of the radar return from a radar-acoustic sounding system (RASS) due to atmospheric refractive turbulence. Radio Science 13:985-989, 1978. 498

Clifford, S. F.: The classical theory of wave propagation in a turbulent medium. In Laser Beam Propagation in the Atmosphere (J. W. Strohbehn, ed.), 9-43, Springer-Verlag, Berlin-Heidelberg-New York, 1978. 503

Derr, V. E.: A basic comparison of lidar and radar for remote sensing of clouds. NOAA Technical Report ERL 397-WPL 52, March, 1978. (Abstract only). 538

Evans, M. W.: Surface current mapping radar: Theory and Application. Society of Petroleum Industry Biologists, Symposium on Energy/Environment, '78, 259-264, 1978. 539

Gossard, E. E.: The distribution of radio refractive index structure parameter in boundary layers undergoing spatial or temporal transition. Radio Science 13:255-259, 1978. 551

Gossard, E. E.: The height distribution of refractive index structure parameter in an atmosphere being modified by spatial transition at its lower boundary. Radio Science 13:489-500, 1978. 556

Hill, R. J.: Spectra of fluctuations in refractivity, temperature, humidity, and the temperature-humidity cospectrum in the inertial and dissipation ranges. Radio Science 13:953-961, 1978. 568

Hill, R. J.: Models of the scalar spectrum for turbulent advection. Journal of Fluid Mechanics 88(part 3):541-562, 1978. 577

Hill, R. J.: Optical propagation in turbulent water. Journal of the Optical Society of America 68:1067-1072, 1978. 599

Hill, R. J. and S. F. Clifford: Modified spectrum of atmospheric temperature fluctuations and its application to optical propagation. Journal of the Optical Society of America 68:892-899, 1978. 605

Hill, R. J. and G. R. Ochs: Fine calibration of large-aperture optical scintillometers and an optical estimate of inner scale of turbulence. *Applied Optics* 17:3608-3611, 1978. 613

Sweezy, W. B., W. R. Moninger, and R. G. Strauch: Simulation of radar-measured Doppler velocity profiles in low-level wind shear. FAA-RD-78-46, U. S. Department of Transportation, February, 1978. (Abstract only). 618

Weber, B. L.: Gravity wave propagation in the presence of a current with an arbitrary vertical profile. NOAA Technical Memorandum ERL WPL-40, 1978. (Abstract only). 619

Wyngaard, J. C. and S. F. Clifford: Estimating momentum, heat, and moisture fluxes from structure parameters. *Journal of Atmospheric Science* 35:1204-1211, 1978. 620

VI. DATA INTERPRETATION AND ANALYSIS TECHNIQUES

Haugen, D. A.: Effects of sampling rates and averaging periods on meteorological measurements. Preprint Volume; Fourth Symposium on Meteorological Observations and Instrumentation, 15-18, American Meteorological Society, Denver, Colorado, 1978. 628

Keeler, R. J.: Non-optimal convergence of adaptive LMS with uncorrelated data. Proceedings of the International Conference on Acoustics, Speech, and Signal Processing, 10-17 April, 91-95, Tulsa, Oklahoma, 1978. 632

Keeler, R. J.: Uncertainties in adaptive maximum entropy frequency estimators. *IEEE Transactions on Acoustics, Speech, and Signal Processing* ASSP-26:469-471, October, 1978. 637

Keeler, R. J. and R. W. Lee: Complex covariance/maximum entropy Doppler estimates for pulsed CO_2 lidar. Proceedings of the International Conference on Acoustics, Speech, and Signal Processing, 10-17 April, 365-368, 1978. 640

Kohn, N. M., A. L. Johnston, and C. Mohr: MUDRAS - multiple Doppler radar analysis system. NOAA Technical Memorandum ERL WPL-35, 1978. (Abstract only). 644

Leise, J. A.: Temperature retrieval from dual Doppler radar wind field data. Preprint Volume; 18th Radar Meteorological Conference, 94-99, Atlanta, Georgia, 1978. 645

Lopez, R. E.: The determination of convective shower populations from radar data. Preprint Volume; 18th Conference on Radar Meteorology, 155-158, American Meteorological Society, 1978. 651

Serafin, R. J. and R. G. Strauch: Meteorological radar signal processing. American Society for Testing and Materials ASTM-653:159-182, 1978. 655

Strauch, R. G., R. A. Kropfli, W. B. Sweezy, W. R. Moninger, and R. W. Lee: Improved Doppler velocity estimates by the poly-pulse-pair method. Preprint Volume; 18th Radar Meteorological Conference, 376-380, American Meteorological Society, Atlanta, Georgia, 1978. 679

Sweezy, W. B.: Comparison of maximum entropy method estimation of Doppler velocity moments with conventional techniques. Preprint Volume; 18th Radar Meteorological Conference, 401-404, American Meteorological Society, 1978. 684

Author Index 689

Boundary Layer Meteorology, 13: 23-43, 1978.

HF RADIO OCEANOGRAPHY—A REVIEW

DONALD E. BARRICK
NOAA/ERL/Wave Propagation Laboratory, Boulder, Colorado, U.S.A.

(Received 2 June, 1977)

Abstract. The understanding and utilization of HF radar sea-echo have enjoyed steady progress since the experimental discovery of the underlying radar/sea interaction process over two decades ago. The agreement of theory with measured data confirms the correctness of currently accepted explanations for both the first-order and second-order portions of the sea-echo Doppler spectrum in terms of the wave-height directional spectrum. Furthermore, experiments have shown that any currents present near the surface produce a readily distinguishable Doppler shift on the wave-scattered echo which is directly related to the current velocity.

Present research activities in HF radio oceanography are of two types. The first involves efforts to extract ocean surface descriptors from the sea echo and thus establish the soundness of a sea-surface remote-sensing concept. The ultimate outcome of successful endeavors of this type, for example, could be the implementation of operational systems for routinely monitoring sea state, ocean surface winds, or surface currents over large areas. The second type of research activity involves the use of radio-oceanographic techniques to advance knowledge in physical oceanography.

Progress on three classes of sea-scatter research programs is reviewed; these three are differentiated by the oceanic variable sought from the echo. The first and most extensive class seeks information about the wave height directional spectral properties; both surface-wave and sky-wave radars are being used for such research. In the second class involving sky-wave radars, surface winds are being related empirically to sea-echo. The third class is concerned with extraction and mapping of near-surface currents from the sea-scattered signal spectrum. Potential future directions in these areas are discussed.

1. Introduction

Radar echo from the sea at high-frequency (HF)* was reportedly first observed in Britain during World War II on air-defense nets around the English Channel. Because it imposed a limitation at times on the detection of aircraft, it was dubbed 'clutter'. The simple processing and display of target echo intensity, however, did not lend itself to an understanding of the physical mechanism of the scatter process. It was not until Crombie (1955) examined the received (temporal) power spectrum of the back-scattered sea echo from shore that the simple physical interaction mechanism was correctly identified. He observed that the echo Doppler spectrum consisted primarily of two well-defined spikes symmetrically placed about the radar carrier frequency (see Figure 1), but not necessarily of equal amplitude. The displacement of these peaks from the carrier appeared to vary with the *square-root* of the carrier frequency, rather than in direct proportion, as the Doppler echo from a discrete target such as an aircraft. Yet the 'spiky' nature of these peaks suggested

---

* The term HF specifically designates frequencies between 3 and 30 MHz (wavelengths between 10 and 100 m). We will use the term here loosely to include frequencies between 500 kHz and 50 MHz (wavelengths between 6 and 600 m), which spans the MF, HF, and VHF bands. Note that 'high frequency' may appear somewhat misleading to one who pictures a microwave radar with its familiar parabolic dish antenna; the latter system operates some three orders of magnitude higher in frequency than a 'high-frequency' radar.

Boundary-Layer Meteorology **13** (1978) 23–43. *All Rights Reserved*
Copyright © 1978 by D. Reidel Publishing Company, Dordrecht, Holland

that the echo was originating from two discrete, identifiable targets, rather than from the randomly moving surface that one observes visually when looking at the sea.

Crombie deduced the scatter mechanism from these peculiar sea-echo Doppler characteristics as follows: since the Doppler echoes consist of two discrete spikes, scatter must be originating from two targets moving at constant velocity. Ocean wave-trains of given wavelength are known to move at given velocity. Therefore, the velocity component of these 'target' wave-trains in the direction of the radar is calculated from the familiar 'Doppler shift' (Δf) formula to be $v_r = \lambda \ \Delta f/2$, where λ is the radar wavelength. From this result he then deduced the wavelength of the ocean wavetrain, L, as seen by the radar from the gravity-wave dispersion relation as $v = \sqrt{gL/2\pi}$, where g is the acceleration of gravity. Equating these two, he found that the wavelength of the backscattering ocean wave-train, L, was precisely one-half the radar wavelength, λ. The 'resonant' effect revealed by this phenomenon is therefore Bragg scatter, or the diffraction-grating mechanism. In other words, all of the ocean wave-trains present on the sea interact with the radar wave, but the only two which can backscatter energy toward the radar are those that have wavelengths precisely one-half the radar wavelength, and moving toward (positive Doppler frequency) and away from (negative Doppler frequency) the radar. That this is the correct explanation of HF sea echo is confirmed by the correspondence of the unique observed square-root relation between the carrier and Doppler frequencies and the square-root gravity-wave dispersion equation. The fact that one always observes discrete Doppler spikes in the echo (even though he may not be able to discern the half-wave backscattering train) arises because any Fourier decomposition of a random but finite patch of sea always contains wave spectral energy at and near the required wavelength and directions. Crombie recognized in his original article that this discovery should lead to the development of sea-state radar remote-sensing techniques. Indeed his finding forms the underlying basis of *all* HF (i.e., MF through VHF) radar sea-surface remote sensing, as well as a large portion of microwave radar sea-surface sensing techniques.

About a decade later, theoretical studies began to appear which confirmed Crombie's experimental discovery, and in addition quantitatively related the sea-echo Doppler spectral strength to the ocean wave-height spectral strength. Looking at a single, sinusoidal wave-train, Wait (1966) showed that one could relate the strength of the signal voltage at the Doppler-echo peak to the height of the Bragg-resonant wave-train. Wetzel (1966) – using a physical-optics approach (which is not entirely appropriate for the sea-surface boundary at HF) – obtained a result for a random sea echo relating the average Doppler spectral peak strength to the sea-surface spatial height spectrum evaluated at the Bragg wave-number. Barrick and Peake (1967, 1968) and Barrick (1972a) employed a boundary perturbation approach put forward by Rice (1951) which quantitatively explained first-order HF sea echo from a random sea surface, including the observed polarization dependence lost in physical optics solutions to the problem. This solution shows that – in the absence of propagation effects which increase the signal bandwidth – the average echo power spectrum consists of two impulse functions (in the frequency domain), located at Doppler frequency shifts $\pm\sqrt{gf_0/\pi c}$ Hz from the carrier frequency, f_0 (c is the free-space radio-wave propagation velocity). The amplitude factor multiplying these impulse functions is precisely the ocean wave-height directional spectrum evaluated at the Bragg wavenumbers $k_{rx} = 2k_0 \cos \phi$, $k_{ry} = 2k_0 \sin \phi$; here $k_0 = 2\pi f_0/c = 2\pi/\lambda$ is the radar wave-number and ϕ is the angle between the (backscatter) radar direction and the x-axis of the coordinate system. Barrick (1972a) also obtained general results valid for arbitrary bistatic incidence/scattering angles, as well as all polarization state combinations. Again, these solutions clearly obey the Bragg or diffraction-grating scatter mechanism. The sea surface is effectively decomposed (over the scattering patch) into series of wave-trains; to first order, each of these scatters the incident energy in a unique direction determined by the wave-train wavelength and orientation. The Doppler shift in turn is precisely the wave frequency of this ocean wave-train. This simple mechanism underlies many of the experiments to be described in subsequent sections.

Sea-echo Doppler spectra measured with modern radar systems clearly show these 'first-order' spikes resembling impulse functions. Figure 1 is an example. This plot was taken at San Clemente Island looking westward at 13.4 MHz. The basic Fourier transform was taken over 200 s, providing a Doppler resolution (or system band-width) of ~0.005 Hz. Nine consecutive 200-s spectra were added together (incoherently averaged) to produce Figure 1. The scattering patch was located 30 km from the radar, and was approximately 3 km in radial extent by 5 km in azimuthal extent.

Also in evidence in nearly all records such as Figure 1 is a broad echo continuum surrounding the first-order spikes. This continuum has been proven experimentally to be sea echo (rather than system noise), and has been observed to vary both in amplitude and shape with sea state and radar frequency. Since 'first-order' theories predict zero echo in these regions of Doppler space, it was concluded that this continuum is of 'higher order'; hence investigators began extending the theories to second order. Barrick (1971, 1972b) derived a result which related the second-order Doppler spectrum to an integral involving the wave-height directional spectrum, the latter quantity appearing as a factor twice and evaluated at two sets of ocean wave-vectors. The result was obtained from second-order terms in the perturbation expansion of the nonlinear equations for both (i) the electromagnetic boundary conditions at the ocean surface, and (ii) the hydrodynamic boundary conditions at the free air-water interface under the influence of gravity. The interpretation of the mathematical expressions for second-order sea echo indicates that a double interaction is responsible for the scatter. Formally, one can express the Bragg-scatter relationships for the first-order Doppler spectrum as

$$\bar{k}_s - \bar{k}_i \equiv \bar{k}_r = \bar{\kappa} \quad \text{and} \quad \omega_s - \omega_i \equiv \omega_r = \omega_0 , \tag{1}$$

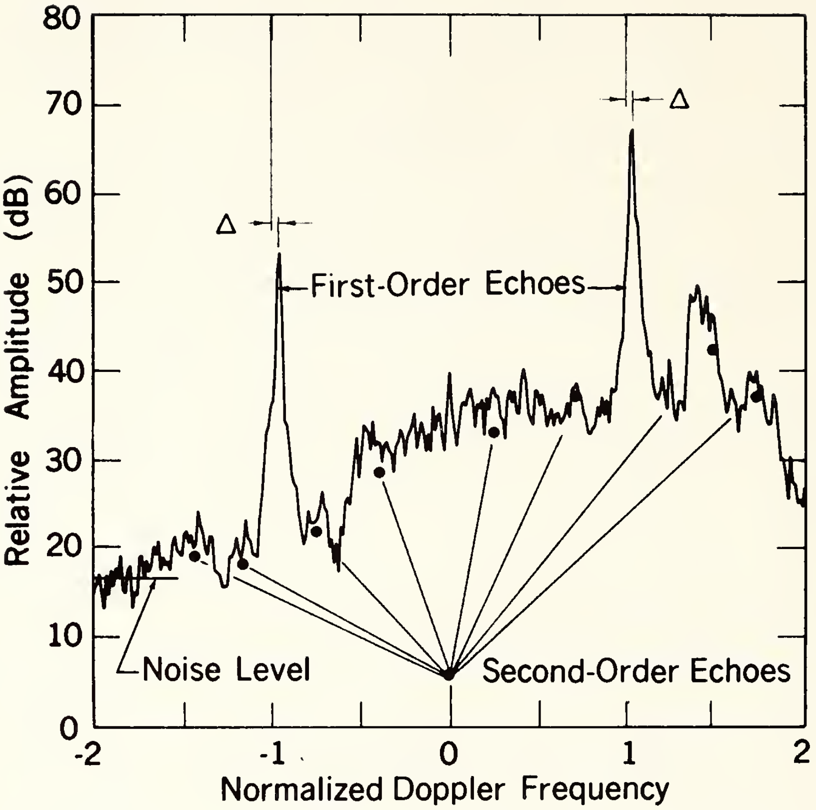

Fig. 1. Measured surface-wave sea-echo Doppler spectrum at 13.4 MHz from San Clemente Island on 4 December 1972. Nine consecutive 200-s power spectra were incoherently averaged to obtain the above record. The Doppler frequency axis is normalized, with 0 corresponding to the transmitted carrier frequency position, and ±1 being the first-order Bragg frequency ($\pm\sqrt{gf_0/\pi c} = \pm 0.3734$ Hz).

(where $\bar{k}_s$, $\bar{k}_i$ are the horizontal projections of the scattering and incident wavevectors, $\bar{\kappa}$ is the wavevector of the Bragg-interacting ocean wave, ω_s and ω_i are the scattered and incident (radian) frequencies of the radar signal, with ω_0, the frequency of the Bragg-scattering oceanwave satisfying the lowest-order dispersion equation $\omega_0 = \pm\sqrt{g\kappa}$). Thus theory shows the Doppler shift, $\omega_s - \omega_i$, of the first-order scatter process is identically $\omega_r = \sqrt{2gk_0}$ $(=\omega_B)$, the value discovered experimentally by Crombie. In the same manner, the second-order theory illustrates the double-interaction Bragg process:

$$\bar{k}_s - \bar{k}_i \equiv \bar{k}_r = \bar{\kappa}_1 + \bar{\kappa}_2 \quad \text{and} \quad \omega_s - \omega_i \equiv \omega_r = \omega_{01} + \omega_{02} \tag{2}$$

where $\bar{\kappa}_1$ and $\bar{\kappa}_2$ are now the wave-vectors of the two ocean waves interacting simultaneously to produce the scatter, and the lowest-order dispersion equation again relates the temporal to the spatial wavenumbers, $\omega_{01} = \pm\sqrt{g\kappa_1}$ and $\omega_{02} = \pm\sqrt{g\kappa_2}$. Without repeating the cumbersome expressions for the Doppler spectrum found in Barrick (1971, 1972b) and Barrick and Weber (1977), Equation (2a) shows that there are whole series of ocean waves whose wave-vectors form two sides of a triangle which participate in the scattering process. Equation (2b) reduces the degrees of freedom of the vector sets satisfying this triad relationship from two to one, thereby evidencing itself as an integral over a single variable for the second-order sea-echo Doppler spectrum.

That these first- and second-order scatter theories correctly explain HF sea echo has been demonstrated experimentally. Figure 2 is a comparison of theory and experiment, using the same data as shown in Figure 1. Here, however, the measured spectrum of Figure 1 was 'filtered' to remove much of the noise-like structure due to the finite sample size. Likewise the theoretical data – computed for the sea conditions modeled by a Phillips spectrum with a $\cos^4(\theta/2)$ azimuthal wave pattern – have been 'filtered' by the same amount to permit comparison. That the Phillips model was applicable for use in calculating the predicted Doppler spectrum was verified by both buoy measurements and hindcasts made for the scattering area. Many comparisons such as this suggest that first- and second-order models available today correctly explain scatter. Hence, the models can be safely used to develop and test inversion techniques.

One final feature shown in Figure 1 illustrates the remaining remote-sensing application to be reviewed in this paper: the measurement of near-surface ocean

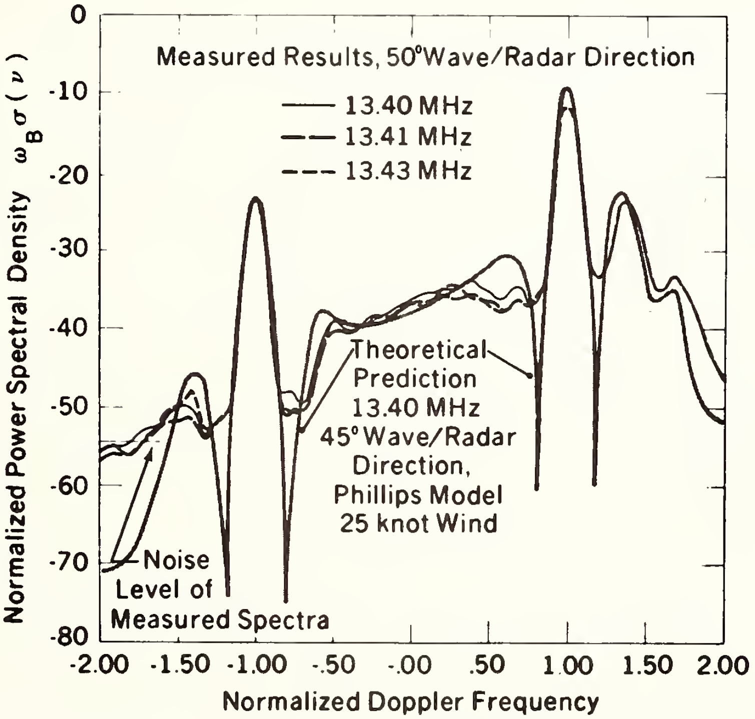

Fig. 2. Comparison of smoothed versions of theoretical Doppler spectrum and measured results shown in Figure 1.

currents. One observes a small overall displacement of the entire spectrum (by a normalized amount, Δ) as seen from the shifts of the sharp first-order peaks from their expected positions at $\pm\omega_B/2\pi$. This displacement arises from the fact that the scattering wave-trains are being transported by underlying currents. Using the same data set from which Figure 1 was made – along with drogue buoys in the scattering area – Stewart and Joy (1974) showed that this explanation in fact accounts for the displacement, while conversely, the current velocity can be calculated from the displacement. Furthermore, both Stewart and Joy (1974) as well as Barrick *et al.* (1974) examined the meaning of this shift when a current 'shear' vs depth is present.

2. Nature of HF Remote Sensing and Research Programs

The nature of HF radars for oceanic remote sensing differs considerably from the more familiar microwave radars characterized by parabolic dish antennas. As a result, the types of experiments to be discussed can only be appreciated if one understands these differences. Because the HF wavelength is three orders of magnitude greater (typically 30 m), the most obvious hardware difference involves the antenna. The type of narrow beam used in any scanning radar requires an antenna aperture many wavelengths in extent.* Thus it is obvious that it is not possible to scan a 2° beam by mechanically rotating an HF antenna as with microwave radars. If one wishes to scan a narrow beam at HF, he is forced to do so by electronically controlling the signal phase at each element of a linear antenna array several hundred meters in length. Therefore, HF experimental facilities either involve long, fairly expensive phased arrays requiring a considerable amount of real estate; or experiments must be designed around either omni-directional or broad-beamed shorter antenna elements and – if direction of arrival is important – by resorting to alternate techniques.

A second very important difference has to do with the propagation of HF radio waves. All electromagnetic waves propagate along straight lines in free space. Thus microwave and optical rays leaving a point near or on the surface of the earth cannot generally propagate to other surface points below the horizon. HF radio waves, however, have two alternate modes by which they can reach surface points beyond the horizon. The first has to do with diffraction by the curved earth; at HF, a vertically polarized wave can be diffracted a considerable distance beyond the horizon due to the much longer wavelength and the highly conductive properties of sea water at these frequencies. With typical powers available today, such radars located at ocean level can observe sea echo as far away as 200 km. The theory behind this mode of radio propagation began with Sommerfeld (1909) over 75 years ago, and today is referred to as the 'ground-wave' or 'surface-wave' mode. We will use the term surface wave here to avoid the confusion which could result from referring to 'ground' waves above the 'sea'.

---

* More precisely, the beamwidth in the plane of an aperture having length L is λ/L radians.

The second 'different' mode of HF propagation – referred to as 'skywave' – results from the presence of the ionosphere above the Earth. The charged particles comprising this layer cause a departure of the effective refractive index within this region from unity, and this departure varies inversely with the square of the radio frequency. Hence, while the ionosphere is virtually invisible to microwaves, it can appear at HF (below 30 MHz) as a concentric mirror at 100–400 km above the Earth. As one goes lower in frequency, however (i.e., less than 3 MHz typically), the effect of lower-altitude charged particles is felt in the form of increased attenuation to the propagating signal. Thus there is a fairly narrow window of frequencies, usually in the mid and upper HF region, within which HF radar operation is practicable. Even within this window, however, moving ionospheric inhomogeneities and multiple layers often distort a skywave signal to the point where it is unusable. Skywave propagation distances – based on a single reflection from the ionosphere – can reach a maximum of 4000 km.

As a consequence of the wavelengths, antenna sizes, and propagation modes at HF, one is faced with several constraints on ocean remote sensing experiments. To observe the important lower end of the gravity-wave spectrum using first-order scatter (where the ocean wavelength observed is one-half the radar wavelength), one must use frequencies typically between 500 kHz and 2 MHz. Besides the presence of the universally used AM band (550 kHz to 1.6 MHz) which would interfere with radar operation in this region, huge antennas would be required to form a fairly narrow beam. Furthermore, observations of a given patch of ocean from two or more directions would be necessary to infer any directional information about the longer ocean waves. Finally, the ionospheric attenuation at these lower frequencies is such as to preclude skywave propagation to greater distances, restricting one to shorter-range surface-wave observations. Even with these constraints, however, several promising techniques have been tested as low as 2 MHz, which give important information about the lower end of the wave-height directional spectrum; these will be discussed subsequently.

On the other hand, use of the upper HF band – more ideally suited to long-range skywave propagation – implies that to first order, the less interesting shorter ocean waves (5–15 m in length), are being observed, which on the open oceans are nearly always developed to their maximum possible height. Because of this and because of unknown ionospheric path losses, it is not possible to use the first-order skywave sea echo to obtain information about the lower end of the gravity-wave spectrum. Such information is therefore obtained by employing the second-order sea echo, normalized against the 'fully-developed' first-order echo.

Two other factors are peculiar to HF systems. All sensing systems are plagued with additive noise; in the microwave band, the prevailing noise is 'internal', due to random electron motion. At HF, however, the dominant noise is external, generated by (i) atmospheric sources, such as thunderstorms, (ii) extraterrestrial or galactic sources, and (iii) man-made sources, such as automobile ignition systems. At 10 MHz, for example, total external noise typically exceeds internal noise by

4–5 orders of magnitude. This dominance of external over internal noise influences choice of antennas and also can cause a diurnal or geographical variation of system sensitivity. A final factor which facilitates implementation of HF systems is the low data rates attendant with the lower operating frequencies (compared with microwaves). The state of the art today is such that all HF receiver signal processing can be done with reliable, inexpensive digital minicomputers or microprocessors. Microwave radars are still forced to rely on analog devices for most of their signal processing.

Research and experiments in HF radio oceanography can be divided into two categories. In the first, the research is focussed upon the development, interpretation, and application of the radar sensor to a particular problem; the emphasis here can be thought of as research and development of a remote sensing technique. The second type of research has to do with the application of a proven HF remote sensing technique to a particular research task in physical oceanography. Traditionally, the radar specialist has emphasized research of the former category, whereas the oceanographer has been more interested in the latter. By promoting interdisciplinary meetings, it is hoped the 'radio oceanographer' of the future will be able to produce contributions more effectively and proficiently in both categories, rather than being bound strictly to the area of his academic training.

The remainder of this paper will review research, experiments, and potential future HF radio oceanographic techniques which fall into one of three classes, based upon the oceanographic observable desired: (i) the wave-height directional spectrum or properties thereof; (ii) the wind field near the sea surface; (iii) ocean currents near the surface.

3. The Wave-Height Directional Spectrum

Crombie (1955) suggested over two decades ago that HF radars could be used to measure sea state. Very little was done in the next decade to further this suggestion, either experimentally or theoretically. Beginning in about 1966, a series of theoretical discoveries (discussed earlier) showed the quantitative relationships – to first and second order – between the wave-height directional spectrum and the sea-echo Doppler spectrum. These theoretical advances spurred further experimental investigations, employing a variety of novel concepts with both bistatic as well as backscatter geometries, and by moving the receiver as well as keeping it fixed.

A. SURFACE-WAVE EXPERIMENTS

Having the theories for first-order sea scatter put forward and extended by a number of investigators (Barrick and Peake, 1967, 1968; Munk and Nierenberg, 1969; Barrick, 1970; Barrick and Grimes, 1970), a number of organizations initiated various scatter experiments. Joint efforts between Scripps and Stanford University were first directed at examining the nature of surface-wave bistatic scatter. Using LORAN-A signals (~1.85 MHz) transmitted from various points along the California coast, this group received sea-echo signals and spectrally analyzed them. Employing the mathematical models for first-order bistatic sea scatter, they derived the relationships which permitted them to 'map' the echo intensity from time-delay/Doppler-frequency space to x/y wavenumber space (see Teague, 1971a, 1971b; Peterson *et al.*, 1970; Barrick, 1972b). While this technique does not uniquely allow the determination of the wave-height directional spectrum at all wave-numbers from a single set of measurements at a given frequency and receiver location, it was shown experimentally to yield a considerable amount of wave-height directional spectral information. One must assume that these wave statistics are homogeneous over the coastal radar coverage area, typically 200 × 200 km. The advantage of this technique – as employed by Scripps and Stanford – is that it uses existing navigational transmissions, requiring only a receiver and processor. Barrick and Grimes (1970; see also Barrick, 1972b) examined the characteristics of bistatic scatter at mid-HF (5, 10, and 15 MHz) using a buoy transmitter. Still later mid-HF experiments of the Riverside Research Institute (1974) were aimed at mapping the average bistatic scatter intensity vs time delay and Doppler frequency.

The Scripps–Stanford team also pioneered another novel concept for measuring the azimuthal variation of the wave-height directional spectrum at a given ocean wave-number. The direction of arrival is obtained by translating the small, omnidirectional receiving antenna along the surface at a constant velocity. This imparts a different Doppler shift to the sea echo arriving from each azimuth angle, the receiver-induced Doppler component varying as $\Delta f(\theta) = v \cos \theta/\lambda$, where θ is the azimuthal echo arrival angle from the receiver velocity direction. (The configuration here was essentially a backscatter geometry, with the transmissions again originating from a LORAN-A tower.) Thus the solitary first-order Doppler spikes – represented by the impulse functions – are spread into bands about their first-order positions ($\sqrt{g/\pi\lambda}$) of width $2v/\lambda$, with each Doppler shift in this band corresponding to a different direction of arrival. The ambiguity in angle, θ (due to the even nature of the cosine function) was resolved by making runs at different angles. In Teague *et al.* (1973) and Tyler *et al.* (1974), an experiment of this type is described which was conducted on Wake Island. The receiver was driven in an automobile along aircraft runways. Since the frequency being transmitted was ~1.95 MHz, the portion of the ocean wave spectrum being observed had wavelengths of 77 m and periods of 7 s. Hence, models were developed from these data relating the angular pattern of the waves at a given frequency to the wind speed.

The 'synthetic aperture' technique* tested at Wake Island has already proven to be a useful tool for oceanographic research; two significant results have emerged thus far. First, the angular dependencies (shown in Figure 3) for the first time reveal that significant amounts of wave energy propagate against the wind, a fact which was predicted years ago from nonlinear wave–wave interaction theories. Secondly, these measurements permitted development of an angular model of the form $\cos^s \theta/2$, in which s depends upon the wind speed (for fully developed seas) and the ocean wavelength being observed (see Tyler *et al.*, 1974). Presently, Scripps and Stanford are conducting experiments in the Gulf of Mexico off Galveston using this technique to study wave growth with distance from shore.

---

* The use of motion of one or both of the terminals is referred to in radar terminology as forming a synthetic antenna aperture because the antenna is being translated in time to the positions that would normally be occupied simultaneously by many elements of a phased-array antenna.

Other techniques have been proposed for observing the wave-height directional spectrum by exploiting motion at one or both of the transmitter/receiver terminals and using the first-order portion of the wave-height spectrum. One method employs a satellite (or aircraft) for one of the terminals and a buoy or tower-based stationary point for the other. Sea echo at a given delay after reception of the direct signal is recorded, spectrum analyzed, and normalized in intensity using the direct signal. Barrick (1972b) describes this concept. Experiments were conducted by Battelle Memorial Institute (Ruck *et al.*, 1972; Ruck, 1975) which showed that the technique can indeed provide useful information at a variety of ocean wavenumbers and wave angles. Barrick (1972b) also discusses using a ship with a back-scatter radar to measure the directional spectrum, again utilizing the known ship velocity to relate wave angle to first-order sea-echo Doppler shift. This technique has been tried experimentally by Stanford and also works satisfactorily; appreciable limitations on the angular accuracy in this case can be imposed by uncertainties in ship velocity, however.

The final type of surface-wave experiment involves shore-based back-scatter radars which can look at a given patch of sea from a single direction. The antenna beamwidths in these experiments have varied between ~7° and ~180°. The first reported experiments (following Crombie's original experiments two decades ago) were by Crombie in the mid 1960's (Crombie *et al.*, 1970; Crombie, 1971) in connection with the BOMEX program on Barbados Island. The Naval Research Laboratory conducted surface-wave experiments in the late 1960's on the Chesapeake Bay which verified the quantitative predictions of the first-order sea-echo amplitude (see Barrick, 1972a). Stanford University reported measurements at 30 MHz (Tyler *et al.*, 1972) with a nearly omnidirectional antenna system; second-order echo features were clearly in evidence on these Doppler records. Surface-wave sea-echo back-scatter Doppler data were observed within many Defense Department programs in the early 1970's, but the primary emphasis in these efforts was the elimination of this echo as unwanted 'clutter' rather than in its use as a remote sensing mechanism. A French program is presently underway (de Maistre *et al.*, 1978), which is investigating the potential of surface-wave sea-echo for measuring wave characteristics. A fairly extensive set of surface-wave measurements was made looking westward from San Clemente Island in late 1972 and early 1973 in a joint NOAA/ITS/NAVY program (Barrick *et al.*, 1974). These data taken on frequencies from 2 to 25 MHz were gathered primarily for the purpose of testing theories relating the second-order Doppler spectrum to characteristics of

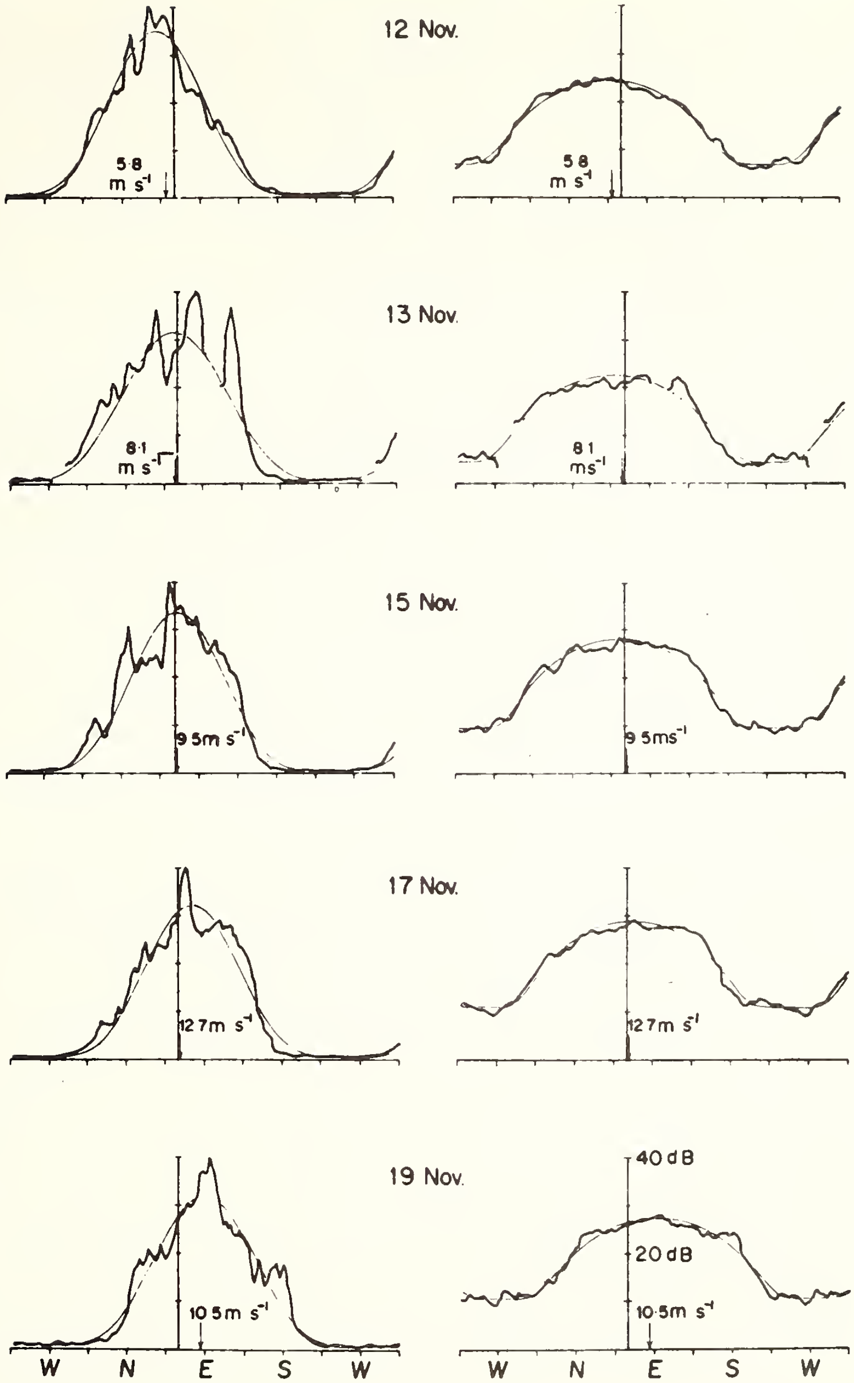

Fig. 3. Directional spectra of 0.14 Hz waves approaching Wake Island as measured by synthetic-aperture HF radar at 1.95 MHz in 1972 (from Tyler *et al.*, 1974). Plotted is energy density on a linear scale (left) and logarithmic scale (right); smooth curves are least-square fits. Wind averages over preceding eight hours are indicated.

the wave-height directional spectrum. Figures 1 and 2 were taken from these measurements. The results of these analyses are discussed in the next section.

Using data gathered at the San Clemente Island facility, Barrick and Snider (1977) showed that the sea-echo signal amplitude is for all practical purposes a Gaussian random variable; this applies to both the first- and second-order portions of the echo. Furthermore, they determined that the time between independent Doppler spectral samples at mid-HF is approximately 30–50 s. These two facts are useful for system design and analyses because they provide statistical confidence limits of spectral sample averages as a function of radar observation time.

B. SECOND-ORDER ECHO-INVERSION EFFORTS

It was mentioned previously that few features of the wave-height directional spectrum can be extracted from practicable non-moving backscatter radars using the first-order echo. Essentially, only two points in the directional spectrum are sampled by the first-order interaction; these are the two sets of ocean wave-trains half the radar wavelength moving toward and away from the radar. For radar frequencies between 3 and 30 MHz, for example, that portion of the spectrum with temporal frequencies between 0.18 and 0.56 Hz are sampled; waves at these frequencies on the open ocean are nearly always developed to their maximum 'equilibrium' heights. The dominant wave direction of the Bragg-scattering waves with respect to the radar direction can be inferred if one uses a directional model such as that put forth in Tyler *et al.* (1974). It is generally not satisfactory to attempt to extrapolate wave directional features at the more important, lower wave-numbers from a single set of such measurements at higher wave-numbers.

As soon as theoretical models for the second-order sea-echo Doppler spectrum were published (Barrick, 1971), it was obvious that from this portion of the echo one could hope to extract many more important wave-height spectral features, still employing only a single radar frequency and direction for a given patch of sea. The mathematical relationship is a nonlinear integral equation, with the desired wave-height directional spectrum appearing as a factor twice in the integrand, evaluated at the double Bragg-scattering wave-vectors $\bar{\kappa}_1$ and $\bar{\kappa}_2$ forming two sides of a triangle. Hasselmann (1971) first suggested that this integral equation could be approximated under certain circumstances to yield the wave-height nondirectional spectrum; furthermore, he pointed out that by dividing by the first-order echo as a normalization, one could remove unknown path losses and/or system gain factors. Stewart (1971) explored Hasselmann's claim, employing only the hydrodynamic second-order contribution and a restrictive directional model. Barrick (1977b), using the general second-order expression, derived and tested this suggested result. He found that much of the directional dependence of this inversion technique could be removed by dividing the Doppler spectrum by a known weighting function; upon testing this inversion method theoretically, Barrick showed that reasonable accuracy was obtainable for $k_0 h > 0.2$, where k_0 is the radar wave-number and h is the rms wave-height.

The first testing of second-order inversion techniques against measured data (supported by independent wave buoy measurements) was done with the San Clemente Island data discussed above. Barrick (1977a) showed that rms wave-height and mean wave period could be deduced to acceptable accuracies. The technique – based upon the weighting-function approach described in the preceding paragraph – requires neither the assumption of a given wave directional model nor the assumption that the seas are fully developed. Figure 4 shows data points for wave-height. The ordinate represents the correction factor, relating radar-deduced wave-height, h_*, to buoy-measured wave-height, h. Some small, residual directional dependence can be expected, as seen from the theoretical curves. The experimental data show that for $k_0h_* > 0.3$, the rms wave-height error is ~22%.

The ultimate objective is to invert the second-order Doppler spectrum exactly, obtaining the entire wave-height directional spectrum. Because of the nonlinearity of the integral equation and the two-dimensional nature of the desired quantity, this is indeed a formidable problem. Stanford University and NOAA's Wave Propagation Laboratory are presently investigating this task. Lipa (1977) has derived and discussed a simplified but quite promising solution.

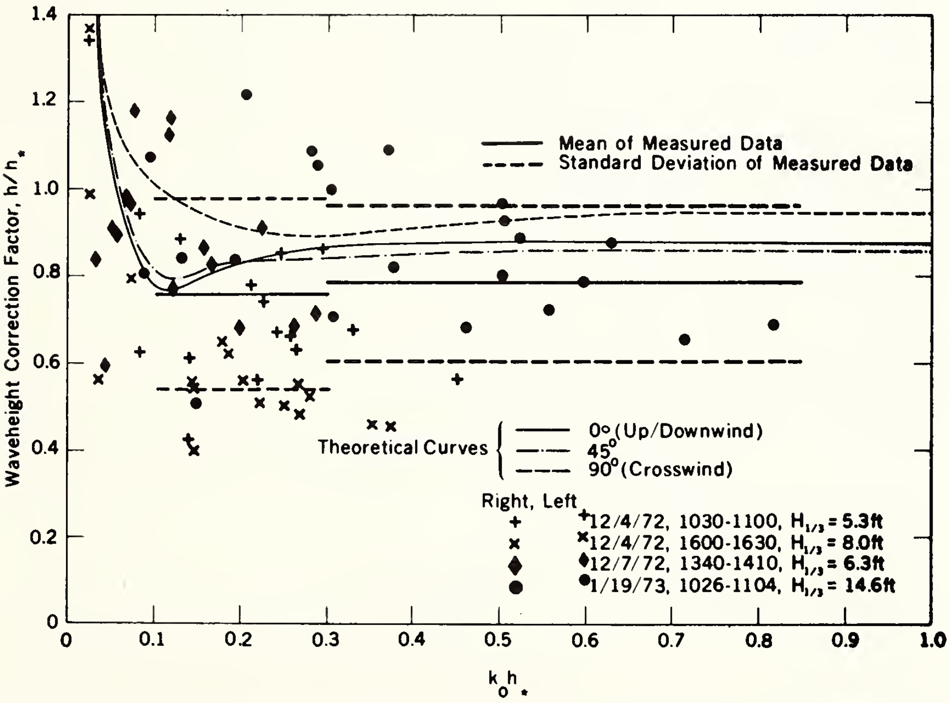

Fig. 4. Theoretical and experimental results of use of waveheight inversion model; h_* is radar-deduced rms wave-height, while $h(=H_{1/3}/4)$ is buoy-measured rms wave-height. Measured data were taken at San Clemente Island on azimuthal bearings of 240° (left) and 270° (right), and are inverted from averages of nine 200-s spectra on frequencies from 3 to 20 MHz.

C. SKYWAVE EXPERIMENTS

Ever since Crombie's initial surface-wave discovery two decades ago, many have been intrigued by the concept of using skywave radars to measure 'sea state' remotely over vast ocean expanses at great distances. Tveten (1967) first published skywave Doppler records of sea echo around Florida measured from Boulder, Colorado, which exhibited the characteristic, symmetrically placed first-order Bragg peaks. Ward (1969) published similar skywave sea-echo data. Both the Stanford Research Institute and Naval Research Laboratory have often observed sea echo with skywave radars, which also clearly shows the expected second-order spectral features; these observations have thus suggested the possibility that the inversion techniques mentioned above – using the second-order echo – can be exploited to obtain important parameters of the wave-height directional spectrum.

Since the second-order sea echo must be utilized in order to recover anything more than crude wave direction estimates at the shorter ocean wavelengths, this portion of the Doppler spectrum must be clearly recognizable. Yet it is well known that a time-varying ionosphere will smear the Doppler record, sometimes to the point where one cannot recognize or utilize the second-order echo. Hence inversion techniques – for example, those discussed in the preceding section which proved so useful for obtaining wave-height and wave-period from surface-wave data – may only be useful for a small percentage of the time with skywave radars. NOAA's Wave Propagation Laboratory has embarked on a research program to determine the utility and accuracy of a skywave radar for obtaining wave-height directional spectral parameters. Located on the north end of San Clemente Island, the radar looks into the North Pacific and Gulf of Alaska. Real-time ionospheric diagnoses and use of adaptive techniques can permit the skywave radar user to recognize bad operating times and areas and, in some cases, to work around these difficulties. In addition, simulations – in which previously recorded surface-wave data are distorted to resemble ionospherically smeared skywave data – are being used to develop and test inversion techniques for dealing directly with the skywave sea echo. If the program indicates that the skywave radar can observe wave parameters a reasonable percentage of the time with adequate accuracy, this remote sensing instrument should prove to be a very useful tool both for routine monitoring of sea state over large areas and for specific oceanographic experiments.

4. Ocean Surface Winds

Inasmuch as the waves on the ocean are produced by the winds near the surface, it was recognized some time ago that the skywave radar would ultimately become a useful tool for remotely sensing oceanic winds. Since only two parameters are required to describe the wind vector (magnitude and direction), it was felt (Long and Trizna, 1973) that these quantities could be deduced from readily recognizable features of the Doppler spectrum. The emphasis was toward deriving empirical techniques for extracting wind velocity from the echo signal, since no direct link between the radar echo and wind is possible.*

As was mentioned earlier, the strengths of the positive and negative first-order Doppler peaks are proportional to the heights of advancing and receding ocean waves equal to roughly one-half the radar wavelength. At skywave radar operating frequencies, these ocean wavelengths are 5 to 15 m. Inasmuch as these shorter ocean waves respond fairly quickly to wind changes, several investigators recognized that the ratio of the two first-order peaks might be a useful indicator of wind direction. One must of course assume a directional model in order to relate this ratio to the wind vector orientation with respect to radar direction, and all such models are symmetrically ambiguous about the radar direction.

The first group to map ocean surface winds with a skywave radar system was the Naval Research Laboratory (NRL). Looking into the North Atlantic from their Chesapeake Bay facility, they plotted wind directional arrows which clearly exhibited the features of both cyclonic storm patterns and frontal systems (Long and Trizna, 1973; Ahearn *et al.*, 1974). Radar-deduced arrows were compared with weather maps based on ship reports. Most of these efforts attempted to deduce only wind directions from the first-order echo ratios; features of the sea-echo Doppler spectrum which could be used to deduce wind speed were less obvious. NRL investigated the comparison of the first-order echo peaks with the (second-order) echo floor between the peaks as an indicator of wind speed; this empirical correlation met with only limited success.

Scripps and the Stanford Research Institute (SRI) conducted skywave tests for several days in which they compared radar-deduced wind directions and speeds with those measured from a buoy, FLIP, northeast of Hawaii (Stewart and Barnum, 1975). (Their radar facility is located in California near San Francisco.) They employed an improved model for deducing wind direction, viz., the result of their LORAN-A Wake Island radar experiment discussed in Tyler *et al.*, (1974). They obtained quite acceptable direction accuracies of ± 16° with this model. For wind speed, they attempted to develop an empirical model, relating the width of the echo at the first-order peak position to the speed; the results were somewhat discouraging. The width of this peak is inherently insensitive to wave-height, and hence would be even less sensitive to wind speed. In addition, however, ionospheric smearing and poor Doppler processor resolution further degraded the accuracy of this technique.

Quite promising results have been obtained recently by SRI, using their skywave radar facility to locate and track hurricanes and severe storms over the ocean. Their radar is capable of looking into the Gulf of Mexico as well as the Pacific Ocean. During 1975 and 1976, they observed several hurricanes in the Gulf of Mexico. The primary output of these observations has been wind direction, using the ratio of the two first-order echo peaks to infer this quantity. The deduction of hurricane wind speeds from the echo has not thus far been successfully demonstrated, although the search for empirical relationships yielding this quantity from the echo is continuing. Figure 5 is an example of radar-inferred wind directions during Hurricane Eloise in 1975 (Maresca and Barnum, 1977). The black circle represents the 'radar-inferred' hurricane center, and the black square is the hurricane center derived from satellite and reconaissance aircraft observations; the difference between these 'centers' is 35 km. The heavy arrows are wind directions measured at NOAA buoys EB-04 and EB-10. Further research in this area at SRI is aimed at deriving methods of determining the position, speed, size, circulation, and wind intensity throughout the hurricane at the ocean surface. They are also exploring the possibility of inferring wind intensity from skywave-derived ocean surface currents, in which land echo is used as a zero-velocity reference. There is little doubt that skywave observations of hurricane and storm areas will ultimately provide information which is difficult and expensive to obtain by other means.

---

* It should be stressed that at HF, a radar does not respond to winds, nor in fact to rain, snow, or other meteorological phenomena which are frequently used as microwave targets.

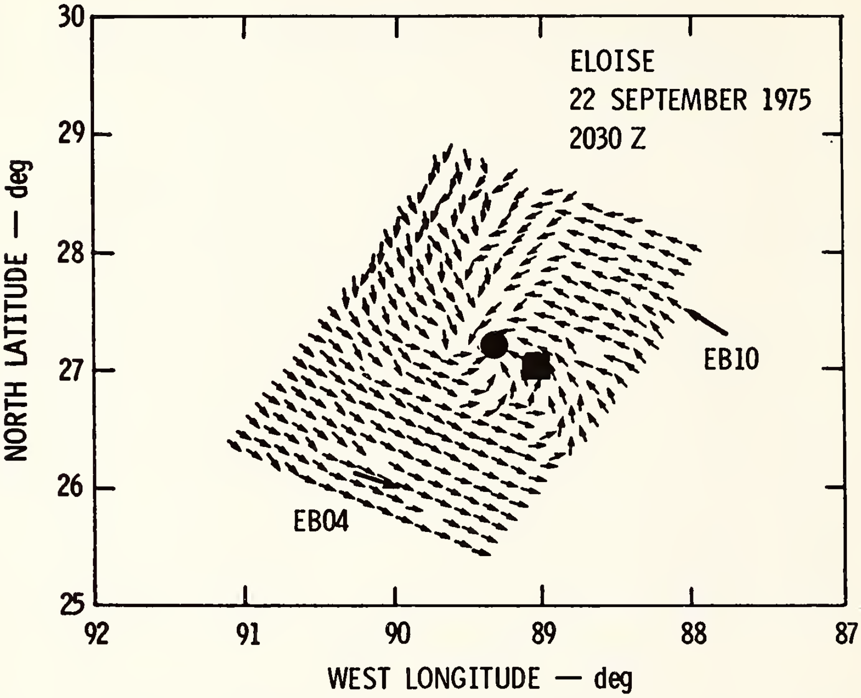

Fig. 5. Wind circulation estimates (direction only) for Hurricane Eloise in Gulf of Mexico measured by SRI over-the-horizon radar. Hurricane center estimated from radar denoted by circle; center estimated from satellite and aircraft reconnaissance denoted by square. Wind direction vectors shown as measured at NOAA buoys EB-04 and EB-10.

5. Ocean Surface Currents

The first study of surface currents using an HF surface-wave radar was done by Crombie (1972). He located a radar on the east coast of Florida and looked toward the Gulf Stream. In these experiments he also pioneered another novel concept: the use of the phase between the echo signal at two omnidirectional receiving antenna elements as a technique for obtaining the angular direction of arrival. Thus the need for a long antenna array to determine direction was circumvented.

Additional experiments done at San Clemente Island in 1972 were aimed at studying the current velocity resolution (Stewart and Joy, 1974; Barrick *et al.*, 1974). The resolution – deduced from independent (buoy) drifter observations – appeared to be better than $10\,\mathrm{cm\,s^{-1}}$. The above investigators also analyzed the effect of a varying current profile with depth, and concluded that the radar senses the mean current speed to a depth of $\sim\lambda/8\pi$ from the (average) surface level.

NOAA's Wave Propagation Laboratory has undertaken a program to develop and test a small, transportable coastal backscatter radar system for mapping near-surface currents in real time (Barrick and Evans, 1976). The system consists of two radar units, because a single radar can measure only one component of the total current vector (that component pointing toward the radar). The two units are positioned along the coast about 40 km apart, and – operating in the surface-wave mode between 25 and 30 MHz – have a maximum range from the coast of about 70 km. Design and construction of the first radar unit pair was completed in June 1976.

These radar units – and others to be constructed in the near future – are to be used to map current patterns along the U.S. coasts. In particular, they are to be employed in environmental studies aimed at assessing the impact of possible offshore oil recovery operations. It is surface currents that will determine whether an oil spill or leak may dissipate harmlessly at sea or do irreparable damage to the coast. Oceanographic research experiments are also planned with these radars; with the ability to obtain thousands of current vectors every 3 × 3 km after only several minutes' operation, the oceanographer will have a wealth of data heretofore unobtainable.

The concept behind the NOAA radars is similar to that employed by Crombie (1972). Here, however, three receiving antennas (3 m apart) are used instead of two to obtain the echo's angle of arrival. This permits one to resolve signals unambiguously at the same Doppler frequency from two different directions.

Only several days data have been gathered thus far with the recently constructed radars, and these have been obtained using only one of the two units required to obtain a complete vector field. This radar was operated near Fort Lauderdale, Florida looking eastward into the Gulf Stream. The other site will soon be on the air simultaneously at Miami. Therefore the 'maps' obtained thus far show only the radial component of the current vector, pointing in the direction of the radar site. For comparison, current values for the Gulf Stream averaged over time are shown in radial map form in Figure 6a; these were obtained from Düing (1975). They show a South–North flow which reaches a maximum about 40 km from shore. Figure 6b is a map of radial currents measured by the radar based upon about five minutes of operation. It is obvious from the general agreement of the two maps that the radar does in fact provide massive amounts of surface current data. Further experiments using both sites will be conducted to measure more precisely the accuracy of the system; first indications are that this accuracy should exceed 10 cm s^{-1}.

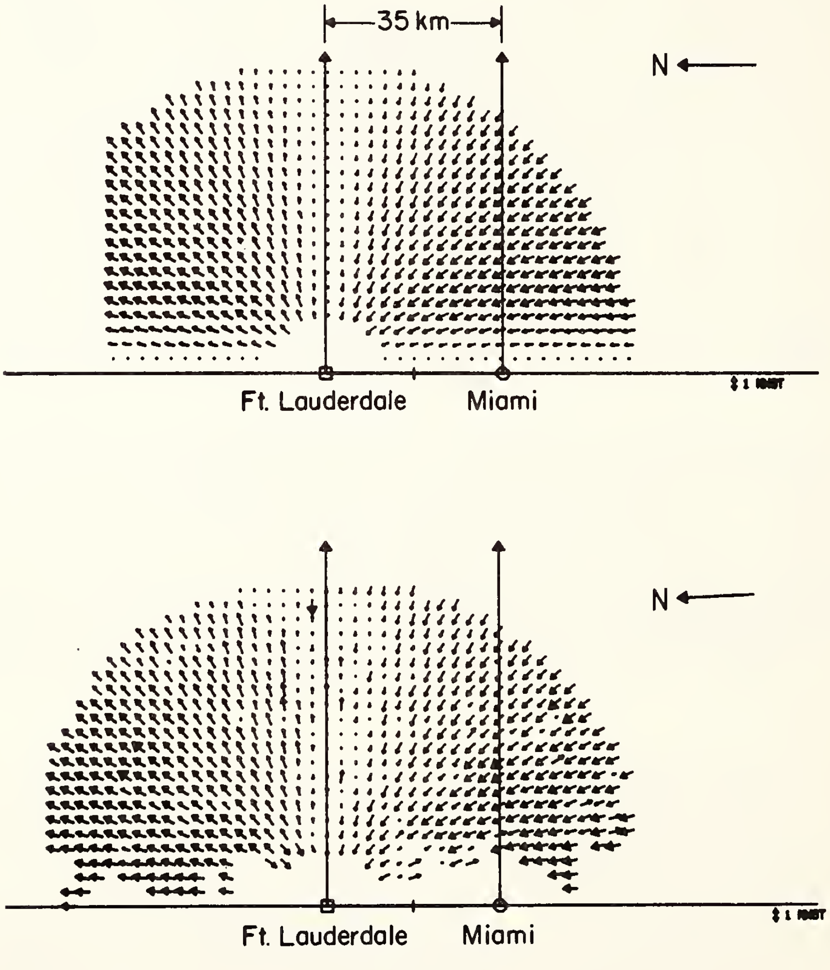

Fig. 6. Radial current-vector maps as seen by transportable NOAA HF surface-wave radar system at Ft. Lauderdale, Florida; comparisons of expected, typical flow pattern vs radar-measured data with no averaging or filtering. (Top) One-site map of typical, mean Gulf-stream current taken from Düing (1975). (Bottom) One-site map of radar-deduced Gulf Stream currents with no averaging or filtering.

6. Conclusions

Historically, radio oceanography began first at HF, both in terms of experiments and theory. The HF scatter mechanism is soundly established, and there is no question as to the adequacy of the theoretical scatter models, both to first and second order. Hence, as this paper has shown, the HF region presently offers a wider variety of radar remote sensing techniques than other regions of the radio spectrum.

Many of these techniques, such as low-HF synthetic aperture surface-wave radars and mid-HF phased-array systems, have already led to oceanographic discoveries. Others, such as current-mapping radars and possibly shipboard radars, will undoubtedly advance our knowledge and understanding of wave and current structures on the ocean's surface.

Skywave radars have for many years held out the exciting possibility of monitoring wave and wind fields over vast ocean areas. Because there are several such radars in the world which can observed the seas, measurements of sea surface conditions will certainly continue. The question of whether the ionosphere will permit sufficiently reliable and timely measurements to justify the implementation of operational skywave radars that will routinely monitor sea state has not yet been answered; present research programs should soon provide the answer.

References

Ahearn, J. L., Curley, S. R., Headrick, J. M., and Trizna, D. B.: 1974, 'Tests of Remote Skywave Measurement of Ocean Surface Conditions', *Proc. IEEE* **62**, 681–687.

Barrick, D. E. and Peake, W. H.: 1967, 'Scattering from Surfaces with Different Roughness Scales: Analysis and Interpretation', Battelle Research Report BAT-197A-10-3, Columbus, Ohio, available from Clearinghouse for Federal Scientific and Technical Information, Springfield, Virginia, Accession No. AD 662 751.

Barrick, D. E. and Peake, W. H.: 1968, 'A Review of Scattering from Surfaces with Different Roughness Scales', *Radio Sci.* **3**, 865–868.

Barrick, D. E. and Grimes, J. A.: 1970, 'Predicted and Measured Ground-wave Sea Clutter Spectrum at 6 MHz', presented at Fall USNC/URSI Meeting, Sept. 15–17, Columbus, Ohio.

Barrick, D. E.: 1970, 'The Interaction of HF/VHF Radio Waves with the Sea Surface and its Implications', *Electromagnetics of the Sea*, AGARD Conference Proceedings No. 77, available from Clearinghouse for Federal Scientific and Technical Information, Springfield, Virginia, Accession No. AD 716 305.

Barrick, D. E.: 1971, 'Dependence of Second-order Sidebands in HF Sea Echo upon Sea State, *IEEE G-AP International Symposium Digest*, Sept. 21–24, Los Angeles, California, pp. 194–197.

Barrick, D. E.: 1972a, 'First-order Theory and Analysis of MF/HF/VHF Scatter from the Sea', *IEEE Transactions on Antennas and Propagation*, AP-**20**, 2–10.

Barrick, D. E.: 1972b, 'Remote Sensing of Sea State by Radar', in V. E. Derr (ed.) *Remote Sensing of the Troposphere*, Ch. 12, U.S. Government Printing Office, Washington, D.C.

Barrick, D. E., Headrick, J. M., Bogle, R. W., and Crombie, D. D.: 1974, 'Sea Backscatter at HF: Interpretation and Utilization of the Echo', *Proc. IEEE* **62**, 673–680.

Barrick, D. E. and Evans, M. W.: 1976, 'Implementation of Coastal Current-mapping HF Radar System', Progress report No. 1, NOAA Technical Report ERL 373-WPL 47.

Barrick, D. E. and Snider, J. B.: 1977, 'The Statistics of HF Sea-echo Doppler Spectra', *IEEE Transactions on Antennas and Propagation*, AP-**25**, 19–28.

Barrick, D. E. and Weber, B. L.: 1977, 'On the Nonlinear Theory for Gravity Waves on the Ocean's Surface, Part II: Interpretation and Application', *J. Phys. Oceanog.* **7**, 11–21.

Barrick, D. E.: 1977a, 'Extraction of Wave Parameters from Measured HF Sea-Echo Doppler Spectra', *Radio Sci.* **12**, 415–424.

Barrick, D. E.: 1977b, 'The Ocean Waveheight Nondirectional Spectrum from Inversion of the HF Sea-echo Doppler Spectrum', *Remote Sensing of Environment* **6**, 201–227.

Crombie, D. D.: 1955, 'Doppler Spectrum of Sea Echo at −13.56 Mc/s', *Nature* **175**, 681–682.

Crombie, D. D., Watts, J. M., and Beery, W. M.: 1970, 'Spectral Characteristics of HF Ground Wave Signals Backscattered from the Sea', *AGARD Conference Proceedings No. 77*, available from Clearinghouse for Federal Scientific and Technical Information, Springfield, Virginia, Accession No. AD 716 305.

Crombie, D. D.: 1971, 'Backscatter of HF Radio Waves from the Sea', in J. R. Wait (ed.), *Electromagnetic Probing in Geophysics*, The Golem Press, Boulder, Colorado, pp. 131–162.

Crombie, D. D.: 1972, 'Resonant Backscatter from the Sea and its Application to Physical Oceanography', *IEEE International Conference Proceedings on Engineering in the Ocean Environment*, Ocean '72, Newport, Rhode Island, Sept. 13–15, 1972, IEEE Publication 72 CHO 660-1 OCC, 174–179.

Düing, W.: 1975, 'Synoptic Studies of Transients in the Florida Current', *J. Marine Res.* **33**, 53–73.

Hasselmann, K.: 1971, 'Determination of Ocean Wave Spectra from Doppler Radio Return from the Sea Surface', *Nature* **229**, 16–17.

Lipa, B. J.: 1977, 'Derivation of Directional Ocean-wave Spectra by Integral Inversion of Second Order Radar Echoes', *Radio Sci.* **12**, 425–433.

Long, A. E. and Trizna, D. B.: 1973, 'Mapping of North Atlantic Winds by HF Radar Sea Backscatter Interpretation', *IEEE Transactions on Antennas and Propagation*, AD-**21**, 680–685.

de Maistre, J. C., Broche, P., and Crochet, M.: 1978, 'Off-shore Wind Measurements by HF Doppler Ground-wave Radar', this volume, pp. 55–60.

Maresca, J. R. and Barnum, J. R.: 1977, 'Remote Measurement of the Position and Surface Circulation of Hurricane Eloise by Skywave Radar', accepted for publication in *Mon. Weather Rev.*

Munk, W. H. and Nierenberg, W. A.: 1969, 'High Frequency Radar Sea Return and the Phillips Saturation Constant', *Nature* **224**, 1285.

Peterson, A. M., Teague, C. C., and Tyler, G. L.: 1970, 'Bistatic Radar Observation of Long-period Directional Ocean-wave Spectra with LORAN A', *Science* **170**, 158–161.

Rice, S. O.: 1951, 'Reflection of Electromagnetic Waves from Slightly Rough Surfaces', in M. Kline (ed.), *Theory of Electromagnetic Waves*, Interscience Publishers, New York, 351–378.

Riverside Research Institute: 1974, Technical Reports T-1/278-4-00, Volumes I, II, and III, 'True Course, Phase I Program Reports', 80 West End Avenue, New York, N.Y. 10023.

Ruck, G. T., Barrick, D. E., and Kaliszewski T.: 1971, 'Bistatic Radar Sea State Monitoring', Battelle, Columbus Laboratories, Columbus, Ohio, Technical Report, Contract NAS6-2006, Dec. 1971.

Sommerfeld, A.: 1909, 'The Propagation of Waves in Wireless Telegraphy', *Annalen Physik* **28**, 665–682.

Stewart, R. H.: 1971, 'Higher Order Scattering of Radio Waves from the Sea, IEEE G-AP International Symposium Digest, Sept. 21–24, 1971, Los Angeles, California, pp. 190–193.

Stewart, R. H. and Joy, J. W.: 1974, 'HF Radio Measurements of Surface Currents', *Deep Sea Research* **21**, 1039–1049.

Stewart, R. H. and Barnum, J. R.: 1975, 'Radio Measurements of Oceanic Winds at Long Ranges: An Evaluation', *Radio Sci.* **10**, 853–857.

Teague, C. C.: 1971a, 'High-frequency Resonant Scattering Techniques for the Observation of Directional Ocean-wave Spectra', Technical Report No. 3615–1, Stanford Electronics Laboratory, Stanford University, August 1971.

Teague, C. C.: 1971b, 'Bistatic-radar Techniques for Observing Longwavelength Directional Ocean-wave Spectra', *IEEE Transactions on Geoscience Electronics* GE-**9**, 211–215.

Teague, C. C., Tyler, G. L., Joy, J. W., and Stewart, R. H.: 1973, 'Synthetic Aperture Observations of Directional Height Spectra for 7s Ocean Waves', *Nature* **224**, 98–100.

Tveten, L. H.: 1967, 'Ionospherically Propagated Sea Scatter', *Science* **157**, 1302–1304.

Tyler, G. L., Faulkerson, W. E., Peterson, A. M., and Teague, C. C.: 1972, 'Second-order Scattering from the Sea: Ten-meter Observations of the Doppler Continuum', *Science* **177**, 359–351.

Tyler, G. L., Teague, C. C., Stewart, R. H., Peterson, A. M., Munk, W. H., and Joy, J. W.: 1974, 'Wave Directional Spectra from Synthetic Aperture Observations of Radio Scatter', *Deep Sea Res.* **21**, 989–1016.

Wait, J. R.: 1966, 'Theory of HF Ground Wave Backscatter from Sea Waves', *J. Geophys. Res.* **71**, 4839–4842.

Ward, J. F.: 1969, 'Power Spectra from Ocean Movements Measured Remotely by Ionospheric Radio Backscatter', *Nature* **223**, 1325–1330.

Weber, B. L. and Barrick, D. E.: 1977, 'On the Nonlinear Theory for Gravity Waves on the Ocean's Surface, Part I: Derivations', *J. Phys. Oceanog.* **7**, 3–10.

Wetzel, L. B.: 1966, unpublished manuscript.

Proceedings of AMS/NWS Conference on Weather Forecasting and Analysis
and Aviation Meteorology, 228-233, 16-19 October 1978.

PROFS: A STRATEGY TO IMPROVE LOCAL WEATHER SERVICES

D. W. Beran and C. G. Little

Wave Propagation Laboratory
Environmental Research Laboratories
National Oceanic and Atmospheric Administration
Boulder, Colorado 80302

1. INTRODUCTION

The continuing debate concerning the quality and accuracy of weather forecasts in the United States (see, for example, Ramage, 1978, Sanders, 1978) is interesting to follow. One side points to the advances that have been possible as the result of centralized numerical prognoses (Shuman, 1978), while others believe that it is this centralized product which has resulted in what they view as a leveling of forecast skill (Ramage, 1978a, Snellman, 1977).

While this kind of dialogue within the scientific community is healthy and thought-provoking, it misses an important point. Has the level of overall *service* been improved in relationship to any measure of forecast skill which we care to apply? This end product, the service, is after all the fundamental reason for making a forecast in the first place and unless we can show that services are improved as the result of a better forecasting or observing technique, we are left with a nagging doubt about the magnitude of the "improvement."

Measurement of service quality is difficult. We must go beyond the well-ordered scientific disciplines and enter the area of sociology and human behavior in order to gauge the users' reactions to the products which are supplied. There is some evidence that our final weather service output does not match increasing forecast skill scores. For example, in a recent survey in a region near Denver, Colorado, a randomly selected sample of 100 farmers were asked to give their impression of the accuracy of currently available weather forecasts. Nearly 50% of the sample felt that the forecasts were accurate only about 25% of the time. Another indication of the quality of the final output of our weather services comes from the excellent response of the public to the CRAB experiment (Scofield and Weiss, 1977). This experiment concentrated on providing nowcast service to users in the Chesapeake Bay region. Providing timely information based on existing observing and forecasting techniques formed the main thrust of this experiment. This relatively simple exercise apparently generated more favorable user response than all of the skill score improvements that have occurred in the past 10 years.

Lest there be some misunderstanding, let us emphasize now that we are not suggesting that forecasting skill is not of fundamental importance to the overall effectiveness of a weather service; it most emphatically is. Our point is that a weather service is a complex system, made up of several important elements. Major improvements in one area will not necessarily improve overall system performance, if some other element of the system is really the limiting factor.

A weather service can be divided into the general elements of observing, forecasting (including analysis), communication, and dissemination. Each of these elements contain specialists in fields that relate most closely to that element. Often, there is little cross-disciplinary experience or training within a single element, and even less communication between elements. Hence, we see the observational field with a predominance of engineers and physicists, the forecasting element with mostly meteorologists, and the dissemination area with a large proportion of people skilled in broadcasting and journalism. While this division of disciplines is by no means total, it is great enough to be suspected as one of the reasons for less than perfect system performance.

Let us now change our tack slightly and examine weather service in terms of those it serves. Clearly, the weather service is designed to meet the needs of users ranging from the general public to such specialized groups as aviation. Meeting these needs may indeed be the ultimate goal of a weather service, but we do not believe that this goal has yet been reached. We are getting closer, but there is still much to be done.

Let us explain. Few meteorologists would argue with the importance of understanding large-scale meteorological process. The global and synoptic scales are fundamentally important to any forecasting attempt. These larger scale motions had to be observed and quantified before there was even any thought of applying powerful numerical techniques to help provide weather predictions. Once we have a high degree of skill in dealing with the larger scales of motion we can turn our attention more to the smaller, mesoscales. This, it seems, is exactly what we are doing and from the meteorologist's point of view is the only correct way to proceed.

Now let us introduce another concept of scale. For want of a better name we will call it the users' scale. Its size depends only on the area covered by any given individual for any given length of time. On a day-to-day basis, most people stay within a few 10's of km of their home, so we can say that in general the users' scale is not much larger than the area encompassed by a large city. There are, of course, exceptions such as the traveler, but the vast majority of users fit comfortably within this scale size.

When we say that there is still much to be done before we achieve the ultimate goal of a weather service we are simply making the observation that we do not now provide highly site specific localized weather services on the user scale as we have defined it. In order to avoid becoming involved in the ongoing forecasting debate, we take the comfortable position that both schools of thought are correct. The synoptic scales and larger mesoscales are most effectively dealt with by a centralized, numerical facility. This capability forms the essential base from which smaller scale forecasts can be made. As the scales of interest become smaller, however, it is necessary to place more emphasis on the skills and capabilities of the local forecaster, the dissemination component, and on improved observations.

Researchers in the numerical modeling discipline are well aware of the need to provide higher resolution predictions. Their efforts have resulted in the Limited Area Fine Mesh Model (LFM) and the Very Fine Mesh Model (VFM), (Fawcett, 1977) for example. Relative to the global scale these are indeed high resolution models, but when we consider that even the VFM has a grid spacing of about 100 km and we compare this to the size of any large city, it is clear that even these models cannot provide the site specific forecasts needed for a truly local weather service. Further, it would appear that there are fundamental limits to this "come down from the large scale" approach. Despite the near exponential growth of computer capacity, use of these new models is pushing the limits of computer technogloy. Shuman (1978) observes that "nowhere does nature support exponential growth indefinitely," suggesting that we cannot rely on the growth of computer technology to reach the very small scales with ever more sophisticated models. A second limitation is inherent in the data base that is available to initialize the smaller scale models. Our present observational network is compatible with the synoptic scale. The spacing and timing of radiosonde launches, the surface network, and the generally large overview of the satellite provide a data base that is well matched to the larger atmospheric scales. Again, as higher-resolution models are designed, they must be initialized by higher-resolution (both time and space) data. These high-resolution data sets are not now available, even for testing the finer mesh models.

Those who suggest that the centralized large scale prognoses are not effective on the local scale perceive the problem of weather services more from the users' viewpoint. Their number, understandably, includes many people who have local forecast responsibility. Their approach is characterized by pleas to place "the man" more fully in the forecasting loop and to make fuller use of such techniques as Model Output Statistics (MOS) (Glahn and Lowry; 1972) and Lagrangian Extrapolation Models (LEM). This approach too has fundamental limitations. Local data sets are usually derived from a single radiosonde profile taken twice per day, regional surface stations, satellite input, precipitation sensing radar, and in some cases local spotter networks. This data set contains local information not used for the larger scales, but it is still firmly based on devices and a network density that are designed primarily for larger-scale applications.

If we accept that providing more locally specific user oriented weather services is a common goal and that both approaches discussed above have validity, we are in a position to start creating an improved strategy for achieving our objective. There is evidence that the meteorological community is starting to respond to this need (Fritsch and Kreitzberg, 1978), but we have yet to create a focused program that addresses the entire local scale weather service system design problem. In doing this, we must look at each of the components of a total weather service system and determine how they can best be integrated to meet locally specific user needs. By concentrating on the user scale we are in a sense entering a new frontier where innovative design techniques can be effectively used without disrupting the existing service system. The interface between the two cannot be neglected, but the design task is much easier if we can deal with the internal workings of a separate subsystem, at least in the early stages. Later, local-scale services must complement the existing services, bearing in mind that the meteorological scales are intimately connected.

In taking this approach we uncover other issues that must be addressed. Paramount among these are the physical and organizational limitations to more effective technology transfer between disciplines and from the research community to the operational service elements. The record of mesoscale technology transfer and interdisciplinary activity in the meteorological community can be improved. Many discoveries and techniques that could help the forecaster provide better mesoscale services are not used for a variety of reasons. A natural selection process eliminates concepts that look good in the research environment but do not effectively address an operational need. However, useful discoveries and techniques are lost through lack of a systematic mesoscale exploratory development effort, the next logical step after research. Such development is essential if we are to avoid thrusting raw and untested research products onto operational activity where there is neither time nor resources to evaluate them. To achieve this, the weeding out process should happen at an earlier stage of the development cycle where new research devices and techniques can be combined into research prototype systems. It is imperative that the people involved in such early exploratory development be fully cognizant of the unique operational environment into which new systems will eventually be integrated.

In considering the need for more effective interdisciplinary work and technology transfer, we must look at the organizational structure of government agencies that have the charter for providing weather services. Attention to early mesoscale exploratory development is lacking in present organizational structures, a shortcoming that must be corrected before we can attempt to implement a new approach to the design of local weather services.

2. A NEW APPROACH

A new NOAA initiative called PROFS (Prototype Regional Observing and Forecasting Service) addresses the issue of improving local weather services. The program is designed to provide comprehensive localized, short-term weather services that are characterized by dramatically improved accuracy and timeliness.

This service system design will be guided by specific user requirements in a given urban region and it will make optimum use of recent advances in observing, data processing, communications, forecasting, and dissemination. The local system will be designed to complement our existing synoptic-scale services, making services on all scales more effective because of stronger user orientation. In addition, the PROFS program calls for the creation within NOAA of an Exploratory Development Facility that would develop a research prototype service system for small scale applications and would introduce, test, and integrate new research capabilities into that system.

2.1 PROFS-The Overview

The PROFS program is divided into three phases:

Phase I. Exploratory development of a research prototype service system.

Phase II. Development of an engineering prototype.

Phase III. Operational implementation.

Phase I has two distinct objectives. First, a facility and associated staff dedicated to exploratory development will be created within NOAA. Second, a research prototype of a local weather service will be designed and tested. These two objectives are compatible and mutually beneficial. A primary function of the new organization will be to use the facility for producing prototype service system designs for any given location and set of requirements. A systems analysis of the components of a local weather service will serve as a guide in determining the various capabilities required at the facility. In addition, the facility must have a high level of flexibility; access to the latest research devices and techniques; and the capacity to computer simulate different demographic, climatic, and economic conditions.

This systems analysis will also serve as the first stage in the design of a prototype service. The detailed design of the prototype service will then proceed in parallel with the installation and checkout of the facility components.

Briefly then, the facility consists of essential devices, techniques, offices, labs, communication networks, and people. The prototype service is, on the other hand, created by the interaction of the components of the facility to produce a desired output.

Phase I will require 3 years to complete. The first 2 years will concentrate on the creation of the facility and the detailed design of the prototype service. The third year will be devoted to demonstrating the feasibility of the prototype service.

This demonstration will concentrate on testing and integrating various observational methods, forecasting techniques, and communication systems. The actual service output will be limited to test populations and will not be made available to the general public.

During the last year of Phase I, an urban area (not necessarily the same as the site of the development facility), will be selected for testing of a Phase II engineering prototype (fully engineered for operational application). This engineering prototype will be designed on the basis of a careful user need survey, and will be an adaptation of the research prototype service. The first level design of the engineering prototype will be produced at the Exploratory Development Facility through use of the simulation capability and the mix of observational and forecasting techniques that make up the facility. The engineering prototype will then be created and installed in an urban region and the final public impact test will be conducted. This Phase II system will be operated by the NWS as part of their existing services, with on site assistance from the development facility staff. This critical and final test of the service will be a primary objective of Phase II.

If the expected improvements are demonstrated during the engineering prototype tests, the third and final phase will begin. Local weather service systems for other urban regions will be designed, again on the basis of carefully determined user needs in a given area and the optimum mix of system elements to meet those needs. These systems will then be installed and following a checkout period will become operational local service components of NWS.

2.2 Other Issues

An important feature of the general plan outlined above is that an organization will be created that will foster and encourage interdisciplinary activity and help to close the gap between research and operations. It is imperative that this organization be staffed by people who represent a wide range of disciplines from both the research and operational communities. A second consideration is to insure that the organization does not develop its own set of inward looking attitudes; staff rotation back to parent organizations will be encouraged. In addition, industrial fellowships, research grants, and interagency staff exchange will be used to insure that the private and academic sectors, and other agencies all have an impact.

2.3 Mesoscale Forecast Research

The PROFS facility will help to revitalize mesoscale forecasting research through the provision, for the first time, of data sets comparable to mesoscale motion. These direct observations of the smaller scale atmospheric processes on a continuing basis will first be used to create an effective nowcasting capability. The natural extension of this capability will be renewed research on the development of short-term extrapolation techniques and finally the more difficult research area of creating mesoscale numerical models that are continually updated by the richer data sets.

This approach is not meant to replace present efforts to improve mesoscale forecasting by coming down from the large scale, but to complement these efforts by starting on the very short-range small scale and then expanding the efforts until they merge with the larger mesoscale activity.

2.4 Observations

The point has been made that new forecasting research would be based on a vastly improved data set. Although the precise details of the Exploratory Development Facility's observational component must await completion of the final design, a brief description of some of the available capabilities will indicate its potential.

New observing techniques can be divided into the general categories of *in situ* and remote sensors. The latter can be either ground-based, or mounted on aircraft or satellites. Through application of microprocessors and new communication techniques, fully automated ground stations capable of measuring nearly all standard meteorological variables are available at relatively low cost. New optical techniques have also been developed to monitor more difficult-to-sense parameters such as precipitation types at remote unmanned stations.

Remote sensors on satellites already provide a broad overview of cloud formations, and the new GOES and TIROS N instruments promise quantitative temperature, moisture, and cloud motion derived wind measuring capabilities with high horizontal resolutions. A single ground-based remote sensor collects data over a much smaller area than is covered by a satellite, but it does provide very high resolution quantitative data. The temperature and moisture profiles produced by ground-based radiometers have demonstrated accuracies equivalent to those of the radiosonde and superior to the low level portion of satellite-sensor derived profiles. An observing system that combines the complementary capabilities of ground-based and satellite-derived temperature and moisture data could produce these profiles continuously in near real time. The development of new processing techniques that allow radar systems to measure winds in the clear air has made it possible to produce high resolution wind profiles to heights well into the stratosphere. A system that combines the temperature and humidity profiles derived from satellite and ground-based radiometers with the ground-based radar-derived wind profiles could be the forerunner of a fully automated device that would not only replace the radiosonde, but would be capable of producing atmospheric profiles on an essentially continuous, real time, basis. The early development of such a system is part of Phase I of PROFS and it will become a major element of the facility's observational capability.

The FM-CW radar, another instrument candidate, can sense wind fields with resolution that is high enough to detect shear zones only a few meters deep along the approach to an airport, and to detect the precise altitude of temperature inversions. Storm surveillance radars with full Doppler capability and special cloud-sensing radar would be available to monitor in-cloud motions. With the addition of a clear air capability, the storm surveillance system could monitor a component of the entire wind field within perhaps 100 km of the instrument. If we add line-of-sight optical devices which measure an integrated crosswind component over paths many km long, and sensitive microbarographs capable of detecting the cold air outflow from thunderstorms, a very dense mesoscale data set could be obtained to support the mesoscale research efforts.

2.5 Dissemination

Many knowledgeable people believe that the weakest component of present weather services is dissemination, the critical final link with the user. They contend that if we could simply find more effective ways of transmitting existing weather information to the user, we could make a significant improvement in our services without changing our observing or forecasting methods.

The problem of dissemination could be the most difficult to solve. We are dealing with the diverse areas of human behavior, FCC regulations, the interface between private and public broadcast services, and almost incidentally the science of meteorology. Accurate information must be provided in an easily understood format. A fine balance must be achieved between general information and that required to elicit a rapid response to warnings of danger. Ways must be found to provide accurate warning information to only that segment of the population that will suffer from a weather-related disaster; overwarning is possible cause for a loss of credibility. Furthermore, the information must be communicated effectively.

It is in this area, perhaps more than any other, that government weather services have much to learn from the private sector. The much maligned T.V. weatherman and the disk jockey who "rips and reads" may not understand all of the subtleties of atmospheric dynamics, but the majority know how to communicate. If their message doesn't get through, they stand to lose their job.

The PROFS program is sensitive to the problem of achieving the best interface between the private and public meteorological sectors without infringing on the legitimate concerns of either group. The dissemination component of a local weather service is a logical interface. But we must review who should have the ultimate responsibility for providing warnings, whether that responsibility can, or should be delegated, and how quality control of weather services can be achieved when several different groups are active in the same region.

3. THE PROFS SCENARIO

To demonstrate how a truly local, user-oriented weather service might operate let us consider the following scenario.

Assume that we have an observational component capable of providing an exact, high-resolution representation of all important meteorological elements in near real time. Assume further that the dissemination component is capable of continually presenting all relevant weather information to the total population of an urban area, and that any desired smaller segment of that population can be warned selectively. For an optimum local service, the forecaster must be able to react rapidly. He must be able to monitor continually the evolving weather patterns and to update or modify the forecast rapidly. Similarly, he must be able to get updated numerical guidance (4-dimensional, mesoscale) for periods up to 12 hours. Such capabilities, only available now to a limited extent (radar, satellite), should be part of the local scale PROFS system.

The following might then occur. Assume that the 12-24 hour guidance forecast includes the possibility of severe thunderstorms. The local forecaster, alerted by the NMC and NSSFC outputs, would be ready to employ the local service capability for the 0-12 hour time frame. The first public forecast might simply note the possibility of the severe storm conditions over a broad region, much like present forecasts. The high resolution numerical model would then produce 3-12 hour predictions narrowing the possible region of severe storm activity. As much as 12 hours before the event, a "watch" area covering perhaps several counties could be shown on a dedicated T.V. weather channel with parallel broadcasts over NOAA radio and commercial outlets, alerting the populace and telling them to monitor the weather channel occasionally for updated information.

As the forecast time is reduced within 3-6 hours of the event, the mesoscale model would produce more refined predictions of the time and location of severe storm activity. This information could be combined with real time Doppler radar data of wind fields, clouds, and precipitation, plus ground based and satellite radiometric data on moisture and temperature patterns, a relatively dense array of remote *in situ* surface observations, and information from conventional sources such as storm spotters. Animated displays of the predicted storm motion and severity over a smaller watch area could be produced and disseminated.

At less than 3 hours before the event, the numerical model would cease being a central part of the forecast procedure. During this shorter time frame, the forecaster would rely on near real time observations and sophisticated extrapolation techniques that are preprogrammed and available for immediate call-up from a minicomputer. As the storms develop, the watch area could be further narrowed to a highly specific warning area.

The forecaster would now be almost completely dependent on his observation network, aided by rapid data processing techniques. Assume that during this time the Doppler radar detects the first in-cloud motions known to be associated with tornadoes. The forecaster could continuously monitor and extrapolate these features, eventually making a prediction of a possible tornado touchdown. With the aid of his computer and a highly specific dissemination network, he could activate a system that would alert just the people in the potential path of the tornado several minutes to one-half hour or more before the tornado touches down.

This example demonstrates the different operational forecasting philosophy that must be adopted for an effective short-range local service. Events occur rapidly, so the forecaster must be supported with a high level of automation and accurate high resolution data. He can update or modify his predictions right up to the time of the event and these changes would be disseminated quickly, avoiding the situation in which outdated information confuses the user. The accuracy and precision of the forecast would increase as the time before the event became less. The implications for improved credibility are obvious. Forecasts would be viewed as highly accurate, because they would be continually updated and refined until the verification time.

4. PRE-PROFS EXPERIMENT

As with all initiatives the time lag between germination of the idea and the final approval of funding is painfully long. Even if the program is approved and funded for an FY-80 start, full operational impact will not occur until the latter part of Phase II, 7 or 8 years after the work starts. This wait is especially frustrating to those operational personnel who are continually asked to provide more and better service with decreasing resources. These people see developments taking place in the research community and are justifiably concerned that it takes so long for new technology, which could help in meeting the demands for their services, to reach the operational arena.

As a partial solution, a preliminary experiment is now being planned for the Denver region. It will involve local research organizations and local operational forecast groups (hopefully, both government and private). The exercise will be patterned after the highly successful CRAB experiment that has been conducted for several summers in the Chesapeake Bay area. It will differ in that the large number of advanced research techniques and devices that are under development in the Denver-Boulder area such as two-channel radiometers, continuous wind profilers, and chinook wind models, will be applied to the local service problem. These advanced systems will be interfaced directly with the Denver forecast office and used by the meteorologists in their daily operations. Resources for this experiment will come from individual groups that wish to participate, and success will depend, to a large extent, on a spirit of cooperation.

Close relationship with the Denver office is expected to continue throughout the PROFS program. In this way, research subsystems still under development can be tested in actual operations before the total system design is complete.

5. SUMMARY

The PROFS program addresses the need for developing an effective local-scale, short-range weather service in the nation's urban regions. It applies a user-oriented, systems engineering approach to the creation of such a service. The PROFS concept also recognizes certain organization and communication improvements within NOAA that must be achieved before the program can be fully effective. These will foster and encourage interdisciplinary activities and the transfer of new technology from research to operations. A basic feature of the PROFS program is the creation of an Exploratory Development Facility, which would provide the needed organizational focus.

The PROFS concept recognizes that a major portion of the technology necessary for creating effective local-scale weather services for the cities of the nation exists in separate disciplines, in both research and operational organizations. The missing element is a coordinated effort to bring these separate technologies together into a blanced, user-oriented system which is neither technology-driven nor user-dominated. PROFS would provide this missing effort.

ACKNOWLEDGMENTS: The PROFS concept was first generated nearly two years ago and has evolved into the proposed NOAA initiative mentioned in the text. The people both within NOAA and from other organizations who contributed their time and ideas during the formulation of this plan are too numerous to mention, but their contributions are gratefully acknowledged.

6. REFERENCES

Fawcett, E. B., 1977: Current capabilities in prediction at the National Weather Services, National Meteorological Center, 58, 143-149.

Fritsch, J. M. and C. W. Kreitzberg, 1978: Workshop on local scale forecast techniques — 1980 and beyond (meeting review), *Bull. Amer. Meteor. Soc.*, 59, 293-296.

Glahn, H. R. and D. A. Lowry, 1972: The use of model output statistics (MOS) in objective weather forecasts, *J. Appl. Meteor.*, 11, 1203-1211.

Ramage, C. S., 1978: Response (to Sanders 1978), *Bull. Amer. Metero. Soc.*, 59, 644-645.

Ramage, C. S., 1978a: Further outlook - hazy, *Bull. Amer. Meteor. Soc.*, 59, 18-21.

Sanders, F., 1978: Comments on "Further Outlook - Hazy", *Bull. Amer. Meteor. Soc.*, 59, 643-644.

Scofield, R. A. and C. E. Weiss, 1977: A report on the Chesapeake Bay Region Nowcasting Experiment, NOAA Tech. Memo., NESS 94, 51 p.

Shuman, F. G., 1978: Numerical weather prediction, *Bull. Amer. Meteor. Soc.*, 59, 5-17.

Snellman, L. W., 1977: Operational forecasting using automated guidance, *Bull. Amer. Meteor. Soc.*, 58, 1036-1044.

Reviews of Geophysics and Space Physics 16: 47-110, 1978.

Advances in Atmospheric Acoustics

EDMUND H. BROWN AND FREEMAN F. HALL, JR.

NOAA/ERL Wave Propagation Laboratory, Boulder, Colorado 80302

We give a detailed review of developments in atmospheric acoustics of the last decade. These developments include new ways to use refractive effects, studies of phase and amplitude fluctuations during propagation of sound along a path, nonlinear effects near high-powered acoustic antennas, problems related to noise, insights into large-scale atmospheric processes gained from infrasound, applications dependent on the Doppler frequency shift, and hybrid devices using both acoustic and electromagnetic waves. The introduction of the echosonde approximately 10 years ago results in the considerable emphasis given to advances in active acoustic remote sensing of atmospheric structure.

CONTENTS

Introduction 47
The atmosphere 50
  The quiet atmosphere 50
  The turbulent atmosphere 52
Propagation in a quiet atmosphere 53
  Refraction 53
  Attenuation 54
  Sound in fogs 55
  Nonlinear effects 56
Interaction of sound with turbulence 57
  Separating sound from turbulence 57
  General equations 59
  Interaction mechanisms 60
  Scattering 62
  Propagation 64
Acoustic systems 71
Atmospheric science investigations with echosondes 73
  Convection in the unstable atmosphere 73
  Inversions, fronts, and turbulent layers 78
  Ground-based shear layers 78
  Multiple-layer echoes 81
  Subsidence inversions 81
  Fronts 81
  Acoustic scattering from clouds 81
Echosonde applications 83
  Wind sensing 83
  Doppler echosondes in the computer era 84
  Quantitative measurement of structure parameters with echosondes 89
  Echosonde applications in air pollution meteorology 92
  Echosonde facsimile interpretation 93
Hybrid acoustic and electromagnetic systems 94
  Lasers and acoustics 94
  Radar and echosonde investigations 96
  Radio acoustic sounding systems (RASS) 96
Passive acoustics and infrasound 97
The future of atmospheric acoustics 98
Appendix A: A derivation of the acoustic equation 99
Appendix B: A selection of useful theoretical results 100
Notation 101

INTRODUCTION

The decade previous to this review has seen impressive contributions to science through the newly expanding study and use of sound waves in the atmosphere. This reawakening of interest in acoustics for atmospheric geophysical research was stimulated in great part by *McAllister*'s [1968] invention of the echosonde.

In the *Iliad* of Homer, 'echo' meant simply 'sound,' as the sound of spears striking shields in battle. After half a millennium, echo acquired the additional meaning of 'resound' and, later still, the meaning that we continue to use today, sound repeated by scattering or reflection. In Ovid's *Metamorphoses* the nymph Echo personified the latter meaning. Echo could speak only by repeating the words of others. *Derham* [1708] used echo in the word 'echometry,' the application of acoustics to range-finding. 'Sonde' refers to one of the some dozen definitions of the root word 'sound' not identified with acoustic vibrations and has the exact meaning of 'a remote sensing device.' So the name 'echosonde' accurately depicts the physical process underlying the operation of an acoustic sounder, the use of echoes for remote sensing.

The introduction of the echosonde has been followed by many other advances in atmospheric acoustics. We consider here all of those developments following a brief review of their historic roots. The echosonde itself will be seen to play a major role throughout the 10-year period.

Modern atmospheric acoustics has a dual character. First, it is that part of the science concerned with the effects on sound of the vagaries and inhomogeneities of the earth's atmosphere (as opposed to a sample of the same gases confined to a laboratory vessel). Figure 1 gives an example of such effects, the random deformation of plane wave phase fronts and their amplitudes (indicated by the thickness) as they propagate through atmospheric fluctuations. Second, atmospheric acoustics is the application of sound to atmospheric research and man's weather-dependent activities.

Greek science considered mainly the musical aspects of acoustics, and this emphasis continued with the acoustical research of Galileo, Mersenne, Sauveur, and others during the rebirth of science in the seventeenth century. The early outdoor measurements of the speed of sound used the free atmosphere but only to obtain long path lengths. (Note that much of the early work briefly mentioned here has become relatively inaccessible in original form. However, descriptions of most of the results appear in *Rayleigh*'s [1877] *The Theory of Sound* or *A. Wood*'s [1946] *Acoustics*. And references to the research appear in Lindsay's 'Historical Introduction' to the 1945 American edition of Rayleigh's book, in the review by *Ingard* [1953], in the 'Historical Introduction' to the monograph of *Skudrzyk* [1971], and in *Acoustics: Historical and Physical Development* by *Lindsay* [1973].)

An English clergyman named Derham apparently initiated the field of atmospheric acoustics in 1704. In response to a letter claiming greater audibility of sound in England than in Italy, Derham and an Italian acquaintance, Averrani, conducted experiments in England and Italy which showed that after a proper accounting for the effects of wind, sound propagation did not differ in the two countries. However, the first sustained development of atmospheric acoustics did not begin

Copyright © 1978 by the American Geophysical Union.

Paper number 7R0813.
0034-6853/78/017R-0813$06.00

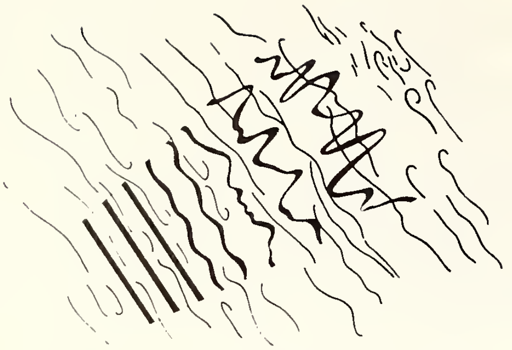

Fig. 1. Distortion of a plane wave propagating through turbulence. Heavy curves denote phase fronts. Amplitudes are indicated by the thickness of the fronts. Fluctuations are exaggerated for easier visibility. (From *Brown and Keeler* [1975].)

until the last half of the nineteenth century. During this period, *Reynolds* [1876] studied atmospheric temperature profiles and their effects on the refraction of sound. *Stokes* [1857] briefly considered the refractive effects of winds and wind profiles, and *Tyndall* [1874] investigated the scattering of sound by atmospheric fluctuations both in the laboratory and over the sea. Using the siren developed by Brown and reported by *Henry* [1874] fitted with a huge horn for impedance matching (Figure 2), Tyndall explained the scattering of sound by an apparently still, clear atmosphere noted earlier by *Derham* [1708]. Tyndall showed in a laboratory demonstration that the scattering resulted mainly from temperature fluctuations, incidentally disproving Derham's assertion that mists and fog necessarily inhibit sound propagation. However, other researchers, such as *Henry* [1874] and, to some extent, even *Rayleigh* [1877], did not accept Tyndall's results and instead tended to ascribe the observed effects to refraction. In consequence, interest in the atmospheric scattering of sound remained negligible for nearly a century.

Most of the turbulence-dependent processes in the earth's atmosphere take place in the lowest 10–20 km, called the 'troposphere,' a layer ending in a temperature minimum at the 'tropopause.' By balloon measurements, *Teisserenc de Bort* [1902] discovered an 'isothermal' layer, the 'stratosphere,' lying just above the troposphere. At about the same time, observers such as *van den Borne* [1910] noticed the anomalous propagation of sound: audibility of an explosion within a circle of about 100-km radius, surrounded by a ring-shaped 'dead zone' of silence about another 100 km wide, followed by a return of audibility at greater distances. *Emden* [1916] developed a theory of refraction that could explain such anomalous propagation if a temperature inversion, that is, increasing temperature with height, existed at some altitude. *Schrödinger* [1917] showed that even though negligible dispersion exists at audible frequencies the strong frequency dependence of the attenuation of sound implies that lower-frequency sound can refract back to earth with detectable intensity from a greater altitude than can a higher-frequency sound.

Observations of meteor trails proved that the upper part of the stratosphere did indeed have an increasing temperature, a rise to a maximum at about 50 km, the 'stratopause,' caused by absorption of solar radiation by atmospheric ozone. *Whipple* [1923] used this evidence as a basis for a description of the anomalous propagation of sound by refraction caused by the temperature inversion in the upper stratosphere. *Barton* [1901] continued the approach of *Stokes* [1857] (which was little more than a suggestion) and confirmed that in the presence of winds, zones of audibility or inaudibility would lose their symmetric form. In following years, organizations interested in atmospheric research carried out numerous programs on the anomalous propagation of sound from explosions, such as the experiment performed by the International Commission for the Investigation of the Upper Atmosphere, reported by *Duckert et al.* [1934], or the Helgoland explosion described by

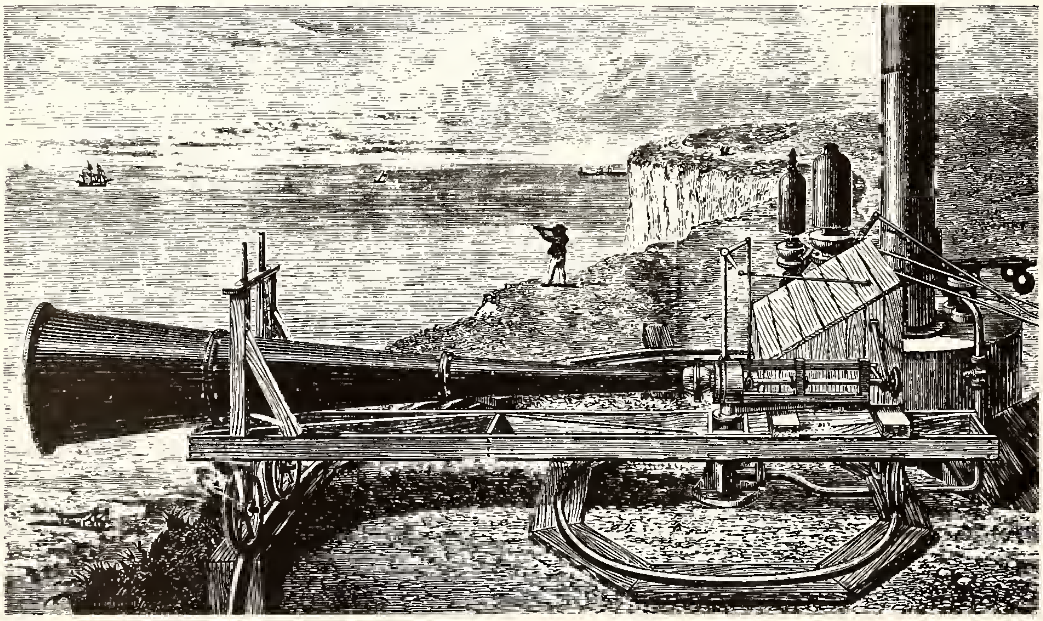

Fig. 2. Tyndall's apparatus for studying sound propagation in the atmosphere [from *Tyndall*, 1875].

E. F. Cox [1949*a*, *b*]. During many tests, observers such as *Gowan* [1929] noted hitherto unrecognized very low frequency sound waves, now called 'infrasound.' Subsequently, *Gutenberg* [1938] began extensive investigations into the sources and propagation of such infrasonic waves. A later section will sketch more modern developments in the detection of infrasound and applications to mesoscale atmospheric research. For refraction the report of Frank, Bergmann, and Yaspan reprinted in the collection of *Lindsay* [1974] gives an excellent description of ray theory. The annotated bibliography of *Wescott and Kushner* [1965] provides a comprehensive survey of the literature to that date.

Although zones of silence indicate a rise in temperature above the tropopause, this phenomenon provides good quantitative information on the temperature profile only with difficulty. Because of low atmospheric densities above 30 km, research balloons cannot fly very much higher. However, an acoustic technique using rocket grenades, developed at the White Sands missile range by *Stroud et al.* [1956], gives measurements not only of temperature but also of wind in the upper atmosphere to heights of 80 km. Researchers used the method at several different locations during the International Geophysical Year (1956–1957) to obtain temperature (by time-of-transmission measurements) and winds (by angle-of-arrival measurements) before the rocketsonde network method superseded the technique. *Nordberg and Stroud* [1961] give a summary of the rocket grenade results.

The gradual introduction of turbulence theory to studies of the small-scale dynamic structure of the atmosphere by *Taylor* [1915] and others revived interest in the scattering of sound by what *Tyndall* [1874] had called 'flocculence.' In 1941, the same year that *Kolmogorov* [1941] and *Obukhov* [1941] had obtained the '$\frac{2}{3}$ law' for inertial range turbulence, *Obukhov* [1941] related the acoustic scattering cross section to a general expression for the spectral density of turbulent kinetic energy. Obukhov's derivation neglected the fact that the gradient of the acoustic refractivity, as well as the acoustic refractivity itself, appears in the 'source term' of the inhomogeneous wave equation. However, his analysis represents the first attempt at a quantitative explanation of sound scattering by the atmosphere. In the case of 'smooth' (i.e., nonturbulent) atmospheres, *Bergmann* [1946*a*] showed that the presence of the static density gradient produces dispersion in the propagation of sound, that is, a dependence of the phase velocity on the frequency. In the same year, *Bergmann* [1946*b*] began the study of scattering from the point of view of correlation functions.

For the turbulent atmosphere, *Blokhintzev* [1946] introduced the assumption that only wave numbers in the inertial range of turbulence affect the propagation of audible and high-frequency sound, thus permitting the use of the Kolmogorov spectrum in the scattering cross section. *Kraichnan* [1953] and *Lighthill* [1953] simultaneously found the correct form of the velocity-dependent part of the scattering cross section in 1953. Four years later, *Batchelor* [1957] obtained the scattering cross sections used today, both the same velocity-dependent part found by Kraichnan and Lighthill and the part dependent on the spectral density of fluctuations of a passive additive such as acoustic velocity or temperature. Although Batchelor did not express the total cross section as the sum of the velocity-dependent and temperature-dependent parts, such a summation is implicit, since the cross section represents a normalized energy flow and thus partial cross sections are additive.

Evidently unaware of the earlier work, *Tatarskii* [1961] obtained the total scattering cross section expressed as the sum of a velocity-dependent part and a temperature-dependent part. Unfortunately, the derivation followed Obukhov in neglecting gradients and thus omitted a factor $\cos^2 \theta$ dependent on the scattering angle θ. The striking divergence in scattering angle dependence near 90° between Tatarskii's theoretical expression and the extensive experimental results of *Kallistratova* [1959*a*, *b*] first prompted *Kallistratova and Tatarskii* [1960] and then *Monin* [1962] to reexamine the derivation. Monin's analysis obtained the same results found earlier by Batchelor and again expressed the total cross section as the sum of a velocity-dependent part and a temperature-dependent part. In his monograph on wave propagation in turbulent atmospheres and in its revision, *Tatarskii* [1961, 1971] collected a wealth of results, many from his previous papers, on the propagation and scattering of light and high-frequency sound. These results included amplitude and phase structure functions, two-dimensional spatial spectra of amplitude and phase for planes perpendicular to the propagation path, and the frequency spectrum of the amplitude fluctuations in a continuous wave propagating through turbulence convected by a mean crosswind.

The sharing of one common arena, the atmosphere, places atmospheric acoustics in close contact with several other disciplines, particularly tropospheric radio propagation and optical, or laser, propagation. In pursuit of the cause of signal fading on so-called 'troposcatter' transhorizon microwave paths, *Gilman et al.* [1946] built a precursor of the echosonde, a device acting like an 'acoustic radar' which they named the 'sodar' (for sonic detection and ranging). In the sodar a loudspeaker transmitted sound pulses upward into the atmosphere, a microphone received scattered or reflected waves, and after filtering and detection a motion picture camera recorded the display of the received signal on an oscilloscope. Because of the poor antenna beam pattern, ground clutter required operation at the relatively high carrier frequency of 4 kHz. Since absorptivity increases approximately as the square of the frequency, attenuation limited the range of a sodar to a little over 100 m. Although the recording procedure allowed no pulse-to-pulse integration or averaging, the authors observed scattered signals, especially from low-level inversions, and found correlations between radio signal fading and inversions. Since a calculation showed that even in a strong inversion the gradient could not account for the strength of the returned signal, the authors ascribed the scattering of the sound to some unknown inhomogeneities or turbulence in the atmosphere.

Pursuit of the same problem, understanding troposcatter radio propagation, induced *McAllister* [1968] to return to the earlier concept of the sodar but with three major changes: a vastly improved transmitting antenna permitting operation just below 1000 Hz and at ranges up to 1.5 km; use of the transmitting antenna itself (with a transmit-receive switching circuit) for the receiver; and perhaps most important, use of the facsimile recorder, adopted from sonar, for the received signal. (Echo sounding and echo sounders for use in the ocean date from 1924.) In the facsimile recorder, each pulse produces a vertical trace whose darkness varies with the received signal strength from a particular height in the atmosphere, a height proportional to the ordinate on the chart. Since the traces from successive pulses are closely spaced along the abscissa, the eye can easily integrate corresponding features and detect the evolution of atmospheric structure with time. With his new instrument, which he preferred to call an 'acoustic sounder,' McAllister obtained very clear pictures of inversions, includ-

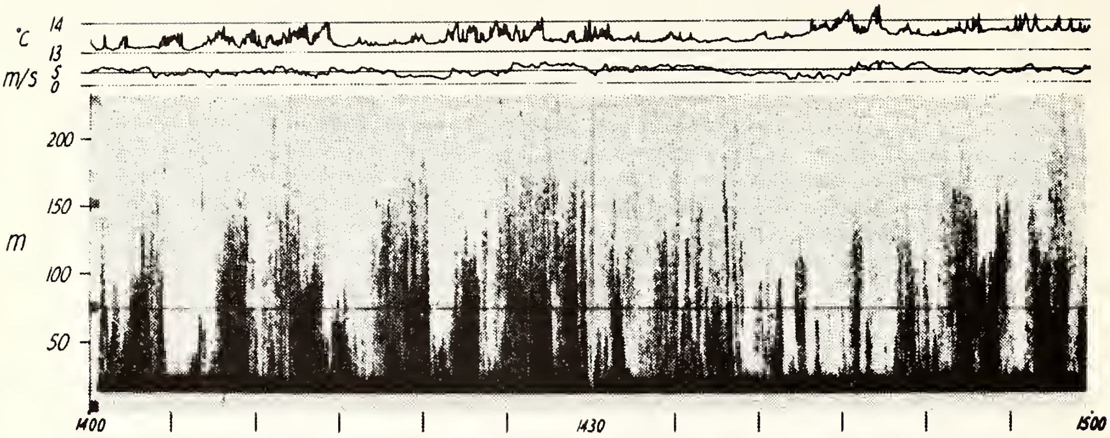

ing one showing the striking presence of internal waves ('gravity waves'). Following Gilman et al., McAllister attributed the scattering of the sound waves to 'temperature discontinuities' or atmospheric inhomogeneities.

During this period, Little had initiated a program at the Wave Propagation Laboratory of the National Oceanic and Atmospheric Administration for the study of optical propagation and remote sensing of the atmosphere by means of laser beams. The program resulted in a new acquaintance with the work of the Russian school, particularly the monograph of *Tatarskii* [1961] and the related acoustic studies of *Kallistratova* [1961] and *Monin* [1962]. Consequently, Little could communicate details of the Russian work on scattering of waves by turbulence during a visit to Australia during the same year that McAllister's short paper was published.

The following year saw the appearance of a pair of coordinated papers by *Little* [1969] and *McAllister et al.* [1969]. Using turbulent scattering theory, Little for the first time obtained quantitative estimates of the received signal strength, estimates in good agreement with later experimental results. Little also compared several remote sensing methods in addition to the echosonde, such as passive sensing of natural atmospheric sounds, measurement of acoustic propagation over a path, and the use of electromagnetic waves; for example, the study showed that the strength of the scattering interaction with turbulence for acoustic waves exceeds the strength for electromagnetic waves by a factor of about 10^6. In the same paper, Little suggested elaborations of echosonde techniques that in addition to the display of atmospheric structure would give vertical profiles of winds (by using the Doppler effect), three-dimensional spectra of temperature and wind fluctuations, and vertical profiles of humidity (by using a multifrequency system). Later research has followed up all of these suggestions. The companion paper of *McAllister et al.* [1969] gave a more complete description of the experimental conditions (including correlation of the results with observations from a meteorological tower), adopted turbulent scattering as the likely mechanism for production of the return signals, and showed a beautiful set of facsimile recordings of various atmospheric structures, such as thermal plumes, inversions, inversion growth and decay, internal waves, and breaking waves (Figure 3 reproduces one of these records.)

This detailed review of developments in atmospheric acoustics of the last decade includes new ways to use refraction, studies of phase and amplitude fluctuations during propagation of sound along a path, insights into larger-scale atmospheric processes gained from infrasound, nonlinear effects near high-powered acoustic antennas, problems related to noise, applications dependent on the Doppler effect, and hybrid devices using both acoustic and electromagnetic waves. The echosonde takes a major share because of its importance in applications and its influence on other aspects of atmospheric acoustics. However, the development of the echosonde has reached a crucial turning point. The form of the instrument producing only displays of turbulent structures limits the results to, at best, semiquantitative information. But serious atmospheric research requires incorporation of components that will provide direct quantitative data on temperature and velocity fluctuation strengths and on Doppler-measured wind speeds. The next few years will tell whether the instrument can meet these needs.

THE ATMOSPHERE

The Quiet Atmosphere

In a sense the 'quiet atmosphere' is a statistical artifact, since the air in the earth's atmosphere is never quite still. As an illustration, suppose that a bare-armed picnicker can just detect a wind speed of $U = 1$ m s^{-1} on a sunny late afternoon. Instead of the height of the 'boundary layer' (the lowest few hundred to few thousand meters of the atmosphere influenced by wind shear and heat flow at the surface), which determines

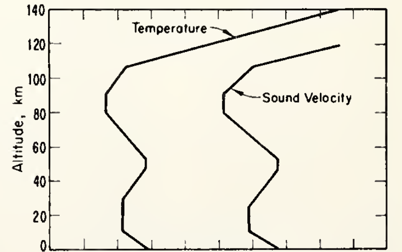

Fig. 4. Mean temperature T_0 (°C) and sound velocity c_0 (m s^{-1}) in the troposphere as a function of altitude [from *Cook*, 1962].

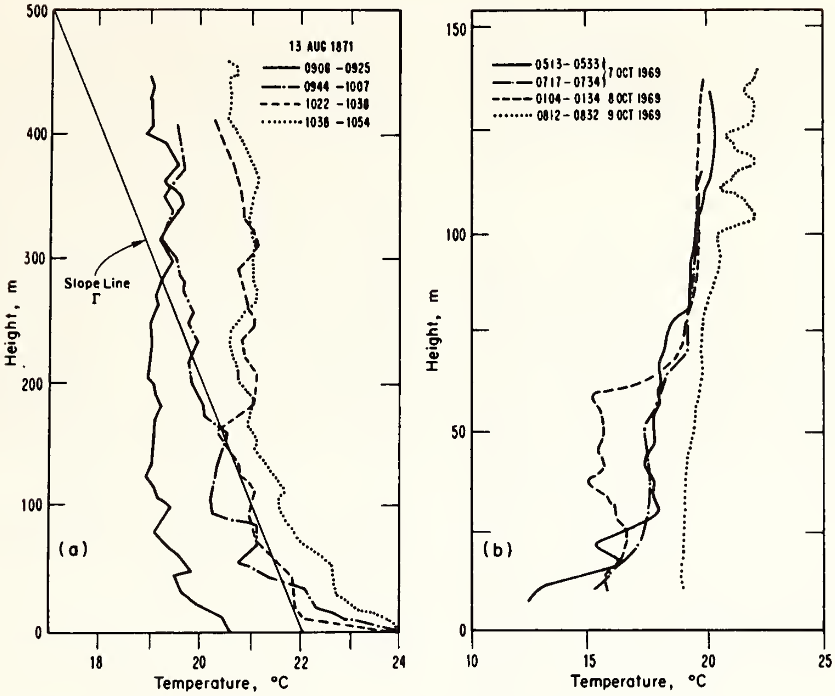

Fig. 5. Temperature profiles in the boundary layer (in degrees Celsius). (*a*) Daytime convective profiles [from *Hall et al.*, 1975]. (*b*) Nighttime inversion profiles [from *Emmanuel et al.*, 1972]. Note the differences between the scales.

the turbulence at all scales, choose the height of the picnicker (say, L = 180 cm) as the largest relevant scale. Then, with a nominal value of the kinematic viscosity of ν = 0.15 cm^2 s^{-1}, the apparent Reynolds number of the flow becomes $Re = UL/\nu \approx 1200$, a number twice as large as that which usually indicates the onset of turbulence in a boundary layer without pressure gradients. But for large experimental scales and especially for long wavelengths the concept of a smooth, mean atmosphere possessing certain agreed-on average properties remains a useful tool.

Even at sea level the atmosphere behaves like a perfect gas to a high degree of approximation. And throughout the troposphere and stratosphere the dry atmosphere retains a constant molecular composition, having an average molecular weight of m = 28.97 g mol^{-1}. Since air obeys the perfect gas law $p_0 = (R/m)\rho_0 T_0$, measurement of the static pressure p_0 (in millibars) and the absolute temperature T_0 (in kelvins) immediately furnishes the static density ρ_0, the equilibrium sound speed $c_0 = 20.05(T_0)^{1/2}$ in meters per second, and the acoustic impedance $\rho_0 c_0$. Figure 4, from *Cook* [1962], shows accepted standard values of T_0 and c_0 as functions of altitude up to the tropopause. Unfortunately, such a standard atmosphere does not give a very good picture of the variability of the temperature gradient from night to day, particularly in the first few hundred to some thousand meters above the ground (the boundary layer). In particular, 'inversions' caused by rapid radiation cooling of the ground at night with a consequent increase (rather than the usual daytime decrease) in the temperature of the air with altitude changes the character of acoustic propagation. Uncertainty of temperature profiles and wind is the main cause for error in sound ranging, such as ranging against enemy artillery [*Trowbridge*, 1920; *Golden*, 1961].

Inversions are more precisely defined in terms of the gradient in the 'potential temperature' θ_0 rather than the absolute temperature T_0 (θ_0 is the temperature that a parcel of air would assume if it were brought adiabatically to the pressure at sea level). For a perfect gas, $\theta_0 = T_0 + (g/c_p)z$, where g is the acceleration of gravity, c_p the specific heat at constant pressure, and z the height above the ground. For z measured in kilometers, g/c_p has the value 9.8 K km^{-1}. The usefulness of θ_0 lies in the fact that gradients in θ_0 imply upward or downward transfers of heat and also indicate whether a parcel of air is 'stable' or 'unstable,' that is, whether an accidental displacement of the parcel will result in either a restoring motion or an increasing change. Thus in discussing states of the atmo-

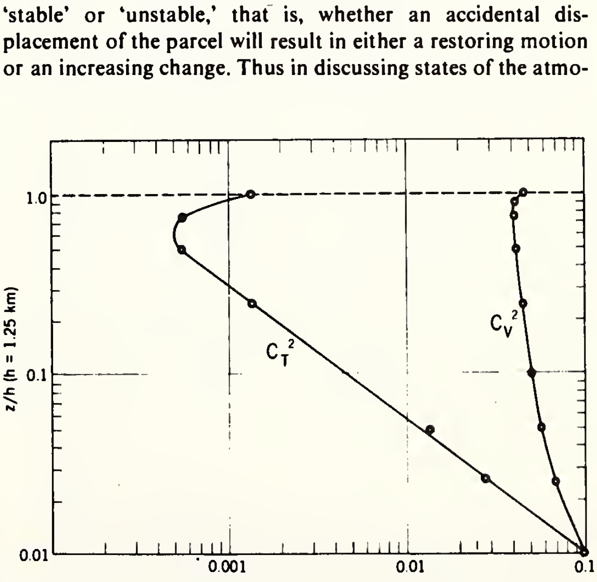

Fig. 6. Typical daytime profiles of C_T^2 (K^2 m$^{-2/3}$) and C_v^2 (m$^{4/3}$ s^{-2}) [from *Brown and Clifford*, 1976].

sphere, θ_0 is the relevant quantity; in discussing acoustic propagation, in which the speed of sound depends on the actual temperature, T_0 remains the important variable. Figure 5 shows typical daytime and nighttime temperature profiles. The strongest known inversion, reaching a value of 30 K in 100 m, occurred at the south pole during an austral winter [*Neff and Hall*, 1976*a*, *b*].

The Turbulent Atmosphere

As was suggested above, the distinction between a smooth, refracting atmosphere and a turbulent, scattering atmosphere lies partially in the application at hand, whether the propagating sound has a long wavelength or a short wavelength. And because of the frequency dependence of attenuation this distinction also affects the path lengths over which the sound propagates. Infrasound, sound having a frequency below about 20 Hz, propagates over thousands of kilometers and interacts mainly with the refractive structure of the troposphere and stratosphere. In contrast, practical considerations limit the frequencies of sound used in active devices for remote sensing of the turbulent boundary layer (the lowest few hundred to few thousand meters of the atmosphere influenced by wind shear and heat flow at the surface) to the range of several hundred to a few thousand hertz. Such shorter wavelengths lie just in the middle of the range of turbulent velocity correlation lengths or 'eddy' scales, typically having values between about 1 cm and many tens of meters. Of course, other distinctions exist which may come into play strongly in areas such as atmospheric dynamics. One of these differences springs from the fact that the mean refractive structure depends mainly on a single dimension, height in the atmosphere, whereas true turbulence possesses an inherently three-dimensional character.

Because of the vast size of the literature on turbulence, even atmospheric turbulence, this review of atmospheric acoustics will reference only a few, fairly comprehensive treatises. The text of *Tennekes and Lumley* [1972] serves as a good introduction. The two-volume monograph of *Monin and Yaglom* [1971, 1974] covers most of the older literature, with especially complete coverage of the Russian school. A proceedings edited by *Haugen* [1973] contains both general material on atmospheric turbulence and analyses of results of one of the classical field programs, the so-called 'Kansas experiment.' A recent study by *Kaimal et al.* [1976] determines both of the turbulence intensity parameters C_T^2 and C_v^2 (defined below). *Brown and Clifford* [1976] have abstracted the data of Kaimal et al. for daytime unstable conditions, shown here in Figure 6, to give an impression of the typical behavior of atmospheric turbulence. *Weill et al.* [1976] have made experimental studies of the effect of intermittency on C_T^2 and on the slope of the spectrum of the temperature fluctuations.

Because of the acoustic wavelengths ordinarily found in problems of the propagation of sound through turbulence, one can almost always assume that the structure function of the turbulent velocity fluctuations,

Definition of trace of velocity
structure function

$$D(\mathbf{r}_1, \mathbf{r}) = \langle |\mathbf{v}(\mathbf{r}_1 + \mathbf{r}) - \mathbf{v}(\mathbf{r}_1)|^2\rangle \qquad (1)$$

(where angle brackets denote ensemble averaging) satisfies both conditions of isotropy and local homogeneity, $D(\mathbf{r}_1, \mathbf{r}) = D(r)$, and the Kolmogorov-Obukhov inertial range law

Structure function for inertial
range turbulence

$$D(r) = C_v^2 r^{2/3} \qquad (2)$$

where $r = |\mathbf{r}|$. Equation (2) also defines the turbulent velocity fluctuation 'structure constant' C_v^2. Figure 6 shows that for the unstable case, C_v^2 varies with altitude. For stable atmospheres, C_v^2 becomes small except for large values in layers of large shear associated either with winds or with internal waves. Theoretical analysis of the interaction of sound with turbulence requires, instead of $D(r)$, the corresponding one- and three-dimensional spatial spectra of the velocity fluctuations. These spectra result from a Fourier transformation of the coordinate space $x_i = (x, y, z)$ to the associated Fourier space of the variables $\kappa_i = (\kappa_1, \kappa_2, \kappa_3)$. In terms of the magnitude $\kappa = (\kappa_i \kappa_i)^{1/2}$ (repeated indices imply summation over the squares of components) the kinetic energy spectrum $E(\kappa)$ associated with $D(r)$ becomes

Spectrum of inertial range kinetic energy

$$E(\kappa) = 0.76 C_v^2 \kappa^{-5/3} \qquad (3)$$

and the corresponding three-dimensional velocity spectrum (which appears in later scattering formulations) becomes

Tensor velocity spectrum for
incompressible turbulence

$$\Phi_{ij}(\kappa) = [\delta_{ij} - \kappa_i \kappa_j/\kappa^2] E(\kappa)/(4\pi\kappa^2) \qquad (4)$$

where δ_{ij} is the 'Kronecker delta,' equal to 1 for $i = j$ and 0 otherwise.

An additional simplification of the equations of sound propagation introduces the assumption that the acoustic refractive index $n = c_0/c$, c being the true velocity of sound and c_0 the reference velocity, behaves like a 'passive additive.' This assumption implies that the fluctuations in n derive from the effect of the turbulent velocity fluctuation field acting on the mean vertical gradient of n in the atmosphere. The condition usually holds because the time scales associated with atmospheric heat and humidity fluxes far exceed the wavelengths and pulse lengths of sound. With this assumption the structure function of refractive index fluctuations $D_n(r) = \langle |n(\mathbf{r}_1 + \mathbf{r}) - n(\mathbf{r}_1)|^2\rangle$ also satisfies the Kolmogorov-Obukhov law in the form

Structure function of inertial range
refractivity fluctuations

$$D_n(r) = C_n^2 r^{2/3} \qquad (5)$$

The velocity of sound in a mixture of perfect gases depends on the temperature T and the combined molecular weight m according to the formula $c^2 = \gamma kT/m$, where γ is the combined specific heat ratio and k the Boltzmann constant. Writing $T = T_0 + T'$, where T_0 is the equilibrium temperature, and e/p_0 for the ratio of the vapor pressure of water to the total pressure, *Wesely* [1976] obtained the formula

Structure constant for refractivity
fluctuations

$$C_n^2 = C_T^2/4T_0^2 + 2(0.307)C_{eT}/4p_0T_0 + (0.307)^2 C_e^2/4p_0^2 \qquad (6)$$

for the refractive index structure constant. (Wesely uses C_{eT}^2 for the parameter for cross correlation of humidity and temperature fluctuations. Since C_{eT} sometimes becomes negative and a square root would imply an imaginary C_{eT}, the above notation appears both more logical and in agreement with the formal rule $C_{xx} = C_x^2$.) The approximation $e/p \approx 1.61r$ will convert the humidity terms in (5) to functions of the water vapor mixing ratio r. *Tatarskii* [1971] drops the factor $\frac{1}{4}$ appearing in (6) and in the work of *Tatarskii* [1961]. This change is appropriate when the electric permittivity ϵ is used, since $n = \epsilon^{1/2}$ implies $\langle n'^2 \rangle$. But the relation between the refractive index n and the temperature T of a perfect gas suggests retention of the factor in acoustic propagation.

Friehe et al. [1975] have studied the behavior of C_e^2 and C_{eT} for use in the corresponding optical refractive index structure function. (Of course, C_e^2 and C_{eT} retain the same values, although C_n^2 changes.) They found that C_{eT} may contribute a negative correlation over lakes near deserts but that it produces a positive contribution over a warm ocean. Using their typical values of $T' \approx 0.1$ K, $r' \approx 0.5\rho_0$, ρ_0 being in micrograms per cubic centimeter, gives $T'/T_0 \approx 0.3 \times 10^{-3}$, $r' \approx 0.3 \times 10^{-3}$. Unlike the optical C_n^2, C_T^2, C_{eT}, and C_e^2 may have comparable contributions to the acoustical C_n^2 for acoustic waves. Unfortunately, there do not yet exist any inertial subrange investigations of profiles of C_{eT} and C_e^2 with altitude, although *Gossard* [1960] has obtained correlations of e and T fluctuations at a single elevated level of 500 ft (150 m). When such profiles are obtained, they will have great value for the interpretation of echosonde recordings in marine atmospheres.

The above information on atmospheric turbulence gives a rough picture of the average behavior of the boundary layer. In reality, the boundary layer is rarely horizontally homogeneous. During unstable daytime conditions, thermal plumes and humidity plumes, having various diameters, move past observing stations with speeds close to the mean wind speed. During stable nighttime or inversion conditions, long-wavelength internal waves and breaking waves produce horizontal inhomogeneity. But since the full extent of such horizontal inhomogeneity became known only after the introduction of the echosonde, further information will fall more logically into the later section on uses of the echosonde in atmospheric research. (Many of the statements made above hold for the mixed layers in the ocean as well. A theoretical analysis of such effects by *Emmanuel and Mandics* [1973] has been borne out in experiments performed by *Proni and Apel* [1975].)

PROPAGATION IN A QUIET ATMOSPHERE

Refraction

Temperature gradients, wind, and wind gradients affect the propagation of sound in a nonturbulent atmosphere. Of course, a constant wind alone (meteorologically unlikely! a logarithmic wind profile near the ground appears typical of mean wind behavior) has an immediate solution by transforming to a coordinate system moving with the mean wind (Galilean transformation). The approaches to solutions of more complicated problems of refraction fall into two classes: (1) full solutions of the generalized wave equation for particular simple boundary conditions, usually using the method of expansion in modes; and (2) treatment of refraction by the ray theory method in which (under the criterion that dimensions, such as beam diameters and reciprocals of refractive index gradients, remain much larger than the wavelength) only the paths of energy flow and the energy flow density retain any significance.

The work of *Pekeris* [1946] exemplifies the first type, that of wave solutions. *D. H. Wood* [1969] has used such work to determine the Green's functions for propagation in a medium with a constant refractivity gradient. In turn, *D. H. Wood* [1970] has applied his results to obtaining correction factors for acoustic direction and range determinations and to giving parameterless wave solutions [*D. H. Wood*, 1973]. *Raphael* [1971] has rederived the results of *D. H. Wood* [1970] by the alternative ray path method. *Hartman* [1975] obtained solutions for the behavior of the propagation of a 'wave packet' in a particular stratified flow. *Bretherton* [1969], *Garrett* [1969], *Pierce and Posey* [1971], *Wenzel* [1974], and *Donato* [1976*a*, *b*] have studied the effect of the surface wave along an impedance boundary on the full wave solutions above it. The surface wave effect has had immediate practical application, as it has in the study of the effect of ground impedance by *Embleton et al.* [1976*a*, *b*]. *Ingard and Maling* [1963] have studied the more complex effects caused by the combination of turbulence and ground reflections.

The ray path approach to refraction suffered a brief confusion because of an error in the older literature. Much of the early work concerns correction of that error and analysis for obtaining the equations of the ray paths alone. *Blokhintzev* [1946] properly accounted for the effect of wind on the equations of sound propagation. *Heller* [1953] gave the correct form of the generalized eikonal equation:

$$|\nabla S|^2 = n^2(\mathrm{r})[1 - \mathrm{m}(\mathrm{r}) \cdot \nabla S]^2 \tag{7}$$

where $n(\mathrm{r}) = c_0/c(\mathrm{r})$ represents the refractive index and $\mathrm{m}(\mathrm{r})$ denotes the Mach number $\mathrm{v}(r)/c_0$, $\mathrm{v}(r)$ being the wind. The solutions of (7) give the paths over which the acoustic energy travels, which differ from the trajectories of the wave vectors when $\mathrm{v} \neq 0$. *Kornhauser* [1953] used Heller's result to obtain the equation for the ray path in the two-dimensional case, in which sound propagates in the direction of the wind and n and v depend only on altitude z. *Kornhauser* [1953] also derived a generalization of Snell's law which, if ψ represents the angle between the ray and the horizontal and $m^2 = |\mathrm{m}|^2$, takes the form

$$\frac{n \cos \psi[1 - m^2n^2 \sin^2 \psi]^{1/2} - mn^2 \sin^2 \psi}{1 + mn \cos \psi[1 - m^2n^2 \sin^2 \psi]^{1/2} - m^2n^2 \sin^2 \psi} = C \tag{8}$$

where C is a constant on each ray. Clearly, when the wind vanishes, $m = 0$, and (8) reduces to $n \cos \psi = C$, the form of the ordinary Snell's law suitable for horizontal stratification. *Warren* [1964] reemphasized the validity of the new results. *Thompson* [1974*a*, *b*] gives a more thorough treatment for derivation of the equations of the ray path in the three-dimensional case. Much of the remainder of the work on ray paths consists of numerical methods, alternative derivations, and treatment of simple cases such as horizontal stratification and constant refractivity gradient with altitude. Such work includes that of *Sager* [1974], *Chuprynin* [1975], *White* [1973], *Chessel* [1973], *Kong* [1970], and *Mathur and Sagoo* [1975]. The papers of *Pedersen et al.* [1975] and *Weinberg* [1975] contain a number of techniques which, although they were intended for underwater sound propagation, are also applicable to refraction in the atmosphere. *Hassab* [1975] has described methods for treating refraction in a layer with an arbitrary refractivity profile. Refraction in complex three-dimensional atmospheric wind and temperature fields can be treated by computerized ray-tracing algorithms, such as the modification of the Jones-Haselgrove program given by *Georges* [1971].

Since the rays studied in the above papers represent paths of energy flow, the convergence or divergence of ray bundles essentially determines the sound intensity. A number of authors have studied sound intensities from this geometric point of view. *Uginčius* [1969*a*, *b*, 1970, 1972] has obtained equations for the energy flow that bypass the need for solution of the wave equation. Other techniques and applications appear in the papers of *Krol* [1973*a*, *b*], *MacKinnon et al.* [1972], *Chen and Ludwig* [1973], and *Solomon and Armijo* [1971]. *Barnes and Solomon* [1973] give some interesting special cases for ray acoustics. Most of the above theoretical studies assume both horizontal homogeneity and constancy in time. For the real atmosphere an intermediate, time-dependent scale exists, which causes random fluctuations in the effective ray paths and in their phase path lengths. One can consider such effects as being due either to 'small-scale' refraction or to 'large-scale' anisotropic turbulence. *Chessel* [1976] has studied these random effects by obtaining the correlation function of the propagation times on the fluctuating paths. He finds the fluctuations to be determined by atmospheric scale sizes in the range from 200 to 500 m. Measurements of such large-scale fluctuations are included also by *Gonter* [1975].

Recently, interest has revived in the phenomenon of 'ducting' by ground-based or elevated inversions, such as the phenomenon studied much earlier by *King* [1919]. *Embleton et al.* [1976*a*, *b*] have studied the effect of ground impedance on such ducting, and *Kriebel* [1972] has considered both the focusing and the attenuation. *Greenfield et al.* [1974] have used observations of propagation times to measure temperature profiles in inversions. *Burkhard and Shealy* [1974] have made a theoretical study of the way refraction by a gradient affects the wave reflected by an arbitrary shape. As a final application of refraction theory, *Georges and Clifford* [1972, 1974] and *Spizzichino* [1974*a*, *b*] have obtained correction formulas for the effect of refraction on Doppler echosonde measurements of wind. For the case of realistic horizontal winds, Georges and Clifford found that the correction remained small up to at least 1-km range and that the correction depended on the square of the wind Mach number m.

Attenuation

The attenuation of sound by molecular absorption represents one of the most thoroughly studied subjects in acoustics. This review will include only a few highlights of this practically important aspect of atmospheric acoustics. The reader interested in more details can pursue them in the review of *Piercy et al.* [1977] or the report of *Sutherland* [1975]. Many of the empirical results depend on the careful experimental results of *Harris* [1963, 1966] and *Harris and Tempest* [1964]. The suggestion of *Piercy* [1969] that at frequencies below about 4 kHz the vibrational modes of N_2 in addition to those of O_2 play an important role in absorption brought about agreement between theoretical predictions, such as those of *Evans et al.* [1972], and experimental values.

Given an (infinite) plane sound wave with an intensity (ensonification or energy flux density) S_0 at the origin and an intensity S after propagation over a path length L (m) in a direction perpendicular to the phase fronts, the equation

Definition of attenuation coefficient

$$aL = 10 \log (S_0/S) \tag{9}$$

defines the absorption coefficient a in decibels per meter. Clearly, any finite source will have additional losses caused by diffraction ('spreading losses'). These losses in the far field vary inversely as the square of the distance. Additional losses are caused by turbulent scattering ('excess attenuation'), considered in a later section of this paper.

A simplified but adequate model of absorption divides the absorption coefficient into contributions from classical viscous losses (cl), molecular rotation losses (rot), and molecular vibration losses (vib) in the principal atmospheric components, O_2 and N_2. The latter two losses typify so-called relaxation processes. For molecules with internal degrees of freedom, some of the kinetic energy imparted to the molecules by the sound transfers to internal energy modes. Then the internal energy more or less slowly transforms back (relaxation) to translational energy but is now more or less out of phase with the initial wave. In air, third-body collisions with water vapor molecules drastically affect the rate of such relaxation. In accordance with this physical picture the absorption coefficient takes on the form

Contributions to the absorption coefficient

$$a = a_{\text{cl}} + a_{\text{rot}} + a_{\text{vib}}(O_2) + a_{\text{vib}}(N_2) \tag{10}$$

For the sum of the classical and rotational contributions to the absorption coefficient a the report of *Sutherland* [1975] recommends the equation

Empirical form of classical and
rotational absorption

$$a_{\text{cl}} + a_{\text{rot}} = 5.847 \times 10^{-10} \frac{p_0/p}{(T_0/T) + 2.654} f^2 \text{ dB m}^{-1} \tag{11}$$

where f is in hertz, p is the pressure (p_0 = 101,325 N m^{-2}), and T is the absolute temperature (T_0 = 293 K). Equation (10) combines the constants in Sutherland's equation in a slightly different way. Thus at 'room temperature' and 1 atm the contribution amounts to $1.6 \times 10^{-7} f^2$ dB km^{-1}, for practical purposes a negligible amount until the frequency rises above about 3000 Hz.

The vibrational contributions to the absorption coefficient assume an especially simple form when they are expressed as a loss per wavelength. When $\alpha = a\lambda$, each molecular species adds an amount

Resonance form for vibrational absorption

$$\alpha_{\text{vib}} = \alpha_{\max} \frac{2f/f_r}{1 + (f/f_r)^2} \text{ dB} \tag{12}$$

where f_r represents the frequency of the particular absorption peak and $\alpha_{\max}$ the magnitude of α_{vib} at the peak. The parameter $\alpha_{\max}$ depends on temperature but not on humidity. In contrast, f_r depends on both temperature and humidity. Most of the literature uses the dimensionless loss in nepers per wavelength, $\hat{\alpha}_{\max}$, in place of $\alpha_{\max}$ in decibels; thus $\alpha_{\max} = 10(\log e)\hat{\alpha}_{\max} = 4.343\hat{\alpha}_{\max}$. Figure 7, from *Sutherland* [1975], shows the behavior of $\hat{\alpha}_{\max}(O_2)$ and $\hat{\alpha}_{\max}(N_2)$.

The following empirical formula from *Sutherland* [1975] gives the relaxation frequency for O_2, abbreviated as f_o:

Empirical expression for O_2 resonance peak

$$f_o \frac{T/T_0}{p/p_0} = 24 + 44{,}100q \frac{0.05 + q}{0.391 + q} \text{ Hz} \tag{13}$$

where q represents the mole ratio (in percent) of H_2O molecules to the total number. In terms of vapor pressure e, q = $100e/p$ mol % ratio. Similarly, and again from *Sutherland* [1975], the relaxation frequency for N_2, abbreviated as f_n, has the empirical representation

Empirical expression for N_2 resonance peak

$$f_n \frac{T/T_0}{p/p_0} = 9 + 350q \text{ Hz} \tag{14}$$

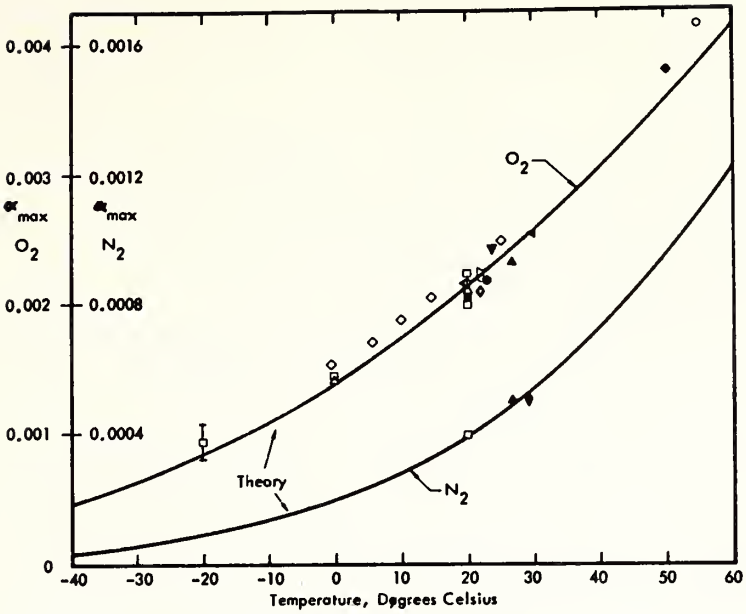

Fig. 7. Maximum absorption coefficients per wavelength due to O_2 and N_2 [from *Sutherland*, 1975].

Use, of course, requires conversion of the values of α_{vib} found from (11) to the ordinary absorption coefficient by the relation $a_{vib} = \alpha_{vib} f/c$ with $c = 343.15(T/T_0)^{1/2}$ m s^{-1}. Figure 8, from *Sutherland* [1975], shows the qualitative behavior of both the total absorption coefficient a and the absorption per wavelength, α.

Sound in Fogs

Propagation of sound in fog historically represents the second problem, after effects of mean wind, to arise in atmospheric acoustics. *Derham* [1708] concluded that fog introduced extra attentuation and thus inhibited the propagation of sound. *Tyndall* [1874] carried out field experiments that contradicted Derham's results. Tyndall suggested that the decrease in temperature fluctuations associated with fog conditions could explain observations of decreased attenuation of sound through fogs. Only the last decade has brought a resolution of the controversy: in the low audible and infrasonic range, heat and momentum transfer relaxations and mass transfer and latent heat release between droplets and vapor cause increased attenuation; above the relaxation frequencies, however, attenuation in fog becomes lower than that associated with water vapor.

A satisfactory theory of sound in fogs became possible with the development of a model that treated the 'sea' of water droplets as a continuum, a third gas added to the air-water vapor mixture. *Marble* [1969] and *Marble and Wooten* [1970] developed equations for such a mixture. *Cole and Dobbins* [1970, 1971] obtained both numerical predictions, from a similar theory, and experimental results, which did not entirely agree with their predictions. *Davidson* [1975] found that *Cole and Dobbins* [1970] had discarded some terms of the same order as those retained in their final equations. Reintroduction of such terms led to satisfactory agreement between the revised predictions found by *Davidson* [1975] and the observations of *Cole and Dobbins* [1971]. *Einaudi and Lalas* [1973] used a similar model to analyze the propagation of internal waves ('gravity waves') in the atmosphere. For infrasound the same mechanism that produces increased attentuation causes a slight amount of dispersion (frequency dependence of the sound speed).

Two dimensionless numbers simplify a discussion of the results of the above authors. The first, the Prandtl number $Pr = c_p\mu_m/\kappa_m$ (where c_p is the specific heat at constant pressure, μ_m the shear viscosity of the mixture, and κ_m the thermal conductivity of the mixture), represents the ratio of energy dissipated by viscosity to energy transferred by heat conduction. The second, the Lewis number $Le = \kappa_m/(\rho_m c_p D_m)$ (where ρ_m is the density and D_m the thermal diffusion coefficient of the mixture), represents the ratio of energy transferred by heat conduction to energy transferred by thermal diffusion. From Appendix B of *Davidson* [1975] we can define a basic characteristic time $\tau_0 = 2\pi(\rho_l/\rho_m)(r_l^2/3\nu_m)$, where ρ_l is the density of the liquid phase, r_l the liquid droplet radius, and ν_m the kinematic viscosity of the mixture (the introduction of the factor 2π permits expressing all frequencies in hertz). Then the characteristic relaxation times associated with interchange (between vapor and droplets) of momentum, heat, and mass become $\tau_{mom} = \frac{2}{3}\tau_0$, $\tau_{therm} = Pr\cdot\tau_0$, and $\tau_{mass} = Le\cdot Pr\cdot\tau_0$, respectively. But for air and light fogs, $Pr \approx 0.75$ and $Le \approx 0.84$ imply that all the characteristic times have the same order of magnitude.

As an example, for large fog droplets with $r_l = 10\ \mu$m, $\nu_m = 0.1$ cm^2 s^{-1}, $\rho_l = 1$ g cm^{-3}, and $\rho_m = 10^{-3}$ g cm^{-3}, the characteristic time τ_0 becomes $\tau_0 = 0.06$ s, corresponding to a frequency of 16 Hz. However, the solutions of the equations for the above model show that two peaks in the attenuation exist. For practical purposes the highest of these satisfies the equation $f\tau_0 = 1$, where f is in hertz. But a much lower peak, related to mass (and latent heat) effects, also exists. The position of the lower peak always lies in the infrasound region (or below) and depends on the mass fraction Q_l of water droplets to the mass of the air-water vapor mixture according to the equation $f\tau_0 = Q_l$ (using the same molecular weight factor that appeared in the equation for absorption by molecules shows that $Q_l = 0.621q_l$, where q_l is the mole fraction of liquid

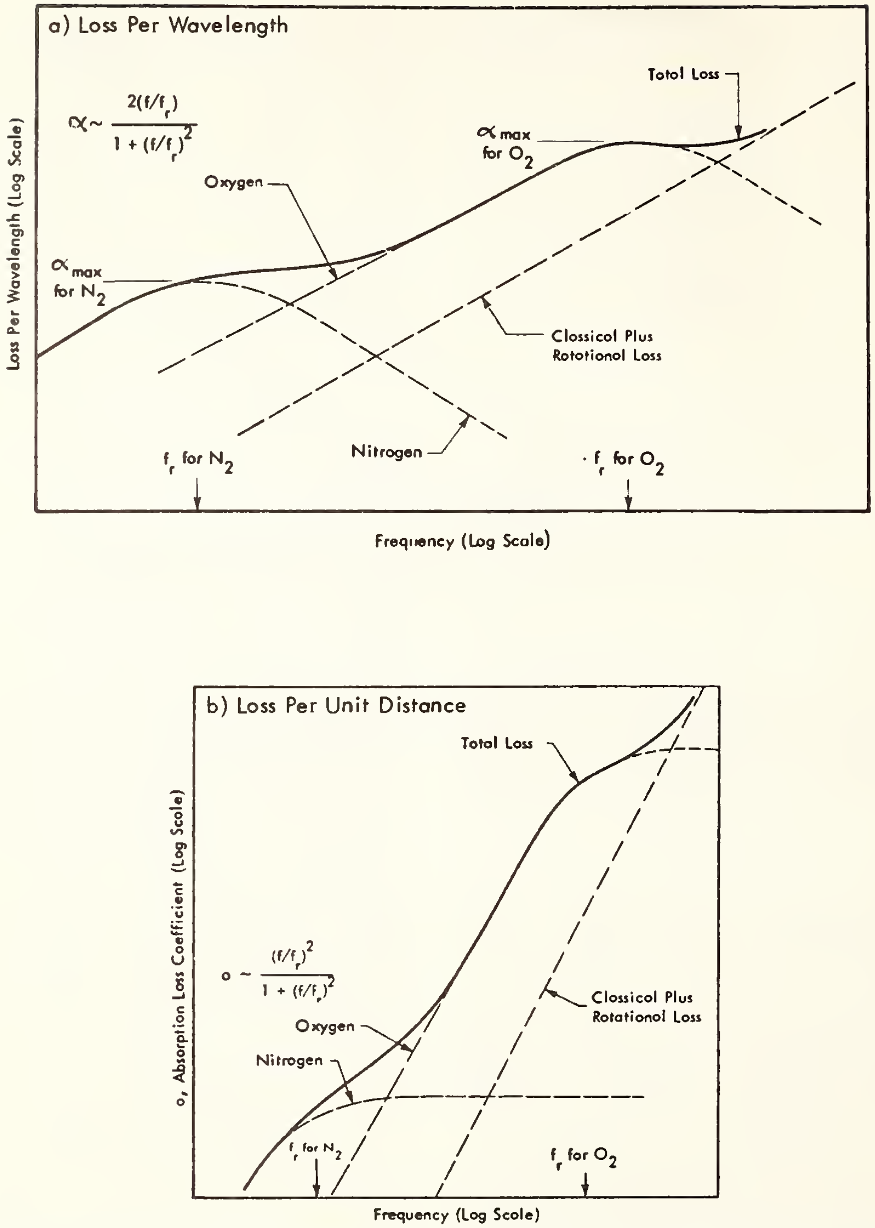

Fig. 8. Schematic behavior of absorption coefficient per unit wavelength α and per unit distance a. [from *Sutherland*, 1975].

droplets). A value of $Q_l = 0.001$ is typical for fogs, and a value of $Q_l = 0.01$ is probably the upper limit of the range. Thus the highest values of attenuation in fogs appear at frequencies below 1 Hz, or at periods of about 6–60 s. Figure 9, from Davidson, gives an illustrative example for the variation of attenuation with frequency. The figure shows values of the dimensionless attenuation $2\pi\tilde{\alpha}$ in nepers per wavelength as a function of the dimensionless frequency $f\tau_0$.

Nonlinear Effects

As a particular kind of fluid flow, sound waves must satisfy the conservation equations (of mass, momentum, and energy) of fluid mechanics and, in addition, the special conditions that distinguish sound from other fluid motions such as steady laminar flow or turbulence. As a consequence, sound waves do not obey the 'wave equation' (*Whitham* [1974] justly remarks that the wave equation does not govern the motions of the majority of waves). The wave equation for sound results only from the linear approximation of 'very small' amplitudes. But, as an example, the acoustic power output of recently developed echosondes has risen to the point at which nonlinear motions in front of the transmitters or in the feed horns may seriously affect performance.

If we denote the velocity of a particle in a sound wave by $\mathbf{u} = u_i$, the equations contain terms that lead to an 'interaction of the sound with itself.' As long as the magnitude $u = |\mathbf{u}|$ remains very much smaller than the average phase velocity c of the wave, the nonlinear term has a negligible effect. But with

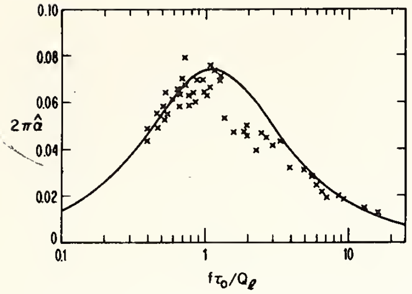

Fig. 9. Absorption coefficient $2\pi\hat{\alpha}$ ($\hat{\alpha}$ in nepers per wavelength) due to fog as a function of nondimensional frequency $f\tau_0/Q_l$, where f is the sound frequency in hertz, Q_l is the mass fraction of water droplets, and τ_0 is the characteristic time of the mixture [from *Davidson*, 1975].

increasing u (so-called 'finite-amplitude' sound) a number of phenomena appear that spring from this essential nonlinearity. Most important, at any point within each positive velocity half cycle the instantaneous phase velocity becomes $c + 1.2u$, and within the negative velocity half cycle, $c - 1.2u$. (The factor $(\gamma + 1)/2 = 1.2$ arises from convection and the relation between adiabatic pressure and density changes in a perfect gas.) As a result the crests of a simple sine wave begin to overtake the zeros, while the negative portions lag increasingly. At some point a shock front for each cycle begins to form, and shortly afterward the wave becomes distorted into a sawtooth.

Fourier analysis shows that the distortion appearing in the wave form of finite amplitude sound represents a flow of energy out of the fundamental frequency into higher harmonics. Since sound absorptivity varies as f^2, the appearance of higher frequencies results in greatly increased attenuation. Ultimately, even with increasing input power, nonlinear effects prevent any increase in the wave amplitude at a distant point in a sound beam, a phenomenon best called 'nonlinear saturation' (as distinct from the process of 'turbulent saturation,' discussed later). A large body of literature has arisen both on the mathematical theory of nonlinear propagation and on the applications to underwater sound. This review considers only the literature that has immediate applications to atmospheric acoustics, referring the reader to the article of *Blackstock* [1972] for broader theoretical background.

A paper of *Shooter et al.* [1974] contains a very readable description of the increasing distortion with path length of a sufficiently intense sound wave, together with expressions for the characteristic distances associated with each stage: the distance $\bar{r}$ for shock formation, the distance $\hat{r}$ for a fully developed sawtooth or N wave, and the 'old-age' distance $r_{\max}$, where the wave returns to an approximately sinusoidal form of greatly reduced amplitude propagating linearly. The same authors obtain results applicable to the nonlinear saturation of sound in air (although their data concern only underwater sound), the phenomenon predicted by *King* [1919] and first observed by *Allen* [1950]. Shooter et al. also consider the deterioration of the beam pattern of a transmitter produced by nonlinear effects. Beam broadening attenuates the high-amplitude sound in the main lobe more than the weaker sound in the side lobes. *Lockwood et al.* [1973] also have studied the dependence on direction of the generation of higher harmonics by nonlinearity. *Fenlon* [1971] has given a method for calculating saturation in spherical waves from the acoustic Burgers' equation, but again his comparisons between theory and experiment refer only to underwater sound. *Pestorius* [1973] analyzed an alternative method, a revision of the so-called 'weak shock' theory, and *Pestorius and Williams* [1974] discussed the limits for the use of the weak shock approach. This review does not try to cover the work of a number of other researchers on the special problem of high-intensity sound in pipes, even though the results may have important applications to transducer or horn design.

Just as nonlinearity results in a self-interaction of a sound beam, the same phenomenon permits interference with respect to the parallel components of the particle velocities of two sound beams of different frequencies. (That perpendicular particle velocities would not affect each other seems almost immediately clear on physical grounds.) A study of such nonlinear interaction between two sound beams led *Westervelt* [1963] to suggest the application known as a 'parametric array.' In such an array a high-frequency primary interacts with a primary of slightly lower frequency to create a secondary wave beam having a low frequency equal to the difference between the original two frequencies. The fact that the difference frequency beam originates physically from the long, extended and tapered region of nonlinear interaction in front of the actual transmitters implies that diffraction and side lobes become negligible. However, the applications of such arrays appear to show greater promise for underwater sound than for atmospheric acoustics, since the side lobe suppression costs additional amounts of power. *M. B. Bennett and D. T. Blackstock* [1975] have achieved such side lobe suppression with a parametric array operating in air. An earlier work of *Muir* [1971] also studied the parametric array. But the antenna design used in typical present-day echosondes (using feed horns, reflecting dishes, and flared absorbing cuffs) can easily, and more cheaply, match or better the beam patterns of parametric arrays, at least in their present state of development.

In a study of jet engine noise, *Ffowcs Williams* [1974] noted that for the high-intensity noise the wave form appeared as a sequence of sharp spikes rather than the expected sawtooth. An accompanying theoretical study indicated that such an extreme wave form follows from the spatially extended nature of the source. The study developed the solution for high-intensity sound from a sphere in a Taylor expansion and then showed that energy tends to flow from the first term of the expansion to the second and, presumably, with still more intense sound to still higher-order terms. Theobald et al. noticed similar spiking in the radiation field of an exponential horn similar to the horns used in echosonde antennas. Such results are discussed briefly by *Theobald* [1977] and *Webster* [1976]. They relate the effect to a diffraction phenomenon associated with finite piston sources in which the wave diffracted from the edge of the piston combines with the wave radiated directly from the piston face in such a way that the far field wave form becomes the derivative of the signal near the piston. Thus a sawtooth near the piston would become a sequence of spikes in the far field. Since the second term in a Taylor expansion determines the strength of the first derivative of a function, the explanations of Theobald et al. and Ffowcs Williams represent the same physical process. Clearly, this phenomenon may severely limit higher-powered echosonde antennas.

Interaction of Sound With Turbulence

Separating Sound From Turbulence

The title of this section suggests that a clear distinction exists between the fluid motion called sound and that called turbulence. We think of sound as a wave motion and of turbulence as a random velocity field. Now we must consider flows that are simultaneously waves and random motions, recognizing that even the word 'wave' has no precise meaning. *Whitham* [1974] adopts, but it is not completely happy with, the definition by *Tolstoy* [1973] that a wave is a process that transfers energy from one point at one time to a distant point at a later time without a corresponding transfer of mass. Clearly, the definition does not cover the possibility of treating a moving electron as a de Broglie wave. Physics cannot be neatly packaged. In fact, our definitions of sound and turbulence can be only approximate and will fail outside of certain limits. Instead, we must circle around a phenomenon in a series of partial descriptions that ultimately will give the reader a pragmatic understanding.

One such description, one used in some form by so many authors that it can almost be considered classic, depends on two approximations: first, that the density changes in sound represent a reversible adiabatic process, that is, that the entropy of each 'particle' or 'parcel' of air remains constant in time (particles are not molecules); and second, that turbulence represents an incompressible random flow, that is, that the density of each particle remains constant. The adiabatic condition fails to hold when the frequency of the sound increases toward the molecular collision frequency and, for the lowest infrasound at the other end of the spectrum, when the radiative absorption studied by *Gille* [1968] and others begins to have a slight effect. In typical atmospheric conditions, turbulence behaves in approximately the same way as in an incompressible fluid. But since turbulence itself produces random aerodynamic sound, the approximation can hold only if we either neglect some minimum noise level or restrict the intensity of turbulence considered.

Making use of the above approximations involves the tricky step of getting them into the equations of motion. That is, we must find an unambiguous way to separate the particle velocity $\mathbf{v}$ into a part $\mathbf{w}$ associated with turbulence and a part $\mathbf{u}$ associated with sound. Following *Tatarskii* [1971] or *Brown* [1972], for example, we can 'freeze' the dynamic and thermodynamic states of the fluid at successive points in time. Then at each point we can apply temporary additional pressure or body forces that selectively compress or expand the particles (or parcels) of fluid isentropically to the densities $\rho_0(\mathbf{X})$ that they would have in the absence of both sound and turbulence. Here we use the 'material' coordinates $\mathbf{X}$ to label each particle of fluid to distinguish from the geometric coordinates $\mathbf{x}$ of a point in space; also, we will need the symbols $\nabla = \partial/\partial\mathbf{x} = \partial/\partial x_i$ and $\partial_t = \partial/\partial t$.

For each time t we denote the velocity of a particle after each adiabatic process by $\mathbf{w}(\mathbf{X})$ but require the velocity to remain unchanged, that is, $\mathbf{w}(\mathbf{X}) = \mathbf{v}(\mathbf{X})$. Since particles must move about during the adiabatic process to permit the desired adjustments in the density ρ, we must also have $\mathbf{w}(\mathbf{x}) \neq \mathbf{v}(\mathbf{x})$; that is, we have defined (almost!) a new velocity field $\mathbf{w}(\mathbf{x})$ associated with incompressible turbulence. This procedure is not unique since, for example, with a given spherical density concentration, each particle could move either on radial or spiral paths during the rearrangement. To remove this ambiguity, we introduce here a third assumption. Although $\mathbf{w}(\mathbf{X}) = \mathbf{v}(\mathbf{X})$, the particle displacements during the adiabatic process require $\nabla\mathbf{w}(\mathbf{X}) \neq \nabla\mathbf{v}(\mathbf{X})$. But except for sound near boundary surfaces and except for infrasound the vorticity associated with sound is negligible. Turbulence, on the other hand, as a three-dimensional random velocity field, necessarily possesses nonvanishing vorticity. Thus introducing the third condition, that $\nabla \times \mathbf{w}(\mathbf{X}) = \nabla \times \mathbf{v}(\mathbf{X})$, leads to a unique turbulent velocity field $\mathbf{w}(\mathbf{x})$ and a unique sound particle velocity field $\mathbf{u}(\mathbf{x}) = \mathbf{v}(\mathbf{x}) - \mathbf{w}(\mathbf{x})$. We note in passing that the above procedure also requires $\partial_t\mathbf{w}(\mathbf{X}, t) = \partial_t\mathbf{v}(\mathbf{X}, t)$, but $\partial_t\mathbf{w}(\mathbf{x}, t) \neq \partial_t\mathbf{v}(\mathbf{x}, t)$. Again, however, our procedure must have limits of validity: the nonzero mean density gradient in the atmosphere implies that particle paths gradually change from line segments to ellipses on descending to the infrasound region, which in turn implies nonvanishing vorticity. And even in the audible range the boundary condition that the tangential component of the particle velocity must vanish at solid surfaces cannot be met in general without some vorticity. However, *Skudrzyk* [1971] suggests that at 1000 Hz such vorticity is confined to a film less than 0.06 mm thick.

The above description of the separation of sound and turbulence becomes less useful in certain areas, such as infrasound. We can obtain a second description if, in Tolstoy's definition of a wave, we replace the word 'energy' by 'information'. In information theory the complement of information is entropy (here the entropy associated with the velocity fluctuations, not the entropy of the gas). Thus information is a result of wave propagation, and entropy is a result of turbulence, the process that decreases the information observable with increasing propagation time. Despite the abstract nature of this second approach, its usefulness lies almost entirely in the procedures of observation; as yet, no attempt has been made to use it in the equations or theory of sound propagation. *Georges and Young* [1972] briefly discuss the method as applied to separation of infrasound signals from the pressure fluctuations associated with turbulence and other noise.

In the simplest form of the method, signals at one or more receivers are correlated by using various time delays. The delay giving maximum correlation provides the horizontal velocity and direction of the wave, and the correlation process itself tends to remove noise and maximize information in the signal. However, the method depends to a certain extent on the existence of a recognizable 'signature,' that is, on sufficient information. A more sophisticated technique suggested by *Gossard* [1967] depends on first Fourier analyzing the signal and then correlating only the same frequency components. Although the method is useful for more complicated signals, it would still fail, for instance, for sound in the form of a band of white noise and also for the sound generated by turbulence aerodynamically. A separate and distinct method of removing turbulent pressure fluctuations uses spatial averaging: for a given frequency range, acoustic waves have longer wavelengths (higher speeds) than the turbulence, allowing spatial filtering of 'shorter-wavelength' turbulence.

We mention only briefly a third approach that avoids the whole problem of separating sound from turbulence by adopting a form of the random wave equation 'by assumption' and then studying its solutions for whatever cases of sound propagation may happen to satisfy it. This is the approach followed by the first book of *Tatarskii* [1961] (the second book [*Tatarskii*, 1971] uses the more correct approach, described above). This approach is used as well in the early work of *Mintzer* [1953*a*, *b*, 1954]. However, as was remarked by *Batchelor* [1957], 'this procedure has its dangers, since mistakes in the form of the governing equations cannot be detected by the usual checks on consistency of the analysis . . . the ideas are plausible, but actually they are too simple, and lead to correct results only in special circumstances.'

General Equations

The three conditions of the first approach, described above, that sound is adiabatic and rotationless, whereas turbulence is incompressible, could lead to very general equations for sound propagation. But since the resulting equations would be quite unwieldy, two additional assumptions are introduced that abandon any attempt to treat both turbulent and nonlinear effects simultaneously. Let A represent any normalized acoustic variable (random or not), and T any normalized turbulence variable. Then the equations of sound propagation are enormously simplified if all terms of order A^2 or higher and all terms of order AT^2 or higher are dropped.

Before giving the resulting equations we need to introduce some notation regarding temporal and spatial wave number space, in particular, the Fourier transforms $\mathfrak{F}_t$ and $\mathfrak{F}_{\mathbf{x}}$ defined by

Fourier time transform

$$F(k) = c_0 F(\omega) = \mathfrak{F}_t\{f(t)\} = (2\pi)^{-1} c_0 \int_{-\infty}^{\infty} dt\,(\exp ikc_0 t) f(t)$$

$$f(t) = \mathfrak{F}_k{}^{\dagger}\{F(k)\} = \int_{-\infty}^{\infty} \backslash dk\,(\exp -ikc_0 t) f(k) \tag{15}$$

where $k = \omega/c_0$ and the dagger indicates the complex conjugate or inverse transform, and

Fourier space transform

$$F(\boldsymbol{\kappa}) = \mathfrak{F}_{\mathbf{x}}\{f(\mathbf{x})\} = (2\pi)^{-3} \int_{-\infty}^{\infty} d^3\mathbf{x}\,(\exp -i\boldsymbol{\kappa}\cdot\mathbf{x}) f(\mathbf{x})$$

$$f(\mathbf{x}) = \mathfrak{F}_{\kappa}{}^{\dagger}\{F(\boldsymbol{\kappa})\} = \int_{-\infty}^{\infty} d^3\boldsymbol{\kappa}\,(\exp i\boldsymbol{\kappa}\cdot\mathbf{x}) F(\boldsymbol{\kappa}) \tag{16}$$

where c_0 is the constant sound speed in the absence of turbulence and where $\boldsymbol{\kappa} = \kappa_i$ are the spatial Fourier coordinates. After Fourier transform of functions, ordinary multiplications transform into the convolution products given by

Definition of one-dimensional convolutions

$$\mathfrak{F}_t\{f(t)g(t)\} = F(k) * G(k) = \int_{-\infty}^{\infty} dk'\, F(k-k')G(k')$$

$$\mathfrak{F}_k{}^{\dagger}\{F(k)G(k)\} = f(t) * g(t) = \int_{-\infty}^{\infty} dt' f(t-t')g(t') \tag{17}$$

Definition of three-dimensional convolutions

$$\mathfrak{F}_{\mathbf{x}}\{f(\mathbf{x})g(\mathbf{x})\} = F(\boldsymbol{\kappa}) \odot G(\boldsymbol{\kappa}) = \int_{-\infty}^{\infty} d^3\boldsymbol{\kappa}'\, F(\boldsymbol{\kappa}-\boldsymbol{\kappa}')G(\boldsymbol{\kappa}')$$

$$\mathfrak{F}_{\kappa}{}^{\dagger}\{F(\boldsymbol{\kappa})G(\boldsymbol{\kappa})\} = f(\mathbf{x}) \odot g(\mathbf{x}) = \int_{-\infty}^{\infty} d^3\mathbf{x}'\, f(\mathbf{x}-\mathbf{x}')g(\mathbf{x}') \tag{18}$$

Since for the linear case (neglecting terms A^2) the Fourier transforms of the acoustic pressure p_α and the ratio of the acoustic density to turbulent density, ρ_α/ρ_σ, differ only by a constant, that is, $p_\alpha/p_0 = \gamma\rho_\alpha/\rho_\sigma$, we will use $P(k)$ for either. (We note that density changes are more fundamentally associated with sound but that pressure changes are the only true observables.) In addition to neglecting A^2 and AT^2 terms, *Tatarskii* [1971] assumed zero mean wind and rates of change of the turbulence very much less than the acoustic frequency ('frozen turbulence'). Thus *Tatarskii* [1971] obtained the acoustic equation

Acoustic equation for zero-wind
frozen turbulence

$$\nabla^2 P + k^2 P = 2\partial_j(N'\partial_j P) + 2ik^{-1}\partial_j\partial_h(M_j{}'\partial_h P) \tag{19}$$

where $N'(\mathbf{x})$ is the fluctuation in refractive index and $\mathbf{M}' = M_i{}' = W_i{}'/c_0$ is the time Fourier transform of the turbulence Mach vector given by the fluctuations of the velocity from the mean. If we write P_0 for the acoustic field that would exist in the absence of turbulence, the 'Born approximation' consists of replacing P by P_0 in the right-hand side of (19), that is, in the terms containing the fluctuations N' and $M_i{}'$. Then the unit vector $\mathbf{e} = e_i$ normal to a phase front of the initial wave P_0 is nonrandom. Consequently, we can write an 'effective refractivity fluctuation' in the form used by *Monin* [1962]:

Definition of effective refractivity

$$N_e{}' = N' - \mathbf{e}\cdot\mathbf{M}' \tag{20}$$

Using the effective refractivity leads to a simplied form of (18), that is,

Born approximation to acoustic equation

$$\nabla^2 P_1 + k^2 P_1 = 2\partial_i(N_e{}'\partial_i P_0) \tag{21}$$

where the acoustic field has been split into the initial and scattered fields, $P = P_0 + P_1$. If we denote ensemble averaging by angle brackets, then $P_1 = \langle P_1\rangle + P_1{}'$, and $\langle P_1{}'\rangle = 0$. We should emphasize that only in the Born approximation is it true that $\langle P_1\rangle = 0$ and $P_1 = P'$.

If sound is transmitted from (or received by) an antenna fixed on the ground into (or from) an atmosphere moving with some mean wind $\bar{\mathrm{w}}$, or if the turbulence is not frozen, we can no longer neglect time changes. But we can obtain a more general equation (see Appendix A):

Acoustic equation

$$\nabla^2 P + (k + i\bar{\mathbf{M}}\cdot\nabla)^2 P = 2\partial_j(N' * \partial_j P) + 2i\partial_j\partial_h[M_j{}' * (k^{-1}\partial_h P)] \tag{22}$$

where $\bar{\mathbf{M}}$ is the mean wind Mach vector. By using the Born approximation, *Brown* [1972] obtained a simplified form of (22), not recognizing that the more general form followed directly from the A^2 and AT^2 assumptions. We emphasize that (22) permits both a nonzero mean wind and a nonnegligible evolution of turbulence with time. *Krasil'nikov and Pavlov* [1975] and *Goncharov et al.* [1976] have studied an alternative Hamiltonian formulation that takes into account gradients in atmospheric properties.

All of the above equations have assumed negligible shear viscosity μ_v and volume viscosity λ_v. *Clifford and Brown* [1970] studied the effect of nonnegligible viscosity on the solutions in the first-order approximation (which will be discussed later). Defining a length $l_v = (2\mu_v + \lambda_v)/(2\rho_0 c_0)$, these authors show that for $l_v \ll l_0$, viscosity effects can be accounted for in (21) by replacing k by the quantity $h = k(1 + ikl_v)$ and the effective refractivity $N_e{}'$ by $\tilde{N}_e{}' = (h^2/k^2)N_e{}'$ (l_0 is the 'inner scale' of turbulence, the size of the smallest correlations, or eddies). Since they retain the imaginary part of h only in the phase for their subsequent analysis, they actually write down only the real part of $\tilde{N}_e{}'$. However, the main result of their analysis is that for reasonable values of the 'outer scale' of turbulence L_0 ($L_0 \geq 1$ m) the spectrum of turbulence causes a more rapid decay than absorption in the first-order two-dimensional amplitude and phase spectra as the magnitude of the two-dimensional spatial wave number approaches the temporal wave number k. In consequence, most of the single-scattering results found by Tatarskii with the restriction $\lambda \ll l_0$ can be applied for the weaker condition $\lambda \leq L_0$. As far as we know, no similar results have yet been published for the case of acoustic propagation through strong turbulence, in which the single-scatter assumption becomes invalid.

As was mentioned above, a number of other authors have extensively analyzed the 'random wave equation' or its Fourier counterpart, the random Helmholtz equation, which may govern the propagation of sound in certain cases. In the absence of motion the random wave equation merely replaces the static sound speed c_0 by a random speed $c(\mathbf{x}, t)$. With velocity fluctuations $\mathbf{w}(\mathbf{x}, t)$ as well, this approach requires replacement of the time derivative ∂_t by the random 'substantial derivative' $d_t = \partial_t + \mathbf{w} \cdot \nabla$. Analyses using the random wave equation include those of *Neubert* [1970], *Neubert and Lumley* [1970, 1972], *Wenzel and Keller* [1971] (who also study more general sound equations, but not in turbulence), *Wenzel* [1972], and *Rosenbaum* [1972].

Interaction Mechanisms

Like many words, 'propagation' and 'scattering' have a number of different meanings. For example, the particular case of refraction of a wave moving in the direction of a smooth refractivity gradient can be called 'coherent forward scatter.' Here we wish to use the words only in much more restricted senses. At the same time, our attempt to make the terms more precise will again result in a more approximate correspondence with actual physical processes. We will use the following definition of scattering (one which might better be called 'simple scattering'): if we produce an initial wave P_0, if we can choose (say, by gating) a finite region of time, space, or propagation direction in which P_0 is zero, and if we can find an acoustic wave P_1 propagating in this region, then we will call P_1 the 'scattered' wave produced by the interaction of P_0 with a volume V_s of scatterers. The much more complex process in which both P_0 and P_1 propagate in the same region and interfere with each other will be called simply 'propagation.' Since scattering spreads a part of the initial energy flowing in one direction into a distribution over many directions, the magnitude of the intensity of the scattered wave at one scattering angle θ_s is always very much less than the initial intensity. Consequently, we can frequently treat scattering by the Born or 'single-scatter' approximation. The single-scatter approximation assumes that if a portion of the wave has been scattered once by the turbulence, most of the time the scattered wave will reach the receiver without being scattered again; the approximation does not imply that there is only a single scatterer, a single interacting center. In contrast, the Born approximation for propagation (frequently called 'line-of-sight' propagation) usually leads to more restricted predictions, given typical path lengths and intensities of atmospheric turbulence.

The right-hand side of (22) clearly shows that the physical process of acoustic wave interaction with turbulence depends on the fluctuations in refractive index N', which in turn depend on fluctuations in temperature T' and water vapor pressure e', and on fluctuations in the turbulence Mach vector $\mathbf{M}' = \mathbf{W}'/c_0$. Consider first only fluctuations in temperature. For homogeneous turbulence, *Kraichnan* [1953] showed that since T' fluctuations are proportional to the turbulent pressure fluctuations that are second order in M', interaction with temperature fluctuations can be neglected. But, as usually occurs in the atmosphere, the existence of a mean potential temperature gradient leads to a quite different conclusion. If both turbulence and potential temperature gradients exist together, the turbulence will mix particles of air having different potential temperatures. In consequence, the resulting turbulent mixture can have normalized temperature fluctuations of the same order of magnitude as normalized velocity fluctuations. Note that a potential temperature gradient rather than a temperature gradient is required. Also, note that it is entirely possible to have a potential temperature gradient with little turbulence and, conversely, to have turbulence due to wind shear when the mean potential temperature gradient is small. The requirement of simultaneous gradients and turbulence has considerable significance for the interpretation of monostatic echosonde facsimile records.

When sound travels through a region of random refractivity fluctuations N', the various points on the phase fronts travel with different random velocities. Applying Huygens' principle to the resulting irregular phase fronts shows that a part of the energy flux is redirected into random forward directions different from the direction of the initial wave. However, with large enough refractivity gradients, backward traveling or reflected waves are also produced. For an actual plane discontinuity ΔN the classical Fresnel formula gives a power reflection coefficient Γ^2 equal to $\Gamma_0^2 = |\Delta N/2|^2$. For smooth refractivity profiles the power reflection coefficient may be obtained by integrating over the profile. For a profile of a layer of thickness l, *Ottersten* [1970] found that Γ^2 is within 70% of Γ_0^2 when $l/\lambda < 0.1$ but that Γ^2 drops to less than 1% of Γ_0^2 when $l/\lambda > 0.5$. Thus if turbulence has sufficiently large random refractivity gradients, sound will be scattered into the backward hemisphere as well as into forward scatter angles. However, a peculiarity of acoustic-turbulence interactions implies that no energy will be scattered at $\theta_s = 90°$ from either N or $\mathbf{M}$ fluctuations. This peculiarity arises from the fact that the derivatives of N' and $\mathbf{M}'$, as well as N' and $\mathbf{M}'$ themselves, appear in (22), the acoustic equation.

In the discussion of the separation of turbulent motions from sound waves we noted that with a slow push against the atmosphere the air behaves like an incompressible fluid, merely flowing around the moving object. With a rapid push, however, like that from a transducer or an explosion, sound is produced. This behavior implies that slow motions cannot couple with fast motions but merely advect them. Turbulent motions, then, produce a vector addition of the random turbulence velocity fluctuations to the phase velocities of the waves. When the waves have traveled far enough into the turbulence to have random wave vectors in the forward hemisphere, the components of the wave vectors in the plane perpendicular to the initial direction of propagation may be of the same magnitude as the turbulent velocity fluctuations and result, with one exception, in scattering into the backward hemisphere as well. The exception arises because velocities are always merely the vector sum of the wave and turbulence velocities; the only components in the pure backscatter (or $\theta_s = 180°$) direction are the original turbulence velocity fluctuations. These fluctuations do not constitute a propagating wave with some nonzero mean frequency of oscillation. Thus there will be no backscatter from velocity fluctuations, and in particular, only the refractivity fluctuations will contribute to the signal in a monostatic echosonde.

We can gain further insight into the difference between scattering by refractivity fluctuations and scattering by velocity fluctuations from the following comparison. As was noted above, a sufficiently intense uniform refractivity gradient, a partial mirror, will produce a backscattered wave, a partial reflection. Assume that we could also arrange a uniform laminar flow with a gradient of velocity in the direction of the flow but without any change in refractivity. Then, if a sound wave propagated in the direction of the flow, we could expect only an acceleration or deceleration of the phase fronts by the advection of the mean motion. We could not expect the creation of a backscattered or reflected wave, since at any point we could make a Galilean transformation to a local coordinate system moving at each point with the velocity of the mean flow. Of course, the physical processes involved remain the same when we change from uniform to random gradients (although we must now add diffractive effects). We note that even when it is mathematically correct, the use of the effective refractivity N_e' in place of N' and $\mathbf{M}'$ conceals the physical differences between refraction by N' and advection by $\mathbf{M}'$.

Unlike a mirror, the atmosphere cannot sustain actual discontinuities in N' or $\mathbf{M}'$. Both types of fluctuations remain smoothly varying and are correlated over appreciable distances. Customarily, we use the distance l_0, the inner scale, as the smallest distance for which turbulence retains inertial range characteristics and L_0, the outer scale, as the largest distance for nonnegligible correlation of isotropic turbulence. Measurements indicate that l_0 varies from a few millimeters to about 1 cm, whereas L_0 lies between about 10 m and a few tens of meters. However, as was indicated earlier, correlations in anisotropic eddies may extend up to several hundred meters. Thus even though turbulence is random, the nonzero correlation distances imply a quite different kind of interaction or scattering than that from a field of randomly spaced point scatterers. As long as the wavelength λ is no greater than L_0, waves scattered from nearby regions can interfere both constructively and destructively to produce a partially coherent scattered wave. Thus the interaction itself can be described as a 'coherent scattering process.' Such a process is due to the integrated effect of many small scatterings over a nonzero region of space. Note the distinction between a coherent wave, as described in the chapter on partial coherence by Wolf [*Born and Wolf*, 1970], and the process of coherent scattering.

One practical consequence of the above distinction is that for typical acoustic wavelengths the intensities in coherent scattering are very much larger than those in incoherent scattering, such as Rayleigh scattering. A second consequence is that for backscattering the refractivity fluctuations can be treated as if they were a set of partially reflecting parallel mirrors with a spacing equal to $\lambda/2$. Or more generally, and for any scattering angle, the turbulence can be treated as a regular crystal lattice with a lattice spacing l satisfying the Bragg condition $l = (\lambda/2)/\sin(\theta_s/2)$. As long as $(\lambda/2) \leq L_0$, we can decompose the random turbulence field by a spatial Fourier transform and find a Fourier component that will satisfy the Bragg condition and produce coherent scattering. It is for this reason that Fourier transforms, and the three-dimensional spatial spectrum of the fluctuations, play such a major role in the theoretical analysis of the interaction of sound with turbulence.

Before turning to the particular processes of scattering and propagation we need to consider briefly the kinds of measurements made on sound. Unlike measurements in optical propagation, in which the wave itself, that is, the combined amplitude and phase, is difficult to observe, acoustical wave and phase measurements (such as those of *Mandics* [1971] or *Brown and Keeler* [1975]) can be performed fairly easily. But even so, most measurements, especially with echosondes, are restricted to those of acoustic power and the acoustic power spectrum. Thus we need to define two quantities, the power, or the acoustic energy flow rate per unit cross-sectional area, $S(\mathbf{x})$, and the power spectrum, or the power spectral density, $I(\mathbf{x}, k)$, the amount of energy flux per unit frequency interval per unit cross-sectional area. Since $p(\mathbf{x}, t)$ is the force per unit area and $\mathbf{u}(\mathbf{x}, t)$ is the displacement per unit time, the product $p(\mathbf{x}, t)\mathbf{u}(\mathbf{x}, t)$ is the instantaneous energy flux per unit area in the direction of $\mathbf{u}$. (Note that we are considering the real acoustic pressure and velocity rather than the complex equivalents.) For propagation of single-frequency CW sound through a nonrandom medium the energy flux density of interest is the average of $p(\mathbf{x}, t)\mathbf{u}(\mathbf{x}, t)$ over a cycle. But this definition becomes useless for multifrequency sound and for sound interacting with random velocity fluctuations in the turbulent atmosphere. Instead, we consider propagation and scattering of sound pulses with a pulse length, say, l_p, which requires us to use one of two types of 'gating' of the received signal.

For propagation we are interested in 'time gating,' that is, turning the receiver on and off for a period l_p/c_0 about the time T that the pulse passes by. Although it is less obvious, we are interested only in a similar measurement for scattering. If, for instance, we consider backscattering, for each range R the scattered signal from a pulse of length l_p comes from a region of thickness $l_p/2$; thus $l_p/2$ is the minimum spatial resolution of the atmosphere, and the corresponding region produces a scattered signal of length l_p. For scattering, then, we are interested in 'range gating,' that is, in the average of the received signal for a period l_p/c_0 about the time $2R/c_0$. This average gives us all the information that we can obtain on the $l_p/2$ thick slab of the atmosphere at the range R. Thus for both propagation and scattering the acoustic power of interest is the time average of the instantaneous power at times T or $2R/c_0$ over the pulse length l_p averaged over the ensemble of pulses:

Acoustic energy flux density

$$\mathbf{S}(\mathbf{x}) = l_p{}^{-1}c_0 \int_{-l_p/2}^{l_p/2} dt\, \langle p(\mathbf{x}, t)\mathbf{u}(\mathbf{x}, t)\rangle \tag{23}$$

If we express $p(t)$ and $\mathbf{u}(t)$ in terms of their Fourier transforms $P(k)$ and $\mathbf{U}(k) = -ik^{-1}\nabla P(k)$ and if we assume that there are many wavelengths in a pulse length (in practice, at least 10), (23) can be rewritten as

Fourier form of acoustic energy flux density

$$\mathbf{S}(\mathbf{x}) = (2\pi/l_p) \int_{-\infty}^{\infty} dk\, \langle P^\dagger(k)[-ik^{-1}\nabla P(k)]\rangle \tag{24}$$

If in addition we assume that $P(k)$ is not too broad, we can make the approximation $-ik^{-1}\nabla P(k) \approx \mathbf{e}P(k)$, where $\mathbf{e}$ is a unit vector in the direction of $\mathbf{S}$, giving

Approximate vector acoustic
energy flux density

$$\mathbf{S}(\mathbf{x}) = \mathbf{e}(2\pi/l_p) \int_{-\infty}^{\infty} dk\, \langle P(k)P^\dagger(k)\rangle \tag{25}$$

or, if we define $S(\mathbf{x}, \theta_s) = \mathbf{e}\cdot\mathbf{S}(\mathbf{x})$ with θ_s the direction of $\mathbf{S}$,

Scalar acoustic energy flux density

$$S(\mathbf{x}, \theta_s) = (2\pi/l_p) \int_{-\infty}^{\infty} dk\, \langle P(k)P^\dagger(k)\rangle \tag{26}$$

In statistical theory the 'power spectral density' of a function is defined as the Fourier transform of the autocovariance of the function. Texts such as those of *Jenkins and Watts* [1968] or *Koopmans* [1974] show that the basic definition can be modified sufficiently to account for nonergodic, or even nonstationary, processes. *Brown and Clifford* [1973*a*] have shown that such methods can also be applied to a sequence of pulses, essentially by omitting the periods of time between pulses that are of no interest. Their method consists of a double averaging procedure: the product of two pressures with a time delay τ between them is averaged in time over each pulse, creating an ensemble of random functions of τ alone with the starting time of each pulse now reduced to being merely a label for each member of the ensemble; then the doubly averaged function is Fourier transformed from τ to k to obtain the power spectral density. Using such an 'intermittent' autocovariance of the acoustic pressure, they show that the statistical power spectral density of the pressure is given by

Power spectral density

$$I(k) = (2\pi/l_p)\langle P(k)P^\dagger(k)\rangle \qquad (27)$$

Comparing (27) with (26), we see that the total power (per unit area) is just the integral of $I(k)$ over all wave numbers:

Relation between spectrum and energy flux

$$S(\mathbf{x}) = \int_{-\infty}^{\infty} dk\, I(k) \qquad (28)$$

that is, $I(k)$ is just the density of $S(\mathbf{x})$ in frequency space. Thus the statistical power spectral density of the pressure is, in fact, the acoustic power spectral density, the rate of energy flow per unit area per unit frequency interval. We note that for CW sound of wave number k_0 and with no spectral broadening, (27) reduces to $I(\mathbf{x}, k) = S(\mathbf{x})\delta(k - k_0)$, where $\delta(k - k_0)$ is the Dirac measure. (We prefer the term 'measure' rather than 'function,' since a function is an object that gives back a number (the 'value' of the function) whenever a number (the variable) is put into it. This description is not useful for $\delta(k)$ which, as a function, has the value 0 for all $k \neq 0$ and is undefined for $k = 0$. But as a measure for integration or as a 'unit' for convolution products, $\delta(k)$ has the valuable property $\delta(k - k_0) * F(k) = F(k - k_0)$ for any function $F(k)$.)

Scattering

Scattering of sound by atmospheric fluctuations in N and $\mathbf{M}$ is the physical mechanism underlying the operation of the echosonde. Measurement of the characteristics of the received signal and comparison with the known properties of the transmitted signal provide all the information acoustically obtainable about the atmosphere in the scattering volume V_s at the range R. Such a comparison must be made in several steps: first, comparison of the scattered energy flux density with the energy flux density incident on V_s; second, determination of the changes in the energy flux densities due to diffraction spreading going to and from transmitting and receiving antennas, molecular absorption, and effects of mean motions; and third, determination of the relations between acoustic signals and electrical signals. If Ω is the solid angle in the direction θ_s into which the energy flux density is scattered and if l_s is the thickness in the direction of incidence of the volume of scatterers, then $V_s = \Omega R^2 l_s$. Thus we can compare incident and scattered radiation at the scattering volume by defining the scattering cross section as the ratio of the scattered energy flux density $S(\mathbf{x}, \theta_s)$ per unit solid angle per unit thickness of scatterers to the incident energy flux density $S_0(\mathbf{x})$ or by using the above expression for V_s:

Definition of scattering cross section

$$\sigma_s(\theta_s) = R^2 S(\theta_s)/(V_s S_0) \qquad (29)$$

We note that for a plane wave, $S_0(\mathbf{x}) = (2\rho_0 c_0)^{-1} A_0^2(\mathbf{x})$, where A_0 is the amplitude of P_0.

If we introduce the incompressibility condition into the relation between wave scattering and the inertial range three-dimensional spectrum of turbulence and, in addition, use (21), the Born approximation to the acoustic equation, we can obtain an exact solution for $\sigma_s(\theta_s)$. The Green's function for the wave equation is the function satisfying the elementary equation

$$\nabla^2 G + k_0^2 G = \delta(\mathbf{x}) \qquad (30)$$

where $\delta(\mathbf{x})$ is the spatial Dirac measure. With an obvious notation we have $\delta(\mathbf{x}) = \delta(x)\delta(y)\delta(z)$ in Cartesian coordinates. The well-known solution of (30) is the Green's function

$$G(\mathbf{x}, k_0) = (-\exp ik_0 R)/(4\pi R) \qquad (31)$$

where $R = |\mathbf{x}|$. In terms of G the Born solution of (21) for frozen turbulence and zero mean wind becomes

Born approximation

$$P_1(\mathbf{x}, k_0) = 2G \odot \nabla\cdot(N_e'\nabla P_0) \qquad (32)$$

where the three-dimensional $\mathbf{x}$ space convolution is defined in (18).

Introducing (32) into (26) and (29) gives the inertial range scattering cross section as expressed by *Monin* [1962] (with our slight revision to include the effect of water vapor):

Inertial range scattering cross section

$$\sigma_s(\theta_s) = 1.52 k_0^{1/3} \cos^2\theta_s \{0.13 C_n^2 + \cos^2(\theta_s/2) C_v^2/(4c_0^2)\}[2\sin(\theta_s/2)]^{-11/3} \qquad (33)$$

where C_n^2 depends on temperature and water vapor fluctuation intensities according to (6). We see that when $\theta_s = 90°$, the scattering cross section vanishes and when $\theta_s = 180°$, only the fluctuations in N contribute to σ_s. We remark that since the size l of a turbulent eddy contributing to the scattering is $l = (\lambda/2)/\sin(\theta_s/2)$ and since $l \to \infty$ as $\theta_s \to 0$, points near $\theta_s = 0$ can never admit far field scattering (the far field is given by $R \geq 2l^2/\lambda$); in particular, we can no longer use (33) for propagation. We should expect some changes in $\sigma_s(\theta_s)$ when the mean wind is no longer zero even if the frozen turbulence condition applies in a coordinate system moving with the mean wind. *Clifford and Brown* [1974] have found the principal effect, a shift in the position of the zero cross section at $\theta_s = 90°$ to a nearby angle, resulting from rotations of the wave vectors of the initial and scattered waves. Figure 10, from their paper, gives a typical example of the effect and shows that large fluctuations may occur in measurements near $\theta_s = 90°$. For backscattering and near backscattering the presence of a mean wind makes little change in σ_s.

The remaining steps in the comparison of received power with transmitted power can be expressed in what *Neff* [1975*a*] has called the 'echosonde equation,' in analogy to the electromagnetic 'radar equation.' With a narrow angular width transmitting beam, diffraction loss in the initial energy flux density can be small over the transmitting beam path length R_0. The scattered sound, however, is always subject to such losses, which in the far field, result in a factor R_s^{-2}. Both transmitted and received beams are attenuated by molecular absorption over their respective paths. Following the approach of *Lighthill* [1953], *Huang* [1976] has shown that when a scattering volume moves away from or toward a transmitter, the rate that energy is received at the volume is decreased or raised, respectively. A similar effect occurs between the scattering volume and the receiver. If $\mathbf{e}_0$ is a unit vector in the direction of the transmitted wave, the initial energy flux density is changed by the factor $(1 + \mathbf{e}_0 \cdot \bar{\mathbf{M}})^{-1}$ on traveling to the scattering volume. And if $\mathbf{e}_s$ is the unit vector at V_s in the direction of the receiver, the scattered energy flux density is changed by the factor $(1 - \mathbf{e}_s \cdot \bar{\mathbf{M}})^{-1}$ on traveling to the receiver. At the same time the pulse length is stretched by the mean wind in such a way that the scattering volume referred to pulse lengths and beam widths at the ground is also changed by the factor $(1 + \mathbf{e}_0 \cdot \bar{\mathbf{M}})^{-1}$. Thus in a comparison of transmitted and received powers, only the factor $(1 - \mathbf{e}_s \cdot \bar{\mathbf{M}})^{-1} \approx 1 + \mathbf{e}_s \cdot \bar{\mathbf{M}}$ remains. (This is exactly the factor obtained by Huang and given in his notation by $[1 - M \cos(\theta - \phi)]^{-1}$.) Despite the changes in energy flow rate, no energy is lost or gained. Since we are considering only linear sound propagation, the total energy is merely stretched differently over the time-varying ranges between the ground and the scattering volume. For energy reflection from a rigid moving mirror the change in energy flow rate would be twice that in scattering from V_s, corresponding exactly to the Doppler frequency shift. Here, when $\mathbf{e}_0 \cdot \bar{\mathbf{M}}$ is positive, the stretching of V_s by the wind compensates for the decrease in transmitted power due to the same wind, leaving only the decrease in flow of the scattered radiation to the receiver.

If we use $\mathcal{P}_R$ for received electrical power, ϵ_R for efficiency of acoustic-to-electrical conversion, $\mathcal{P}_T$ for transmitted power, ϵ_T for efficiency of electrical-to-acoustic conversion, $\hat{a}$ for the effective intensity attenuation coefficient in nepers per meter, A_R/R_s^2 for the solid angle subtended by the antenna aperture A_R in square meters at the range R_s, A_T for the transmitter area, A_C for the area common to both transmitter and receiver beams, and g for the antenna directivity gain factor, we can write

Echosonde equation

$$\mathcal{P}_R/\epsilon_R = \epsilon_T \mathcal{P}_T \exp\left[-\hat{a}(R_0 + R_s)\right] \cdot (1 + \mathbf{e}_s \cdot \bar{\mathbf{M}}) \mathcal{A}(\theta_s)(l_p/2)(gA_R/R_s^2)\sigma_s(\theta_s) \qquad (34)$$

The dimensionless aspect factor $\mathcal{A}(\theta_s)$ equals 1 for monostatic echosondes and approximately equals A_C/A_T for angles near 180°. For the general bistatic case, exact values of $\mathcal{A}$ require computer solutions, such as those given by *Thomson and Coulter* [1974]. We can immediately check that (34) is merely the definition of σ_s in (29), rewritten with the substitution of the relations between energy fluxes at V_s and those at the transmitter and receiver. (Note that for backscatter, $\mathbf{e}_s = -\mathbf{e}_0$.) Equation (34) represents the key link between theory and experiment, the link between echosonde electrical power measurements and the values of C_n^2 and C_v^2 appearing in the theoretical relationships between wave scattering and turbulence.

In an early paper, *Ford and Meecham* [1960] studied the power spectral density $I(k)$ expected at an angle θ_s from scattering from velocity fluctuations alone. They assumed that since the scattering depends on eddies of order of magnitude $\lambda/2$, if $\lambda \ll L_0$ (with L_0 the outer scale), an approximate separation can be made of small, scattering eddies from large eddies advecting the small ones. Such a condition can be called the 'locally frozen' hypothesis. And by making a local Galilean transformation to the advecting velocity coordinate system we can apply the usual locally isotropic, homogeneous, inertial range turbulence spectra. If $\mathbf{K}$ is the wave scattering vector given by $K(\mathbf{e}_0 - \mathbf{e}_s)$ with $K = 2k_0 \sin(\theta_s/2)$ (the Bragg condition), if $\mathbf{M}_L$ is the Mach vector of the large-scale eddies, and if τ is the time delay introduced into the correlations by the large-scale motion, the time-varying turbulence spectrum is related to the locally fixed spectrum by

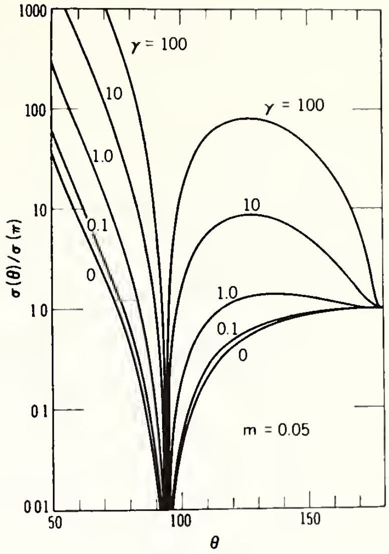

Fig. 10. Typical deformation in the scattering cross section due to a 15 m s^{-1} mean wind, where $\gamma = C_v^2 T_0^2 / C_T^2 c_0^2$ [from *Clifford and Brown*, 1974].

Locally frozen turbulence spectrum

$$\Phi_{ij}(\mathbf{K}, \tau) = \langle \exp(i\mathbf{K} \cdot \mathbf{M}_L c_0 \tau) \rangle_V \Phi_{ij}(\mathbf{K}) \qquad (35)$$

where the angle brackets with subscript V indicate a volume average of the large-scale motions.

Using (35), Ford and Meecham obtain $I(k)$ for velocity scattering. But by assuming the Born approximation and using the effective refractivity N_e' we can extend their result to both velocity and refractive index fluctuations. Then $I(k)$ can be written in the form

$$I(k - k_0) = S(x, k)\mathfrak{F}_\tau \langle \exp(i\mathbf{K} \cdot \mathbf{M}_L c_0 \tau) \rangle_V \qquad (36)$$

Tatarskii [1971] follows essentially the same procedure and obtains the same result. If we now assume that the components of $\mathbf{M}_L$ have Gaussian probability distributions, we can use the identity $\langle \exp x \rangle = \exp \bar{x} \exp(1/2\langle x'^2 \rangle)$, where $x = \bar{x} + x'$ and $\bar{x} = \langle x \rangle$, with the result that (36) becomes

Gaussian form of locally frozen
turbulence spectrum

$$I(k) = S(\mathbf{x})[2\pi\langle(\mathbf{K} \cdot \mathbf{M}_L')^2\rangle]^{-1/2} \exp\left[-(k - k_0 + \mathbf{K} \cdot \bar{\mathbf{M}}_L)^2 / 2\langle(\mathbf{K} \cdot \mathbf{M}_L')^2\rangle\right] \qquad (37)$$

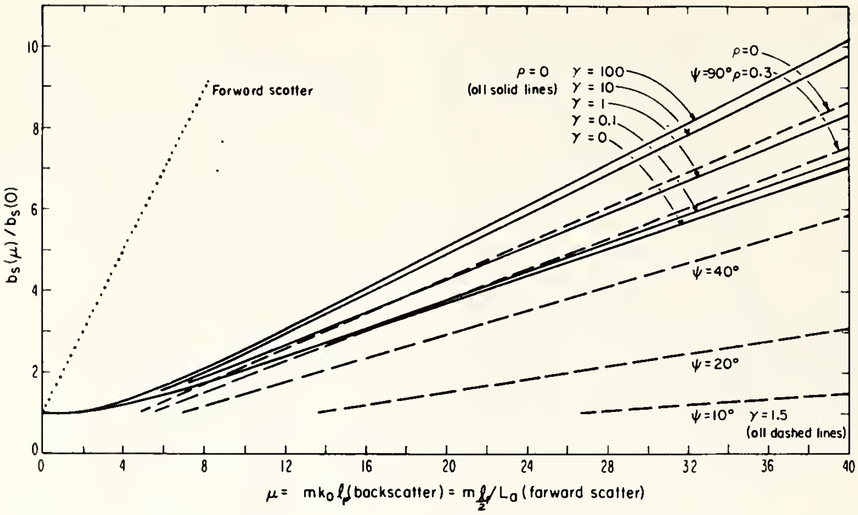

Fig. 11. Equivalent width b_s of the backscattered spectrum broadened by the effect of the mean wind; ψ is the half-angle beam width.

Equation (37) is exactly the result given by *Tatarskii* [1971, p. 130] if we write $K^2\sigma_M^2 = 3\langle(\mathbf{K}\cdot\mathbf{M}_L')^2\rangle$, where σ_M^2 is the variance of the components of the Mach vector in the direction of the scattering vector **K**.

When acoustic wave fronts propagate through or are scattered by turbulence, the fronts acquire random bumps and irregularities. And as these irregularities drift across the path, the phase will change in time, and the instantaneous frequency $d\phi/dt$ also will fluctuate. Thus the observed signal will undergo a spectral broadening dependent on the magnitude of the mean transverse wind. *Ho and Kovasznay* [1976*a*] have made an experimental study of the advection by the mean flow of the diffraction patterns created by turbulence in a beam of sound that appears to give some information on the phenomenon underlying such spectral broadening by the transverse motion of the distorted wave fronts. If we set $\mathbf{M}_L' = 0$ in (35) or (37), $I(k)$ does not reduce to the broadened spectrum caused by the mean wind alone. Such a step reduces the Gaussian function in (37) to a Dirac measure and suggests that $I(k) = S(x)\delta(k - k_0 + \mathbf{K}\cdot\bar{\mathbf{M}})$, that is, that $I(k)$ is an unbroadened spectrum, one merely Doppler shifted in position by the wind. The discrepancy arises because the locally frozen approach neglects phase fluctuations.

A more careful analysis would both include phase fluctuations and make use of the locally frozen hypothesis to determine the effect on the scattered frequency spectrum. ***Brown*** [1974*a*] has only combined phase fluctuations with the frozen turbulence assumption (Taylor's hypothesis) to determine $I(k)$. His study considers a finite scattering volume V_s, defined by a finite pulse length l_p and a finite receiver half beam width ψ. Because of the finite beam width, not all the scattering elements lie at $\theta_s = 180°$, and thus both refractivity fluctuations and velocity fluctuations contribute to the spectrum. A finite length pulse will have a nonzero spectral width. Also, but to a smaller extent, the finiteness of V_s will broaden the spectrum. Thus Brown's study includes all broadening mechanisms other than the advection of scattering eddies by larger eddies. Figure 11 shows the equivalent width b_s of the wind-broadened backscatter spectrum. We remark that oversight of the additional factor k_0^{-1} appearing in the part of Brown's solution symbolized by H_m led to an incorrect comment on k_0 dependence. The spectra of Ford and Meecham, Tatarskii, and Brown all have the $k_0^{-2/3}$ dependence to be expected in an energy flux density per unit wave number, since the energy flux density itself varies as $k_0^{1/3}$. An analysis that included all effects by first applying the locally frozen hypothesis in a coordinate system moving with the mean wind and then transforming to a fixed system, as was done by Brown, would be a valuable contribution to turbulent scattering theory.

Propagation

We now consider the problem of sound traveling over a path, where the 'forward scatter' waves continually interfere with the propagating initial wave and where the cumulative effects of phase fluctuations change the nature of the solutions. We have already noted the result of *Clifford and Brown* [1970], that the solutions for the various statistical properties of the wave for weakly interacting sound and turbulence that have been obtained with the condition $\lambda \ll l_0$ can be extended to hold under the much weaker condition $\lambda \leq L_0$. The significance of the inequality $\lambda \ll l_0$ is immediately apparent. Since we can rewrite the Bragg condition $2 \sin(\theta_s/2) = \lambda/l$ in the form $\theta_s = \lambda/l$ when θ_s is small, the inequality requires that $\theta_s = \lambda/l \leq \lambda/l_0 \ll 1$ for an eddy of size l. That is, all the eddies 'scatter' into angles negligibly different from zero. For this reason an analysis treating fluctuations of phase in the direction of propagation, fluctuations that vary randomly over the surfaces perpendicular to the direction of propagation, provides a far better model for propagation through turbulence than scattering theory does. We reemphasize that 'eddy size' refers to the spatial Fourier decomposition of the turbulent fluctuation field, not to actual 'blobs' in the atmosphere. The Kolmogorov spectrum for inertial range turbulence implies that increasing the eddy size $l = 2\pi\kappa^{-1}$ means increasing the fluctuation in effective refractivity N_e. Thus the largest eddies cause the greatest phase fluctuations in the direction of propagation and the smallest values of θ_s. The difference between the inequality $\lambda \ll l_0$ and the inequality $\lambda \leq L_0$ given by *Clifford and Brown* [1970] appears then as a difference between a kinematic condition and a dynamic condition. The first inequality permits no scattering at large angles, whereas the second requires only that the energy flow scattered into large angles be negligible.

The above discussion does not touch on the role of amplitude fluctuations in propagation. Figure 1 depicted in a schematic fashion both the increasing random irregularities in the phase fronts (shown by the darker lines) and the wave amplitudes (indicated by the varying thickness of the lines) as a plane wave travels through turbulence. The fluctuations in amplitude arise because random changes in the wave vectors normal to the phase fronts cause interference at various distances farther along the path. We will see later that for weakly interacting turbulence the most effective eddies for creating interference at the path length L in a spherical wave from a transmitter at the beginning of the path are those of half Fresnel zone size $(\lambda L)^{1/2}/2$ lying at the center of the path, $L/2$. Since these dimensions correspond with an interference angle $\lambda/(\lambda L)^{1/2} = (\lambda/L)^{1/2}$, we must also require that $(\lambda/L)^{1/2} \ll 1$. Clearly, the latter requirement is satisfied under any practical conditions, and only the inequality $\lambda \leq L_0$ needs consideration. *Ho and Kovasznay* [1976*b*] have found experimental confirmation that in weakly interacting turbulence the statistical properties of the wave retain the same form under the relaxed condition $\lambda \leq L_0$. The results change drastically, however, when we turn to strongly interacting sound and turbulence. Not only do the statistical properties obtained with the Rytov approximation become quantitatively incorrect, but entirely new phenomena appear. We will call one such phenomenon 'turbulent saturation' (to distinguish the term from nonlinear saturation), which we discuss later in this section. Analysis of sound propagation in 'strong turbulence' has required entirely new theoretical techniques, such as the Markov approximation. At this time, such techniques still depend on the assumption $\lambda \ll l_0$. Thus the degree of approximation and the errors involved in applying the theoretical results from optical propagation to acoustic propagation in strong turbulence are unknown. However, we will use these theoretical results with the excuse that, at the moment, we have nothing better.

Since for propagation, P_0 does not vanish identically in the region of interest, we can define logarithmic quantities in the following way:

Logarithmic wave function

$$\psi(\mathbf{x}, k) = \ln (P/P_0) = \chi + i\Delta\phi \tag{38}$$

Log-amplitude function

$$\chi(\mathbf{x}, k) = \ln (A/A_0) \approx A'/A_0 \tag{39}$$

Phase function

$$\Delta\phi(\mathbf{x}, k) = \phi - \phi_0 = \phi' \tag{40}$$

When the random wave equation is transformed into an equation for ψ, as was done by *Tatarskii* [1971, sect. 45], the approximation of first order in N_e', called the Rytov approximation, holds for somewhat longer path lengths or somewhat greater turbulence intensities than does the Born approximation. As an additional convenience the real and imaginary parts of ψ immediately give the amplitude and phase fluctuations. *Tatarskii* [1961, 1971], *R. W. Lee and J. C. Harp* [1969], and *Clifford* [1971], among others, have obtained a number of the statistical properties of a propagating wave in the 'weak turbulence,' or Rytov approximation, limit.

Before quoting some of the results on statistical properties for weak turbulence we need to introduce the structure parameter C_{ne}^2 of the effective refractivity fluctuations N_e'. From *Tatarskii* [1971] we can write

Effective refractivity structure constant

$$C_{ne}^2 = C_n^2 + C_v^2/c_0^2 \tag{41}$$

We should note that the numerical constants appearing in the scattering cross section in (33) differ from those in (41), since N_e' is a function of the angle between the wave normal and the fluctuating wind. More important, C_{ne}^2 is a function of position, especially on vertical paths, and the structure constants C_T^2, C_e^2, C_{eT}, and C_v^2 contributing to C_{ne}^2 according to (6) vary differently with altitude, as is shown in the example in Figure 6. We can considerably simplify the display of the results by following *Brown and Keeler* [1975] and introducing various weighted integral averages of C_{ne}^2 over the path. Such weightings depend on whether the waves are plane or spherical, indicated by subscripts p or s. The weightings also depend on whether the averages are to be used in amplitude or phase statistical properties, which will be given the respective subscripts χ and ϕ. We observe that on vertical paths, where C_{ne}^2 varies strongly with height, some of the weighted averages depend on whether the beginning of the integration path is elevated or on the ground. To avoid confusion we will always consider a transmitter located at the point $s = 0$ and a receiver at the point $s = L$. With these precautions we can write the appropriate weighted averages of C_{ne}^2 in the following forms:

Plane wave average C_{ne}^2 for phase properties

$$[C_{ne}^2]_{\phi p} = L^{-1} \int_0^L ds\, C_{ne}^2(s) \tag{42}$$

Spherical wave average C_{ne}^2 for
phase properties

$$[C_{ne}^2]_{\phi s} = L^{-1} \int_0^L ds\, [s/L]^{5/3} C_{ne}^2(s) \tag{43}$$

Plane wave average C_{ne}^2 for
amplitude properties

$$[C_{ne}^2]_{\chi p} = L^{-1} \int_0^L ds\, [1 - s/L]^{5/6} C_{ne}^2(s) \tag{44}$$

Spherical wave average C_{ne}^2 for
amplitude properties

$$[C_{ne}^2]_{\chi s} = L^{-1} \int_0^L ds\, [(s/L)(1 - s/L)]^{5/6} C_{ne}^2(s) \tag{45}$$

When C_{ne}^2 is constant, integration for the last three averages introduces the respective factors $\frac{3}{8}$, $\frac{6}{11}$, and the beta function of $\frac{11}{6}$, $B(\frac{11}{6}, \frac{11}{6}) = \Gamma^2(\frac{11}{6})/\Gamma(\frac{11}{3})$.

As sound travels along a path from a transmitter at $s = 0$ to a receiver at $s = L$, the turbulent interactions produce random fluctuations in the pressure (that is, in both the amplitude and the phase of the pressure) over the surfaces orthogonal to the direction of propagation. Let $\mathbf{x}$ be a point on the axis of propagation at a distance s from the source and $\boldsymbol{\rho}$ a vector perpendicular to the axis having a magnitude ρ. If the turbulence is locally homogeneous and isotropic in the three-dimensional space, then the wave will be statistically homogeneous and isotropic in the two-dimensional orthogonal surfaces. For turbulent propagation, the important quantities are correlations of wave properties at pairs of points $\mathbf{x}$, $\mathbf{x} + \boldsymbol{\rho}$ expressed as functions of ρ, s. Perhaps the most fundamental function in propagation is the one called 'modulation transfer function' in optical theory and 'mutual coherence function' in communications theory. We will define this function $\mathfrak{M}$ as

Definition of mutual coherence function

$$\mathfrak{M}(\rho, s) = \langle P(\mathbf{x})P^{*}(\mathbf{x} + \boldsymbol{\rho})\rangle \tag{46}$$

We will define the various other structure functions and covariances in a similar manner:

Logarithmic wave structure function

$$D_{\psi}(\rho, s) = \langle|\psi(\mathbf{x} + \boldsymbol{\rho}) - \psi(\mathbf{x})|^2\rangle = D_{\chi} + D_{\phi} \tag{47}$$

Phase structure function

$$D_{\phi}(\rho, s) = \langle[\phi(x + \rho) - \phi(x)]^2\rangle \tag{48}$$

Log-amplitude covariance

$$B_{\chi}(\boldsymbol{\rho}, s) = \langle\chi(\mathbf{x} + \boldsymbol{\rho})\chi(\mathbf{x})\rangle = \sigma_{\chi}^2 - \tfrac{1}{2}D_{\chi}(\boldsymbol{\rho}, s) \tag{49}$$

Log-amplitude variance

$$\sigma_{\chi}^2(s) = B_{\chi}(0, s) \tag{50}$$

Experiments show that the phase fluctuations in propagation have approximately normal, or Gaussian, probability distributions, whereas in weak turbulence the energy flux density fluctuations are approximately log-normal; but a log-normal energy flux implies normal distribution in the log-amplitude χ. Thus if we substitute $P = P_0e^{\psi}$ in (46) and again use the identity $\langle e^x\rangle = e^{\bar{x}} \exp[\frac{1}{2}\langle x'^2\rangle]$ for a Gaussian random variable x, we obtain

Mutual coherence function

$$\mathfrak{M}(\rho, s) = \exp[-\tfrac{1}{2}D_{\psi}(\rho, s)] \tag{51}$$

after introducing the relation $\bar{\chi} = -\sigma_{\chi}^2$ required for energy conservation.

Since we wish to give an economical display of solutions in the recent literature for weak turbulence propagation theory, we introduce the function of path distance $\beta = \beta(s)$ defined by $\beta = 1$ for plane waves and $\beta = s/L$ for spherical waves. Since the atmosphere is not homogeneous, we follow *Tatarskii* [1961] in using the spectrum for slowly varying turbulence given by $\Phi_{ne}(s, \kappa) = C_{ne}^2(s)\Phi_{ne}^{(0)}(\kappa)$, where $C_{ne}^2(s)$ is a local structure parameter. Also, we introduce a weighting function $H_f(s, \kappa)$ for each property $f(\rho)$, which varies the importance of different path positions and different eddy sizes. With these conventions we can write all the structure functions given by *Lawrence and Strohbehn* [1970] in the form

Weak turbulence structure functions

$$D_f(\rho) = 8\pi^2k^2\int_0^L ds\, C_{ne}^2(s)\int_0^{\infty} d\kappa\, \kappa\Phi_{ne}^{(0)}(\kappa)$$

$$\cdot[1 - J_0(\beta\rho\kappa)]H_f(s, \kappa) \tag{52}$$

where J_0 is the Bessel function of the first kind and zero order and where, if the wave propagates in the x_3 direction, we must set $\kappa_3 = 0$ and $\kappa = (\kappa_1^2 + \kappa_2^2)^{1/2}$. The weighting functions for the logarithmic wave ψ, the phase ϕ, and the log-amplitude χ are given by

Weak turbulence weighting functions

$$H_{\psi} = 1$$

$$H_{\phi} = \cos^2[\beta(s)(1 - s/L)\kappa^2L/2k] \tag{53}$$

$$H_{\chi} = \sin^2[\beta(s)(1 - s/L)\kappa^2L/2k]$$

Consortini and Ronchi [1969], *Consortini et al.* [1973], and *Lutomirski and Yura* [1969, 1971*a*] have pointed out that when ρ is not small, the finite outer scale L_0 in the atmosphere can seriously affect the behavior of ψ and ϕ. For such cases, more realistic results are obtained by replacing the Kolmogorov spectrum with the empirical von Kármán spectrum

Von Kármán spectrum

$$\Phi_{ne}^{(0)}(\kappa) = 0.0330 \exp[-(\kappa/\kappa_0)^2][\kappa^2 + K_0^2]^{-11/6} \tag{54}$$

where $K_0 = 2\pi/L_0$ and $\kappa_0 = 5.92/l_0$. (The analysis leading to the constant 5.92 instead of 2π is given by *Tatarskii* [1971].) If (52) for $D_{\psi}(\rho)$ using the spectrum given by (54) is differentiated with respect to ρ, formula 11.4.44 of *Abramowitz and Stegun* [1964] gives

Slope of weak turbulence wave
structure function

$$\partial_{\rho}D_{\psi}(\rho) = 3.1097k^2\rho^{2/3}\int_0^L ds$$

$$\cdot\beta^{5/3}(s)C_{ne}^2(s)\{(\beta\rho K_0)^{1/6}\mathcal{K}_{1/6}(\beta\rho K_0)\} \tag{55}$$

where $\mathcal{K}_{1/6}$ is the modified Bessel function of the second kind. Equation (55) can be immediately integrated by using formula 11.3.27 of *Abramowitz and Stegun* [1964] to give

Weak turbulence wave structure function

$$D_{\psi}(\rho) = 2.914k^2\rho^{5/3}\int_0^L ds\, \beta^{5/3}(s)C_{ne}^2(s)\cdot f(\beta\rho K_0) \tag{56}$$

where $f(\beta\rho K_0)$ is given exactly by

$$f(\beta\rho K_0) = 1.067(\beta\rho K_0)^{-5/3}\{2^{-1/6}\Gamma(\tfrac{5}{6})$$

$$-(\beta\rho K_0)^{5/6}\mathcal{K}_{5/6}(\beta\rho K_0)\} \tag{57}$$

or approximately by

$$f(\beta\rho K_0) \approx 1 - 0.8048[\beta(s)\rho K_0]^{1/3} \qquad \rho K_0 < 1 \tag{58}$$

The constant appearing in (58) is the same as that given by *Fante* [1975] for the plane wave case, where $\beta(s) = 1$. For constant C_{ne}^2 the function $\beta(s)$ can be integrated to give the function f_s appropriate for spherical waves:

$$f_s(\rho K_0) \approx \tfrac{3}{8}[1 - 0.7154(\rho K_0)^{1/3}] \tag{59}$$

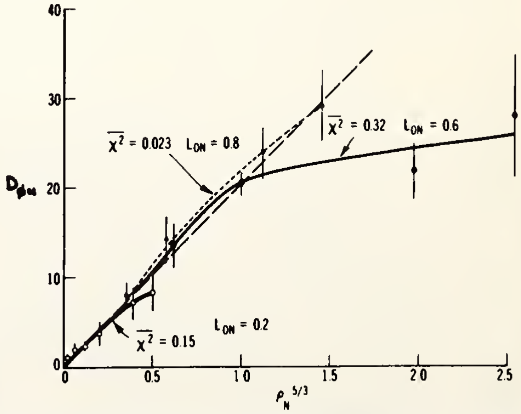

Fig. 12. Experimental phase structure functions. D_{ϕ} is normalized by the log-amplitude variance $\sigma\chi^2$, and the transverse separation ρ is normalized by a Fresnel zone $(\lambda L)^{1/2}$ [from *Brown and Keeler*, 1975].

with the same constant as that given by *Lutomirski and Yura* [1971*b*]. The additional factor $\frac{3}{8}$ appearing in (59) implies that wave (and phase) fluctuations in a spherical wave will be only three-eighths as large as the fluctuations in a plane wave.

Tatarskii [1961] has shown that since D_χ remains bounded while D_ϕ continually increases with ρ, $\rho \geq (\lambda L)^{1/2}$ implies $D_\phi \gg D_\chi$, and thus $D_\phi \approx D_\psi$. Much more roughly, when $\rho \ll (\lambda L)^{1/2}$, $D_\phi \approx D_\chi$, and thus $D_\phi \approx \frac{1}{2}D_\psi$. We can see the reason for the approximate equality of D_χ and D_ϕ for very small ρ by considering the factor $1 - J_0(\beta\rho\kappa)$ in (52). For small ρ this factor is close to zero unless κ is very large. But if κ is very large, the cosine squared and sine squared functions in (53) oscillate very rapidly in comparison with the slowly varying Bessel factor, and the $\pi/2$ phase difference between the two sinusoidal functions becomes unimportant. If we neglect the effect of the variation of $\beta(s)$ on the correction term appearing in (58), we can then write the phase structure function as

Weak turbulence phase structure function

$$D_\phi(\rho) = 2.914k^2\rho^{5/3}L[C_{ne}{}^2]_\phi\{1 - 0.805(\rho K_0)^{1/3}\} \qquad \rho \geq (\lambda L)^{1/2}$$

$$D_\phi(\rho) = (2.914/2)k^2\rho^{5/3}L[C_{ne}{}^2]_\phi\{1 - 0.805(\rho K_0)^{1/3}\} \qquad \rho < (\lambda L)^{1/2} \tag{60}$$

where $[C_{ne}{}^2]_\phi$ is taken from (42) or (43). Figure 12, from *Brown and Keeler* [1975], shows typical experimental phase structure functions, here normalized by $\sigma_\chi{}^2$, as functions of the normalized separation distance $\rho_n = \rho/(\lambda L)^{1/2}$, where $(\lambda L)^{1/2}$ is the size of a Fresnel zone. The effects of the outer scale correction given by (58) that cause the curves to bend over are clearly evident. The numbers L_{on} above the curves are estimates of the normalized outer scale $L_{on} = L_0/(\lambda L)^{1/2}$. A similar integration for D_χ or B_χ in closed form has not yet been performed. The log-amplitude variance, however, has been found to be

Weak turbulence log-amplitude variance

$$\sigma_\chi{}^2 = 4\pi^2k^2 \int_0^L ds\, C_{ne}{}^2(s) \int_0^\infty d\kappa\, \kappa\Phi_{ne}{}^{(0)}(\kappa)H_\chi(s, \kappa) \approx 0.5628k^{7/6}L^{11/6}[C_{ne}{}^2]_\chi \tag{61}$$

with $[C_{ne}{}^2]_\chi$ from (44) or (45). For constant $C_{ne}{}^2$ the averaging process introduces a factor $\frac{6}{11}$ into (61) for plane waves and a factor $B(\frac{11}{6}, \frac{11}{6}) = \Gamma^2(\frac{11}{6})/\Gamma(\frac{11}{3}) \approx 0.2205$ for spherical waves. The ratio of the two numbers shows that the amplitude fluctuations of a spherical wave are less than half as large as the fluctuations of a plane wave.

Spectra of the various random functions that are properties of a wave propagating through turbulence should depend on weighting functions determined by the amplitude $a_0(\mathbf{x}, t)$ of the 'initial' wave, that is, the wave that would exist in the absence of turbulence, a wave that is completely determined by the propagation equations and the boundary conditions. The uniqueness of the initial amplitude for spectral weighting follows from the fact that the other functions, phase, frequency (phase derivative), logarithmic wave, or log-amplitude, are undefined when $a_0(\mathbf{x}, t) = 0$. The initial wave also determines a field of wave vectors $\mathbf{k}_0(\mathbf{x})$, for simplicity assumed not to be a function of time or, at least, very slowly varying. For convenience we introduce the vector field $\boldsymbol{\varepsilon}(\mathbf{x}) = \mathbf{k}_0(\mathbf{x})/\omega_0$, where ω_0 is the angular frequency of the initial wave. Now, given that the transmitter is at $\mathbf{x} = 0$, we can transform from the time t to the local 'retarded time' $t' = t - \boldsymbol{\varepsilon}\cdot\mathbf{x}$. We define the autocovariance of the random function $f(\mathbf{x}, t)$ in the usual way:

Autocovariance of a function $f(t)$

$$R_f(\mathbf{x}, t'; \tau) = \langle f(\mathbf{x}, t')f^\dagger(\mathbf{x}, t' + \tau)\rangle \tag{62}$$

Then, for the most general case, including CW propagation and pulses of arbitrary shape, we can define the 'frequency spectrum' of any function $f(\mathbf{x}, t)$ associated with a wave by

Definition of frequency spectrum

$$W_f(\mathbf{x}, \omega) = \mathfrak{F}_\tau \lim_{T\to\infty} \left\{ \left[\int_{-T}^{T} dt'\, a_0(\mathbf{x}, t')a_0(\mathbf{x}, t' + \tau)R_f(\mathbf{x}, t'; \tau) \right] \cdot \left[\int_{-T}^{T} dt'\, [a_0(\mathbf{x}, t')]^2 \right]^{-1} \right\} \tag{63}$$

where $\mathfrak{F}_\tau$ is the Fourier transform given by (15) with t replaced by τ. Equation (62) states that the frequency spectrum of $f(\mathbf{x}, t)$ equals the Fourier transform of the weighted average of the autocovariance of $f(\mathbf{x}, t)$.

For CW propagation, where $a_0(\mathbf{x}, t)$ is constant in time, (62) reduces immediately to the definition of a spectrum given by *Jenkins and Watts* [1968]:

CW frequency spectrum

$$W_f(\omega) = \mathfrak{F}_\tau \lim_{T\to\infty} \left\{ \frac{1}{2T} \int_{-T}^{T} dt'\, R_f(\mathbf{x}, t'; \tau) \right\} \tag{64}$$

If $f(\mathbf{x}, t)$ is also a stationary random function, (64) reduces to

Spectrum of a stationary random function

$$W_f(\omega) = \mathfrak{F}_\tau R_f(\mathbf{x}; \tau) \tag{65}$$

For the case of a pulse we define the characteristic length τ_p in exactly the same manner for time as we define the equivalent width of a spectrum in frequency space, that is,

Characteristic length of a pulse

$$\tau_p = \left\{ \int_{-\infty}^{\infty} dt'\, [a_0(\mathbf{x}, t')]^2 \right\} \{\max\, [a_0(\mathbf{x}, t)]^2\}^{-1} \tag{66}$$

where max implies the maximum value for all t at a fixed $\mathbf{x}$. For a rectangular pulse the definition (66) gives the actual physical length of the pulse. Now, for a pulse the general definition (63) reduces to the pulse spectrum $W_{f(P)}$:

Frequency spectrum of a pulse

$$W_{f(P)}(\omega) = \left\{ \mathfrak{F}_\tau \int_{-\infty}^{\infty} dt'\, a_0(\mathbf{x}, t')a_0(\mathbf{x}, t' + \tau)R_f(t', \tau) \right\} \{\tau_p \cdot \max\, [a_0(\mathbf{x}, t)]^2\}^{-1} \tag{67}$$

If we define the normalized pulse shape by $d_0(\mathbf{x}, t') = a_0(\mathbf{x}, t')/\max a_0(\mathbf{x}, t)$ and the envelope spectrum by $\mathfrak{D}_0(\omega) = \mathfrak{F}_t d_0(t)$, we can rewrite (67) in a simpler form. If we also assume both that the pulse f is merely a sample of a stationary CW function f_{CW} and that τ_p is much greater than the largest time scale in f_{CW}, then since $R_{f(CW)}(t, \tau) = R_{f(CW)}(0, \tau)$, the pulse spectrum can be related to the CW spectrum by

Relation between pulse spectrum
and CW spectrum

$$W_{f(P)}(\omega) = (2\pi/\tau_p)\mathfrak{D}_0{}^2(\omega) * W_{f(CW)}(\omega) \tag{68}$$

where the asterisk indicates convolution with respect to ω defined by (17) with k replaced by ω. Equation (68) is the relation between pulse spectrum and CW spectrum noted by *Brown* [1974*b*] for the case of the acoustic pressure as found by

Brown and Clifford [1973*a*] and for the case of the amplitude of the pressure as found by *Brown and Clifford* [1973*b*]. The significance of (68) is that we can immediately apply all the CW spectra, such as those found by *Tatarskii* [1971] for plane waves or those found by *Clifford* [1971] for spherical waves, to the corresponding pulse spectra.

At this point the reader should be warned that the generality of (68) could lead to confusion between two quite different types of spectra. The first is associated with signals usually obtained by 'incoherent detection.' Such detection is the only type readily available for optical propagation because of the extremely high frequencies. For this kind of spectrum the differences between signals separated by the time delay τ arise only from advection of turbulence by mean winds (for frozen turbulence) or from the slow evolution of turbulence, which we will not consider, since each case depends on particular circumstances. The slow rates involved imply that the corresponding 'incoherent spectra' are nonzero only in a frequency region near zero. The second type of spectrum is associated with the wave itself, such as the acoustic pressure, and is derived from signals obtained by 'coherent detection,' that is, by including both amplitude and phase. For these signals the rates are related to the speed of sound, and the corresponding spectra are nonzero only in a much higher region located at about the frequency of the initial wave. Such 'coherent spectra' seldom have a counterpart in optical propagation experiments.

Consider a wave after its propagation through turbulence, one that initially possessed a single angular frequency ω_0. We can write $f(\mathbf{x}, t) = \tilde{f}(\mathbf{x}, t)e^{-i\omega_0 t}$, where $\tilde{f}(\mathbf{x}, t)$ is a function slowly varying in comparison with the exponential factor. Then, $\mathfrak{F}_\tau R_f(\mathbf{x}, \tau) = \{\mathfrak{F}_\tau R_{\tilde{f}}(\mathbf{x}, \tau)\} * \delta(\omega - \omega_0)$; or, writing $\Delta\omega = \omega - \omega_0$ and substituting in (68), we obtain

Frequency spectrum of a wave

$$W_{f(P)}(\omega) = (2\pi/\tau_p)\mathfrak{D}_0^2(\Delta\omega) * W_{\tilde{f}(CW)}(\Delta\omega) \qquad (69)$$

where, as usual, the convolution product is with respect to the variable explicitly indicated in the two factors, that is, in this case the variable $\Delta\omega$. If there are roughly 10 cycles in a pulse, $\mathfrak{D}_0^2(\Delta\omega)$ is a narrow function of $\Delta\omega$ centered on ω_0. Then (69) implies that all the spectral density is concentrated in a narrow region around ω_0. We should note that the above spectral expansions are made with respect to both positive and negative frequencies. Experimentally, however, results are given for positive frequencies only and as functions of f in hertz rather than ω in radians per second. If we designate the experimental spectra by $W^+(f)$, we can relate the two by defining $W(f) = \frac{1}{2}[W^+(f) + W^+(-f)]$ so that $W(f)$ does not vanish for $f < 0$ and, in fact, is symmetric with frequency reflection. But the definition of $\mathfrak{F}_t$ given in (17) implies that $W(f) = 2\pi W(\omega)$, and thus $W^+(f) = 4\pi W(\omega) = (4\pi/c_0)W(k)$ for $\omega > 0$. Then the transforms between the autocovariance $R(\tau)$ (definition unchanged) and the experimental spectrum $W^+(f)$ become

Transforms for experimental spectra

$$W^+(f) = 4\int_0^\infty d\tau \cos(2\pi f\tau)R(\tau)$$
$$R(\tau) = \int_0^\infty df \cos(2\pi f\tau)W^+(f) \qquad (70)$$

The frozen turbulence assumption relates the time autocovariance $R_f(\tau)$ of a property f slowly varying because of a crosswind $w_\perp$ to the spatial covariance $B_f(\rho)$ of f and thus permits a calculation of the incoherent frequency spectrum of f. From the assumption, $R_f(\mathbf{x}, \tau) = R_f(\mathbf{x} - w_\perp\tau, 0) = B_f(w_\perp\tau)$. Replacing ρ by $w_\perp\tau$ in all the covariances or structure functions given earlier and substituting in (65) then lead to the corresponding frequency spectra $W_f(\omega)$ or $W_f^+(f)$. *Mandics et al.* [1973] display numerous experimental spectra obtained for most properties of acoustic waves propagating in turbulence. *Clifford* [1971] lists the weak turbulence theory limiting form of spectra found by *Tatarskii* [1961] and himself for the cases of log-amplitude χ, phase fluctuation ϕ, and phase difference fluctuation $\delta\phi$ at two points separated by the transverse distance ρ. To display these results in compact form, we introduce the following notation: $\rho_n = \rho/(\lambda L)^{1/2}$, $f_w = w/(\lambda L)^{1/2}$, $f_n = f/f_w$, and, for use in $\delta\phi$ spectra, $\langle\sigma_\chi^2\rangle = (\sigma_{\chi 1}^2\sigma_{\chi 2}^2)^{1/2}$. Again we use the subscripts p and s for the variances of plane and spherical waves. Then for weak turbulence and with the additional conditions $l_0 \ll (\lambda L)^{1/2} \ll L_0$ and $w/L_0 < f$ we have

Plane waves

$$\sigma_{\chi p}^2 = 0.308k^{7/8}L^{11/8}C_{ne}^2$$

Spherical waves

$$\sigma_{\chi s}^2 = 0.124k^{7/8}L^{11/6}C_{ne}^2$$

Log-amplitude spectra for plane waves

$$f_w W_\chi^+(f) = 1.103\sigma_{\chi p}^2(1 + 0.92f_n^{4/3}) \qquad f_n < 1$$
$$f_w W_\chi^+(f) = 0.24\sigma_{\chi p}^2 f_n^{-8/3} \qquad f_n > 1 \qquad (71a)$$

Log-amplitude spectra for spherical waves

$$f_w W_\chi^+(f) = 0.614\sigma_{\chi s}^2(1 + 0.405f_n^{4/3}) \qquad f_n < 1$$
$$f_w W_\chi^+(f) = 0.606\sigma_{\chi s}^2 f_n^{-8/3} \qquad f_n > 1 \qquad (71b)$$

Phase spectra for plane waves

$$f_w W_\phi^+(f) = 0.489\sigma_{\chi p}^2 f_n^{-8/3} \qquad f_n < 1$$
$$2f_w W_\phi^+(f) = 0.489\sigma_{\chi p}^2 f_n^{-8/3} \qquad f_n > 1 \qquad (72a)$$

Phase spectra for spherical waves

$$f_w W_\phi^+(f) = 1.215\sigma_{\chi s}^2 f_n^{-8/3} \qquad f_n < 1$$
$$2f_w W_\phi^+(f) = 1.215\sigma_{\chi s}^2 f_n^{-8/3} \qquad f_n > 1 \qquad (72b)$$

Phase difference spectra for plane waves

$$f_w W_{\delta\phi}^+(f) = 0.99\langle\sigma_{\chi p}^2\rangle f_n^{-8/3}[1 - \cos(2\pi\rho_n f_n)] \qquad \rho_n > 1$$
$$2f_w W_{\delta\phi}^+(f) = 0.99\langle\sigma_{\chi p}^2\rangle f_n^{-8/3}[1 - \cos(2\pi\rho_n f_n)] \qquad \rho_n < 1 \qquad (73a)$$

Phase difference spectra for spherical waves

$$f_w W_{\delta\phi}^+(f) = 2.46\langle\sigma_{\chi s}^2\rangle f_n^{-8/3}\frac{1 - \sin(2\pi\rho_n f_n)}{2\pi\rho_n f_n} \qquad \rho_n > 1$$
$$2f_w W_{\delta\phi}^+(f) = 2.46\langle\sigma_{\chi s}^2\rangle f_n^{-8/3}\frac{1 - \sin(2\pi\rho_n f_n)}{2\pi\rho_n f_n} \qquad \rho_n < 1 \qquad (73b)$$

The coherent spectrum of the pressure itself, found by *Brown and Clifford* [1973*a*], can be put into a form similar to that above if we introduce the symbol $\Delta f_n = (f - f_0)/f_w$, with f_0 the carrier frequency and the abbreviation $L_{on} = L_0/(\lambda L)^{1/2}$. Then their result becomes

Frequency spectrum of the pressure

$$f_w W_{p(P)}^+(f) = (2\pi/\tau_p)\mathfrak{D}_0^2(\Delta f)$$
$$* \{0.144\sigma_{\chi p}^2 L_{on}^{8/3}[1 + (L_{on}\Delta f_n)^2]^{-4/3}\} \qquad (74)$$

The right-hand factor in the convolution product in (74) is just the CW frequency spectrum of the pressure. In the wings of the spectrum, when $\Delta f_n \gg L_{on}^{-1}$, the factor reduces to $0.144\sigma_{\chi p}^2 \Delta f_n^{-8/3}$. A similar calculation for spherical waves has not yet been carried out.

Strong interactions between turbulence and sound bring about quantitative and qualitative changes in propagation. All of the results given so far apply to acoustics whenever the interactions are weak and $\lambda \leq L_0$. Now we will give a physical criterion for the meaning of 'strong' and describe some of the equivalent phenomena in optical propagation through strong turbulence that may serve as reasonable approximations in acoustics. Equation (61) quotes the first-order solution for the variance σ_χ^2 of the log-amplitude fluctuations, a solution that predicts that the variance will increase linearly with the path-averaged value of C_{ne}^2 and as the $\frac{11}{6}$th power of the path length L. Following *Clifford et al.* [1974], we will introduce a new symbol σ_t^2 for the weak turbulence result, $\sigma_t^2 = 0.563k^{7/6}L^{11/6}[C_{ne}^2]_\chi$. (The subscript t stands for at least one of the words 'turbulence,' 'theory,' or 'Tatarskii'!) Then, the weak turbulence prediction is that $\sigma_\chi^2 = \sigma_t^2$. However, optical propagation measurements find such behavior only for short path lengths or low turbulence intensities. For longer paths or higher intensities, observations of σ_χ^2 level off or perhaps even decrease slightly with increasing σ_t^2. This result is the phenomenon originally termed 'saturation,' but which we will call turbulent saturation. The modifier distinguishes it from the leveling off of received power with increasing transmitter power that earlier we termed nonlinear saturation. Examination of a time series of the amplitude during progressive turbulent saturation shows a change from continuously random fluctuations to intermittent spikiness, essentially concentrating all the energy in higher but less frequent peaks.

That a phenomenon similar to turbulent saturation in optical propagation occurs in acoustic propagation can hardly be doubted, although the amount of experimental evidence is slimmer by several orders of magnitude. A study by Embleton et al., presented at the fall 1973 meeting of the Acoustical Society of America but unfortunately still unpublished, presented measurements of σ_χ^2 clearly showing turbulent saturation. The paper of *Brown and Keeler* [1975] also found indirect evidence of turbulent saturation in the behavior of their measured curves of the log-amplitude covariance B_χ. Explanation of the phenomenon requires introduction of an additional parameter, the lateral coherence length ρ_0, defined as the separation of two points in the plane perpendicular to the sound waves for which the mutual coherence function $\mathcal{M}(\rho)$ becomes equal to e^{-1}. *Fante* [1974] showed that $\mathcal{M}(\rho)$ has the same form as (51) and, in fact, that using the weak turbulence result for $D_\psi(\rho)$ in (51) gives a good approximation to $\mathcal{M}(\rho)$ for strong turbulence. Thus ρ_0 is defined as the value of ρ for which $D_\psi(\rho) = 2$ rad and $\mathcal{M}(\rho)$ becomes $\exp\{-(\rho/\rho_0)^{5/3}\}$. Then ρ_0 can be found by setting $D_\psi(\rho) = 2$ in (56) and solving for ρ_0. To first order in ρ/L_0 this procedure gives $\rho_0 \approx \{1.46k^2L[C_{ne}^2]_\phi\}^{-3/5} + 0.483K_0^{1/3}\{1.46k^2[C_{ne}^2]_\phi\}^{-4/5}$. We should note that the examples of ρ_0 given by Brown and Keeler are not completely realistic, since they were obtained from the assumption that the altitude profile of C_{ne}^2 was the same as that of C_T^2 rather than the more typical behavior appearing in Figure 6. *Fante* [1975] includes more elaborate solutions for ρ_0 in the case of finite angular width beams, where a distinction must be made between short-term averaging and long-term averaging because of the effects of beam wander.

First we consider which eddies have the greatest effect on the log-amplitude variance σ_χ^2. Using the Kolmogorov spectrum and the weighting function H_χ given by (53) leads to a κ integrand in (61) equal to $\kappa^{-8/3}\sin^2[(\beta/s)(1 - s/L)\kappa^2L/2k]$ for the weak turbulence case. Differentiating this expression with respect to κ gives

Maximizing equation for log-amplitude

$$\tan[\beta(s)(1 - s/L)\kappa^2L/2k] = \tfrac{3}{2}[\beta(s)(1 - s/L)\kappa^2/2k] \qquad (75)$$

with the root $\beta(s)(1 - s/L)\kappa^2L/2k = 0.988$. For plane waves and constant C_{ne}^2 the eddies having most influence are located at $s = 0$, whereas for spherical waves they are located at $\beta(s) = s/L = \frac{1}{2}$. The corresponding eddy sizes $l = 2\pi/\kappa$ then are given by $l = 1.78(\lambda L)^{1/2}$ for plane waves and $l = 1.26(\lambda L)^{1/2}$ for spherical waves, that is, roughly equal to a Fresnel zone. The same result can be obtained by a more physical argument by noting that if part of the sound travels through the 'center' of an eddy and part past the 'edge' at the radius $r = l/2$, then interference between the two parts requires a total path length difference of at least $\lambda/2$, which implies $r \geq [\beta(s)(1 - s/L)]^{1/2}(\lambda L)^{1/2}$. Note that an 'eddy' is a spatial Fourier decomposition of the random three-dimensional refractivity fluctuation field, so that in one realization, one eddy of a given size contains one corresponding given value of refractivity. However, a refractivity change over the distance r between center and edge results in a diffraction angle $\theta \leq \lambda/r$, whereas the diffraction angle needed for the sound to reach the receiver at L is $\theta \geq (r/s)/(1 - s/L)$. Putting all these conditions together gives $r = [\beta(s)(1 - s/L)(\lambda L)]^{1/2}$. At the most effective location, $r = (\lambda L)^{1/2}$ for plane waves, and $r = (\lambda L)^{1/2}/2$ for spherical waves. For spherical waves a refractivity change over r will be magnified by the factor L/s at the receiver. Curves showing the resulting most effective eddy size and most important pattern size are included by *Clifford* [1976]. The curves show another important feature, that is, that small-scale fluctuations result from the effects of irregularities near the receiver and large-scale fluctuations from the effects of irregularities near the transmitter.

The correlation of amplitude over various pattern sizes, given as a function of transverse separation ρ, can be expressed by the log-amplitude covariance $B_\chi(\rho)$. *Clifford* [1976] gives a curve of $B_\chi(\rho)/\sigma_\chi^2$ as a function of $\rho_n = \rho/(\lambda L)^{1/2}$ for spherical waves, and a similar curve for plane waves appears in the work of *Tatarskii* [1961]. The above discussion presupposes homogeneous turbulence, that is, constant C_{ne}^2. For vertical paths the profile of C_{ne}^2 is usually much higher near the ground, and thus the most effective location will be shifted toward the ground. For such a profile, if the transmitter is on the ground, all pattern sizes will be increased, and the corresponding curve of B_χ/σ_χ^2 will lie everywhere above the homogeneous curve for $\rho_n > 0$. Experimental curves for this case were obtained by *Mandics* [1971]. In contrast, if the receiver is on the ground and the transmitter elevated, all pattern sizes will be decreased, and the curve of B_χ/σ_χ^2 will fall everywhere below the homogeneous curve for $\rho_n > 0$. If we limit ourselves to monotonic C_{ne}^2 profiles, all the various profiles lead to a family of nonintersecting covariance curves. All the members of the family lying above the curve for constant C_{ne}^2 result from profiles decreasing along the path, and all the members lying below result from profiles increasing along the path.

We noted earlier that the approximation $\sigma_\chi^2 = \sigma_t^2$ holds only in weak turbulence, that for increasing σ_t^2 greater than some value (≈ 0.3 for optical propagation in homogeneous turbulence) the values of σ_χ^2 increase less and less rapidly, eventually leveling off. Under these conditions the behavior of the B_χ^2/σ_χ^2 curves also changes, as is shown by the experimen-

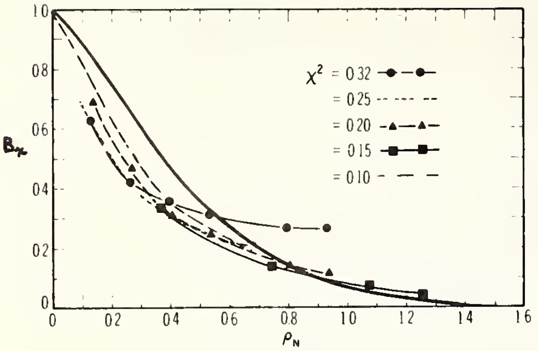

Fig. 13. Experimental log-amplitude covariances. B is normalized by the log-amplitude variance $\sigma_\chi{}^2$, and the transverse separation ρ is normalized by a Fresnel zone $(\lambda L)^{1/2}$ [from *Brown and Keeler*, 1975].

tal data in Figure 13, from *Brown and Keeler* [1975]. At the spring 1973 meeting of the Optical Society of America, Clifford proposed a physical theory that would account for the changes in behavior of $\sigma_\chi{}^2$ and B_χ. This theory was given quantitative form in the paper of *Clifford et al.* [1974]. A theory of *Yura* [1974] for the same phenomena was shown to be completely equivalent to the first by *Clifford and Yura* [1974]. Using the Markov approach described by *Tatarskii* [1971], *Fante* [1975] obtained similar results. Briefly, the weak turbulence theory assumes that the most important eddies intercept plane or spherical waves and that subsequent diffraction produces interference at the receiver. But in strong turbulence the wave fronts reaching the most important eddies have already been randomly distorted during propagation over the partial distance. The lateral coherence length ρ_0 measures the mean size of the wave irregularities. As ρ_0 becomes equal to or less than a Fresnel zone, the eddies at the center of the path become less effective in producing amplitude fluctuations, and their place is taken by smaller eddies closer to both the receiver and the transmitter. As a result the variance begins to saturate, and the covariance receives greater emphasis in small pattern scales (from smaller eddies nearer the receiver) and in large pattern scales (from the magnified effect of smaller eddies farther away from the receiver). Thus the normalized covariance $B_\chi/\sigma_\chi{}^2$ drops more rapidly for $\rho_n < 1$ and decreases less rapidly for $\rho_n > 1$ than the constant $C_{ne}{}^2$ curve for weak turbulence and intercepts the latter curve at about $\rho_n = 0.6$. For a profile of $C_{ne}{}^2$ along the path $s = 0$ to $s = L$ the point of intersection moves toward smaller ρ_n for decreasing profiles and toward larger ρ_n for increasing profiles. (This difference accounts for the fact that it is difficult to find evidence for saturation in the experimental curves of *Mandics* [1971], while the curves of *Brown and Keeler* [1975] appear to show such saturation.) *Brownlee et al.* [1974] have proposed an alternative explanation for turbulent saturation. They attempt to obtain saturation in the weak scattering case by a truncation of the wave numbers contributing to the fluctuation field. However, their result shows a leveling off of $\sigma_\chi{}^2$ only with increasing path length L rather than with the parameter $\sigma_t{}^2$. Consequently, the result implies that $\sigma_\chi{}^2$ continues to increase with $C_{ne}{}^2$ contrary to experimental observation.

A quite different approach to the problem of the propagation of sound through turbulence was initiated by *Keller* [1964] and continued by *Wenzel and Keller* [1971], *Howe* [1971], and *Wenzel* [1972]. In this method the wave is artificially split up into a 'coherent' wave with unchanged phase but decreasing amplitude and a growing 'incoherent' wave. Since many theorists have confused the phenomenon of the transfer of energy from the coherent wave to the incoherent wave with the phenomenon of turbulent saturation described above, we will coin a term and call this energy transfer 'coherent extinction' and emphasize that coherent extinction is not turbulent saturation. The energy transfer between a coherent spherical wave and an incoherent spherical wave can be simply modeled if we neglect absorption. If we write $p = \bar{p} + p'$, then energy conservation requires $\langle pp^\dagger \rangle = a_0{}^2/(4\pi r^2)$. At the same time, each differential scattering process is linear, that is, the same fraction of the coherent wave is transferred to the incoherent wave for each differential element of the path. Thus the coherent wave must decrease exponentially, or $\langle \bar{p}\bar{p}^\dagger \rangle = a_0{}^2 \exp{[-2\eta r]}/(4\pi r^2)$, where the relation defines the coherent extinction coefficient η. Combining these relations immediately gives $\langle p'p'^\dagger \rangle = a_0{}^2\{1 - \exp{(-2\eta r)}\}/(4\pi r^2)$, a result found through a much more involved argument by *Wenzel* [1976].

Brownlee [1973] has studied the Mintzer parameter $\mathcal{V}^2$ (related to $\sigma_\chi{}^2$) from the coherent-incoherent wave approach for the geometric acoustics case $(\lambda L)^{1/2} \ll l_0$ and for the 'wave' case $(\lambda L)^{1/2} \gg L_0$. For these two cases the behavior of $\sigma_\chi{}^2$ mimics the phenomenon of turbulent saturation but, in fact, does not result from diffraction or depend in any way on the structure of the turbulence. The similarity in behavior arises from the fact that in the geometric acoustics case, for instance, the ray path segments between multiple scatterings form a 'random walk' with a consequent Rayleigh probability distribution. But in the diffraction case, fluctuations that are initially normal go through a transitional probability distribution with increasing $\sigma_t{}^2$ and also eventually become Rayleigh distributed at high levels. *Howe* [1973] has studied the flow of kinetic energy, instead, for thermal scattering and turbulent scattering separately and obtained solutions in both the wave case $(\lambda L)^{1/2} \gg L_0$ and the geometric acoustics case $(\lambda L)^{1/2} \ll l_0$. For the thermal scattering case, Howe uses the propagation equation for the acoustic density fluctuations ρ_α, $\partial_t{}^2\rho_\alpha = \nabla^2(c^2\rho_\alpha)$, which for the atmosphere is not quite correct. In the atmosphere the density can be written as $\rho = \rho_\sigma + \rho_\alpha$, with $\rho_\sigma = \rho_0 + \rho_\sigma'$, where ρ_σ' are the density fluctuations in the absence of sound due to turbulent mixing of particles having different specific entropies σ from different altitudes. Such turbulent mixing is slow enough for the pressures to reach equilibrium with the local turbulence pressures, so that a fluctuation in c^2 requires a fluctuation in ρ_σ. Thus the correct equation should be $\partial_t{}^2\rho = \nabla^2(c^2\rho_\alpha)$ or, equivalently, $\partial_t{}^2(\rho_\alpha/\rho_\sigma) = \nabla\cdot[c^2\nabla(\rho_\alpha/\rho_\sigma)]$, an equation which includes the density changes resulting from the forced sloshing back and forth of ρ_σ due to the passage of the sound wave.

Although knowledge of the effects of turbulence on propagation is useful in itself, such information also has applications in other areas. An important example is in the quantitative interpretation of echosonde returns, particularly in corrections for the measurement of $C_T{}^2$ and $C_v{}^2$. *Brown and Clifford* [1976] have used the recent theory of *Yura* [1971] for beam broadening by strong turbulence to determine the amount of 'excess attenuation,' such as that considered by *DeLoach* [1975], produced by turbulence in a finite acoustic beam. If D_0 is the diameter of the source and a_e represents the 'excess attenuation coefficient,' the excess loss in intensity in decibels over a path length L is given by

Excess attenuation

$$a_eL = 10 \log \left\{1 + 1.56k^{12/5}D_0{}^2 \cdot \left[\int_0^L ds\,(1 - s/L)^{5/3}C_{ne}{}^2(s)\right]^{6/5}\right\} \qquad (76)$$

When (33) and (34) are used for measurements of C_T^2 and C_v^2, excess attenuation can introduce considerable errors into the results. However, the use of bootstrap computer programs based on (74) will furnish a method to remove most of such errors.

Acoustic Systems

The most common form of the echosonde is the monostatic configuration, in which the transmitting and receiving transducers are identical or, at least, nearly collocated. The simplified block diagram shown in Figure 14 describes the equipment of *McAllister* [1968], and it is still representative of most of the more advanced systems utilized in research laboratories at the present time or available commercially. In this system an acoustic tone burst is amplified, and the audio signal P_T is sent through a switching device to the transmit transducer. After a suitable delay the transducer is switched to the receive mode, in which the echo signal P_R is passed to the receiver amplifier and thence to a display or recording device, usually a facsimile recorder. Similar designs using an A-scope cathode ray tube (CRT) display much like that of *Gilman et al.* [1946] have been employed by *List et al.* [1972], and a design with a *Z* axis modulated CRT display was used by *Singal and Pancholy* [1972]. The earliest complete sounder system, reported by *Gilman et al.* [1946], was essentially the same as that indicated in Figure 14 except that a separate loudspeaker transmitter was used; the receiving transducer was a microphone in a 60-cm parabolic dish. The backscatter echoes were displayed on an oscilloscope which was photographed with a time-lapse camera. Likewise, the system used by *Kallistratova* [1961] to investigate the theoretical predictions of sound scattering by turbulence in the real atmosphere utilized separate receivers and transducers, in each case a large-area electrostatic transducer, the transmitter and receiver being placed in proximity for monostatic or backscatter investigations and separated and aimed at the appropriate angles for bistatic studies to scattering angles as small as 16°.

The echosonde used by *McAllister* [1968] had the important distinction that the display was a real-time facsimile machine in which the correlation and structure of the scattering volumes in the atmosphere could be graphically displayed. McAllister used the same transducers for transmitting and receiving, at first using an electrodynamic driver and horn at the focus of a large dish [*Mahoney*, 1966] and later an array of 196 commercial loudspeakers, each 20 cm in diameter. The peak pulse power for the array was over 500 W of electrical input. Switching to the transmit mode was accomplished with electromagnetic relays. *Mahoney* [1966] has described the design requirements of the echosonde, which initiated the 'new era' in atmospheric acoustics, the era leading to this review paper. In studying nocturnal radio propagation in Australia it was noted that over-the-horizon signal strengths could be explained only if significant temperature inversions existed for prolonged time periods. Since radiosondes could not continuously monitor the temperature structure, Mahoney studied the expected intensity of sound 'specularly reflected' from the temperature gradients sometimes measured. On the basis of these calculations the previously mentioned 15-m parabolic concrete dish antenna was constructed, and atmospheric return was successfully obtained. Because the returned intensity was stronger than was expected (confirming the work of *Gilman et al.* [1946]), the 'portable' array antenna sounder [*Mahoney*, 1967] was also constructed to supplement the obviously immovable first sounder. This array design was still based on the assumption of specular reflection from gradients; a multiple-gradient model was assumed to be necessary to explain the larger than expected signal strengths.

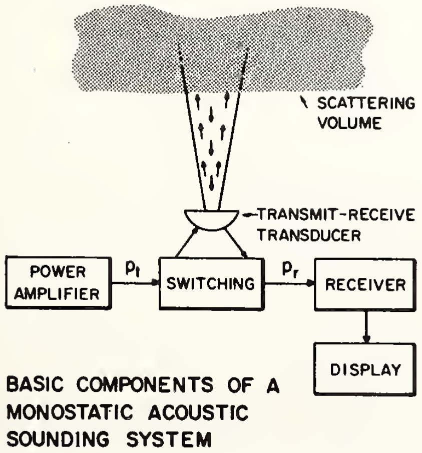
SCATTERING VOLUME
TRANSMIT-RECEIVE TRANSDUCER
POWER AMPLIFIER
P_t
SWITCHING
P_r
RECEIVER
DISPLAY
BASIC COMPONENTS OF A MONOSTATIC ACOUSTIC SOUNDING SYSTEM

Fig. 14. Simplified block diagram of a monostatic echosonde.

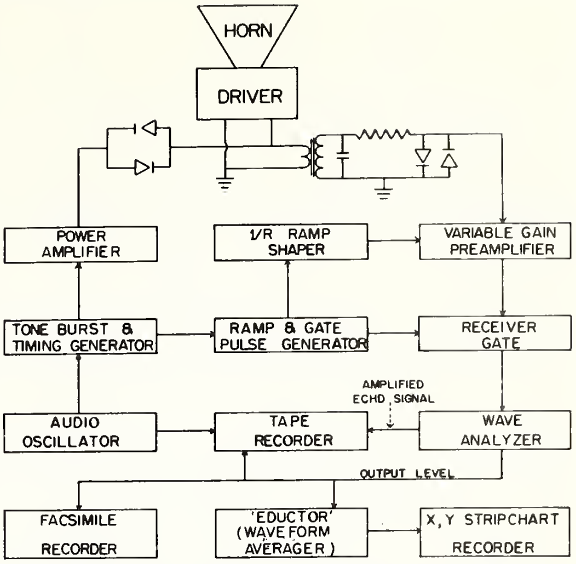

Fig. 15. Block diagram of an echosonde fabricated largely from off-the-shelf components.

The first comprehensive systems analysis of echosondes, performed by *Little* [1969], considered the effects of environmental noise. The desirable sensitivity and directivity of the receiver were determined, and estimates were made of the scattered signal strength to be expected from the knowledge then available on the turbulent temperature and velocity structure in the atmosphere. For example, Little calculated that for 10 W of transmitted acoustic power and a receiving area of 1 m², nominal temperature structure in the atmospheric boundary layer would lead to a return signal-to-noise ratio of +26 dB for a range of 150 m. Later investigations have shown this performance estimate to be quite representative of conditions found in nature.

A subsequent comparison of sensitivities between echosondes and electromagnetic radars shows the acoustic sounder to have a 10-dB advantage over comparable electromagnetic devices for viewing temperature irregularities; the electromagnetic units have a significant signal-to-noise advantage for viewing humidity fluctuations or hydrometeors [*Chadwick and Little*, 1973].

The first NOAA echosonde was designed and placed in operation during 1969 [*Wescott et al.*, 1970]. The design of this unit was based on the analysis of *Little* [1969] and used off-the-shelf units for many of the discrete components, such as the power amplifier, tone burst generator, wave analyzer, and facsimile recorder. Figure 15 shows a block diagram of the all-solid-state electronics unit (no relays were used in the switching circuits). The $1/R$ ramp shaper is to compensate for the spherical spreading of the scattered acoustic echoes; the transducer is sensitive to pressure amplitude rather than power, so that $1/R$ provides the proper range compensation, if other attenuating effects in the atmosphere are neglected. When the system was equipped with a 1.2-m cone paraboloid reflector antenna and a 40-W receive-transmit transducer, it provided a useful range of several hundred meters in the atmosphere [*Wescott et al.*, 1970].

As sounder technology has advanced, more sophisticated and specialized designs have been tested and applied. The NOAA Mark II unit, described in a report by *Simmons et al.* [1971], utilized a crystal-stabilized clock. The report is explicit in defining the various control signals found useful in operating monostatic echosondes.

Problems in obtaining satisfactory performance from echosondes can frequently be traced to an inadequate preamplifier. If one is to obtain the ultimate performance from an echosonde system, it is necessary to be limited by the inherent system noise, the Johnson, or thermal, noise generated in the receiver element [*Nyquist*, 1928]. The usual impedance of electrodynamic voice coils being a few ohms, it is easy to calculate the expected noise voltage across the voice coil by $V = (4kTR\Delta f)^{1/2}$, where k is the Boltzmann constant (1.38×10^{-23} J K^{-1}), T is the temperature, R is the ohmic resistance of the voice coil, and Δf is the electronic bandwidth of the measurement. For example, consider a 10-ohm voice coil at room temperature with a typical echosonde bandwidth of 100 Hz. Then we obtain $V = 4 \times 10^{-9}$ V. If we want an echosonde that is truly systems noise limited, we must be able to handle such small signals.

Admittedly, it takes an extremely quiet environment to allow enough amplification to see the Johnson noise. Usually environmental noise dominates (eolian tones from winds blowing across the antenna, eolian tones from wind in nearby foliage or around structures, insects, or birds, and, in urban areas, man-made noise from vehicles or other human activities), but on occasion in still, rural settings, one can find quiet conditions that enable the Johnson noise to be the limiting factor in echosonde performance. The preamplifier must obviously be placed near the transducer to prevent other sources of noise from being picked up in long cables, and it is usually necessary to use a step-up transformer in coupling the voice coil to the input stage, say, with a turn ratio of 100:1, since typical input noise voltages for solid-state amplifiers are frequently near 1 μV. Preamplifiers to achieve this desirable performance have been discussed by *Wescott et al.* [1970] and *Simmons et al.* [1971].

By 1972, echosondes of the type described above were being operated by some twenty-two different groups around the world [*Hall*, 1973]. Following the lead set by the Weapons Research Establishment (WRE) in Australia, two groups at the University of Melbourne quickly developed echosonde programs. In the Department of Meteorology, *Beran* [1970] exploited echosondes in a diversified study of turbulence detection methods. Several reports on project EAR (Environmental Acoustic Research) were published. Cooperative experiments were performed with WRE on the extension of acoustic sounding to the upper troposphere [*Beran et al.*, 1972*a*]. Acoustic scattering layers at heights of 3 km and more were detected by using the 15-m concrete dish at WRE and utilizing a feed of 19 paper cone loudspeakers. Experiments with a sound source on a glider were conducted to investigate the propagation and attenuation of sound in the real atmosphere [*Beran*, 1970].

In the Physics Department of the Royal Australian Air Force Academy, *Bourne and Shaw* [1970] developed a monostatic echosonde to study the classes of echoes observed and to relate these to meteorological conditions. The results obtained by *Shaw* [1971] are useful in interpreting facsimile records; interpretation will be discussed in a later section of this review.

The radio research laboratories in Japan have operated an echosonde with a 16-m concrete reflector antenna patterned after the WRE unit since 1970 [*Fukushima et al.*, 1971] and more recently a portable unit [*Fukushima et al.*, 1976]. The objective of this project is to supply inversion information for the local weather services and to study the radiometeorological structure of the lower troposphere.

In India the group at the National Physical Laboratory has developed acoustic techniques to aid in the study of radio wave propagation [*Singal*, 1973, 1975]. The ability of the echosonde to anticipate the dispersion of nocturnal inversions is regarded as especially valuable [*Singal et al.*, 1975].

Centre National d'Etudes de Télécommunications in France has the goal of real-time wind profile measurement from the surface to 1 km for its echosonde program [*Aubry et al.*, 1974]. Special parabolic antennas for acoustic use have been designed, and the understanding and extraction of Doppler-shifted signals have been emphasized. (More will be said on wind studies in the applications section.) A recent progress report [*Aubry*, 1975] presents striking multicolor displays to depict the backscatter intensity and the Doppler shift in the echoes.

The objective of the acoustic program at Laboratorium für Atmosphärenphysik, Eidgenössische Technische Hochschule, in Zurich, Switzerland, is to develop an echosonde to monitor the gravity waves induced by foehn winds over the Alps. The pressure fluctuations associated with these waves give rise to a malaise commonly noted in Switzerland. *Nater* [1974] has reviewed these plans and provides a comprehensive review and bibliography of the field of atmospheric acoustic research.

The program at the Swedish National Defense Research Institute [*Joelsson*, 1974] has as its objective the understanding of radio ducting, especially over the Baltic [*Ottersten*, 1975]. More will be said on this program in the section on atmospheric science investigations.

Since 1972, utilization of integrated circuits and logic circuit design techniques has reduced the size and cost of echosondes while providing extremely reliable and flexible devices [*Owens*, 1974, 1975]. A low cost commercially available echosonde has also been placed on the market, and more than 100 are in use at this writing [*AeroVironment, Inc.*, 1976]. Digital data reduction methods have also been incorporated into echosondes to provide plots of quantitative values of the returned echo to supplement the, at best, semiquantitative facsimile records [*Werner*, 1977].

The acoustic antenna remains one component of the echosonde system in which there is still room for increased understanding and better design. Microwave antennas, suitably damped and shielded, provide reasonably well-defined main beams and suppressed side lobes [*Hall and Wescott,* 1974], but the difficulty in actually measuring far-field beam patterns over a horizontal outdoor range leads to uncertainties of several decibels in the gain characteristics. A study by *Strand* [1971] showed that absorbing cuffs around the antennas can reduce the 90° side lobes by 20–30 dB if they are properly designed. *Adekola* [1975, 1976] has extended Strand's treatment and concludes that both the height and the upper diameter of the absorbing cuff should be 3 times the lower aperture for optimum performance.

For bistatic configurations, linear arrays of horns designed to exhibit a fan beam shape have been suggested [*Carsey,* 1972], but experience has shown that extreme care needs to be employed to limit the beam width of such receiving arrays or, at least, to decrease significantly the gain in the horizontal direction, in which the acoustic horizon is generally too noisy to allow efficient operation of such units. Of course, a fan beam transmitting antenna and vertically directed receiving beam can be used [*Davey,* 1976; *Kaimal and Wescott,* 1976] if the noise nuisance is acceptable.

Singal et al. [1974] have compared the performance of on-axis and horn-reflector parabolic antennas and arrays of loudspeakers and have offered tips on fabrication techniques. They conclude that the horn-reflector configuration is a highly efficient design, in agreement with the results of *Hall and Wescott* [1974] and of *Kurze* [1976].

In order to obtain quantitative measurements of the echo intensity return to study the turbulent parameters leading to acoustic scattering it is necessary to know precisely the gain pattern of the antenna in the far field. A measurement technique in which a microphone is suspended on a three-point tether from a balloon has been described by *Willmarth et al.* [1975]. This technique overcomes many of the objections and uncertainties in utilizing a horizontal range or an anechoic chamber where only the near field can be measured.

A properly shielded acoustic antenna can achieve 50-dB suppression of the 90° side lobes [*Adekola,* 1976]. If insufficient side lobe suppression occurs, there is a good chance that scattering or reflection of the transmitted pulse by nearby structures, hills, or trees can produce the appearance of horizontal layers on the facsimile record, which might be interpreted as being of atmospheric origin. Here the experimenter is cautioned that the atmosphere is never completely at rest and that true horizontal layers will always show some undulations from gravity waves or shear instabilities and will change with time as different striae advect over the site.

Similarly, problems with proper triggering in time of the transmit pulse can lead to leak-throughs of improperly timed tone bursts that may give the appearance of atmospheric echoes. This may have been the case in the thin sloping layer reported by *Petersen and Jensen* [1976].

ATMOSPHERIC SCIENCE INVESTIGATIONS WITH ECHOSONDES

Earlier reviews of echosonde science investigations have provided preliminary information on the temperature structure in convective plumes [*Hall,* 1972], have provided information on the types of echo patterns observed for the stable and unstable atmosphere [*R. Cox,* 1971], or have listed the fundamental equations for propagation, scattering, and Doppler extraction from the returned echosonde signal [*Morris and Hall,* 1975]. *Thomson* [1975] discussed the various scientific applications of echosondes. Other reviews have compared echosonde results and capabilities with optical or microwave remote sensors [*Little,* 1972*a*, *b*, 1973]. This review of atmospheric research performed with echosondes gives particular attention to new information and insight into atmospheric structure that such studies have provided.

Convection in the Unstable Atmosphere

As was pointed out earlier, the backscatter of acoustic waves is caused primarily by temperature fluctuations, or C_T^2, in the atmosphere. When the surface of the earth is heated by the sun in midday, it becomes much warmer than the surrounding atmosphere, and a superadiabatic lapse rate develops in the lower few meters. The air heated by conduction from the earth rises in turbulent eddies characterized by a high value of C_T^2. It is not surprising then, as was pointed out by *McAllister et al.* [1969], that the most characteristic and repeatable pattern of acoustic returns depicts convective plume structures rising to several hundred meters on sunny days with light winds. Here it should be noted that turbulent overturning of a stable layer may also be called convection [*Parry and Sanders,* 1972] or, more definitively, forced convection. We will follow the more usual meteorological use of the term [*Huschke,* 1959] to imply buoyant (or free, or gravitational) convection. Over a typical dry prairie terrain the vertical convective plume structures first appear an hour or two after sunrise and lift and modify the characteristic stable atmosphere echoes, which will be described in the next subsection. A typical facsimile record of the monostatic acoustic probing of convective plumes is shown in Figure 3, where the darkness of the trace is proportional to the value of C_T^2 in the plumes. Typical maximum values of C_T^2 in plumes over dry prairie terrain at a height of 100 m are near 3×10^{-2} °C^2 m$^{-2/3}$. Because of the intermittent nature of the plumes the average value of C_T^2 at the same height would be more than 1 order of magnitude lower. Typical isopleths of C_T^2 derived by sounder backscatter measurements are given by *Hall et al.* [1975]. They also document the average lack of wind shear as determined by Doppler echosonde at heights from 30 m to several hundred meters under convective conditions. This lack of shear results in an average vertical orientation of the plumes; maximum vertical velocities in summertime prairie plumes average 2 m s^{-1}. Under certain specialized prairie conditions, thermal plume characteristics may show little seasonal variation [*Hall et al.,* 1971], evidently because the lower winter insolation on dry, perhaps overgrazed grasslands is compensated for by taller grass and more evapotranspiration during summer months.

By applying Taylor's hypothesis and knowing that the plumes advect with the mean wind in the well-mixed layer, one finds an average dimension for individual plumes at a height of 100 m to be between 200 and 400 m in the direction of the mean wind. The plumes seem to come in clusters, however, so that an even larger scale of organization, measuring several kilometers, may be found by spectral analysis of the scattered acoustic intensity or of the wind fields that converge into the plumes [*Fitzjarrald,* 1976].

The C_T^2 signature of convective plumes is an expected consequence of similarity theory modeling of the planetary boundary layer. *Wyngaard et al.* [1971] show that C_T^2 is related to the turbulent surface temperature flux Q_0 by

Relation of C_T^2 to surface heat flux

$$C_T^2 \simeq (4/3k^{2/3})(\bar{T}/g)^{2/3}(Q_0/z)^{4/3} \tag{77}$$

Here $\bar{T}$ is the mean atmospheric temperature, g is the acceleration of gravity, k is von Kármán's constant, and z is the height

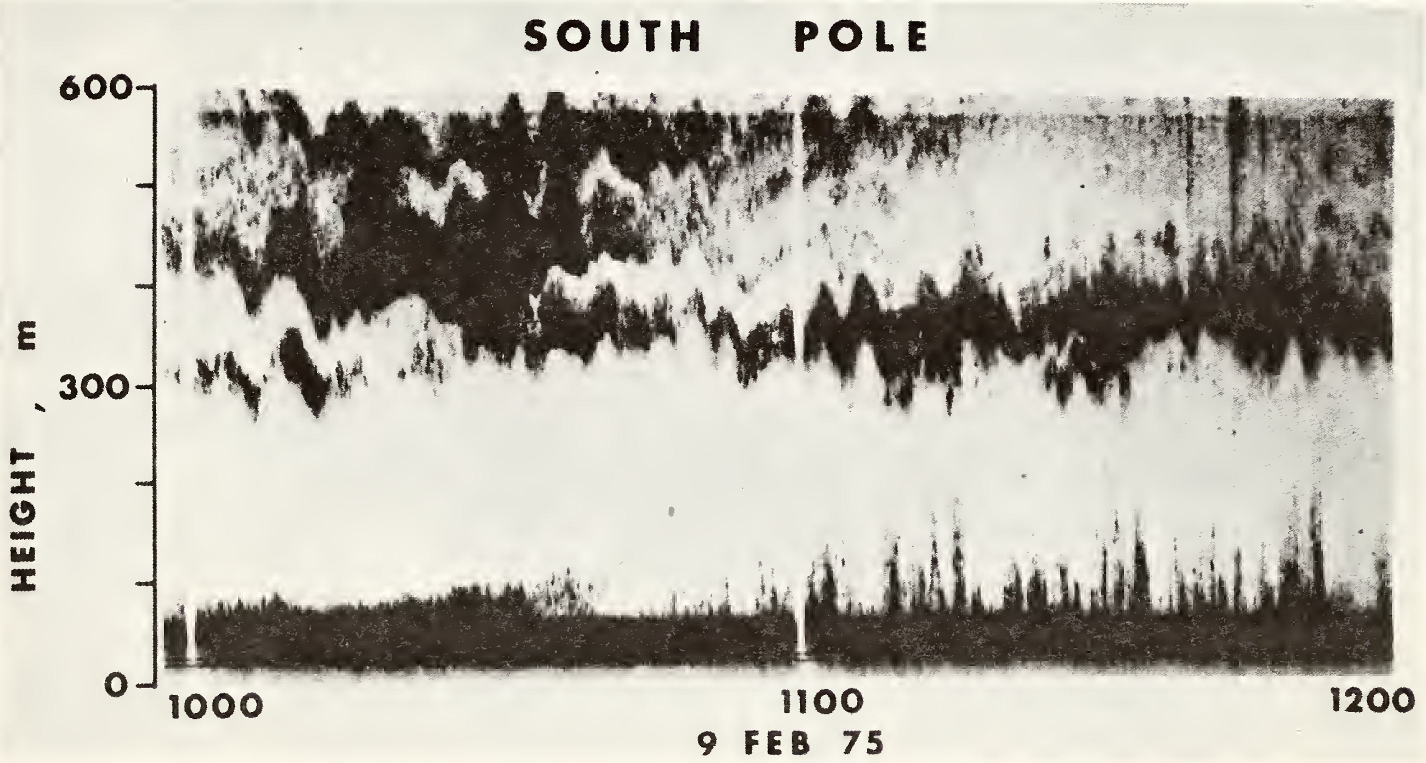

Fig. 16. Facsimile record of convective plumes at the south pole. The cold front shows as the undulating layers aloft.

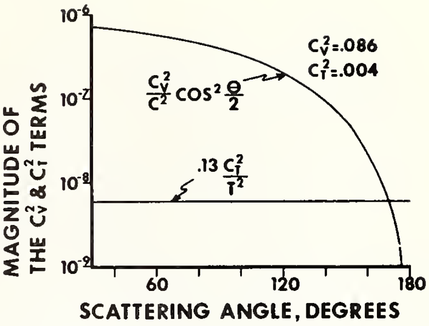

Fig. 17. Magnitude of the two structure parameter terms of (33) for typical dry, convective conditions. C_v^2 units are $m^{4/3}\ s^{-2}$; those of C_T^2 are $K^2\ m^{-2/3}$.

above the surface. As might be expected, the typical temperature profile when plumes are present will be dry adiabatic, superadiabatic lapse rates being found near the surface [*Fukushima*, 1975].

Over warm tropical oceans the echosonde will reveal a truly ubiquitous pattern of convective plumes, continuing night and day because of the absence of diurnal temperature patterns. Such plumes were measured during Gate [*Mandics et al.*, 1975*a*, *b*; *Mandics and Hall*, 1976]. In the equatorial mid-Atlantic these plumes extend to 300–400 m and represent warm moist columns of rising air with maximum vertical velocities near 1 m s^{-1}. Because the ratio of latent heat to sensible heat in such plumes may be 10:1 or higher [*Gaynor et al.*, 1976], the contribution of the humidity fluctuations to acoustic backscatter can be significant, accounting for 28% or more of the echo intensity [*Wesely*, 1976]. If the temperature and humidity fluctuations are correlated, as aircraft measurements by *Coulman and Warner* [1976] near a moist land surface imply, then the humidity influence becomes even more important.

Fukushima et al. [1976] also observed continuous convective plumes over a warm ocean current in the northwest Pacific. In other oceanic regions the atmospheric stability may change from a convectively unstable lapse rate to a stratified, stable lapse rate depending upon the history of the air mass overlying the nearly constant temperature ocean surface. *Ottersten et al.* [1974] present typical examples of convective plume records recorded aboard the research vessel *Planet* in the North Sea during 1973. A ship can be a noisy, rolling, and pitching platform, not necessarily ideal for acoustic work, but Ottersten and his co-workers obtained excellent results by mounting their equipment on a stabilized platform (to overcome the ship movement) isolated from ship vibrations. With the ship anchored and much of the machinery shut down, good results were obtained, in no small measure because of the excellent acoustic cuff surrounding the antenna during the experiment.

By mounting their antenna on the foredeck of the NOAA ship *Oceanographer*, *Mandics and Owens* [1975] were able to operate with the ship underway. They reported convective plumes when air cooler than the ocean surface was being probed off the coast of Baja California and in the Caribbean Sea.

NOAA has operated echosondes through two winters near Frasier, Colorado, in a high mountain valley well known for its low temperatures and deep snowpack. Surprisingly, even under these conditions, convective plumes to several hundred meters frequently develop on sunny days. For such cases the sensible heat is not added to the atmosphere from the high-albedo snow cover but rather through the heating of conifer foliage, which generally shakes loose the snow cover a day or two after each storm. This effect has been studied by *D. H. Miller* [1956].

The plumes observed in an urban environment with echosondes seem to have the same dimensions and vertical velocities as those over uniform land surfaces or water [*List and Melling*, 1974]. When such plumes are observed to heights of several hundred meters without the capping inversion echo, one can be assured that good vertical mixing is occurring and that there is little threat of an air pollution episode.

Convective plumes may even be detected over the Antarctic ice sheet. A NOAA sounder operating at the south pole recorded the facsimile shown in Figure 16 as a cold air mass at −40°C advected over the somewhat warmer ice, conditioned by several days at −30°C. Until the ice cooled, 4 hours after the cold front passed at 1030 LT on February 9, 1975, convective plumes were detected to heights of 200 m. A radiosonde at 1115 showed a superadiabatic lapse rate in the lowest 138 m of the atmosphere [*Hall and Owens*, 1975; *Neff and Hall*, 1976*a*].

During midafternoon in temperate regions, convection frequently lifts the previous night's capping inversion to heights of 1 km or more over typical prairie terrain. Most monostatic sounder facsimile records show convective plumes extending to only 600 m or so, yet we know that convection and vertical transport of heat must still be going on at the higher levels. Indeed, *Frisch and Ochs* [1975] have shown from in situ measurements that the model of C_T^2, decreasing with height as the $-\frac{2}{3}$ power, extends to at least 80% of the convectively mixed layer. The plumes do not show in most sounder records to greater heights because of this decrease in temperature structure and the increasing attenuation caused by both molecular absorption and because of the scattering process. (The analysis of *Brown and Clifford* [1976] shows that if a wider transmitting and receiving beam width is used, the effects of scattering or excess attenuation will be decreased, but this is usually not practical because the decreased directivity lowers the signal-to-noise ratio and side lobe rejection of noise by the antenna may also be degraded by the wider beam.)

By significantly increasing the transmitted acoustic power to 1 kW or more, one may improve the signal-to-noise ratio and record monostatic echoes to heights of several kilometers. This approach has been taken by *Bourne and Keenan* [1974], who report rather consistent returns to heights of 2 km or more from elevated inversions and from only slightly lesser heights for the convective plumes. Another approach to obtaining improved signal-to-noise ratio is to abandon the monostatic configuration and use the combined scattering from temperature and velocity fluctuations in a bistatic configuration. If a scattering angle of 150° is used, compared with the 180° for the monostatic case, the scattering cross section will usually increase by more than 10 dB. The plot of Figure 17 shows the contribution of the two scattering terms for scattering angles varying from 30° to 180°; it uses typical values of the velocity and temperature structure parameters found low in the prairie summertime surface layer. Additionally, C_v^2 is nearly constant with height throughout the mixing layer, not exhibiting the falloff with height as does C_T^2 [*Frisch and Clifford*, 1974]. Thus when a bistatic return is compared with a monostatic one, the convective plumes are less well delineated because C_v^2 scattering between the plumes will contribute more scattered power to the bistatic receiver than C_T^2 within the plumes [*Hall and*

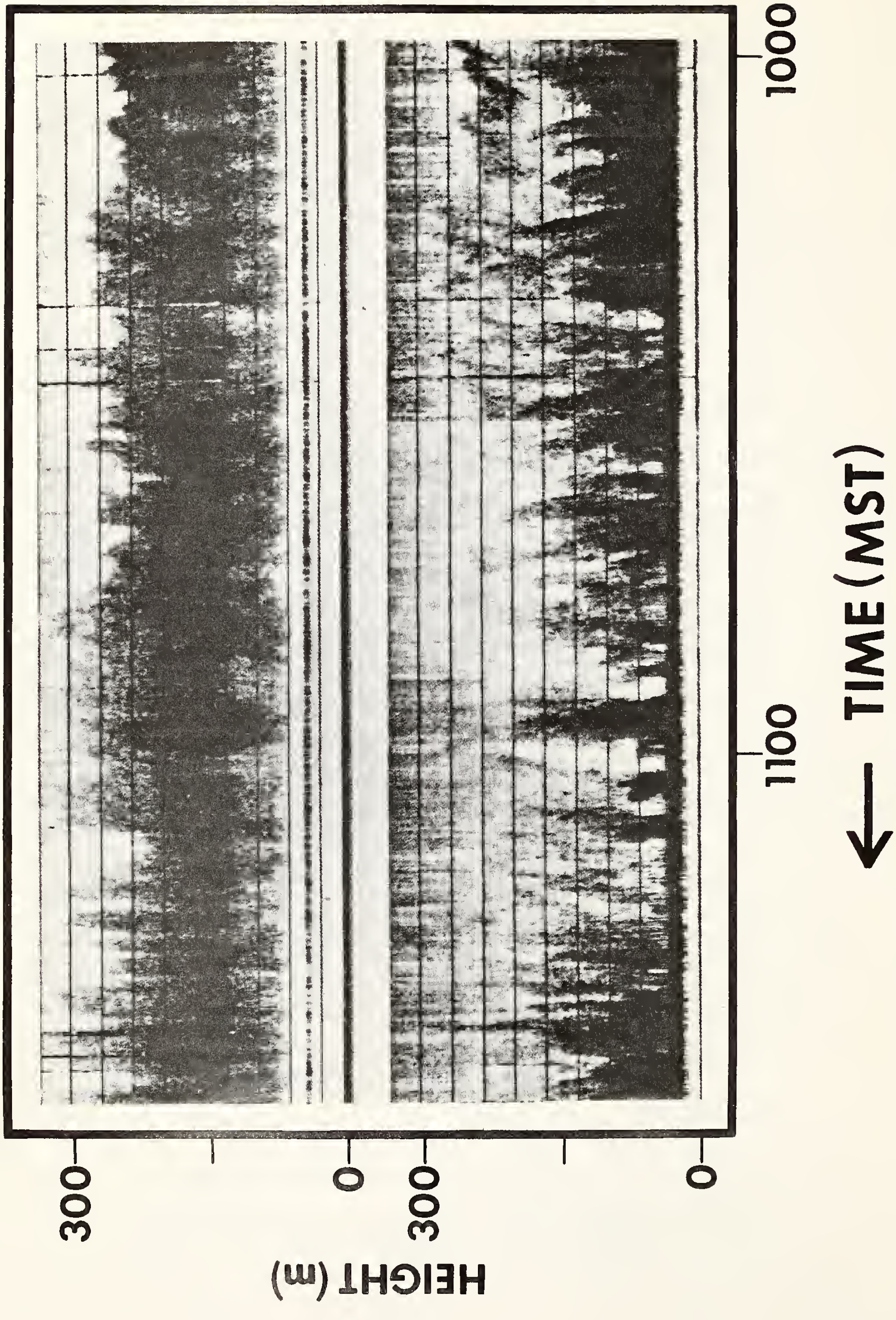

Fig. 18. Facsimile records of convective plumes. The lower record is from a monostatic echosonde; the upper is the bistatic return with a scattering angle $\theta = 150°$. Data were taken at Table Mountain, Colorado, during March 1977.

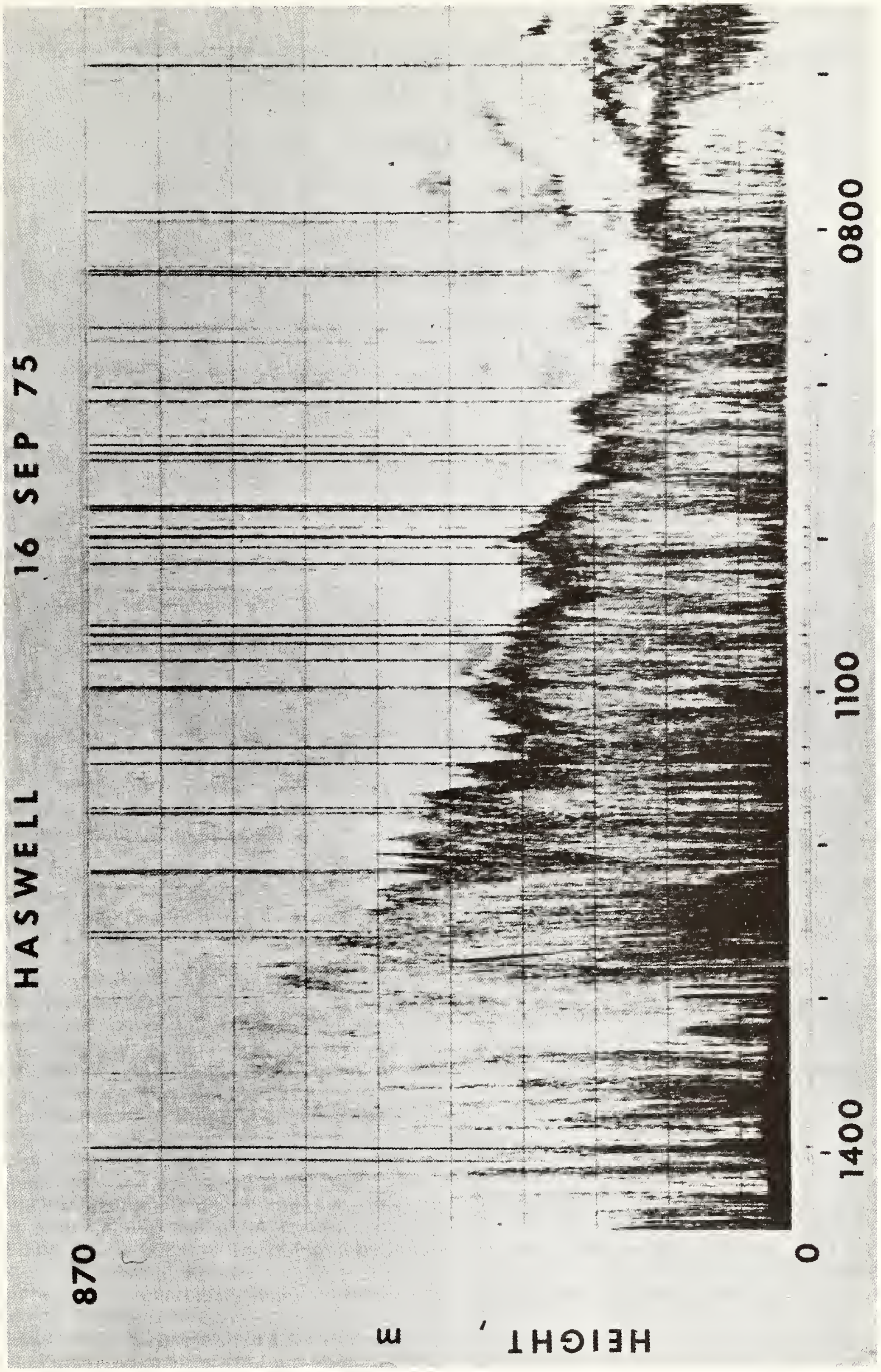

Fig. 19. Increase in depth of the convective mixed layer with time during dry, sunny conditions. The elevated temperature inversion lifts from 180 m at 0800 to 700 m at 1300.

Beran, 1974]. An example of this filling in between plumes in the bistatic mode is shown in Figure 18, where the limited height range for the bistatic returns is the result of the limited volume of beam interception produced by the experiment geometry.

Bistatic scattered intensity can exceed monostatic during nighttime conditions also. *McAllister and Pollard* [1969] show an example from a nearly neutrally stratified atmosphere in which the monostatic return is hardly detectable, while at a 120° scattering angle a strong echo shows.

Spizzichino and van Grunderbeeck [1975] have used a three-axis Doppler echosonde equipped with a minicomputer for real-time data processing to study the structure of thermal plumes. In particular, they obtained time of passage as a function of altitude, height profiles of vertical velocity, and scattering cross sections. They compared their observations with theoretical models of thermal plume structure. Generally, most of the hypotheses used in these models, such as that of 'self-preservation' of profiles, seemed to be supported.

Inversions, Fronts, and Turbulent Layers

As free convection develops over land on sunny mornings, the nocturnal temperature inversion, which usually develops during nighttime hours, is lifted by the plumes. It shows on echosonde facsimile records as a darker 'envelope echo' rising with time. A typical facsimile picture of this effect is shown in Figure 19. That the interpretation of this envelope echo as the lifting inversion is correct has been shown by a number of studies [*Cronenwett et al.*, 1972; *Wyckoff et al.*, 1973; *Fukushima*, 1975; *Edinger*, 1975; *Stilke et al.*, 1976]. We have seen why a large acoustic return is to be expected from buoyant thermal plumes, rich in C_T^2, but what is the explanation of echoes from statically stable layers? The answer can be readily obtained when one of the criteria for turbulence is examined, the gradient Richardson number, Ri_g. Recalling that the definition is

Gradient Richardson number

$$Ri_g = \frac{g\,(\partial\theta/\partial z)}{\theta\,(\partial U/\partial z)^2} \tag{78}$$

where the potential temperature θ and the wind speed U are measured as a function of height z, and that turbulent flows are experienced when Ri_g assumes values lower than 0.25, we see that although the buoyantly unstable thermal plumes give rise to echoes because of the zero or negative numerator term, wind shear, even in statically stable layers, can lead to low Richardson numbers. Overturning of the air in turbulent eddies occurs even though $\partial\theta/\partial z$ may have a large positive value, as was discussed earlier. In situ instrument profiles of the wind and temperature through elevated inversions show that Ri_g assumes values between 0.1 and 0.2 [*Hall et al.*, 1975]. It seems that nature has some feedback mechanism whereby the thickness of stably stratified shear regions changes so that the region is turbulent but not too turbulent. Thus the acoustic return from elevated inversions is because of scattering from turbulence and is not a reflection of the sound waves from a smooth gradient in acoustic index of refraction. In a specific attempt to see if such gradient returns could be measured in the extremely stable, only slightly sheared inversions over Fairbanks, Alaska, *Beran et al.* [1973] found no change in backscatter for a vertically pointed sounder compared with one tilted 35° from the zenith. Stronger returns to the vertical sounder would be expected from horizontal, specular layers.

In spite of this evidence against specular returns, *Petersen and Jensen* [1976] believe that they observed such a gradient in a sea breeze front. This interpretation is challenged by *Hall and Neff* [1977], who attribute the pattern observed to noise or equipment problems. *Petersen and Jensen* [1977] hope to resolve the argument through use of a bistatic system.

When the atmosphere exhibits a uniform, adiabatic temperature lapse rate, or $\partial\theta/\partial z = 0$, no amount of turbulence or overturning of different air parcels will produce C_T^2 structure. Frequently, the real atmosphere approaches such an adiabatic lapse around sunset on clear days and beneath thick cloud cover at almost any time. Under such conditions a monostatic echosonde will produce a rather featureless facsimile record; no acoustic scattering centers are present.

Ground-Based Shear Layers

When the lowest several tens of meters of the atmosphere show an increase in potential temperature of, say, 4–10 K accompanied by a wind shear of 5–10 m s^{-1} across this region, the echosonde will characteristically display an intense band of closely spaced, turbulent, sloping regions. *McAllister et al.* [1969] were the first to describe this ground-based wind shear layer, noting its frequent similarity to a herringbone structure. The shear instabilities within such layers were examined by *Emmanuel* [1972, 1973], who measured the gradient Richardson number within these layers by using an instrumented carriage on a meteorological tower. A number of shallow regions within the herringbone structure showed Ri_g values of 0.25 or less, although the 'layer (or bulk) Richardson number' throughout the band of acoustic echoes frequently averaged near 0.5. As was pointed out by Emmanuel, the kinetic energy of the turbulent breaking waves has its source in the kinetic energy of the wind. The greater the wind shear, the greater the depth of the instability with its consequent downward transport of momentum and heat to the surface. The intermittency of the waves represents a cycling process between the turbulent breaking waves and the background wind field. Amplification of these instabilities and maintenance of the turbulent layer demand a continued excess of shear kinetic energy over buoyant energy. Emmanuel shows that the Helmholtz instability, although it was derived to explain a more limited class of waves, serves quite well to describe the uniform amplitude and spacing of the sloping regions in the ground-based shear layer (GBSL).

When the pulse repetition rate or the paper advance speed in the facsimile is increased, the sloping regions of the echo band closely resemble braided (or breaking wave, or cat's eye) structures [*Gossard et al.*, 1970; *Emmanuel et al.*, 1972]. On occasion, bursts of even larger amplitude breaking waves may appear superposed over the ground-based layer [*Hooke et al.*, 1973]. Such events may represent the dumping of large quantities of energy and momentum from low-level jets to the ground.

Where better to find the ubiquitous ground-based shear layers than in the polar regions, characterized by boundary layers of strong static stability and persistent winds? *Holmgren and Jacobsson* [1976] show a typical ground-based layer recorded at Barrow, Alaska, in the late winter, repeated in Figure 20*a*. A 6.5 m s^{-1} shear across a 200-m-deep layer with only 1 K static stability shows a persistent, closely spaced turbulent wave return hour after hour. Similarly, *Neff and Hall* [1976*b*] find the GBSL to be the typical return at the south pole, characterizing more than 4000 hours of data acquired during 1975. An example is shown in Figure 20*b*.

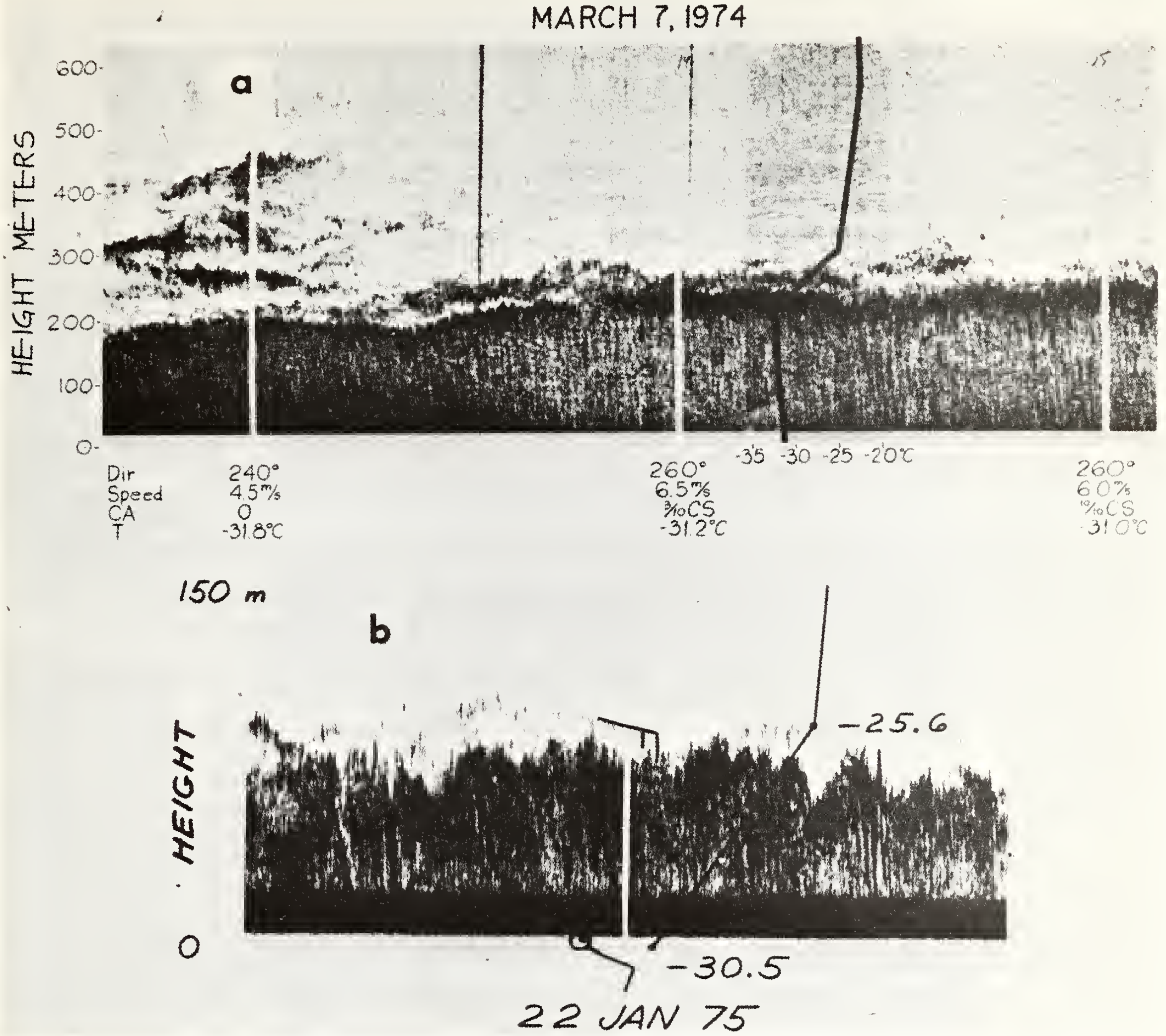

Fig. 20. Ground-based shear layer echo structure recorded (*a*) at Barrow, Alaska, and (*b*) at the south pole. Both records indicate a stable, sheared boundary layer. (Part *a* courtesy of B. Holmgren.)

When the ground-based shear layer is observed over the central United States, the maximum height of the echoes may correspond to the nocturnal jet wind maximum [*Kelly*, 1973]; as the wind speed increases in the jet, a sudden jump of a thin ground-based layer to the jet altitude may be observed.

When air warmer than the ocean surface intruded over the North Sea, *Ottersten et al.* [1974] observed the typical stably stratified returns, similar in appearance to those observed over land. Ocean-based shear layers with herringbone appearance, ranging in depth up to 300 m, were monitored as well as complex, multilayered, undulating inversions.

A slightly modified appearance for a ground-based shear layer is typically found during cold air outflow or gust front episodes from thunderstorms. Here we have both conditions for the herringbone pattern, static stability and strong winds, but the events are much more transient than the more ubiquitous nocturnal or polar layers. Figure 21 is a typical facsimile recording of a gust front as described by *Hall et al.* [1976]. In this case a shallow ground-based layer, representing the surface-based inversion, is lifted and modified by the still colder air from the thunderstorm. Although the original storm had dissipated 20 km away, the typical abrupt nose to the current and the descending shear layers are still clearly in evidence. Knowledge of the existence of such sloping shear interfaces can be of value in interpreting in situ tower anemometers to delineate properly the wind patterns within the currents.

Marks [1973] compared two cases of thunderstorm density current echoes against in situ instruments on a 444-m tower and also found good correlation between temperature and wind measurements and the appearance of the facsimile records. He points out that echo-free regions sometimes found in such currents are explained by volumes of homogeneous air that are entrained in the currents. With a little practice the user of the echosonde can come to recognize the different patterns presented from sudden jumps in the layer, from nocturnal jet coupling, or from density currents.

Another mechanism for establishing statically stable ground-based shear layers operates when cool air from lakes or the sea is advected over the heated land. The echoes from such occurrences closely resemble those of weak density cur-

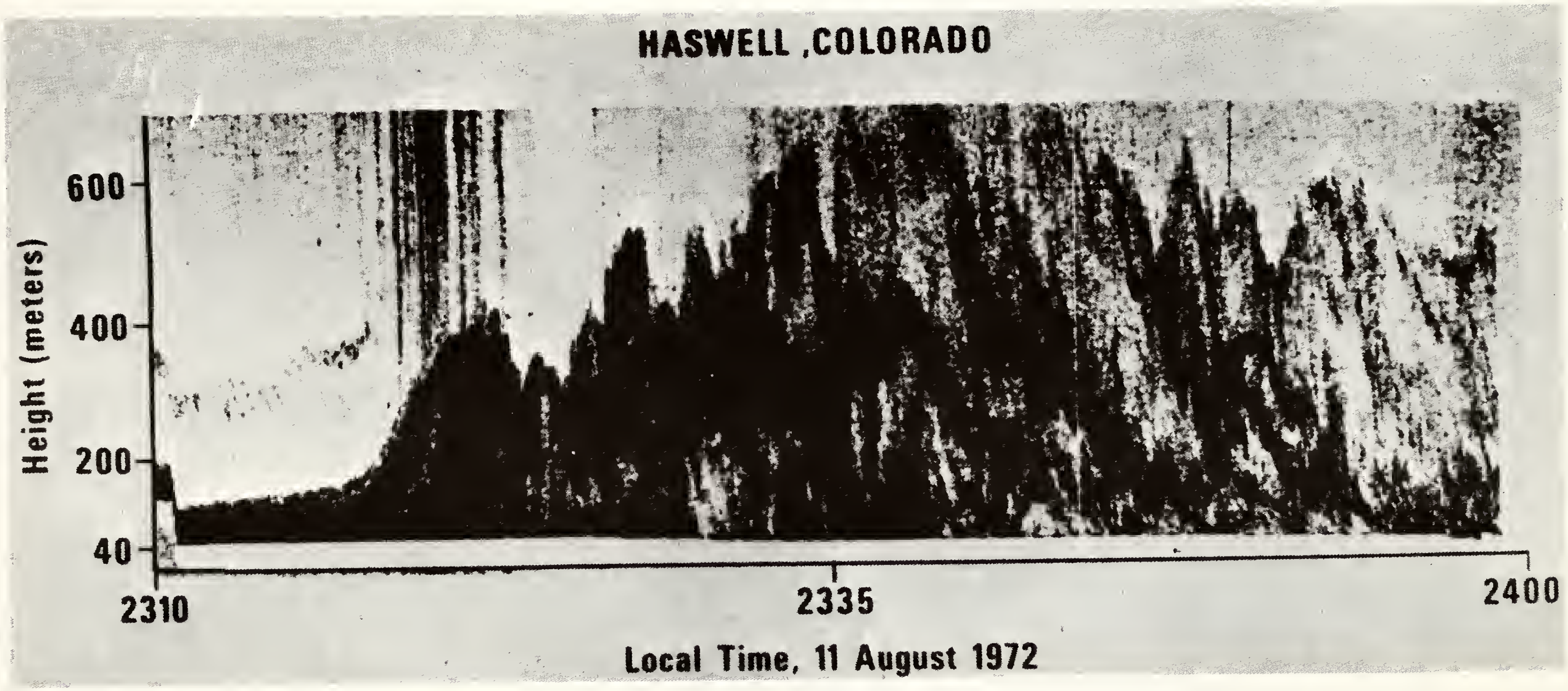

Fig. 21. Echosonde facsimile record of a density current or gust front from a thunderstorm.

rents. *R. C. Bennett and R. List* [1975] show facsimile records of the breeze from Lake Ontario as it blows across Toronto. Following the lifting of the nocturnal inversion by convective plumes in the early morning, the lake breeze shows a typical ground-based shear layer appearance for several hours, or even all day, depending upon the synoptic forcing of the circulation. Similar records are shown by *Rizzo* [1975], who used a monostatic echosonde to investigate the circulation from Lake Michigan in Milwaukee.

Cold, drainage winds (katabatic winds) also produce density current type echoes. *Mahoney et al.* [1973*a*] show three such facsimile records, complete with wind profiles, of the so-called 'gully wind' in south Australia.

When winds exceed 15–20 m s^{-1}, even 200 m above a strong surface-based inversion, the turbulence generated may be strong enough to erode the continuous ground-based layer, leaving only bursts or spikes of turbulent patches. Such echoes closely resemble buoyant convective plumes on the facsimile record. Spiky ground-based layer returns may be more prevalent over rough terrain, since they have not been seen often in the south pole facsimile records. Nonetheless, the reader is warned of this possibility of confusing facsimiles in the stably stratified, strong wind situation.

Multiple-Layer Echoes

When wind speeds drop to only a few meters per second, the facsimile record of the nocturnal inversion usually assumes a form showing multiple layers of acoustic return with little evident temperature structure between the layers. Such returns are typical of those found in Fairbanks, Alaska, where the valley location of the city leads to a trapping of cold air drainage from the nearby mountains. A typical Fairbanks facsimile record is shown in Figure 22. Some 14 scattering layers may be identified. The lower 200 m of the atmosphere had a lapse of $\theta = -30$ K, and the winds were light and variable at speeds less than 2 m s^{-1}. Other examples of such extreme numbers of multiple layers are described by *Holmgren et al.* [1973]; they give plots of temperature and wind speed with height for six such cases with further descriptions of the change from the herringbone appearance GBSL to the multiple-layer returns as wind shear decreased. The nocturnal marine layer in the Los Angeles basin also is often characterized by such multiple layers [*Edinger,* 1975]. Hazy inversions with low wind speed in Italy also are characterized by such layers [*Bervoets and Hasenjäger,* 1975].

Frequently, wavelike undulations are observed in the multiple-layer returns. These undulations originate as Kelvin-Helmholtz instabilities [*Emmanuel*, 1972]. By using an array of three vertically pointed echosondes, *Kjelaas et al.* [1974] were able to show that these gravity waves propagate nearly at the speed and direction of the wind at the height of the waves. Sensitive microbarographs can detect the pressure changes under such propagating waves, and arrays of these instruments can also provide wave direction information, as was shown by *Kjelaas et al.* [1974] and also by *Hooke et al.* [1972]. Although the herringbone ground-based shear layers can transport significant momentum and heat downward, the decoupled potential temperature inversions in the multiple-layer echo are much less efficient transporters of turbulent fluxes [*Bean et al.*, 1973].

Subsidence Inversions

In their classical study of synoptic scale subsidence, *Petterssen et al.* [1947] show that a characteristic temperature inversion develops at the base of the subsiding air, which is frequently found in association with anticyclonic vorticity. Such subsidence inversions may be found anywhere from 300 m to several kilometers above the surface; they are frequently detected by echosondes, as was pointed out by *Beran* [1970]. In his thesis, *Shaw* [1971] discusses 11 cases of subsidence inversions, showing the facsimile records and radiosonde-derived temperature profiles through the inversions. One of Shaw's records is shown in Figure 23. The height of this inversion holds steady at 900 m through the early morning hours but appears to weaken and dissipate as convective activity builds below the stable layer. If the subsidence is strong and continuing, the elevated layers will be seen to lower with time, sometimes even merging with the top of a ground-based nocturnal inversion, as occurs in the event described by *Wyckoff et al.* [1973].

Fronts

We have seen that even small temperature differences and low wind shears can produce strong acoustic echoes from nocturnal and subsidence inversions. It is not surprising that the possibly larger temperature differences and greater wind shears associated with synoptic scale fronts will also lead to significant echoes. Cold air sliding under and lifting warmer air masses or warmer air overrunning low-level, colder volumes results in a turbulent interface temperature inversion. An example taken from the thesis by *Ahmet* [1976] is shown in Figure 24. This event, recorded at Melbourne on December 7, 1975, at 1940 LT, was accompanied by an 8°C temperature drop at the surface and a change in wind direction from north to southwest. Notice the sudden onset of the echo region, sloping upward with time as the front passes, and the complex internal structure of the cold air mass, accentuated by the strongly echoing envelope region where synoptic scale shear occurs.

An almost identical facsimile record obtained during a cold front passage in Oklahoma has been published by *Cronenwett et al.* [1972]. *Shaw* [1971] reports on three such events, in one of which the frontal surface was traced to an altitude of nearly 2 km. *Neff and Hall* [1976*a*] show that similar frontal passages can be observed even at the south pole. *Trettel and Rai* [1976] have also discussed complex frontal echoes.

When the echosonde is located near a long wave on the frontal surface, even more complex patterns may be recorded. *Parry et al.* [1975] report on two such occurrences; their surface maps and measurements of winds aloft, coupled with the facsimile records, very clearly indicate the structure and timing of the overrunning air masses. Using a high-power sounder, they were able to follow inversion surfaces to 3 km, confirming the results of *Bourne and Keenan* [1974], who also used a high-power array transmitter to obtain returns from such altitudes.

Acoustic Scattering From Clouds

Although the acoustic scattering from cloud droplets and precipitation must be rather small [*Little,* 1972*c*], the turbulent mixing within convective clouds and especially the turbulent boundaries between clear air and cumulus cloud boundaries would be expected to provide large values of temperature and water vapor fluctuations. *Shaw* [1971] proved quite convincingly that convective clouds within the range of his echosonde (1500 m) were consistently detected, especially the tropical cumulus so frequently observed at Darwin, Australia. The echoes were described by Shaw as 'blobs,' the vertical extent of which frequently exceeded several hundred meters. Similar echoes reported by *Gaynor et al.* [1976], recorded during Gate,

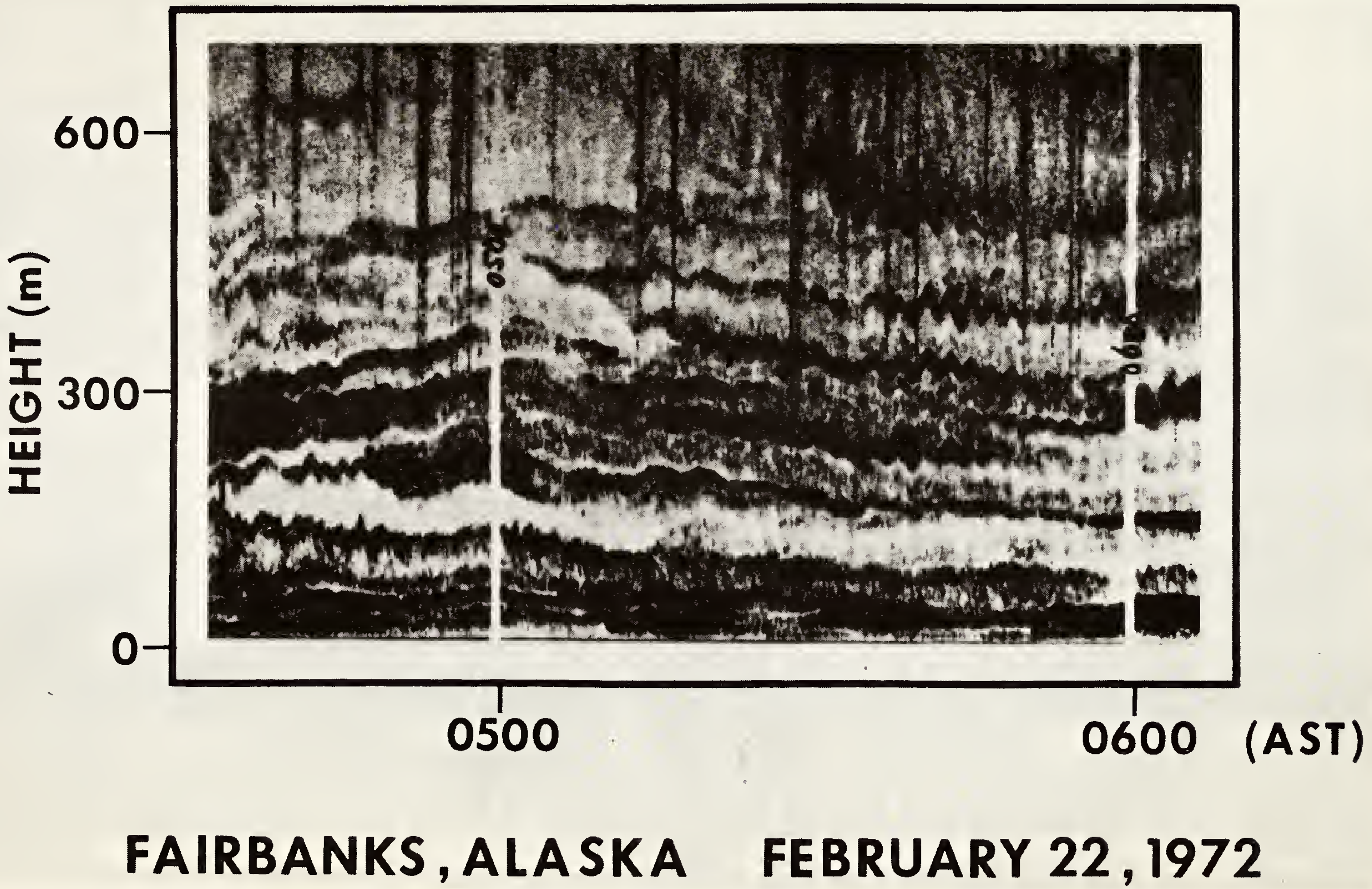

Fig. 22. Multiple layers in a highly stable, low-wind condition. Notice that the waves in the layer near 600 m cusp and break. Greater wind shear existed at this level.

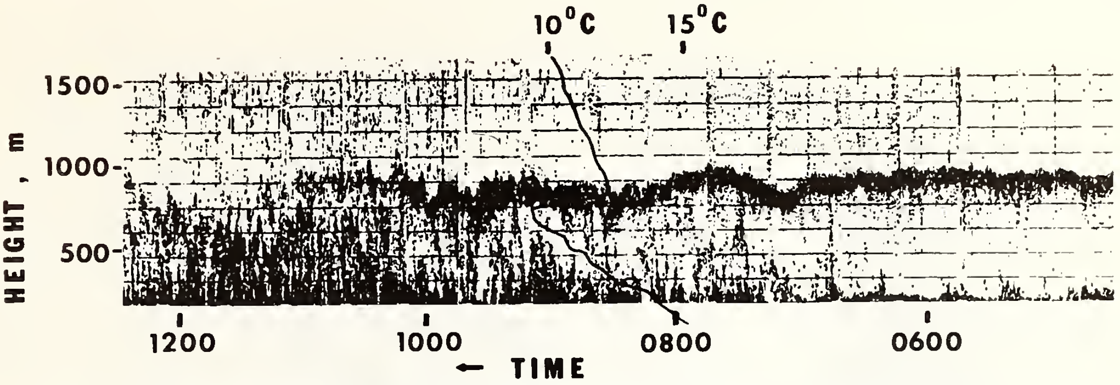

Fig. 23. Subsidence inversion recorded at Melbourne, Australia, showing a radiosonde temperature profile as an overlay. (Courtesy of N. A. Shaw.)

show good correlation to all-sky camera pictures of low-level cumulus clouds advecting over the echosonde and to the in situ measurement of water vapor mixing ratio provided by a balloon-borne sensor. Figure 25 shows the typical blob or hummocky echoes, quite similar in appearance to those reported by Shaw; these echoes are most certainly associated with low-level cumulus. Both Shaw's results and those obtained during Gate indicate that such echoes are more prevalent during the nighttime hours, but the statistical significance of this apparent trend has not been verified.

Radiative cooling and wind shear at the top of stratus decks can also produce overturning of stable air, resulting in acoustic echoes. *Beran* [1971] noted this effect and the deep wave oscillations that can occur in extremely stable but rare supercooled stratus in Boulder, Colorado. *Shaw* [1971] also noticed the correlation in layer type echoes with stratus and described the abrupt change in acoustic facsimile records as the stratus cleared, the cessation of the strong, uniform layer echo from the top of the stratus bank. That the acoustic echoes do indeed originate near the top of stratus clouds was verified by *Cronenwett et al.* [1972]; they flew a light aircraft through the cloud and correlated cloud top observations with echosonde observations.

During the formation phases of stratus, either aloft or as ground-based fog, complex, multilayered patterns are frequently observed, relating to the stably stratified, low-wind conditions typical for such occurrences. As the stratus thickens, the radiative exchange and mixing may eliminate the multilayered appearance of the record [*Ahmet*, 1974], resulting in a single cloud top echo with possibly some surface-caused structure in the lower part of the facsimile. An example of this featureless type of facsimile record is shown in Figure 26; it shows a stratus top at 700 m capping the marine layer in the Los Angeles basin. Note that before sunrise, which occurred at 0632 PDT, short-lived turbulent patches appear near the surface. These are probably stably stratified turbulent zones, the stable lapse rate near the surface being revealed by the 0700 rawinsonde. The beginnings of buoyant plumes start shortly thereafter, and by 0930 the stratus top echo begins to thicken and become wavy in nature, indicating that convection is reaching this level and producing some overturning and downward mixing of dryer air aloft as well as heating the air below. The sky condition changes from overcast to broken (0.6 to 0.9 cloud cover) at about the same time. By 1200 on this date the stratus has completely dissipated. *Edinger* [1975] notes that the sounder indication of a thickening stratus return with waves correlates extremely well with the beginning of the stratus breakup. Thus the echosonde is a useful tool for monitoring this condition.

The ability of the echosonde to indicate the presence of stratus may be of value in Arctic studies in determining when open leads of water exist upwind of the instrument site. *Holmgren and Spears* [1974] have shown that the cessation of the ground-based shear layer returns and the initiation of an elevated, thin line echo occur when stratus begins to form. Upon clearing of the stratus the ground-based shear layer return is again depicted. In such stratus returns, some correlation with satellite observations of open water leads in the Arctic ice was obtained in this preliminary study.

Echosonde Applications

In this section we review how echosondes have been applied to measurements of wind velocity and other atmospheric parameters of interest to the meteorologist and to air pollution assessment. We will also consider how the user can recognize the state of the atmosphere from the facsimile record.

Wind Sensing

Sonic anemometry, whereby the transit time of an acoustic signal between two transducers is measured, is a well developed technology, and we will not dwell on it here. Suffice it to say that *Schotland* [1955] constructed a continuous wave, phase comparison sonic anemometer and demonstrated its accuracy in field tests, using 1-m path lengths between the transducers. A much larger device for use at airports was tested by *John* [1960], using 100- to 300-m path lengths. In an up-to-date summary of sonic anemometry, *Kaimal et al.* [1974] discuss the operating principles, errors, and utilization of the device for measuring turbulent power spectral density. It is interesting to note the accuracy of Schotland's prediction, more than 20 years ago, that sonic anemometers would find their principal use as a research instrument.

We emphasize here acoustic measurements of wind through refractive or Doppler effects. The first use of acoustic Doppler for wind sensing seems to have been made by *Kelton and Bricout* [1964]. They used a whistle source near 10 kHz. The source beam was scattered off atmospheric turbulence to two receivers located at right angles to the vertical plane of the source. We know now that scattering from turbulence has a minimum at 90°, but nonetheless, because of finite beam

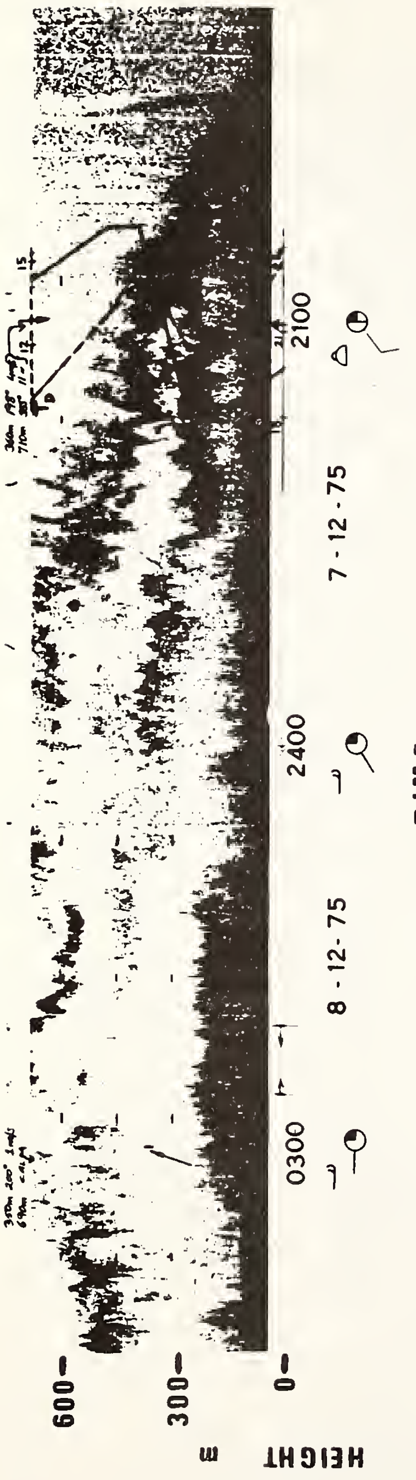

Fig. 24. Synoptic scale cold front record during the austral winter. (Courtesy of S. Ahmet.)

widths and slight departures from the 90° geometry due to beam elevations, Kelton and Bricout were able to detect the scattered signals and measure the Doppler shift. Their anemometer-measured winds and the Doppler-measured winds show rather good agreement. The high frequency and geometry used limited the technique to short ranges.

The refraction of sound by wind and temperature in the atmosphere has long been recognized as a potential for wind profiling if multiple receivers are positioned around a transmitting source. *Fox* [1969] showed that transit time measurements are a far more suitable method of obtaining vertical wind profiles; the spatial intensity distribution is rather insensitive to the wind. This technique has never been developed for operational use, probably because of the need for a large array of sensors.

Little [1969], utilizing the correct scattering theory from atmospheric turbulence, predicted that monostatic Doppler wind sounders should have a nominal range of several hundred meters and that an optimum frequency might be near 1 kHz. He also raised a number of questions on the feasibility of Doppler echosondes. Most of these questions have since been answered, as will be discussed presently. *Little* [1969] also discussed the possibility of correlating atmospheric turbulent structures advected over an array of sounders utilizing the observed lag times to measure wind. This possibility was investigated experimentally by *Wescott et al.* [1970], but it was found that there was little correlation in the appearance of convective plumes among three sounders spaced 50 m apart. Although good results were obtained to 200-m height (0.2 m s^{-1} error bars in a 2.5 m s^{-1} wind), the errors rapidly increased to more than 2 m s^{-1} at 300-m ranges.

Doppler Echosondes in the Computer Era

The first monostatic echosonde Doppler velocity measurements were reported by *Beran et al.* [1971], who measured vertical velocities in convective plumes and in overturning waves during a frontal passage. In this experiment the backscattered acoustic signal was recorded on an analog tape recorder with a bandwidth wider than the carrier frequency. The Doppler shift was determined after the experiment was completed by repeatedly running the analog tape through a two-channel digital wave analyzer. An *x-y* plotter then drew the spectra of the carrier and the returned signal, from which the Doppler shift was estimated. Needless to say, this tedious procedure limited the number of data points obtained; a total of 16 min of data are reported upon in this pioneering paper. A facsimile record of convective plumes with the corresponding vertical current isotachs as presented by *Beran et al.* [1971] is repeated in Figure 27. Such vertical velocity measurements have been confirmed by using tethered balloons [*Caughy et al.*, 1976].

Shortly after this first experiment the same technique was extended to a two-sounder configuration with one antenna tilted from the vertical, its beam intersecting the vertically pointed unit positioned 80 m distant. Both monostatic and bistatic runs were made. The superior scattered intensity of the bistatic configuration provided much better signal-to-noise ratio and cleaner Doppler plots. As was done in the first experiment, the data were evaluated after the experiment had been completed [*Beran and Willmarth*, 1971]. Note that the Doppler extraction technique used is essentially incoherent, no reference being made to the phase of the scattered signal compared with the transmitted tone. This is Doppler extraction in its most simple, least elegant form, a straightforward measure-

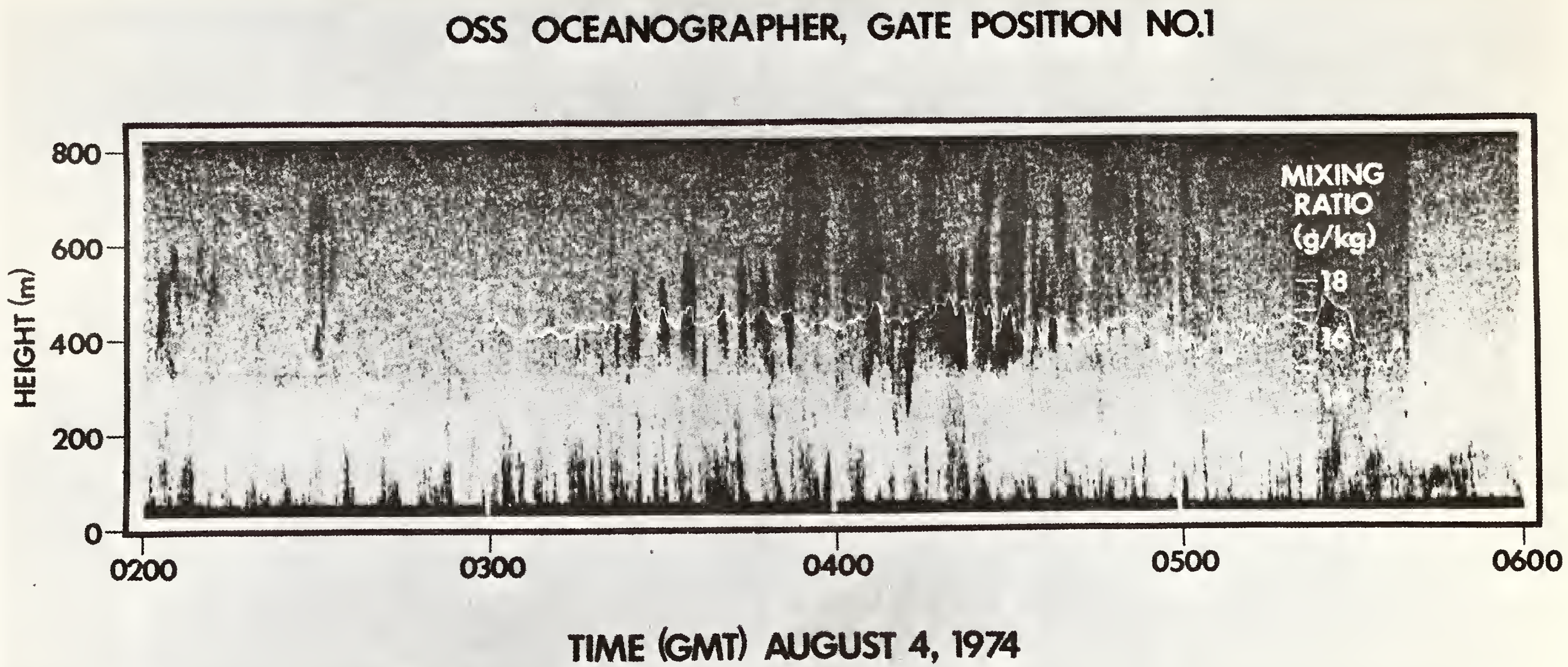

Fig. 25. Hummocky echoes from cumulus clouds in the tropical Atlantic. The saturation mixing ration was 17 g kg^{-1}; tethered balloon measurements show that the hummocks were saturated.

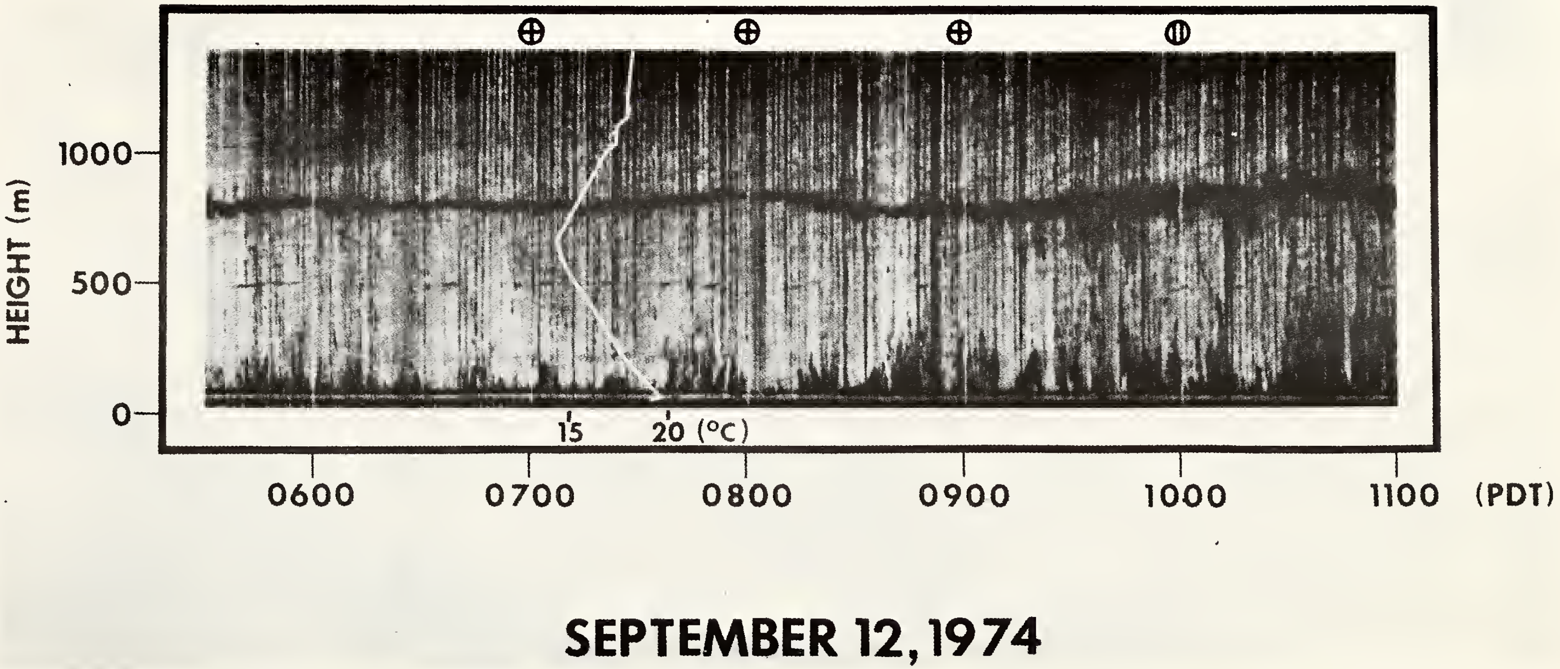

Fig. 26. Facsimile record showing a typical stratus top return at 700 m. The echo thickens and becomes undulating as the stratus breaks up.

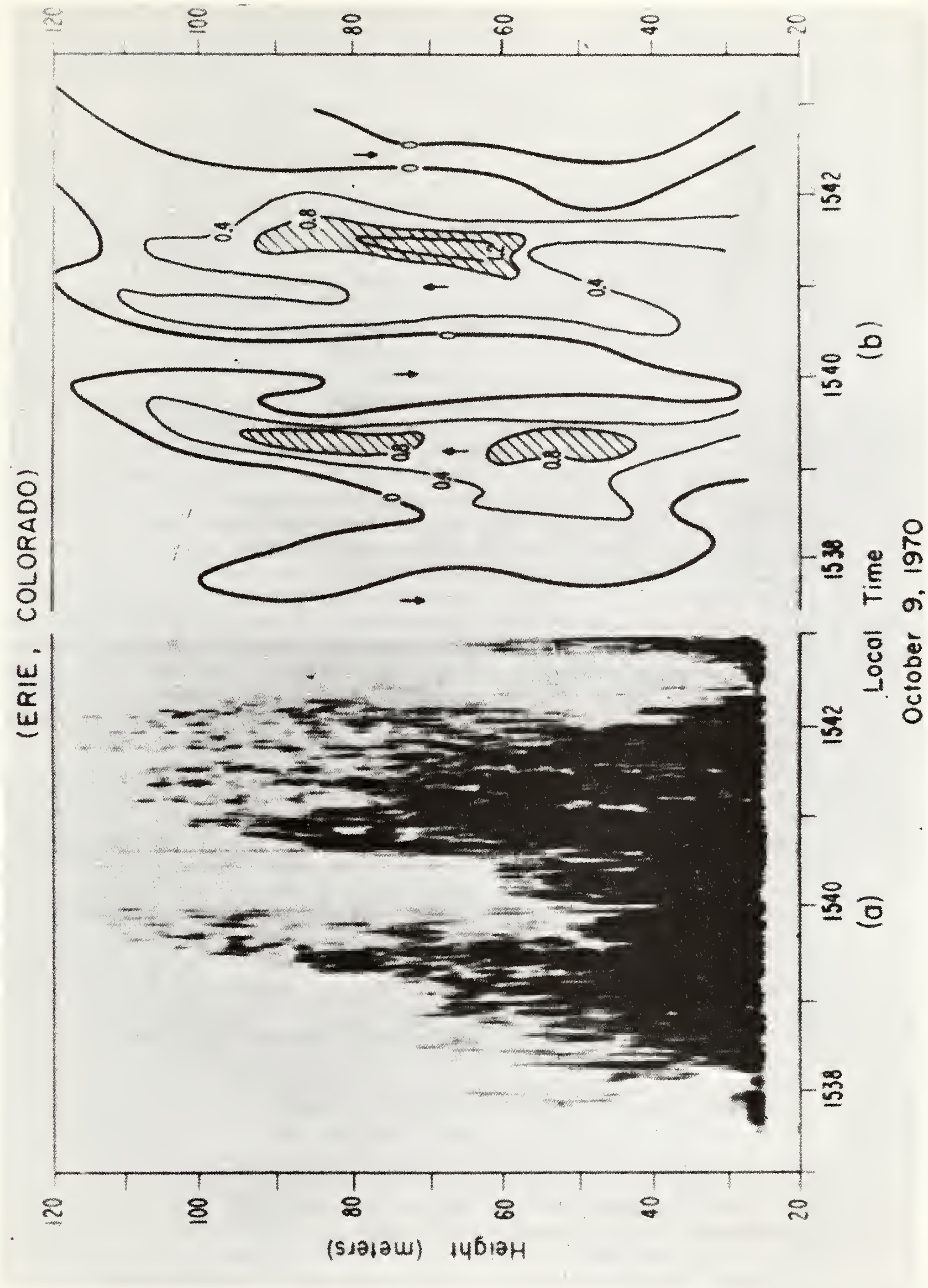

Fig. 27. (*a*) Convective plume facsimile record. (*b*) Record with Doppler-derived vertical velocities in meters per second. Note that part *b* overlies part *a*. (Courtesy of D. Beran, C. G. Little, and B. Willmarth.)

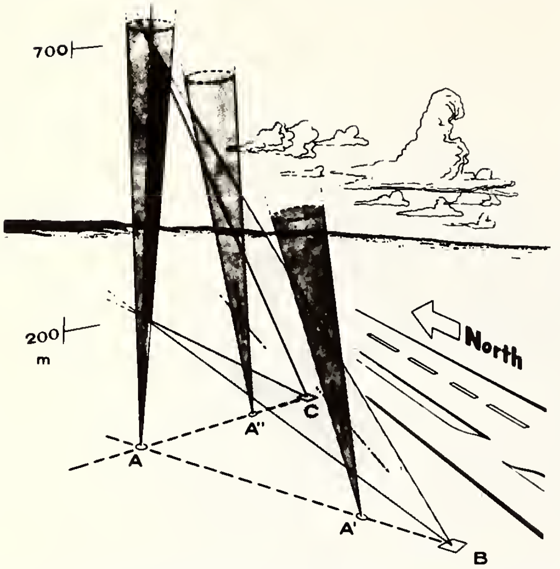

Fig. 28. Configuration of the Doppler echosonde tested at Stapleton Airport, Denver, during 1973. A vertical transmitter at A, supplemented by transmitters A' and A'', and fan beam receivers at B and C were used.

ment of the frequency of the scattered signal, possible in the acoustic regime because of the low frequencies used.

Another approach to Doppler processing was adopted by *McAllister* [1971]. He used a tracking filter, the output voltage of which was proportional to the frequency shift of the scattered power relative to the transmitted frequency. In a monostatic sounder he was able to show correlation of vertical velocities with the convective plume facsimile records in real time. He operated in oblique monostatic modes and in bistatic modes as well. McAllister also discussed acoustic wind sensing by angle-of-arrival measurements. With this demonstrated ability to profile real-time winds coupled with the information that echosondes can provide on inversion heights and stratus tops the suggestion for acoustic applications in the airport environment was not long in coming [*Beran*, 1971].

The excellent temporal and spatial resolution of the Doppler echosonde led to its application in atmospheric science problems. For instance, a detailed study of vertical velocity structure in thermal plumes was reported by *Mahoney et al.* [1973*a*], who also demonstrated the good agreement between Doppler and angle-of-arrival measurements under ground-based shear layer, katabatic wind conditions. They showed the existence of the Ekman wind spiral through the turbulent layer, an angular shear of 40° between the surface and 400 m being a typical value.

In the bistatic configuration the Doppler in the scattered signal represents a velocity along the bisector of the angle between the transmitter and the receiver, as was shown by *Beran and Clifford* [1972]. The excellent agreement between Doppler-derived winds and winds measured with an anemometer suspended below a tethered balloon is also shown in this study, in which the measurement of the total horizontal wind vector is reported. The development of the nocturnal jet wind maximum above the surface-based inversion at an altitude of 300–400 m was also described by *Beran and Clifford* [1972].

The feasibility of measuring the profile of the total wind vector from a height of 30 m to over 600 m, even in a noisy airport environment, was demonstrated during 1973 [*Beran et al.*, 1974*a*]. Their Doppler echosonde used a vertically directed transmitter and a bistatic receiver buried in subterranean bunkers to minimize the effect of wind noise. The configuration is shown in Figure 28. Auxiliary transmiters at A' and A'' were used to avoid the signal minima near the 90° scattering angle for the lower levels of the profile. This system utilized a minicomputer for processing the Doppler voltage derived from the analog tracking filter. The calibration and test procedures for the system, documenting how low-signal-to-noise episodes were eliminated from the data processing, are described in more detail by *Beran* [1974]. This system was designed to monitor wind shear as it might affect aircraft landing and taking off. Slight and rather steady-state errors because of refraction [*Spizzichino*, 1974*a*] were not accounted for in the data processing. Another problem encountered with the system arose when low-level strong turbulence yielded a stronger received signal from the transmitter side lobes than, at the same time delay, the signal scattered from the main transmitter beam, a possibility of which we are warned by *Spizzichino* [1974*b*]. It was difficult to obtain smooth wind profiles across the regions of the satellite and main transmitter beam patterns also [*Beran et al.*, 1974*b*]. The experiment was useful in demonstrating that in spite of snow and dust accumulation in the antennas an acoustic system could be made to perform adequately in the noisy airport environment. It also demonstrated that the analog tracking filter approach to Doppler extraction needed improvement.

As a result of the lessons learned in the tests at Stapleton Airport, Denver, an alternative signal-processing technique was adapted for a follow-on system. In this later system the scattered signal is digitally sampled and transformed into a 128-line spectrum for each height gate by use of a dedicated fast Fourier transform (FFT) processor in the minicomputer. This is the system used in a Doppler echosonde wind profiler now installed and operating at Dulles Airport near Washington, D. C. [*Beran et al.*, 1976].

A similar signal-processing technique, also utilized in a system employing a vertically directed transmitter and three bistatic receivers, is reported by *Balser et al.* [1976]. This system was tested against anemometers on a 150-m meteorological tower at the White Sands missile range, and the extracted Doppler results showed good agreement with the tower anemometer data. Balser et al. reported the 1-min averages of data for this test, in which the transmitter was located only 10 m from the tower. In subsequent tests of a similar system, *Haugen* [1976] showed that tower reflections, which are non-Doppler shifted, can cause significant errors in the comparison. It is probably necessary to locate Doppler echosondes some distance from towers to avoid this improper spectral weighting, but then it is necessary to average the comparison periods for longer times because the tower- and echosonde-sampled volumes will be significantly displaced. Even then, errors because of ringing in the transducers and antennas or side lobe reflections from the ground can produce ambiguous results. It is certainly best to compare any Doppler echosonde with data from properly averaged conventional anemometers to be assured that the remote sensing system is operating properly.

The bistatic Doppler echosonde with a vertically directed transmitter has the great advantage that the transmitter beam causes a minimum of noise nuisance, since the 90° side lobes can be depressed 50 dB below the main lobe [*Adekola*, 1976]. However, in those instances in which the noise nuisance is not objectionable (at remote locations or even at airports), there are advantages to switching the transmitter and receiver configuration. An acoustic system with a fan beam, inclined transmitting antenna, and a vertical receiving antenna has the advantage of better environmental noise shielding for the receiver. Since the background noise so frequently sets the limits on performance of a Doppler echosonde, this configuration can be quite advantageous. This is the geometry adopted by *Kaimal and Wescott* [1976] in two different systems, both of which demonstrated quite adequate performance when they were compared with tower-mounted anemometers. Analog tracking filters were used in both Kaimal's and Wescott's echosonde for processing the Doppler shift, but analog filtering techniques and logic were used in Wescott's sounder, compared with a minicomputer and digital processing in Kaimal's unit. The sectoral horn, cuffed transmitting antenna developed by Kaimal demonstrated a beam pattern uniform to within 5 dB over 60° of elevation angle; a vertical section through the antenna beam pattern showed a main lobe less than 10° wide at 3.6 kHz and good side lobe rejection at larger angles. A fanned transmitting antenna, similar in concept but with an inclined receiver, was used in a system developed by *Davey and MacCready* [1976] in a so-called 'simple wind shear detector.' The Doppler signal was extracted by using FFT techniques in off-the-shelf spectral analyzers.

A three-axis monostatic Doppler echosonde that measures the Doppler shift through use of a 100-point FFT has been described by *Chong* [1976]. Wind speed and direction data from this system were compared with data taken from pilot balloons at heights of 30–500 m. Demonstrated accuracy was about 1 m s^{-1} over a wind velocity range from 1 to 10 m s^{-1}. The standard deviation for wind direction was about 40°.

The question of optimum Doppler processing for echosondes is still open. Although FFT methods have demonstrated their utility in several semioperational devices, there is no denying that this method is oversophisticated. All that is really needed for wind measurements is the first moment of the Doppler spectrum and not the entire spectral envelope defined by the multipoint FFT. *Keeler* [1976] has demonstrated that even a four-pole adaptive inverse filter can accomplish a very good measure of the first moment of the Doppler. Considerably less digital hardware is needed than that in dedicated FFT circuits. He has shown the utility of a least mean square adaptive coefficient adjustment that uses a maximum entropy spectral analysis method for finding the first moment of the spectrum.

An even simpler Doppler technique has been developed by *Owens* [1977]. He has demonstrated that a real covariance approach to spectral moment estimation is extremely simple to implement in an all-digital echosonde design. The Doppler estimation results agree very well with both FFT and adaptive filter methods. Certainly, more tests will need to be performed on the real covariance method (easily expandable to a complex covariance processing) in the future. Zero-crossing Doppler methods are also well adapted to digital techniques, and if proper attention is given to the rapidly varying signal-to-noise ratio typical of echosondes, this method may also show significant promise [*Melling and List*, 1976]. In analyzing several Doppler extraction techniques, *Baudin* [1977] finds digital methods to be far superior to analog methods in the presence of realistic noise backgrounds.

Quantitative Measurement of Structure Parameters With Echosondes

As was discussed earlier, the temperature structure and velocity structure (and to a lesser extent the humidity structure) in the atmosphere lead to the strong scattering of acoustic waves, making the echosonde a feasible device. The early test of *Kallistratova* [1961] demonstrated the shortcomings of scattering theory as it existed 17 years ago and pointed to the improvements necessary as embodied in the present *Tatarskii* [1971] theory. Implicit in this theory is the assumption of a homogeneous, isotropic inertial subrange of turbulence giving rise to the acoustic scatter. These ideal conditions are expected to prevail during unstable, free convective conditions, in which the outer scale of turbulence is many meters. But can these conditions be expected to hold in thin shear layers found in nocturnal inversion conditions? The question of the accuracy of the scattering theory was addressed by *Neff* [1975*a*, *b*]. He found that during free convection, measurements of backscattered acoustic intensities taken with a carefully calibrated echosonde agreed with predictions based on measurements of the temperature structure C_T^2 taken with fast response, spaced temperature probes [*Lawrence et al.*, 1970]. For the unstable conditions at a range of 92 m the agreement was consistently within 3 dB.

However, during statically stable conditions the echosonde consistently measured a larger value of backscattered intensity than would be expected from the in situ measurements. There was little aspect sensitivity to these errors, indicating that the problem did not arise from gradient or specular reflections from temperature structure. Neff suggests that under the stable conditions a quasi-horizontal spatial ordering of small-scale turbulence structure may introduce sampling and averaging errors in the in situ instruments relative to the finite volume echosonde measurements. This explanation is supported, since better agreement was obtained between echosonde and in situ data when the pulse length (and thus the scattering volume) of the echosonde was reduced. It is still possible that the assumption of homogeneous isotropic conditions in the inertial subrange is not correct for some of the rather thin shear regions that may sometimes exist in temperature inversions.

Neff's comparisons were made at a range of 92 m from the echosonde. Because the insonifying intensity at the scattering volume may be reduced by turbulence structure, the accuracy of echosonde measurements at greater ranges may be reduced because of this excess attenuation. *Haugen et al.* [1975] have shown that at larger ranges the accuracy of C_T^2 determination from backscattered intensities will significantly decrease. Recent tests have shown that by purposefully defocusing the acoustic antenna to broaden the main lobe the discrepancy can be reduced, indicating that this is indeed a scattering attenuation effect. Of course, it is also necessary to know the profiles of temperature and humidity and to know the atmospheric density in order to account properly for molecular attenuation in the echosonde equation.

Similarly, *Asimakopoulos et al.* [1976] conclude from echosonde tests under both stable and convective conditions that the device can provide reliable estimates of C_T^2 but that the apparent errors in echosonde measurements increase with increasing turbulence. Their in situ probes were carried by a large tethered balloon; the measurements were made at a range of 90 m. Their better agreement between in situ and echosonde measurements for the stably stratified case may be attributable to the lack of layered structure in the inversion that they measured. Their inversion shows a stronger, more continuous ground-based shear layer facsimile appearance compared with the thin breaking wave pattern sampled by Neff. In general, the agreement between in situ and echosonde measurements was between 7% and 25%.

Fukushima et al. [1975*a*] have attempted to use echosondes to profile C_T^2 to heights of 900 m. Because of the rather narrow main lobe produced by their 16-m-diameter antenna it is quite possible that the nighttime profiles of the temperature structure parameter evaluated by them may fall off less rapidly with height than they indicate.

In principle, it should be possible to derive C_v^2 values from intensity measurements of the bistatic echo after the contribution from C_T^2 is subtracted. This has not yet been accomplished, primarily because of uncertainties in accounting for the excess attenuation in the monostatic C_T^2 measurements, although for many bistatic geometries, C_v^2 scattering will overwhelm C_T^2. Another approach to obtaining C_v^2 values from echosonde values has been reported by *Gaynor* [1977]. He shows that it is possible to obtain the velocity structure function D_z over scale sizes ranging from 10 to 200 m by range gate resolution of Doppler differences in separated scattering volumes. Of course, these larger separation distances may approach the outer scale of turbulence under some atmospheric conditions, but at 10 m, one is probably within the inertial subrange for almost all conditions. Doppler-differenced values of C_v^2 so obtained should be equal to those defined by the scale of the acoustic wavelength, assuming a Kolmogorov spectrum of turbulent energy cascading downscale. Since C_v^2 can be related directly to the turbulent energy dissipation ϵ by

Dissipation relationship to
velocity structure

$$2\epsilon^{2/3} = C_v^2 \tag{79}$$

this Doppler-differencing echosonde method can be used to study the profiles of the dissipation of turbulent kinetic energy in the boundary layer. During periods of convective plume activity the profile of ϵ is nearly constant with height. Figure 29 compares echosonde measurements of dissipation from Doppler-differenced C_v^2 calculations with measurements obtained from bivanes on a 150-m tower. Also shown for reference is a surface layer value of dissipation measured during the Air Force Cambridge Research Laboratories Kansas experiment [*Izumi*, 1971].

During nocturnal conditions, isolated patches of elevated breaking waves may appear on the facsimile record. Gaynor shows that these regions correspond with enhanced values of C_v^2. An example of contours of the velocity structure parameter in the direction of the mean wind (obtained by assuming Taylor's hypothesis as turbulent eddies advect over a sounder) is shown in Figure 30. It can also be seen that the ground-based shear layer exhibits enhanced values of C_v^2, typically of the order of 10^{-3} m$^{4/3}$ s^{-2}. This value is typically 10^{-2} of the typical daytime values found in convective plumes, however.

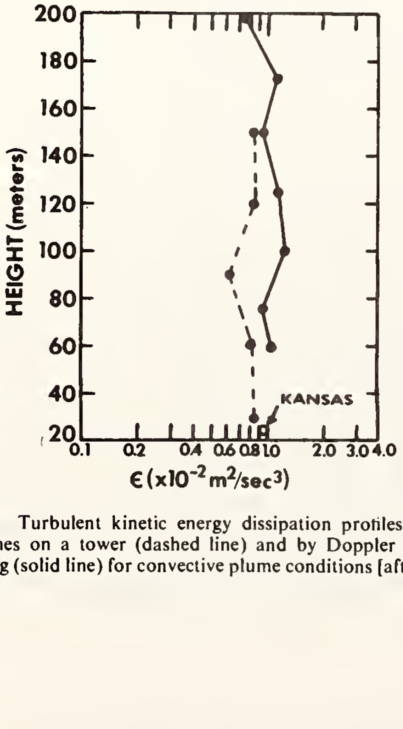

Fig. 29. Turbulent kinetic energy dissipation profiles measured with bivanes on a tower (dashed line) and by Doppler echosonde differencing (solid line) for convective plume conditions [after *Gaynor*, 1977].

Thus we see that echosondes have demonstrated their ability to measure the turbulent atmospheric parameters C_T^2 and C_v^2 in the planetary boundary layer with reasonable accuracies. Is there any hope that echosondes will be able to measure profiles of temperature and humidity? *Little* [1969] speculated on the possibility of utilizing the differences in molecular absorption caused by humidity to obtain humidity profiles by using a multifrequency echosonde. An attempt to exploit this method was reported by *Gething and Jenssen* [1971], who performed a theoretical analysis on the ability of a four-frequency echosonde to derive both humidity and temperature profiles, relying upon the known molecular absorption dependence of these two variables. The fourth frequency was added to account for excess or scattering attenuations. By expanding the molecular attenuation coefficient in series form they derived the frequency-dependent backscatter intensity relations and then attempted to calculate temperature and water vapor profiles from simulated data. The error bars, even for exactly calculated backscatter data, were about 1 mbar in water vapor pressure and 2 K in temperature. When realistic error bars were added to the backscatter intensity, the solutions blew up rather badly, water vapor errors averaging 2 mbars and temperature errors 10 K. In later unpublished results using actual experimental data, Gething reported that even greater errors were obtained (private communication, 1974).

These rather discouraging results have been confirmed more recently by *van Grunderbeeck* [1975], who performed a similar theoretical analysis of a three-frequency echosonde and then attempted to extract water vapor and temperature profiles from experimental data. The errors experienced were of the same order of magnitude as that predicted by the Gething and Jenssen study.

Another approach to temperature profiling utilizing a phase coherent echosonde had been reported by *Closs and Surridge* [1974]. They occasionally observed dark bands in facsimile records made with the phase coherent part of the backscattered signal, bands that appeared to vary in apparent altitude with the temperature of the atmosphere. However, they were not able to suggest a mechanism for the production of such bands, other than the possible Doppler shift due to slow mean vertical motion. Later, *Surridge* [1975] found that the mean phase of the backscattered signal obtained with the same equipment was not zero but varied in a way that appeared to be closely correlated with temperature changes. *Brown et al.* [1977] speculated that the appearance of dark bands might be due to interference. To test this possibility, they built an echosonde interferometer that produced banding in facsimile records. However, the motion of the apparent altitude of the fringes with temperature changes appeared to have only marginal sensitivity for use as a remote temperature-sensing device. In contrast, Surridge's comparison of mean phase and temperature seemed to suggest a much stronger dependence.

Are there any other methods by which the temperature or humidity profile can be extracted from a now improved knowledge of echosonde characteristics? Certainly, when convective

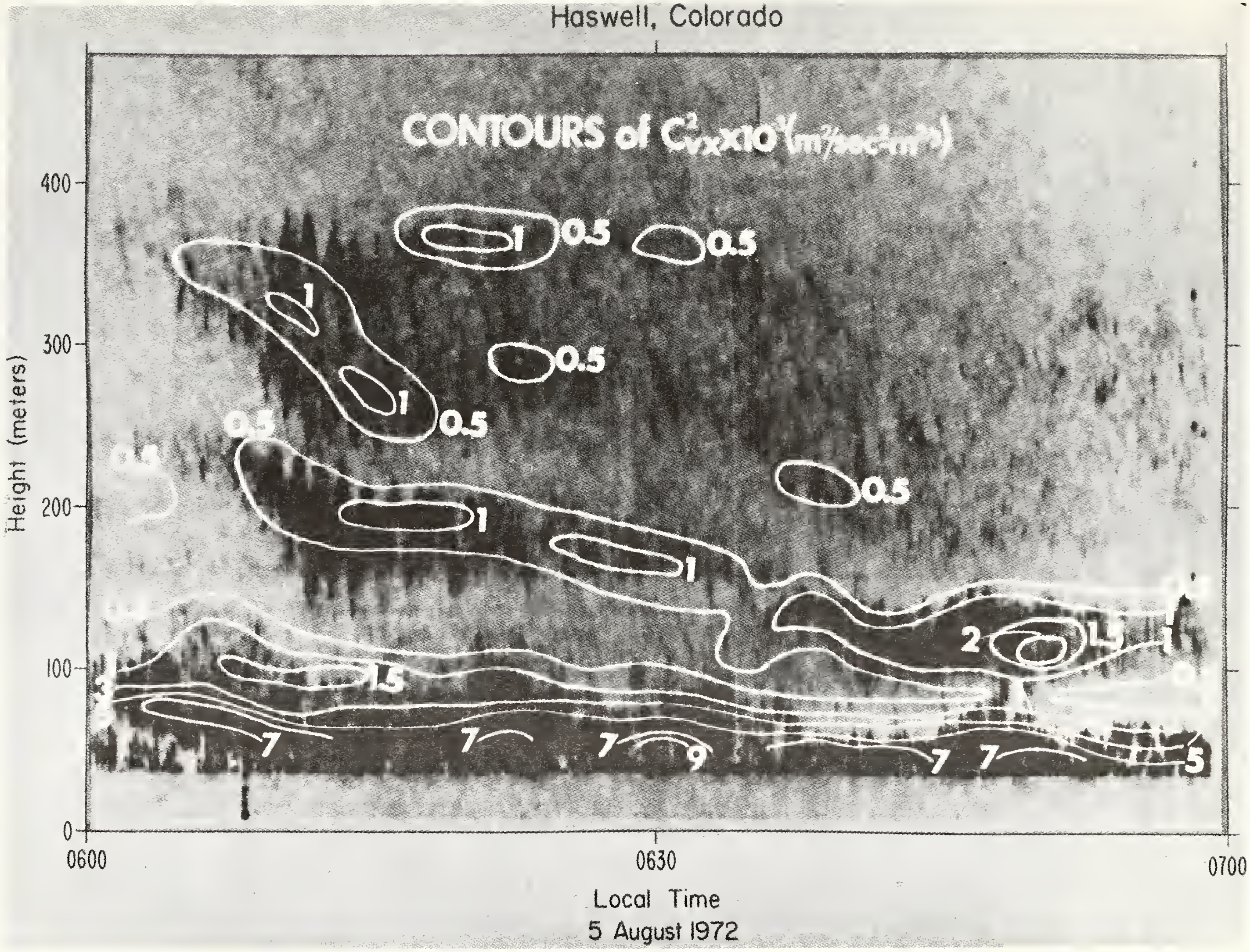

Fig. 30. Contours of horizontal velocity C_v^2, determined by echosonde Doppler differencing, overlying the facsimile record of turbulent breaking waves and a ground-based shear layer [after *Gaynor*, 1977].

plumes are depicted on the facsimile recording, one can be assured of an adiabatic lapse rate, at least to the top of the observed plumes, with possibly a superadiabatic lapse in the lower few tens of meters, documented for typical convective conditions by *Hall et al.* [1975]. When ground-based shear layers are present, there is undoubtedly some information relating to atmospheric stability by the frequency of the turbulent breaking wave pattern presented. If the frequency N of these waves is governed by the Brunt-Väisälä equation

Brunt-Väisälä frequency

$$N^2 = (g/\theta)(\partial\theta/\partial z) \tag{80}$$

then by a spatial frequency analysis of the wave periods, properly compensated for by the motion of the waves (which could be measured with a Doppler echosonde), it may be possible to extract $\partial\theta/\partial z$. Similarly, from the expression for the gradient Richardson number, if the wind shear term can be measured with the Doppler echosonde and if the layer-averaged Richardson number can be derived through a measure of the intermittency of the observed turbulence, there may be an additional approach to extracting $\partial\theta/\partial z$. More thought and research must be directed toward this approach, but for now, absolute temperature profiling can be obtained only through hybrid acoustic systems such as the radar acoustic sounding system (RASS) to be discussed in a following section.

Echosonde Applications in Air Pollution Meteorology

Air pollution is essentially an urban problem. It is therefore important to determine if echosondes can be operated in built-up neighborhoods without being a noise nuisance and without being degraded in performance by the urban noise level. This question was addressed by *Simmons et al.* [1971], who determined that with proper shielding of the echosonde antenna the noise nuisance can be effectively eliminated (especially when the masking effect of the urban noise background is considered). Except near airports or busy highways the urban noise level should not significantly degrade the ability of an echosonde to detect elevated temperature inversions and the deepening of the mixing layer by unstable convection.

The addition of a Doppler capability to echosondes makes them an even more attractive air pollution meteorology tool [*Beran et al.*, 1972*b*]. The ability to detect large-scale subsidence inversions, which can lead to an intensification of nocturnal surface-based inversions, is another attribute of the echosonde. Such large-scale subsidence is shown by Beran et al. to have merged with the surface-based inversion, resulting in an unpredicted pollution episode in Denver, Colorado.

To test the feasibility of operating in the urban environment, a test was conducted during the winter of 1971–1972 in Denver. Data from slow ascent radiosondes, launched specifically for air pollution meteorology predictions, were compared with echosonde facsimile records [*Wyckoff et al.*, 1973]. A good agreement was found between the ground-based shear level top, or striae in multilayered returns, and the principal temperature inflection point measured with the radiosondes. The echosonde used in the experiment was located near a warehouse and trucking terminal area next to an interstate freeway, and in spite of these noise sources it produced quite usable facsimile records during the entire test. It was concluded that through further tests it might be possible to develop improved predictions of inversion breakup. *Parry* [1974] stresses the advantage of the echosonde in continuously monitoring the atmospheric mixing layer depth, thus providing the updated information between radiosonde launches on the time rate of change of this depth.

To explain further the correlation between the echosonde facsimile records and analytical models of the inversion rise during morning hours, *Shaw* [1974] compared echosonde records with the predictions of a simplified mixing layer depth development model. The experiment was performed in the Chicago area, and although reasonable agreement was obtained, the distance separating the radiosonde and echosonde site, 16 km, undoubtedly contributed to some of the discrepancies. It was found that better agreement was obtained by adding about 1° to the observed surface temperature and using this corrected temperature in the model for comparison with echosonde-observed mixing depths.

The model used by Shaw was a simple 'filling model' in which the heating of the ground directly drives convection in the layer below the capping inversion. Turbulent mixing at the top of the convective layer was not considered. More recent models by *Tennekes* [1973], later improved by *Zilitenkevich* [1975] and *Zeman* [1975], included turbulent mixing through the inversion. The suitability of the Zeman-Tennekes model was tested by *Benkley* [1977], who compared echosonde facsimile records of capping inversion height as a function of time with the predictions of the model. Benkley points out the importance of knowing in detail the stable lapse rate in the free atmosphere above the ground-based shear layer at sunrise and graphically illustrates the difference in inversion breakup for conditions with similar heating rates but differing background stabilities. For example, inflection points in the stability profile above the ground-based shear layer result in inflections of the inversion rise rate.

Shaw's model was similar to one derived by *Deardorff et al.* [1969], in which the mixed layer depth h changes with time:

Rate of change of mixed layer depth

$$dh/dt = Q_0/\gamma h \tag{81}$$

where Q_0 is the surface turbulent heat flux and γ is the potential temperature lapse rate.

The Tennekes model, improved by Zilitenkevich, includes the ratio of downward turbulent flux through the inversion to surface heat flux. This ratio, defined as a constant C_F, has a value of approximately $\frac{1}{4}$, and in addition, a temporal constant $C_T \sim \frac{5}{8}$ is included in the growth rate equation given by

Mixed layer depth change with entrainment

$$dh/dt = (C_F/C_T)(gQ_0h/T_0)^{1/3} \tag{82}$$

Zeman improved the Tennekes-Zilitenkevich model by adding a third constant parameterizing the dissipation rate in the surface layer. The comparison with echosonde data obtained at Haswell, Colorado, shows that the comparison works quite well. However, comparison with echosonde data from the Los Angeles basin, where large-scale subsidence and advection in the basin are important, indicates that there are still some shortcomings in modeling planetary boundary layer growth rates.

Tombach et al. [1973] summarized the ability of the monostatic echosonde in air pollution applications to measure the following parameters: (1) the time of onset of unstable convection and the period of persistence, (2) the time of onset of stably stratified conditions and the period of persistence, (3) a minimum height to which the convective plumes will carry surface-generated pollutants, (4) the thickness of the turbulent ground-based shear layer in stable conditions, and (5) the heights of various stable layers and inversions aloft.

In addition, they point out that when the echosonde is combined with other in situ meteorological instruments (rawinsondes, anemometers, or vertically separated temperature probes) or with other remote sensing instruments, the information available to the air pollution meteorologist is much more useful. Simplified models for developing a quantitative estimate of dispersion based on the echosonde and in situ measurements are presented. *Beran and Hall* [1973, 1974] and *Tombach and Chan* [1976] show that when echosondes are combined with arrays of other remote sensors or rawinsondes, especially when Doppler echosondes are used, a valuable measure of urban area mixing depths and wind patterns can be deduced. The combination of an echosonde array within an urban area ringed by transverse laser wind sensors would answer many of the questions that the air pollution meteorologist must answer on pollutant concentration and the time rates of change of these levels.

The operation of a monostatic echosonde in the Los Angeles area made it possible to monitor the depth of the convectively mixed layer to the base of the marine inversion most of the time as well as to document the arrival of the sea breeze front at an inland site. In addition, *Edinger* [1975] makes the interesting observation of the precursors to stratus breakup observed by the sounder. Since the breakup of the clouds allows for greater surface heating and an increase in mixing layer depth, this ability of the echosonde also has important air pollution meteorology applications. When an array of echosondes is deployed in an urban area, it is possible to map the topography of elevated inversions and the area-wide development of the mixing layer. Such an experiment has been performed in the San Francisco Bay area by *Russell and Uthe* [1977], who correlated the facsimile records of the mixing layer depth with measurements of the concentration of particulate matter. In general, good agreement was obtained: increasing the mixing layer depth lowers particulate concentration. They viewed the three-station experiment as being successful enough to justify the expansion to a 13-station echosonde network. It needs to be pointed out, however, that the low-lying inversions in the San Francisco Bay area, where Russell and Uthe performed their study, are ideally suited for echosonde studies. They caution against indiscriminately extending the results and conclusions of their investigation to other urban areas.

The array of echosondes deployed around St. Louis during the Metromex program in 1973 indicated that nocturnal inversion depths near St. Louis averaged 50–100 m greater than those in the surrounding rural areas [*E. L. Miller*, 1974]. Further measurements since made in the Chicago region seem to confirm this indication.

Echosonde Facsimile Interpretation

Although the feasibility of quantitative acoustic echo interpretation has been demonstrated, most echosondes record data only on facsimile machines; the darkening of the facsimile record is related qualitatively to the intensity of the scattered sound. The patterns of atmospheric turbulence versus time so displayed can tell the experienced observer much about the status of the atmosphere, and much more can be extracted when additional meteorological observations are made in conjunction with the facsimile.

A paper summarizing the typical facsimile record appearance with in situ measurements of temperature, humidity, and wind has been published by *Estival and Aubry* [1976]. They used a tethered balloon for the in situ measurements and documented the general enhancement of wind shear in elevated layers along with the usually slight temperature stability in elevated shear layers. The earlier explanation, that the gradient Richardson number within portions of the layers is small enough to cause the turbulent mixing, is not contradicted by this paper. However, we clearly need to obtain more highly resolved turbulence data in both ground-based shear layers and in elevated layers, along with measures of the intermittency of this turbulence, to be absolutely sure that the interpretation presented here is correct.

In a pioneering effort to bring some order out of the chaos of the diversity of facsimile record patterns, *Clark and Bendun* [1974] proposed a numerical classification scheme. Briefly, their pattern types are characterized as follows: type 0, noisy record or no structure visible; types 1–5, ground-based shear layers of increasing depth, showing some horizontal stratification for types 4 and 5; types 6–10, ground-based shear layers with complex, separated elevated bands, descending with time in types 9 and 10; types 11 and 12, ground-based shear layers with additional elevated layers rising with time; and type 13, convective plumes.

In a similar manner, *Fukushima et al.* [1975*b*] devised a pictorial scheme in which monthly summary charts of facsimile patterns are characterized by alphabetic symbols for wind, precipitation noise, or equipment problems; stratified returns are shown by thick solid lines giving some indication of the structure and appearance in the facsimile charts, and vertical accent symbols are used to characterize convective thermal plumes. In a brief survey paper, *Thomson* [1975] has provided references to papers treating these various classes of facsimile records.

It seems desirable, however, to develop a classification scheme with descriptors that indicate the status of the atmosphere. Enough is now understood about why characteristic facsimile patterns develop to allow this kind of classification.

Let us consider first the stably stratified atmosphere. The fundamental echo structure here is the ground-based shear layer, shown in Figures 20*a* and 20*b*. Such layers, measuring from a few tens of meters to several hundred meters thick, show as featureless black bands when the facsimile chart is compressed in time, but they will show distinct, sloping, turbulent wave patterns when the record is stretched out. As was discussed earlier, such echoes develop when significant wind shear occurs across the ground-based stable layer. When this echo appears alone, the facsimile can be classified as GBSL followed by the depth of the layer in meters. The classification can be further modified by the adjective 'thickening' or 'pinching' (T or P) if the layer depth is increasing with time or decreasing with time.

When strong low-level jets or wind sheets occur within the lower stably stratified region, the GBSL may present a divided appearance. On stretching out such a facsimile record the turbulent waves will be found to slope in opposite directions away from the clear, bifurcating region. This pattern represents a modification of the simple shear layer, so it is suggested that the letter B be appended as an adjective to GBSL when the bifurcation appears. Under the strong wind conditions when the GBSL is broken into intermittent bursts, the suffix I may be appended to the descriptor.

The GBSL classification may be modified when separated layers aloft occur on the facsimile record. When such layers are clearly not directly associated with the GBSL (as occurs in the bifurcated pattern), it is suggested that 'EL' (elevated layers aloft) be appended to the GBSL designation. In addition, the adjectives 'ascending' or 'descending' may be appended to the EL modifier, since the appearance of these layers may be important in depicting mesoscale subsidence or convergence above the GBSL.

A second general category of the stably stratified atmospheric echoes involves layers separated from the surface, multiple layers, or density currents. When a single elevated shear layer (perhaps quite similar to the GBSL but clearly separated from the surface) is observed, it can be classified as an elevated shear layer (ESL) followed by the elevation in meters or, for thick layers, the elevation range. When the layer is known to correspond with a stratus top, this designation may be appended to the descriptor.

Under low-wind conditions the appearance of multiple, decoupled layers may occur, as is shown in Figure 22. It is suggested that these be simply identified as 'multiple layers' (ML), the range in elevation being appended. Such additional descriptors as 'undulating' (U) may be appended when wave amplitude in the layers significantly exceeds layer thickness. In addition, when complex breaking wave, descending, ascending, or interleaved layers appear, it is suggested that the ML pattern be described as 'complex' (C), this being indicative of significant changes occurring in the elevated patterns but probably associated with rather low kinetic energies, for otherwise the patterns would not be separately discerned and decoupled.

Finally, density currents, be they caused by synoptic or mesoscale fronts, cool outflows from storms, or katabatic winds, may be described as 'DC.' These are transient events, which will probably decay into one or another of the preceding designations after 1 hour or so. A source descriptor can be appended when the cause of the density current echo is known. When breaking waves appear within the current, as is exemplified by Figure 21, that appearance also seems dynamically significant enough to merit an appending descriptor (BW).

When we come to the convectively unstable atmosphere, the convective plume (CP) will be the typical echo. An example has already been shown in Figure 3. It may be desirable to append to the CP designation the height to which the plumes can be observed.

Combinations of the above descriptors will often occur on a single facsimile record. It is suggested that the classifications provided can be used in sequence, progressing upward from the surface to describe the features depicted. For example, in Figure 19 we find convective plumes capped by an elevated shear layer; the classification for this record would be CPESL, the additional qualifier 'ascending' being applied to the elevated layer.

It is believed that the descriptors suggested above can be made to fit any facsimile record. When an echosonde is being used to obtain a climatology of the planetary boundary layer, tables of descriptors and appropriate heights for each hour (or possibly somewhat longer) can be assembled, thus providing a semiquantitative record of what the boundary layer is doing at a particular site. *Schubert* [1975] gives examples of such climatological record use at two sites in the eastern United States. In any tabular classification of boundary layer structure it is almost essential to have a 'remarks' column for further explanation of unusual events, such as the mesoscale or occluded synoptic scale fronts described by *Parry et al.* [1975].

A tabular boundary layer climatology format is convenient for digital processing, by which statistics of the mixed layer depth or the relative frequency of different types of patterns can be obtained. Alternatively, the range-gated raw signal from the echosonde may be processed by an analog-to-digital converter and directly coupled to a computer for processing. One method of achieving this has been described by *Hess and Wesely* [1973]. They store data compactly on magnetic tape, so that such information as inversion heights, relative intensities of the acoustic echoes, or the statistics of different facsimile patterns can be obtained as required. A similar method has been described by *Werner* [1977], who correlated the echosonde returns with lidar and visibility measurements of the boundary layer. A somewhat different digitization scheme has been employed by *Carsey and Leavitt* [1977], who identify the height of successive layers occurring in echosonde returns obtained in polar regions. Their work has resulted in a first development of echosonde boundary layer climatologies over the Arctic ice cap.

HYBRID ACOUSTIC AND ELECTROMAGNETIC SYSTEMS

We have mentioned already the advantages of using the attributes of atmospheric acoustic waves in combination with electromagnetic waves, be they in the optical or radio frequency range. As was pointed out by *Derr and Little* [1970], the interaction of acoustic waves with temperature or velocity structure in the atmosphere is indeed complemented by optical scattering from aerosols or scintillation from temperature structure. Radar waves scatter strongly from precipitation particles and also from fluctuations in the water vapor mixing ratios in the atmosphere. As was predicted by Derr and Little, many significant experiments combining acoustic and electromagnetic probing of the atmosphere have now been performed; more details follow immediately.

Lasers and Acoustics

During the 1971 Metromex air pollution meteorology experiment in the St. Louis area, the Stanford Research Institute operated a vertically directed pulsed ruby lidar and compared the results with the Argonne Laboratories' echosonde [*Uthe and Russell*, 1974]. An example of the comparison between the time height displays provided by the lidar and those provided by the echosonde is given in Figure 31. It will be seen that both instruments trace the top of the mixing layer as it is heated by convection from below but that after noon the sudden growth of the mixed layer documented by the lidar, which clearly shows the maximum altitude of this mixing layer depth to be near 1.2 km, is lost by the sounder, which shows only convective plumes to about 1 km. Because of the difference in scattering centers observed with the two instruments, much more is learned about the evolution and decay of the planetary boundary layer when both are used than when either instrument is used alone.

A similar lidar-echosonde experiment in the 1972 Metromex has been described by *Russell et al.* [1974]. Comparing the results, the authors conclude that in the early morning hours the lidar and echosonde generally perform equally well in defining the depth of the mixed layer, although the lidar traces the activity to its full vertical extent when the convective regime matures in midday. The echosonde depicts the reformation of subsidence layers in the early evening hours; the lidar does not show these layers because there is evidently no difference in the turbidity, as might be expected because of the very low settling speeds of the aerosol particles. Both instruments frequently revealed wave structures in the early morning inversions, and there may be a possibility of utilizing

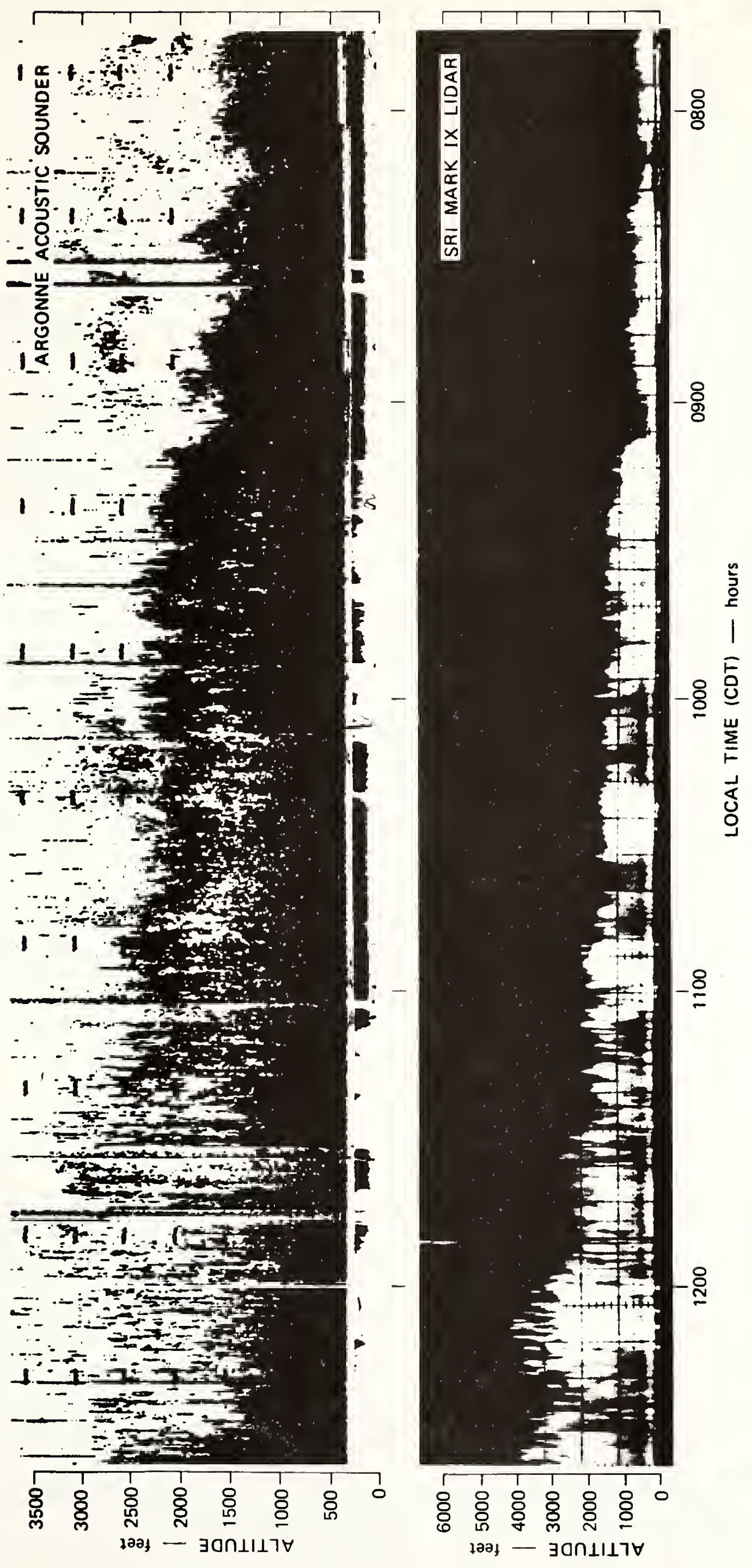

Fig. 31. Comparison of echosonde (top panel) and lidar (bottom panel) displays of the growth of a convectively mixed layer. Note the difference between the vertical scales. (Courtesy of E. Uthe and P. Russell.)

both instruments to understand the transport of aerosols through these sometimes turbulent shear layers.

In a quite different study, *Werner* [1977] compared lidar and echosonde returns with transmissometer results in order to determine how the remote sensing instruments aided the forecasting of visibility. The echosonde determined the top of the radiation fog, whereas the lidar indicated the depth into which the optical radiation penetrated the stratus, complementing the echosonde results in visibility predictions.

Radar and Echosonde Investigations

With the development of the FM/CW high-resolution radar, it became possible to monitor fine-scale fluctuations in the radio refractive index in the atmosphere, caused principally by fluctuations in the water vapor mixing ratio [*Gossard et al.*, 1970]. Multiple layers, breaking waves, and convective cells were detectable in the southern California marine layer by use of this technique. *Mandics* [1973] attempted to correlate returns from a monostatic echosonde with radio refractivity fluctuations, at least qualitatively. When radio refractivity results at different levels on an instrumented tower showed little correlation, indications were found on the echosonde facsimile records that there was considerable decoupling between the two layers, so that agreement might not be expected. This suggested that a combined radar and echosonde experiment might be useful in providing a more complete picture of atmospheric layering, gravity waves, and other structures characteristic of the dynamic boundary layer. The results to be gained and the resulting insight into the organization of turbulence in the stratified atmosphere were reviewed by *Ottersten et al.* [1973].

An experiment performed at Wallops Island, Virginia, during late 1973 utilized both an echosonde and an FM/CW radar [*Richter et al.*, 1974; *Arnold et al.*, 1975]. During the passage of a weak cold front a density-current-like pattern observed with the echosonde was also traced out by the FM/CW radar, which sensed the moisture fluctuations outlining the frontal surface. Further experiments in the marine boundary layer in California [*Richter and Jensen*, 1975] showed that while the echosonde frequently detected the large temperature structure convective plumes, the FM/CW radar depicted the top of the marine inversion (where moisture discontinuities are quite dramatic), which the echosonde missed.

A detailed, quantitative evaluation of the Wallops Island experiment is given by *Noonkester* [1976]. Mixing layer depths determined with the echosonde, the FM/CW radar, and a high-power pulse radar were compared by using supplementary radiosonde information. The agreement between data from the three remote sensors is remarkably good for the ground-based shear layers and for the development of the convectively mixed layers during the early morning hours. However, the echosonde is unable to observe the decay of the top of the convective field in the afternoon hours, whereas the two radars continue to do a reasonably good job. Noonkester points out the caution that must be used when considering convection, whether the measurements have been obtained through the C_T^2 sensing of the echosonde or the radio C_n^2 sensing of the radars. The echosonde frequently observed layered structure in the nocturnal inversion to a higher level than the FM/CW radar did. Such structures obviously represent temperature turbulence events not associated with the top of the moist, ground-based layer.

Echosondes, lidar, and FM/CW radar have been compared by the Naval Electronics Laboratory group [*Noonkester et al.*, 1976]. The marine fogbanks along the California coast show significant returns for the echosonde and FM/CW radar, but on occasion, the fog is dense enough that the lidar is unable to penetrate to the top of the layer.

Another method of comparing echosonde returns with radar data is to utilize chaff to outline the atmospheric patterns, thus making possible the utilization of lower sensitivity radars. Chaff dispensed in convective plumes will remain dispersed for long periods of time, allowing comparative measures of the mixing layer depth and velocity structure by radar and by echosonde. Such an experiment has been reported by *Frisch and Clifford* [1974], who show that the regions within the echosonde plumes, in the low echo level region immediately above the plumes, and in the capping inversion are regions of nearly uniform dissipation of kinetic energy. The dissipation measurements were achieved by using dual pulsed Doppler radars and estimating the dissipation by means of the second moment of the Doppler spectrum. The result confirms the nearly uniform bistatic appearance of the convective plume pattern already mentioned, since dissipation can be directly related to C_v^2 by means of (79). The echosonde can also be used to advantage in depicting the scale size of a convective event for comparison with the size of a convective cell revealed by radar detection of chaff [*Frisch et al.*, 1976].

Radar Acoustic Sounding Systems (RASS)

As was discussed earlier, sound waves propagating through the atmosphere may be characterized as periodic pressure fluctuations. These fluctuations in pressure produce a change in the electromagnetic index of refraction as well. *Smith* [1961] and *Fetter* [1961] proposed using the advection of this pressure field as a measure of wind velocity, the probing being done by electromagnetic radiation. The 22-kHz sound waves used lost coherence so rapidly that the system was limited to ranges of 30 m, however.

By operating at a lower acoustic frequency (85 Hz) *Marshall et al.* [1972] proved the feasibility of obtaining radar echoes from the acoustic tone burst at ranges of more than 1 km. They proposed to utilize the temperature dependence of sound velocity as a method for remote probing of the temperature profile in the lower atmosphere. Marshall et al. show that the received radar power P_r is given by

RASS equation

$$P_r = 1.38 \times 10^{-16} \frac{P_t P_a g n^2}{R^2} \left\{ \frac{\sin [(k_a - 2k_e)(n\lambda_a/2)]}{(k_a - 2k_e)(n\lambda_a/2)} \right\}^2 \qquad (83)$$

where P_t is the transmitted power of the radar, P_a is the acoustic radiated power, g is the directivity of the acoustic antenna, and n is the number of wavelengths in an acoustic pulse. The received power falls off with range R because of the decreasing acoustic intensity in the spherically diverging pressure wave; the wave numbers of the acoustic wave and electromagnetic wave are k_a and k_e, respectively. The expression assumes perfectly coherent acoustic and electromagnetic waves so that when the ratio $k_a/k_e = 2.0$, the reflection coefficient is maximized. Marshall et al. calculated that the match in wavelength ratio is critical when $n > 10$. More details on the development of RASS are given in reports by *Marshall* [1970] and by *North and Frankel* [1972].

A comparison of RASS temperature profiles with radiosonde measurements of temperature to heights of 2.7 km has been reported by *North et al.* [1973]. The Doppler radar, operating at a frequency of 36.8 MHz was a continuous wave unit with transmitting and receiving Yagi antennas placed symmetrically about the pulsed acoustic transmitter. This was a folded horn design, for use at 85 Hz, as described by *Frankel and Peterson* [1976]. North et al. discussed the potential errors in RASS measurements due to water vapor and vertical currents in the atmosphere. Realistic errors in the water vapor mixing ratio amount to 1 K or less, but each meter per second of vertical current speed produces a temperature error of 1.7 K. Thus when convective plumes are present, it may be necessary to average the RASS-derived profiles for many minutes to remove the vertical currents (which can exceed 2 m s^{-1}) in convection. Profiles accurate to within about 1 K were indeed obtained in the field tests by North et al.

The range limitation imposed on a RASS because of turbulence, which reduces the coherence of the acoustic wave, has been analyzed by *Clifford and Wang* [1977]. They show that the turbulent effects change the range dependence from R^{-2} to $R^{-16/5}$. Strong turbulence can thus reduce the range, even at the low acoustic frequency of 85 Hz used by North et al., to several hundred meters. A newer, higher-frequency RASS reported by *Frankel et al.* [1977], utilizing an acoustic frequency of 1.0 kHz, would be more strongly influenced by turbulence. This system has, however, operated to ranges of almost 1 km.

An even more severe limitation to RASS performance is caused by the advection of the acoustic pulse by wind. The ideal, spherical, coherent acoustic grating reflects the electromagnetic signal directly back in the collocated acoustic-electromagnetic antenna configuration. *Frankel et al.* [1977] report that when the wind speed exceeded 4 m s^{-1}, it was necessary to reconfigure RASS as a bistatic radar. In such a configuration the radar antennas were aligned with the wind direction, the transmitting antenna being upwind from the acoustic source and the receiving antenna being placed symmetrically downwind. Because the reflected electromagnetic signal may drop to one-tenth the perfect focus intensity at a radius of only several meters from this ideal point, it appears that it might be necessary to deploy an array of electromagnetic transmitting and receiving antennas symmetrically about the acoustic transmitter to optimize RASS performance in the presence of realistic boundary layer winds. Nevertheless, the potential of RASS for obtaining temperature profiles is of such importance in boundary layer meteorology, and especially for air pollution prediction, that the system is a worthy candidate for further development.

PASSIVE ACOUSTICS AND INFRASOUND

Up to this point we have considered the use of active sound sources in probing the atmosphere, a process in which the received signals are caused by scattering or refraction in atmospheric structure. One can also utilize naturally occurring sounds to probe the atmosphere. Examples of such passive sources are thunder in the audible region and infrasound from atmospheric turbulence and waves, from storms, or from the ocean at the lower acoustic frequencies.

Thunder is the spectrum of sound generated by lightning in the atmosphere, stretched out in time because of the differing transmission path lengths from the extended channel source. If one places an array of microphones on the ground, it is possible to reconstruct the shape of the lightning channel by correlating the direction cosines and the arrival times of identifiable temporal segments of the thunder. This technique has been proven feasible by *Few* [1970] in a continuing series of investigations. Typically, three or four microphones are laid out in each array; a Y-shaped array with spacings of 30–100 m between microphones has proven to be most useful. It is the tortuous nature of the lightning channel (the many kinks and bends) that gives rise to the time variability of the acoustic signature [*Few*, 1969]. Of course, sound that arrives from more distant portions of the channel will be attenuated in the higher frequencies because of molecular absorption in the atmosphere. Typical power spectra corresponding to differing arrival times have been given by *Few* [1969].

In evaluating thunder data it is important to know the temperature and wind as functions of height in reconstructing the sound rays back to their point of origin. The method of analysis and the expected errors in establishing the lightning channel geometry are discussed by *Teer and Few* [1974] from data gathered by using a triangular array of three microphones 100 m apart. During the mature and decaying times of an Arizona thunderstorm, 17 cloud-to-ground and 20 intracloud lightning discharges were mapped. The results indicate that horizontal lightning structures within clouds are more persistent and extended than has been previously determined from electric field measurements from the ground. Typically, the horizontal extent of a lightning discharge will be 3 times the vertical extent. The accuracy with which the channels can be reconstructed has been confirmed by overlaying acoustic records onto photographs of visible portions of cloud-to-ground strokes [*Few and Teer*, 1974]. Typical positional errors seem to be within 4% when wind and temperature profiles are well known. (A 90-m error at a range of 2.5 km was documented.) When supportive wind measurements are not available, errors may be about 10%.

As a result of the acoustic thunder research we have learned that lightning activity is predominantly horizontal and is concentrated in the zone within the cloud associated with freezing [*Few*, 1974]. A positive correlation between radar reflectivity values within the cloud and lightning activity has also been found. Thus this acoustic method is already having impact in an important area of cloud physics.

Besides the audible acoustic waves in the atmosphere, there is a class of wave in which the force of gravity can no longer be neglected. These so-called 'acoustic gravity waves' occur in the frequency region from about 1 to 10^{-4} Hz or less [*Georges and Young*, 1972]. Sensors for these waves have historically been of the microbarograph type. To eliminate background noise, such as eolian wind tones, it is usual practice to connect the pressure-sensing instrument to a noise-reducing multiple-aperture pipe, typically 100 m long [*Burridge*, 1971]. When the pressure sensor is capable of measuring changes of about 1 part in 10^8, or 0.01 μbar, with sufficient noise rejection, a number of atmospheric wave motions are detectable [*Cook*, 1962; *Cook and Young*, 1962]. It is usually necessary to arrange the sensors with their noise-reducing pipes in an array so that the direction of arrival of the wave can be used to discriminate further against random background noise. When this is done, the most characteristic wave patterns observed have a period of approximately 5 s and an amplitude of about 5 μbar. These are the so-called 'microbaroms' frequently observed with infrasonic microphones spaced 1 km apart in an array. Microbaroms are seldom detectable in larger arrays. The direction of arrival of the microbarom signal is not limited to a single direction: the spatial correlation is low, indicating a wide-area source. This source is now believed to lie in oceanic waves. Correlating directions of arrival by using arrays spaced many hundreds of kilometers apart usually leads to intersections in oceanic areas.

Another class of infrasonic wave, typically with periods of about 40 s, originates in mountainous regions. *Larson et al.* [1971] report on triangulation using arrays at Pullman, Washington, and Edson, Alberta, Canada, and identify a region of the Canadian Rocky Mountains as the source region. The signals also showed a correlation with wind speed and direction at the 500-mbar level. Typical amplitudes for this mountain-associated infrasound are near 0.5 μbar.

In a more recent study, *Bedard* [1977] shows excellent correlation between 500-mbar winds and aircraft reports of turbulence in apparent wave source generating regions to the lee of Pike's Peak or Long's Peak (both peaks higher than 4.3 km) in Colorado. There seems to be no doubt that turbulent eddies in the mountain wake are responsible for the infrasound, but the exact generation mechanism (quadrupoles or eolian tones) is still not well understood.

Another source of atmospheric infrasound is auroral disturbances. *Wilson* [1969] has shown that typical auroral infrasonic wave packets have amplitudes of several microbars and that the waves at the beginning of the packet may exhibit periods of a few seconds, stretching out to periods of 1 min or longer toward the end of the packet. A typical packet of waves is identifiable for periods of 5 min or longer. Auroral infrasound is easily separated from infrasound originating lower in the atmosphere, since the trace velocity across an array of microbarographs will average about 500 m s^{-1}. This is because the angle of arrival (at least in Alaska) averages 45° in elevation. The source of the infrasound is associated with supersonic motion in auroral arcs. This explanation has been supported by correlating infrasonic events with all-sky photographs of the aurora.

Another interesting subset of infrasonic waves originates in severe convective storms. *Georges* [1973] has examined the evidence that infrasonic waves do originate in such storms and are detectable at distances of several hundred to 1000 km. He shows a strong correlation between infrasonic observations and electromagnetic Doppler soundings of wavelike ionospheric motions, concluding that both events are manifestations of a single source process. As potential sources of infrasound, *Georges* [1976] analyzes models of pressure pulses in growing convective cells, of infrasound emission from turbulence in storm clouds, of thermal-mechanical mechanisms related to the heat release in clouds, and of the electrical activity in storms. He concludes, however, that the most likely model for the infrasonic emission is a vortex radiation mechanism, which suggests that the tornadic cyclones may be the infrasound emitters. This mesoscale rotation is sometimes noted (by radar observation) 1 hour before tornadoes touch the ground. This early development of the mesoscale rotation could explain the infrasound observed at distances of several hundred kilometers from tornadoes being observed at the same time.

In analyzing the propagation of infrasound from convective storms into the upper atmosphere, *Jones and Georges* [1976] conclude that the observed spectrum of infrasound is explained by the source-to-ionosphere transfer function imposed by the atmosphere. The model, however, fails to match accurately the observed high-frequency spectral roll-off rate, which leads to the hypothesis of a source power spectral density proportional to $f^{-7/2}$. This is the same spectral variation expected of a turbulent sound source. Because of the finite transit time through the atmosphere, it is not probable that infrasound from storms will be useful for storm warning. It is more likely that infrasonic detection will be a useful supplement to the present forecasting and radar net warning system. In a study of false alarm rate, detection rate, location accuracy, and timeliness, *Georges and Greene* [1975] show that at a 1000-km range, infrasound from tornadic storms is measurable 65% of the time and that the location of the storm can be determined to within 50–100 km when three direction-finding arrays are utilized. A later study by *Beasley et al.* [1976], in which electrical activity is compared with infrasound from convective storms, shows that the infrasonic emission does precede the electrical activity by 1 hour or more.

Thus there is now little doubt that severe convective storms, especially tornadic storms, can produce infrasonic waves of great intensity with periods of about 0.2–2 min. One must be some distance (at least 15 km) from the storm to observe its sound because of the propagation path. There can be little forewarning of the severe storm presence. More work remains to be accomplished in explaining the source of this infrasound.

As is true with any passive technique, infrasonic measurements of the state of the atmosphere must be taken as the information comes to the observer. For instance, noise from strong winds at the observing site can eliminate the possibility of any measurements. Nevertheless, infrasonic observations have shed considerable light on atmospheric processes that would be inaccessible to echosondes for probing.

THE FUTURE OF ATMOSPHERIC ACOUSTICS

In the introduction to this paper we speculated that the echosonde may represent only a passing fancy. *Little* [1972*d*] has shown that the present range limitations on echosonde applications in the planetary boundary layer can be overcome by increasing the transmitted power, increasing the integration time, increasing the effective antenna area, and improving data processing through the use of matched filters and coherent integration. A potential sensitivity gain of 80 dB over currently used systems may be possible.

With the improvements and simplification in Doppler processing now available through microcomputers and real correlation methods, there is no doubt that a Doppler echosonde wind profiler can be significantly less costly in the very near future. Such a tool will undoubtedly find significant application in air pollution meteorology problems, especially if adaptive methods can be developed so that the echosonde can be made to recognize the depth of the mixed layer without needing an expert meteorologist to interpret the facsimile recording for this information. Further processing of the Doppler signal for velocity variance should lead to applications of echosondes in predicting the dispersion of air pollutants in the turbulent planetary boundary layer. But perhaps the future is brightest for the echosonde in combination with other remote sensors, such as radars (as in the RASS method), or with lidars for better measurements of the mixed layer characteristics. Certainly, the details of atmospheric turbulence revealed by echosondes cannot help but provide modelers of boundary layer dynamics with new clues on the organization of turbulent waves in the atmospheric fluid. Turbulence organization must also provide critical tests for the predictions of temperature or velocity structure functions. Improvements in data processing, perhaps using coherent detection techniques or acoustic interferometers, may hold promise for echosonde temperature profiling without supporting instruments.

Scientists and engineers working in the field of atmospheric acoustics can feel some satisfaction with the rapid acceptance of acoustic methods over the past several years. There is still plenty of work for those interested in atmospheric research, in feasibility experiments, and in operational meteorological predictions, work using to advantage the inherently straightforward and inexpensive acoustic technology now available and supported by the rapid improvements in digital data processing techniques.

APPENDIX A: A DERIVATION OF THE ACOUSTIC EQUATION

Because some confusion exists regarding the conditions introduced by various authors in the derivation of the acoustic equation, we append one such derivation here. We use both the A^2 and AT^2 assumptions and the assumptions involved in the separation into turbulence and acoustic velocities described earlier. Recall that the A^2 assumption requires us to neglect second-order or higher acoustic pressure and density changes normalized by equilibrium values of pressure and density (with respect to first-order changes) and second-order or higher acoustic particle velocities normalized by the equilibrium sound speed c_0. Similarly, the AT^2 assumption requires us to neglect products of normalized acoustic quantities with higher than first-order normalized turbulence properties. The separation into acoustic and turbulence properties implies that turbulence property changes of the types T, T^2, etc., satisfy their own equations and thus drop out of the acoustic equation. However, the mean wind Mach number $\bar{m} = |\bar{\mathbf{w}}|/c_0$ requires special treatment, since $\bar{m}$ can reach values of approximately 0.1 (or even exceed this value in hurricanes and chinooks), whereas the rms value of the Mach number of the turbulent velocity fluctuations $m_{\mathrm{rms}}' = (|w'|^2)^{1/2}/c_0$ rarely reaches values of approximately 0.01. But most of the effects of the mean wind can be taken into account very generally without any restriction on the results by using the 'mean substantial derivative.' That is, if we write the total velocity as $V_i = v_i + \bar{w}_i$ and if $d_t = d/dt$ represents the ordinary substantial derivative $d_t = \partial_t + V_i\partial_i$, where $\partial_i = \partial x_i$, then the mean substantial derivative is $\bar{d}_t = \partial_t + \bar{w}_i\partial_i$. The exception that will arise is a term involving an acoustic fluctuation, a turbulent fluctuation of order m_{rms}', and the mean wind Mach number $\bar{m}$. But since this term will still be small compared with the others, we will neglect it also.

In accordance with the separation into turbulent and acoustic velocities we write $v_i = w_i' + u_i$, where u_i is the acoustic particle velocity. Similarly, we write the pressure as $p = p_\omega + p_\alpha$, where the subscript ω reminds us that turbulence is a random vorticity (ω) field and the subscript α suggests the acoustic field. But since $p_\omega = \bar{p}_\omega + \bar{p}_\omega' = p_0 + p_\omega'$ and since p_ω' is second order in w_{rms}', we can set $p_\omega \approx p_0$ in any terms containing acoustic properties. Since the turbulence is assumed to be incompressible, we would similarly have $\rho_\omega = \rho_0$ for the turbulence density in the homogeneous case. However, for an atmosphere in which turbulence mixes air parcels originally having different potential temperatures the turbulence density is no longer constant or uniform. If we label such parcels with the symbol σ, where $\sigma = s/c_v$ represents the ratio of entropy density s to specific heat c_v, we can write the turbulence density after mixing as $\rho_\sigma = \rho_0 + \rho_\sigma'$, where ρ_σ' is a nonzero random turbulence variable. If in addition to the adiabatic condition $d_t\sigma = 0$ we assume that ρ_σ is a 'passive additive,' that is, the turbulence density of each parcel does not change during its motion (which also assumes that the excursions of a parcel are not great enough for the gravity field to produce appreciable changes), we obtain an additional equation $d_t\rho_\sigma = 0$. Since the characteristic times of turbulence motions are small in comparison with those associated with heat flow, we can assume that the pressure on a parcel of different density ρ_σ has reached the pressure in the turbulent field. Consequently, for a perfect gas we can write $d \ln \rho_\sigma = -d \ln c^2$ for any displacement d in time or space, where c is the random speed of sound associated with the turbulent field.

With the above notation and assumptions the equation for conservation of mass, the equation for conservation of momentum, the adiabatic condition, and the restriction that ρ_σ (or c^2) is a passive additive take the forms

$$\bar{d}_t\rho + \partial_j(\rho v_j) = 0 \tag{A1}$$

$$\bar{d}_t(\rho v_i) + \partial_j(\rho v_i v_j) = -\partial_i p \tag{A2}$$

$$\bar{d}_t\sigma + v_j\partial_j\sigma = 0 \tag{A3}$$

$$\bar{d}_t\rho_\sigma + v_j\partial_j\rho_\sigma = 0 \tag{A4}$$

We note that using the rule for the derivative of a product for the $\bar{d}_t$ term in (A2) and then substituting for $\bar{d}_t\rho$ from (A1) leads to the Euler equation (the Navier-Stokes equation for zero viscosity)

$$\bar{d}_t v_i + v_j\partial_j v_i = -\rho^{-1}\partial_i p \tag{A5}$$

Taking the divergence of (A2), however, and substituting for $\partial_j(\rho v_j)$ from (A1) immediately give

$$\partial_i\partial_j(\rho v_i v_j) + \nabla^2 p - \bar{d}_t^2\rho = 0 \tag{A6}$$

Now we must use some care in subtracting strictly turbulence properties from (A6). The distinction between the turbulence field and the acoustic field determines the velocities w_i' and u_i. But ρ_σ is defined differently; that is, ρ_σ is the result of adiabatic motion between different locations in a gradient atmosphere. Stated in another way, ρ_σ is a passive additive, not only for the turbulent motions represented by w_i', but also for the acoustic motions denoted by u_i. Consequently, for a given gradient in ρ_σ, (A4) requires that the time derivative $\bar{d}_t\rho_\sigma$ be split into two parts, a part $(\bar{d}_t\rho_\sigma)_\omega = -w_j'\partial_j\rho_\sigma$ representing the time rate of change caused by the advection of ρ_σ by the turbulence, and a part $(\bar{d}_t\rho_\sigma)_\alpha = -u_j\partial_j\rho_\sigma$ representing the change caused by the sloshing back and forth of ρ_σ during the passage of sound. As a result the equations corresponding to (A5) and (A6) for the purely turbulence field reduce to

$$\bar{d}_t w_i' + w_j'\partial_j w_i' = -\rho_\sigma^{-1}\partial_i p_\omega \tag{A5$'$}$$

and

$$\partial_i\partial_j(\rho_\sigma w_i' w_j') + \nabla^2 p_\omega - \partial_i(w_i' w_j'\partial_j\rho_\sigma) + (\partial_i\rho_\sigma)\bar{d}_t w_i' = 0 \tag{A6$'$}$$

Because of the sloshing effect, the acoustic equation presents a much simpler form when it is written in terms of the ratio $\xi = \rho_\alpha/\rho_\sigma$ than when it is given for ρ_α alone. Thus we set $\rho = \rho_\sigma(1 + \xi)$ in (A6) and expand the time derivative as

$$\bar{d}_t^2\rho = (1 + \xi)\bar{d}_t^2\rho_\sigma + 2\bar{d}_t\rho_\sigma\bar{d}_t\xi + \rho_\sigma\bar{d}_t^2\xi \tag{A7}$$

From (A4) we can write $\bar{d}_t^2\rho_\sigma = -\bar{d}_t(u_i\partial_i\rho_\sigma) - \bar{d}_t(w_i'\partial_i\rho_\sigma)$, and thus from the A^2 and AT^2 assumptions the first term of (A7) reduces to

$$(1 + \xi)\bar{d}_t^2\rho_\sigma = -\bar{d}_t(u_i\partial_i\rho_\sigma) - \bar{d}_t(w_i'\partial_i\rho_\sigma) \tag{A8}$$

From the same assumptions and (A4), $\bar{d}_t\rho_\sigma = -u_j\partial_j\rho_\sigma - w_j'\partial_j\rho_\sigma$, the second term of (A7) vanishes. Continuing the process, we find that the first term of (A8) becomes $-\bar{d}_t(u_i\partial_i\rho_\sigma) = -(\bar{d}_t u_i)(\partial_i\rho_\sigma)$ and that the second term of (A8) reduces to purely turbulence properties, $-\bar{d}_t(w_i'\partial_i\rho_\sigma) = -(\bar{d}_t w_i')\partial_i\rho_\sigma + w_i'\partial_i(w_j'\partial_j\rho_\sigma)$. If we substitute these results in (A6), subtract all purely turbulence properties by means of (A5′) and (A6′), and again use the A^2 and AT^2 assumptions, we obtain

$$2\rho_0\partial_i\partial_j(w_i'u_j) + \nabla^2 p_\alpha + (\bar{d}_t u_i)(\partial_i\rho_\sigma) - \rho_\sigma \bar{d}_t^2\xi = 0 \quad \text{(A9)}$$

We note that the third term of (A9) is already of type AT. Thus we can use the Euler equation, (A5), with all T and A^2 terms removed, to substitute $\bar{d}_t u_i = -\rho_0^{-1}\partial_i p_\alpha$ plus a purely turbulence term that vanishes because (A5′) implies that one of its factors is zero. But considering the order, we can also write $\rho_0^{-1}\partial_i\rho_\sigma = \partial_i \ln \rho_\sigma = -\partial_i \ln c^2$. With this change, (A9) becomes

$$2\rho_0\partial_i\partial_j(w_i'u_j) + \nabla^2 p_\alpha + (\partial_i \ln c^2)(\partial_i p_\alpha) - \rho_\sigma \bar{d}_t^2\xi = 0 \quad \text{(A10)}$$

Before continuing the process of simplification we need to introduce the adiabatic condition, (A3), which without the averaging bar reads merely $d_t\sigma = 0$. But from the relation $T\,ds = c_v\,dT - (p/\rho^2)\,d\rho$ satisfied by a perfect gas, for $\sigma = s/c_v$ we can write $d_t\sigma = d_t \ln (p/p_0) - \gamma d_t \ln (\rho/\rho_0)$. Again using $\rho = \rho_\sigma(1 + \xi)$, $p = p_0 + p_\alpha$, and (A4), that is, $d_t\rho_\sigma = 0$ (note no overbar), then $d_t \ln (1 + p_\alpha/p_0) = \gamma d_t \ln (1 + \xi)$, or with the A^2 assumption, $d_t(p_\alpha/p_0) = \gamma d_t\xi$. If we assume that no acoustic field existed at some earlier time (at $t = -\infty$ if need be), we can in principle integrate the last equation along the path of each parcel to obtain finally

$$p_\alpha/p_0 = \gamma\xi = \gamma\rho_\alpha/\rho_\sigma \quad \text{(A11)}$$

The relation (A11) will permit us to write the acoustic equation in terms of either ξ or p_α. Briefly, if we substitute for p_α from (A11) in (A10), divide through by ρ_σ, and use the relation $c^2 = \gamma p_0/\rho_\sigma$, we obtain

$$2\partial_i\partial_j(w_i'u_j) + \partial_i(c^2\partial_i\xi) - \bar{d}_t^2\xi = 0 \quad \text{(A12)}$$

We note that the first term of (A12) is also of the type AT, so that we can again employ (A5) with all A^2 and T terms removed. From (A11) we can write this reduced version of (A5) as $\bar{d}_t u_i = -c_0^2\partial_i\xi$. But before we can use the equation, we need to convert the time derivative by applying a Fourier time transform $\mathfrak{F}_t$ to all quantities, which implies that we must transform (A12) as well. If we write $P = P(k) = \mathfrak{F}_t\xi$ (which differs only by a constant from $\mathfrak{F}_t p_\alpha$), $U_i = \mathfrak{F}_t u_i$, $N' = \mathfrak{F}_t n'$ (where $n = c/c_0 = 1 + n'$), $M_i' = \mathfrak{F}_t w_i'/c_0$, $\bar{M}_i = \bar{m}_i\delta(k)$, and $c_0^{-1}\,\mathfrak{F}_t\bar{d}_t = -ik + \bar{m}_i\partial_i$, then the reduced version of (A5) becomes

$$U_i/c_0 = -ik^{-1}\partial_i P - ik^{-1}\bar{M}_j\partial_j U_i/c_0 \quad \text{(A13)}$$

We could continue to remove U_i from the right side of (A13) by iteration. But we notice that after the first right-hand term the result substituted in the Fourier transform of the first term of (A12) would contribute terms containing all of the small factors $\bar{M}$, M', and P. As was mentioned at the end of the first paragraph of this appendix, such terms will still be 1 order of magnitude less than the others and thus can be neglected. Since w_i', u_i, c^2, and ξ are all functions of time, in general, application of the Fourier transform $\mathfrak{F}_t$ to (A12) will convert all products of time-dependent functions to k convolution products, which we will symbolize by an asterisk. In addition, the AT^2 assumption implies that we must approximate N^{-2} in the second term by $1 - 2N'$. Introducing all the above transforms in (A12) and rearranging terms finally give the acoustic equation

$$\nabla^2 P + (k + i\bar{M}_j\partial_j)^2 P = 2\partial_j(N' * \partial_j P) + 2i\partial_j\partial_h[M_j' * (k^{-1}\partial_h P)] \quad \text{(A14)}$$

We remark that the above derivation has made no assumptions about 'frozen turbulence,' so that the result applies also to time-varying turbulence statistics. Nor has it made any assumptions on the spatial homogeneity, so that it applies equally well to the atmosphere and to moving finite turbulent regions.

APPENDIX B: A SELECTION OF USEFUL THEORETICAL RESULTS

Structure constant for refractivity fluctuations (6)

$$C_n^2 = C_T^2/4T_0^2 + 2(0.307)C_{eT}/4p_0T_0 + (0.307)^2C_e^2/4p_0^2$$

Effective refractivity structure constant (41)

$$C_{ne}^2 = C_n^2 + C_v^2/c_0^2$$

Inertial range scattering cross section (33)

$$\sigma_s(\theta_s) = 1.52k_0^{1/3}\cos^2\theta_s\{0.13C_n^2 + \cos^2(\theta_s/2)C_v^2/(4c_0^2)\}[2\sin(\theta_s/2)]^{-11/3}$$

Echosonde equation (34)

$$\mathcal{P}_R/\epsilon_R = \epsilon_T\mathcal{P}_T \exp[-\hat{a}(R_0 + R_s)] \cdot (1 + \mathbf{e}_s\cdot\bar{\mathbf{M}})\mathcal{A}(\theta_s)(l_p/2)(gA_R/R_s^2)\sigma_s(\theta_s)$$

Gaussian form of locally frozen turbulence spectrum (37)

$$I(k) = S(\mathbf{x})[2\pi\langle(\mathbf{K}\cdot\mathbf{M}_L')^2\rangle]^{-1/2}\exp[-(k - k_0 + \mathbf{K}\cdot\bar{\mathbf{M}}_L)^2/2\langle(\mathbf{K}\cdot\mathbf{M}_L')^2\rangle]$$

Weak turbulence structure functions (52)

$$D_f(\rho) = 8\pi^2k^2\int_0^L ds\, C_{ne}^2(s)\int_0^\infty d\kappa\, \kappa\Phi_{ne}^{(0)}(\kappa)[1 - J_0(\beta\rho\kappa)]H_f(s,\kappa)$$

Weak turbulence spectral weighting functions (53)

$$H_\psi = 1$$
$$H_\phi = \cos^2[\beta(s)(1 - s/L)\kappa^2L/2k]$$
$$H_\chi = \sin^2[\beta(s)(1 - s/L)\kappa^2L/2k]$$

Weak turbulence wave structure function (56)

$$D_\psi(\rho) = 2.914k^2\rho^{5/3}\int_0^L ds\,\beta^{5/3}(s)C_{ne}^2(s)\{1 - 0.805[\beta(s)\rho K_0]^{1/3}\}$$

Weak turbulence phase structure function (60)

$$D_\phi(\rho) = D_\psi(\rho) \qquad \rho \geq (\lambda L)^{1/2}$$
$$D_\phi(\rho) = \tfrac{1}{2}D\psi(\rho) \qquad \rho < (\lambda L)^{1/2}$$

Weak turbulence log-amplitude variance (61)

$$\sigma_\chi^2 \approx \sigma_l^2 = 0.563k^{7/6}L^{11/6}[C_{ne}^2]_\chi$$

Log-amplitude spectra for plane waves (71*a*)

$$f_wW_\chi^+(f) = 1.103\sigma_{\chi p}^2(1 + 0.92f_n^{4/3}) \qquad f_n < 1$$
$$f_wW_\chi^+(f) = 0.24\sigma_{\chi p}^2f_n^{-8/3} \qquad f_n > 1$$

Log-amplitude spectra for spherical waves (71*b*)

$$f_wW_\chi^+(f) = 0.614\sigma_{\chi s}^2(1 + 0.405f_n^{4/3}) \qquad f_n < 1$$
$$f_wW_\chi^+(f) = 0.606\sigma_{\chi s}^2f_n^{-8/3} \qquad f_n > 1$$

Phase spectra for plane waves (72*a*)

$$f_w W_\phi^+(f) = 0.489\sigma_{\chi p}^2 f_n^{-8/3} \qquad f_n < 1$$

$$2f_w W_\phi^+(f) = 0.489\sigma_{\chi p}^2 f_n^{-8/3} \qquad f_n > 1$$

Phase spectra for spherical waves (72*b*)

$$f_w W_\phi^+(f) = 1.215\sigma_{\chi s}^2 f_n^{-8/3} \qquad f_n < 1$$

$$2f_w W_\phi^+(f) = 1.215\sigma_{\chi s}^2 f_n^{-8/3} \qquad f_n > 1$$

Phase difference spectra for plane waves (73*a*)

$$f_w W_{\delta\phi}^+(f) = 0.99\langle\sigma_{\chi p}^2 f_n^{-8/3}[1 - \cos(2\pi\rho_n f_n)] \qquad \rho_n > 1$$

$$2f_w W_{\delta\phi}^+(f) = 0.99\langle\sigma_{\chi p}^2\rangle f_n^{-8/3}[1 - \cos(2\pi\rho_n f_n)]^\cdot \qquad \rho_n < 1$$

Phase difference spectra for spherical waves (73*b*)

$$f_w W_{\delta\phi}^+(f) = 2.46\langle\sigma_{\chi s}^2\rangle f_n^{-8/3}\frac{1 - \sin(2\pi\rho_n f_n)}{2\pi\rho_n f_n} \qquad \rho_n > 1$$

$$2f_w W_{\delta\phi}^+(f) = 2.46\langle\sigma_{\chi s}^2\rangle f_n^{-8/3}\frac{1 - \sin(2\pi\rho_n f_n)}{2\pi\rho_n f_n} \qquad \rho_n < 1$$

Frequency spectrum of the pressure (74)

$$f_w W_{p^+(P)}(f) = (2\pi/\tau_p)\mathfrak{D}_0^2(\Delta f)$$
$$* \{0.144\sigma_{\chi p}^2 L_{on}^{8/3}[1 + (L_{on}\Delta f_n)^2]^{-4/3}\}$$

Excess attenuation (76)

$$a_e L = 10\log\left\{1 + 1.56k^{12/5}D_0^2\left[\int_0^L ds(1 - s/L)^{5/3}C_{ne}^2(s)\right]^{6/5}\right\}$$

NOTATION

Because of the breadth of the field of atmospheric acoustics a number of symbols are used in several ways. When such overlap occurs, the correct meaning will be clear from the context.

a	absorption coefficient, decibels per meter.
a	amplitude of sound pressure as a function of time, decibels referred to 2×10^{-5} N m^{-2}.
$\hat{a}$	absorption coefficient, nepers per meter.
a_e	excess attenuation coefficient, decibels per meter.
a_0	amplitude of initial wave sound pressure as a function of time, decibels referred to 2×10^{-5} N m^{-2}.
α	absorption coefficient per wavelength, decibels.
$\hat{\alpha}$	absorption coefficient per wavelength, nepers.
A	amplitude of sound pressure as a function of temporal wave number, decibels referred to 2×10^{-5} N m^{-1}.
A	area of cross section of scattering volume subtended by receiving antenna, square meters.
A_0	amplitude of initial wave sound pressure as a function of temporal wave number, decibels referred to 2×10^{-5} N m^{-1}.
$\mathfrak{A}$	aspect ratio for scattering volume changes in bistatic echosondes.
b_s	equivalent width of spectrum, s^{-1} or m^{-1}.
β	plane wave/spherical wave characteristic function.
B_f	covariance of an arbitrary function f.
c	speed of sound, meters per second.
c_0	equilibrium speed of sound as a function of altitude, meters per second.
c_p	specific heat at constant pressure, J K^{-1} mol^{-1}.
c_v	specific heat at constant volume, J K^{-1} mol^{-1}.
C_v^2	structure parameter for velocity fluctuations, m$^{4/3}$ s^{-2}.
C_T^2	structure parameter for temperature fluctuations, K^2 m$^{-2/3}$.
C_e^2	structure parameter for vapor pressure fluctuations, N^2 m$^{-14/3}$.
C_{eT}	structure parameter for cross correlation of vapor pressure and temperature fluctuations, K N m$^{-8/3}$.
C_n^2	structure parameter of refractive index fluctuations, m$^{-2/3}$.
C_{ne}^2	effective structure parameter of refractive index and velocity fluctuations, m$^{-2/3}$.
$[C_{ne}^2]_{\phi p}$	C_{ne}^2 average over a path for plane wave phase properties, m$^{-2/3}$.
$[C_{ne}^2]_{\chi p}$	C_{ne}^2 average over a path for plane wave log-amplitude properties, m$^{-2/3}$.
$[C_{ne}^2]_{\phi s}$	C_{ne}^2 average over a path for spherical wave phase properties, m$^{-2/3}$.
$[C_{ne}^2]_{\chi s}$	C_{ne}^2 average over a path for spherical wave log-amplitude properties, m$^{-2/3}$.
d_0	normalized pulse shape of initial wave as a function of time.
D_0	diameter of transmitting antenna, meters.
D_f	structure function of arbitrary function f.
D_m	thermal diffusivity of air-fog mixture, square meters per second.
$\mathfrak{D}_0$	normalized pulse shape of initial wave as a function of temporal wave number, meters.
δ	Dirac delta measure.
δ	difference (for phase at two points).
δ_{ij}	Kronecker delta.
Δ	difference.
∂_t	time derivative, equal to $\partial/\partial t$.
∇	gradient or spatial derivative, equal to $\partial/\partial \mathbf{x} = \partial/\partial x_i = \partial_i$.
$\nabla\cdot$	divergence (of a vector).
∇x	curl (of a vector).
∇^2	Laplacian operator, equal to $\nabla\cdot\nabla$.
e	vapor pressure of water in air, newtons per square meter.
e_i	unit vector, equal to $\mathbf{e}$.
$\mathbf{e}_0$	unit vector in direction of initial wave.
$\mathbf{e}_s$	unit vector in direction of scattered wave.
ϵ	kinetic energy dissipation rate, m^2 s^{-3}.
$\boldsymbol{\varepsilon} =$	$\mathbf{k}_0/\omega_0$, seconds per meter.
ϵ_T	electric-to-acoustic efficiency of transmitter.
ϵ_R	acoustic-to-electric efficiency of receiver.
E	kinetic energy density, m^2 s^{-2}.
η	coherent extinction coefficient, m^{-1}.
f	arbitrary function of time.
f	frequency of sound wave, hertz.
f_0	frequency of initial sound wave, hertz.
$\tilde{f}$	part of wave varying slowly with time.
f_w	effective frequency due to crosswind $w_\perp$, equal to $w_\perp/(\lambda L)^{1/2}$, hertz.
f_n	sound frequency normalized by crosswind frequency, equal to f/f_w.
F	arbitrary function of temporal wave number.
$\mathfrak{F}_t$	Fourier time transform.
$\mathfrak{F}_k^\dagger$	inverse of Fourier time transform.
$\mathfrak{F}_\mathbf{x}$	Fourier space transform.
$\mathfrak{F}_\kappa^\dagger$	inverse of Fourier space transform.
ϕ	phase of a wave, radians.

Φ_{ij}	spatial velocity spectrum.
Φ_{ne}	spatial effective refractivity spectrum.
$\Phi_{ne}^{(0)}$	local spatial effective refractivity spectrum in a gradient atmosphere.
g	antenna gain factor.
g	acceleration of gravity, m s^{-2}.
γ	ratio of specific heats, equal to c_p/c_v.
γ	parameter for scattering cross section, equal to $C_v^2 T_0^2/(C_T^2 c_0^2)$.
G	Green's function.
Γ^2	power reflection coefficient.
h	complex temporal wave number, equal to $k(1 + ikl_v)$, m^{-1}.
H_f	weighting function for wave property f.
i	imaginary number unit, equal to $(-1)^{1/2}$.
I	spectral density of a wave.
k	temporal wave number, equal to $\omega/c_0 = 2\pi/\lambda$, m^{-1}.
k	Boltzman constant, equal to 1.38×10^{-23} J K^{-1}.
k	von Kármán constant.
k_0	temporal wave number of initial wave, m^{-1}.
$\mathbf{k}$	wave vector, m^{-1}.
$\mathbf{k}_0$	wave vector of initial wave, m^{-1}.
κ	magnitude of spatial wave number, equal to $\lvert\boldsymbol{\kappa}\rvert$, m^{-1}.
$\boldsymbol{\kappa}$	spatial wave number coordinates, equal to κ_i, m^{-1}.
κ_0	inner scale wave number, equal to $5.92/l_0$, m^{-1}.
κ_m	thermal conductivity of fog-air mixture, J K^{-1} m^{-1} s^{-1}.
K_0	outer scale wave number, equal to $2\pi/L_0$, m^{-1}.
$\mathbf{K}$	wave scattering vector, equal to $K_i = 2k_0 \sin(\theta_s/2)(\mathbf{e}_0 - \mathbf{e}_s)$, m^{-1}.
l	thickness of scattering layer, meters.
l	eddy size, equal to $2\pi/\kappa$, meters.
l_0	inner scale of turbulence, meters.
l_p	characteristic length of pulse, meters.
l_v	characteristic viscosity length, equal to $(2\mu_v + \lambda_v)/(2\rho_0 c_0)$, meters.
λ	wavelength of sound, meters.
λ_v	volume viscosity, kg m^{-1} s^{-1}.
L	path length of sound beam, meters.
L_e	Lewis number of fog-air mixture, equal to $\kappa_m/(\rho_m c_p D_m)$.
L_0	outer scale of turbulence, meters.
L_{on}	outer scale of turbulence normalized by a Fresnel zone, equal to $L_0/(\lambda L)^{1/2}$.
m	molecular weight, kilograms per mole.
$\bar{m}$	magnitude of mean wind Mach number.
$m =$	turbulence Mach number, equal to $\lvert\mathbf{w}\rvert/c_0$.
M	time Fourier transform of turbulence Mach number, meters.
M_L	time Fourier transform of turbulence Mach number for large-scale eddies, meters.
$\mathbf{M}$	turbulence Mach vector, meters.
$\mathcal{M}$	mutual coherence function of a wave.
μ_v	shear viscosity, kg m^{-1} s^{-1}.
μ_m	shear viscosity of fog-air mixture, kg m^{-1} s^{-1}.
n	acoustic refractive index as a function of time, equal to c_0/c.
N	temporal Fourier transform of acoustic refractive index as a function of wave number, meters.
N_e	effective refractivity, equal to $N - \mathbf{e}\cdot\mathbf{M}$, meters.
$\tilde{N}_e$	complex effective refractivity, equal to $(h^2/k^2)N_e$, meters.
N	Väisälä frequency, hertz.

ν	kinematic shear viscosity, square meters per second.
ω	angular sound frequency, radians per second.
ω_0	angular sound frequency of initial wave, radians per second.
Ω	solid angle, steradians.
p	acoustic pressure as a function of time, decibels referred to 2×10^{-5} N m^{-2}.
p_0	equilibrium pressure of the atmosphere as a function of altitude, newtons per square meter.
P	temporal Fourier transform of acoustic pressure, decibels referred to 2×10^{-5} N m^{-1}.
P	temporal Fourier transform of ratio of acoustic density to tubulence density, dimensionless.
P_0	temporal Fourier transform of acoustic pressure of initial wave, decibels referred to 2×10^{-5} N m^{-1}.
Pr	Prandtl number of fog-air mixture, equal to $c_p\mu_m/\kappa_m$.
$\mathcal{P}_T$	transmitted electrical power, watts.
$\mathcal{P}_R$	received electrical power, watts.
q	mole ratio of water vapor to mixture, percent.
Q	vertical turbulent heat flux, J m^{-2} s^{-1}.
Q_l	mass fraction of droplets in fog.
r	spatial separation for structure function, meters.
r	water vapor mixing ratio.
r_l	liquid drop radius, micrometers.
$\bar{r}$	distance for shock formation, meters.
$\hat{r}$	distance for fully developed sawtooth wave, meters.
$r_{\max}$	old-age distance for wave, meters.
R	range, equal to $\lvert\mathbf{x}\rvert$, meters.
R_0	range to scattering volume from transmitter, meters.
R_s	range to scattering volume from receiver, meters.
R_f	time autocovariance of an arbitrary function f.
R	perfect gas constant, equal to 8.314 J K^{-1} mol^{-1}.
R	electrical resistance, ohms.
Re	Reynolds number, equal to vl/ν.
Ri_f	flux Richardson number.
Ri_g	gradient Richardson number.
ρ	separation in a plane perpendicular to a sound beam, meters.
ρ_n	transverse separation normalized by a Fresnel zone, equal to $\rho/(\lambda L)^{1/2}$.
ρ_0	equilibrium density in a gradient atmosphere as a function of altitude, kilograms per cubic meter.
ρ_σ	turbulence density in a gradient atmosphere, equal to $\rho_0 + \rho_\sigma'$, kilograms per cubic meter.
ρ_α	acoustic density change, kilograms per cubic meter.
s	distance from transmitter along a path, meters.
S	sound energy flux density, decibels referred to 10^{-12} W m^{-2}.
S_0	sound energy flux density of initial wave, decibels referred to 10^{-12} W m^{-2}.
σ	specific entropy, J K^{-1} mol^{-1}.
σ_s	scattering cross section, m^{-1}.
σ_f^2	variance of an arbitrary random function f.
σ_t^2	parameter for comparing weak turbulence to strong turbulence, equal to $0.563 k_0^{7/6} L^{11/6} [C_{ne}^2]_\chi$.
$\langle\sigma_\chi^2\rangle$	geometric mean of log-amplitude variances at two points in a transverse plane, equal to $(\sigma_{\chi_1}^2 \sigma_{\chi_2}^2)^{1/2}$.
t	time, seconds.
τ	time delay for autocovariance, seconds.
τ_0	characteristic time for fogs, seconds.
τ_p	characteristic length of a pulse, seconds.

T	temperature, kelvins.
T_0	equilibrium temperature of a gradient atmosphere as a function of altitude, kelvins.
T_0	reference temperature, kelvins.
u_i	particle velocity in a sound wave, equal to **u**, meters per second.
U	magnitude of horizontal mean wind, meters per second.
v_i	total fluid velocity, equal to **v**, meters per second.
V	potential difference, volts.
V_s	scattering volume, cubic meters.
w	magnitude of turbulence and wind velocity, equal to $\|\mathbf{w}\|$, meters per second.
$w_\perp$	mean crosswind, meters per second.
w_i	velocity of turbulence and wind, equal to **w**, meters per second.
W_i	time Fourier transform of turbulence and wind velocity, equal to **W**, s^{-1}.
W_f	temporal frequency spectrum of a wave property f.
$W_{f(CW)}$	CW frequency spectrum.
$W_{f(P)}$	frequency spectrum of a pulse.
W_f^+	positive frequency spectrum of a property f.°
x_i	spatial coordinates, equal to **x**, meters.
X_i	particle coordinate label, equal to **X**.
z	height above ground, meters.
θ_0	potential temperature, kelvins.
θ_s	scattering angle, radians.
ψ	refraction angle, radians or degrees.
ψ	angular width of a sound beam, radians or degrees.
ψ	logarithmic wave function.
χ	log-amplitude, equal to log (A/A_0).
$\dagger$	complex conjugate.
$*$	convolution with respect to time or temporal wave number (see (17)).
$\odot$	convolution with respect to space or spatial wave number (see (18)).
$\langle\ \rangle$	ensemble average over a sequence of pulses.
$\langle\ \rangle_V$	volume average.

Acknowledgments. We should like to thank C. G. Little for advice and support, S. F. Clifford for extensive consultation on the theoretical sections, and the entire Atmospheric Acoustics Group at NOAA for their inputs. J. C. Kaimal, R. M. Jones, and T. M. Georges read early versions of the paper and made many helpful suggestions. Audrey Ralphs and Clark King helped prepare the first draft and figures, and Mildred Birchfield did a superlative job of typing the entire paper.

REFERENCES

Abramowitz, M., and I. A. Stegun, *Handbook of Mathematical Functions*, U.S. Government Printing Office, Washington, D. C., 1964.

Adekola, S. A., A study of the radiation patterns of a shielded quasi-tapered aperture antenna for acoustic echo-sounding, Ph.D. dissertation, 301 pp., Ohio State Univ., Columbus, 1975.

Adekola, S. A., Toward a more general integral formulation of the pressure field of an echosonde aperture antenna, *J. Acoust. Soc. Amer., 60*, 230–239, 1976.

AeroVironment, Inc., *Monostatic Acoustic Radar*, 60 pp., Pasadena, Calif., 1976.

Ahmet, S., Acoustic sounding of fog, *Meteorol. Note 77*, 6 pp., Bur. of Meteorol., Canberra, Australia, 1974.

Ahmet, S., Development of acoustic sounding technique for operational use, M.S. thesis, 106 pp., Roy. Aust. Air Force Acad., Univ. of Melbourne, Melbourne, Australia, 1976.

Allen, C. H., Finite amplitude distortion in a spherically diverging sound wave in air, Ph.D. dissertation, Pa. State Univ., University Park, 1950.

Arnold, A., et al., Simultaneous observations of clear air convection by a pulse radar, an FM-CW radar, an acoustic sounder, and an instrumented aircraft, in *Preprints of the 16th Radar Meteorology Conference*, pp. 290–295, American Meteorological Society, Boston, Mass., 1975.

Asimakopoulos, D. N., R. S. Cole, S. J. Caughey, and B. A. Crease, A quantitative comparison between acoustic sounder returns and the direct measurement of atmospheric temperature fluctuations, *Boundary Layer Meteorol., 10*, 137–147, 1976.

Aubry, M., Les sondages acoustiques de l'atmosphère, *Note Tech. CRPE/7*, 34 pp., Centre Nat. de la Rech. Sci., Issy-les-Moulineaux, France, 1975.

Aubry, M., R. Chezlemas, and A. Spizzichino, Preliminary results of the atmospheric sounding program at CNET, *Boundary Layer Meteorol., 7*, 513–519, 1974.

Balser, M., C. A. McNary, A. E. Nagy, R. Loveland, and D. Dickson, Remote wind sensing by acoustic radar, *J. Appl. Meteorol., 15*, 50–58, 1976.

Barnes, A., and L. P. Solomon, Some curious analytical ray paths for some interesting velocity profiles in geometrical acoustics, *J. Acoust. Soc. Amer., 53*, 147–155, 1973.

Barton, E. H., On the refraction of sound by wind, *Phil. Mag., 1*, 159–165, 1901.

Batchelor, G. K., Wave scattering due to turbulence, in *Symposium on Naval Hydraulics*, edited by F. S. Sherman, pp. 409–423, National Academy of Sciences, Washington, D. C., 1957.

Baudin, F., Estimateurs de fréquence pour mesurer la dèrive Doppler sodar, *Rep. CRPE NT/38*, 60 pp., Centre de Rech. en Phys. de l'Environ. Terr. et Planetaire, Orleans Cedex, France, 1977.

Bean, B. R., Application of FM-CW radar and acoustic echo sounder techniques to boundary layer and CAT studies, in *Remote Sensing of the Troposphere*, edited by V. E. Derr, pp. 20-1–20-20, U.S. Government Printing Office, Washington, D. C., 1972.

Bean, B. R., A. S. Frisch, L. G. McAllister, and J. R. Pollard, Planetary boundary-layer turbulence studies from acoustic echo sounder and in-situ measurements, *Boundary Layer Meteorol., 4*, 449–474, 1973.

Beasley, W. H., T. M. Georges, and M. W. Evans, Infrasound from convective storms: An experimental test of electrical source mechanisms, *J. Geophys. Res., 81*, 3133–3140, 1976.

Bedard, A. J., Jr., Infrasound and airflow over mountains, *J. Appl. Meteorol.*, in press, 1977.

Benkley, C. W., Model of planetary boundary layer growth using sodar validation: Applications to pollutant dispersion, M.S. thesis, 110 pp., Pa. State Univ., University Park, 1977.

Bennett, M. B., and D. T. Blackstock, Experimental verification of the parametric array in air, *J. Acoust. Soc. Amer., 57*, 562–568, 1975.

Bennett, R. C., and R. List, Lake breeze detection with an acoustic radar, in *Preprints of the 16th Radar Meteorology Conference*, pp. 260–262, American Meteorological Society, Boston, Mass., 1975.

Beran, D. W., Turbulence detection, Ph.D. dissertation, 257 pp., Univ. of Melbourne, Melbourne, Australia, 1970.

Beran, D. W., Acoustics: A new approach for monitoring the environment near airports, *J. Aircr., 8*, 934–936, 1971.

Beran, D. W., Remote sensing wind and wind shear system, *Rep. FAA-RD-74-3*, 115 pp., Dep. of Transp., Washington, D. C., 1974.

Beran, D. W., and S. F. Clifford, Acoustic Doppler measurements of the total wind vector, in *Preprints of the 2nd Symposium on Meteorological Observations*, pp. 100–110, American Meteorological Society, Boston, Mass., 1972.

Beran, D. W., and F. F. Hall, Jr., Remote sensing applications in air pollution meteorology, in *Proceedings of the 2nd Joint Conference on Sensing Environmental Pollutants*, pp. 231–246, Instrument Society of America, Washington, D. C., 1973.

Beran, D. W., and F. F. Hall, Jr., Remote sensing for air pollution meteorology, *Bull. Amer. Meteorol. Soc., 55*, 1097–1105, 1974.

Beran, D. W., and B. C. Willmarth, Doppler winds from a bistatic acoustic sounder, in *Proceedings of the 7th International Symposium on Remote Sensing of the Environment*, pp. 1699–1714, University of Michigan Press, Ann Arbor, 1971.

Beran, D. W., C. G. Little, and B. C. Willmarth, Acoustic Doppler measurements of vertical velocities in the atmosphere, *Nature, 230*, 160–162, 1971.

Beran; D. W., L. G. McAllister, and A. R. Mahoney, Extension of acoustic sounding experiments to the upper troposphere, *Rep. A208 (AP)*, 31 pp., Dep. of Supply, Weapons Res. Estab., Salisbury, Australia, 1972*a*.

Beran, D. W., F. F. Hall, Jr., J. W. Wescott, and W. D. Neff, Application of an acoustic sounder to air pollution monitoring, in *Proceedings of the Symposium on Air Pollution, Turbulence, and Diffu-*

sion, edited by H. W. Church and R. E. Luna, pp. 66–72, Sandia Laboratories, Albuquerque, N. Mex., 1972*b*.

Beran, D. W., W. H. Hooke, and S. F. Clifford, Acoustic echo-sounding techniques and their application to gravity-wave, turbulence, and stability studies, *Boundary Layer Meteorol.*, *4*, 133–153, 1973.

Beran, D. W., B. C. Willmarth, F. C. Carsey, and F. F. Hall, Jr., An acoustic Doppler wind measuring system, *J. Acoust. Soc. Amer.*, *55*, 334–338, 1974*a*.

Beran, D. W., F. F. Hall, Jr., B. C. Willmarth, R. J. Keeler, and D. Hunter, Operational test results of acoustic Doppler wind shear detector, in *Preprints of the 6th Conference on Aerospace and Aeronautical Meteorology*, pp. 412–417, American Meteorological Society, Boston, Mass., 1974*b*.

Beran, D. W., P. A. Mandics, A. J. Bedard, and R. G. Strauch, A wind shear and gust front warning system, in *Preprints of the 7th Conference on Aerospace and Aeronautical Meteorology*, pp. 167–174, American Meteorological Society, Boston, Mass., 1976.

Bergmann, P. G., The wave equation in a medium with a variable index of refraction, *J. Acoust. Soc. Amer.*, *17*, 329–333, 1946*a*.

Bergmann, P. G., Propagation of radiation in a medium with random inhomogeneities, *Phys. Rev.*, *70*, 486–492, 1946*b*.

Bervoets, A., and H. Hasenjäger, Notes on experience gained during operation of an acoustic sounder and in interpretation of the records, *Rep. EUR/C-IS/216/75*, 26 pp., Eur. At. Energy Community, Ispra, Italy, 1975.

Blackstock, D. T., Nonlinear acoustics (theoretical), in *American Institute of Physics Handbook*, edited by D. E. Gray, chap. 3, pp. 183–204, McGraw-Hill, New York, 1972.

Blokhintzev, D., The propagation of sound in an inhomogeneous and moving medium I, II, *J. Acoust. Soc. Amer.*, *18*, 322–334, 1946.

Born, M., and E. Wolf, *Principles of Optics*, 4th ed., Pergamon, New York, 1970.

Bourne, I. A., and T. D. Keenan, High power acoustic radar, *Nature*, *251*, 206–208, 1974.

Bourne, I. A., and N. Shaw, A preliminary report on acoustic sounding of the lower atmosphere, *Res. Rep. 55*, 14 pp., Roy. Aust. Air Force Acad., Univ. of Melbourne, Melbourne, Australia, 1970.

Bretherton, F. P., Lamb waves in a nearly isothermal atmosphere, *Quart. J. Roy. Meteorol. Soc.*, *95*, 754–757, 1969.

Brown, E. H., Acoustic Doppler radar scattering equation and general solution, *J. Acoust. Soc. Amer.*, *52*, 1391–1396, 1972.

Brown, E. H., Turbulent spectral broadening of backscattered acoustic pulses, *J. Acoust. Soc. Amer.*, *56*, 1398–1406, 1974*a*.

Brown, E. H., Some recent NOAA theoretical work on echo sounding in the atmosphere, *J. Geophys. Res.*, *79*, 5567–5571, 1974*b*.

Brown, E. H., and S. F. Clifford, Spectral broadening of an acoustic pulse propagating through turbulence, *J. Acoust. Soc. Amer.*, *54*, 36–39, 1973*a*.

Brown, E. H., and S. F. Clifford, Amplitude spectra of acoustic pulses in the ocean, *J. Acoust. Soc. Amer.*, *54*, 461–464, 1973*b*.

Brown, E. H., and S. F. Clifford, On the attenuation of sound by turbulence, *J. Acoust. Soc. Amer.*, *60*, 788–794, 1976.

Brown, E. H., and R. J. Keeler, Applications of propagation parameters to atmospheric echosondes, in *Proceedings of the 16th Radar Meteorology Conference*, pp. 272–277, American Meteorological Society, Boston, Mass., 1975.

Brown, E. H., C. G. Little, and W. M. Wright, An echosonde interferometer for atmospheric research, *J. Acoust. Soc. Amer.*, in press, 1977.

Brownlee, L. R., Rytov's method and large fluctuations, *J. Acoust. Soc. Amer.*, *53*, 156–161, 1973.

Brownlee, L. R., F. H. Sagar, and D. E. Ash, Measurement of wave propagation in a weakly inhomogeneous medium—The sea, *J. Acoust. Soc. Amer.*, *56*, 1059–1070, 1974.

Burkhard, D. G., and D. L. Shealy, Equation for the intensity of acoustic rays deflected by an object in a variable velocity medium, *J. Acoust. Soc. Amer.*, *56*, 1327–1335, 1974.

Burridge, R., The acoustics of pipe arrays, *Geophys. J. Roy. Astron. Soc.*, *26*, 53–69, 1971.

Carsey, F., A linear zipper array for probing the wind and structure profile of the lower atmosphere (abstract), *J. Acoust. Soc. Amer.*, *52*, 1309, 1972.

Carsey, F., and E. Leavitt, Pibal/acoustic radar data in measurement and computation of air stress over pack ice, *Aidjex Bull.*, *36*, 87–128, 1977.

Caughy, S. J., B. A. Crease, D. N. Asimakopoulos, and R. S. Cole, *Nature*, *262*, 274–276, 1976.

Chadwick, R. B., and C. G. Little, The comparison of sensitivities of atmospheric echo-sounders, *Remote Sens. Environ.*, *2*, 223–234, 1973.

Chen, K. C., and D. Ludwig, Calculation of wave amplitudes by ray tracing, *J. Acoust. Soc. Amer.*, *54*, 431–436, 1973.

Chessel, C. I., Three-dimensional acoustic-ray tracing in an inhomogeneous anisotropic atmosphere using Hamilton's equations, *J. Acoust. Soc. Amer.*, *53*, 83–87, 1973.

Chessel, C. I., Observations of the effects of atmospheric turbulence on low-frequency sound propagation, *J. Acoust. Soc. Amer.*, *60*, 29–33, 1976.

Chong, M., Mesure des profils de vent par sodar-Doppler, *Note Tech. CRPE/22*, 103 pp., Centre de Rech en Phys. de l'Environ. Terr. et Planetaire, Orleans Cedex, France, 1976.

Chuprynin, V. I., Sound propagation in an inhomogeneous medium, *Sov. Phys. Acoust.*, Engl. Transl., *20*, 574–575, 1975.

Clark, G. H., and E. O. K Bendun, Meteorological research studies at Jervix Bay, Australia, *Rep. AAEC/E309*, 97 pp., Aust. At. Energy Comm., Lucas Heights, Australia, 1974.

Clifford, S. F., Temporal-frequency spectra for a spherical wave propagating through atmospheric turbulence, *J. Opt. Soc. Amer.*, *61*, 1285–1292, 1971.

Clifford, S. F., Physical properties of the atmosphere in relation to laser probing, *Opt. Quantum Electron.*, *8*, 95–104, 1976.

Clifford, S. F., and E. H. Brown, Propagation of sound in a turbulent atmosphere, *J. Acoust. Soc. Amer.*, *48*, 1123–1127, 1970.

Clifford, S. F., and E. H. Brown, Acoustic scattering from a moving turbulent medium, *J. Acoust. Soc. Amer.*, *55*, 929–933, 1974.

Clifford, S. F., and T.-I. Wang, The range limitation on radar-acoustic sounding systems (RASS) due to atmospheric refractive turbulence, *IEEE Trans. Antennas Propagat.*, *AP-25*, 319–326, 1977.

Clifford, S. F., and H. T. Yura, Equivalence of two theories of strong optical scintillation, *J. Opt. Soc. Amer.*, *64*, 1641–1643, 1974.

Clifford, S. F., G. R. Ochs, and R. S. Lawrence, Saturation of optical scintillation by strong turbulence, *J. Opt. Soc. Amer.*, *64*, 148–154, 1974.

Closs, R. L., and A. D. Surridge, The temperature profile in the lower atmosphere obtained by acoustic sounding, *J. Phys. E Sci. Instrum.*, *7*, 369–371, 1974.

Cole, J. E., III, and R. A. Dobbins, Propagation of sound through atmospheric fog, *J. Atmos. Sci.*, *27*, 426–434, 1970.

Cole, J. E., III, and R. A. Dobbins, Measurements of the attenuation of sound by a warm air fog, *J. Atmos. Sci.*, *28*, 202–209, 1971.

Consortini, A., and L. Ronchi, Some comments on the theory of EM propagation in a turbulent atmosphere, *Lett. Nuovo Cimento*, *2*, 683–688, 1969.

Consortini, A., L. Ronchi, and E. Moroder, Role of the outer scale of turbulence in atmospheric degradation of optical images, *J. Opt. Soc. Amer.*, *63*, 1246–1248, 1973.

Cook, R. K., Strange sounds in the atmosphere, I, *Sound*, *1*, 12–16, 1962.

Cook, R. K., and J. M. Young, Strange sounds in the atmosphere, II, *Sound*, *1*, 25–33, 1962.

Coulman, C. E., and J. Warner, Aircraft observations in the sub-cloud layer over land, in *Preprints of the International Conference on Cloud Physics*, pp. 270–274, American Meteorological Society, Boston, Mass., 1976.

Cox, E. F., Upper-atmosphere temperatures from Helgoland big bang, *J. Meteorol.*, *6*, 300–311, 1949*a*.

Cox, E. F., Abnormal audibility zones in long distance propagation through the atmosphere, *J. Acoust. Soc. Amer.*, *21*, 6–16, 1949*b*.

Cox, R., Remote sensing with sound waves, *Rep. 18*, pp. 3–12, Facil. for Atmos. Res., Nat. Center for Atmos. Res., Boulder, Colo., 1971.

Cronenwett, W. T., G. B. Walker, and R. L. Inman, Acoustic sounding of meteorological phenomena in the planetary boundary layer, *J. Appl. Meteorol.*, *11*, 1351–1358, 1972.

Davey, R. F., A coherent acoustic Doppler radar for real-time wind measurement, in *Preprints of the 17th Radar Meteorology Conference*, pp. 270–275, American Meteorological Society, Boston, Mass., 1976.

Davey, R. F., and P. B. MacCready, Jr., Feasibility demonstration of an acoustic radar wind shear detection system, final report, contract DOT-TSC-1158, 40 pp., AeroVironment, Inc., Pasadena, Calif., 1976.

Davidson, G. A., Sound propagation in fogs, *J. Atmos. Sci.*, *32*, 2201–2205, 1975.

Deardorff, J. W., G. E. Willis, and D. K. Lilly, Laboratory investigation of non-steady penetrative convection, *J. Fluid Mech., 35,* 7–31, 1969.

DeLoach, R., On the excess attenuation of sound in the atmosphere, *NASA Tech. Note D-7823,* 1975.

Derham, W., Experimenta et observationes de soni motu, *Phil. Trans. Roy. Soc. London, 26,* 2–35, 1708.

Derr, V. E., and C. G. Little, A comparison of remote sensing of the clear atmosphere by optical, radio, and acoustic radar techniques, *Appl. Opt., 9,* 1976–1992, 1970.

Donato, R. J., Propagation of a spherical wave near a plane boundary with a complex impedance, *J. Acoust. Soc. Amer., 60,* 34–39, 1976*a*.

Donato, R. J., Spherical-wave reflection from a boundary of reactive impedance using a modification of Cagniard's method, *J. Acoust. Soc. Amer., 60,* 999–1002, 1976*b*.

Duckert, P., O. Meisser, H. Martin, H. Regula, H. Jung, B. Sandmann, and J. Kölzer, Sprengungen zu Forschungszwecken mit Unterstützung der Notgemeinschaft der Deutschen Wissenschaft, *Z. Geophys., 10,* 119–221, 1934.

Edinger, J. G., Acoustic sounding of the lowest one and one-half kilometers over Los Angeles, in *Preprints of the 16th Radar Meteorology Conference,* pp. 253–256, American Meteorological Society, Boston, Mass., 1975.

Einaudi, F., and D. P. Lalas, The propagation of acoustic-gravity waves in a moist atmosphere, *J. Atmos. Sci., 30,* 365–376, 1973.

Embleton, T. F. W., J. E. Piercy, and N. Olson, Outdoor sound propagation over ground of finite impedance, *J. Acoust. Soc. Amer., 59,* 267–277, 1976*a*.

Embleton, T. F. W., G. J. Thiessen, and J. E. Piercy, Propagation in an inversion and reflections at the ground, *J. Acoust. Soc. Amer., 59,* 278–282, 1976*b*.

Emden, R., Beiträge zur Thermodynamik der Atmosphäre, *Meteorol. Z., 33,* 351–360, 1916.

Emmanuel, C. B., Observations of Helmholtz waves in the lower atmosphere with an acoustic sounder, Ph.D. dissertation, 94 pp., Colo. State Univ., Fort Collins, 1972.

Emmanuel, C. B., Richardson number profiles through shear instability wave regions observed in the lower planetary boundary layer, *Boundary Layer Meteorol., 5,* 19–27, 1973.

Emmanuel, C. B., and P. A. Mandics, A feasibility study for the remote sensing of underwater currents using acoustic Doppler techniques, *Tech. Rep. ERL 278-WPL 25,* 36 pp., Nat. Oceanic and Atmos. Admin., Boulder, Colo., 1973.

Emmanuel, C. B., B. R. Bean, L. G. McAllister, and J. R. Pollard, Observations of Helmholtz waves in the lower atmosphere with an acoustic sounder, *J. Atmos. Sci., 29,* 886–892, 1972.

Estival, A., and M. Aubry, Interprétation des échos sodar en terme de stratifications atmosphériques, *Meteorologie, VI*(5), 33–42, 1976.

Evans, L. B., H. E. Bass, and L. C. Sutherland, Atmospheric absorption of sound: Theoretical predictions, *J. Acoust. Soc. Amer., 51,* 1565–1575, 1972.

Fante, R. L., Mutual coherence function and frequency spectrum of a laser beam propagating through atmospheric turbulence, *J. Opt. Soc. Amer., 64,* 592–598, 1974.

Fante, R. L., Electromagnetic beam propagation in turbulent media, *Proc. IEEE, 63,* 1669–1692, 1975.

Fenlon, F. H., Asymptotic and numerical methods for solving Burger's equation, in *Proceedings of the Symposium on Nonlinear Acoustics, Birmingham 1971,* pp. 52–99, British Acoustical Society, London, 1971.

Fetter, R. W., Remote measurement of wind velocity by the electromagnetic probe, II, Experimental system, Conference Proceedings of the 5th National Convention on Military Electronics, Washington, D. C., *Rep. 420,* Midwest Res. Inst., Kansas City, Mo., 1961.

Few, A. A., Power spectrum of thunder, *J. Geophys. Res., 74,* 6926–6934, 1969.

Few, A. A., Lightning channel reconstruction from thunder measurements, *J. Geophys. Res., 75,* 7517–7523, 1970.

Few, A. A., Lightning sources in severe thunderstorms, in *Preprints of the Conference on Cloud Physics,* pp. 387–390, American Meterological Society, Boston, Mass., 1974.

Few, A. A., and T. L. Teer, The accuracy of acoustic reconstruction of lightning channels, *J. Geophys. Res., 79,* 5007–5011, 1974.

Ffowcs Williams, J. E., Nonlinear generation of secondary waves in fluids, in *Finite-Amplitude Wave Effects in Fluids, Proceedings of the 1973 Symposium, Copenhagen,* edited by L. Bjørnø, pp. 9–18, IPC Press, Guildford, England, 1974.

Fitzjarrald, D. E., A field observation of atmospheric free convection, *J. Appl. Meteorol., 15,* 259–263, 1976.

Ford, G. W., and W. C. Meecham, Scattering of sound by isotropic turbulence of large Reynolds number, *J. Acoust. Soc. Amer., 32,* 1668–1672, 1960.

Fox, H. L., Vertical profiles of wind and temperature by remote acoustical sounding, in *Atmospheric Exploration by Remote Probes,* vol. 2, pp. 671–679, National Research Council, Washington, D. C., 1969.

Frankel, M. S., and A. M. Peterson, Remote temperature profiling in the lower troposphere, *Radio Sci., 11,* 157–166, 1976.

Frankel, M. S., N. J. F. Chang, and M. J. Sanders, Jr., A high-frequency radio acoustic sounder for remote measurement of atmospheric winds and temperature, *Bull. Amer. Meteorol. Soc., 58,* 928–934, 1977.

Friehe, C. A., J. C. LaRue, F. H. Champagne, C. H. Gibson, and G. F. Dreyer, Effects of temperature and humidity fluctuations on the optical refractive index in the marine boundary layer, *J. Acoust. Soc. Amer., 65,* 1502–1511, 1975.

Frisch, A. S., and S. F. Clifford, A study of convection capped by a stable layer using Doppler radar and acoustic echo sounders, *J. Atmos. Sci., 31,* 1622–1628, 1974.

Frisch, A. S., and G. R. Ochs, A note on the behavior of the temperature structure parameter in a convective layer capped by a marine inversion, *J. Appl. Meteorol., 14,* 415–419, 1975.

Frisch, A. S., R. B. Chadwick, W. R. Moninger, and J. M. Young, Observations of boundary-layer convection cells measured by dual-Doppler radar and echosonde and by microbarograph array, *Boundary Layer Meteorol., 10,* 55–68, 1976.

Fukushima, M., Status of Sodar observations in Japan, *J. Radio Res. Lab. Jap., 22,* 151–164, 1975.

Fukushima, M., K. Akita, and I. Kasuya, Experiments on the lower troposphere using an acoustic sounder, *Rev. Radio Res. Lab. Jap., 17,* 401–406, 1971.

Fukushima, M., K. Akita, and H. Tanaka, Night time profiles of temperature fluctuations deduced from two-year sodar observations, *J. Meteorol. Soc. Jap., 53,* 487–491, 1975*a*.

Fukushima, M., K. Akita, and H. Tanaka, Sodar probing of small-scale temperature structures in the clear troposphere, *J. Radio Res. Lab. Jap., 22,* 23–43, 1975*b*.

Fukushima, M., K. Akita, Y. Masuda, and H. Tanaka, Features of Sodar echoes observed at Miyakojima Island during Amtex '75, *J. Radio Res. Lab. Jap., 23,* 235–246, 1976.

Garrett, C. J. R., Atmospheric edge waves, *Quart. J. Roy. Meteorol. Soc., 95,* 731–753, 1969.

Gaynor, J. E., Acoustic Doppler measurement of atmospheric boundary layer velocity structure functions and energy dissipation rates, *J. Appl. Meteorol., 16,* 148–155, 1977.

Gaynor, J. E., P. A. Mandics, A. B. Wahr, and F. F. Hall, Jr., Studies of the tropical marine boundary layer using acoustic backscattering during Gate, in *Preprints of the 17th Radar Meteorology Conference,* pp. 303–306, American Meteorological Society, Boston, Mass., 1976.

Georges, T. M., A program for calculating three-dimensional acoustic-gravity ray paths in the atmosphere, *Tech. Rep. ERL 212-WPL 16,* 43 pp., Nat. Oceanic and Atmos. Admin., Boulder, Colo., 1971.

Georges, T. M., Infrasound from convective storms: Examining the evidence, *Rev. Geophys. Space Phys., 11,* 571–594, 1973.

Georges, T. M., Infrasound from convective storms, II, A critique of source candidates, *Tech. Rep. ERL 380-WPL 49,* 59 pp., Nat. Oceanic and Atmos. Admin., Boulder, Colo., 1976.

Georges, T. M., and S. F. Clifford, Acoustic sounding in a refracting atmosphere, *J. Acoust. Soc. Amer., 52,* 1397–1405, 1972.

Georges, T. M., and S. F. Clifford, Estimating refractive effects in acoustic sounding, *J. Acoust. Soc. Amer., 55,* 934–936, 1974.

Georges, T. M., and G. E. Greene, Infrasound from convective storms, IV, Is it useful for storm warning?, *J. Appl. Meteorol., 14,* 1303–1316, 1975.

Georges, T. M., and J. M. Young, Passive sensing of natural acoustic-gravity waves at the earth's surface, in *Remote Sensing of the Troposphere,* edited by V. E. Derr, chap. 21, pp. 21-1–21-23, U.S. Government Printing Office, Washington, D. C., 1972.

Gething, J. T., and D. Jenssen, Measurement of temperature and humidity by acoustic echo sounding, *Nature Phys. Sci., 231,* 198–200, 1971.

Gille, J. C., Acoustic wave propagation in a non-gray radiating atmosphere, *J. Atmos. Sci., 25,* 808–817, 1968.

Gilman, G. W., H. B. Coxhead, and F. H. Willis, Reflection of sound signals in the troposphere, *J. Acoust. Soc. Amer., 18,* 274–283, 1946.

Golden, A., Evaluation of meteorological corrections for sound ranging, Proceedings of the Symposium on Atmospheric Acoustic Propagation, *Rep. AD 408 716*, pp. 149–161, U.S. Army Signal Support Agency, White Sands Missile Range, N. Mex., 1961.

Goncharov, V. P., V. A. Krasil'nikov, and V. I. Pavlov, On the theory of wave interactions in stratified media (in Russian), *Izv. Akad. Nauk SSSR Fiz. Atmos. Okeana, 12*, 1143–1151, 1976.

Gonter, R. H., Intensity fluctuations of aircraft flyover noise, *J. Acoust. Soc. Amer., 57*, 273–275, 1975.

Gossard, E. E., Power spectra of temperature, humidity and refractive index from aircraft and tethered balloon measurements, *IEEE Trans. Antennas Propagat., AP-8*(2), 186–201, 1960.

Gossard, E. E., The apparent movement of the spectral components in fading records of ionospherically reflected radio waves, *J. Geophys. Res., 72*, 1563–1569, 1967.

Gossard, E. E., J. H. Richter, and D. Atlas, Internal waves in the atmosphere from high-resolution radar measurements, *J. Geophys. Res., 75*, 3523–3536, 1970.

Gowan, E. H., Low frequency sound waves and the upper atmosphere, *Nature, 124*, 452–454, 1929.

Greenfield, R. J., M. Teufel, D. W. Thomson, and R. L. Coulter, A method for measurement of temperature profiles in inversions from refractive transmission of sound, *J. Geophys. Res., 79*, 5551–5554, 1974.

Gutenberg, B., The velocity of sound-waves from gun-fire in southern California, *Eos Trans. AGU, 19*, 156, 1938.

Hall, F. F., Jr., Temperature and wind structure studies by acoustic echo-sounding, in *Remote Sensing of the Troposphere*, edited by V. E. Derr, chap. 18, U.S. Government Printing Office, Washington, D. C., 1972.

Hall, F. F., Jr., Report on the July 1972 workshop in atmospheric acoustics, *Tech. Memo. ERL WPL 8*, 23 pp., Nat. Oceanic and Atmos. Admin., Boulder, Colo., 1973.

Hall, F. F., Jr., and D. W. Beran, Real time measurements of boundary layer winds and turbulence by acoustic echo sounding, in *Preprints of the Symposium on Atmospheric Diffusion and Air Pollution*, pp. 79–82, American Meteorological Society, Boston, Mass., 1974.

Hall, F. F., Jr., and W. D. Neff, Comments on 'A mesoscale phenomenon revealed by an acoustic sounder,' *J. Appl. Meteorol., 16*, 109–110, 1977.

Hall, F. F., Jr., and E. J. Owens, Atmospheric acoustic echo sounding investigations at the south pole, *Antarct. J. U.S., 10*, 191–192, 1975.

Hall, F. F., Jr., and J. W. Wescott, Acoustic antennas for atmospheric echo sounding, *J. Acoust. Soc. Amer., 56*, 1376–1382, 1974.

Hall, F. F., Jr., J. W. Wescott, and W. R. Simmons, Acoustic echo sounding of atmospheric thermal and wind structure, in *Proceedings of the 7th International Symposium on Remote Sensing of the Environment*, pp. 1715–1732, University of Michigan Press, Ann Arbor, 1971.

Hall, F. F., Jr., J. G. Edinger, and W. D. Neff, Convective plumes in the planetary boundary layer, investigated with an acoustic echo sounder, *J. Appl. Meteorol., 14*, 513–523, 1975.

Hall, F. F., Jr., W. D. Neff, and T. V. Frazier, Wind shear observations in thunderstorm density currents, *Nature, 264*, 408–411, 1976.

Harris, C. M., Absorption of sound in air in the audio-frequency range, *J. Acoust. Soc. Amer., 35*, 11–17, 1963.

Harris, C. M., Absorption of sound in air versus humidity and temperature, *J. Acoust. Soc. Amer., 40*, 148–159, 1966.

Harris, C. M., and W. Tempest, Absorption of sound in air below 1000 cps, *J. Acoust. Soc. Amer., 36*, 2390–2394, 1964.

Hartman, R. J., Wave propagation in a stratified shear flow, *J. Fluid Mech., 71*, 89–104, 1975.

Hassab, J. C., The acoustic field in non-uniform layers, *J. Sound Vib., 38*, 215–224, 1975.

Haugen, D. A. (Ed.), *Workshop on Micrometeorology*, American Meteorological Society, Boston, Mass., 1973.

Haugen, D. A., Performance test results for a Xonics acoustic Doppler system, *Tech. Memo. ERL WPL-16*, 13 pp., Nat. Oceanic and Atmos. Admin., Boulder, Colo., 1976.

Haugen, D. A., J. C. Kaimal, and J. T. Newman, The use of an acoustic echo sounder for optical tracking applications, *Rep. AFCRL-TR-75-0454*, 59 pp., Meteorol. Lab., Air Force Cambridge Res. Lab., Bedford, Mass., 1975.

Heller, G. S., Propagation of acoustic discontinuities in an inhomogeneous moving liquid medium, *J. Acoust. Soc. Amer., 25*, 950–951, 1953.

Henry, J., *Report of the Lighthouse Board of the United States*, U.S. Government Printing Office, Washington, D. C., 1874.

Hess, P. E., and M. L. Wesely, Digitization of acoustic sounder data, *Rep. ANL-8060*, part IV, pp. 85–92, Radiol. and Environ. Res. Div., Argonne Nat. Lab., Argonne, Ill., 1973.

Ho, C. M., and L. S. G. Kovasznay, Acoustical shadowgraph, *Phys. Fluids, 19*, 1118–1123, 1976*a*.

Ho, C. M., and L. S. G. Kovasznay, Propagation of a coherent acoustic wave through a turbulent shear flow, *J. Acoust. Soc. Amer., 60*, 40–45, 1976*b*.

Holmgren, B., and C. Jacobsson, Sondering av atmosfärens gränsskikt med vertikalsodar, *FOA Rep. C 30077-El*, 75 pp., *Försvarets Forskningsanst.*, Huvudenket 3, Stockholm, 1976.

Holmgren, B., and L. Spears, Sodar investigation of the effect of open leads on the boundary layer structure over the Arctic basin, *Aidjex Bull., 27*, 167–179, 1974.

Holmgren, B., L. Spears, C. Wilson, and C. Benson, Acoustic soundings of the Fairbanks temperature inversions, in *Proceedings of the 24th Alaska Science Conference, Climate of the Arctic*, pp. 293–306, University of Alaska Press, Fairbanks, 1973.

Hooke, W. H., J. M. Young, and D. W. Beran, Atmospheric waves observed in the planetary boundary layer using an acoustic sounder and a microbarograph array, *Boundary Layer Meteorol., 2*, 371–380, 1972.

Hooke, W. H., F. F. Hall, Jr., and E. E. Gossard, Observed generation of an atmospheric gravity wave by shear instability in the mean flow of the planetary boundary layer, *Boundary Layer Meteorol., 5*, 29–41, 1973.

Howe, M. S., Wave propagation in random media, *J. Fluid Mech., 45*, 769–804, 1971.

Howe, M. S., Multiple scattering of sound by turbulence and other inhomogeneities, *J. Sound Vib., 27*, 455–476, 1973.

Huang, M. N., Sound scattering from atmospheric turbulence, *Progr. Astronaut. Aeronaut., 46*, 35–50, 1976.

Huschke, R. E. (Ed.), *Glossary of Meteorology*, 638 pp. American Meteorological Society, Boston, Mass., 1959.

Ingard, U., A review of the influence of meteorological conditions on sound propagation, *J. Acoust. Soc. Amer., 25*, 405–411, 1953.

Ingard, U., and G. C. Maling, Jr., On the effect of atmospheric turbulence on sound propagation over ground, *J. Acoust. Soc. Amer., 35*, 1056–1058, 1963.

Izumi, Y. (Ed.), Kansas 1968 field program data report, *Rep. AFCRL-72-0041*, 79 pp., Air Force Cambridge Res. Lab., Bedford, Mass., 1971.

Jenkins, G. M., and D. G. Watts, *Spectral Analysis and Its Applications*, Holden-Day, San Francisco, Calif., 1968.

Joelsson, H., Ljudpulser, Spårar luftföroreningar, *FOA Tidn. Stockholm, 12*(4), 3–5, 1974.

John, R. S., Field tests of a sonic anemometer-thermometer, *Bull. Amer. Meteorol. Soc., 41*, 618–626, 1960.

Jones, R. M., and T. M. Georges, Infrasound from convective storms, III, Propagation to the ionosphere, *J. Acoust. Soc. Amer., 59*, 765–779, 1976.

Kaimal, J. C., and J. W. Wescott, An acoustic Doppler sounder for measuring wind profiles in the lower boundary layer, in *Preprints of the 17th Radar Meteorology Conference*, pp. 290–296, American Meteorological Society, Boston, Mass., 1976.

Kaimal, J. C., J. T. Newman, A. Bisberg, and K. Cole, An improved three-component sonic anemometer for investigation of atmospheric turbulence, in *Flow: Its Measurement and Control in Science and Industry*, vol. 1, edited by R. B. Dowdell, Instrument Society of America, Pittsburgh, Pa., 1974.

Kaimal, J. C., J. C. Wyngaard, D. A. Haugen, O. R. Coté, Y. Izumi, S. J. Caughey, and C. J. Readings, Turbulence structure in the convective boundary layer, *J. Atmos. Sci., 33*, 2152–2169, 1976.

Kallistratova, M. A., An experimental investigation into the scattering of sound in turbulent atmosphere (in Russian), *Dokl. Akad. Nauk SSSR, 125*, 69–72, 1959*a*.

Kallistratova, M. A., Procedure for investigating sound scattering in the atmosphere, *Sov. Phys. Acoust.*, Engl. Transl., *5*, 512–514, 1959*b*.

Kallistratova, M. A., Experimental investigation of sound wave scattering in the atmosphere (in Russian), Tr. Inst. Fiz. Atmos., Atmos. Turbulentnost, *4*, 203–256, 1961. (English translation, U.S. Air Force FTD TT-63-441.)

Kallistratova, M. A., and V. I. Tatarskii, Accounting for wind turbulence in the calculation of sound scattering in the atmosphere, *Sov. Phys. Acoust.*, Engl. Transl., *6*, 503–505, 1960.

Keeler, R. J., A frequency discriminator vs FFT Doppler extraction, *Tech. Memo. ERL WPL-17*, 23 pp., Nat. Oceanic and Atmos. Admin., Boulder, Colo., 1976.

Keller, J. B., Wave propagation in random media, *Proc. Symp. Appl. Math., 16,* 145–170, 1964.

Kelly, E. H., Acoustic sounding in the planetary boundary layer, M.S. thesis, 80 pp., Univ. of Okla., Norman, 1973.

Kelton, G., and P. Bricout, Wind velocity measurements using sonic techniques, *Bull Amer. Meteorol. Soc., 45,* 571–580, 1964.

King, L. V., On the propagation of sound in the free atmosphere and the acoustic efficiency of fog-signal machinery: An account of experiments carried out at Father Point, Quebec, September, 1913, *Phil. Trans. Roy. Soc. London, Ser. A, 218,* 211–293, 1919.

Kjelaas, A. G., D. W. Beran, W. H. Hooke, and B. R. Bean, Waves observed in the planetary boundary layer using an array of acoustic sounders, *J. Atmos. Sci., 31,* 2040–2045, 1974.

Kolmogorov, A. H., The local structure of turbulence in an incompressible viscous fluid for very large Reynolds numbers (in Russian), *Dokl. Akad. Nauk SSSR, 30,* 301, 1941.

Kong, J. A., Interaction of acoustic waves with moving media, *J. Acoust. Soc. Amer., 48,* 236–241, 1970.

Koopmans, L. H., *The Spectral Analysis of Time Series,* Academic, New York, 1974.

Kornhauser, E. T., Ray theory for moving fluids, *J. Acoust. Soc. Amer., 25,* 945–949, 1953.

Kraichnan, R. H., The scattering of sound in a turbulent medium, *J. Acoust. Soc. Amer., 25,* 1096–1104, 1953.

Krasil'nikov, V. A., and V. I. Pavlov, Systematic acceleration of phonons in a turbulent medium (in Russian), *Zh. Eksp. Teor. Fiz., 68,* 1797–1805, 1975.

Kriebel, A. R., Refraction and attenuation of sound by wind and thermal profiles over a ground plane, *J. Acoust. Soc. Amer., 51,* 19–23, 1972.

Krol, H. R., Intensity calculations along a single ray, *J. Acoust. Soc. Amer., 53,* 864–868, 1973*a*.

Krol, H. R., Some ray and intensity solutions in the complex plane, *J. Acoust. Soc. Amer., 54,* 96–98, 1973*b*.

Kurze, U. I., Antennas for sodar systems, *J. Acoust. Soc. Amer., 60,* Suppl. 1, S114, 1976.

Larson, R. J., L. B. Craine, J. E. Thomas, and C. R. Wilson, Correlation of winds and geographic features with production of certain infrasonic signals in the atmosphere, *Geophys. J. Roy. Astron. Soc., 26,* 201–214, 1971.

Lawrence, R. S., and J. W. Strohbehn, A survey of clear-air propagation effects relevant to optical communications, *Proc. IEEE, 58,* 1523–1545, 1970.

Lawrence, R. S., G. R. Ochs, and S. F. Clifford, Measurements of atmospheric turbulence relevant to optical propagation, *J. Opt. Soc. Amer., 60,* 826–830, 1970.

Lee, R. W., and J. C. Harp, Weak scattering in random media, with applications to remote probing, *Proc. IEEE, 57,* 375–406, 1969.

Lighthill, M. J., On the energy scattered from the interaction of turbulence with sound or shock waves, *Proc. Cambridge Phil. Soc., 49,* 531–555, 1953.

Lindsay, R. B., *Acoustics: Historical and Physical Development,* 465 pp., Dowden, Hutchinson, and Ross, Stroudsburg, Pa., 1973.

Lindsay, R. B. (Ed.), *Physical Acoustics,* Dowden, Hutchinson, and Ross, Stroudsburg, Pa., 1974.

List, R., and H. Melling, Plume convection over an urban area as observed by acoustic sounding, *Atmosphere, 12,* 144–153, 1974.

List, R., R. C. Bennett, and U. Rentsch, Acoustic echo soundings in urban Toronto. *Atmosphere, 10,* 73–79, 1972.

Little, C. G., Acoustic methods for the remote probing of the lower atmosphere, *Proc. IEEE, 57,* 571–578, 1969.

Little, C. G., Status of remote sensing of the troposphere, in *Remote Sensing of the Troposphere,* edited by V. E. Derr, pp. 30-1–30-16, U. S. Government Printing Office, Washington, D. C., 1972*a*.

Little, C. G., Status of remote sensing of the troposphere, *Bull. Amer. Meteorol. Soc., 53,* 936–949, 1972*b*.

Little, C. G., On the detectability of fog, cloud, rain and snow by acoustic echosounding methods, *J. Atmos. Sci., 29,* 748–755, 1972*c*.

Little, C. G., Prospects for acoustic echo sounding, in *Remote Sensing of the Troposphere,* edited by V. E. Derr, chap. 19, pp. 19-1–19-10, U.S. Government Printing Office, Washington, D. C., 1972*d*.

Little, C. G., Remote sensing of the atmosphere, *Atmos. Technol., 2,* 51–56, 1973.

Lockwood, J. C., T. C. Muir, and D. T. Blackstock, Directive harmonic generation in the radiation field of a circular piston, *J. Acoust. Soc. Amer., 53,* 1148–1153, 1973.

Lutomirski, R. F., and H. T. Yura, Modulation-transfer function and phase-structure function of an optical wave in a turbulent medium, *J. Opt. Soc. Amer., 59,* 999–1000, 1969.

Lutomirski, R. F., and H. T. Yura, Wave structure function and mutual coherence function of an optical wave in a turbulent atmosphere, *J. Opt. Soc. Amer., 61,* 482–487, 1971*a*.

Lutomirski, R. F., and H. T. Yura, Propagation of a finite optical beam in an inhomogeneous medium, *Appl. Opt., 10,* 1652–1658, 1971*b*.

MacKinnon, R. F., J. S. Partridge, and S. H. Toole, On the calculation of ray-acoustic intensity, *J. Acoust. Soc. Amer., 52,* 1471–1480, 1972.

Mahoney, A. R., Tropospheric sounding: A feasibility study, *Tech. Memo. CPD (T) 130,* Weapons Res. Estab., Adelaide, Australia, 1966.

Mahoney, A. R., Tropospheric sounding: A portable acoustic sounder, *Tech. Memo. CPD (T) 141,* 22 pp., Weapons Res. Estab., Adelaide, Australia, 1967.

Mahoney, A. R., L. G. McAllister, and J. R. Pollard, The remote sensing of wind velocity in the lower troposphere using an acoustic sounder, *Boundary Layer Meteorol., 4,* 155–167, 1973*a*.

Mahoney, A. R., K. Gage, H. Ottersten, and H. Tennekes, Turbulence in stable layers and their effects on EM propagation, *Boundary Layer Meteorol., 5,* 219–226, 1973*b*.

Mandics, P. A., Line-of-sight acoustical probing of atmospheric turbulence, Ph.D. dissertation, Stanford Univ., Stanford, Calif., 1971.

Mandics, P. A., Generation and dissipation of microwave refractive-index fluctuations in the boundary layer, *Boundary Layer Meteorol., 4,* 311–322, 1973.

Mandics, P. A., and F. F. Hall, Jr., Preliminary results from the Gate acoustic echo sounder, *Bull. Amer. Meteorol. Soc., 57,* 1142–1147, 1976.

Mandics, P. A., and E. J. Owens, Observations of the marine atmosphere using a ship-mounted acoustic echo sounder, *J. Appl. Meteorol., 14,* 1110–1117, 1975.

Mandics, P. A., R. W. Lee, and A. T. Waterman, Jr., Spectra of short-term fluctuations of line-of-sight signals—Electromagnetic and acoustic, *Radio Sci., 8,* 185–201, 1973.

Mandics, P. A., F. F. Hall, Jr., and E. J. Owens, Observations of the tropical marine atmosphere using an acoustic echosounder during Gate, in *Preprints of the 16th Radar Meteorology Conference,* pp. 253–256, American Meteorological Society, Boston, Mass., 1975*a*.

Mandics, P. A., F. F. Hall, Jr., and E. J. Owens, Preliminary results of acoustic echo sounding of the marine boundary layer during Gate, *Gate Rep. 14, Prelim. Sci. Res.,* vol. II, pp. 225–228, World Meteorol. Organ., Geneva, 1975*b*.

Marble, F. E., Some gas dynamic problems in the flow of condensing vapors, *Astron. Acta, 14,* 585–614, 1969.

Marble, F. E., and D. C. Wooten, Sound attenuation in a condensing vapor, *Phys. Fluids, 13,* 2657–2664, 1970.

Marks, J. R., Acoustic radar investigations of boundary layer phenomena, scientific report, contract NAS8-28659, 65 pp., Dep. of Meteorol., Univ. of Okla., Norman, 1973.

Marshall, J. M., A radio acoustic sounding system for the remote measurement of atmospheric parameters, *Rep. AFCRL-70-0438, SU-SEL-70-050,* 139 pp., Stanford Univ., Stanford, Calif., 1970.

Marshall, J. M., A. M. Peterson, and A. A. Barnes, Jr., Combined radar-acoustic sounding system, *Appl. Opt., 11,* 108–112, 1972.

Mathur, S. S., and M. S. Sagoo, Focusing of acoustic waves in inhomogeneous media, *Acustica, 32,* 51–53, 1975.

McAllister, L. G., Acoustic sounding of the lower troposphere, *J. Atmos. Terr. Phys., 30,* 1439–1440, 1968.

McAllister, L. G., Wind velocity measurements in the lower atmosphere using acoustic sounding techniques, *Tech. Note-A204 (AP),* 20 pp., Weapons Res. Estab., Salisbury, Australia, 1971.

McAllister, L. G., and J. R. Pollard, Acoustic sounding of the lower atmosphere, in *Proceedings of the 6th International Symposium on Remote Sensing of the Environment,* pp. 436–450, University of Michigan Press, Ann Arbor, 1969.

McAllister, L. G., J. R. Pollard, A. R. Mahoney, and P. J. R. Shaw, Acoustic sounding—A new approach to the study of atmospheric structure, *Proc. IEEE, 57,* 579–587, 1969.

Melling, H., and R. List, Doppler velocity extraction from atmospheric acoustic echoes using a level crossing technique (abstract), *J. Acoust. Soc. Amer, 60,* Suppl. 1, S69, 1976.

Miller, D. H., The influence of open pine forest on daytime temperature in the Sierra Nevada, *Geogr. Rev., 46,* 209–218, 1956.

Miller, E. L., Multiple site acoustic sounding in Metromex, *Bull. Amer. Meteorol. Soc., 55,* 114–115, 1974.

Mintzer, D., Wave propagation in a randomly inhomogeneous medium, I, *J. Acoust. Soc. Amer.*, *25*, 922–927, 1953*a*.

Mintzer, D., Wave propagation in a randomly inhomogeneous medium, II, *J. Acoust. Soc. Amer.*, *25*, 1107–1111, 1953*b*.

Mintzer, D., Wave propagation in a randomly inhomogeneous medium, III, *J. Acoust. Soc. Amer.*, *26*, 186–190, 1954.

Monin, A. S., Characteristics of the scattering of sound in a turbulent atmosphere, *Sov. Phys. Acoust.*, Engl. Transl., *7*, 370–373, 1962.

Monin, A. S., and A. M. Yaglom, *Statistical Fluid Mechanics I*, MIT Press, Cambridge, Mass., 1971.

Monin, A. S., and A. M. Yaglom, *Statistical Fluid Mechanics II*, MIT Press, Cambridge, Mass., 1974.

Morris, A. L., and F. F. Hall, Jr., Remote sensing of the atmosphere by sound, *Atmos. Technol.*, *6*, 84–93, 1975.

Muir, T. G., An analysis of the parametric acoustic array for spherical wave fields, Ph.D. dissertation, Univ. of Tex., Austin, 1971.

Nater, W., Voruntersuchungen zum Bau eines akustischen Echo-Sounders, *Rep. LAPETH-9*, 67 pp., Lab. für Atmosphärenphys. Eidgenöss. Tech. Hochsch., Zurich, 1974.

Neff, W. D., Quantitative evaluation of acoustic echoes from the planetary boundary layer, *Tech. Rep. ERL 322-WPL 38*, 34 pp., Nat. Oceanic and Atmos. Admin., Boulder, Colo., 1975*a*.

Neff, W. D., An investigation of acoustic scatter from small scale thermal fluctuations in the planetary boundary layer, in *Preprints of the 16th Radar Meteorology Conference,*, pp. 263–270, American Meteorological Society, Boston, Mass., 1975*b*.

Neff, W. D., and F. F. Hall, Jr., Acoustic sounder measurements of the south pole boundary layer, in *Preprints of the 17th Radar Meteorology Conference,*, pp. 297–302, American Meteorological Society, Boston, Mass., 1976*a*.

Neff, W. D., and F. F. Hall, Jr., Acoustic echo sounding of the atmospheric boundary layer at the South Pole, *Antarct. J. U.S.*, *11*, 143–144, 1976*b*.

Neubert, J. A., Asymptotic solution of the stochastic Helmholtz equation for turbulent water, *J. Acoust. Soc. Amer.*, *48*, 1203–1211, 1970.

Neubert, J. A., and J. L. Lumley, Derivation of the stochastic Helmholtz equation for sound propagation in a turbulent fluid. *J. Acoust. Soc. Amer.*, *48*, 1212–1218, 1970.

Neubert, J. A., and J. L. Lumley, Approach to stochastic Lagrangian integrals and their asymptotic evaluation for sound propagation in continuous stochastic media, *J. Math. Phys. N. Y.*, *13*, 169–183, 1972.

Noonkester, V. R., The evolution of the clear air convective layer revealed by surface-based remote sensors, *J. Appl. Meteorol.*, *15*, 594–606, 1976.

Noonkester, V. R., J. H. Richter, and D. R. Jensen, Marine fog investigations in San Diego, in *Preprints of the 17th Radar Meteorology Conference*, pp. 282–289, American Meteorological Society, Boston, Mass., 1976.

Nordberg, W., and W. G. Stroud, Results of IGY rocket grenade experiments to measure temperature and winds above the Island of Guam, *J. Geophys. Res.*, *66*, 455–464, 1961.

North, E. M., and M. S. Frankel, Two radar techniques for remote measurement of atmospheric parameters, *Rep. AFCRL-72-0070, SU-SEL-72-001*, 35 pp., Stanford Univ., Stanford, Calif., 1972.

North, E. M., A. M. Peterson, and H. D. Parry, RASS, a remote sensing system for measuring low-level temperature profiles, *Bull. Amer. Meteorol. Soc.*, *54*, 912–919, 1973.

Nyquist, H., Thermal agitation of electric charge in conductors, *Phys. Rev.*, *32*, 110–113, 1928.

Obukhov, A. M., Scattering of sound in turbulent flow (in Russian), *Dokl. Akad. Nauk. SSSR*, *30*, 611, 1941.

Ottersten, H., Radar angels and their relationship to meteorological factors, *FOA Foresvarets Forskningsanst. Rep.*, *4*, 1–33, 1970.

Ottersten, H., Remote sensing med speciell inriktning på att utnyttja radiovågor för sondering av troposfären, *FOA Rep. D 30026-E 1*, 21 pp., Res. Inst. of Nat. Def., Stockholm, 1975.

Ottersten, H., K. R. Hardy, and C. G. Little, Radar and sodar probing of waves and turbulence in statically stable clear-air layers, *Boundary Layer Meteorol.*, *4*, 47–89, 1973.

Ottersten, H., M. Hurtig, G. Stilke, B. Brümmer, and G. Peters, Shipborne sodar measurements during Jonswap 2, *J. Geophys. Res.*, *79*, 5573–5584, 1974.

Owens, E. J., Development of a portable acoustic echo sounder, *Tech. Rep. ERL 298-WPL 31*, 38 pp., Nat. Oceanic and Atmos. Admin., Boulder, Colo., 1974.

Owens, E. J., NOAA Mark VII acoustic echo sounder, *Tech. Memo. ERL WPL-12*, 71 pp., Nat. Oceanic and Atmos. Admin., Boulder, Colo., 1975.

Owens, E. J., Microcomputer-controlled acoustic echo sounder, *Tech. Memo. ERL WPL-21*, 76 pp., Nat. Oceanic and Atmos. Admin., Boulder, Colo., 1977.

Parry, H. D., The acoustic sounder: Pollution fighter's tool, *Tech. Memo. NWS-EDL-12*, 16 pp., Nat. Weather Serv., Silver Spring, Md., 1974.

Parry, H. D., and M. J. Sanders, Jr., The design and operation of an acoustic radar, *IEEE Trans. Geosci. Electron.*, *GE-10*, 58–64, 1972.

Parry, H. D., M. J. Sanders, Jr., and H. P. Jensen, Operational applications of a pure acoustic sounding system, *J. Appl. Meteorol.*, *14*, 67–77, 1975.

Pedersen, M. A., D. White, and D. W. Johnson, Generalized expansions of ray theory in terms of phase velocity, I, *J. Acoust. Soc. Amer.*, *58*, 78–96, 1975.

Pekeris, C. L., Theory of propagation of sound in a half-space of variable sound velocity under conditions of formation of a shadow zone, *J. Acoust. Soc. Amer.*, *18*, 295–315, 1946.

Pestorius, F. M., Propagation of plane acoustic noise of finite amplitude, Ph.D. dissertation, Univ. of Tex., Austin, 1973. (Also available as *Rep. ARL-TR-73-23*, Appl. Res. Lab., Univ. of Tex., Austin, 1973.)

Pestorius, F. M., and S. W. Williams, Upper limit on the use of weak shock theory, *J. Acoust. Soc. Amer.*, *55*, 1334–1335(L), 1974.

Petersen, E. L., and N. O. Jensen, A mesoscale phenomenon revealed by an acoustic sounder, *J. Appl. Meteorol.*, *15*, 662–664, 1976.

Petersen, E. L., and N. O. Jensen, Reply, *J. Appl. Meteorol.*, *16*, 110–111, 1977.

Petterssen, S., P. A. Sheppard, C. H. B. Priestly, and K. R. Johannessen, An investigation of subsidence in the free atmosphere, *Quart. J. Roy. Meteorol. Soc.*, *73*, 43–62, 1947.

Pierce, A. D., and J. W. Posey, Theory of the excitation and propagation of Lamb's atmospheric edge mode from nuclear explosions, *Geophys. J. Roy. Astron. Soc.*, *26*, 341–368, 1971.

Piercy, J. E., Role of the vibrational relaxation of nitrogen in the absorption of sound in air, *J. Acoust. Soc. Amer.*, *46*, 602–604, 1969.

Piercy, J. E., T. F. W. Embleton, and L. C. Sutherland, Review of noise propagation in the atmosphere, *J. Acoust. Soc. Amer.*, *61*, 1403–1418, 1977.

Proni, J. R., and J. R. Apel, On the use of high-frequency acoustics for the study of internal waves and microstructure, *J. Geophys. Res.*, *80*, 1147–1151, 1975.

Raphael, D. T., Wood's refraction correction equations for a constant gradient medium: An alternative derivation, *J. Acoust. Soc. Amer.*, *50*, 955–959, 1971.

Rayleigh (J. W. Strutt), *The Theory of Sound*, Macmillan, New York, 1877. (American editor, Dover, New York, 1945.)

Reynolds, O., On the refraction of sound in the atmosphere, *Phil. Trans. Roy. Soc. London*, *166*, 315, 1876.

Richter, J. H., and D. R. Jensen, Simultaneous acoustic sounder and FM-CW radar observations, in *Preprints of the 16th Radar Meteorology Conference*, pp. 282–289, American Meteorological Society, Boston, Mass., 1975.

Richter, J. H., et al., Clear air convection: A close look at its evolution and structure, *Geophys. Res. Lett.*, *1*, 173–176, 1974.

Rizzo, K. R., Determining the mixing depth climatology using an acoustic sounder in a lakeshore environment, *Spec. Rep. 28*, 78 pp., Center for Great Lake Stud., Univ. of Wis., Milwaukee, 1975.

Rosenbaum, S., Backscatter from gated fluctuating regions: A Bremmer series approach, *IEEE Trans. Antennas Propagat.*, *AP-20*, 618–624, 1972.

Russell, P. B., and E. E. Uthe, Acoustic and direct measurement of atmospheric mixing at three sites during an air pollution incident, *Atmos. Environ.*, in press, 1977.

Russell, P. B., E. E. Uthe, F. L. Ludwig, and N. A. Shaw, A comparison of atmospheric structure as observed with monostatic acoustic sounder and lidar techniques, *J. Geophys. Res.*, *79*, 5555–5566, 1974.

Sager, G., Eine Methode zur Bestimmung der Schallausbreitung in quasiruhender Atmosphäre, *Z. Meteorol.*, *24*, 117–129, 1974.

Schotland, R. M., The measurement of wind velocity by sonic means, *J. Meteorol.*, *12*, 386–390, 1955.

Schrödinger, E., Zur Akustik der Atmosphäre, *Phys. Z.*, *18*, 445–453, 1917.

Schubert, J. F., A climatology of the mixed layer using acoustic methods, in *Preprints of the 3rd Symposium on Meteorological Ob-*

servation and Instrumentation, pp. 151-156, American Meteorological Society, Boston, Mass., 1975.

Shaw, N. A., Acoustic sounding of the atmosphere, Ph.D. dissertation, 266 pp., Roy. Aust. Air Force Acad., Univ. of Melbourne, Melbourne, Australia, 1971.

Shaw, N. A., Observations of atmospheric structure using an acoustic sounder, *Rep. ANL/RER/75-2*, 37 pp., Argonne Nat. Lab., Argonne, Ill., 1974.

Shooter, J. A., T. G. Muir, and D. T. Blackstock, Acoustic saturation of spherical waves in water, *J. Acoust. Soc. Amer., 55*, 54-62, 1974.

Simmons, W. R., J. W. Wescott, and F. F. Hall, Jr., Acoustic echo sounding as related to air pollution in urban environments, *Tech. Rep. ERL 216-WPL 17*, 77 pp., Nat. Oceanic and Atmos. Admin., Boulder, Colo., 1971.

Singal, S. P., Remote sensing of the troposphere using sodar technique, *J. Acoust. Soc. India, 1*, 64-68, 1973.

Singal, S. P., Sodar—The atmospheric sensor using acoustic waves, *Rep. 16*, 83 pp., Centre for Res. on the Troposphere, Nat. Phys. Lab., New Delhi, 1975.

Singal, S. P., and M. Pancholy, Acoustic sounder for probing of the lower atmosphere, *Indian J. Radio Space Phys., 1*, 202-204, 1972.

Singal, S. P., J. R. Anand, B. S. Gera, and S. K. Aggarwal, Design, fabrication and studies of the acoustic antennas for use in acoustic sounding of the lower atmosphere, *Rep. 14*, 23 pp., Centre for Res. on the Troposphere, Nat. Phys. Lab., New Delhi, 1974.

Singal, S. P., B. S. Gera, S. K. Aggarwal, and M. Saxena, Use of monostatic sodar in probing the lower atmosphere, *Indian J. Radio Space Phys., 4*, 146-156, 1975.

Skudrzyk, E., *The Foundations of Acoustics*, Springer, New York, 1971.

Smith, P. L., Jr., Remote measurement of wind velocity by the electromagnetic acoustic probe, I, System analysis, *Conference Proceedings of the 5th National Convention on Military Electronics*, Washington, D. C., Rep. 419, Midwest Res. Inst., Kansas City, Mo., 1961.

Solomon, L. P., and L. Armijo, An intensity differential equation in ray acoustics, *J. Acoust. Soc. Amer., 50*, 960-963, 1971.

Spizzichino, A., The refraction of acoustic waves in the atmosphere and its effect on sodar wind measurement, *Ann. Telecommun., 29*, 301-310, 1974*a*.

Spizzichino, A., Discussion of the operating conditions of a Doppler sodar, *J. Geophys. Res., 79*, 5585-5591, 1974*b*.

Spizzichino, A., and P. van Grunderbeeck, Etude des plumes convectives de la basse atmosphère par sondage acoustique Doppler, *CRPE Tech. Note 34*, Centre Nat. de la Rech. Sci., Issy-les-Moulineaux, France, 1975.

Stilke, G., C. Wamser, and G. Peters, Untersuchen über den Abbau einer Bodeninversion mit direkten und indirekten Messverfahren, *Meteorol. Rundsch., 29*, 181-186, 1976.

Stokes, G. G., On the effect of wind on the intensity of sound, report, p. 22, Brit. Ass., Dublin, 1857. (Reprinted in *Mathematical and Physical Papers of G. G. Stokes*, vol. 4, pp. 110-111, Cambridge University Press, New York, 1904.

Strand, O. N., Numerical study of the gain pattern of a shielded acoustic antenna, *J. Acoust. Soc. Amer., 49*, 1698-1703, 1971.

Stroud, W. G., W. Nordberg, and J. Walsh, Atmospheric temperatures and winds between 30 and 80 km, *J. Geophys. Res., 61*, 45-56, 1956.

Surridge, A. D., Tropospheric acoustic sounding, Ph.D. dissertation, 259 pp., Univ. of Otago, Dunedin, New Zealand, 1975.

Sutherland, L. C., Review of experimental data in support of a proposed new method for computing atmospheric absorption losses, *Rep. TST-75-87*, Dep. of Transp., Washington, D. C., 1975. (Available from National Technical Information Service, Springfield, Va.)

Tatarskii, V. I., *Wave Propagation in a Turbulent Medium*, translated from Russian by R. A. Silverman, Dover, New York, 1961.

Tatarskii, V. I., *The Effects of the Turbulent Atmosphere on Wave Propagation*, translated from Russian by J. W. Strohbehn, Israel Program for Scientific Translations, Jerusalem, 1971. (Available from National Technical Information Service, Springfield, Va.)

Taylor, G. I., Eddy motion in the atmosphere, *Phil. Trans. Roy. Soc. London, Ser. A, 215*, 1-26, 1915.

Teer, T. L., and A. A. Few, Horizontal lightning, *J. Geophys. Res., 79*, 3436-3441, 1974.

Teisserenc de Bort, L. P., Variations de la température de l'air libre dans la zone comprise entre 8 km et 13 km k'altitude, *C. R. Acad. Sci., 134*, 987-989, 1902.

Tennekes, H., A model for the dynamics of the inversion above a convective boundary layer, *J. Atmos. Sci., 30*, 558-567, 1973.

Tennekes, H., and J. L. Lumley, *A First Course in Turbulence*, MIT Press, Cambridge, Mass., 1972.

Theobald, M. A., Experimental study of outdoor propagation of spherically spreading periodic acoustic waves of finite amplitude, M.S. thesis, Univ. of Tex., Austin, 1977.

Thompson, R. J., Ray theory for an inhomogeneous moving medium, *J. Acoust. Soc. Amer., 51*, 1675-1682, 1972.

Thompson, R. J., Ray-acoustic intensity in a moving medium, I, *J. Acoust. Soc. Amer., 55*, 729-732, 1974*a*.

Thompson, R. J., Ray-acoustic intensity in a moving medium, II, A stratified medium, *J. Acoust. Soc. Amer., 55*, 733-737, 1974*b*.

Thomson, D. W., Acdar meteorology: The application and interpretation of atmospheric acoustic sounding measurements, in *Preprints of the 3rd Symposium on Meteorological Observation and Instrumentation*, pp. 144-150, American Meteorological Society, Boston, Mass., 1975.

Thomson, D. W., and R. L. Coulter, Analysis and simulation of phase coherent acdar sounding measurements, *J. Geophys. Res., 79*, 5541-5549, 1974.

Tolstoy, I., *Wave Propagation*, McGraw-Hill, New York, 1973.

Tombach, I., and M. Chan, Estimation of mixing depth and inversion height by acoustic radar—A comparison with in-situ measurements, in *Preprints of the 17th Radar Meteorology Conference*, pp. 313-320, American Meteorological Society, Boston, Mass., 1976.

Tombach, I., P. MacCready, and L. Baboolal, Use of a monostatic acoustic sounder in air pollution diffusion estimates, in *Proceedings of the 2nd Joint Conference on Sensing Environmental Pollutants*, pp. 139-149, Instrument Society of America, Washington, D. C., 1973.

Trettel, D. W., and D. Rai, Acoustic radar as a tool in local weather prediction, in *Preprints of the 17th Radar Meteorology Conference*, pp. 276-281, American Meteorological Society, Boston, Mass., 1976.

Trowbridge, A., Sound ranging, *J. Franklin Inst., 189*, 133-146, 1920.

Tyndall, J., On the atmosphere as a vehicle of sound, *Phil. Trans. Roy. Soc. London, Ser. A, 164*, 183-244, 1874.

Tyndall, J., *Sound*, 3rd ed., Appleton, New York, 1875.

Ugincius, P., Intensity equations in ray acoustics, I, *J. Acoust. Soc. Amer., 45*, 193-205, 1969*a*.

Ugincius, P., Intensity equations in ray acoustics, II, *J. Acoust. Soc. Amer., 45*, 206-209, 1969*b*.

Ugincius, P., Intensity equations in ray acoustics, III, Exact two-dimensional formulation, *J. Acoust. Soc. Amer., 47*, 339-341, 1970.

Ugincius, P., Ray acoustics and Fermat's principle in a moving inhomogeneous medium, *J. Acoust. Soc. Amer., 51*, 1759-1763, 1972.

Uthe, E. E., and P. B. Russell, Experimental study of the urban aerosol structure and its relation to urban climate modification, *Bull. Amer. Meteorol. Soc., 55*, 115-121, 1974.

van den Borne, G., Über die Schallverbreitung bei Explosions-katastrophen, *Phys. Z., 11*, 483-488, 1910.

van Grunderbeeck, P., Etude de la détermination des profils atmosphériques de température et humidité par sondage acoustique multifréquence: Faisabilité, vérification experimentale, *Rep. NT CRPE/5*, 47 pp., Centre de Rech. en Phys. de l'Environ. Terr. et Planetaire, Orleans Cedex, France, 1975.

Warren, C. H. E., A note on the refraction of sound in a moving gas, *J. Sound Vib., 1*, 175-178, 1964.

Webster, D. A., Saturation of plane acoustic waves and notes on the propagation of finite-amplitude waves, M.S. thesis, Univ. of Tex., Austin, 1976.

Weill, A., M. Aubry, F. Baudin, and J. Heissat, A study of temperature fluctuations in the atmospheric boundary layer, *Boundary Layer Meteorol., 10*, 337-346, 1976.

Weinberg, H., Applications of ray theory to acoustic propagation in horizontally stratified oceans, *J. Acoust. Soc. Amer., 58*, 97-109, 1975.

Wenzel, A. R., Propagation speed and attenuation coefficient for plane coherent acoustic waves in a turbulent medium, *J. Acoust. Soc. Amer., 51*, 1683-1687, 1972.

Wenzel, A. R., Propagation of waves along an impedance boundary, *J. Acoust. Soc. Amer., 55*, 956-963, 1974.

Wenzel, A. R., Saturation effects associated with sound propagation in a turbulent medium, *Prog. Astronaut. Aeronaut., 46*, 67-75, 1976.

Wenzel, A. R., and J. B. Keller, Propagation of acoustic waves in a turbulent medium, *J. Acoust. Soc. Amer., 50*, 911-920, 1971.

Werner, C., Digital sodar system, *J. Appl. Meteorol.*, in press, 1977.

Wescott, J. W., and S. S. Kushner, Propagation of sound in air, *Rep. 2900-185-B*, 632 pp., Inst. of Sci. and Tech., Univ. of Mich., Ann Arbor, 1965.

Wescott, J. W., W. R. Simmons, and C. G. Little, Acoustic echo sounding measurements of temperature and wind fluctuations, *Tech. Memo. ERLTM-WPL 5*, Environ. Sci. Serv. Admin., Boulder, Colo., 1970.

Wesely, M. L., The combined effect of temperature and humidity fluctuations on refractive index, *J. Appl. Meteorol., 15*, 43–49, 1976.

Westervelt, P. J., Parametric acoustic array, *J. Acoust. Soc. Amer., 35*, 535–537, 1963.

Whipple, F. J. W., The high temperatures of the upper atmosphere as an explanation of zones of audibility, *Nature, 111*, 187, 1923.

White, R. W., Acoustic ray tracing in moving inhomogeneous fluids, *J. Acoust. Soc. Amer., 53*, 1700–1704, 1973.

Whitham, G. B., *Linear and Nonlinear Waves*, John Wiley, New York, 1974.

Willmarth, B. C., E. H. Brown, J. T. Priestley, and D. W. Beran, Beam pattern measurements for large acoustic antennas, in *Preprints of the 16th Radar Meteorology Conference*, pp. 278–281, American Meteorological Society, Boston, Mass., 1975.

Wilson, C. R., Auroral infrasonic waves, *J. Geophys. Res., 74*, 1812–1836, 1969.

Wood, A., *Acoustics*, Interscience, New York, 1946.

Wood, D. H., Green's functions for unbounded constant gradient media, *J. Acoust. Soc. Amer., 46*, 1333–1339, 1969.

Wood, D. H., Refraction correction in constant-gradient media, *J. Acoust. Soc. Amer., 47*, 1448–1452, 1970.

Wood, D. H., Parameterless examples of wave propagation, *J. Acoust. Soc. Amer., 54*, 1727–1736, 1973.

Wyckoff, R. J., D. W. Beran, and F. F. Hall, Jr., A comparison of the low-level radiosonde and the acoustic echo sounder for monitoring atmospheric stability, *J. Appl. Meteorol., 12*, 1196–1204, 1973.

Wyngaard, J. C., Y. Izumi, and S. A. Collins, Jr., Behavior of the refractive-index structure parameter near the ground, *J. Opt. Soc. Amer., 61*, 1646–1650, 1971.

Yura, H. T., Atmospheric turbulence induced laser beam spread, *Appl. Opt., 10*, 2771–2772, 1971.

Yura, H. T., Physical model for strong optical-amplitude fluctuations in a turbulent medium, *J. Opt. Soc. Amer., 64*, 59–67, 1974.

Zeman, O., The dynamics of entrainment in the planetary boundary layer: A study in turbulence modeling and parameterization, Ph.D. thesis, 216 pp., Pa. State Univ., University Park, 1975.

Zilitenkevich, S. S., Comments on 'A model for the dynamics of the inversion above a convective boundary layer,' *J. Atmos. Sci., 32*, 991–992, 1975.

(Received August 23, 1977;
accepted August 25, 1977.)

Bulletin of the American Meteorological Society, 59: 1334-1342,
October 1978.

What Should the NWS Be Doing to Improve Short-Range Weather Forecasting?— A Panel Discussion with Audience Participation

12 April 1978, Boulder, Colo.

Joseph H. Golden, C. F. Chappell, C. G. Little,
A. H. Murphy, E. B. Burton, and E. W. Pearl

1. Introduction

Joseph H. Golden.[1] The Denver Chapter of the American Meteorological Society sponsored a panel discussion on the evening of 12 April 1978 in connection with the Fourth Symposium on Meteorological Observations and Instrumentation being held in Denver that week. The topic was selected both for its relevance to the symposium and its timely and controversial nature. We were fortunate to secure five scientists from the local research and operational community who could, we thought, provide new perspectives and stimulate audience reaction to the question, "What should the NWS be doing to improve short-range weather forecasting?" The panelists were Charles Chappell, Deputy Director of NOAA's Atmospheric Physics and Chemistry Laboratory, C. Gordon Little, Director of NOAA's Wave Propagation Laboratory, Allan Murphy of NCAR's Environmental and Societal Impacts Group, Ellis Burton, Meteorologist-in-Charge of the Denver Weather Service Forecast Office, and Edward Pearl, Meteorologist and Executive Vice-President of Geophysical R & D Corp., a private firm in Denver. Each of the panelists was asked to prepare a short talk of up to 10 minutes in length on the above topic and to be prepared to answer questions and defend his position with audience and panel interaction, following the presentations from the panel. The panelists represented a broad spectrum of interests and views on the discussion topic. They did not collaborate with one another, to my knowledge, prior to the meeting and did not know beforehand the order in which I, acting as moderator, would call upon them. As it turned out, this uncertainty allowed for more spontaneous reaction and rebuttal to the previous panelists' remarks. Some of their prescriptions are somewhat radical, but in most cases they agreed that strong measures are becoming necessary. Finally, I think that all concerned meteorologists would agree that the short-term forecasting problem is *not* just an NWS issue but a vital national one.

2. Panel presentations

FIG. 1. Panel members were (l to r): C. Gordon Little, Ed Pearl, Charles Chappell, Allan Murphy, and Ellis Burton.

C. F. Chappell. I would like to present a few personal observations and interpretations of the present NWS approach to short-range weather prediction and how it might be improved.

The NWS tries to do all things for all people on a finite budget and with shrinking manpower. The climax of this trend, if it continues uninterrupted, will be that they will do little of substance for anyone.

The NWS apparently sees the forecaster as the weak link in the prediction chain. More and more resources go into providing more and more technology. Less and less resources and attention are given to other needs of the forecaster. Instead of the forecaster controlling the use of technology, he is subservient to technology, and the day approaches when technology will ring a bell in the forecast office and tell him what to do. Actually, it will probably not stop there. Technology will probably go ahead and disseminate the forecast without disturbing him.

The difficulty in predicting weather is second only to, perhaps, predicting human behavior. Many forecasters in the NWS are undertrained for the very complex task they face. They work in, and are conditioned to, a routine, scheduled, and deadline-meeting environment and then are expected to shift quickly and sporadically into a role in which they must make life and death decisions in a matter of seconds. Are they really trained properly to do this? Is it even possible to train them for this very difficult dual role they must fulfill?

Does 20 hours of meteorology from any college provide an adequate education for a weather forecaster? I think not. Can you imagine a psychoanalyst trying to unlock

---

[1] President of the Denver Chapter.

0003-0007/78/1334-1342$05.00
© 1978 American Meteorological Society

the mysteries of the human mind with a couple of introductory courses in psychology? Why not demand equally high educational standards for weather forecasters, whose jobs are just as complex?

Funny things happen to the weather coming down from the synoptic scale to the people. Mountains, lakes, oceans, and cities modify and modulate the synoptic weather patterns and can radically alter the evolution of weather to be experienced by people. These very important mesoscale influences on our weather are now handled only very subjectively by the forecaster, if at all.

So, what should the NWS do to improve short-range weather forecasting? They should quit trying to be all things to all people. The NWS should provide the basic observations and numerical predictions on the synoptic scale and issue short-range predictions and warnings to the public only when weather conditions threaten life and property. Otherwise, let the private sector furnish routine forecasts to business, industry, and the public.

The forecaster should be conditioned to operate in a "firehouse" mode by putting him in an operational environment conducive to predicting the elusive and sporadic, out of the ordinary, weather event.

People, not machines, make things happen. The forecaster should be put back in control of the prediction chain. Let him ring the bell in the weather station and wake up technology. Then, with the forecaster calling the shots, let him and available technology team up to attack the difficult weather situation.

The educational requirements for a weather forecaster should be raised. As a minimum, he should have a master's degree in meteorology or atmospheric science, preferably more. He should be carefully prepared for the job through appropriate screening, training, and experience. His name should appear on every forecast and warning that leaves the office and, like a doctor, he should be held accountable by the public for his work. He also should be paid at a level that will generate a line of top-notch students waiting to enter the program. Forecasters who perform consistently below an acceptable threshold must be removed and steered toward other efforts. The variability between a good and a bad forecaster is not insignificant.

Improved short-range predictions also await the development and implementation of mesoscale numerical models. These are needed to fill the gap between present synoptic-scale forecasts and the weather experienced by people. Stationary mesoscale influences, such as mountain terrain, lakes, oceans, cities, etc., must be included in regional models if we are to provide more detailed numerical weather predictions for short time periods. Important small-scale processes, such as convection and cloud and precipitation processes, must be included in these models.

Development of these mesoscale numerical weather predictions should be encouraged by the NWS and followed by timely implementation.

Finally, technology must supply the required data necessary to initialize these regional-scale models so that we can eventually fill this mesoscale prediction gap.

If and when we do the things I have just outlined, I predict that people will notice the improvement in the performance of the NWS.

C. G. Little. During the past year or two, I have had the opportunity to spend an appreciable amount of time considering what could be done to improve local weather services.

Early on, we decided that we would try to take the "systems view," that is, we would try to look at local weather services as a single system whose overall performance was to be optimized. The systems approach requires that one start first by identifying the desired goal of the system. In our case the goal clearly is improved local weather services to the users. By this we mean that we will seek to provide improved weather information to the users that they can then use to guide their own weather-related decisions. The weather information to be provided is to be improved in the sense that it is more accurate, more timely, more complete, more relevant to the user needs, and/or more accessible to them.

Who then are the users and what are their needs? The users are indeed the total community of U.S. residents. They need this information for three main purposes. These are, first, public safety. Lives can be saved if persons are warned in time of tornadoes, flash floods, hazardout winds, wind shear at airports, etc. Second is economic efficiency. Each day, tens of thousands of persons in industries such as aviation, agriculture, construction, recreation, surface transport, and fishing make weather-related decisions based on their estimates of what the weather conditions will be. Weather information that is more accurate, more complete, more timely, and more relevant to their needs will help increase the economic efficiency and reduce economic losses in these industries. Third is general convenience. Each day, millions of our citizens are affected by significant weather changes. Occasionally, these are hazardous but in many cases they affect little more than the convenience of the persons involved. However, the cumulative effect of improved local weather services, when it is integrated over millions of persons each day, will be large.

These improved weather services are, of course, needed on all time and space scales. Analyses have shown, however, that the principal unmet needs for improved weather services lie in the area of short-term (0–12 h) local (0–100 km) weather forecasts, both because existing NWS functions are already successfully meeting most of the need for longer-term synoptic-scale services and because weather is experienced by the individual on the local scale.

Many studies have shown that persons use the longer-term forecast to make plans but that decisions are usually made on the basis of shorter-term (0–12 h) forecasts. The most demanding of these user needs are in the area of public safety, for example, tornadoes and airport wind shear conditions. Both of these require observational and dissemination time scales of the order of minutes and space scales of the order of kilometers—far beyond the present capabilities of the NWS.

These, then, are the user needs. What do they imply about the dissemination process? Obviously, in order to be optimum, the dissemination process should have at least the following characteristics:

1) The forecasts and warning should be available to all (broadcast).
2) They should be continuously available on demand.
3) They should be updated frequently.
4) They should include automatic warning capability.
5) Because of the very diverse needs and interests of the users, essentially all the local weather information existing in the NWS system should be potentially available to the user.
6) Since each user, in fact, is interested in only a very limited subset of these data, the service should be interactive and allow the user to select the specialized data that he needs.
7) The system should provide an effective feedback mechanism whereby users can, over time, indicate if the service is or is not effectively meeting their needs.

In this connection, it is clear that the NWS FM weather radio is a very important advance in that it broadcasts continuously and includes an automatic warning capability. However, two severe limitations are that the information transfer rate is limited to that of the human voice and the effective range is line of sight (severely limited in mountainous terrain).

Looking to the future, we recognize that major advances in dissemination are being made, particularly by the private meteorologist. These can be identified as lying in two areas: broadcast services to the general user and special services to specific users. We are all, perhaps, accustomed to PPI plots of precipitation on black and white screens. Advances at NOAA and elsewhere have resulted in digitized and contoured color video maps of the precipitation. Soon computer-prepared animated sequences of pictures for TV will be available. In addition, recent advances in Doppler radar indicate that it will be practical to prepare color maps of wind fields as well as of precipitation. The private meteorologists are very active in the use of video techniques for the dissemination of weather information, and it is noteworthy that several dozen television stations now have their own weather radars.

In addition to improvements in broadcast dissemination, there are equally important improvements in dissemination to special users. One example of such a concept is the NWS/Department of Agriculture cooperative observer program in which a local farmer, for example, would enter into a local computer, using Touch-Tone telephone, his own local weather observations. In return, he would receive, via a telephone modem or interface ("Green Thumb Box"), data on local weather conditions and forecasts, agricultural prices, etc., for display on his television screen. I understand that it is contemplated that the farmer would be able to select at will from any of 80 data sets available in the local Department of Agriculture computer. Thus, such a system would have many additional desirable characteristics of a dissemination system, including interactive video capabilities.

The next question is, "What do the user needs have to say about the nature of the forecasts that are required?" Although weather services are required on all time and space scales, as indicated earlier, dominant needs are for time scales from 0 to 12 h and space scales of from 0 to 100 km. The cutoff at time periods of 12 h is because of the 12 h cycle of the NWS; the cutoff at 100 km range matches the normal maximum commuting range of an individual from the center of some urban area and also the service area of a broadcast television station. The forecasts available for selection should, of course, cover all the relevant parameters, including wind, temperature, pressure, humidity, precipitation, clouds, visibility, cloud height, icing, turbulence, wind shear, etc.

To meet these needs, the forecaster will have to use two approaches. One may be thought of as the standard approach—"come down from the large scale." To use Verner Suomi's memorable phrase, "The synoptic scale is the choreographer of the mesoscale," that is, it sets up conditions for the mesoscale "to do its own thing." The local weather is the product of the synoptic scale forcing as modulated by local forcing functions such as orography and other terrain features, such as urban heat islands and land-sea boundaries. In recent years, there has been major progress in the development of numerical models capable of including these focal forcing functions. For example, colleagues in NOAA's Atmospheric Physics and Chemistry Laboratory have models whose total domain is comparable to a single grid point spacing on the standard National Meteorological Center (NMC) numerical weather prediction models.

The second, and proposed new approach, is to build up to the mesoscale from the small scale. In recent years, there has been major progress in the automatic monitoring of the atmospheric conditions by ground-based and satellite-borne remote sensors. Similar progress in data processing and display techniques makes it feasible to contemplate the preparation of what has been termed "nowcasts," that is, *video presentations* of the current state of the atmosphere over some local area. Such nowcasts could be displayed over a broadcast or cable television channel in essentially real time. Obviously, the information content of such pictures is enormously greater than can be conveyed by the human voice.

The next step will involve learning how to extrapolate the nowcasts for time periods of the order of 2 or 3 h. Since we do not yet have these much richer data sets, it will take appreciable time to learn how to extrapolate them in an optimum fashion. Filling the gap in the time interval between the 2–3 h nowcasts and the twice per day, 12 h cycle of the existing NWS forecasts will be the most difficult one. Here we anticipate that the use of locally specific numerical models, operated within some nested grid model whose boundaries are driven, for example, by the NMC synoptic-scale models, will be effective in improving the local mesoscale forecasts for time periods of 3–12 h.

Having identified the user needs, dissemination mechanisms, and forecast requirements, what do these have to say about the required observations? Obviously, three-dimensional measurements in essentially real time will be needed out to beyond the 100 km radius. We envisage networks of cooperative observers, surface arrays of automatic weather stations, geostationary and orbiting satellites, and digitized weather radar data (including Doppler information) plus some of the new remote sensors, especially the new capabilities for the automatic, unmanned profiling of winds, temperature, and humidity to tropopause heights. Such data sets should permit the preparation of nowcasts for the local area and their extrapolation for the next 2 or 3 h. For numerical weather prediction to longer time spans, three-dimensional data out to 500–1000 km will be required. Here, major use will need to be made of satellites, especially the vertical atmospheric sounding (VAS) capabilities planned for the early 1980s (e.g., the VAS sounding device on GOES-D). Major use should also be made of the continuous profiling capabilities of the new ground-based remote sensors. In addition, we may expect that at least in the most densely populated areas of the country, nowcasting capabilities for neighboring large urban populations will give contiguous coverage over large regions.

Thus I foresee major opportunities for improved local weather services by the creation of an integrated system that incorporates some of the latest advances in dissemination, forecasting, and observing and successfully integrates the new local weather services into the existing NWS synoptic-scale services.

One last point. I feel that the local atmospheric science community has both a major opportunity and responsibility to begin to face the problem of improved short-term local weather services. We have, in the Boulder/Denver area, the largest single concentration of atmospheric research talent in the country or, for that matter, in the world. Therefore, if we choose to focus on this problem, we may expect to make progress more rapidly and more effectively than any other group. The facilities available to us in NCAR, the universities, Environmental Research Laboratories/NOAA, and the Bureau of Reclamation are in many cases unique and together make for a very attractive opportunity. In addition, some metropolitan TV stations have new color radars and spotter networks that can add information. The meteorological challenge provided by the Denver area is also large and will fully test our capabilities. The challenge, opportunity, and need all exist; I urge that together we begin to focus upon them the attention they deserve. If we don't, who will?

Allan H. Murphy. I don't think that it is possible to conduct a meaningful discussion concerning what the NWS should be doing to improve short-range weather forecasts without briefly reviewing recent trends in the quality of forecasts and examining some possible explanations for these trends. Thus, I shall attempt to summarize the current state of the art in weather forecasting and then offer several suggestions concerning ways in which forecasts could be improved. Even before we consider the quality of weather forecasts, however, it is necessary to define several terms.

First, we must distinguish between what I shall call "meteorological forecasts" and "weather forecasts." The former are forecasts of variables such as pressure, temperature, and humidity at various levels in the atmosphere; the geopotential heights of pressure surfaces on prognostic charts are examples of such forecasts. The latter are forecasts of variables such as precipitation, temperature, and wind velocity generally at or near the earth's surface. Meteorological forecasts prepared by the NWS are based upon numerical models and are produced almost exclusively by machine. Weather forecasts, on the other hand, are prepared both objectively by numerical-statistical procedures and subjectively by NWS forecasters. The public weather forecasts currently issued by the NWS are produced by the forecasters with the aid of objective guidance information. It may also be useful in this discussion to distinguish between objective and subjective forecasts, where the former refers to both meteorological and weather forecasts produced exclusively by machine and the latter refers to the weather forecasts produced by the "man-machine mix."

Second, we must decide what is meant by "improvements" in weather forecasts. Do we mean increases in the accuracy, reliability, skill, etc., of such forecasts or do we mean increases in their usefulness and value? Generally, because we have little if any information concerning the value and/or use of forecasts, we interpret improvements to mean increases in attributes such as accuracy and skill and we assume implicitly that increases in value will follow from these scientific advances. However, it should be emphasized that increases in (for example) accuracy may or may not lead to increases in value; in fact, increases in accuracy can lead to decreases in value (Murphy and Thompson, 1977).[2] Moreover, the results of several recent studies suggest that, in many situations, substantial increases in forecast accuracy may be necessary before appreciable increases in value are realized (e.g., Howe and Cochrane, 1976; Phillips *et al.*, 1978). Nevertheless, we shall assume that improvements in the context of this discussion refer to increases in scientific attributes of the forecasts such as accuracy and skill.

---

[2] References are given at the end of Section 3.

A look at recent trends in the quality of weather forecasts reveals that meteorological forecasts have generally improved throughout the period since the introduction of numerical weather prediction (NWP) models into the forecast system about two decades ago (e.g., Fawcett, 1977; Shuman, 1978). Statistical-numerical or model output statistics (MOS) weather forecasts, based upon these meteorological forecasts, have also demonstrated an improvement over the 10 years since they were first introduced (e.g., Glahn, 1976; Klein, 1976). Some tendency toward a decreasing rate of improvement in both types of machine-produced objective forecasts has been noted in recent years.

On the other hand, weather forecasts produced by the man-machine mix and disseminated to the public have improved very little over the last 5–10 years (e.g., Cook and Smith, 1977; Sanders, 1977; Shuman, 1978; Snellman, 1977). While some differences of opinion certainly exist concerning the extent to which both objective and subjective forecasts have improved in recent years, I think that it is generally agreed that the rate of improvement of subjective forecasts has been less than that of objective forecasts. Thus, the difference in, say, accuracy between objective guidance forecasts and the forecasts formulated by forecasters has decreased; specifically, the human forecaster's contribution to the quality of the ultimate product appears to have diminished. Two general explanations have been offered to account for this phenomenon, and an examination of these explanations provides some insights into what, in my opinion, should be done to improve short-range weather forecasts.

One possible explanation for this phenomenon is based upon the belief that improvements in models and machine-produced forecasts in recent years have been such that forecasters can no longer make significant improvements in these objective forecasts (except perhaps in the first 12 h). Currently, this belief is quite widely held in meteorological circles, principally by those involved in model formulation, objective forecast development, and weather service management. Although it is true that when objective forecasts approach perfection, the forecasters' contributions must necessarily decrease, I will leave it to the audience to decide whether or not we need to concern ourselves with such a utopian state of affairs at this time. If we examine the basis for this belief from a more realistic point of view, we find that very little "uncontaminated" evidence exists to support this position. By uncontaminated, I mean evidence obtained from comparative evaluations conducted in the absence of explicit or implicit directives, guidelines. "penalty functions," etc., to the general effect that "objective guidance forecasts are now almost as good as subjective forecasts and therefore forecasters should not modify these objective forecasts unless they are almost certain that they can improve upon them." Since this statement leads almost immediately to the creation of a closed loop with positive (i.e., reinforcing) feedback, it is not particularly surprising that the forecasters' contributions have decreased in recent years!

An alternative explanation, and one that has been gaining some adherents very recently, is based upon the belief that many NWS policies and practices, as well as the current and evolving structure of the NWS forecast system as a whole, have tended to limit the role of the forecaster and have prevented or at least discouraged him from making effective use of his knowledge and experience. Many examples of such policies and practices could be cited, and I will mention only a few here. First, explicit guidelines exist regarding departures from guidance forecasts for the second and third periods (i.e., 12–24 and 24–36 h, respectively), and forecasters are generally encouraged to adhere closely to these objective forecasts in most cases. Moreover, the forecasters are subjected to (implicit) asymmetric penalty functions when they depart from guidance. Specifically, they are "penalized" for departures that lead to poorer forecasts but they are not similarly "rewarded" for departures that lead to better forecasts.

The very existence and availability of these guidance forecasts provide an example involving more fundamental issues. The problem of concern here is summarized quite well in the following quotation from Snellman (1977, p. 1036):

> . . . today's forecaster can, if he chooses, and many do, come to work, accept Numerical Weather Prognoses (NWP) and MOS guidance, put this into words, and go home. Not once does he have to use his meteorological knowledge and experience. This type of practice is taking place more and more across the United States, and it will be made easier to do with Automation of Field Operations and Services (AFOS). . . .

While the basic concept and potential usefulness of guidance forecasts are not at issue here, the nature of their impact upon the ultimate product—the forecasts produced by the man-machine mix—would seem to be an open question. There is, in my opinion, a fundamental difference between basic guidance—that is, guidance information in the form of analyses and prognostic charts—and forecast guidance in the form of objective forecasts. I believe that these two types of information have quite different psychological impacts on forecasters and on the process by which they arrive at their forecasts. For example, is it reasonable to expect a forecaster to treat the guidance forecast (as he should) as simply another source of information to be assimilated during the process of formulating his forecast? It seems to me at least possible if not probable that guidance forecasts have had an adverse impact on forecasters and thereby on the quality of the forecasts produced by the man-machine mix. In any case, there is a clear and urgent need to investigate the role and impacts of guidance forecasts in the current forecasting system.

Finally, I will mention the current policy of concentrating highly trained and experienced weather forecasters in a relatively few forecast offices. The lack of qualified forecasters at the local level means that local weather forecasts are unlikely to depart from guidance even under those meteorological conditions in which such departures are appropriate. The fact that most experienced public and aviation weather forecasters are now largely removed from contact with users of weather information in many areas (except for certain specialized services) is another undesirable aspect of this policy.

In my opinion, the evidence currently available lends considerably more support to the explanation involving NWS policies and practices and the structure of the forecast system than it does to the explanation based upon the inability of NWS forecasters to improve upon current objective guidance forecasts. Since I subscribe to the point of view characterized by the policies/practices explanation, my ideas concerning what the NWS should do to improve short-range forecasts are necessarily influenced and shaped by this belief. Someone who subscribes to the alternative (or some other) point of view would presumably have different suggestions and proposals.

First, I should indicate that, in suggesting ways of improving short-range forecasts, I will emphasize procedures and practices that I believe can lead to immediate improvements. In this regard, it is certainly true that better observations and more refined models will contribute significantly to improvements in weather forecasts in the future. However, the phrase "in the future" should perhaps be emphasized, since such improvements are likely to be slow in coming and modest when they do arrive. Moreover, I personally have little confidence in approaches to this problem that are largely technological in nature. After all, if either weather radar or weather satellites had fully lived up to their advance billing, then the problem of short-range weather forecasting would have been solved years ago! Consider the fact that contoured, digitized radar was demonstrated for research purposes at the National Severe Storms Laboratory in 1965, and there are still only a fraction of such radars that effect improved warnings.

One set of my suggestions relates to modifications or changes in current policies and practices or in the forecast system itself. First, I would like to see the explicit directives, implicit penalty functions, etc., related to the forecasters' departures from guidance forecasts removed or at least greatly relaxed. In this regard, it would be useful to conduct detailed studies related to the performance of forecasters as a function of departures from guidance. (One or more pilot studies of this type have been conducted recently (see MacDonald, 1977).) Second, the tendency toward centralization both in staffing by highly trained and experienced forecasters and in forecast technique development, refinement, and application should be reversed. Such a change in policy could reasonably be expected to provide the resources and "know-how" at or near the local level that could lead to more successful short-range forecasts. Third, it seems to me critically important to include flexibility within the AFOS system for local forecast technique development and application (it should be noted that this suggestion is meaningful only if appropriately trained and experienced personnel are available at the local level). As presently envisaged, the AFOS system is largely a communications tool, and the original plans to provide local computer capability may not materialize for some time.

Another suggestion involves the explicit recognition of the possibility (if not the probability) that guidance forecasts can have adverse as well as beneficial impacts on the forecasters and on their forecasts. Carefully designed experiments and analytical studies need to be conducted to investigate the role and impacts of guidance forecasts within the existing system and to aid in the development of a more nearly optimal man-machine mix. I firmly believe that the current system, as it has evolved, makes it difficult if not impossible for the forecaster to assimilate and weigh the available guidance information properly (particularly the guidance forecasts) and discourages him from using his training and experience to depart from this guidance. With regard to the former, there is a need to develop procedures that enable forecasters to process information and formulate forecasts in a more nearly systematic, rational manner. Can we really afford to have a forecast system that is clearly not obtaining "full value" from either the machine or the man?

A training program is needed within NWS to renew and sharpen the diagnostic and analytic skills of the forecasters. The quotation from Snellman (1977) given earlier provides dramatic evidence that these skills are rapidly falling into disuse. The need for such a training program has recently been emphasized by Angulis (1978).

An urgent need exists for an improved program for the quality control of weather forecasts within the NWS. Such a program should include, as one of its major components, the facility for providing rapid feedback to both local forecast offices and individual forecasters. Some of the potential benefits of such a program have been demonstrated recently by the staff of the Western Region Headquarters of the NWS (MacDonald, 1977; Snellman, 1977). The results from the first year of their so-called "Man/MOS Program" demonstrate convincingly that NWS forecasters can still improve significantly on guidance forecasts for all three 12 h periods.

Finally, I believe that the NWS should give greatly increased attention to the nature of the requirements for and uses of weather forecasts for all time periods. An example of one possible improvement in this context relates to the need (by users) for information concerning the uncertainty in forecasts. Thompson (1972) has shown that the economic benefits to be expected from operational improvements in forecasts (i.e., from the quantification of uncertainty) are of the same order of magnitude as those to be expected from scientific advances (i.e., from improvements leading to essentially perfect forecasts). Recently, it has also been shown that reliable probabilistic forecasts are generally of greater value to actual and potential users of these forecasts than either climatological or traditional categorical forecasts (Murphy, 1977). The fact that reliable and skillful probabilistic forecasts for a variety of weather variables can be formulated both objectively and subjectively has been demonstrated in a variety of experimental and operational programs conducted over the last 25 years (see Murphy, 1978).

I have attempted to outline briefly a few ways of improving and increasing the usefulness of short-range weather forecasts. These suggestions are not as glamorous as those embodied in some of the large, highly visible, and expensive programs that have been proposed or are now in the process of being implemented. However, I believe that the benefits that would result from following up on these and other similar suggestions would be large, perhaps larger than those associated with the more glamorous programs. Moreover, these so-called "operational" benefits can be realized in the immediate or foreseeable future without the need for major technological developments or scientific advances.

Ellis B. Burton. NWS operations have, in the past decade, been augmented by some instrumentation and procedures to increase capability in short-range prediction. These efforts have only scratched the surface of the problem. The continuing restriction on manpower and equipment, coupled with program expansions and demands, has had a frustrating impact on operations. A genuine impact on the problem can only be approached by operations and research bridging the technology transfer gap and beginning to work and talk together.

Mesoscale sensor networks, with real-time communication capabilities, in weather vulnerable regions of high population density are a must to ensure sufficient warning and short-range forecast capability.

Nothing can prevent or alter the path of severe local storms. Public safety must be enhanced through community action planning, education, and timely warnings. The NWS has primary responsibility within the federal government to provide meteorological forecasts and warnings for the protection of life and property. No legal restriction inhibits the private meteorology sector from issuing warnings on severe weather. Doing so must be coupled with acceptance of legal actions involved or emanating from these issuances.

Of primary concern is the possibility of confusion. Confusion by the public in some cases could nullify or impede safety actions taken by them. Overwarning by multiple sources could conceivably be worse than no warning. The meteorology profession, as a whole, must show responsibility for solution of this problem.

Edward W. Pearl. When we speak of short-range forecasting we must look at two areas: first, the timeliness with which the forecast is disseminated, and, second, the medium of dissemination, i.e., radio, television, CRTs, etc. Forecasts must be constantly updated during changing weather periods. I am disenchanted with the present system of forecast updating practiced by the NWS on the NOAA Weather Radio. In all three of the major metropolitan areas where I have lived, I have heard outdated tapes describing events or forecasts that had occurred 10 or more hours earlier. Frequently, the weather forecast tape continued to broadcast invalid forecasts for hours while quite different weather events were taking place. This situation presents the worst possible image for *all* meteorologists. If we are not able to update the public weather properly, perhaps we should not disseminate it at all, except for immediate emergency situations. If we don't inform the public in a timely, accurate manner, no one will want a weather service, be it government or private.

The second issue, the mode of forecast dissemination, reflects on the "Big Brother" desire (or image) of the NWS to have instant radio, television, and computer access to the public in the near future. The NWS has trouble enough just trying to keep the NOAA Weather Radio current and communicate weather information on it in an understandable form. It would be very premature for the NWS to expand its services to other media forms if it cannot maintain the ones it already offers. Private meteorologists and firms have been offering specialized media weather services for decades and are quite cognizant of the special skills required to effectively communicate on these media. Perhaps the best solution would be for these skilled private firms and individuals to act as the only weather dissemination link with the public.

Dissemination is the key to an immediate upgrading of present-day weather services, whether they be public or private. One advantage that the private service has (such as the one I am a part of) is the direct immediate broadcast. In other words, the radio stations we interact with allow us to go on the air immediately with bulletins of severe weather, hazardous driving conditions, or other weather conditions that may cause harm (the "nowcast").

There are several key factors that must be satisfied before one is able to provide timely and accurate weather information:

1) A sense of trust must be established between the radio station personnel and the broadcast meteorologist. The trust is earned through consistently reliable forecasting combined with an entertaining presentation.
2) Station management must provide the broadcast meteorologist with instant access to the public. This access is absolutely crucial, and it is possible if the management trusts the reliability and authenticity of the meteorologist and his product.
3) The broadcaster must develop a rapport with his audience. The public responds more quickly to a trusted, understandable friend than it does to a cold, abstract authority or figure. The rapport thereby established allows for two-way communication and an additional source of input to a nowcast.

At our corporation (GRD), we have developed Skywatch, which is used only for weather events that may be hazardous to the public, such as rapidly changing road conditions or visibility, development of potential flooding situations, sighting of tornadoes, and many other weather events. Typically the GRD meteorologist goes on the air within seconds to broadcast such information. A prior call is always given to the NWS (Denver) for general dissemination purposes. GRD does not issue watches or warnings but simply observations of weather events and what might be termed an "alert."

I also wanted to ask the other panelists what they thought of the precipitation percentage game? What does a chance of showers with a 30% probability mean to the public? From my experience with the media, it means little if anything. People do understand "chance of, isolated, scattered, likely, probable and possible," but not the percentages. A prime example of the problem of percentages occurred in Chicago a year ago. A "comic" television weatherman discussed a 1% chance of snow for the following day despite the fact that his forecast called for partly cloudy skies and temperatures in the 70s. The following day I was in an elevator with two women. One woman was carrying her boots. The other woman said, "What are those for?" The reply was that the weatherman on television said it would snow. The fact is that many people only hear the word "snow" or "rain" and not what the percentages are.

Two major questions were asked after the above discussion: 1) should private services put out watches or warnings?, and 2) don't multiple forecasts on various radio stations add to confusion?

In response to the first, I believe that private services should be able to alert the public to significant weather events such as severe storms, hail, tornadoes, and floods. Often the private service has modern equipment that the NWS does not possess. In other cases, trained observers may call in reports to a private service (we have our own observer network, the Severe Weather Activity Team, SWAT) or simply one group's equipment may fail while the other's continues to function normally. Without totally evading the question, I believe that just because a private service calls their severe weather bulletin an alert or Skywatch makes it no less effective. Therefore, "watch" or "warning" can be left to the NWS, but I don't see why it should be. There may be a problem with quality control for either a government or private service, but this is not easily resolvable and I don't believe it will ever be resolved.

Regarding the second question on whether multiple forecasts on various radio stations add to confusion, I would say that in some ways they do and in some ways they don't. In the case of the severe weather event, if one station uses the terms "watch" or "warning" based on the NWS bulletins and another uses an "alert" to define a similar situation, there is certainly confusion in the public's mind due to a lack of awareness of a standard definition. Perhaps we should study this further, and possibly the terms should eventually be the same for each.

Very little confusion arises from various local stations carrying different general forecasts, either between different private services or the private and public services. Competition is the name of the game for the private service. Those who listen to the stations learn what to expect from the station they listen to. The fact that the private service is able to update immediately gives an advantage in terms of getting the information to the public when it is needed. Second, the private service is constantly under scrutiny, whether by the media or other business customers. Therefore, private services are forced to put out a better product. If a severe storm is in the area, the private meteorologist will stay with the storm until it has weakened. There are no set hours and therefore no problems with shifts during important weather events. It is the public and private industry that keeps the private services in business; if we don't succeed with a superior product, then our business will fold. Perhaps most forecasts should be made by the private services, as the public and the dollar are our own special quality control.

3. Discussion

Joseph H. Golden. Some of the provocative ideas expressed in the formal presentation by the panelists, as reconstructed above, should pique the intellect of many Bulletin readers. I, for one, welcome a continuing constructive dialog on this important topic, including our foreign colleagues.

Many of us who were present during the open discussion following the formal, short presentations were impressed with the development of a growing consensus within the local meteorological community that a severe short-range prediction problem exists. Although much of the discussion consisted of detailed follow-up questions on the formal presentations, I tried to elicit statements on the following topics: Is the growing number of sometimes conflicting local forecasts received by the public from NWS and competing private firms a healthy trend? Will this add to public confusion on whom to believe? Do private meteorologists have either the right or the responsibility to issue their own severe weather watches and warnings (independent of NWS)? Do we really know anything about user needs for local weather forecasts?

Ellis Burton emphasized his belief that the NWS has no need to be in competition with the private sector. Ideally, the NWS should be a data collection and dissemination agency, but few private industrial forecasting companies would be willing to accept the responsibility for issuing severe weather warnings. Furthermore, some private forecasters have more modern equipment (e.g., color radar systems) than the WSFOs and can offer more specialized forecasts to clients. Ed Pearl agreed with these last two points and suggested that the existing warning system operates too slowly. Another view expressed was that a centralized agency must issue the severe weather warnings to avoid confusion from state to state and region to region.

Finally, several comments from the audience suggested that the Department of Commerce (DOC), not the NWS, should be held accountable for the manpower shortage and overall decline in effectiveness of the NWS operations. Improved forecaster training programs, especially in mesoscale dynamics and analysis, must be adequately budgeted from the DOC. The NWS is perceived by many to be a frequent victim of DOC cutbacks.

The short-range forecast problem is one that elicits strong views not only from operational meteorologists but also from the government and academic atmospheric research community. For this reason, and because of its special regional significance, it seems to be a growing focus of discussion at AMS chapter meetings. By encouraging such a dialog, the AMS chapters may have their best opportunity in many years to serve their profession and the nation. We invite further exchanges on this topic through correspondence to the BULLETIN.

The most important idea brought out in the discussions was that the large communications gap that currently exists between forecasters and researchers must be bridged before the rift becomes too great and neither side is yet able to understand or appreciate the contributions being made to solve important operational problems. We simply must learn to communicate more effectively with one another!

Acknowledgments. At the suggestion of Kenneth Spengler and Evelyn Mazur from AMS Headquarters, who were among the 115 participants, and at the urging of several other attendees, I asked each of the panelists to supply me with copies of their presentation notes for editing, fitting together, and submission to the BULLETIN. I wish to express my many thanks for encouragement and editorial assistance to D. K. Lilly and C. W. Newton.

References[3]

Augulis, R. P., 1978: Observations. *Nat. Wea. Dig.*, **3** (1), 32–33, 30.

Cook, D., and D. R. Smith, 1977: Trends in skill of public forecasts at Louisville, Ky. *Bull. Amer. Meteor. Soc.*, **58**, 1045–1049.

Fawcett, E. B., 1977: Current capabilities in prediction at the National Weather Service's National Meteorological Center. *Bull. Amer. Meteor. Soc.*, **58**, 143–149.

Glahn, H. R., 1976: Numerical-statistical forecasting in the U.S. National Weather Service. *Weather Forecasting and Weather Forecasts: Models*, NCAR, Boulder, Colo., pp. 448–522.

Howe, C. W., and H. C. Cochrane, 1976: A decision model for adjusting to natural hazard events with application to urban snowstorms. *Rev. Econ. Statis.*, **58**, 50–58.

Klein, W. H., 1976: Statistical forecasting of local weather from numerical prognoses. *Proceedings of WMO Symposium on the Interpretation of Broad-Scale NWP Products for Local Forecasting Purposes (Warsaw), WMO No. 450*, World Meteorological Organization, Geneva, pp. 85–92.

MacDonald, A. E., 1977: The Man/MOS Program. *NOAA Tech. Memo. NWS WR-112*, NWS Western Region, Salt Lake City, 21 pp.

Murphy, A. H., 1977: The value of climatological, categorical and probabilistic forecasts in the cost-loss ratio situation. *Mon. Wea. Rev.*, **105**, 803–816.

——, 1978: Subjective quantification of uncertainty in real-time weather forecasts in the United States. *Recent Developments in Real-Time Forecasting/Control of Water Resource Systems*, edited by A. Szollosi-Nagy and E. F. Wood, John Wiley, New York, in press.

——, and J. C. Thompson, 1977: On the nature of the non-existence of ordinal relationships between measures of the accuracy and value of probability forecasts: An example. *J. Appl. Meteor.*, **16**, 1015–1021.

Phillips, L. D., C. R. Peterson, and T. W. Keelin, 1978: The value of improved forecasts of climate for agricultural decision making. Final report, *PR 77-7-44*, Decisions and Designs, Inc., McLean, Va., 148 pp.

Sanders, F., 1977: Comments on forecast accuracy at the National Meteorological Center and elsewhere. *Bull. Amer. Meteor. Soc.*, **58**, 606.

Shuman, F. G., 1978: Numerical weather prediction. *Bull. Amer. Meteor. Soc.*, **59**, 5–17.

Snellman, L. W., 1977: Operational forecasting using automated guidance. *Bull. Amer. Meteor. Soc.*, **58**, 1036–1044.

Thompson, J. C., 1972: The potential economic benefits of improvements in weather forecasting. Final report, Grant No. NGR 05-046-005, Dept. of Meteorology, California State University, San Jose, 80 pp. ●

---

[3] *Editor's note:* All references are for the presentation by A. H. Murphy, pp. 1337–1340.

NOAA Technical Memorandum ERL WPL-39, July 1978

THE USE OF RADAR FOR STUDIES OF CLOUDS

E. E. Gossard

In the late 1950's and 1960's there were relatively large efforts at several laboratories using radars for studies of clouds. Some of this work, in fact, led to the deployment of the U.S. Air Force TPQ-11 radar ceilometer used operationally around the globe. However, the success of cloud sensing radars was generally marginal. There are several reasons why radars have, so far, been unimpressive in cloud studies: 1) except for the TPQ-11, the radars used have usually been designed for other purposes. For example, the wavelengths used have been in the centimeter range or longer. 2) The radar-observed bases and tops of clouds often did not agree well with the visible bases and tops. 3) No simple relationship was found between the radar observations and the cloud classification system of the meteorological services. According to Plank et al. (1954), of 89 periods during which echoes were received, slightly less than 50% could be classed as echoes from internationally defined cloud types. 4) For reasons never well understood, only about 50% of the clouds visually observed were detected by radar, and the presence of ice crystals seemed to be important. Harper (1964) reported that only about 50% of high clouds and 75% of medium clouds were detectable with a 0.86 cm wavelength radar in southern England.

For the reasons given above, radar cloud-sensing has generally not been vigorously pursued in the 1970's. However, in the last decade there have been several developments in radar technology that suggest that radar cloud-studies should be resumed. These include the ready availability of low-noise components which can significantly improve the sensitivity of radar receivers. Furthermore, the technology of satellite communications has produced, and made commercially available, microwave components at wavelengths of only a few millimeters—components that would have been expensive and inefficient a decade ago. Finally, new radars have been designed and built specifically for atmospheric investigations. Some of them, such as the FM-CW Doppler radar, have great flexibility in spatial and temporal resolution, and have the ability to sense the clear air in addition to hydrometeors. The incorporation of computers into the new radar systems provides many options in the processing of data. It now seems clear that operational wind-sensing radars will eventually be deployed as part of the routine observational system of the weather services, and it is important to determine early what cloud-sensing capabilities may be anticipated from such radars. Lending further urgency to the development of cloud-sensing systems, is the increasing realization that detailed short-term prediction of storm development requires observation at a much earlier stage in storm evolution than is provided by conventional weather radars.

Proceedings of the IEE International Conference on Antennas and Propagation, Part 2: 110-113, November 1978.

MILLIMETER WAVES - PROPAGATION AND APPLICATION

David C. Hogg

Wave Propagation Laboratory, National Oceanic and Atmospheric Administration, Boulder, CO., U.S.A.

INTRODUCTION

The impact of mm wavelength radio on both industry and government has so far been minimal. But some applications are now surfacing quite strongly: satellite and, to lesser extent, terrestrial communications, remote-sensing of the atmosphere for weather-forecasting purposes, and recognition systems for the military. Radio-astronomy has always had a lively vested interest. An appraisal of the first two of these activities will be given, emphasis being on the role played by the propagation and antennas in design of such systems.

Communications

Terrestrial. The conventional radio-relay approach, used so successfully in the past at centimeter wavelengths, encounters such strong attenuation by rain at millimeter wavelengths that the economic viability of communication systems at those wavelengths becomes questionable. Path lengths between repeaters become very short and the number of repeaters large. Nevertheless, application in urban areas where high information capacity is required may become worthwhile.

An interesting alternative to the conventional radio-relay arrangement, the so-called Hertzian cable (Arnaud et al (1), Arnaud (2)), may result in a larger available margin for rain attenuation. It consists of a series of pairs of focussing and redirecting cylindrical mirrors mounted on suitably high buildings as shown schematically in Figure 1. At 100 GHz (3 mm) for example, if the redirectors are of area one square meter, the interspacing can be at least 100 m; experiments (Anderson and Ruscio (3)) at 105 GHz utilizing 10 pair over an 0.8 km path show that a clear-day attenuation of less than 3 dB from transmitting to receiving waveguide can be achieved. Thus this type of system can have very little associated "path loss" and therefore a considerably larger fading range (to accommodate rain) than a conventional system.

The magnitude of attenuation by rain is demonstrated by measurements (DeLange et al (4)) at 60 GHz (5 mm) taken on a 1-km path throughout 1970 in New Jersey, U.S.A.

A cumulative distribution, given in Figure 2, shows that an attenuation of 30 dB is exceeded 0.005 percent of the time (about 25 minutes per year); at 100 GHz the attenuation would be about ten percent larger. Thirty dB at 60 GHz corresponds to an average rainrate of about 100 mm per hour over a 1-km path.

Microwaves have recently been observed to be subject to significant differential attenuation (Semplak (5)) and depolarization (Semplak (6)) in propagation through rain because of large oblate drops. But at millimeter wavelengths, both theory (Chu (7)) and experiment (4) show these effects to be small; a theoretical computation (7) of the depolarization at various frequencies as a function of attenuation by a 100 mm/hr rain is given in Figure 3. The marked change in behavior with wavelength occurs for two reasons: because the refractive index of water decreases rapidly from cm to mm wavelengths (less differential phase shift at the latter), and because the small rain drops (which do not deform because of surface tension) are most influential at mm wavelengths. From Figure 3, a rain-induced fade of 40 dB results in a cross-polarized component of -15 dB at 11 GHz, but only -35 at 100 GHz.

Satellite. Beacons at wavelengths near 1 cm have been mounted on synchronous satellites for measurements of earth-space propagation. ATS-5 (Ippolito (8)) and ATS-6, which afforded intermittent transmission at 30 GHz, have been followed by COMSTAR 1 (A and B) which continuously illuminate the contiguous U.S.A. at 28.5 GHz; several ground stations in locations of various climate are taking observations of 28.5 GHz attenuation and depolarization. It is found, in addition to the now familiar depolarization occurring during (Hogg and Chu (9)), preceding, and following fades caused by heavy rain, that some depolarization also occurs in the absence of fading. These occurrences (Cox et al (10)) are associated with ice crystals in high clouds which produce differential phase shift in orthogonal components of the polarization. However, the cross-polarized power thus produced is small, resulting in acceptable crosstalk levels in PCM transmission systems.

The large mm-wave attenuation produced at times by rain in most locations make site diversity mandatory if good all-weather reliability in communications is required. Separation of two sites by several miles on a baseline normal to the earth-space path (9) provides adequate reliability at cm wavelengths, but at mm wavelengths more than two sites may be necessary and experiments have yet to be done.

Remote Sensing

Passive remote probing of the atmosphere is somewhat more subtle than the communications problem. For example, in temperature profiling, the weather forecaster requires absolute temperature to an accuracy within 1^{o}C as a function of altitude. Multi-channel radiometers near the 60 GHz absorption line* are used to monitor continuously the temperature profile; this means that the absorption (emission) coefficients must be accurately known, the equipment be both sensitive and stable, and the profiles be retrievable in the presence of other absorbing constituents such as water vapor and liquid water. It is also useful, for forecasting and weather modification, to measure the water vapor and liquid in the atmosphere. The remote sensing can be performed from the earth, and from orbiting or synchronous satellites; but from satellites, the radiometers must contend with a changing background, land or sea. An example of profiles retrieved (Westwater (11)) from a five-channel earth-based radiometer is shown in Figure 4. Also shown in this Figure are profiles that can be retrieved using a combination of active and passive techniques.

---

*The channels are chosen on the side of the line such that the radiometers receive more or less radiation from various altitudes.

In the case of water vapor, detailed profiling will have to await research at frequencies on the side of the strong absorption line near 180 GHz (1.65 mm).

Antennas for Remote Sensing

The requirements on antennas for terrestrial remote sensing are similar to those for satellite communications; in both cases, performance must not be degraded by precipitation at the site. Unfortunately, radomes and the like do not alleviate the problem because the attenuation and noise generated by a liquid layer on a transmission window degrade performance much more than that same layer on a reflecting surface (9). For this reason, antenna systems such as that shown in Figure 5 are designed for remote sensing (Hogg et al (12)). The radiometers and the antenna are in a sheltered environment; radiation from the atmosphere enters the antenna by way of an exposed flat reflector and a thin window protected from the elements by a cowling. In remote sensing from satellites (Staelin et al (13)), these problems of course do not arise, and the constraints on the antennas are simply low loss, equal beamwidth (where several frequencies are used), and light weight. In both terrestrial and satellite passive sensors, equal beamwidth at the several frequencies is necessary to enable correction for emission from clouds.

We can conclude, therefore; that there are applications of millimeter waves, beyond those of the military and radio astronomy, which are reaching the practical state. The future looks particularly promising in remote sensing, where the losses and other electromagnetic properties of atmospheric constituents offer useful characteristic signatures.

REFERENCES

1. Arnaud, J. A., Hogg, D. C., and Ruscio, J. T., 1972, "Focussing of 52-GHz beams by cylindrical mirrors", IEEE, MTT-20, 5, 344-5.

2. Arnaud, J. A., 1976, "Beam and fiber optics", Academic Press, New York, NY.

3. Anderson, I., and Ruscio, J. T., 1975, "106 GHz low-loss beam waveguide", Electronics Letters, 11.

4. DeLange, O. E., Dietrich, A. F., and Hogg, D. C., 1975, "An experiment on propagation of 60 GHz waves through rain", Bell Syst. Tech. J., 54, 1.

5. Semplak, R. A., 1970, "Effect of oblate raindrops on attenuation at 30.9 GHz", Radio Sci., 5, 559-564.

6. Semplak, R. A., 1974, "Simultaneous measurements of depolarization by rain using linear and circular polarization at 18 GHz", Bell Syst. Tech. J., 53, 400-404.

7. Chu, T. S., 1974, "Rain induced cross polarization at centimeter and millimeter wavelengths", Bell Syst. Tech. J., 53, 1557-1579.

8. Ippolito, L. J., 1971, "Effects of precipitation on 15.3 and 31.6 GHz earth-space transmissions with the ATS-5 satellite", Proc. IEEE, 59, 189-205.

9. Hogg, D. C., and Chu, T. S., 1975, "The role of rain in satellite communication", Proc. IEEE, 63, 9, 1308-1331.

10. Cox, D. C., Arnold, H. W., and Hoffman, H. H., "Depolarization of 19 and 28 GHz earth-space signals by ice particles", (to be published in the May-June issue of Radio Science).

11. Westwater, E. R., 1978, "Improved determination of vertical temperature profiles of the atmosphere by a combination of radiometric and active ground-based sensors", Proc. 4th Symp. Meteor. Observ. & Instru., American Meteorological Society, Denver, CO., Apr. 10-14, 153-157.

12. Hogg, D. C., Guiraud, F. O., Howard, J., Newell, A. C., Kremer, D. P., and Repjar, A. G., "An antenna for remotely sensing the troposphere simultaneously at 21 and 32 GHz", (to be submitted to IEEE AP/S).

13. Staelin, D. H., Cassel, A. L., Kunzi, K. F., Pettijohn, R. L., Rosenkranz, P. W., and Waters, J. W., 1975, "Microwave atmospheric temperature sounding: effects of clouds on the Nimbus 5 satellite data", J. Atmos. Sci., 32, 1970-1976.

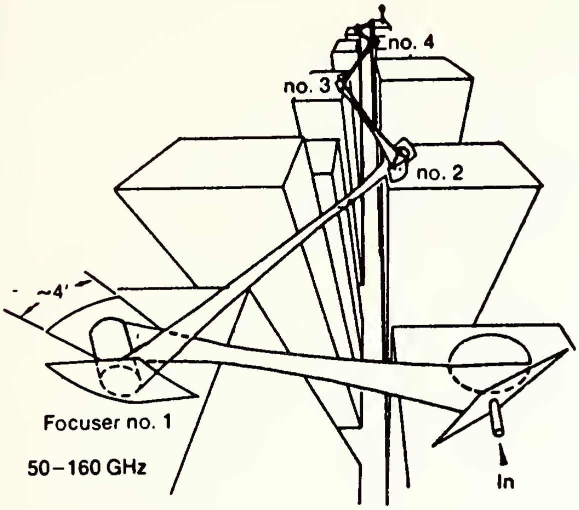

Fig. 1 A Millimeter-Wave Beam-Wave System Called the Hertzian Cable.

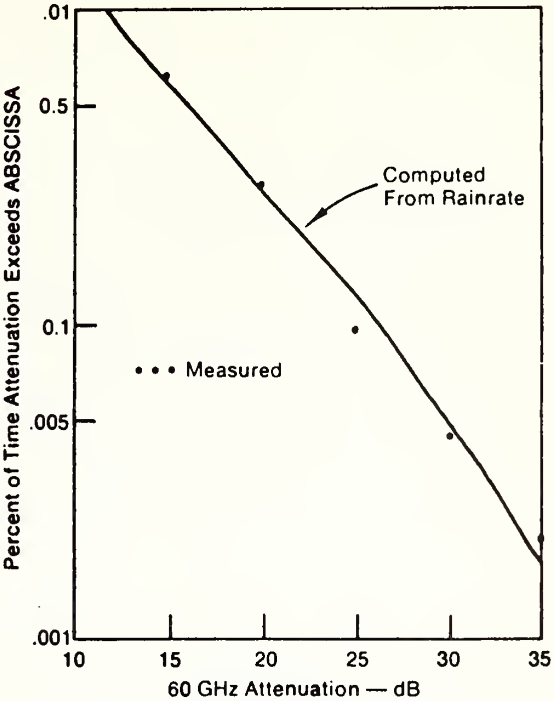

Attenuation Measured on a 1 Km Path Compared With Computation Using Point Rain Rate.

Fig. 2 Cumulative Distribution of 60 GHz Attenuation by Rain — One Year in N.J., U.S.A.

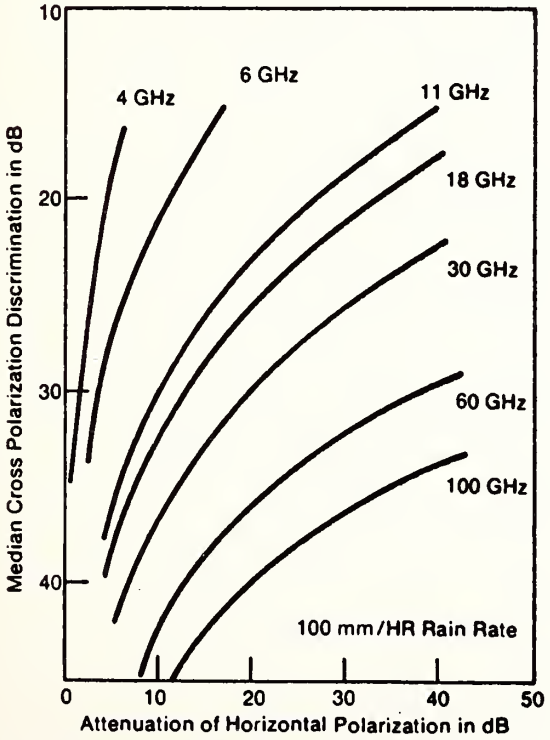

Fig. 3 Cross Polarization Produced by a 100 mm/hr Rainfall at Various Frequencies.

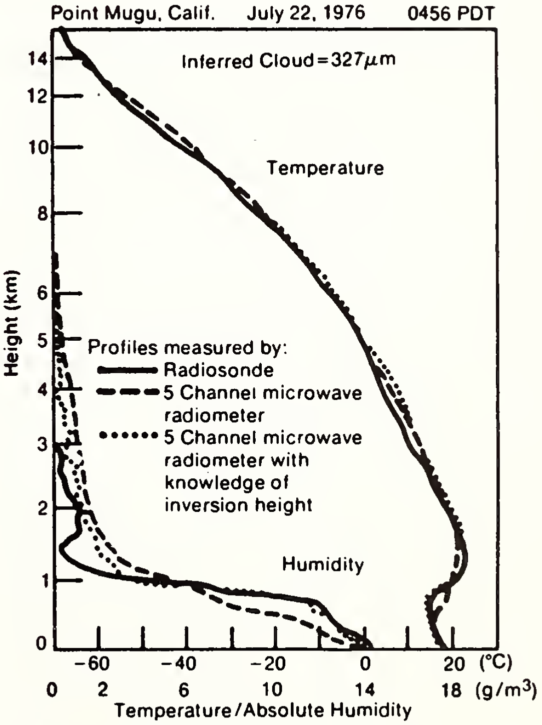

Fig. 4 Profiles of the Temperature and Humidity of the Troposphere Measured by Ground-Based Millimeter-Wave Remote Sensors.

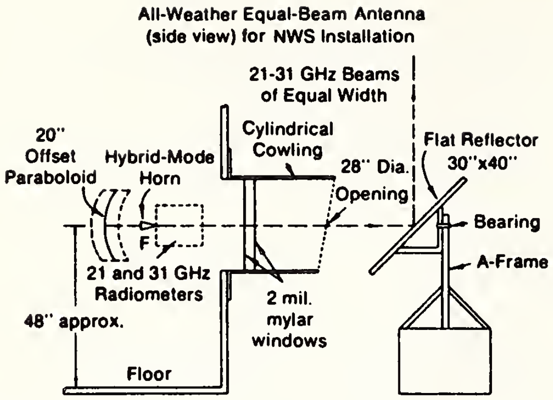

Fig. 5 Design of an Antenna System for Passive Remote Sensing.

Proceedings of the Third U. S. National Conference on Wind Engineering Research, 81-88, February 26-March 1, 1978.

THE BOULDER ATMOSPHERIC OBSERVATORY

William H. Hooke
Chief, Atmospheric Studies Program Area
NOAA/ERL/Wave Propagation Laboratory
Boulder, Colorado 80302

The Wave Propagation Laboratory (WPL) of NOAA, in cooperation with the National Center for Atmospheric Research (NCAR), has just completed construction of the Boulder Atmospheric Observatory (BAO), a facility for meeting a wide range of needs within the research community. Showpiece of the facility is a 300-m tower, instrumented at eight fixed levels with fast-response temperature sensors and sonic anemometers for measuring not only mean wind and temperature but also turbulent fluctuations in these quantities. The tower also has available an instrumented carriage for providing continuous height profiles of quantities of interest. In addition to the tower, the facility features remote-sensing systems such as acoustic echo sounders and optical anemometry for studying the planetary boundary layer (PBL). A quarter-million dollar minicomputer system provides for data acquisition, processing, and archiving. We intend to operate the facility ultimately on a continuous basis, in order to provide a climatology of PBL turbulence statistics.

Although the BAO is intended for use by the parent organizations, power and a number of extra data channels are available at each instrumented tower level for experiments of other groups. Data may be fed into the central data-processing facility or recorded separately. We are developing our computer system so that it may be readily used by outside workers, either at the BAO site itself or by remote terminal. Already we have been approached with plans to use the BAO on experiments including bird flight, micrometeorology, instrument calibration, and studies of the tower structural dynamics itself.

The talk concludes with an outline of the major work to be accomplished at the BAO in 1978.

1. Introduction

Since its founding in 1967, the Wave Propagation Laboratory (WPL) of NOAA has endeavored to improve the nation's geophysical research and services through the development and application of remote sensors. The past decade has seen a stream of devices and systems flowing from the laboratory to the outside world, covering the gamut from lidars, radars, and acoustic echo sounders, to radiometry, thunderstorm gust-front-detection systems for use at airports, and sea-state and sea-current radars. As each of these systems has progressed through a sequence of concept identification, technique development, and application, it has been necessary to provide independent tests and evaluations of the system's performance. For many years in the past, the laboratory has attempted to carry out such comparisons and calibration using a meteorological tower at Haswell, Colorado, several hundred kilometers distant from Boulder. Repeatedly we have found that the logistics associated with mounting experiments at this facility were so cumbersome and expensive as to preclude field work of more than two weeks' duration in any given year. Our activity at this site was thus limited to field programs in 1969, 1972, 1974, and 1975. While these were quite productive (see, e.g., Little and Gossard, 1975), they often left many questions unanswered. For this reason, WPL has worked for some time to develop a facility within easy commuting distance from Boulder, where we could:

a) test and calibrate new meteorological remote-sensing systems.
b) make initial application of such systems to atmospheric research
c) develop an economic, mobile remote-sensing capability for carrying out boundary-layer studies in other parts of the world.

The result is the Boulder Atmospheric Observatory (BAO).

2. The Instrumented Tower

The major feature of the BAO is its 300-m meteorological tower, of guyed open-lattice design. The structure is galvanized steel with three legs, spaced 3 m apart. Designed (a) to support an additional 200 m should that ever prove desirable and economically feasible, and (b) to withstand 77 ms^{-1} winds with 1.3 cm of radial ice on all exposed surfaces, the tower is a very impressive structure (figure 1). It is located on gently rolling prairie some 25 km east of the foothills of ~~the~~ Rockies (figure 2). Although many of the surrounding sections of land have been undermined to tap a major coal field in the area, the tower site itself lies over a block upthrust or horst area that has not been undermined, thus providing sufficient support for the tower weight and the guy wire tension. The tower proper rests on a foundation cap which in turn surmounts three concrete piers each 1.5 m in diameter and 17 m deep.

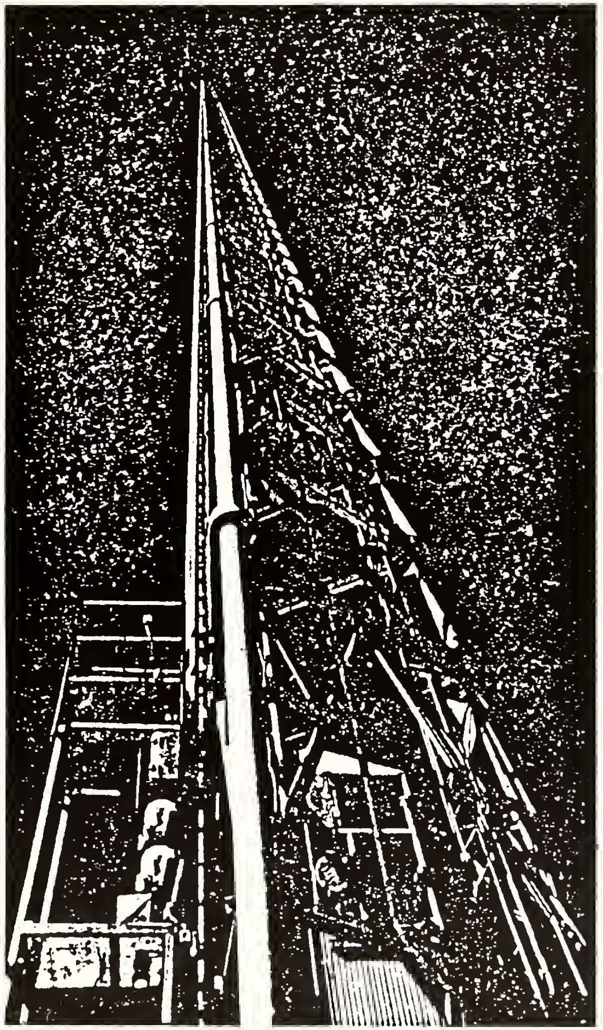

Vern Walker, Courtesy of the Boulder Daily Camera

Figure 1. The BAO Tower

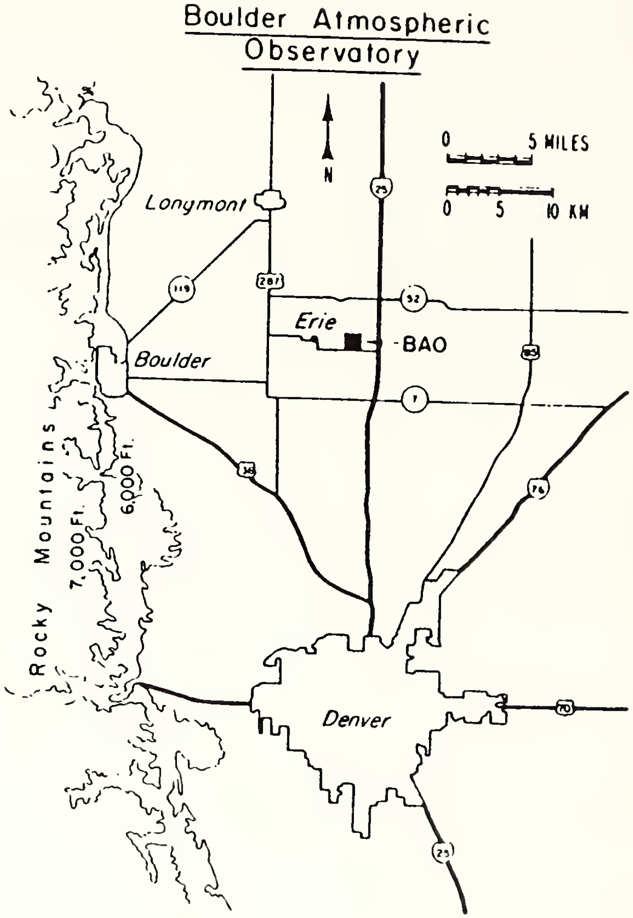

Figure 2. Location of the BAO

A two-man elevator inside the tower provides access to the eight instrumented levels; these are fixed at heights of 10m, 22m, 50m, and every 50m above (figure 3). All levels have identical instrumentation.

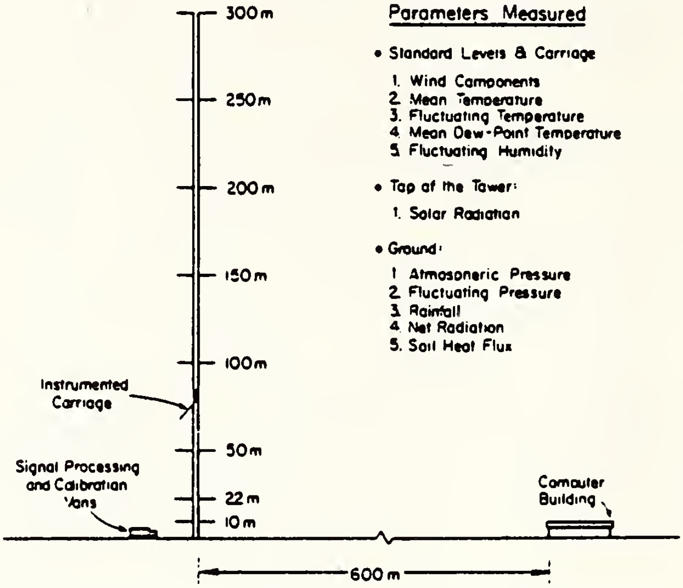

Figure 3. The Tower Instrumentation

At each level the instruments are mounted on a 4m telescoping boom attached to a hinged support with fine adjustments for leveling. Figure 4 is a drawing of a boom and its instrumentation. Fluctuat-

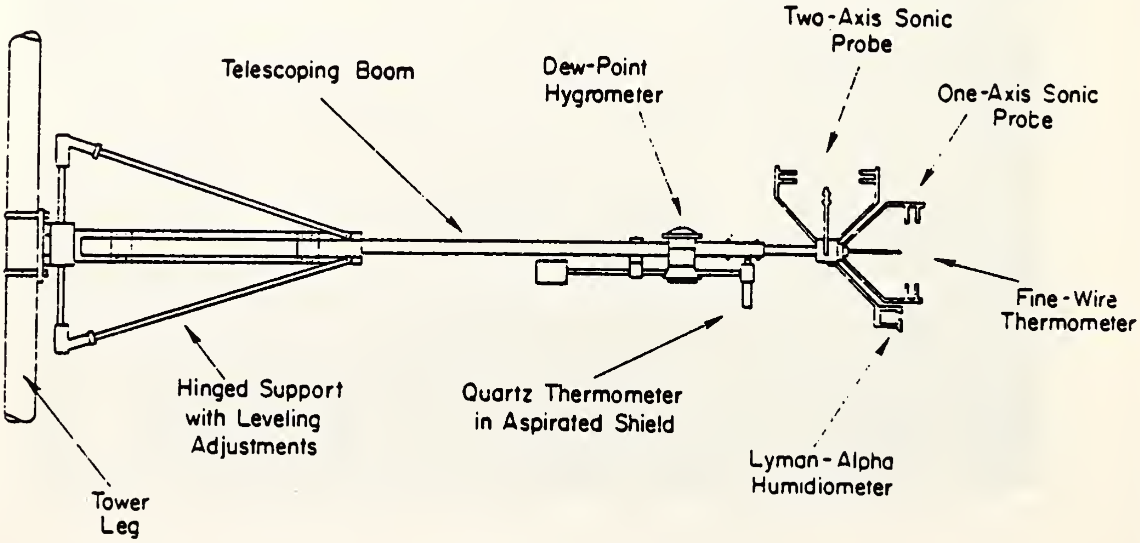

Figure 4. A Tower Boom

ing temperature is measured by a platinum-wire thermometer. Three-axis sonic anemometers are used to measure both the mean wind and turbulent fluctuations in the mean wind. Humidity fluctuations are measured by a Lyman-α humidiometer. (Ultimately all levels will have these expensive humidity sensors; however, initially this particular instrumentation will be sparse.) The other two sensors on the boom are slow-response devices for measuring mean temperature and mean dewpoint. More detailed descriptions of the instruments and their operation may be found in the paper by Kaimal (1978) and the references therein. Because the limited climatological data available from the Denver area suggest that prevailing winds at the site are from the southeast during the summer and from the northwest during the winter, we have two booms at each level for switching the sensors on a seasonal basis in order to obtain optimal exposure. Obviously, however, there will be periods when data will be less meaningful because the instruments are in the lee of the tower.

In addition to the fixed levels of instrumentation, a moveable carriage on the southwest face of the tower permits continuous profiling or fixed-level operation at any desired height. A boom on the carriage supports the full complement of instruments available at the fixed levels. The carriage can support an additional 1200 kg of equipment for special experiments. The carriage and each fixed level of the tower carry 110-120 AC power and signal cables additional to the cabling and power for the standard instrumentation.

3. Ground-Based Sensors

There are two major categories of ground-based meteorological sensors at the BAO. The first are in situ sensors measuring atmospheric pressure, rainfall, net radiation and soil heat flux. In addition, a spatial array of eight microbarographs distributed over a 2 km radius about the tower senses small amplitude pressure fluctuations (as small as 10^{-4} mb) associated with gust fronts and gravity waves (Hooke, 1975). The second category is made up of remote sensors developed by WPL over the past decade. These include a triangular array of optical crosswind anemometers located at the outer guy anchors (Lawrence et al., 1972) for measuring surface winds and horizontal convergence. (Recognizing that the outer guy anchors are likely to prove popular points for locating ground-based equipment, we are making additional power and signal cables available at these sites as well.) An FM-CW Doppler radar (Chadwick et al., 1976) will be available, at least initially, to measure winds in the clear air to altitudes of 1 km. Three acoustic echo sounders, one at each of the outer guy anchors, will be used to document planetary-boundary layer (PBL) heights, the presence of convective plumes, and the structure of stably stratified layers. In addition, one of the sounders will have a bistatic Doppler wind-sensing capability through the addition of two fan-beam acoustic transmitters.

Although the basic facility comprises these remote probes, additional WPL probing systems, including microwave radiometers, pulsed and FM-CW lidar systems, and pulse dual-Doppler radar systems can be made available for brief periods by arrangement.

4. Data Acquisition and Processing

A digital computer at the BAO site itself will handle data acquisition from the tower and ground-based systems. Originally, a Mobile Micrometeorological Observation System (MMOS) used in past PBL experiments (Haugen et al., 1971; Kaimal et al., 1976) will be used for this purpose. Ultimately the task will be taken over by a new PDP 11/34 computer, supplied by NCAR. This system will be housed in temporary buildings some 600m southwest of the tower, pending construction of a permanent building by NCAR's Field Observing Facility at the same site. Underground cables will link the computer to the tower instrumentation. Since it has been clear to us from the outset that with the exception of certain special periods of data collection we will not be able to record all the sampled data (fast-response data of 10 Hz and slow-response data at 1 Hz) on a climatological basis, we have settled on a procedure for storing high-frequency turbulence information in the form of smoothed spectral and cospectral estimates and low-frequency information as times series. In this way we can reduce the storage of high-frequency information in each 20-minute period to roughly 24 data words per channel. Details are given by Kaimal (1978). The low-frequency information is contained in two simultaneous time series. To compute the low-frequency portion of the meteorological spectra, we store 10-second block-averaged data (100 points of 10 Hz data). The block-averaging reduces aliasing. However, in order to compute variances, fluxes and moments, we also store a grab sample (the last sample in each 10-second block).

Ultimately, the PDP 11/34 system will be in communication with a PDP 11/70 system at our laboratory in Boulder, which will feature (a) a 100-million-word disc memory, able to store the last month of BAO data, and (b) interactive computer terminals and peripheral analyses of the data. Connections with NOAA and NCAR central computer systems are also contemplated.

5. Future Plans

Our major plans for the immediate future include the following:

1) Completion of the tower instrumentation. This has not been done at the time of this writing, but it should be done by the time of presentation.

2) A site-evaluation experiment in April 1978. Most boundary-layer theory has been developed for level, homogeneous terrain. This site does not meet those standards, raising

the twin issues of (a) departures from the idealized case, and (b) the representativeness of the tower site. We will investigate both these points in April using the NCAR PAM network and aircraft flybys on 20-km legs downwind and crosswind of the tower.

3) An August 1978 workshop of PBL researchers.

4) An August 1978 study of the convective PBL, using dual Doppler radars and chaff, aircraft, and the NCAR PAM network. This experiment has multiple objectives in the areas of remote-sensor development, PBL processes, transport and diffusion in the PBL, and PBL modeling. Some severe-storm PBL work will also be attempted.

5) A summer 1979 WMO/CIMO intercomparison of low-level sounding systems for the World Meteorological Organization.

We encourage outside use of this facility, and we particularly solicit comments from you concerning applications of this facility to wind engineering. Anyone wishing to mount an experiment at the BAO should either write to me or phone (303) 499-1000, x6378.

References

Chadwick, R. B., K. P. Moran, R. G. Strauch, G. E. Morrison, and W. C. Campbell, A new radar for measuring winds, Bull. Am. Meteorol. Soc., 56, 964-969 (1976).

Haugen, D. A., J. C. Kaimal, and E. F. Bradley, An experimental study of Reynolds stress and heat flux in the atmosphere surface layer, Quart. J. Roy. Meteorol. Soc., 97, 168-180 (1971).

Hooke, W. H., Sensitive microbarographs used to study atmospheric gravity waves, Proc. Third AMS Symposium on Meteorological Observations and Instrumentation, Washington, D.C., February 10-13, 1975, 175-178 (1975).

Kaimal, J. C., J. C. Wyngaard, D. A. Haugen, O. R. Coté, Y. Izumi, S. J. Caughey, and C. J. Readings, Turbulence structure in the convective boundary layer, J. Atmos. Sci., 33, 2152-2169 (1976).

Kaimal, J. C., NOAA instrumentation at the Boulder Atmospheric Observatory, Proc. Fourth AMS Symposium on Meteorological Observations and Instrumentation, Denver, Colorado, April 10-14, 1978 (to be published).

Lawrence, R. S., G. R. Ochs, and S. F. Clifford, Use of scintillations to measure average wind across a light beam, Appl. Optics, 11, 239-243 (1972).

Little, C. G., and E. E. Gossard, The 1972 Haswell, Colorado, atmospheric boundary layer experiment, Proc. Third AMS Symposium on Meteorological Observations and Instrumentation, Washington, D.C., February 10-13, 1975, 187-192 (1975).

NOAA Technical Memorandum ERL WPL-37, September, 1978

FEASIBILITY STUDY OF SATELLITE-BORNE LIDAR GLOBAL WIND MONITORING SYSTEM

R. M. Huffaker (Editor)

We have analyzed the feasibility of monitoring the global wind patterns from orbital altitudes to 800 km using a coherent infrared lidar. A one-meter diameter telescope is assumed on the satellite, collimating the 10 J pulses that are 3-7 μs in duration from a CO_2 isotope gas laser. Pointing accuracy of 50 or 100 μrad is assumed with short-term pointing jitter of 2 μrad during the 4 ms pulse time-of-flight. The lidar scans in a conical pattern around the nadir point in 12s while pulsing at an average rate of 8 Hz. Using realistic models of atmospheric attenuation and aerosol backscatter, we show that it should be possible to measure global winds by means of the Doppler shift at 1 km height intervals throughout the troposphere with an accuracy of 1-2 m s^{-1}, so long as dense clouds do not obstruct the line-of-sight. Even for stormy conditions, case studies using actual cloud statistics show that for most cases the wind velocity can be accurately measured in a 300 X 300 km patch to 1-2 m s^{-1} down to altitudes of 1 km above the surface. Cirrus clouds only slightly attenuate the beam and actually provide enhanced backscatter for measuring upper-tropospheric winds. A conceptual design for a Space Shuttle feasibility demonstation lidar has been completed.

Program Development Plan for Prototype Regional Observing and Forecasting Service (PROFS), September 1978

PROFS PDP Panel
C. G. Little (Chairman)
D. W. Beran (Editor-in-chief)

This Program Development Plan is an updated version of the original document completed by the Profs PDP panel in August 1977. While the basic concept and goals of PROFS have remained intact this plan incorporates the thinking of a wider constituency. Many of the changes and improvements resulted from a PROFS PDP workshop held in March, 1978, which was attended by representatives from NOAA's research and operational components, other government agencies with an interest in local weather services, and the private sector.

Preprint Volume; Fourth Symposium on Meteorological
Observation and Instrumentation, 150-152, American
Meteorological Society, April 1978.

GROUND-BASED PASSIVE MICROWAVE SENSING OF WATER VAPOR AND CLOUD LIQUID

Ed R. Westwater and F. O. Guiraud

NOAA/ERL/Wave Propagation Laboratory
Boulder, Colorado 80302

1. INTRODUCTION

Total precipitable water is an important component of many moisture-related processes in the atmosphere. For example, the occurrence of convective clouds and precipitation is closely related to the amount of water vapor in the layer from the surface to 400 mb (Battan and Kassander, 1960). Consequently, measurements of integrated vapor have been used in the design of cloud seeding experiments (Dennis and Koscielski, 1969). Continuous observations of this quantity may also be useful in operational precipitation forecasting, and in meteorological research applications such as the estimation of water vapor flux into convective cells (Leichter and Dennis, 1974).

At the present time, integrated water vapor can be measured in several ways. Operationally, this quantity can be obtained by integrating radiosonde soundings and can be estimated, between soundings, by statistical regression of surface observations. Other measurement techniques include the spectral hygrometer and aircraft soundings using a microwave cavity refractometer.

None of the above techniques is completely appropriate for long term, continuous, and near all-weather operation. Because of its operational simplicity, and its proven performance in such areas as long term attenuation monitoring, microwave radiometry seems ideally suited for routine monitoring of moisture and its changes with time. We will summarize below, following Westwater (1978), how a dual-channel microwave radiometer can provide near all-weather measurements of integrated water vapor and cloud liquid.

2. FACTORS DETERMINING THE ACCURACY OF RADIOMETRIC DETERMINATION OF LIQUID AND WATER

It is conventional in microwave radiometry to express atmospheric radiative emission intensity as an equivalent black body temperature, or brightness temperature. As shown by Hogg and Chu (1975), brightness temperature can be related to total absorption under conditions of low attenuation (optical depth < ∿ 1). This absorption can, in turn, be directly related to corresponding amounts of integrated water vapor V and cloud liquid L. Thus emission measurements of low attenuation at a vapor sensitive frequency and a cloud sensitive frequency allow separation of the two water phases. Various errors, both in measurement and in physical constants, affect the accuracy of this separation:

(a) Errors in mean radiating temperature. These errors result from the unknown spatial distributions of temperature, water vapor, and cloud liquid which affect the determinations of V and L.

(b) Measurement errors in brightness temperature.

(c) Uncertainties in dry attenuation. This attenuation arises from the "wing" contribution of the 5 mm oxygen band. It can be predicted climatologically to about 10%.

(d) Errors in water vapor absorption coefficients. These errors arise from uncertainties in molecular constants, spectral line shape, etc., and through variations in atmospheric profiles that cannot be predicted climatologically. Errors in this category are the limiting factor in the determination of V during clear conditions.

(e) Errors in cloud liquid attenuation coefficient. For non-precipitating clouds, this uncertainty arises primarily from uncertainties in cloud temperature. Rain will cause difficulties but it seems likely that useful estimates of V can still be obtained for low rain rates (< 5 mm/hr).

3. ESTIMATION OF ACCURACY OF INTEGRATED VAPOR AND LIQUID DETERMINATION

We estimated the accuracy in V and L determination for two pairs of frequencies (20.6, 31.65) and (22.235, 31.65) GHz. The 20.6 and 22.235 GHz channels are vapor sensitive; the 31.65 is sensitive to clouds. The (22.235, 31.65) is already in an operational sounder on a satellite (Staelin et al., 1975); the (20.6, 31.65) pair uses a water channel at which the uncertainties in vapor absorption coefficient are small.

Typical results on overall accuracy of vapor and liquid retrievals, for values of average moisture ranging from 4 to 45 mm, and cloud attenuations up to 15 dB, are shown in Fig. 1 (in this and Fig. 2, relative accuracy means standard deviation divided by true value). Several features are evident from this figure: (1) for clear skies, the 20.6 GHz frequency yields a better accuracy in V than the 22.235 GHz frequency; for V > 10 mm, this accuracy generally is better than ∿ 15%. (2) at some cloud density the accuracy for determining V at 22.235 GHz will exceed that of the lower frequency channel; (3) except for the extremes of the cloud error curves, the relative accuracy of the derived

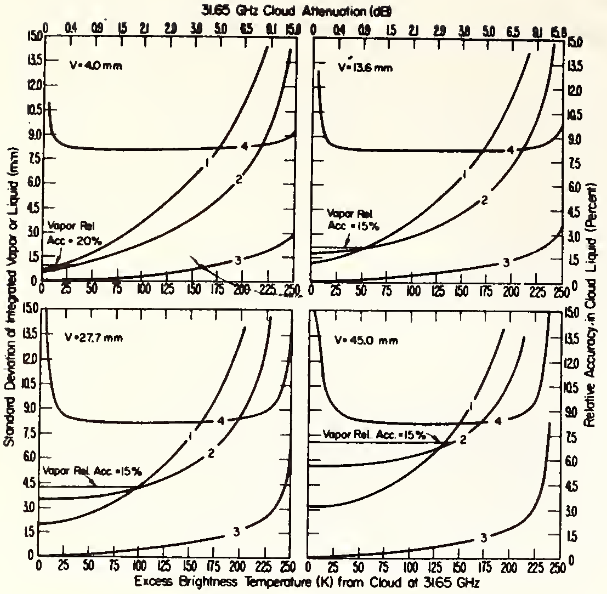

Figure 1. Errors in the determination of precipitable water as a function of cloud emission. 1 = vapor determination with (20.6, 31.65 GHz) system, 2 = vapor determination with (22.235, 31.65 GHz) system, 3 = liquid determination with (22.235, 31.65 GHz) system, 4 = relative accuracy in liquid with (22.235, 31.65 GHz) system.

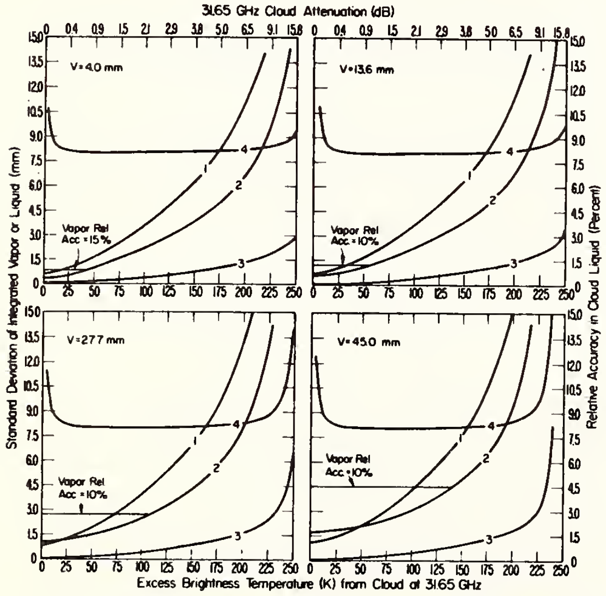

Figure 2. Errors in the determination of precipitable water as a function of cloud emission. Same notation as in Figure 1. Molecular constants and absorption equations are assumed to be correct.

amount of cloud liquid is better than 10% and is quite insensitive to the amount of water vapor present. To estimate system reliability from these curves, it is necessary to know the percentage of time that cloud attenuation levels (or excess brightness temperature levels) are exceeded. Lo et al., (1975) reported attenuation at 35 GHz for various types of non-precipitating clouds. Even in pre-rain clouds, the largest observed liquid attenuation was 2.3 dB. In addition, some long term statistics are available. For example, at Holmdel, N.J., Wilson (1969) determined that the excess attenuation at 30 GHz exceeded 3 dB about 1% of the time for nighttime zenith observations, and it exceeded 3 dB 2% of the time for daytime solar tracking. Our extrapolation to 30 GHz of Bergmann and Muller's (1976) observations of sky brightness at 13 and 18 GHz, taken at Longmont, Colorado, implies that 3 dB would be exceeded only about 0.1% to 0.2% of the time. Thus, for many locations at least, these rather conservative attenuation estimates along with the accuracies indicated in Fig. 1 suggest a high degree of system reliability.

A large component of the total error in water vapor mass absorption coefficient and in dry absorption is the error due to uncertainties in molecular absorption equations. If theoretical and experimental developments would lead to substantial improvement of these calculations, then a large improvement would be obtained in the accuracy of deriving water vapor V during clear and moderately cloudy skies. To show this, we repeated our calculations with conditions identical to those used in calculating Fig. 1, except that uncertainties in path-averaged gaseous absorption were from profile variation only, molecular absorption equations being assumed exact. The results are shown in Fig. 2. Note that the two water channels yield roughly the same accuracy for clear conditions, with the 22.235 GHz channel exhibiting a clear superiority during cloudy conditions. As is evident by comparison with Fig. 1, a large reduction in error in V occurs when the molecular component of absorption error is eliminated.

An important factor in correcting V for clouds whose 31 GHz attenuation is greater than ∿ 1 dB is the average cloud temperature. Curves of Fig. 3, calculated assuming no error in molecular constants, show this accuracy for various standard deviations of cloud temperature δT_c. Thus, for example, a standard deviation of 1.5 mm in V could arise from a cloud whose attenuation is 0.9 dB and whose temperature uncertainty is 7.4 K or from one whose attenuation is 2.5 dB but whose δT_c is 1 K. Similar calculations investigating the sensitivity to noise levels in the measurement system indicate that the accuracy in V does not degrade seriously until the brightness temperature error exceeds 1 K.

4. CONCLUDING REMARKS

Calculations indicate that, when the 31 GHz cloud attenuation is less than 3 dB, a dual frequency ground-based radiometric system can provide useful measurements (usually within 15%) of integrated water vapor and cloud liquid water. These calculations, coupled with available attenuation statistics, imply that such a system could operate 98 - 99% of the time for many locations.

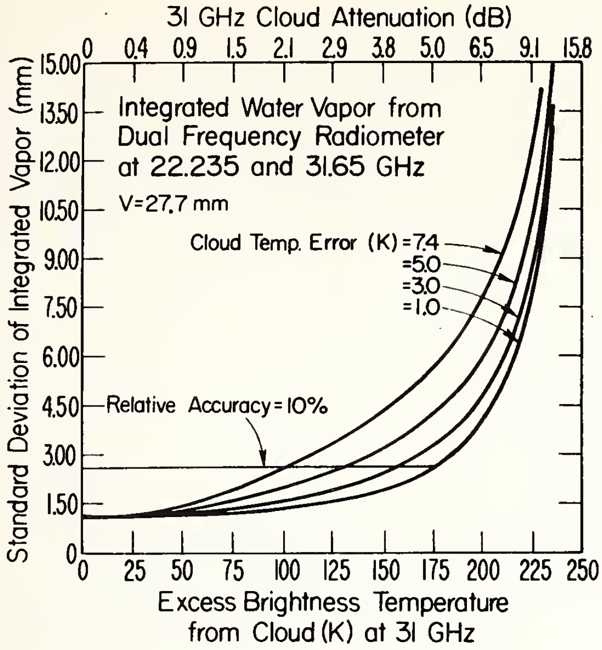

Figure 3. Errors in the determination of precipitable water for different uncertainties in cloud temperature.

We have recently constructed a dual-channel system at 20.6 and 31.65 GHz. The system is now undergoing performance tests. Current plans include the initial operation of the system at Stapleton International Airport, Denver, Colorado, for about 6 months in 1978. Later, the system will be taken to a more humid location for further tests and evaluation.

5. REFERENCES

Battan, L. J., and A. R. Kassander, 1960: Design of a program of randomized seeding of orographic cumuli. *J. Meteorol.*, 17, 583-590.

Bergmann, H. J., and E. E. Muller, 1976: A radiometer experiment at 13 and 18 GHz to study satellite system site diversity. *IEEE International Conference on Communication*, Philadelphia, PA. June 14-16, 1976, Vol. I, 12.1.

Dennis, A. S., and A. Koscielski, 1969: Results of a randomized cloud seeding experiment in South Dakota. *J. Appl. Meteor.*, 8, 556-565.

Hogg, D. C., and T. Chu, 1975: The role of rain in satellite communications. *Proc. IEEE*, 63, 1308-1331.

Leichter, I., and A. S. Dennis, 1974: Moisture flux and precipitation studies of convective storms in western South Dakota using pibal and radar data. *Conference on Cloud Physics*, Oct. 21-24, 1974, Tucson, Arizona, American Meteorological Society, 438-441.

Lo, L., B. M. Fannin, A. W. Straiton, 1975: Attenuation of 8.6 and 3.2 mm radio waves by clouds. *IEEE Trans. Ant. Prop., AP-23*, 782-786.

Staelin, D. H., A. L. Cassel, K. F. Kunzi, R. L. Pettyjohn, R. K. L. Poon, P. W. Rosenkranz and J. W. Waters, 1975: Microwave temperature sounding: effects of clouds on the Nimbus 5 satellite data. *J. Atmos. Sci.*, 32, 1970-1976.

Westwater, E. R., 1978: The accuracy of water vapor and cloud liquid determination by dual-frequency ground-based microwave radiometry. To be published in *Radio Science*.

Wilson, R. W., 1969: Sun tracker measurements of attenuation by rain at 16 and 30 GHz. *Bell Syst. Tech. J.*, 48, 1383-1404.

(Reference: II.1)

Preprint Volume; WMO Symposium on Boundary Layer Physics Applied to Specific Problems of Air Pollution, 39-43, 19-23 June, 1978.

PROGRESS IN RESEARCH ON TURBULENT FLOW

John C. Wyngaard
Cooperative Institute for Research in Environmental Sciences
University of Colorado/NOAA
Boulder, CO 80309
and
Wave Propagation Laboratory, NOAA
Boulder, CO 80302

1. Introduction

Our understanding of turbulent flow is limited not only by the intractability of the governing equations, which have defied several generations of researchers, but also by the difficulties involved in making the accurate, detailed measurements of turbulence structure necessary to shed light on the underlying physics. In spite of these formidable obstacles, turbulence research proceeds, and in this brief review we discuss some recent advances which have increased (or promise to increase) our understanding of turbulence.

Virtually every portion of the atmosphere is, at one time or another, turbulent. The general circulation of the atmosphere is often treated as two-dimensional (2-D) turbulence, but 2-D turbulence is dynamically quite different from the 3-D variety, as discussed by Tennekes (1978). We will cover only the 3-D variety here; this is the type of turbulence found continuously in the planetary boundary layer (PBL), where it transfers heat, momentum, and moisture between the surface and the free atmosphere and causes a variety of other effects which impact on society. The PBL is a rich turbulence research medium, and many of the advances cited here stem from studies of the PBL.

2. Advances through computation

Large, fast digital computers have created new opportunities in turbulence research. Calculations which were out of the question only 20 years ago can now be cheaply done. These can be separated naturally into three general types, which we now consider in turn.

a) Numerical solutions of Navier-Stokes equations

Turbulence is inherently three dimensional with complex spatial structure; its basic nonlinearity couples dynamically all its scales of motion, from the largest, energy-containing eddies to the smallest, dissipative ones. Thus any direct, numerical solution of the Navier-Stokes (N-S) equations must be 3-D and must resolve the entire scale range. While scientific computers have increased dramatically in size and speed over the past 20 years, they remain hopelessly inadequate for the task of calculating 3-D geophysical turbulence directly.

Nevertheless, there is continuing interest in 3-D numerical solutions of the N-S equations, since they do reveal structure inaccessible in other ways. One of the largest, fastest, and newest machines, the CRAY-1 at NCAR in Boulder, Colorado, is now being programmed for numerical solution of the N-S equations on a $(64)^3$ grid in wavenumber space; $(128)^3$ calculations seem feasible within a few years. These calculations are, within numerical approximations and certain idealizations involving forcing and boundary conditions, exact; they use none of the closure approximations needed in other calculation schemes. Their limitation is simply their low ratio of energy-containing to dissipative range scale sizes; in other words, their low turbulence Reynolds number Re. For turbulent flows in general the ratio of the largest ($\sim \ell$) and smallest ($\sim \eta$) scale sizes goes as (Tennekes and Lumley, 1972) $\ell/\eta \sim (q\ell/\nu)^{3/4} \sim Re^{3/4}$, which indicates that the CRAY-1 computations will have very small Re values by geophysical standards (in a typical convective PBL, $q \sim 1$ m/s, $\ell \sim 200$ m, $Re \sim 10^7$).

Thus while we can never hope to do "exact" calculations of large Reynolds number geophysical turbulence, such calculations do provide a rich source of turbulence information unavailable in any other way. Further, since the large-scale structure of turbulent flows is thought to be, to a good approximation, independent of the value of Re (providing Re is sufficiently large) these direct calculations might some day provide insight into geophysical turbulence structure through simulations at lower, accessible Re values.

b) 3-D (large eddy) calculations

Clearly any numerical simulation of PBL turbulence based on the governing equations must involve some compromises, since computer limitations will not allow all the dynamically essential scales to be calculated. One attractive compromise is to calculate explicitly the 3-D, time-dependent structure of only the largest eddies; i.e., to use the available grid starting from the large-scale end. Such calculations are no longer "exact", of course, since the unresolvable, sub-grid scale eddies must be parameterized; their average effect is to extract energy from the resolvable eddies.

The pioneering work here in PBL applications has been done by Deardorff; his approach is summarized in his 1973 article, which also includes many additional references. This approach continues to find applications to lower atmospheric flows. Sommeria (1976) has extended Deardorff's convective PBL simulations to include moist processes with condensation (cloud formation), infrared radiative cooling, and flow disturbances from large-scale effects. As another example, Klemp and Wilhelmson (1978) have used a 3-D model to study convective storm dynamics in a 24 km × 24 km (horizontal) × 10 km (vertical) volume.

Such studies have given valuable insight into the gross structure and dynamics of important tropospheric flows. Unfortunately, however, it is generally not clear to what extent one can trust the details of the calculated structure, since parameterizations of uncertain validity are used in the models. Broadly speaking, the closure parameterizations become less important as Δ/ℓ becomes smaller, where Δ is a characteristic grid scale. In Deardorff's PBL calculations Δ was of the order of 50 m, which made Δ/ℓ small in mid-regions; most of the turbulent kinetic energy and fluxes were carried by the directly-resolved, large-scale eddy motion. Often, however, this Δ/ℓ restriction is not met, particularly when a large flow volume is needed; in such cases the detrimental influences of inadequate sub-grid scale parameterizations are probably stronger.

The 3-D modeling efforts at Stanford by Reynolds and colleagues, while not concerned specifically with atmospheric turbulence, are particularly interesting. Their work is touched on briefly in the survey paper by Reynolds (1976) and covered in more detail by Mansour *et al.* (1977) and Ferziger *et al.* (1977). They have paid much attention to the formal details of the decomposition into resolvable and sub-grid scale components, have used various mathematical filters to effect this separation, and have found that certain filters allow some of the inertial transfer to smaller eddies to be resolved explicitly (see Leonard, 1974).

The parameterizations in 3-D turbulence models are attempts to express the sub-grid scale effects in terms of the resolvable-scale field. This parameterization problem differs from the usual variety in that here one is dealing with instantaneous, random sub-grid effects; one seeks to express them in terms of the (also random) resolved motion. Even if an eddy viscosity relationship is valid on the average, there seems no guarantee that it will hold locally in space and time. This question is also the subject of current research.

c) Second-order closure

While the equations governing the evolution of second-order, single-point moments have been known since the time of Osborne Reynolds, they were evidently not examined in detail again until the work of Chou (1945). Attempts to solve them numerically have followed, and in recent years they have come into increasingly wide use in applications ranging from engineering to geophysical flow research. Since this field is evolving rapidly and our space here is limited, we will cite only certain advances and some remaining challenges.

In second-order modeling one attempts to establish equations for the Reynolds terms which result from averaging of the flow equations. Traditionally *ensemble* averaging has been used, but recently second-order closure has also been introduced into 3-D calculations which use *grid-volume* averaging. There are so many contemporary approaches to establishing these turbulence "constitutive equations" that any comprehensive classification and discussion of them is itself an advance. Thus we mention the recent survey paper by W.C. Reynolds (1976) which, although restricted to shear-driven turbulence, is the most complete and up-to-date survey of second-order models.

Unfortunately, most second-order model development is not rooted as deeply in turbulence physics as one would wish; in fact, many model parameterizations have no detectable roots at all. This situation is perhaps inevitable, because in developing a second order model one confronts the turbulence closure problem, a problem often called one of the most difficult in all of physics.

The model development efforts of Lumley and colleagues stand in contrast to most others. His recent paper (1978) is the most significant attempt to date to provide a physical basis for the necessary parameterizations. This paper, in itself, represents a remarkable advance in the field of second-order modeling.

Because of the Reynolds and Lumley papers, we will not discuss in any detail any of the contemporary versions of second-order models, or the physical bases (or lack of them) for their parameterizations; their papers cover these areas remarkably well. Rather, we will touch on some of the highlights of second-order modeling as it applies to the PBL, and on recent advances in our understanding of PBL structure and its impact on the models.

Numerous journal articles concerning the application of second-order models to lower atmospheric structure have appeared in the past few years, and in a broad sense the bulk of these represent advances over the traditional eddy-diffusivity approach. In fact, many of the models essentially allow the eddy diffusivity to be calculated from the flow structure as it evolves. This has been one of the benefits of second-order modeling: it has provided a systematic means of determining eddy diffusivities. This is not to say these eddy diffusivity predictions are always correct, or even always useful; but they are *often* useful, and remain about the only way to proceed, short of prescribing eddy diffusivity or mixing length distributions at the outset, a perilous undertaking.

A second major benefit of second-order modeling, from a research point of view, is that it has highlighted and reinforced the traditional role of experimental work in advancing our fundamental knowledge of turbulent flow. Second order models need closure parameterizations; these have been, in many cases, tested, refuted, and reformulated through analysis of turbulence data from the PBL and other flows.

We can illustrate this process by considering some of the history of the parameterization of turbulent transport--i.e., the divergence of the turbulent second moment flux. In the equation for $\partial\overline{u_i u_k}/\partial t$, for example, the turbulent transport term is $\partial\overline{u_i u_k u_j}/\partial x_j$. Traditionally (and even today in shear-flow applications) this is parameterized with a gradient-diffusion model of the type

$$\overline{u_i u_j u_k} \propto -\frac{\ell}{q}\left[(\overline{u_i u_j})_{,m}\,\overline{u_m u_k} + (\overline{u_i u_k})_{,m}\,\overline{u_m u_j} + (\overline{u_j u_k})_{,m}\,\overline{u_m u_i}\right] \qquad (1)$$

where $q^2 = (\overline{u_i u_i})$ and repeated indices are summed. This has certain appealing symmetry properties, but little theoretical justification; in addition, it has been found to be incorrect in buoyancy-driven turbulence (Wyngaard, 1973).

Lumley and colleagues were the first second-order modelers to suggest an alternative to (1) for transport modeling. They considered the rate equations for the third moments involved in transport, and showed that the direct effects of buoyancy in these equations made relations such as (1), which are often approximately true in shear flows, invalid in convective turbulence. Zeman and Lumley (1976) have used this approach--i.e., carrying third-moment equations for convective turbulence--and have obtained the most realistic model simulation to date of the convective PBL. Further developments along these lines are presented by Lumley *et al.* (1978).

Experimentalists, having pointed out that gradient diffusion models such as (1) do not hold in convective turbulence, have now seen theoreticians develop yet more complicated parameterizations; these are capable of being tuned to fit the observations, but at the same time they introduce more unknown physics. We can expect this evolutionary process to continue, with experimentalists in turn studying new details of buoyant transport. This process is the traditional one in turbulence research, and judging from past history should gradually give improved understanding and better models.

We do not imply that PBL turbulence measurements alone can provide the data source necessary for formulating improved understanding of second-order modeling. Rather, it is clear that well-designed laboratory experiments can be extremely useful, particularly for the second major type of parameterizations needed, those for the fluctuating pressure covariances. Lumley's (1978) paper gives the state of understanding of these covariances and their parameterization, which seems an even more difficult task than transport parameterization.

Recent measurements support the conclusion from the 1968 Kansas experiments (Wyngaard & Coté, 1971) that the turbulence energy budget in the unstable surface layer of the atmosphere receives a substantial gain from the pressure transport term $\partial(\overline{pw}/\rho)\partial z$. Some of these new data are direct measurements of the fluctuating pressure field (McBean & Elliott, 1975), and others allow inferences from the imbalance of the other measured energy budget terms; together, they support the conclusion that the "pressure transport" term is not negligible, as previously widely supposed and as often true in shear flows. These findings of important pressure transport effects provide a further challenge for second-order modelers.

Possibly even more difficult than pressure covariance parameterization is the problem of dealing with the molecular terms in the second moment equations. Under the local isotropy hypothesis, these occur as dissipative (sink) terms in the component turbulent energy equations, and in the scalar variance and scalar covariance equations, but are negligible elsewhere. Lumley (1978) has summarized our understanding of the physics of dissipation maintenance equations, pointing out that we know less about these than any other equations encountered in second order modeling.

We can look forward to the possibility that carefully done 3-D simulations will supplement direct measurements in providing the sort of turbulence information needed to test and refine second-order models. The possibilities here are intriguing; a well-done, fine-mesh 3-D simulation could resolve explicitly most of the transport and pressure covariance statistics, for example. These are quantities which are difficult or (in the case of pressure statistics) all but impossible to measure. There is also the possibility that 3-D calculations, by varying the mesh size, could be used to test and refine their own sub-grid scale parameterizations.

Second-order models, as ordinarily formulated, can at times produce unphysical behavior such as negative variances and, in diffusion applications, negative concentrations; they can also violate Schwartz's inequality by producing correlation coefficients larger than one in magnitude. This is called the "realizability" problem, and as discussed by Schumann (1976) can be interpreted in terms of the physics of second-moment maintenance. Schumann derives some constraints on Reynolds stress models which insure realizability, and these are extended and generalized by Lumley (1978).

Deardorff (1978) has pointed out some disturbing properties of second and third-order model solutions of diffusion from an instantaneous source in homogeneous turbulence. This is a problem whose solution is well-established, but Deardorff found that contemporary second-order model results were inaccurate in some respects. Deardorff was able to deduce how the transport parameterizations, for example, should behave in order to achieve proper predictions, and it is interesting that Lumley's (1978) thinking was independently evolving in the same direction on the basis of different considerations.

3. Advances through experiment

Pressure fluctuations, and their covariance with vertical velocity, have been measured in the surface layer by McBean and Elliott (1975). Earlier, others have measured pressure fluctuations over water waves. There are unanswered questions concerning the performance of pressure sensors of the type used (specially-shaped bodies with pressure ports carefully located on the surface) but these are first steps toward a very important goal in turbulence research. The ability to measure pressure fluctuations accurately within a turbulent flow, with adequate spatial and temporal resolution in a device suitable for tower or aircraft use, would be a tremendous experimental advance. It would make possible, for example, measurement of the all-important pressure covariance terms in the turbulence second-moment equations and thus could provide a greatly broadened data base for second-order model development.

Experimental activity in the area of turbulent fine structure seems to have decreased somewhat since the flurry of efforts from the mid 1960's to early 1970's. Much of that work was stimulated by refinements in Kolmogorov's original hypotheses about the fine structure of large Reynolds number turbulence, and in particular by some new hypotheses about the effects of intermittency on the statistical properties of these smallest-scale motions. Experimental work in this area has been impeded somewhat by recent discoveries of heretofore unexpected sensor problems, including salt spray effects on fine-scale temperature sensors operated in a marine environment, and the mutual contamination of temperature and velocity signals at high frequencies. Nonetheless new findings have emerged, including persistent evidence (which has yet to be reconciled with prevailing hypotheses about turbulent fine structure) of anisotropic scalar fine structure (temperature derivative skewness) in a variety of large Reynolds number flows (Mestayer *et al.*, 1976). Some very detailed studies of the fine structure of the velocity field in the dissipative range were interpreted in the context of the original and refined Kolmogorov hypotheses by Champagne (1978).

Most research-quality PBL turbulence data continues to be obtained from conventional sensors mounted either on towers, balloon cables, or aircraft. While there are concerns that fixed-point sensors in PBL flow can require excessively long averaging times for sufficiently stable statistics (Wyngaard, 1973), towers in particular remain the best platforms available for a wide range of turbulence research objectives. The 300 m tower at the Boulder Atmospheric Observatory, described in some detail in the companion article by Hooke, is a new facility providing research-quality PBL turbulence data and is now open to outside users.

Acknowledgment

I am grateful to S. Orszag for helpful discussions on direct simulations of turbulence and to J. Trebing for expertly typing the manuscript.

References

Champagne, F. H., 1978: The fine-scale structure of the turbulent velocity field. To appear, *J. Fluid Mech.*

Chou, P. Y., 1945: On the velocity correlations and the solutions of the equations of turbulent fluctuation. *Quart. Appl. Math.* *3,* 38-54.

Deardorff, J. W., 1973: Three-dimensional numerical modeling of the planetary boundary layer. In *Workshop on Micrometeorology,* 271-311. AMS, Boston, MA.

Deardorff, J. W., 1978: Closure of second- and third-moment rate equations for diffusion in homogeneous turbulence. To appear, *Phys. Fluids.*

Ferziger, J. H., V. B. Mehta, and W. C. Reynolds, 1977: Large eddy simulation of homogeneous isotropic turbulence, *Proceedings, Symposium on Turbulent Shear Flows,* Univ. Park, PA, April 1977.

Klemp, J. B. and R. B. Wilhelmson, 1978: The simulation of three-dimensional convective storm dynamics. To appear, *J. Atmos. Sci.*

Leonard, A., 1974: Energy cascade in large-eddy simulations of turbulent flows. In *Advances in Geophys., 18A,* 237-248. Academic Press, N.Y.

Lumley, J. L., 1978: Computational modeling of turbulent flows. To appear, *Adv. in Appl. Mech.*

Mansour, N. N., P. Moin, W. C. Reynolds and J. H. Ferziger, 1977: Improved methods for large-eddy simulations of turbulence, *Proceedings, Symposium on Turbulent Shear Flows,* Univ. Park, PA, April 1977.

McBean, G. A. and J. A. Elliott, 1975: The vertical transports of kinetic energy by turbulence and pressure in the boundary layer. *J. Atmos. Sci., 32,* 753-766.

Mestayer, P. G., C. H. Gibson, M. F. Coantic, and A. S. Patel, 1976: Local anisotropy in heated and cooled turbulent boundary layers. *Phys. Fluids, 19,* 1279-1287.

Reynolds, W. C., 1976: Computation of turbulent flows. In *Annual Review of Fluid Mech., 8,* 183-208. Annual Reviews, Inc., Palo Alto, CA.

Schumann, U., 1976: Realizability of Reynolds stress turbulence models. *Phys. Fluids, 20,* 721-725.

Sommeria, G., 1976: Three-dimensional simulation of turbulent processes in an undisturbed trade wind boundary layer. *J. Atmos. Sci., 33,* 216-241.

Tennekes, H. and J. L. Lumley, 1972: A first course in turbulence. MIT Press, Cambridge.

Tennekes, H., 1978: Turbulent flow in two and three dimensions. *Bull. Am. Meteor. Soc., 59,* 22-28.

Wyngaard, J. C. and O. R. Coté, 1971: The budgets of turbulent kinetic energy and temperature variance in the atmospheric surface layer. *J. Atmos. Sci., 28,* 190-201.

Wyngaard, J. C., 1973: On surface-layer turbulence. In *Workshop on Micrometeorology,* 101-149. AMS, Boston, MA.

Zeman, O. and J. L. Lumley, 1976: Modeling buoyancy driven mixed layers. *J. Atmos. Sci., 33,* 1974-1988.

Preprint Volume; 18th Conference on Radar Meteorology, 100-103,
American Meteorological Society, 1978.

MEASUREMENTS TOWARD A C_n^2 CLIMATOLOGY

R. B. Chadwick, K. P. Moran, G. E. Morrison

NOAA/ERL/Wave Propagation Laboratory
Boulder, Colorado 80302

1. INTRODUCTION

One of the problems in designing an operational radar to measure winds in the clear air is the lack of a data base on the expected signal strength of the return. This paper describes some preliminary results of an experimental program to determine statistics of clear air radar return in the boundary layer.

The return signal for a monostatic radar using refractive-index fluctuations as the backscattering mechanism is directly proportional to C_n^2, the structure constant for radio refractive index. This quantity varies greatly in the boundary layer. An in-situ sensor on an aircraft routinely measures a 20 dB variation in C_n^2 in a short period (minutes) and a 40 dB variation over a longer period (days) (Lawrence, 1976). Using radar measurements of C_n^2, in the Boulder, Colorado area, we have measured a variation of 63 dB over longer periods. These kinds of variation make it clear that specifying the required sensitivity of an operational clear air radar is not simple and depends on user needs.

The large scale spatial variation of C_n^2 further complicates the matter of selecting the sensitivity of a clear air radar. This large scale variation depends on the types of air masses occupying a particular geographic area. The characteristics of C_n^2 for different types of air masses has been studied by Gossard (1976). He gives values of the radio C_n^2/C_T^2 for many different air masses and different locations. Mean values of C_T^2 can be obtained from a variety of sources, e.g., Ochs and Lawrence (1972). These allow a rough extrapolation of the C_n^2 measurements given in this paper to other geographical areas.

2. EXPERIMENTAL PROCEDURE

The radar used to collect the data presented is an FM-CW radar that can measure Doppler shift and hence radial velocity. Because the radar measures a velocity spectrum, it can separate the clear-air returns from ground returns and from the noise baseline. The return power is then related to the area under the velocity spectrum and from this area the C_n^2 estimate can be obtained.

The particular processing scheme is described in Chadwick et al. (1976a) and some examples of wind measurements are given in Chadwick et al. (1976b). Values of pertinent radar parameters are given in Table I.

Table I. FM-CW Radar Parameters

Power	200 W
Beamwidth	2.8°
Range cell	160 m
Velocity cell	.30 m/s
Wavelength	10 cm
Az scan rate	3°/s
El scan rate	0.75°/s
Number of range cells	9
Coherent averaging time	0.15 s
Incoherent averaging time	51 s

A new estimate of the velocity spectrum for each range cell is obtained every coherent averaging period. These estimates are exponentially weighted in time and averaged with a time constant of 51 sec and the data recorded on magnetic tape every 60 sec. This record of data consists of 500 points. Each velocity spectrum consists of 50 points and there are 9 spectra, one for each range cell. The first cell (0-80 m) is not used.

Data are acquired continuously in an unattended mode of operation. The radar can be controlled and checked remotely by phone lines. Over phone lines, we can: start and stop the magnetic tape, rewind the tape, access earlier data on that tape, calculate statistics for the individual records, measure transmitted power, check antenna direction, and move the antenna to a new direction. Under normal conditions, we need only to visit the radar every 8 days to change tapes.

3. CALIBRATION FOR C_n^2 MEASUREMENTS

We considered antenna and electronics calibrations. Since the antenna calibration for a two antenna system such as ours is not a standard procedure, it will be covered in greater detail than the electronics calibration.

Our radar uses two antennas, transmitting continuously from one and receiving continuously on the other. Suppose the antenna centers are separated by a distance D, and the boresight axes are parallel. Figure 1 shows that there is little overlap at short ranges, but this overlap increases at greater ranges. We need to quantify this overlap by finding a function of range, F(R), which can be multiplied by the antenna gain to give the effective two-antenna gain. The overlap can be found by multiplying and integrating the two antenna patterns. Using small angle approximations in Fig. 1, we see that

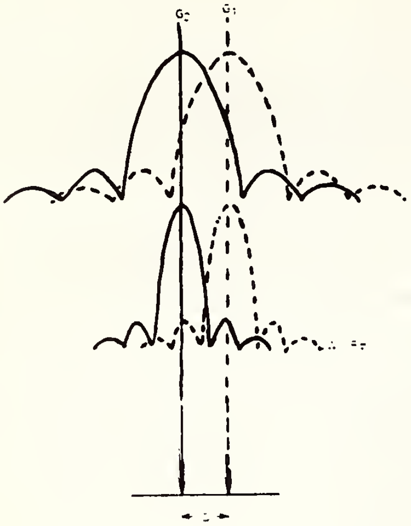

Figure 1. Side-by-side antenna patterns.

$$F(R) = \frac{C}{R} \int_{-\infty}^{\infty} G_1\left(\frac{W + \frac{D}{2}}{R}\right) G_2\left(\frac{W - \frac{D}{2}}{R}\right) dW$$

where $G_1(\cdot)$ and $G_2(\cdot)$ are the antenna patterns of the two side-by-side antennas. The term outside the integral sign is necessary to ensure the boundary conditions, i.e., $F(R \to 0) = 0$ and $F(R \to \infty) = 1$. Changing the variable of integration and evaluating the constant gives us

$$F(R) = \frac{\int G_1(\theta + \frac{D}{2R})\, G_2(\theta - \frac{D}{2R})\, d\theta}{\int G_1(\theta)\, G_2(\theta)\, d\theta} .$$

However, it is clear that this is simply the cross-correlation between the two antenna patterns. If the two patterns are the same, this becomes the autocorrelation function, $\mathcal{R}_G(\cdot)$, of the antenna pattern $G(\theta)$. $\mathcal{R}_G(\cdot)$ is calculated by lagged products. So the effective antenna pattern for our measurements is

$$G_E(\theta,R) = \mathcal{R}_G(\tfrac{D}{R})\, G(\theta) .$$

The two terms making up this effective antenna pattern are shown in Fig. 2 and 3.

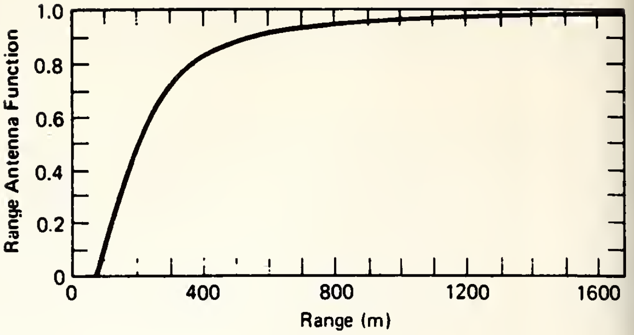

Figure 2. Range weighting function due to antenna beam overlap.

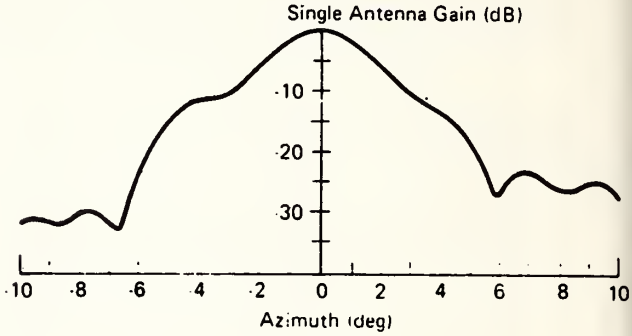

Figure 3. Measured antenna pattern.

The electronic calibration is determined by taking a known sample of the transmitted signal, attenuating it by a known amount, delaying it in a 10 μs electro-acoustic delay line, and coupling it into the receiver. The response from the delay line represents a signal of known power and this calibrates the portion of the receiver after the point at which the delayed signal is coupled in. Since this coupling point is after the r-f amplifier, we must know the gain of this amplifier to complete the calibration. The amplifier was kept at a constant temperature during the experiment and the gain checked periodically. The gain variations did not exceed 1.6 dB. This is acceptable considering the large variation of the quantity being measured.

Once the antenna and electronic calibrations are completed, the received power (the integral of the output velocity spectrum) can be related to the average value of C_n^2 in that particular range cell. The derivation of the equation relating the receiver output to C_n^2 is straightforward and starts with a slight variation of the standard meteorological radar equation. If P_T is the transmitted power and A_e is the aperture effective area, the return power, P_r, from a range cell Δ at range R with radar cross section σ, is

$$P_r = \frac{P_T \mathcal{R}_G (\frac{D}{R}) \Delta A_e \eta}{4\pi R^2}$$

where the units are all MKS. For clear-air scattering in the inertial subrange (Ottersten, 1969)

$$\eta = 0.38 C_n^2 \lambda^{-1/3}$$

where λ is the wavelength and C_n^2 has units of $m^{-2/3}$. If we designate A_r as the area under a clear air velocity spectrum, P_s as the equivalent test signal power, and A_s as the area of the test signal output, it is obvious that

$$P_r = \frac{A_r}{A_s} P_T .$$

Combining these equations and solving for C_n^2, we obtain

$$C_n^2 = \frac{8.43}{\mathcal{R}_G(\frac{D}{R})} \frac{A_r}{A_s} \frac{P_s}{P_T} \frac{R^2}{\Delta} \quad (\text{meters})^{-2/3} .$$

So, given an output clear-air velocity spectrum, we can obtain an estimate of C_n^2. An error analysis has not been performed, but the rms errors are probably in the range of 2-3 dB.

4. HISTOGRAMS OF C_n^2

At the time of this writing (November 1977) only a small amount of data has been processed. These results are presented as histograms on a logarithmic scale of C_n^2. Each decade of C_n^2 values is broken into three bins of equal size (on a log scale) and a histogram for each range bin constructed for each hour of data. Figure 4 shows such a histogram obtained about sundown under clear sky conditions. The numbers shown indicate how many of the one minute estimates of C_n^2 fell into that bin every hour. Figure 5 shows another histogram obtained at midnight. Note the difference in the change of C_n^2 with height. Sometimes the C_n^2 values are greater in the surface layer and decrease with height, but often they increase with height. This is perhaps due to an elevated temperature inversion that is unresolved by the radar. Both Fig. 4 and 5 were obtained such that no storms occurred within 24 hours before or after the data were taken.

Height (m)							
1449	3	5	6	11	11	15	8
1288	1	5	2	8	20	15	9
1127	2	1	6	15	18	15	2
966		1	11	27	16	5	
805				6	36	18	
644			4	28	23	4	1
483				13	34	13	
322				10	30	20	
161						27	33

10^{-16} 10^{-15} 10^{-14} 10^{-13}

C_n^2 value ($m^{-2/3}$)

Figure 4. Range ordered C_n^2 histograms.

Height (m)							
1449				5	7	19	29
1288					10	26	24
1127					12	37	11
966				3	21	36	
805			2	18	32	8	
644		7	25	24	4		
483	3	21	30	6			
322	26	28	5	1			
161		56	4				

10^{-16} 10^{-15} 10^{-14} 10^{-13}

C_n^2 value ($m^{-2/3}$)

Figure 5. Range ordered C_n^2 histograms.

Diurnal variations in C_n^2 can be seen in Fig. 6, a time history of C_n^2 histograms at a height of 1127 m. Our results indicate that there is extensive diurnal variation, however we have not been able to establish this variation from the limited amount of data we have processed.

The upper sides of the histograms are due to large returns from insects. Such returns generally have a different character when viewed on an A-scope. So we are well aware that there are many insects in Colorado. However, we are confident that the lower portions of the histograms are valid estimates of C_n^2.

5. CONCLUSIONS

Since we have not yet processed all of the data, it is difficult to make general conclusions on C_n^2. However, based on a year's operating experience, we can present conclusions on radar performance. These are: 1) winds can always be measured to several hundred meters; 2) during the summer, winds can usually be measured to heights exceeding 1.6 km; 3) C_n^2 values at heights up to 1.6 km seem to be positively correlated with surface wind speed.

Negative Power of ten in C_n^2 value

Hours (MDT)

```
   12 12 12 13 13 13 14 14 14 15 15 15 16 16 16 17 17 17
20                         16 26 11  5  1        1
21                    8 15 30  3  1  1  2
22              16 31  7  3  3
23               2 18 13 10  9  7  1
 0           15 39  6
 1            3  5 21 24  7
 2                 1 14 19  5  5  3  3  2  2  1  3
 4                      13 10  6  8  4  2  2  3  1
 5                         15 11 14 11  5  1  1  2
 6                       6 10 15  9 10  4  1     1
 7                       7 14  9  7  7  3  3  4  5
 8                      10 24 16  7     2  1
 9                       6 39 11  3              1
10                      38  9  3  2  3  1  1
11                      21 30  2     3  1
12                      16 33  8  1  1  1
13                    1 37 22
14                       8 33 18     1
15                         19 16  8  8  2  2     5
16                   16 17 20  4  2  1
17                    3  7 18 23  6  2  1
18                      10 25 16  8  1
19                      17 26 15  2
19            1 10  4  4  5 16 12  3  4  1
20                    3 11 20 26
21                 47 11  2
22               1 28 28  3
23               6 20 21 13
 0               5 26 23  2  1  1        2
 1            2 13 42  3
 2              12 36  8  4
 3               2 31  8  5  5  4  2        1  1
 4                 12 29 10  3  4  1
 5                    2  5 19 19 14  1
 6                    1  4 19 17 16  3
 7                    1  1  4 12 28  8  3     3
 8                          5 24 26  4  1
 9                       1 15 36  8
10                   12 34 12  2
11                 2 57  1
12                28 25  3  1                    2
13               1 34 25
14                38 22
15               2 24 30  4
16               1  4 36 19
17                    3 54  3
18                      54  6
19                    4 56
20                 1 16 43
21                 8 45  5  2
22                    1 12 29  9  4  4  1
23                    5 12 16 20  5  1           1
 0                    1 15 34 10
 1                 1  1  7 24 18  4  4  1
 2                      13 30 11  4  1           1
 3                       1 29 18  9  1  1
 4                          6 10 24  4  5  4     4
 5                       3  8 13 19  6  5  2  3
 6                       1  7 30 17  3  1  1
 7                          2 14 28  9  3     1  1
 8                          2 26 10 16  4  1  1
 9                    1  7 36 15  1
10                 1  1 13 42  3
11                 1  3 48  8
12                 1 17 42
13                   26 34
14                 6 35 19
15                 3 41 15     1
16               8 50  2
17               5 40  7  7                  1
18               1 24 13 16  5        1
19                       2 45 13
20                    2 35 22  1
21                 2  8 19 23  5  2  1
22                    5 10 17  8 11  7        1  1
23                    8 19 15  8  3  3  2     1
 0                 2  8 26 17  2  3  1  1
 1                   23 24  8  2  1        1
 2                 6 24 11  9  5  4     1
 3                19 19  5 10  3  2  1        1
 4                33 20  3  1  1              2
 5                 2 17  7 24  6  4
 6                    5 21 27  7
 7                       9 14 16 11  5     3  2
 7                       2  6 19 21  8  4
 8                          1 20 19 18  2
10                    1 18 24 12  2  1
11                         10 42  8
12                         11 24 18  5        1
13                            27 28  5
14                         25 30  3        1
15                          9  5 25 16  4     1
16                          7 13 14  8 15  1     1
17                                4  9  9  5  6 10  1  5
18                             6  4  8  6  4 10  5  4  4
19                          4  7  9  3  7 17  5  4     2
20                             5 42 12  1
```

Figure 6. Time ordered C_n^2 histograms.

6. ACKNOWLEDGMENTS

This work was fully supported by Air Force Project Order No. Y77-847, entitled "FM-CW Doppler Radar Wind Shear Detector." We wish to thank Ralph Donaldson of AFGL for support and encouragement.

7. REFERENCES

Chadwick, R. B., K. P. Moran, R. G. Strauch, G. E. Morrison, and W. C. Campbell, 1976a: Microwave wind measurements in the clear air, *Radio Sci.*, 11 (10); 795-802.

Chadwick, R. B., K. P. Moran, R. G. Strauch, G. E. Morrison, and W. C. Campbell, 1976b: A new radar for measuring winds, *Bull. Amer. Meteorol. Soc.*, 57 (9); 1120-1125.

Gossard, E. E., 1976: Refractive index variance and its height distribution in different air masses, NOAA Tech. Report ERL 369-WPL46.

Lawrence, R. S., 1976: Private communication.

Ochs, G. R. and R. S. Lawrence, 1972: Temperature and C_n^2 profiles measured over land and ocean to 3 km above the surface, NOAA Tech. Report ERL 251-WPL22.

Ottersten, H. 1969: Atmospheric structure and radar backscattering in clear air, *Radio Sci.*, 4; 1179-1193.

U. S. Department of Air Force Report AFGL-TR-78-0160, 1978

MEASUREMENTS SHOWING THE FEASIBILITY FOR RADAR DETECTION OF HAZARDOUS WIND SHEAR AT AIRPORTS

R. B. Chadwick, K. P. Moran, G. E. Morrison, W. C. Campbell

Measurements of the strength of clear-air backscattered power for a 10 cm radar were made over a 12 month period in Colorado. The main conclusion is that radar offers a viable option for warning of hazardous low-level wind shear at airports. There were 161 days of operation and diurnal and seasonal trends of the return are identified. It is shown that the back-scattered power can be considered as a single parameter log-normal random variable. The problems encountered in low elevation angle operation are discussed and one solution, a clutter suppression system is presented.

Journal of Geophysical Research, 83: 4791-4797, October 1978.

Neutral Atmospheric Motions Manifested in Radar Echo Doppler Shifts From Two-Stream Irregularities in the Equatorial Electrojet

ROBERT COHEN[1]

Aeronomy Laboratory, Environmental Research Laboratories, National Oceanic and Atmospheric Administration
Boulder, Colorado 80302

WILLIAM H. HOOKE

Wave Propagation Laboratory, Environmental Research Laboratories, National Oceanic and Atmospheric Administration
Boulder, Colorado 80302

Theoretical expressions are derived describing the effect of neutral atmospheric motions (prevailing winds, gravity waves, and tides) on observed propagation velocities of type 1 ionospheric irregularities in the equatorial electrojet. The theory takes account of two ways in which the neutral motions may influence the observed plasma wave phase velocities—directly, through their influence on the ion motion, relative to which the plasma waves propagate, and indirectly, through motion-associated temperature perturbations which affect the ion acoustic velocity. The theoretical results together with what little independent information is available on neutral motions within the equatorial electrojet suggest that they should produce variations in the observed plasma wave phase velocities of the order of several percent. Results are shown to be consistent with variations in the plasma phase velocity observed at Jicamarca, Peru.

1. INTRODUCTION

The equatorial *E* region occupies a unique place in ionospheric physics because global electric fields associated with the atmospheric dynamo combine with the horizontal magnetic field there to produce an especially strong electric current, which has been given the name of the equatorial electrojet. Some 30% of the time (the major exception, of course, being the periods each day near sunrise and sunset when the equatorial electrojet reverses direction) the drift velocity $\mathbf{v}_D \equiv \mathbf{v}_e - \mathbf{v}_i$ of the electrons relative to the ions is sufficiently great to give rise to two-stream instability generated plasma waves [*Farley*, 1963]. These ionospheric irregularities scatter VHF radio waves and have been studied by this means for a number of years [*Bowles et al.*, 1960, 1963; *Cohen et al.*, 1962; *Cohen and Bowles*, 1963*a*, *b*, 1967; *Balsley*, 1965; *Cohen*, 1973]. *Balsley* [1969] confirmed a suspicion of long standing that in addition to plasma waves generated by the two-stream instability (hereafter referred to as type 1 irregularities) the equatorial electrojet contained another type of plasma wave motion of quite different character (the associated irregularities are hereafter referred to as type 2). Balsley pointed out that the type 2 irregularities displayed properties analogous to turbulent eddies in a shear flow; *Sato* [1968, and subsequent work] and others have interpreted these as evidence of nonlinear cross-field instability. Parallel to the observational work of the past 15 years there has been considerable development of the theory of the two types of plasma irregularities, in both their linear and nonlinear aspects, by a number of researchers. *Sato* [1973] gives many of the pertinent references. A number of properties distinguish the type 1 from the type 2 irregularities, but the two that are most pertinent to the present work can be characterized briefly (and in a somewhat oversimplified fashion) as follows:

1. Type 1 irregularities are generated only when the component of $\mathbf{v}_D$ in the direction of the plasma wave propagation, i.e., $(\mathbf{v}_D \cdot \mathbf{k}_p/k_p)$, where $\mathbf{k}_p$ is the plasma wave vector and k_p is its scalar magnitude, exceeds a certain critical value v_C. For the plasma wave numbers of interest here, v_C lies just above the ion acoustic speed v_{ia}, defined as $[K(T_i + T_e)/m_i]^{1/2}$, where K is Boltzmann's constant, T_i and T_e are the ion and electron temperatures, respectively, and m_i is the ion mass. (To help fix ideas, $v_{ia} \approx 360$ m s^{-1} in the equatorial electrojet.) By contrast, type 2 irregularities are detected at all values of $\mathbf{v}_O$ exceeding a minimal threshold, ~30 m s.

2. Once they are generated, type 1 irregularities are observed to propagate with phase speeds v_θ relative to the ions that have constant values just greater than v_{ia}, independent of the magnitude of $\mathbf{v}_D$; however, type 2 irregularities appear to move at velocities comparable with the drift velocity $\mathbf{v}_O$ regardless of its value.

Thus a major goal of theoretical development over the years has been to explain the observed wave phase speeds of the type 1 irregularities, revealed by Doppler shifts of the radar echoes. In particular, theorists have attempted to answer the following questions:

1. Why do type 1 irregularities propagating over a wide range of angles from vertical appear nearly simultaneously, when linearized theory predicts that it is the component of the drift velocity $\mathbf{v}_D$ in the direction of wave propagation that must exceed a certain critical value?
2. Why are type 1 irregularities observed on occasion to propagate vertically?
3. Why does v_θ appear to be independent of v_O for values $v_D > v_C$, when linear theory predicts that v_θ should be proportional to v_D in this regime?
4. Why are the Doppler shifts of the radar echoes from type 1 irregularities observed to fluctuate by amounts up to 10% or so over periods ranging between several minutes and a day and over horizontal distances of the order of 100 km?

Farley and Balsley [1973] and *Sato* [1973] attempt to resolve the first three of these questions in the following way: The regions of type 1 echo returns are observed to be patchy rather

---

[1] Currently at the Ocean Systems Branch, Division of Solar Energy, Washington, D. C., 20545.

This paper is not subject to U.S. copyright. Published in 1978 by the American Geophysical Union.

Paper number 8A0466.

than homogeneous, reflecting the influence of the large-scale (~2 km) type 2 irregularities on $\mathbf{v}_D$ itself. These irregular motions produce local variations in both the magnitude of $\mathbf{v}_D$ and the angle it makes with the horizontal, so that the radar views a mixture of type 1 irregularities, some growing in amplitude and some damped. On the average they are at the threshold of growth and propagating with a wave phase speed ($\sim v_c$) just greater than v_{ia} (as the linear theory predicts). The spread in the local directions of $\mathbf{v}_D$ relative to the vertical produces corresponding spread in the angles of wave propagation relative to the vertical. These authors take the explanation of the fourth question to lie either in statistical fluctuations or in the effects of neutral atmospheric motions.

This latter possibility was first raised by W. B. Hanson (private communication, 1966); subsequently, we treated the subject orally in a paper presented at the Seventh International Association of Geomagnetism and Aeronomy Symposium, held in St. Gallen, Switzerland, in 1967. The idea is certainly not lacking in intuitive appeal, but hitherto we had not set down in writing its theoretical basis, and it now seems appropriate and desirable to do so. Specifically, we examine theoretically the effects on the type 1 radar echo Doppler shifts to be expected from three major classes of neutral atmospheric motions: (1) prevailing winds, (2) atmospheric gravity waves, and (3) the atmospheric tides. While very little is actually known about *E* region neutral atmospheric motions at equatorial latitudes, we can extrapolate from what is known from observations of *E* region winds at temperate latitudes, from observations of mesospheric motions at the equator, and from theoretical estimates of amplitudes at the equator of atmospheric gravity waves and tides, and we can use these figures to estimate the magnitude of the type 1 radar echo Doppler shifts to be produced by these motions. This discussion constitutes section 2. In section 3 we present observational data from power spectra of 50-MHz radar echoes returned from type 1 irregularities, showing temporal and spatial Doppler shift variations which we believe can be interpreted reasonably as revealing neutral atmospheric motions. Section 4 contains brief concluding remarks.

2. THEORY: NEUTRAL ATMOSPHERIC MOTIONS MANIFESTED IN TYPE 1 WAVE PROPAGATION VELOCITIES

As was mentioned in the introduction, type 1 irregularities are found to propagate in relation to the ambient *E* region ions with phase speeds v_θ which are independent of the magnitude of $\mathbf{v}_D$ (as long as v_D exceeds v_C), as was established by a detailed analysis of the correlation between observed two-stream wave phase velocities and the phase velocities of type 2 irregularities [*Cohen*, 1973]. Although the theoretical basis for this is still a matter of some uncertainty [*Farley and Balsley*, 1973; *Sato*, 1973], we shall accept this motion as given, and write

$$v_\theta = \alpha(k_p) v_{ia} \tag{1}$$

where α is a constant for a given plasma wave wave number k_p (for the wave numbers of concern here, α is just slightly greater than unity). Thus we take v_θ to be proportional to v_{ia}, so that to the extent that neutral atmospheric motions produce associated temperature changes those changes will (weakly) affect v_{ia} and hence v_θ.

Moreover, v_θ is the phase speed of the plasma wave relative to the ions. The observed wave phase speed v_R must therefore include a contribution arising directly from the mean velocity of the electrojet ions in the radar scattering volume. At the *E* region heights in question the ions are constrained to move with the velocity $\mathbf{v}_N$ of the neutral molecules [e.g., *Hines et al.*, 1965].

Thus neutral atmospheric motions influence the Doppler shift of type 1 radar echoes in two ways: (1) directly, through the motion they induce in the ion rest frame with respect to which the wave phase speed v_θ is fixed, and (2) indirectly, through atmospheric temperature changes associated with the neutral atmospheric motions. *Sato* [1975] has argued that in the equatorial region, neutral winds produce a velocity change in both the ion and the electron velocity equal to that of the neutral wind itself. Whatever physical picture one adopts does not change any of the conclusions which follow, however.

While little is known about neutral atmospheric winds in the equatorial *E* region, if we extrapolate from the considerable body of data available on neutral atmospheric motions in the temperate latitude *E* region, we can conclude that the influence of these motions on the Doppler shift of the type 1 radar echoes will be small. Specifically, if we write

$$v_R = v_{R0} + v_{R1} \tag{2}$$

where v_{R0} is the unperturbed value of the type 1 irregularity phase speed observed and v_{R1} represents the departure produced by neutral atmospheric motions, then

$$v_{R1}/v_{R0} \ll 1 \tag{3}$$

In an analogous manner we can define $v_\theta \equiv v_{\theta 0} + v_{\theta 1}$, $v_{ia} \equiv v_{ia0} + v_{ia1}$, etc., and using (1) and (2), we can now write

$$v_{R0} = \frac{\mathbf{1}_D \cdot \mathbf{1}_R}{|\mathbf{1}_D \cdot \mathbf{1}_R|} v_{\theta 0} \tag{4}$$

where $\mathbf{1}_D$ and $\mathbf{1}_R$ are unit vectors oriented in the direction of $\mathbf{v}_D$ and the radar beam, respectively (the observational geometry is shown in Figure 1). Here we have expressed v_{R0} in the form shown in order to retain the sign of the observed wave phase speed; thus for $v_R < 0$, wave propagation is toward the radar, while for $v_R > 0$, wave propagation is away from it.

The neutral atmospheric motions perturb v_R by an amount

$$v_{R_1} = \frac{\mathbf{1}_D \cdot \mathbf{1}_R}{|\mathbf{1}_D \cdot \mathbf{1}_R|} \alpha v_{ia1} + \mathbf{v}_N \cdot \mathbf{1}_R \tag{5}$$

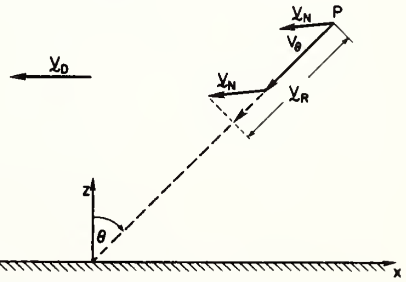

Fig. 1. The observational geometry. Here the plane of the figure is the east-west plane. The velocity vectors $\mathbf{v}_D$, $\mathbf{v}_N$, $\mathbf{v}_\theta$, and $\mathbf{v}_R$ are the electron-ion drift velocity, the neutral velocity, the wave phase velocity relative to the ions, and the observed radar phase velocity, respectively.

where the subscript 1 on the vector $\mathbf{v}_N$ has been dropped because it is redundant; by definition, $v_{N0} = 0$. Carrying our perturbation treatment one step further, we may write

$$v_{R1} = \frac{1}{2}\frac{\mathbf{1}_D\cdot\mathbf{1}_R}{|\mathbf{1}_D\cdot\mathbf{1}_R|}\alpha v_{\iota a0}\frac{T_{\iota 1} + T_{e1}}{T_{\iota 0} + T_{e0}} + \mathbf{v}_N\cdot\mathbf{1}_R \tag{6}$$

where we have expressed the motion-induced perturbations of v_θ in terms of the corresponding perturbations of the ion and electron temperatures T_e and T_ι. Thus our problem becomes one of determining $T_{\iota 1}$, T_{e1}, and $\mathbf{v}_N$ for each case of interest. Note that the first term in this equation does not vary with the radar zenithal look angle θ ($\equiv \cos^{-1}(\mathbf{1}_r\cdot\mathbf{1}_z)$ where $\mathbf{1}_z$ is a unit vector in the vertical; see Figure 1), except insofar as $T_{\iota 1}$ and T_{e1} vary spatially. The second term of the equation does, however, vary with θ if $\mathbf{v}_N$ is a spatial constant. In addition, the type 1 irregularities propagate only in the east-west vertical plane; hence north-south neutral atmospheric motions produce no detectable effect except as they result in temperature changes $T_{\iota 1}$ and T_{e1}. Thus the effects of temperature and velocity perturbations enter the expression for the observed wave phase velocity in fundamentally different ways.

Case 1: Prevailing neutral winds. By prevailing winds we mean motions of planetary scale that persist without change over periods of many days. Very little is known about such winds at *E* region heights near the equator, although they are believed to be light. *Murgatroyd* [1965, Figures 1 and 2] puts them at no more than a few meters per second. Since any temperature changes induced by prevailing winds will be spatial constants, the winds themselves can be studied by looking for a θ dependent variation in v_{R1} with radar look angle that persists in averages over several days. However, using the Murgatroyd estimate of the prevailing winds, we would put the magnitude of this variation at about 1%, which is probably undetectable. This magnitude would be reduced still further by any significant amplitude variation through the random scattering value resulting from changes in prevailing wind speed with height. We have made no attempt to estimate prevailing winds in our observational study.

Case 2: Atmospheric gravity waves. Still less is known about the spectrum of atmospheric gravity waves in the equatorial *E* region. However, the properties of the wave spectra at temperate latitude *E* region heights are fairly well documented. The summary given by *Hines* [1960] remains valid today: (1) The waves have vertical wavelengths at *E* region heights in excess of 5 km, with the dominant vertical wavelengths just in excess of 10 km. (2) Wave periods vary between several minutes and several hours, with dominant periods of the order of 1 hour. (3) The dominant horizontal wavelength is something like an order of magnitude greater than the vertical. (4) Wave-associated winds are of the order of tens of meters per second in amplitude. *Woodman and Guillén* [1974] report gravity wave wind fluctuations at 80 km of the order of 10 m s⁻¹. Recalling that wave-associated wind speeds increase with height as exp $(z/2H)$ [*Hines*, 1960], where H (~5 km) is the atmospheric scale height, we can infer that wave-associated wind speeds in the equatorial electrojet, four scale heights above, would be ~70 m s⁻¹. However, these speeds approach the prevailing speed of sound (~360 m s⁻¹), and nonlinear effects can be expected to reduce the wave-associated wind speeds somewhat. It thus seems reasonable to suppose that gravity waves in the equatorial *E* region have spectra similar to their temperate latitude counterparts.

Since the wave-associated motions are adiabatic, they induce perturbations in the neutral atmospheric temperature T_n, as was pointed out by *Hines* [1965]. In the *E* region, ion temperatures are so closely tied to the neutrals that it is valid to take

$$T_{\iota 0} = T_{n0} \qquad T_{\iota 1} = T_{n1} \tag{7}$$

At night, when there is little or no photo-ionization and hence little or no electron heating, it seems reasonable to take

$$T_{e0} = T_{n0} \qquad T_{e1} = T_{n1} \tag{8}$$

as well, and indeed this hypothesis is supported by observation [*Cohen*, 1973]. Even during the day it seems that (8) is sufficiently accurate for our purposes, but here the demonstration is more involved. *Gleeson and Axford* [1967] give

$$T_e = T_n + (\tfrac{3}{2}qKT_e\dagger/L_{en}{}^*n_e) \tag{9}$$

where q is the photo-ionization rate, n_e is the electron density, $T_e\dagger$ is an 'injection temperature' of energetic photoelectrons, which they take to be 8000 K, and

$$L_{en}{}^* = 1.55 \times 10^{-15}n(\mathrm{N_2})$$
$$+ (5 \times 10^{-18}T_e - 1.0 \times 10^{-15})n(\mathrm{O_2}) \tag{10}$$

where $n(\mathrm{N_2})$ and $n(\mathrm{O_2})$ are number densities of $\mathrm{N_2}$ and $\mathrm{O_2}$, respectively, measured in units per cubic centimeter. Using reasonable values for the terms in (9), we find $T_e - T_n \sim 20$ K $\sim 0.1T_n$ at electrojet heights.

In the unperturbed state, then,

$$T_e = T_{e0} = T_{n0} + (\tfrac{3}{2}q_0KT_e\dagger/L_{en0}{}^*n_{e0}) \tag{11}$$

while during wave passage the electron temperature is perturbed by an amount

$$T_{e1} = T_{n1} + \left[\frac{q_1}{q_0} + \frac{n_{n1}}{n_{n0}} - \frac{n_{e1}}{n_{e0}}\right](T_{e0} - T_{n0}) \tag{12}$$

where n_n is the neutral atmospheric particle number density; (12) follows from a slight manipulation of expressions given by *Hooke* [1969*a*, *b*]. The next step in this procedure would involve the expression of q_1/q_0 and n_{e1}/n_{e0} in terms of n_{n1}/n_{n0}. While this is possible under various simplifying assumptions [*Hooke*, 1969*b*], it is rather difficult in general. However, we can note that but for certain truly exceptional cases, the term in brackets should be $\sim n_{n1}/n_{n0}$, which itself is $\sim T_{n1}/T_{n0}$, so that

$$T_{e1} \doteq T_{n1} + 0.1T_{n1} \doteq T_{n1} \tag{13}$$

to the accuracy of this analysis.

Thus for gravity waves, (6) becomes

$$v_{R1} = \frac{1}{2}\frac{\mathbf{1}_D\cdot\mathbf{1}_D}{|\mathbf{1}_D\cdot\mathbf{1}_D|}\alpha v_{\iota a0}\frac{T_{n1}}{T_{n0}} + \mathbf{v}_N\cdot\mathbf{1}_R \tag{14}$$

To proceed further, we require a relation between T_{n1}/T_{n0} and v_n. Let us confine our attention to the equations governing gravity wave propagation in an isothermal inviscid atmosphere stationary in the absence of wave motions; we can then write

$$v_n \propto \exp(z/2H)\exp i(\omega t - k_x x - k_y y - k_z z)$$

where ω is the angular wave frequency of the gravity wave and $\mathbf{k}$ is its wave vector (see Figure 1). Then, after making some slight notational changes in the polarization relations given by *Hines* [1960, 1965] we find that

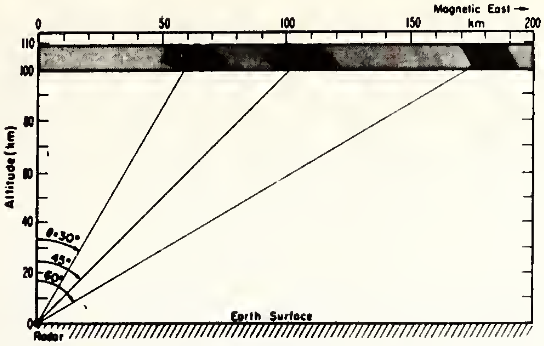

Fig. 2. Separation of the scattering regions for radar look angles of $\theta = 30°, 45°$, and $60°$

$$\frac{T_{n1}}{T_{n0}} = \frac{(\gamma - 1)\omega^2 k_z - i(\gamma - 1)g(k_x^2 + k_y^2) + i\gamma\omega^2(\gamma - 1)g/2C^2}{\omega(k_x^2 + k_y^2)^{1/2}C^2 k_z - i(1 - \gamma/2)g/C^2} \cdot v_{nx}^2 + v_{ny}^2)^{1/2} \quad (15)$$

where γ is the ratio of specific heats, g is the acceleration of gravity, and $C^2 = \gamma g H$. Since the plasma waves are generated only in the east-west vertical plane and the radar echoes are confined to this plane,

$$\mathbf{v}_N \cdot \mathbf{1}_R = v_{Nx} \sin\theta + v_{Nz}\cos\theta \quad (16)$$

Thus knowledge of the background atmospheric parameters C^2, γ, and g and the gravity wave wave vector **k** and amplitude $|\mathbf{v}_N|$, together with (14)–(16), enables us to calculate gravity-wave-associated changes in v_{R1}.

While (15) looks complicated, it is really very simple in form, and for gravity waves of small vertical wavelength and long period, specifically waves for which $k_z^2 \gg 1/4H^2$ and $\omega^2 \ll (\gamma - 1)g^2/C^2$, it simplifies (*Hines* [1965], with some notational changes) to

$$\frac{T_{n1}}{T_{n0}} = -i(\gamma - 1)^{1/2}(v_{Nx}^2 + v_{Ny}^2)^{1/2}/C \quad (17)$$

Noting that $v_{i00}/C = 2/\gamma = 1.4$, we have from (14) and (16) that

$$v_{R1} = 0.4i\frac{\mathbf{1}_D \cdot \mathbf{1}_R}{|\mathbf{1}_D \cdot \mathbf{1}_R|}(v_{Nx}^2 + v_{Ny}^2)^{1/2} + v_{Nx}\sin\theta + v_{Nz}\cos\theta \quad (18)$$

(Note that the imaginary unit vector i appears in this expression, indicating a phase relation between the various contributions to v_{R1}. In the applications the real part of this and subsequent expressions should be used to evaluate v_{R1}.)

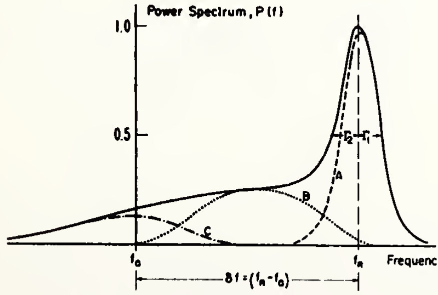

Fig. 3. Power spectrum of the radar echoes decomposed into the sum of three Gaussian spectra A, B, and C, following *Cohen* [1973].

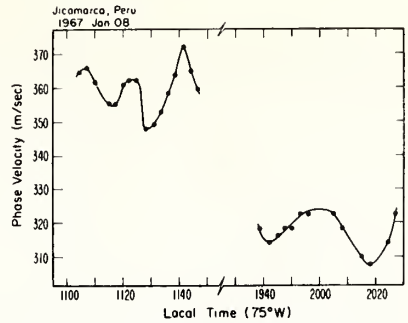

Fig. 4. Observed phase velocity v_R as a function of time for January 8, 1967 (θ = 50°W).

Thus for gravity waves propagating east-west ($k_y = 0$) we have

$$v_{R1} = 0.4i\frac{\mathbf{1}_D \cdot \mathbf{1}_R}{|\mathbf{1}_D \cdot \mathbf{1}_R|}v_{Nx} + v_{Nx}\sin\theta + v_{Nz}\cos\theta \quad (19)$$

while for gravity waves propagating north-south ($k_x = 0$, $v_{Nx} = 0$) we have

$$v_{R1} = 0.4i\frac{\mathbf{1}_D \cdot \mathbf{1}_R}{|\mathbf{1}_D \cdot \mathbf{1}_R|}v_{Ny} + v_{Nz}\cos\theta \quad (20)$$

For waves of long period, $v_{Nz} \ll (v_{Nx}^2 + v_{Ny}^2)^{1/2}$ [*Hines*, 1960], so that these equations simplify still further to

$$v_{R1} = \left(0.4i\frac{\mathbf{1}_D \cdot \mathbf{1}_R}{|\mathbf{1}_D \cdot \mathbf{1}_R|} + \sin\theta\right)v_{Nx} \quad (21)$$

and

$$v_{R1} = 0.4i\frac{\mathbf{1}_D \cdot \mathbf{1}_R}{|\mathbf{1}_D \cdot \mathbf{1}_R|}v_{Ny} \quad (22)$$

respectively, except for near-zenith radar look angles θ. Thus we see that in these limits, gravity waves propagating east-west will be somewhat more effective in producing Doppler shifts changes in the type 1 radar echoes than will gravity waves propagating north-south, all else being equal. The response of the fluctuations v_{R1} to the gravity wave motions is anisotropic.

It would be possible to use the formulas given above to generate plots showing changes induced in v_{R1} as a function of azimuth of gravity wave propagation and the wave parameters (period, phase speed, wavelength, etc.). However, that does not appear to be worthwhile at this juncture, and we shall content ourselves with the observation that gravity waves having the properties summarized at the beginning of this subsection, i.e., having wind amplitudes something like 10% of the

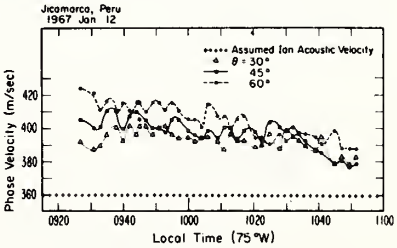

Fig. 5. Observed phase velocity v_R as a function of time and radar look angle for January 12, 1967.

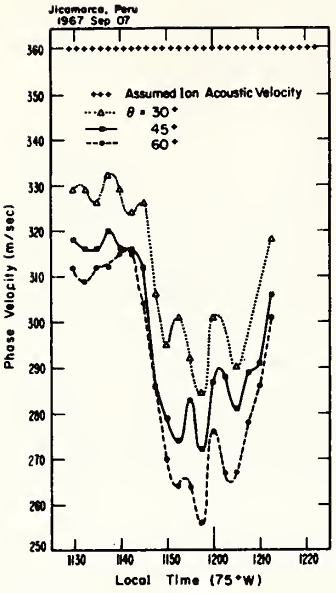

Fig. 6. Observed phase velocity v_R as a function of time and radar look angle for September 7, 1967.

speed of sound, will produce fluctuations in v_{R1} of the order of 10%. It should be noted, however, that this statement is true only to the extent that the gravity wave wavelengths of interest here are large in comparison with the dimensions of the radar scattering volume; otherwise, considerable cancellation inside the volume would occur. Thus the above estimate would tend to exaggerate the effect on v_{R1} of gravity waves of small wavelengths. Note also that while the prevailing winds are of large spatial scale, so that v_{Nx} and v_{Ny} are constant over the spatial distances between radar scattering volumes for different look angles θ, the gravity-wave-associated velocities may vary considerably, even reversing sign over these distances. Thus varying the radar look angle θ yields results that will be somewhat ambiguous in this case.

Case 3: The atmospheric tides. The theory governing atmospheric tides at altitudes between the earth's surface and 100 km [*Lindzen*, 1967; *Lindzen and Chapman*, 1969] appears to be reasonably consistent with observations [*Reed et al.*, 1969]. However, there are discrepancies between the predicted and the observed semidiurnal tide [*Reed*, 1972], and there may be some cause for concern about *Woodman and Guillén*'s [1974] failure to discern any tidal oscillations in their analyses of mesospheric winds at equatorial latitudes. The situation at altitudes above 100 km is somewhat more uncertain because of the effects of thermospheric heating and geomagnetic constraints on the ion and electron motion at such heights. Nevertheless, one should conclude that the weight of the evidence suggests E region diurnal and semidiurnal motions at equatorial latitudes of the order of several tens of meters per second, with accompanying temperature fluctuations of the order of several tens of degrees Kelvin. Thus using (14), we conclude that the atmospheric tides will induce fluctuations in v_{R1} of the order of several tens of meters per second or 10% of v_{R0}.

Because tidal motions are of global scale, the phase variations over the range of distances which can be scanned by a single radar are negligible. It is thus possible in principle to distinguish between the effects of the tidal motions and those of the tidal temperature fluctuations on v_{R1}, since the former vary sinusoidally with θ while the latter do not, as is seen from (6). Thus in principle, such observations would provide a check between the phase and amplitude relationships between v_{nx} and T_{n1}/T_{n0} for the tides. (Note that here it is assumed that $(v_{nz})_{\text{tides}} = 0$, which is valid to a quite high degree of accuracy.)

3. OBSERVATIONS: NEUTRAL ATMOSPHERIC MOTIONS MANIFESTED IN TYPE I WAVE PROPAGATION VELOCITIES

In this section we report briefly on results of a preliminary observational study carried out at the Jicamarca Radar Observatory of the temporal and spatial variability of observed type 1 irregularity phase speeds. While the results are not by themselves definitive, they serve to illustrate the type of approach that might be made to the data analysis.

A few prefatory remarks should be made concerning the observational geometry depicted in Figure 1. Recall that a family of type 1 irregularities emanates from each point P in the electrojet where the threshold requirement for the two-stream instability is satisfied. The irregularities move in relation to the ions with phase velocity v_θ. An observing radar with an antenna beam inclined to the vertical at angle θ in the magnetic east-west vertical plane obtains echoes from those Fourier components of the irregularities which are moving in that direction. As is emphasized in Figure 2, for the radar look angles $\theta = 30°$, $45°$, and $60°$ used in these studies, the scattering regions being compared are not collocated but rather are separated by distances of about 60–120 km in the east-west direction. The separation between the regions viewed at angles $\pm\theta$ in the east-west direction can amount to 300 km. Gravity wave motions typically exhibit considerable phase variation over horizontal distances of this order. Observations at angles $\theta < 45°$ are complicated by the increased difficulty of resolving the spectrum into its two-stream and type 2 components, so that v_{R1} is best measured by observing at angles $\theta > 45°$. Measurements reported here were typically taken simultaneously at angles $\theta = 45°$ and $\theta = 60°$, corresponding to an east-west spatial separation of about 70 km.

The antenna beam width used in these studies was rather large—about 35°—so that the angular resolution is obtained by taking advantage of the narrow vertical extent of the equa-

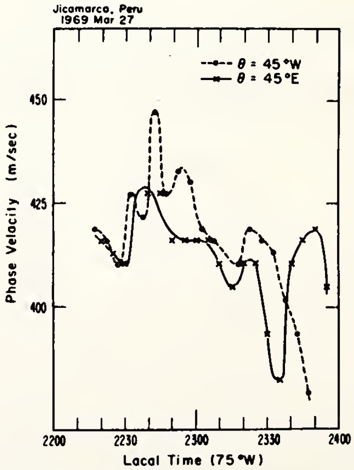

Fig. 7. Observed phase velocity v_R as a function of time and radar look angle for March 27, 1969.

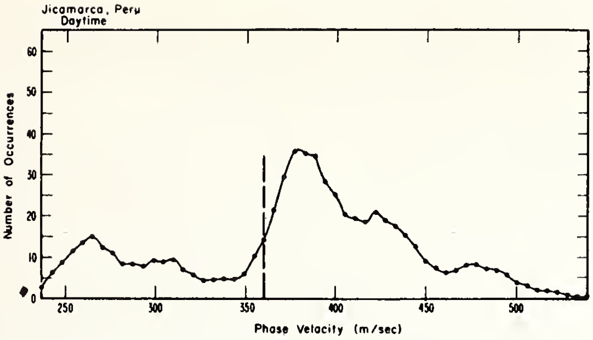

Fig. 8. Daytime distribution of phase velocities v_R.

torial electrojet and range gating to study echoes at different ranges, which correspond to different inclination angles from the vertical (Figure 2). Because the electrojet itself is some 5 km or so in thickness, the observing technique effectively filters out the effects produced by atmospheric motions on smaller scales.

The basic data sets consist of power spectra $P(f)$ of the echoes, which are decomposed into the sum of three Gaussian spectra, labeled A, B, and C in Figure 3, following a procedure developed and discussed in detail by *Cohen* [1973]. Gaussian A is associated with the type 1 or two-stream echo. Gaussian B is associated with type 2 irregularities in the same echo stratum. Gaussian C is associated with slower moving type 2 irregularities in another echo stratum. The electron drift velocities in the two strata can be estimated [*Balsley,* 1969] by converting the frequency shifts at the centers of Gaussians B and C to phase velocities, using the Doppler shift formula

$$v_d = \frac{c}{2}\frac{\delta f}{f_0}\csc\theta \qquad (23)$$

where δf is the frequency shift and the peak of the Gaussian measured from the transmitted frequency f_0, and c is the velocity of light. In the present measurements, f_0 = 59.92 MHz, and the proportionality factor $c/2f_0$ is about 300 $\text{ms}^{-1}/100$ Hz.

Thus the principal measurement discussed in the present paper is the time-varying Doppler shift $\delta f = (f_R - f_0)$, where f_R is the frequency associated with the peak of the composite spectrum, normalized so that $P(f_R) = 1$. This peak value, it will be noted from Figure 3, occurs at a slightly lower frequency than the frequency at which the Gaussian A attains its maximum. However, the error introduced by utilizing this value rather than that obtained through spectral decomposition is slight. Other quantities taken from the composite spectra are Γ_1 and Γ_2, defined as the spectral 'half widths' of the two-stream portion of the spectrum of the 'far' and 'near' frequency sides, respectively. From f_R we determine v_R using the relation

$$v_R = \frac{c}{2}\frac{(f_R - f_0)}{f_0} = \frac{c}{2}\frac{\delta f}{f_0} \qquad (24)$$

Figures 4–7 show plots of v_R as functions of time (and, in some instances, radar look angle θ) for five brief observing intervals over a 3-year period. Each of the figures reveals considerable temporal variability (amounting in some cases to as much as ±10%), over all periods in excess of several minutes (the minimum period resolvable in the data). In light of the discussion in section 2 it would appear probable that these fluctuations are produced by atmospheric gravity waves, which would only have to have wind amplitudes of $\pm 20\ \text{ms}^{-1}$ to produce the Doppler shifts detected here. The fluctuations at each of the different look angles θ show some degree of correlation (better in some cases than in others). The consistent difference between the velocities v_R seen at the three look angles in Figure 6 would also be consistent with the existence of a fairly substantial mean wind during the observing interval, amounting to some 90 ms^{-1}, but whether this wind is a prevailing wind, a tidal wind, or simply a very long period gravity wave wind cannot be determined directly from such a short span of data. However, measurements of gravity wave amplitudes at other latitudes and of prevailing winds at low latitudes suggest that these amplitudes are typically too small to account for the 90 ms^{-1} wind detected here, arguing in favor of the tidal or prevailing wind interpretation. Superimposed on this wind composite is a half cycle of wind change of $\pm 30\ \text{ms}^{-1}$, at about 1 hour period.

To infer any diurnal variations in v_R, we have examined a large quantity of Jicamarca electrojet spectra for the period August 4, 1967, through November 15, 1968, kindly provided by B. B. Balsley. Those spectra for which there was an adequate development of type 1 irregularities were analyzed for $v_R(t)$, resulting in data during portions of about 50 days. 'Daytime' two-stream data, obtained during periods when v_D was westward, were mainly available between 0900 and 1500 hours LT. 'Nighttime' two-stream data, obtained when v_D was directed eastward, were mainly available between 1900 and 0600 hours LT. The results are shown in Figures 8 and 9 and indicate a diurnal variation of $\approx 30\ \text{ms}^{-1}$.

4. CONCLUDING REMARKS

We have shown in the theoretical analysis in section 2 how neutral atmospheric motions, including prevailing winds, atmospheric tides, and atmospheric gravity waves, can be expected to produce detectable changes in the wave phase speed v_R of observed two-stream instability plasma waves of the equatorial electrojet. These changes would appear to offer a plausible explanation for the changes in v_R actually observed, although definitive comparisons will require a much more extensive analysis of radar data. Such studies might also be used to see whether any influence of the semiannual variation, the quasi-biennial oscillation, or the five-day oscillation—prominent features of tropical meteorology—can be detected at E region heights.

However, it should be realized that the validity of the analysis rests on the applicability of (1), and the theoretical basis for this result remains vague. Specifically, the analysis also as-

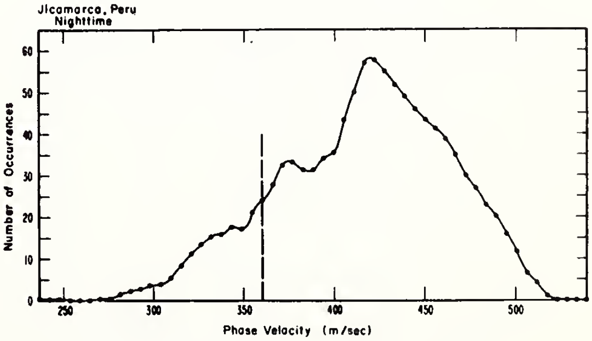

Fig. 9. Nighttime distribution of phase velocities v_R.

sumes that neutral atmospheric motions will be unable to influence $\mathbf{v}_R$ through motion-associated changes either in $\mathbf{v}_D$ or in $\mathbf{v}_i$. However, a more sophisticated analysis could be evolved to include such effects.

Acknowledgments. We wish to thank B. B. Balsley, G. C. Reid, and others of the Aeronomy Laboratory of NOAA, as well as D. T. Farley, Jr., of Cornell, for useful discussions and comments on the manuscript.

The Editor thanks T. Sato and R. Kaw for their assistance in evaluating this paper.

REFERENCES

Balsley, B. B., Some additional features of radar returns from the equatorial electrojet, *J. Geophys. Res., 70,* 3175–3182, 1965.

Balsley, B. B., Some characteristics of non-two-stream irregularities in the equatorial electrojet, *J. Geophys. Res., 74,* 2333–2347, 1969.

Bowles, K. L., R. Cohen, G. R. Ochs, and B. B. Balsley, Radio echoes from field-aligned ionization above the magnetic equator and their resemblance to auroral echoes, *J. Geophys. Res., 65,* 1853–1855, 1960.

Bowles, K. L., B. B. Balsley, and R. Cohen, Field-aligned *E* region irregularities identified with acoustic plasma waves, *J. Geophys. Res., 68,* 2485–2501, 1963.

Cohen, R., Phase velocities of irregularities in the equatorial electrojet, *J. Geophys. Res., 78,* 2222–2331, 1973.

Cohen, R., and K. L. Bowles, The association of plane wave electron density irregularities with the equatorial electrojet, *J. Geophys. Res., 68,* 2503–2525, 1963*a*.

Cohen, R., and K. L. Bowles, Ionospheric VHF scattering near the magnetic equator during the International Geophysical Year, *J. Res. Nat. Bur. Stand., Sect. D, 67,* 459–480, 1963*b*.

Cohen, R., and K. L. Bowles, Secondary irregularities in the equatorial electrojet, *J. Geophys. Res., 72,* 885–894, 1967.

Cohen, R., K. L. Bowles, and W. Calvert, On the nature of equatorial slant sporadic *E, J. Geophys. Res., 67,* 965–972, 1962.

Farley, D. T., Jr., A plasma instability resulting in field-aligned irregularities in the ionosphere, *J. Geophys. Res., 68,* 6083–6097, 1963.

Farley, D. T., and B. B. Balsley, Instabilities in the equatorial electrojet, *J. Geophys. Res., 78,* 227–239, 1973.

Gleeson, L. J., and W. I. Axford, Electron and ion temperature variations in temperate zone sporadic-*E* layers, *Planet. Space Sci., 15,* 123–136, 1967.

Hines, C. O., Internal atmospheric gravity waves at ionospheric heights, *Can. J. Phys., 38,* 1441–1481, 1960.

Hines, C. O., Dynamical heating of the upper atmosphere, *J. Geophys. Res., 70,* 177–183, 1965.

Hines, C. O., I. Paghis, T. R. Hartz, and J. A. Fejer (Eds.), *Physics of the Earth's Upper Atmosphere,* Prentice-Hall, Englewood Cliffs, N. J., 1965.

Hooke, W. H., Electron, ion, and neutral gas temperatures in temperate latitude sporadic *E* layers, *Planet. Space Sci., 17,* 737–748, 1969*a*.

Hooke, W. H., *E*-region ionospheric irregularities produced by internal atmospheric gravity waves, *Planet. Space Sci., 17,* 749–765, 1969*b*.

Lindzen, R. S., Thermally driven diurnal tide in the atmosphere, *Quart. J. Roy. Meteorol. Soc., 93,* 18–42, 1967.

Lindzen, R. S., and S. Chapman, Atmospheric tides, *Space Sci. Rev., 10,* 3–188, 1969.

Murgatroyd, R. J., Winds in the mesosphere and lower thermosphere, *Proc. Roy. Soc. London, Ser. A, 288,* 575–589, 1965.

Reed, R. J., Further analysis of semidiurnal tidal motions between 30 and 60 kilometers, *Mon. Weather Rev., 100,* 579–581, 1972.

Reed, R. J., M. J. Oard, and M. Sieminski, A comparison of observed and theoretical diurnal tidal motions between 30 and 60 kilometers, *Mon. Weather Rev., 97,* 456–459, 1969.

Sato, T., Brillouin scattering in plasmas as applied to ionospheric irregularities, *J. Geophys. Res., 73,* 2941–2949, 1968.

Sato, T., Unified theory of type I and II irregularities in the equatorial electrojet, *J. Geophys. Res., 78,* 2232–2243, 1973.

Sato, T., Neutral winds and electrojet irregularities, *J. Geophys. Res., 80,* 2835–2838, 1975.

Woodman, R. F., and A. Guillén, Radar observations of winds and turbulence in the stratosphere and mesosphere, *J. Atmos. Sci., 31,* 493–505, 1974.

(Received January 10, 1978;
revised April 28, 1978;
accepted May 1, 1978.)

Preprint Volume; Fourth Symposium on Meteorological Observation and Instrumentation 148-149, American Meteorological Society, April 1978.

TESTS OF MICROWAVE RADIOMETRIC SENSING OF ATMOSPHERIC TEMPERATURE AND WATER IN THE GULF OF ALASKA

M. T. Decker, E. R. Westwater, and F. O. Guiraud

NOAA/ERL/Wave Propagation Laboratory
Boulder, Colorado 80302

1. INTRODUCTION

The feasibility of using multichannel microwave radiometers mounted on ocean data buoys for remote sensing of atmospheric temperature and water vapor structure is being investigated. Algorithms have been developed for inferring temperature and water vapor profiles in the presence of clouds as well as under clear skies (Westwater et al., 1976). These algorithms also predict the accuracies that should be achieved in a particular climate with known instrumental accuracies. Briefly, microwave thermal radiation from the atmosphere is measured by zenith-pointing radiometers at three frequencies in the 50 to 60 GHz oxygen absorption band, one at the 22 GHz water vapor absorption line, and one at 31 GHz in the window region between these. Information from the latter two frequencies can be used to correct for the contaminating effect of cloud radiation and at the same time to derive water vapor and cloud liquid content. The cloud correction allows us to estimate equivalent clear radiation for the microwave channels. These data and surface measurements of temperature, pressure, and relative humidity are then used to infer profiles of temperature and water vapor using statistical inversion techniques (Westwater et al., 1975).

2. EXPERIMENTS

To test these methods a series of experiments was performed jointly by NOAA and the Jet Propulsion Laboratory under various atmospheric conditions. The microwave radiometer is similar to that used on the Nimbus 6 satellite. Radiation from the zenith was measured once each minute with a dwell time of 1 second. In general, 18 to 24 of these measurements were averaged to give the radiation data used in retrieval of profiles. Concurrent rawinsonde data were used to evaluate the accuracy of the radiometric profiles.

Measurements were made at the Pacific Missile Test Center, Pt. Mugu, California, during the periods February 24 to March 17 and July 16 to 30, 1976. The 21 profiles analyzed for the first period were all under essentially clear skies; 16 of 22 profiles during the second period were classified as cloudy. A more severe environmental test was made aboard the Canadian Ship Quadra at Ocean Station P in the Gulf of Alaska from February 15 to March 26, 1977. Of the 45 profiles from this location 35 were cloudy.

3. RESULTS

Predicted accuracies and those actually achieved for temperature profiles during the three experimental periods are shown in Figures 1, 2, and 3. Height of the vertical scale is given in pressure difference from the surface. Note that a pressure difference of 100 mb corresponds to a geometrical height of about 0.9 km, 300 mb corresponds to 3 km, 500 mb to 5.6 km, and 800 mb to 12 km. The curves labeled a and b are the theoretical accuracies in profile retrieval for the appropriate seasonal climatology. Curve a is the expected accuracy if the climatological mean profile is used as the predictor of all profiles, i.e., no measurement is made. Curve b shows the theoretical accuracy if the five radiation measurements together with the surface measurements are used to determine the profiles. Curves c and d are the corresponding quantities observed during the experimental periods. Curve c is the RMS difference between the climatological mean profile and the experimental rawinsondes, and curve d is the RMS difference between the radiometric profiles and the corresponding rawinsondes. In this analysis we assume that there are no errors in the rawinsonde data.

Our analysis shows that the temperature profile accuracies achieved during the experimental periods are quite close to the theoretical predictions of accuracy. Tests were made to determine temperature errors that resulted if corrections were not made for the radiation from clouds. The results showed that without the corrections there would be a substantial increase in error.

Profiles and line integrals of water vapor have also been derived from the radiometric data but are not shown here. Errors in these measurements are somewhat larger than predicted. It is likely that discrepancies arise partly from inaccuracies in the rawinsonde itself and partly from uncertainties in our knowledge of water vapor absorption coefficients.

4. CONCLUSIONS

Temperature profiles retrieved from surface-based microwave radiometric measurements have been compared with rawinsonde profiles to show that reasonable agreement with predicted accuracy has been achieved. This increases confidence in our ability to predict the performance of radiometric systems under various climatological, seasonal, or other conditions.

Corrections for the radiation from non-precipitating clouds have been successfully applied to microwave radiometric temperature profile measurements. This greatly improves the usefulness of the radiometric technique by increasing the time during which valid data can be obtained.

While the radiometric technique tends to produce a smoothed temperature profile, the accuracies achieved should make it particularly useful in applications that require the mean temperature between standard pressure levels

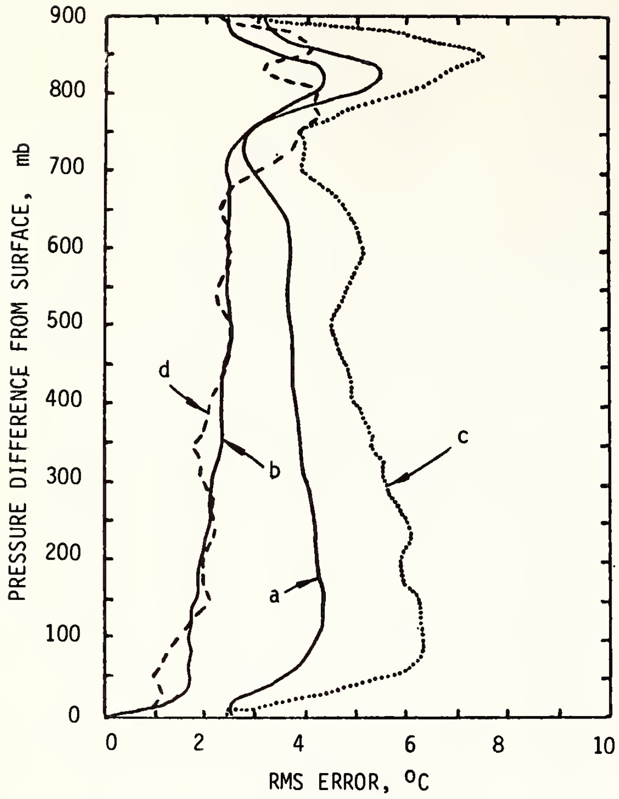

Figure 1. Predicted and observed accuracies of temperature profiles measured by microwave radiometry at Pt. Mugu, California, in February-March 1976. See text for explanation of curves.

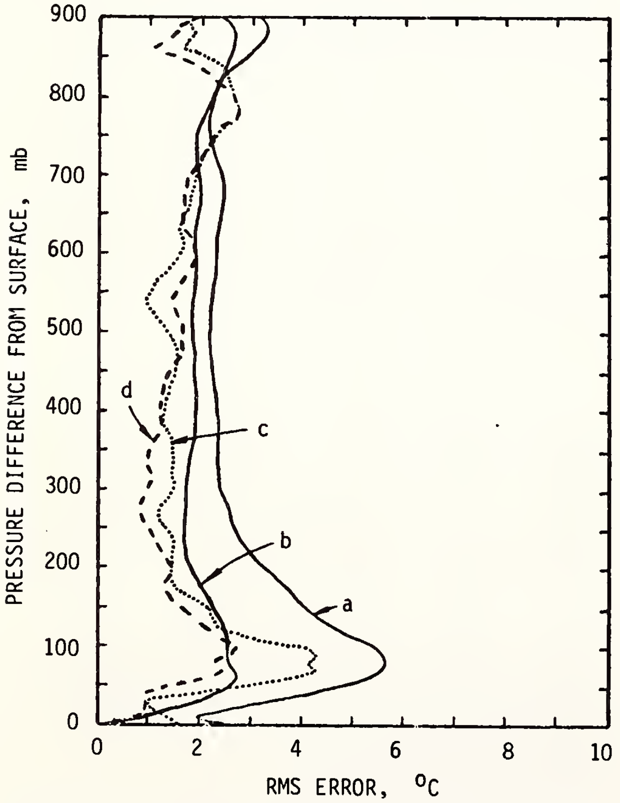

Figure 2. Same as Figure 1 except at Pt. Mugu, California, in July 1976.

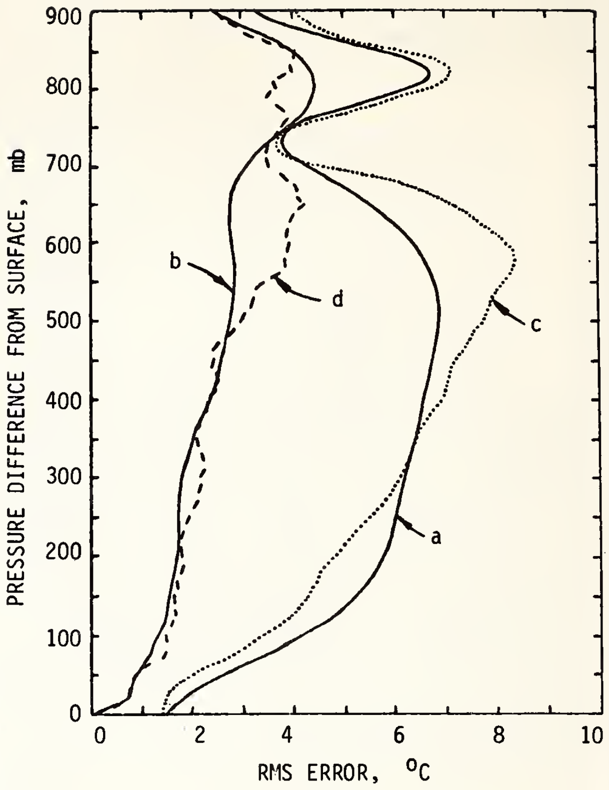

Figure 3. Same as Figure 1 except at Ocean Station P in the Gulf of Alaska in February-March 1977.

(layer thickness). The ocean data buoy application would be especially appropriate for obtaining temperatures in data-sparse regions to be used in numerical weather prediction.

5. ACKNOWLEDGMENTS

The radiometric measurements reported here were made under the direction of B. L. Gary and N. I. Yamane of the Jet Propulsion Laboratory, with support from the NOAA Data Buoy Office. We express our appreciation to personnel of the Pacific Missile Test Center and the Canadian Ship Quadra for providing meteorological data and facilities for the experiments.

6. REFERENCES

Westwater, E. R., M. T. Decker, and F. O. Guiraud, 1976: Feasibility of atmospheric temperature sensing from ocean data buoys by microwave radiometry. *NOAA Technical Report ERL 375-WPL 48*, National Technical Information Service, Springfield, Va.

Westwater, E. R., J. B. Snider and A. V. Carlson, 1975: Experimental determination of temperature profiles by ground-based microwave radiometry. *J. Appl. Meteor.*, 14, 524-539.

Department of U. S. Army Report
ASL-CR-78-8017-1, July 1978

MEASURES OF INHOMOGENEITY OF AEROSOLS

V. E. Derr
G. M. Lerfald
M. J. Post

A statistical analysis of atmospheric inhomogeneities was conducted to determine the design criteria of a transit time lidar. An experimental transit time lidar was built and employed to gather wind data. Other atmospheric sensors were also employed to measure relevant atmospheric parameters. System recommendations based on the collected and reduced data are presented in the last chapter.

Journal of Applied Meteorology, 17: 895-899, 1978.

Measuring Temperature Structure Parameter Profiles with an Acoustic Sounder

DUANE A. HAUGEN AND J. CHANDRAN KAIMAL

NOAA/ERL/Wave Propagation Laboratory, Boulder, Colo. 80302

11 October 1977 and 19 December 1977

ABSTRACT

A preliminary evaluation of acoustic sounders for measuring C_T^2 has been completed. Results show that the radar equation used to derive C_T^2 from sounders must be modified to include the effects of excess attenuation due to turbulence and beam bending due to horizontal winds. Both effects are strongly dependent on beam width and, taken together, can lead to errors of 400% or more in C_T^2 estimates.

---

1. Introduction

Since McAllister *et al.* (1969) first demonstrated the feasibility of using acoustic waves for remotely sensing the temperature structure of the atmosphere a great deal of information has been gathered by investigators on such features as convection plumes, capping inversions, nocturnal inversions and gravity waves. To a large extent these studies have been descriptive, based mainly on qualitative interpretations of facsimile records. The time-height displays obtained from monostatic sounders show the evolution and decay of boundary layer turbulence events and have found wide application in air pollution studies.

The potential for quantitative studies of atmospheric turbulence from the scattered acoustic energy was outlined by Little (1969). However, estimation of the temperature structure parameter C_T^2 from monostatic returns has received relatively limited attention (Neff, 1975; Asimakopoulos *et al.*, 1976). The objective of the work described by these workers was to compare *in situ* measurements of C_T^2 with estimates of C_T^2 derived from acoustic sounders. In each case, the transmitting and receiving efficiencies of the acoustic antenna were measured and the derived values of C_T^2 were compared directly with the *in situ* measurements. Comparisons were obtained at only one height above ground.

In the work to be reported here, no attempt was made to measure the antenna efficiencies. Instead, estimated values were used. Adjustments to these estimated values were then made as a result of the comparison tests.

The significant difference between our work and that by Neff and Asimakopoulos *et al.* is that we performed simultaneous comparisons at three heights above ground. Thus, we are able to determine whether the resulting "comparison factors" are a function of height. In the course of evaluating two monostatic sounders with somewhat different operating characteristics, we discovered that the conventional radar equation used to derive C_T^2 systematically underestimates its values. Analyses indicate the underestimation to be a function of height and stability. Here we will describe the two comparison experiments and the results obtained from them.

2. Theory

The theoretical basis for computing C_T^2 from the sounder backscatter is described in detail by Neff (1975). Therefore only a brief outline is presented here. The temperature structure parameters C_T^2 is defined by

$$C_T{}^2=\overline{[T(\bar{x})-T(\bar{x}+\bar{r})]^2/r^{\frac{2}{3}}}, \tag{1}$$

where T is the temperature at two points in space separated by distance r and the overbar represents a time average. This equation is valid only if the magnitude of r lies within the inertial subrange of the temperature fluctuations. To measure C_T^2 directly one simply measures the variance of the temperature difference between two points separated by distance r.

To measure C_T^2 from acoustic sounder returns, one starts with the radar equation for backscattered energy,

$$\frac{P_R}{E_R}=[P_T\cdot E_T][e^{-2\bar{\alpha}R}][\tfrac{1}{2}c\tau][(A/R^2)\cdot G]\cdot\sigma, \tag{2}$$

where

P_R	measured received electrical power
E_R	efficiency of antenna system in converting received acoustic to electrical power
P_T	transmitted electrical power
E_T	efficiency of antenna system in converting electrical to acoustic power
$e^{-2\bar{\alpha}R}$	power loss due to atmospheric attenuation of sound as it travels to scattering volume and back
α	attenuation coefficient, strongly dependent on frequency and humidity, weakly dependent on temperature and pressure
R	travel distance to scattering volume of interest
c	speed of sound
τ	duration of transmitted sound pulse
A	geometrical area (antenna aperture) of antenna
G	aperture gain factor related to distribution of scatterers within the sampling volume
σ	backscattering cross section.

The cross section σ is in turn related to C_T^2 by

$$\sigma = 0.0039\, k^{1/3} C_T^2 / T^2, \tag{3}$$

where k is the wavenumber of the transmitted sound and T the mean temperature of the air over the range of interest. From (2) and (3) we have an expression for C_T^2 in terms of atmospheric and instrument parameters which are either known or can be measured or estimated.

A number of references can be found describing techniques for computing the attenuation coefficient $\bar{\alpha}$ from measurements of pressure, temperature and humidity as a function of height (Harris, 1966; Sutherland, 1968; Neff, 1975). Suffice it to say that the techniques are straightforward and do not give rise to any difficulties, although it should be noted that in practice these atmospheric parameters should probably be measured with *in situ* sensors at various heights. This tends to limit the use of an acoustic sounder for obtaining C_T^2 to situations in which direct sensing of these parameters is accomplished in some manner using towers, balloons or airplanes as sensor platforms, particularly in stable conditions.

Estimating values for the antenna efficiencies E_T and E_R and the aperture gain factor G for a given acoustic sounder is considerably more difficult than estimating the attenuation factor. One can measure the antenna efficiencies to a fair degree of accuracy, but the aperture gain factor depends on the distribution of scatterers in the irradiated volume (Hall and Wescott, 1974). The scatterers in this case are the sharp temperature gradients in the atmosphere caused by turbulence. It is not well known whether these scatterers are distributed uniformly through the sound beam or whether variations in their distribution could seriously affect the received power. Our results seem to suggest that uncertainties in the estimates of C_T^2 arising from variations in the distribution of scatterers could be no greater than a factor of 2 and are probably considerably less.

In the work being reported here we assumed values of 0.1 for E_T and E_R and 0.4 for G. We then adjusted the value of the product of these terms so the C_T^2 comparison factor was normalized to unity at the lowest comparison height for unstable conditions.

3. Experiments

The first experiment was conducted in October 1974 at the Nevada Test Site (NTS) of the Energy Research and Development Administration (ERDA). The acoustic sounder used in this experiment was the WPL Mark VII (Owens, 1975) built for the Rome Air Development Center by the Wave Propagation Laboratory (WPL). A 50 ms burst of 2000 Hz acoustic energy was transmitted upward once every 2 s. After a delay of 150 ms, the transmitting antenna switches to its receiving mode to measure the energy scattered back by the transmitted pulse. The received signal was recorded on an FM-analog magnetic tape recorder for subsequent quantitative analysis as well as on a facsimile recorder for an immediate visual display.

The *in situ* measurements were made at three levels (45, 87 and 133 m) on the 450 m tower at NTS. Each level was equipped with a pair of finewire, platinum resistance thermometers spaced vertically 1 m apart. The sensor outputs were sampled at a rate of 20 times per second, recorded on digital magnetic tape, and processed in real time by a computer-controlled data acquisition system (Kaimal *et al.*, 1966). The sounder was located 450 m away from the tower to avoid possible sidelobe reflections from the tower. Data were gathered only during periods when the wind was blowing from the sounder toward the tower. In this direction the fetch was uniform for a distance of over 10 km.

The second experiment was conducted in January 1977 at WPL's Table Mountain test site about 20 km north of Boulder. The acoustic sounder used in these experiments was built by WPL for the Air Force Optical Observatory at Cloudcroft, N.M. The only significant difference between the two sounders was the design of the antenna cuffs used for sidelobe suppression. The cuff used in the NTS experiment was a four-sided plywood enclosure (Owens, 1975), flared at an angle of 11°, and lined internally with convoluted foam. The cuff used in the Table Mountain experiment was a fiberglass conical enclosure, flared at an angle of 16°, and lined on the inside with a sound absorbing material which consists of lead septum sandwiched between layers of foam. Sidelobe suppression was significantly improved with the conical cuff design. In addition, this design provided a narrower main beam, which will be seen to be a significant factor in interpretation of our results.

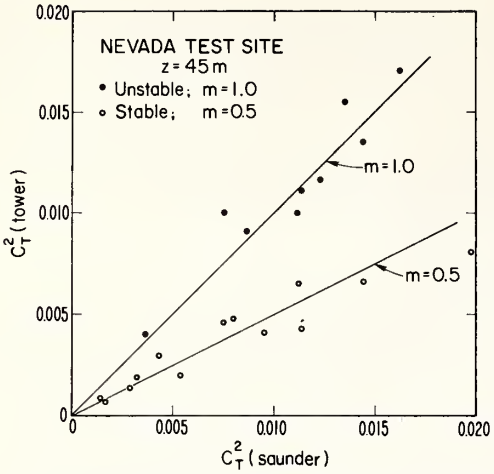

FIG. 1. Tower C_T^2 vs sounder C_T^2 at 45 m, Nevada.

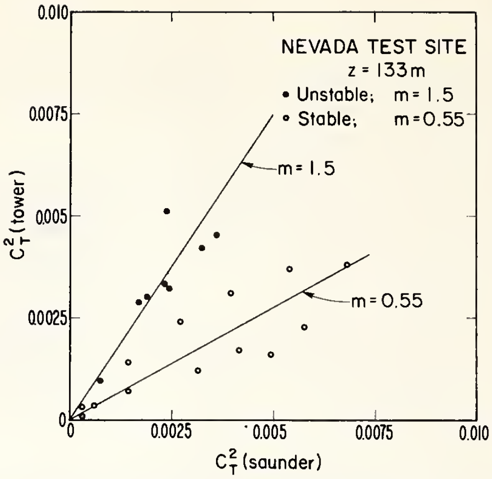

FIG. 3. As in Fig. 1 except at 133 m, Nevada.

The *in situ* sensors used in the Table Mountain experiment were similar to those used in the Nevada experiment and were mounted at heights of 38, 95 and 145 m on a 150 m tower. The sounder was located about 150 m north of the tower; data were collected only for easterly winds with a uniform fetch of 3 km.

Temperature and dew point temperature were measured at each of the three tower heights in the NTS experiment but only at the surface (~2 m) at Table Mountain, since the NTS results had shown that the attenuation coefficient $\bar{\alpha}$ did not change appreciably over the height range of interest. Pressure was measured at the surface for both sets of experiments. Careful calibration of the sounder electronics was accomplished through insertion of a known signal at the receiver input.

4. Results

Data obtained from the NTS and Table Mountain experiments are presented in Figs. 1–6 as scatter diagrams. Time-averaged C_T^2 values from the sounder at heights corresponding to the tower levels are plotted against the direct C_T^2 measurements averaged over the same time interval. The sounder C_T^2 values for each height were also averaged over the pulse width. The data selected for analysis were for those cases where convective plume activity (unstable) or the nocturnal inversion layer (stable) exceeded 150 m. Sounder facsimile records were used to control the data selection process as a qualitative check that the layer being observed was uniformly stable or unstable. Separate scatter diagrams were prepared for each height and for stable and unstable atmospheric conditions. The slope of the line of best fit is by definition the "comparison factor" of the sounder. The actual value of these comparison factors is not important for our purposes. Our interest is to examine the height and stability dependence of these factors.

Long-term averages were used for all the comparisons in an attempt to minimize any differences

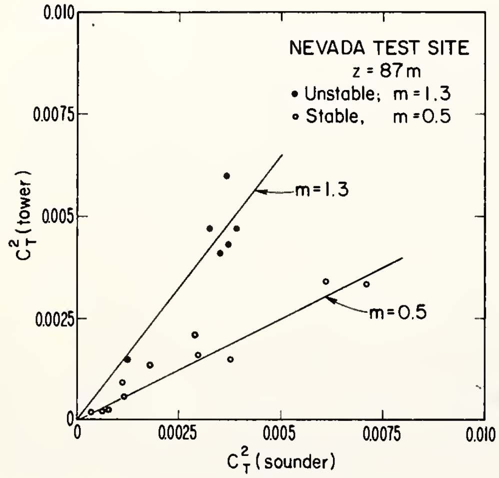

FIG. 2. As in Fig. 1 except at 87 m, Nevada.

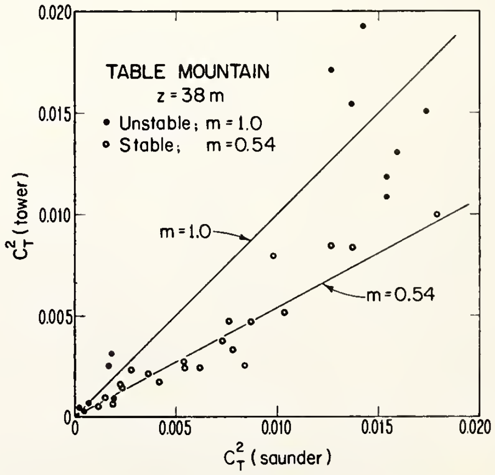

FIG. 4. Tower C_T^2 vs sounder C_T^2 at 38 m, Table Mountain.

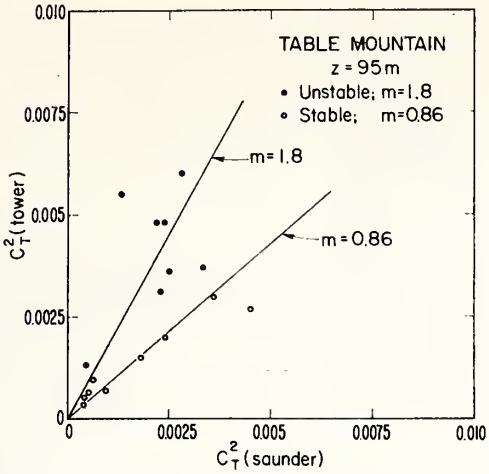

FIG. 5. As in Fig. 4 except at 95 m, Table Mountain.

that might exist due to the large spatial separation between the sounder and the *in situ* samples of C_T^2. Sixty minute averages were used for the NTS data; 30 min for the Table Mountain data. It is to be expected, of course, that some scatter will exist in the plots because of differences in sampling techniques and spatial variability of temperature fluctuations (Wyngaard, 1973).

Two observations emerge from these data. First, the scatter shown on any given plot appears reasonably small, implying that the assumption of a uniform distribution of scatterers through the acoustic beam is justified within a factor of 2 since some of the scatter must be attributed to spatial variability. Second, the slopes of the best-fit lines, i.e., the "comparison factors," vary markedly with atmospheric stability and with height. At any given height, the comparison factor for unstable conditions is about twice that for stable conditions. The variation with height is much greater for the Table Mountain data than for the NTS data, a fact that most likely reflects differences in sounder antenna characteristics, atmospheric conditions, or both.

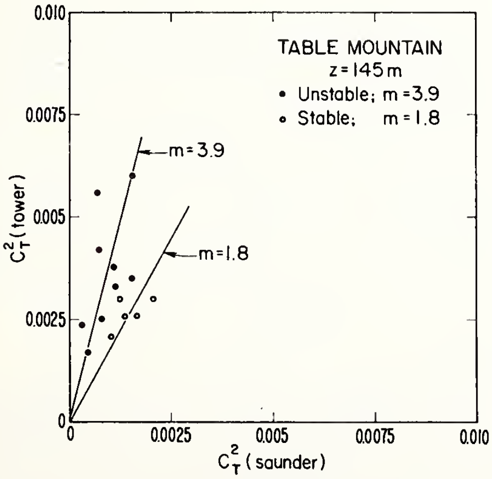

FIG. 6. As in Fig. 4 except at 145 m, Table Mountain.

In general, the atmospheric conditions at NTS varied from strongly stable to strongly unstable with a well-developed, deep planetary boundary layer. At Table Mountain, conditions varied from moderately unstable to moderately stable with a relatively shallow planetary boundary layer.

Our results are consistent with a theory of excess attenuation of sound propagated through a turbulent medium recently presented by Brown and Clifford (1977). They suggest that the turbulent wind field scatters acoustic energy outside the beam in a manner that is dependent on the intensity of turbulence. This leads to a beam-broadening effect of a loss of scattered energy that is not accounted for in the antenna equation (2). We are not able to verify the theory in detail with the data presented here, but the results are strongly supportive of the theory they propose. In particular, the narrower beam for the sounder used in Table Mountain experiment should indeed be significantly more susceptible to excess attenuation as observed.

5. Conclusions

The results illustrate that deriving C_T^2 from an acoustic sounder operating in a monostatic mode is seriously complicated by changes in comparison factor for the sounder with height and stability. At present, this means that any given sounder must be calibrated over the range of stabilities and heights against *in situ* measurements in order to provide the most accurate values of C_T^2 possible. The only alternative that we can suggest at the moment is to operate acoustic sounders in a bi-static mode in an attempt to derive both temperature and wind fluctuations so that excess attenuation can be explicitly accounted for in the radar equation. We are presently conducting a pilot study to explore the feasibility of this approach and hope to report the results in the near future.

Acknowledgments. The NTS experiment was supported by Mr. Ray Urtz of the Rome Air Development Center while we were members of the Air Force Cambridge Research Laboratories. The Table Mountain experiment was supported by Capt. James Lyon of the Air Force Optical Observatory after we joined the Wave Propagation Laboratory. We would also like to thank W. D. Neff, E. J. Owens and L. A. Vohs for their assistance and many helpful discussions during the course of both experiments. J. T. Newman and N. Szczepczynski participated fully in all the Table Mountain work and Mr. Newman also worked with us during the NTS experiment. The manuscript was typed by M. F. Birchfield.

REFERENCES

Asimakopoulos, D. N., R. S. Cole, S. J. Caughey and B. A. Crease, 1976: A quantitative comparison between acoustic sounder returns and the direct measurement of atmospheric temperature fluctuations. *Bound.-Layer Meteor.*, **10**, 137–147.

Brown, E. H., and S. F. Clifford, 1977: On the attenuation of sound by turbulence. *J. Acoust. Soc. Amer.*, **60**, 788–794.

Hall, Jr., F. F., and J. W. Westcott, 1974: Acoustic antennas for atmospheric echo sounding. *J. Acoust. Soc. Amer.*, **56**, 1376–1382.

Harris, C. M., 1966: Absorption of sound in air versus humidity and temperature. *J. Acoust. Soc. Amer.*, **40**, 148–159.

Kaimal, J. C., D. A. Haugen and J. T. Newman, 1966: A computer-controlled mobile micrometeorological observation system. *J. Appl. Meteor.*, **5**, 411–420.

Little, C. G., 1969: Acoustic methods for the remote probing of the lower atmosphere. *Proc. IEEE*, **57**, 571–578.

McAllister, L. G., J. R. Pollard, A. R. Mahoney and P. J. R. Shaw, 1969: Acoustic sounding—A new approach to the study of atmospheric structure, *Proc. IEEE*, **57**, 579–587.

Neff, W. D., 1975: Quantitative evaluation of acoustic echoes from the planetary boundary layer. NOAA TR ERL 322-WPL 38, 34 pp.

Owens, E. J., 1975: NOAA Mark VII acoustic echo sounder. NOAA TR ERL WPL 12, 71 pp.

Sutherland, L. C., Ed., 1968: Sonic and vibration environments for ground facilities—A design manual, Wyle Lab. Rep. No. WR-68-2, NASA Contract NAS8-11217, Huntsville, Ala., Chap. 7, pp. 1–14.

Wyngaard, J. C., 1973: On surface layer turbulence. *Workshop in Micrometeorology*, Amer. Meteor. Soc., 101–149.

Preprint Volume; Fourth Symposium on Meteorological Observations and Instrumentation, 278-280, American Meteorological Society, 1978.

MEASURING C_T^2-PROFILES WITH ACOUSTIC SOUNDERS

Duane A. Haugen and J. Chandran Kaimal

NOAA/ERL/Wave Propagation Laboratory
Boulder, Colorado 80302

1. INTRODUCTION

We have conducted two experiments using acoustic sounders to obtain measurements of the temperature structure parameter, C_T^2. The first one was conducted at ERDA's Nevada Test Site in October 1974, the second one at WPL's Table Mountain site in January 1977. In each experiment, the desired result was to establish calibration data that would permit one to obtain C_T^2-profiles with sufficient accuracy to be useful for optical tracking applications. The results of these experiments have been reported elsewhere (Haugen and Kaimal, 1978). Only a brief summary will be presented here.

2. THEORETICAL BACKGROUND

A detailed description of the theoretical basis for deriving C_T^2 from acoustic sounders has been given by Neff (1975). It can be shown that acoustic energy backscattered by temperature discontinuities in a turbulent atmosphere depends in part on the intensity of the temperature fluctuations in the inertial subrange. Hence, estimates of C_T^2 may be derived from measurements of the backscattered energy of acoustic pulses along with measurements of the sounder antenna characteristics and atmospheric conditions that affect sound propagation. In general, the antenna characteristics are independent of range whereas the atmospheric effects are strongly range dependent. Thus, in practice one can establish calibration data for a sounder by merely estimating values for the antenna characteristics and carefully measuring the range-dependent terms in a series of comparison measurements between the sounder and direct, in-situ sensors. One test of the theoretical basis for sounder-derived C_T^2-values is to determine whether the calibration data is independent of range and atmospheric conditions. It is this test of the theory which we have attempted.

3. EXPERIMENTAL PROCEDURES

Direct measurements of C_T^2 were made at three levels on a tower with in-situ sensors in each experiment. The sounder-derived C_T^2-values were based on estimates of the various antenna characteristics and measurement of the atmospheric, range-dependent parameters. Long term averages (60 minutes for the Nevada and 30 minutes for the Table Mountain experiments) were obtained in order to minimize spatial variability effects between the two methods of obtaining C_T^2. Separate scatter diagrams were then prepared for stable and unstable conditions for each observation height. A separate set of scatter diagrams was prepared for each experiment as well. The acoustic sounder used in the Table Mountain experiment had a significantly narrower beam than the one used in the Nevada Test Site experiment. Other antenna characteristics also differed so the two sets of calibration data should not be identical. However, each set of calibration data has similar characteristics with respect to dependencies on range or atmospheric conditions.

4. RESULTS

The calibration data revealed a dependency on height as well as on atmospheric stability. The data were therefore normalized to give a one-to-one comparison between the tower and sounder C_T^2-values for the lowest height under unstable conditions. A simple measure of the height and atmospheric stability dependency is to note the slope of the line of best fit relative to one. The various scatter diagrams we prepared are summarized in Figs. 1 through 4 where we show the slopes of the various lines but not the individual data points. The scatter of the data was generally within a factor of two as may be seen in the paper by Haugen and Kaimal (1978).

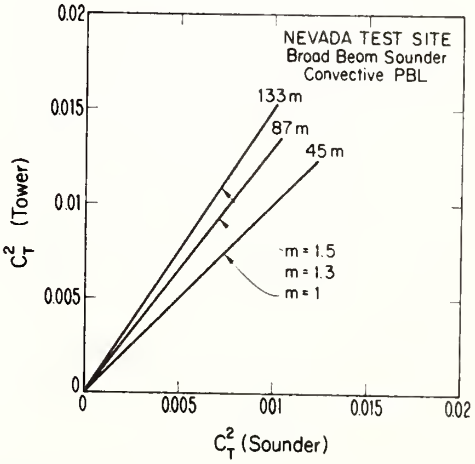

Figure 1. Tower C_T^2 vs sounder C_T^2, convective PBL, Nevada.

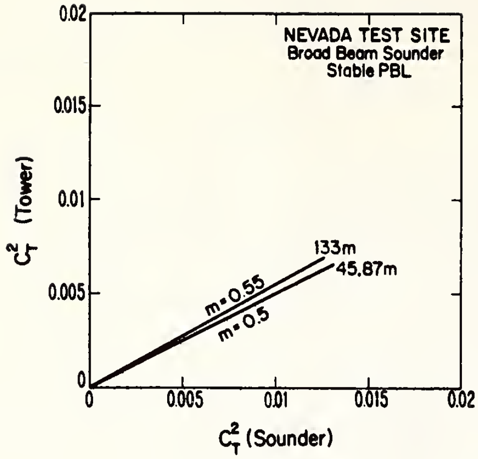

Figure 2. Tower C_T^2 vs sounder C_T^2, stable PBL, Nevada.

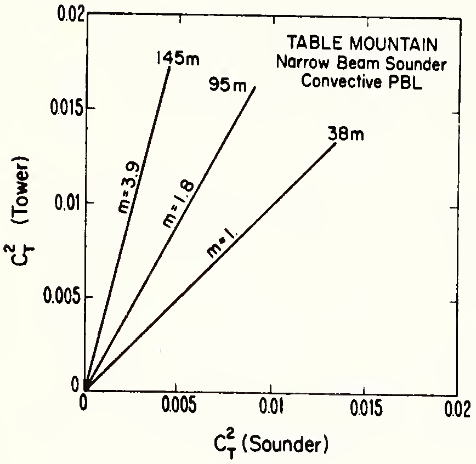

Figure 3. Tower C_T^2 vs sounder C_T^2, convective PBL, Table Mountain.

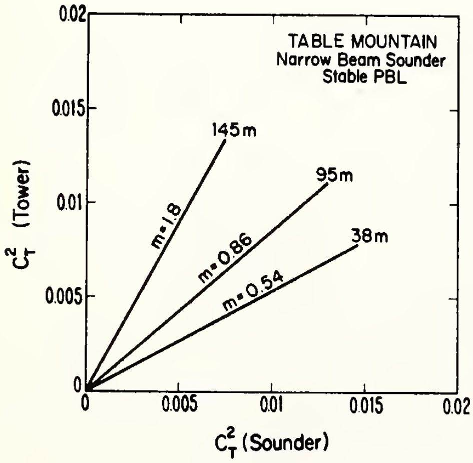

Figure 4. Tower C_T^2 vs sounder C_T^2, stable PBL, Table Mountain.

Looking first at the Nevada Test Site results, we note that the slope increases from 1.0 to 1.5 over a height range of 45 to 133 m under convective conditions. Under stable conditions, the slope changes only slightly with height, but is one-half to one-third the slopes found for convective conditions. At the time we obtained these results, we learned of some work later reported by Brown and Clifford (1977) describing excess sound attenuation caused by turbulence. This attenuation is not accounted for in the equations used to derive C_T^2 from the sounder and it is range dependent. Therefore our results are consistent with their predictions since the Nevada stable cases were nearly laminar flow conditions for which little excess attenuation would be expected. The difference between stable and unstable cases had been observed previously by Neff (1975) and is not yet fully understood. One possible explanation is that the inertial subrange of the stable temperature spectra may not be well developed for the eddy sizes causing the acoustic backscatter. But, to our knowledge, this aspect of acoustic echo behavior has not yet been studied by anyone.

The Table Mountain results are similar to the Nevada Test Site results, but the variation with height is much greater and occurs for stable as well as unstable cases. The dependency on stability is the same otherwise, the slopes for stable cases being roughly one-half those for unstable cases. There are at least three possible explanations for the increased height dependency. The antenna beam for the Table Mountain experiment was considerably narrower than for the Nevada experiment. Excess attenuation due to turbulence is generally more effective for a narrow antenna beam. Next, the wind speeds and turbulence levels were generally higher at Table Mountain, which should lead to greater excess attenuation for both stable and unstable cases, all other factors being equal. Finally, another source of apparent excess attenuation is high wind speeds which cause beam bending. Detailed explanation of our results is not possible with the limited amount of data we gathered in these experiments. However, further research being carried out at Table Mountain to better understand these possible effects is reported on in the following paper (Neff and Haugen, 1978).

5. CONCLUSIONS

These results show that problems of excess attenuation with acoustic sounders appear to have potential for serious inaccuracies in the measurement of C_T^2-profiles if ignored. A well-documented method for including these effects in the theory does not exist at present, but we have every reason to expect research efforts to accomplish this in the near future. Certainly, the need for C_T^2-profiles in many types of research problems makes the use of remote probes such as the acoustic sounder very attractive which in turn makes the resolution of this excess attenuation question very important.

6. ACKNOWLEDGMENTS

The Nevada Test Site experiment was supported by Mr. Ray Urtz of the Rome Air Development Center while we were members of the Air Force Cambridge Research Laboratories. The Table Mountain experiment was supported by Capt. James Lyon of the Air Force Optical Observatory, Cloudcroft, N. Mex., after we joined the Wave Propagation Laboratory. We are grateful for this support as well as for the assistance and interest we received from our colleagues during the course of both experiments.

7. REFERENCES

Brown, E. H., and S. F. Clifford, 1977: On the attenuation of sound by turbulence, *J. Acoust. Soc. Am.*, 60, 788-794.

Haugen, D. A., and J. C. Kaimal, 1978: Measuring temperature structure parameter profiles with an acoustic sounder, *J. Appl. Meteor.*, 17, to be published.

Neff, W. D., 1975: Quantitative evaluation of acoustic echoes from the planetary boundary layer, *NOAA TR ERL 322-WPL 38*, U.S. Govt. Printing Off., Washington, D.C., 34 pp.

Neff, W. D., and D. A. Haugen, 1978: Multibeamwidth studies of excess acoustic attenuation, *Fourth Symp. Meteor. Obs. and Inst.*, *Preprints*, Am. Meteor. Soc., Boston, Mass.

Journal of Applied Meteorology, 17: 1514-1520, 1978.

Beamwidth Effects on Acoustic Backscatter in the Planetary Boundary Layer

W. D. Neff

NOAA/ERL/Wave Propagation Laboratory, Boulder, CO 80302

(Manuscript received 19 January 1978, in final form 15 June 1978)

ABSTRACT

An "excess attenuation" experiment is described that uses an acoustic sounder (or echosonde) operating at simultaneous frequencies of 1250 and 2500 Hz. The relative error in the received powers at these two frequencies is shown to be a beam-width-dependent effect. The magnitude of this effect at 150 m ranged typically from 50% in free-convection conditions to 400% with wind speeds of 10 m s^{-1}, consistent with a number of previous comparison experiments. The results of this experiment are interpreted in terms of models of the broadening of the beam by small-scale turbulence and the refraction of the beam by a transverse wind.

1. Introduction

Acoustic sounders (or echosondes) are widely used for boundary layer and air pollution studies. Many of these applications have relied solely on qualitative interpretations of facsimile records. With increasing use, for example, of microprocessor technology (Owens, 1977) it is now possible to obtain quantitative information on boundary layer turbulence on a routine basis. The first comparisons of acoustic backscatter intensities with predictions from *in situ* tower instruments at a single height (Neff, 1975; Asimakopoulos *et al.*, 1976) showed reasonable agreement with the scattering theory proposed by Tatarskii (1971). However, vertical profiles of the temperature structure parameter C_T^2 in Neff (1975) indicated a more rapid decrease of intensity with increasing height than was expected from theory. Additional measurements recently reported by Haugen and Kaimal (1978) at several tower levels confirmed an apparent attenuation of the sound with range in excess of that expected from viscous and molecular-relaxation effects.

The structure functions of temperature and velocity are useful descriptors of boundary layer turbulence (Kaimal, 1973). Developing a technology to derive these quantities from echosonde returns is of considerable interest (Brown, 1975; Kerman, 1976). Resolution of the "excess attenuation" problem constitutes an essential first step if the errors in such measurements are to be minimized. Brown and Clifford (1976) reviewed the so-called excess attenuation problem and applied forward-scatter optical results to predict the magnitude of acoustic beam-broadening produced by small-scale turbulence. Their results, however, applied only to the reduction of the intensity in the forward-scatter direction. Fig. 1 shows this effect schematically where A_0 represents the area of the beam in the absence of turbulence and A_T+A_0, the area after turbulent broadening. For application to echosondes, we estimated the effect of the broadening on the power received by the antenna. This required the assumption that any signal backscattered from the region outside of A_0 could only return to the main beam (defined by A_0) through a second scattering (a small effect) and ignores further effects of turbulence on the scattered beam. Brown and Clifford's results showed that the ratio $A_0/(A_T+A_0)$ depended strongly on frequency or equivalently on beamwidth. This then suggested, as a critical test of this interpretation of their theory and as a means of measuring the excess attenuation, the simple multi-beamwidth acoustic scattering experiment described here.

The theory and results of this experiment, which show the beamwidth and range dependence of the excess attenuation, are described first. Profile data from Neff (1975) are then interpreted to show relative errors comparable with those found in this experiment. Further analysis of data from an attempt to "calibrate" an echosonde, using a "corner reflector" mounted on a tower, suggests that refraction (or bending) of the beam by a transverse wind may also be significant. This then leads to an interpretation of the data in terms of the combined effects of broadening and refraction.

2. Formulation of the experiment

Our analysis uses the monostatic echosonde equation (Neff, 1975), which relates the received power to the corresponding scattering cross section per unit

0021-8952/78/1514-1520$05.00
© 1978 American Meteorological Society

volume. We have included an additional term $L_E(f)$ which we expected to correspond to the ratio $A_0/(A_0+A_T)$. While the behavior of $L_E(f)$ may be a complicated function of range and turbulence parameters, we have not specified a particular functional form leaving this to be determined by the experiment. Because of the differences in the underlying physical processes we have separated $L_E(f)$ from the viscous and molecular absorption term which follows a well-known exponential law.

In terms of measured and/or calculated quantities,

$$\frac{P_R}{E_R}=P_TE_Te^{-2\bar{\alpha}R}\left[\sigma_0(R,f)\frac{c\tau}{2}\frac{A}{R^2}G\right]L_E(f), \qquad (1)$$

where:

P_R/E_R	received power, where P_R is the measured electrical power and E_R the efficiency of conversion from received power
P_TE_T	radiated power, where P_T is the electrical power applied to the transducer and E_T the efficiency of conversion to radiated acoustic power
$e^{-2\bar{\alpha}R}$	round-trip loss of power resulting from attenuation by viscous and molecular-relaxation processes, where $\bar{\alpha}$ is the average attenuation (m^{-1}) to the scattering volume at range R(m)
$\sigma_0(R,f)$	scattering cross section per unit volume, i.e., the fraction of incident power backscattered per unit distance into unit solid angle at frequency f
$c\tau/2$	maximum effective-scattering volume thickness, where c is the local speed of sound ($\mathrm{m\ s}^{-1}$) and τ the pulse length (s)
$4G/R^2$	solid angle subtended by the antenna aperture A (m^2) at range R (m) from the scattering volume, modified by an effective-aperture factor G, arising from the antenna's directivity
$L_E(f)$	excess attenuation, whose magnitude and behavior is to be determined by the experiment and compared with the theory of Brown and Clifford.

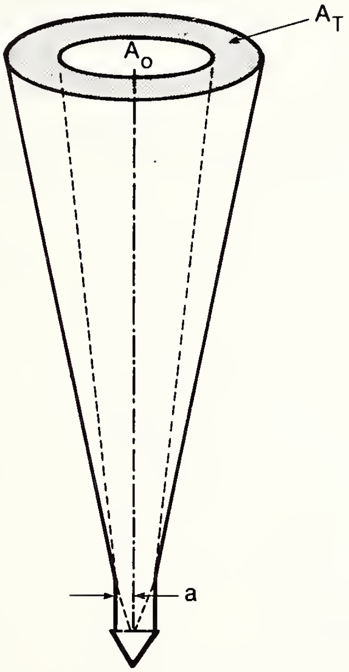

FIG. 1. The effect of forward-scatter turbulent broadening on an echosonde beam. A_0 indicates the area illuminated in the absence of turbulence while A_T represents the increase in area after broadening. Since total power is conserved, the ratio $A_0/(A_0+A_T)$ approximates the decrease in intensity with this interpretation.

Tatarskii (1971) expresses the acoustic backscatter cross section per unit volume σ_0 as

$$\sigma_0\simeq(\pi/2)k^4\phi_T(2k)/T_0^2, \qquad (2)$$

where ϕ_T is the isotropic, three-dimensional spectral density of temperature fluctuations, $k=2\pi/\lambda$ the incident acoustic wavenumber at wavelength λ, and T_0 the local mean temperature. When the spectrum is expressed in terms of the temperature structure parameter

$$C_T^2=\langle[T(\mathbf{x})-T(\mathbf{x}+\mathbf{r})]^2\rangle/r^{\frac{2}{3}}, \qquad (3)$$

where angle braces indicate an ensemble average, $\mathbf{x}$ denotes the location at which C_T^2 is evaluated, and $\mathbf{r}$ is the separation between the sensors, Tatarskii (1971) finds the following expression for the cross section:

$$\sigma_0=0.0039k^{\frac{1}{3}}(C_T^2/T_0^2). \qquad (4)$$

When (4) is inserted into (1), a number of unknowns remain. However, if at every range gate one takes the ratio of the received power at each of two frequencies, a number of these unknowns cancel. For an echosonde operating at frequencies f_1 and f_2 (wavenumbers k_1 and k_2), we then have at range R

$$\frac{P_R(f_1)}{P_R(f_2)}=\frac{E_1}{E_2}\exp[-2(\bar{\alpha}_1-\bar{\alpha}_2)R]\left(\frac{f_2}{f_1}\right)^{\frac{1}{3}}L_{12}, \qquad (5)$$

where $E_i=E_R(f_i)E_T(f_i)$ with $i=1$, 2, and $L_{12}=L_E(f_1)/L_E(f_2)$. Since the efficiencies were not measured and may change with time, the ratios L_{12}, which we calculated from (5) at each range gate (31, 67, 95, 125 and 150 m), were normalized by L_{12} at the lowest gate (31 m) to eliminate E_1/E_2. If excess attenuation is present at this lowest level, this procedure may introduce some error in the absolute values of L_{12}.

The classical and molecular attenuations included in the coefficients $\bar{\alpha}_1$ and $\bar{\alpha}_2$ were calculated using the equations of Sutherland (1975). Surface values of humidity and temperature were used for this calculation. We estimated that this use of surface

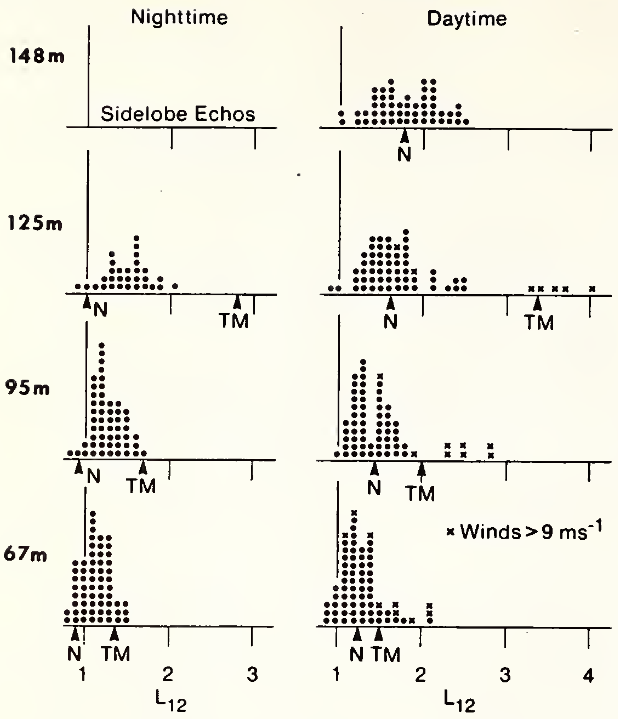

FIG. 2. Histograms of L_{12}, the excess attenuation error at 2500 Hz relative to that at 1250 Hz, as a function of height and time of day with individual samples normalized to values at 30 m. *In situ* echosonde ratios of the temperature structure parameter $C_T{}^2$ from Haugen and Kaimal (1978) are indicated by arrows. Their Nevada data (N) were obtained under conditions of light winds and moderate daytime convection whereas their Table Mountain data (TM) were obtained under windier conditions.

data would produce an error of only a few percent at the short ranges of interest to us (150 m).

The frequency dependence in (5) depends on a $-5/3$ spectral slope. Any anomalies in the spectral slope will change the interpretation of the scattering cross section in terms of $C_T{}^2$ as discussed by Neff (1975). Recent modeling of the large-wavenumber region of the temperature spectrum (Hill, 1978) suggests that a non-5/3 behavior does occur and is a function of the dissipation rate. However, for the convective boundary layer where one finds the largest excess attenuation, the dissipation rate varies only slowly with height and is large enough that the anomalous spectral region lies largely outside the wavenumber range of the sounder. Such anomalies should not, therefore, introduce any significant complication in the range-dependence of L_{12} under these conditions.

3. Experimental results

The experiment was run over an 8-day period in August 1977 at NOAA's Table Mountain field site. This site, atop a mesa, was instrumented with a 150 m tower to measure wind speed and direction. Received powers $P_R(f_1)$ and $P_R(f_2)$ in (5) were averaged for 30 min periods from a multi-frequency echosonde like that described by Neff (1975). Altogether some 66 h of data were obtained; each normalized, 30 min average for L_{12} was calculated and is represented by a dot within the histograms in Fig. 2. We have interpreted the value of $L_E(f)$ as the ratio of $A_0/(A_T+A_0)$ (cf. Fig. 1). If the excess attenuation increases with increasing frequency, then one expects that $L_E(f_1) > L_E(f_2)$ for $f_2 > f_1$. In the presence of excess attenuation one should thus find values of $L_{12} = L_E(f_1)/L_E(f_2)$ that are greater than 1.0. Some values in Fig. 2 are less than 1.0 because of scatter in the normalizing values of L_{12} calculated at 31 m. This implies some excess attenuation at low levels that cannot be resolved by the experiment because the minimum reliable range of the echosonde is only slightly less than 31 m.

Although the data are separated according to night and day, the nighttime cases should not be considered fully representative of the nocturnal boundary layer because of the higher winds and decreased static stability during the periods of observation. Data obtained during high wind (9–11 m s⁻¹) conditions are identified as such. Although it is not a strictly valid comparison [unless one assumes minimal excess attenuation at our lower frequency (1250 Hz)], we have included in Fig. 2 the *in situ* echosonde $C_T{}^2$ comparison errors from Haugen and Kaimal (1978). Their Nevada data (labeled N) were obtained under conditions of moderate convection and light winds

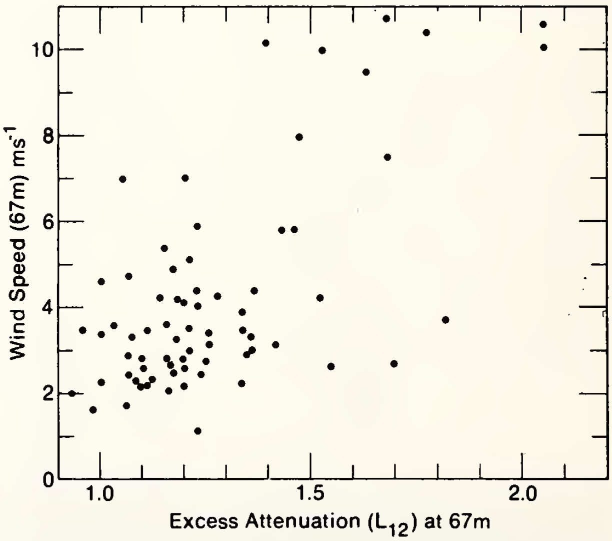

FIG. 3. Scatter plot of the excess attenuation factor L_{12} during convective conditions against wind speed at the 67 m tower level.

similar to those prevailing during the majority of our daytime cases. Their Table Mountain data (labeled TM) were obtained under generally windier conditions. Excluding the higher wind cases, Fig. 2 shows a nearly linear increase in the median values of L_{12} with range that agrees well with the Nevada data of Haugen and Kaimal. Both the scatter of the points about the median and the variability in the individual profiles (not shown) suggest, however, a complicated relation between excess attenuation and atmospheric parameters.

Because the data of Haugen and Kaimal indicated some effects due to windiness, we show in Fig. 3 a scatter diagram relating the magnitude of the excess attenuation at 67 m to the wind speed at that height. Although the excess attenuation depends on ambient meteorological conditions, it is clear from the large scatter in this figure that more extensive *in situ* instrumentation will be required to determine functional relationships. Similar plots of excess attenuation versus wind shear showed even greater scatter.

Fig. 4 shows profiles of C_T^2 obtained by Neff (1975), comparing typical echosonde data with the $Z^{-4/3}$ profile predicted by free-convection theory (Wyngaard *et al.*, 1971). These data were obtained under convective conditions with a capping inversion where, from the data of Frisch and Ochs (1975), it was expected that the falloff would be less rapid than the free-convection prediction. Although it was speculated (Neff, 1975) that the discrepancy was due to excess attenuation, there was no theory at that time to adequately describe the effect. When the profile between 50 and 200 m is extrapolated to 30 m (to be directly comparable with our normalized values of L_{12}) and compared with the $Z^{-4/3}$ prediction, a value of $L_{12}=1.6$ results, which is remarkably consistent with the data in Fig. 2. A frequency of 2250 Hz was used in this experiment.

Data were also analyzed from an experiment carried out in 1972 at the Haswell, Colorado, field site of the Wave Propagation Laboratory using the multifrequency echosonde described by Neff (1975). This experiment used a corner reflector mounted at the top of a 150 m tower as pictured in Fig. 5. The antenna was aimed at this reflector. The reflector acts as a diffraction-limited source with a 1 m diameter which reradiates in the direction of the receiving antenna. The amount of power received at each frequency depends on the molecular attenuation, the transducer efficiencies, and the fraction of each beam intercepted by the corner reflector and the receiving antenna.

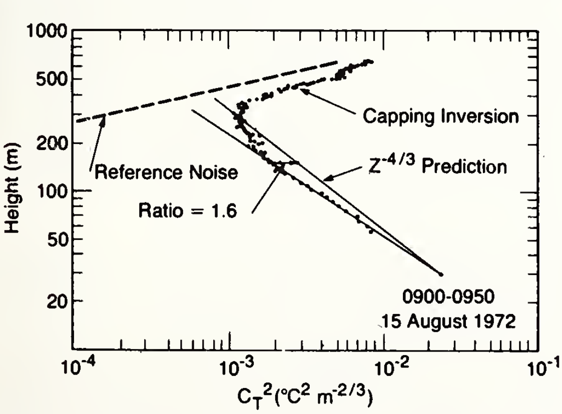

Fig. 4. Profiles of C_T^2 derived from echosonde data by Neff (1975) compared with the $Z^{-4/3}$ profile predicted by free-convection theory. The discrepancy at 150 m corresponds to an $L_{12}=1.6$.

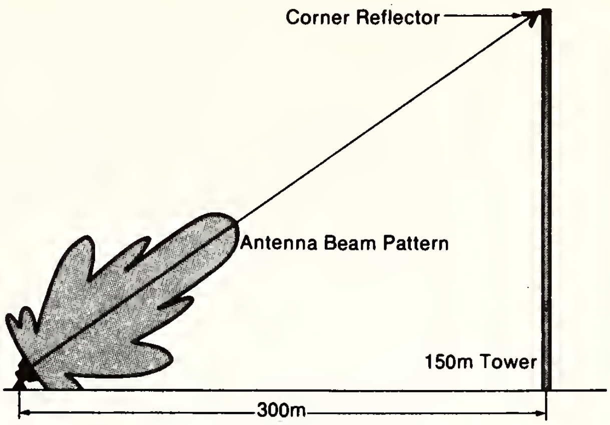

Fig. 5. Schematic diagram of corner-reflector experiment.

The data shown in Fig. 6 were obtained during a 7 min calibration run during the early evening on 13 August 1972. We used a 50 ms pulse length with a 4 s repetition period. The amplitude of the return-signal varied from 25 to 50%; peak values are plotted at 4 s intervals in Fig. 6. The temperature profile to the top of the tower was isothermal. The wind was about 7 m s^{-1} from the southeast which was transverse to the propagation path. The effects of molecular attenuation and differing transducer efficiencies have been removed from the 3200 Hz data so as to be directly compared with those at 1250 Hz. The same amount of power was applied at each frequency so that the narrowest of the beams (i.e., that corresponding to the highest frequency) was expected to lead to a much stronger return. In fact, we observed comparable peak values (posed in terms of the receiver voltage in Fig. 6) but much reduced average amplitudes and more rapid fading between peaks at the higher frequencies. This suggested refraction effects (or beam-bending by the wind) that would be more noticeable with the narrower beam. Because the first sidelobes were down by about 15–30 dB at 1250 and 2500 Hz, respectively, we expected minimal interference from ground reflections. Because of the difficulty in calculating the fraction of power subtended by the corner reflector (because of refraction) it was not possible to calculate a factor equivalent to L_{12} which we used in our Table Mountain data.

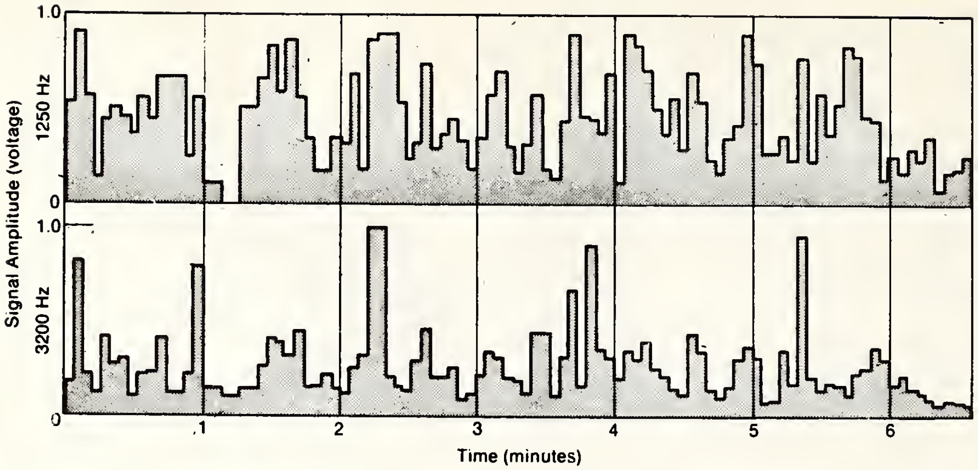

FIG. 6. Return signals from corner reflector (Fig. 5) at simultaneous frequencies of 1250 and 3200 Hz showing diminishment and more rapid fading of the signal with narrower beams.

4. Interpretation of results

Both our data and those of Haugen and Kaimal (1978) clearly confirm the presence of an excess attenuation mechanism. However, interpretation of these backscatter results in terms of existing theory requires some care. Brown and Clifford (1976) calculated the beam broadening (in the absence of beam wander) in terms of the acoustic refractive index structure function

$$C_n^2=\frac{C_T^2}{4T^2}+\frac{C_v^2}{C^2}, \tag{6}$$

where C_T^2 and C_v^2 are the structure parameters for temperature and velocity inhomogeneities, T the mean temperature and C the speed of sound. The fraction of the acoustic energy remaining within the non-broadened beam pattern corresponding to the ratio $A_0/(A_0+A_T)$ in Fig. 1 (at range R with antenna diameter D_0) is then given by (Brown and Clifford, 1976, Eq. 5)

$$\frac{A_0}{A_0+A_T}=\left\{1+1.56k^{12/5}D_0^2\times\left[\int_0^R ds\left(\frac{R-s}{R}\right)^{5/3}C_n^2(s)\right]^{6/5}\right\}^{-1}, \tag{7}$$

where s is measured along the beam. For constant C_n^2 this becomes

$$\frac{A_0}{A_0+A_T}=\{1+0.48k^{12/5}D_0^2R^{6/5}C_n^{12/5}\}^{-1}. \tag{8}$$

For $C_n^2=10^{-6}$ and $D_0=2$ m, this gives a maximum loss of about 33% out of the non-broadened beam at 150 m with $f=2500$ Hz. Now, if one assumes that only a negligible fraction of this energy is returned to the receiver, this is approximately the error for the backscatter intensity. Relative to the error at 1250 Hz this gives an equivalent $L_{12}=1.37$ which is somewhat less than the values in Fig. 2. Eq. (7) does not apply in the near field of the antenna although that is the most important region for generation of the broadening by virtue of the path weighting function multiplying C_n^2. We have not therefore, normalized by its predictions at 30 m as we did in the experiment analysis.

Table 1 shows both absolute and relative errors predicted using time-averaged C_n^2 profiles derived from the data of Kaimal *et al.* (1976) that are typical for a moderately convective boundary layer. However, in a convective boundary layer, C_T^2 varies considerably over periods of several minutes. Since the experimental values of L_{12} are biased by those times when C_T^2 is

TABLE 1. Relative and absolute errors predicted by Eq. (7) (relative errors in parentheses correspond to a doubling of C_T^2).

	Antenna radius = 0.6 m			Antenna radius = 1.0 m		
Height	Absolute error		Relative (L_{12}) error	Absolute error		Relative (L_{12}) error
(m)	1250 Hz	2500 Hz		1250 Hz	2500 Hz	
60	0.97	0.87	1.11 (1.18)	0.93	0.72	1.29 (1.44)
90	0.97	0.86	1.13 (1.20)	0.92	0.69	1.34 (1.49)
120	0.97	0.85	1.14 (1.21)	0.91	0.67	1.37 (1.53)
150	0.96	0.83	1.16 (1.23)	0.91	0.65	1.40 (1.56)

large we made a second calculation, doubling the values of C_T^2 used in $C_n^2(z)$. This produced as much as a 16% increase in the relative error, as is shown by the values in parentheses in Table 1. Variability in C_n^2 may thus account for much of the scatter in L_{12} shown in Fig. 2. Since the antenna beamwidth is a function of both frequency and aperture size (see below), two radii were used for the calculations in Table 1 to give an indication of the range of errors to be expected.

Examination of the data in Table 1 and the dependence on range shown in (8) suggests that the linear increase in L_{12} with range (shown by the data in Fig. 2) requires a nearly constant and large value of C_n^2 along the propagation path. Mean profiles of C_n^2 may not, therefore, be appropriate to a careful test of the theory behind (7) and its more detailed modifications (Clifford and Brown, 1978) that include a direct calculation of propagation effects to and from the scattering volume.

A second effect to consider is refraction or bending of the transmitting beam by the wind, as suggested by the data in Fig. 6. To estimate this effect, we first calculated the change in angle of arrival ϕ due to a horizontal wind acting on a vertical beam. This is given by Georges and Clifford (1972) as

$$\phi(z)=2\bar{u}(z)/c, \quad \bar{u}(z)=\frac{1}{z}\int_0^z u(s)ds, \tag{9}$$

where $u(s)$ is the wind speed as a function of height, c the speed of sound, z the height of the scattering volume and temperature gradients are neglected. This effect can be interpreted as a shifting of the apparent scattering volume off-axis. Because of the narrow receiving beam, the scattered sound received from off-axis is weighted less than that received on the main axis of the antenna.

To calculate this effect we assumed a beam pattern characteristic of a defraction-limited circular aperture (Born and Wolf, 1964) which approximates the radiation field of acoustic antennas (Hall and Wescott, 1974). We define for a uniformly illuminated antenna aperture, the radiation pattern

$$P(\theta)=\left[\frac{2J_1(2\pi a\theta/\lambda)}{(2\pi a\theta/\lambda)}\right]^2, \tag{10}$$

where J_1 is a first-order Bessel function, a the aperture radius, θ the angle from the center of the beam, and λ the acoustic wavelength. We integrated the product $P_1(\theta_1)P_2(\theta_2)$ on a horizontal grid where the separation of the beam centers was a function of the wind speed through (9) and θ_1 and θ_2 were transformed to Cartesian coordinates. This calculation of the received power from the integration of $P_1(\theta_1)P_2(\theta_2)$ follows the formulation of Probert-Jones (1962) for the effective aperture factor used in (1). We then normalized the results of the integration to that obtained with no separation to find the reduction in received power due to refraction.

Table 2. Ratio of errors at 2500 Hz to those at 1250 Hz (L_{12}) at 150 m with antenna radii of $a=0.6$ m and $a=1.0$ m.

Wind speed ($\bar{u}$) (m s^{-1})	Error due to refraction of nonbroadened beam $a=0.6$ m	$a=1.0$ m	Total error due to refraction of a broadened beam $a=0.6$ m	$a=1.0$ m
0	1.00	1.00	1.15	1.40
3	1.03	1.07	1.17	1.45
6	1.12	1.36	1.26	1.64
9	1.27	2.00	1.39	2.03
12	1.53	3.35	1.62	2.67

Since the transmitted beam will tend to be broadened by small-scale turbulence, this will reduce the apparent effect of beam refraction. This effect was evaluated by adjusting the wavelength in (10) for the refracted beam to produce a broadening equivalent to that implied by (7) at 150 m [using C_n^2 profiles derived from Kaimal *et al.* (1976) for moderate convection] and again computing $\int P_1P_2$. Since the power distribution in (10) is quite sensitive to the antenna aperture radius a, we used two values of this parameter. For compatibility with Fig. 2, the results are posed as the relative error between 1250 and 2500 Hz in Table 2. Evidently refraction is typically important for mean winds greater than 6 m s^{-1} while turbulent broadening diminishes the relative importance of refraction. The antenna used in our experiment had an aperture radius of $a=1.0$ m but was somewhat nonuniformly illuminated so that its effective radius may lie between the values $a=0.6$ and $a=1.0$ used in our calculations.

5. Conclusions

The simple multi-frequency experiment described above shows that the effects of turbulent beam broadening and refraction by a mean wind on acoustic backscatter intensities can be significant. The magnitudes of the errors observed are consistent with *in situ* echosonde comparisons of the temperature structure parameter C_T^2, as measured by Haugen and Kaimal (1978), but somewhat greater than those predicted by present theory. Our calculations suggest that the greatest accuracy will be obtained at low frequencies using narrow aperture antennas with errors in the calculation of C_T^2 predicted to be as small as 4%. For higher frequencies and wider aperture antennas the errors are predicted to be as large as 100% at 150 m under typical convective conditions and as much as 400% under windy conditions. Our comparisons with theory ignored such features as nonuniform illumination of the antenna aperture and short-term variability in the profile of C_n^2. These will be addressed by a future experiment that will also examine the ability of the technique to yield layer-averaged values of C_n^2 and hence the kinetic energy dissipation rate.

Acknowledgments. The author is indebted to Duane Haugen for many helpful discussions and for his assistance in implementing this experiment. Comments and criticisms by Chandran Kaimal, Edmund Brown, Steven Clifford and Thomas Georges have been most useful. Norbert Szczepczynski, Daniel Wolfe and Jim Newman aided in the field operation.

REFERENCES

Asimakopoulos, D. N., R. S. Cole, S. J. Caughey and B. A. Crease, 1976: A quantitative comparison between acoustic sounder returns and the direct measurement of atmospheric temperature fluctuations. *Bound. Layer Meteor.*, **19**, 137–147.

Born, M., and E. Wolf, 1964: *Principles of Optics*, 4th ed. Pergamon, 808 pp.

Brown, E. H., 1975: Some applications of atmospheric acoustics. *J. Acoust. Soc. Amer.*, **58** (Supp. 1), 108.

——, and S. F. Clifford, 1976: On the attenuation of sound by turbulence. *J. Acoust. Soc. Amer.*, **60**, 788–794.

Clifford, S. F., and E. H. Brown, 1978: Excess attenuation in echosonde signals. Submitted to *J. Acoust. Soc. Amer.*

Frisch, A. S., and G. R. Ochs, 1975: A note on the behavior of the temperature structure parameter in a convective layer capped by a marine inversion. *J. Appl. Meteor.*, **14**, 415–419.

Georges, T. M., and S. F. Clifford, 1972: Acoustic sounding in a refracting atmosphere. *J. Acoust. Soc. Amer.*, **52**, 1397–1405.

Hall, F. F., Jr., and J. W. Wescott, 1974: Acoustic antennas for atmospheric echo sounding. *J. Acoust. Soc. Amer.*, **56**, 1376–1382.

Haugen, D. A., and J. C. Kaimal, 1978: Measuring temperature structure parameter profiles with an acoustic sounder. *J. Appl. Meteor.*, **17**, 895–899.

Hill, R. J., 1978: Acoustic scattering cross section determined from an accurate model of the spectrum of temperature fluctuations. *J. Acoust. Soc. Amer.* (in press).

Kaimal, J. C., 1973: Turbulence spectra, length scales and structure parameters in the stable surface layer. *Bound. Layer Meteor.*, **4**, 289–309.

——, J. C. Wyngaard, D. A. Haugen, O. R. Coté, Y. Izumi, S. J. Caughey and C. J. Readings, 1976: Turbulence structure in the convective boundary layer. *J. Atmos. Sci.*, **33**, 2152–2169.

Kerman, B. R., 1976: A note on the interpretation of acoustic sounder returns. *Bound. Layer Meteor.*, **10**, 303–310.

Neff, W. D., 1975: Quantitative evaluation of acoustic echoes from the planetary boundary layer. NOAA Tech. Rep. ERL 322-WPL-38, 34 pp. [NTIS No. PB-253 207].

Owens, E. J., 1977: Microcomputer-controlled acoustic echo sounder. NOAA Tech. Memo. ERL WPL 21. 76 pp. [NTIS PB No. 268 033].

Probert-Jones, J. R., 1962: The radar equation in meteorology. *Quart. J. Roy. Meteor. Soc.*, **88**, 485–495.

Sutherland, L. C., 1975: Review of experimental data in support of a proposed new method for computing atmospheric absorption losses. DOT Rep. TST-75-87 [NTIS No. PB 245 016].

Tatarskii, V. I., 1971: *The Effects of the Turbulent Atmosphere on Wave Propagation.* Nauka, Moscow, 1967. Israel Program for Scientific Translations, U.S. Dept. of Commerce, 472 pp. [NTIS No. TT 68-50464].

Wyngaard, J. C., J. Izumi, and S. A. Collins, 1971: Behavior of the refractive-index structure parameter near the ground. *J. Opt. Soc. Amer.*, **61**, 1646–1650.

Preprint Volume; Fourth Symposium on Meteorological Observations and Instrumentation, 281-284, American Meteorological Society, 1978.

MULTI-BEAMWIDTH STUDIES OF EXCESS ACOUSTIC ATTENUATION

W. D. Neff and D. A. Haugen

NOAA/ERL/Wave Propagation Laboratory
Boulder, Colorado 80302

1. INTRODUCTION

Acoustic sounders (or echosondes) are widely used in boundary layer and air pollution studies. Many of these applications have relied on qualitative interpretations of facsimile records. With increasing use of microprocessor technology (Owens, 1977) it will be possible to obtain quantitative information on boundary layer turbulence routinely. Early comparisons of acoustic backscatter intensities with predictions from in-situ tower instruments (Neff, 1975; Asimakopoulos et al., 1976) showed reasonable agreement with the scattering theory proposed by Tatarskii (1971), but the measurements were carried out at only one height. Vertical profiles of the temperature structure parameter C_T^2 in Neff (1975) showed a more rapid fall-off of intensity with height than was expected from theory or experiment. Later measurements by Haugen and Kaimal (1978) at several tower levels confirmed a sound attenuation with range in excess of that due to classical and molecular absorption.

Since the structure functions of temperature and velocity are useful descriptors of boundary layer turbulence (Kaimal, 1973), the development of a technology to derive these quantities from echosonde returns is of considerable interest (Brown, 1975; Kerman, 1976). A resolution of the "excess attenuation" problem is an essential first step in this development to improve the quantitative evaluation of echosonde data. Brown and Clifford (1976) reviewed the so-called "excess attenuation" problem and applied forward-scatter optical results to predict the magnitude of acoustic beam-broadening produced by small-scale turbulence which reduces the intensity of the backscattered signal. Brown and Clifford's results suggested that the broadening effect was strongly beam-width dependent. This stimulated the simple multi-beamwidth acoustic scattering experiment described here. We describe the theory and results of the experiment which confirm the frequency or beamwidth dependence of the excess attenuation. Our results suggest that multi-frequency sounders may provide a means to correct for the attenuation. A more complete interpretation of the data in terms of Brown and Clifford's results with the added effect of refraction of the beam by a mean wind is provided by Neff (1978).

2. THEORY

Our analysis uses the monostatic echosonde equation (Neff, 1975) which relates the range-gated transducer output to the corresponding scattering cross section per unit volume. In terms of measured and/or calculated quantities

$$\frac{P_R}{E_R} = [P_T E_T][e^{-2\bar{\alpha}R}][\sigma_o(R,f) \cdot \frac{c\tau}{2} \cdot \frac{A}{R^2} G] \cdot L_E \quad (1)$$

with

$\frac{P_R}{E_R}$ = received power, where P_R = measured electrical power and E_R = efficiency of conversion from received power,

$P_T \cdot E_T$ = radiated power where P_T = electrical power applied to the transducer and E_T = efficiency of conversion to radiated acoustic power,

$e^{-2\bar{\alpha}R}$ = round trip loss of power resulting from attenuation by air where $\bar{\alpha}$ = average attenuation (m^{-1}) to the scattering volume at range R(m),

$\sigma_o(R,f)$ = scattering cross section per unit volume; that is, fraction of incident power backscattered per unit distance into unit solid angle at frequency, f,

$c\tau/2$ = maximum effective-scattering volume thickness where c = local speed of sound (ms^{-1}) and τ = pulse length (s),

$\frac{A}{R^2} \cdot G$ = solid angle subtended by the antenna aperture A (m^2) at range R(m) from the scattering volume, modified by an effective-aperture factor G, arising from the antenna's directivity.

L_E = excess attenuation.

Tatarskii (1971) expresses the acoustic backscatter cross section per unit volume σ_o as,

$$\sigma_o = \frac{\pi}{2} k^4 \frac{\phi_T(2k)}{T_o^2} \quad (2)$$

where ϕ_T is the isotropic, three-dimensional spectral density of temperature, $k = 2\pi/\lambda$ is the incident acoustic wavenumber at wavelength λ, and T_o is the local mean temperature. When the spectrum is expressed in terms of the temperature structure parameter

$$C_T^2 = [(T(\vec{x}) - T(\vec{x} + \vec{r}))^2]/r^{2/3} \quad (3)$$

where [ ] indicates an ensemble average, $\vec{x}$ denotes the location at which C_T is evaluated and $\vec{r}$ is the separation between the sensors, Tatarskii

(1971) finds the following expression for the cross-section:

$$\sigma_o = 0.0039\ k^{1/3}\ \frac{C_T^2}{T_o^2} \qquad (4)$$

When Eq. (4) is inserted into Eq. (1), a number of unknowns remain. However if at each range gate one takes the ratio of the received power at each of two frequencies, a number of these unknowns cancel. For a sounder operating at frequencies f_1 and f_2 (wave numbers k_1 and k_2) we have at range R

$$\frac{P_R(f_1)}{P_R(f_2)} = \frac{E_1}{E_2} \cdot e^{-2(\alpha_1-\alpha_2)R} \cdot \left(\frac{f_2}{f_1}\right)^{1/3} \cdot L_{12} \qquad (5)$$

where $E_i = E_R(f_i)\ E_T(f_i)$ and $L_{12} = L_E(f_1)/L_E(f_2)$. Since the efficiencies were not measured and may change with time, the ratios L_{12} which we calculated from Eq. (5) at each range gate were normalized by that at the lowest gate, 31 m, to eliminate E_1/E_2. The classical and molecular attenuation included in the coefficients α_1 and α_2 were calculated using the equations of Sutherland et al. (1975). Surface values of humidity and temperature were used for this calculation: We estimated that this use of surface data would produce an error of only a few per cent at the short ranges of interest to us (150 m). Normalized values of L_{12} were obtained from Eq. (5) at range gates of 67, 95, 125, and 150 m. If excess attenuation is greater at higher frequencies then the ratios L_{12} should be greater than 1.0 for $f_1 < f_2$.

3. RESULTS

The experiment was run over an eight day period in August 1977 at NOAA's Table Mountain field site. This site atop a mesa was instrumented with a 150 m tower to measure wind speed and direction. Received powers, $P_R(f_1)$ and $P_R(f_2)$ in (5) were averaged for 30-minute periods from a multifrequency sounder like that described by Neff (1975). Altogether some 66 hours of data were obtained; with each half-hour represented by a dot in Fig. 1. Although the data are separated according to night and day in Fig. 1, the nighttime cases should not be considered as fully representative of the nocturnal boundary layer because of the higher winds and decreased stability during the periods of observation. Data obtained during high wind (10 m s^{-1}) conditions are identified as such. We have included the in situ-sounder C_T^2 comparison errors from Haugen and Kaimal (1978) although this is not a strictly valid comparison unless the excess attenuation error is minimal at our lower frequency (1250 Hz). Their Nevada data (N) were obtained under conditions of moderate convection and light winds similar to those prevailing during the majority of our daytime cases. Their Table Mountain data (TM) were obtained under generally windier conditions.

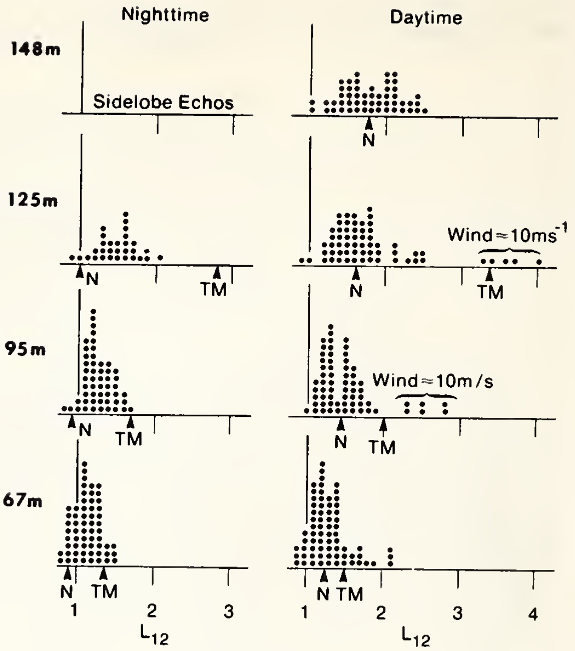

Figure 1. Distributions of L_{12}, the excess attenuation error at 2500 Hz relative to that at 1250 Hz as a function of height and time of day with individual samples normalized to values at 30 m. In-situ echosonde ratios of the temperature structure parameter C_T^2 from Haugen and Kaimal (1978) are shown.

Figure 2 shows a scatter diagram relating the magnitude of the excess attenuation at 67 m to the wind speed at that height. Although a crude relation exists it is clear from the large scatter in this figure that more extensive in-situ instrumentation will be required to relate the excess attenuation to atmospheric parameters.

4. INTERPRETATION OF RESULTS

Both our data and those of Haugen and Kaimal (1978) clearly confirm the presence of an "excess attenuation" mechanism. However interpretation of these backscatter results in terms of existing theory requires some care. Brown and Clifford (1976) calculated the beam broadening (in the absence of beam wander) in terms of the acoustic refractive index structure function:

$$C_N^2 = \frac{C_T^2}{4T^2} + \frac{C_v^2}{C^2} \qquad (6)$$

where C_T^2 and C_v^2 are the structure parameters for temperature and velocity inhomogeneities, T is the mean temperature, and C is the speed of

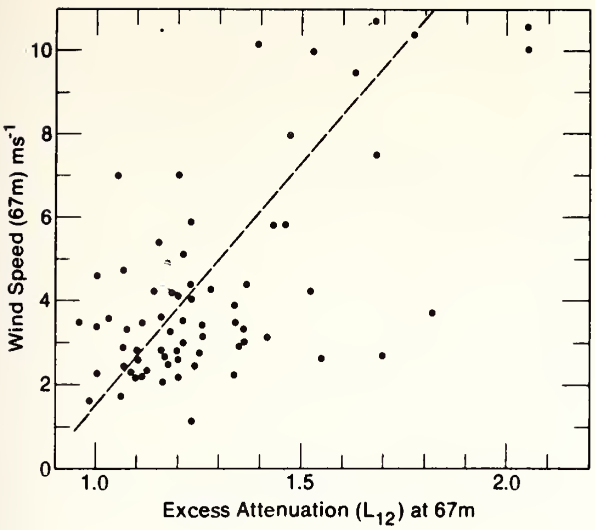

Figure 2. Scatter plot of the excess attenuation factor L_{12} against wind speed at the 67-m tower level.

sound. The fraction of the acoustic energy now remaining within the non-broadened beam pattern (at range R with antenna diameter D_o) is then given by (Brown and Clifford, 1976, Eq. 5)

$$\{1 + 1.56\ k^{12/5}\ D_o^2\ [\int_o^R ds\ (\frac{R-s}{R})^{5/3}\ C_N^2(s)]^{6/5}\}^{-1} \tag{7}$$

or for constant C_n^2

$$\{1 + 0.48\ k^{12/5}\ D_o^2\ R^{6/5}\ C_N^{12/5}\}^{-1}\ .$$

For $C_n^2 = 10^{-6}$ and $D_o = 2$ m, this gives a maximum loss out of the original beam at 150 m with f = 2500 Hz of about 33 percent. Now if one assumes that only a small fraction of this energy is returned to the receiver, then this is approximately the error for the backscatter intensity. Relative to the error at 1250 Hz this gives an equivalent $L_{12} = 1.37$ which is somewhat less than the values in Fig. 1. This suggests that a rigorous derivation of the theory for the broadening effect on backscatter may be necessary.

4. CONCLUSIONS

The simple multi-frequency experiment described here shows that beamwidth is a significant factor in the excess attenuation of acoustic backscatter signals. The magnitudes observed are partially accounted for by theoretical predictions and are consistent with in-situ echosonde comparisons of the temperature structure parameter C_T^2 as measured by Haugen and Kaimal (1978). More extensive discussion of these results in terms of beam broadening and beam refraction is provided by Neff (1978). An experiment is anticipated at the new Boulder Atmospheric Observatory (Hall, 1977) when it becomes operational during 1978. With the instrumentation available on this new 300 m tower it will be possible to explore the detailed relationship between meteorological parameters and the observed attenuation and possibly to use the excess attenuation effect as a means of inferring information about boundary layer turbulence structure and to provide a means of correcting for the attenuation as well.

5. ACKNOWLEDGMENTS

Comments and criticisms by Chandran Kaimal, Edmund Brown, and Freeman Hall have been most useful. Norbert Szczepczynski, Daniel Wolfe, and Jim Newman aided in the field operation.

6. REFERENCES

Asimakopoulos, D. N., R. S. Cole, S. J. Caughey, and B. A. Crease (1976), "A quantitative comparison between acoustic sounder returns and the direct measurement of atmospheric temperature fluctuations," *Boundary Layer Meteorol.* 10, pp. 137-147.

Brown, E. H. (1975), "Some applications of atmospheric acoustics," *J. Acous. Soc. Amer.*, 58, Supp. 1, 108.

Brown, E. H., and S. F. Clifford, (1976), "On the attenuation of sound by turbulence," *J. Acoust. Soc. Amer.*, 60, 788-794.

Hall, F. F., Jr. (1977), "The Boulder Atmospheric Observatory and its meteorological research tower," *Optics News*, 3(2), 14-18.

Haugen, D. A., and J. C. Kaimal (1978), "Measuring temperature structure parameter profiles with an acoustic sounder," (Submitted to *J. Appl. Meteorol.*)

Kaimal, J. C. (1973), "Turbulence spectra, length scales and structure parameters in the stable surface layer," *Boundary Layer Meteorol.* 4, 289-309.

Kerman, B. R., (1976), "A note on the interpretation of acoustic sounder returns," *Boundary-Layer Meteorol.*, 10, 303-310.

Neff, W. D., (1975), "Quantitative evaluation of acoustic echoes from the planetary boundary layer," NOAA Tech. Rept. ERL 322-WPL-38, 34 pp. (U.S. Government Printing Office, Washington, D.C. 20402 or from the author, NOAA Laboratories/WPL, Boulder, CO 80302.)

Neff, W. D. (1978), "Beam-width effects on acoustic backscatter in the planetary boundary layer," (Submitted to *J. Appl. Meteorol.*)

Owens, E. J., (1977), "Microcomputer-controlled acoustic echo sounder," NOAA Tech. Memo. ERL WPL-21, Boulder, Colorado, 76 pp.

Sutherland, L. C., (1975), "Review of experimental data in support of a proposed new method for computing atmospheric absorption losses, DOT Report TST-75-87 (National Technical Information Service, Springfield, Va. 22151.)

Tatarskii, V. I., (1971), *The Effects of the Turbulent Atmosphere on Wave Propagation* (Nauka, Moscow, 1967), transl. Israel Program for Scientific Translations, U.S. Dept. of Commerce, Nat. Tech. Inform. Serv., Springfield, VA., 472 pp.

Optics Letters, 2: 166-168, June 1978.

Experimental measurements of atmospheric aerosol inhomogeneities

Madison J. Post

Wave Propagation Laboratory, Environmental Research Laboratories, NOAA, Boulder, Colorado 80302

Received February 27, 1978

Experimental measurements of inhomogeneities in the spatial distribution of boundary-layer aerosols, including structure and probability density functions, are presented. Correlations between the statistics and meteorological conditions are discussed.

Introduction

Recently, a great deal of effort has been spent in understanding the nature and origin of refractive-index fluctuations in the lower atmosphere. These fluctuations strongly affect optical propagation for bistatic systems. Another fluctuating quantity, the aerosol backscatter coefficient, is of equal or greater importance in its effects on monostatic lidar systems. Differential absorption techniques, for instance, assume constant backscatter coefficients between spatially or temporally separated observations. Such an assumption may be good or bad, depending on the scales involved. Designers of systems measuring transit times of aerosol inhomogeneities also need to understand the spatial properties of their tracers. Zuev *et al.*[1] have studied several aspects of the problem, using a He–Ne two-point sensor and a limited data set.

This Letter presents observations of the fluctuations in the aerosol-volume backscatter signal, I, for $\lambda = 10.6$-μm radiation for a period of one year near Boulder, Colorado. The observed-signal fluctuations are strongly related to inhomogeneities in the total number of large aerosols. Analysis of the signals provides this first reported experimental verification of the applicability of turbulence theory to boundary-layer aerosols, using a single sensor.

Characterization of aerosol inhomogeneities is made through features of the spatial structure function for aerosols, defined as $D_a(r) = \langle [A(x) - A(x + r)]^2 \rangle$, and the separation at which outer-scale effects[2] occur. Here $A(x)$ is the concentration of aerosols at position x.

Observations

Data were taken using a CO_2 Doppler lidar (a cw system) aligned parallel to the mean wind and focused to a range of 150 m, positioned 30 m above the surface. Between ranges of 60 and 600 m the sensitivity of the lidar is essentially invariant. The sensing volume was approximately a cylinder 3 cm in diameter and 20 m long, elevated 11° above horizontal. Observations consisted of a large number of frequency spectra of the Doppler-shifted signal backscattered from aerosols moving with the wind. Approximately two spectra were processed per second, and ten were averaged before recording. The effective averaging time was thus 5 sec. Data runs were normally 20–30 min long. The mean velocity $V(t)$ and the total backscattered intensity versus time $I(t)$ are available from these data.

A Climet Model CI-108 particle counter determined aerosol size distributions while data were taken. It became apparent that variations in the signal I arise mainly from inhomogeneities in the number of large aerosols (>1-μm radius), although the shape, composition, orientation, and number of small aerosols affect the signal slightly. This observation agrees well with the theoretical response of the system $R(r)$ to the measured size distributions $n(r)$ (Fig. 1), which peaks near 1.5 μm. $R(r)$ is a convolution over r of the expected signal per particle of radius r with the particle size distribution. Note that in all cases the observed number densities for larger aerosols did not diminish

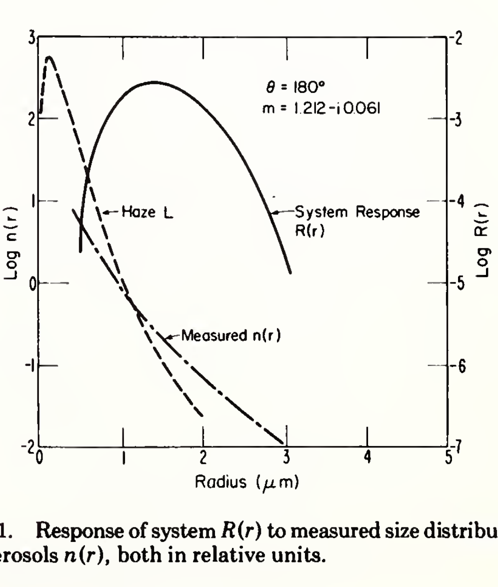

Fig. 1. Response of system $R(r)$ to measured size distribution of aerosols $n(r)$, both in relative units.

0146-9592/78/0600-0166$0.50/0 © 1978, Optical Society of America

so rapidly with radius as Diermendjian's[3] Haze L model.

It should be stressed that the results presented in this Letter, therefore, hold only for particles 0.5 to 3.0 μm in radius. It is not known, for instance, whether concentrations of smaller aerosols fluctuate over the same percentage range as the larger ones, whether they fluctuate in synchronism with the larger particles, etc. However, because the lidar signal I is directly proportional to the concentration of large aerosols A, it is justifiable to state that $D_a(r) \propto D_I(r)$.

Analysis

For the experimental configuration used, the spatial distribution of inhomogeneities in the backscatter $I(x)$ may be derived from the temporal observations by associating a position x with each observation time t as follows:

$$t_0 = x_0 = 0,$$

$$x_n = x_{n-1} + \left[\frac{V(t_n) + V(t_{n-1})}{2}\right] (t_n - t_{n-1}), \quad n = 1, 2 \ldots N,$$

where $V(t)$ is the mean velocity for time t and N is the total number of measurements.

Strictly speaking, to make this transformation properly, one must show that the advecting atmosphere is "frozen," or stationary, for the entire observation period. This cannot be done. However, having made many observations, we observe that the shape of the spatial frequency spectrum is essentially maintained from day to day, indicating that the spatial structure of atmospheric aerosols is in some sort of steady-state motion.

Using $I(x)$, the structure function $D_I(r)$ for each data run is computed using the formula

$$D_I(r) = \langle [I(x) - I(x + r)]^2 \sim D_a(r) \rangle .$$

$D_I(r)$ thus computes the average difference (squared) between all $I(x)$ in the data set that are separated by the distance r and, by arguments presented previously, represents the strength of the aerosol-concentration irregularities below a scale size r. Theoretically, in the lower atmosphere, $D_a(r)$ will take the form $D_a(r) = C_A^2 r^{2/3}$ for r in the inertial subrange, or for separations r between the inner and outer scales, l_0 and L_0, respectively. C_A^2 represents the intensity of the aerosol fluctuations and is proportional to the variance in the aerosol density.[4] For $r < l_0$, $D_a(r)$ is reduced below the theoretical level, since very small eddies (<5 mm) cannot exist because of viscous effects. The length of the sensing volume in this experiment did not permit observations in this regime. In the outer-scale regime, large eddies (greater than observation height) cannot exist, or more precisely cannot be handled properly by isotropic theory, because of surface effects. Measurements presented here, however, do show the form of $D_a(r)$ beyond the outer-scale limit of 30 m.

Typical structure functions for day and night conditions, plotted on a log–log format, are shown in Fig. 2. A summary of all data runs, with characterization of features of their structure functions, is given in Table 1.

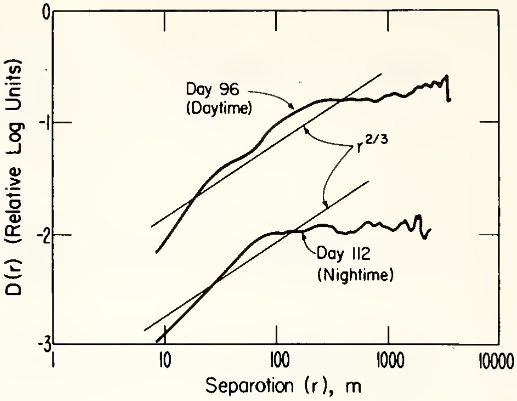

Fig. 2. Typical aerosol structure functions for daytime and nighttime conditions.

It was found that these, as well as all the other structure functions, approximately follow the predicted $r^{2/3}$ relation for classical isotropic passive additives. Several significant departures appear, however. During daylight conditions, the outer scale "roll-off" of the structure functions occurs at larger r values, typically 200–300 m, than are predicted by theory for the 30-m level. At night, the outer scale drops to 40–60 m, so isotropic theory holds more closely for this nonconvective condition.

Another departure appears at small separations. Consistently, the slope of the structure function was greater in this region, typically nearer 4/5 than 2/3, a 20% increase. Maximum errors in data taking and reducing can account for only an 8% increase. This departure is due to the poor radial resolution of the lidar. Aerosol inhomogeneities smaller than 20 m in diameter are averaged together throughout the sensing volume, thereby enhancing the slope of the structure function by decreasing signal variations at small scales. Frisch and Clifford[5] have treated this effect theoretically. Hill and Clifford[6] postulate an additional increase in the slope at small scales due to viscous-convective effects. Without making more detailed measurements of the aerosol population, the combination of these effects cannot be treated analytically.

The diurnal change in the level of the structure function (the nighttime data being lower than the daytime) is approximately one order of magnitude. This variability is considerably less than that experienced for similar temperature fluctuations but is approximately the same as that for velocity fluctuations. This means that the mechanism creating and maintaining aerosol inhomogeneities is probably more strongly velocity related than temperature related.

No strong correlation to general weather conditions is apparent, nor does season of the year affect the form of $D_a(r)$ significantly. An interesting run is indicated by "smoke day" in the comments column. A forest fire approximately 10 km upwind of Boulder created dense smoky conditions in town. While the level of the scattered signal increased dramatically ($>10^2$), all the

Table 1. Summary of Data Runs and Structure Function Characteristics

Day	Time (MDT)	Weather	Visibility (km)	Outer Scale Rollover (m)	Relative Rollover Level	Notes
140	1501	Overcast	50	>1000	10^{-1}	W winds
163	1446	Clear	80	1400	9.0×10^{-1}	Smoke day
163	1534	Clear	80	750	2.2×10^{-1}	Smoke day
176	1506	Partly cloudy	>100	1900	1.6×10^{-1}	NW winds
176	1538	Partly cloudy	>100	850	1.7×10^{-1}	NW winds
46	1353	Partly cloudy	50	140	1.5×10^{-2}	S winds, snow melt
73	1421	Overcast	50	375	5.2×10^{-1}	NW winds
82	1556	Cloudy	70	1000	2.9×10^{-1}	Winds variable
83	1345	Clear	100	250	5.8×10^{-2}	NE winds
84	0942	Clear	20	190	1.6×10^{-1}	SE winds
96	1328	Clear	>100	260	1.6×10^{-1}	SE winds
101	0907	Overcast	75	140	4.1×10^{-2}	NE winds, stratus
101	2119	Overcast	10	590	6.0×10^{-2}	E winds, foggy
104	1429	Partly cloudy	75	250	7.6×10^{-2}	Small cumulus
112	1356	Partly cloudy	>100	100	2.3×10^{-2}	Winds variable
112	1356	Clear	>100	100	3.0×10^{-2}	SW winds
112	2014	Clear	>100	80	7.5×10^{-3}	SW winds
114	2134	Clear	>100	900	7.1×10^{-2}	SW winds
114	2220	Clear	>100	60	1.2×10^{-3}	SW winds
115	1406	Partly cloudy	75	160	1.7×10^{-1}	N winds
115	2139	Clear	>100	60	1.2×10^{-3}	W winds

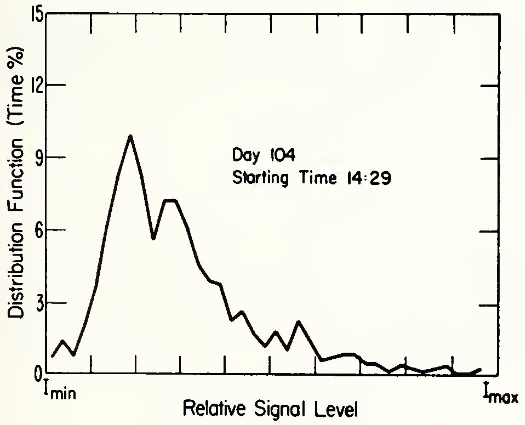

Fig. 3. Probability density (distribution) function for typical data run.

characteristic features of the structure function were normal for daytime. This indicates that, in a 50-km/h wind condition, steady state had been reached in less than 10 kM (or 12 min).

In addition to the structure function, the probability density function was calculated for each data run. This function measures the fractional time a signal spends between I and $I + dI$, normalized to the total range in I. The pattern of all data was a consistent one: bell-shaped but skewed toward lower intensity levels, as illustrated in Fig. 3. This log-normal character is consistent with the concept of infrequent enhancement of large aerosol concentrations, which give rise to disproportionately strong increases in signal, and is typical of fluctuating quantities in the atmosphere.

References

1. V. E. Zuev, Yu. M. Vorevodin, G. G. Matvienko, and V. I. Samokhvalov, "Investigation of structure and dynamics of aerosol inhomogeneities in the ground layer of the atmosphere," Appl. Opt. 16, 2231–2235 (1977).
2. J. W. Strohbehn, "Line-of-sight wave propagation through the turbulent atmosphere," Proc. IEEE 56, 1301–1318 (1968).
3. D. Deirmendjian, *Electromagnetic Scattering on Spherical Polydispersions* (Elsevier, New York, 1969), p. 75.
4. V. I. Tatarskii, *The Effects of the Turbulent Atmosphere on Wave Propagation*, translated from Russian by Israel Program for Scientific Translations (Kefer Press, Jerusalem, 1971).
5. A. S. Frisch and S. F. Clifford: "A study of convection capped by a stable layer using Doppler radar and acoustic echo sounders," J. Atmos. Sci. 31, 1622–1628 (1974).
6. R. J. Hill and S. F. Clifford: "The modified spectrum of atmospheric temperature fluctuations and its application to optical propagation," to be published in J. Opt. Soc. Am. 68 (1978).

Preprint volume: Fourth Symposium on Meteorological Observations and Instrumentation, 47-50, American Meteorological Society, 10-14 April 1978.

AN OPTICAL HEAT FLUX EXPERIMENT

J. C. Wyngaard

Cooperative Institute for Research in Environmental Sciences
University of Colorado/NOAA
Boulder, Colorado 80309

and

Wave Propagation Laboratory, NOAA
Boulder, Colorado 80302

J. C. Kaimal, G. R. Ochs, R. J. Hill* and D. C. Sorensen**

Wave Propagation Laboratory, NOAA
Boulder, Colorado 80302

1. INTRODUCTION

A laser beam transmitted through a turbulent field will develop scintillations due to optical refractive index fluctuations. In the linear theory (Lawrence and Strohbehn, 1970) the log-amplitude variance σ_χ^2 of these scintillations is

$$\sigma_\chi^2 = AC_n^2\kappa^{7/6}R^{11/6}f\left(\frac{\eta^2}{\lambda R}, \frac{D_t^2}{\lambda R}, \frac{D_r^2}{\lambda R}\right) \tag{1}$$

Here A is a constant which depends on the optical wave type (spherical or plane), C_n^2 is the refractive index structure parameter, $\kappa = 2\pi\lambda^{-1}$ is the optical wavenumber, R is the path length, η is the Kolmogorov microscale of the (homogeneous) turbulence along the path (Tennekes and Lumley, 1972), and D_t and D_r are the diameters of the transmitter and receiver apertures. The function f approaches unity as all three of its arguments approach zero.

In a dry atmosphere C_n^2 and the temperature structure parameter C_T^2 are related by

$$C_n^2 = \left[\frac{79\times10^{-6}P}{T^2}\right]^2 C_T^2 \tag{2}$$

where P is the pressure in millibars and T is mean temperature in Kelvin. Thus we have, from (1) and (2), a proportionality between optical scintillations (σ_χ^2) and a property of the intervening thermal turbulence field (C_T^2). Since C_T^2 has been demonstrated to be closely related to the surface heat flux (Wyngaard et al., 1971), this provides a potential means of inferring heat flux from optical scintillations (Little, 1972). Here we will briefly report on a recent experimental attempt to develop such a technique.

2. SURFACE-LAYER THEORY

In the surface layer (the first few tens of meters) of a horizontally homogeneous atmospheric boundary layer, the turbulence structure is believed to follow rather simple similarity scaling. This scaling is discussed in detail in a recent survey volume (Haugen, 1973). For C_T^2, data reported by Wyngaard et al. (1971) follow

$$C_T^2 = T_*^2 z^{-2/3} g_3(z/L) \tag{3}$$

where T_* is a scaling temperature, L is a scaling length, and z is the height. Under very unstable (convective) conditions, it was found that

$$g_3 \simeq \frac{4}{3}\left(-\frac{z}{L}\right)^{-2/3} \tag{4}$$

so

$$C_T^2 \simeq \frac{4}{3} T_*^2(-L)^{2/3} z^{-4/3} \tag{5}$$

the $z^{-4/3}$ dependence is observed to extend well above the surface layer (Kaimal et al., 1976). We introduce the definitions of T_* and L,

$$L = \frac{-u_*^3 T}{kgQ_o}$$

$$T_* = -Q_o/u_* \tag{6}$$

---

[*] NRC Resident Research Associate

[**] Junior Fellow

where $u_* = \sqrt{\tau_o/\rho}$ (τ_o is the surface stress and ρ the air density), $k \approx 0.35$ is the von Kármán constant, and Q_o is the surface temperature flux (ms^{-1} C), which we will loosely call the heat flux. Combining (5) and (6) gives

$$C_T^2 \approx 2.7\left(\frac{g}{T}\right)^{-2/3} Q_o^{4/3}\, z^{-4/3} \qquad (7)$$

under very unstable (convective) conditions. By combining (1), (2), and (7) we see that in this unstable limit,

$$Q_o \propto (\sigma_\chi^2)^{3/4} \qquad (8)$$

Thus the detection of scintillations over a horizontal path in the unstable surface layer should allow one to infer the vertical heat flux Q_o.

3. THE EXPERIMENT

We used a 300 m path on Table Mountain, north of Boulder. The fetch was extremely flat and uniform for 2 km upwind of the path. A He-Ne laser (λ=.6328 µm) was mounted at z=4 m; it had a 0.8 mm transmitter aperture (effectively a point source) and a 16 mm receiver aperture. Three-component sonic anemometers, each with 13 µm diameter Pt fast-response thermometers, were located at 4 m height, 120 m and 180 m from the laser. C_T^2 was measured directly, at the mast nearer the laser, by means of the temperature-difference variance relationship

$$C_T^2 = \overline{(\theta_1 - \theta_2)^2}\, r^{-2/3} \qquad (9)$$

at z=4 m, using r=0.30 m and 2.5 µm diameter Pt wires. Fig. 1 shows a schematic of the experiment.

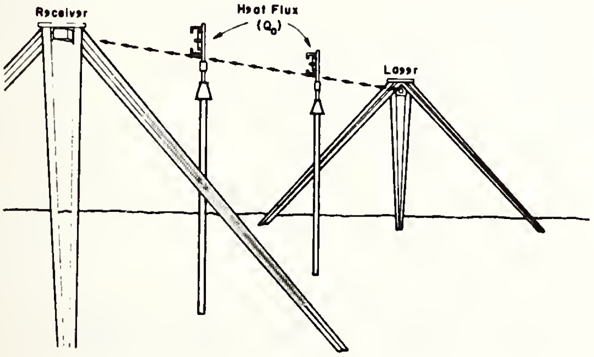

Figure 1. A schematic of the optical heat flux experiment. The 300 m path was 4 m above the surface.

All data were recorded digitally and processed for 1024 sec runs. We processed over 100 such runs, and analyzed the data carefully. Complete results will be presented in a journal article, but we will briefly survey them here.

Fig. 2 shows scatter plots of mean wind $\overline{u}$, wind component standard deviations σ_u, σ_v, σ_w, friction velocity u_* (found via a profile technique), stress $\overline{uw}$, heat flux $\overline{\theta w}$, and temperature standard deviation σ_θ, all obtained from the two 4 m masts along the optical path. There is no indication of systematic differences, which is consistent with (but of course does not prove) horizontal homogeneity.

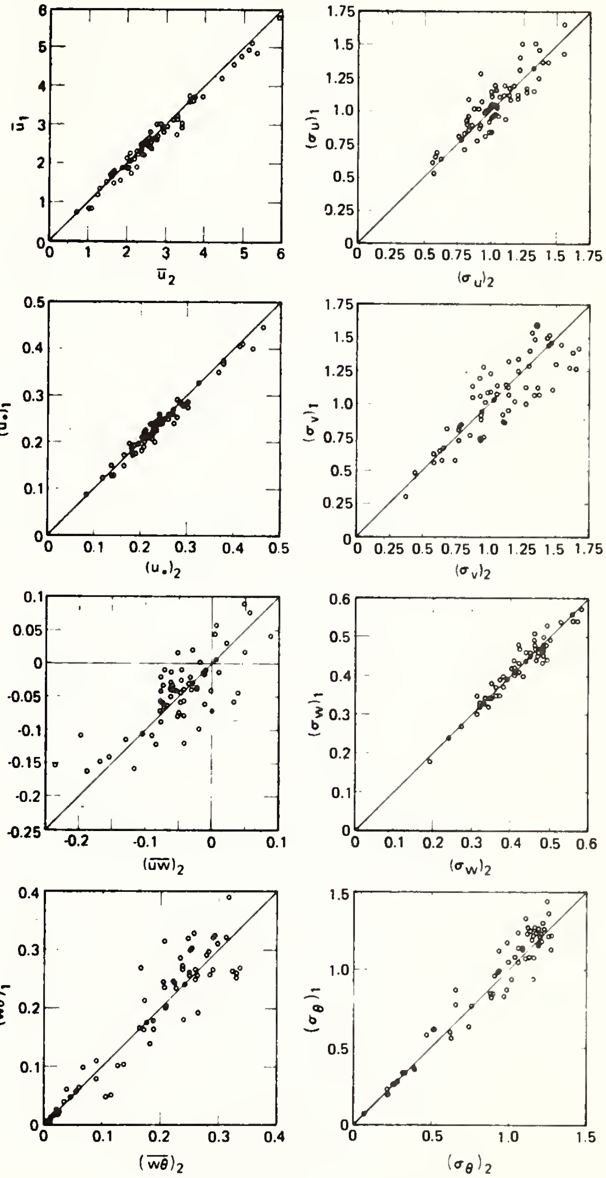

Figure 2. Scatter plots of the statistics at the two 4 m masts. The solid lines indicate equality. Units m, s, C.

The temperature structure parameter C_T^2 ranged over two orders of magnitude during the runs. We examined the C_T^2 values inferred from the scintillations with those measured directly to determine if the optical effects remained within the range of the linear theory of (1). We define, from (1) and (2)

$$C_T^2\Big)_{laser} = \sigma_\chi^2 \left(\frac{79\times10^{-6}P}{T^2}\right)^{-2} A^{-1} \kappa^{-7/6} R^{-11/6} f^{-1} \qquad (10)$$

We used A=0.123 (spherical wave) and f values based on the aperture sizes and the Tatarskii (1971) form of the temperature spectrum (a Kolmogorov inertial range and a Gaussian tail). The η values were found from its definition, $\eta \equiv (\nu^3/\varepsilon)^{1/4}$, where ν is kinematic viscosity and ε is the dissipation rate of turbulent kinetic energy per unit mass. We inferred ε from σ_w^3/z, using a similarity relation deduced from the Kansas 1968 and Minnesota 1973 experiments.

The ratio $C_T^2)_{laser}/C_T^2$ for all data is shown in Fig. 3. Apart from a few anomalously high points at very low C_T^2 values (which might be due to spurious scintillation from causes other than refractive index fluctuations), there is no indication of a trend. Thus we conclude that the linear theory holds, and that there is no evidence of saturation of scintillations, a nonlinear effect.

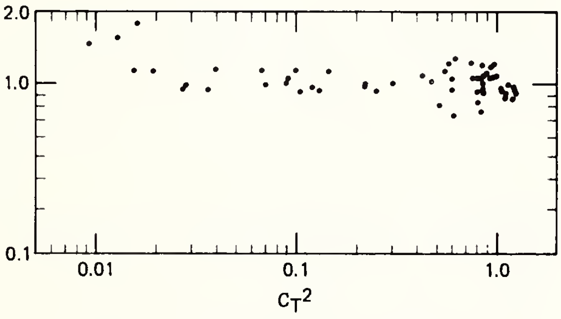

Figure 3. The ratio of C_T^2 values inferred from the scintillations to those measured directly, versus C_T^2.

The linear theory also assumes the temperature field is locally isotropic, which implies that the temperature difference variance is independent of the direction of the (small) separation r. We tested this by using two sets of temperature difference sensors at the same (4 m) height, and the same (0.30 m) separation, but with different separation directions. The results of several 300 sec runs (Fig. 4) are consistent with local isotropy.

Another test of local isotropy is the relation (Wyngaard et al., 1971)

$$C_T^2 = 4\,\kappa_1^{5/3}\,\phi_T \qquad (11)$$

where ϕ_T is the inertial subrange of the one-dimensional (streamwise) temperature spectrum.

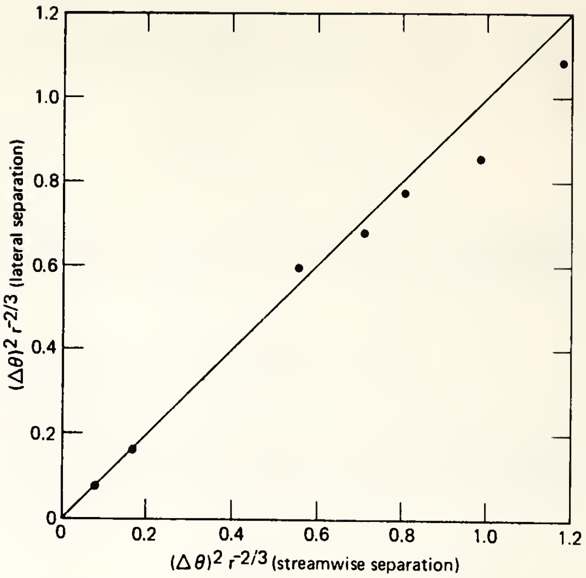

Figure 4. A test of local isotropy of the temperature field.

We evaluated the right side of (11) using a modified Taylor's hypothesis (Wyngaard and Clifford, 1977b) to convert frequency spectra to ϕ_T. We evaluated the left side of (11) using the temperature difference variance, (9). The results for 1024 sec runs, using frequencies near 10 Hz, are compared in a scatter plot in Fig. 5. They too are consistent with local isotropy.

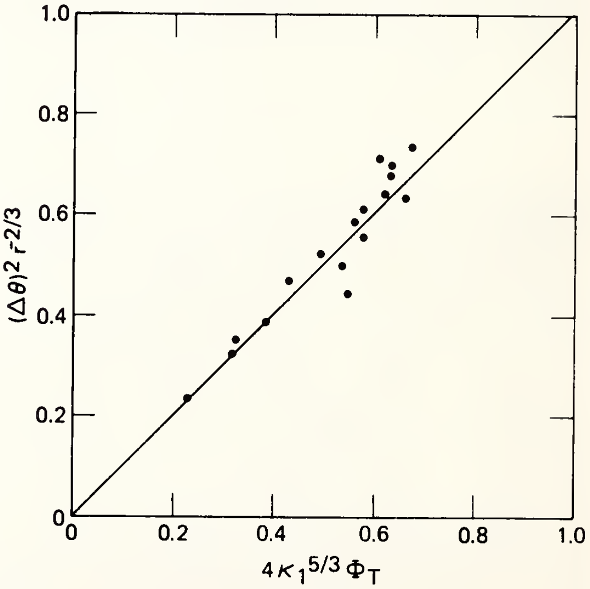

Figure 5. A comparison of directly-measured C_T^2 values (ordinate) with those inferred from inertial range spectral levels (abscissa).

In summary, the results presented in Figs. 2-5 are consistent with horizontal homogeneity, linear optical propagation, and locally isotropic turbulence. These are the principal assumptions underlying the propagation theory and its prediction (1).

The prediction (1) also includes a dependence on the function f. The determination of f is difficult for two reasons. First, it requires knowledge of the Kolmogorov microscale η, which is difficult to measure. Second, f requires knowledge of the form of the temperature spectrum at dissipation range scales, and there is recent evidence (Champagne et al., 1977; Hill, 1977) that the Tatarskii form is not a good model. Therefore from an applications point of view, it would be desirable if f could be treated as a calibration factor to be determined.

With this in mind, we prepared a plot of Q_o versus $(\sigma_\chi^2)^{3/4}$, which as suggested earlier should be linear under very unstable conditions. We took Q_o to be the average of the $\overline{w\theta}$ values measured at the two 4 m masts. Fig. 6 shows the results for all unstable data; surprisingly, the linear relation holds well for the entire experiment. The proportionality factor depends on f, κ, R, and A, and thus will change with experiment geometry, of course, but the nearly linear relation between $(\sigma_\chi^2)^{3/4}$ and Q_o should be general.

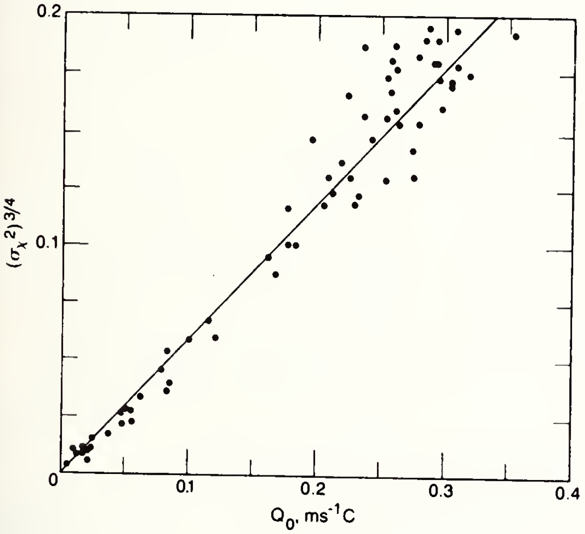

Figure 6. The 3/4 power of the log-amplitude variance versus the heat flux.

4. CONCLUSIONS

We have found that the linear relation between vertical heat flux and the 3/4 power of log-amplitude variance, expected for very unstable surface layer conditions, is a useful approximation even for only slightly unstable conditions. There are reasons to believe a path-averaged heat flux measurement is more representative and requires much less averaging time than point measurements (Wyngaard and Clifford, 1977a). Thus for operational applications the optical heat flux technique is attractive.

Acknowledgments

We are grateful to S. Clifford, D.A. Haugen, R. Lawrence, S. Maximon, G. Miller, J. Newman, N. Szczepczynski, T. Wang, D. Wolfe, and J. Young for their invaluable assistance during the experiment and analysis, and to Ms. J. Trebing for skillfully typing the manuscript.

References

Champagne, F. H., C. A. Friehe, J. C. LaRue, and J. C. Wyngaard, 1977: Flux measurements, flux estimation techniques, and fine-scale turbulence measurements in the unstable surface layer over land, J. Atmos. Sci., 34, 515-530.

Haugen, D. A., Ed., 1973: Workshop on Micrometeorology, AMS, Boston, 392 pp.

Hill, R., 1977: Models of the scalar spectrum for turbulent advection. Submitted to J. Fluid Mech.

Kaimal, J. C., J. C. Wyngaard, D. A. Haugen, O. R. Coté, Y. Izumi, S. J. Caughey, and C. J. Readings, 1976: Turbulence structure in the convective boundary layer, J. Atmos. Sci., 33, 2152-2169.

Lawrence, R. S. and J. W. Strohbehn, 1970: A survey of clear-air propagation effects relevant to optical communications, Proc. IEEE, 58, 1523-1545.

Little, C. G., 1972: Status of remote sensing of the troposphere, Bull. Amer. Meteorol. Soc., 53, 936-949.

Tatarskii, V. I., 1971: The Effects of the Turbulent Atmosphere in Wave Propagation, NTIS, Springfield, VA, TT-68-50464.

Tennekes, H. and J. L. Lumley, 1972: A First Course in Turbulence, MIT Press, Cambridge, 300 pp.

Wyngaard, J. C., Y. Izumi, and S. A. Collins, Jr., 1971: Behavior of the refractive index structure parameter near the ground, J. Opt. Soc. Am., 61, 1646-1650.

Wyngaard, J. C. and S. F. Clifford, 1977a: Estimating momentum, heat and moisture fluxes from structure parameters, submitted to J. Atmos. Sci.

Wyngaard, J. C. and S. F. Clifford, 1977b: Taylor's hypothesis and high-frequency turbulence spectra. J. Atmos. Sci., 34, 922-929.

Preprint Volume; Fourth Symposium on Meteorological Observation
and Instrumentation, 115-124, American Meteorological Society, 1978.

THE DULLES AIRPORT PRESSURE-SENSOR ARRAY FOR GUST-FRONT DETECTION — SYSTEM DESIGN AND PRELIMINARY RESULTS

A. J. Bedard, Jr. and W. H. Hooke

NOAA/ERL/Wave Propagation Laboratory
Boulder, Colorado 80302

1. INTRODUCTION

In response to an urgent need for low-level wind-shear information at air terminals, the Wave Propagation Laboratory of NOAA has developed and installed an experimental wind-shear detection system at Dulles International Airport, where it is currently being evaluated. Dangerous wind shear can normally be classified in two ways: either as extending over large areas, as it does when associated with warm frontal passages, or as being highly localized, as it is when resulting from thunderstorm downbursts (as described by Fujita and Byers, 1977) or gust fronts (extensively documented by Goff, 1976, Greene, et al., 1977 and the references therein). The Dulles system consists of two major elements -- a hybrid acoustic-microwave-radar system for providing a detailed height profile of the wind directly above the sensor (and hence providing a useful picture when the shear condition is widespread) and a dense surface array of pressure jump detectors for detecting the development and motion of the more localized features. This system in its dual and complementary aspects has been described recently in companion papers appearing in the Society's Bulletin (Hardesty, et al., 1977; Bedard, et al., 1977). In addition, the design of the pressure jump detectors themselves has been described by Bedard and Meade (1977); Bedard and Cairns (1977) and Bedard and Beran (1977) give further information.

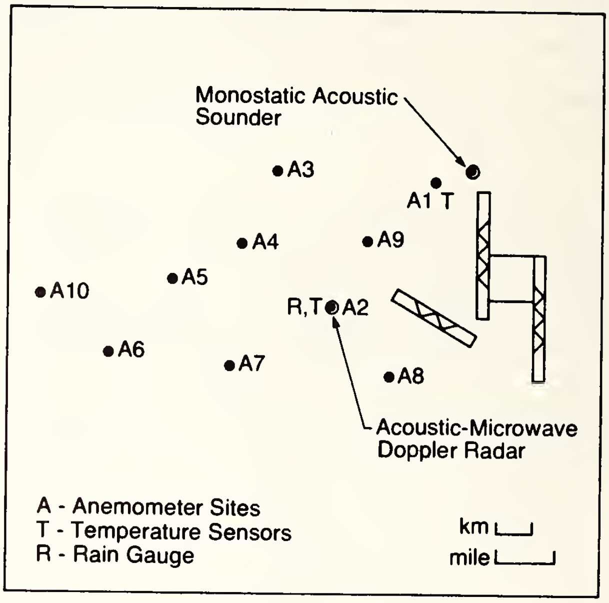

Figure 1. Anemometer sites in the Dulles system.

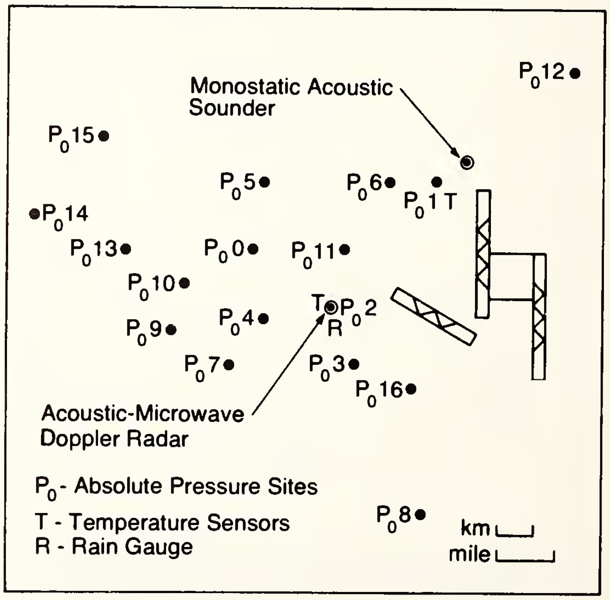

Figure 2. Absolute pressure sensor sites in the Dulles system.

While it is generally agreed that surface arrays of in situ sensors are useful for tracking the progress of thunderstorm gust fronts, there remains some unofficial but nonetheless spirited controversy concerning which kind of surface sensor should be optimum for gust-front detection. To put it more precisely, the question is whether we should monitor gust-front-associated changes in wind speed and direction or whether we should focus on the related pressure changes. Proponents of the former argue that it is wind velocity itself that is most relevant to aviation and hence wind velocity that ought to be measured, whereas proponents of the latter point out that the surface-pressure changes are better indications of conditions aloft, where the plane is, because they measure changes in the integrated air mass above the sensor. Auxiliary questions also remain concerning the optimum geometry and spatial density of the sensor arrays, false alarm rate, and miss rate of the system, etc. To resolve these issues requires data, and the Dulles system has been designed and operated with just such a goal in mind. In addition to approximately 120 pressure-jump (dP) sensors (Bedard and Meade, 1977) deployed, it also includes ten anemometers, sixteen pressure sensors, and two temperature sensors. Figures 1 and 2 show the positioning of these instruments relative to the Dulles runways. Thus the Dulles system provides a means for detecting cold-air outflows from thunderstorms, measuring the spatial structure of their surface properties, and relating these to the resulting wind shear and the local meteorology. This complex of instruments has been operating for several months now, and while data acquisition is continuing and our statistical analysis is only in the early stages, it is already possible to see some of the advantages and shortcomings of the various monitoring approaches. This paper highlights these approaches by presenting data from selected events. The results, though quite preliminary, suggest (perhaps unsurprisingly) the advantages of hybrid systems (including both wind and pressure sensors) for operational use.

2. THE SELECTED EVENTS

From the available Dulles data we have selected well over one hundred events, including not only gust fronts, but other phenomena that range from intense squall lines to the very weakest wind gusts. These manifest themselves through wind surges, pressure rises recorded by the pressure sensors, pressure jumps sufficient to trigger the jump detectors, large wind-shear recorded by the acoustic-sounder system, and combinations of the above. Here we present a selection of these observations which we feel show the diversity inherent in the phenomenon. All are either related to gust fronts (through association with thunderstorms reported by the Weather Service or on radar) or illustrate some property important for use in detection systems. The cases include the following:

I. 20 July 1977 — Spatially uniform and readily interpretable surface wind surges accompanying a gust-front cold-air outflow.

II. 25 July 1977 — a gust-front change in wind direction with no accompanying change in speed.

III. 7 August 1977 — a gust front showing the impulsive nature common to many wind-speed surges caused by thunderstorms.

IV. 2 May 1977 — a gust front associated with large and continuous changes in wind azimuth and speed.

V. 10 June 1977 — a gust-front showing considerable spatial irregularity in winds but not in surface pressure.

VI. 8 August 1977 — a gust front showing spatial complexity in both the surface-wind and pressure fields.

VII. 8 July 1977 — large-amplitude pressure changes caused by gravity waves.

Case I. Spatially uniform and readily interpretable surface wind surges accompanying a gust-front cold-air outflow.

On 20 July 1977, nocturnal thunderstorms occurred to the north of the Dulles system causing a gust surge in the wind to pass over the site at about 0400 EDT, as shown in Figure 3. Figure 4 presents the pressure data for the absolute pressure sensor near the anemometer A1 location, which indicates that the gust surge and pressure rise arrived essentially simultaneously. For this event, the pressure rise was about 1.4 millibars and was constant across the array of pressure sensors to within 0.15 millibar, as it moved with a nearly uniform propagation speed of about 8 m s^{-1} from the north. Figure 5 depicts the maxima for the wind surges observed by all of the (operating) anemometers. The solid-line vector at the lower left of the figure defines the wind speed scale for all the maximum winds associated with the event. (In corresponding figures for the case studies to follow, a dashed line vector also appears at the lower left of the figure, defining the wind-speed scale for the winds measured just prior to the onset of the event. However, for this case the winds prior to the event are essentially calm and hence are not shown.) There is very

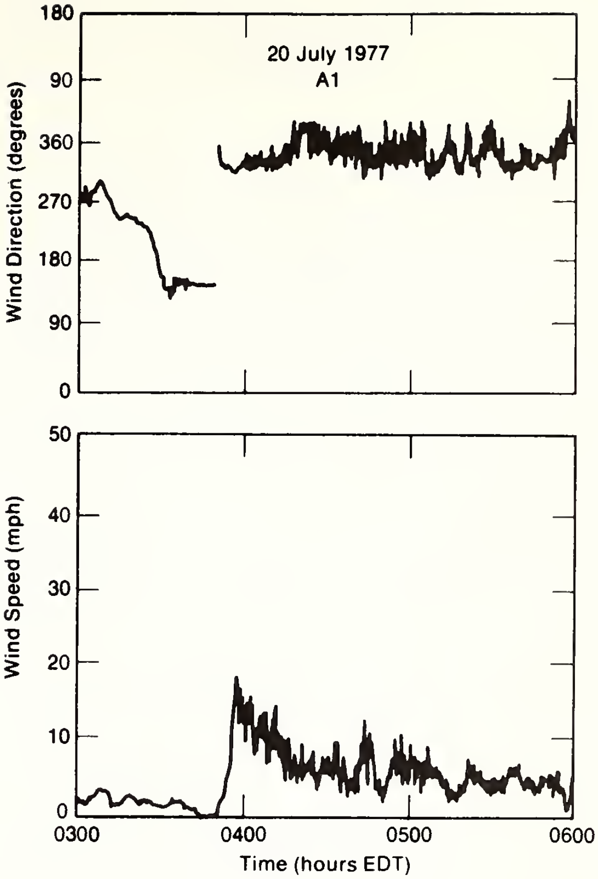

Figure 3. Example of a wind surge for the case of 20 July 1977.

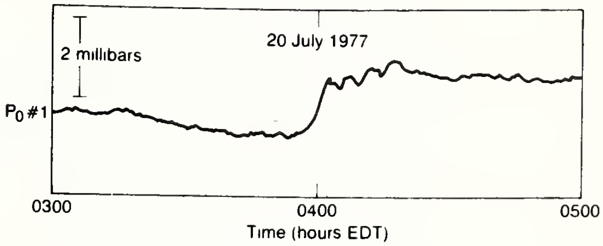

Figure 4. Absolute pressure data for the case of 20 July 1977.

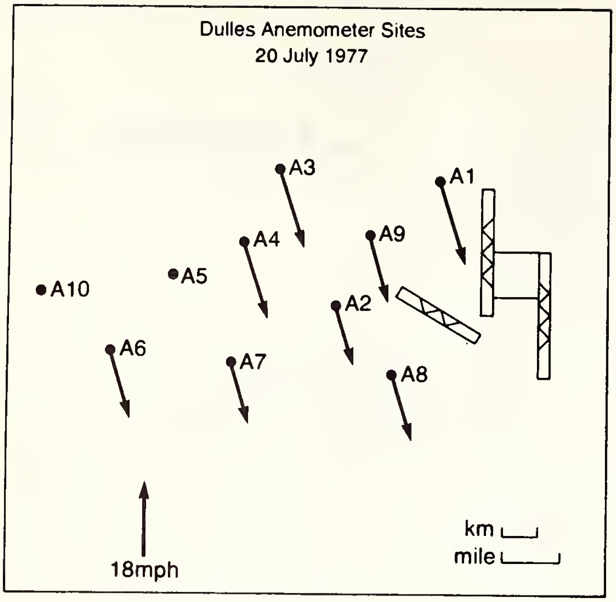

Figure 5. Surface wind vectors before and at the peak of the disturbance of 20 July 1977.

little spatial variability revealed in either the pressure or anemometer data for this event. Unfortunately, from the standpoint of airport operation, such unique events, showing relatively uniform surface effects and easily interpreted azimuth variations, do not appear to be the rule. The cases that follow indicate that the detection problem is frequently more complex.

Case II. A gust-front change in wind direction with no accompanying change in speed.

On 25 July 1977, the Dulles area experienced thundershower activity with cloud tops reaching 7 km. Shortly before 1800 EDT, a disturbance from storms northwest of the site, propagated across the array at a speed of 13 m s^{-1}, producing a pressure rise of about 0.9 mb over a 450-second period. This event was particularly noteworthy because the gust front produced a change in wind direction with little corresponding change in the wind speed itself. As indicated in Figure 6, the event is clearly evident in the wind direction data but not immediately discernible in the wind speed; the average change in the wind vector amounted to some 4.7 m s^{-1}. However, all other events detected at Dulles have shown a significant change in wind speed. While this case does suggest the importance of measuring the wind vector rather than the wind speed, it has proved so far to be unique, a point considered in more detail in the discussion of Case IV. Case II also illustrates considerable spatial and temporal variability in the wind. Figure 7, which shows wind vectors before and during the event, reveals large differences in the wind behavior from site to site; for example, the difference between the anemometer readings during the event at sites A6 and A3 amounts to a factor of three. The corresponding spatial variations in pressure are relatively minor amounting to no more than a factor of 30%. This point is considered in more detail in the discussion of Cases V and VI.

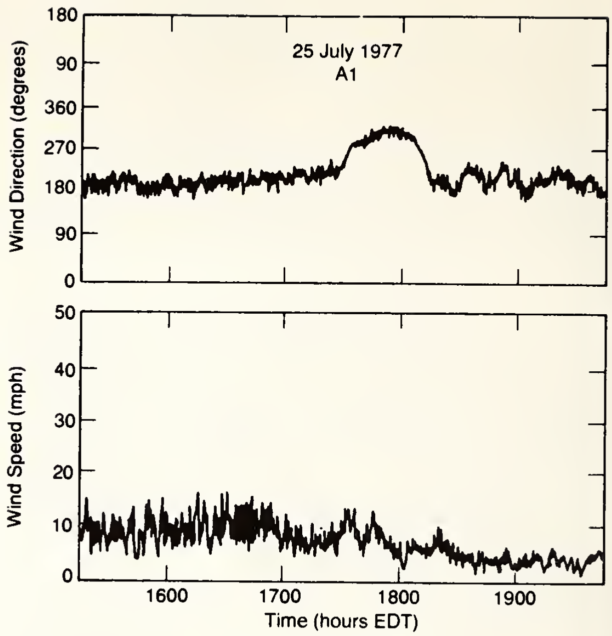

Figure 6. Case of 25 July 1977 showing an abrupt change in wind vector with little surface wind speed disturbance.

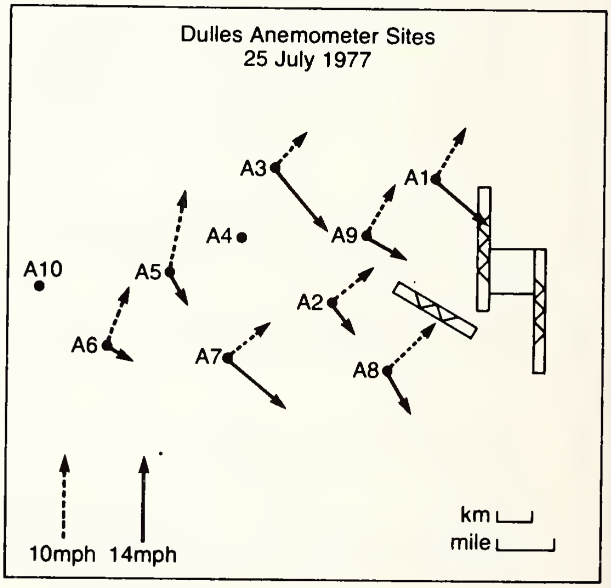

Figure 7. Surface wind vectors before and after the direction shift on 25 July 1977.

Case III. A gust-front showing the impulsive nature common to many wind-speed surges caused by thunderstorms.

Two events of 7 August 1977 provide examples of impulsive wind surges caused by thunderstorm outflows. Figure 8 shows the wind speed and direction data for one of the anemometers (A9) and indicates the two events. In both cases the largest fraction of the wind

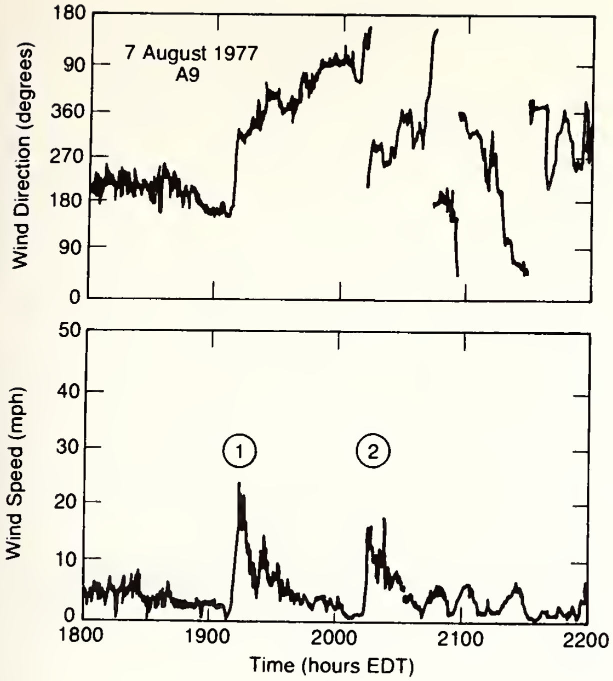

Figure 8. Example of anemometer data on 7 August 1977 illustrating the impulsive nature of gust fronts.

speed change occurs in well under 10 minutes, the onset of the surge being more rapid than the following decay. The relatively short duration of the peak winds compared to the duration of the events themselves suggest that the gust front is most violent in a relatively small region (e.g., 2 km) near the head. Some change in wind azimuth also occurs during the events. Figures 9 and 10 show the corresponding wind-vector summaries from the anemometer array. Although there is some spatial variability in the surface peak-wind surges, the vector maxima are all within a factor of two of one another. A pressure jump of 1.1 mb was recorded on a standard barograph near the A1 site with rise times of 7 minutes and 2 minutes for the first and second events respectively. Unfortunately, a lightning strike caused the loss of the absolute pressure sensor array data. The pressure-jump-detector array did not respond to the slower rise time of the first event, but it did trigger on the second event and revealed that the speed of the gust front changed considerably as it propagated over the site. When it entered the array, the gust front was moving with a 20 m s^{-1} motion from the northwest; by the time it was exiting, however, its speed had been reduced to 5 m s^{-1}. This is statistically unusual; by far the majority of such disturbances are observed to propagate with nearly uniform speed across the array.

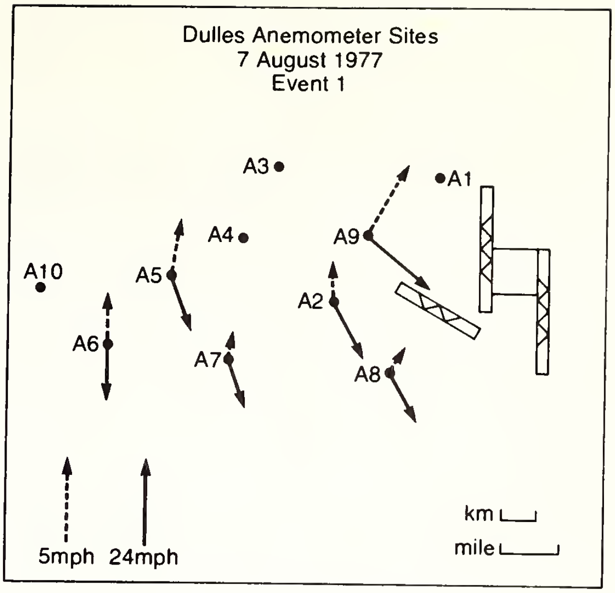

Figure 9. Surface wind vectors before and at the peak of the first disturbance on 7 August 1977.

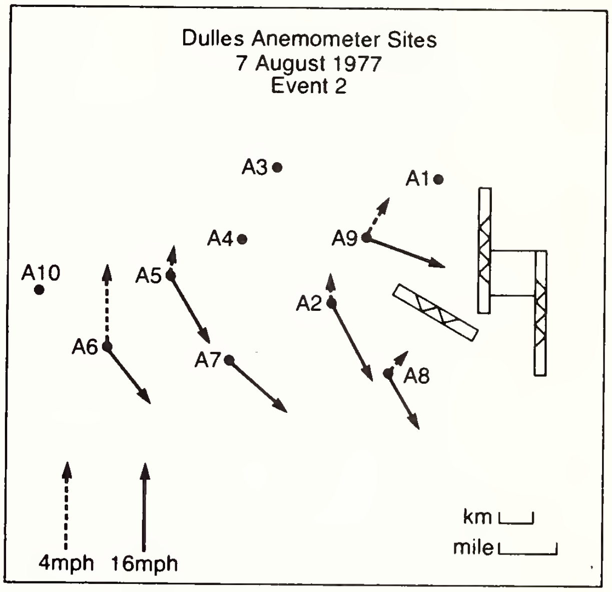

Figure 10. Surface wind vectors before and at the peak of the second disturbance on 7 August 1977.

Case IV. A gust-front associated with large and continuous changes in wind azimuth and speed.

On 2 May 1977 an abrupt wind surge occurred, with wind speed increasing by more than 10 m s^{-1} within 5 minutes (Figure 11), in a fashion analogous to that of the events in Case III. During the event, wind direction changed dramatically and continuously from 270° clockwise through north to 20°. Even after passage of the gust front itself, the wind kept changing continuously in time, eventually coming from due east and finally from the southeast before the winds died down. Interestingly, the event was detected only by the northeast sector of the

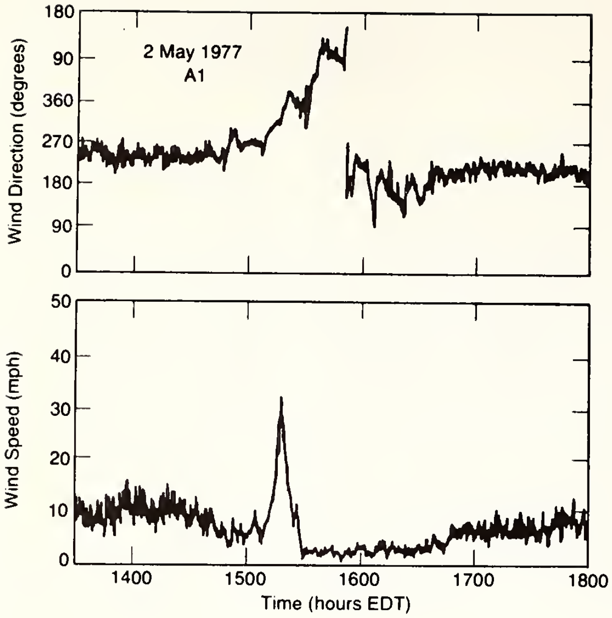

Figure 11. Example of anemometer data on 2 May 1977 illustrating the large changes in wind direction that can accompany the disturbed portion of a gust surge.

array, making velocity determinations more difficult. However, indications from the acoustic sounder data indicate that it was propagating from the northwest. This event points up the need for relatively densely spaced multiple sensors for such events in order to provide accurate estimates of the shape of the front and its propagation.

Case V. A gust front showing considerable spatial irregularity in winds but not in surface pressure.

On 10 June 1977, the Dulles area experienced rain with cloud tops at the 7 km level in the late afternoon and early evening. During this time, the system data showed a pressure jump propagating from the north at just under 11 m s^{-1}; the pressure increase amounted to 2 mb over 500 seconds, as shown in Figure 12, for the P_o1 and P_o2 sites. Figures 13 and 14 show the corresponding wind traces from the respectively colocated anemometers. At site A1 only a single wind surge with a 12 m s^{-1} maximum is evident, occurring at about 1820 EDT. At A2 a smaller initial surge (8 m s^{-1}), occurring at about 1830 EDT is followed by yet another surge (9 m s^{-1}). During both events, wind-direction changes are small. Clearly, in a case like this, a large number of wind sensors in a surface array is required to provide an unambiguous picture of the low-level airflow; a few sensors might give a quite misleading picture of the event. It should also be noted that the apparent discrepancy between the anemometry data and the pressure-sensor system can be resolved if we recall that the wind sensor measures the local wind while the pressure sensor measures the total mass of the air above it (if we ignore inertial effects). Because the two instruments are sensing different height regions of the atmosphere, we may quite naturally expect them to show different results on occasion.

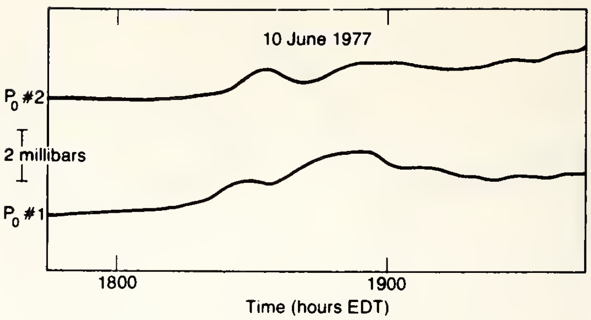

Figure 12. Absolute pressure data for the case of 10 June 1977.

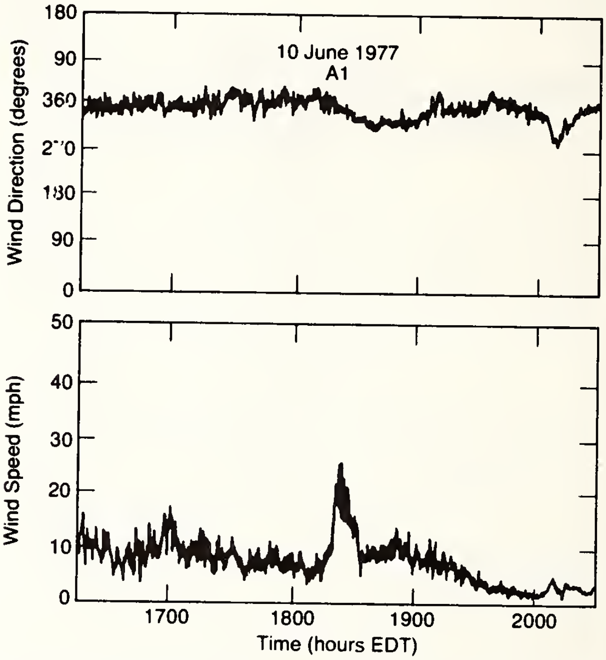

Figure 13. Example of anemometer data on 10 June 1977 for A1.

Case VI. A gust front showing spatial complexity in both the surface-wind and pressure fields.

In the afternoon and early evening of 8 August 1977 severe storms hit the Dulles area, causing 1-1/2" rains and leveling trees. These storms began to the south and then broke out to the north. The Dulles array data show that three pressure jumps occurred during a one-hour interval, the third and largest amounting to about 2 mb in 5 minutes. Each of the pressure jumps showed surface wind changes during a period when the surface winds remained generally disturbed and exhibited significant veering.

Figure 15 shows the event as it appeared on the pressure jump detectors. Solid circles

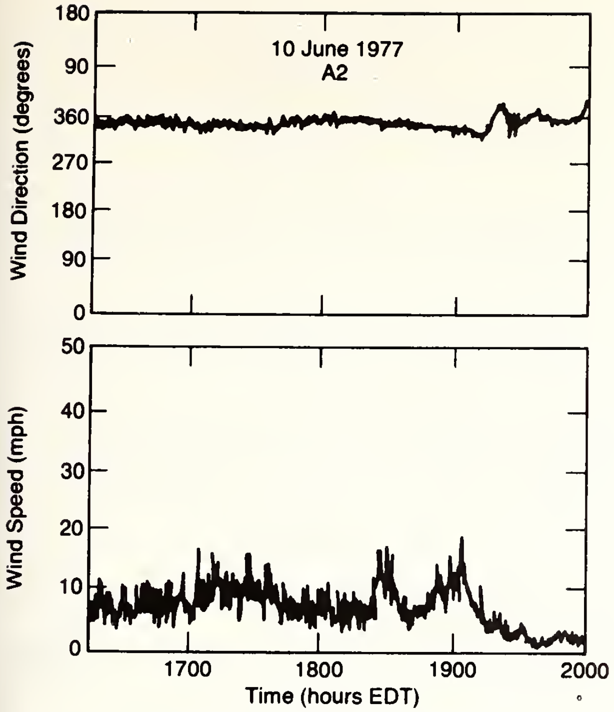

Figure 14. Example of anemometer data on 10 June 1977 for A2.

on the figure show the locations of the detectors, whereas the numbers above the sensor location refer to the key at left, giving the time interval during which the respective sensors first detected the gust-front-associated pressure rise. Thus, for example, designator 2 (D2) refers to the time interval between 1915 and 1918 EDT, at which time D3 is set. (The sites that apparently did not respond were, in fact, either unconnected at this time (western segment) or had phone-line problems (south-west) because of lightning damage.) Thus the progression of the numbers indicates the progress of the pressure jumps. The initial disturbance propagated from the southwest at 10 m s^{-1}, producing a small surge in surface wind. A subsequent "burst" of triggers developed to the north, as indicated by designator 3, in an area shaded for emphasis. Although analysis of this event is in its preliminary stages, it would appear that a "downburst" of the type described by Fujita and Caracena (1977) could have caused the pattern. Thus, this case again indicates the importance of using dense arrays in order to detect and interpret complex situations.

It might be noted parenthetically that in addition to the pressure-jump detectors, a large number of anemometers, pressure sensors, and the acoustic sounder installation were knocked out by lightning. This points up the

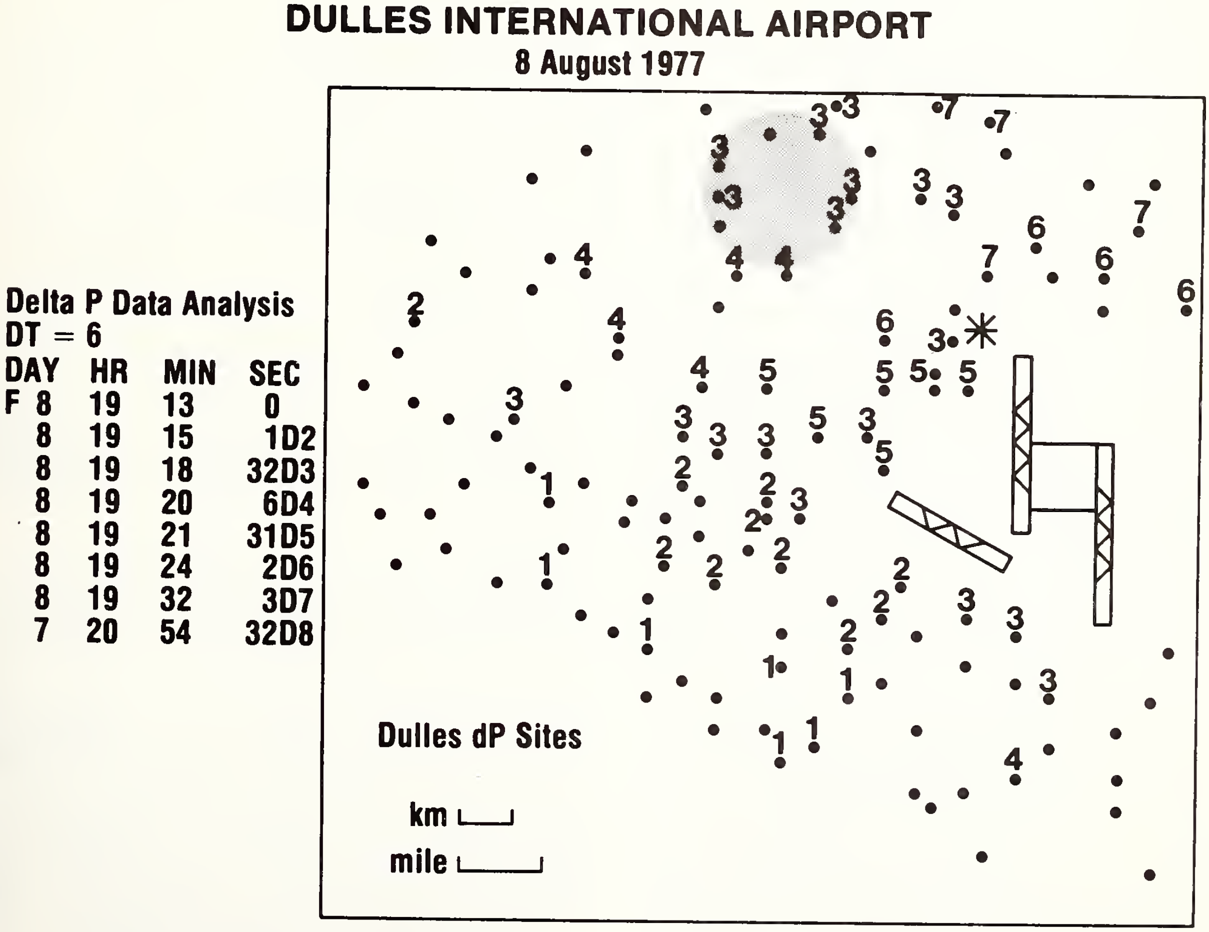

Delta P Data Analysis
DT = 6

DAY	HR	MIN	SEC
F 8	19	13	0
8	19	15	1D2
8	19	18	32D3
8	19	20	6D4
8	19	21	31D5
8	19	24	2D6
8	19	32	3D7
7	20	54	32D8

Figure 15. Pressure jump detector array data for the case of 8 Aug. 1977 illustrating a spatially complex event.

critical need for "hardening" the system by providing auxiliary power sources, etc., in order to keep the system operational under such adverse but important conditions.

Case VII. Large amplitude pressure changes caused by gravity waves.

During the night of 8 July 1977, a wave-like pressure disturbance, with a 400-second period, propagated across the array with a phase speed of about 8 m s^{-1} from the north (Figure 16). The weather radar summary showed no echoes in the region at the time of this event and were unable to relate this disturbance (which did cause pressure-jump detector triggers) to any surface weather feature. The most probable explanation is that the event is due to a gravity wave of the type reviewed by Gossard and Hooke (1975) and routinely detected by acoustic echo sounders (e.g., Hooke et al., 1972; Beran et al., 1973). Indeed, the Dulles monostatic sounder records indicate an inversion of about 350 meters depth with 200-m perturbations at the time of the event. Further support to the wavelike nature of the disturbance is given by the validity of the impedance relation (Gossard and Munk, 1954; Kjelaas et al., 1975) applied to this case, which relates the phase speed, c, to the ratio of the pressure and velocity perturbations (dp and du respectively) through the formula

$$c = \frac{dp}{\rho_o du} ,$$

where ρ_o is the background atmospheric density. The measured and computed values of the induced velocity perturbations are 9.3 m s^{-1} and 8.4 m s^{-1} respectively. It should be noted that while this event was not associated with a gust front per se, it did produce updrafts and downdrafts of the order of ±1 m s^{-1} near the ground, which could be hazardous to aircraft especially if there were many cycles which excited an aircraft or control resonance (e.g., Chimonas, private communication). Further, even the horizontal wind field vector changes (9 m s^{-1} accompanied by wind direction shifts of 180°) themselves could be dangerous. It is therefore doubtful whether such events should be considered false alarms.

3. THE TIME HISTORIES OF THE INDIVIDUAL EVENTS

Bedard and Beran (1977) review past measurements treating the relative arrival times of pressure, temperature and wind disturbances. However, more statistics are needed concerning these temporal relationships. Figure 17 (after Bedard and Cairns, 1977) presents data taken near O'Hare International airport during the summer of 1976, depicting the time differences between the arrival of the peak of the pressure and the peak of the wind disturbances. Using propagation speeds determined from the pressure sensor array, we computed equivalent distances for each of the time differences. In eight out of eleven cases the pressure disturbance arrived coincident with or prior to the arrival of the surface wind surge. In the two cases in which the wind surge occurred well prior to the pressure jump, dp triggers were not caused. They also seemed to be weaker events.

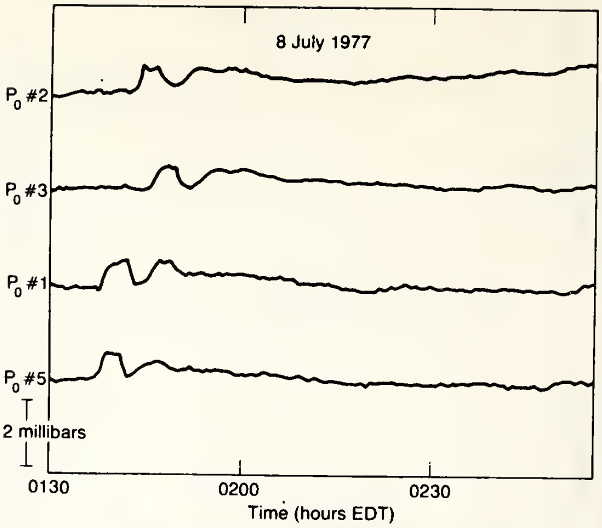

Figure 16. Absolute pressure data for a gravity-wave event.

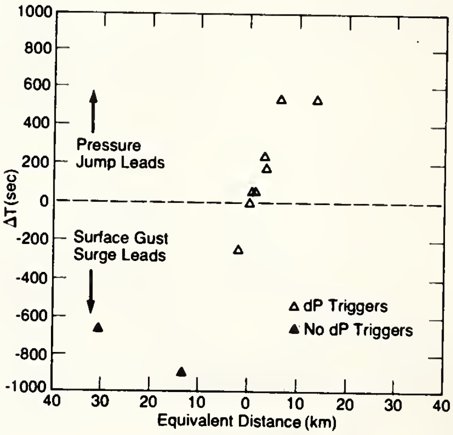

Figure 17. Relative arrival times of pressure jump and gust surge maxima as a function of equivalent distance in km.

Future studies of both the O'Hare 1977 and the Dulles data sets should make the statistics of these relationships clearer. For example, the value of temperature sensors relative to pressure or wind sensors is best treated by the O'Hare airport 1977 experiment which recorded data from six towers with collocated temperature, pressure and wind sensors. On the basis of observations made thus far, surface temperature sensors, although valuable for scientific studies of thunderstorm density currents, frequently show little or no response to the passage of a leading portion of a thunderstorm outflow. Therefore,

Table 1. Use of Anemometers for Gust-Front Detection of Thunderstorm Outflows.

Advantages

1. Directly measures surface winds and attendant danger to aircraft on the ground, as well as to airport surface facilities.
2. Also provides runway winds, knowledge of surface winds for general facility needs, inputs to wake vortex prediction systems, etc.
3. Detects surface gust surges related to thunderstorms as well as other meteorological phenomena (such as sudden downflows of warm air).

Disadvantages

1. Requires processing to define a significant event.
2. Is difficult to deploy dense arrays.
3. Does not detect some density currents at the surface, particularly in the presence of surface based inversions.
4. Is affected by the fact that some gust surges are accompanied by complex wind shifts, so as to greatly reduce confidence in wind vector computations and hence determinations of motion of the discontinuity.
5. Is susceptible to damage because of exposed mechanical moving parts (both natural and vandalism).

Table 2. Use of Pressure Jump Detectors for Detection of Thunderstorm Outflows.

Advantages

1. Is low-cost and highly reliable.
2. Can be mounted indoors as well as in sheltered or exposed outside locations.
3. Provides a level of processing at the sensor.
4. Allows data to be handled easily, thus permitting deployment in dense arrays.
5. Can detect density currents not reaching the surface of the earth.
6. Provides an early warning, as the pressure jump frequently precedes the gust surge.
7. Should detect "downbursts".
8. Is less influenced by boundary layer effects, so that pressure data show less spatial variability.

Disadvantages

1. Can produce false alarms due to gravity-shear waves or hydraulic jumps aloft (although some of these events may constitute an aviation hazard in and of themselves). This is overcome if pressure jump detectors are used in conjunction with wind speed detectors.
2. May not detect significant pressure jumps during certain events, such as warm air downflows or outflows of cold air occurring in thin layers.

although they respond to the cold air in the down-flow region itself and in some cases respond well to a thin, slowly moving flow of cold air with strong surface interaction, it seems that temperature sensors are not well suited for use as part of a warning system.

4. ANEMOMETERS VERSUS PRESSURE SENSORS — RELATIVE STRENGTHS AND WEAKNESSES

Tables 1 and 2 summarize the advantages and disadvantages of anemometers and pressure jump detectors pertinent to their use as part of an airport warning system. A number of the disadvantages of anemometers, such as their susceptibility to damage and higher costs, might be removed by using the inherently rugged and low cost wind-speed threshold sensor described in these proceedings by Bedard and Fujita (1978). Another advantage of this device is that it also eases the data transmission problems by answering the question "Is an event occurring?" A comparison between the tables indicates that the sensors can complement each other. Pressure sensors promise to detect downbursts and currents that do not reach the surface, whereas wind sensors can detect outflows of limited depth or of warmer air. Both sensor types should be capable of responding reliably to the most energetic events. The pressure detector would (statistically speaking) provide an earlier warning which in turn could be "verified" by a surface wind-speed surge.

It should be noted in closing that these results are only preliminary and indicative. The final, more conclusive study is still in process.

5. OUTLOOK FOR THE FUTURE

We still need to identify the optimum configuration and density for airport warning arrays, which will require statistics concerning surface effects in the vicinity of thunderstorms. These needs should be met at least in part by the data sets from the O'Hare and Dulles experiments. The forthcoming NIMROD experiment (Fujita, 1977) should also provide valuable insights into the meteorology of these events. Our current plans call for optimizing both the pressure-jump detectors and wind-threshold sensors, testing these "final" designs and completing analyses of existing data sets. After accomplishing this, we should be able to make our best possible recommendations concerning the design of an airport warning system. Present indications are that configurations like the one shown in Figure 18 will represent a reasonable compromise between reliability for detection and practicability in implementation. (The execution and operation of the Dulles system has required great and continuing effort from a large number of people). In the long term, future advances in remote sensing methods should eventually provide alternative solutions to this aircraft safety problem.

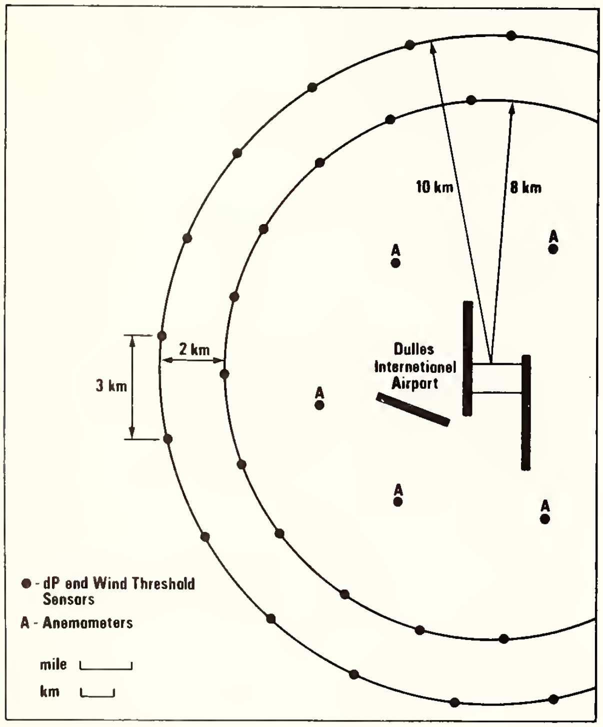
10 km
8 km
A
A
A
A
A
Dulles International Airport
2 km
3 km
● - dP and Wind Threshold Sensors
A - Anemometers
mile
km

Figure 18. Possible warning system for detecting thunderstorm density currents in the vicinity of airports.

6. ACKNOWLEDGMENTS

The Systems Research and Development Office of the Federal Aviation Administration supported both the experimental field programs and the analysis efforts that led to the development of the valuable data sets described. We are grateful to many individuals within the FAA for their guidance and encouragement; these include Messrs. R. Colao and J. Sowar as well as F. Coons and G. Tinsley. The data sets shown represent a small portion of data planned for a report to the FAA by the Wave Propagation Laboratory. We also wish to acknowledge WPL/ERL support at a critical juncture. The many people who assisted in the implementation of the Dulles System are acknowledged in the paper by Bedard et al. (1977). Professor T. T. Fujita has provided encouragement and valuable advice in these efforts. He suggested the value of collocating wind threshold and pressure jump detectors and his suggestion seems validated by the data sets obtained to date. The monostatic acoustic radar (Parry and Sanders, 1972) operated independently of the experiment by the Equipment Development Laboratory of NOAA's Weather Service. However, we plan future cooperative studies, relating gust front structure (as indicated by the monostatic and Doppler radars) to surface effects.

7. REFERENCES

Bedard, A. J., Jr. and D. W. Beran (1977). Detection of gust fronts using surface sensors. NOAA Tech. Memo. ERL WPL-20, 15 p.

Bedard, A. J., Jr. and M. M. Cairns (1977). Atmospheric pressure jumps measured with arrays of sensitive pressure sensors in the vicinity of Chicago's O'Hare International Airport. NOAA Tech. Memo. ERL WPL-28, 29 p.

Bedard, A. J., Jr., W. H. Hooke and D. W. Beran (1977). The Dulles airport pressure jump detector array for gust front detection. *Bull. Amer. Meteor. Soc.*, 58, no. 9, p. 920-926.

Bedard, A. J., Jr. and H. B. Meade (1977). The design and use of sensitive pressure-jump sensors to detect thunderstorm gust fronts. Part I: Pressure-jump detector design. *J. Appl. Meteor.* 16, no. 10, p. 1049-1055.

Bedard, A. J., Jr. and T. T. Fujita (1978). An omnidirectional, tilt insensitive, wind speed threshold detector. Proc. 4th Symposium on Meteorological Observations and Instrumentation, April 10-14, Denver, Colorado. Amer. Meteor. Soc. Boston, Mass.

Beran, D. W., W. H. Hooke, and S. F. Clifford (1973). Acoustic echo-sounding techniques and their application to gravity-wave, turbulence, and stability studies, *Boundary Layer Meteorology*, 4, 133-153.

Fujita, T. T. (1977., Project Nimrod (First Report), University of Chicago, p. 12.

Fujita, T. T. and H. R. Byers (1977). Spearhead echo and downburst in the crash of an airliner. *Mon. Weather Rev.*, 105, p. 129-146.

Fujita, T. T. and F. Caracena (1977). Common denominator of three weather-related aircraft accidents. Proc. 10th Conference on Severe Local Storms, Oct. 18-21, Omaha, Nebr., Amer. Meteor. Soc., Boston, Mass, p. 135-142.

Goff, R. C. (1976). Vertical structure of thunderstorm outflows. *Mon. Wea. Rev.*, 104, no. 11, 1429-1440.

Gossard, E. E. and W. H. Hooke (1975). *Waves in the Atmosphere,* Elsevier Press.

Gossard, E. E. and W. H. Munk (1954). On gravity waves in the atmosphere, *J. Meteorol.,* 11, 259-269.

Greene, G. E., H. W. Frank, A. J. Bedard, Jr., J. A. Korrell, M. M. Cairns and P. A. Mandics (1977). Wind shear characterization. Final report to the Federal Aviation Administration, prepared by the Wave Propagation Laboratory, NOAA.

Hardesty, R. M., P. A. Mandics, D. W. Beran and R. G. Strauch (1977). The Dulles airport acoustic/microwave radar wind and windshear measuring system. *Bull. Amer. Meteorol. Soc.*, 58, no. 9, 910-918.

Hooke, W. H., J. M. Young and D. W. Beran, (1972). Atmospheric waves observed in the planetary boundary layer using an acoustic sounder and a microbarograph array, *Boundary-Layer Meteorol.,* 2, 371-380.

Kjelaas, A. G., E. E. Gossard, J. M. Young and W. R. Moninger (1975). Dispersion and spectra of gravity waves probably generated by a convective storm, *Tellus,* 27, no. 1, 25-33.

Parry, H. D. and M. J. Sanders, Jr. (1972). The design and operation of an acoustic radar. IEEE Transactions on Geoscience Electronics GE-10, No. 1, 54-64.

Preprint Volume; Fourth Symposium on Meteorological Observation and Instrumentation, 83-86, American Meteorological Society, 1978.

AN OMNIDIRECTIONAL, TILT INSENSITIVE, WIND SPEED THRESHOLD DETECTOR

A. J. Bedard, Jr.

NOAA/ERL/Wave Propagation Laboratory
Boulder, Colorado

and

T. T. Fujita

University of Chicago
Chicago, Illinois

1. INTRODUCTION

The impetus for the design of this relatively simple wind-speed threshold detector (more generally called a wind-speed and wind-speed threshold sensor) arose from a need to develop surface sensors for use in preventing wind-shear related accidents at airports. Originating with dense currents of cold air in thunderstorms, downflows and the resulting outflows of dense air can produce wind-shear dangerous to aircraft (Fujita and Byers, 1977 and Fujita and Caracena, 1977) as well as variations in surface winds, temperature and pressure (Goff, 1976; Bedard and Beran 1977). The optimum detection of these systems could involve combinations of surface sensors until an active remote sensing method (e.g., involving FM-CW radar) can be developed.

Pressure sensor arrays at Dulles (Bedard, Hooke and Beran, 1977) and O'Hare (Bedard and Cairns, 1977) international airports have shown the feasibility of using arrays of surface sensors to detect and track the motion of the leading edge of atmospheric density currents. A paper in these proceedings (Bedard, 1978) discusses the relative strengths and weaknesses of temperature, wind and pressure sensing approaches. There is a need for surface sensors of high reliability that can be obtained at reasonable costs for use in large numbers. Bedard and Meade (1977) have presented a pressure jump detector developed in answer to these needs. Similarly, we developed the wind-speed detector described here. One of us (Fujita) originated the concept of using such a device, and the final design evolved during a semi-empirical investigation.

We must emphasize that the detector indicates wind speed and not wind direction. Although in some instances wind vector information is necessary at a point (e.g., little change in wind speed could occur in the presence of a large wind vector difference), there is evidence that the most dangerous density currents will produce significant wind speed surges (Fujita, 1977). Thus, it seems a simple wind-speed sensor can find applications for the detection of thunderstorm gust fronts. Moreover, the advantages offered by the sensor suggest a variety of other uses, including down-slope wind studies, wind caution signs for roads and bridges, as well as wind machine protection and site surveys.

2. SENSOR DESIGN

The detector (see Fig. 1 for a cutaway view) consists of two omnidirectional probes. These are configured so that the induced pressures for each differ from each other at a given wind speed. A differential pressure transducer can detect the pressure difference between the two probes and the wind speed deduced through the relationship

$$U = K\left(\frac{2\Delta P}{\rho}\right)^{1/2}$$

where U is the horizontal wind speed, ρ is the air density, ΔP is the pressure difference produced between the two probes and K is a constant determined during calibration.

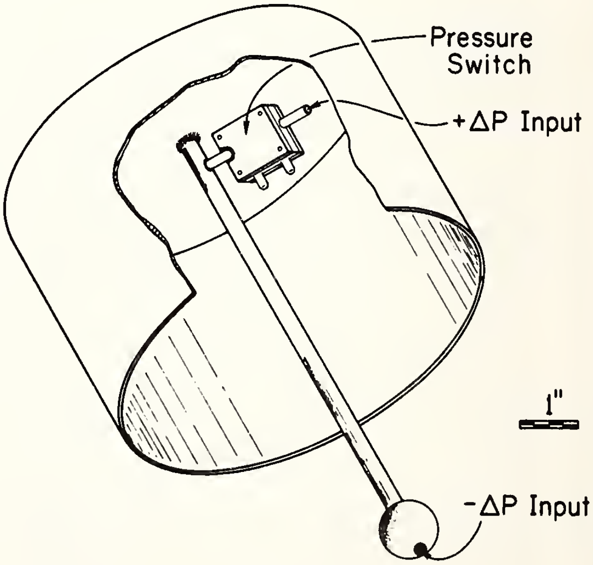

Figure 1. Cross-sectional view of wind speed threshold sensor.

One probe consists of a sphere with a sampling port at the base. But what considerations are important to the choice of the dimensions of such a probe? If the goal is a probe of maximum sensitivity (permitting the use of transducers with lower sensitivities and possibly lower costs), then one approach is to use a sphere with a small radius of curvature which accelerates the streamlines in the vicinity of the probe, increases the local velocity of the medium near the inlet, and reduces the local pressures relative to the free stream.

However, for atmospheric measurements, problems presented by dust, insects and sensor susceptibility to water and icing are important. Locating the sampling inlet at the base of the sphere reduces the problem of dust in the probe and makes the response independent of the azimuth of the horizontal winds. The length of the tube from the sensor to the sphere and its vertical orientation should further prevent dust from reaching the transducer. A small screen inserted in the tube prevents insects from entering. Even the size of the inlet port can be important. We have computed the maximum wavelength for stability of an air-water interface. Considering the effects of gravity and the surface tension of water we have made the diameter of the port larger than that required to produce a stable surface (e.g., Joseph, 1976). A large enough diameter port size (> 1.7 cm) helps to prevent water from collecting at the port opening and should inhibit ice formation.

The second probe could take a number of forms. For example, we have tested probes that consisted of a large number of small diameter holes (#54 to #71 drill size) drilled at equal distances around the surface of a cylinder by measuring the pressure inside the cylinder. This configuration acts as an averaging device or a form of a d-c pneumatic summator (Bedard, 1977). We have built several versions of these, and although they operated satisfactorily, the requirement of keeping the numerous ports clean and open is an impractical feature of this approach for atmospheric applications.

However, we have found that a cylinder closed at the top and open at the bottom can be an effective, practical probe. The flow of the medium produces internal pressures less negative than those obtained from the spherical probe already described (under identical free stream velocity conditions). One problem with using an open cylinder is that complex circulations occur because of complex detachments at the leading edge of the open portion of the cylinder. These make reproducibility of the pressure measurements poor. Fortunately, the simple addition of a central tube (in our case a tube holding the spherical probe) serves to stabilize the basic flow. The inverted cylinder can act as an area averaging device, displacing the measurement point from the free stream. Also, vertical velocity components, resulting from induced circulations within the cylinder, can increase the pressure with respect to the free stream Bernoulli pressure. This results in a less negative pressure than that obtained from the spherical probe reference port. Sensitivity to tilt is reduced if the two probes share a common axis and the pressures induced in each vary approximately equally and in the same direction with orientation to the mean flow, as is the case with the probes described here.

3. EXPERIMENTAL TESTS

Initially we tested sensor response by holding the unit out of the window of an automobile and measuring the differential pressure as a function of the speedometer reading. These rough measurements agreed with the wind tunnel tests described below. The sensor (mounted on a heavy brass plate) was tested in a wind tunnel at the University of Colorado (see Figs. 2 and 3 for photographs showing the sensor and the testing configuration). We routed the probe pressures to a differential pressure transducer located outside the wind tunnel using 1/4 inch inner

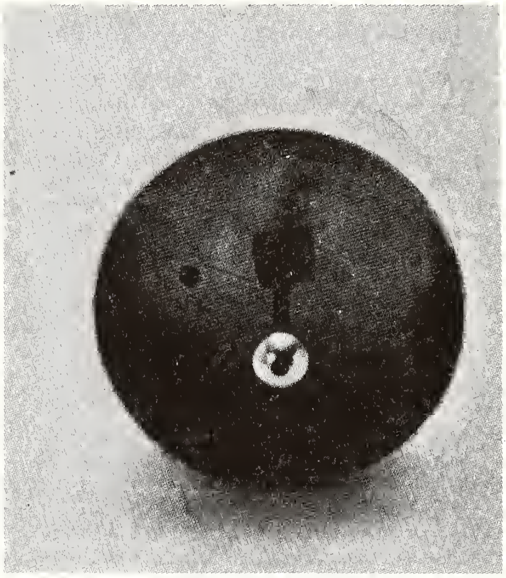

Figure 2. Photograph of wind speed threshold sensor.

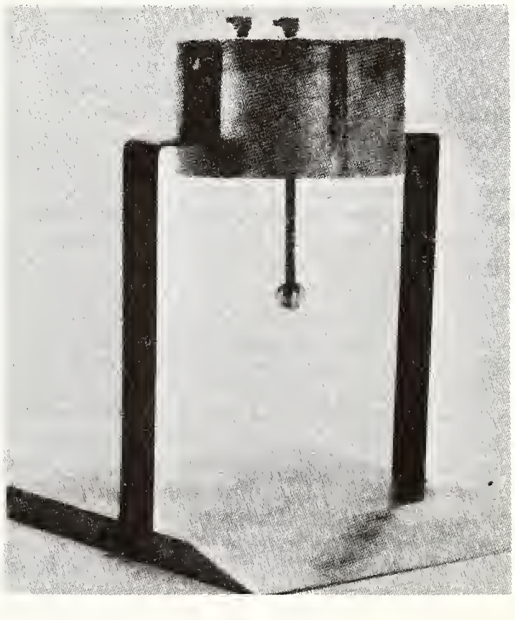

Figure 3. Photograph showing configuration for wind tunnel testing.

diameter tubing. We compared each probe pressure measurement with the static probe of a pitot-static tube that monitored the free stream of the wind tunnel. In addition we measured the pressure difference between the two sensor probes. For each run, we checked the noise level and zero of the differential pressure transducer by connecting the transducer inputs together. A pneumatic switching arrangement enabled us to make these measurements promptly and easily. Results from these tests appear in Fig. 4. Note that the pressure difference is a function of the square of the mean wind speed with little scatter in the data points. As a reference we noted the free-stream Bernoulli pressure variation on the plot. The agreement is not fortuitous since this was set as a practical goal for the detector sensitivity.

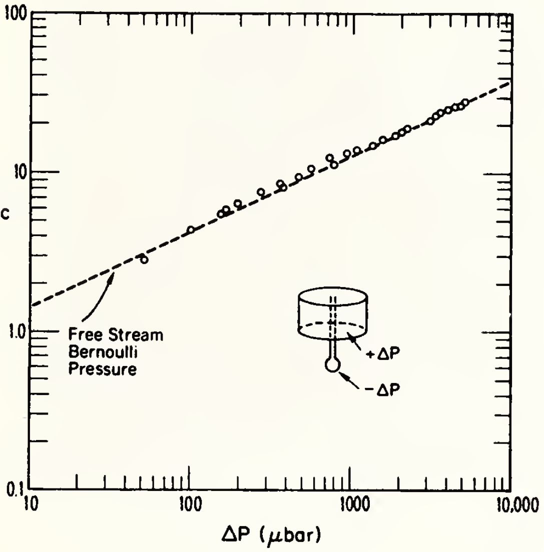

Figure 4. Pressure difference between probes as a function of horizontal wind speed.

We tested the influence of the spherical probe diameter and found that decreasing the probe diameter from 2 inches to 1 inch increased the sensitivity by about 50%. For the 1-inch diameter probe we found a tilt sensitivity for the entire detector of less than ± 5% for a ± 10 degree deflection of the sensor from the direction of the mean flow. Near the earth's surface the vertical components of the wind tend to be quite small compared with the horizontal components, so that, for purposes of most atmospheric applications, the tilt sensitivity can be considered negligible. This was for a 5/16 inch-diameter port opening. We found a similar tilt sensitivity by using a 2 inch diameter probe with the same size port opening. We plan to test other configurations for tilt sensitivity.

4. PRACTICAL APPLICATIONS

The advantages of ruggedness, low projected costs, and the fact that one question is answered (i.e., Is the threshold exceeded or not?) at the detector, suggest a great variety of practical applications.

a. Control of wind-caution warning signs for roads and bridges.

b. Control of wind-caution indicators for high-speed railroads.

c. Obtaining wind statistics for evaluation of sites for wind machines. (This detector could indicate the percentage of time the threshold for operation of a particular wind machine is exceeded.)

d. Automatic control of devices for protecting wind machines at high wind speeds.

e. Obtaining wind measurements under severe weather conditions.

f. Use in dense arrays to indicate patterns of downslope wind storms and provide real-time information to police and firemen as well as the public. Such downslope wind storms will become a more significant hazard as the front range areas of mountainous regions become more populated (e.g., Rocky Mountain region wind storms described by Henz, 1977).

g. Single unit use in the approach zones of small airports. We hope to evaluate the sensor for use in at least some of these areas.

h. Use as part of a wind-shear detection and warning system for major airports.

5. CONCLUDING REMARKS

In order to obtain experience with their operation under field conditions, current plans call for the fabrication of five of these wind speed threshold detectors for installation in the Dulles airport wind-shear detection system. We will use pressure switches set so that the wind-speed detectors indicate at approximately $10\ m\ s^{-1}$. Note that the set point of the pressure switch can be calibrated in the field using the pressure calibrator described by Bedard (1977). Additional tests will investigate the effects of adding a screen across the open portion of the inverted cylinder. This screen will prevent insects from entering the inverted cylinder and should further improve the stability and reduce turbulence.

For other applications we can modify the sensitivity by changing the diameter of the sphere used and/or the cylinder size. Note that although wind direction information is not obtained from the sensor, when arrays of these sensors are used vectors can be computed for gust surges using arrival time information at various sensors. In many cases, especially when complex shifts in the local wind vector occur, such computations can be more representative of system motion. In spite of the fact that this sensor is quite simple it seems that a variety of practical applications are possible.

6. ACKNOWLEDGMENTS

We are grateful to M. S. Uberoi and R. A. Kadlec at the University of Colorado for use of wind tunnels in the Aerospace Department's laboratories. We are also grateful to the Systems Research and Development Office of the Federal Aviation Administration for providing support for future testing of the sensor.

7. REFERENCES

Bedard, A. J., Jr. (1977). The d-c pressure summator: Theoretical operation, experimental tests and possible practical uses. *Fluidics Quarterly*, 9, no. 1, 26-51.

Bedard, A. J., Jr. (1978). The Dulles airport pressure-sensor array for gust-front detection ... system design and preliminary results. Proc. 4th Symposium on Meteorological Observations and Instrumentation, April 10-14, Denver, Colorado. Amer. Meteor. Soc., Boston, Mass.

Bedard, A. J., Jr. and D. W. Beran (1977). Detection of gust fronts using surface sensors. NOAA Tech. Memo. ERL WPL-20, 15 p.

Bedard, A. J., Jr. and M. M. Cairns (1977). Atmospheric pressure jumps measured with arrays of sensitive pressure sensors in the vicinity of Chicago's O'Hare International Airport. NOAA Tech. Memo. ERL WPL-28, 29 p.

Bedard, A. J., Jr., W. H. Hooke and D. W. Beran (1977). The Dulles airport pressure jump detector array for gust front detection. *Bull. Amer. Meteor. Soc.*, 58, no. 9, p. 920-926.

Bedard, A. J., Jr. and H. B. Meade (1977). The design and use of sensitive pressure-jump sensors to detect thunderstorm gust fronts. Part I: Pressure-jump detector design. *J. Appl. Meteor.* 16, no. 10, p. 1049-1055.

Fujita, T. T. (1977). Project Nimrod (First Report), University of Chicago, p. 12.

Fujita, T. T. and H. R. Byers (1977). Spearhead echo and downburst in the crash of an airliner. *Mon. Wea. Rev.*, 105, p. 129-146.

Fujita, T. T. and F. Caracena (1977). Common denominator of three weather-related aircraft accidents. Proc. 10th Conference on Severe Local Storms, Oct. 18-21, Omaha, Nebr., Amer. Meteor. Soc., Boston, Mass, p. 135-142.

Goff, R. C. (1976). Vertical structure of thunderstorm outflows. *Mon. Wea. Rev.*, 104, no. 11, 1429-1440.

Henz, J. F. (1977). On the predictability and formation of Colorado severe downslope windstorms. Proc. 10th Conference on Severe Local Storms, Oct. 18-21, Omaha, Nebr., Amer. Meteor. Soc., Boston, Mass., p. 201-206.

Joseph, D. D. (1976). Stability of fluid motions II. Springer-Verlag, New York p. 254.

Journal of the Acoustical Society of America, 63: 694-699, 1978.

Echosonde interferometer for atmospheric research

Edmund H. Brown and C. Gordon Little

Wave Propagation Laboratory, NOAA, Boulder, Colorado 80302

Wayne M. Wright[a]

Cooperative Institute for Research in Environmental Sciences Boulder, Colorado 80302

(Received 24 February 1977; revised 9 September 1977)

A preliminary version of an echosonde interferometer is described and some of the first results obtained with it are presented. The results demonstrate that the formation of an acoustic interference pattern from a pair of coherent sources extends to the sound field scattered by turbulent fluctuation and that an echosonde interferometer is practicable. Possible applications to the remote sensing of atmospheric temperature profiles are discussed.

PACS numbers: 43.28.Fp, 43.20.Fn

INTRODUCTION

In 1968 McAllister[1] constructed the first *echosonde*, an instrument that he called an *acoustic sounder*. This invention combined an improved version of a precursor of the echosonde—the device of Gilman, Coxhead, and Willis[2] that they named the *sodar*—with a facsimile recorder. The underlying physical mechanism of the echosonde consists of the scattering of sound waves by random temperature and velocity fluctuations in the atmosphere. In consequence, the echosonde represents a powerful instrument for mapping many aspects of the atmospheric boundary layer, using the naturally occurring atmospheric temperature and velocity fluctuations as tracers. However, though the echosonde can measure the strength of *temperature fluctuations*, it can provide neither *absolute temperatures* nor *temperature profiles* of the atmosphere. Temperature, perhaps the paramount quantity needed in meteorological studies, has until now resisted measurement by any simple remote sensing techniques. This lack has restricted temperature observations to *in situ* measurements provided by radiosondes. The costs of such radiosonde flights preclude fine enough space and time separations of the measurement grid for good meteorological prediction.

Typically, the interpretation of an echosonde facsimile record is based upon the assumption of narrow beams from the transducers. That is, the acoustic source and receiver (which correspond to the same device for a monostatic sounder) are considered to have radiation patterns with narrow major lobes and negligible side lobes. During examination of some particular echosonde records, Closs and Surridge[3] noted horizontal bands or fringes of scattered intensity, superimposed on the patterns that were anticipated due to atmospheric turbulence. These records were obtained with a coherent detection scheme. We speculate that the bands might have resulted from nonuniform ensonification of the lower atmosphere, corresponding to the directivity pattern for an array of real acoustic sources. Backscattered acoustic energy implies the existence of atmospheric irregularities, and these can be expected to restrict coherence length of the transmitted acoustic signals and thus to smear out the radiation pattern of the source transducer or source array.

A primary goal of the work described here was to ensonify only limited regions of the atmosphere above a directive receiving antenna of a bistatic echosonde and thus to attempt to generate predictable horizontal bands in the facsimile records. A secondary goal, given initial success at producing these bands, was to devise a means by which exploitation of this phenomenon might lead to the remote measurement of atmospheric temperature.

The radiation pattern of a single pistonlike acoustic source involves relatively little power in the side lobes, which consequently could not be expected to lead to measurable atmospheric scattering. An array of identical point sources, on the other hand, can have a radiation pattern with the same acoustic power in each of several major lobes (similar to the interference fringes produced by a set of coherent optical sources or slits) separated by regions of destructive interference (i.e., nulls of the array radiation pattern). The effects of interest to us are obtained from consideration of two or more interfering sets of waves, and we hence refer to the presence of a three-dimensional interference pattern throughout a small region of the atmosphere.

In this paper we present the first systematic research that provides evidence for such interference, namely facsimile records (obtained with the equipment described in this paper) showing bands at the predicted time delays. Since the facsimile recorder produces a darker trace with a more intense signal, regions of constructive interference in the atmosphere produce dark bands on the recordings. We have found that the sound waves (traveling upward through turbulence) from the transmitter, retain enough phase coherence to form interference fringes in space, and that the fringes are detectable by the increased scattering of the sound by the fluctuations within the regions of constructive interference.

---

[a] Permanent address: Kalamazoo College, Kalamazoo, MI 49007.

0001-4966/78/6303-0694$00.80

© 1978 Acoustical Society of America

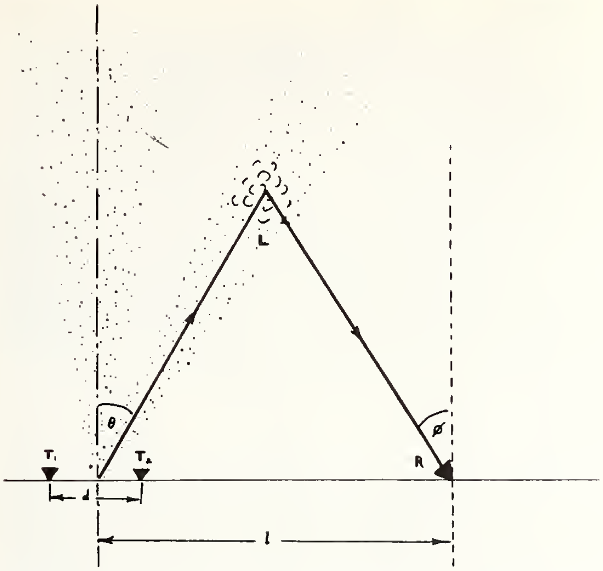

FIG. 1. Geometry of the interference experiment in the vertical plane through the receiver and two transmitters. Zenith angle θ measured from the vertical axis through the center of the transmitting array; zenith angle ϕ measured from the vertical axis through the receiver. Separation of transmitters denoted by d; separation of receiver from center of transmitting array denoted by l; L represents the total pathlength traveled by sound from transmitter to receiver.

I. THEORY

Figure 1 shows the configuration of our experiment. In the vertical receiver–transmitters plane the maxima of constructive interference in the farfield should appear at the zenith angles θ satisfying

$$\sin\theta = n\lambda/d, \tag{1}$$

with λ the wavelength, d the separation of transmitters, and n the fringe order. However, the positions of the horizontal bands on the facsimile recordings depend on the travel time for the total path length L. This path consists of one leg from transmitter to scattering volume in the fringe, and one from scattering volume to receiver.

First, for the simple case of temperature constant with altitude, L depends on the receiver–transmitters horizontal separation l according to the formula

$$L = l(\sec\theta + \sec\phi)/(\tan\theta + \tan\phi), \tag{2}$$

with ϕ the zenith angle of the receiver.

Since the speed of sound c in meters per second is related to the Kelvin temperature T by $c = 20.05\sqrt{T}$, the time delays $t = L/c$ are inversely proportional to $\sqrt{T}$ for large ϕ, but become inversely proportional to T as $\phi \to 0$. In particular, for $\phi = 0$, the above equations show that the time delay t resulting from a constructive interference fringe of order n is

$$t = (fld/nc^2)\{1 + [1 - (nc/fd)^2]^{1/2}\}, \tag{3}$$

where f is the frequency of the transmitted sound, and where all distances are in meters. If we assume that $(nc/fd)^2 \ll 1$ then we have approximately

$$t \approx fld/(200\,nT). \tag{4}$$

Thus, with a receiving bandwidth narrow enough to resolve returns from adjacent fringes, a vertical receiver beam will give relative changes in relative band position on the recorder equal in magnitude to the relative changes in absolute temperature, that is,

$$\delta t/t = -\delta T/T. \tag{5}$$

Temperature profiles can be treated by more complicated analysis. For most of the distance on the paths between the radiating elements and a point of interference, the different paths traverse approximately the same temperature profiles. Therefore the locations of the interference fringes in space are determined primarily by the few extra wavelengths in one path near the ground and thus by the temperature near the ground. But the time delays for the recorded bands will depend on both the fringe positions and the temperature profiles aloft. Let us, for example, assume that the lower half of a region extending to the altitude of the intersection of a fringe and the receiver beam remains a uniform constant temperature T, but that the upper half changes temperature by a uniform amount δT. Then if θ is the angular position of the fringe, the relative change in time delay can be shown to be

$$\delta t/t = -\tfrac{1}{4}\,(1 + \sec\theta)(\delta T/T). \tag{6}$$

As an example, for $\theta = 45°$, Eq. (6) gives approximately two-thirds the change indicated by Eq. (5) for the same temperature change in a uniform atmosphere.

Measurement of the variation of temperature altitude would require closely spaced narrow fringes, with an optimum narrow-beam receiver, to obtain distinguishable bands. Such a configuration could employ either a "boot-strap" type of calculation (in which the path-averaged sound speed obtained from one time delay is used to determine the altitude of the scattering volume in the next fringe) or a calculation based on measuring band delay times at two or more frequencies.

II. EQUIPMENT

With the objective of experimentally observing intentional interference fringes by means of the bands produced in echosonde facsimile recordings, we set up an acoustic receiver and a pair of transmitters at NOAA's Table Mountain field site, a flat-topped mesa about 1 by 2 miles in size, located a few miles north of Boulder, Colorado. The receiving antenna consisted of a 24-Ω compression driver (Altec-Lansing 288-C) together with an exponential feed horn, mounted at the focus of a 5-ft parabolic dish, with the total assembly placed in a square cuff lined with acoustic absorbing foam. Each transmitting element consisted of a 4-Ω compression driver (Altec-Lansing 290-4G) rated for 100 continuous electrical watts, together with a 1000-Hz exponential feed horn. The parabolic dish was omitted to reduce the directionality of each individual transmitting beam pattern and to permit close spacing of the acoustic

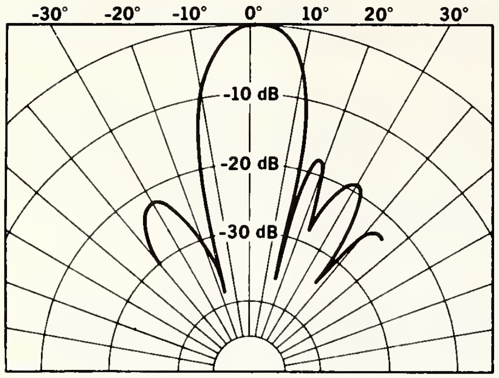

FIG. 2. Receiver radiation pattern at 1250 Hz. Amplitude of acoustic pressure in decibels as a function of angle from the zenith.

sources. We placed a 4-ft-high absorbing cuff on the three sides of the transmitter array away from the direction of the receiver. The elements of the transmitting array sat directly on the ground, pointing straight up and with centers separated by about $3\lambda/2$ at 1000 Hz and 3λ at 2000 Hz. The receiving antenna was located at a horizontal distance of 50 m from the transmitting array in the vertical plane through the elements of the array. After some initial problems with reflections from fixed objects, we positioned this entire assembly about 1000 ft from any object higher than rocks a few inches above the ground.

Thousand-foot cables connected the receiving and transmitting antennas to an echosonde (Mark VII Wave Propagation Laboratory, see Owens[4]) arranged to permit separation of the signals from the receiving and transmitting antennas. The transmitting circuits included a two-channel power amplifier (Crown 300A) which allowed equalizing of the farfield axial pressure of the two transmitters. The output of the echosonde corresponding to the scattered wave went either directly or *via* a postdetection integrating device (a Princeton Applied Research "Waveform Eductor" TDH-9) to a facsimile recorder (Raytheon Universal Graphic Recorder 196-C).

To independently confirm the existence of three-dimensional spatial interference fringes in the atmosphere, we used the field beam-pattern measuring method described in Willmarth *et al.*[5] Briefly, in this method a balloon-borne microphone is swung in a circular arc in the farfield over the antenna to provide sound pressure as a function of angle. Figures 2 and 3 show the resulting measurements for the radiation from the receiver and the transmitter array, respectively, for a 1250-Hz signal and a 24-in. transmitter separation. Evidently, the receiver has a total angular beamwidth, as defined by the 3-dB points, of about 14°. For the transmitting array, fringe intensity drops only slowly with increasing order, and individual fringes have spacings of about 30°.

III. RESULTS

With the considerations of the Sec. I in mind, we adopted the configuration with the two transmitter drivers and feed horns pointed up, with a transmitter spacing of $d = 18$ in. and a receiver zenith angle of 0°. In addition, since we appeared to obtain better results at higher frequencies, most of our further tests used either 2000 or 2500 Hz; thus, the facsimile records included two or more bands. Figure 4 shows a record obtained with the experimental arrangement. The top part of Fig. 4 gives the direct results, the bottom part, the results after integrating and smoothing with the Waveform Eductor. At the beginning of the record at the right (time in our facsimile records runs from right to left) two darker bands, corresponding to constructive interference, appear clearly. Halfway through the record we reversed the electrical connections to one of the transmitters, thus reversing the phase relationship. As expected, whatever had appeared dark became light, and conversely.

During the course of our experiments we noticed that faint horizontal bands frequently remained on the facsimile record even with only one transmitter in operation. Figure 5, which gives only the Waveform Eductor-processed part of the recording, shows such faint bands in the right-hand two thirds of the record. At the time marked by a thin, vertical white stripe (when transmission was interrupted), we raised the single transmitter by exactly $\lambda/4$. The shift had a startling effect on the intensity and position of the bands. Though more difficult to see than in Fig. 4, again dark bands appear to become light, and light fringes dark. We suggest that many of the dark bands seen in facsimile records of some previous researchers may have resulted from interference between the direct beam and a reflected beam from the ground and other nearby surfaces.

Finally, we ran a test to simulate the effect of temperature change on band position by altering the frequency instead. Figure 6 gives the results: At the right two bands appear at the appropriate positions corresponding to the operating frequency of 2500 Hz; halfway through the record we changed the frequency to 2000 Hz; the bands drop abruptly to two lower positions. Measurements indicate that this 500-Hz frequency shift corresponds to a 100 °K temperature shift. Clearly, obtain-

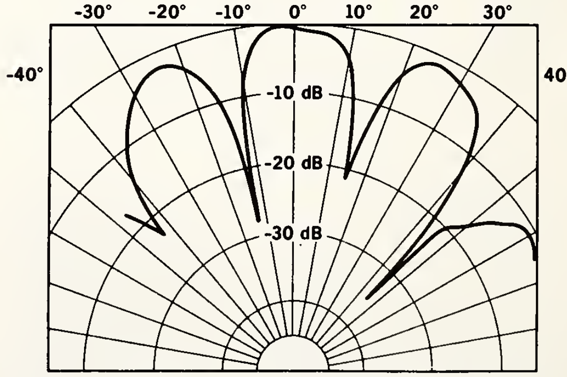

FIG. 3. Transmitter array radiation pattern at 1250 Hz. Acoustic pressure in decibels as a function of angle from the zenith in the vertical plane through the array: two compression drivers and feed horns at a 24-in. spacing, pointed upwards.

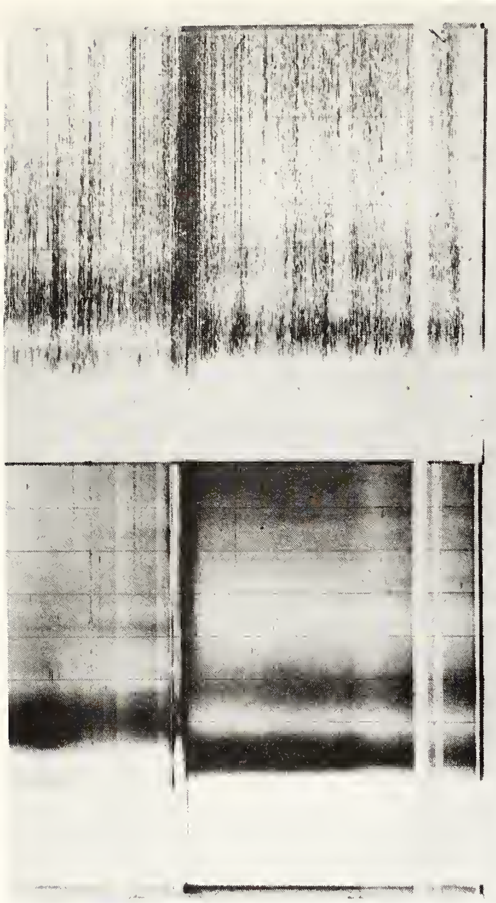

FIG. 4. Interference from two sources: effect of phase reversal. Regions of constructive interference result in darker bands on facsimile record. Time begins at right of all records and runs to the left. Vertical scale on all records is 0.1 s per division for time delay. Two-thirds through the record the phase of one transmitter changed by 180°. Thus regions of destructive interference (white) change to constructive (dark) and conversely. Top part of figure derived directly from the echosonde; bottom part represents signal after amplitude integration and smoothing.

ing meteorologically useful temperature measurements to about 1 °K from time delays alone would require considerable sophistication in the data-processing electronics of an echosonde temperature-measuring system.

IV. FUTURE DESIGN FACTORS

Obtaining improved facsimile record bands requires both narrow fringes in the radiation pattern and a narrow receiver beam to prevent band overlap and smearing. A receiving antenna dish of larger diameter would have a smaller angular beamwidth. However, without a proportionately higher cuff, a larger dish also would accept more nearfield noise and drastically lower the signal-to-noise ratio. Since reduction of band overlap requires a narrow receiving beam only in the vertical plane through transmitters and receiver, the use of *two* receivers in the same plane, with electrical correlation of their signals, should permit effective reductions of up to about one-third in the previously measured 14° beam angles. Using *more* than two receivers does not appear practical, since each receiver must have the now fairly standard form of compression driver, feed-horn, reflecting dish, and absorbing cuff.

An even greater improvement should occur with the use of multiple transmitters to narrow the angular width of the interference fringes. With these less bulky transmitters (consisting only of drivers and impedance-matching horns), a larger number than for the receiver appears practical. Now, the need to obtain and maintain approximately the same phase of the sound from all drivers (which drift with ambient conditions and age) will control the maximum useable number of transmitters. An analysis based on M point sources gives an approximate idea of the improvement in fringe definition expect over only two sources. If the sources run from $m=1$ to $m=M$, the phase path length of the mth source to the point P becomes

$$\phi_m = kr + \tfrac{1}{2}(M+1-2m)kd\sin\theta, \qquad (4)$$

to first order in d/r, with r the distance from the center of the array to P, θ the zenith angle, k the wave number $2\pi/\lambda$, and d the distance between sources (assumed ev-

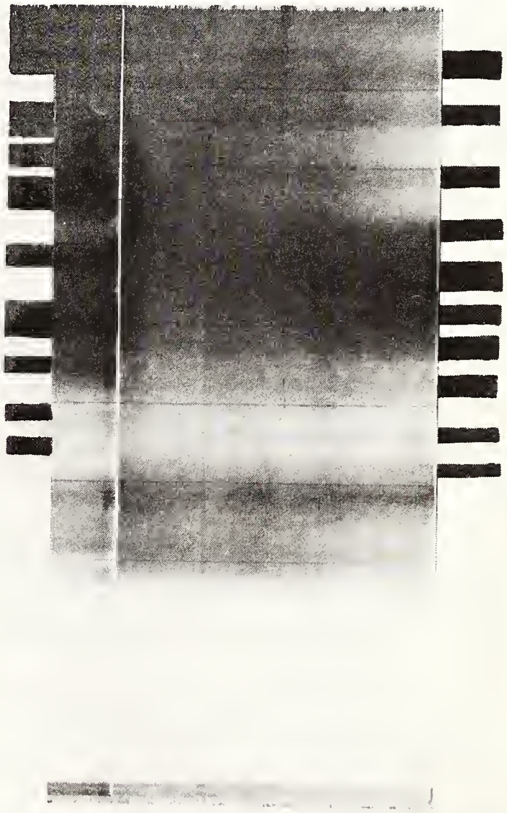

FIG. 5. Interference from one source and reflections. Faint bands visible in right-hand four-fifths of record shift intensity and position when the single transmitter is raised by $\lambda/4$. (Change takes place at point marked by thin white vertical strip.) Bars drawn on each side of this reproduction show where bands appeared more clearly in original record. The irregular dark band running across the record below the marked bands is due to a weak transmitter sidelobe.

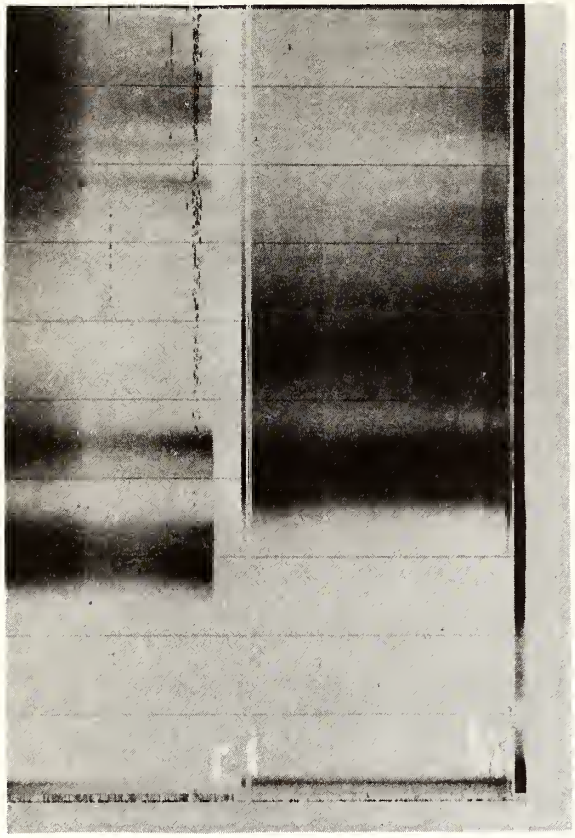

FIG. 6. Interference from two sources: effect of frequency shift. Bands appear on right-hand half of record for 2500 Hz. At center of record, frequency shift to 2000 Hz causes drop in position of two most visible bands.

erywhere equal). Neglecting the diffraction pattern of the individual elements, a standard result [such as Eq. (10) of Sec. 8.6 in Born and Wolf[6]] shows that the amplitude of the pressure $a(\theta)$ as a function of zenith angle θ is related to the initial amplitude a_0 by

$$a(\theta)=\frac{a_0}{r}\,\frac{\sin(\frac{1}{2}Mkd\sin\theta)}{\sin(\frac{1}{2}kd\sin\theta)}\,. \qquad (5)$$

Figures 7 and 8 show computer evaluated curves of the sound pressure for two and five sources, for element spacing given by $d/\lambda=\frac{3}{2}$ and 4. The curves show a striking increase in fringe sharpness with increasing number M of transmitters.

Despite the above direct methods for increasing sensitivity of measurements to temperatures, Fig. 6 suggests that these methods, alone, may not achieve results acceptable to meteorologists. However, recently developed minicomputer echosonde systems such as that reported by Owens,[7] show promise of providing adequate sensitivity. Such systems, recently become commercially available,[8] will permit sampling the scattered echos at rates above the Nyquist frequency of the wave. Thus, the systems furnish the possibility of using coherent detection noise cancellation techniques. With these techniques, sufficiently precise definition of the fringes may become possible. And, obtaining such

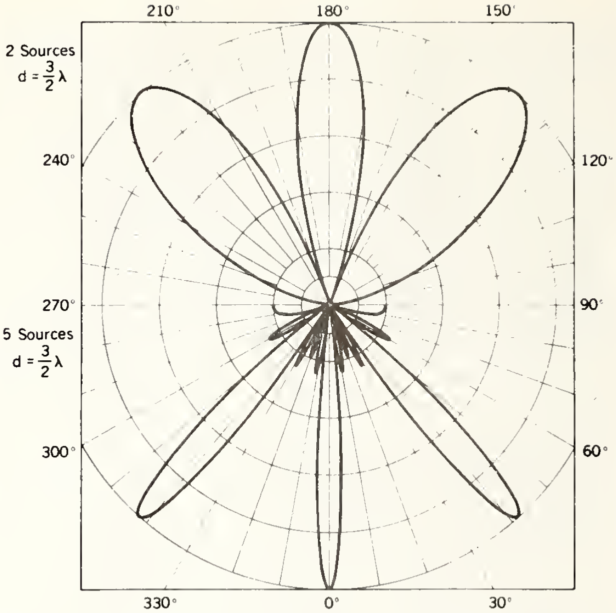

FIG. 7. Multiple source interference. Calculated improvement in fringe width defined in terms of acoustic pressure (linear rather than decibel scale) obtained by increasing number of sources in transmitting array. Top half: two sources with separation $3\lambda/2$; bottom half: five sources with separation $3\lambda/2$.

results require only minor changes in the programs written for the minicomputers.

An additional complication results from the effect of mean wind on the motion of the acoustic phase fronts and the position of the fringes. One method to correct

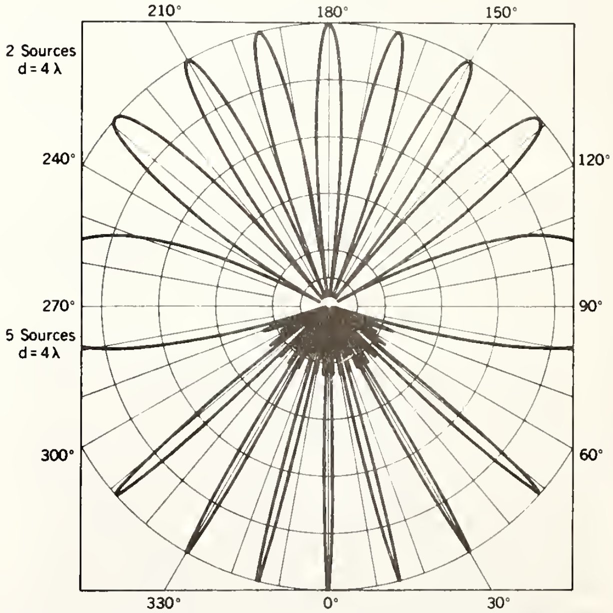

FIG. 8. Multiple source interference. Similar to Fig. 7. Top half: two sources with separation 4λ; bottom half: five sources with separation 4λ.

for the wind would use a symmetric receiver–transmitter configuration. For example, balancing the set of receivers on one side of the transmitting array by a similar set 180° from the first would permit cancelling the effect of wind on temperature measurements and, perhaps, also lead to another measure of the wind itself.

V. CONCLUSIONS

We have built an echosonde interferometer and demonstrated both that it produces interference fringes in space and that the regions of constructive interference produce observable differences in the sound scattered to a receiver; these differences appear as darker bands on the facsimile recordings. We have investigated phase reversal and simulated the effects of temperature changes by producing wavelength changes due to shifts in frequency. We have shown that, when a single transmitter does not have adequate shielding from the ground or nearby objects, the observed bands vary with changes in the height of the transmitter above the ground. This strongly suggests that the occasional bands seen by previous researchers might have resulted from interference between the direct transmitter beam and reflected beams. Finally, we have suggested design improvements including the addition of a minicomputer for correlation detection and the use of noise cancellation techniques.

ACKNOWLEDGMENTS

We would like to thank Dr. F. F. Hall, Jr., L. A. Vohs, and C. E. Case in the Wave Propagation Laboratory's Atmospheric Acoustics group for advice and assistance during this study, and Drs. R. L. Closs and A. D. Surridge for helpful correspondence.

[1] L. G. McAllister, "Acoustic sounding of the lower troposphere," J. Atmos. Terr. Phys. 30, 1439–1440 (1968).

[2] G. W. Gilman, H. B. Coxhead, and F. H. Willis, "Reflection of sound signals in the troposphere," J. Acoust. Soc. Am. 18, 174–283 (1946).

[3] R. L. Closs and A. D. Surridge, "The temperature profile in the lower atmosphere obtained by acoustic sounding," J. Phys. E, 7, 369 (1974).

[4] E. J. Owens, "NOAA Mark VII acoustic echosounder," NOAA Tech. Memo. ERL WPL-12 (Wave Propagation Laboratory, Boulder, CO, 1975).

[5] B. C. Willmarth, E. H. Brown, J. T. Priestley, and D. W. Beran, "Beam pattern measurements for large acoustic antennas," *Preprints of the* 16th AMS *Radar Meteorology Conference* (Am. Meteor. Soc., Boston, MA, 1975), pp. 278–281.

[6] M. Born and E. Wolf, *Principles of Optics* (Pergamon, New York, 1970), 4th ed.

[7] E. J. Owens, "Microcomputer controlled acoustic echo sounder," M.S. thesis (University of Nevada, 1976) (unpublished).

[8] See Bull. Am. Soc. 57, 1181 (1976).

Proceedings of the Dynamic Flow Conference, Baltimore, Md., 551-565, 1978.

Sonic Anemometer Measurement of Atmospheric Turbulence

by

J.C. Kaimal
Wave Propagation Laboratory
NOAA/ERL, Boulder, Colorado 80302

1. Introduction

The study of atmospheric turbulence and its role in transporting momentum, heat, water vapor and other constituents within the layers close to the ground has been a central goal in micrometeorology. Essential to such a study is detailed information on the fluctuations of all relevant parameters. The frequencies of interest cover a range of nearly five decades, corresponding to scales of motion ranging from a few centimeters to several kilometers, presenting a serious challenge to the experimentalist. Over the last 50 years a number of different measurement techniques have been tried with varying degrees of success. Particular attention was given to fluctuations in the velocity field because of their importance to turbulent transport in the atmosphere.

The earliest attempt to estimate momentum flux through direct measurements of velocity fluctuations was made by F.J. Scrase (1930), a British meteorologist. He made his measurements in 1962 over Salisbury Plain using an airmeter, a swinging plate anemometer, and a simple bivane attached to a recording pen. His instrumentation was replaced by more sensitive bivanes and hot-wire anemometers in later experiments at other sites, but a clear understanding of the structure and dynamics of turbulences in the first 50 m or so of the atmosphere, usually referred to as the surface layer, did not emerge until the late 1960's. To a large extent this breakthrough was possible because of advances in sonic anemometry which, coupled with developments in the rapidly growing data processing and recording field, enabled scientists to analyze large quantities of turbulence data in a relatively short time.

The sonic anemometer offered several advantages over the bivane and hot-wire systems. It has no moving parts to come into dynamic equilibrium with the flow, so its frequency response is limited only through the attenuation in the spatial response imposed by line averaging along the path. It responds linearly to wind velocity and is relatively free of contamination from other velocity components or temperature. As an absolute instrument, its calibration is established by its design parameters.

The use of sonic anemometers in micrometeorological studies was pioneered by Suomi (1957). In his instrument, acoustic pulses were propagated in opposite directions along a 1-m path to determine wind velocity along the path. He demonstrated the feasibility of sonic anemometry for turbulence measurement but encountered substantial difficulties in detecting the leading edge of the received pulses. This problem led later workers in the United States (Kaimal and Businger, 1963) and the USSR (Gurvich, 1959; Bovsheverov and Voronov, 1960) to turn to continuous wave techniques, which avoided some of the difficulties of the pulse technique. Measuring transit time differences with phase comparators proved more dependable, so the early field instruments used the continuous-wave technique. However, inherent drifts in the zero-wind calibration due to thermal drifts in the transducers and the need for a multiplicity of frequencies in any three-axis configuration led investigators to reexamine the pulse approach and overcome some of the problems encountered in the earlier versions. The instruments described by Mitsuta (1966) and Kaimal et al. (1974) use the pulse approach to advantage. In the USSR continuous-wave systems still remain in use (Koprov and Sokolov, 1973), and a three-dimensional version utilizing one transmitter and four receivers is described by Bovsheverov et al. (1973).

Recent developments in sonic anemometry have been aimed at adapting it for continuous operation on towers and reducing its cost. The author's orthogonal, three-dimensional array used on the Boulder Atmospheric Observatory's 300-m tower is designed for wider azimuth coverage of wind directions than was possible in earlier versions. Kaijo Denki Co. of Tokyo, Japan, offers several array configurations including the type mentioned above. A single-axis prototype of a low-cost phase locked loop system has been tested successfully by the Atmospheric Sciences Department at the University of Washington, but further development work is needed to convert it into an operational three-axis system.

2. Principle of Operation

The sonic anemometer measures wind velocity components from arrival times (or phase) of acoustic signals transmitted in opposite directions across a fixed path. Fig. 1 illustrates the effect of wind V on the sound ray vectors for a single-axis, dual-path sonic anemometer. The paths are parallel and closely spaced to minimize errors arising from velocity and temperature differences between the two paths. Assuming a uniform wind and temperature field within the array the transit times for two opposing pulses traveling from T_1 to R_1 and T_2 to R_2 can be approximated by

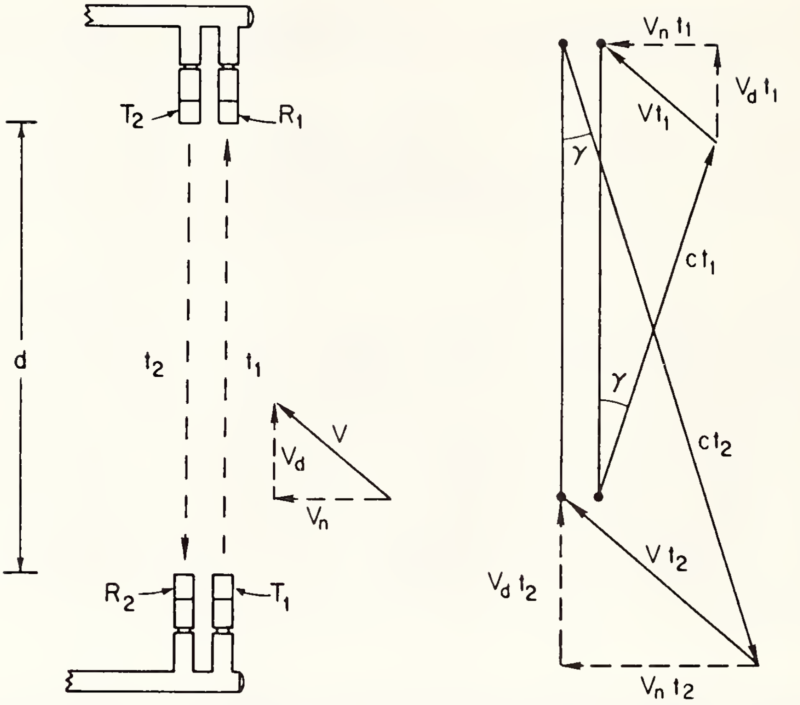

Fig. 1. Sound ray vectors for single-axis sonic anemometer showing principle of operation. Symbols T and R represent the transmitter and receiver, respectively.

$$t_1 = \frac{d}{c \cos\gamma + V_d} \qquad [1]$$

$$t_2 = \frac{d}{c \cos\gamma - V_d} \qquad [2]$$

where t_1 and t_2 are the transit times for the two pulses, d is the path length, V_d is the velocity component along the path, c is the velocity of sound in air, and $\gamma = \sin^{-1}(V_n/c)$, V_n being the velocity component normal to the path. The transit time difference is therefore

$$\Delta t = t_2 - t_1 = \frac{2\,V_d d}{c^2 - V^2}\,, \qquad [3]$$

where $V^2 = V_d^2 + V_n^2$. Assuming $V^2 << c^2$,

$$\Delta t = \left[\frac{2d}{c^2}\right] V_d\,. \qquad [4]$$

The speed of sound is a function of temperature and water vapor content and can be expressed in the form (Kaimal and Businger, 1963)

$$c^2 = 403\ T(1+0.32\ e/P) \qquad [5]$$

where T is the absolute temperature, e is the vapor pressure of water and P is the atmospheric pressure with all terms expressed in SI units. The vapor pressure term is small and usually negligible, as are fluctuations in T compared to the mean absolute temperature. From [4] and [5] we have

$$V_d = \left[\frac{201.5\ \overline{T}}{d}\right] \Delta t. \qquad [6]$$

When $\overline{T}$ (mean temperature) is known, the measurement of V_d reduces to a simple measurement of transit time difference whereas the sign of Δt indicates the direction of the velocity component. Therefore the accuracy of the measured velocity depends on the precision of the Δt measurement. For typical values of d = 0.2 m and $\overline{T}$ = 25°C, a minimum resolution of 0.1 μs (3 cm/s^{-1}) is needed. The effective resolution can be improved by averaging 10 or 20 successive acoustic transmission so that each data point is a block average over the preceding sampling interval (Kaimal et al. 1974). This prefiltering has the added advantage of reducing distortions at the high frequency end of spectra due to aliasing.

Sonic anemometers using only one transducer at each end of the path, switching alternately between transmitter and receiver modes, are now available from Kaijo Denki Co. The benefits include reduced interference to airflow and smaller temperature drifts in the measurements. The drawbacks are a lower sampling rate (<10 Hz) to allow for settling times in the transducers and consequent inability to block average data by transmitting more frequently than is needed.

It is instructive to examine the error introduced by the simplifying assumption $c^2 \cong 403\ \overline{T}$ which led to the expression in Eq. [6]. Separating the terms in Eq. [5] into their mean and fluctuating parts (denoted by overbars and primes, respectively), and neglecting the higher order terms,

$$\frac{c'}{c} \cong \left(\frac{T'}{2\overline{T}}\right) + 0.16\left(\frac{e'}{\overline{P}}\right). \qquad [7]$$

The humidity fluctuation term is usually negligible. The effect of the temperature fluctuations on the velocity measurement can then be expressed as

$$(V_d)_m \cong V_d(1 - \frac{T'}{\overline{T}}), \qquad [8]$$

where the subscript m indicates the measured value. The error is less than 1 %, but could be large if a significant temperature trend occurs during the observation period. Hourly updating of $\overline{T}$ is essential especially during the transition periods. Friehe (1976) has shown that error introduced by the temperature fluctuation term in Eq. [8] is negligibly small in the variance and heat flux calculations but can be as large as −3.6 % in the momentum flux.

An alternate approach avoids the velocity error caused by fluctuations in c^2. If instead of $(t_2 - t_1)$, the difference between their reciprocals $(1/t_1 - 1/t_2)$ is computed, the resulting term 2V/d is independent of c^2. The difficulty of measuring small differences between the reciprocals of two relatively large numbers with sufficient accuracy diminishes its attraction to the instrument designer. However, Kaijo Denki offers this option in the digital version of its sonic anemometer.

In addition to wind measurement some sonic anemometers (Mitsuta, 1974) provide temperature measurements by computing the sum of the transit times. But the temperature information is contaminated by the crosswind V_n and by humidity (to a lesser extent) since they have the same effect on t_1 and t_2. Under convective conditions in the first 30 m or so of the boundary layer, the contamination is negligible, but in neutral and stable air where the actual temperature fluctuations are small, the fluctuations in V_n appear prominently in the measured temperature signal (Kaimal, 1969).

3. Measuring the Vertical Component of the Wind

The geometry of the single-axis sonic anemometer array is particularly well suited for measuring the vertical wind component w since the transducers interfere little if at all with airflow along the path when the path is oriented normal to the flow. This is significant since in most other wind sensors w is the hardest component to measure accurately. Shifts in azimuth wind directions do not affect the accuracy of the measurement except when the acoustic path is in the wake of the supporting frame. Bivanes and hot-wire x-probes do not measure the w component directly, but provide inclination angle measurements from which w must be computed.

Fig. 2 is one of the first records of simultaneous w and temperature measurements. It shows a convective plume at 3.5 m, with pronounced updraft within the core of the plume (as defined by the sawtooth temperature burst), and downdrafts in the thermally quiescent regions upwind and downwind of it.

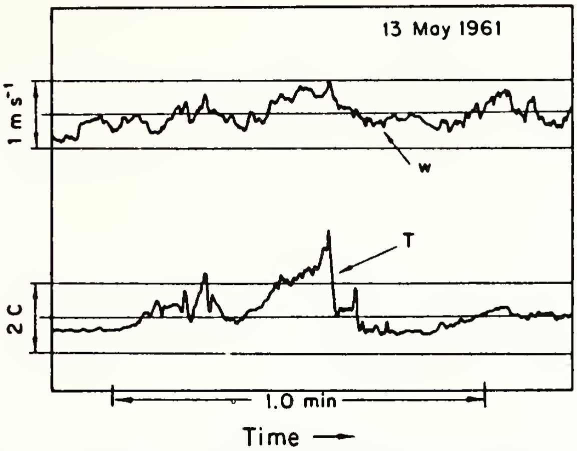

Fig. 2. Simultaneous records of vertical velocity and temperature fluctuations in a convective plume obtained with a sonic anemometer-thermometer.

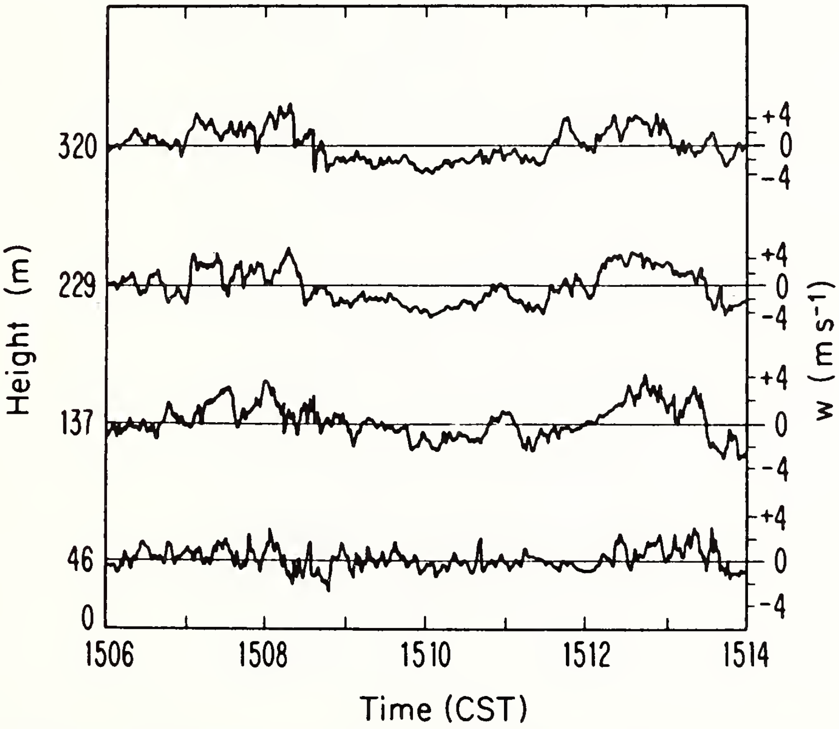

Fig. 3. Vertical velocity fluctuations measured on a 430-m tower show large-scale convective plume formed by merging of smaller ground-based plumes.

These individual updrafts merge into larger plumes as they ascend above 100 m as seen in sonic anemometer records in Fig. 3 obtained from four levels on a 430-m tower (Kaimal and Haugen, 1967). Peak vertical velocities observed here are of the same order as the horizontal wind speeds (5 to 6 ms^{-1}) during that period. Thus, sonic anemometers intended for measuring w on tall towers should have a range comparable to that needed for horizontal velocity measurements.

4. Measurement of Horizontal Velocity Components

The integration of two horizontal axes to the vertical array should, in principle, provide the full three-dimensional information on the wind field needed for turbulence studies. But the problem of designing a three-dimensional array with unobstructed exposure for all the axes is not a trivial one. A non-orthogonal array which has evolved in recent years (Kaimal et al. 1974; Mitsuta, 1974) has its horizontal axes separated by a 120-deg. angle to provide a reasonably wide (90 deg) azimuth coverage (see Fig. 4). Even with such a coverage the array often must be reoriented once every hour to ensure that the natural variations in wind direction do not exceed the desired range. Such reorientation of the array can be achieved remotely if the array is mounted on an antenna rotor (see Fig. 5). The wind outputs from the horizontal axes are monitored on a strip-chart recorder to determine the orientation of the array with respect to the wind.

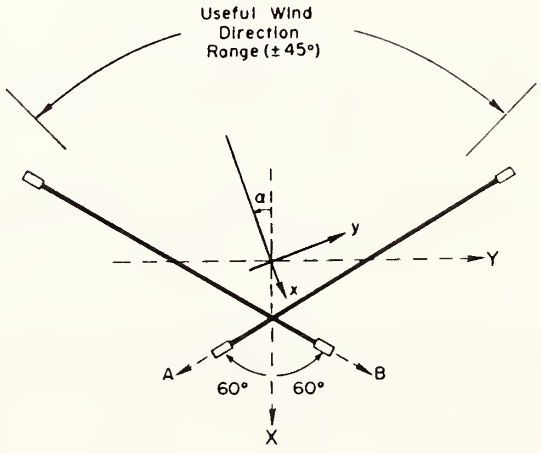

Fig. 4. Relationship between the horizontal axes of a three-axis sonic anemometer and the vector-mean axes of the wind. Coordinate transformation for converting wind measurements to velocity components along the vector-mean axes are given in Eq. [9].

In the array of Fig. 5 the vertical component (w) is obtained directly from the vertical axis, but the streamwise (u) and lateral (v) components must be computed from velocities V_A and V_B measured along the horizontal paths A and B (see Fig. 4). If α is the angle between the vector-mean wind directions and the axis of symmetry for the array,

$$u = V_A\left(\cos\alpha - \frac{1}{\sqrt{3}}\sin\alpha\right) + V_B\left(\cos\alpha + \frac{1}{\sqrt{3}}\sin\alpha\right); \qquad [9a]$$

$$v = -V_A\left(\frac{1}{\sqrt{3}}\cos\alpha + \sin\alpha\right) + V_B\left(\frac{1}{\sqrt{3}}\cos\alpha - \sin\alpha\right); \qquad [9b]$$

$$\alpha = \tan^{-1}\left[\frac{\bar{V}_B - \bar{V}_A}{\sqrt{3}(\bar{V}_B + \bar{V}_A)}\right] \qquad [9c]$$

The overbar denotes time average over a suitably long interval. In the instance of $\alpha = 0$ we have $u = V_A + V_B$ and $v = (1/\sqrt{3})(V_B - V_A)$

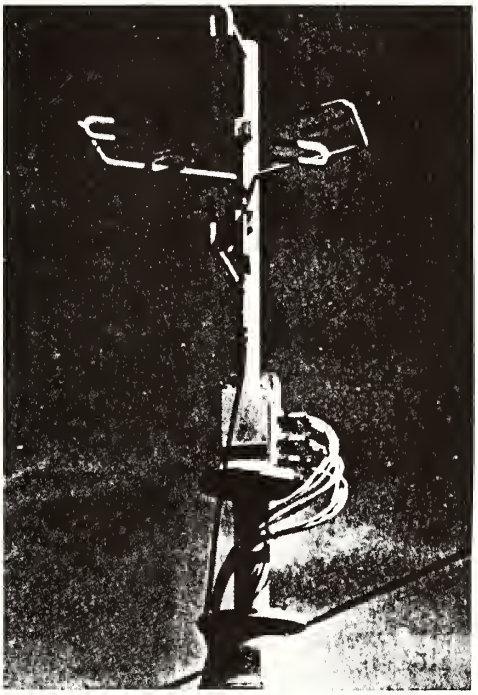

Fig. 5. Three-axis sonic anemometer array (EG&G Model 198-3) using the geometry of Fig. 4 avoids the need for support members upwind of acoustic paths. Array is mounted on a remotely-controlled, antenna rotor and periodically oriented into the mean wind. Path length in each axis is 20 cm.

Although this arrangement is ideal for surface layer measurements where observation periods can be conveniently broken up into hourly segments it is not well-suited for continuous, unattended operation on tall towers. A different configuration of the axes is needed. One such array, designed for use on the Boulder Atmospheric Observatory (BAO) 300-m tower, is shown in Fig. 6. The axes are orthogonal, with the vertical axes kept upwind of the other axes to optimize the vertical velocity measurement. The acceptable azimuth range for the vertical axis is clearly much larger in this array than in the array in Fig. 5; the unacceptable segment would be useless anyway because of shadowing caused by the tower. However, the horizontal wind measurements fare less well in this arrangement. An underestimation in the wind (Mitsuta, 1974) can be expected when the mean wind direction is along either axis. This error is corrected in the data processing routine by a first order approximation of the wind direction (see Section 8). Interference from supports for the crosswind axis is also minimized by vertically separating the horizontal paths. The main disadvantage for surface layer measurements is the large spatial separation between the horizontal axes and the vertical axis.

5. Some Consequences of Array Geometry

The dimensions of the array and the configuration of the acoustic paths have pronounced effect on the spectral responses at wavelengths (λ) approaching the size of the array.★ Line-averaging along the acoustic path attenuates wavelengths smaller than $2\pi d$. The shape of the transfer function varies with orientation of the path relative to the mean wind direction (Kaimal et al., 1968; Horst, 1973). In the streamwise direction the response drops as $\sin^2 x/x^2$, approaching zero at wavelength d. In the crosswind direction the roll-off is more gradual, with the half-power point at wavelength d. When measurements along the different axes are combined to resolve the wind fluctuations along the streamwise (x) and lateral (y) directions (Fig. 4), the response is more complex because of the spatial separation between the axes. Transfer functions for u, v, and w measured by the array of Fig. 5 are presented in Fig. 7. The term transfer function is used rather loosely here for the ratio of measured to true spectral density. Strictly speaking the curves are not transfer functions since they require an assumption of the spectral form for the velocity field. The curves were computed for the specific instance of $d = 0.2$ m and a horizontal separation distance, $s = 0.6\ d$, between the midpoints of the paths.

★Wavelength λ is approximated by $\overline{V}_H/n$ where $\overline{V}_H$ is mean horizontal wind vector and n is the cyclic frequency.

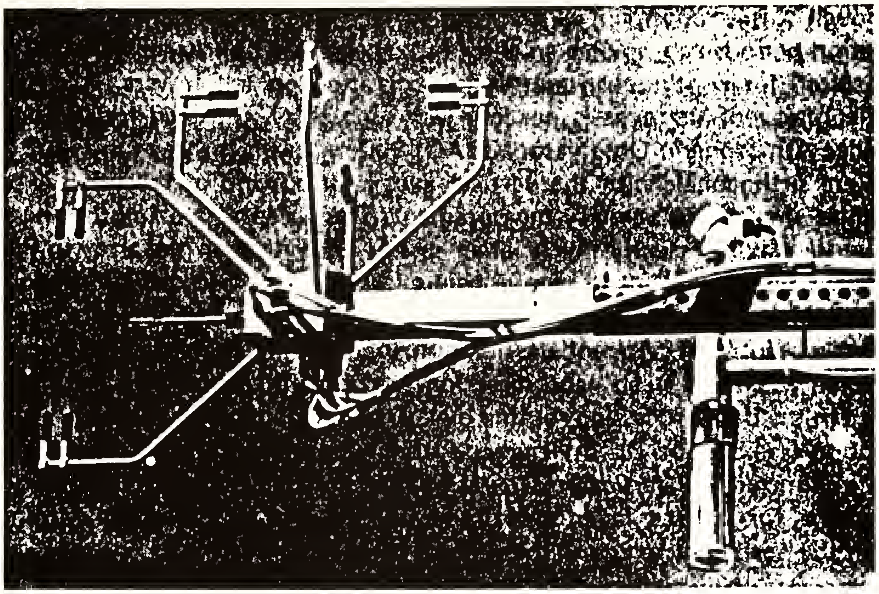

Fig. 6. Three-axis sonic anemometer array (Ball Bros. Model 125-197, 198) designed for fixed-boom operation uses an orthogonal configuration with 25-cm path length on each axis. Array provides wide azimuth coverage for vertical axis and for fast-response temperature sensor mounted in vertical probe. Horizontal velocity measurements need correction for blockage from transducers.

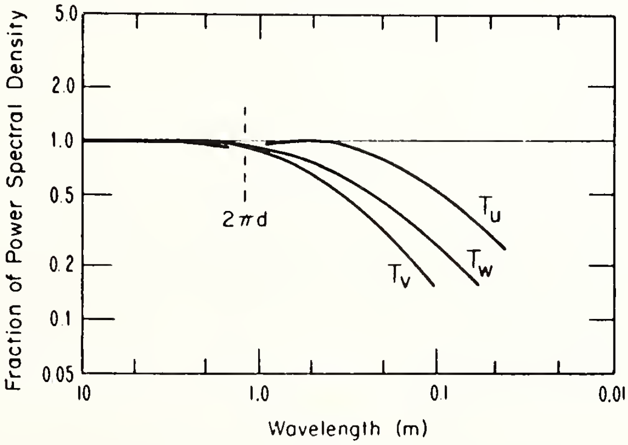

Fig. 7. Transfer functions for u, v, and w for three-axis array in Fig. 5. Distortions in spectral response become apparent at wavelengths smaller than 2πd (1.26 m for this array).

The effects of spatial separation merit further discussion. Distortions in the spectral response of u and v arise because wavelengths smaller than $2\pi s$ are not properly transformed by Eq. [9]. As the wavelength decreases, the Fourier components of velocity observed along A and B become increasingly uncorrelated. In the limit when no correlation exists, the u spectrum is overestimated by a factor of 2.5 and the v spectrum is underestimated by a factor of 0.625 (Kaimal et al., 1974).

Spatial separation between sensors (e.g. the w path and the fast-response temperature and humidity sensors) also introduces a limitation on the high-frequency response in flux cospectra. A diminishing correlation between the sensors at wavelengths smaller than 2π times the separation distance can be expected, which leads to the simple requirement that the separation distance be made no larger than the length of the w path in the sonic anemometer.

In the orthogonal array of Fig. 6, partial shadowing of the acoustic path by the transducers causes the velocity readings to be underestimated. Results of wind tunnel and atmospheric tests indicate a linear drop in response for angles between 0 and 75 deg relative to the acoustic path (see Fig. 6). For the path length-to-transducer diameter ratio of 25 appropriate to this array (heavy line in Fig. 8), the measured wind component $(V_d)_m$ can be approximated by

$$(V_d)_m = \begin{cases} V_d(0.87 + 0.13\,\theta/75), & \text{for } 0 \leqslant \theta \leqslant 75 \\ V_d & \text{for } 75 \leqslant \theta \leqslant 90 \end{cases} \qquad [10]$$

where

$$\theta = \tan^{-1} \frac{|V_n|}{|V_d|} \; . \qquad [11]$$

A first order approximation to the instantaneous angle θ using wind components measured along the two horizontal axes is found to be adequate for correcting the two wind components. With such a correction, the effect of transducer shadowing is hardly apparent in the mean wind profiles and in the second moments involving u and v.

Another type of error can result from small offsets in the array geometry and in the leveling of the array. The parameter most affected is the covariance of u and w, which represents the vertical momentum flux. Kaimal and Haugen (1969, 1971) have shown that the error can be very large in unstable air (typically 25 % for 1-deg tilt) and recommend a 0.1-deg accuracy in the mechanical

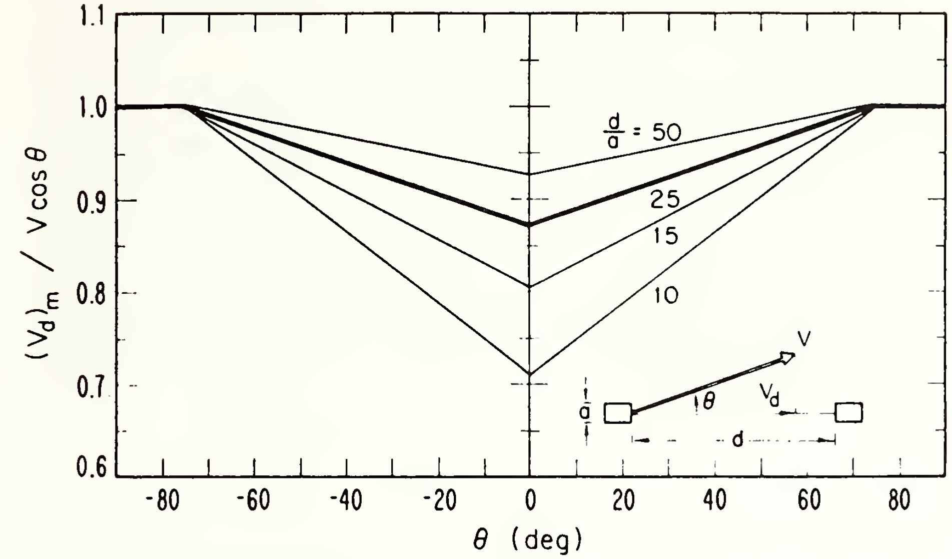

Fig. 8. Sonic anemometer response to wind component along acoustic path for various path length to transducer diameter ratios shown as a function of wind direction. Heavy line represents velocity error in the sonic anemometer of Fig. 6 (see Eq. [10]).

alingment of the probe and in the leveling. This requirement is stringent but worth pursuing for accuracy in the momentum flux measurement. Heat flux and variance measurements, on the other hand, are not as sensitive to alignment and tilt errors.

6. Sampling Rates and Run Lengths

The upper frequency limit dictated by the array dimensions determines the maximum sampling rate for sonic anemometer data. Allowing an additional octave at the high-frequency end for aliasing effects, this sampling rate n_s may be specified in terms of the path length and the mean horizontal wind vector (V_H) as

$$n_s = 2V_H/\pi d. \qquad [12]$$

For typical 5 to 6 ms^{-1} winds and a path length of 0.2 m the sampling requirement can be rounded off to 20 Hz. This restriction on bandwidth imposed by array size is not a serious limitation for most turbulence studies at heights above 4 m since the inertial subrange is usually well established at 10 Hz in that height range and no significant contributions to the turbulent fluxes are expected from higher frequencies.

The relation between observation height and high-frequency spectral behavior is highlighted in Fig. 9 by a line marking the frequency at which λ equals z, the height above ground. The spectra shown here are typical for velocity fluctuations over flat, unobstructed terrain. Their behavior is predictable for wavelengths $\lambda(\cong V_H/n)$ smaller than z/2. The −2/3 slope at the high-frequency (or short-wavelength) end corresponds to the Kolmogorov −5/3 power law predicted for a one-dimensional velocity spectrum in the inertial subrange. The 4/3 ratio between the transverse (v and w) and longitudinal (u) spectral intensities predicted for local isotropy is also apparent in that frequency range. Thus, with the spectral curves established down to at least an octave into the inertial subrange, their behavior through the rest of the inertial subrange can be obtained by simple extrapolation.

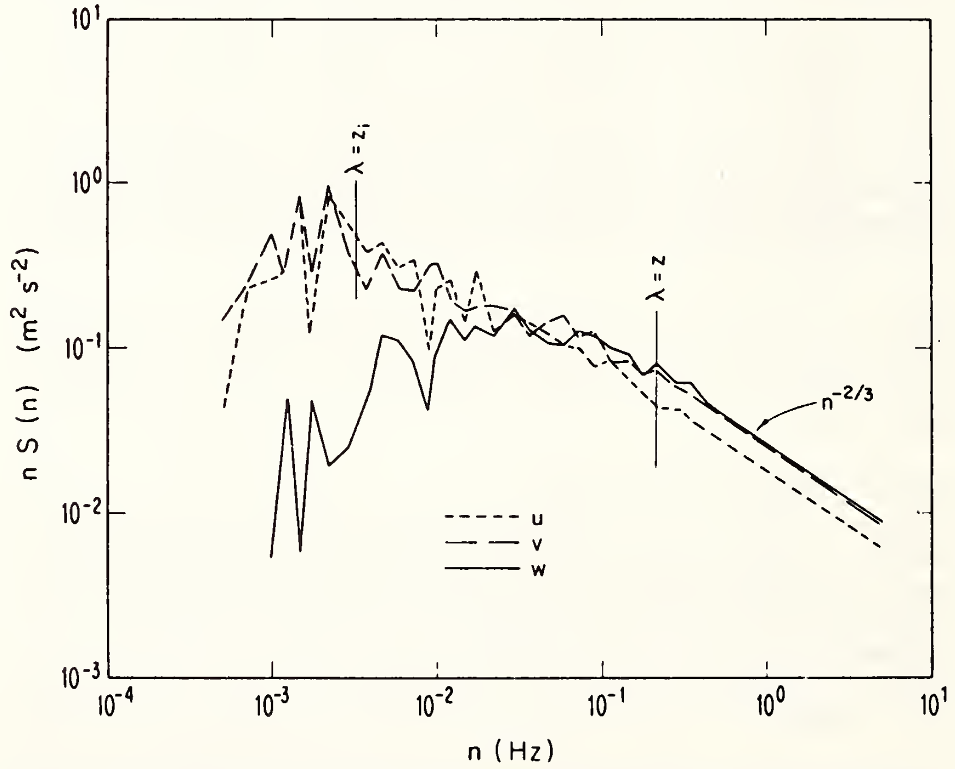

Fig. 9. Typical surface layer velocity spectra for unstable daytime conditions obtained with the sonic anemometer shown in Fig. 5 at z = 32 m. The high-frequency ends of spectra have been corrected for distortions introduced by the anemometer's spatial response and by aliasing. The boundary layer depth z_i *for this run was 2095 m.*

On the low-frequency side, the day-time w spectrum rolls off as n^{+1}, peaking at a wavelength roughly 5.9 times z (Kaimal et al., 1972) which suggests that in principle a height-dependent, low-frequency cutoff can be specified for w. This is not possible with u and v since they tend to scale with z_i, the convective boundary layer depth, rather than z. The wavelength at the peak corresponds to roughly $\lambda = 1.5z_i$ (Kaimal, 1978) as seen in Fig. 9. In contrast to w, the u and v spectra often show a tendency to rise again in response to the large-scale, two-dimensional fluctuations in the velocity field (not shown in figure). An optimum cutoff point for boundary layer studies would be the spectral minimum which occurs roughly a decade below the peak frequency. Record lengths of 1-hr duration provide spectral information down to approximately 0.0003 Hz, close to the expected u and v spectral minima. For most surface layer work the bandwidth offered by data collected at 20 Hz rate over 1-hr observational periods should prove adequate.

7. Concluding Remarks

The sonic anemometer with its rapid response, linear output and stable calibration has become a valuable tool for atmospheric research. It has provided high-quality turbulence data in a number of field experiments conducted during the last decade. A new three-axis configuration is currently being used for continuously monitoring the wind at eight levels on the Boulder Atmospheric Observatory's 300 m tower.

Because of its complexity and high cost, the sonic anemometer is likely to remain a research instrument. Attempts are being made to reduce cost and to simplify its operation. Even if these attempts are successful, the sonic anemometer has an inherent limitation which precludes its use in adverse weather conditions. The instrument fails to respond in rain, wet snow, and heavy fog. Formation of water drops on the transducer temporarily affects its operation. Thus the sonic anenometer's main contribution will be in fair-weather observations of atmospheric turbulence, where it is still the instrument of choice amoung boundary-layer physicists.

References

Bovsheverov, V.M. and Voronov, V.P., 1960 Acoustic anemometer. *Izv. Geophys. Series,* **6**, 882-885

Bovsheverov, V.M., Koprov, B.M., and Mordukhovich, M.I., 1973 Spatial correlation functions of velocity and temperature components in the surface layer of the atmosphere. *Izv. Atmos. Oceanic Phys.,* 9, 434-437

Friehe, C.A., 1976 Effects of sound speed fluctuations on sonic anemometer measurements. *J. Appl. Meteorol.,* **15**, 607-610

Gurvich, A.S., 1959 Acoustic microanemometer for investigation of the microstructure of turbulence. *Acoust. J.* (USSR), 5, 368-369

Horst, T.W., 1973 Spectral transfer functions for a three-component sonic anemometer. *J. Appl. Meteor.,* **12**, 1072-1075

Kaimal, J.C., 1969 Measurement of momentum and heat flux variations in the surface boundary layer. *Radio Sci.,* 4, 1147-1153

Kaimal, J.C., 1978 Horizontal velocity spectra in an unstable surface layer. *J. Atmos. Sci.,* 35, 18-24

Kaimal, J.C. and Businger, J.A., 1963 A continuous wave sonic anemometer-thermometer. *J. Appl. Meteorol.,* 2, 156-164

Kaimal, J.C. and Haugen, D.A., 1967 Characteristics of vertical velocity fluctuations observed on a 430-m tower. *Q.J.R. Meteorol. Soc.,* 93, 305-317

Kaimal, J.C. and Haugen, D.A., 1969 Some errors in the measurement of Reynolds stress. *J. Appl. Meteorol.,* 8, 460-462

Kaimal, J.C. and Haugen, D.A., 1971 Comments on "Minimizing the levelling error in Reynolds stress measurement by filtering". *J. Appl. Meteorol.,* **10**, 337-339

Kaimal, J.C., Wyngaard, J.C., and Haugen, D.A., 1968 Deriving power spectra from a three-component sonic anemometer. *J. Appl. Meteorol.,* 7, 827-837

Kaimal, J.C., Wyngaard, J.C., Izumi, Y., and Coté, O.R., 1972 Spectral characteristics of surface layer turbulence. *Q.J.R. Meteorol. Soc.,* **98**, 563-589

Kaimal, J.C., Newman, J.T., Bisberg, A. and Cole, K., 1974 An improved three-component sonic anemometer for investigation of atmospheric turbulence. *Flow – Its Measurement and Control in Science and Industry,* Vol. **1** (Instrum. Soc. Amer.), 349-359

Koprov, B.M. and Sokolov, D. Yu., 1973 Spatial correlation functions of velocity and temperature components in the surface layer of the atmosphere. *Izv, Atmos. Oceanic Phys.,* **9**, 178-182

Mitsuta, Y., 1966 Sonic anemometer-thermometer for general use. *J. Meteorol. Soc., Japan,* **44**, 12-24

Mitsuta, Y., 1974 Sonic anemometer-thermometer for atmospheric turbulence measurements *Flow – Its Measurement and Control in Science and Industry,* Vol. **1**, (Instrumen. Soc Amer.), 341-347

Scrase, F.J., 1930 Some characteristics of eddy motion in the atmosphere. Meteorological Office Geophysical Memoirs, No. 52. His Majesties Stationary Office, London, England

Suomi, V.E., 1957 Sonic Anemometer. *Exploring the Atmosphere's First Mile,* Vol. **1**, Pergamon, New York, 356-266.

Proceedings of the International Conference on Lasers '78, 40-47, Society of Photo-optical Instrumentation Engineers, Orlando, Florida, 11-15 December 1978.

APPLICATIONS OF LIDAR TO ATMOSPHERIC SENSING

Vernon E. Derr
National Oceanic and Atmospheric Administration
Environmental Research Laboratories
Wave Propagation Laboratory
Boulder, Colorado 80302

Abstract

Applications of lidar techniques to the study of atmospheric particles, and the use of particles as tracers are discussed. A comparison of radar and lidar for cloud studies is presented. The study of cloud processes, the detection, identification and tracing of particulate pollution, and the measurement of atmospheric vortices and wind by lidar are described.

Introduction

In 1962, Fiocco demonstrated backscatter of laser beams from atmospheric constituents. Since then lasers have been used to measure characteristics and motion of clouds and aerosols, the variation of refractive index, the concentration of gases, and meteorological variables such as wind velocity, temperature, and humidity profiles. Because such a wide range of applications can be examined only superficially in the space and time available, this paper is confined to applications of lidar to the sensing of atmospheric particles and to some techniques depending on particle backscatter. Important developments such as line-of-sight techniques, differential absorption or Raman scatter are not covered.

Specifically, the study of cloud development processes by lidar, the use of lidar combined with other sensors, applications of lidar to tracking of smoke-stack effluent, the identification of aerosols by lidar and other remote sensing techniques, and the use of CW Doppler lidar techniques will be considered. In addition, crucial problems of calibration and mathematical inversion techniques required for precise evaluation of atmospheric data will be briefly reviewed. First we consider the relative effectiveness, the differing roles, and the importance of combined uses of radar and lidar techniques.

Roles of Radar and Lidar in Cloud Studies

In the final analysis, a complete understanding of the comparative signal-to-noise ratio of a lidar and a radar system depends on the mission and specific system configurations. It is possible, however, to gain considerable insight into comparative performance by a nearly "system-free" analysis. This analysis depends on the target and medium characteristics, namely the backscatter coefficient β and the extinction coefficient β_{ext}. The analysis depends on the mission through the range, R, and the cloud thickness H. It is not possible to achieve a completely system-free analysis because the fundamental noise characteristics of detectors are frequency dependent.

Active electromagnetic remote sensors may detect rain, ice and water clouds, aerosols, turbulence (inhomogeneities in refractive index) and Rayleigh scatter from molecules. (We do not consider inelastic scatter such as Raman or fluorescence effects.) Table 1 lists approximate relative backscatter coefficients for ruby lidar and 1 cm radar. The coefficients for turbulence were calculated from the formula

$$\eta = 0.39\, C_n^{2} \lambda^{-1/3} \tag{1}$$

assuming $C_n^2 = 10^{-12}$ to $10^{-16} (m^{-2/3})$. The use of the formula at visible wavelengths overestimates turbulence because of the rapid falloff of turbulent energy at small scales. Turbulence contributes to optical beam wander (scintillations) but not to backscatter.

Table 1. Typical Backscatter Coefficients ($m^{-1}sr^{-1}$)

			Particles			Turbulence	Molecular Scatter (Total)
	Rain L	**Cont Cu**	C.3	Cirrus	Aerosols		
Lidar (.7μm)		2.9×10^{-2}	2.6×10^{-3}	4.6×10^{-3}	1×10^{-6}	10^{-35} (or less)	3.5×10^{-7}
Radar (1 cm)	2.7×10^{-5}	5.6×10^{-10}	1.2×10^{-13}	7×10^{-13}	1.3×10^{-15}	$(10^{-13}$ to $10^{-16})$*	$\simeq10^{-23}$

*Assume $C_n^2 = 10^{-12}$ to $10^{-16} m^{-2/3}$ perhaps greater in layers.

Rain L and Cloud C.3 are Deirmendjian models. Cont Cu is an abbreviation for continental cumulus.

The essential, or irreducible noise temperature, $T^e = h\nu/k$, where h is Planck's constant, k is Boltzmann's constant and ν is the radiation frequency. Actual (effective) noise temperatures may be much greater. The effective noise temperature $T_{eff} = T^e/Q$, where Q is the quantum efficiency. (At microwave frequencies, the noise characteristics are usually given by the noise figure.) The essential noise temperature for a 10 cm radar is 0.14 K, and for ruby lidar at 0.69 µm is 20732 K.

Combining the essential factors, a relative signal-to-noise ratio is defined as:

$$SNR = \frac{\beta e^{[-2\beta_{ext}(R-H)]}}{R^2 T_{eff}} \qquad (2)$$

This criterion of performance may be used to determine the relative signal-to-noise ratios of microwave and optical systems. The formula incorporates the assumption that the detector noise T_{eff} dominates all other noise sources; it is not applicable to background limited systems. We may make the comparison by determining a mission, from which the range, R, and the cloud depth H are determined, and by determining the appropriate backscatter and extinction coefficients for optical and microwave frequencies.

Extinction and radar backscatter coefficients, and effective temperatures are given in Table 2. The extinction and radar backscatter coefficients are given for the Deirmendjian cloud model C.1 to illustrate their very large range from microwave to ultraviolet wavelengths. The effective temperatures are chosen by assuming maser amplifiers are used from 0.10 to 0.0321 (m) wavelengths, traveling wave tubes are used from 0.124 to .002 m wavelengths and representative commercial detectors are available for wavelengths 1.2×10^{-5} to $.347 \times 10^{-6}$m.

Table 2. Backscatter Coefficients, Radar and Lidar

System	Wavelength (m)	T_{eff} (K)	β^*_{ext} (m^{-1})	β^* ($m^{-1} sr^{-1}$)
S-band radar	1×10^{-1}	34.8	1.3×10^{-7}	9.9×10^{-16}
X-band radar	3×10^{-2}	34.8	1.3×10^{-6}	1.2×10^{-13}
K-band radar	1×10^{-2}	600	1.2×10^{-5}	9.4×10^{-12}
CO_2 lidar	1×10^{-5}	2878	1.1×10^{-2}	2.4×10^{-4}
Ruby lidar	6.94×10^{-7}	518293	1.7×10^{-2}	1.1×10^{-2}
Ruby lidar (second harmonic)	3.47×10^{-7}	138211	1.7×10^{-2}	1.1×10^{-2}

*For Deirmendjian model cloud C.1.

The large noise temperature in the optical range of wavelengths is offset by the very large advantage (by fourteen orders of magnitude) of the radar backscatter coefficient. The effect of the extinction coefficient is to limit penetration. Table 3 illustrates the penetration depths of lidar and microwave radar in three different clouds.

Table 3. Penetration Depths (m)

	3-cm Radar	Ruby lidar
Continental Cumulus	9896	216
Cloud C.1	10589	408
Cloud C.3	(Very large)	2142

The penetration depth is defined as the greatest range within the cloud from which a signal-to-noise ratio of one is obtained, given a signal-to-noise ratio of 1000 at the nearest edge of the cloud. Clouds C.1 and C.3 are young clouds with relatively small droplets and continental cumulus is a well-developed cloud of high water content. Their characteristics are shown in Table 4 (Page 3).

The comparison of relative signal-to-noise ratio for 3 cm radar and .694 µm lidar is shown in Table 5 for the detection of a closest edge of a cloud. Clearly, for all cases except Rain L, the lidar has the greatest signal-to-noise ratio.

On the other hand, if we consider the problem of detecting a cloud parcel lying 1 km within a cloud, we see by Table 6 that the lidar has greater relative signal-to-noise ratio only for the lightest of clouds.

Table 4. Cloud Characteristics

Cloud Type	Density (kg/m^3)	Radius (μm)		
		Minimum	Maximum	Modal
C.3	0.4×10^{-5}	0.5	4.3	2.0
C.1	0.6×10^{-4}	0.03	12.3	4.0
Rain L	0.1×10^{-3}	4.0	1540.0	70.0
Cont. Cu.	0.3×10^{-3}	5.0	20.0	11.8

Table 5. Relative Signal-To-Noise Ratio (db)
(Cloud leading edge detection)

Cloud Type	3 cm Radar	Ruby Lidar
C.3	0	60
C.1	0	115
Rain L	0	-20
Cont. Cu.	0	60

Table 6. Relative Signal-To-Noise Ratio (db)
(Cloud Penetration)

Cloud Type	3 cm Radar	Ruby Lidar
C.3	-60	0
C.1	90	0
Rain L	150	0
Cont. Cu.	160	0

The results given above make precise a conclusion that is intuitively recognized: a simultaneous use of radar and lidar can extend our ability to study cloud growth from early formation to precipitation. Simultaneous observations by calibrated systems will allow estimates of drop-size distributions and the observation of droplet growth. If both instruments measure depolarization, glaciation processes can be studied from early cloud development to precipitation.

Applications of Lidar to the Study of Cloud Glaciation Processes

If the electromagnetic plane wave incident on a spherical particle is polarized, the wave scattered directly backward retains the same polarization. Non-spherical particles may produce changes of polarization in backscatter. A simple pair of detectors, one polarized in the same direction as the transmitted wave, and one accepting cross-polarized radiation, can reveal the presence of non-spherical particles in a cloud.

The process of glaciation is very important in cloud development. Although "warm rain" has been observed, almost all rain occurs because of ice formation and attendant processes. Studies have shown that the fractional depolarization is a reasonable guide to the fraction of the cloud water substance that is ice. However, even for clouds composed of spherical droplets, depolarization may occur if the density of droplets is large enough to cause appreciable multiple scatter. Because multiple scatter effects increase rapidly with density, it is important to determine when polarization measurements are affected. For a large class of clouds, it can be shown that an algorithm may be defined to distinguish cases in which depolarization is only shape-dependent from those in which multiple scatter plays a role.

To form this algorithm, we first observe that multiple scatter depends on the density of scatterers and the sample volume of the (pulsed) lidar system. The average diameter of a sample volume for which L is 1/2 the lidar pulse length, R the range to the sample volume, and θ = aperture angle is:

$$\left(\frac{\pi L R^2 \theta^2}{32}\right)^{1/3} \tag{3}$$

To keep in mind a specific example, we assume $L = 5$ m, $R = 300$ m, and $\theta = 4 \times 10^{-3}$ radians. For this representative case, the average diameter is 6.2 m.

When the extinction coefficient, β_{ext} is given the optical depth of the sample volume is defined as:

$$\tau = \int \beta_{ext}\, dz, \tag{4}$$

and is a function of the number and size of particles in the sample volume. The integral extends over the diameter of the sample volume. One optical depth is such that the sum of electromagnetic cross sections of the particles equals the cross section of the incident radiation beam. Statistically, of course, this means that in traversing the medium, 1/e of the energy is lost from the beam and the probability of a second scattering is appreciable. The criterion for the strength of multiple scatter is thus clearly dependent on the optical depth of the sample volume. (Higher order scatter may arise from energy leaving the sample volume, being reflected back in, and then reflected to the receiver. At least third order scattering is required.) A generally accepted value for the greatest permissible optical depth in the sample volume is $\tau = 0.3$ to avoid multiple scatter effects.

The sample volume is defined by characteristics of the lidar, but the optical depth requires a knowledge of the extinction coefficient. The extinction coefficient may be determined from the backscatter coefficient, measured by a calibrated lidar, only if the size distribution of the particles is known. However, the ratio of the coefficients β/β_{ext} is quite stable for a large class of clouds. Calculations for 28 different cloud distributions give an average value of 0.65 with a standard deviation of 0.27 for a wavelength of 0.7 μm. The radar backscatter coefficients for these clouds range from 1.5×10^{-7} to 0.14 ($m^{-1}sr^{-1}$) the β_{ext} ranges from 2.0×10^{-5} to 0.16. The densities range from 9.6×10^{-9} to 1.1×10^{-3} kg/m^{-3}, and the model radii of the distributions range from .05 to 27μm. Thus we may deduce approximately the extinction coefficient from the radar backscatter coefficient by the formula $\beta_{ext} = 1.54\beta$. The formula is applicable to all clouds except cirrus with very large particles (greater than 200 μm) and very young clouds with very small particles (less than .05 μm).

To restrict the sample volume diameter (6.2 m in our own example) to 0.3 optical depths, β_{ext} must be less than .048 (m^{-1}) or β must be less than .031 ($m^{-1}sr^{-1}$). Thus if β is less than .031 ($m^{-1}sr^{-1}$), we may assume significant depolarization in clouds is caused by nonsphericity. Note that a specific range (3000 m) is assumed. As the range increases, the sample diameter increases as $R^{2/3}$.

Two techniques may be used to reduce the depolarization caused by multiple scatter. The first is to decrease the angular aperture of the receiver. Practical limits of mounting stability and transmitter beam wander prevent apertures much less than 10^{-3}r. A second method is to use a rectangular field stop in the receiver to eliminate scatter from particles at angles other than those nearly 90° from the transmitter polarization vector. The technique requires a large signal-to-noise ratio, but clouds are large lidar targets and frequently permit sacrificing some of the signal.

Table 7 lists the scatter coefficients for three cloud types. We see that the lighter clouds have sufficiently low extinction that depolarization must be caused by ice formation. Fairweather cumulus, a rather dense, well-formed cloud, would show some depolarization from multiple scatter. In principle, the size of the effect can be estimated. In practice, the compensation for multiple scatter is difficult.

Table 7. Scatter Coefficients for Clouds

Cloud Type	Density (kg/m^3)	β_{ext} (m^{-1})	β ($m^{-1}sr^{-1}$)
Cont. Cu.	2.9×10^{-4}	3.2×10^{-2}	2.9×10^{-2}
Fairweather Cu.	1.1×10^{-3}	1.6×10^{-3}	1.1×10^{-1}
Deirmendjian C.3	3.8×10^{-6}	3.0×10^{-6}	2.6×10^{-3}

One of the principal uses of the measurement of depolarization of lidar signals is the study of glaciation in clouds. Figure 1 (page 5) shows glaciation in newly-formed summer cumulus clouds. The early glaciation in these clouds appears to be related to the presence of organic ice nuclei active at higher temperatures, -5° to 0°, in the summer air of the Rocky Mountain Region. Winter clouds may remain liquid at substantially lower temperatures. The precipitation processes in the two instances may be substantially different; as different as summer thunder storms and slowly developing winter snowstorms. Lidar is essential for the study of early clouds. As the clouds develop, radar is required to achieve the necessary penetration.

Identification of Aerosols

Depolarization measurement of lidar signals is one of the techniques used in remote identification of aerosols, but this difficult problem requires further measurements. In its most general form, the identification of atmospheric aerosols by lidar backscatter is impossible. A complex, arbitrary collection of aerosols with varied indices of refraction, size, shape and concentration requires many parameters to describe the sample and at least as many independent measurements to solve for the unknown factors. If, however, the parameters which must be measured to describe the sample are limited by prior knowledge or if

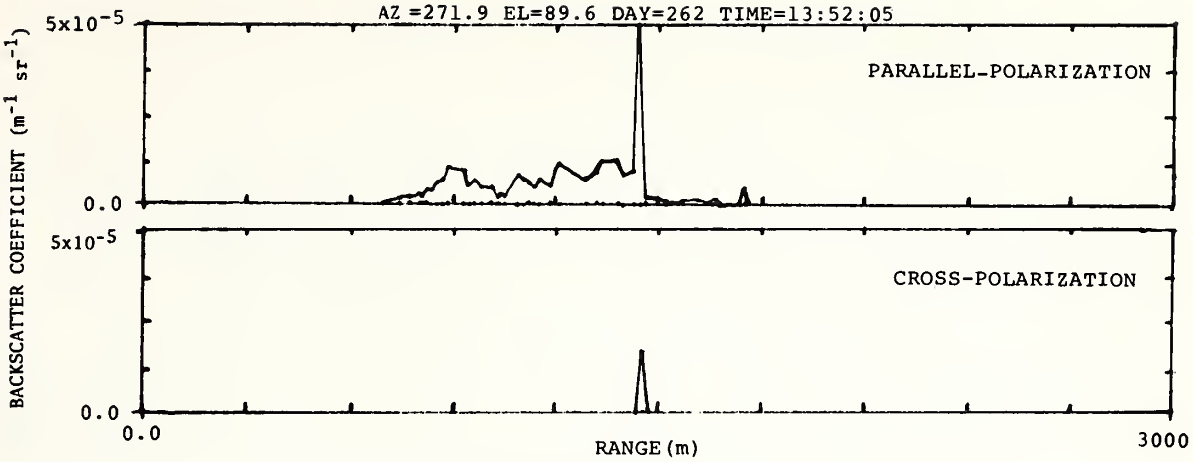

Fig. 1. Unpolarized and polarized lidar backscatter signals from a cloud.

the observer requires only an incomplete description, then, a smaller number of observations may provide the desired information. Figure 2 shows a lidar signal which permits discriminating between nearly risen strip mine dust and the plume of a large power plant by a simple depolarization method. Experience in tracing smoke-stack plumes, invisible to the eye, has shown the utility of this identification in an otherwise clear atmosphere. Figure 3 shows the ability of the lidar to trace a plume for considerable distance downwind. Dust plumes are eliminated from the data.

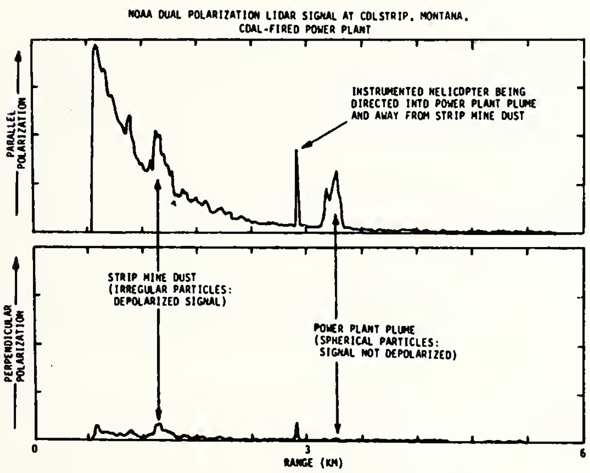

Fig. 2. Unpolarized and polarized lidar backscatter signals from dust and a power plant smoke-stack plume.

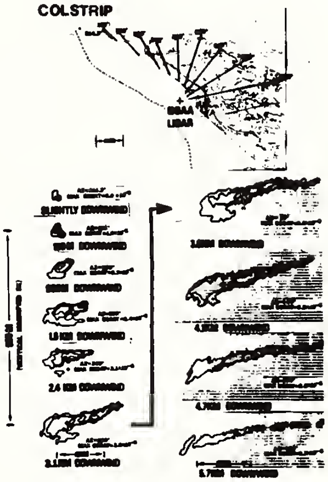

Fig. 3. Cross sections of a plume from a power plant smoke-stack.

Identification of more complicated targets requires additional data. Let us consider the specific problem of determining size distributions of water cloud droplets. Clouds may be examined by polarized lidar and identified as water if they exhibit no depolarization. It has been shown that measurement of the scattering coefficient at many well-separated scattering angles gives a good estimate of size distribution. Angle measurements require either movable lidar systems or homogeneous samples. These requirements are incompatible with the study of rapidly moving and growing clouds, although angle scatter has been successfully used to study aerosols. Thus it is necessary to consider what can be done to determine size distributions solely by the use of backscatter information.

The limitation to backscatter requires that we vary parameters that are affected by particle sizes. The backscatter coefficient of a spherical particle is completely specified by the complex index of refraction and the radius of the particle, and by the incident wavelength of steady state illumination. Only the wavelength of the radiation is at the control of the experimenter and the characteristics of the medium must be deduced from the backscatter coefficients at a number of wavelengths.

The wavelengths chosen for interrogating the medium must be chosen in accordance with three conditions. The first is the wavelengths must span the radii in the significant parts of the distribution. Secondly, the wavelengths must be sufficiently different that the backscatter signals are statistically independent, that is, uncorrelated. Third, they must be sufficiently numerous to determine the parameters of the distribution. When a simple distribution such as the two-parameter Marshall-Palmer, or four-parameter Deirmendjian distribution may be assumed (based on a climatology), the number of wavelengths may be chosen appropriately. To probe an entirely unknown distribution of many modes requires a corresponding expansion of the number of wavelengths.

It is relatively easy to use two wavelengths simultaneously from a powerful ruby lidar by frequency doubling. Unless filtered, the ultraviolet wavelength (.374 μm) and the red wavelength (.694 μm) are transmitted simultaneously. In spite of the complications of complex samples, many atmospheric measurements can be accomplished simply. Table 8 shows that the two wavelengths given above discriminate between clear air, clouds and smoke-stack plumes.

Table 8. Dual Wavelength Measurements, Colstrip, Montana
(Preliminary Results)

	Relative Scattering Cross Section		
Scatterer	UV	Red	UV/Red Ratio
Clear Air (23000 Ft MSL)	16.5	1.03	16.0 (By Definition)
Clear Air (1000 Ft AGL)	29.0	3.18	9.1
Cloud (29000 Ft MSL	47.4	41.3	1.1
Cooling Tower Condensation	4840	2000	2.4
Plume (At Stack)	32.8	2.12	15.5
Plume (Downwind	3350	252	13.3

Because of their large range of radii, clouds are the most difficult atmospheric aerosols to measure. To obtain a drop-size distribution by backscatter requires at least four wavelengths. A near optimum choice, determined by mathematical inversion studies, is the set: 0.374 μm, 0.694 μm, 10.6 μm, and 1 mm. In practice, a 1 cm radar is used rather than 1 mm. Recent observations, comparing in-situ measurements with backscatter at 0.374 μm, 0.694 μm, and 1.24 cm, are encouraging, but show the need for 10.6 μm radiation to discriminate drop-sizes between ten and several hundred micrometers.

Continuous Wave Doppler Techniques

Studies of atmospheric motion have been made with a CW CO_2 Doppler lidar. The characteristics of the lidar are given in Table 9.

The lidar system depends on aerosols as tracers of air motion to provide the Doppler shifted backscattered signal.

Because of the poor range resolution of this system, it is best employed on concentrated targets. The range resolution is achieved by focusing, and rapidly deteriorates with range. Objects readily distinguished from the ambient air or background, such as dust devils, waterspouts, or smoke-stack plumes are natural targets of study. The high angular resolution permits scanning across an atmospheric vortex and obtaining velocity profiles as seen in Figure 4. This figure shows the velocity profile of a waterspout measured as the airborne lidar passed in steady horizontal flight past the vortex. Each curve is a sweep of the frequency analyzer, at the indicated distance from the center of the vortex. The curves indicate minimal velocity, generally, in the center of the vortex. The width of the velocity distribution is a measure of the turbulence in the waterspout. The difference of the peak velocities of two adjacent traces are a measure of the shear. (Of course, only motion parallel to the beam is measured.) The double peaks indicate shears that can be interpreted as nested sheaths. Visual observations have been made of the sheath structure of waterspouts.

Table 9. Characteristics of a CW CO_2 Doppler Lidar

Range	5 Km	Velocity range	0-200 ms^{-1}
Range resolution	10 m at 100 m	Velocity resolution	3 cm s^{-1}
Angle resolution	0.2 mr	Laser power	5 W

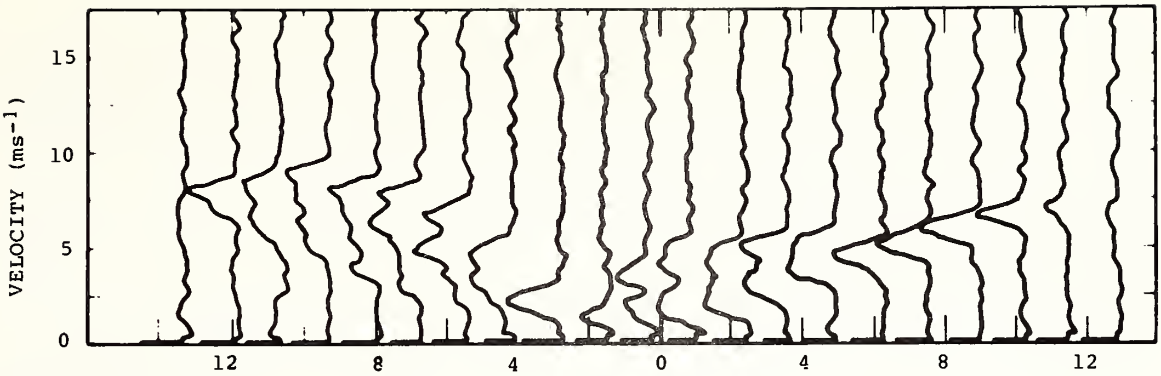

Fig. 4. Profile of vortex velocity across a waterspout.

These Doppler lidar techniques have also been successfully applied to measure boundary layer wind shear to ranges of a kilometer, vertical velocities of convective cells, wind profiles to a range of 1 km, and building effects on wind driven stack effluent. The latter measurements indicate important problems in the design of exhaust vents in nuclear power plants to avoid ingress of exhausted air through intake vents under variable wind conditions.

Perhaps the greatest significance of the CW and pulse Doppler lidar devices now in existence is the impetus given, because of their success, to major developments in satellite-borne Doppler lidar. The feasibility of measurement of wind profiles from satellites is now well-established. If the benefits are worth the cost, such devices can be built.

Inversion Techniques

A fundamental problem in atmospheric remote sensing is the determination of characteristics of the medium by analysis of signals from it. Mathematical inversion, the technique of recovering characteristics from emitted or scatter signals, has many forms. One of the simplest, and most effective, is to graph the signals and choose from the possible set of functions describing the medium, those which fit best. More sophisticated techniques, such as Phillips-Twomey or Backus-Gilbert techniques, may be used if the quality of the data permits. One of the major problems in lidar data analysis for size distributions is to find a simple technique without the complications of the highly mathematical methods requiring extensive computer time that can be employed to determine a few parameters of the size distribution without requiring recovery of the entire function.

The Backus-Gilbert technique is perhaps the easiest to convert to recover the mean and width of the distribution curve. The measured backscatter coefficients g_i, where i = 1,n, may be expressed (excluding noise) as:

$$g_i = \int_a^b W_i(r)f(r)dr \qquad (5)$$

where f(r) is the required size distribution to be recovered from the measurements, and $W_i(r)$ is the backscatter coefficient (from Mie theory) as a function of r. The subscript i refers to the set of parameters varied by the experimenter, say wavelengths of scattering angles. In the usual form of the theory, the sum:

$$\sum_i a_i g_i = \int_a^b \sum_i a_i W_i f(r)dr \qquad (6)$$

is formed and the coefficients are chosen so that $\Sigma a_i W_i(r)$ forms an approximate delta function that yields f(r). However, we may choose[1] the coefficients so that $\sum_i a_i W_i(r)$ is approximately r (or r^2), and thus recover moments of the distribution. Because data is usually insufficient to warrant extraction of complete functions, it is imperative that mathematical techniques be developed to determine optimally a few important characteristics of the target.

Calibration

The use of many wavelengths imposes a major burden of calibration on the experimenter. Photometric and power measurement methods differ at ultraviolet, visible, infrared and microwave frequencies and intercomparisons are very difficult. Perhaps the best method is to use a calibrated target and face the problems of evaluating the target on the basis of laboratory measurements or by mathematical calculation as in the case of a metallic spherical target in the microwave region.

Great care must be taken to ensure that detectors are operating in a linear dynamic region and that optical alignment is maintained. A significant portion of the effort in remote sensing is in calibration procedures.

Conclusions

The field of optical remote sensing is extraordinarily rich in potential applications in atmospheric science, operations, and services. In those portions of the spectrum where transmission is not severely limited, in the range from ultraviolet through infrared, radiation interacts with molecules and particles and is affected by inhomogeneities. Each of these interactions is an opportunity to identify constituents and measure important atmospheric parameters. In addition to molecular and particulate absorption and scatter, the motion of the particles is detected by Doppler shifts, and the resulting spectral shifts and broadening may be interpreted as wind velocity and related to local temperature. Thus, atmospheric parameters such as wind velocity, temperature and humidity can be measured with lidar techniques. Gases and particles can be identified and concentrations measured. Important weather processes such as cloud development can be explored and parameters important in climate prediction may be measured.

In spite of present success and clear potential, applications of lidar to atmospheric measurements develop slowly. One reason for this is a fundamental limitation of optical lidar in turbid media. Because of the strong interactions with the medium which account for the sensitivity of the technique, the extinction coefficients are comparatively large, preventing a full "all-weather" capability. A second limitation is caused by the slowness of laser development. The comparison with radar development is useful. Before large defense requirements financed the development of radars, transmitters and components, advanced radar techniques were largely unrealized. Similarly, advancing laser development will permit realization of much of the present potential. Many applications are limited by inability to find laser transmitters meeting all requirements of power, tunability, coherence and modulation characteristics. (Recent developments in metal lasers, chemical lasers, excimer lasers, and narrow-line dye lasers give promise of removing some of these barriers.) For example, the development of a laser with the power of a ruby laser, but sufficiently coherent for Doppler techniques, at visible or u.v. wavelengths, would permit wind and temperature profile measurement in the clear air, eliminating the need for tracer particles.

The field of lidar atmospheric sensing has gone through the maturing stages of optimism, frustration, disillusion, realism and renewed expectations. One of the most important signs of this deepening understanding is the tendency to improve atmospheric remote sensing by appropriate synthesis with other remote sensors such as radar, radiometry and solar photometry. No technique provides all the data needed on atmospheric constituents. The insularity of the technique developer results from focusing on his challenging opportunity. Only by appropriate combinations of techniques can we perform the atmospheric measurements required.

In addition to the requirement for measuring many parameters by multiple remote sensors is the need for intercomparison and calibration of remote sensors. In many cases, the proof of validity of remote sensors depends on intercomparison of remote sensors, rather than on in-situ instruments, because of differences in sample volumes, averaging times and parameter measured.

Journal of Applied Meterology, 17: 1476-1481, 1978.

A Feasibility Study of Identifying Weather by Laser Forward Scattering

K. B. Earnshaw, Ting-i Wang, R. S. Lawrence and R. G. Greunke

NOAA/ERL Wave Propagation Laboratory, Boulder, CO 80302

(Manuscript received 10 April 1978, in final form 2 July 1978)

ABSTRACT

The possibility of identifying weather through the observation of forward scatter of a laser beam has been investigated. Preliminary observations with a prototype instrument suggest that it is possible to distinguish clear air, rain, snow, hail and fog using laser weather identification. After additional measurements are made in various weather conditions, it should be practical to design a simple automatic instrument to provide such information.

---

1. Introduction

Techniques for identifying weather have traditionally relied on human judgment. In recent years devices have been introduced to make automatic weather observations but their ability to identify weather is quite limited. For example, most of the automatic devices can only measure the total water content of the precipitation, and are unable to identify the type of precipitation such as rain, snow or hail without the help of human observers. Recent efforts devoted to the effects of wind (Lawrence *et al.*, 1972; Clifford *et al.*, 1975, Ochs *et al.*, 1976) and precipitation (Hogg, 1964; Chu and Hogg, 1968; Atlas, 1953; Wilson and Penzias, 1966; Atlas and Ubrich, 1974; Kurnick *et al.*, 1960; Arnulf and Bricard, 1957; Wang and Clifford, 1975; Wang *et al.*, 1977, 1978; Wang and Earnshaw, 1977; Derr *et al.*, 1974) on optical and infrared wave transmissions through the atmosphere suggest that optical identification of weather may provide an inexpensive and reliable method for monitoring weather conditions, making possible more complete remote weather sensing at automatic unmanned weather stations.

When a visible or infrared light beam passes through an irregular medium, the irregulatities in the medium produce changes in both the phase and the intensity (or irradiance) of the wave front. This phenomenon has long been known as "scintillation." The twinkling of stars is a familiar example. Different weather conditions produce different signatures of the detected scintillations. Here we discuss the use of weather-induced scintillations to identify, for example, wind, rain, hail and snow. Either phase or irradiance scintillations might be used but phase measurements at optical wavelengths are more difficult than irradiance measurements. We discuss only the use of irradiance fluctuations. In clear air, turbulence combined with temperature gradients causes scintillations of a projected optical beam. The scintillations, which result from variations of refractive index in the air, are similar to the irregular moving patterns on the bottom of a swimming pool in direct sunlight. The turbulence scintillations are always present but often decrease during extended periods of rain or snow. A principal challenge of laser weather identification is to identify the weather-induced signals, usually small in amplitude, in the presence of the larger turbulence-scintillation signals.

A distinctive characteristic of precipitation is that the particles introduce finely structured interference patterns (Wang and Clifford, 1975; Wang *et al.*, 1977, 1978; Wang and Earnshaw, 1977) that are moving downward through the projected laser beam. These moving patterns suggest that weather can be identified by measuring the speed of pattern movement, and by observing the increase in high-frequency components caused by the fine interference patterns as they sweep past a light detector. We have observations to indicate that the terminal velocities can be measured optically, and can be used to identify separately rain, snow and hail. In fact, even the simpler measurement of the frequency spectrum of the scintillation signals may permit separate identification of snow, rain and clear-air turbulence. Raindrops are several thousand times larger than the wavelength of light so their forward-scattering angle is only a few milliradians. By contrast, fog particles are comparable in size to the optical wavelength, so light is forward-scattered to relatively large angles of several degrees. The large scattering angle and the high number density of particles combine to average out individual scintillations, producing attenuation and off-axis forward-scattering signals. Measurement of attenuation and off-beam forward scatter are straightforward optical methods for detecting fog.

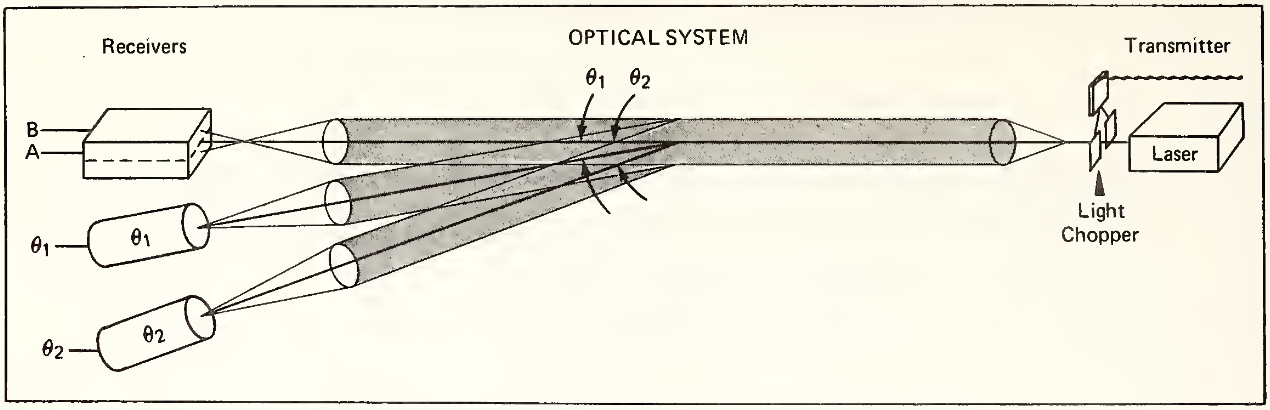

Fig. 1. Schematic diagram of the prototype laser weather identifier.

2. The prototype laser weather identifier

We built an optical system to detect the scintillations in a projected laser beam and to measure the light scattered from the beam at two forward-scattering angles. A chopper-type light modulator in the optical transmitter permits sensitive detection of light in the forward-scatter detectors when the beam is strongly attenuated by fog or heavy precipitation. Fig. 1 is a schematic diagram of the optical system. An earlier prototype instrument has been described in detail by Earnshaw and Keebaugh (1977). The laser transmitter simply collimates light from the laser beam and projects it onto one of the receiving telescopes. The modulator chops the laser beam prior to beam expansion, and may be switched on or off at the signal processing chasis. Fig. 2 is a photograph of the transmitter.

The receiver system consists of three independently mounted detecting telescopes. The scintillation-measuring telescope is aligned with the transmitted laser beam and is apertured by two narrow horizontal slits that are spaced 2 cm apart vertically. Light from the slits is detected by a dual-diode photodetector placed slightly behind the focus of the telescope objective lens. The signals from the upper and lower photo-detectors, designated A and B, respectively, are amplified and transmitted to the signal-processing circuits. The two off-axis forward-scatter telescopes detect light within 0.06° conical volumes. The telescope axes are aimed at the midpoint of the laser beam and are set to detect the forward-scatter light at angles of approximately 0.5° and 1°. The detected forward-scatter light signals, designated θ_1 and θ_2, are amplified and transmitted to the signal-processing circuits. Fig. 3 is a photograph of the optical receiver. The A and B signals from the

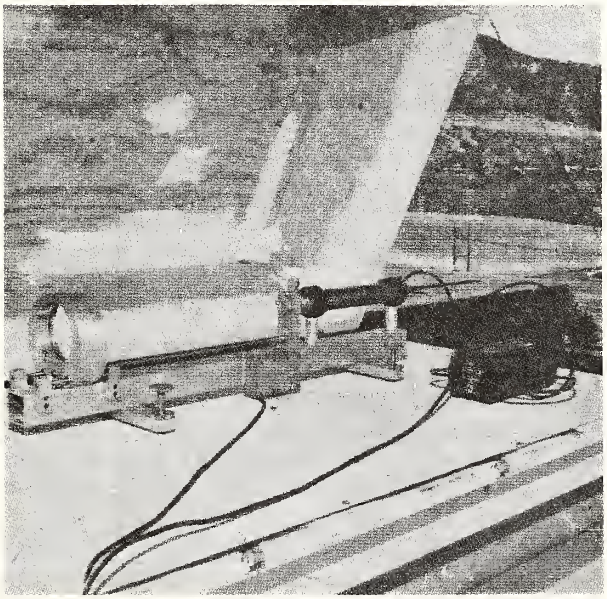

Fig. 2. The laser transmitter.

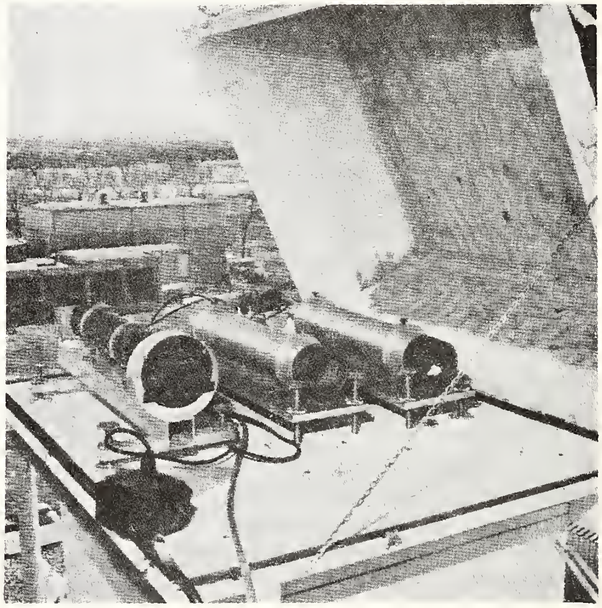

Fig. 3. The three optical-detecting telescopes of the receiver system. The one at left is aimed to detect the direct beam through two horizontal entrance slits. The two other telescopes are off-axis detectors.

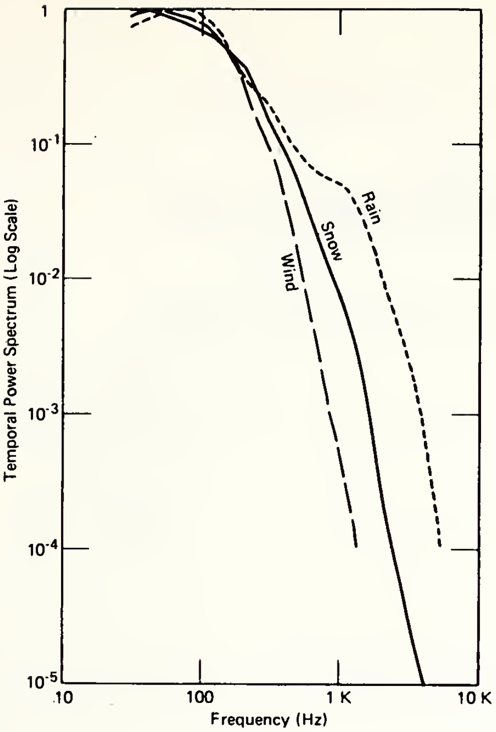

FIG. 4. Temporal power spectra of rain-, snow- and wind-induced scintillation detected by a horizontal line detector on a 50 m line-of-sight path.

upper and lower slit apertures are processed in a correlator to obtain the time-lagged covariance and, from it the terminal velocity distribution of falling particles (Wang *et al.*, 1977; Wang and Earnshaw, 1977). The B signal is also used to analyze the spectrum of the scintillations by selecting six frequency bands (0∼200, 200∼500, 500∼1000, 1000∼2000, 2000∼4000, 4000∼10000 kHz). As an option, the beam can be modulated by a 400 Hz chopper. The B signal and the two off-axis detected signals (θ_1 and θ_2) are amplified by 400 Hz narrow-band amplifier filters and converted to dc signals. All outputs are slowly varying voltages suitable for low-speed chart recording.

3. Results and interpretations

The instrument was used during the summer and fall of 1976 in Boulder, Colorado. Unprocessed signals from rain, hail, snow, fog and turbulence-induced scintaillations were detected and recorded on an audio stereo tape recorder. These data were later replayed through the processing electronics. Because of the uneventful weather of Colorado, we could not obtain enough data for convincing statistical analysis, but our measurements do provide enough samples to encourage us to continue to pursue this approach.

Turbulence, combined with temperature gradients, causes scintillation of a projected optical beam passing through clear air. If the beam is observed by a thin horizontal line detector, the typical spectrum (labeled "wind" in Fig. 4) of atmospheric turbulence-induced optical scintillation signals observed over a path length of 50 m shows large signals at low frequencies with rapidly decreasing amplitudes at higher frequencies. This frequency spectrum is typical for most clear weather, though increased wind speed shifts the spectrum to somewhat higher frequencies. Methods for using the optical scintillations to make quantitative path-averaged crosswind velocity measurements are available at the present time (Lawrence *et al.*, 1972; Clifford *et al.*, 1975; Ochs *et al.*, 1976).

Precipitation-induced scintillation has more high-frequency components than that induced by turbulence

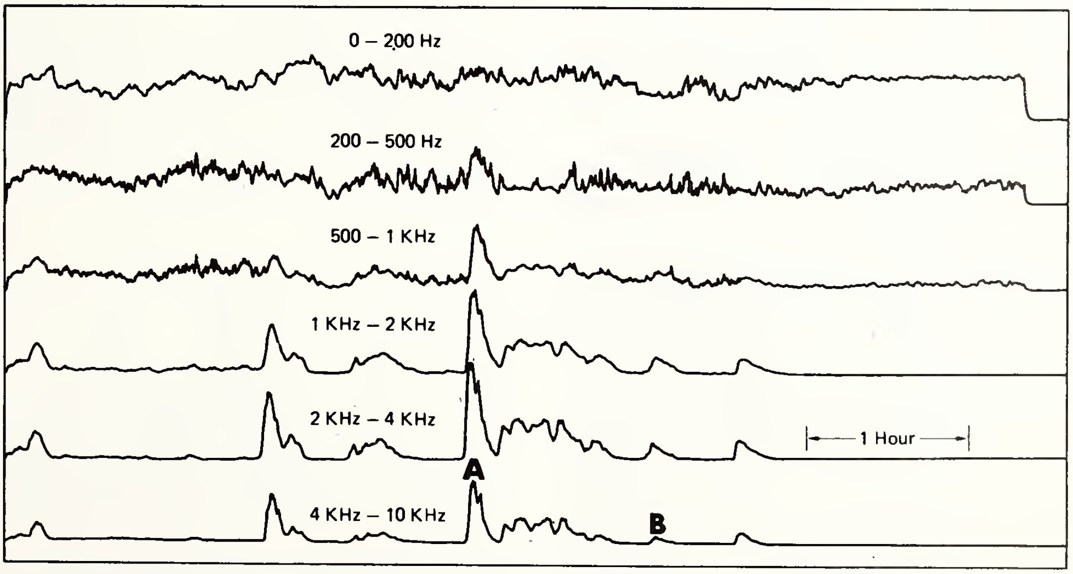

FIG. 5. Sample six-band analyzer recording of rain-induced scintillation, using a horizontal line detector and a 50 m path length. Signals in the three highest frequency bands are produced by rain.

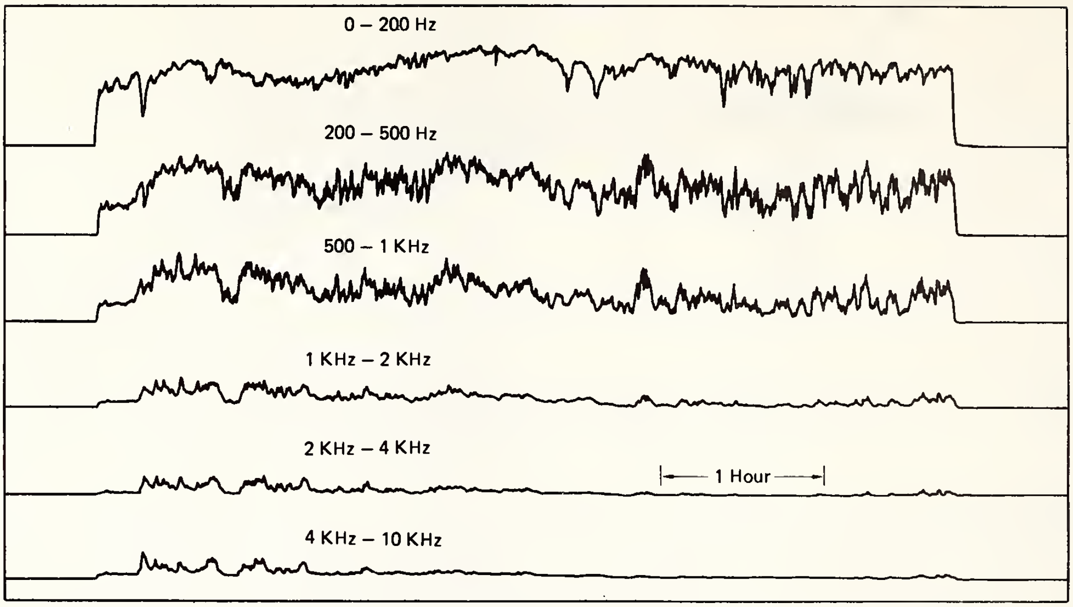

Fig. 6. As in Fig. 5 except for snow-induced scintillation. Signals in the three highest frequency bands are produced by snow. Compared to rain (Fig. 5), snow signals are stronger in band 4 than in band 5.

(Wang and Clifford, 1975; Wang, *et al.*, 1978). Typical temporal power spectra of rain- and snow-induced irradiance scintillation observed with a horizontal line detector appear in Fig. 4. Rain-induced scintillations have substantial frequency components above 2 kHz; for snow the scintillations are usually below 2 kHz and for turbulence, below 1 kHz. Figs. 5 and 6 show sample results from the six-band analyzer in the presence of rain and snow, respectively. The gains of the six bands are arbitrarily set, but they remain fixed for comparison between the two figures. The low-frequency signal of band 1 indicates the strength of turbulence-induced scintillations and very little effect of precipitation appears in this band. Bands 2 and 3 respond to both turbulence (wind) and precipitation. The three upper frequency bands respond for this storm to precipitation only, and we found that the signal in band 6 is sensitive to precipitation. For example, at Point B in Fig. 5, the rain rate was about 0.1 mm h^{-1}; at point A, it was about 7.5 mm h^{-1}. It appears that, to distinguish rain from snow, the ratio of band 4 to band 5 can be used whenever band 6 indicates that some kind of precipitation is present, though additional observations are needed to see if such discrimination is invariably successful. Although the spectrum seems to be able to discriminate precipitation from clear air, strong wind might occasionally produce enough high-frequency components to be comparable to snow-induced scintillation. The reliability of identifying precipitation by spectrum analysis must still be assessed by collecting more weather data in various locations and seasons.

A more reliable method for identifying precipitation involves the fact that particles are falling with noticeable vertical speed. We have demonstrated a technique (Wang *et al.*, 1977; Wang and Earnshaw, 1977) for measuring the path-averaged terminal velocity distribution of raindrops with two horizontally oriented, vertically spaced line detectors. The technique measures accurately the path-averaged rain rate and the drop-size distribution. The same technique can be used to measure the fall velocity of snow or hail. Typical path-averaged velocity distributions of snow, rain and hail appear in Fig. 7, though the values may vary in storms having different hail or drop sizes. The terminal velocity of raindrops usually ranges from 3 to 8 m s^{-1}. For snow, it is usually less than 2 m s^{-1} and for hail, greater than 8 m s^{-1}. Thus, with only occasional ambiguity, the measured terminal velocities can be used to identify separately rain, snow and hail. For

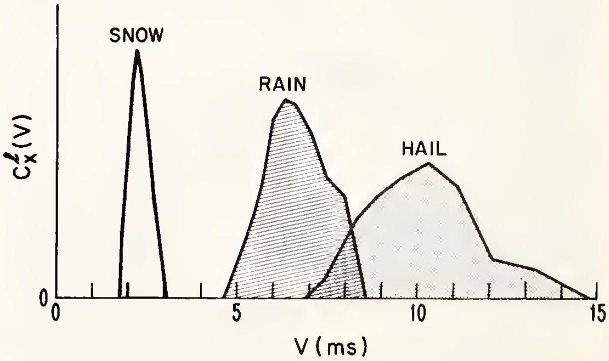

Fig. 7. The optically measured, path-averaged (pathlength, 200 m) terminal velocities of snow, rain and hail. Each curve represents only one 40 s average of a specific storm.

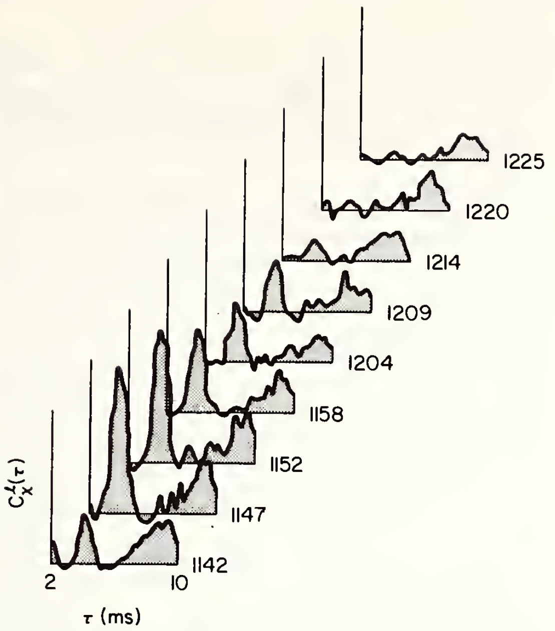

FIG. 8. The time-lagged covariance functions of the signals detected by two vertically separated line detectors with a separation of 4 cm on a 200 m path at Table Mountain during a mixture of rain and hail on 23 June 1976.

example, a bimodal velocity distribution was detected on 23 June 1976 during a mixture of rain and hail. The time-lagged covariance functions, each averaged over 5 min and taken with a slit spacing of 4 cm, are shown in Fig. 8. The peak at 4 ms contributed by hail-induced scintillations corresponds to a terminal velocity of 10 m s^{-1}. The 9 ms peak is caused by raindrops with terminal velocity of 4.5 m s^{-1}. Near the end of the storm the hail disappeared while small raindrops were still falling.

In fog the relatively large scattering angles and the high number density of particles combine to average out individual scintillations, producing only extinction of light in a directly received beam. Measurement of this extinction is a straightforward optical method for detecting fog, through it should also be practical to use off-beam forward scattering. Significant light scattering by a particle of diameter d larger than the wavelength λ of the light occurs at all scattering angles less than about λ/d rad. For raindrops with $d \approx 2$ mm, the scattering angles for optical wavelengths extend to about 3×10^{-4} rad, while fog particles with $d \approx 6$ μm produce scattering angles as great as about 0.1 rad. Thus an off-beam detector arranged to detect the forward scattering at about 1° (actually 0.64° was used) will be sensitive to particles <20 μm (e.g., fog, haze, dust and smoke) and insensitive to larger particles (e.g., rain, snow and hail). To discriminate against the background light, the laser was modulated by a 400 Hz chopper and a narrow-band 400 Hz filter was used to process the received signals. Fig. 9 shows measurements of direct transmission and scattered light during a very light fog. The upper trace is the transmittance and the lower trace the off-axis scattering. Because the fog was extremely light, no loss of transmittance was detected on the 50 m path (the small dips shown in the upper diagram were caused by manual beam blocking) but the off-axis signal clearly showed the presence of fog. The effect of a heavier fog is shown in Fig. 10. Here the agreement between the attenuation and the off-axis signal is good. The slow drift of the transmittance trace was caused by the beam wandering as a result of a change in vertical temperature gradient of the atmosphere. The off-axis signal is less affected by beam wandering and is more sensitive to light fog, so we believe this is the more reliable method for identifying the presence of fog.

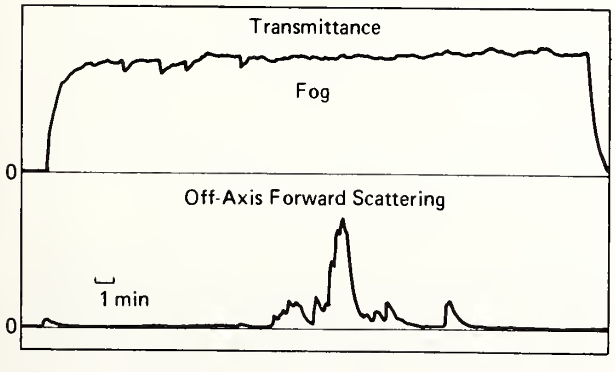

FIG. 9. Transmittance and off-axis forward-scattering measurements during a light fog. (The small dips shown in the upper diagram were caused by manual beam blocking.)

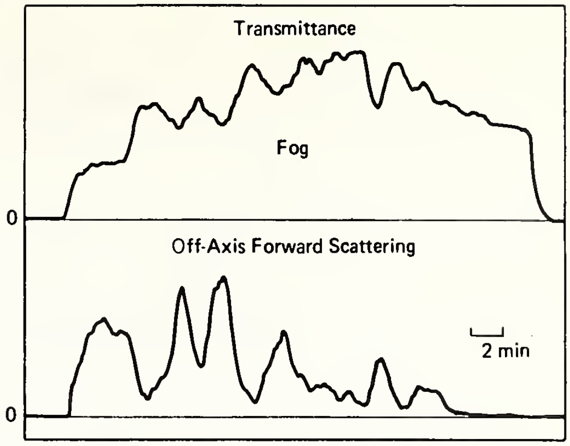

FIG. 10. Transmittance and off-axis forward-scattering measurements during a heavy fog. (The slow change in the transmittance was caused by the beam wandering as a result of a change in vertical temperature gradient of the atmosphere.)

4. Summary

It appears that signals from a laser forward-scattering system can indeed identify different types of weather. Preliminary results show that clear air (wind), snow, rain and hail can be identified by the unmodulated forward-scattered signal. With the help of a modulator and an off-axis receiver, fog and haze can be detected. Because of the large capture volume of this system, the time resolution of the observations is very short, typically 20 s.

Any remaining ambiguity in the identification of weather could be removed by adding to the system additional information channels. The detected signals at the rainbow angle (~138°) can be used to positively identify raindrops. This would discriminate rain from fast-falling snow pellets. Depolarization measurements can surely be helpful in separating spherical from irregular particles (in the single-scattering regime) and may occasionally be necessary to separate rain from snow or hail. We have made no attempt to build an instrument that will serve as an automatic weather identifier because optimum design of such a system requires extensive data collection in various types of weather. We expect that a reliable identifier can be developed using the results of measurements like those we have described.

Acknowledgments. This work was partially supported by the Air Force Geophysics Laboratory at Bedford, MA, and the Test and Evaluation Division of the National Weather Service at Sterling, VA.

REFERENCES

Arnulf, A., and J. Bricard, 1957: Transmission by haze and fog in the spectral region 0.35 to 10 microns. *J. Opt. Soc. Amer.*, **47**, 491–498.

Atlas, D., 1953: Optical extinction by rainfall. *J. Meteor.*, **10**, 486–488.

——, and C. W. Ubrich, 1974: The physical basis for attenuation–rainfall relationships and the measurement of rainfall parameters by combined attenuation and radar methods. *J. Rech. Atmos.*, **8**, 275–298.

Chu, T. S., and D. C. Hogg, 1968: Effects of precipitation on propagation at 0.63, 3.5 and 10.6 microns. *Bell Sys. Tech. J.*, **47**, 723–759.

Clifford, S. F., G. R. Ochs and Ting-i Wang, 1975: Optical wind sensing by observing the scintillations of a random scene. *Appl. Opt.*, **14**, 2844–2850.

Derr, V. E., M. J. Post, R. L. Schwiesow, R. F. Calfee and G. T. McNice, 1974: A theoretical analysis of the information content of lidar atmospheric returns. NOAA Tech. Rep. ERL 296-WPL29, 284 pp.

Earnshaw, K. B., and B. Keebaugh, 1977: A research laser weather identification instrument. NOAA Tech. Memo. ERL WPL-23, 63 pp.

Hogg, D. C., 1964: Scattering and attenuation due to snow on optical wavelengths. *Nature*, **203**, 396.

Kurnick, S. W., R. N. Zitter and D. B. Williams, 1960: Attenuation of infrared radiation by fog. *J. Opt. Soc. Amer.*, **50**, 578–583.

Lawrence, R. S., G. R. Ochs and S. F. Clifford, 1972: Use of scintillations to measure average wind across a light beam. *Appl. Opt.*, **11**, 239–243.

Ochs, G. R., S. F. Clifford and Ting-i Wang, 1976: Laser wind sensing: the effects of saturation of scintillation. *Appl. Opt.*, **15**, 403–408.

Wang, Ting-i, and S. F. Clifford, 1975: Use of rainfall-induced optical scintillations to measure path-averaged rain parameters. *J. Opt. Soc. Amer.*, **47**, 927–937.

——, and K. B. Earnshaw, 1977: An optical velocimeter for precipitation. *Topical Meeting on Optical Propagation through Turbulence, Rain and Fog*, Tech. Digest ThB5 1-4, Opt. Soc. Amer., Washington, DC, 1–5.

——, G. Lerfald, R. S. Lawrence and S. F. Clifford, 1977: Measurement of rain parameters by optical scintillation. *Appl. Opt.*, **16**, 2236–2241.

——, K. B. Earnshaw and R. S. Lawrence, 1978: Simplified optical path-averaged rain gauge. *Appl. Opt.*, **17**, 384–390.

Wilson, R. W., and A. A. Penzias, 1966: Effect of precipitation on transmission through the atmosphere. *Nature*, **211**, 1081.

Proceedings of the Fourth Joint Conference on Sensing
of Environmental Pollutants, 294, 1978.

Applications of a Laser Beam Average Wind Sensor to Pollution Meteorology

081

R. S. Lawrence, G. R. Ochs and S. F. Clifford
Environmental Research Laboratories
National Oceanic and Atmospheric Administration
Boulder, Colorado 80302

WE HAVE DEVELOPED AN OPTICAL WIND SENSOR that uses the naturally occurring density fluctuations in the atmosphere to obtain a spatially-averaged wind. The optical refractivity variations, produced largely by temperature fluctuations, drift through the optical path and modulate the received signal irradiance. Using a correlation technique at the receiver, we extract a path-averaged transverse wind speed. This optical sensor has two important advantages over conventional anemometers. First, it measures transverse mean flow over long paths up to several tens of kilometers. Second, it is not limited by bearing friction or other mechanical constraints and consequently has an extremely low velocity threshold. These properties enable it to contribute higher quality and more appropriate wind information in certain applications. For example, by enclosing an area with horizontal laser-beam paths we can measure the outward flux or convergence of air, a useful quantity in the monitoring for pollution events in cities. In a similar context, the mean flow of air down a valley is a critical parameter to know before initiating such pollution-causing events as agricultural burning. We illustrate the measurement of convergence with results from an experiment, using an optical triangle with each leg 300 m long. This relatively small enclosed area is adequate for measurements of the strength of local convective activity. We found excellent agreement between our optical triangle measurements of convergence and simultaneous indications of thermal plume activity from tower-mounted anemometers and from acoustic echo-sounder data.

Our first report of the use of scintillations to measure the average wind across a light beam was prepared by Lawrence, Ochs, and Clifford - (1).* Figure 1 shows how well the winds measured by that system compared with anemometer measurements. Kjelaas and Ochs (2) demonstrated the use of three light beams arranged in a triangular pattern to measure horizontal convergence. Figure 2 compares daytime measurements showing convective thermal plumes with nighttime measurements.

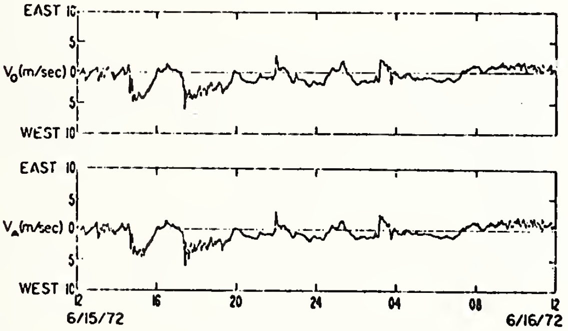

Fig. 1. - A comparison of the average wind speed (V_o) measured optically with the average of the readings of six propellor anemometers (V_A) uniformly spaced along the optical path. Both the anemometers and the optical system measure the component of wind that is horizontal and at right angles to the path. The path is 300 m long, oriented north-south, and 3 m above the ground.

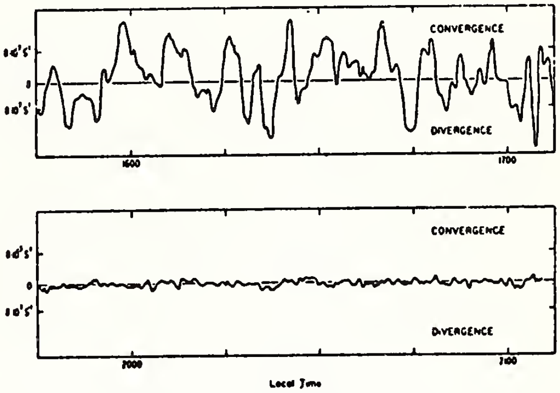

Fig. 2. - Ten-second average divergence readings for typical afternoon and nighttime periods, made with an optical triangle 300 m on a side.

While these early systems worked well on paths shorter than 1 km, they were influenced on longer paths by a phenomenon known as saturation of the scintillations. The effect of saturation and the development of a saturation-resistant optical crosswind sensor were reported by Ochs, Clifford, and Wang - (3). The saturation-resistant system has since been used successfully on long paths and around a 10-km triangle.

REFERENCES

1. R. S. Lawrence, G. R. Ochs, and S. F. Clifford, "Use of Scintillations to Measure Average Wind Across a Light Beam," Applied Optics, 11, No. 2, 239 (1972).

2. A. G. Kjelaas and G. R. Ochs, "Study of Divergence in the Boundary Layer Using Optical Propagation Techniques," Applied Meteorology, 13, No. 2, 242 (1974).

3. G. R. Ochs, S. F. Clifford, and Ting-i Wang, "Laser Wind Sensing: The Effects of Saturation of Scintillation," Applied Optics, 15, No. 2, 403 (1976).

---

*Numbers in parentheses designate References at end of paper.

Proceedings of the Society of Photo-Optical Instrumentation Engineers, 161: 109-113, November 1978.

EXPERIMENTAL ATMOSPHERIC EXTINCTION MEASUREMENTS AT NINE WAVELENGTHS BETWEEN 0.3 AND 10 μm*

Gordon Lerfald and Vernon Derr
National Oceanic and Atmospheric Administration
Boulder, Colorado 80302

Abstract

Accurate determinations of the widely varying spectral extinction of the direct solar beam by the earth's atmosphere has applications in several fields; these include solar energy, optical communication and remote sensing of atmospheric parameters. A system used to make extinction measurements at nine wavelengths in the 0.3 to 10 μm range is described and sample results are presented. Plans to use the data to study remotely the characteristics of clouds and aerosols, particularly the size distributions of the particles along the transmission path, are discussed.

Introduction

The atmosphere acts as a continually varying filter to solar radiation penetrating it. Some of the more important processes include molecular scattering, absorption by the various atmospheric gases, and scattering by hydrometeors (e.g., cloud droplets, rain drops and ice crystals) and by lithometeors (suspended solid particles). Of these, the only one which remains nearly constant for a given site and which can be computed reliably is molecular (Rayleigh) scattering. Absorption due to water vapor varies widely because of large variations in the amount of this gaseous component in the atmosphere, and absorption due to stratospheric ozone also fluctuates significantly.

The concentration and size distribution of lithometeors and hydrometeors may take on a wide range of values and may sometimes be highly variable in time and space. An obvious example of the latter is cumulus clouds which may form, then dissipate in a matter of minutes.

The spectral transmission characteristics of the atmosphere are of obvious interest to designers of solar energy systems and optical communications systems. Other important applications of spectral transmission data include climate studies and determination of the radiation budget of the earth. Also, measured spectral transmission can be used to deduce the amount and characteristics of absorbing and scattering components in the atmosphere. This paper involves measurements of the extinction at nine wavelengths in the range 0.3 to 10 μm. The instrumentation used, the analysis procedures employed and sample results are presented.

Instrumentation

During the past decade, the concept of using several experimental techniques simultaneously to make atmospheric measurements has been gradually implemented in the Wave Propagation Laboratory (WPL) of NOAA. The data thus obtained usually leads to a more complete description of atmospheric conditions than can be obtained by a single technique and allows the different techniques to be cross-checked and calibrated. Among the methods used are backscatter lidar, microwave radar, acoustic sounder, time-lapse photography, photometry, radiometry and in situ sampling by aircraft-borne probes.

This paper describes atmospheric transmission results obtained from narrow beamwidth photometers at wavelengths ranging from 0.3 to 10 μm using the sun as a source. Other data types will be mentioned only in a peripheral way to indicate their usefulness in analysis of the photometric data.

---

* The research work leading to this paper was partially funded by the United States Department of Energy Division of Solar Technology, Environmental and Resource Assessment Branch.

Narrow Bandwidth Solar Photometer (8-channel)

A photometer with eight bandpass filters, each about 0.01 μm (100 Å) wide, was designed and built in WPL. The instrument characteristics are outlined in Table I. The primary emphasis in instrument design were large dynamic range, time response of a few seconds and good relative accuracy in measuring the optical thickness changes (actually, radiant flux changes) at the different wavelengths. These characteristics were obtained by using a common lens, photodetector, and logarithmic amplifier, and rotating a filter wheel at 1 rps so as to update the data for each filter once per second. The instrument is operated on a solar tracker which keeps it pointed at the sun. The data are averaged by an integrator with time constant of about 3 sec and a data point recorded once per second. The data are normally digitized, stored temporarily in computer memory then written onto magnetic tape for permanent data storage.

Table I

Band Pass Filter Center Wavelengths:	0.305, 0.317, 0.338, 0.382, 0.511, 0.875, 0.941 and 1.06 μm.
Response to Radiant Flux:	Logarithmic
Dynamic Range:	5 orders of magnitude (∿ 12 optical thicknesses)
Resolution:	2%
Relative accuracy:	2%
Time constant of response:	3 secs.
Angular Field of View:	1.5 degrees.

Infrared (8-13 μm) Solar Photometer

A photometer for use at this wavelength range was obtained by modifying a commercially available radiometer for the purpose. An aperture about 0.25 cm in diameter was positioned in front of the lens (∿ 1 cm diameter) to reduce the radiation incident on the detector to a safe level. The detector head was then mounted on the solar tracker with other photometric instruments. The instrument response is linear and the dynamic range is limited to about two orders of magnitude. Data are recorded at a one Hertz rate in the same way as is described above for the eight channel photometer.

Extent of the Data Collected

The extinction measurements have been recorded during a number of intensive data collecting programs when several other types of data were simultaneously taken. At other times, the extinction data, time lapse photography and standard solar pyranometer and pyrheliometer data, were the only data types recorded. During the intensive observing periods, data were generally taken from sunrise to sunset. Most of these data have been surveyed to check quality but not analyzed in detail. Intensive observations have been conducted at Colstrip, Montana (26 days), Pt. Mugu, California (13 days), Fairplay, Colorado (28 days), and Grover, Colorado (29 days). Observations at Boulder, Colorado (40 days) have mostly included only the photometric and photographic data types. Examples of data taken at Pt. Mugu are presented below.

Data Processing and Analysis

The data for each of the wavelengths of the 8-channel photometer and the 8-12 μm infrared photometer are converted to atmospheric optical thickness by processing on a computer. This step has the prerequisite of knowing the radiant intensities, $I_{o\lambda}$, which would be measured by the instrument if there were no atmospheric absorption. The latter values are determined primarily by the Langley method in which values of the logarithm of intensity are plotted against relative air mass. For stable atmospheric conditions and a range of air mass values the points on such a graph should lie along a straight line which can be extrapolated to zero air mass, which represents the desired intensity, $I_{o\lambda}$. There is an advantage to using summertime data, when the noon air mass approaches 1.00. Also time periods when stable atmospheric conditions exist, are chosen to improve the reliability of the results. Saturation of strong gaseous absorption lines within some of the filter bandwidths lead to non-linear response with air mass. This means the extrapolation to zero air mass must be done by a curved line on the Langley plots.

The approach taken in the development of software to analyze the data is to work directly from copies of the field-recorded tapes. The computer programs are mostly implemented as operator-interactive with choices for such parameters as averaging intervals, corrections to remove Rayleigh scattering and scale factors on output plots. Much of the analysis is performed by viewing output plots on a CRT display and making hard copy prints of the display when a permanent record is desired. Time lapse photographs by a camera mounted on the solar tracker (sun's disc occulted) and another camera which views the entire sky are taken routinely at intervals of 15 seconds. These films, played back in a movie mode, have been found to be extremely valuable when doing data analysis. Cloud geometry and motion and general sky and weather conditions are used to select periods of special interest or to categorize the type of condition present at any given time.

Time Series Plots

The time variation of the optical thickness at each wavelength measured by the photometric instruments can be plotted on almost any desired time and optical thickness scales. The differential in optical thickness between pairs of wavelengths can also be automatically plotted. The latter method is routinely applied to obtain values of the total precipitable water vapor along the propagation path by taking the difference between the optical thickness measured in a wavelength band centered at 0.941 μm, where water vapor absorption bands occur, and at 0.875 μm which is essentially free of gaseous absorption bands.

The slant-path values of measured optical thickness can be adjusted to the equivalent vertical optical thickness by dividing by the relative optical air mass(1). This correction assumes horizontal uniformity, which appears to be reasonably well satisfied for the atmospheric gases (including water vapor), but often is not satisfied for clouds and particulate aerosols.

Optical Thickness vs Wavelength Plots

The optical thickness measured for each of the eight narrow bandwidth channels and the 8-12 μm band can be plotted versus wavelength (latter on logarithmic scale). Averaging may be applied to data intervals ranging from one second to 5 minutes. The optical thickness scale can be chosen to have any desired upper and lower limits and be either linear or logarithmic. Rayleigh scattering or clear day optical thickness values may be subtracted from each measured value. These types of plots provide a versatile means of analyzing the wavelength dependence of optical thickness under various conditions.

Results

The analysis to date has consisted mainly of routine plotting of output in a survey mode to check quality and consistency of the data. In a few cases, more detailed analysis of selected time periods of special interest has been done. Time series plots of the optical thickness measured at the wavelengths 0.317, 0.501 and 0.875 μm are routinely obtained for each observing day. These serve to point up any problems with the quality of the data and give a good indication of the atmospheric transmission conditions. Optical thickness vs wavelength plots are also obtained at approximately half-hourly intervals using five minute segments of data.

Examples

Figures 1 and 2 show plots of optical thickness versus wavelength for transmission through thin cirrus clouds. Five minute segments of data centered on the times indicated for each data set were averaged. The clear-day extinctions obtained from data on other days are subtracted from the optical thickness values. It is seen that optical thickness increases with longer wavelengths; this is consistent with the evidence that cirrus clouds consist primarily of ice crystals with typical dimensions the order of tens of micrometers.(2) The general theory of scattering(3) shows that the energy scattering coefficient for radiation interacting with particles will peak roughly when the wavelength of the radiation, λ, is nearly equal to the size parameter, $a = 2\pi r/\lambda$, of a scattering particle with radius r.

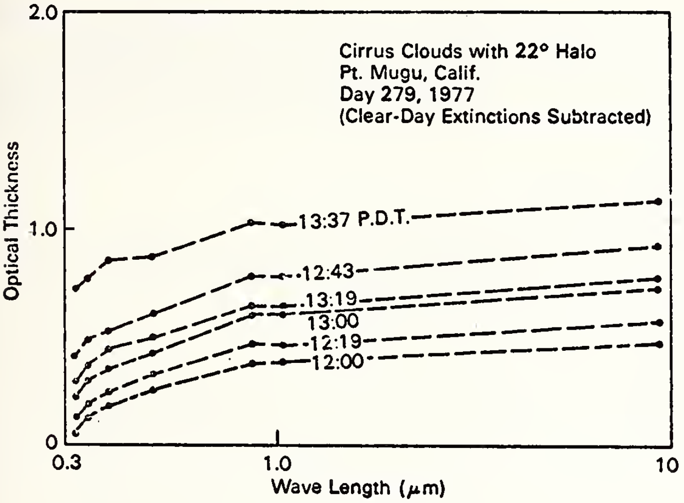

Fig. 1. Optical thickness vs wavelength observed for cirrus clouds.

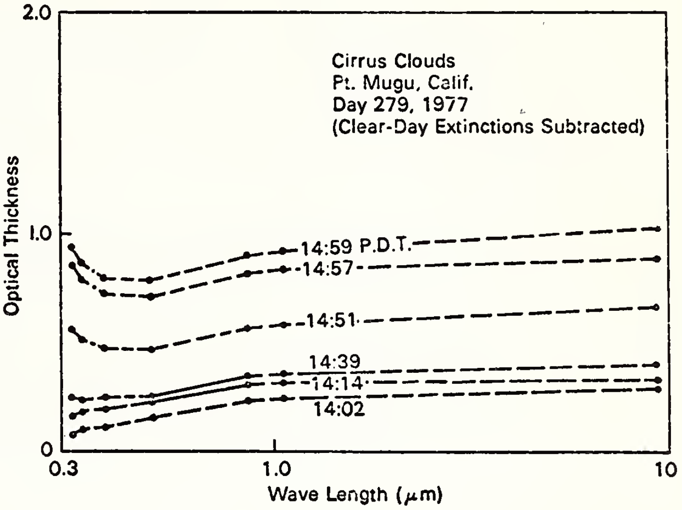

Fig. 2 Same as Fig. 1 for later times.

Figure 3 shows plots of optical thickness versus wavelength for low altitude clouds which dissipated with time. The peak in optical thickness between 0.5 and 1.0 μm indicates the presence of particles having radii of a few tenths of micrometers. The optical thickness and the height of the peak are seen to decrease with time in Figure 3 and the sequence is continued in Figure 4. The steep increase in the optical thickness at shorter wavelengths after 16:00 PDT is due to the increasing path length through heavy aerosol pollution as the sun approaches the horizon. The wavelength dependence observed implies a distribution of particles with radii mostly below 0.1 μm.

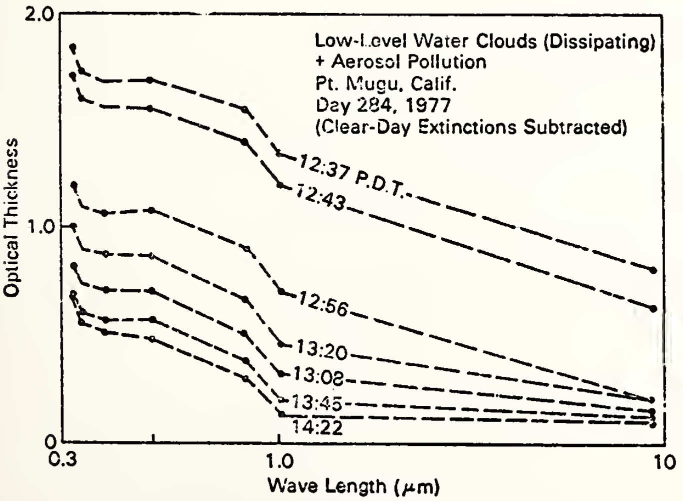

Fig. 3. Optical thickness vs wavelength observed for low altitude clouds which were dissipating and heavy aerosol pollution.

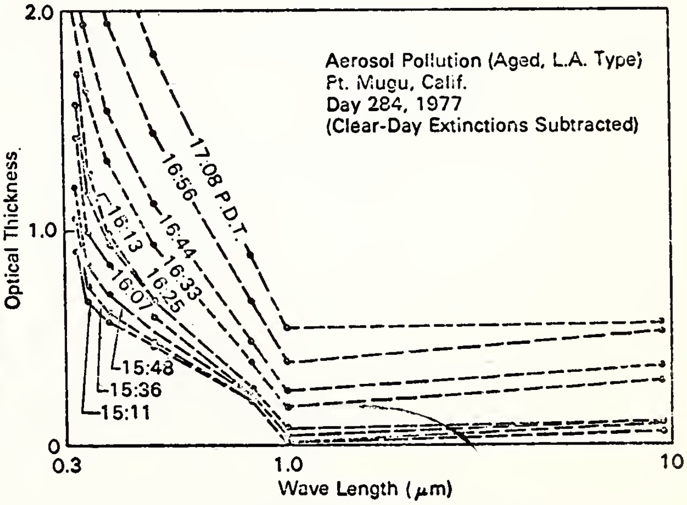

Fig. 4. Same as Fig. 3 after low altitude clouds had largely dissipated.

Returning to figure 3, it seems likely that the particles causing the peak at wavelengths between 0.5 and 1.0 μm were aerosol particles with water coatings. As the air dried out these particles lost their water coatings and the peak gradually disappeared.

Conclusion

It is planned that the optical thickness data will be analyzed in conjunction with other types of data collected simultaneously. One of the objectives will be to assemble data sets which can be used to develop and test computer models of the transmission of solar radiation through the atmosphere. One approach will be to derive parameters which characterize the spectral transmission properties of differing types of clouds and aerosols

The data will also be used as a means of remotely measuring the microphysical properties of clouds and aerosols. In order to optimize the amount of information which can be derived, it is necessary to perform a mathematical inversion which relates the observed wavelength dependence of optical thickness to the microphysical properties of the scattering particles. Work is in progress to implement a routine process of performing such inversions.

References

1. Kasten, Fritz, "A New Table and Approximate Formula for the Relative Optical Air Mass." Arch. Meteorol. Geophys. Bioklimatol. Ser. B, 14(2); 206-223, 1966.

2. Heymsfield, A. J. and R. G. Knollenberg, "Properties of Cirrus Generating Cells," J. Atmos. Sci., 29, 1358-1366. 1972.

3. Kerker, M., The Scattering of Light and Other Electromagnetic Radiation, Academic Press, 1969.

Applied Optics, 17: 3774-3778, 1978.

Finite aperture optical scintillometer for profiling wind and C_n^2

G. R. Ochs and Ting-i Wang

A new optical technique is described for measuring the path profiles of crosswind and of a refractive-index structure parameter C_n^2 along a line-of-sight path. Different sizes of transmitters and receivers are used to control the path-weighting function so that it will peak at different path locations. Various linear combinations of these measurements yield the path profile of crosswind and C_n^2. A prototype instrument has been built and tested. Experimental results show good agreement with the theoretical predictions.

I. Introduction

In recent years, many authors[1-16] have considered the possibility of remotely probing the crosswind and refractive-index structure parameter C_n^2 using line-of-sight optical, microwave, and acoustic techniques. One laser beam system that has operated successfully uses the naturally occurring scintillations produced by atmospheric refractivity variations to derive the path-averaged transverse wind.[1] By measuring a time-lagged covariance function with spaced detectors, the path-averaged wind speed can be found directly from the slope of this function at zero time lag. A change in the separation between detectors emphasizes different regions of the path, as shown in Fig. 1. Although this system performs well when measuring path-averaged wind (in the weak scattering regime), it is not suitable for path profiling because of its broad weighting function.

Recent theoretical and experimental work has shown that it is possible to measure the transverse wind across an optical path, and the refractive-index structure parameter (C_n^2) along the path, by observing the scintillation of an extended incoherent light source.[12,13] In fact, for both measurements there are distinct advantages over the use of coherent light sources because the deleterious effects of the saturation of scintillation for paths of high integrated refractive turbulence as well as the inner scale of refractive turbulence on short paths are largely eliminated. It has also been shown that by using the proper ratios of transmitter and receiver aperture diameters, it is possible to position the maximum of the weighting function in different portions of the path.

Spatial-filter techniques are also effective in restricting the measurement to a portion of the optical path.[2,14-16] These techniques require more apertures, however, and the array of apertures must be large to avoid saturation effects on horizontal paths of several kilometers. While, in principle, a rather sharp path definition may be obtained by cross-path techniques, in practice, on paths of 0.5 km or more, the intermittent nature of C_n^2 seems to require long averaging times, making the sharp path definition less useful. These considerations led us to develop a profiler with less sharp path definition and based upon the use of different-sized, extended, incoherent transmitting sources with different-sized tangent receiver apertures for each path location to be measured.

II. Theory

Recently, Clifford *et al.*[17] developed an equation for the log-amplitude covariance function in strong Kolmogorov turbulence,[18] i.e.,

$$C_\chi(\rho) = 2.94 \int_0^1 du\,\sigma_T^2(u)[u(1-u)]^{5/6} \int_0^\infty dy\,y^{-11/6}\sin^2 y$$
$$\exp\{-\sigma_T^2[u(1-u)]^{5/6}F(y)\}J_0\left\{\left[\frac{4\pi y u}{(1-u)}\right]^{1/2}\rho\right\}, \qquad (1)$$

where $\sigma_T^2(u) = 0.124k^{7/6}L^{11/6}C_n^2(u)$, $u = z/L$ is the normalized path position, ρ is the separation between two detectors in Fresnel zones $(\lambda L)^{1/2}$, J_0 is the zero-order Bessel function of the first kind, and $F(y)$ is given by

$$F(y) = 7.02y^{5/6}\int_{0.7y}^{\infty} d\xi\,\xi^{-8/3}[1 - J_0(\xi)], \qquad (2)$$

The authors are with NOAA/ERL, Wave Propagation Laboratory, Boulder, Colorado 80302.

Received 27 April 1978.
0003-6935/78/1201-3774/$0.50/0.
© 1978 Optical Society of America.

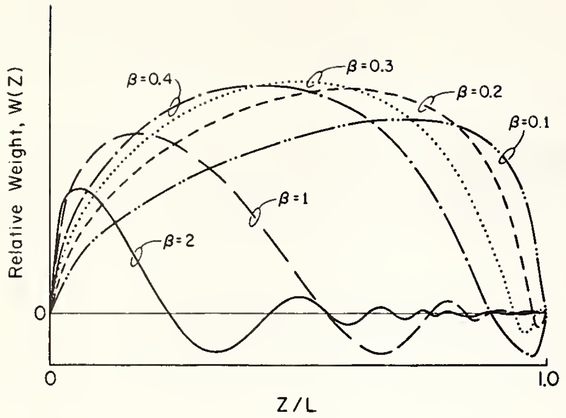

Fig. 1. The relative weights of the different portions of the path in determining the optically measured wind. The parameter $\beta = \rho(\lambda L)^{-1/2}$ is the normalized separation of the sensors. These curves are calculated for a point source and for point sensors.

where y is the normalized spatial wavenumber. Equation (1) can be written in a more convenient form

$$C_\chi(\rho) = \int_0^1 du C_n^2(u) W(u), \tag{3}$$

where

$$W(u) = 0.365 k^{7/6} L^{11/6} [u(1-u)]^{5/6} \int_0^\infty dy g(u,y) \times J_0 \left\{ \left[\frac{4\pi y u}{(1-u)} \right]^{1/2} \rho \right\} \cdot \tag{4}$$

$$g(u,y) = y^{-11/6} \sin^2 y \exp\{-\sigma_T^2 [u(1-u)]^{5/6} F(y)\}. \tag{5}$$

In Eq. (4), $W(u)$ is the path-weighting function to measure C_n^2 using a point source and a point receiver. To incorporate the effects of wind into Eq. (1), we use Taylor's hypothesis and replace ρ by $|\rho - \mathbf{v}\tau (\lambda L)^{-1/2} u^{-1}|$. Information about the wind is then derived from the slope at zero time lag, i.e., $m = \partial C_\chi(\rho,\tau)/\partial\tau$ at $\tau = 0$. After differentiating, we obtain

$$m = 2.95 \int_0^1 du \sigma_T^2(u) [u(1-u)]^{1/3} (\hat{\rho} \cdot \mathbf{v}_n) \times \int_0^\infty dy g(u,y) (4\pi y)^{1/2} J_1 \left[\left(\frac{4\pi y u}{1-u} \right)^{1/2} \rho \right], \tag{6}$$

where J_1 is the first-order Bessel function of the first kind, $\mathbf{v}_n = \mathbf{v}/(\lambda L)^{1/2}$, and $\hat{\rho} = \rho/\rho$. (Note that only winds parallel to $\hat{\rho}$ will contribute to the measured wind speed.) When we use the one-bit correlator technique[1] to obtain $C_\chi(\rho,\tau)$, this function is automatically normalized to the signal variance $C_\chi(0,0)$, and we actually obtain a normalized slope m_N of the form

$$(\lambda L)^{1/2} m_N = \int_0^1 du v(u) W_1(u) \bigg/ \left[\int_0^1 du W(u) \right], \tag{7}$$

where

$$W_1(u) = 0.365 k^{7/6} L^{11/6} [u(1-u)]^{1/3} \int_0^\infty dy g(u,y) (4\pi y)^{1/2} \times J_1 \left[\left(\frac{4\pi y u}{1-u} \right)^{1/2} \rho \right] \cdot \tag{8}$$

[Note that in using the particular form of Eq. (7), we have assumed a uniform distribution along the optical path, i.e., that C_n^2 is a statistically uniform function of u.] Under this assumption, $W_1(u)$ is proportional to the path-weighting function for the transverse wind speed under all refractive-turbulence conditions.

To generalize Eqs. (4) and (8) to the case of finite circular, incoherent transmitting and receiving apertures, the essential modification of the theory is to replace $g(u,y)$ by[7]

$$g'(u,y) = g(u,y) \left\{ \frac{2J_1 \left[\left(\frac{\pi y u}{1-u} \right)^{1/2} \alpha_r \right]}{\left(\frac{\pi y u}{1-u} \right)^{1/2} \alpha_r} \right\}^2 \times \left\{ \frac{2J_1 \left\{ \left[\frac{\pi y (1-u)}{u} \right]^{1/2} \alpha_t \right\}}{\left[\frac{\pi y (1-u)}{u} \right]^{1/2} \alpha_t} \right\}^2 \tag{9}$$

where α_r and α_t are, respectively, the diameters of the receiver and transmitter, each normalized to a Fresnel zone for the optical path. It has been shown[13] that for a sufficiently large size of transmitting aperture or receiving aperture, there will be no saturation effect even in strong integrated turbulence. Sufficiently large means that

$$\alpha_r + \alpha_t > 1.95(\sigma_T^2)^{3/5}. \tag{10}$$

In this case, the weighting function and the calibration remain unchanged for both weak and strong refractive turbulence. For all the following calculations, we assume that Eq. (10) is satisfied, hence the exponential term in $g(u,y)$ is ignored.

III. Implementation

We have designed and constructed a profiling instrument based upon these principles, which simultaneously measures the crosswind and C_n^2 at six locations along an optical path from 0.5 km to 2 km long. The transmitter consists of two incoherent light sources 8.4 cm and 27.9 cm in diameter, illuminated by quartz–iodine lamps. The smaller source uses a frosted bulb at the focus of a concave mirror; the larger source has its lamp at the focus of a fresnel lens and uses a separate piece of frosted glass to insure sufficient uniformity of illumination over the aperture.

The receiver (Fig. 2) has three pairs of circular apertures, 15.2 cm, 9.8 cm, and 6.7 cm in diameter. The distances between the apertures are equal to the aperture diameters so they are tangent to each other. Dual photodiodes placed at the focus of concave mirrors measure the irradiance of the apertures. By spacing the transmitters and aligning the receiver properly, the irradiance of six apertures by one transmitter is measured by one group of six diodes, and the irradiance of the six apertures by the second transmitter is measured by the

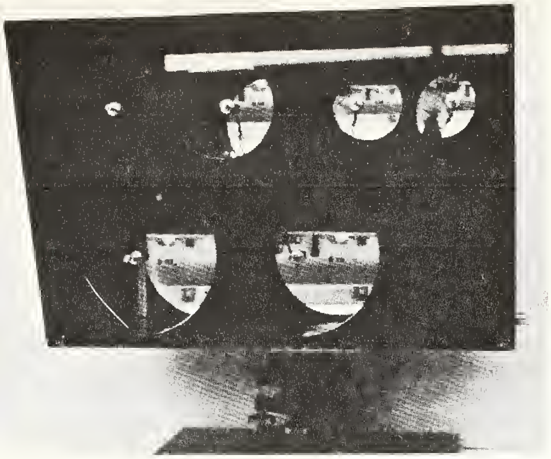

Fig. 2. A front view of the receiver showing the three pairs of different-sized apertures.

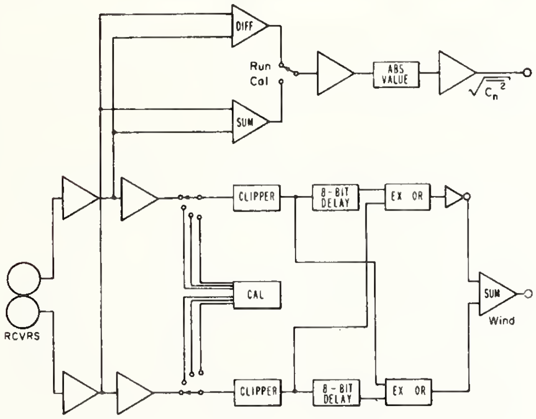

Fig. 3. Block diagram of the system.

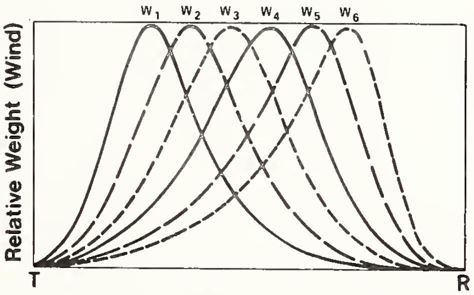

Fig. 4. The wind path-weighting functions using the six transmitter–receiver pairs shown in Table I. The horizontal axis is the relative path position, and T and R represent transmitting and receiving ends, respectively.

Table I. Transmitter Size [= $\alpha_t(\lambda L)^{1/2}$] and the Receiver Size [= $\alpha_r(\lambda L)^{1/2}$] for the Six Transmitter–Receiver Pairs

n	1	2	3	4	5	6
α_t	2.99	2.99	2.99	9.88	9.88	9.88
α_r	5.39	3.49	2.37	5.36	3.49	2.37
R_{n-2}	0	0	−0.27	−0.33	−0.31	−0.28
R_{n-1}	0	−0.26	0	0	0	−0.21
R_{n+1}	−0.49	0	0	0	−0.19	0
R_{n+2}	0	−0.22	−0.23	−0.16	0	0
C_f	1.96	1.93	2.00	1.98	2.00	1.96

Note: The linear combination coefficients R are used to obtain better path resolution according to Eq. (13). The calibration factors C_f are calculated according to Eq. (14) for each case.

second set of six photodiodes. In this way six transmitter–receiver pair aperture ratios are obtained with two transmitting apertures and three receiving aperture pairs. Twelve preamplifiers at the receiver provide both a low-gain signal suitable for C_n^2 measurement and a high-gain signal that can be clipped for wind measurement purposes. The signal processor uses these signals to calculate both transverse wind and C_n^2 at six locations along the optical path.

A block diagram of the circuit used to compute wind and C_n^2 at one path location is shown in Fig. 3. Six of these circuits, which differ only in calibration, are used so that measurements are made simultaneously at the six locations. The circuit used to compute wind utilizes the slope system and is similar to that employed in the saturation-resistant optical wind measurement systems.[12] The wind calibration is independent of pathlength over the 0.5–2.0-km range.

The C_n^2 circuit is arranged so that, for received signals A and B, a calibrated measurement of the ratio

$$\sigma_I^2 = \langle (A - B)^2\rangle/[(A_0 + B_0)^2] \tag{11}$$

is obtained. It can be shown that[13]

$$C_n^2 = (K\sigma_I^2 D_t{}^{7/3})/L^3, \tag{12}$$

where L is the pathlength, D_t is the incoherent transmitting aperture diameter, and K is a function of the ratio of transmitting and receiving aperture sizes.

Based on Eq. (8), the six calculated path-weighting functions for wind are shown in Fig. 4. Each curve is normalized to its own peak value. The curves peaking to the left of the center of the light path represent the weighting functions for the small ratio of transmitter size to receiver size, while the curves to the right represent the weighting functions for the large ratio. Comparing Figs. 4 and 1, it is clear that using extended transmitting and receiving sizes yields sharper weighting functions than can be obtained with a point transmitter and receivers. To obtain even better path resolution, we linearly combine the weighting functions to obtain new weighting functions:

$$W'_n = C_f(R_{n-2}W_{n-2} + R_{n-1}W_{n-1} + W_n + R_{n+1}W_{n+1} + R_{n+2}W_{n+2}), \tag{13}$$

where

$$C_f = (R_{n-2} + R_{n-1} + 1 + R_{n+1} + R_{n+2})^{-1}, \tag{14}$$

W_n is the original weighting function, and R_n is the coefficient. If we use the values of R_n shown in Table I, the weighting functions are shown in Fig. 5.

The instrument is primarily designed to measure wind profiles, and the optical arrangement is not optimum for C_n^2. Useful measurements can be made,

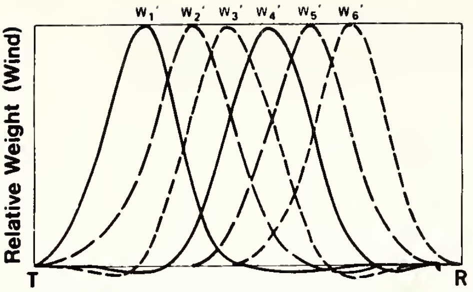

Fig. 5. The wind path-weighting functions using linear combinations according to Eq. (13) and the coefficients listed in Table I. The horizontal axis is the relative path position, and *T* and *R* represent transmitting and receiving ends, respectively.

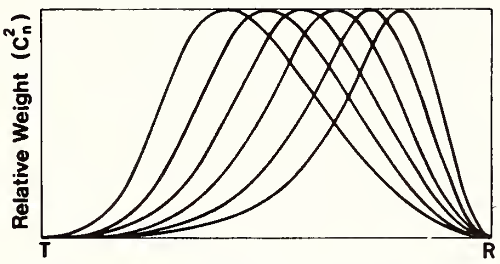

Fig. 6. The C_n^2 path-weighting functions using the six transmitter–receiver pairs shown in Table I. The horizontal axis is the relative path position, and *T* and *R* represent transmitting and receiving ends, respectively.

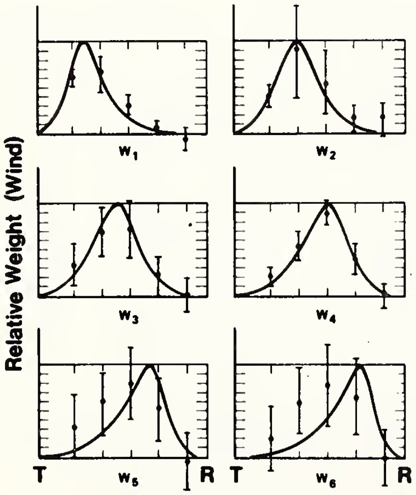

Fig. 7. Experimentally measured wind path-weighting functions of the six transmitter–receiver pairs before linear combination. The horizontal axis is the relative path position, and *T* and *R* represent transmitting and receiving ends, respectively. The solid curves represent the theoretical weights. The dots are the measured weights averaged, in most cases, over 24-h periods. The error bars represent the standard deviation of the hourly averages throughout the measuring period. The pathlength is 500 m.

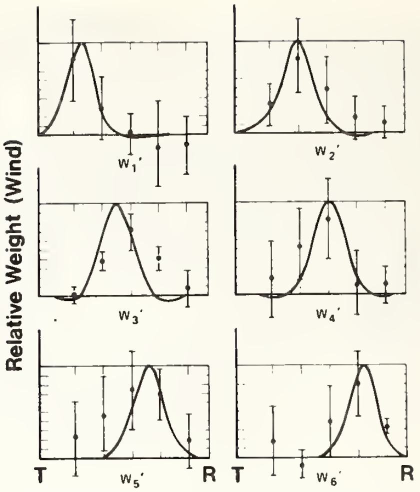

Fig. 8. Similar to Fig. 7 but after the linear combinations.

however. Based on Eq. (4), the calculated weighting functions for the C_n^2 measurement are shown in Fig. 6. The aperture sizes chosen for profiling wind in the middle ⅔ of the path do not produce the same weighting functions for C_n^2; hence the C_n^2 weights obtained are not symmetric with respect to the center of the optical path.

For wind measurements, we performed an experiment on a uniform 500-m path to check the path-weighting function shown in Figs. 4 and 5. Our path was 1.5 m above the ground and was equipped with ten propeller anemometers to measure the component of the horizontal wind at right angles to the optical path. Clifford *et al.*[11] give a procedure by which the simultaneous measurement of wind optically and with spaced anemometers is used to determine the path-weighting function. We analyzed the data with an on-line minicomputer and compared the optical and *in situ* crosswind measurements, averaged in pairs. The comparisons of measured and theoretical path-weighting functions are shown in Fig. 7 (no linear combination) and Fig. 8 (after linear combination according to the coefficients listed in Table I). The solid curves in Figs. 7 and 8 represent the theoretically calculated path-weighting functions. The dots are the measured weights over a 24-h or longer period. The error bars represent the standard deviation of hourly averages throughout the measuring period. Their size is partly dependent upon the spatial variation of the wind component along the path, because weighting information can only be obtained during variable wind conditions. Thus the error bars tend to be larger when the wind is more nearly uniform over the optical path, and smaller for highly variable winds.

The experimental results generally show reasonable agreement with the theoretical predictions. However, probably due to the intermittency of the C_n^2 distribution along the path, the measured weights are usually broader than the theoretical weights, the latter having been calculated on the assumption of uniform C_n^2 along the path. Likewise, the averaging periods necessary for a given wind-measurement accuracy increase with increasing C_n^2 intermittency. Also, the effective SNR for wind profiling vary with path position. The midpath positions are much better than those near the transmitter or receiver, and the original wind measurements are less noisy than the sharper ones we have obtained by combining weighting functions.

Some other effects, not specifically evaluated, very likely contribute to the measurement error. We have assumed in the analysis a Kolmogorov spectrum of turbulence and an instrument operation wholly within the inertial subrange. Both assumptions may be violated in certain regions of operation. For optical paths near the ground the largest transmitting and receiving apertures may be influenced by changes in the outer scale of turbulence. However, since the C_n^2 measurement employs a differential technique, the effect is small.[11] Due to the bump in the spectrum of turbulence at high wavenumbers,[19] the smallest transmitting and receiving apertures will observe somewhat higher scintillation levels than predicted. We estimate that the maximum error for wind measurement is less than 10% and less than 15% for C_n^2 for a 1-min averaging period.

IV. Conclusions

We have shown, both theoretically and experimentally, that by changing the ratio of the transmitting aperture to the receiving aperture, measurements of the crosswind and the refractive-index structure parameter weighting functions can be maximized at different path positions, and that difficulties due to the saturation of scintillation and inner scale effects are minimized by the use of extended incoherent apertures. By linearly combining several such measurements, using different ratios of the transmitting aperture to receiving aperture, we obtain a set of reasonably sharp weighting functions peaked in the middle ⅔ of the path. A prototype instrument, designed on these principles, has performed satisfactorily on a horizontally homogeneous path.

This work was partially supported by the U.S. Army Electronics Command, Atmospheric Sciences Laboratory, White Sands, New Mexico. Thomas H. Pries and Reuben Rodrigues were the Project Monitors.

References

1. R. S. Lawrence, G. R. Ochs, and S. F. Clifford, Appl. Opt. 11, 239 (1972).
2. R. W. Lee, J. Opt. Soc. Am. 64, 1295 (1974).
3. T-i Wang, S. F. Clifford, and G. R. Ochs, Appl. Opt. 13, 2602 (1974).
4. L. C. Shen, IEEE Trans. Antennas Propag. AP-18, 493 (1970).
5. A. Ishimaru, IEEE Trans. Antennas Propag. AP-20, 10 (1972).
6. P. A. Mandics, R. W. Lee, and A. T. Waterman, Jr., Radio Sci. 8, 185 (1973).
7. J. C. Harp, "A Line-of-Sight Microwave Propagation Experiment for Resolving the Motions and Turbulent Structure of the Atmosphere," Ph.D. Thesis, AFCRL-71-0451, SV-SEL 71-042, Scientific Report 1 (1971).
8. P. A. Mandics, "Line-of-Sight Acoustical Probing of Atmospheric Turbulence," Ph.D. Dissertation, Stanford U., Stanford, Calif. (1971).
9. A. G. Kjelaas and G. R. Ochs, J. Appl. Meteorol. 13, 242 (1974).
10. R. W. Lee and J. C. Harp, Proc. IEEE 57, 375 (1969).
11. S. F. Clifford, G. R. Ochs, and Ting-i Wang, Appl. Opt. 14, 2844 (1975).
12. G. R. Ochs, S. F. Clifford, and Ting-i Wang, Appl. Opt. 15, 403 (1976).
13. Ting-i Wang, G. R. Ochs, and S. F. Clifford, J. Opt. Soc. Am. 63, 334 (1978).
14. G. R. Ochs, R. S. Lawrence, Ting-i Wang, and P. Zieske, "Stellar-Scintillation Measurement of the Vertical Profile of Refractive-index Turbulence in the Atmosphere," in *Imaging through the Atmosphere* (Soc. Photo-Opt. Instrum. Eng., 75, 48 (1976).
15. G. R. Ochs, Ting-i Wang, R. S. Lawrence, and S. F. Clifford, Appl. Opt. 15, 2504 (1976).
16. G. R. Ochs, S. F. Clifford, and Ting-i Wang, "Wind and C_n^2 Profiling with Crossed Laser Beams and Spatial Filter Detectors," NOAA Tech. Rept. ERL 367-WPL 45 (GPO, Washington, D.C., 1976).
17. S. F. Clifford, G. R. Ochs, and R. S. Lawrence, J. Opt. Soc. Am. 64, 148 (1974).
18. A. N. Kolmogorov, Dokl. Akad. Nauk SSSR 30, 299 (1941).
19. R. J. Hill and S. F. Clifford, J. Opt. Soc. Am. 68, 892 (1978).

Proceedings of the Fourth Joint Conference on Sensing
Environmental Pollutants, 403-406, 1978.

Measurement by Doppler Lidar of Atmospheric Velocities Relevant to Environmental Monitoring

R. L. Schwiesow, M. J. Post, and V. E. Derr
Wave Propagation Laboratory
Environmental Research Laboratories, NOAA
Boulder, Colorado 80302

ABSTRACT

We are using an infrared, Doppler lidar system to measure velocities in the atmosphere. Applications to air quality problems for which the Doppler lidar is being evaluated include measurements of atmospheric diffusion, stack effluent velocity, and structural loading from the localized winds of vortices, and determination of the urban ventilation factor. The Doppler lidar measures the line-of-sight component of the velocity of aerosols in its sensing volume. Properly applied, it can measure wind profiles to at least 300 m altitude at a distance of up to 1 km from the lidar, sub-resolution-volume scale turbulence, and 10.6 μm backscatter intensity. The Doppler lidar system acts as a vertical anemometer array and is completely mobile. Profiles obtained from variable range or variable elevation scans apply to diffusion and ventilation problems. Considerations of data interpretation for stack effluent velocity have dictated refined Doppler approaches. Better signal-to-noise ratio in data processing, development of a differential Doppler technique, and use of Doppler lidar to measure plus and minus velocity are improvements under way.

THE DOPPLER LIDAR TECHNIQUE has demonstrated usefulness in a number of environmental monitoring applications. This paper presents representative applications of Doppler lidar velocity measurements to inform the pollutant sensing community about the measurement capability and to stimulate those with measurement needs to identify other applications that can benefit from the capabilities and limitations unique to the Doppler lidar.

Doppler lidar is a subcategory of active remote sensing. It uses a narrow-frequency laser transmitter (lidar = light detection and ranging) and a telescope-receiver of scattered light to detect the motion of atmospheric aerosols at a distant location, which may be generally inaccessible to conventional *in situ* anemometers.

ATMOSPHERIC VELOCITIES IN ENVIRONMENTAL MONITORING

Four types of sensing problems illustrate applications of Doppler lidar. These problems are not inclusive of all the possibilities, nor are they completely solved at this stage.

DIFFUSION - Mean wind-speed profiles are used as a direct measure of the transport of airborne pollutants. Wind profiles are affected by meteorological conditions and terrain configurations. Present Doppler lidars cannot provide a complete three-dimensional map of the wind field over the entire space of interest. They are effective as highly mobile anemometer arrays with considerable flexibility in positioning.

Wind profiles at suitably chosen locations can characterize the wind field in a more cost-effective fashion than tower-mounted sensors when portability (short-term experiments) and sensing heights above 50 m are involved. Lidar-obtained wind profiles can be taken continuously over a chosen point, in contrast to pilot balloon measurements, which can be taken only occasionally and with significant shortcomings in accuracy and representativeness. The lidar's mobility and remote sensing capability is especially valuable in uneven terrain.

There are diffusion applications of lidar wind measurements in research, where wind speed data for extensions of Pasquill-Gifford stability classifications for elevated sources and for evaluation of complex terrain diffusion models are required. There are also applications in operational transport predictions, where both profiles and knowledge of horizontal inhomogeneities are important.

URBAN VENTILATION - An important variable for pollution episode prediction in urban areas is the product of the thickness of the (aerosol) mixed layer and the flow velocity through that layer.

The flow is conveniently measured by a Doppler lidar wind profile. As in diffusion applications, the Doppler lidar has significant operational advantages over towers and radiosondes for boundary layer wind measurements. Possible effects of severe weather on operational lidar range are not significant for this application because during severe weather urban ventilation is not a concern.

Many alternatives are available for inferring the thickness of the mixed layer. Simple modifications of the infrared Doppler lidar allow it to measure profiles of infrared backscatter from aerosols in the 1 to 3 μm diameter range. The thickness of the mixed layer is taken to be the height at which the backscatter decreases sharply and/or falls below a predetermined threshold. This technique compares favorably with other alternatives. Thickness measurement from airborne platforms is expensive; inferences from acoustic-sounder-sensed thermal data are indirect; visible-wavelength lidars are preferentially sensitive to much smaller particles, suffer from sky background interference, are less eye-safe, and are not yet operationally useful for wind measurements.

STACK EFFLUENTS - The mass loading of a stationary source is a product of concentration and effluent velocity. The infrared Doppler lidar has been shown to be useful for effluent velocity measurements in preliminary tests (1)*. Various technique refinements are needed.

At low elevation angles, the line-of-sight velocity component of the principally vertical effluent flow is small. This fact leads to two sources of error. First, the presence of large turbulent velocities can mask the small mean flow component. A homodyne lidar, which does not determine the sign of the velocity, can produce a misleading velocity spectrum from pure isotropic turbulence, for example. A heterodyne lidar, discussed later, is indicated. Second, at low elevation angles, the lidar is preferentially sensitive to the ambient wind, which is largely horizontal. In this case, sign information is helpful, and a lidar configuration that senses flow transverse to the line of sight would be more helpful than a longitudinal component sensor.

---

*Numbers in parentheses designate references at the end of the paper.

Particularly in the case of stacks, it is important to compare lidar principles to the sensing needs to achieve a reasonable measurement solution.

LOCALIZED WIND LOADING - One environmental-energy problem relates to effects on containment structures from tornados. From localized wind measurements, structural effects can be estimated.

DOPPLER LIDAR PRINCIPLES

GEOMETRY AND DATA - The types of wind data available from a Doppler lidar are limited by the backscatter geometry that is the only practical way of sensing atmospheric motions at ranges beyond a few meters. Actual velocity information comes from the Doppler shift of infrared radiation backscattered from aerosols in the sensing volume. Only the component of velocity in the backscatter (line-of-sight) direction gives a shift. At 10.6 µm in the middle infrared, a velocity component of 1 ms^{-1} gives a shift of 189 kHz.

The sensing volume is determined by the focus region of the transmit-receive telescope for the present coaxial, CW lidar systems that are practical for environmental monitoring. Within this volume, the aerosol tracers are assumed to follow air motion. Since in general the scatterers are not in uniform motion, a frequency (velocity) spectrum represents the distribution of velocity components in the sampling region. From the spectrum, information on the total backscattered intensity (0th spectral moment), mean velocity (1st moment), and velocity spread or sub-resolution-volume turbulence (2nd moment) is available.

Measurement of more than one component of velocity requires multiple beams. Azimuth-elevation diversity using a single system in a scanned, time-shared mode is workable if the atmosphere is both horizontally homogeneous and stationary in time. Multiple beams from spatially separated systems converging at a single resolution volume, as used for Doppler radars, have not yet been used for infrared Doppler lidars.

FIELD HARDWARE - We are using a compact, mobile lidar that has been operated aboard a light aircraft and a pickup truck. The system uses a standard laboratory laser, 30 cm Newtonian optics, a commercially-available detector, and an electronic spectrum analyzer. Appropriate flat mirrors steer the coaxial transmit-receive beams anywhere within a full hemisphere in azimuth and elevation, although most work is done between -5° and +18° elevation or at 90° elevation. Radiated power is 3 W, continuous wave.

A velocity spectrum is available every 16 ms. The resolution volume at the focus is roughly a cylinder less than 0.2 mrad in azimuth and elevation, but 10 m along the line of sight at 100 m range. This length increases with the square of the range out to approximately 1 km where no range resolution remains. Velocity accuracy is to within the uncertainty in the speed of light and the frequency calibration of the spectrum analyzer (typically less than 0.1% full scale). Velocity resolution is limited by the laser linewidth to ±3 cms^{-1} and by the spectrum analyzer to approximately 1% full scale. For example, instrumental uncertainty is less than 0.1 ms^{-1} for a full scale range of 10 ms^{-1}. Full scale velocity can range to 200 ms^{-1} with present equipment.

Work on aerosol statistics with this lidar (2) showed that approximately 5×10^3 scatterers per m^3, of diameter 2 µm and larger, are required for a working range of 200 m with 5 s integration time and 6 dB signal-to-noise ratio. This typically corresponds to a clean rural environment with 50 km visibility. In urban or seacoast environments, the typical operating range is 1 km because of the larger backscatter than in rural cases.

ILLUSTRATIVE FIELD MEASUREMENTS

The first task for any new measurement technique is to establish its validity by comparison with known methods. Comparisons between the lidar at a range of 150 m and a tower-mounted anemometer centered on the resolution volume showed excellent agreement for one minute averages of data taken under a variety of conditions (3).

A related observation, familiar to anyone working in boundary layer wind measurements, is that in many cases the lower atmosphere is anything but homogeneous in space and stationary in time. This fact places significant restrictions on azimuth-elevation diversity techniques for multicomponent wind sensing.

PROFILES - The sample volume may be scanned in height by fixing an elevation angle and scanning in range or by choosing a range and scanning the elevation angle. Either scan with a fixed azimuth measures only one component of the wind. If the elevation angle is kept small (for example less than 18°) then the component measured is primarily horizontal. Various assumptions about the atmosphere may be appropriate for particular measurement situations.

Figure 1 shows a fixed elevation, variable range scan. Since information was desired along the line of sight in this case, no assumptions on horizontal homogeneity were made. The most restrictive assumption was that of time stationarity for three minutes measurement time under the daytime convection conditions present.

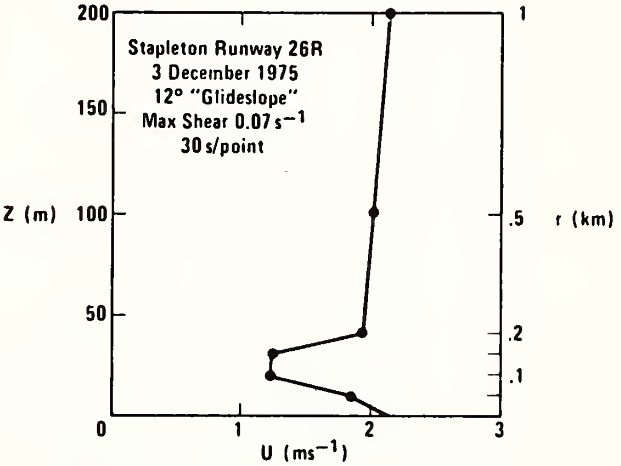

Figure 1. Fixed elevation, variable range wind profile.

Improved scanning speed, repetitive scanning, and/or more efficient data processing, discussed in the next major section, would relax the need for time stationarity. If the atmospheric situation justified an assumption of horizontal homogeneity, a profile taken at a different azimuth would indicate the other horizontal wind component.

Figure 2 presents a pair of profiles upwind and downwind of a change of terrain feature. In this case, an assumption of horizontal homogeneity was obviously invalid. Because of an inversion above the highest point measured, an assumption of negligible vertical velocity was used to convert the measured line-of-sight component to the horizontal component in the vertical plane containing the maximum terrain change gradient (perpendicular to the shore). The stable sea breeze condition indicated that an assumption of stationarity was appropriate for the measurement.

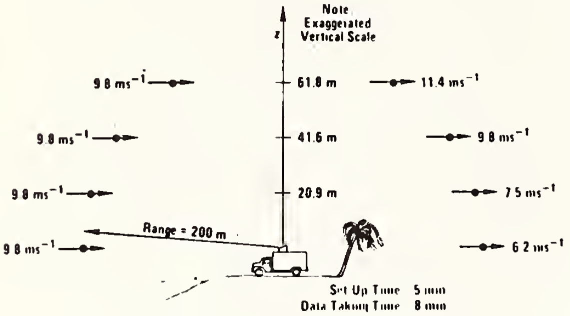

Figure 2. Sea breeze wind profiles using fixed range, variable elevation scan.

More data were available from the lidar velocity spectra than are indicated in figure 2. Profiles of sub-resolution-scale turbulence show interesting variations upwind and downwind of the terrain change. For this case, no significant velocity fluctuations were observed on scales larger than the resolution volume. This situation is consistent with the stationarity assumption.

Profiles such as these are applicable to environmental monitoring problems of diffusion and urban ventilation, among others. At this state of system development we have demonstrated field measurement capability for velocity spectra to a distance of 1 km from the lidar and profiles to a height of 300 m using naturally-occurring aerosols. The setup time for a measurement is approximately one minute.

AEROSOLS - At any time when the aerosol backscatter is strong enough to provide a usable signal, the aerosol backscatter value is accessible from the signal spectrum. If the velocity is very small, extracting that value can be quite difficult.

We have experimented with a frequency-modulated, continuous-wave (FM-CW) technique to measure velocity-independent backscatter values. It turns out that FM-CW modification of a Doppler lidar is operationally difficult because of problems in linearizing the frequency sweep. Developing pulsed modifications to the lidar should increase the system's effectiveness and ease in backscatter measurement.

One important application of the backscatter measurement is to determine the thickness of the mixed layer for urban ventilation factor monitoring. It is important to note that the aerosol backscatter at 10.6 μm does not by itself measure aerosol concentration or mass loading. The relation between backscatter and concentration depends on the aerosol size distribution and refractive index. The infrared backscatter is an important contributor to remote measurement of aerosol concentration.

STACKS - Visual density of a stack plume does not guarantee a strong lidar signal. Actual measurements on coal-fired power plant plumes at 400 to 600 m range showed signal-to-noise ratios of 15 dB and greater. Signal intensity from the test stack varied more than 10 dB over a few minutes, presumably because of varying burner loads or tube cleaning. We did not compare in-stack monitors and the lidar because demonstration of feasibility was the only objective. Full scale tests should be based on the improved lidar capabilities of offset local oscillator (for sign determination) and perhaps differential Doppler (see next section).

A white plume from a cement plant with efficient emission controls was not visible to the lidar, even though it was visible to the eye. In this case, the emitted aerosols were less than 1 μm diameter, consistent with the observed plume color. For aerosols less than approximately 3 μm in diameter, the return intensity is proportional to the diameter to the fourth power. Thus, submicron particles give very weak backscatter for an infrared lidar.

The lidar is able to detect clouds to ranges of 2 km even though liquid water is strongly absorbing at 10.6 μm. It was not surprising therefore to observe 10 dB and stronger signals from cooling tower plumes. Detailed condensation plume studies await system improvements as in the case of stack studies.

VORTICES - A first step in demonstrating the potential of lidar tornado measurements is to measure smaller vortices. The largest dust devil velocity observed in a two-state field program was 22 ms^{-1} (4). Waterspout maximum velocities are still under analysis, but observed spectra (5) are generally similar to dust devil results for maximum winds. Tornados have not yet been measured by lidar.

DEVELOPING CAPABILITIES

It is worthwhile to indicate Doppler lidar capabilities that should soon be available for environmental monitoring. These expected improvements are based on the field-tested techniques outlined earlier in this presentation.

DIFFERENTIAL DOPPLER - By breaking up a large sensing beam into three or more smaller beams with interbeam convergence angles of 6 mrad, for example, it is possible to measure all three components of velocity at a single point (6). When this technique is applied to aerosol targets, significantly better wind measurements for environmental monitoring purposes should be available than are obtained with present systems.

Wind profiles in support of diffusion and urban ventilation applications measured by differential Doppler will not depend on assumptions of horizontal homogeneity and negligible vertical velocity. Time stationarity of approximately 60 seconds or time averaging for 15 minutes would still be required. For profile purposes, we envision a fixed, vertically-pointing system.

The differential Doppler technique measures the velocity component transverse to the nominal lidar axis, as well as along it. For low elevation angle views of stacks, the transverse component is generally the larger. Optical systems for non-vertical differential systems at long ranges could be quite bulky.

DATA PROCESSING - The currently used scanning spectrum analyzer has a duty cycle given by the resolution bandwidth divided by the full scan. For our application this duty cycle is between 0.3% and 1%, which rejects 99% or more of the available signal.

Much more signal is usable in situations where the required bandwidth is 5 MHz or less (<25 ms^{-1} velocity). In these cases, we are testing a digital autocorrelator to estimate the first three spectral moments. A chirped spectrum analyzer is also under investigation. The significance of these processing improvements is that measurements can be made in lower-aerosol environments or more rapidly than is now possible. Preliminary tests indicate a signal-to-noise improvement of 10 dB ±5dB for the correlator over the swept analyzer.

SIGN DETERMINATION - We have frequency-locked a small laser at 10 MHz offset from the lidar transmitter and used the system to measure the velocity component, including sign (toward or away), from a hard (non-aerosol) target.

One application of this capability is to large-turbulence, small-mean-velocity situations as in the case of stack effluents. Vertical velocity measurements in support of diffusion experiments under convective conditions require clear differentiation of upward and downward velocities.

SUMMARY

The infrared Doppler lidar technique for wind measurement has already proved its capability in a number of environmental sensing applications. System improvements are underway to increase the sensing capabilities of the lidar.

Measurements of wind profiles are relevant to many types of diffusion research and to monitoring urban ventilation, for example. Direct measurements of stack exit velocity are an important part of total mass loading assessment. Aerosol backscatter data are available as a side benefit.

Present profiling operations include 300 m altitude, 1 km range, and hemispherical scanning for a single component of the wind. Multi-component sensing with present systems requires a number of assumptions about the wind field. An important advantage of lidar measurements is the speed with which the equipment can be set up and data taken.

This work was supported in part by the Environmental Protection Agency under task EPA-IAG-D5 (E77BEB) and by the Nuclear Regulatory Commission under agreement AT(49-25)-1004.

REFERENCES

1. W. F. Herget, C. R. Miller, and C. M. Sonnenschein, "Remote Measurement of Power Plant Stack Effluent Velocity," in Applications of Laser Spectroscopy Conference (Optical Society of America), March 19-21, 1975.

2. M. J. Post and R. L. Schwiesow, "Temporal- and Spatial- Frequency Spectra for Atmospheric Aerosols," in Atmospheric Aerosols, Report NASA CP-2004, Dec. 13-15, 1976.

3. M. J. Post, R. L. Schwiesow, R. E. Cupp, D. A. Haugen, and J. T. Newman, "A Comparison of Anenometer- and Lidar-Sensed Wind Velocity Data," submitted to J. Appl. Met.

4. R. L. Schwiesow and R. E. Cupp, "Remote Doppler Velocity Measurements of Dust Devil Vortices," Appl. Opt., 15, No. 1, 1-2 (1976).

5. R. L. Schwiesow, R. E. Cupp, M. J. Post, R. F. Abbey, Jr., and P. C. Sinclair, "Velocity Structures of Waterspouts and Dust Devils as Revealed by Doppler Lidar Measurements," 10th Conf. on Severe Local Storms (Am. Met. Soc.), Oct. 18-21, 1977.

6. R. L. Schwiesow, R. E. Cupp, M. J. Post, and R. F. Calfee, "Coherent Differential Doppler Measurements of Transverse Velocity at a Remote Point," Appl. Opt., 16, No. 5, 1145-1150 (1977).

Scientific Monthly, Taipei, Taiwan, The Republic of China, Volume 9, 48-53, February, 1978 (In Chinese)

OPTICAL REMOTE SENSING ON TURBULENCE AND CROSS-WIND

Ting-i Wang

This paper is an introductory description of the ground-based optical remote sensing. First, we describe the basic principle of optical sensing for atmospheric turbulence and cross-wind. We then describe several practical instruments developed by the optical group of the Wave Propagation Laboratory. Finally, we point out the potential usage of these instruments.

Summaries of the 1978 International Symposium on Antennas and Propagation, Sendai, Japan, 493-495, 29-31 August 1978.

C–9–4 A FAST-RESPONSE OPTICAL SENSOR FOR MEASURING RAINFALL RATE AND RAINDROP SIZE DISTRIBUTION

Ting-i Wang, K. B. Earnshaw, and R. S. Lawrence
National Oceanic and Atmospheric Administration
Environmental Research Laboratories
Wave Propagation Laboratory
Boulder, Colorado 80303

I. SUMMARY

We have developed a laser-beam system to measure rain rate and drop-size distribution averaged over a 200 m horizontal path.[1] The technique correlates the laser-beam scintillations produced by the raindrops at two optical detectors separated vertically by a few centimeters. We first obtain the path-averaged drop-velocity distribution by computing the covariance, as a function of time delay, between the scintillations recorded by the two detectors. Assuming a known monotonic relation between a raindrop's size and its terminal velocity,[2] we convert the velocity distribution to drop-size distribution. Our earlier optical measurements have verified that path-averaged drop-size distribution of a steady rain follows a Marshall-Palmer distribution.[3,4] Total path-averaged rain rate is obtained by integrating the drop-size distribution using a suitable weighting function. Optically measured path-averaged rain rate agrees well with simultaneous tipping-bucket rain-gauge measurements.[3]

II. THE INSTRUMENT

Our prototype system consists of a laser transmitter, two line detectors and an analog correlator whose output feeds a computer that calculates precipitation quantities. The transmitter is a 4 mW He-Ne laser and optical collimator that produces a uniform beam 20 cm in diameter. The two receivers are horizontal linear detectors 25 cm long and 0.15 cm high with a variable vertical separation that is typically a few centimeters. To minimize interference from other light sources, filters exclude all light except a 0.002 μm passband centered at 0.6328 μm, and a telescopic aperture restricts the field of view to 2°. Correlation between the scintillations from the two receivers is accomplished in analog delay devices that multiply and integrate to obtain time-lagged covariance functions. In our prototype system, the scintillations were recorded on analog tape and processed by computer later, but implementing a real-time readout of precipitation quantities would be straightforward.

III. SAMPLE MEASUREMENTS

We operated our system on June 23, 1976 at Boulder, Colorado, during a storm that produced a mixture of rain and hail. Detector separation was 4 cm and path length was 200 m. Figure 1 shows the time-lagged covariance functions for nine 5-min averaging intervals. The peaks at 4 ms delay correspond to a vertical velocity of 10 m s^{-1}, which is the terminal velocity of the hail component, whereas the 9 ms peaks are caused by raindrops whose terminal velocity was 4.5 m s^{-1}. Near the end of this storm (1220-1225), the hail disappeared, whereas rain was still falling.

We analyzed another storm on August 2, 1976 for a 2 1/2-hour period. Raindrop-size distributions for each 42-sec interval are shown in Figure 2. Total rain rate is also indicated for each interval by the height of the vertical line at the left end of each distribution. Both the rain rate and the drop-size distribution changed rapidly during this storm. The heaviest rainfall tends to be correlated with larger drop size, except in the beginning of the storm, where large drops occurred with rates of only 7 mm hr^{-1}.

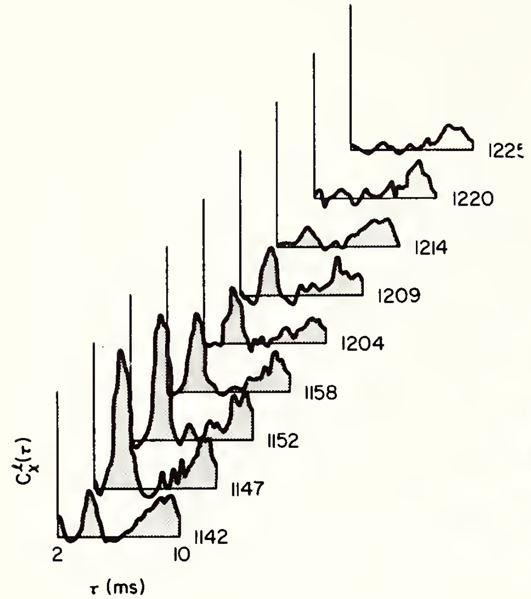

Fig. 1. The time-lagged covariance functions of the signals detected by two vertically separated line detectors with a separation of 4 cm on a 200-m path at Table Mountain during a mixture of rain and hail on June 23, 1976.

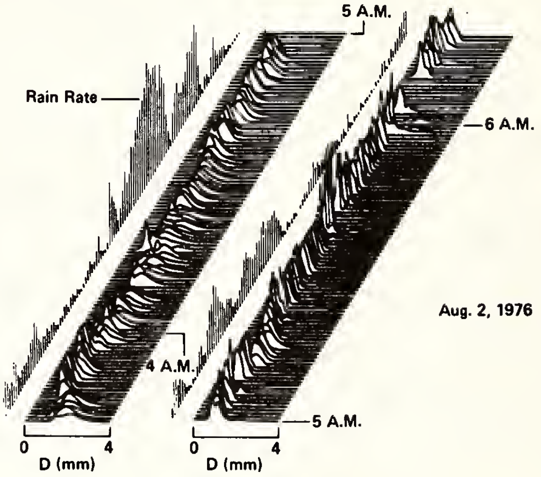

Fig. 2. The raindrop size distribution for every 42 seconds. The vertical axis is the relative fraction of rain rate contributed by drop-size intervals. The horizontal axis denotes the raindrop diameter. Total rain rate is also indicated for each interval by the height of the vertical line at the left end of each distribution.

Figure 3 compares the optically deduced rain rate during this storm with the rate measured by a single tipping-bucket rain gauge near the optical receiver. The agreement is good but might have been better if readings of several rain gauges along the path were averaged.

Figure 4 shows the mean raindrop size vs rain rate during this storm. The solid line shows the relation predicted by the Marshall-Palmer distribution.[4] The scatter of experimental points is substantial for rain rate less than 10 mm hr^{-1}, whereas a linear relationship falling somewhat below the Marshall-Palmer line is evident for the higher rates.

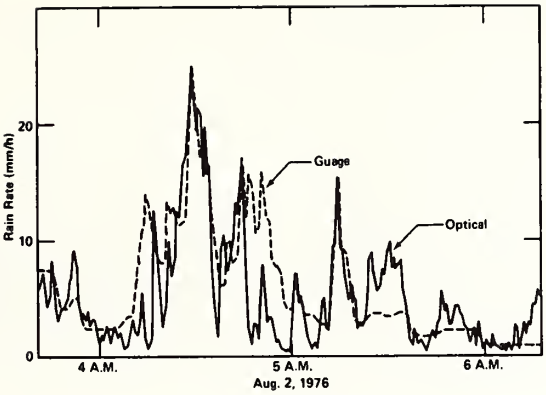

Fig. 3. A comparison between optically detected rain rates (solid-line) and rain rates measured by a tipping-bucket rain gauge near the receiving end of the path (dash-line).

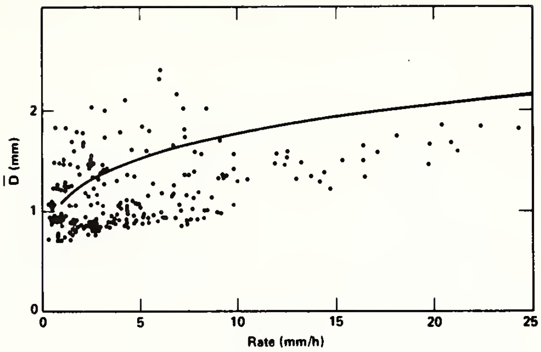

Fig. 4. The mean raindrop size as a function of rain rate. The solid-line indicates the mean drop-size if raindrops follow the Marshall-Palmer distribution.

IV. CONCLUSIONS

We have demonstrated an optical device that measures path-averaged rainfall rate and drop-size distribution. The technique offers the following advantages: 1) The measured quantities are path-averages and do not depend on variations whose spatial scale is smaller than the optical path length. 2) Prior knowledge of the drop-size distribution is not required to obtain total rainfall rate. 3) The actual path-averaged drop-size distribution can be measured. 4) Because spatial integration (path averaging) is used, shorter time integration is required and time resolution as short as 20 sec is possible.

V. REFERENCES

[1] T-i Wang and S. F. Clifford, J. Opt. Soc. Am. 65, 927 (1975).

[2] R. Gunn and G. D. Kinzer, J. Meteorol. 6, 243 (1949).

[3] T-i Wang, G. Lerfald, R. S. Lawrence, and S. F. Clifford, Appl. Opt. 16, 2236 (1977).

[4] T. S. Marshall and W. McK. Palmer, J. Meteorol. 4, 186 (1948).

Applied Optics, 17: 384-390, 1978.

Simplified optical path-averaged rain gauge

Ting-i Wang, K. B. Earnshaw, and R. S. Lawrence

It has previously been shown that the scintillations produced by raindrops falling through a collimated laser beam can be used to measure the drop-size distribution and the rainfall rate, both averaged over the path. We now present a theoretical analysis, verified by observation, showing that the variance of the scintillations detected by a line-detector measured at frequencies near 1 kHz is closely related to rain rate and is nearly independent of drop-size distribution. If only rain rate is desired, the variance type of optical rain gauge has several advantages over the earlier model. It could use a diverging beam, thus eliminating the practical difficulties of maintaining adjustment and pointing of a collimated beam. Furthermore, it is less sensitive to the presence of updrafts and downdrafts along the beam and can thus be used over rough terrain.

I. Introduction

Wang and Clifford[1] and Wang *et al.*[2] have presented a technique for measuring path-averaged rain parameters which utilizes the temporal–spatial covariance function of the rainfall-induced scintillations of a laser beam. One advantage of the technique is that it requires no prior assumption of the form of drop-size distribution, since path-averaged drop-size distribution is part of the measurement. The technique was successfully confirmed by experiment.[2] We now describe a simpler technique for measuring the path-averaged rain rate which utilizes the standard deviation of the rainfall-induced amplitude scintillation detected by a single line-detector. We discuss the reasons for using a line detector instead of a point detector, and then we compare the standard deviation technique with the covariance technique. Finally, we show sample measurements of path-averaged rain rate.

II. Amplitude Variance

Figure 1 illustrates the geometry of an incident plane wave propagating along the x direction and scattered by randomly located raindrops. We assume that the raindrops are spherical and that the wavelength λ of the incident wave is much smaller than the radius a of the raindrop. In the far field, the normalized amplitude scintillation χ induced by a raindrop located at coordinates (x,y,z), measured by a horizontal line-detector with an infinitesimal width, is expressed by Eq. (2) of Wang *et al.*,[2] i.e.,

$$\chi(x,y,z) = \begin{cases} -(\eta/k)(2\pi x/k)^{1/2}\sin[kz^2/(2x)+\pi/4]J_1(\eta z/x)/z; & \text{if } |y| < l/2 \\ 0 \quad ; & \text{if } |y| > l/2, \end{cases} \tag{1}$$

where $\eta = ka$ is the drop-size parameter, a is the drop radius, $k = 2\pi/\lambda$, and l is the length of the line-detector, extending in the horizontal (y) direction.

The variance of the amplitude scintillation detected by the single line-detector is $\sigma_\chi{}^2 = \langle\chi^2\rangle$, where the bracket represents the ensemble average. Using Eq. (1), replacing η/k by a, we have

$$\sigma_\chi{}^2 = \frac{2\pi}{kl}\int_0^L xdx\int a^2 dN_V(a,x) \times \int_{-\infty}^{\infty} dz\,\sin^2[\pi/4 + kz^2/(2x)]\,\frac{J_1{}^2(\eta z/x)}{z^2}, \tag{2}$$

where L is the pathlength.

In Eq. (2), $dN_V(a,x)$ is the differential number density of raindrops with radius a at path position x. The subscript V denotes the number density measured for a fixed volume. From Eq. (7) of Ref. 1, we have

$$dN_V(a,x) = \frac{dh(a,x)}{4.8\pi \times 10^6 a^3 v}, \tag{3}$$

where v is the terminal velocity of the drop with radius a, and $dh(a,x)$ is the differential rain rate contributed by raindrops with radius a at path position x. It can be shown (see Sec. IV, Ref. 1) that

$$dh(a,x) = h(x)p(a,x)da, \tag{4}$$

where $h(x)$ is the total rain rate at position x and $p(a,x)$ is the probability–density function of raindrop size at that position given by

---

The authors are with NOAA Environmental Research Laboratories, Wave Propagation Laboratory, Boulder, Colorado 80302.

Received 30 June 1977.
0003-6935/78/0201-0384$0.50/0.
© 1978 Optical Society of America.

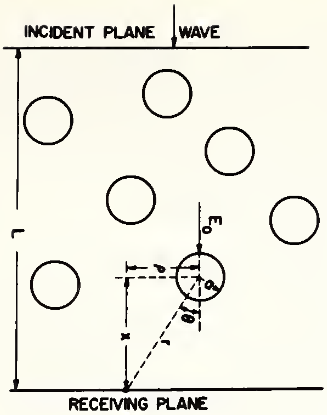

Fig. 1. Geometry of an incident plane wave scattered by randomly placed raindrops of radius a, where $\rho = (y^2 + z^2)^{1/2}$.

$$p(a,x) = \frac{N_t(a,x)\frac{4}{3}\pi a^3}{\int_0^\infty da N_t(a,x)\frac{4}{3}\pi a^3} \tag{5}$$

[see Eq. (25), Ref. 1]. In Eq. (5), $N_t(a,x)$ is the number density of raindrops measured in a fixed time period. [The difference between the number densities $N_V(a,x)$ and $N_t(a,x)$ is discussed in detail in the Appendix of Ref. 2.].

Inserting Eqs. (3) and (4) into Eq. (2), we obtain

$$\sigma_\chi{}^2 = \frac{1.04 \times 10^{-9}}{kl} \int_0^L dx h(x) x \int_0^\infty da a^{-3/2} P(a,x) \times \int_{-\infty}^{\infty} dz [1 + \sin(kz^2/x)] \frac{J_1{}^2(\eta z/x)}{z^2}. \tag{6}$$

In obtaining Eq. (6), we used the relationship[3] $v = 200 \sqrt{a}$, where v is terminal velocity in m/sec, and a is drop radius in m [see Eq. (19) of Ref. 1]. Since it is easy to see that the contribution from the second term in the bracket is small compared with the first term, provided that $a \ll (\lambda x)^{1/2}$, we have

$$\sigma_\chi{}^2 = 8.84 \times 10^{-10} l^{-1} \int_0^L h(x) dx \int_0^\infty da a^{-1/2} p(a,x). \tag{7}$$

In obtaining Eq. (7), we have used the relationship

$$\int_{-\infty}^{\infty} dz \frac{J_1{}^2(z)}{z^2} = \frac{8}{3\pi}. \tag{8}$$

For the purpose of comparison it is necessary to know the variance of the amplitude scintillation detected by a single point detector. This is given by [Eq. (23) of Ref. 1]

$$\sigma_p{}^2 = 5.22 \times 10^{-10} \int_0^L dx h(x) \int_0^\infty da a^{-3/2} p(a,x). \tag{9}$$

Inserting Eq. (5) for $p(a,x)$ into Eqs. (9) and (7), respectively, using the relationships $N_t(a) = N_V(a)v(a)$ and $v(a) \sim \sqrt{a}$, we obtain, for a point detector,

$$\sigma_p{}^2 \sim \int_0^L dx h(x) \frac{\int_0^\infty da a^2 N_V(a,x)}{\int_0^\infty da a^3 N_t(a,x)}, \tag{10}$$

and, for a line detector,

$$\sigma_\chi{}^2 \sim \int_0^L dx h(x) \frac{\int_0^\infty da a^3 N_V(a,x)}{\int_0^\infty da a^3 N_t(a,x)}, \tag{11}$$

The denominator of both Eqs. (10) and (11) is proportional to the total amount of precipitation at path position x. The variance for a point detector is proportional to the total cross-section area of raindrops in a fixed volume, because the strength of the drop-induced diffraction pattern is proportional to the cross-section area of the raindrops. By contrast, the variance for a line detector is proportional to the total water content in a fixed volume. The difference between the signals detected by a point detector and by a line detector can be explained by Fig. 2. When a raindrop-induced diffraction pattern sweeps through a point detector, the interference fringes can be detected by the point detector as long as the detector is inside the pattern. The intensity detected is proportional to the cross-section area of the raindrop. However, for a line detector, the detected signal is an average over the whole line and so is sensitive only to the central part of the diffraction pattern where the fringes are horizontal. This can also be seen from Eq. (1). When the center of the diffraction pattern is outside the line detector (i.e., $|y| > l/2$), there is very little contribution to the detected signal from the outside fringes of the pattern. Hence, for a line detector, there is almost no discrimination between large and small drops as long as the center of the diffraction pattern passes across the line detector. On the other hand,

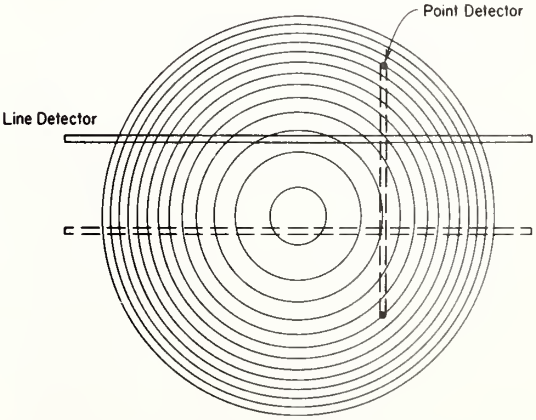

Fig. 2. The raindrop-induced diffraction pattern at the receiving plane. Point-detector and line-detector geometries are shown for comparison.

for a point detector the signal will depend on the separation between the detector and the center of the diffraction pattern of raindrops. Since the size of the pattern is inversely proportional to the drop radius, the intensity scintillation detected by a line detector has one more linear dependence on the drop size compared with that detected by a point detector, which explains the difference between Eqs. (10) and (11).

From Eq. (11), the raindrop-induced amplitude scintillation of a line detector is proportional to the path-averaged total water content per unit volume M, and that differs from the path-averaged rainfall rate by only a terminal-velocity dependence. This is a weak dependence,[3] proportional to the square root of the drop size.

To demonstrate how to obtain the path-averaged rain rate, we assume that the raindrop size distribution follows the Marshall-Palmer model,[4] i.e.,

$$N_V(a,x) = N_o \exp[-2\Lambda(x)a], \tag{12}$$

where N_o is the value for $a = 0$ and $\Lambda(x)$ is a function of rainfall rate $h(x)$. It has been reported[4] that

$$N_o = 8 \times 10^6 \text{ m}^{-4}, \tag{13}$$

and that

$$\Lambda(x) = 4100 h(x)^{-0.21} \text{m}^{-1}, \tag{14}$$

where $h(x)$ is the rainfall rate in mm/h. The number density is $N_t(a) = N_V(a)v(a)$. Inserting Eqs. (12) and (14) into Eq. (11), we obtain

$$\sigma_\chi{}^2 = 4.13 \times 10^{-8} l^{-1} \int_0^L h^{0.895}(x)dx \simeq 4.13 \times 10^{-8} l^{-1} L h^{0.895}, \tag{15}$$

or

$$h = 1.78 \times 10^8 (L/l)^{-1.117} (\sigma_\chi)^{2.235}, \tag{16}$$

where h is the path-averaged rain rate in mm/h, and l and L are in meters. Although Eq. (16) is obtained by assuming that the drop-size distribution follows a Marshall-Palmer distribution, the dependence is not critical. From Eq. (15), it is evident that the path-weighting function is roughly uniform.

III. Temporal Power Spectrum

One problem involved in measuring the path-averaged rain rate from the variance of the amplitude scintillation is that turbulent variations of refractive index produce scintillations that contaminate the rain-induced scintillation. This is especially true at frequencies below 500 Hz. In order to separate the contributions from turbulence and from rain, a temporal-frequency filter must be applied to the signal before the variance measurement is made. To choose this filter, we first calculate the temporal power spectrum of the rain-induced amplitude scintillations measured by a single line detector. The spectrum is defined by

$$\omega_\chi(f) \equiv \int_{-\infty}^{\infty} \exp(-i\omega\tau) c_\chi(\tau) d\tau, \tag{17}$$

where $c_\chi(\tau)$ is the temporal autocovariance function of the amplitude scintillation. Following the development of Secs. II and III of Ref. 1, we obtain the time-lagged autocorrelation function of the rain induced amplitude scintillation of a single line detector, i.e.,

$$\begin{aligned} C_\chi(\tau) = \frac{2\pi}{kl^2} \int_0^L xdx \int_0^\infty a^2 dN_V(a,x) \\ \times \int_{-l/2}^{l/2} dy \int_{-\infty}^{\infty} dz \sin[kz^2/(2x) + \pi/4] \\ \times \sin[k(z + v\tau)^2/(2x) + \pi/4] \frac{J_1(\eta z/x)}{z} \frac{J_1[\eta(z + v\tau)/x]}{(z + v\tau)}. \end{aligned} \tag{18}$$

Inserting Eqs. (3), (4), and (18) into Eq. (17) and performing the integration over y, we obtain

$$\omega_\chi(f) = 2.08 \times 10^{-9} k^{-1} l^{-1} \int_0^L dxxh(x)(I_1 + I_2), \tag{19}$$

where

$$\begin{aligned} I_1 = \int_0^\infty daa^{-3/2} p(a,x) \int_{-\infty}^{\infty} dz \int_0^\infty d\tau \cos(2\pi f\tau) \\ \times \cos\left(\frac{kzv\tau}{x} + \frac{kv^2\tau^2}{2x}\right) \frac{J_1(kaz/x)}{z} \frac{J_1[ha(z + v\tau)/x]}{z + v\tau}, \end{aligned} \tag{20}$$

and

$$\begin{aligned} I_2 = \int_0^\infty daa^{-3/2} p(a,x) \int_{-\infty}^{\infty} dz \int_0^\infty d\tau \cos(2\pi f\tau) \\ \times \sin\left(\frac{kz^2}{x} + \frac{kzv\tau}{x} + \frac{kv^2\tau^2}{2x}\right) \frac{J_1(kaz/x)}{z} \frac{J_1[ka(z + v\tau)/x]}{z + v\tau}. \end{aligned} \tag{21}$$

In obtaining Eqs. (20) and (21), we used the relationship between the drop radius and the terminal velocity given by $v = 200\sqrt{a}$. If we assume that the Fresnel-zone size $(\lambda x)^{1/2}$ is much larger than the drop size a (a reasonable assumption for $x > 10$ m in the optical band and $a \sim 1$ mm), the integrations over τ and z in Eqs. (20) and (21) can be obtained by the method of stationary phase at $\tau = -z/v \pm \omega x/(kv^2)$ and $z = \mp\omega x/(kv)$, respectively. (See Sec. V and Appendix II of Ref. 1 for details of the restrictions on the application of the method of stationary phase.) Accordingly, we obtain

$$\left.\begin{matrix} I_1 \\ I_2 \end{matrix}\right\} = \frac{\pi k}{100x} \int_0^\infty da \frac{J_1{}^2(2\pi fa/v)}{(2\pi fa/v)^2} p(a,x) \begin{cases} \times 1 \\ \times \cos[4\pi^2 f^2 x/(kv^2)] \end{cases} \tag{22}$$

Inserting Eq. (19) into Eq. (16) gives

$$\begin{aligned} \omega_\chi(f) = \frac{2.08\pi \times 10^{-11}}{l} \int_0^L dxh(x) \int_0^\infty dap(a,x) \frac{J_1{}^2(2\pi fa/v)}{(2\pi fa/v)^2} \\ \times \{1 + \cos[4\pi^2 f^2 x/(kv^2)]\}. \end{aligned} \tag{23}$$

To see how sensitively the temporal power spectrum depends on drop-size distribution, we assume that the rain rate is uniform along the path [i.e., $h(x) \equiv h$ and $p(a,x) = p(a)$]. Then Eq. (23) can be simplified as

$$\begin{aligned} \omega_\chi(f) = \frac{2.08\pi \times 10^{-11} hL}{l} \int_0^\infty dap(a) \frac{J_1{}^2(\pi f\sqrt{a}/100)}{(\pi f\sqrt{a}/100)^2} \\ \times \left[1 + \frac{\sin(\pi^2 \times 10^{-4} f^2 k^{-1} a^{-1} L)}{\pi^2 \times 10^{-4} f^2 k^{-1} a^{-1} L}\right]. \end{aligned} \tag{24}$$

For the special case where the drop-size distribution follows a Marshall-Palmer model, we have

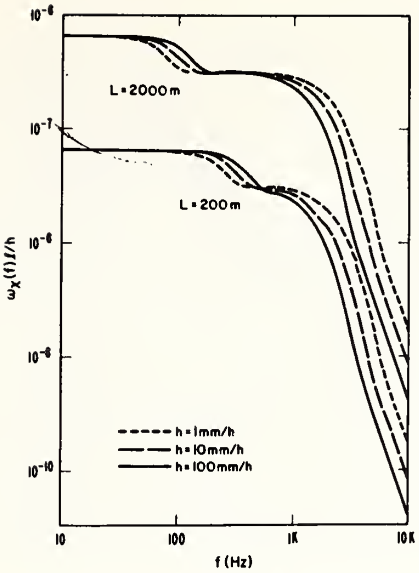

Fig. 3. Temporal power spectra, normalized to rain rate, of the amplitude scintillation induced by rainfall on a line detector. The drop-size distribution is assumed to follow a Marshall-Palmer model (l = length of the detector in m).

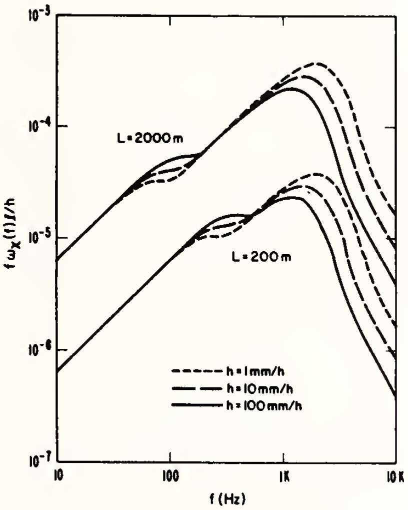

Fig. 4. Frequency distribution of energy of the temporal power spectra shown in Fig. 3.

$$\omega_\chi(f) = \frac{5.62 \times 10^{-12} hL}{l} \times \int_0^\infty da' a'^{7/2} e^{-a'} \frac{J_1{}^2[3.47 \times 10^{-4} f a'^{1/2} h^{0.105}]}{[3.47 \times 10^{-4} f a'^{1/2} h^{0.105}]^2} \times \left[1 + \frac{\sin(8.09 h^{-0.21} f^2 k^{-1} a'^{-1} L)}{(8.09 h^{-0.21} f^2 k^{-1} a'^{-1} L)}\right], \quad (25)$$

where $a' = 8200 h^{-0.21} a$. Equation (25), normalized to rain rate, is plotted in Fig. 3 for rainfall rates h of 1, 10, and 100 mm/h. The terminal velocity is proportional to the square root of the drop size, and the cutoff frequency is on the order of the ratio of the velocity to the radius of the raindrops, i.e., $a_0{}^{-1/2}$, where a_0, the mean drop size, is proportional to $h^{0.21}$ for a Marshall-Palmer distribution. Since a smaller rainfall rate has smaller drops, the temporal power spectrum has more high-frequency content. To see the true frequency distribution of energy, Fig. 4 shows the normalized temporal power spectrum $f\omega_\chi(f)l/h$. It is obvious that for a smaller mean size a_0, or a smaller rainfall rate, the peak power is at a higher frequency. Again, the frequency of the peak power is proportional to $a_0{}^{-1/2}$ or $h^{-0.105}$. For pathlengths L varying from 200 m to 2 km, the spectra are similar except that the low-frequency bump moves to a lower frequency proportional to $L^{-1/2}$.

Note that the variance and the temporal power spectrum of the log-amplitude scintillations are not dependent on the wavenumber k as long as the wavelength is small compared with the sizes of raindrops. Furthermore, all of the above results are based on the far-field assumption, i.e., $x \gg 4a^2/\lambda$. If we assume that the radius of the raindrops is 1 mm and $\lambda = 0.63\ \mu$m, then $4a^2/\lambda = 6.3$ m. Hence all drops except those very close to the detector are sufficiently distant to satisfy the far-field condition.

The results plotted in Figs. 3 and 4 are based on the assumption that the rainfall rate is uniform along the path. While this is not true for a practical case, we found from Figs. 3 and 4 that the temporal power spectra are quite insensitive to rainfall rate. It seems reasonable, therefore, to replace the path dependent rainfall rate $h(x)$ by the path-averaged rainfall rate h in Eq. (25), and we can show that the changes in the temporal power spectrum due to this substitution will be small.

IV. Filtered Amplitude Variance

Figures 3 and 4 show that the low frequency region of the temporal power spectrum of rain-induced scintillations detected by a line detector is proportional to the path-averaged rain rate regardless of the drop-size distribution. However, observation of this portion of the spectrum will be contaminated by contributions from turbulence-induced scintillations. To discriminate between the contributions from turbulence and from rain-induced scintillation, some filtering must be used. In the high frequency region, the spectrum becomes sensitive to rain rate (or drop-size distribution). This is because the diffraction pattern is smaller (hence, has a lower frequency response) for larger drops. In this region, the advantage of a line detector over a point detector (see Sec. II) vanishes, and the spectra coincide with the case of a point detector.

It is easy to show that, in the high frequency region ($f \geq 500$ Hz), the second term in the brackets of Eq. (24) can be ignored. The filtered amplitude variance is given by

$$\sigma_f{}^2 = \frac{2.08\pi \times 10^{-11} hL}{l} \int_0^{\infty} dap(a) \int_{f_1}^{f_2} df \frac{J_1{}^2(\pi f\sqrt{a}/100)}{(\pi f\sqrt{a}/100)^2}, \tag{26}$$

where f_1 = low cutoff frequency and f_2 = high cutoff frequency. For $f_1 < f_2 \leq 1.5$ kHz, the Bessel function in Eq. (26) could be approximated by

$$\frac{J_1{}^2(x)}{x^2} \simeq \frac{1}{4}(1 - x^2/4). \tag{27}$$

Inserting Eq. (27) into Eq. (26) and performing the integration over f give

$$\sigma_f{}^2 = 1.63 \times 10^{-11} hLl^{-1}(f_2 - f_1) \times \left[1 - \frac{\pi(f_1{}^2 + f_1f_2 + f_2{}^2)}{12 \times 10^4} \int_0^{\infty} daap(a)\right]. \tag{28}$$

In obtaining Eq. (28), we have used the identity

$$\int_0^{\infty} dap(a) \equiv 1.$$

For a Marshall-Palmer distribution, Eq. (28) reduces to

$$\sigma_f{}^2 = 1.63 \times 10^{-8} hLl^{-1}(f_2 - f_1)[1 - 0.0451h^{0.21}(f_1{}^2 + f_1f_2 + f_2{}^2)], \tag{29}$$

where f_1 and f_2 are in kHz. The results of the filtered standard deviation of the amplitude scintillation for various values of f_1 and f_2 vs $h^{1/2}$ are shown in Fig. 5. In the low frequency region, the standard deviation σ_f is linearly proportional to $h^{1/2}$. This dependence indicates that the measurement is independent of the drop-size distribution. However, this information is contaminated by the turbulence-induced scintillation. The higher the frequency band, the more nonlinearity appears in the relationship between σ_f and $h^{1/2}$ and the more dependent the measurements become on drop size. (For comparison, the point-detector case is also plotted in Fig. 5.)

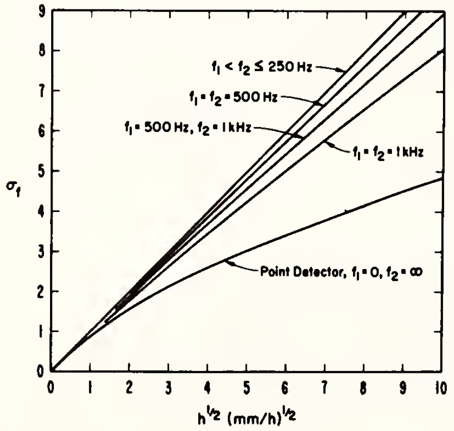

Fig. 5. Bandpassed filtered standard deviation of the amplitude scintillation induced by rainfall on a line detector vs (path-averaged rain rate)$^{1/2}$. f_1 = low cutoff frequency; f_2 = high cutoff frequency.

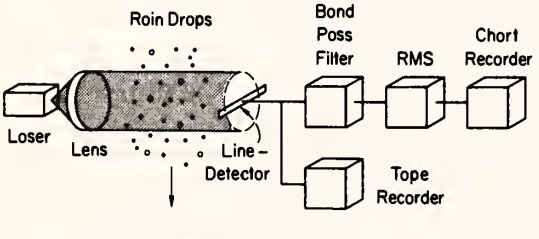

Fig. 6. Schematic diagram of the prototype optical rain gauge.

To improve linearity, we wish to use as low a frequency band as possible. But we have found that, even in the 500-Hz to 1-kHz band, contamination by turbulence scintillation cannot always be ignored, particularly when the wind is strong. Therefore, we are forced to use a narrowband filter at 1 kHz. Measurements of path-averaged rain rate at this frequency depend only slightly on drop-size distribution.

V. Experimental System and Results

A schematic diagram of the prototype system appears in Fig. 6. The transmitter is a 4-mW He–Ne laser followed by an optical system that expands the beam to produce a collimated beam 20 cm in diameter. The receiver is a horizontal line detector 25 cm long and 0.15 cm high. The 0.15-cm height of the line detector will average some high frequency signals producing a cutoff frequency of the order of v/d, where v is the velocity of the drop pattern and d is the height of the detector. If we assume that the terminal velocity of the most effective drop size (a = 1 mm) is 6 m/sec, the cutoff frequency is about 4 kHz, comfortably higher than the 1-kHz frequency of interest. Interference filters with a passband of 0.002 μm are used. Also, multiple field stops are used to exclude background light. The detected scintillation signal passes through a bandpass filter, and its rms value is recorded on a chart recorder.

The system was used during the summer of 1976 on a 200-m flat path at Table Mountain, a mesa located 12 km north of Boulder, Colorado. A tipping-bucket rain gauge, which sent a pulse to a chart recorder for each 0.25 mm of accumulated rainfall, was located under the path at 15 m from the receiver. More than 20 h of rain data were recorded. Two 3-h sections with various rain rates were selected to test the technique against theoretical expectations.

The measured standard deviation of the amplitude scintillations is shown by the solid lines in Figs. 7 and 8. In these figures, the dashed lines are the quantity $h^{1/2}(1 - 0.135h^{0.21})^{1/2}$, where h is the rain rate measured by a tipping-bucket rain gauge. From Eq. (29), for $f_1 = f_2 = 1$ kHz, this quantity should be proportional to the standard deviation σ_f. Because the rain rate measured by a tipping bucket is a point measurement while the optical measurement is a path average, a 40-sec time constant was used on both gauge and optical measurements in Fig. 8 and on the upper graph of Fig. 7. The

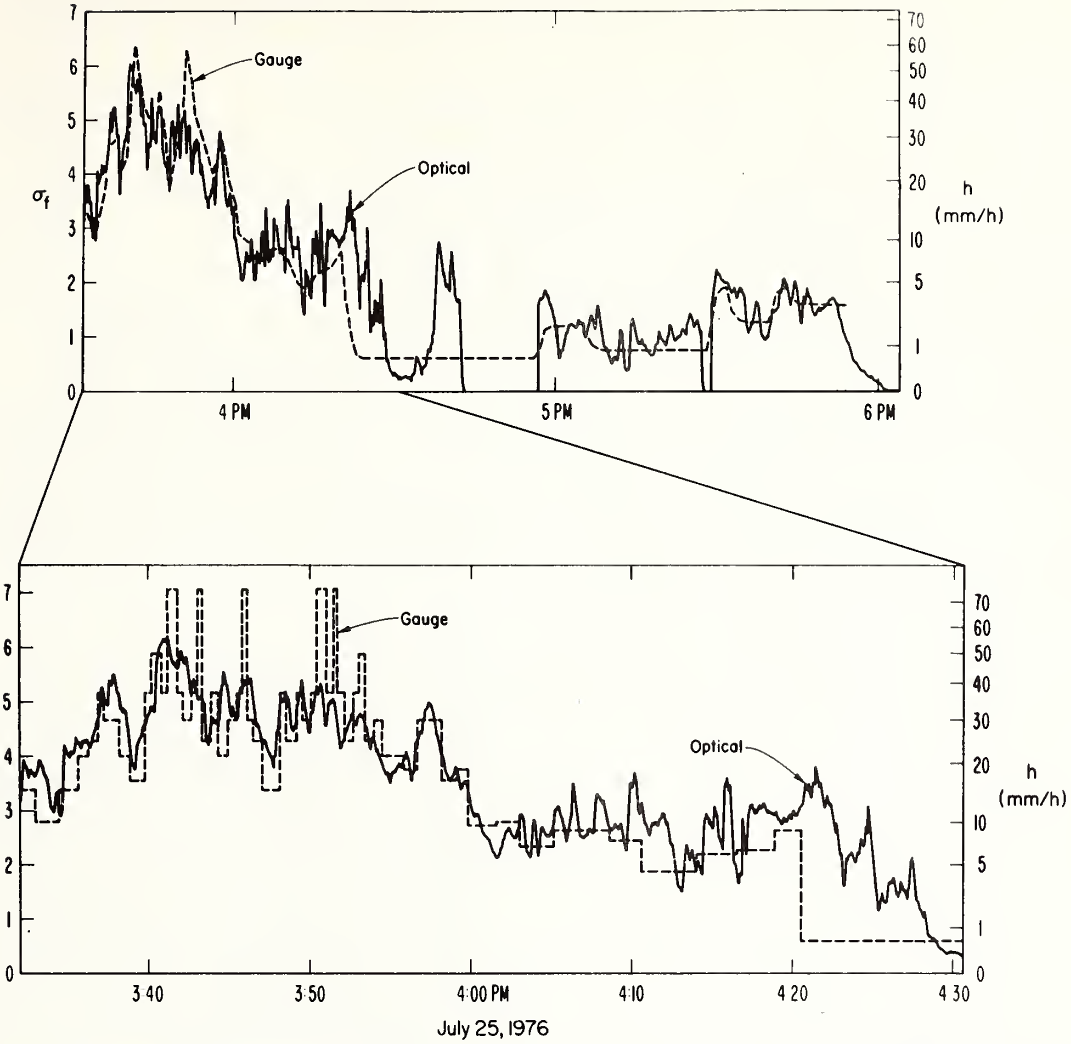

Fig. 7. The time variation of rain rates measured by a tipping-bucket rain gauge and by an optical rain gauge on 25 July 1976. The time scale of the lower diagram is expanded.

vertical scale, σ_f is arbitrarily adjusted to give the best linear regression with tipping-bucket data. The linear regression of these two quantities is shown in Fig. 9. For high rain rate ($h \gtrsim 5$ mm/h), the results are plotted for a fixed 1-min time constant (shown by dots in Fig. 9). For low rain rate, the time resolution of the tipping-bucket rain gauge is insufficient to compare with the optical measurements. We decided to take the average of the optical data between tips of the tipping-bucket gauge and to plot this against the tipping-bucket gauge reading (shown by circles in Fig. 9). In all three figures, the agreement between the rain gauge and the optical measurements is good and might have been further improved by using several rain gauges deployed along the path. For a detailed comparison, the heavy rain-rate section of the 25 July 1976 data is expanded and shown in the lower graph of Fig. 7. A 40-sec time constant is used on the optical data, but no smoothing is applied to the rain-guage data. It is clear, in the heavy-rate section, that the gauge measurements have more variation than the optical measurements. This is because the tipping-bucket values represent point measurements while the optical measurements are path averaged.

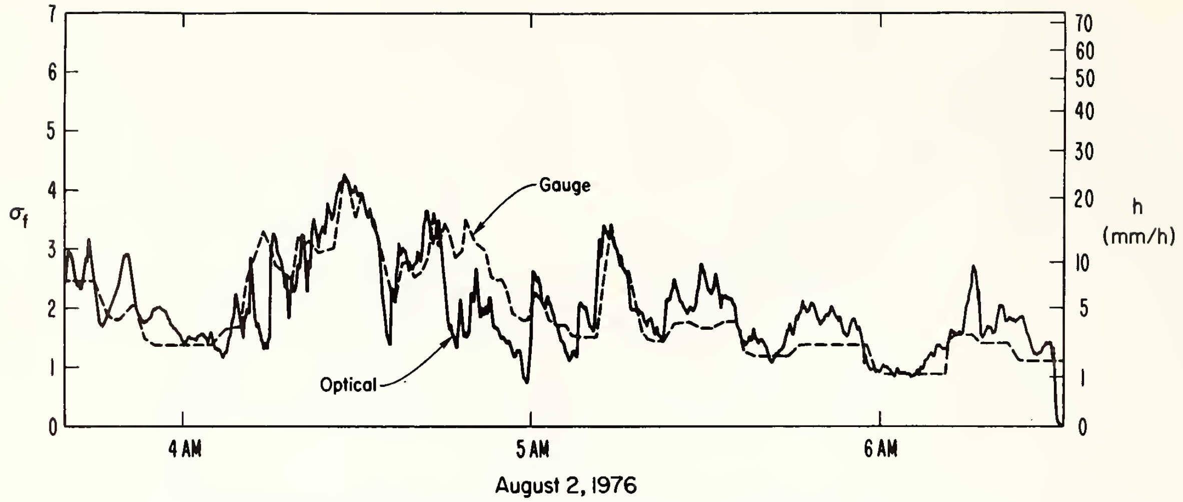

Fig. 8. The time variation of rain rates measured by a tipping-bucket rain gauge and by an optical rain gauge on 2 August 1976.

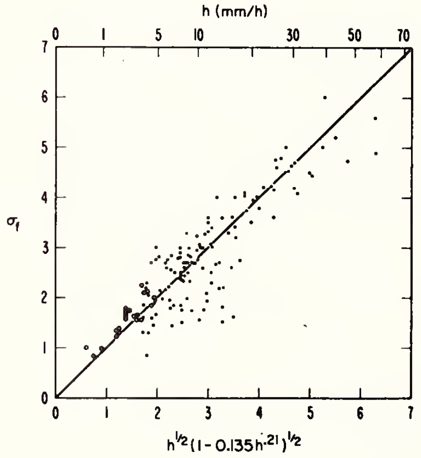

Fig. 9. Filtered standard deviation vs $h^{1/2}(1-0.135h^{0.21})^{1/2}$ (see detail in text) of Figs. 7 and 8. The straight line shows the best linear regression fit. Dot: 1-min averaging time constant; circle: averaged value between tips of the tipping-bucket rain gauge.

VI. Conclusions

We have demonstrated that the path-averaged rain rate can be measured by using the variance (or standard deviation) of the rainfall-induced amplitude scintillation detected by a single line detector. Comparing this single-detector variance technique to the two-detector temporal–spatial covariance technique,[2] the rain rate obtained from single-detector variance is dependent on drop-size distribution, though the dependence is weak (see Fig. 5). However, the new method has several advantages. The instrument is simpler and less expensive, and the construction of the source is less critical than for the two-detector instrument which requires a well-collimated beam. Furthermore, the measurement of the path-averaged rain rate by the new technique is less sensitive to vertical wind. Accordingly the path for the variance technique could be high above the ground (e.g., from mountain top to mountain top) or a slant path. This feature permits the new technique to be used in various geographic areas, especially in the mountainous terrain. We believe this to be a simple and potentially useful device for measuring the path-averaged rain rate.

This work was partially supported by the U.S. Army Electronics Command, Atmospheric Sciences Laboratory, White Sands, N. Mex. The ASL Scientific Monitor was T. Pries.

The authors are indebted to T. G. Cumberland and R. G. Gruenke for their effort on instrumentation and data analysis.

References

1. T-i. Wang and S. F. Clifford, J. Opt. Soc. Am. 65, 927 (1975).
2. T-i. Wang, G. Lerfald, R. S. Lawrence, and S. F. Clifford, Appl. Opt. 16, 2236 (1977).
3. R. Gunn and G. D. Kinzer, J. Meteor. 6, 243 (1949).
4. T. S. Marshall and W. Mck. Palmer, J. Meteor. 4, 186 (1948).

Summaries of the 1978 International Symposium on Antennas and Propagation, Sendai, Japan, 497-500, 29-31 August 1978.

C-9-5

AN OPTICAL CROSS-WIND PROFILER

Ting-i Wang and G. R. Ochs
National Oceanic and Atmospheric Administration
Environmental Research Laboratories
Wave Propagation Laboratory
Boulder, Colorado 80303

I. INTRODUCTION

We have previously reported the development of a laser-beam instrument that measures the average wind across an optical path by processing the scintillations caused by natural atmospheric refractivity fluctuations.[1] The scintillations recorded by detectors spaced a few centimeters apart are cross-correlated, and the path-averaged cross wind is derived from the slope of the covariance function at zero time lag. Theoretical calculations have shown that such a path average contains a weighting function that emphasizes different portions of the path, depending on the separation between the detectors.[1] Thus, by varying the detector separation, we could, in principle, emphasize any desired part of the optical path; however, the practical utility of such a system for path profiling is limited because the true profile is "smeared" by a rather broad weighting function.

Further theoretical and experimental work has shown that it is possible to sharpen the path-weighting function by employing an extended incoherent light source and larger receiving apertures. Furthermore, the location of the weighting function along the path can be adjusted by varying the ratio of the source to receiving apertures.[2,3] Even better resolution along the path can be obtained by linearly combining data obtained with different weighting functions using different transmitter-to-receiver aperture ratios. Figure 1 shows such a set of weighting functions calculated from linear combinations of weighting functions for different transmitter/receiver aperture ratios.

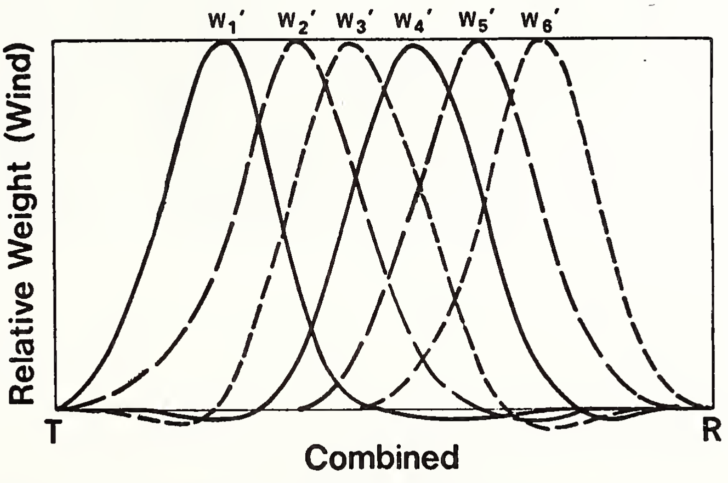

Fig. 1. The wind path-weighting functions using linear combinations of the weighting functions obtained by six transmitter-receiver pairs.

In principle, then, improved cross-wind profiling should be possible with an incoherent optical system in which one or both apertures are variable. Another advantage of extended incoherent sources over coherent illumination is that scintillation-saturation is largely eliminated. To test this concept, we made wind measurements with a prototype profiler that uses six aperture ratios.

II. THE INSTRUMENT

The transmitter consists of two incoherent light sources 8.4 cm and 27.9 cm in diameter. Each uses a quartz-iodine lamp. The smaller source uses a frosted bulb at the focus of a concave mirror; the larger source uses a separate piece of frosted glass between the bulb and a Fresnel lens to obtain uniform aperture illumination.

The receiver, shown in Figure 2, consists of three pairs of concave mirrors 15.2, 9.8 and 6.7 cm in diameter with two photodiodes at each focus that integrate the illumination over each aperture. The field of view of each photodiode is restricted by masks so that one of each pair sees one of the sources and the other photodiode sees the other source. In this way six transmitter-receiver aperture ratios are obtained with two transmitting apertures and three receiving apertures.

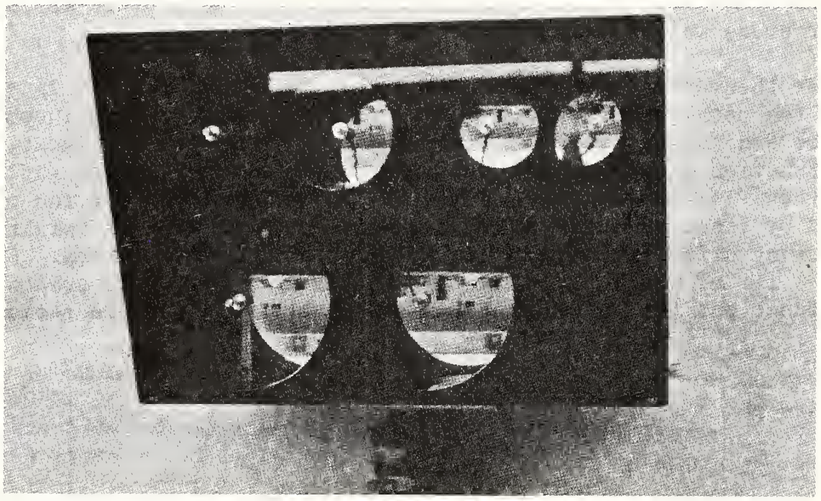

Fig. 2. A front view of the receiver showing the three pairs of different-sized apertures.

III. EXPERIMENTAL VERIFICATION

To test the profiler, we equipped a 500-m optical path with ten propeller anemometers to measure the transverse component of the horizontal wind. To smooth the anemometer data, we averaged them in pairs. By solving a system of equations involving the cross correlations among the wind fluctuations recorded at all the anemometers, as well as the optically measured weighted-average wind, we can recover the actual weighting function of the profiler. Details of this procedure are described in Reference 4. Figure 3 shows the measured weighting functions for the six aperture ratios, compared with the appropriate theoretical weighting functions. The error bars associated with the measurements represent the standard deviations of hourly measurements over a recording period at least 24 hours long. The error bars are large, even for a 24-hour period, because only the spatial variations of the transverse wind can be used to calculate the weighting function. The measured weights appear to be broader than the theoretical ones. This could be caused by intermittence of the refractive-index structure parameter (C_n^2) along the path, whereas the theory assumes a uniform C_n^2.

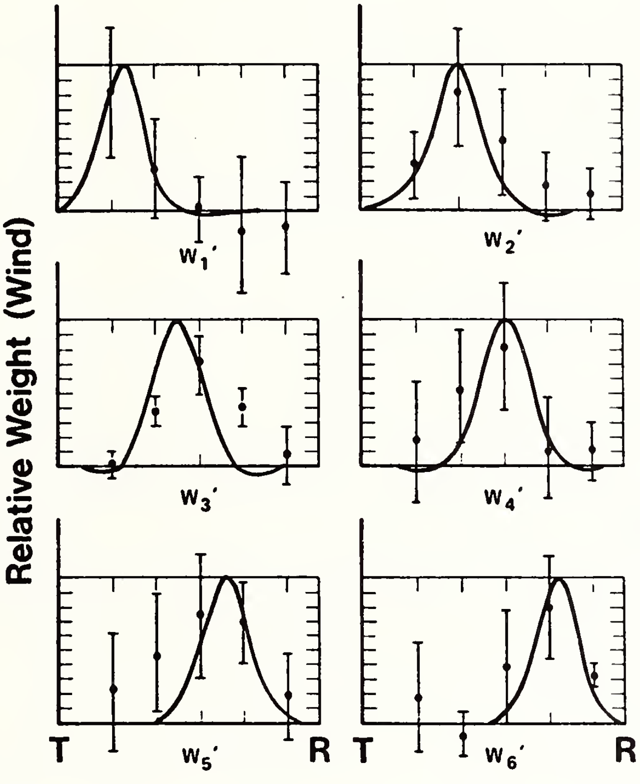

Fig. 3. Experimentally measured wind path-weighting functions of the six transmitter-receiver pairs after linear combination. The solid curves represent the theoretical weights. The dots are the measured weights averaged, in most cases, over 24-hr periods. The error bars represent the standard deviation of the hourly averages throughout the measuring period. The path length is 500 m.

IV. CONCLUSIONS

We have shown theoretically and have verified by measurement that, by changing the ratio of transmitting aperture to receiving aperture, the path-weighting function for cross wind can be moved along the middle two-thirds of the path. By linearly combining several measurements using different aperture ratios, we can further sharpen the weighting functions and provide greater profile resolution. A prototype instrument, designed on these principles, has performed satisfactorily.

V. REFERENCES

[1] R. S. Lawrence, G. R. Ochs, and S. F. Clifford, Appl. Opt. 11, 239 (1972).

[2] G. R. Ochs, S. F. Clifford, and Ting-i Wang, Appl. Opt. 15, 403 (1976).

[3] Ting-i Wang, G. R. Ochs, and S. F. Clifford, J. Opt. Soc. Am. 68, (1978).

[4] S. F. Clifford, G. R. Ochs, and Ting-i Wang, Appl. Opt. 14, 2844 (1975).

Journal of the Optical Society of America, 68: 334-338, 1978.

A saturation-resistant optical scintillometer to measure C_n^2

Ting-i Wang, G. R. Ochs, and S. F. Clifford
National Oceanic and Atmospheric Administration, Environmental Research Laboratories, Wave Propagation Laboratory, Boulder, Colorado 80302

(Received 27 June 1977)

This paper describes a new optical technique for measuring the refractive-index structure parameter C_n^2. By using relatively large incoherent transmitting and receiving optics, the scintillometer maintains its calibration and path-weighting function throughout the range of observed refractive turbulence values, even to the case of saturated scintillation.

I. INTRODUCTION

It is known[1-3] that the path-averaged refractive turbulence C_n^2 in the weak-scattering region can be measured by the irradiance (or amplitude) scintillation of a monochromatic wave propagating through the atmosphere. The variance of the log-amplitude σ_T^2 for a spherical wave propagating through a statistically homogeneous and isotropic refractivity field is given by[1]

$$\sigma_T^2 = 4\pi^2 k^2 \int_0^L dz \int_0^\infty dK K \Phi(K) \times \sin^2\left(\frac{K^2 z(L-z)}{2kL}\right), \quad (1)$$

where k is the wave number of the radiation, L is the path length, and $\Phi(K)$ is the three-dimensional spectrum of the refractive-index fluctuations. The most commonly accepted form of the spectrum of refractive turbulence is that of Kolmogorov,[4] i.e.,

$$\Phi(K) = 0.033\, C_n^2(z) K^{-11/3}. \quad (2)$$

Inserting Eq. (2) into Eq. (1), we obtain

$$\sigma_T^2 = 0.124\, k^{7/6} L^{11/6} \overline{C}_n^2, \quad (3)$$

where $\overline{C}_n^2$ is the path-averaged value of $C_n^2(z)$ with a weighting function $[(z/L)(1-z/L)]^{5/6}$. Equation (3), which is based on the first-order scattering theory, is applicable only as long as the integrated amount of refractive turbulence σ_T^2 is small, i.e., $\sigma_T^2 \leq 0.3$. As the strength of refractive turbulence increases, the scintillations saturate[4] and any scintillometer whose performance is based on the proportionality of σ_T^2 and $\overline{C}_n^2$ will fail. Besides the saturation effect, another difficulty of measuring $\overline{C}_n^2$ on short paths ($L < 300$ m) is that the weighting function and the calibration will vary with the microscale of the refractive turbulence l_0.

In this paper we derive the formulas that describe the performance of the optical C_n^2 sensor in strong turbulence and, based on this theory, describe the design and testing of an optical C_n^2 sensor that maintains its path-weighting function and calibration throughout the observed range of refractive turbulence values. The measurements are also independent of the microscale of the refractive turbulence so that the same technique may be used on short optical paths.

II. THEORY

To obtain the path-weighting function, we rewrite Eq. (1) in a more convenient form:

$$\sigma_T^2 = \int_0^L dz C_n^2(z) W(z), \quad (4)$$

where $W(z)$ is the path-weighting function for C_n^2, given by

$$W(z) = 4\pi^2 k^2 \int_0^\infty dK K \Phi(K) \sin^2\left(\frac{K^2 z(L-z)}{2kL}\right). \quad (5)$$

To include the effect of the microscale, we use the spectrum suggested by Tatarskii,[1] i.e.,

$$\Phi(K) = 0.033\, C_n^2(z) K^{-11/3} \exp(-K^2/K_m^2), \quad (6)$$

where $K_m = 5.92/l_0$. The resultant path-weighting functions are shown in Fig. 1. The solid-line curve represents the case when $l_0 = 0$. The dashed-line curve is the case for $l_0 = 0.435\,(\lambda L)^{1/2}$, which corresponds to $l_0 = 6$ mm for $L = 300$ m, and $\lambda = 0.6328\ \mu$m (He-Ne laser). Both the shape of the weighting function and the calibration (area under the curve) change. Because it is difficult to give the value of the microscale accurately, the effect of the microscale will introduce errors in the measurements of path-averaged C_n^2.

Recently, Clifford *et al.*[5] developed an equation for the log-amplitude covariance function in strong Kolmogorov turbulence,[4] i.e.,

$$C_\chi(\rho) = 2.94 \int_0^1 du\, \sigma_T^2(u) [u(1-u)]^{5/6} \int_0^\infty dy\, y^{-11/6} \sin^2 y \times \exp\{-\sigma_T^2 [u(1-u)]^{5/6} F(y)\} J_0\{[4\pi y u/(1-u)]^{1/2} \rho\}, \quad (7)$$

where $\sigma_T^2(u) = 0.124\, k^{7/6} L^{11/6} C_n^2(u)$, $u = z/L$ is the normalized path position, ρ is the separation between two detectors in Fresnel zones $(\lambda L)^{1/2}$, J_0 is the zero-order Bessel function of the first kind, and $F(y)$ is given by

$$F(y) = 7.02\, y^{5/6} \int_{0.7y}^\infty d\xi\, \xi^{-8/3} [1 - J_0(\xi)]. \quad (8)$$

Equation (7) can be written in a more convenient form:

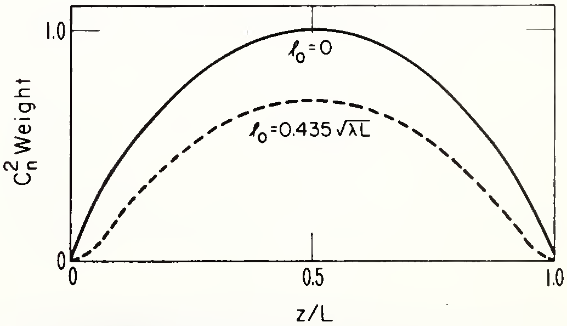

FIG. 1. The effect of the microscale on the weighting function of a point transmitter and detector system.

© 1978 Optical Society of America

$$C_\chi(\rho) = \int_0^1 du\, C_n^2(u) W(u), \tag{9}$$

where

$$W(u) = 0.365\, k^{7/6} L^{11/6} [u(1-u)]^{5/6} \times \int_0^\infty dy\, g(u,y) J_0 \{[4\pi y u/(1-u)]^{1/2} \rho\}, \tag{10}$$

and

$$g(u,y) = y^{-11/6} \sin^2 y \exp\{-\sigma_T^2 [u(1-u)]^{5/6} F(y)\}. \tag{11}$$

Equation (11) differs from the first-order scattering theory by only the exponential term. For weak turbulence this term can be neglected. Figure 2 illustrates the C_n^2-weighting functions as calculated from Eq. (10) for σ_T^2 ranging from 0.1 to 5. The C_n^2 calibration of the instrument is proportional to the area under the curves. For small values of σ_T^2 (≤ 0.1), the weighting function agrees with that calculated from first-order theory (see solid-line curve in Fig. 1). The change in shape of the weighting function and the decrease in area under the curve are pronounced at larger values of σ_T^2; this can be explained by noting that the most effective size of the turbulent eddies varies from Fresnel-zone size in the weak turbulence case to wave-coherence length[6] in strong turbulence. One way to avoid the change of weighting function and calibration is to devise an optical system that avoids observing the Fresnel-zone-size eddies. A system with spatially incoherent transmitter and receiver optics more than a Fresnel zone in diameter satisfies this requirement[7] because it biases the refractive-turbulence weighting toward larger sizes.

To generalize Eqs. (9) and (10) to the case of finite circular, incoherent transmitting and receiving apertures, the essential modification of the theory is to replace $g(u,y)$ with[7]

$$g'(u,y) = g(u,y) \left(\frac{2J_1\{[\pi y u/(1-u)]^{1/2}\, \alpha_r\}}{[\pi y u/(1-u)]^{1/2}\, \alpha_r}\right)^2 \times \left(\frac{2J_1\{[\pi y (1-u)/u]^{1/2}\, \alpha_t\}}{[\pi y (1-u)/u]^{1/2}\, \alpha_t}\right)^2, \tag{12}$$

where α_r and α_t are, respectively, the diameters of the receiver and transmitter normalized to a Fresnel zone for the optical path. To see what sizes of α_t and α_r are required so that saturation effects may be ignored, we rewrite Eq. (12) as

$$g'(u,y) = y^{-11/6} \sin^2 y A, \tag{13}$$

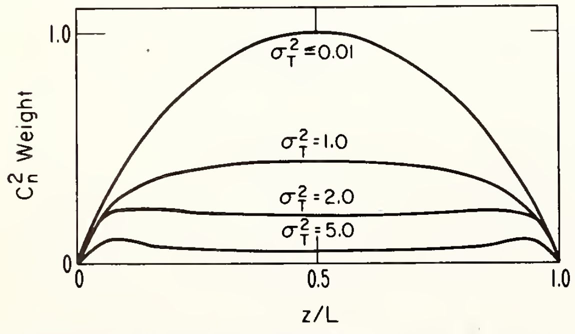

FIG. 2. The effect of saturation of scintillation on the weighting function of a point transmitter and detector system, where $\sigma_T^2 \doteq 0.124\, k^{7/6} L^{11/6} C_n^2$.

where

$$A \equiv \exp\left(\frac{-F(y)}{F(y_s)}\right) \left(\frac{2J_1[(y/y_r)^{1/2}]}{(y/y_r)^{1/2}}\right)^2 \times \left(\frac{2J_1[(y/y_t)^{1/2}]}{(y/y_t)^{1/2}}\right)^2, \tag{14}$$

$$y_r \equiv (1-u)/\alpha_r^2 \pi u, \tag{15}$$

$$y_t \equiv u/[\alpha_t^2 \pi (1-u)], \tag{16}$$

and

$$F(y_s) \equiv \{\sigma_T^2 [u(1-u)]^{5/6}\}^{-1}. \tag{17}$$

Clifford and Yura[6] gave an asymptotic expression for both $y \leq 1$ and $y \geq 1$, i.e.,

$$F(y) \simeq \begin{cases} 7.9 y^{5/6} & \text{if } \quad y \leq 1 \\ 7.9 y^{-5/6} & \text{if } \quad y \geq 1 \end{cases}. \tag{18}$$

In obtaining Eq. (18), we use the value of the cutoff $\alpha = 0.685$ (see Ref. 6 for details). Equation (18) indicates that the maximum value of $F(y)$ is 7.9. If $F(y_s) \gg 7.9$ in Eq. (14), the exponent is always small compared with unity. Hence the saturation effect can then be ignored. It can easily be shown that for $\sigma_T^2 < 0.3$, $F(y_s) \gg 7.9$. In this case, the first-order scattering theory is adequate. This conclusion agrees with observations.[5] For $F(y_s) \leq 7.9$, the saturation effect will be important if the exponent is larger than unity for the most important region of integration over y. If we assume that either y_r or y_t is less than one throughout the range of u integration, the region for which y makes a significant contribution over the integration of y is $y \leq 1$. In this case, $F(y)$ can be approximated by $7.9 y^{5/6}$. There are three scale sizes y_s, y_r, and y_t in Eq. (14). The term containing the smallest of them has the largest contribution to the covariance. Hence, if $y_s > y_r$ or $y_s > y_t$, i.e.,

$$0.084\, (\sigma_T^2)^{-6/5} u^{-1} (1-u)^{-1} > (1-u)/(\alpha_r^2 \pi u) \tag{19a}$$

or

$$0.084\, (\sigma_T^2)^{-6/5} u^{-1} (1-u)^{-1} > u/[\alpha_t^2 \pi (1-u)], \tag{19b}$$

the contribution of the exponential term can be ignored. In other words, the first-order scattering theory is adequate. Rearranging Eq. (19), we have

$$\alpha_r > 1.95 (\sigma_T^2)^{3/5} (1-u) \tag{20a}$$

or

$$\alpha_t > 1.95 (\sigma_T^2)^{3/5} u. \tag{20b}$$

The inequalities in Eq. (20) depend on path position u. However, if we combine the two inequalities, we obtain

$$\alpha_r + \alpha_t > 1.95 (\sigma_T^2)^{3/5}. \tag{21}$$

Equation (21) illustrates that for a sufficiently large size of transmitting aperture or receiving aperture, there will be no saturation effect even in strong integrated turbulence. The weighting function and the calibration will remain unchanged in both weak and strong refractive turbulence. For all the following calculations, we assume that Eq. (21) is always satisfied, hence the exponential term in Eq. (14) is ignored.

Besides getting rid of the saturation problem, there are some other advantages of using large incoherent transmitting

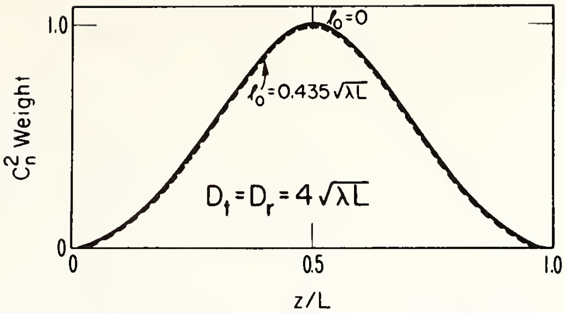

FIG. 3. The effect of the microscale on a finite transmitter and detector system $[D_t = D_r = 4(\lambda L)^{1/2}]$.

and receiving apertures. Because only the large eddy sizes will contribute to the measurements, the effect of inner scale length is small. Figure 3 illustrates this point. For both the transmitting and receiving apertures equal to four Fresnel zones the path-weighting function is plotted for $l_0 = 0$ (solid line) and for $l_0 = 0.435\ (\lambda L)^{1/2}$ (dashed line). The change with l_0 as shown in the point-source and point-detector case (see Fig. 1) is diminished. Hence the measurements of path-averaged C_n^2 will be nearly independent of the microscale when both transmitter and receiver are large. Another advantage is that by changing the ratio of the transmitting-to-receiving apertures, we can change the shape of the path-weighting function. For $D_t = 4(\lambda L)^{1/2}$, and varying D_r from 1.28 $(\lambda L)^{1/2}$ to 9.52 $(\lambda L)^{1/2}$, the path-weighting function is shown in Fig. 4. For large detector size, the weighting function moves toward the transmitter end. Although the path resolution is broad, it is possible to profile C_n^2 along the path by this technique.

One more advantage is that the calibration is relatively simple for different pathlengths or different sized apertures. For fixed transmitting and receiving apperture ratios, $\overline{C}_n^2$ can be obtained by

$$\overline{C}_n^2 = C\,\sigma_\chi^2 D_t^{7/3} L^{-3}, \tag{22}$$

where σ_χ^2 is the log-amplitude variance, D_t is the transmitting aperture in meters, L is the pathlength in meters, C_n^2 is in $\mathrm{m}^{-2/3}$, and C is a calibration constant that is only a function of the ratio of the receiving aperture to the transmitting aperture. For the case of equal receiving and transmitting apertures, $C = 4.48$.

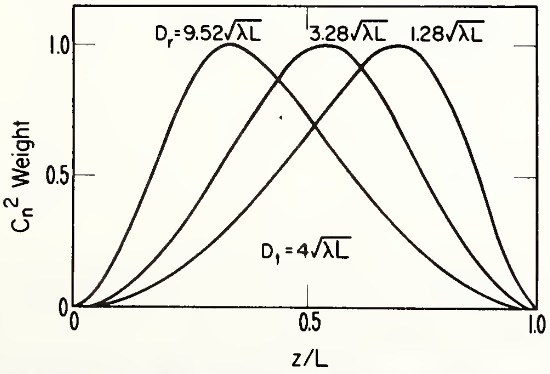

FIG. 4. The path-weighting function for different receiving aperture diameters.

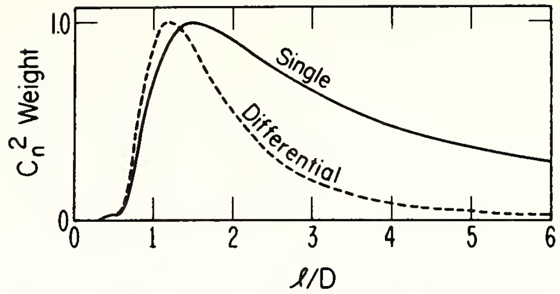

FIG. 5. The C_n^2 weighting versus the eddy size normalized to the receiver aperture size. Solid-line: for single detector. Dashed-line: for two equal-aperture tangent detectors.

For measurement purposes, there are advantages in using the difference of the signals detected by two receiving apertures instead of the single-aperture technique described above. The advantages arise from the fact that any noise, whether atmospherically or electrically induced, that is common to both apertures will be removed by the subtraction process. For the case of two circular tangential detectors, the calculation of the calibration factor and the path-weighting function are straightforward. For equal transmitting and receiving apertures ($D_t = D_r = D$), we obtain

$$C_n^2 = 0.689 \frac{\langle (I_A - I_B)^2 \rangle}{\bar{I}^2} D^{7/3} L^{-3}, \tag{23}$$

where I_A and I_B are the intensities detected by the two detectors, and $\bar{I}$ is the average intensity. In Eq. (23) and Eq. (24) to follow, we assume that the relative scintillation level $\langle (I_A - I_B)^2 \rangle / \bar{I}^2$ is sufficiently small, because of aperture averaging, and that this quantity is linearly related to σ_χ^2. The path-weighting function is also changed; however, the peak moves only a small percentage of the path toward the receiving end. We will call this method the differential method in the following discussion.

It is known[1–3] that for a point transmitter and detector the most effective eddy sizes are on the order of a Fresnel-zone size. For aperture sizes larger than Fresnel zone, the refractive-turbulence weighting is biased toward larger sizes. Assuming a Kolmogorov spectrum, for equal transmitting and receiving apertures, we obtain the relative weight for C_n^2 as a function of the eddy size normalized to the aperture size as shown in Fig. 5. The solid line is for a single receiver, the dashed line represents the result of the differential method using two detectors. Both of them are peaked at a scale size of the order of D; however, the differential method gives much better rejection for larger eddy sizes as demonstrated by the more rapid fall-off of the dashed curve for $l/D > 1$.

III. IMPLEMENTATION

Experiments, performed over flat terrain at the Wave Propagation Laboratory Table Mountain Field Station near Boulder, Colorado, confirm the theory. The light sources used were frosted quartz-iodine incandescent bulbs placed at the focus of concave spherical mirrors, and the receivers used concave spherical mirrors with photodiodes placed at the focus. The light source must be both incoherent and uniformly illuminated across its aperture. While there was no

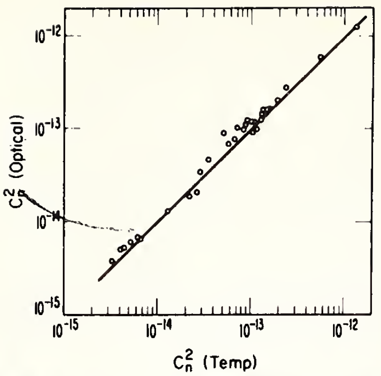

FIG. 6. Measurements of C_n^2 ($m^{-2/3}$) obtained from the saturation-resistant optical scintillometer vs C_n^2 derived from a differential thermometer placed at the center of a 500 m optical path 1.5 m above the ground. Each point is a 5 min average. Transmitting and receiving apertures were 15 cm in diameter; the differential thermometers were separated 20 cm in the vertical direction.

problem with coherence, we found it necessary to frost the bulb to obtain sufficiently uniform illumination.

Measurements were first made using a 15-cm-diam transmitter and receiver, on an optical path 500 m long, and 1.5 m above the ground. Over the path lengths and apertures for which inequality (21) applies, Eq. (22) may be rewritten in terms of a fractional variance of irradiance I as

$$C_n^2 = \frac{C}{4}\frac{\langle (I-\bar{I})^2\rangle}{(\bar{I})^2} D^{7/3} L^{-3}. \tag{24}$$

In this form, background light, as long as it does not fluctuate rapidly, does not interfere with the measurement. The initial calibration must of course be made in a way that does not affect the measurement of $\bar{I}$. Values of C_n^2 were calculated from Eq. (24) and compared with values of C_n^2 derived from high-speed differential thermometers separated 20 cm vertically and placed at the center of the optical path.[8] The results are shown in Fig. 6 where each data point represents a 5 min average. A substantial part of the upper portion of the plot lies in the region where saturation of scintillation would have occurred using a laser scintillometer.

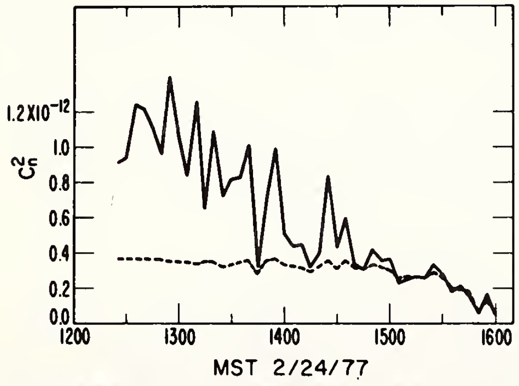

FIG. 7. Comparison of C_n^2 ($m^{-2/3}$) measurements made with the saturation-resistant optical scintillometer and with a laser scintillometer on a 500 m optical path 1.5 m above the ground. Each point is a 5 min average. The differential saturation-resistant system used 15 cm diameter optics; the laser system used a spherical wave front which irradiated a 1-mm-diam receiving aperture.

While the agreement with the thermometer measurements is quite good, considerable care must be taken to insure that the light source and receiver are solidly mounted and that there is no fluctuating background light in the receiver field of view. One way to substantially reduce these effects, as mentioned above, is to take the difference of two tangent apertures. In this case, Eq. (23) defines the calibration factor, and the data in Figs. 7 and 8 illustrate the performance of the differential technique. In Fig. 7 we compare a measurement of C_n^2 obtained from a differential saturation-resistant system using 15 cm apertures with C_n^2 values obtained from a laser scintillometer; 5 min averages are plotted. The laser system provided a spherical wave front that irradiated a 1-mm-diam aperture observed by a photomultiplier tube. The refractive-index structure parameter C_n^2 was calculated from Eq. (3). No correction was made for microscale effects. The laser system is clearly in saturation (corresponding to $\sigma_\chi^2 = 0.5$ to 0.6) until about 1500. After this time both systems are in reasonable agreement.

Differential saturation-resistant optical scintillometers with different aperture diameters and pathlengths were compared in a final experiment to verify the relationships expressed in Eqs. (23) and (24). We have plotted 1 h averages in Fig. 8 and all paths are 1.5 m above the ground. The solid line represents data obtained from the system using 15 cm apertures on a 500 m path. The dotted-line data to the left of the break in the graph were obtained using 7.5 cm apertures on a parallel 500 m path; to the right of the break, the dotted-line data is from 7.5 cm apertures on a 250 m path also parallel to the 500 m path. Some differences are expected since the scale sizes observed differ by a factor of 2, and in addition, for the pathlength comparison, the light paths are parallel over only one-half of the 500 m path. However, it is apparent that conditions were quite uniform over the region of the test, and the refractive turbulence closely approximated a Kolmogorov spectrum, as the data averages differ by less than 5%.

Both single-aperture and differential-aperture measurements of C_n^2 were made over the period of time shown in Fig. 8. Both methods gave results within 4% for data to the left of the break. For data to the right, the 7.5-cm-diam aperture

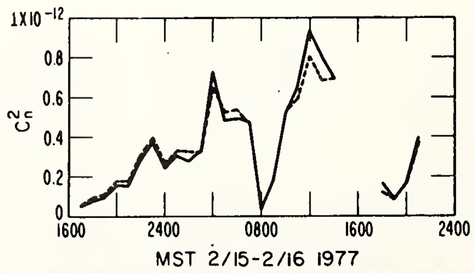

FIG. 8. Comparison of differential saturation-resistant optical scintillometers of different path lengths and aperture diameters. Each point is a 1 h average and all paths are 1.5 m above the ground. The solid line represents data obtained from the system using 15 cm apertures on a 500 m path. The dotted line data to the left of the break in the graph was obtained using 7.5 cm apertures on a parallel 500 m path; to the right of the break, the dotted line data is from 7.5 cm apertures on a 250 m path also parallel to the 500 m path. The data averages differ by less than 5%.

measurements became more than 10 times the differentiated ones because high winds were vibrating the light source. We conclude that the differential technique minimizes such sources of noise.

IV. CONCLUSIONS

This paper demonstrates that an optical instrument for measuring C_n^2 can be designed to perform satisfactorily even in the case of strong or saturated refractive turbulence. By using relatively large apertures on both the incoherent transmitters and receivers, the optical scintillometer maintains its calibration and path-weighting function throughout the range of expected C_n^2 values. By using a differential technique we minimize the ambient noise observed by both detectors, rendering the instrument insensitive to problems such as wind-induced mount fluctuations and fluctuating background light.

[†] This work was supported in part by the U.S. Army Electronics Command, Atmospheric Laboratory, White Sands, N.M. 88002.

[1] V. I. Tatarskii, *Wave Propagation in a Turbulent Medium* (McGraw-Hill, New York, 1961).

[2] V. I. Tatarskii, *The Effect of the Turbulent Atmosphere on Wave Propagation*, IPST Catalog 5319 (National Technical Information Service, Springfield, Va., 1971).

[3] R. W. Lee and J. C. Harp, Proc. IEEE **57**, 375 (1969).

[4] A. N. Kolmogorov, Dokl. Akad. Nauk, SSSR **30**, 299 (1941).

[5] S. F. Clifford, G. R. Ochs, and R. S. Lawrence, J. Opt. Soc. Am. **64**, 148 (1974).

[6] S. F. Clifford and H. T. Yura, J. Opt. Soc. Am. **64**, 1641 (1974).

[7] G. R. Ochs, S. F. Clifford, and Ting-i Wang, Appl. Opt. **15**, 403 (1976).

[8] R. S. Lawrence, G. R. Ochs, and S. F. Clifford, J. Opt. Soc. Am. **60**, 826 (1970).

Journal of Applied Meteorology, 17: 1788-1795, December 1978.

Experimental Evaluation of Ground-Based Microwave Radiometric Sensing of Atmospheric Temperature and Water Vapor Profiles

M. T. Decker, E. R. Westwater and F. O. Guiraud

NOAA/ERL/Wave Propagation Laboratory, Boulder, CO 80302

(Manuscript received 13 January 1978, in final form 16 September 1978)

ABSTRACT

Profiles of atmospheric temperature and water vapor derived from ground-based microwave radiometric measurements are compared with concurrent rawinsonde profiles including both clear and cloudy cases. Accuracies of the temperature profiles including the cloudy cases are quite close to predicted accuracies. Mean virtual temperatures between commonly used pressure levels are also compared and resulting rms accuracies are 1.1, 1.6, 2.0 and 2.8°C for the 1000–850, 850–700, 700–500 and 500–300 mb layers, respectively. The microwave technique is potentially useful in applications requiring high time resolution or in data-sparse regions of the oceans that might be covered by an ocean data buoy system.

---

1. Introduction

Thermal radiation from the atmosphere at microwave frequencies originates primarily from oxygen, water vapor and liquid water, and depends on their temperature and spatial distribution. For a well-mixed gas such as oxygen, and given the surface pressure, the radiation contains information primarily on the atmospheric temperature. It is thus possible to infer temperature structure from surface-based radiation measurements in the 60 GHz oxygen absorption complex. These measurements are "contaminated" by radiation from water vapor and especially from cloud liquid. Hence improved accuracy and operation during cloudy conditions are possible if measurements are also made of radiation from these constituents at frequencies outside the oxygen band. In addition to their use in temperature profiling these observations can be used to infer line integrals of water vapor and cloud liquid. In some cases vapor profile information can also be obtained.

Previous field experiments (Hosler and Lemmons, 1972; Miner *et al.*, 1972; Snider, 1972; Westwater *et al.*, 1975; Gurvich and Yershov, 1976) demonstrated that, under clear conditions, smoothed features of vertical temperature profiles can be recovered. Westwater *et al.* (1976) used a computer simulation to examine the feasibility of sensing temperature profiles from ocean data buoys. This study presented methods for correcting measurements for the radiation from clouds and water vapor, and concluded that useful data could be obtained under both clear and cloudy conditions. As a further step in this evaluation a series of field experiments has been carried out jointly by NOAA and the Jet Propulsion Laboratory. The purpose of these experiments was to confirm our ability to predict accuracies of radiometrically derived temperature profiles for a known season and geographical locations, especially under cloudy conditions. We present here a comparison of 88 simultaneous rawinsonde and radiometer temperature and water vapor profiles. Clouds were present in 54 of these cases and the cloud-correction techniques are shown to reduce the temperature profile errors very nearly to those expected in the clear-sky cases.

2. Experiment description

Measurements were made at the Pacific Missile Test Center (PMTC), Pt. Mugu, California, during the periods 24 February–17 March and 16–30 July 1976. The 21 profiles analyzed for the first period were all under essentially clear skies; 16 of 22 profiles during the second period were classified as cloudy. A more severe environmental test was made aboard the Canadian Ship *Quadra* at Ocean Station P in the Gulf of Alaska from 15 February–26 March 1977. Of the 45 profiles from this location 35 were cloudy.

The microwave radiometer, operated by personnel from the Jet Propulsion Laboratory, is similar to that used on the Nimbus 6 satellite (Staelin *et al.*, 1975). It has three channels in the oxygen absorption band at 52.85, 53.85 and 55.45 GHz, one channel in the water vapor absorption line at 22.235 GHz, and a window channel at 31.65 GHz. The radiometer was operated in an angular scan mode over ±45° from the zenith in steps of 7.5°. Dwell time at each zenith angle is 1 s with the sequence being repeated approximately once each minute. The antennas also scan temperature-controlled targets which are used together with the angular-scan data for calibration purposes. Although radiation from the various zenith angles could be used in retrieving atmospheric profiles, we have restricted ourselves to zenith-pointing data because of the difficulty in correcting for buoy motion in an operational system. In general, 18 to 24 of the measurements at 1 min intervals were averaged to give the radiation data used in retrieval of profiles. In addition to the five channels of radiometric data, surface measurements of temperature, pressure and relative humidity available from regular rawinsonde launch procedures were used in our profile retrievals.

Rawinsondes used for comparison purposes were routine launches by personnel of the PMTC for the Pt. Mugu measurements and by personnel of the *Quadra* for the Gulf of Alaska measurements. The radiometers were at the rawinsonde release location in all cases. Radiometric measurements began at rawinsonde release time in all but three cases; in these three instances (aboard the *Quadra*) time differences were less than 1 h.

3. Analysis

Statistical retrieval algorithms have been used extensively to extract temperature profiles from both microwave (Waters *et al.*, 1975; Westwater *et al.*, 1975; Yershov *et al.*, 1975) and infrared (Smith *et al.*, 1970; Rodgers, 1970) radiation measurements. These algorithms also predict retrieval accuracies if realistic estimates of measurement uncertainties are known.

Previous experiments have used thermal emission in the oxygen complex under clear-sky conditions to determine temperature profiles. Cloud emission, however, can introduce non-negligible departures from the corresponding emission from clear air for the upward-looking case. Microwave emission below about 45 GHz is insensitive to temperature structure and depends strongly on water, so measurements at the lower frequencies may be used to correct for the effects of clouds. Since the lower frequency emission depends on both water vapor and liquid water, two frequencies are required. As described by Westwater *et al.* (1976), our technique is to estimate the equivalent clear air radiation from the cloudy measurements both within and outside the oxygen band. Similar work has been published by Fowler *et al.* (1975). In a procedure identical to our commonly used profile retrieval algorithm, we use an eight-element data vector consisting of the five cloudy radiation measurements and surface temperature, pressure and relative humidity (and perhaps higher order products of these quantities) as a minimum variance estimator of the equivalent clear air radiation for the five radiometer channels. In this algorithm the statistical ensemble is representative of cloudy atmospheres only. The resulting data sets representing equivalent radiation from a clear sky may then be used in an inversion algorithm constructed from a statistical ensemble of clear profiles to retrieve temperature and water vapor profiles. The equivalent clear sky radiation may be used with an effective noise level different from that used with measurements under clear sky conditions, depending on frequency and the range of liquid water thickness present in the cloud ensemble. In using the above algorithm we assume that it is known whether or not clouds are present. This initial categorization is made by using the same eight-element data vector as above to determine the integrated amounts of liquid water and water vapor. The measurement is classified as cloudy if the inferred liquid amount exceeds some threshold, usually taken to be an integrated thickness of 20 μm. The statistical ensemble upon which this algorithm is based includes a representative sample of both clear and cloudy profiles.

In summary, our analysis uses statistical retrieval algorithms 1) to determine the integrated amount of cloud liquid and water vapor, and thus categorize the sky at the time of measurement as clear or cloudy; 2) to estimate, for cloudy cases, the equivalent radiation from the clear atmosphere; and 3) to retrieve temperature and water vapor profiles.

To eliminate biases that might arise from the instruments or from incorrect absorption coefficients, we forced averages of measured and calculated brightness temperatures for a sample of clear sky cases to agree. The brightness temperature calculations were made using contemporary absorption models and assuming the rawinsonde profiles were correct. Since different instruments were used in the three experimental runs, the corrections were made separately for each run. From 11 clear cases in the first run, 5 in the second and 10 in the third, the bias adjustments listed in Table 1 were calculated and applied to radiometric data of each run. These cases are included in the statistical summaries presented later. The standard deviations after the biases have been subtracted are also included in Table 1.

TABLE 1. Brightness temperature bias adjustments.

Frequency (GHz)	22.235	31.65	52.85	53.85	55.45
Pt. Mugu, Feb–Mar 1976 ($n=11$)					
Bias (K)	−2.8	−1.7	−0.2	−0.1	+1.2
Standard deviation (K)	2.2	0.7	1.5	0.7	0.5
Pt. Mugu, July 1976 ($n=5$)					
Bias (K)	−4.0	+0.1	−2.3	−3.8	+1.2
Standard deviation (K)	1.7	1.1	0.8	1.6	0.4
Gulf of Alaska, Feb–Mar 1977 ($n=10$)					
Bias (K)	−1.6	−1.0	+1.1	−0.1	−1.0
Standard deviation (K)	2.5	1.6	1.1	0.6	0.4

4. Cloud models

Construction of algorithms of the previous section require representative ensembles of cloud conditions, in-

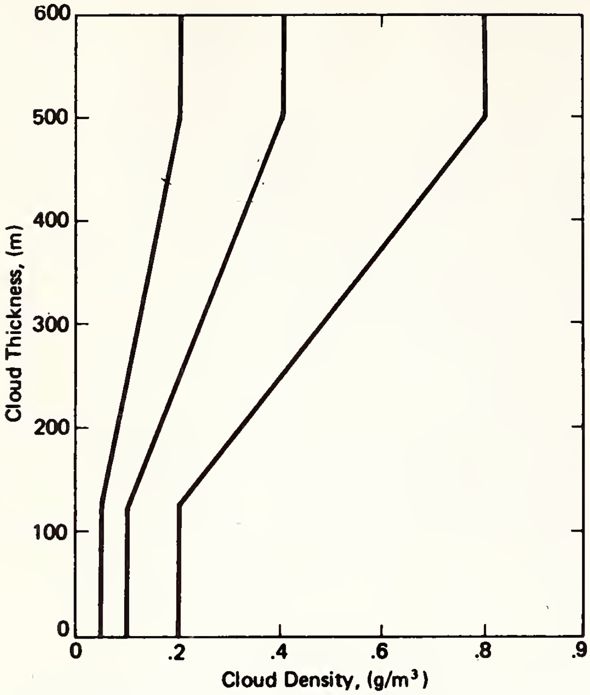

FIG. 1. Cloud thickness-liquid density models used in thermal emission simulations.

cluding realistic statistical distributions of base height, thickness, liquid water content, temperature, etc. Our ensembles were obtained by inserting clouds into our *a priori* set of rawinsonde data if at any point the relative humidity exceeded 95%. Base heights were taken to be the (interpolated) levels at which the humidity first exceeded 95% and thicknesses were determined using the points at which the humidity dropped below 95%. Some profiles will contain two or more cloud layers. Since liquid density is not measured by rawinsondes, completion of our ensemble required modeling of this parameter. We assumed that the liquid density within a given cloud was constant with height. For each cloudy rawinsonde profile we picked three values of density, one from each of the cloud thickness-liquid density models of Fig. 1. These models cover a reasonable range of observed liquid densities for non-precipitating clouds, and restrict thin clouds to low densities. Each rawinsonde profile with relative humidity above 95% was therefore used to generate four profiles—a clear case, and three cases with different liquid densities. Westwater *et al.* (1976) show the resulting distributions of cloud parameters for five ocean weather stations. The wide range of variation of these parameters provides a stringent test of our hypothesis that we can correct for clouds without knowledge of the details of cloud structure. The study shows that the accuracy to which clear air emission can be inferred from a set of cloud-contaminated emission measurements closely approaches the instrumental noise level for frequencies above 54 GHz. Below this frequency the effective noise level increases and should be considered in assigning errors to the statistical ensemble used for generating the profile retrieval algorithms.

Statistical ensembles of atmospheric profiles for the PMTC February–March experiment reported in this paper are derived from archived Pt. Mugu rawinsondes for the two 3-month periods February–March–April of 1973 and 1974. June–July–August data for the same years are used for the second experimental period. February–March–April data of 1966 and 1967 from Ocean Station P are used for the third period.

5. Results

Examples of retrieved temperature and water vapor profiles are shown in Fig. 2. Height on the vertical scale is given in pressure difference from the surface. Note that a pressure difference of 100 mb corresponds to a geometrical height of about 0.9 km, 300 mb to 3 km, 500 mb to 5.6 km and 800 mb to 12 km. Point values are retrieved at 10 mb increments in these profiles.

These examples indicate the characteristic smoothing of the radiometric profiles, especially for elevated temperature structure and for water vapor at all heights. We note that this system is not designed specifically for water vapor profile retrieval. Radiometric data for the examples on 16 and 22 July indicated that clouds were present with equivalent liquid thickness of 150 and 327 μm, respectively. Clouds with this liquid amount contribute significantly to radiation in the radiometric channels other than that at 55.45 GHz.

Fig. 3 shows the theoretical accuracies (curves with prefix T) in profile retrieval expected for the appropriate clear sky climatology and an rms instrument accuracy of 1 K together with the achieved accuracies during the three experimental periods (curves with prefix E). The rms error in retrieved profiles is taken to be the rms difference between the rawinsonde values and the radiometrically retrieved values. Thus, we assume that there are no errors in the rawinsonde measurements. Curves labeled T3 are the theoretical accuracies expected if the mean of the *a priori* statistical ensemble is used as the predictor of all profiles, i.e., no measurement is made. This then is the standard deviation of the *a priori* ensemble about its mean. Curves E3 are the corresponding experimentally observed quantities, i.e., the rms difference between the *a priori* mean and the rawinsonde profiles for the experimental cases. If surface values of temperature, pressure and relative humidity are used as predictors some improvement in accuracy over the *a priori* mean may be obtained as indicated by the curves labeled T2 and E2. Finally, accuracies predicted and actually observed when the full data set of five radiometric channels and three surface quantities are used are given by the curves labeled T1 and E1.

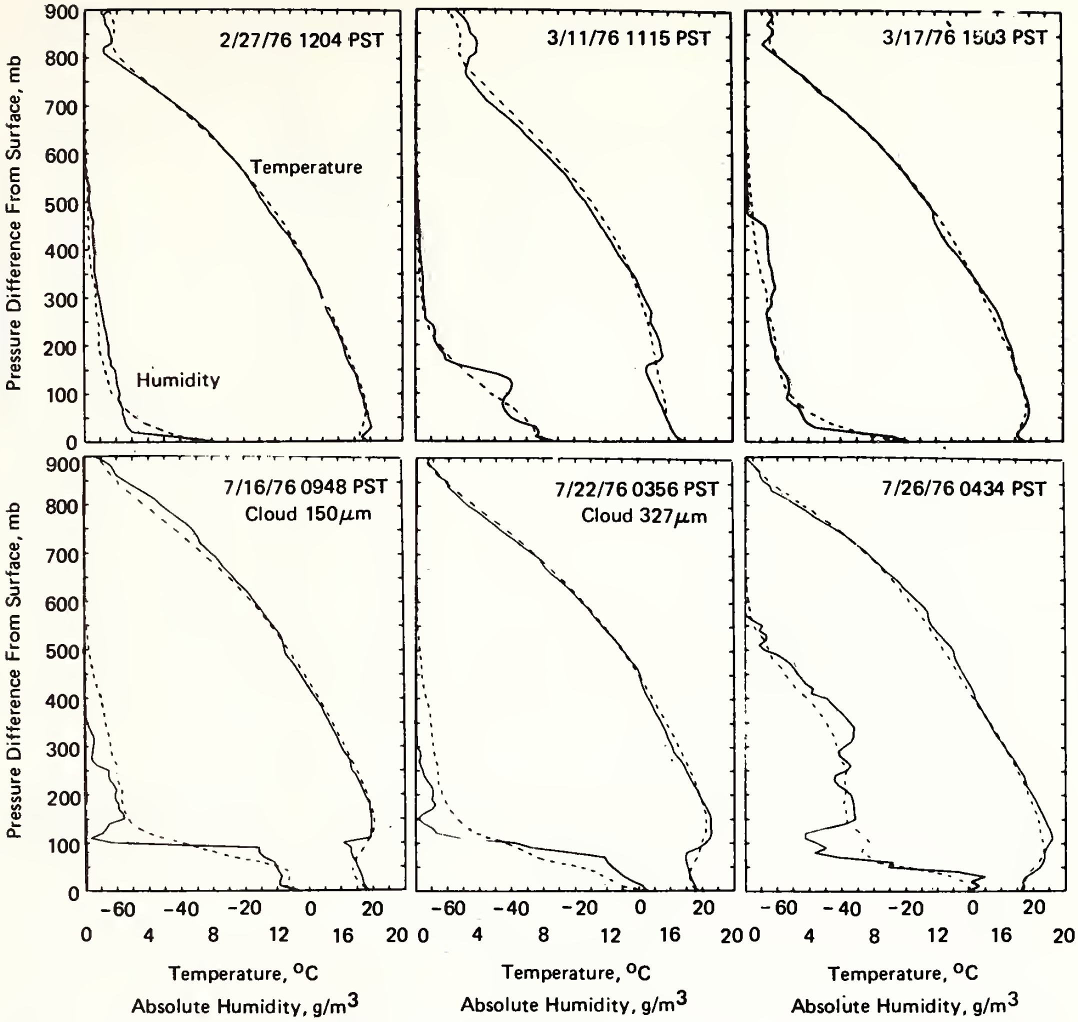

Fig. 2. Examples of retrievals of temperature and water vapor profiles. Solid lines, rawinsonde; dashed lines, radiometer.

This analysis shows that the achieved temperature profile accuracies are quite close to the theoretical prediction of accuracy. Temperature variations during the February–March experimental period at Pt. Mugu were larger than in the *a priori* sample as indicated by curve E3 of Fig. 3a, but this variance was reduced to the predicted value as shown by curve E1. On the other hand, temperature variations during the PMTC July period were quite small, and except for heights near 100 mb above the surface there is little improvement over the *a priori* mean. This experimental period did have clouds during many of the measurements and provided a test of our cloud-correction algorithm. These clouds were generally low-level stratus with integrated liquids inferred from the radiometric measurements ranging from about 100 to 300 μm; Fig. 4 illustrates the improvement in retrieval accuracies, the curves being similar to the E1 curves of Fig. 3b. It is evident that without the correction for clouds there would be a substantial increase in error and that the correction algorithm effectively eliminates this error.

The third experimental period in the Gulf of Alaska also included a large fraction of cloudy cases with line integrals of liquid up to about 900 μm. The accuracies achieved during the experimental period shown in Fig. 3c agree with the predicted values up to 500 mb pressure difference from the surface, but are somewhat larger at heights just above this as shown by curve E1.

In each of the three experimental periods the temperature error curves imply that significant information is obtained at altitudes well above the 500 mb pressure difference, including altitudes above the tropopause. However, it is likely that this is a result of the correlation of these temperatures with those at lower levels and hence the temperature information at the higher levels would not be reliable in statistically anomalous situations. This is also evident from the shape of the temperature weighting functions for these frequencies which are maximum at the

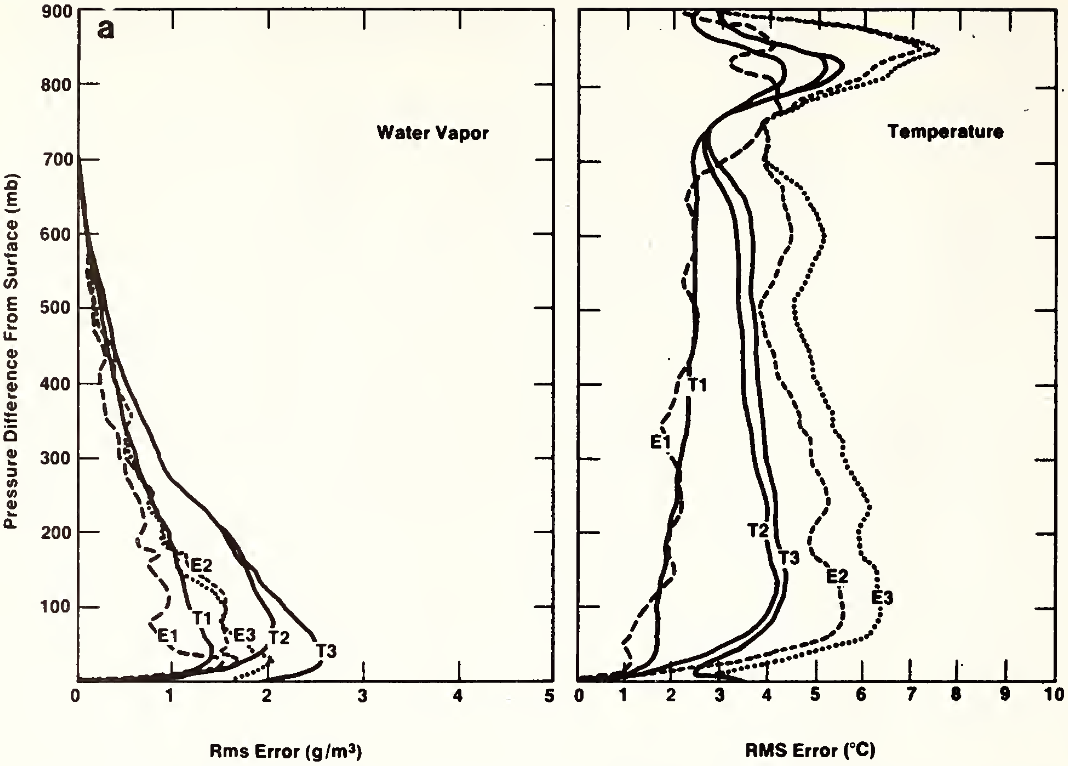

FIG. 3a. Comparison of theoretically predicted and experimentally observed accuracies of temperature and water vapor profiles for Pt. Mugu, February–March 1976. T, theoretical; E, experimental; 1, profiles retrieved using five radiometric channels and surface temperature, pressure and humidity; 2, profiles from surface data only; 3, *a priori* mean.

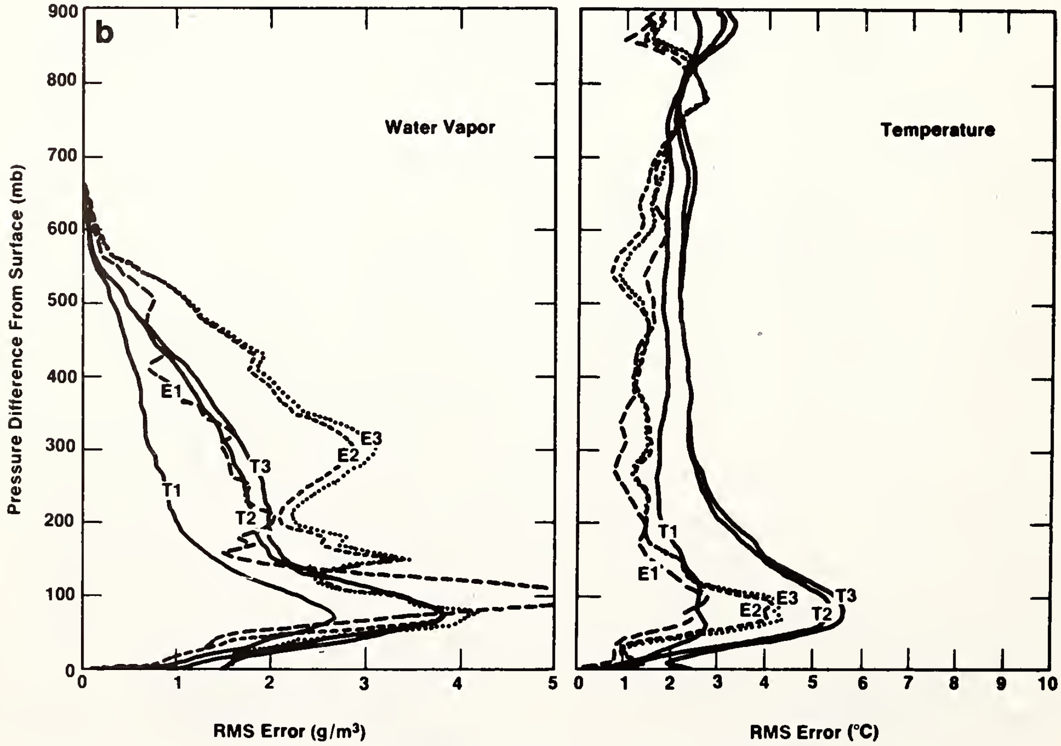

FIG. 3b. As in Figure 3a, except for Pt. Mugu, July 1976.

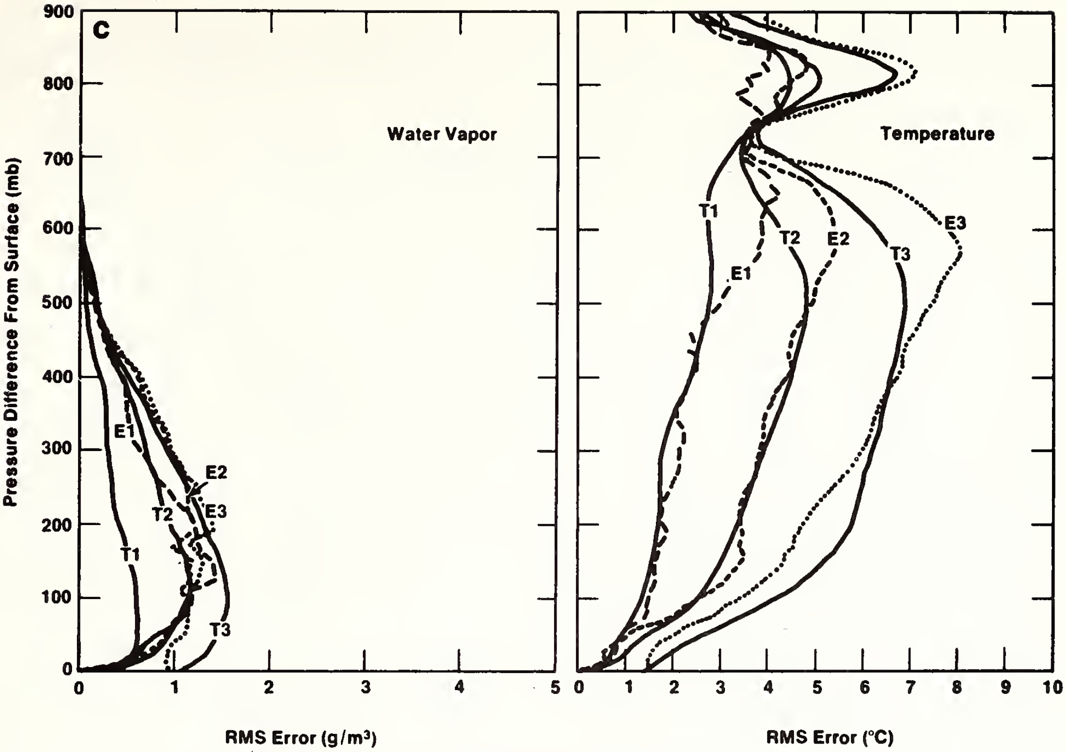

FIG. 3c. As in Figure 3a, except for Gulf of Alaska, February–March 1977.

surface and decrease to very low values at these heights.

The rather large error in temperature and especially water vapor profiles near 100 mb above the surface in the July measurements at Pt. Mugu shown in Fig. 3b is largely the result of the smoothing of the sharp boundary of the marine subsidence inversion. This is illustrated by the July examples of Fig. 2. However, for some meteorological applications, and in particular the numerical models that might use ocean buoy data, average temperatures between specified pressure levels may be used, making the detailed structure less important. We have used the radiometric and rawinsonde profiles to compute the thickness (equivalent to mean virtual temperature) between commonly used pressure levels. These are illustrated in the scatter diagrams of Fig. 5, where data for the three experimental periods are combined. The rms differences between radiometric and rawinsonde thicknesses are given for each layer. The 5.0 m rms difference for the 1000–850 mb layer corresponds to an rms mean temperature difference of 1.1°C. Similarly the 850–700 mb layer corresponds to 1.6°C, the 700–500 mb layer to 2.0°C, and the 500–300 mb layer to 2.8°C.

A comparison of the vertical line integral of water vapor (or precipitable water) as derived from the rawinsonde and radiometer is given in Fig. 6. The general agreement in the two measurements is apparent, but the rms difference of 0.32 cm is significantly larger than the predicted value of about 0.1 cm. Similar results have been reported by Staelin *et al.* (1976) and Grody (1976) for the measurement of water vapor from satellites, where rms differences between radiometer and rawinsonde are about 0.4 cm compared with predicted values of about 0.2 cm. These

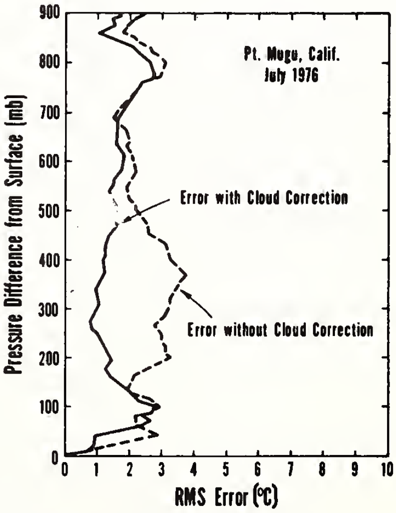

FIG. 4. Experimentally observed accuracies of temperature profiles using a five-channel radiometer with and without correction for radiation from clouds.

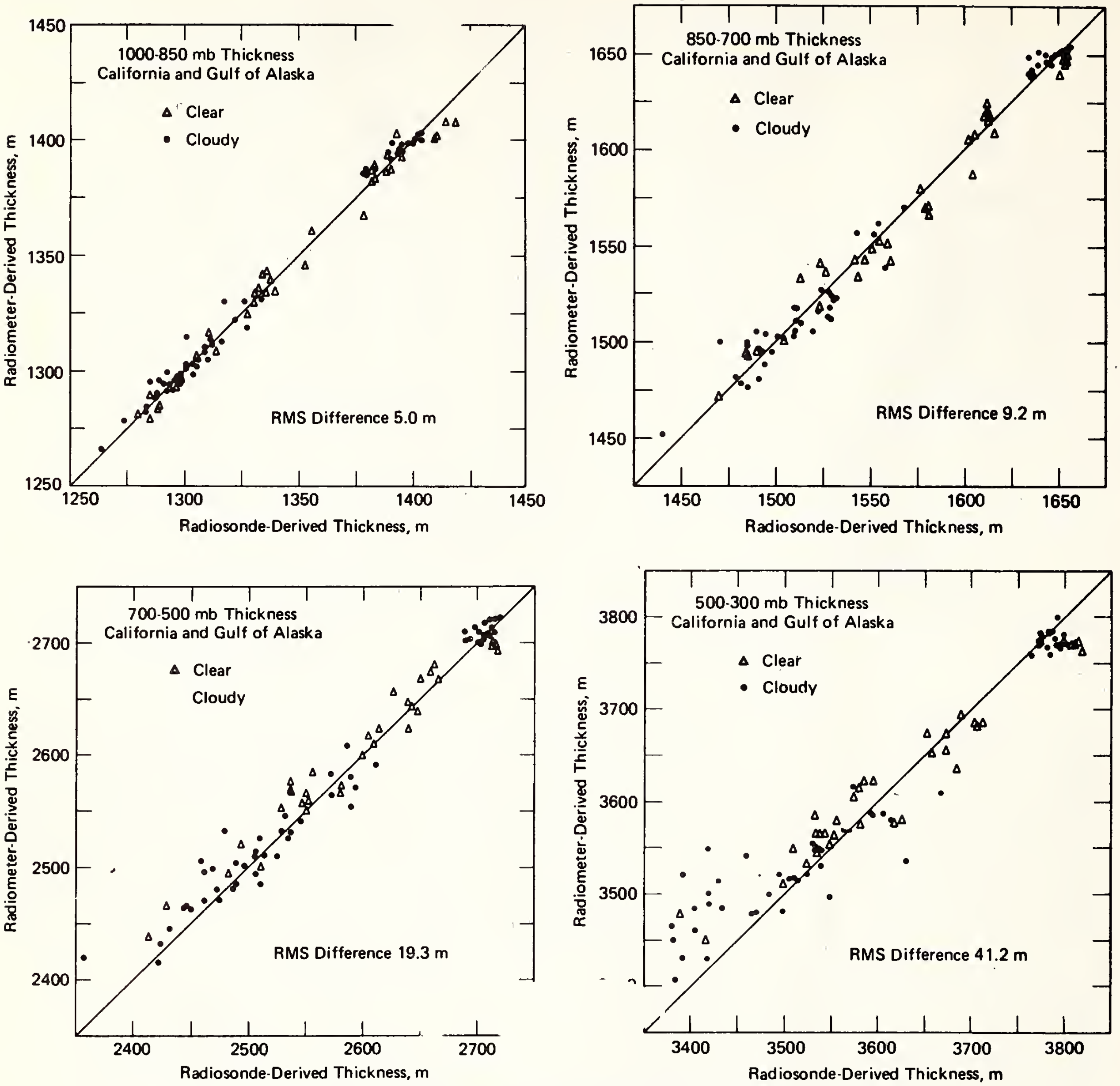

Fig. 5. Comparison of layer thicknesses as derived from rawinsonde and radiometer.

discrepancies could arise from a number of sources, including inaccuracies in the radiometric and rawinsonde measurements and, in the satellite case, errors in earth surface emissivity and temperature. Uncertainties in the absorption coefficient of water vapor may also be a significant source of error.

6. Conclusion

Temperature profiles retrieved from ground-based microwave radiometric measurements under both clear and cloudy conditions have been compared with rawinsonde profiles to show that reasonable agreement with predicted accuracy has been achieved. Root-mean-square accuracies between 1 and 2°C for the mean temperature between standard pressure levels up to 500 mb were obtained for the combined data from the three experimental periods. Measurements with these accuracies will be useful in numerical weather prediction, especially in data-sparse regions.

Water vapor profiles and line integrals from the radiometric data have also been compared with rawinsonde data, but differences of these quantities are somewhat larger than expected. It is likely that discrepancies arise partly from inaccuracies in the rawinsonde itself and partly from uncertainties in our knowledge of water vapor absorption coefficients.

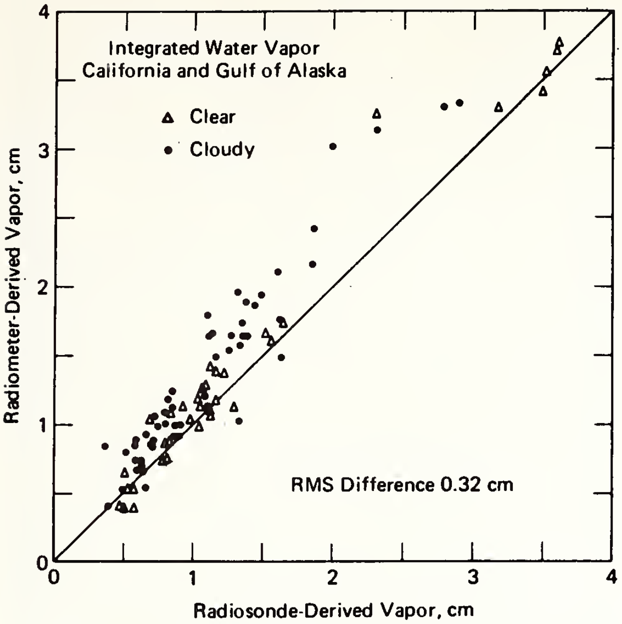

FIG. 6. Comparison of the line integral of water vapor as derived from rawinsonde and radiometer.

Acknowledgments. The radiometric measurements reported here were made under the direction of B. L. Gary and N. I. Yamane of the Jet Propulsion Laboratory, Pasadena, California, with support from the NOAA Data Buoy Office. We express our appreciation to personnel of the Geophysics Division of the Pacific Missile Test Center and of the Canadian Ship *Quadra* for providing meteorological data and facilities for the experiments.

REFERENCES

Fowler, M. G., N. D. Sze and N. E. Gaut, 1975: The estimation of clear sky emission values from cloudy radiometric data. Air Force Cambridge Research Laboratories, TR-75-0440, 57 pp.

Grody, Norman C., 1976: Remote sensing of atmospheric water content from satellites using microwave radiometry. *IEEE Trans. Antennas Propag.*, **AP-24**, 155–162.

Gurvich, A. C., and A. T. Yershov, 1976: On remote determination of anomalous distributions of atmospheric temperature and moisture. *Izv. Acad. Nauk USSR Atmos. Ocean. Phys.*, **12**, 1320–1323.

Hosler, C. R., and T. J. Lemmons, 1972: Radiometric measurements of temperature profiles in the planetary boundary layer. *J. Appl. Meteor.*, **11**, 341–348.

Miner, G. F., D. D. Thornton and W. J. Welch, 1972: The inference of atmospheric temperature profiles from ground-based measurements of microwave emission from atmospheric oxygen. *J. Geophys. Res.*, **77**, 975–991.

Rodgers, C. D., 1970: Remote sounding of the atmospheric temperature profile in the presence of cloud. *Quart. J. Roy. Meteor. Soc.*, **96**, 654–666.

Smith, W. L., H. M. Woolf and W. J. Jacob, 1970: A regression method for obtaining real-time temperature and geopotential height profiles from satellite spectrometer measurements and its application to Nimbus 3 SIRS observations. *Mon. Wea. Rev.*, **98**, 582–603.

Snider, J. B., 1972: Ground-based sensing of temperature profiles from angular and multi-spectral microwave emission measurements. *J. Appl. Meteor.*, **11**, 958–967.

Staelin, D. H., A. H. Barrett, P. W. Rosenkranz, F. T. Barath, E. J. Johnson, J. W. Waters, A. Wouters and W. B. Lenoir, 1975: The scanning microwave spectrometer (SCAMS) experiment. *Nimbus 6 Users Guide*, Goddard Space Flight Center, Greenbelt, Md.

——, K. F. Kunzi, R. L. Pettyjohn, R. K. L. Poon and R. W. Wilcox, 1976: Remote sensing of atmospheric water vapor and liquid water with the Nimbus 5 microwave spectrometer. *J. Appl. Meteor.*, **15**, 1204–1214.

Waters, J. W., K. F. Kunzi, R. L. Pettyjohn, R. K. L. Poon and D. H. Staelin, 1975: Remote sensing of atmospheric temperature profiles with the Nimbus 5 microwave spectrometer. *J. Atmos. Sci.*, **32**, 1953–1959.

Westwater, E. R., J. B. Snider and A. V. Carlson, 1975: Experimental determination of temperature profiles by ground-based microwave radiometry. *J. Appl. Meteor.*, **14**, 524–539.

——, M. T. Decker and F. O. Guiraud, 1976: Feasibility of atmospheric temperature sensing from ocean data buoys by microwave radiometry. NOAA Tech. Rep. ERL 375-WPL 48 [NTIS No. 262-421].

Yershov, A. T., Yu. V. Lebskiy, A. P. Naumov and V. M. Plechkov, 1975: Determination of the vertical temperature profile from ground-based measurements of the atmospheric radiation at $\lambda = 5$ mm. *Izv. Acad. Nauk USSR Atmos. Ocean. Phys.*, **11**, 1220–1229.

EOS Transactions of the American Geophysical Union, 59:
843-847, 1978.

Measurement of Ocean Wave Heights With a Satellite Radar Altimeter

L. S. Fedor and D. E. Barrick

Introduction

The launch of Geos 3 on April 9, 1975, by the U.S. National Aeronautics and Space Administration (NASA) represented the first step toward the goal of ocean surface remote sensing from space. Microwave radars and radiometers orbiting aboard a network of unmanned satellites are expected ultimately to offer an all-weather capability for routinely monitoring sea state, ocean surface topography, temperature, currents, and (indirectly) surface winds on a global scale. The availability of such data in real time should produce a quantum increase in the quality of long-term weather forecasts, as well as provide needed information for the efficient and safe conduct of burgeoning maritime operations.

Geos 3 is the first unmanned satellite to carry a radar system for observations of the sea. In particular, it carries a microwave short-pulse altimeter capable of measuring rms ocean wave height along its nadir track. Although the instrument can measure other quantities of geodetic and oceanographic interest (such as the instantaneous mean sea level from which currents and geoidal features can be extracted), we consider here only the measurement of sea wave height; this is without a doubt the most important single parameter characterizing that general but often used term, 'sea state.' The mathematical model and physical principles describing the sea echo have been understood for years. This paper, however, presents some of the first wave height plots made from a spacecraft radar. These wave height plots are shown versus distance along the satellite track; they agree reasonably well with ocean wave hindcasts and laser profilometer measurements of wave height, the errors being consistent with system resolution and internal and tracking loop noise.

This page may be freely copied.

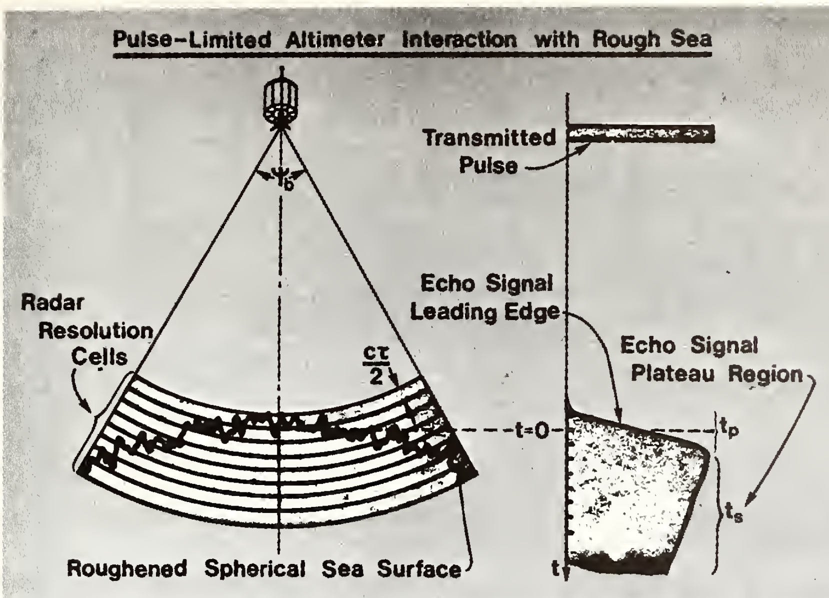
Pulse-Limited Altimeter Interaction with Rough Sea
Transmitted Pulse
ψ_b
Radar Resolution Cells
$\frac{c\tau}{2}$
Echo Signal Leading Edge
Echo Signal Plateau Region
t=0
t_p
t_s
t
Roughened Spherical Sea Surface

Fig. 1. Sketch showing consecutive radar resolution cells for altimeter in pulse-limited mode and the resulting average echo power shape versus time.

The Radar

The Geos 3 microwave radar operates in a pulse-limited mode, as illustrated in Figure 1. Operating at 13.9 GHz, the system transmits a pulse whose effective nominal temporal width is 12.5 ns, providing a radar cell spectral width of 1.875 m [*McGoogan*, 1975]. The peak pulse radiated power is 2 kW, and the pulse repetition frequency is 100 Hz, providing for a typical effective signal-to-noise ratio at the receiver of 12 dB. The satellite orbit is nearly circular, approximately 843 km above the earth. Figure 1 illustrates how the received sea echo increases in amplitude from the noise level as the short pulse scatters from the highest ocean wave crests directly below the satellite. This echo signal rises to a peak value, representing a circle of illuminated sea surface whose diameter is typically 4 km (independent of beam width, but dependent upon pulse width and, to some extent, wave height). This sea echo then remains at a 'plateau' level because constant sea area is intercepted by a spherical pulse, but it falls off eventually because of the finite antenna beam width of 2.6°. It is the stretching or rise time of the leading edge of the echo signal which is a direct measure of wave height at nadir. Because the ocean wave height is random, the instantaneous echo signal is also random; hence averaging must be used to obtain rms wave height estimates.

This paper is primarily concerned with inversion of the sea echo to obtain wave height and an interpretation of the results. The discussion is brief and elementary, with the purpose of acquainting the geophysics community with the principles and potential of the instrument for wave height measurement. Other groups besides ours are presently involved in the analysis of Geos 3 data. The National Environmental Satellite Service (NESS) of the National Oceanic and Atmospheric Administration (NOAA) will ultimately have the responsibility for the effective processing, utilization, and dissemination of data from an operational network of such satellites; our present research efforts within NOAA's Environmental Research Laboratories (ERL), and the work of others, are paving the way toward that time. (Further details of the satellite instrumentation and additional applications of the altimeter can be found in the work of *McGoogan* [1975].)

Signal Processing

The echo voltage time signal is square law detected on board the satellite and sampled over the leading edge every 6.25 ns. Inasmuch as the nominal transmitted pulse width is 12.5 ns, sampling every 6.25 ns does not represent an increase in range resolution; the increased number of samples does, however, produce some degree of smoothing along the leading edge as a result of overlap and hence will aid in improving wave height extraction accuracy. The 'effective' pulse width is somewhat longer than the 12.5 ns quoted above because of (1) stretching of the pulse due to finite receiver bandwidth, (2) range-gate jitter, and (3) errors in range-gate amplitudes. Estimates of these instrumental errors are made and transmitted with the altimeter data.

Sixteen range-gate channels are sampled and digitized over the leading edge, as shown in Figure 2. An average consisting of the sum of 320 consecutive pulses for each gate is formed. This average represents 3.2 s of data, over a path approximately 21 km long. Pulse to pulse autocorrelations were formed for several sets of data. The correlations all exhibit correlation distances of less than 500 m so that the distance between independent observations is of the order of 886 m. This indicates that each average over 3.2 s contains approximately 24 independent samples.

Many investigators [*Walsh et al.*, 1978; *Dooley et al.*, 1976] are employing maximum likelihood fits along the leading edge to deduce wave height. We have merely used finite difference techniques to estimate digitally the leading edge derivative, along with the simple expression given above from our model. This technique employs six points from the midregion shown in Figure 2, corrected to include best estimates of the effective pulse width and a multiplicative constant which relates the finite difference derivative estimate to the derivative of a continuous Gaussian process. In order to increase the independent samples, wave height means are computed for three consecutive 320-pulse sample averages, representing a total rms wave height for each 63-km ocean path length segment.

This page may be freely copied.

Sample Wave Height Tracks

Of the many altimeter passes across the North Atlantic, two typical examples were selected for display here, one representing low sea conditions (April 23, 1975) and the other representing high sea conditions (May 6, 1975). The rms wave height was extracted and averaged as described above. Plotted in Figures 3 and 4 is significant wave height in meters (a convenient oceanographic term which is 4 times the rms wave height) versus position along the satellite track. The track is given as a function of latitude and longitude, and a distance scale (in kilometers) is included for convenience.

Independent, reliable measurements of wave height under the satellite have been available only rarely for comparison with altimeter observations. During the two passes displayed an aircraft profilometer measurement of wave height was available at only one point; the agreement is good. Otherwise, weather charts and hindcasting were used to estimate wave height [*Parsons and Goodman*, 1975]; these values are displayed across the top. The first number of the upper set of two is wave height (in meters), and the second is wave period (in seconds) for the wind-driven wave field along the track. The estimated winds are shown as flags, giving the direction with respect to north (up), with the number of full bars denoting wind speeds in 10-kn increments (5.144 m/s = 10 kn); half bars denote 5-knot steps. A lower set of numbers refers to the wave height and period of any swell component present.

Hindcasts such as this are of questionable accuracy over the open ocean, where even winds themselves are estimated. Hindcasted wave heights are likely to be least reliable for low wind speeds, because unknown swell heights always present may be as large or larger than the wind-driven waves. In addition, radar-deduced wave heights will typically be less accurate for calm seas, because a constant error in measuring the width, t_p, of the leading edge will produce larger wave height variances when t_p is close to τ, the pulse width (as seen from the above equation for h). In general,

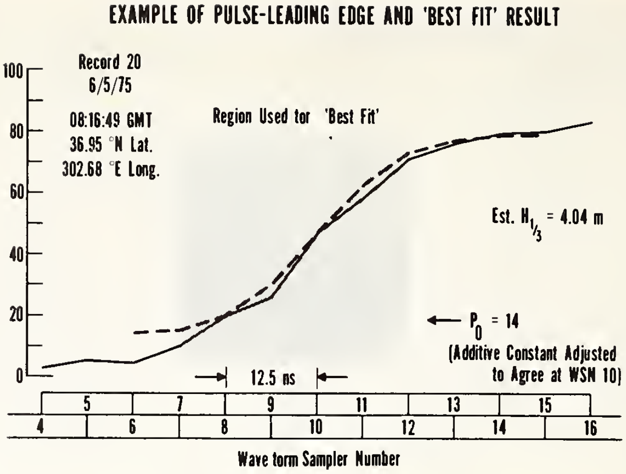

Fig. 2. Example of measured 'leading edge' Geos 3 altimeter echo data, along with 'best fit' (dashed curve) to signal derivative.

Echo Model

Many theoretical models [*Barrick*, 1972*a*, *b*; *Berger*, 1972; *Miller and Hayne*, 1972; *Walsh*, 1974] have appeared in the literature for the average scattered power versus time as seen by a short-pulse altimeter. A particularly convenient representation, based on a specular point approach derivable from physical optics, was obtained by *Barrick* [1972*a*] for pulse-limited operation. Assumed in this model (for convenience) are Gaussian antenna beam pattern (of half-power width ψ_B), Gaussian pulse shape (of half-power width τ), Gaussian ocean wave height, and wave slope probability distributions (of rms height h and rms total slope s). These approximations are reasonably valid for a first-order representation of the echo signal leading edge and initial portion of the plateau region. The product of the antenna gain squared times the average radar cross section of the sea versus time is

$$G^2\sigma(t) = (\pi^{3/2}Hx_w/s^2) \cdot [1 + \Phi(t/t_p)] \exp(-2t/t_s)$$

where H is the altitude of the satellite, $x_w = c\tau/[4(\ln 2)^{1/2}$, $c = 3 \times 10^8$ m/s, $t_p = 2(x_w^2 + 2h^2)^{1/2}/c$, $t_s = 2H\psi_e^2/c$, and $1/\psi_e^2 = (8 \ln 2)/\psi_B^2 + 1/s^2$. Here $\Phi(x)$ is the error function of argument x. Time $t = 0$ is taken to occur at the radar when the center of the pulse intercepts the mean (smooth) sea surface. The constants t_p and t_s have particularly meaningful interpretations. First, t_p represents the temporal leading edge stretching of the original pulse of width τ due to the waves of rms height h and, second, t_s represents the temporal extent of the plateau region and contains the combined effects of antenna beam width and surface slope.

Pulse-limited operation by definition implies that $t_s >> t_p$. Since the stretching of the echo signal leading edge is known to contain the wave height information, a particularly meaningful representation of this stretching is obtained by taking the derivative of this portion of the signal; it has the Gaussian pulse shape characteristic of the probability distribution of wave heights.

$$[G^2\sigma(t)]' = [2\pi Hx_w/(s^2t_p)] \cdot \exp(-t^2/t_p^2)$$

Thus by measuring the width of this leading edge derivative, t_p, one has a simple estimator of rms wave height h from $h = [c/2(2)^{1/2}][t_p^2 - (\tau^2/4 \ln 2)]^{1/2}$

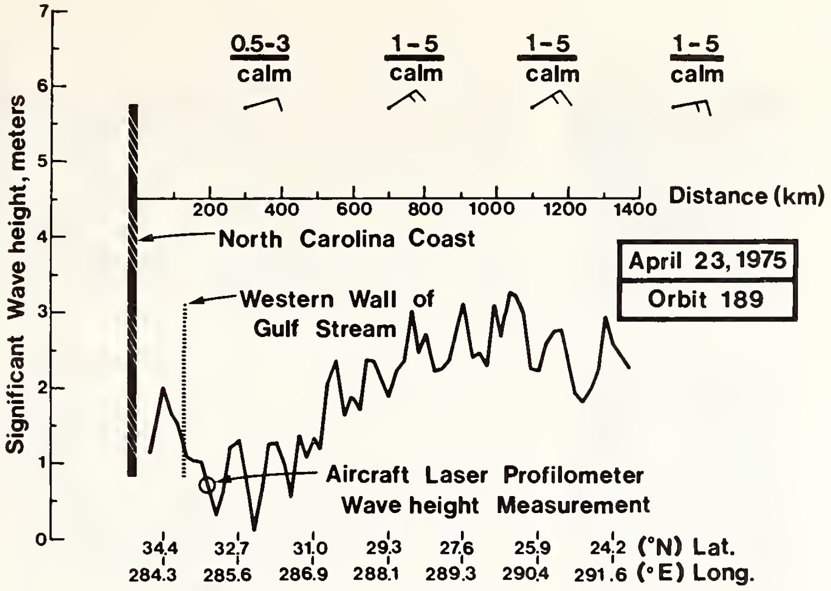

Fig. 3. Wave height track over the Atlantic during low sea conditions on April 23, 1975. Wave hindcasts and wind flags shown at various track positions are defined in text.

however, the radar-deduced wave heights and hindcasted wave heights do show good agreement and similar trends across the tracks.

We have had only one additional set of Geos 3 data during which an aircraft profilometer measured wave-height along a portion of the satellite track. This was a run on April 25, 1975, when the aircraft underflew the satellite along a 120-km section of track. The rms profilometer-measured wave height, averaged over this entire track, was reported as 3.51 m [*Parsons and Goodman*, 1975]. The satellite-measured wave heights, $H_{1/3}$, for the corresponding six 21-km (320 pulse) sample averages are given in the tabulation below.

$H_{1/3}$, m	σ_I, m
3.22	1.43
3.18	1.51
4.48	1.29
5.85	1.40
1.81	1.53
2.03	1.41

Also given are the tracking errors (converted from rms time-gate error to significant wave height, σ_I) as measured on board the satellite and transmitted with the data. The mean altimeter wave height obtained from these six numbers is 3.43 m, and the wave height standard deviation is 1.53 m.

Conclusions

Short-pulse microwave radar altimeters operating from space offer the potential of measuring ocean wave height along the nadir track, as demonstrated by preliminary Geos 3 data. Limited ground truth and hindcasts show favorable agreement. Very close laser profilometer agreement with altimeter wave heights (0.73 versus 0.65 m and 3.51 versus 3.43 m) are more likely fortuitous than indicative of altimeter accuracy. Geos 3 wave height standard deviations from the second profilometer test were 1.53 m, giving an rms normalized error of 45% for these tests. As can be seen from the second column of the tabulation, these wave height errors are explained almost entirely by instrumental errors, σ_I. The latter are due not only to tracking loop and range-gate jitter but also to a relatively low signal-to-noise ratio on the midportion of the leading edge used in the analysis (9-10 dB). The next generation altimeter to be flown aboard Seasat-A will be a more precise instrument, having a higher signal-to-noise ratio and shorter pulse width; such improvements should result in ocean wave height measurement accuracies of the order of tens of centimeters.

References

Barrick, D. E., *Remote Sensing of the Troposphere*, chap. 12, edited by V. E. Derr, U.S. Government Printing Office, Washington, D. C., 1972*a*.

Barrick, D. E., *Sea Surface Topography From Space*, vol. 1, chap. 16, U.S. Government Printing Office, Washington, D. C., 1972*b*.

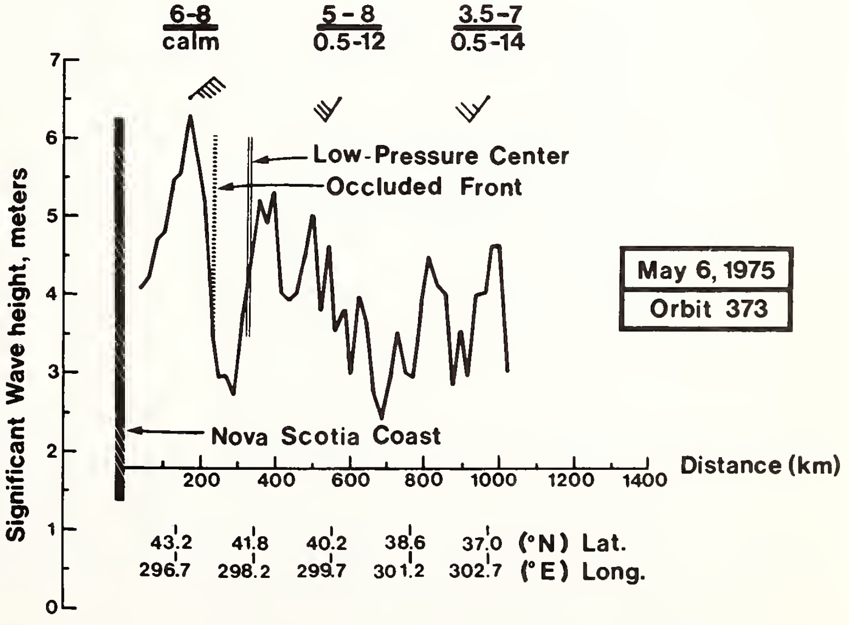

Fig. 4. Wave height track over the Atlantic during higher sea conditons on May 6, 1975. Wave hindcasts and wind flags shown at various track positions are defined in text.

This page may be freely copied.

Berger, T., Satellite altimetry using ocean backscatter, *IEEE Trans. Antennas Propagat.*, *AP-20*, 295-309, 1972.

Dooley, R. P., L. W. Brooks, and Khoury, Optimization of sate altimeter and wave height measurement, *Final Rep. NAS6-2601*, NASA Wallops Flight Center, Wallops Island, Va., 1976.

McGoogan, J. T., Satellite altimetry application, *IEEE Trans. Microwave Theory Tech.*, *MTT-23*, 970-978, 1975.

Miller, L. S., and G. S. Hayne, *Sea Surface Topography From Space*, vol. 1, chap. 12, U.S. Government Printing Office, Washington, D. C., 1972.

Parsons, C. I., and L. R. Goodman, Geos 3 phase B ground truth summary, *NASA Tech. Memo. X-69360*, Wallops Flight Center, Wallops Island, Va., 1975.

Walsh, E. J., Analysis of experimental NRL radar altimeter data, *Radio Sci.*, *9*, 711-722, 1974.

Walsh, E. J., E. A. Uliana, and B. S. Yaplee, SWH measurement with a high-resolution pulse-limited radar altimeter, *Boundary Layer Meteorol.*, *13*, 263-278, 1978.

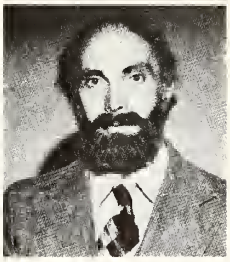

Donald E. Barrick received his B.S., M.Sc., and Ph.D. degrees in electrical engineering from the Ohio State University. He is presently the Program Chief of the Sea State Studies Area of NOAA's Wave Propagation Laboratory in Boulder, Colorado. This group is responsible for research and development of radio techniques for remote sensing of ocean surface parameters and has perfected several shore-based and satellite-borne concepts for monitoring sea state and ocean currents.

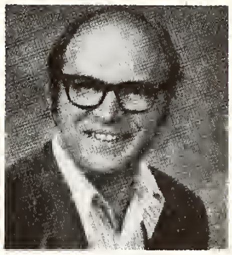

Leonard S. Fedor received his B.S. in physics from San Diego State College and his M.S. in meteorology from the Massachusetts Institute of Technology. He is currently a Project Leader in the Wave Propagation Laboratory of NOAA in Boulder, Colorado. For the past 17 years he has been involved in research in various aspects of remote sensing of the environment. These studies have included wave propagation, motions of ionospheric irregularities, and, for the past 4 years, ocean waves.

This page may be freely copied.

Radio Science, 1 285-289, 1978.

Observation of winds in the clear air using an FM-CW Doppler radar

E. E. Gossard, R. B. Chadwick, K. P. Moran, R. G. Strauch, G. E. Morrison, and W. C. Campbell

Wave Propagation Laboratory, Environmental Research Laboratories, National Oceanic and Atmospheric Administration, US Department of Commerce, Boulder, Colorado 80302

(Received June 29, 1977; revised September 8, 1977.)

The Wave Propagation Laboratory of NOAA has developed a frequency-modulated, continuous-wave, clear-air radar with a Doppler capability for measuring both the mean wind and turbulent intensity. In this paper, observations of turbulence are shown and related to the background wind and temperature structure. The radar's capability for measuring the structure parameters and dissipation rates of both velocity and refractive index in the inertial subrange is discussed.

1. INTRODUCTION

It has been known for some time [*Richter*, 1969], that frequency-modulated, continuous-wave (FM-CW) radar has the capability of revealing many details of clear-air structures in the planetary boundary layer. Its value lies mainly in its ability to "see" structure close to the radar (near the ground), and in the fine resolution with which the atmosphere can be observed. It is fundamentally very flexible, and the range resolution, observed range, and integration time can be varied more or less at will.

The capabilities of the FM-CW radar for observing the atmosphere attracted considerable attention for some time after its invention, and much was learned about wave motions and convection in the lower atmosphere [*Gossard et al.*, 1970; *Atlas et al.*, 1970; *Bean et al.*, 1971]. However, acoustic sounders were under development at about the same time [*Little*, 1969; *McAllister*, 1968], and the acoustic sounders had the great advantage that Doppler velocity information was easy to extract from the backscattered signal. Although it was well known that Doppler velocity information about discrete targets could be obtained by the FM-CW radar, it was widely believed that the extraction of velocity information from backscatter that was continuous in range was impossible because this kind of radar uses the frequency difference between the outgoing and returning signal to get range information. How, then, could the backscattered signal also be used to provide Doppler velocity information?

Strauch et al. [1975] of NOAA's Wave Propagation Laboratory have recently described the theory of how Doppler information can be extracted through digital processing, and demonstrated the technique [*Strauch et al.*, 1976] by observing the fall velocity of rain and snow. The essence of the technique is to observe phase changes in the return signal from sweep to sweep. They further pointed out the potential of the radar for clear-air studies and showed examples of clear-air vertical velocity.

2. MEAN WIND OBSERVATIONS

Still more recently, *Chadwick et al.* [1976*a,b*] have made clear-air observations of the horizontal wind velocity and discovered the startling fact that the Doppler information is fundamentally available even without additional digital data processing if the FM-CW radar is suitably configured. This is because the output of this radar appears in the frequency domain. The equipment configuration is similar to that used by *Richter* [1969], the only changes being in parameters. The FM sweep period used by Richter was 50 ms while *Chadwick et al.* [1976*a,b*] used a few-ms sweep period. Richter coherently processed over only one sweep while Chadwick *et al.* coherently processed over 50 or more sweeps. An example of velocity spectra displayed on an A-scope without digital processing is shown in Figure 1. Figure 2 (from Chadwick *et al.*) shows the corresponding wind profile acquired along an azimuth of 225° at an elevation angle of 45°. The profile is compared with winds measured by a captive balloon (solid lines) at the beginning times of ascent and descent indicated.

Copyright © 1978 by the American Geophysical Union.

0048-6604/78/0304-0285$03.00

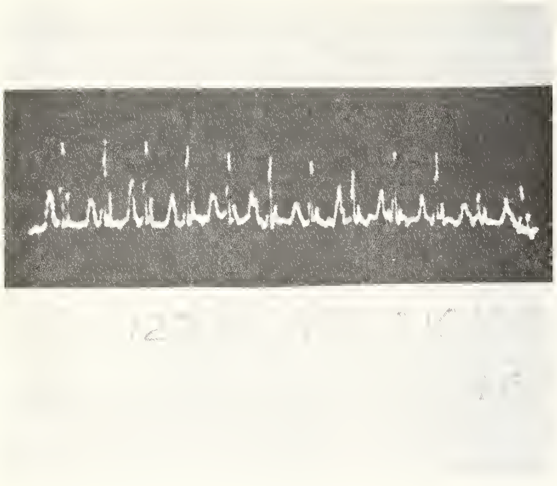

Fig. 1. A-scope display of clear air Doppler wind spectra. Spikes are from ground clutter and represent zero velocity point in range cells spaced 122 m apart from 465 m range out to 1805 m. The velocity scale is 20 m/sec between spikes; the clear-air spectra are the broad peaks shifted from zero by the horizontal wind.

The circles show a Rawinsonde ascent made at the same time. The radar sounding represents a 10-sec average, whereas many minutes were needed for the balloon soundings. In the system used by Chadwick *et al.*, the radial wind and wind-shear data can easily be displayed on a PPI, revealing the clear-air wind structure over a volume in the vicinity of the radar.

3. TURBULENCE INTENSITY MEASURED BY FM-CW DOPPLER RADAR

The mean radial velocity is found from the displacement of the wind velocity spectrum from zero as shown in Figure 1. However, the finite width of the velocity spectrum is a result of either random turbulent air motions toward and away from the radar within the range cell or of shear of the radial wind transverse or parallel to the beam axis. However, shear transverse to the beam axis can usually be determined by scanning the beam; shear parallel to the beam can be found from the range cell-to-cell wind information, and shear effects then removed. When the radar is pointing vertically, the shear component is nearly always negligible because the mean radial wind component is then almost always small. Thus the width of spectra measured by Doppler radars can be interpreted in terms of mechanical turbulence intensity [*Frisch and Clifford,* 1974]. They find that the turbulent dissipation rate is given by

$$\varepsilon \simeq \delta^{-1}\,[\sigma^2_{11}/1.35A(1-\gamma^2/15)]^{3/2}$$

where σ^2_{11} is the variance in the radial velocity component. When $\beta/\alpha \leq 1$, $\delta = \alpha$ and $\gamma^2 = 1 - (\beta/\alpha)^2$. When $\beta/\alpha > 1$, $\delta = \beta$ and $\gamma^2 = 4[(\alpha/\beta)^2 - 1]$. Their analysis assumes that turbulence scales within the radar range cell lie in the inertial subrange where the spectral density $E(k) = A\,\varepsilon^{2/3}\,k^{-5/3}$ and that the antenna pattern corresponds to the three-dimensional gaussian distribution

$$P(x,y,z) = [(2\pi)^{3/2}\beta\alpha^2]^{-1} \cdot \exp[-(z^2+y^2)/(2\alpha^2) - x^2/(2\beta^2)]$$

where x is the direction of the radar beam. For our radar, the half-power beamwidth was 2.7° and the cell size was $\beta = 87$ m. The radar wavelength is 10 cm. The constant $A \simeq 0.53$. Except in the heart of the inversion layer, the assumption that

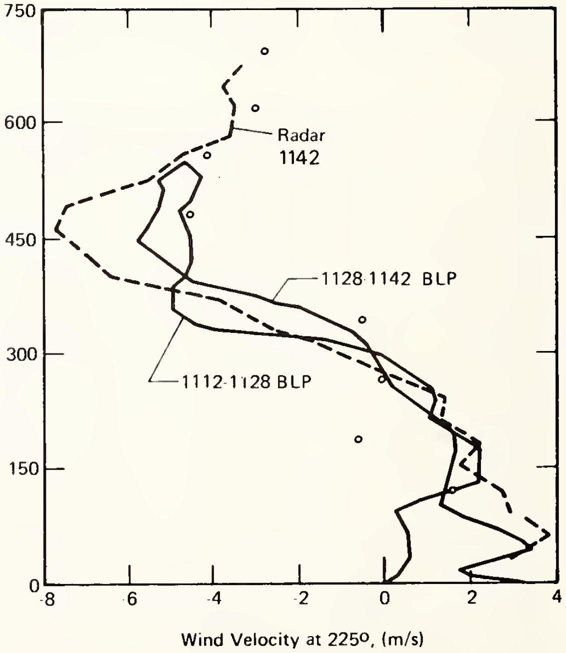

Fig. 2. FM-CW radar and tethered balloon wind profiles for 16 September 1975. Wind component is at 225° aximuth. Small circles show results of Rawinsonde release at 1100 MDT. Tethered balloon and Rawinsonde release about 300 m east of radar site.

the inertial subrange extends to scales of the cell size seems safe.

Figure 3 shows an example of an FM-CW radar record obtained on 29 April 1976 with the antennas pointing vertically. The left-hand side shows intensity of the backscatter on a height vs. time display. An A-scope display of log intensity vs. height is shown by the left-hand solid curve. The backscattered intensity is a direct measure of the turbulent structure parameter C_n^2, as demonstrated by *Ottersten* [1969]. The Doppler spectra in 87 m height increments are shown by the curves at the right. As in Figure 1, the range axis is also a velocity axis. In this case the vertical velocity is zero within the error of reading from the display so the peaks of the spectra are at zero velocity. The velocity range from peak-to-peak is 10 m/s and the corresponding height range is 87 m. The first and second moments of the spectra were calculated from the mean-value theorem using the trapezoidal rule.

On 29 April there was a nearly stationary front along the eastern slope of the Rocky Mountains so the boundary layer displayed by the radar was in a nearly steady-state condition. We therefore have compared the radar data with the Rawinsonde data from Denver, Colorado, almost 60 km from Boulder where the radar was located. The Rawinsonde data taken at 0500 MST show the frontal inversion to be 1400 m above the ground, in remarkable agreement with the thin, intense scattering layer on the radar record. The sounding data are shown in Figure 4 with profiles of ε and C_n^2 shown for

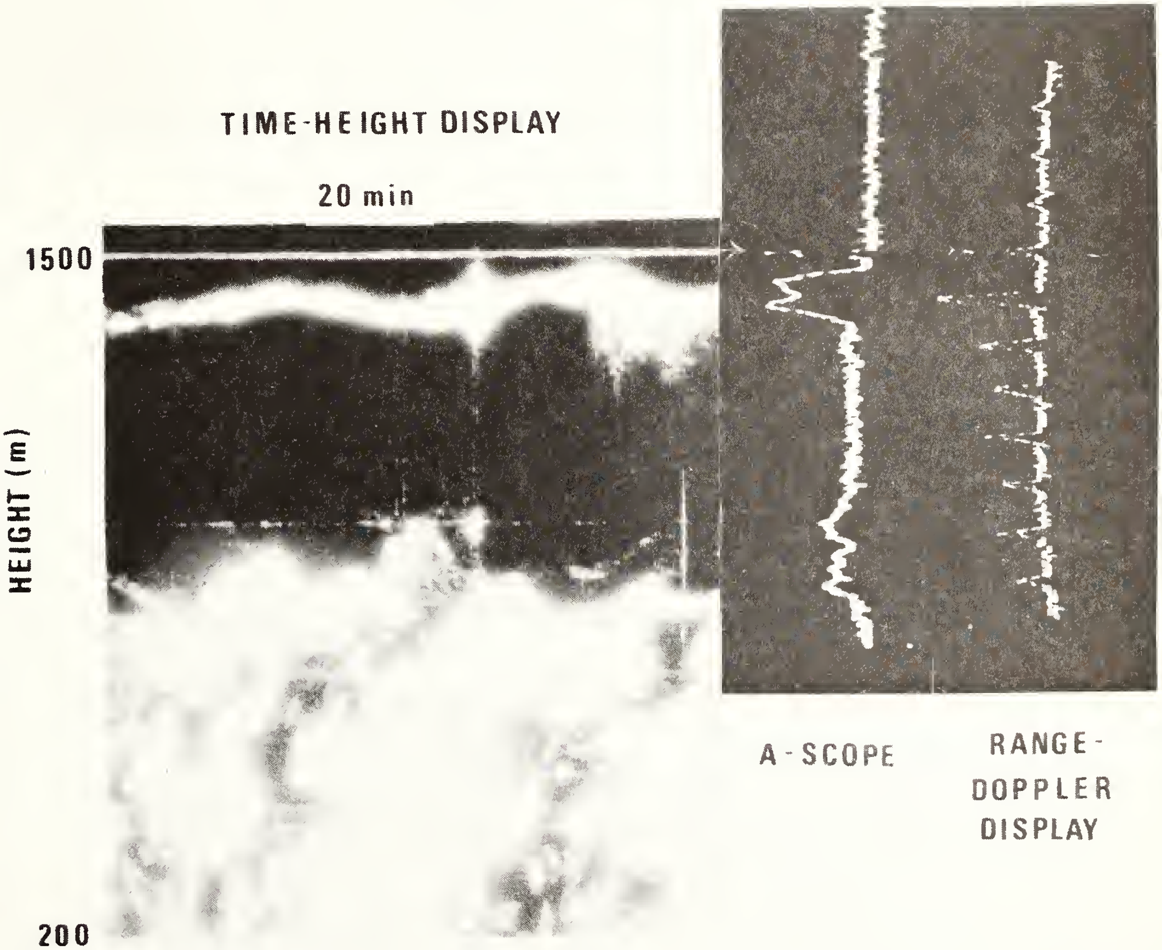

Fig. 3. Backscattered intensity vs. height and time with wind spectra shown at far right. Spectra are centered on zero velocity because radar is pointing vertically.

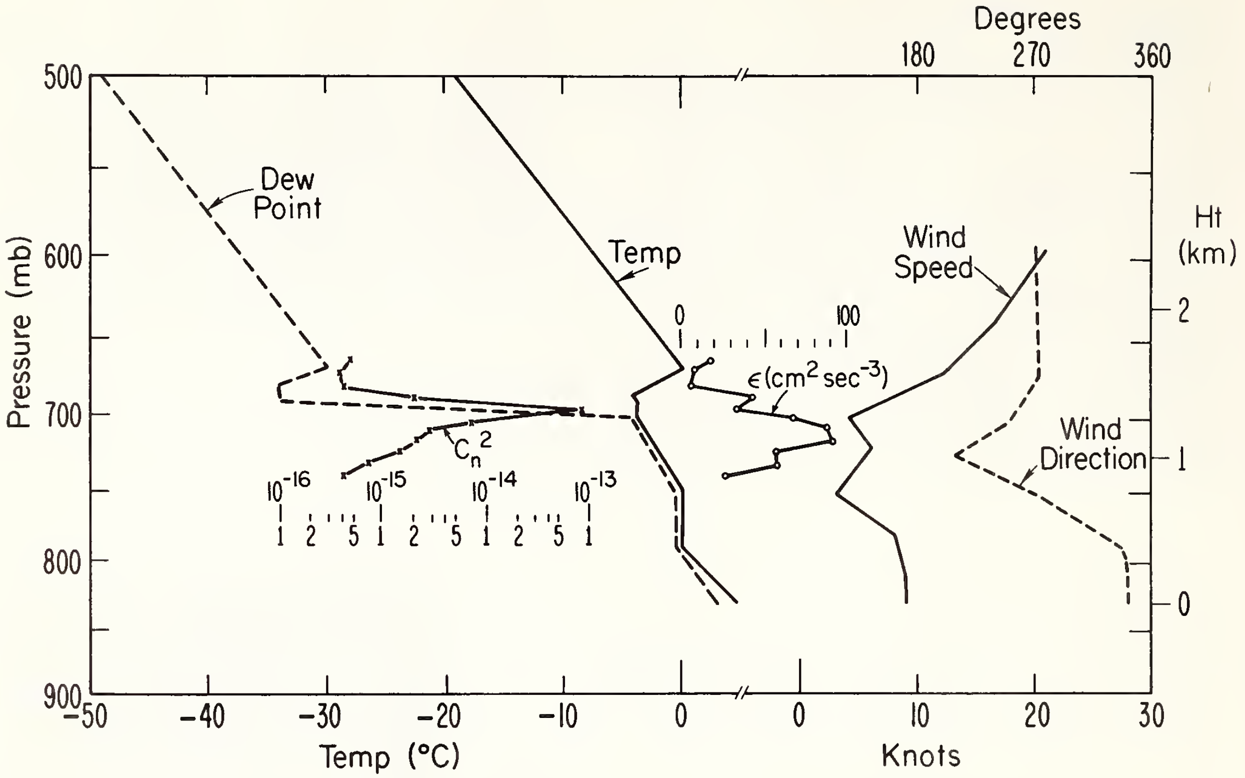

Fig. 4. Meteorological sounding data from Denver Rawinsonde shown with turbulent dissipation rate ε and C_n^2 measured by the radar.

comparison. Both ε and C_n^2 reach a maximum below the inversion, with ε falling to less than a tenth of its maximum value above the inversion. The structure constant C_n^2 (or equivalently, the back-scattered intensity) also has a strong maximum at the base of the inversion, in agreement with aircraft-borne-refractometer results reported by *Gossard* [1960] and with balloon-borne-refractometer results reported by *Lane* [1967].

4. CONCLUSIONS

The FM Doppler radar is a powerful new research tool for studying wind structure and turbulence in the planetary boundary layer. If it can be established that it can operate to several-km ranges a large percent of the time, it will have many practical applications as well as research applications. These include the monitoring of wind shear and severe turbulence in the neighborhood of airports.

REFERENCES

Atlas, D., J. I. Metcalf, J. H. Richter, and E. E. Gossard (1970), The birth of "CAT" and microscale turbulence, *J. Atmos. Sci.*, *27*, 903–913.

Bean, B. R., R. E. McGavin, R. B. Chadwick, and B. D. Warner (1971), Preliminary results of utilizing the high resolution FM radar, *Boundary-layer Meteorol.*, *1*, 466–473.

Chadwick, R. B., K. P. Moran, R. G. Strauch, G. E. Morrison, and W. C. Campbell (1976*a*), A new radar for measuring winds, *Bull. Amer. Meteorol. Soc.*, *57*, 1120–1125.

Chadwick, R. B., K. P. Moran, R. G. Strauch, G. E. Morrison and W. C. Campbell (1976*b*), Microwave radar wind measurements in the clear air, *Radio Sci.*, *11*, 795–802.

Frisch, A. S., and S. F. Clifford (1974), A study of convection capped by a stable layer using Doppler radar and acoustic echo sounders, *J. Atmos. Sci.*, *31*, 1622–1628.

Gossard, E. E. (1960), Spectra of atmospheric scalars, *J. Geophys. Res.*, *65*, 3339–3351.

Gossard, E. E., J. H. Richter, and D. Atlas (1970), Internal waves in the atmosphere from high-resolution radar measurements, *J. Geophys. Res.*, *75*, 3523–3536.

Lane, J. A. (1967), Measurements with a spaced-cavity microwave refractometer, in *Atmospheric Turbulence and Radio Wave Propagation*, edited by A. M. Yaglom and V. I. Tatarsky, pp. 201–204, Nauka, Moscow.

Little, C. G. (1969), Acoustic methods for the remote probing of the lower atmosphere, *Proc. IEEE, 57*, 571–578.

McAllister, L. G. (1968), Acoustic sounding of the lower troposphere, *J. Atmos. Terr. Phys., 30*, 1439–1440.

Ottersten, H. (1969), Atmospheric structure and radar backscattering in clear air, *Radio Sci., 4*, 1179–1193.

Richter, J. R. (1969), High resolution tropospheric radar sounding, *Radio Sci., 4*, 1261–1268.

Strauch, R. G., W. C. Campbell, R. B. Chadwick, and K. P. Moran (1975), FM-CW boundary layer radar with Doppler capability, *NOAA Tech. Rep. ERL 329-WPL 39*, US Government Printing Office, Washington, DC.

Strauch, R. G., W. C. Campbell, R. B. Chadwick, and K. P. Moran (1976), Microwave FM-CW Doppler radar for boundary layer probing, *Geophys. Res. Lett., 3*, 193–196.

Journal of Geophysical Research, 83: 5011-5018, 1978.

Measurement of Ocean Wave Heights Using the Geos 3 Altimeter

CLIFFORD L. RUFENACH

NOAA/ERL Wave Propagation Laboratory, Boulder, Colorado 80302

WERNER R. ALPERS

Institute of Geophysics, University of Hamburg and Max-Planck-Institute of Meteorology, Hamburg, West Germany

Radar altimeter signals transmitted from the low-orbiting satellite Geos 3 were analyzed for two selected orbits over high seas associated with hurricane 'Caroline' in the Gulf of Mexico and a North Atlantic storm. The measured values of significant wave height are in reasonable agreement with surface measurements, provided that the altimeter data are properly edited. The internal consistency of estimated wave heights for the North Atlantic storm, a standard deviation of 0.6 m or less, and the good agreement with surface truth lend credence to the method. A statistical analysis of the pulse slope variation gives estimated values of significant wave height within ±1 m of the true values 75% of the time for spatial averaging over 70 km.

INTRODUCTION

Short-pulse radar altimeters aboard low-orbiting satellites have the capability of measuring the mean height of the ocean surface, the geoid, and the roughness of this surface, the wave height. The mean height measurement uses the round trip travel time of radar pulses to estimate the distance from the satellite to the surface. The roughness of the ocean surface causes stretching of the return pulse leading edge which is a direct measure of the ocean wave height (see, for example, *Barrick* [1972]; *Brown* [1977]). In the present work the significant wave height $H_{1/3}$ is inferred from the shape of the average received pulse.

Short-pulse altimeters are aboard two satellites, Skylab S-193 and Geos 3 [*McGoogan,* 1975]. Both altimeters have similar pulse widths, about 15 ns, allowing the measurement of higher wave heights, whereas the altimeter scheduled for launch aboard Seasat-A in May 1978 will have a nominal pulse width of 3 ns, allowing measurement of lower wave heights.

Contributions to the received radar signal occur when the scattered energy from specular points on the rough ocean surface is returned to the radar antenna. However, these points will be received at different delays, since they come from different depths into the rough surface. Therefore the delayed signals add randomly, causing stretching of the leading edge of the return pulse. This scattering process for a short-pulse satellite altimeter requires that the spherical nature of the transmitted wave be considered [*Moore and Williams,* 1957; *Barrick,* 1972]. Thus the received pulse increases in amplitude after being reflected from the surface up to a peak (plateau) value. This plateau value is reached when the trailing edge of the transmitted pulse first intersects the mean surface, for a flat sea an area about 4 km in diameter for Geos 3, whereas for high seas it occurs when the trailing edge reaches the lowest trough, which could be 6-7 km in diameter.

The purpose of the present work is to develop a method for analyzing the Geos 3 altimeter signals in terms of ocean wave heights. The technique must take into account the peculiarities associated with the Geos 3 altimeter. Indeed, several altimeter parameters are observed in order to determine when and if the altimeter data required to calculate $H_{1/3}$ are reliable. A more accurate method for analyzing Geos 3 data may evolve in the future; however, it is believed that the method presented here leads to useful results. Data from two orbits were selected for analysis: overflights of hurricane Caroline in the Gulf of Mexico and a North Atlantic storm.

THEORY

The time evolution of the backscattered signal as recorded by the receiver is given by the convolution of the incoming pulse $I_0(t)$ with the impulse response function $H(t)$:

$$I(t) = H(t)*I_0(t) = \int_{-\infty}^{+\infty} H(t-t')I_0(t')\,dt' \qquad (1)$$

where $H(t)$ is the convolution of the radar sea surface impulse response function $S(t)$, which describes the backscattering of the pulse and the receiver response function $R(t)$:

$$H(t) = S(t)*R(t)$$

The antenna beam width effects were not included, since they have a negligible effect on the shape of the leading edge of the pulse.

For the simplified case, a nearly smooth flat sea surface, the mean backscattered signal is proportional to the area illuminated by the pulse. For this simplification the signal energy is a linear function of time if $t_0 - \tau/2 < t < t_0 + \tau/2$ and remains constant for $t > t_0 + \tau/2$ [*Brown,* 1977]. Assuming that the surface impulse response $S(t)$ is a step function, the receiver response $R(t)$ is a delta function, and the incoming pulse is rectangular, then a linear response is obtained as shown by the solid line in Figure 1.

If the sea surface is rough, however, specular points are encountered above and below mean sea level. This causes the linear rise to be stretched as illustrated by the dashed line in Figure 1. For a rough sea the surface response function $S(t)$ is then the convolution of a step function and the probability density function $P_3(\zeta, \mathbf{n})_{\eta=0}$ for specular points having heights ζ above the mean level ($\mathbf{n}$ represents the vector normal of the specular points). Specular points for a nadir-looking altimeter are characterized by tangent planes on the ocean waves where the normals of these planes are vertical to the mean sea surface; i.e., $\mathbf{n} = (\eta_x, \eta_y) = 0$ [*Barrick,* 1968].

In the analysis of a rough surface we can assume that the ocean wave field obeys Gaussian statistics and that the backscattered energy per unit illuminated area is independent of height above the mean sea level. *Shapiro et al.* [1972] have

This paper is not subject to U.S. copyright. Published in 1978 by the American Geophysical Union.

Paper number 8C0452.

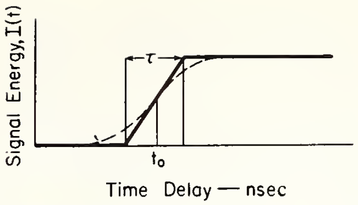

Fig. 1. Simplified representation of average received pulse shape.

shown evidence that the radar energy near vertical incidence increases linearly with increasing distance below the wave crests. However, these small effects are unlikely to be detectable with the Geos 3 altimeter because of its limited resolution.

The ocean wave field is assumed to be Gaussian distributed with independent wave heights and the wave normals,

$$P_3(\zeta, \mathbf{n}) = P_1(\zeta)P_2(\mathbf{n}) \tag{2}$$

For a nadir-looking altimeter, (2) can then be represented by [*Brown*, 1977]

$$P_3(\zeta, \mathbf{n})_{\eta=0} \sim \exp -\zeta^2/2\sigma_s^2 \tag{3}$$

where σ_s is the rms wave height and is related to $H_{1/3}$ by

$$\sigma_s = \tfrac{1}{4}H_{1/3} \tag{4}$$

In this analysis it is implied that the reflected pulse contains contributions from so many specular points that the statistics of the returned pulse envelope can be described by a Rayleigh distribution or, equivalently, its square by an exponential distribution.

The receiver response function is useful in characterizing the effect of pulse jitter on the average received pulse shape. The altimeter pulse acquisition requires continuous adjustment of the individual pulse positions. The random portion of this adjustment is termed pulse jitter and may be assumed to be Gaussian distributed with an rms value σ_j [*Hofmeister et al.*, 1976]. Therefore the receiver response function $R(t)$ is approximately

$$R(t) \sim \exp\,[-(t - t_0)^2/2\sigma_j^2] \tag{5}$$

and the incoming pulse can also be approximated by a Gaussian shape with rise time σ_T:

$$I_0(t) \sim \exp\,(-t^2/2\sigma_T^2) \tag{6}$$

TABLE 1. Geos 3 Satellite Characteristics

Characteristic	Value
Orbital	
Mean altitude	843 km
Inclination	115°
Eccentricity	0
Period	101.8 min
Satellite velocity	~7 km/s
Radar Altimeter	
Transmitting frequency	13.9 GHz
Pulse width (one-half power width)*	14–15 ns
Pulse width ($\sigma_T = e^{-1/2}$ width)†	6.2 ns
Pulse repetition frequency	100 pulse/s
Detector characteristic	square law
Antenna beam width (one-half power)	2.6°
Tracking loop jitter (σ_j)*	~4 ns for $H_{1/3} \lesssim 2$ m ~9 ns for $H_{1/3} \cong 10$ m

*Based on electrical tests of the flight model altimeter [*Hofmeister et al.*, 1976].

†Based on one-half power width of 14.6 ns.

The average return pulse includes the convolution of three Gaussian functions:

$$P_3(\zeta = ct/2, \mathbf{n})_{\eta=0} \quad R(t) \quad I_0(t) \tag{7}$$

where c is the speed of light. The resulting Gaussian expression is $G_{\sigma_c}(t)$ with rise time

$$\sigma_c = [(2\sigma_s/c)^2 + \sigma_T^2 + \sigma_j^2]^{1/2} \tag{8}$$

Therefore the resulting analytical expression for the average return signal is

$$I(t) = \int_{-\infty}^{\infty} \theta(t - t_0 - t')G_{\sigma_c}(t')\,dt'$$

$$= \frac{I_\infty - I_{-\infty}}{2}\left(1 + \operatorname{erf}\frac{t - t_0}{(2)^{1/2}\sigma_c}\right) + I_{-\infty} \tag{9}$$

where

$$\theta(t - t_0) = I_\infty \qquad t > t_0$$

$$\theta(t - t_0) = I_{-\infty} \qquad t < t_0$$

and $\operatorname{erf} t = 2/(\pi)^{1/2} \int_0^t e^{-\lambda^2}\,d\lambda$ is the error function.

From (4) and (8) we obtain

$$H_{1/3} = 0.6(\sigma_c^2 - \sigma_T^2 - \sigma_j^2)^{1/2} \tag{10}$$

where $H_{1/3}$ is in meters and σ_c, σ_T, and σ_j are in nanoseconds. Equations (9) and (10) are used to deduce the significant wave height in the examples examined.

DESCRIPTION OF ALTIMETER

The Geos 3 satellite was launched on April 9, 1975, into a circular orbit with each consecutive orbit precessing about 25° to the west. The principal orbital and altimeter characteristics are given in Table 1. The tabulated altimeter characteristics refer to the instantaneous short-pulse (intensive) mode of operation relevant for sea state studies. The altimeter probes the ocean surface 100 times per second resulting in a spatial period of 70 m. Each radar pulse is sampled in the radar receiver by 16 sampling gates as illustrated in Figure 2. These gates of a width of 12.5 ns and uniformly spaced at 6.25 ns intervals sample the pulse at discrete levels of 8 mV. Furthermore, the receiver continuously adjusts the position of these 16 gates to track the leading edge of the return pulse, which gives a measure of the satellite altitude. This tracking adjustment is accomplished by a split-gate tracking loop which minimizes the loop error voltage $E = 2I_{10} - I_\infty$, where I_{10} is the sampled energy in gate number 10 and I_∞ is the sampled energy in the plateau region (see Figure 2). The loop bandwidth is approximately 4 Hz, which means that any real or apparent changes in

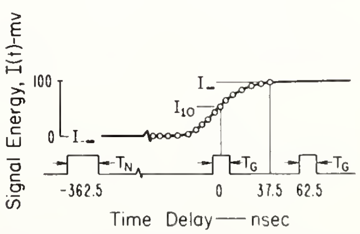

Fig. 2. Geos 3 sampling gate configuration for intensive mode: T_G = 12.5 ns, T_N = 200 ns. I_{10} is the sampled energy gate 10, I_∞ is the sampled energy plateau region, and $I_{-\infty}$ is the sampled energy noise region.

altitude slower than 4 Hz will appear as a tracking adjustment.

The random fluctuations in this error voltage, termed jitter, are important for sea state studies, since jitter in position of the individual pulses causes additional stretching of the average received pulse. The expected standard deviation of tracking loop jitter is about 4 ns for low sea states and increases to about 9 ns for high sea states (see Table 1).

The 16 sampling gates are also available through a resistance-capacitance low-pass filter with a 1-s time constant. These average gate values, hereafter designated as analog averages, are sampled at discrete levels of 2 mV and transmitted to the earth every 3.2 s.

Several other parameters are used to determine if the altimeter was operating properly or might bias the estimates of $H_{1/3}$. These parameters include (1) altimeter status, (2) satellite altitude, (3) position of the average received pulse relative to the 16 sampling gates t_0, and (4) Automatic Gain Control (AGC), which is a measure of received signal level.

ANALYSIS METHOD

The analysis method is separated into (1) the statistical analysis of data and (2) the development of criteria for deleting unreliable data that could bias the estimates of $H_{1/3}$.

The average pulse shapes were obtained by digitally averaging 320 instantaneous pulses over 3.2 s, defined as one frame of data. This corresponds to a spatial resolution of about 23 km, the distance the satellite travels in 3.2 s. Other statistical parameters, i.e., variance, skewness, kurtosis, intergate, and interpulse correlation coefficients, were calculated, and the results are given in Appendix A.

The average received pulse shape is represented by the error function of (9),

$$I(t_i) = \frac{I_\infty - I_{-\infty}}{2}\left(1 + \operatorname{erf}\frac{t - t_0}{(2)^{1/2}\sigma_c}\right) + I_{-\infty} \qquad (11)$$

where the parameters I_∞ and $I_{-\infty}$ are available from the altimeter output, average plateau, and noise gate energies, respectively; t_i is the time delay of the transmitted pulse as shown in Figure 3, and σ_c is a measure of the pulse stretching. The pulse stretching is given in Figure 3 for $0 \leq H_{1/3} \leq 12$ m based on (10) and (11).

The significant wave height ($H_{1/3}$) is estimated from the average pulse shape by a standard least square error analysis using gate 10 and the four adjacent gates. This analysis was performed for the analog and digitally averaged gates. The locations of the five points selected for the analysis are shown with open circles in Figure 3.

The form of the least square error is

$$\epsilon = \sum_{i=8}^{12} [I(t_i) - I_i]^2 \qquad (12)$$

where I_i represents the average gate values. The minimization was numerically performed by selecting successive values of σ_c and t_0.

The justification for selecting only five points is as follows: The results of intergate correlation analysis for several different orbits show an unexpected and consistent decrease in correlation between gates 13 and 14 and a corresponding unexpected increase in correlation between gates 12 and 13 as illustrated in Figure A1. These correlation coefficients show that the position of gate 13 is mislocated with a delay nearly identical to that of gate 12. Therefore including gate 13 in the analysis could bias the estimates.

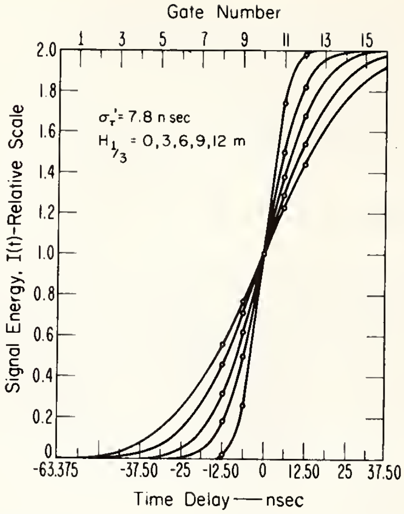

Fig. 3. Theoretical shape of received pulse for Geos 3 altimeter. Open circles indicate the four sampled points (gates) adjacent to gate 10, $\sigma_T' = (\sigma_T^2 + \sigma_J^2)^{1/2}$, $I_\infty = 2$, $I_{-\infty} = 0$, and $t_0 = 0$.

The jitter is calculated from the range servo error voltage y_i. The servo error voltage is proportional to the satellite altitude rate (E. L. Hofmeister, private communication, 1977). Therefore the random jitter fluctuations are obtained first by calculating the running sum, $z_i = \sum_{j=1}^{i} y_j$, where y is given in centimeters. The resulting values are then detrended and converted to time units by using $t_j(\text{ns}) = y_j(\text{cm})/15$ to obtain the jitter fluctuations. In the present work a quadratic least square error analysis was used to subtract both altitude rate and acceleration. Similar results were obtained by using several slightly different analytic methods.

The Geos 3 overflight (orbit 2024) of hurricane Caroline was selected to illustrate the method of analysis. This includes the least square analysis described above to estimate $H_{1/3}$, t_0, and ϵ. In addition, the altimeter status and the satellite altitude were monitored in an attempt to determine when the altimeter data should be edited. Figure 4 shows the result of this analysis. Figure 4*a* shows the variation of ϵ, the mean square error which is a measure of the goodness of fit to the error function. Figure 4*b* shows the variation of t_0, which is a measure of how effectively the altimeter receiver is positioning the incoming pulses. Figure 4*c* shows the standard deviation of the jitter σ_J, which is a measure of the random time shifts between instantaneous pulses. This jitter is expected to increase with increasing $H_{1/3}$ and decreasing signal level. Figure 4*d* shows the variations of the satellite altitude with four values of altitude averaged to obtain altitude values every 0.4 s. Finally, and most importantly, Figure 4*e* gives the estimates of $H_{1/3}$. The solid circles represent the $H_{1/3}$ values based on an effective pulse width $\sigma_T' = (\sigma_T^2 + \sigma_J^2)^{1/2} = 7.8$ ns, whereas the open circles represent $H_{1/3}$ values based on measured values of σ_J from the method described above using (10). Both methods of calculating $H_{1/3}$ use (10) with $\sigma_T = 6.2$ ns. The dashed lines refer to portions along the ground track where the data were deleted by using the editing criteria described below.

The principal features of Figure 4 are the large negative spikes in satellite altitude (see points A, B, and C); these spikes are directly correlated with large values of σ_J. The estimates of $H_{1/3}$ without jitter correction exhibit less deviation from adjacent values than estimates with jitter correction exhibit for the

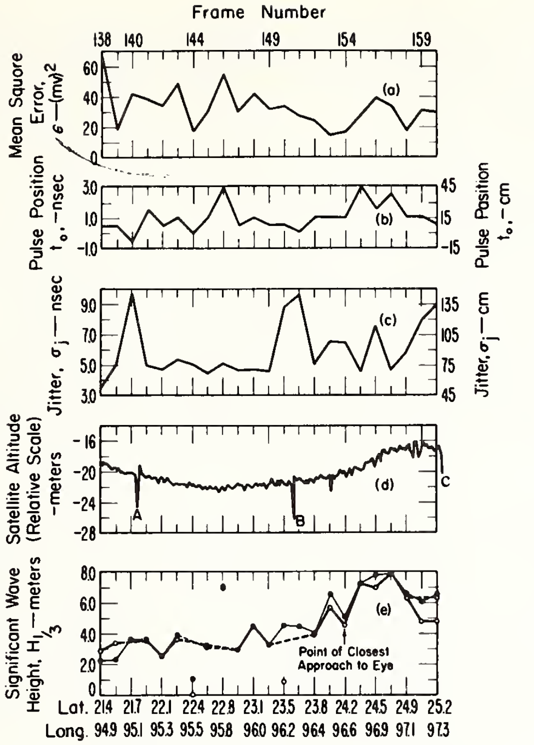

Fig. 4. Plots of altimeter parameters from selected portions of orbit 2024 in the Gulf of Mexico near hurricane Caroline, August 31, 1975. Solid circles represent $H_{1/3}$ based on $\sigma_T' = 7.8$ ns. Open circles represent $\sigma_T = 6.2$ ns with σ_j correction. $H_{1/3}$ values using σ_j correction underestimate the wave height when negative spikes are present in satellite altitude (e.g., $\sigma_T' > \sigma_c$ for frames 140 and 150). Points A, B, and C indicate negative spikes in altitude.

negative spike associated data The smaller values of t_0 appear to correlate with these negative spikes.

A similar analysis was undertaken for orbit 4546 with data over a much larger area and range of sea states. The results from this North Atlantic orbit are shown in Figure 5. First, the satellite altitude output did not exhibit the large negative spikes present for orbit 2024. Therefore continuous unbiased estimates of $H_{1/3}$ are available except for a small area near frame 15 where the signal level dropped below the minimum threshold. The parameters selected for display in Figure 5 are t_0, σ_j, and $H_{1/3}$. The values of $H_{1/3}$ were computed by using a three-frame running average resulting in a spatial resolution of about 70 km; the other parameters are based on one-frame averages or 23-km resolution. The pulse position t_0 appears to decrease with decreasing sea state from approximately $t_0 \cong 2$ ns to 1 ns as is illustrated in Figure 5*a*. Figure 5*b* illustrates typical values for jitter σ_j of about 8 ns for high sea states. These values gradually decrease with decreasing sea states to 4 or 5 ns. These results are in agreement with tests on the flight model altimeter. The estimates of $H_{1/3}$ using analog-averaged pulse shapes exhibit wider scatter than digital averages with or without jitter correction. Therefore only the digital-averaged values are used here.

The following criteria were applied to edit data that might bias the $H_{1/3}$ estimates. First, and most important, data associated with large negative spikes in satellite altitude were edited when the peak values of the spikes were greater than 2 m, e.g., see frames 140, 150, 151, and 160 of orbit 2024.

Two other parameters that have indicated bias are t_0 and a nonmonotonic shape for the average pulse in the plateau region. The values of t_0 that bias $H_{1/3}$ are taken as $t_0 < 1$ ns or $t_0 > 3$ ns as described in Appendix B. Deleting data based on pulse shape may seem somewhat arbitrary; nevertheless, useful results were obtained after carefully analyzing the data, leading to the criterion to delete data when $|I_{\max} - I_{\min}| > 10$ mV in the plateau region where the average values of $I_{\max}$ are usually located near gates 12 or 13 and $I_{\min}$ near gates 15 or 16. The values of $I_{\max}$ and $I_{\min}$ were calculated every 3.2 s.

The criteria $|I_{\max} - I_{\min}| > 10$ mV and $t_0 < 1$ ns or $t_0 > 3$ ns may delete valid data occasionally. For example, the standard deviation of $I_{\max}$ or $I_{\min}$ is $1/(320)^{1/2} = 5.6\%$ of the mean value which for typical plateau values of 90 mV implies a standard deviation of about 5 mV. Therefore if one gate is greater than one standard deviation high and another is less than one standard deviation low, valid data would be deleted.

RESULTS

Two orbits were selected for estimating $H_{1/3}$ during high sea conditions. The subsatellite tracks for these orbits are shown in Figure 6. Figure 6*a* illustrates the track for orbit 2024 at 0100 UT on August 31, 1975, near hurricane Caroline. The point of closest approach to the eye (point A) is about 40 km. Figure 6*b* illustrates the track for orbit 4546 when it passed near a low-pressure system associated with a North Atlantic storm at 0800 UT on February 25, 1976.

The variation in $H_{1/3}$ along the ground track for hurricane Caroline shows the following general variations provided the data are properly edited (see Figure 4*c*). The values are nearly constant for distances of 300 to 100 km (frames 140–150) from the eye; beyond this point, however, there is a gradual trend for $H_{1/3}$ to increase up to a maximum (frame 156) about 40 km beyond the point of closest approach. The motion of the hurricane toward the north and west is consistent with an asymmetry in $H_{1/3}$ around the point of closest approach based on wind-driven waves, since the counterclockwise circulation causes larger winds in the northeast quadrant (hurricane winds are known to increase up to a maximum corresponding to a radius typically 25 km). For orbit 2024 the ground track passes close to the radius of maximum winds at the point of closest approach. These results are in agreement with expected values based on wave model analysis of similar hurricanes [*Cardone*

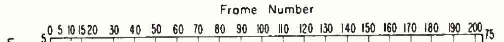

Fig. 5. Plots of altimeter parameters from orbit 4546 in the North Atlantic, February 25, 1976. Heavy line represents $H_{1/3}$ based on $\sigma_T' = 7.8$ ns. Light line represents $H_{1/3}$ based on $\sigma_T = 6.2$ ns with σ_j correction. Here $\sigma_T' = (\sigma_T^2 + \sigma_j^2)^{1/2}$.

et al., 1976]. No ship reports were available near the satellite track.

The estimates of $H_{1/3}$ for orbit 4546 are shown in Figure 7, where less data editing was required. Therefore a continuous plot is available, illustrating a definite trend: At the beginning of the orbit the wave heights are near 9 m, increasing to about 10 m before gradually decreasing to about 4 m. The scatter in the values is considered to be internally consistent and reasonable. The standard deviation is calculated to be about 0.6 m or less over the entire ground track. It was based on a quasi-linear regression analysis, the data being separated into three linear segments.

Ship reports and surface weather maps (available from NOAA/EDS, National Climate Center, Asheville, North Carolina, 28801) are compared with orbit 4546. The (0600 UT) northern hemisphere surface chart was analyzed for February 25, as well as the charts from the 2 previous days, along the subsatellite path. Both the isobar contours and the ship reports were used to estimate the magnitude of the wind. The winds near the northern coast of Scotland had been blowing for 50 hours with velocities of about 20 m/s. Therefore the waves were considered to be fully developed or nearly fully developed; see, for example, *Kinsman* [1965]. Wave heights for a fully developed sea correspond to a nondimensional peak frequency $\nu = 0.13$ as given by *Hasselmann et al.* [1976] and adjusted by *Pierson* [1977]:

$$H_{1/3}(\mathrm{m}) = 9.4 \times 10^{-4} \nu^{-10/6} U_{10}^{2} \quad \mathrm{m/s} \tag{13}$$

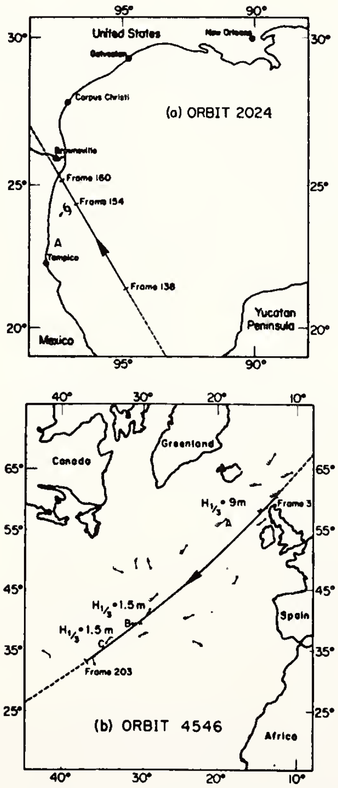

Fig. 6. Surface maps of subsatellite tracks. (*a*) Orbit 2024, Gulf of Mexico. Point A indicates the location of the hurricane eye (frame 154 corresponds to point of closest approach). (*b*) Orbit 4546, North Atlantic. Flags indicate surface winds. Points A, B, and C indicate location of ship weather reports.

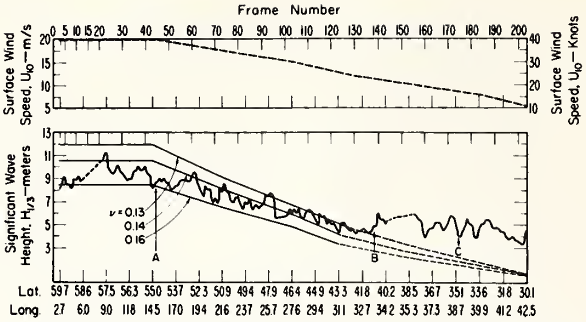

Fig. 7. Plot of significant wave height and surface winds along subsatellite path for orbit 4546 in the North Atlantic, February 25, 1976. $H_{1/3}$ is corrected for instrument jitter. Light lines show parametric model fit to $H_{1/3}$. Points A, B, and C correspond to the points of closest approach to the ship weather reports.

where U_{10} is the wind speed referred to a height of 10 m. The surface winds taken at a 10-m height are assumed to be equal to the winds reported in the surface charts. Hasselmann's parametric model defines the wave height in terms of two parameters, ν and U_{10}; however, his model considers only wind-driven waves. When wind wave heights are small, swell wave heights may be dominant. Ship reports were used in conjunction with wind wave heights based on the parametric model to determine that the swell probably did not contribute significantly to the wave height for the ground track considered here.

The estimated values of the surface winds along the satellite track are given in Figure 7. The corresponding wave heights for the wind-driven sea are given using (13) for three values of peak frequency, $\nu = 0.13$, 0.14, and 0.16. The fully developed case implies a 20-m/s wind blowing over a long fetch for approximately 36–48 hours. That is consistent with the weather maps off the northern coast of Scotland. In contrast, $\nu = 0.14$ and $\nu = 0.16$ represent lower wave heights and shorter duration winds. The dotted lines in Figure 7 refer to the portion of the analysis when the wind waves are small and the $H_{1/3}$ measurements deviate from the model values. On the basis of the available surface truth and the results of Figure 7, the wave height is overestimated when $H_{1/3} \lesssim 4$ m; this discrepancy is thought to be caused by bias error which is known to be more sensitive to the lower wave heights. Other analysis methods and/or a slight adjustment of σ_τ could decrease this discrepancy.

The statistical significance of the $H_{1/3}$ estimates, analyzed in terms of the regression slope variance, is discussed in Appendix C. When $H_{1/3} \gtrsim 4$ m, the estimates of $H_{1/3}$ are within ±1 m for 75% of the data. For this analysis, three frames were averaged for each data point which corresponds to spatial averaging over 70 km.

CONCLUSIONS

A method of analyzing the Geos 3 radar altimeter pulses has been developed which gives estimates of $H_{1/3}$ with sufficient accuracy for global measurements, provided $H_{1/3} \gtrsim 4$ m. However, this method requires that the altimeter data be properly edited to ensure this accuracy.

The small scatter in $H_{1/3}$, standard deviation of 0.6 m or less, is in reasonable agreement with the statistical analysis, ±1 m of the true values 75% of the time.

The bias errors in significant wave height are more sensitive to the analysis method including transmitter pulse width for the lower wave heights. The sensitivity to these errors should be improved with narrower pulse altimeters such as the one scheduled for launch on Seasat-A in May 1978. Indeed, the method employed here may be useful in developing techniques for analyzing altimeter pulses from the Seasat-A satellite scheduled for launch in May 1978.

APPENDIX A. STATISTICAL ANALYSIS OF INDIVIDUAL PULSES

The purpose of this work has been to infer significant wave height from average pulse shape. However, additional information related to sea state and the validity of the theory is available from the statistical fluctuations of the individual pulses. Furthermore, these fluctuations can indicate when the altimeter is operating properly. The statistical analysis is separated into two categories: (1) the correlation analysis between individual pulses and gates and (2) the moments of the amplitude statistics of the individual gates.

The interpulse and intergate correlation analyses are useful in assessing the validity of theoretical assumptions and in checking on the spacing of the 16 sampling gates, respectively. The interpulse correlation analysis is useful, since one would expect that the amplitudes of the square law detected return pulses are uncorrelated from pulse to pulse. Normally, many specular points in the illuminated footprints contribute to the backscattering, causing uniform distributed phase between many instantaneous pulses [*Berger,* 1972]. However, an exception to this could occur in the gate, which measures the backscattered energy when the pulse first intersects the top of the sea surface, i.e., when it has encountered only a few specular points. Theoretically, one would expect a detectable correlation in this one gate only for a sea with very long dominant waves, where the distance between specular points is large. But with the Geos 3 altimeter such a correlation may not be detectable, because even after correcting for jitter of the position of the gates, the 1.56-ns quantization level results in an indeterminacy of the illuminated area of 1.18 km² from pulse to pulse. Even for large swell the pulse most likely illuminates at least 5–10 specular points, which assuming uniform distributed phase is usually sufficient to approach Gaussian statistics.

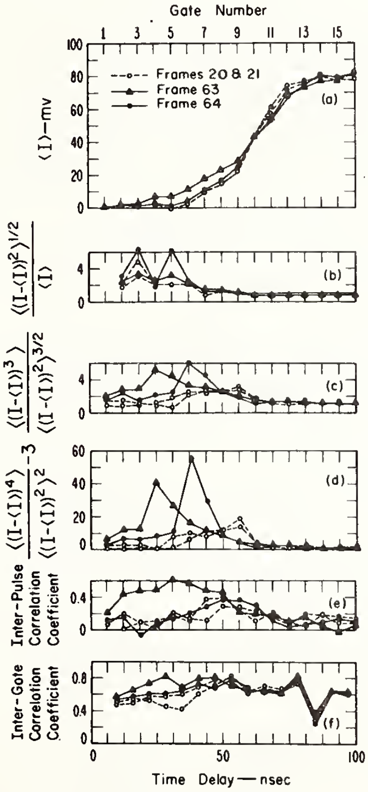

Fig. A1. Typical example for moments of statistical amplitude distribution, and intergate and interpulse correlation coefficients for four individual frames. Upper plot is average pulse shape, first-order moment; lower plots correspond to second-, third-, and fourth-order moments and correlation coefficients.

The intergate correlation analysis is one method of estimating the relative location of the individual gates. Indeed, an abnormally low intergate correlation coefficient would imply a larger than normal spacing between adjacent gates. The nominal altimeter design specifications are gates 12.5 ns wide, spaced 6.25 ns apart.

The correlation, for example, between gates 1 and 2 is calculated by using

$$R_{12} = \frac{\sum_{j=1}^{320} y_{1j} y_{2j}}{\left\{ \sum_{j=1}^{320} y_{1j}^2 \sum_{j=1}^{320} y_{2j}^2 \right\}^{1/2}}$$

where

$$y_{1j} = I_{1j} - \mu \qquad y_{2j} = I_{2j} - v$$

$$\mu = \frac{1}{320} \sum_{j=1}^{320} I_{1j} \qquad v = \frac{1}{320} \sum_{j=1}^{320} I_{2j}$$

I_{1j}, I_{2j} are the instantaneous energies in gates 1 and 2, respectively. A similar procedure was used to calculate other intergate and the interpulse correlation coefficients.

Figure A1 illustrates typical variations in the correlation coefficients and statistical moments for four different sets of data. Two sets, designated as frames 20 and 21, were selected for low seas, $H_{1/3} \lesssim 4$ m, whereas the remaining two sets of data were selected at times of higher seas, $H_{1/3} \cong 8$ m. Frame 64 is typical, whereas frame 63 is associated with a large negative spike in satellite altitude. These spikes have previously been considered to bias the estimates of $H_{1/3}$. Plot a shows the average pulse shape, first moment, for the four data sets, whereas plot e illustrates the variation in the interpulse correlation as a function of delay time or gate number. The correlation coefficients for the noise gates 1–6 and the plateau gates 13–16 are smaller than those for the transitionary gates 7–12, which have typical values of 0.2–0.3. However, an exception occurs at times of large negative spikes in satellite altitude as illustrated by frame 63, which displays coefficients 0.4–0.6 in the noise gates. Therefore the interpulse correlation is considered a useful indicator of negative spikes in altitude. Plot f illustrates the variation in intergate correlation. Again the larger correlation for frame 63 is evident although not as

TABLE A1. Statistical Moments for Exponential Distribution

	Distribution	
	$P(I)$	$(1/a)e^{-I/a}$
First moment	$\langle I \rangle$	a
Second moment	$\langle (I - \langle I \rangle)^2 \rangle^{1/2} / \langle I \rangle$	1
Third moment	$\langle (I - \langle I \rangle)^3 \rangle / \langle (I - \langle I \rangle)^2 \rangle^{3/2}$	2
Fourth moment	$[\langle (I - \langle I \rangle)^4 \rangle / \langle (I - \langle I \rangle)^2 \rangle^2] - 3$	6

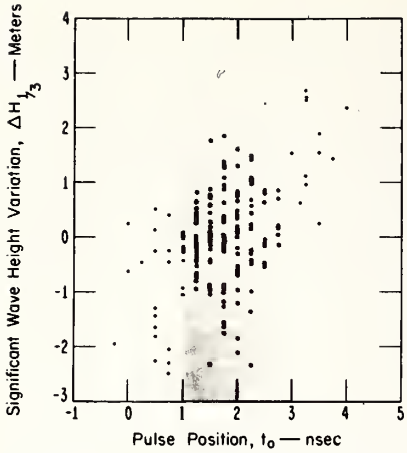

Fig. B1. Mass plot showing relationship between changes in wave height and pulse position.

pronounced. The consistent unexpected decrease in correlation between gates 13 and 14 and the increase in correlation between gates 12 and 13 are interpreted as a mislocation of gate 13 such that it is nearly in the same location as gate 12. The remaining lower plots illustrate the variations in the individual gate amplitude distributions. The expected values based on Gaussian statistics and the square law detector result in an exponential distribution for the individual gates. The expected values for the first four moments are given in Table A1. The second moment is a first indicator of how close the amplitude statistics can be approximated by exponential distribution, since the mean equals the standard deviation for this distribution. The large values of the second moment for the noise gates should be ignored, since $\langle I \rangle$ may be $\cong 0$ for these gates. The third moment, skewness, and the fourth moment, kurtosis, give more detailed information about the amplitude statistics. These parameters are higher for the high sea state conditions, which suggests that they may be a measure of sea state, changes in altitude, or perhaps some other related effect.

APPENDIX B. OBSERVATIONAL BIASES IN $H_{1/3}$ ESTIMATES

Some scatter in the values of $H_{1/3}$ is expected because the results are only estimates of the true values. The statistical significance of the estimates can be calculated (see Appendix C). The purpose of this section is to show that other systematic factors can bias these $H_{1/3}$ estimates.

The results for orbits 2024 and 4546 were carefully analyzed in an attempt to determine if a relationship could be found between the large positive and/or negative excursion from the trends in $H_{1/3}$ and other altimeter-related parameters. This analysis showed a definite relationship between both positive and negative excursions in $H_{1/3}$, hereafter designated $\Delta H_{1/3}$, and the position of the average received pulse, t_0. Figure B1 illustrates the correlation between $\Delta H_{1/3}$ and t_0 for orbit 4546; indeed, typical pulse positions are 2 ns, larger delays being associated with positive excursions of $H_{1/3}$ and smaller delays with negative excursions. The correlation between $\Delta H_{1/3}$ and t_0 as illustrated in Figure B1 is 0.78 provided that only values associated with $t_0 > 3$ ns and $t_0 < 1$ ns are considered in the analysis. Therefore the largest and smallest values of t_0 bias the estimates of $H_{1/3}$. The data associated with $t_0 > 3$ ns and $t_0 < 1$ ns were deleted from the data analyzed here.

APPENDIX C. STATISTICAL SIGNIFICANCE OF $H_{1/3}$ ESTIMATES

The random variations in the estimates of $H_{1/3}$ are important in determining the measurement accuracy of the altimeter. The estimates of $H_{1/3}$ are obtained by a least square fit of an error function to five data points defining the pulse shape near its midrange. The argument of the error function is related to $H_{1/3}$ by (9) and (10). The purpose of this section is to determine the statistical significance of the estimates. However, since a direct method using the error function is mathemati-

TABLE C1. Statistical Analysis of Regression Line for $H_{1/3}$, Orbit 2024

Frame	Slope Estimate b, mV/ns	Standard Deviation of Slope Estimate $S(b)$, mV/ns	Constant d	Standard Deviation of $H_{1/3}$ Estimates $S(H_{1/3})$, m	75% Confidence Limits		$H_{1/3}$, m
					Lower	Upper	
138	3.26	0.34	1369	2.18	−2.3	6.72	2.21
139	3.37	0.24	1436	1.40	−0.59	5.21	2.31
140	3.02	0.30	1402	1.52	0.48	6.76	3.62
141	3.05	0.23	1380	1.10	1.38	5.94	3.66
142	3.33	0.25	1425	1.39	−0.38	5.37	2.49
143	3.02	0.25	1425	1.18	1.52	6.40	3.96
144	3.45	0.26	1391	3.05	−5.27	7.35	1.04
145	3.23	0.21	1414	1.03	0.95	5.21	3.08
146	2.35	0.20	1380	1.08	4.82	9.28	7.05
147	3.23	0.21	1391	1.07	0.71	5.13	2.92
148	2.90	0.20	1369	0.90	2.61	6.33	4.47
149	3.14	0.23	1391	1.13	0.96	5.64	3.30
150	2.87	0.22	1380	1.02	2.42	6.64	4.53
151	2.87	0.24	1380	1.14	2.08	6.80	4.44
152	2.96	0.20	1369	0.94	2.08	5.97	4.03
153	2.46	0.15	1369	0.76	4.98	8.12	6.55
154	2.76	0.17	1406	0.79	3.55	6.81	5.18
155	2.32	0.15	1376	0.83	5.49	8.93	7.21
156	2.25	0.21	1421	1.21	5.28	10.3	7.78
157	2.19	0.15	1440	0.94	5.94	9.82	7.78
158	2.49	0.15	1428	0.76	5.02	8.16	6.59
159	2.50	0.19	1325	0.96	4.07	8.04	6.06

cally complicated, for simplicity a linear regression analysis is applied and shown to be a good approximation.

If two variables can be correlated linearly, the regression coefficient is the slope of the line used to correlate the variables. We are interested in the estimated deviations of this slope which can easily be related to $H_{1/3}$. If higher-order correlation is required (i.e., terms of order higher than linear can be obtained by using a series expansion of the error function), then a least square error analysis would give regression coefficients for each of the higher-order regression coefficients, a so-called curvilinear regression analysis. The curvilinear method is useful, since it permits the stepwise removal of each successive lower degree of the error function series expansion such that the calculation can be terminated at any level when the regression is adequate. Therefore in practice one need show only that the first few higher-order terms are small in comparison with the first-order (linear) term to establish that the linear regression is a valid method of determining the confidence bounds.

The curvilinear regression analysis was applied to selected frames of data from orbit 2024 by using a method described by *Volk* [1969]. The results showed that second-degree and third-degree terms may be removed with negligible error. Therefore a linear regression analysis is deemed sufficient to determine the statistical significance of the $H_{1/3}$ estimates. The error bars are obtained by applying a standard regression analysis, in terms of the least squares line $I = a + bt$, over the range of the five data points, where b is the slope estimate or regression coefficient. The results of this analysis give a correlation coefficient between 0.98 and 0.99, which is in agreement with the curvilinear regression result that only linear regression is required. The regression analysis gives the standard deviation of this slope estimate, $S(b)$. However, a transformation is required to convert to the standard deviation of $H_{1/3}$, $S(H_{1/3})$. Using (10) in a slightly different form we have

$$H_{1/3} = 0.6[d/b^2 - (\sigma_T')^2]^{1/2} \quad \text{(C1)}$$

where $d = [(I_\infty - I_{-\infty})^2]/2\pi$ and $\sigma_T' = 7.8$ ns. Then, using $S(H_{1/3}) = (dH_{1/3}/db)S(b)$, we obtain

$$S(H_{1/3}) = \frac{0.36d}{b^3 H_{1/3}} S(b) \quad \text{(C2)}$$

Table C1 shows the relevant statistical parameters for each frame of orbit 2024. The confidence limits are given as $H_{1/3} \pm tS(H_{1/3})$, which for a 75% chance of being within the range $H_{1/3} \pm tS(H_{1/3})$ gives $t = 2.069$. The results in Table C1 illustrate the high percent of change in the confidence limits for the lower sea states. Furthermore, the lowest values of $H_{1/3}$, such as the value for frame 140, which are normally deleted from the analysis using the editing criteria discussed above, give the most unreliable estimates of $H_{1/3}$. The estimates of $H_{1/3}$ can be considered to be statistically significant within about ±2 m for 75% of the data when $H_{1/3} \gtrsim 4$ m for spatial averaging over 23 km.

The $H_{1/3}$ estimates are statistically more significant for orbit 4546, since a running average of three points (frames) was used. Indeed, $S(H_{1/3})$ will be smaller by a factor $(3)^{1/2}$, i.e., $S_3(H_{1/3}) = 0.577S_1(H_{1/3})$, or in other words the confidence interval will be reduced by a factor of about 2 from the values of Table C1. When $H_{1/3} \gtrsim 4$ m, the estimates of $H_{1/3}$ can be considered to fall within ±1 m for 75% of the data for spatial averaging over 70 km.

Acknowledgments. The authors wish to thank K. Hasselmann and Duncan Ross for their encouragement and guidance during this work. The computer programing help from Bruce Gritton, Allan Yanaway, and Ruth Alpers is kindly acknowledged. This work was partially supported by NATO research grant SRG/A1.10., NOAA contract 03-022-35163, and NASA contract 855-33-05-09-53.

REFERENCES

Barrick, D. E., Rough surface scattering based on the specular point theory, *IEEE Trans. Antennas Propagat., 16*(4), 449–454, 1968.

Barrick, D. E., *Remote Sensing of the Troposphere*, chap. 12, edited by V. E. Derr, U.S. Government Printing Office, Washington, D. C., 1972.

Berger, T., Satellite altimetry using ocean backscatter, *IEEE Trans. Antennas Propagat., 20*(3), 295–309, 1972.

Brown, G. S., The average impulse response of a rough surface and its applications, *IEEE Trans. Antennas Propagat., 25*(1), 67–74, 1977.

Cardone, V. J., W. J. Pierson, and E. G. Ward, Hindcasting the directional spectra of hurricane-generated waves, *J. Petrol. Technol.*, 385–394, 1976.

Hasselmann, K., D. B. Ross, P. Muller, and W. Sell, A parametric wave prediction model, *J. Phys. Oceanogr., 6*(2), 200–228, 1976.

Hofmeister, E. L., B. N. Keeney, T. W. Godbey, and R. J. Berg, *Data Users Handbook and Design Error Analysis*, Aircraft Equipment Division, General Electric Company, Utica, N. Y., 1976.

Kinsman, B., *Wind Waves; Their Generation and Propagation on the Ocean Surface*, Prentice-Hall, Englewood Cliffs, N. J., 1965.

McGoogan, J. T., Satellite altimetry applications, *IEEE Trans. Microwave Theory Tech., 23*(12), 970–978, 1975.

Moore, R. K., and C. S. Williams, Jr., Radar terrain at near vertical incidence, *Proc. IRE, 45*, 228–238, 1957.

Pierson, W. J., Comments on a parametric wave prediction model, *J. Phys. Oceanogr., 7*(1), 127–137, 1977.

Shapiro, A., E. A. Uliana, and B. S. Yaplee, Radar pulse shape versus ocean wave height, edited by J. R. Apel, *Tech. Rep. ERL 228-AOML 7*, p. 11-1, Nat. Oceanic and Atmos. Admin., Washington, D. C., 1972.

Volk, W., *Applied Statistics for Engineers*, 2nd ed., pp. 323–328, McGraw-Hill, New York, 1969.

(Received November 8, 1977;
revised March 30, 1978;
accepted April 7, 1978.)

Radio Science 13: 677-685, July 1978.

The accuracy of water vapor and cloud liquid determination by dual-frequency ground-based microwave radiometry

Ed R. Westwater

Wave Propagation Laboratory, Environmental Research Laboratories, National Oceanic and Atmospheric Administration, Boulder, Colorado 80302

(Received September 6, 1977.)

A dual frequency ground-based radiometer operating in the 1 to 1.4 cm wavelength range can provide continuous measurements of integrated water vapor and cloud liquid water. Using climatological data, the accuracy of the vapor and liquid determinations is estimated as a function of cloud amount. Limiting factors in the water determination are uncertainties in water vapor absorption coefficients and, during cloudy conditions, uncertainties in cloud temperature. For integrated water vapor content greater than 10 mm, the accuracy of the vapor determination is better than 15% for a wide range of cloudy conditions.

1. INTRODUCTION

Total precipitable water is an important component of many moisture-related processes in the atmosphere. For example, the occurrence of convective clouds and precipitation is closely related to the amount of water vapor in the layer from the surface to 400 mb [*Battan and Kassander*, 1960]. Consequently, measurements of integrated vapor have been used in the design of cloud seeding experiments [*Dennis and Koscielski*, 1969]. Continuous observations of this quantity may also be useful in operational precipitation forecasting, and in meteorological research applications such as the estimation of water vapor flux into convective cells [*Leichter and Dennis*, 1974]. Other problems that require integrated water vapor, although not necessarily in the zenith direction, include electrical path length correction [*Westwater*, 1967; *Schaper et al.*, 1970], and real-time prediction of transmission for both infrared and millimeter wave propagation.

At the present time, precipitable water V can be measured in several ways. Operationally, V can be obtained by integrating radiosonde soundings and can be estimated, between soundings, by statistical regression of surface observations [*Reitan*, 1963; *Tomasi*, 1977]. However, single wavelength radiometric observations of precipitable water, obtained during clear conditions, have indicated frequent occurrences in which the total water content changed by 50% in periods of one or two hours and during which either the surface moisture remained nearly constant [*Gurvich et al.*, 1972] or the emission showed no correlation with surface dew point temperature [*Fogarty*, 1975]. Clearly, under such conditions prediction from surface conditions is unreliable. Another measurement technique, and one that gives both good accuracy and continuity in time, uses the spectral hygrometer to infer V from the infrared attenuation of solar radiation [*Tomasi et al.*, 1974]. However, this method is strongly affected by dense clouds, requires an assumption of horizontal stratification, and is restricted to daytime. Aircraft soundings, using a microwave cavity refractometer and a temperature sensor [*Gilmer et al.*, 1965], are capable of high accuracy in point measurements, but are too expensive for routine observations and are not ideal for vertical soundings.

None of the above techniques is completely appropriate for long-term, continuous, and near all-weather operation. Because of its operational simplicity and its proven performance in such areas as long-term attenuation monitoring, microwave radiometry seems ideally suited for routine monitoring of moisture and its changes with time.

The relationship between microwave thermal emission and atmospheric moisture was first observed by *Dicke et al.* [1946]. Although most of their measurements were taken during clear conditions, they mentioned that some cumulus clouds were quite absorbing at centimeter wavelengths.

Copyright © 1978 by the American Geophysical Union.

0048-6604/78/0708-0677$01.00

Subsequently, *Barrett and Chung* [1962] and *Staelin* [1966] discussed the determination of profile information from multispectral emission or extinction observations. In addition, Staelin discussed the possibilities of simultaneous vapor and cloud liquid determination. These possibilities were experimentally demonstrated by *Toong and Staelin* [1970] who obtained vapor and cloud liquid from emission observations at five frequencies. In addition, the Russian literature contains many descriptions of experimental determinations of vapor and liquid [*Plechkov*, 1968; *Gorelik et al.*, 1973; *Yershov and Plechkov*, 1977]. For down-looking systems, *Rosenkranz et al.* [1972] gave accuracy estimates for radiometric moisture determination.

In spite of the large amount of work on the problem, several important questions have not been addressed in the literature. Among these are the following: What is the range of cloud amounts over which useful vapor determinations can be obtained and, hence, what degree of reliability can dual frequency systems be expected to have? What effects do errors in molecular absorption parameters have on the vapor determination, and how can these errors be minimized? What are optimum frequencies for the system?

To answer these questions we describe below our accuracy estimates of radiometric determination of liquid and vapor. These results imply that, even with present uncertainties in absorption calculation, accuracies usually better than 15% can be achieved for a wide range of cloudy conditions.

2. DETERMINATION OF INTEGRATED WATER VAPOR AND CLOUD LIQUID FROM RADIOMETRIC OBSERVATIONS

Under conditions of low attenuation (optical depth $\leqslant 1$), total absorption can be derived from atmospheric emission [*Hogg and Chu*, 1975]. This absorption can, in turn, be directly related to corresponding amounts of integrated water vapor V and cloud liquid L. As discussed by *Staelin* [1966] measurements of low attenuation at a vapor-sensitive frequency and a cloud-sensitive frequency allow separation of the two water phases. Various separation algorithms are possible [*Staelin*, 1966; *Grody*, 1976]; we briefly describe a physically transparent method in which the effect of uncertainties (both in measurement and of physical constants) can easily be evaluated.

If the total atmospheric transmission at frequency ν is written as $\exp(-\tau_\nu)$, then measurements of microwave brightness temperature $T_{b\nu}$ can be converted to this opacity τ_ν by

$$\tau_\nu = -\ln[(T_{mr} - T_{b\nu})/(T_{mr} - T_{bb})] \tag{1}$$

where T_{bb} is the cosmic background "big bang" brightness temperature equal to 2.8 K, and T_{mr} is an estimated "mean radiating temperature." For nonprecipitating clouds, we can write

$$\tau_\nu = \kappa_{V\nu} V + \kappa_{L\nu} L + \tau_{d\nu} \tag{2}$$

where $\kappa_{V\nu}$ and $\kappa_{L\nu}$ are path-averaged mass absorption coefficients of vapor and liquid, and $\tau_{d\nu}$ is the dry absorption. since microwaves interact only weakly with ice clouds [*Staelin et al.*, 1975], their effect is neglected here. From measurements at two frequencies, we can form two equations and solve for the two unknowns V and L:

$$V = (\kappa_{Lu} f_l - \kappa_{Ll} f_u)/(\kappa_{Vl}\kappa_{Lu} - \kappa_{Vu}\kappa_{Ll}) \tag{3}$$

$$L = (-\kappa_{Vu} f_l + \kappa_{Vl} f_u)/(\kappa_{Vl}\kappa_{Lu} - \kappa_{Vu}\kappa_{Ll}) \tag{4}$$

where

$$f_\nu = -\tau_{d\nu} - \ln[(T_{mr} - T_{b\nu})/(T_{mr} - T_{bb})] \tag{5}$$

for $\nu = l, u$. In (3), (4), and (5), we use the notation l and u to refer to lower (water-vapor-sensitive) and upper (liquid-water-sensitive) frequencies. Physically, f_ν is a measure of the opacity at ν from water vapor and cloud liquid. Observe that in (3), the estimate of V depends only on the ratio of κ_{Lu} and κ_{Ll} and not on their absolute values. The implication of this when measuring water vapor in the presence of light rain is discussed in the next section.

As discussed in section 3, (3)–(5) can be used to derive V and L from measurements of T_b. This first requires the calculation of mass absorption coefficients and dry attenuation from a model profile of the vertical temperature, pressure, and humidity distributions.

3. FACTORS CONTRIBUTING TO ERROR IN RADIOMETRIC DETERMINATION OF LIQUID AND VAPOR

Radiometric determination of V and L requires both the physical measurement of radiation and

TABLE 1. Calculations of mean (κ_{V_ν}) and standard deviation σ of water vapor absorption coefficient.

A. Weather ship D						
Frequency (GHz)	19.35	20.6	21.5	22.0	22.235	31.65
κ_{V_ν} (nepers per cm of H_2O)	.02503	.04239	.06032	.06867	.07099	.02562
$\sigma(\kappa_{V_\nu})$ (nepers per cm of H_2O)	.00027	.00033	.00124	.00180	.00190	.00065
(σ/κ) (percent)	1.08	0.78	2.06	2.62	2.68	2.54
B. Weather ship P						
κ_{V_ν} (nepers per cm of H_2O)	.002504	.04280	.06139	.07013	.07259	.02556
$\sigma(\kappa_{V_\nu})$ (nepers per cm of H_2O)	.00034	.00022	.00157	.00241	.00252	.00058
(σ/κ) (percent)	1.35	0.51	2.56	3.44	3.47	2.27

the *estimation* of a number of quantities entering into (3)–(5). A small uncertainty ε_i in any of these parameters p_i contributes to the total uncertainty in V, for example, an amount $(\partial V/\partial p_i)\varepsilon_i$. We examine below the uncertainty in each of these factors.

Errors in mean radiating temperature (T_{mr}). The zenith thermal emission depends on the vertical distributions of temperature and composition and, hence, the true T_{mr} cannot be determined unless these distributions are known. However, using climatological and/or surface meteorological measurements to estimate T_{mr}, we have found that, over the frequency interval 15–35 GHz, the standard deviations of this quantity are typically about 3–5 K.

Errors in measurement of brightness temperature. Absolute values of water content are related to the absolute measurement of T_{b_ν}; hence all of the many factors determining the absolute calibration of the instrument will influence the moisture determination. For many of the calculations of section 4, we assume an uncertainty in brightness temperature measurement of ±0.5 K.

Uncertainties in dry attenuation. For a given location and season, dry attenuation varies about 5% due to changes in temperature and pressure. With knowledge of surface pressure and temperature, some of this variation can be predicted. Another source of uncertainty in dry attenuation is the inaccuracy in calculating the dry absorption coefficients as a function of temperature and pressure. Our calculations agree to within about 10% with measurements at 6 GHz by *Hogg and Semplak* [1961] and with those of *Altshuler et al.* [1968] at 15 GHz.

Errors in water vapor attenuation coefficients. As in the case of dry absorption, errors in effective water mass attenuation coefficient arise in two fundamentally different ways: first, through uncertainties in molecular constants, spectral line shape, etc.; and second, through variations in the vertical absorption profile that cannot be predicted climatologically.

To determine typical ranges of variation of κ_{V_ν}, means and standard deviation of the quantity were calculated from a data base of radiosonde soundings from two weather ships taken during the years 1967–1968. The climatological variation of each of these stations, ship D in the North Atlantic (44°N, 41°W) and ship P in the Gulf of Alaska (50°N, 145°W), was large. The statistical results are shown in Table 1. For frequencies less than ~31 GHz, the largest climatological variation in water vapor mass absorption coefficient κ_{V_ν} occurs at the resonant frequency ν = 22.235 GHz. Note also the reduced variation at 20.6 GHz.

As discussed by *Waters* [1976], the absorption by molecular water vapor is not completely understood, particularly in the windows between resonant lines. With empirical corrections, the discrepancy between measured and calculated absorption can be reduced to within 10%. Another source of error is the value of the line width constant and its temperature, pressure, and humidity dependence. For example, *Becker and Autler's* [1946] measurements of water vapor absorption lead to a line width constant of water vapor, broadened by one atmosphere of dry air, of 2.78 GHz (T = 300 K). *Liebe's* [1969] measurement of the same quantity by dispersion spectroscopy yielded $\Delta\nu_{H_2O-AIR} = 2.87$ GHz (T = 300 K), whereas the value suggested by *Waters* [1976] is 2.96 GHz. Calculations of the water vapor mass absorption coefficient for changes of ±10% in $\Delta\nu$ are shown in Figure 1. The results shown were calculated for the Van Vleck-Weisskopf line shape, using the parameters of *Liebe* [1969], and for the Zhevakin-Naumov-Gross line shape using

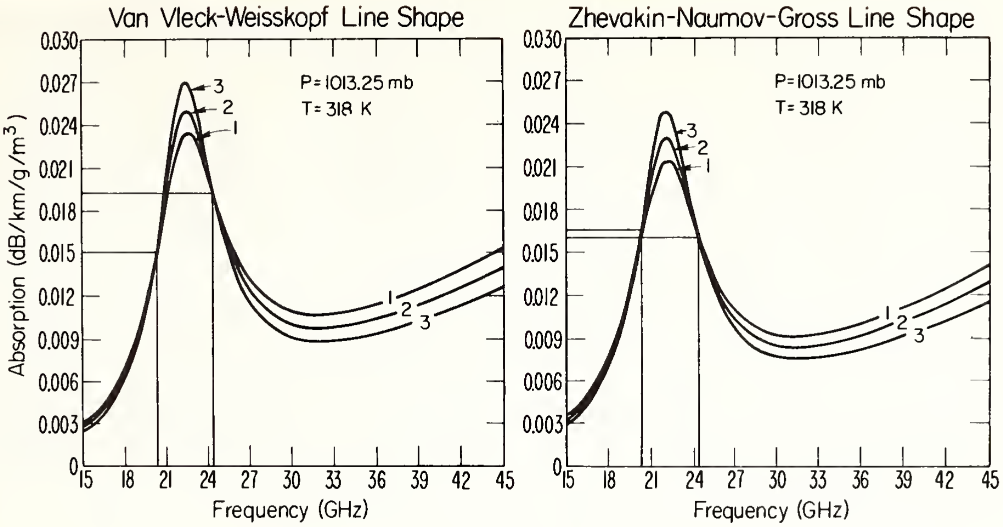

Fig. 1. Calculations of water vapor mass absorption coefficient for ±10% change of line width constant $\Delta\nu_0$. 1 = line width increased by 10%, 2 = original line width, 3 = line width decreased by 10%. For details, see text.

the parameters of *Waters* [1976]. Note that around 20.6 and 24.4 GHz, the absorption changes little for the different line widths. In addition, the differences in absorption for the two line shapes are small at 20.6 GHz. Thus, radiometric observations at the 20.6 GHz frequency could minimize both the effects of uncertainties in the choice of line width parameter and line shape, and the effects due to climatological variation of water vapor and temperature profiles.

Errors in cloud liquid attenuation coefficient. Measurements of the microwave dielectric constant of liquid water show a strong dependence on wavelength and temperature [*Grant et al.*, 1957]. For the wavelengths considered in this paper, and for nonprecipitating conditions, i.e., for maximum particle diameters less than 100 μm, the Rayleigh equation may be used to calculate the absorption from the dielectric constant and the cloud water content [*Mason*, 1971]. Such calculations show that the liquid attenuation changes (decreases) about 2% per °C (increase) in temperature. However, the sensitivity to temperature is somewhat ameliorated for a two-channel system because of the known dependence of the attenuation on frequency and temperature. Without independent information on such cloud parameters as base temperature, base height, or thickness, the uncertainty in average cloud temperature can easily be ±5°C.

For frequencies greater than 15 GHz and during rains that contain an appreciable number of drops whose diameters exceed 1 mm, the Rayleigh approximation is not valid. Furthermore, for the same frequency restriction and for rain rates greater than 1 mm/hr, the scattering contributions to extinction exceed 5%, so that scattering becomes increasingly important in radiative transfer, as either the frequency, or the rain rate, increases. However, *Zavody's* [1974] calculations at 37 GHz indicated that, for rain attenuation less than ~3 dB, the error due to neglecting scattering and estimating the attenuation directly from emission is about 20%. As was pointed out in section 2, the dual-frequency vapor determination requires not the separate values of the upper and lower channel liquid attenuation but only their ratio. This ratio, calculated at 22.235 and 30 GHz, for a rain rate of 0.25 mm/hr differed by about 10% from the ratio calculated for Rayleigh particles. Thus, in light rain, although the Rayleigh assumption could result in an error in liquid determination of a factor of 2 or 3, the effect on vapor determination would be much less serious.

4. RESULTS

Proceeding on the assumption that cloud absorption is Rayleigh, and by using the standard statistical rule for the propagation of errors of correlated

TABLE 2. Error standard deviations used in evaluating resultant errors in the determination of water vapor *V* and cloud liquid *L*.

Frequency (GHz)	Vapor absorption coefficient (percent)	Liquid absorption coefficient (percent)	Dry attenuation (percent)	Mean radiating temperature (K)	Brightness temperature (K)
20.6	5.9	16.6	10.4	4.1	0.5
22.235	10.9	16.5	10.4	3.9	0.5
31.65	5.2	15.7	10.4	5.0	0.5

variables, we have combined the error factors discussed in section 3 with the appropriate partial derivatives to yield a resultant error in both *V* and *L*. The results strongly suggest that most, if not all, non-precipitating clouds will not seriously degrade retrievals of water vapor *V*.

In determining suitable frequencies for dual channel remote sensing, we investigated the pairs

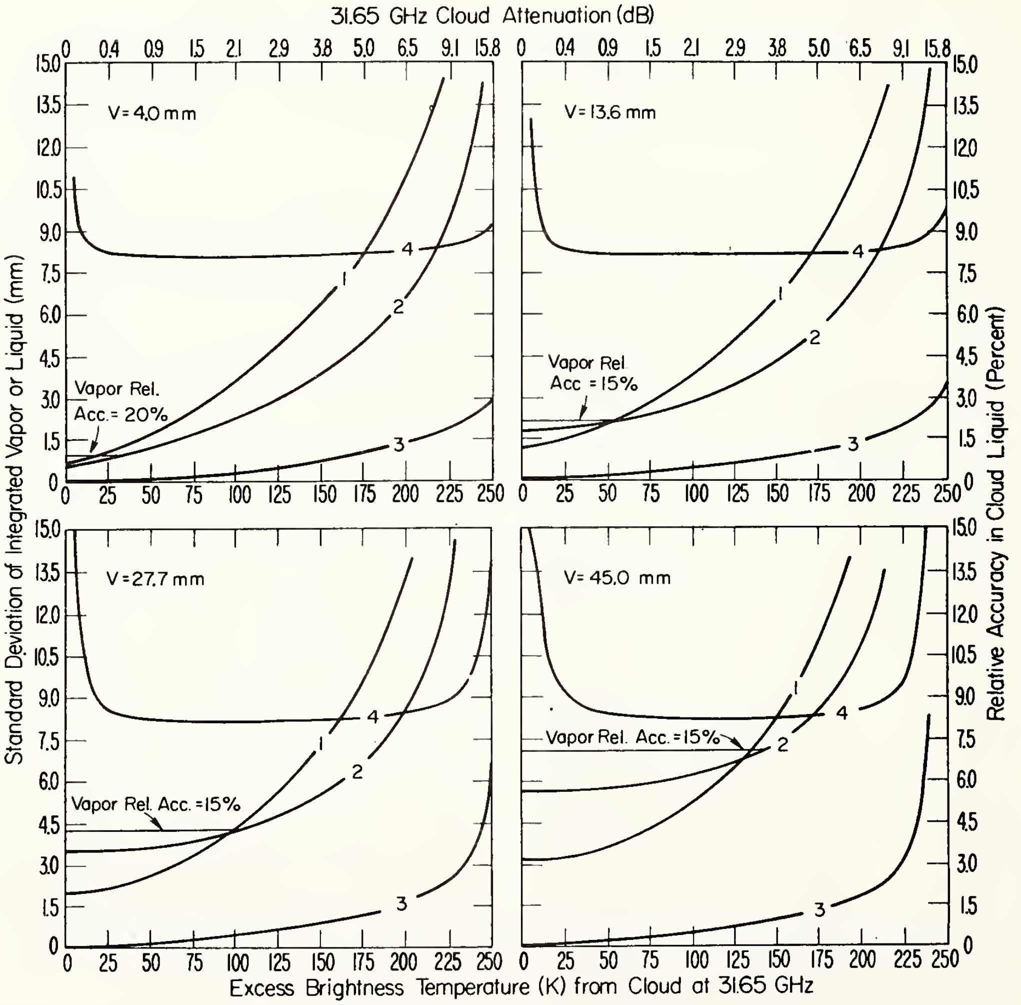

Fig. 2. Errors in the determination of precipitable water as a function of cloud emission. 1 = vapor determination with (20.6, 31.65 GHz) system, 2 = vapor determination with (22.235, 31.65 GHz) system, 3 = liquid determination with (22.235, 31.65 GHz) system, 4 = relative accuracy in liquid with (22.235, 31.65 GHz) system. Error factors of Table 1 are assumed.

(20.6, 31.65) and (22.235, 31.65) GHz. The (22.235, 31.65) pair is already in an operational sounder [*Staelin et al.*, 1975]; the (20.6, 31.65) pair uses a channel, 20.6, at which the error in vapor attenuation coefficient is small. For these frequencies, the error factors in Table 2 were used to evaluate the resultant errors in V and L. The climatological variation of the factors was derived from two years of radiosonde data obtained at weather ship D. The total uncertainties in water vapor and dry absorption coefficients were determined by adding the variance from errors in molecular constants to the climatological variance. We used least-squares parameter fitting to the data of *Becker and Autler* [1946], assuming the Van Vleck-Weisskopf line shape, to estimate the uncertainty in calculating water vapor attenuation, given that temperature, pressure, and humidity are known. Our fit resulted in an rms percentage residual of about 7%, which is more than double the precision of the Becker-Autler data. We are currently investigating this enigma.

Typical results on overall accuracy of vapor and liquid retrievals, for values of average moisture ranging from 4 to 45 mm, and cloud attenuations up to 15 dB, are shown in Figure 2 (in this and subsequent figures, relative accuracy means standard deviation divided by true value). The reader is cautioned, however, that most attenuations greater than 3 dB are caused by rain; therefore, the portions of the curves beyond this value will not

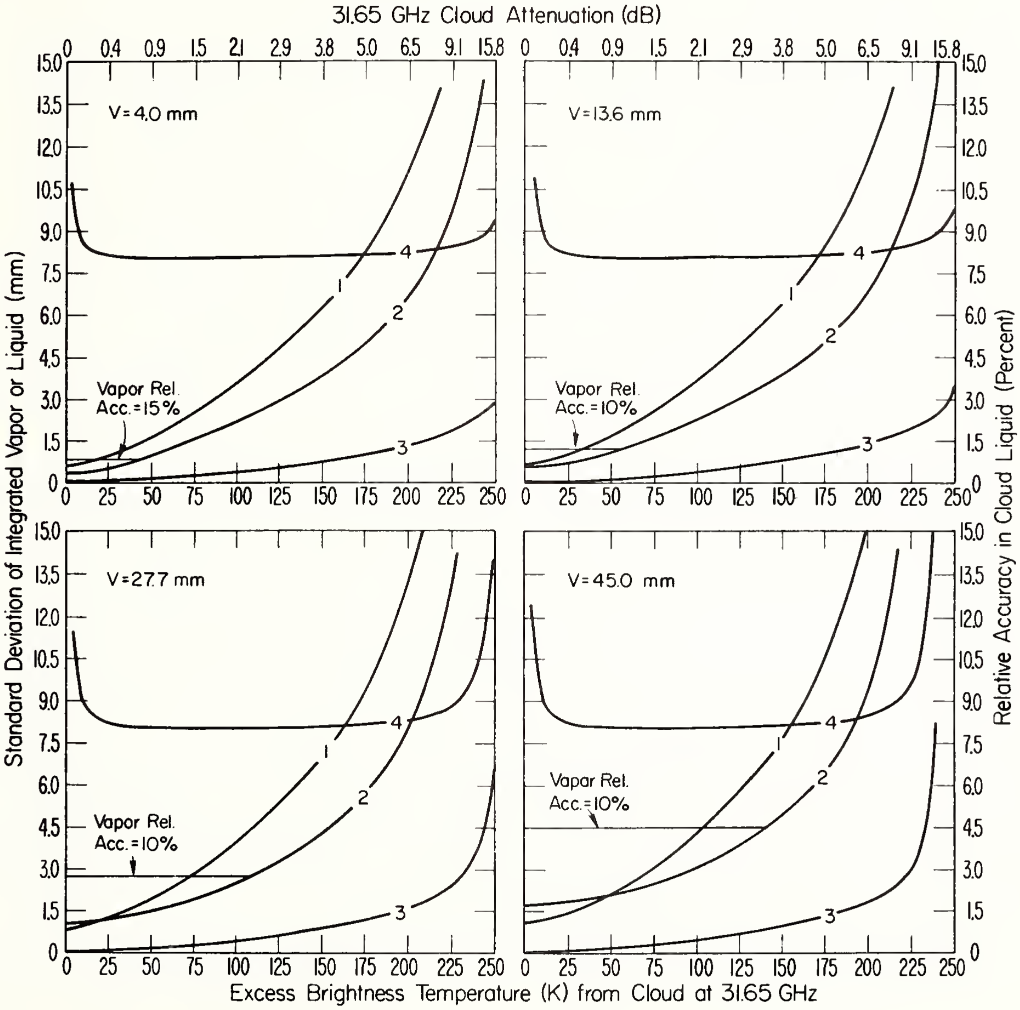

Fig. 3. Errors in the determination of precipitable water as a function of cloud emission. Same notation as in Figure 2. Molecular constants and absorption equations are assumed to be correct.

apply in all cases. Several features are evident from this figure: (1) For clear skies, the 20.6 GHz frequency yields a better accuracy in V than the 22.235 GHz frequency; for $V > 10$ mm, this accuracy generally is better than ~15%. (2) At some cloud density the accuracy for determining V at 22.235 GHz will exceed that of the lower channel. (3) Except for the extremes of the cloud error curves, the accuracy of the derived amount of cloud liquid is quite insensitive to the amount of water vapor present. To estimate system reliability from these curves, it is necessary to know the percentage of time that cloud attenuation levels (or excess brightness temperature levels) are exceeded. *Lo et al.* [1975] reported attenuation at 35 GHz for various types of nonprecipitating clouds. Even up to pre-rain clouds, the largest observed liquid attenuation was 2.3 dB. In addition, some long-term statistics are available. For example, at Holmdel, New Jersey, *Wilson* [1969] determined that the excess attenuation at 30 GHz exceeded 3 dB about 1% of the time (for nighttime zenith observations), and it exceeded 3 dB 2% of the time for daytime solar tracking. Our extrapolation to 30 GHz of *Bergmann and Mullers'* [1976] observations of sky brightness at 13 and 18 GHz, taken at Longmont, Colorado, implies that 3 dB would be exceeded only about 0.1% to 0.2% of the time. Thus, for many locations at least, these rather conservative attenuation estimates along with the accuracies indicated in Figure 2 suggest a high degree of system reliability.

A large component of the total error in water vapor mass absorption coefficient κ_{V_ν} and in dry absorption τ_{d_ν} is the error due to uncertainties in molecular absorption equations. If theoretical and experimental developments would lead to substantial improvement of these calculations, then a large improvement would be obtained in the accuracy of deriving water vapor V during clear and moderately cloudy skies. To show this, we repeated our calculations with conditions identical to those of Table 2, except that uncertainties in path-averaged gaseous absorption were from profile variation only, molecular absorption equations being assumed exact. At the frequencies 20.6, 22.235, and 31.65 GHz, these remaining errors in κ_{V_ν} were 0.8%, 3.2%, and 2.6%, and those in τ_{d_ν} were 2.7%, 2.7%, and 2.7%. The results are shown in Figure 3. Note that the two water channels yield roughly the same accuracy for clear conditions, with the 22.235 GHz channel exhibiting a clear superiority during cloudy conditions. As is evident by comparison with Figure 2, a large reduction in error in V occurs when the molecular component of absorption error is eliminated.

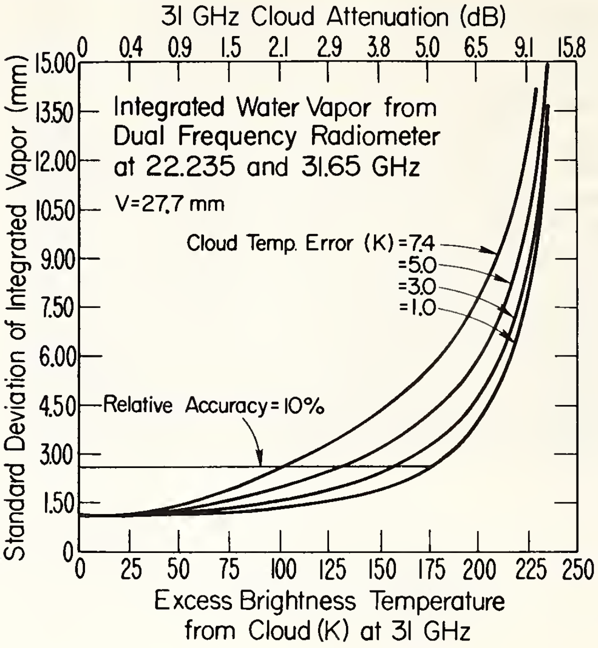

Fig. 4. Errors in the determination of precipitable water for different uncertainties in cloud temperature.

An important factor in correcting V for clouds whose 31 GHz attenuation is greater than ~1 dB is the average cloud temperature. Curves of Figure 4, calculated assuming no error in molecular constants, show this accuracy for various standard deviations of cloud temperature δT_c. Thus, for example, a standard deviation of 1.5 mm in V could arise from a cloud whose attenuation is 0.9 dB and whose temperature uncertainty is 7.4 K or from one whose attenuation is 2.5 dB but whose δT_c is 1 K. Similar calculations investigating the sensitivity to noise levels in the measurement system indicate that the accuracy in V does not degrade seriously until the brightness temperature error exceeds 1 K.

5. DISCUSSION

Calculations indicate that, for 31 GHz cloud attenuation less than 3 dB, a dual frequency ground-based radiometric system can provide useful measurements (usually within 15%) of integrated water vapor and cloud liquid water. These calculations, coupled with available attenuation statistics, imply that such a system could operate 98%–99% of the time for many locations.

The clear-air accuracy of such a system is currently limited by uncertainties in calculation of water vapor absorption as a function of temperature, pressure, and water vapor concentration. To minimize these uncertainties, we are designing a channel at 20.6 GHz, a frequency at which uncertainties in absorption due to uncertainties in line width constants are small. If, however, the uncertainties in knowledge of absorption were eliminated, the 22.235 GHz channel would be an equally good frequency for clear-air probing, and a much better one for separating cloud from vapor.

As was shown in section 4, the cloud effects could be considerably reduced if the effective radiating temperature of the clouds were known. This temperature could be much more accurately estimated if the base height (or base temperature) and thickness were independently measured. Base heights can be measured by a ceilometer, base temperature perhaps by joint infrared-microwave radiometry, and both height and thickness by radar.

The Wave Propagation Laboratory, National Oceanic and Atmospheric Administration, has recently constructed a dual-channel system at 20.6 and 31.65 GHz. After initial performance tests are completed, the system will be operated at Stapleton International Airport, Denver, Colorado, for about six months in 1978. Later, the system will be taken to a more humid location for further tests and evaluation.

A complementary experiment that will independently measure cloud attenuation is also being designed by the Wave Propagation Laboratory (J. B. Snider, personal communication, 1977). The COMSTAR synchronous satellites have a continuously operating beacon at 28.5 GHz. Power levels of this extremely narrow bandwidth beacon will be monitored at the ground by a stable receiver. This measurement, coupled with simultaneous measurements of emission in the same direction and at a closely separated but nonoverlapping frequency band, will provide estimates of both cloud radiating temperature and cloud attenuation. Accuracy estimates of J. B. Snider (personal communication, 1977) suggest that this system can measure attenuation to within ±0.25 dB for attenuation less than 5 dB, and to within ±10% for attenuation between 5 and 10 dB. The accuracy of the mean radiating temperature determination is not high, being about 2.5% at an attenuation of 3 dB. If a dual-frequency system, say 20.6 and 31.65 GHz, were also pointing in the satellite direction, then the estimate of cloud attenuation could receive independent confirmation. The effects of rain on the dual system can also be studied with this experiment.

Acknowledgments. The author expresses appreciation to D. Hogg for many valuable discussions and suggestions during the course of this work, and in addition, to F. O. Guiraud, who performed many of the calculations using climatological data. Finally, the useful suggestions by an anonymous reviewer are acknowledged.

REFERENCES

Altshuler, E. E., V. J. Falcone, and K. N. Wulfsberg (1968), Atmospheric effects on propagation at millimeter wavelengths, *IEEE Spectrum, 5, 83–91.*

Barrett, A. H., and V. K. Chung (1962), A method for the determination of high-altitude water-vapor abundance from ground-based microwave observations, *J. Geophys. Res., 67,* 4259–4266.

Battan, L. J., and A. R. Kassander (1960), Design of a program of randomized seeding of orographic cumuli, *J. Meteorol., 17,* 583–590.

Becker, G. E., and S. H. Autler (1946), Water vapor absorption of electromagnetic radiation in the centimeter wavelength range, *Phys. Rev., 70,* 300–307.

Bergmann, H. J., and E. E. Muller (1976), A radiometer experiment at 13 and 18 GHz to study satellite system site diversity, paper presented at IEEE International Conference on Communication, Philadelphia, PA.

Dennis, A. S., and A. Koscielski (1969), Results of a randomized cloud seeding experiment in South Dakota, *J. Appl. Meteorol., 8,* 556–565.

Dicke, R. H., R. Beringer, R. L. Kyhl, and A. B. Vane (1946), Atmospheric absorption measurements with a microwave radiometer, *Phys. Rev., 70,* 340–348.

Fogarty, W. G. (1975), Total atmospheric absorption at 22.2 GHz, *IEEE Trans. Antennas Propagat., AP-23,* 441–444.

Gilmer, R. O., R. E. McGavin, and B. R. Bean (1965), Response of NBS microwave refractometer cavities to atmospheric variations, *J. Res. Nat. Bur. Stand. Sect. D, 69D,* 1213–1217.

Gorelik, A. G., V. V. Kalashnikov, L. S. Raykova, and Yu. A. Frolov (1973), Radiothermal measurements of atmospheric humidity and the integral water content of clouds, *Atmos. Oceanic Phys., 9,* 527–530.

Grant, E. H., T. J. Buchanan, and H. F. Cook (1957), Dielectric behavior of water at microwave frequencies, *J. Chem. Phys., 26,* 156–161.

Grody, N. C. (1976), Remote sensing of atmospheric water content from satellites using microwave radiometry, *IEEE Trans. Antennas Propagat., AP-24,* 155–162.

Gurvich, A. S., A. T. Yershov, A. P. Naumov, and V. M.

Plechkov (1972), An investigation of atmospheric moisture content by a method of ground-based radiothermal detection (in Russian), *Meteorol. Gidrolog.*, *No. 5*, 22–27.

Hogg, D. C., and T. Chu (1975), The role of rain in satellite communications, *Proc. IEEE*, *63*, 1308–1331.

Hogg, D. C., and R. A, Semplack (1961), The effect of rain and water vapor on sky noise at centimeter wavelengths, *Bell Syst. Tech. J.*, *40*, 1331–1348.

Leichter, I., and A. S. Dennis (1974), Moisture flux and precipitation studies of convective storms in western South Dakota using pibal and radar data, *Proceedings of Conference on Cloud Physics, Oct. 21–24, 1974, Tucson, Arizona*, pp. 438–441, American Meteorology Society, Boston, Mass.

Liebe, H. J. (1969), Calculated tropospheric dispersion and absorption due to the 22-GHz water vapor line, *IEEE Trans. Antennas Propagat.*, *AP-17*, 621–627.

Lo, L., B. M. Fannin, and A. W. Straiton (1975), Attenuation of 8.6 and 3.2 mm radio waves by clouds, *IEEE Trans. Antennas Propagat.*, *AP-23*, 782–786.

Mason, B. J. (1971), *The Physics of Clouds*, p. 427, Oxford University Press, London.

Plechkov, V. M. (1968), Preliminary results of determining the moisture content of the atmosphere from measurements of its thermal emission near $\lambda = 1.35$ cm, *Atmos. Oceanic Phys.*, *4*, 102–105.

Reitan, C. H. (1963), Surface dew point and water vapor aloft, *J. Appl. Meteorol.*, *2*, 776–779.

Rosenkranz, P. W., F. T. Barath, J. C. Blinn III, E. J. Johnson, W. B. Lenior, D. H. Staelin, and J. W. Waters (1972), Microwave radiometric measurements of atmospheric temperature and water from an aircraft, *J. Geophys. Res.*, *77*, 5833–5844.

Schaper, L. W., Jr., D. H. Staelin, and J. W. Waters (1970), The estimation of atmospheric electrical path length by passive microwave radiometry, *Proc. IEEE*, *58*, 272–273.

Staelin, D. H. (1966), Measurements and interpretation of the microwave spectrum of the terrestrial atmosphere near 1-centimeter wavelength, *J. Geophys. Res.*, *71*, 2875–2881.

Staelin, D. H., A. L. Cassel, K. F. Kunzi, R. L. Pettyjohn, R. K. L. Poon, P. W. Rosenkranz, and J. W. Waters (1975), Microwave temperature sounding: Effects of clouds on the Nimbus 5 satellite data, *J. Atmos. Sci.*, *32*, 1970–1976.

Tomasi, C. (1977), Precipitable water vapor in atmospheres characterized by temperature inversions, *J. Appl. Meteorol.*, *16*, 237–243.

Tomasi, C., R. Guzzi, and O. Vittore (1974), A search for the *e*-effect in the atmospheric water vapor continuum, *J. Atmos. Sci.*, *31*, 255–260.

Toong, H. D., and D. H. Staelin (1970), Passive microwave spectrum measurements of atmospheric water vapor and clouds, *J. Atmos. Sci.*, *27*, 781–784.

Waters, J. W. (1976), Absorption and emission by atmospheric gases, in *Methods of Experimental Physics, Vol. 12, Astrophysics*, Part B: Radio Telescopes, Chap. 2.3, Academic Press, New York.

Westwater, E. R. (1976), An analysis of the correction of range errors due to atmospheric refraction by microwave radiometer techniques, *ESSA Tech. Rep. IER 30-ITSA 30*, available from National Technical Information Service, Springfield, Virginia.

Wilson, R. W. (1969), Sun tracker measurements of attenuation by rain at 16 and 30 GHz, *Bell Syst. Tech. J.*, *48*, 1383–1404.

Yershov, A. T., and V. M. Plechkov (1977), Evaluation of the accuracy of radiometric measurements of atmospheric moisture content from data of the expedition ATEP 74, *Atmos. Oceanic Phys.*, *13*, 102–105.

Zavody, A. M. (1974), Effect of scattering by rain on radiometer measurements at millimeter wavelengths, *Proc. Inst. Elec. Eng.*, *121*, 257–263, 1974.

Proceedings of the WMO Symposium on Boundary Layer Physics Applied to Specific Problems of Air Pollution, 259-270, 19-23 June, 1978.

THE IMPLICATIONS OF REMOTE-SENSING DEVELOPMENTS FOR AIR-POLLUTION METEOROLOGY

William H. Hooke
NOAA/ERL/Wave Propagation Laboratory
Boulder, Colorado 80302

1. Introduction

Atmospheric remote sensing — the use of radio, optical, and acoustic techniques to measure atmospheric variables such as wind, temperature, or aerosol concentration, along a line, over an area, or throughout a volume — is currently at the crossroads, for two reasons:

> i) in the past, the majority of remote-sensing techniques were little more than a gleam in a developer's eye. Today we have in hand working prototypes of many of the more important instruments.
>
> ii) in the past, techniques were being developed in isolation, under conditions where the research focus was introspective, concentrating on evaluating a specific measurement concept. Today the field is more outward-looking, searching for applications, and in some instances adopting a top-down user-oriented approach toward developing hybrid systems responsive to the meteorologist's needs.

In this paper, we briefly review this field of atmospheric remote sensing, emphasizing the implications of recent progress for air-pollution meteorology in particular. We begin with a general comparison of remote sensors with in situ instruments in Section 2. We follow this with a discussion of remote sensing as it is being applied to research problems in urban meteorology, the planetary boundary layer (PBL), and turbulence and diffusion processes (Section 3). Section 4 contains brief remarks on the use of remote-sensing data as inputs for initializing and verifying numerical models, on the transfer of remote-sensing technology into the operational sector, and on future uses in operational air-pollution forecasting. An appendix contains a quick (and necessarily incomplete) review of recent hardware developments in remote sensing per se. Let us note before proceeding further that while we have tried to give a fair perspective of progress within the field as a whole, we have perforce drawn heavily for our specific illustrations from work at our home institution. We hope that any imbalances this may have created in the presentation will be excused.

2. Remote Sensors Compared with In Situ Instruments

In this section we contrast the two basic approaches to atmospheric measurement — in situ instrumentation and remote sensors. As its name implies, the former method involves sampling of the medium in the immediate vicinity of the instrument, using some direct effect of the variable in question in order to measure it (for example, the rate at which an airflow turns the cups of an anemometer immersed in it, or the cooling effect of airflow past a hot wire). On the other hand, remote-sensing techniques make use of the fundamental fact that the interaction of radio, optical, and acoustic waves with the medium through which they propagate depends upon the properties of the medium, and in a known way. Thus, for example, sound waves propagate through air at a speed that is determined by the local temperature and the local wind velocity. The Doppler shift introduced into a radio wave by scattering from atmospheric turbulence is proportional to the velocity of the turbulent eddies relative to the radio source. Absorption of an optical wave propagating through a mixture of gases depends upon the composition of the mixture and its density as well as the frequency or color of the incident light.

Passive remote sensors use observed properties of existing radiation of natural origin to draw inferences concerning the medium. For instance, microwave radiometry uses the spectrum of microwave emissions from the clear sky to determine temperature and humidity. While this feature makes them useful for military purposes, where sensor detection is itself a concern, passive sensors are generally much less desirable than active sensors, which supply their own wave radiation. This added control gives active sensors the edge in flexibility, improved spatial resolution, and scanning capability.

In general, because of the difference in complexity of the instruments and their associated electronics, the cost of the first measurement is much greater for remote-sensing systems than for the corresponding in situ instrumentation. Even this is not always the case, however. For example, Wyngaard et al. (1978) describe the operation of an optical method for measuring surface heat flux within the planetary boundary layer over a line path. The equipment for the optical measurement cost several thousand dollars, compared with a figure almost five times as large for the conventional technique, involving fast-response temperature sensors and sonic anemometry. Moreover, remote sensors offer the major intrinsic advantage that they do not perturb the medium being measured (provided, in the case of active remote sensors, that we neglect the slight heating of the medium necessarily resulting from any absorption of the probing wave). By contrast, in situ instruments such as cup anemometers, thermistors, etc., necessarily interfere with the flows of interest, and the platforms on which they must be mounted (e.g., towers or aircraft) introduce even more significant obstacles to the flow.

Where remote-sensing equipment really excels, however, is in the cost of incremental measurements, because most such sensors offer a scanning capability which permits them to interrogate many cells within large volumes. Thus the cost of remote sensors should be compared more appropriately to the cost of in situ sensor arrays in aggregate. In the next few paragraphs we look at the particular advantages of improved spatial and temporal resolution and areal coverage which remote-sensing systems offer, making in each case some general comments and then using dual-Doppler radar data on boundary-layer winds by way of illustration.

Let us consider first the question of spatial resolution. Often the economics of instrument arrays dictates that they be quite sparse. As a result, fine structure in pollutant transport and diffusion cannot be revealed in detail sufficient to evaluate local effects due to terrain, vegetation, urbanization, small-scale meteorological processes, etc. By contrast, remote-sensing systems can often readily supply such detail, as illustrated in Figure 1. This shows dual-Doppler-radar observations made of the wind field at a height of 300 m above St. Louis on a summer afternoon during the 1975 METROMEX experiment. The data were taken using chaff dispersed from a light aircraft as a tracer; the mean wind has been removed from the data in order to better reveal the small-scale structure. Lines of convergence and divergence are evident in the figure, and appear to be associated with an elongated heat island extending from Granite City across the St. Louis central business district (Kropfli and Kohn, 1977). While the data are of considerable meteorological interest, we show them here simply to indicate the ability of dual Doppler radar to provide data with appreciably better than 1 km resolution over an area greater than 100 km^2. An individual anemometer with telemetry and recording system costs perhaps \$$10^3$ if installed near the surface, much less than the \$500 K cost of the dual Doppler radar system. But the array of 300 anemometers required to reproduce the pattern revealed here would cost \$300 K, a figure beginning to approach that of the radars. And if we were to take full advantage of the radar resolution (the equivalent of 10^3 anemometers) the cost of the associated

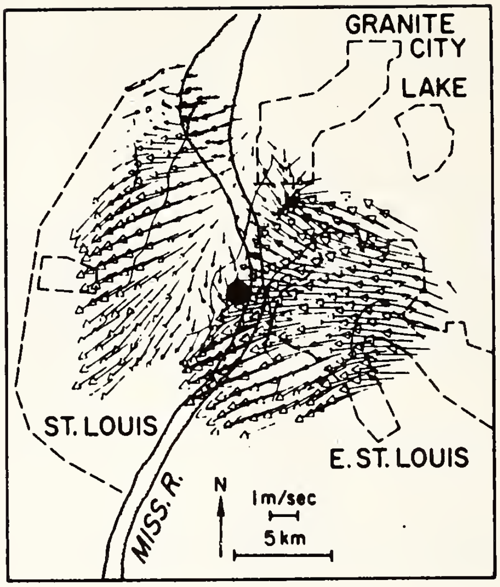

Figure 1. Eddy wind field (mean wind field removed) at 0.3 km above ground level on 28 July 1975. Winds are obtained from an average of 17 volume scans taken during a 70 minute period ending at 1557 CDT. The vertical cuts of Figure 2 lie at the locations Y = 2, 4, 6, 8 km. The Gateway Arch is indicated by the dot just to the west of the Mississippi River at the location X = 22.6 km, Y = 8.5 km.

anemometer array would be double that of the radars. But the comparison does not end here. The anemometer system described above could give only surface data, while the radar data were taken at a height of 300 m. In fact, the radar system provides complete altitude information, up to the top of the boundary layer, as shown in Figure 2, which shows the vertical circulations associated with the horizontal airflow pattern of Figure 1. To provide this information would require four times as many anemometers. And this ignores the cost of the towers on which the anemometry would have to be mounted. Figuring a cost of $10 M/tower for three hundred 1-km towers, an extremely optimistic figure, we find a total system cost for the anemometry of $300 M, some 600 times the cost of the radar system. (Which doesn't interfere with the airflow or blight the landscape, and which is transportable as well.) Note moreover that the radars quite naturally provide data throughout the depth of the mixed layer, no matter how deep it happens to be (several km in extreme cases). By contrast, the technology does not exist for constructing towers meeting this more stringent requirement.

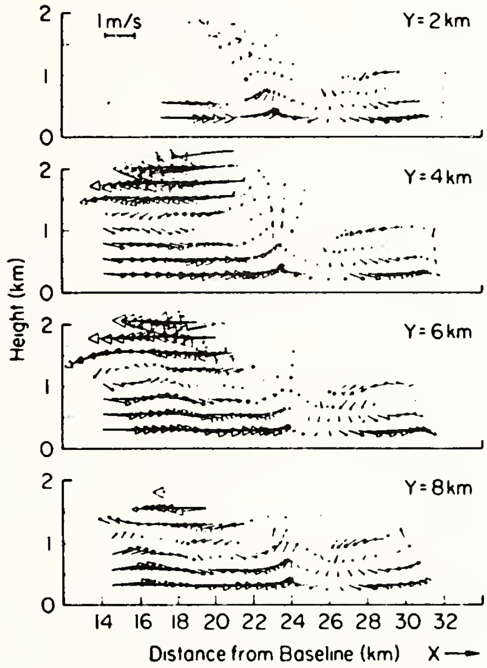

Figure 2. The vertical circulation patterns associated with the circulation of Figure 1.

Remote sensors also offer much improved temporal resolution. We might imagine, for example, that rather than put up 300 tall towers, we could deploy 300 radiosondes, which would each provide a single wind profile for the 70-min period shown here. But the cost of rawinsonde expendables is some $100/profile, so that the incremental cost of the one data set represented by Figures 1 and 2 would be $30 K. The incremental cost of the dual-Doppler radar data is orders of magnitude less than this value. Moreover, the data shown represent averages of seventeen such data sets, and to reproduce this by rawinsondes would have cost some $500 K. Moreover, to acquire a single radiosonde profile through the atmosphere can take up to an hour. Both these factors preclude more frequent measurements that would give us a better look at the effects of small-scale and short-lived changes in atmospheric conditions on pollutant transport and diffusion. In the dual-Doppler example given above, by contrast, the entire velocity field can be mapped out every few minutes. The result is a tremendous improvement in the picture available of the time history of the events.

Associated with the improved spatial and temporal resolution is an improved areal coverage. Often, as the direct result of the first and second factors of the previous two paragraphs, the cost of arrays of instruments precludes their deployment over large areas, limiting our ability to monitor and describe accurately longer-range transport and diffusion of pollutants. Here again, remote sensors are often able to provide better area coverage than point systems by virtue of their scanning capability. The coverage tends to be more uniform, with fewer gaps. There are fewer siting problems associated with meteorological requirements and haggling over rights associated with land ownership. The coverage often can extend over wider geographical areas.

Fourth, and finally, remote sensors typically provide improved representativeness. The deployment of in situ instruments in necessarily sparse arrays gives rise to questions concerning the extent to which the reported observations accurately reflect conditions over the whole of the area being monitored by each instrument. Instrument siting remains something of a black art, whose precise influence on experimental results is poorly understood. Remote sensors alleviate these difficulties in two ways. First, sensors such as the dual-Doppler radars provide many data points over a large area; in some cases this permits evaluation of the representativeness of various sites. Second, remote-sensing data necessarily represent a line, area, or volume average. In the case of the dual-Doppler radars, for example, each wind vector shown in the figures is an average for a sensed volume some 300 m on a side. Thus the remote sensor acts as a low-pass spatial filter on the data, smoothing out smaller-scale fluctuations, some of which reflect siting problems. As another illustration of this same point we can consider the optical heat-flux sensor cited above, which provides a line-average rather than a point measurement of heat flux. This yields more reliable values and permits use of shorter averaging times as well.

As a result of all of these general factors, remote sensors appear to be the instruments of choice, where available, for field experiments, because they provide a look at small-scale, short-lived phenomena, over wide areas, with high reliability.

3. Remote Sensors Applied to Research in PBL Physics, Turbulence and Diffusion and Urban Meteorology

It is in the area of boundary-layer physics and the meteorology of those phenomena and processes which determine pollution dispersion that we can expect remote-sensing to have its biggest initial impact on air pollution meteorology. There are several reasons for this. First, as a brief inspection of the Appendix suggests, while optical remote sensors continue to hold forth great promise for chemically-specific studies of gaseous pollutants as well as aerosols, such studies lie in the future. The greatest progress to date has been in measurements of meteorological fields such as wind, and to a lesser extent temperature. Second, the practical observing range of many remote-sensing devices remains limited to boundary-layer distances ($\sim$1 km or so), and even in those cases where greater range is currently available, the geometry of ground-based remote sensors necessarily restricts their use to areas on the mesoscale (only by going to airborne or satellite platforms or by using arrays of remote sensors is it possible to eliminate this restriction). Third, however, and it is to this point that we shall turn for the moment, there are a number of fundamental problems in PBL physics that require immediate theoretical and observational attention, if we are to understand the backdrop against which the great events of air pollution meteorology occur.

One of the more pressing of these problems is the behavior of the PBL over terrain that is irregular, whether by virtue of its surface contours, thermal properties, or roughness. (Note that the urban-meteorology problem can be considered a specialized example of this.) During the past few decades the PBL over flat, homogeneous terrain under stationary conditions has received an excessive degree of attention. While it might be argued that the problem is of great importance because these are the conditions prevailing over much of the oceans, it is hard to escape the conclusion that the attention lavished on it is more a reflection of the apparent intractability of alternative, more realistic problems. Yet it is precisely the effects of irregular terrain that dominate the meteorology of pollution-prone cities and regional basins, that determine the environmental impact of energy-related activities such as power generation and oil-shale operations in the mountain west of the United States, etc. Although the theoretical difficulties of the problem are themselves overwhelming, there is no question that a major obstacle to progress in the field is a lack of observations, and it is here that remote sensing offers tremendous promise. As pointed out in the previous section, techniques such as dual-Doppler radar provide large areal coverage and detailed spatial resolution. With these it is now feasible to examine the airflow over large urban (or mountainous) areas under a variety of conditions, and to build a picture of the airflow over mesoscale topography as a function of thermal stratification and of mean wind azimuth, speed, and shear. It is possible to see the effects on the circulation of heat sources and terrain obstacles, and to see changes in the wind profile as the air passes from the outlying rural area over the urban center and then resumes its course over rural terrain again. These observations inspire new theories and aid in model verification. They provide the resolution necessary to treat the major features of urban or terrain circulations deterministically. One specific illustration of this was the extensive participation of remote sensing equipment, including the dual Doppler radars, lidar systems and acoustic echo sounders, in the RAPS and METROMEX studies in St. Louis. It will be some time before all the data are analyzed, but even the early results demonstrate the power of the new tools. Kropfli and Kohn (1977) show unmistakably, for example, the urban heat island and its effects on the St. Louis airflow, and how these change with prevailing meteorological conditions. They also show spatial structures within the urban PBL. For the first time it may be possible to relate them directly to the urbanization below. More such studies, even more definitive and larger in scope, undoubtedly lie ahead.

Another development that appears on the near horizon is the use of aerosol-generators to develop plumes of known and simple particle size distribution, for use in quantitative lidar studies of pollutant transport and diffusion over irregular terrain. Already several groups across the United States, our own included, are preparing to carry out such work.

A second major problem area is the nocturnal PBL. Unlike its daytime, convectively-active counterpart, which is relatively well understood, the nighttime, stable boundary layer remains an enigma. Under statically stable conditions, irregular terrain has dramatic influence. At night radiative processes affect the entire depth of the layer rather than merely the very surface. The shift from static instability during the day to dynamic instability at night changes the vertical sense and character of the heat transports. The coupling between top and bottom of the boundary layer, rather than occurring in one step throughout the PBL depth by thermal plumes rooted in the surface layer and penetrating the overlying inversion, occurs in fits and starts, bit by bit, through laminae of turbulence separated by dynamically stable layers containing little or no irregular motion. Gravity waves appear, as a result of shear between these layers, and couple into the turbulence, though their dynamical role is not well understood. Remote sensors are helping in nocturnal PBL studies by providing the spatial and temporal resolution necessary to define the stable-layer turbulence structure, which until now has remained sub-grid-scale to the numerical modelers. Scattered preliminary applications of remote sensors to observational studies often nocturnal PBL have been reported already (e.g., Beran et al., 1973; Hooke et al., 1973; Merrill, 1977; Schubert, 1977) and much more is on the way.

Another challenging area involves study of the cloud-topped mixed layer and the connection interaction between the PBL "cloud roots" and the parent cloud. Here the emphasis is on the processes which transfer water vapor and cloud nuclei from the PBL below into the cloud itself, the "umbilical" through which the cloud receives its life blood. Again, this is a problem area that will yield only to a combination of observations with detailed spatial and temporal resolution and a great chemical specificity, as well as theoretical work.

A key element in much of this research may be the Boulder Atmospheric Observatory, or BAO, a complex of remote-sensing instruments and a 300 m tower (Kaimal, 1978) that is taking form just east of Boulder, under the impetus of the Wave Propagation Laboratory of NOAA and the Field Observing Facility of NCAR. Figure 3 shows the BAO tower.

Figure 3. The 300-m, instrumented meteorological tower at the Boulder Atmospheric Observatory.

Here, at one site, will be combined the best of tower in-situ instrumentation and the newest remote-sensing technology. The former will be used to test and calibrate the latter, and then both technologies will be turned toward these questions of PBL dynamics. In general, then, the BAO can be thought of as an attempt to combine the desirable features of geophysical turbulence — namely a high-Reynolds number flow and an inertial subrange extending over many spectral decades — with the kind of diagnostics that have hitherto been available only in controlled laboratory situations. The sensors at the facility should combine the range capabilities required for doing full PBL research with the resolving power necessary to study the smallest scales of turbulence and turbulent processes. At the time of this writing, the first major experiments planned for the facility are:

i) a site-evaluation experiment in April 1978. The site is located on gently rolling terrain (two-dimensional, 50-m hills of 1-km "wavelength"); the question is to what extent does the site exhibit meteorological characteristics typical over flat terrain and to what extent does the site show the influence of the underlying orography? Aircraft flybys and the NCAR Portable Automated Mesonet (PAM) surface network will be used to answer these questions.

ii) a convective PBL experiment in September 1978, using triple Doppler radars, PAM, and aircraft. Major goals of the experiment include evaluation of radar estimates of terrain-induced irregularities in the flow, Reynolds stress, eddy dissipation rate, and horizontal convergence. For example, radar estimates of Reynolds stress will be compared with aircraft and tower measurements, in an attempt to determine whether the radars' potential in this area is currently realizable or still lies in the future. Can radars be used to carry out definitive studies of PBL turbulence dynamics, and energy budgets like those that made the AFCRL Kansas and Minnesota experiments such classics? Or will we be forced to continue to rely on in-situ instruments for these detailed, quantitative studies? We hope to answer these and similar questions during the September 1978 experiment.

iii) an August-September 1979 WMO/CIMO international comparison of low-level sounding systems.

A major long-term desire of our laboratory is to develop a remote-sensing capability equivalent to the BAO that can be transported, and used to study the meteorology of other environments (arctic, tropical, mountain, desert, urban, marine, to name a few). We know that remote sensors can measure mean quantities well enough — the critical question now is whether they can be used to measure turbulent fluctuations in wind, temperature, and other variables, with accuracy and resolution sufficient to estimate Reynolds stresses, heat fluxes, and other quantities important to turbulence energy budgets. If they can, then we can repeat the success of the truly definitive Kansas and Minnesota PBL experiments in a wide variety of meteorological settings.

4. Remote Sensors Applied to Numerical Modeling and Operational Forecasting

Remote sensors, which feature large areal coverage and good spatial and temporal resolution, are ideally matched to the data-input and data-verification requirements of numerical models on the mesoscale and microscale. Even today, multiple-Doppler radar systems come close to the total capability required for such inputs, particularly if we note (as in the appendix) that there is some hope that mesoscale temperature fields can be derived from the Doppler wind data and surface temperature information. The future should see remote sensors applied routinely to the problem of model initialization and verification.

What is far more interesting, however, in terms of its long-range potential for weather forecasting in general and air-pollution meteorology in particular, is the rise of new system concepts of improved local-weather prediction incorporating recent advances in remote-sensing, mesoscale numerical modeling, data processing, and information dissemination. Using such concepts, we can weld these disparate activities into a coherent whole rather than allowing creation of a patchwork-quilt operational scheme which will function suboptimally. NOAA is currently examining one such proposal, entitled PROFS (Prototype Regional Observing and Forecasting Service) which calls for exploratory development of such a service in the Denver area and then expansion to a nationwide system, focusing on urban areas. Such systems would attempt to improve local weather services to meet increasingly critical needs of aviation, agribusiness, the construction industry, and the general public, and have incorporated in the overall thinking a great concern with air quality problems and their forecasting. Should this concept be implemented, it would mean a tremendous increase over the long term in the quality and quantity of routine National Weather Service data available to the air pollution meteorology community, data that could allow sensible, coherent planning for improvement and maintenance of air quality. An example that comes to mind is the MAP3S (Multi-State Atmospheric Power Production Pollution Study) program which could be much more effective and require considerably less incremental funding for supplemental meteorological instrumentation were the proposed PROFS network already in place.

Such prospects are still relatively far in the future. Closer to the present we see use of remote-sensing technologies in combination to meet the needs of the meteorological community. An example is the wind-shear monitoring system which the Wave Propagation Laboratory has developed for the FAA and installed at Dulles International Airport (Hardesty et al., 1977). This system uses an acoustic echo-sounder to monitor wind profiles in the clear air. However, the noise of rain on the acoustic antennas interferes with the sounder operation to the extent that it becomes unusable. Before this happens, however, the system automatically switches to a microwave radar unit which cannot measure winds in the clear air, but which can use the Doppler shift of precipitation echoes to measure the wind shear as revealed by the rain. Thus the individual sensors are vulnerable to particular weather conditions, but the system as a whole is an all-weather device.

As the field of remote sensing matures, however, it is becoming increasingly apparent that the problem of technology transfer is a major one — perhaps a greater obstacle to progress than the scientific and engineering problems themselves. We have made progress in the field of atmospheric remote sensing as we have (i) identified those wave-medium interactions that supply useful information, (ii) developed techniques for initiating and monitoring the most promising interactions, and developed mathematical procedures for inverting the data to obtain the desired estimate of the meteorological parameter, (iii) applied these new capabilities to atmospheric research, and (iv) transferred this technology into the operational sector. Little (1972), describes this process in somewhat different but equivalent terms.

Step (iv) is a big one. Our own laboratory experience yields many examples (from our viewpoint) of "consumer resistance" and failure to understand our devices. Optical scintillation devices to measure line-average transverse wind speeds have been used by the user community as simple "on-off" switches indicating the presence of precipitation along the optical path. Acoustic sounders that have been turned over to users often fall quickly into disrepair. On the user part, this often represents a reluctance to learn anything new and a resistance to change, as well as overloaded work schedules which simply leave no time for assuming added responsibilities. On our part, this often reflects an insensitivity to the users' real needs, and inexperience in developing operation-hardened (as opposed to breadboard) equipment. Repeatedly we find the process of technology transfer must begin with the initial user-researcher contacts, continue through the entire development phase, and culminate with extensive user-training and follow-up if the transfer is to "take". In the years ahead, this activity may also become routine, but today it represents a severe test of both researcher and operator.

Acknowledgments: R. L. Schwiesow and V. E. Derr provided useful advice and comments during preparation of this manuscript. C. G. Little made numerous improvements in an early draft.

References

Balsley, B. B., N. Cianos, D. T. Farley, and M. J. Baron, Winds derived from radar measurements in the arctic troposphere and stratosphere, J. Appl. Meteorol. 16, 1235-1239 (1977).

Benedetti-Michelangeli, G., F. Congeduti, and G. Fiocco, Measurement of aerosol motion and wind velocity in the lower troposphere by Doppler optical radar, J. Atmos. Sci. 29, 906-910 (1972).

Beran, D. W., W. H. Hooke, and S. F. Clifford, Acoustic echo-sounding techniques and their application to gravity-wave, turbulence, and stability studies, Boundary Layer Meteorology 4, 133-153 (1973).

Brown, E. H., Quantitative acoustic measurements of atmospheric turbulence, Fourth Symposium on Meteorological Observations and Instrumentation of the American Meteorological Society, American Meteorological Society, Boston, Mass. (1978).

Brown, E. H., and F. F. Hall, Jr., Advances in atmospheric acoustics, Rev. Geophys. Space Res. in press (1978).

Chadwick, R. B., K. P. Moran, R. G. Strauch, G. E. Morrison, and W. C. Campbell, A new radar for measuring winds, Bull. Am. Meteorol. Soc. 57, 1120-1125 (1976a)

Chadwick, R. B., K. P. Moran, R. G. Strauch, G. E. Morrison, and W. C. Campbell, Microwave radar wind measurements in the clear air, Radio Sci. 11, 795-802 (1976b).

Clark, G. H., E. Charash, and E. O. K. Bendun, Pattern recognition studies in acoustic sounding, J. Appl. Meteorol. 16, 1365-1368 (1977).

Collis, R. T. H., Lidar, Adv. Geophys. 13, 113-139 (1969).

Cooney, J., Temperature profiles from laser radar measurements of rotational Raman and elastic scattering, Fourth Joint Conference on Sensing of Environmental Pollutants, American Chemical Society, Washington, D.C. (1977).

Derr, V. E. (Ed.), Remote Sensing of the Troposphere, U.S. Govt. Printing Office (1972).

Doviak, R. J., and C. T. Jobson, Mapping clear air winds with dual-Doppler radars, Proc. Open International Symposium on EM wave propagation and non

Fiocco, G., G. Benedetti-Michelangeli, K. Maischberger, and E. Madonna, Measurement of temperature and aerosol to molecule ratio in the troposphere by optical radar, Nature 229, 78-79 (1971).

Frankel, M. S., and A. M. Peterson, Remote temperature profiling in the lower troposphere, Radio Sci. 11, 157-166 (1976).

Frankel, M. S., N. J. F. Chang, and M. J. Sanders, Jr., A high-frequency radio acoustic sounder for remote measurement of atmospheric winds and temperature, Bull. Am. Meteorol. Soc. 58, 928-934 (1977).

Gossard, E. E., J. H. Richter, and D. Atlas, Internal waves in the atmosphere from high-resolution radar measurements, J. Geophys. Res. 75, 3523-3536 (1970).

Green, J. L., J. M. Warnock, R. H. Winkler, and T. E. VanZandt, Studies of winds in the upper troposphere with a sensitive VHF radar, Geophys. Res. Letters 2, 19-21 (1975).

Hall, F. F., Jr., Boundary layer climatologies from acoustic sounder investigations, Fourth Conference on Meteorological Observations and Instrumentation of the American Meteorological Society, American Meteorological Society, Boston, Mass. (1978).

Hardesty, R. M., P. A. Mandics, D. W. Beran, and R. G. Strauch, The Dulles airport acoustic-microwave radar wind and wind shear measuring system, Bull. Am. Meteorol. Soc. 58, 910-918 (1977).

Hooke, W. H., F. F. Hall, Jr., and E. E. Gossard, Observed generation of an atmospheric gravity wave by shear instability in the mean flow of the planetary boundary layer, Boundary Layer Meteorol. 5, 29-42 (1973).

Huffaker, R. M., Laser Doppler detection systems for gas velocity measurement, Appl. Optics 9, 1026 (1970).

Huffaker, R. M., CO_2 laser Doppler systems for the measurement of atmospheric winds and turbulence, Atmospheric Technology, NCAR, p. 71 (1974).

Huffaker, R. M., D. W. Beran, and C. G. Little, Pulsed coherent lidar systems for airborne and satellite-based wind field measurement. Preprints Seventh Conf. on Aerospace and Aeronautical Meteorology and Symposium on Remote Sensing from Satellites, American Meteorological Society, Boston, Mass. (1976).

Kaimal, J. C., and D. A. Haugen, An acoustic Doppler sounder for measuring wind profiles on the lower boundary layer, J. Appl. Meteorol. 16, 1298-1305 (1977).

Kaimal, J. C., NOAA instrumentation at the Boulder Atmospheric Observatory, Proc. Fourth AMS Symposium on Meteorological Observations and Instrumentation, Denver, Colorado, April 10-14, 1978 (to be published).

Kjelaas, A. G., and G. R. Ochs, Study of divergence in the boundary layer using optical propagation techniques, J. Appl. Meteorol. 13, 242-248 (1974).

Kropfli, R. A., and N. M. Kohn, Persistent horizontal rolls in the urban mixing layer as revealed by dual Doppler radar, Preprints Seventh Conference on Inadvertent and Planned Weather Modification of the American Meterological Society, November 10-13, American Meteorological Society, Boston, Mass. (1977).

Kunkel, K. E., E. W. Eloranta, and S. T. Shipley, Lidar observations of the convective boundary layer, J. Appl. Meteorol. 16, 1306-1311 (1977).

Lawrence, R. S., G. R. Ochs, and S. F. Clifford, Use of scintillations to measure average wind across a light beam, Appl. Optics 11, 239-243 (1972).

Lemon, L. R., R. J. Donaldson, Jr., D. W. Burgess, and R. A. Brown, Doppler radar application to severe thunderstorm study and potential real-time warning, Bull. Am. Meteorol. Soc. 58, 1187-1193 (1977).

Little, C. G., Acoustic methods for the remote probing of the lower atmosphere, Proc. IEEE 57, 571-578 (1969).

Little, C. G., Status of remote sensing of the troposphere, Bull. Am. Meteorol. Soc. 53, 936-949 (1972).

McAllister, L. G., J. R. Pollard, A. R. Mahoney, and P.J.R. Shaw, Acoustic sounding — a new approach to the study of atmospheric structure. Proc. IEEE 57, 579-587 (1969).

Merrill, J. T., Observational and theoretical study of shear instability in the airflow near the ground, J. Atmos. Sci. 34, 911-921 (1977).

Noonkester, V. R., D. R. Jensen, J. H. Richter, W. Viezce and R. T. H. Collis, Concurrent FM-CW radar and lidar observations of the boundary layer, J. Appl. Meteorol. 13, 249-256 (1974).

Platt, C.M.R., Lidar observation of a mixed-phase altostratus cloud, J. Appl. Meteorol. 16, 339-345 (1977).

Russell, P. B., and E. E. Uthe, Sodar network measurements of regional mixing depth and stability patterns for an air quality model, Proc. Joint Conference on Applications of Air Pollution Meteorology, American Meteorological Society, Boston, Mass. (1977).

Schubert, J. F., Acoustic detection of momentum transfer during the abrupt transition from a laminar to a turbulent atmospheric boundary layer, J. Appl. Meteorol. 16, 1292-1297 (1977).

Schwiesow, R. L., and R. E. Cupp, Remote Doppler velocity measurements of atmospheric dust devil vortices, Appl. Optics 15, 1-2 (1976).

Schwiesow, R. L., R. E. Cupp, M. J. Post, R. F. Abbey, Jr., and P. C. Sinclair, Velocity structures of waterspouts and dust devils as revealed by Doppler lidar measurements, Preprints Tenth Conf. on Severe Local Storms, American Meteorological Society (1977).

Strauch, R. G., V. E. Derr, and R. E. Cupp, Atmospheric temperature measurement using Raman backscatter, Appl. Optics 10, 2665-2669 (1971).

Strauch, R. G., V. E. Derr, and R. E. Cupp, Atmospheric water vapour measurement by Raman lidar, Remote Sens. Env. 2, 101-108 (1972).

Wesely, M. L., A comparison of two optical methods for measuring line averages of thermal exchanges above warm water surfaces, J. Appl. Meteorol. 15, 1177-1188 (1976).

Westwater, E. R., Improved determination of vertical temperature and humidity profiles of the atmosphere by a combination of radiometers and active ground-based sensors (to be submitted to J. Appl. Meteorol. 1978).

Wyngaard, J. C., J. C. Kaimal, G. R. Ochs, R. J. Hill, and D. C. Sorenson, An optical heat flux experiment, Proc. Fourth Symposium on Meteorological Observations and Instrumentation of the American Meteorological Society, American Meteorological Society, Boston, Mass. (1978).

Appendix — Recent Developments in Remote Sensing

We feel it appropriate to conclude with a partial listing of recent advances in atmospheric remote sensing. In part we are doing this because we are employed by a remote-sensing laboratory; it is impossible to work here and not get excited by the developments as they unfold. More importantly, however, we recognize that the method of presentation used above gives a somewhat fragmented view of the arsenal of techniques now available. We also note that in this rapidly evolving field, two of the latest major reviews available (Derr, 1972; Little, 1972) are falling somewhat out of date. However, our treatment is not by any means exhaustive; we have simply attempted to supply the reader with a sampling of the material available and a few references to direct his first steps. Time (and the spatial limitations) have not permitted any more thorough treatment.

A.1 Acoustic echo sounding

Acoustic echo sounding is analogous to radar except that it uses acoustic pulses to interrogate the atmosphere, detecting acoutic energy scattered by atmospheric turbulence. The subject dates back to papers of McAllister (1969) and Little (1969), although even this work has antecedents in both western and Russian work. Brown and Hall (1978) have recently reviewed the field thoroughly. From the start, acoustic echo sounding has been used to advantage in visualizing conditions in the atmospheric boundary layer — studying the development of the convective boundary layer, monitoring inversion height, etc. In recent years, however, interest has turned to the use of acoustic echo sounding as a quantitative tool. One piece of information yielded readily by the frequency shift of the echo returns is the atmospheric wind velocity. The technique has been used for years; a recent system is described by Kaimal and Haugen (1977). Hardesty et al. (1977) describe a quasi-operational system installed at Dulles International Airport to monitor low-level winds and wind shear. More recently, researchers have begun to investigate the potential of acoustic echo sounding for other quantitative information, including height profiles of the turbulence structure functions C_T^2 and C_V^2, surface heat flux, surface stress, and Monin-Obukhov length, and rudimentary methods of temperature profiling involving heavy use of similarity theory (Brown, 1978) or phase-coherent techniques (Brown, private communication).

While in many cases acoustic methods for measuring these parameters do not seem as promising as radar or lidar techniques, they are worth pursuing because of the lower cost of acoustic methods. This lower cost is making it practicable to install acoustic echo sounders in large arrays, to determine mesoscale structure in PBL height, for example (Russell and Uthe, 1977). Various pattern recognition schemes are currently under development, for use in automated processing of acoustic-sounder facsimile records (Clark, et al., 1977; Hall, 1978).

A.2 Radio techniques.

The use of pulse Doppler radars in PBL studies has been described at length in the body of the paper. For the most part, the work cited has involved the use of chaff; however some installations, e.g., NOAA's National Severe Storms Laboratory, have demonstrated clear-air pulse dual-Doppler radar capability out to ranges of 40 or 50 km (Doviak and Jobson, 1977). For the most part also, the work has involved the use of two radars, to provide two components of the wind directly; the third velocity component has typically been inferred, by assuming incompressibility and using the equation of continuity. However, the use of multiple radars is becoming increasingly frequent, to provide increased area coverage, to provide redundancy and therefore verification of the dual-Doppler approach, and to examine the influence of the lower boundary condition on data recovery. Other research directions are also being pursued in response to the needs of the operational community. Lemon et al. (1977) report use of single Doppler radars for detection of tornado vortex signatures. Strauch (private communication) is currently exploring a variety of single-radar techniques for estimating both horizontal wind components. It has been pointed out recently, by Gal-Chen and by Leise (work in progress) that from the dual-Doppler radar fields and knowledge of the surface boundary conditions, it is possible in principle to deduce mesoscale temperature fields from the Doppler radar data. Tests are currently underway to determine whether the approach is a practicable one. If it is, or if it is true that mesoscale meteorological development is much less sensitive to thermal effects than the initial velocity fields (Anthes, private communication), then radars offer tremendous potential for the initialization of mesoscale models.

FM-CW radar has been in use for the past decade as a powerful tool for studying the clear-air boundary layer with high resolution (e.g., Gossard et al., 1970). In recent years, however, the utility and flexibility of the technique have been greatly increased by the development of a Doppler capability for determining wind velocities, using a VAD scan (Chadwick et al., 1976a,b).

Another radar advance has been the use of VHF radars for probing the clear troposphere and lower stratosphere (e.g., Green et al., 1975; Balsley et al., 1977, and the references therein). While the technique has not been applied to the problem of lower-tropospheric profiling in any detail, it does appear that it can be (Balsley, private communication) and we can anticipate that it will be in the future.

A.3 Optical techniques

Foremost among the optical techniques is lidar, or laser radar. The most common type is the pulsed lidar, which senses echo returns from aerosol scattering; work in this area dates back to the early 1960's, and was reviewed by Collis (1969). Recent papers of interest include a paper comparing FM-CW radar and lidar returns (Noonkester et al., 1974) which shows, as one might expect, that the PBL presents a different characteristic appearance to the two sensors, and a paper describing lidar observations of the convective boundary layer (Kunkel, et al., 1977).

As is the case with both the acoustic sounders and the radars, however, lidars offer tremendous potential for quantitative measurement as well. Huffaker (1970, 1974 and the references therein) describes the principles of Doppler lidar velocity determination. Benedetti-Michelangeli et al. (1972) describe preliminary tropospheric wind measurements using lidar. Schwiesow and Cupp (1976) and Schwiesow et al. (1977) have used truck-mounted and airborne infrared CW Doppler lidar to measure atmospheric velocities in dust devils and waterspouts, paving the way for analogous studies of tornado vortices. And in a recent work, Huffaker et al. (1976) put forth their concept for satellite-based global wind measurement using pulsed coherent lidar systems.

Lidar also offers some promise for temperature profiling. Fiocco et al. (1971), using molecular thermal broadening of the lidar return, and Strauch et al. (1971), using Raman-scatter lidar estimates of N_2 scale heights, report early estimates of atmospheric temperatures. In more recent work, Cooney (1977) has used rotational Raman scattering to estimate temperature profiles.

The area where optical sensing seems to hold the greatest long-term potential is in the area of sensing of gaseous pollutants, where optical radiation offers in principle a tremendous chemical specificity. Unfortunately, such spectroscopic effects are often very weak, however, and despite its glowing future, the subject has only a brief and rudimentary history. The work of Strauch et al. (1972) illustrates the approach. General approaches include Raman spectroscopy and differential absorption. Some of the recent work, including that of the Swedish and Japanese groups, may be found in the Invited Papers and Conference Abstracts of the Eighth International Laser Radar Conference, held at Drexel University on June, 1977 and sponsored by the American Meteorological Society and the Optical Society of America.

Lidar is currently being used to probe cloud microphysical processes. For example, Platt (1977) has used lidar to study phase changes within an altostratus cloud. Derr (private communication) has found recently that cloud glaciation can occur at a much earlier stage in cloud development than previously thought.

Other optical techniques for remote probing include line-of-sight observations of light-beam scintillations which have been used to measure winds (Lawrence et al., 1972), surface convergence (Kjelaas and Ochs, 1974) and surface heat flux (e.g., Weseley, 1976; Wyngaard et al., 1978).

A.4 Hybrid systems

As remote-sensing matures, attention is turning away from the individual technologies themselves and emphasis is shifting to the development of hybrid systems tailored to particular meteorological tasks. Here we discuss a few of these; however, we can expect, from recent work such as that of Noonkester et al. (1974) comparing FM-CW radar and lidar returns from the boundary layer, and from recent joint radar and lidar studies of cloud (Derr, private communication), that much more such research is in the offing.

Microwave radiometry has long been used to retrieve temperature and humidity profiles in the atmosphere from measurements of atmospheric microwave brightness at different frequencies and zenith angles. Recently, Westwater (1978) has shown that should radiometric data be supplemented with data on inversion height then the radiometric inversion techniques can yield much greater resolution of the humidity and temperature variations in the vicinity of the inversion layer itself. Figure A1 shows an example (from a paper study) of the advantages of such a system. Note that since height alone will do (estimates of inversion strength are unnecessary), these supplementary data could readily be supplied by acoustic sounders or FM-CW radar.

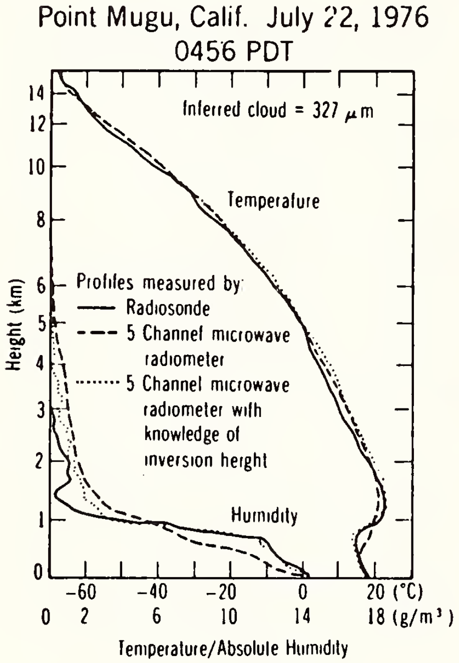

Figure A1. Temperature and humidity profiles recovered by radiometry within and without knowledge of inversion height, compared with radiosonde data.

Another hybrid technique of considerable novelty is the so-called RASS (Radio-Acoustic Sounding System) approach, which provides temperature profiles by using radiowave pulses to follow an acoustic pulse as it propagates through the atmosphere. In this way it is possible to measure the speed of sound and hence the temperature (Frankel and Peterson, 1976; Frankel et al., 1977). While intriguing, RASS suffers from the major disadvantage that it is vulnerable to high winds, which advect the acoustic pulse out of the region scanned by the radar. The result is that even with clever engineering a rather formidable array of antennas is required to overcome this difficulty (Priestley, private communication).

To summarize, remote sensors can now supply 3-D fields of winds, turbulence, precipitation, cloud, and aerosol, as well as profiles of temperature and humidity.

Preprint Volume; Fourth Symposium on Meteorological Observation and Instrumentation, 35-40, American Meteorological Society, 1978.

NOAA INSTRUMENTATION AT THE BOULDER ATMOSPHERIC OBSERVATORY

J. C. Kaimal

NOAA/ERL/Wave Propagation Laboratory
Boulder, Colorado 80302

1. INTRODUCTION

The Boulder Atmospheric Observatory (BAO) is a new research facility operated jointly by the Wave Propagation Laboratory of NOAA and the National Center for Atmospheric Research (NCAR). It is located 20 km east of Boulder (see Fig. 1) on gently rolling terrain. Installations at the site include an instrumented 300 m tower, a variety of remote sensors, and a highly interactive computer system controlling the acquisition and processing of data. The in-situ and remote sensors installed at the site by NOAA are designed to provide basic data for atmospheric studies and testing of other atmospheric sensors. These data will be archived for future use and will be made available to the scientific community. For major experiments these standard measurements will be augmented through the deployment of NCAR's Portable Automated Mesonet (PAM) system and instrumented aircraft, extending the range of the tower measurements over wider horizontal and vertical scales. Other instruments will be operated for specific periods to meet the needs of in-house and visiting scientists.

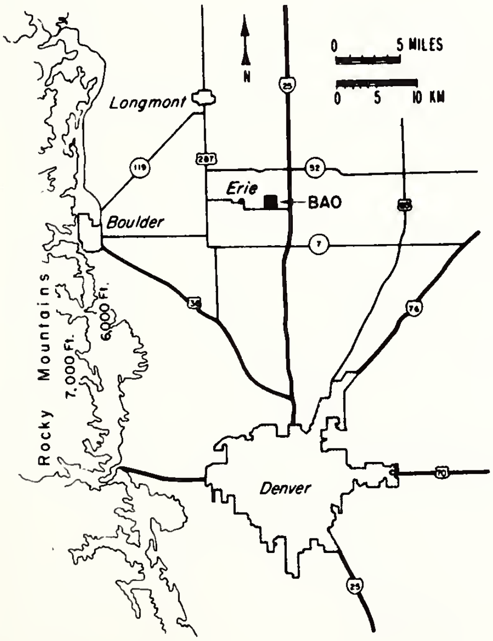

Figure 1. Map showing the location of the Boulder Atmospheric Observatory (BAO) with respect to Boulder, Colorado, and the Rocky Mountains.

This paper will describe the standard instrumentation at the BAO site and discuss briefly the sampling considerations and processing techniques used to minimize tape storage requirements.

2. TOWER INSTRUMENTATION

The tower is a guyed, open-lattice structure of galvanized steel, with three legs spaced 3 m apart. A two-man elevator inside the tower provides access to the eight instrumentation levels while a moving carriage on the southwest face permits continuous profiling or fixed level operation at any desired height. Details of the tower design have been given by Hall (1977).

The standard instrumentation levels on the tower are distributed linearly with height, except for the two lowest levels (see Fig. 2). All levels have identical instrumentation; two booms are available at each level for switching sensors so that the data are not compromised by unexpected changes in wind pattern. Special sensor mounts permit quick transfer of all probes from one boom to the other. Prevailing winds at the site are from the southeast during the summer and from the northwest during the winter. At the very least the sensors will have to be moved twice a year to insure proper exposure.

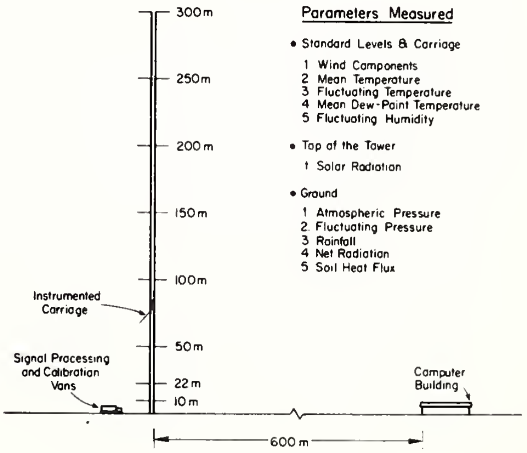

Figure 2. Schematic of the instrumented level on the tower and parameters measured at BAO.

The booms are specially designed for convenience of handling and easy access to the sensors for servicing. Each consists of a 4-m telescoping boom (R. M. Young model 35260-12A) attached to a hinged support with fine adjustments for leveling. If the lateral support member is loosened (see Fig. 3), the entire boom can be swung toward one face of the tower and retracted to bring the sensors within easy reach of the platform.

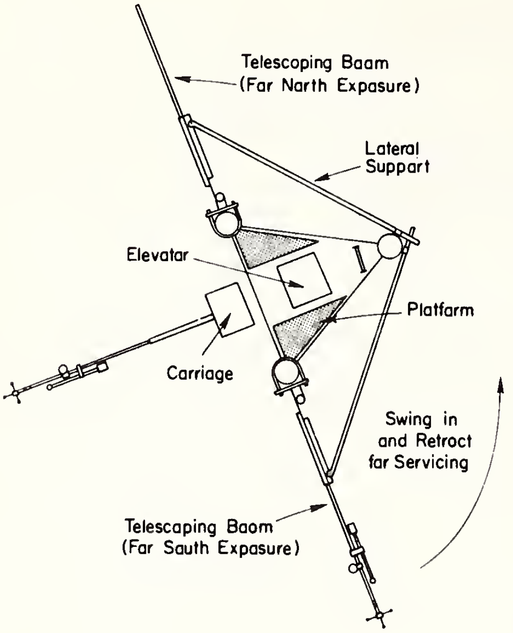

Figure 3. Plan view of an instrumented level on the tower showing the dual boom configuration in relationship to the boom on the movable carriage.

The standard measurements on the tower are listed in Fig. 2. A three-axis sonic anemometer measures wind velocity along three orthogonal directions. This particular configuration provides a wider azimuth coverage for both the vertical component probe and the fast-response temperature sensor nestled in it (see Fig. 4). Non-orthogonal arrays of the type used in past surface layer measurements (Kaimal et al., 1974; Mitsuta, 1974) are not suitable for unattended operation on tall towers since they require periodic reorientation into the wind to accommodate changes in wind direction. They offer unobstructed exposure for the acoustic paths, but only over a limited azimuth range. However, this new configuration has its own limitations. The larger separation between the vertical path and the horizontal paths has the effect of lowering the high-frequency response in the Reynolds stress cospectra. An underestimation in the 10-m stress is expected but little, if any, error should occur at the higher levels. Another limitation (inherent in any fixed array) is the underestimation caused by the blocking effect of the upwind transducer when the wind blows directly along one of the horizontal axes. Correction for this velocity defect is made in the data processing software with a first degree approximation to the wind direction.

The sonic anemometer probes used at BAO include two-axis probes made by EG&G (model 198-2) and by Ball Brothers Research Corporation (model 125-198), and one-axis probes, all made by Ball Brothers Research Corporation (model 125-197). The probe electronics are of the EG&G (model 198-3) type; the computer interface unit (Kaimal et al., 1974) was originally developed at the Air Force Cambridge Research Laboratories for their boundary layer research. The probe electronics located on the tower fire the transmitters on receipt of a signal from the interface unit and select the proper triggering point on the waveform picked up by the receivers. Coaxial cables connect the probe electronics to the computer interface circuit in the van at the base of the tower. The latter contains the timing circuits needed to fire the transmitters and the counters, and holding registers to measure the interval time between pulses arriving at the receivers. To insure proper synchronization in data sampling, the transmitters at all levels are fired simultaneously at a 200 Hz rate. The actual sampling rate for these and other fast response sensors is 10 Hz, so each sample is an average of 20 successive transmissions. This block-averaging is provided to minimize aliasing effects in spectral computations.

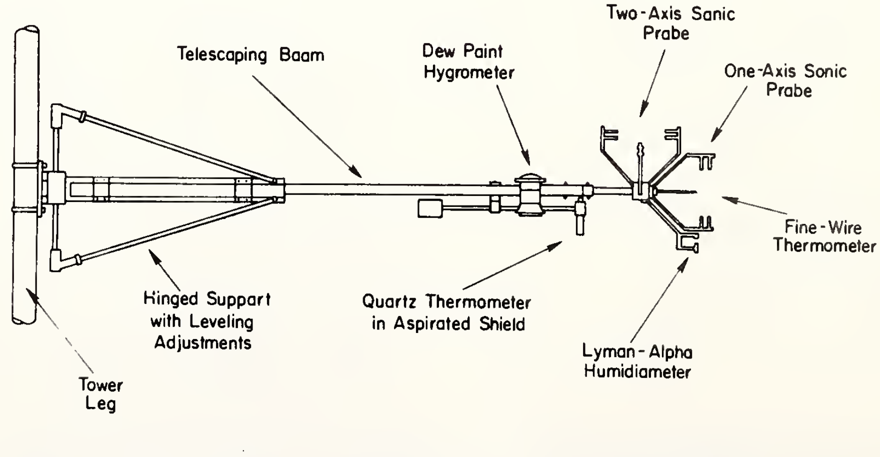

Figure 4. Sketch showing retractable boom and arrangement of sensors on it.

Fluctuating temperature is measured by a platinum wire thermometer (Atmospheric Instrumentation Research, model DT1A) specially engineered for use with the vertical sonic probe. Its frequency response very closely matches the path-averaged response of the sonic wind measurements. The sensor consists of a simple bridge circuit with a length of 12-μ platinum wire (nominally 150Ω at 20°C) on one leg. The wire is wound on a helical bobbin of the author's design attached to the end of a 10-cm rod (see Fig. 4). The mechanical support provided by the bobbin adds considerably to the useful life of the wire without affecting its frequency response in the 0-5 Hz range. Unless hit by debris or exposed to freezing rain, the wire will last for days if not weeks.

The low-noise, low-drift electronic circuitry in the temperature probe has an output range of ± 10 v corresponding to a temperature range of ± 50°C. The wide temperature range makes range switching unnecessary, but shifts the burden of performance to the multiplexer and A/D converter. A 15-bit A/D converter should provide more than adequate resolution in the temperature fluctuation measurements.

An attractive feature of this circuit is its simple calibration scheme which adjusts for probe-to-probe variations in wire resistance and insures proper relative calibration in the output signal. The data acquisition software uses the observed mean temperature reading at that level to correct for the nonlinearity in the platinum temperature-resistance curve.

The Lyman-Alpha humidiometer shown in Fig. 4 represents a modified version of the commercial device made by Electro Magnetic Research Corporation (model BLR). Plans are underway to develop a more compact probe with better exposure of the sampling volume to the airflow. Mean temperature and dew point measurements made at each tower level are used by the data acquisition software to keep the humidiometer in calibration as its sensitivity changes through aging and contamination of the windows.

The other two sensors on the boom are slow-response devices for measuring mean temperature and mean dew point. A Hewlett Packard quartz thermometer (model 2850A) housed in an R. M. Young aspirated shield (model 43404) measures the temperature. An absolute accuracy of ± 0.005°C is maintained by using a single reference oscillator for the probes at all levels, by periodically calibrating all probes at the same time in a precision temperature bath, and by using that information to scale the readings at each level. The dew point is measured with a Cambridge Systems hygrometer (model 110-SM), calibrated in the manner prescribed by the manufacturer. On top of the tower, attached to a vertical mast, is mounted an Eppley pyrheliometer for measuring incoming solar radiation. The outputs of these sensors are sampled once a second by the data acquisition system. Signals from all sensors on the tower are transmitted to the data acquisition system through cables installed in conduits on the tower. Additional signal cables and power outlets are provided at each level to accommodate visitor equipment.

The boom on the carriage is designed to handle the full complement of standard level instrumentation. The carriage can take loads up to 1200 kg so that a large number of other sensors may be added at a later date. For convenience of data transmission all sensors on the carriage yield analog outputs. Transmission of the signals to the data acquisition system is handled through a cable and trolley arrangement which connects to a terminal box at the 150 m level. The carriage sensors are sampled by the same multiplexer used for sampling all other analog sensors on the tower. As new sensors are added, alternate telemetry systems will be used. For the present, however, the direct cable link offers the simplest means for sampling the fast-response channels on the carriage.

3. GROUND-BASED SENSORS

These fall into two categories:

(1.) *In-situ sensors* measuring atmospheric pressure, rainfall, net radiation, and soil heat flux. The raingauge, net radiometer, and soil flux plates are located at a spot removed from the tower and other structures at the site. The barograph for measuring absolute atmospheric pressure is installed in the signal processing van. In addition, a spatial array of eight microbarographs distributed over a 2 km radius around the tower senses small pressure fluctuations signaling the advance of gust fronts and gravity waves (Hooke et al., 1973). Signals from all these sensors are sampled once per second by the analog multiplexer.

(2.) *Remote sensors* such as the laser triangle, the FM-CW Doppler radar, and the acoustic sounder. These remote probes, developed at the Wave Propagation Laboratory in recent years, measure parameters that complement the in-situ measurements on the tower. The laser triangle consists of three crosswind anemometers (Lawrence et al., 1972) spanning the distance between the outer guy wire anchor points. Instantaneous measurements of wind convergence at the base of the tower are computed from the average cross winds measured along the three legs of the triangle. The FM-CW Doppler radar (Chadwick et al., 1976) measures winds to heights up to 1 km in clear air and operates continuously in an unattended mode. The measurements are not degraded by clouds or precipitation. The three acoustic sounders, one at each corner of the laser triangle, document the heights of the boundary layer, the presence of convective plumes, and stably stratified layers. One of the sounders will have bistatic Doppler wind sensing capability through the addition of two fan-beam transmitters.

In addition to these remote probes other WPL devices (e.g., passive microwave radiometers, infrared Doppler lidars, optical heat flux sensors, pulse dual-Doppler radars) will be operated at the BAO as needed. Also, new techniques, as they are developed, will be tested against the in-situ measurements on the tower. Arrangements will be made for intercomparison of remote sensors developed in-house and by visiting groups.

4. DATA ACQUISITION AND RECORDING

A digital computer at the BAO site controls data acquisition from the tower and ground-based sensors. The Mobile Micrometeorological Observation System (MMOS), which performed the data handling in past boundary layer experiments (Haugen et al., 1971; Kaimal et al., 1976), is now used for this purpose. A new system built around NCAR's PDP 11/34 computer will soon take over the data acquisition and recording functions. This system is in a temporary building about 600 m southwest of the tower (see Fig. 2). The system will be housed in more permanent quarters when NCAR's Field Observation Facility moves to the BAO site. Underground cables link the computer to the signal processing circuits at the base of the tower.

The sequence of data handling operations is shown schematically in Fig. 5. This sequence may undergo modification as our requirements evolve. Nevertheless, the block diagram highlights our basic approach to data storage. It was clear from the outset that recording of all sampled data (fast-response data at 10 Hz and slow-response data at 1 Hz) would place an unacceptable burden on the BAO operation. The problem of retaining all relevant information in the bandwidth of our measurements, operating on a continuous mode, is solved by storing the high-frequency information in the form of smoothed spectral and cospectral estimates and the low-frequency information as time series. The high-frequency data are needed for computing dissipation rates (ε) and temperature structure parameters (C_T^2) at the different heights and for a wide range of studies where the inertial subrange behavior of various parameters is of interest. A 1024-pt fast-Fourier transform (FFT) spectrum is computed every 2 min. Successive spectra obtained over a 20 min period are first averaged in time and then block averaged over non-overlapping frequency intervals (the first few estimates excluded) to provide a roughly equal spacing of center frequencies on a logarithmic plot. A density of approximately 10 frequency blocks per decade (shown schematically in Fig. 6) provides a smooth inertial subrange spectrum with more than adequate resolution (Kaimal et al., 1972). Thus the high-frequency information in each 20 min period (synchronized with the line-printer output of data summary) is compressed to roughly 24 data words per channel.

The low-frequency information is contained in two parallel time series. For computations of the low-frequency portion of the spectra, the original 10 Hz data are block-averaged in 10 sec (100-pt) non-overlapping blocks. The block averaging reduces aliasing and confines the mismatch with the real-time high-frequency spectrum to the region of overlap (0.01 to 0.05 Hz). In reconstructing the entire spectrum only spectral estimates below 0.01 Hz are used, while the entire bandwidth of the real-time spectrum is retained.

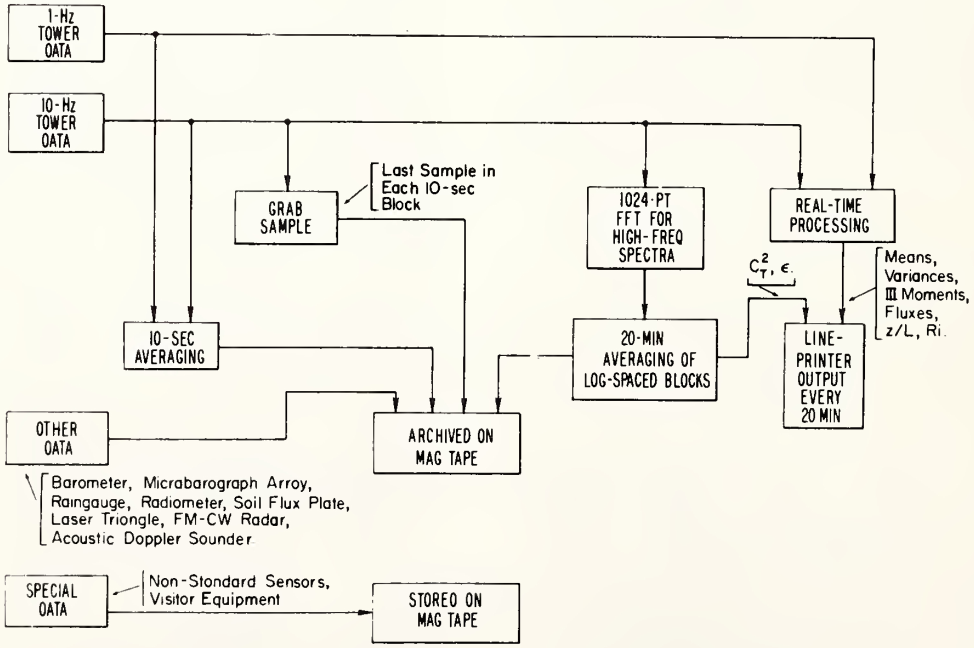
1-Hz TOWER DATA
10-Hz TOWER DATA
GRAB SAMPLE
Last Sample in Each 10-sec Block
1024-PT FFT FOR HIGH-FREQ SPECTRA
REAL-TIME PROCESSING
C_T^2, ε
Means, Variances, III Moments, Fluxes, z/L, Ri
10-SEC AVERAGING
20-MIN AVERAGING OF LOG-SPACED BLOCKS
LINE-PRINTER OUTPUT EVERY 20 MIN
OTHER DATA
ARCHIVED ON MAG TAPE
Barometer, Microbarograph Array, Raingauge, Radiometer, Soil Flux Plate, Laser Triangle, FM-CW Radar, Acoustic Doppler Sounder
SPECIAL DATA
Non-Standard Sensors, Visitor Equipment
STORED ON MAG TAPE

Figure 5. Schematic of data handling for archiving and real-time line printer output.

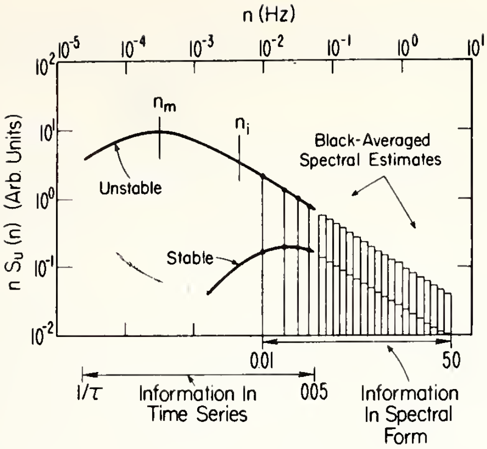

Figure 6. Typical spectra showing bandwidths covered by the smoothed high-frequency spectral estimates and the block-averaged time series. n_m *and* n_i *are the frequencies corresponding to the spectral peak in the logarithmic spectrum and the onset of the -5/3 region, respectively.*

The other time series recorded is a grab sample every 10 sec (last sample in each 10 sec block). This time series contains the turbulence information needed to compute variances, fluxes, third moments and other turbulence parameters. Important high-frequency information is lost in the block-averaging, which renders the first time series useless for turbulence calculations. Haugen's (1978) analyses show that the errors in estimates of variances and fluxes with these 10 sec grab samples are of the same order as the deviations from the ensemble average determined by the properties of the turbulent flow (Wyngaard, 1973).

Typical spectra for unstable and stable stratifications are shown in Fig. 6 to illustrate the approximate range covered by the high frequency spectrum. The daytime spectral peak, n_m, corresponds roughly to a wavelength equal to $1.5z_i$ (Kaimal et al., 1976) over flat terrain, where z_i is the height of the lowest inversion base. Also, for heights above $0.1z_i$, the onset of the -5/3 region in the spectrum (seen as a -2/3 slope in the logarithmic spectral representation), indicated by n_i in Fig. 6, corresponds to a wavelength equal to $0.1z_i$. Under typical daytime conditions at the BAO, the real-time velocity spectrum above 100 m should have much of its -5/3 region covered by the high-frequency spectrum. The relationships for the stable spectra above 22 m have yet to be established but preliminary indications are that n_m will fall roughly in the region where the low and high frequency spectra overlap.

The 1 sec samples from the slow-response sensors are also averaged in 10 sec non-overlapping blocks. Included in this slow-response category, besides the mean profile sensors on the tower, are most of the ground-based sensors at the site. The acoustic sounder and FM-CW radar outputs, which do not lend themselves to the same treatment as the other outputs, are the exceptions. Their outputs are not currently included in the archived tape.

In addition to the recordings on magnetic tape, hard copy outputs are available on the line printer every 20 min listing such parameters as means, variances, fluxes, third moments, dissipation rates, structure parameters, Richardson number and z/L. These outputs serve as a quick summary of meteorological conditions for observational periods on hand, but even more important, they are useful for monitoring sensor performance during experiments. All the data from the sensors (see Fig. 5) are used in the real-time computations for the line printer output.

Non-standard data from special sensors and from visitor equipment installed for the duration of an experiment will be recorded not on the archived tape, but on a separate magnetic tape. It should be pointed out that the system design permits parallel recordings of non-standard sensors as well as other groupings of data from the standard sensors. During episodes of concentrated data gathering all the sampled data may be recorded.

5. FUTURE PLANS

Several experiments have been scheduled at the BAO for the coming year. They range from small experiments verifying new sensor performance against routine tower data to two large cooperative boundary layer experiments involving other agencies and university groups. A site evaluation experiment in April will determine how well the boundary layer at the BAO site approximates boundary layers over flat homogeneous terrain. NCAR's aircraft and PAM system will be in operation at the site for the duration of the experiment. In August a more ambitious boundary layer experiment utilizing several dual-Doppler radars and radiosondes in addition to the aircraft and PAM systems will attempt to study the evolution of the planetary boundary layer and the role played by the boundary layer in the initiation, development, and maintenance of convective storms.

As schedules for future experiments are being drawn up, steps are being taken to link the BAO data acquisition system to a larger computer system at the Wave Propagation Laboratory in Boulder. This larger system, designed around NCAR's PDP 11/70 computer, will have multi-user terminals where several scientists can perform a number of independent computations and analyses of recent data stored in disc memory. The two computer systems are marked Station A and Station B in Fig. 7. When the two stations are linked by dedicated phone lines all standard data will be transmitted to Station B for archiving. Eventually, as the link to NCAR's computing facility is also established, the BAO data will be accessible to an even wider group of users through terminals at NCAR and phone links to other computers across the country.

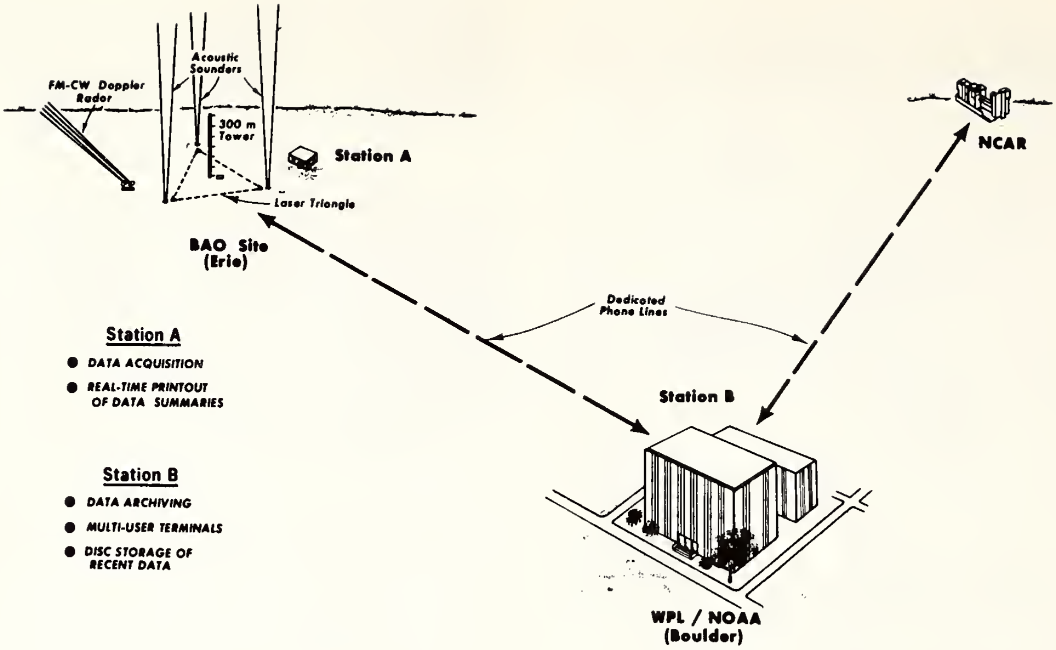

Figure 7. Bird's-eye view of the BAO site indicating data links planned with computer systems at WPL and NCAR.

6. ACKNOWLEDGMENTS

The author is happy to acknowledge the contributions of the BAO staff, Messrs. Robert W. Krinks, Jim T. Newman, Norbert Szczepczynski and Daniel Wolfe to the development of the Boulder Atmospheric Observatory. Drs. John C. Wyngaard and Duane A. Haugen played critical roles in the evolution of the data processing scheme. Mrs. Mildred F. Birchfield prepared the manuscript.

7. REFERENCES

Chadwick, R. B., K. P. Moran, R. G. Strauch, G. E. Morrison and W. C. Campbell, 1976: A new radar for measuring winds. *Bull. Amer. Meteor. Soc.*, 56, 964-969.

Hall, Freeman F., Jr., 1977: The Boulder Atmospheric Observatory. *Optics News*, 3 (2), 14-18.

Haugen, D. A., 1978: Effects of sampling rates and averaging periods on meteorological measurements. *Preprints of the 4th Symposium on Meteorological Observations and Instrumentation, Denver, April, 1978*, Amer. Meteor. Soc., __ __.

Haugen, D. A., J. C. Kaimal and E. F. Bradley, 1971: An experimental study of Reynolds stress and heat flux in the atmospheric surface layer. *Quart. J. Roy. Meteor. Soc.*, 97, 168-180.

Hooke, W. H., F. F. Hall, Jr., and E. E. Gossard, 1973: Observed generation of an atmospheric gravity wave by shear instability in the mean flow of the planetary boundary layer. *Bound.-Layer Meteor.*, 5, 29-41.

Kaimal, J. C., J. T. Newman, A. Bisberg and K. Cole, 1974: An improved three-component sonic anemometer for investigation of atmospheric turbulence. *Flow --Its Measurement and Control in Science and Industry, Vol. 1*, Instr. Soc. Amer., 349-359.

_____, J. C. Wyngaard, Y. Izumi and O. R. Coté, 1972: Spectral characteristics of surface layer turbulence. *Quart. J. Roy. Meteor. Soc.*, 98, 563-589.

_____, J. C. Wyngaard, D. A. Haugen, O. R. Coté, Y. Izumi, S. J. Caughey and C. J. Readings, 1976: Turbulence structure in the convective boundary layer. *J. Atmos. Sci.*, 33, 2152-2169.

Lawrence, R. S., G. R. Ochs and S. F. Clifford, 1972: Use of scintillations to measure average wind across a light beam. *Applied Optics*, 11, 239-243.

Mitsuta, Y., 1974: Sonic anemometer for atmospheric turbulence measurements. *Flow -- Its Measurement and Control in Science and Industry, Vol. 1*, Instr. Soc. Amer., 341-347.

Wyngaard, J. C., 1973: On surface layer turbulence. *Workshop in Micrometeorology*, Amer. Meteor. Soc., Boston, 101-149.

Proceedings of the Fifth National Conference on Energy and the Environment, 335-338, American Institute of Chemical Engineers, 1978.

EFFECTS OF WEATHER AND POLLUTION ON INCIDENT SOLAR ENERGY - BASIC MEASUREMENTS LEADING TO COMPUTER MODELS

G. M. Lerfald and V. E. Derr
U.S. Dept. of Commerce
Environmental Research Laboratories
Boulder, CO 80302

A program of experimental measurements and analysis is being conducted to better define the roles played by the scattering and absorbing components in the atmosphere on the spectral transmission of solar radiation. These components include water vapor, stratospheric ozone, lithometeors, hydrometeors and the standard atmospheric gases. The measurements are being made in several climate regimes. Simultaneous observations by a large backscatter lidar, solar spectral photometers, infrared radiometers, acoustic sounder, in situ particle samplers, and time lapse sky cameras permit determination of each of the absorbing/scattering components, separately. Data sets have been collected at Boulder, Colorado, Fairplay, Colorado, Colstrip, Montana, and Pt. Mugu, California. Measurements are planned for sites in the northeast and southeast USA next year.

The primary objective of the work is to provide uniquely complete data sets useful in the testing and development of computer models to predict and map solar radiation characteristics at ground level.

INTRODUCTION

The earth's atmosphere acts as a complex and constantly varying filter which affects radiation arriving from the sun. The characteristics of the energy which impinges at a ground level site is determined by the amounts of scattering and absorption experienced by the incoming radiation. Among the important components which absorb and scatter are hydrometeors, i.e., precipitation and the water droplets and ice crystals which compose clouds and fog, lithometeors, i.e., suspended particulate matter, water vapor, stratospheric ozone, and the air itself. A considerable amount of experimental data have been collected by various workers on the transmission of the atmosphere in various wavelength ranges, but in most cases auxiliary measurements on the absorbers and scatterers have not been available.

A pilot study completed in 1976(1) showed that a combination of remote sensing and in situ techniques could give rather complete information on the atmospheric components which affect solar radiation. The program described below is based on the results of that pilot study.

EXPERIMENTAL TECHNIQUES

The experimental data are obtained by simultaneous measurements with the following types of equipment: (1) a large backscatter lidar probes the atmosphere to obtain the backscatter coefficients of clouds and aerosols. The lidar is operated either in a dual polarization mode or in a dual wavelength mode. The dual polarized data allows distinguishing spherical from non-spherical particles, e.g., water droplets from ice crystals in clouds and smokestack particles from mining dust or other natural aerosols.

The dual wavelength data gives rough information on the size distribution of the backscattering particles. The lidar (see Figure 1) is fully steerable and gives information on the height

---

Superior numbers refer to similarly-numbered references at the end of this paper.

profiles and horizontal distributions of clouds and aerosols. Scans in a vertical plane, conical scans about a vertical axis (constant elevation angle) and tracking at an angle a few degrees from the sun, may each be used depending on the situation.

(2) An array of solar spectral photometers with both narrow and wide bandwidth filters, in the range 0.3 to 14 μm, are used to obtain the spectral intensity of the solar radiation. Certain of these channels were chosen to yield measurements of the total amounts of water vapor and ozone along the sun-instrument path, and others are analyzed to deduce the size distribution of aerosol and cloud particles.

(3) A solar aureole instrument measures the scattered light as a function of angular distance from the sun (8 degrees above and below) in four wavelength ranges. These data yield estimates of the size distribution of cloud and aerosol particles.

(4) Time lapse color photography of the entire sky and in the direction of the sun (sun blocked out) is used to record the general weather conditions, cloud types, cloud geometry, and atmospheric optical effects.

(5) In situ sampling by airborne probes and filter samples are used to determine aerosol and cloud particle characteristics including size distributions, shapes and chemical composition.

(6) An acoustic sounder is operated to record inversion layers, and thermal plume activity in the 0 to 4000 ft height range.

(7) A Standard Eppley normal incidence pyrheliometer (with four filters) and pyranometer are recorded routinely.

The data are all recorded on magnetic tape for later analysis. Measurements are made intermittently during all seasons at Boulder, Colorado and for periods of two weeks to four weeks (every day) at the other observing sites.

STATUS AND OBJECTIVES

Only partial analysis has been done on the data sets collected at the sites mentioned above. The output from the analysis procedures is, initially, time histories of the measured incident solar spectral intensities and the time histories of the measured and derived physical parameters of the atmospheric absorbers and scatterers. The physical parameters and the method of measurement include:

Physical Parameter	Measurement Method
Total Precipitable Water	Spectrophotometer
Total Ozone Content	Spectrophotometer
Aerosol Height Distribution	Lidar Backscatter
Aerosol Total Loading	Lidar & Spectrophotometer
Aerosol Size Distribution (Remotely Sensed)	Dual Wavelength Lidar, Spectrophotometer and Solar Aureole Photometer
Aerosol Size Distribution, Shape Factors and Chemical Composition	In Situ Sampling (Airborne & Ground)
Cloud Geometry & Height Distribution	Lidar & Time Lapse Photography
Wide Bandwidth Spectral Direct Solar Radiation	Pyrheliometer with Filters
Diffuse Component of Solar Radiation	Pyranometer with Shade Ring

Narrow Bandwidth Spectral Direct Solar Radiation	Eight-Channel Spectrophotometer
Angular Scattering Functions Due To Aerosols and/or Clouds	Solar Aureole Photometer

The initial model development will involve using the measured atmospheric parameters as input to compute the anticipated solar spectral intensities and comparing the latter to the measured spectral intensities. Another objective involves the evaluation of the usefulness of routinely collected weather data as input to solar radiation models and whether or not new types of routine weather data are needed as input to such models.

POTENTIAL USEFULNESS OF MODELS

The development of improved computer models which map and predict solar radiation would be a boon to optimum utilization of solar energy. Such models would permit evaluation of the effects of projected changes in atmospheric quality, e.g., an increase in air pollution near an urban center or pollution due to the expanded use of coal to generate electric power in the western United States.

In order to be useful to the planning of different types of solar energy systems, (e.g., solar heating panels, photovoltaic cells, and solar thermal power stations), the models will need to provide information on the spectral, angular, and time variation characteristics of the incident solar radiation. Our efforts involve development of a physical model only, i.e., relating the atmospheric components to the incoming solar radiation. Statistical models based on solar radiation data networks, cloud cover data, etc., are in existence and being developed further. Eventually, combining physical model results with statistical models and models of costs may permit site and cost evaluations for solar energy systems to be obtained more reliably than is possible at present.

The development of truly adequate solar radiation models is likely to be a challenging task, particularly as concerns the effects of clouds. The data collected in this program should allow the testing of various approaches to improved physical models and hopefully indicate the best methods to apply.

This work is sponsored by the Division of Solar Technology, Environmental and Resource Assessment Branch, U.S. Depart- of Energy.

REFERENCES

(1) Lerfald, Derr, Pueschel and Hulstrom, "Final Report on Phase I of Solar Radiation Atmospheric Transmission Research, NOAA Technical Memorandum, ERL WPL-18, January 1977.

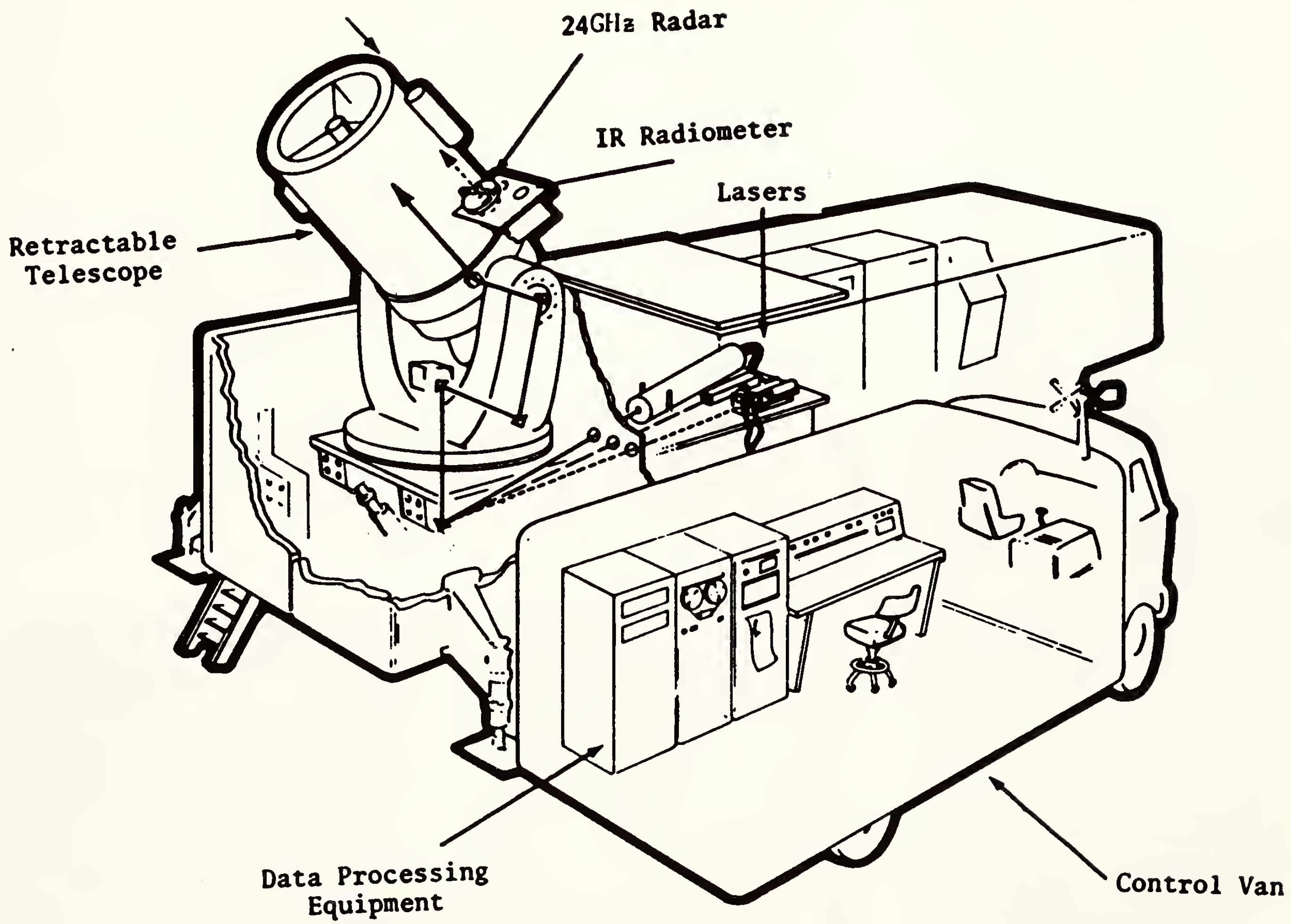

Figure 1.

Cut-Away View of
Remote Sensing Facility.

Journal of Applied Meteorology, 17: 1179-1181, August 1978.

A Comparison of Anemometer- and Lidar-Sensed Wind Velocity Data

M. J. Post, R. L. Schwiesow, R. E. Cupp, D. A. Haugen and J. T. Newman

NOAA/ERL/Wave Propagation Laboratory, Boulder, CO 80302

(Manuscript received 9 February 1978, in final form 1 April 1978)

ABSTRACT

Comparisons between measurements of a wind component by a Doppler lidar and by a conventional anemometer are presented. The two measurement techniques provided thirteen 15 min data sets which agreed within 0.04 m s^{-1} on the average. The maximum difference was 0.12 m s^{-1}, which constitutes less than 3% discrepancy, referred to the period average. The results conclusively demonstrate the ability of Doppler lidar to measure winds with a high degree of velocity resolution and accuracy.

1. Introduction

This report presents the results of an experiment to compare wind measurements obtained from a continuous-wave CO_2 Doppler lidar and from a conventional anemometer. The ability of various types of remote probes to measure winds, particularly within the atmospheric boundary layer, has been frequently demonstrated in recent years. A comprehensive summary, with extensive references, has been given by Little (1972). Two very attractive features of remote probes are their abilities to measure atmospheric parameters without disturbing the flow as *in situ* sensors do and to scan through large volumes of the atmosphere as *in situ* sensors cannot. It is essential, however, that the accuracy and the velocity resolution of a remote probe be assured by comprehensive testing; it is intended that the results presented here provide an example of such a test by comparison. Another test between a CO_2 Doppler lidar and an anemometer, from a different point of view and at shorter range, has been presented by Lawrence *et al.* (1972).

2. Sensor description

The continuous-wave CO_2 Doppler lidar has a transmitted power level of 3 W, a beam diameter when focused at 150 m of 3 cm, and a wavelength of 10.59 μm. The coaxial lidar receiver mixes backscattered energy from atmospheric aerosols within the probing volume with a small fraction of the transmitted energy. The Doppler frequency shift of the backscattered energy is related to the wind component along the laser beam axis by the relationship

$$\Delta f = 2V/\lambda, \qquad (1)$$

where Δf is the Doppler-frequency shift, λ the wavelength and V the wind component along the beam. In actual practice, the backscattered energy is from a volume of the atmosphere within which a random set of velocity values exist. As a result, the returned energy is not found at a single Doppler frequency shift, but is spread over a finite frequency band. It is necessary, therefore, to process the signal return in some manner to obtain a meaningful estimate of Δf for the sample volume selected. In our case the frequency spectra of Δf are obtained every 0.6 s with an electronic spectrum analyzer. The output of the analyzer is then fed to an eductor with a 5 s time constant. The analog output of the eductor, updated every 0.6 s, is then recorded on magnetic tape for off-line processing. The "estimate" of Δf required for Eq. (1) is obtained from the first moment of Doppler spectrum, and these first moments are then averaged over the time interval desired for an averaged value of V. Although not utilized in this study, the total backscattered intensity (zeroth moment) and frequency spread (second moment) are available as well.

The anemometers used were a prop-vane (R. M. Young Model 8002) and a three-axis propeller anemometer (R. M. Young Model 27002). The prop-vane was used to measure the horizontal wind components; the propeller anemometer, the vertical wind component. The prop-vane was mounted on a tower at a height of 31 m; the propeller anemometer at 38 m. Calibration of the anemometers was provided by the manufacturer.

3. Experimental procedures

The laser was located west of the tower with a beam elevation angle of 10.9° and oriented along an azimuth of 101°. The sampling volume was at a slant range of 147 m. This positioned the sampling volume 1 m below the prop-vane. The sampling volume was roughly a cylinder, 20 m long and 3 cm in diameter, centered beneath the prop-vane.

TABLE 1. Statistical results of lidar-anemometer comparisons.

Run no.	Correlation coefficient (1 min)	Averaging period (MDT)	Tower component (m s^{-1})	Doppler component (m s^{-1})
14	—*	1023–1038	3.13	3.19
15	0.972	1340–1353	4.32	4.34
		1353–1407	4.52	4.64
16	0.960	1432–1454	5.00	5.01
18	0.987	0702–0721	1.12	1.14
19	0.994	0745–0801	0.92	0.98
		0801–0816	0.75	0.77
		0816–0830	0.29	0.33
20	0.978	0844–0859	0.45	0.50
		0859–0914	0.62	0.63
		0914–0934	1.18	1.24
22	—*	1335–1350	0.35	0.38
		1350–1405	0.55	0.56

* Only 15 min averages of anemometer data were available.

The *in situ* anemometers were sampled once a second by a computer-controlled data acquisition system (Kaimal *et al.*, 1966) and 1 min averages of the three wind components were computed and listed in real time. The laser data were recorded every 0.6 s and processed later to obtain corresponding 1 min averages by computing the first moment of the 1 min averaged spectra. The anemometer data were used to compute 1 min averaged components along the lidar line of sight. Data for 168 min were obtained over a range of average wind speeds from roughly 0.3 to 5.0 m s^{-1}. Weather conditions ranged from clear skies to moderate snowfall, with mildly convective, nonshear situations predominant.

The 1 min averages were used to obtain correlation coefficients as one statistical measure of the agreement between the two data sets. Average values of the wind components over periods ranging from 12 to 20 min were also computed for direct comparison of absolute mean values.

4. Results

A summary of the results is given in Table 1. The correlation coefficients over runs of ~15 min range from 0.96 to 0.99. The average correlation coefficient is 0.979. The mean values for the 13 periods show differences between lidar and anemometer values ranging from 0.01 to 0.12 m s^{-1}. The overall mean difference between lidar and anemometer values is 0.04 m s^{-1}.

A time-sequence plot of the data for Runs 15 and 16 (Fig. 1) shows how well the two data sets track each other.

From Fig. 1 we note that, under changing wind conditions, the lidar data generally show higher and lower values than the anemometer values. This result was generally true for the entire data set. This is an expected feature of the comparison since the laser is not limited in its response to turbulent fluctuations in the wind whereas the anemometers are.

On the other hand, the comparison of the average values shown in Table 1 is mildly surprising in that the laser values are consistently higher than the anemometer values. In general, one expects the anemometers to overestimate the mean wind speeds in turbulent conditions (Izumi and Barad, 1970).

Nevertheless, the overall conclusion must be that the agreement is excellent and that one may therefore use the laser for atmospheric wind speed measurements with great confidence. There are only two significant practical limitations to the Doppler lidar as a remote sensor. One is that it depends on natural aerosols for the scattered return. In perfectly clear air, no return is obtained. It is estimated (Post and Schwiesow, 1976) that an aerosol concentration of roughly 5000 m^{-3} for particles of radius 2 μm or larger is sufficient to give adequate signal return for this apparatus to make Doppler laser wind measurements to a range of 150 to 200 m. This is an aerosol concentration typical of a clear day in rural areas with visibilities in excess of 50 km. This limitation may be reduced significantly with an improved spectrum analyzer.

The other limitation is a range limitation. Because the length of the volume resolved by the focused lidar beam increases as the square of the range, the practical resolved range of this lidar is limited to roughly 500 m. And, of course, heavy snowfall, rain or dense fog will limit the range of the device because of attenuation from scattering and absorption effects.

However, these limitations do not affect the potential of the device for a number of significant atmospheric studies. Tower-induced turbulence is an ever-present problem with *in situ*, tower-mounted probes

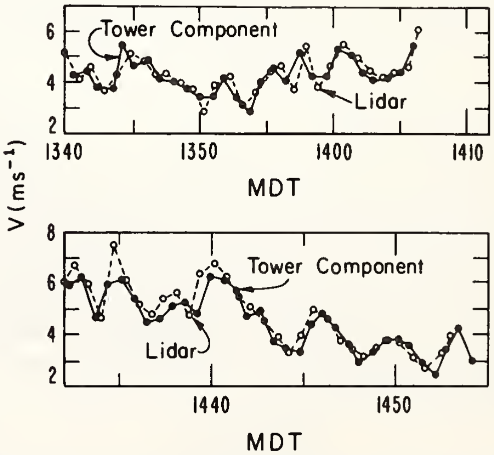

FIG. 1. Runs 15 and 16 of lidar-anemometer comparisons on 27 February 1976. Lidar and anemometer data points occur at different times because of time offsets between the separate data processing procedures.

(Angell and Bernstein, 1976). Absolute calibration of conventional anemometers for measurement of a turbulent wind field is an inexact science at best (MacCready, 1966). It is therefore desirable to exploit remote sensing techniques as much as possible.

The lidar used in this study is limited at the moment in that it measures only the line-of-sight wind component. However, this limitation may be eliminated by operating the laser in a VAD (Velocity-Azimuth-Display) mode or by adopting a coherent differential Doppler mode (Schwiesow *et al.*, 1977).

Work is underway to permit real-time processing of the laser wind data and to introduce various electronic modifications to improve the signal-to-noise ratio of the device. On the basis of the results reported here, we are planning to use the lidar to measure vertical wind speeds over a depth of 300 m at the Boulder Atmospheric Observatory, a new research facility of the Wave Propagation Laboratory (Hall, 1977). We believe that the laser is an excellent device to measure vertical wind speeds with an accuracy impossible to achieve with *in situ* instruments mounted on a tower.

Acknowledgments. We would like to express our thanks for the encouragement and support offered by Drs. V. E. Derr and C. G. Little during the course of this study. Part of the research effort was supported by the Environmental Protection Agency under an inter-agency agreement, number EPA-IAG-D5-1, E77 BEB.

REFERENCES

Angell, J. K., and A. B. Bernstein, 1976: Evidence for a reduction in wind speed on the upwind side of a tower. *J. Appl: Meteor.*, **15**, 187–188.

Hall, F. F., 1977: The Boulder Atmospheric Observatory and its meteorological research tower. *Optics News*, **3**, 14–18.

Izumi, Y., and M. L. Barad, 1970: Wind speeds as measured by cup and sonic anemometers and influenced by tower structure. *J. Appl. Meteor.*, **9**, 851–856.

Kaimal, J. C., Haugen, D. A. and J. T. Newman, 1966: A computer-controlled mobile micrometeorological observation system. *J. Appl. Meteor.*, **5**, 411–420.

Lawrence, T. R., D. J. Wilson, C. E. Craven, I. P. Jones and R. M. Huffaker, 1972: A laser velocimeter for remote wind sensing. *Rev. Sci. Instrum.*, **43**, 512–518.

Little, C. G., 1972: State of remote sensing of the troposphere. *Bull. Amer. Meteor. Soc.*, **53**, 936–949.

MacCready, P. B., Jr., 1966: Mean wind speed measurements in turbulence. *J. Appl. Meteor.*, **5**, 219–225.

Schwiesow, R. L., R. E. Cupp, M. J. Post and R. F. Calfee, 1977: Coherent differential Doppler measurements of transverse velocity at a remote point. *Appl. Opt.*, **16**, 1145–1150.

Post, M. J., and R. L. Schwiesow, 1976: Temporal and spatial frequency spectra for atmospheric aerosols. NASA Rep. CP-2004 [Presented at AMS meeting on Atmospheric Aerosols, Williamsburg].

Preprint Volume; Fourth Symposium on Meteorological
Observation and Instrumentation, 153-157, American
Meteorological Society, April 1978.

IMPROVED DETERMINATION OF VERTICAL TEMPERATURE PROFILES OF THE ATMOSPHERE BY A COMBINATION OF RADIOMETRIC AND ACTIVE GROUND-BASED REMOTE SENSORS

Ed R. Westwater

NOAA/ERL/Wave Propagation Laboratory
Boulder, Colorado 80302

1. INTRODUCTION

Ground-based microwave radiometric techniques have heretofore yielded smoothed, but useful, replicas of vertical temperature (Yershov et al., 1975; Decker et al., 1977). These techniques derive profiles by integral inversion of multi-spectral or multi-angle measurements of atmospheric radiation. Although the gross features of the profiles are inferred, it is known (Conrath, 1972) that the spatial resolution of the derived profiles is inherently limited by the smoothness and interdependence of the weighting functions of radiative transfer.

Returns from active sounders such as the acoustic sounder (Hall, 1972; Russell and Uthe, 1977) or the FM-CW radar (Gossard et al., 1970) have shown a high degree of atmospheric structure, but the received signals are not simply related to the temperature distribution. However Russell and Uthe (1977) have shown that, for altitudes less than about 800 m, the height of nocturnal inversions and the base height of elevated (subsidence) inversions can be deduced accurately (usually to well within 100 m) from acoustic sounder records. Similar agreement between the height of FM-CW radar echoes and the base of the trade wind inversion was obtained by Richter and Gossard (1970).

It is plausible that a combination of the radiometric technique, which yields gross information on the absolute temperature profile, and an active technique, which yields detailed information about the height of significant points of the profile, could significantly improve the profile recovery. We demonstrate that this is indeed the case by first presenting an inversion method that combines the active and passive information. Next we evaluate the theoretical accuracy of the combined system, for a climatology and location at which the passive microwave temperature sensing capabilities had previously been evaluated. Finally, we show profile retrievals, determined from experimental radiometric data and hypothetical height information, and compare these with profiles derived from passive information alone.

2. INVERSION TECHNIQUE

The general principles of microwave radiative transfer and radiometry are discussed, for example, by Staelin (1969) and many of the equations and terms of this field are discussed there. In particular, the microwave atmospheric radiation field, as described by the brightness temperature $T_b(\nu)$, is related to the temperature profile T(u) by

$$T_b(\nu) = \int_0^{U_0} du\, T(u)W(\nu,u) \qquad (1)$$

In (1), $W(\nu,u)$, the weighting function at frequency ν and coordinate u, depends slightly on the spatial distributions of temperature and humidity. The coordinate u can be any monotonically increasing function of height. We choose u to be the difference between the surface pressure P_o and the pressure at altitude h, P(h). By using statistical inversion (Westwater and Strand, 1968; Rodgers, 1971), an estimate of the temperature profile $\hat{T}(u)$ can be derived from a data vector d of brightness temperature and surface meteorological observations:

$$\hat{T}(u) = \langle T(u)\rangle_E + D_E(u)(\underset{\sim}{d} - \langle \underset{\sim}{d}\rangle_E), \qquad (2)$$

where,

$$D_E(u) = \langle T'(u)\, \underset{\sim}{d}'^T\rangle_E \langle \underset{\sim}{d}'\, \underset{\sim}{d}'^T\rangle_E^{-1} \qquad (3)$$

In (2) and (3), primed quantities refer to departures from average values and T means matrix transposition. The notation $\langle\cdot\rangle_E$ means ensemble average over a joint ensemble E of temperature profiles and data vectors $\underset{\sim}{d}$.

Previously (Westwater et al., 1975; Waters et al., 1975), ensembles used in constructing inversion coefficients were chosen strictly on a climatological and/or a geographical basis. If, however, an active sounder can specify that a temperature profile has inflection points within certain altitude ranges, then it is appropriate to infer radiometrically this profile using coefficients derived from an ensemble that contains inflection points only within the appropriate ranges.

In this work, we have constructed inversion coefficients from ensembles determined by the lowest inflection point (inversion base) only. As will be seen below, this single piece of information affords a large reduction in temperature variance, with a subsequent improvement in retrieval of profile details.

3. ACCURACY PREDICTIONS OF COMBINED ACTIVE AND PASSIVE SYSTEMS

By following the methods described by Westwater and Strand (1968), the expected standard deviation in profile retrieval accuracy can be predicted as a function of weighting functions, measurement noise level, and climatology. Assuming that an active sounder can pick out the first temperature inflection point to within 10 mb, we can compute the radiometrically achieved standard deviation for each 10 mb increment up to some cutoff level.

The ensemble from which we constructed inversion coefficients is a set of 340 soundings at Pt. Mugu, California taken during June-July-August of 1973-1974. Table 1 shows the number of profiles that contained first inflection points in the indicated pressure difference interval. About 95% of the inversion bases are contained in the first 100 mb above the surface.

Table 1. Numbers of profiles containing initial temperature inflection-points within selected pressure difference categories.

Pressure difference from surface (mb)			Number of profiles
0.0	-	9.99	62
10.0	-	19.99	37
20.0	-	29.99	33
30.0	-	39.99	39
40.0	-	40.99	47
50.0	-	50.99	29
60.0	-	60.99	26
70.0	-	70.99	22
80.0	-	80.99	15
90.0	-	100.99	8
100.0	-	110.99	8
110.0	-	120.99	5
120.0	-	130.99	3
130.0	-	140.99	4
140.0	-	150.99	0
150.0	-	160.99	1
160.0	-	199.99	0
200.0	-	209.99	1

For each of the sub-ensembles up to 80 mb above the surface, expected standard deviations were computed using as predictors the following variables: surface values of T, P, and rel. hum., brightness temperatures at 22.235 (water vapor channel), 31.65 (cloud channel), 52.85, 53.85 and 55.45 (temperature channels) GHz. Radiometric noise levels of 1 K were assumed. Typical results, namely for the ensemble containing inversion bases in the 70-80 mb interval, are shown in Fig. 1. The radiometer uses the height information to achieve roughly a 5 to 1 reduction in standard deviation over the radiometer alone, in the region below the inversion base. Above this level the reduction is still substantial, being about 30%. As might be expected curve 3 shows that the temperature below the (elevated) inversion base can be well estimated from knowledge of the base height and surface conditions.

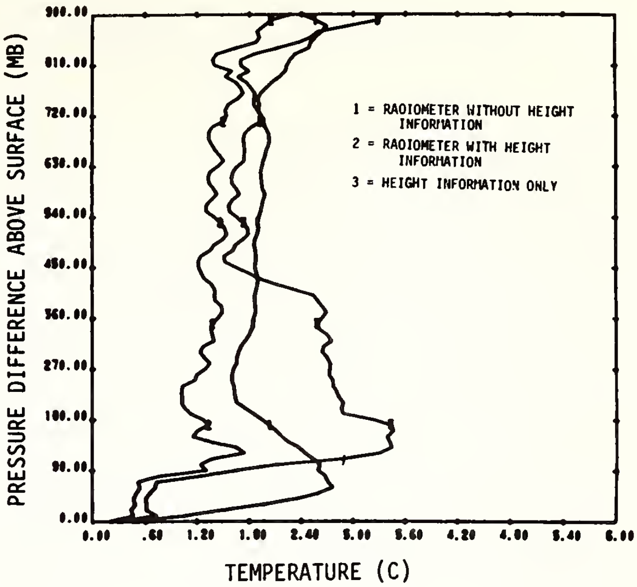

Figure 1. Expected standard deviation in radiometric temperature profile retrievals for ensemble containing inversion bases 70 to 80 mb above the surface. A priori ensemble from Pt. Mugu, California, June-July-August, 1973-1974.

4. TEMPERATURE PROFILE RETRIEVALS

To study the feasibility of passive microwave remote sensing of temperature profiles from an ocean buoy, a joint experiment of the Jet Propulsion Laboratory and the Wave Propagation Laboratory, NOAA, was recently conducted (Decker et al., 1977). Five-channel radiometer data, taken during both clear and cloudy conditions, were inverted to derive vertical temperature (and humidity) profiles. To investigate the improvement in resolution that active measurements could add, the data were also inverted using coefficients determined by lowest inflection point of the profile. Examples of these retrievals are shown in Figs. 2 and 3. Note the improvement in retrieval accuracy below the inversion base. A further retrieval example is given in Fig. 4. This profile has a slight surface based inversion about 10 mb above the surface and a relatively intense elevated inversion about 70 mb above the surface. When the radiometer data are inverted with 0-10 mb coefficients, little improvement over the original retrieval is evident. However, when coefficients appropriate to the 60-70 mb level are used, a much closer correspondence is obtained. This suggests that some discretion is needed in the application of the technique to profiles that contain multiple inversion layers.

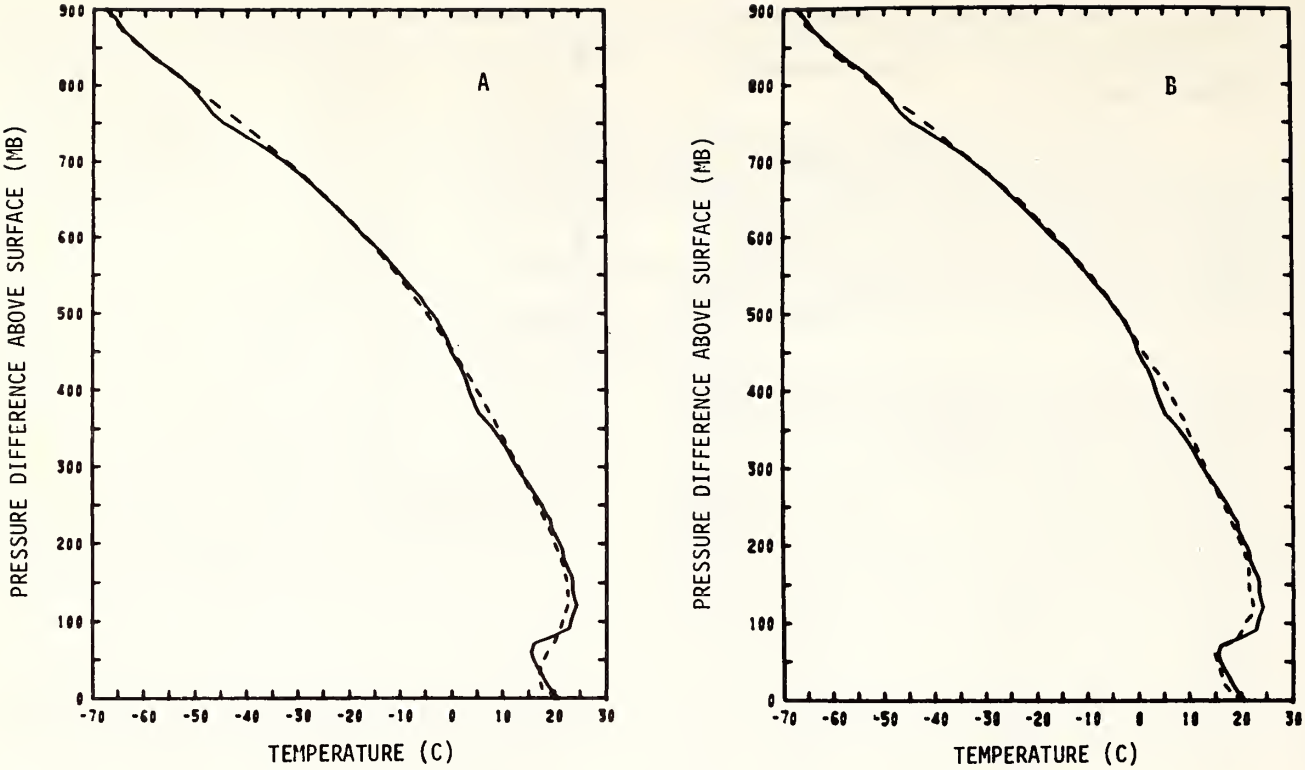

Figure 2. Temperature retrievals at Pt. Mugu, California, 7/21/76, 1101 PDT. A = retrieval without height information. B = retrieval with knowledge of height of elevated inversion. ——— = radiosonde profile. --- = retrieved profile.

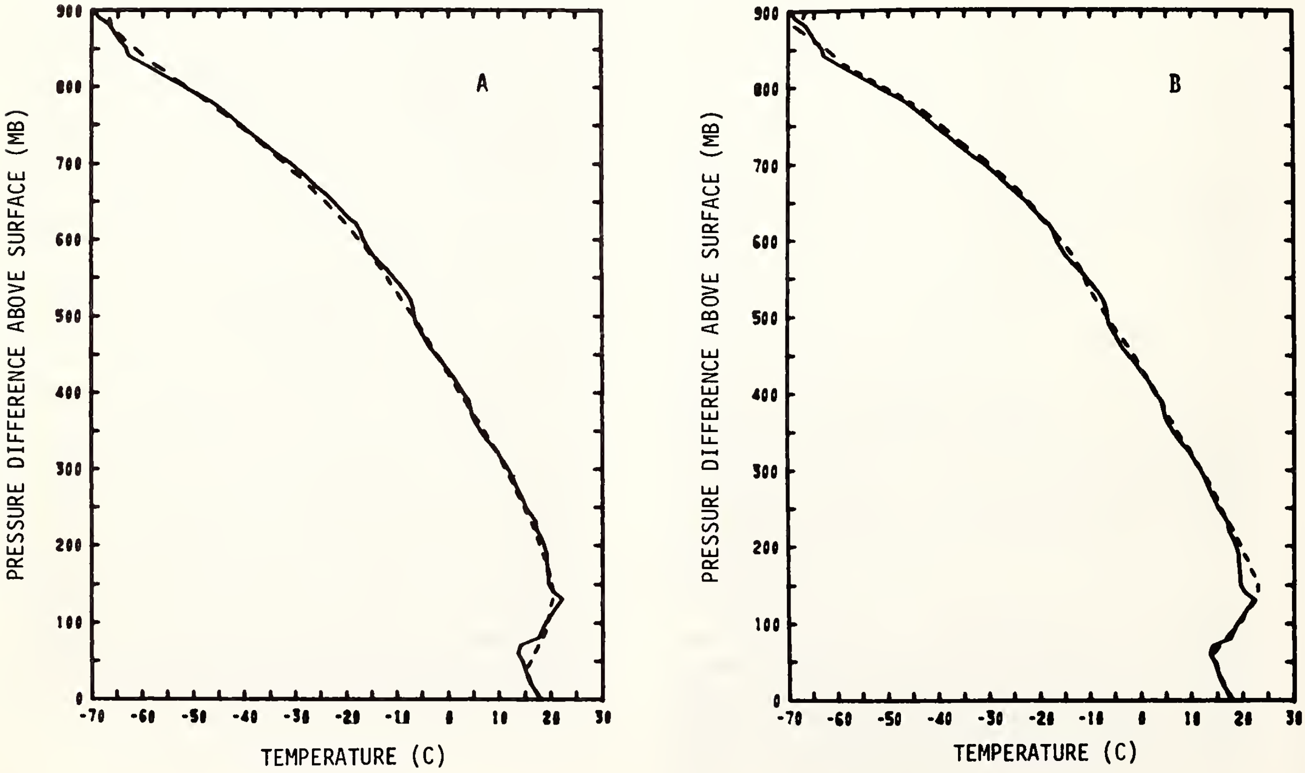

Figure 3. Temperature retrievals at Pt. Mugu, California, 7/29/76, 0459 PDT. A = retrieval without height information. B = retrieval with knowledge of height of elevated inversion. ——— = radiosonde profile. --- = retrieved profile.

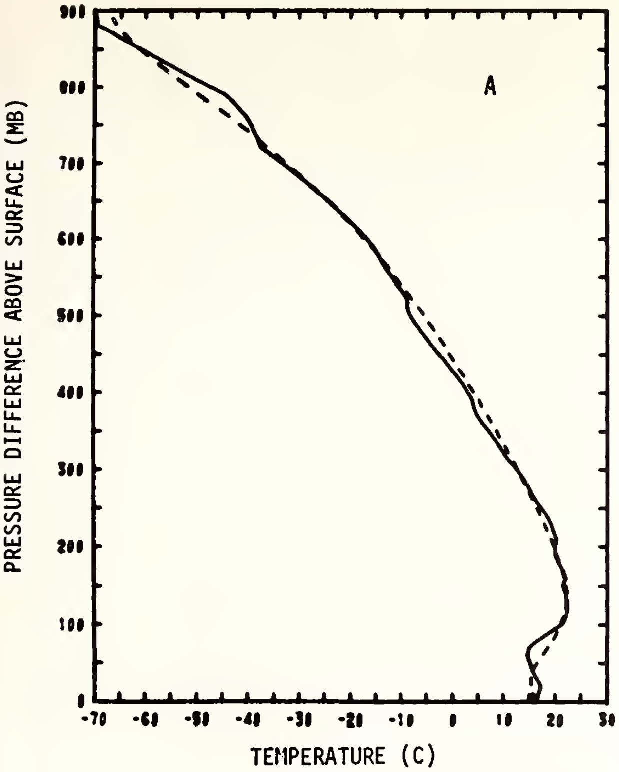

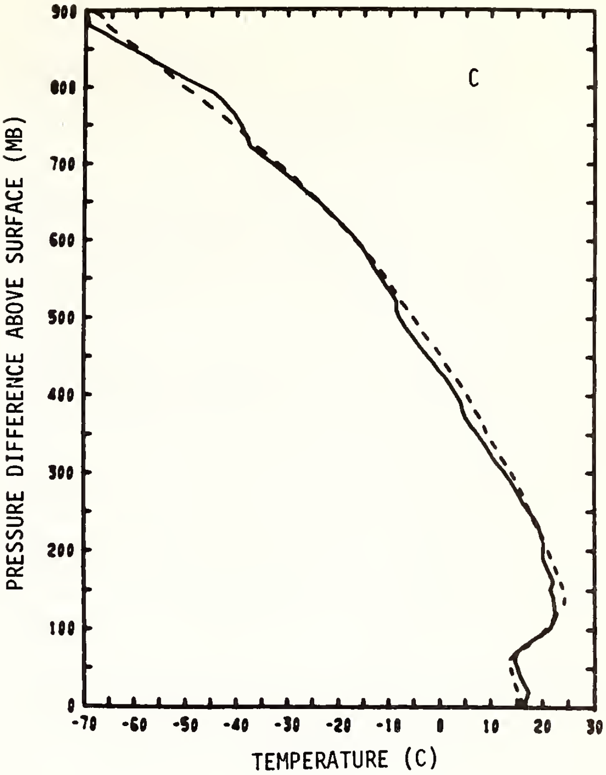

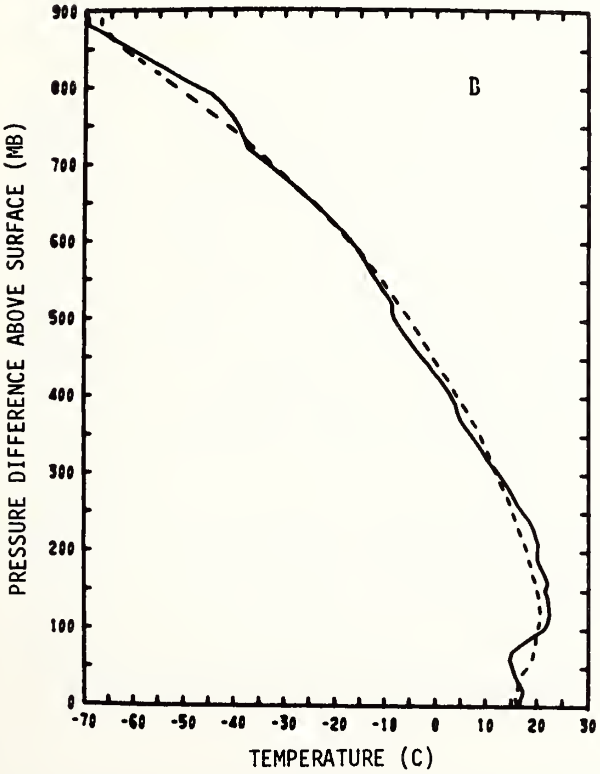

Figure 4. Temperature retrievals at Pt. Mugu, California 7/20/76, 0505 PDT. A = retrieval without height information. B = retrieval using coefficients constructed for inflection points in the 0-10 mb pressure difference interval. C = retrieval using coefficients constructed for inflection points in the 60-70 mb pressure difference interval. ——— = radiosonde profile. --- = retrieved profile.

5. CONCLUDING REMARKS

Both theoretical results, based on predictions of the statistical theory of inversion, and the results of profile retrievals from radiometric data, indicate that improved temperature retrievals can result from the incorporation of profile inflection points into mathematical inversion schemes. Crucial to our presentation is the assumption that active sounders can measure inversion heights to an accuracy of 10 mb (∿ 100 m). In many instances this can easily be done; in other cases, such as complex temperature profiles with many inflection points, ambiguity may arise. Further work is justified in studying the limitations and also, the possible extensions, of combined active-passive systems.

6. ACKNOWLEDGMENTS

The author thanks Mr. Steven Sicola for preparing many of the computer programs used in this study.

Conrath, B. J., 1972: Vertical resolution of temperature profiles obtained from remote radiation measurements. *J. Atmos. Sci.*, 29, 1262-1271.

Decker, M. T., E. R. Westwater, and F. O. Guiraud, 1977: Experimental evaluation of ground-based microwave radiometric sensing of atmospheric temperature and water vapor profiles. Submitted for publication.

Gossard, E. E., J. H. Richter, and D. Atlas, 1970: Internal waves in the atmosphere from high-resolution radar measurements. *J. Geophys. Res.*, 75, 3523-3536.

Hall, F. M., 1972: Temperature and wind structure studies by acoustic echo-sounding. Chapter 18 of *Remote Sensing of the Troposphere.*, V. E. Derr, ed. U.S. Department of Commerce. For sale by Superintendent of Documents, U.S. Government Printing Office, Washington, D.C. 20402.

Richter, J. H. and E. E. Gossard, 1970: Lower tropospheric structure as seen by a high-resolution radar. Naval Electronics Laboratory Center Technical Report, NELC/TR 1718, 66 pp.

Rodgers, C. D., 1971: Some theoretical aspects of remote sounding in the earths atmosphere. *J. Quant. Spectrosc. Radiat. Transfer*, 11, 767-777.

Russell, P. B. and E. E. Uthe, 1977: Sodar network measurements of regional mixing depth and stability patterns for an air quality model /1/. AMS/APCA Conf. Applications of Air Poll. Meteor., 28 Nov.-2 Dec. 1977, Salt Lake City Utah. Published by Amer. Meteor. Soc., Boston, Mass. 02108.

Staelin, D. H., 1969: Passive remote sensing at microwave wavelengths. *Proc. IEEE*, 57, 427-439.

Waters, J. W., K. F. Kunzi, R. L. Pettyjohn, R. K. L. Poon and D. H. Staelin, 1975: Remote sensing of atmospheric temperature profiles with the Nimbus 5 microwave spectrometer. *J. Atmos. Sci.*, 32, 1953-1969.

Westwater, E. R., J. B. Snider, and A. C. Carlson, 1975: Experimental determination of temperature profiles by ground-based microwave radiometry. *J. Appl. Meteor.*, 14, 524-539.

__________, and O. N. Strand, 1968: Statistical information content of radiation measurements used in indirect sensing. *J. Atmos. Sci.*, 25, 750-758.

Yershov, A. T., Yu. V. Lebskiy, A. P. Naumov and V. M. Plechkov, 1975: Determination of the vertical temperature profile from ground-based measurements of atmospheric radiation at $\lambda = 5$ mm. *Izv. Acad. Nauk., USSR, Atmos. Ocean. Phys.*, 11, 1220-1229.

Journal of Atmospheric Sciences, 35: 1427-1440, 1978.

A Model Study of the Stably Stratified Planetary Boundary Layer

R. A. Brost[1]

Cooperative Institute for Research in Environmental Sciences, University of Colorado/NOAA, Boulder 80309

J. C. Wyngaard

Cooperative Institute for Research in Environmental Sciences, University of Colorado/NOAA, Boulder 80309
and
Wave Propagation Laboratory, NOAA, Boulder 80302

(Manuscript received 19 December 1977, in final form 17 April 1978)

ABSTRACT

A second-order turbulence model is used to study the stable boundary layer (SBL). Over a horizontal surface, a constant surface cooling rate drives the SBL to a steady state within a few hours. Parameterizations are developed for eddy diffusivities, the kinetic energy dissipation rate and the geostrophic drag law in this idealized case. Over a sloped surface, a constant cooling rate produces a quasi-steady-state SBL in which some flow properties continue to vary but $h(|f|/u_*L)^{\frac{1}{2}}$ becomes constant; however, this constant is a function of the wind direction relative to the slope and the baroclinity, as measured by the cooling rate times the slope. Calculated eddy diffusivity profiles in the baroclinic (sloping terrain) case compare well with recent data from Antarctica. If a surface energy budget is used rather than a constant cooling rate, the SBL does not reach a steady state even over a horizontal surface; the nondimensional height slowly decays. We conclude that equilibrium models of the SBL are likely to be much less applicable to the real world than are their counterparts for the convective boundary layer.

1. Introduction

The atmospheric boundary layer is often statically stable. Over land, a stable boundary layer (SBL) develops almost every night and in winter it frequently also exists during the day. Over water, an SBL is commonplace at high latitudes and over cold currents.

In this numerical study we describe the broad characteristics of an SBL which, although somewhat idealized, has many of the important features of the real-world case. We examine the influences of terrain slope, the feedback between the surface energy budget and the atmosphere, and the effect of different surfaces. A principal goal is to assess the applicability of the idealizations often made in planetary boundary layer studies (e.g., quasi-steady state, barotropic flow) to the stably stratified case.

There have been several numerical studies of the SBL, but none has adequately addressed the question of the existence of a steady state. Some claimed it did not exist; others claimed it could occur under the proper cooling conditions; still others simply assumed its existence and examined its structure.

Deardorff (1972) simulated the time evolution of a set of SBL observations using height- and stability-dependent eddy diffusivities. He concluded that the depth h of the SBL was time-dependent and could not be parameterized by a diagnostic equation.

Businger and Arya (1974), also using height-dependent and stability-dependent eddy diffusivities, solved directly for the steady-state structure, and found that h obeyed the diagnostic equation of Zilitinkevich (1972); however, they obtained no information on the approach to steady state.

Using a model in which the eddy diffusivities were parameterized in terms of the predicted turbulent energy, Delage (1974) found the SBL approached steady state after several hours with a realistic decaying cooling rate. He concluded that h grew while the inertial velocity overshoot just above the boundary layer was growing and hence the velocity shear across the SBL was increasing, but when the shear decreased h stopped growing and steady state was reached.

Wyngaard (1975) integrated a second-order turbulence numerical model and demonstrated that the SBL could approach steady state after 2–8 h, depending on the specified constant cooling rate at 1 m. He also found that h obeyed Zilitinkevich's similarity prediction.

In this study, we simplify the turbulence model of Wyngaard (1975; hereafter called W75) and reduce it to a means of calculating eddy diffusivities for heat and momentum. Because the closure approximations in

---

[1] Current affiliation: Department of Physics and Geophysical Sciences, Old Dominion University, Norfolk, VA 23508.

0022-4928/78/1427-1440$07.00
© 1978 American Meteorological Society

second-order models remain somewhat controversial, we have chosen not to focus on the details of the calculated SBL structure, which can be somewhat model-dependent. Instead, our emphasis is on the gross dynamics of the SBL and the influences of real-world features such as sloping terrain and a variable cooling rate.

2. The model

We consider an infinite, flat, but sloped (at a small angle β to the horizontal) surface of uniform roughness and temperature. We take the boundary layer thickness to be constant along the slope, and allow mean quantities to vary only in the direction normal to the surface (z) and in time. Following Lumley and Panofsky (1964), we denote the temperature, pressure and density values for an undisturbed, adiabatic atmosphere with a subscript zero. We take these as the values existing throughout the SBL at transition. Thus, for example, mean temperature $\bar{T}$ is written as $T_0+\bar{T}'$, where $\bar{T}'$ is the deviation from the adiabatic state. We choose the x and y directions parallel to the surface, and write the Boussinesq equations for mean wind components U and V in the x and y directions as

$$\frac{\partial U}{\partial t}=fV-\frac{1}{\rho_0}\frac{\partial \bar{P}'}{\partial x}-\frac{g}{T_0}\bar{T}'|\beta|\cos\gamma-\frac{\partial}{\partial z}\overline{uw}, \tag{1}$$

$$\frac{\partial V}{\partial t}=-fU-\frac{1}{\rho_0}\frac{\partial \bar{P}'}{\partial y}+\frac{g}{T_0}\bar{T}'|\beta|\sin\gamma-\frac{\partial}{\partial z}\overline{vw}. \tag{2}$$

Here γ is the angle, measured counterclockwise, from the fall-line vector (the vector perpendicular to the contour lines and pointing down the slope) to the x axis. We assume the pressure gradients in (1) and (2) are independent of z, and define the usual geostrophic wind components U_g and V_g by

$$\rho_0 fU_g=-\partial\bar{P}'/\partial y,\quad \rho_0 fV_g=\partial\bar{P}'/\partial x.$$

For stable conditions $\bar{T}'$ is negative and produces a katabatic (downslope) acceleration. Thus the terrain-slope terms in (1) and (2), when added to the pressure-gradient terms, give an effective pressure gradient that depends on z; a similar situation exists in the baroclinic, unsloped case with a horizontal temperature gradient.

The existence of a height-dependent effective pressure gradient in the SBL over sloped terrain is well-known. It is an important component of Lettau's (1967) explanation of the nocturnal jet over the Great Plains. Also, it must be considered in any description of winds over Antarctic slopes (e.g., Ball, 1960; Dalrymple *et al.*, 1966; Mahrt and Schwerdtfeger, 1970) or over the slopes of Greenland (Schwerdtfeger, 1972).

The mean potential temperature equation is

$$\frac{\partial\Theta}{\partial t}=-\frac{\partial\overline{w\theta}}{\partial z}. \tag{3}$$

Our lower boundary condition on potential temperature is provided by either a constant cooling rate ($\partial\Theta/\partial t$) or a surface energy budget. In Section 3 we follow W75 and specify the cooling rate at $z=1$ m. Later, the ground temperature T_g is calculated using the surface energy budget with one subsoil grid point, i.e.,

$$\frac{\partial T_g}{\partial t}=C_g^{-1}[F\downarrow(0)-\sigma T_g^4-\rho_0C_pQ_0]-1.18\omega(T_g-T_s), \tag{4}$$

where $F\downarrow(0)$ is the magnitude of the (specified) downward longwave radiative flux at the surface, T_s the subsoil temperature, $\rho_0C_pQ_0$ the surface heat flux, ω the angular velocity of the earth and

$$C_g=0.95\left(\frac{\lambda C_s}{2\omega}\right)^{0.5} \tag{5}$$

with λ and C_s the soil thermal conductivity and soil heat capacity per unit volume. Eqs. (4) and (5) were developed by Bhumralkar (1975) and Blackadar (1976) and tested by Deardorff (1978). The surface fluxes of heat and momentum are calculated using transfer coefficients (Sommeria, 1976).

The turbulence equations are those discussed in W75, with the following changes:

1) The time derivatives are neglected (see Appendix B) because they are smaller than the dominant terms. For example, in the turbulent kinetic energy ($q^2/2$) equation the ratio of the production ($\sim q^3/l$) and the time derivative ($\sim q^2/\tau$) terms is of order $q\tau/l$, where l is a characteristic integral scale (Tennekes and Lumley, 1972) and τ a time scale characteristic of the SBL evolution. Taking $q\approx0.3$ m s^{-1}, $l\approx10$ m and $\tau\approx3\times10^3$ s, we find $q\tau/l\approx100$, so that the time change term can be neglected. Examination of the other turbulence second-moment equations indicates that this estimate also applies there.

2) The Coriolis terms are also neglected in comparison to other terms. In the turbulent velocity covariance equations, for example, the ratio of shear production terms ($\sim q^3/l$) to Coriolis terms ($\sim fq^2$) is of order $q/(fl)$. For $q\approx0.3$ m s^{-1}, $l\approx10$ m and $f\approx10^{-4}$ s^{-1}, we find $q/(fl)\approx300$ so the Coriolis terms are negligible.

3) Triple correlations are ignored because surface-layer data show they are small under stable conditions (Wyngaard and Coté, 1971).

4) We parameterize the rate of dissipation of turbulent kinetic energy per unit mass as $\epsilon\propto q^3/l$, where the turbulent length scale $l=z(1+z/l_B)^{-1}$. This is an interpolation between the limits at the wall ($l\approx z$) and at the very stable outer edge of the SBL ($l\approx l_B$). We assume that the limiting scale l_B of the energy-containing eddies in a stably stratified environment is determined by the balance between inertia forces and

TABLE 1. Comparison of steady-state values of boundary-layer parameters of the current model and of Wyngaard (1975) for different cooling rates. $G=10$ m s^{-1}, $z_0=1$ cm.

	Cooling rate							
	0.2 K h^{-1}		0.5 K h^{-1}		1 K h^{-1}		2 K h^{-1}	
	Current model	Wyngaard (1975)	Current model	Wyngaard (1975)	Current model	Wyngaard (1975)	Current model	Wyngaard (1975)
u_* (m s^{-1})	0.25	0.23	0.21	0.20	0.18	0.16	0.15	0.13
Q_0 (K m s^{-1})	−0.0082	−0.0088	−0.015	−0.013	−0.020	−0.016	−0.024	−0.018
L (m)	150	120	46	52	25	25	11	11
α (deg)	28	33	35	39	38	44	42	49
h (m)	220	130	120	70	85	48	50	25
d	0.36	0.24	0.39	0.22	0.40	0.24	0.39	0.21
h/L	1.5	1.1	2.6	1.4	3.4	2.0	4.5	2.3
$u_*/(\lvert f\rvert L)$	17	19	45	38	74	67	130	120

buoyancy forces (Businger and Arya, 1974; Delage, 1974; Zeman and Tennekes, 1977). Requiring these intertia forces ($\sim\sigma_w^2/l_B$) and buoyant forces [$\sim(g/T_0)\times(\partial\Theta/\partial z)l_B$] to be of the same order gives

$$l_B^2 \approx \frac{\sigma_w^2}{\dfrac{g}{T_0}\dfrac{\partial\Theta}{\partial z}} = \frac{\sigma_w^2}{\omega_B^2}, \tag{6}$$

where $\omega_B=[(g/T_0)(\partial\Theta/\partial z)]^{\frac{1}{2}}$ is the Brunt-Väisälä frequency. We used $l_B=C\sigma_w/\omega_B$, with constant $C=1.69$ chosen to give critical flux and gradient Richardson numbers near 0.20 and 0.25, respectively, in agreement with W75.

While the transformation to coordinates in the plane of the slope introduces new terms in the turbulence moment equations, our small-slope assumption insures that these new terms are negligible. The turbulence equations are listed in Appendix B, and Appendix C describes our numerical techniques.

3. Constant cooling rate results

a. Steady-state, horizontal surface

A truly steady-state SBL, in which all parameters are independent of time, can be established by balancing the cooling through turbulent heat flux divergence and the warming through mean advection. In the simplest such case, with mean quantities varying only with x and z, and negligible radiative flux divergence and mean vertical velocity, the mean potential temperature equation is

$$\frac{\partial\Theta}{\partial t} = 0 = -U\frac{\partial\Theta}{\partial x} - \frac{\partial}{\partial z}\overline{w\theta}. \tag{7}$$

This situation could be found in flow over cooler water, for example.

We will use a less stringent definition of "steady state," one which allows Θ to decrease with time but requires the other SBL parameters to be time-independent. This can be approached at night over land when the surface cools. The W75 study found that if the surface cooling rate was constant, the mean potential temperature equation (3) throughout the SBL behaved approximately as

$$\frac{\partial\Theta}{\partial t} = -\frac{\partial\overline{w\theta}}{\partial z} \approx \frac{Q_0}{h} = \text{constant} \tag{8}$$

and the important parameters of the SBL approached time-independence. W75 found this quasi-steady-state structure in 2–8 h, with the shorter times for the larger cooling rates.

Examination of the terms of the surface energy budget (4) indicates the requirements for a constant near-surface cooling rate. Our results and those of W75 indicate that Q_0 is approximately constant after a few hours with a constant cooling rate. Furthermore, the subsoil flux to the surface, which is proportional to (T_g-T_s), must increase with time as the magnitude of (T_g-T_s) increases. To balance these heat inputs the net radiative deficit of the surface [$\sigma T_g^4-F\downarrow(0)$] must increase with time, so the downward radiative flux at the surface $F\downarrow(0)$ must strongly decrease; this can be caused by the breakup of a cloud layer or the advection of drier air aloft. Thus, naturally occurring instances of a persistent constant cooling rate seem unlikely but not impossible.

Nonetheless, a constant cooling rate conveniently produces an idealized, steady-state SBL for study. We generated five such cases with our model by using cooling rates of 0.2, 0.5, 1, 2 and 4 K h^{-1}.

Since our initial conditions are different from those of W75, we will not compare the detailed temporal behavior of the two models. Instead, the steady states for the same cooling rates are compared in Table 1, which shows that the models give quite similar results for most properties.

The steady-state values for the friction velocity u_* and the Monin-Obukhov length L are nearly identical. Thus, for the same cooling rates the two models give

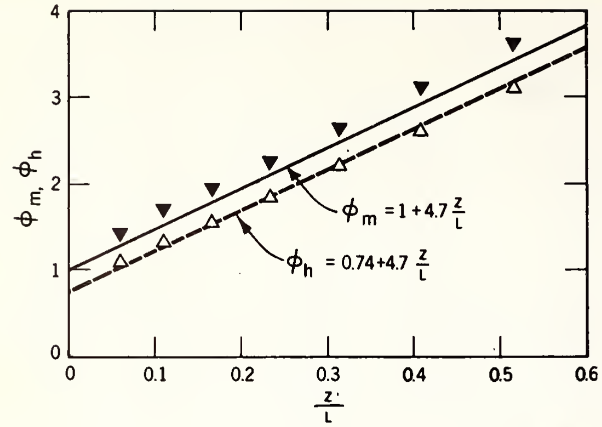

FIG. 1. Dimensionless wind shear ϕ_m (▼) and temperature gradient ϕ_h (△) for a current model run at $h/L=3.4$. Curves are parameterizations of Kansas results (Businger *et al.*, 1971).

virtually identical stabilities as measured by $\mu=u_*/(|f|L)$.

The models differ most in their equilibrium boundary layer depths. Our model predicts values of depth h and the parameter $d=h(|f|/u_*L)^{\frac{1}{2}}$ about twice those of W75.

The steady-state vertical profiles of turbulence quantities from our model are so similar to those of W75 that they will not be presented here.

Fig. 1 compares calculated surface-layer profiles of nondimensional mean wind shear ϕ_m and nondimensional temperature gradient ϕ_h with the Kansas data (Businger *et al.*, 1971). The agreement of ϕ_h is excellent and that of ϕ_m is comparable with that found in model calculations by Mellor (1973), Lewellen and Teske (1973) and W75.

Fig. 2 shows the evolution of the vertical profiles of Θ and $\overline{w\theta}$ for the 1 K h^{-1} cooling rate. The $\overline{w\theta}$ profiles have a slight curvature and the maximum cooling rate is near the ground. Note that the cooling between $t=5$ h and $t=10$ h at 85 m is about half that at the surface. Thus, while (8) is only crudely satisfied, the SBL is essentially in a steady state after 5 h.

In this study, as in W75, h is taken as the height at which the stress is 5% of its surface value. This definition gives $h=85$ m at 10 h, whereas the potential temperature profile would indicate a greater h; however, the Θ profile is a product of the integrated history of $\overline{w\theta}$ and as Fig. 2 shows, the latter can extend to greater heights early in the evening. Thus the Θ profile can be a misleading indicator of h.

1) STABLE BOUNDARY LAYER DEPTH

Several simple expressions for the depth h of the steady-state SBL were tested against the model results. One plausible assumption is that the bulk Richardson number across the boundary layer is a constant, say, a_1. If we take the bulk shear as G/h, with G the geostrophic wind speed, and the bulk potential temperature gradient between 1 m and h as $\Delta\Theta/h$, then we find

$$h=\frac{a_1G^2T_0}{g\Delta\Theta}. \tag{9}$$

However, for our model the "constant" a_1 varies from 0.12 to 0.34 with increasing stability. Taking $\Delta\Theta$ between z_0 and h does not significantly improve (9); however, it is improved somewhat if G^2 is replaced by $(\Delta V)^2$, where ΔV is the magnitude of the difference in wind velocity between h and 1 m. For fixed G, ΔV increases with stability because α and the overshoot at h both increase. Nonetheless, even then a_1 varies from 0.11 to 0.22, and (9) remains a poor indicator of steady-state SBL depth.

A better steady-state depth equation can be derived by integrating between the surface and $z=h$ the equation of motion in the direction of the surface wind, yielding

$$h=\left(\frac{u_*}{\langle V-V_g\rangle}\right)\frac{u_*}{f}, \tag{10}$$

where V and V_g are the mean and the geostrophic wind components perpendicular to the surface wind, and the angle braces indicate averages over h. Since $V_g\equiv -G\times\sin\alpha$, we assume that $\langle V-V_g\rangle \propto G\sin\alpha$ and find

$$h=a_2u_*^2/fG\sin\alpha. \tag{11}$$

This is a fairly successful expression, in the sense that according to model results a_2 has no significant dependence on stability; our model gives $a_2=1.6$ and W75 gives $a_2=1.1$. Fig. 3 shows how a_2 converges to a steady state for the constant cooling rate runs.

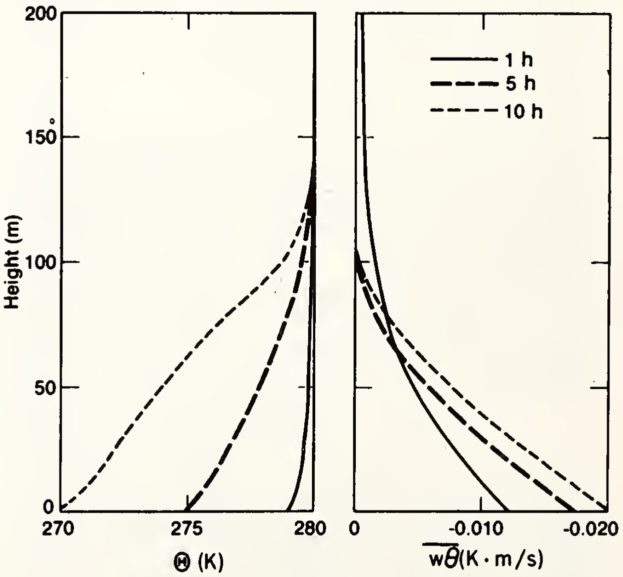

FIG. 2. Calculated time evolution of potential temperature and vertical potential temperature flux profiles for 1 K h^{-1} constant cooling rate at 1 m.

Eq. (11) implies that $u_*/G=C_1(fh\sin\alpha/G)^{\frac{1}{2}}$, where $C_1=(a_2)^{-\frac{1}{2}}$; the current model gives $C_1=0.79$ and W75 gives $C_1=0.95$. The arctic observations of Carsey and Leavitt (1977) give $C_1=0.71$, but have a great deal of scatter.

Our model results show that the assumption that $\langle V-V_g\rangle\propto G\sin\alpha$ becomes very poor under baroclinic conditions. Even a slight amount of baroclinity seriously degrades the predictions of (11).

Another expression for h is the similarity prediction (Zilitinkevich, 1972, 1975)

$$h=d(u_*L/|f|)^{\frac{1}{2}}. \tag{12}$$

The value of the constant d depends on the definition of the depth h, but using the 5% stress criterion W75 found $d=0.22$; our model gives $d=0.40$, about the value found by Businger and Arya (1974). Fig. 3 shows that (12) correlates well the steady-state h values from the present model over a wide range of cooling rates.

The steady-state SBL depth can be strongly model-dependent, perhaps because the height at which turbulence vanishes depends on a delicate balance between production and dissipation. As a result, minor differences in the parameterization of dissipation can yield major changes in h, and hence d. Therefore, we should not look too closely at the value of d; instead, we will emphasize the relative changes in d caused by terrain slope or the variable surface cooling rate.

2) Parameterization of eddy diffusivities

The predicted steady-state profile of eddy diffusivity for momentum K_m is represented well by

$$\frac{K_m}{ku_*h}=\frac{\left(\frac{z}{h}\right)\left(1-\frac{z}{h}\right)^{1.5}}{1+4.7\left(\frac{z}{h}\right)\left(\frac{h}{L}\right)}. \tag{13}$$

Note that for $z/h\ll1$ Eq. (13) gives $K_m=ku_*z/(1+4.7z/L)$, which is the Businger *et al.* (1971) surface layer result for stable conditions. Figs. 4 and 5 illustrate the good agreement between (13) and the predictions of W75 and our model.

That the dimensionless K_m should depend on only z/h and h/L is consistent with similarity reasoning in the steady-state case (Zilitinkevich, 1975). The similarity hypothesis would allow $\mu=u_*/(|f|L)$ to be used instead of h/L, since they are related in steady state through $h/L=d\mu^{\frac{1}{2}}$ [see Eq. (12)]. However, the good fit of our K_m expression (13) to both sets of model results would not have occurred if μ had been used as the stability index, since the two models give different proportionality factors between h/L and $\mu^{\frac{1}{2}}$ (i.e., different d values). The use of h/L as a stability index for stably and unstably stratified boundary layers has been suggested by Melgarejo and Deardorff (1974) and by Zilitinkevich and Deardorff (1974).

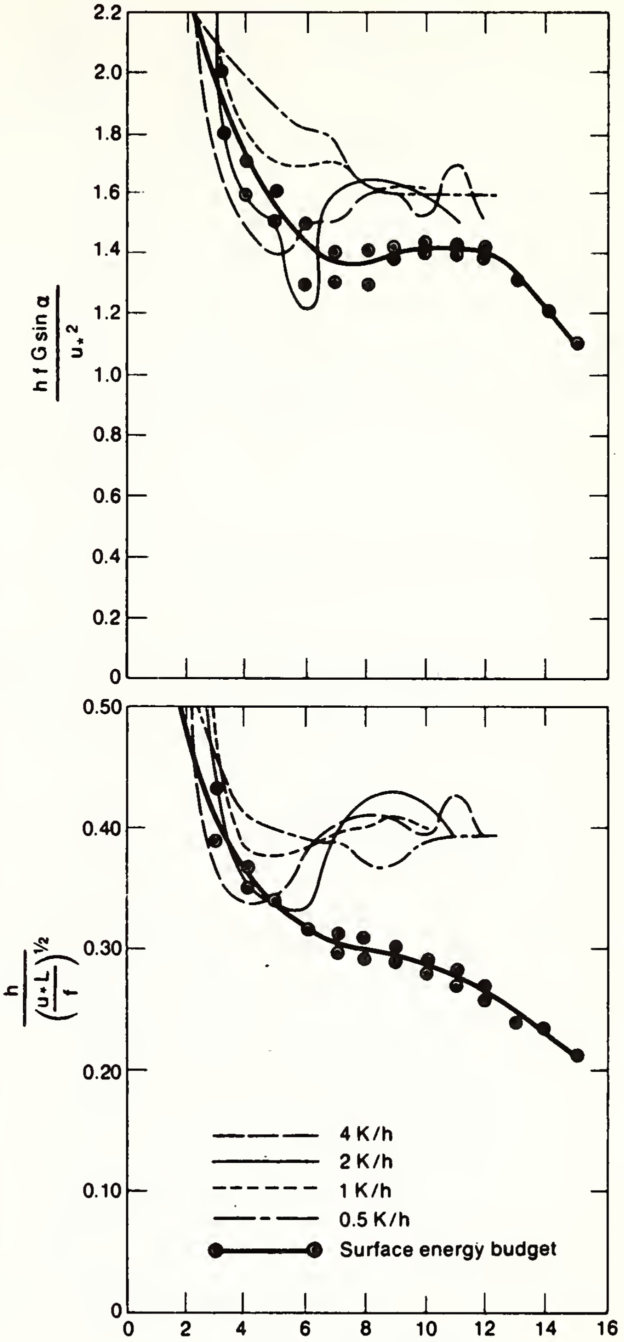

Fig. 3. Calculated time evolution of two dimensionless SBL depths. The convergence to steady state is shown for various cooling rates, along with the steady decay that results when a surface energy budget is used.

Our model results also show that K_h/K_m, where K_h is the eddy diffusivity for temperature, averages about 1.25 in the SBL. In the surface layer it is nearer 1.35, the value implied by the lower boundary conditions, while near h it is about 1.2. The W75 results show somewhat more height dependence, with $K_h/K_m\approx1.0$ above $z\approx0.5$ h. Thus our parameterization (13) works

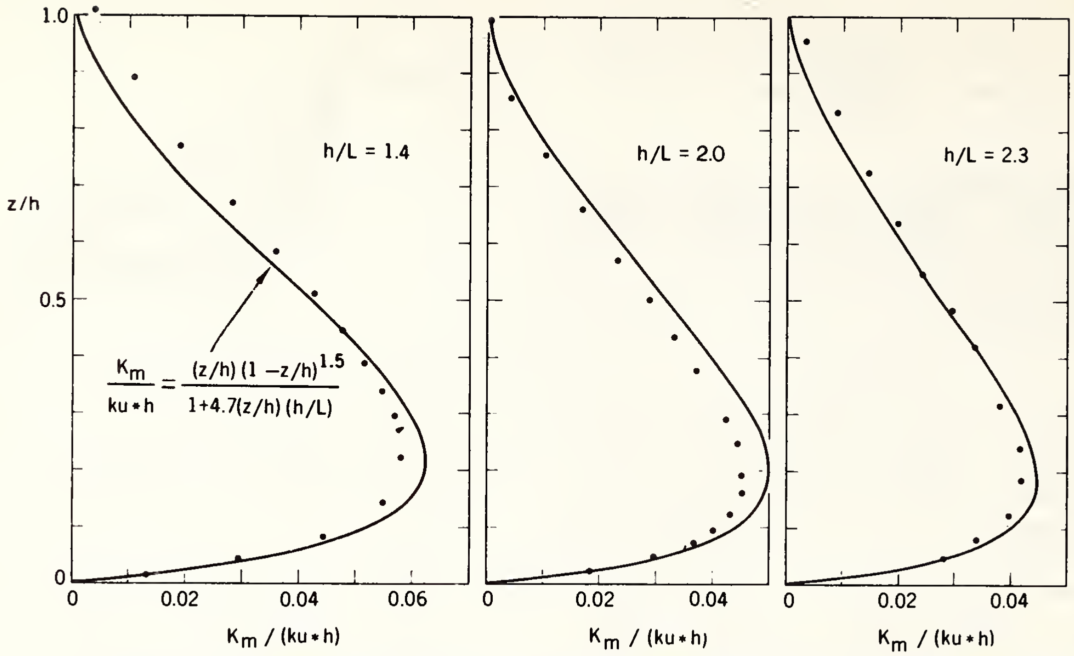

FIG. 4. Comparison of Wyngaard's (1975) predicted dimensionless steady-state K_m (dots) and parameterization (13) (curves) for three cooling rates (0.5, 1 and 2 K h^{-1}).

about as well for K_h if a factor of 1.2 is inserted on the right side.

3) PARAMETERIZATION OF DISSIPATION

Our model's steady-state ϵ profile is fit well by

$$\frac{\epsilon k h}{u_*^3} = \left(\frac{h}{z}\right)\left[1+3.7\left(\frac{z}{h}\right)\left(\frac{h}{L}\right)\right]\left(1-0.85\frac{z}{h}\right)^{1.5}, \quad (14)$$

as shown in Fig. 6. For $z/h \ll 1$, Eq. (14) implies that $\epsilon = [u_*^3/(kz)](1+3.7z/L)$, which as discussed in W75 is the result implied by the Businger *et al.* (1971) data and the negligible turbulent transport of energy found by Wyngaard and Coté (1971) in the stable surface layer.

We can easily derive an integral constraint for ϵ. Multiplying the x equation of motion (1) by U, the

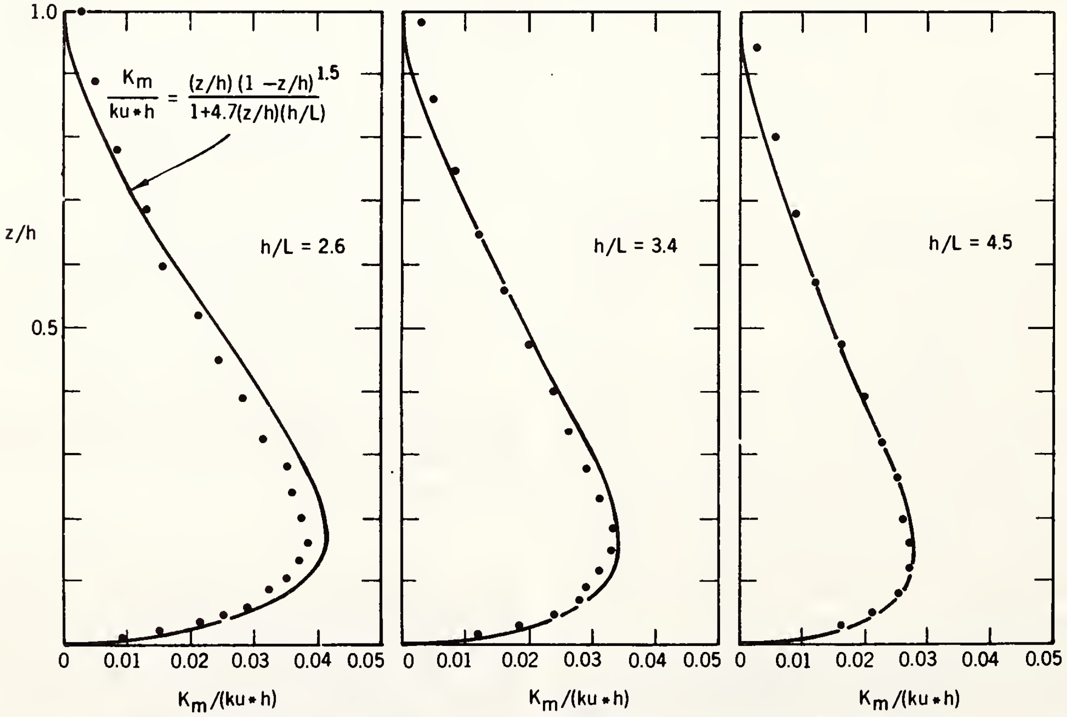

FIG. 5. As in Fig. 4 except for current model's predicted dimensionless steady-state K_m.

y equation of motion (2) by V, adding, and integrating between the surface roughness height z_0 and h gives in the steady, horizontally homogeneous, barotropic case

$$\int_{z_0}^{h}\left(U\frac{\partial}{\partial z}\overline{uw}+V\frac{\partial}{\partial z}\overline{vw}\right)dz=fG\int_{z_0}^{h}Vdz, \qquad (15)$$

where we have here chosen the x axis along the geostrophic wind. The left side of (15) can be evaluated by integrating by parts and using the turbulent kinetic energy equation, yielding

$$\int_{z_0}^{h}\left(U\frac{\partial}{\partial z}\overline{uw}+V\frac{\partial}{\partial z}\overline{vw}\right)dz=-\int_{z_0}^{h}\left(\frac{g}{T_0}\overline{w\theta}-\epsilon\right)dz. \qquad (16)$$

The right side of (15) can be evaluated by integrating (1), yielding

$$fG\int_{z_0}^{h}Vdz=Gu_*^2\cos\alpha. \qquad (17)$$

Combining (15)–(17) gives a kinetic energy balance for the entire layer:

$$-(h/u_*^3)[(g/T_0)\langle\overline{w\theta}\rangle-\langle\epsilon\rangle]=(G/u_*)\cos\alpha. \qquad (18)$$

This constraint, with the buoyant term neglected, is also discussed by Kuhn *et al.* (1977).

If we evaluate the left side of (18) using our ϵ parameterization (14) and a linear $\overline{w\theta}$ profile, we find

$$(G/u_*)\cos\alpha=k^{-1}[\ln(h/z_0)-1.1+2{:}2(h/L)]. \qquad (19)$$

Combining (11) and (12) yields, for the current model

$$(G/u_*)\sin\alpha=10(h/L). \qquad (20)$$

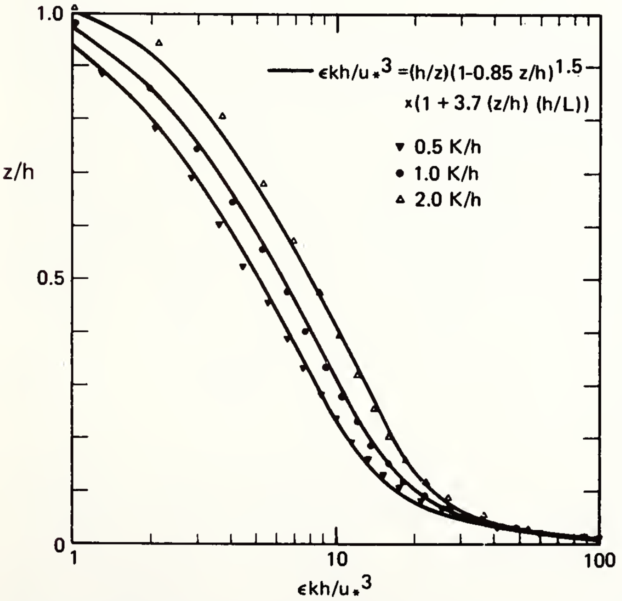

Fig. 6. Comparison of current model's predicted dimensionless steady-state ϵ and parameterization (14) (curves) for three cooling rates (0.5, 1 and 2 K h^{-1}).

Eqs. (19) and (20) comprise a geostrophic drag law which fits our model results (Table 1) well.

The geostrophic drag law is usually written as (Businger and Arya, 1974)

$$(G/u_*)\cos\alpha=k^{-1}[\ln|u_*/fz_0|-A], \qquad (21)$$

$$(G/u_*)\sin\alpha=k^{-1}B\,\mathrm{sgn}(f), \qquad (22)$$

where A and B depend on stability. Our model gives, from (12) and (19)–(22),

$$A=\ln(h/L)-2.2(h/L)+2.9=\tfrac{1}{2}\ln\mu-0.9\mu^{\frac{1}{2}}+2.0, \qquad (23)$$

$$B=3.5(h/L)=1.4\mu^{\frac{1}{2}}, \qquad (24)$$

which agrees fairly well with W75, Zilitinkevich (1975) and Arya (1977).

b. Sloped surface

The "drainage" acceleration over a flat but slightly inclined surface depends on the deviation $\bar{T}'$ from the adiabatic temperature profile and hence is time-dependent. In general, this acceleration can cause L, u_*, the surface temperature flux Q_0, the angle α between the geostrophic wind and the low level flow and h to change with time. However, this acceleration is impressed throughout the SBL directly as a body force, rather than diffused from the lower boundary (e.g., as is the acceleration due to changing surface friction). The model results indicate that the SBL over sloped terrain can reach a quasi-steady state in which $d=h(|f|/u_*L)^{\frac{1}{2}}$ is approximately constant; however, d depends on the wind direction relative to the slope and the magnitude of the baroclinity.

Fig. 7 illustrates the evolution of several significant properties of the SBL over terrain with a slope of 0.002 and a cooling rate of 2 K h^{-1}. For comparison, the results are also shown for the same cooling rate over a horizontal surface. The sloped case is shown for four geostrophic wind directions relative to the fall line vector. As an example, for the Great Plains, where the surface slopes downward going from west to east, 0° represents a geostrophic wind from the west, 90° is a wind from the south, 180° is east and 270° is north. Not surprisingly, the horizontal (barotropic) case is almost always intermediate between the baroclinic extremes.

Note from Fig. 7 that L, u_* and Q_0 are strongly affected by the orientation of the terrain slope. The 0° and the 270° cases are the least stable (largest L) because they represent downslope upper-level and low-level flow, respectively, and therefore have stronger winds near the surface. The 90° case is the most stable (smallest L) because its low-level flow is opposed by the downslope acceleration. This tends to minimize wind shear and turbulence production.

The SBL depths shown in Fig. 7 vary less with time than any of the other quantities we have just examined, and the dimensionless depths are even more nearly constant. At least up to 9 h, there is a perfect correspondence between h and the angle α, where α is a crude measure of velocity shear and hence turbulence production. However, by 9 h the much greater low-level wind, and hence u_*, of the 270° case makes up for its smaller directional shear and the 270° height curve overtakes the 180° curve. Delage (1974) also noted a strong correlation between wind shear across the SBL and boundary layer growth.

Kuhn *et al.* (1977) integrated observed vertical profiles of geostrophic departure to obtain stress and hence eddy diffusivity profiles for five stability and wind direction classes over sloped terrain in Antarctica. Using the observed mean winds and temperatures at 0.5 and 1.0 m we estimated the gradient Richardson number Ri and inverted $\mathrm{Ri}=[0.74z/L+4.7(z/L)^2]/(1+4.7z/L)^2$ (Businger *et al.*, 1971) to obtain z/L and hence L, using $z=0.75$ m. We compare our horizontal-surface parameterization of K_m in Eq. (13) with these sloped surface observations in Fig. 8. (One class is not shown because the observed Ri at 0.75 m exceeded 1/4.7.) To see if the consistent overprediction of (13) is due to terrain slope, Fig. 9 compares (13) and the model predictions for the four sloped cases of Fig. 7. The wind directions of Kuhn *et al.* (1977) vary by only 40° and, considering the different hemispheres, the 270° case in Fig. 9 should be most similar to the observations (Fig. 8), which is the case. (We are ignoring differences in slope and latitude and only making a qualitative comparison since our estimates of L for the Kuhn *et al.*, observations are relatively crude.)

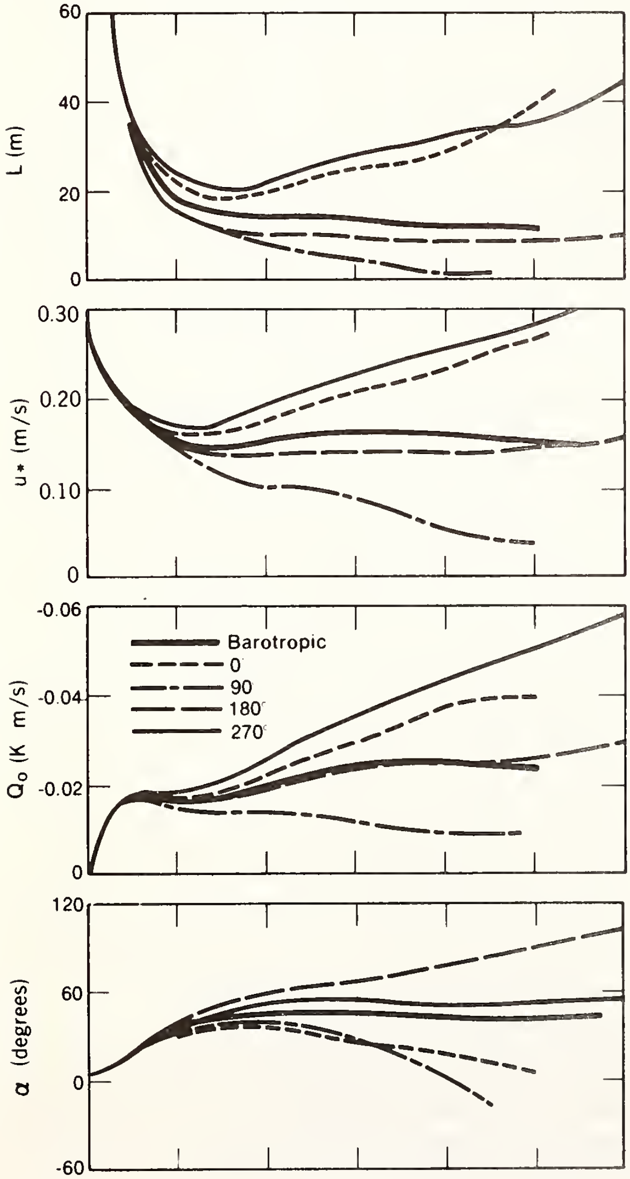

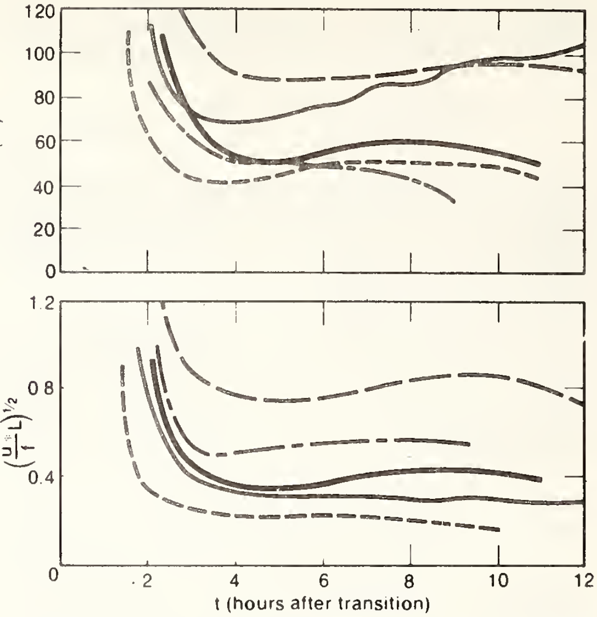

FIG. 7. Time evolution of key SBL parameters for a 2 K h⁻¹ cooling rate over a horizontal surface, and for four values of the angle (γ) between the fall line vector and geostrophic wind for a surface with slope 0.002.

The baroclinic terms in the mean horizontal momentum equations (1) and (2) depend on the product of the temperature deficit $\bar{T}'$ and the terrain slope β. Other things being equal, $\bar{T}'$ is proportional to the near-surface cooling rate. A baroclinic parameter B might be defined as

$$B=\left.\frac{\partial\Theta}{\partial t}\right)_{1\,\mathrm{m}}\cdot\beta\,[\mathrm{K\,h^{-1}}]. \qquad (25)$$

Fig. 10 depicts the time evolution of several key boundary-layer parameters for three different runs that have the same slope orientation, $\gamma=180°$, and the same baroclinic parameter, $B=0.004$ K h⁻¹. The runs have slopes of 0.004, 0.002 and 0.001, and cooling rates of 1, 2 and 4 K h⁻¹, respectively. We notice that runs with the same B value can have significant differences in some properties, so B is not an adequate indicator of slope effects.

We can look more closely at terrain-slope effects by considering the ratio (S) of the magnitudes of the mean drainage and friction forces

$$S \approx \frac{(g/T_0)\bar{T}'\beta}{u_*^2/h}, \tag{26}$$

and we ignore the effect of the orientation of the slope. This ratio depends on z, so it is not directly useful as a bulk index, but it can give us some insight. Note first that if $\beta=0.001$, $\bar{T}'=3$ K, $h=100$ m and $u_*=0.1$ m s^{-1}, then $S=1$; thus with a seemingly mild slope of 0.001 and typical SBL conditions, the drainage forces are of the same order as the turbulent friction. This explains why the results in Fig. 10 are so slope-dependent. Although the runs in Fig. 10 have the same value of B, which is proportional to $\bar{T}'\beta$, their representative values of S differ enough to make their flow properties evolve differently.

Fig. 10 shows that some properties (e.g., L, u_*, h) fairly quickly establish quasi-steady values, while α, for example, continuously increases. This flow cannot attain a true steady state, even though some of its properties seem to, because the parameter S continuously increases with time. However, in all runs d converges to about the same value (0.8). Evidently d is more sensitive to γ than to S.

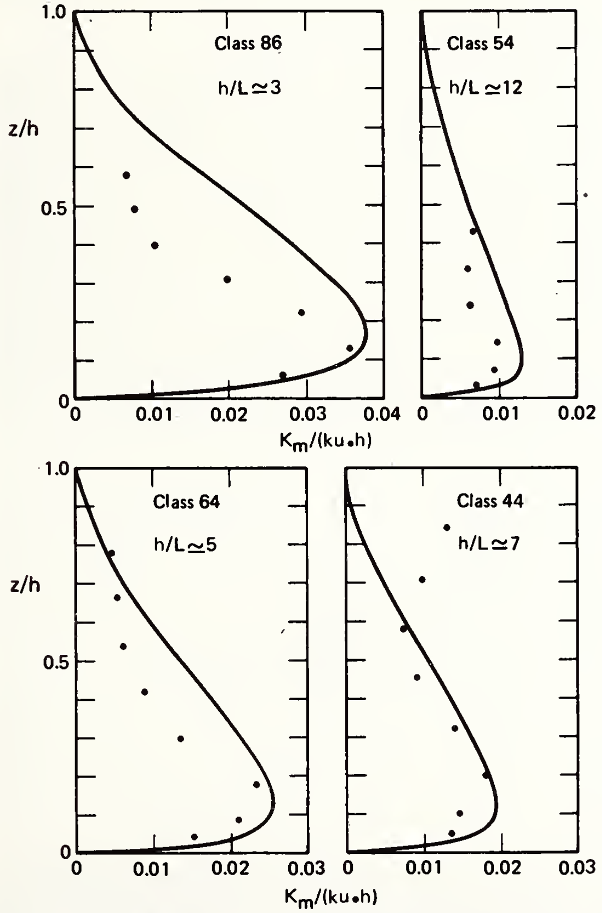

FIG. 8. Comparison of observed dimensionless K_m (dots) over sloped terrain (Kuhn *et al.*, 1977) with parameterization (13) (curves), for four stability classes.

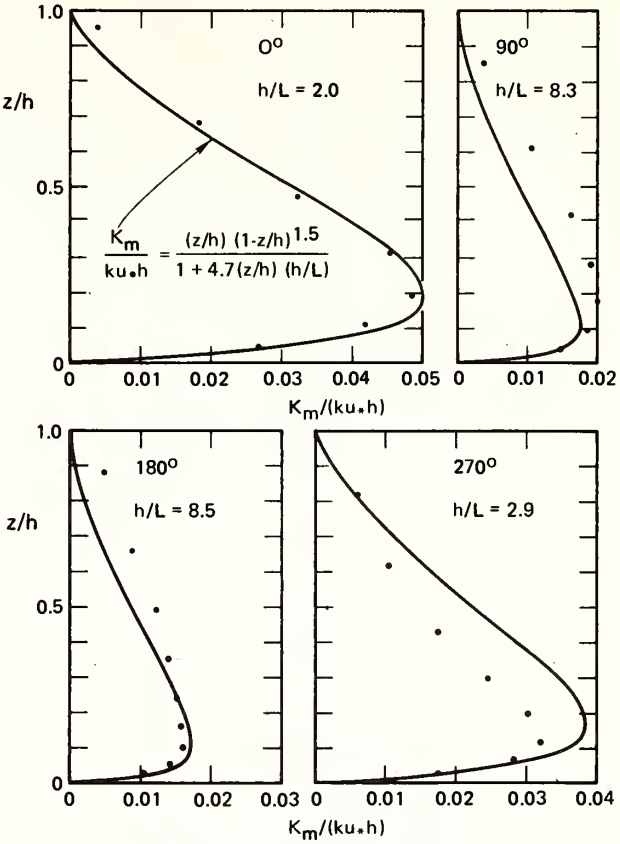

FIG. 9. Calculated dimensionless K_m profiles (dots) for the four cases of Fig. 7. Curves are from (13).

We have shown (Fig. 7) that the greatest d value occurs for $\gamma=180°$ and the smallest for 0°. For a baroclinic parameter $B=0.004$ K h^{-1}, the ratio d_{180}/d_0 is predicted to be 4 and for $B=0.001$ K h^{-1} it is predicted to be 1.5. This comparison indicates a significant dependence of d on B.

Predictions for the geostrophic drag coefficient u_*/G as a function of the stratification parameter μ are shown in Fig. 11. The curve in Fig. 11 is the prediction obtained by squaring and adding (21) and (22), using our parameterizations (23) and (24) for A and B, for a surface Rossby number $G/(|f|z_0)=10^7$. The current model predictions for the horizontal surface case lie on this curve, while the W75 results are slightly below it. (The models would have disagreed strongly had h/L been used as the stability parameter.) Had the sloped-terrain results been plotted in the normal way, they would not have followed the curve well. Instead, for these cases a drag coefficient based on a G calculated from the depth-averaged "effective" pressure gradient was used, and these results follow the barotropic prediction quite well. This use of the layer-averaged

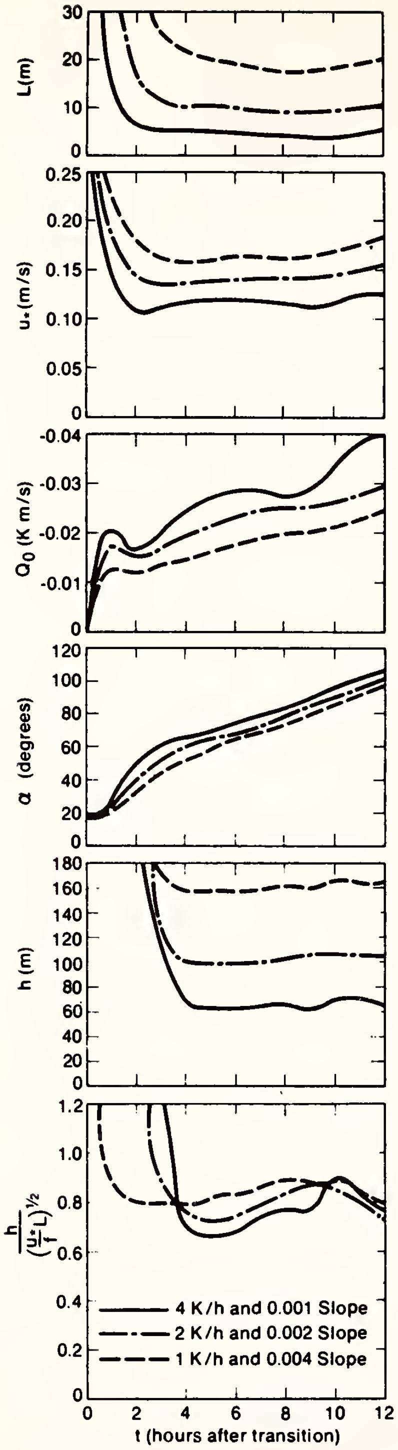

FIG. 10. Time evolution of key SBL parameters for three model runs with $\gamma=180°$ and $B=0.004$ K h^{-1}.

geostrophic wind in the baroclinic case has also been suggested for the convective boundary layer (Arya and Wyngaard, 1975).

4. Surface energy budget

We now use a surface energy budget (Blackadar, 1976), rather than an imposed constant cooling rate at 1 m. In the previous sections this cooling rate was the key variable determining the stratification. The situation now is much more complex as the cooling rate is replaced by several parameters:

1) The temperature difference ΔT between the initial adiabatic atmosphere and subsoil slab. We have tested temperature differences that ranged from -0.5 to $+20$ K.

2) The heat capacity C_g (per unit area) of the subsoil slab, which enters as the parameter $C_g/(\rho_0 C_p)$ with ρ_0 and C_p the density and specific heat of the air. We have used values of $C_g/(\rho_0 C_p)$ corresponding to a poor conductor (snow, 10 m) and an excellent conductor (rock, 221 m). These values of $C_g/(\rho_0 C_p)$ were chosen following Blackadar (1976). From (5), they correspond approximately to $\lambda=0.2\times10^{-3}$ cal (cm s K)$^{-1}$ and $C_s=0.09$ cal (cm^3 K)$^{-1}$ for snow and $\lambda=10^{-2}$ cal (cm s K)$^{-1}$ and $C_s=0.6$ cal (cm^3 K)$^{-1}$ for rock (Geiger, 1966).

3) The imposed downward long wave radiative flux at the surface. We used values of $F\downarrow(0)/(\rho_0 C_p)$ from 16 to 24 K m s^{-1}.

When the surface energy budget is used, the cooling rate of the surface becomes a strong function of time. Initially it is large, making the boundary layer very stable and shallow; however, after 1 or 2 h, L begins to increase again as the cooling rate declines. These variable conditions are not transmitted directly to the fluid as is the body force causing downslope acceleration in the sloping-terrain case. Instead, information about the changing surface conditions (e.g., u_* and L) must diffuse into the SBL from below. We can crudely estimate this diffusion time as of the order of h^2/K_m. From Figs. 4 and 5, we take a typical K_m value representative

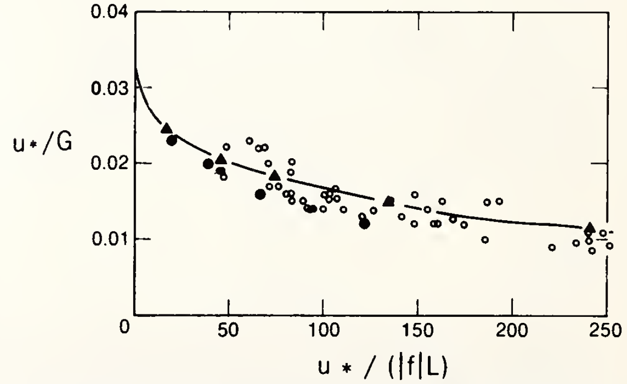

FIG. 11. Stability variation of geostrophic drag coefficient, from model simulations with a constant surface cooling rate. Curve, from Eqs. (21)–(24); (▲) current model results for horizontal terrain; (●) W75 model results; (○) current model results, sloping terrain, G based on layer-averaged effective pressure gradient.

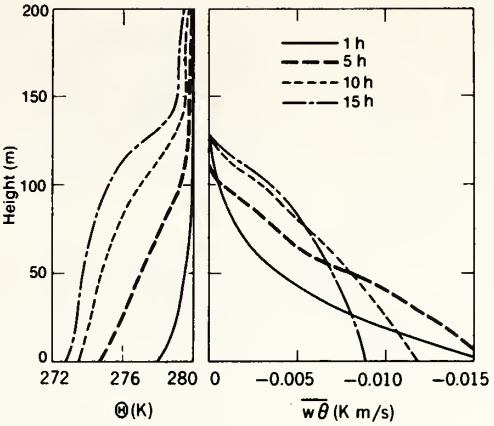

FIG. 12. Calculated time evolution of Θ and $\overline{w\theta}$ profiles for surface energy budget (4) case using $G=10$ m s^{-1}, $\Delta T=5$ K, $C_g/(\rho_0C_p)=221$ m and $F\!\downarrow\!(0)/(\rho_0C_p)=20$ K m s^{-1}.

of the layer as a whole as $K_m \approx 0.03ku_*h$. If $u_*=0.1$ m s^{-1} and $h=100$ m, we find $h^2/K_m \sim 10^5$ s or ∼30 h. By contrast, a convective boundary layer would be expected to respond to changing surface conditions with a time scale $h^2/K_m \approx h/w_*$, where $w_*=[(g/T_0)Q_0h]^{1/3}$ is the convective velocity scale. Under typical conditions we might have $h\approx 10^3$ m, $w_*\approx 2$ m s^{-1}, so $h/w_* \approx 10$ min. Thus, while the convective boundary layer is often quasi-steady, this suggests the SBL probably only rarely is. As evidence of this, note the different behavior of the dimensionless SBL depth in Fig. 3 when a surface energy budget is used.

As an aside, we note that the slowness of the response of the current model to changing surface conditions is not due to the lack of turbulent transport terms in the turbulence equations because we could find no consistent differences in response time between the current model and W75, which has these terms.

Fig. 12 illustrates the evolution of the potential temperature and potential temperature flux profiles for a case with $G=10$ m s^{-1} and $\Delta T=5$ K. This should be contrasted with Fig. 2 which shows the evolution of the same variables under constant cooling rate conditions. With a constant near-surface cooling rate, the cooling rate (turbulent heat flux divergence) initially decreases strongly with height, but by 10 h the cooling is approximately constant with height. With a surface budget, the height of the maximum cooling rate increases with time, creating a tendency to develop a uniform layer with a large potential temperature jump at the top. The Θ and $\overline{w\theta}$ profiles are curved instead of quasi-linear and the curvature changes with time. The relatively large temporal changes in the magnitudes and curvatures of the Θ and $\overline{w\theta}$ profiles indicate that this case does not attain steady state.

Fig. 13 illustrates the evolution of the surface temperature drop for an initially adiabatic atmosphere at 280 K and a surface initially at 279 K. For a fixed, imposed downward longwave radiative flux at the surface (20 K m s^{-1}) and the same surface characteristics [$C_g/(\rho_0C_p)=221$ m], there are four curves (I, G, D, C) corresponding to different temperature drops (2.5, 5, 10 and 20 K) between the initial adiabatic atmosphere and the subsoil slab. The extent to which the surface temperature drops below the subsoil temperature depends on the surface radiative deficit and hence on the absolute temperature; thus, in the 2.5 K case (curve I) the surface temperature drops almost 3 K below the subsoil temperature whereas in the 20 K case (C) it drops only 0.5 K below. For the 5 K case (G) the effects of varying the imposed downward flux and using different surface characteristics are shown. If a larger downward radiative flux is used (H) the surface temperature obviously will not decrease as much below the subsoil temperature. If the soil has a $C_g/(\rho_0C_p)$ value characteristic of snow (B), the surface temperature drops well below (15 K) the subsoil temperature. This curve has a bump due to complex feedback between the atmosphere and the surface.

Several simple analytical theories have been developed to predict the surface or shelter temperature fall at night (Haltiner and Martin, 1957, p. 131). For

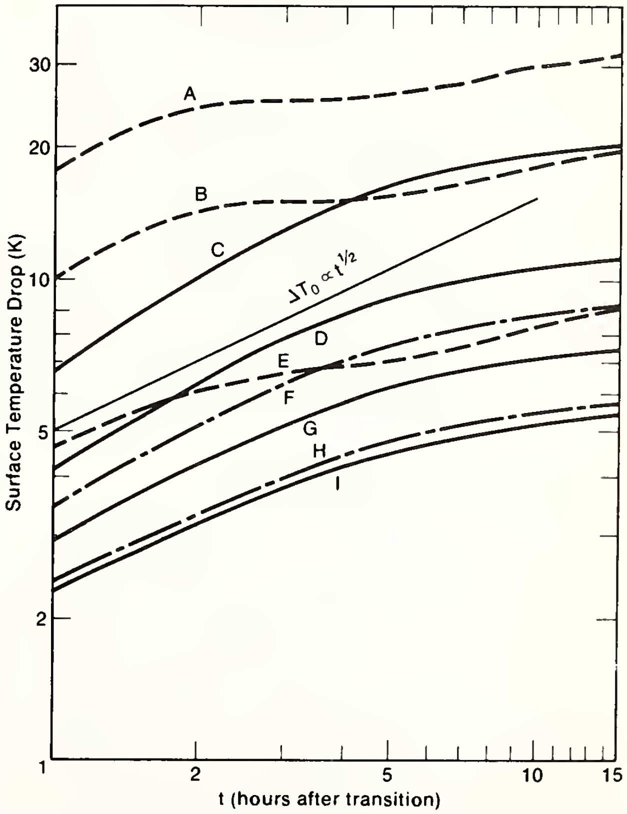

FIG. 13. Calculated surface temperature drop as a function of time for simulations using surface energy budget (4). Run A, $\Delta T=5$ K, $C_g/(\rho_0C_p)=10$ m, $F\!\downarrow\!(0)/(\rho_0C_p)=16$ K m s^{-1}; run B, 5 K, 10 m, 20 K m s^{-1}; run C, 20 K, 221 m, 20 K m s^{-1}; run D, 10 K, 221 m, 20 K m s^{-1}; run E, 5 K, 10 m, 24 K m s^{-1}; run F, 5 K, 221 m, 16 K m s^{-1}; run G, 5 K, 221 m, 20 K m s^{-1}; run H, 5 K, 221 m, 24 K m s^{-1}; run I, 2.5 K, 221 m, 20 K m s^{-1}.

example, Brunt (1939) assumed that the net radiative deficit at the surface was constant and that this deficit was balanced by the soil heat flux alone. He found that the surface temperature drop varied as the square root of time. The theory was subsequently generalized to include the atmospheric heat flux, but the functional dependence on temperature was unchanged if a constant eddy diffusivity was used for heat transfer. [A comparison with Groen (1947), whose theory is more realistic than that of Brunt (1939), though less so than the present study, was not made because it could not be definitive. This is because the cooling in Groen (1947) depends on the assumed value of the derivative with respect to temperature of the net radiative flux at the surface, while here it depends on ΔT and $F\downarrow(0)$.]

Fig. 13 shows that for $C_g/(\rho_0 C_p)=221$ m and for a ΔT of 5 or 10 K (G or D), the surface temperature drop in our model does indeed follow $t^{\frac{1}{2}}$ for the first 3 or 4 h. For the same surface and a larger temperature drop of 20 K (C), the initial tendency is slightly greater. For a smaller temperature drop of 2.5 K (I), the initial tendency is less. For all cases, the present model's predicted rate of temperature drop eventually falls below $t^{\frac{1}{2}}$ as the net radiative deficit at the surface decreases.

The similarity between Brunt's prediction and ours should be greatest for a surface where the ratio of the soil heat flux to the atmospheric heat flux is maximized, e.g., soil with large thermal diffusivity and heat capacity, as in the surface just discussed. If the surface used had a low $C_g/(\rho_0 C_p)$ value, such as that for snow, then the fact that the eddy diffusivity in the air was not constant, as assumed in an extension of Brunt, but was a function of time, as in our model, would be important. Thus, our model's more realistic representation of atmospheric physics should be more important for curves A, B and E. These curves depart from $t^{\frac{1}{2}}$ behavior sooner and more drastically and have a more complicated temporal behavior.

5. Conclusions

This study supports the findings of W75 that a constant cooling rate imposed near a horizontal lower boundary can drive the boundary layer to steady state within a few hours. Although the steady-state layer depth h, together with the changes in speed and potential temperature across the layer, do not give the same bulk Richardson number for all cases, h is uniquely related to other SBL parameters. Calculated eddy diffusivity profiles and drag coefficients agree well with recent observations in the arctic and antarctic.

The scaled SBL depth $d=h(|f|/u_*L)^{\frac{1}{2}}$ over a sloped surface with a constant cooling rate has different steady-state values depending on the wind direction relative to the slope. The slope effect is strong; for example, d varies by a factor of 4 for a slope of 0.002 and a cooling rate of 2 K h^{-1}.

When the lower boundary condition on temperature is provided by a surface energy budget rather than a constant cooling rate, the SBL typically does not reach steady state. The surface temperature drop behaves as $t^{\frac{1}{2}}$ for the first few hours, but eventually decreases more slowly. This failure to reach steady state is due to the slowness of the SBL to adjust to the changing surface conditions.

In addition, we conclude that the real SBL is subject to other influences that greatly complicate its structure and dynamics. First, our finding that h is very sensitive to model parameterizations suggests it can also be affected strongly by turbulence created by unstable gravity waves. Wave-turbulence interactions and their influence on SBL structure remain an important but relatively unexplored problem.

Second, we showed that even slight terrain slopes have strong effects on the SBL. However, real terrain is much more complicated than our constant-slope model, having a spectrum of slopes; the extent to which this affects SBL structure is also unknown.

Finally, we may have missed important features of the SBL because we could not model a full diurnal cycle. We started with balanced, steady-state, slightly stable initial conditions at transition. A more realistic initial condition for the wind would be an imbalance or inertial oscillation dependent on the history of the flow; this inertial oscillation could be important in the growth of the SBL. Also, we compared the SBL development over different soils and with different initial temperature differences between the adiabatic atmosphere and the subsoil slab. It would be valuable to compare full daily cycles over different soils such that the initial temperature difference would depend on the differing storage in the soil and the differing heating of the atmosphere.

Acknowledgments. We are grateful to J. W. Deardorff, J. Businger, W. Hooke, D. Lilly, W. Neff, K. S. Rao, B. Stankov and O. Zeman for helpful discussions, and to Ms. J. Trebing for patiently and skillfully typing many revisions of the manuscript.

APPENDIX A

Table of Symbols

B	baroclinic parameter $[=-(\partial\Theta/\partial t)\beta]$
C_g	heat capacity per unit area of soil slab [Eq. (5)]
C_p	specific heat of air at constant pressure
d	scaled SBL depth [Eq. (12)]
f	Coriolis parameter, taken as 10^{-4} s^{-1} in model
$F\downarrow(0)$	magnitude of the downward longwave radiative flux at the surface
g	gravitational acceleration
G	geostrophic wind speed
h	height of SBL, i.e., height at which stress declines to 5% of surface maximum
k	von Kármán constant, taken as 0.35 in model

K_m, K_h	eddy diffusivity for momentum, temperature
l	integral length scale
l_B	asymptotic value of l $[=C\sigma_w/\omega_B]$
L	Monin-Obukhov length $[=-u_*^3T_0/(kgQ_0)]$
$\bar{P}'$	deviation of mean pressure from background state P_0
q	turbulent velocity scale $[=(\overline{u_iu_i})^{\frac{1}{2}}]$
Q_0	surface potential temperature flux
Ri	gradient Richardson number $\left\{=\frac{g}{T_0}\frac{\partial\Theta}{\partial z}\Big/\left[\left(\frac{\partial U}{\partial z}\right)^2+\left(\frac{\partial V}{\partial z}\right)^2\right]\right\}$
T_g	surface temperature
T_0	adiabatic background temperature of atmosphere
T_*	scaling temperature $[=-Q_0/u_*]$
T_s	temperature of subsoil slab
$\bar{T}'$	deviation from adiabatic background temperature
ΔT	temperature difference between initial atmosphere and subsoil slab $[=T_0-T_s]$
ΔT_0	surface temperature drop $[=T_0-T_g]$
U_i	mean velocity (U,V,W)
u_i	fluctuating velocity (u,v,w)
u_*	surface friction velocity
z_0	surface roughness length, taken as 0.01 m in model
α	angle between geostrophic and surface winds
β	surface slope
γ	angle of geostrophic wind relative to fall line vector
Θ	mean potential temperature
θ	fluctuating potential temperature
$\Delta\Theta$	mean potential temperature increase across SBL
Θ_v	mean virtual potential temperature
μ	stability index $[=u_*/(\lvert f\rvert L)]$
ρ_0	density of air in background adiabatic state
σ	Stefan-Boltzmann constant
σ_w	root-mean-square vertical velocity
ϕ_h	nondimensional potential temperature gradient $[=(kz/T_*)(\partial\Theta/\partial z)]$
ϕ_m	nondimensional velocity gradient $[=(kz/u_*)\times(\partial U/\partial z)]$
ω_B	Brunt-Väisälä frequency $\left[=\left(\frac{g}{T_0}\frac{\partial\Theta}{\partial z}\right)^{\frac{1}{2}}\right]$

APPENDIX B

The Diagnostic Turbulence Equations

Our turbulence equations are derived from those of W75 by neglecting the time change, Coriolis and turbulent transport terms, and by using only some of the full set of equations. The reader is referred to that paper for a full discussion of the parameterizations. The closure constants and lower boundary conditions were unchanged except in a few instances where slight modifications were required because of the model simplifications. Our equations follow:

Vertical velocity variance

$$0.30\left(\overline{uw}\frac{\partial U}{\partial z}+\overline{vw}\frac{\partial V}{\partial z}\right)$$
$$=0.67(g/T_0)\overline{w\theta}-0.093q^3/l-0.51q(\overline{w^2}-q^2/3)/l.$$

Turbulent kinetic energy

$$\overline{uw}(\partial U/\partial z)+\overline{vw}(\partial V/\partial z)=(g/T_0)\overline{w\theta}-0.139q^3/l.$$

Shear stress

$$\left.\begin{aligned}0.14\overline{w^2}(\partial U/\partial z)&=-0.255(\overline{uwq/l})+0.28(g/T_0)\overline{u\theta}\\ 0.14\overline{w^2}(\partial V/\partial z)&=-0.255(\overline{vwq/l})+0.28(g/T_0)\overline{v\theta}\end{aligned}\right\}$$

Heat flux

$$\overline{w^2}(\partial\Theta/\partial z)=-1.35\overline{w\theta}q/l+(1-C_1)(g/T_0)\overline{\theta^2}$$

where $C_1=\begin{cases}0.5+1.5\,\mathrm{Ri}^2-\mathrm{Ri}^3, & 0<\mathrm{Ri}<1\\ 1, & \mathrm{Ri}>1\end{cases}$

$$\overline{uw}(\partial\Theta/\partial z)+0.5\overline{w\theta}(\partial U/\partial z)=-1.35\overline{u\theta}q/l,$$
$$\overline{vw}(\partial\Theta/\partial z)+0.5\overline{w\theta}(\partial V/\partial z)=-1.35\overline{v\theta}q/l.$$

Temperature variance

$$2\overline{w\theta}(\partial\Theta/\partial z)=-0.386\overline{\theta^2}q/l.$$

APPENDIX C

Numerical Methods

The Adams-Bashforth finite-difference scheme was used to march in time. The vertical grid was equally spaced in the transformed variable η, where

$$\eta=\frac{z}{A_1}+\ln\frac{z+A_2}{A_2}.$$

Here A_2 controls the rate at which the logarithmic grid expands near the surface, while A_1 determines the height at which the grid became linear. Values of $A_2=5$ m and $A_1=250$ m were used. The variables were staggered in the vertical with the mean and turbulence quantities calculated on different but interlacing grids.

The computer model was a factor of 10 faster than that of W75 because we used simpler equations, time step control (Zeman and Lumley, 1976), and a grid with variable resolution and vertical extent.

Because spatial rather than temporal resolution limited the accuracy of our solutions, the full set of turbulence equations was not solved every time step. We used the following procedure:

1) We solved the turbulence equations (Appendix B) to form a quadratic equation for q^2. The largest root

always proved to be the desired solution. If Ri exceeded a critical value both roots were negative and q^2 was set at a small positive value.

2) All of the vertical fluxes were then calculated in terms of the known q^2.

3) Effective eddy diffusivities for momentum and heat were formed from these fluxes and the existing mean gradients.

4) These effective eddy diffusivities were used to calculate fluxes while ten time steps were taken with the mean equations.

5) The procedure was repeated.

We tested the accuracy of this procedure by comparing two 10 h model simulations. In one, the procedure was used and, in the other, the full turbulence set was solved each time step. After 10 h, the temperatures differed at most by 1 part in 10^5 and all other significant quantities by no more than 1 part in 10^3.

Our program discarded the top grid point if the stress there fell below a small threshold value for one hour. Typically, after 5 h five grid points had been discarded and the computational domain had shrunk from 500 to 250 m. Then the grid was doubled to 30 points and the mean variables were interpolated onto the new grid. The time evolution of predicted variables did not show any noticeable effects of this grid change. Before the grid change the vertical resolution was 2 m near the surface and increased smoothly to 50 m aloft; after the change it varied from 1 to 25 m.

A dissipation length scale which behaved as $l_B = C\sigma_w/\omega_B$ at large z and the lack of explicit diffusion terms in the turbulence equations allowed the turbulent kinetic energy at adjacent grid points to tend to drift apart. To avoid this we introduced a small amount of diffusion by running a Hanning filter over $l(z)$.

The initial conditions were provided by holding Θ fixed with $\partial\Theta/\partial z = 4\times10^{-5}$ K m^{-1} and integrating to a steady state.

REFERENCES

Arya, S. P. S., 1977: Suggested revisions to certain boundary layer parameterization schemes used in atmospheric circulation models. *Mon. Wea. Rev.*, **105**, 215–227.

——, and J. C. Wyngaard, 1975: Effect of baroclinicity on wind profiles and the geostrophic drag law for the convective planetary boundary layer. *J. Atmos. Sci.*, **32**, 767–778.

Ball, F. K., 1960: Winds on the ice slopes of Antarctica. *Proc. Symp. Antarctic Meteorology*, Melbourne, Pergamon Press, 9–16.

Bhumralkar, C. M., 1975: Numerical experiments on the computation of ground surface temperature in an atmospheric general circulation model. *J. Appl. Meteor.*, **14**, 1246–1258.

Blackadar, A. K., 1976: Modeling the nocturnal boundary layer. *Preprints Third Symp. Atmospheric Turbulence, Diffusion and Air Quality*, Raleigh, Amer. Meteor. Soc., 46–49.

Brunt, D., 1939: *Physical and Dynamical Meteorology*, 2nd ed. Cambridge University Press, 428 pp.

Businger, J. A., and S. P. S. Arya, 1974: Height of the mixed layer in a stably stratified planetary boundary layer. *Advances in Geophysics*, Vol. 18A, Academic Press, 73–92.

——, J. C. Wyngaard, Y. Izmui and E. F. Bradley, 1971: Flux-profile relationships in the atmospheric surface layer. *J. Atmos. Sci.*, **28**, 181–189.

Carsey, F., and E. Leavitt, 1977: Preliminary study of pibal and acoustic radar data over pack ice. Submitted to *J. Appl. Meteor.*

Dalrymple, P. C., H. Lettau and S. Wollaston, 1966: South Pole micrometeorology program: Data analysis. *Studies in Antarctic Meteorology*, Vol. 9, *Antarctic Res. Ser.*, Amer. Geophys. Union, 13–57.

Deardorff, J. W., 1972: Rate of growth of the nocturnal boundary layer. *Proc. Symp. Air Pollution, Turbulence and Diffusion*, H. W. Church and R. E. Luna, Eds., 183–190.

——, 1978: Efficient prediction of ground surface temperature and moisture, with inclusion of a layer of vegetation. *J. Geophys. Res.*, **83**, 1889–1903.

Delage, Yves, 1974: A numerical study of the nocturnal atmospheric boundary layer. *Quart. J. Roy. Meteor. Soc.*, **100**, 351–364.

Geiger, R., 1966: *The Climate Near the Ground*. Harvard University Press, 611 pp.

Groen, P., 1947: Note on the theory of nocturnal radiational cooling of the earth's surface. *J. Meteor.*, **4**, 63–66.

Haltiner, G. J., and F. L. Martin, 1957: *Dynamical and Physical Meteorology*. McGraw-Hill, 470 pp.

Kuhn, M., H. H. Lettau and A. J. Riordan, 1977: Stability related wind spiraling in the lowest 32 m. Meteorological Studies at Plateau Station, Antarctica. Pap. 7, *Antarctic Research Series*, Vol. 25, Amer. Geophys. Union, 93–111.

Lettau, H. H., 1967: Small to large-scale features of boundary layer structure over mountain slopes. *Proc. Symp. Mountain Meteorology*, Atmos. Sci. Pap. 122, Colorado State University.

Lewellen, W. S., and M. Teske, 1973: Prediction of the Monin-Obukhov similarity functions from an invariant model of turbulence. *J. Atmos. Sci.*, **30**, 1340–1345.

Lumley, J. L., and H. A. Panofsky, 1964: *The Structure of Atmospheric Turbulence*. Wiley, 239 pp.

Mahrt, L. J., and W. Schwerdtfeger, 1970: Ekman spirals for exponential thermal wind. *Bound.-Layer Meteor.*, **1**, 137–145.

Melgarejo, J. W., and J. W. Deardorff, 1974: Stability functions for the boundary layer resistance laws based on observed boundary-layer heights. *J. Atmos. Sci.*, **31**, 1324–1333.

Mellor, G. L., 1973: Analytic prediction of the properties of stratified planetary surface layers. *J. Atmos. Sci.*, **30**, 1061–1069.

Schwerdtfeger, W., 1972: The vertical variation of the wind through the friction layer over the Greenland ice cap. *Tellus*, **24**, 13–16.

Sommeria, G., 1976: Three-dimensional simulation of turbulent processes in an undisturbed trade wind boundary layer. *J. Atmos. Sci.*, **33**, 216–241.

Tennekes, H., and J. L. Lumley, 1972: *A First Course in Turbulence*. MIT Press, 300 pp.

Wyngaard, J. C., 1975: Modeling the planetary boundary layer—extension to the stable case. *Bound.-Layer Meteor.*, **9**, 441–460.

——, and O. R. Coté, 1971: The budgets of turbulent kinetic energy and temperature variance in the atmospheric surface layer. *J. Atmos. Sci.*, **28**, 190–201.

Zeman, O., and J. L. Lumley, 1976: Modeling buoyancy driven mixed layers. *J. Atmos. Sci.*, **33**, 1974–1988.

——, and H. Tennekes, 1977: Parameterization of the turbulent energy budget at the top of the daytime atmospheric boundary layer. *J. Atmos. Sci.*, **34**, 111–123.

Zilitinkevich, S. S., 1972: On the determination of the height of the Ekman boundary layer. *Bound.-Layer Meteor.*, **3**, 141–145.

——, 1975: Resistance laws and prediction equations for the depth of the planetary boundary layer. *J. Atmos. Sci.*, **32**, 741–752.

——, and J. W. Deardorff, 1974: Similarity theory for the planetary boundary layer of time-dependent height. *J. Atmos. Sci.*, **31**, 1449–1452.

Proceedings of 11th Technical Conference on Hurricanes and
Tropical Meteorology, 242-246, 1978.

ANALYSIS OF THE DISTURBED BOUNDARY LAYER DURING GATE USING ACOUSTIC SOUNDER DATA

John E. Gaynor

NOAA/ERL/Wave Propagation Laboratory
Boulder, Colorado 80302

1. INTRODUCTION

A vertically pointing monostatic atmospheric acoustic sounder was installed aboard the NOAA Ship OCEANOGRAPHER during the three phases of the GARP Atlantic Tropical Experiment (GATE) in the summer of 1974. The instrumentation and initial data set are described in some detail by Mandics and Owens (1975) and Mandics and Hall (1976).

Briefly, the backscattered echo from the clear atmosphere is caused by small-scale (∿ 0.1 m) turbulent temperature fluctuations and, to a lesser extent, turbulent humidity fluctuations. This turbulent structure is usually caused by relatively warm, moist and, therefore, buoyant thermal plumes originating at the slightly warmer ocean surface, but turbulence due to wind shear also marks stable layers at the top of the mixed layer.

Earlier work by Gaynor et al. (1976) has detailed the types of acoustic echoes appearing on acoustic facsimile recordings during GATE. The recordings clearly showed a dramatic change in the boundary layer during and following precipitation over or near the ship. The stable regime following the precipitation (often referred to as the convective wake during the GATE Workshop, August 1977) has been discussed in some detail by Gaynor and Mandics (1978) using a case study approach.

The earlier work is expanded here to include a possible dynamic mechanism for the break-up or dissipation of the stable layer, the possible effect of waves in the stable layers on in situ measurements, the effect of wind shear on acoustic scattering at the stable layer, and temporal statistics of these wakes during GATE using a categorization scheme appropriate to the acoustic sounder data. In discussing the final item, inferences are made as to the importance of the wake in modulating the development of further moist convection.

2. THE DISTURBED BOUNDARY LAYER — CASE STUDIES

The disturbed boundary layer includes a wake region and the gust front that occurs before the wake. Clear indications of both occurrences are often seen very clearly in the acoustic sounder data, especially when no major rainfall occurs over the ship.

Figure 1 is reproduced from Gaynor and Mandics (1978). It shows an acoustic facsimile recorded during the passage of a squall line in GATE. Thermal plumes, vertically oriented dark regions near the bottom of the record, are prevalent until 1250 GMT* when the rain begins. The dark appearance at the top of the record is due to electronic amplification of the received signal to compensate for acoustic beam broadening. The effect is to increase background noise. The rain noise continues until 1600, after which horizontally oriented structures indicative of stable layers appear. Using slow ascent radiosonde profiles, Gaynor and Mandics (1978) have shown that the layers are not only statically stable, but represent true inversions in temperature. Particularly after 1900, when the thermal plume echoes reappear at the bottom of the record, the stable layers are undulating with apparent wave action. Between 0000 and 0100, echoes indicating breaking waves or Kelvin-Helmholtz shear instability (Hooke et al., 1973, and Merrill, 1977) are clearly seen at about 500 m.

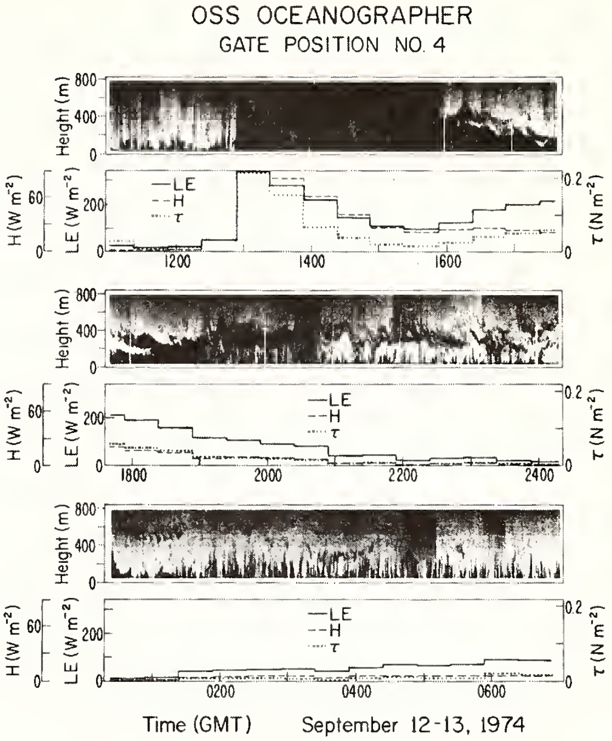

Figure 1. Acoustic facsimile record during a squall-line passage with one-half-hour averaged surface bulk aerodynamic fluxes of latent heat, LE, sensible heat, H, and momentum, τ. (Figure from Gaynor and Mandics, 1978.)

The 1/2-hr averaged surface bulk aerodynamic fluxes (Pond et al., 1974) of sensible heat, H, latent heat, LE, and momentum, τ, are shown beneath the acoustic facsimile records in Fig. 1. The large increase in fluxes at 1250 (by an order of magnitude in some cases) is largely caused by the increase in winds (measured at the 10-m bow boom level) associated with the arrival of the gust front. The cooler and slightly drier air advecting past with the gust front has only a minor effect in increasing H and LE in this case. However, the statistics presented in Section 3 will show this not to be the situation in the average. In Fig. 1, the gust front arrives with the rain, but in some cases it precedes the rain by a few minutes.

---

* All times referred to are GMT.

One of the uses of acoustic sounder records is to analyze the effect of the waves (likely gravity waves) seen so clearly on the stable layers in Fig. 1. These waves appear in all stable layers on the acoustic records during GATE with various frequencies and amplitudes. Calculations of vertical fluxes using tethered balloon data in the regions of these undulating stable layers will most surely be adversely affected. Unfortunately, the wake regions are of most interest for boundary layer flux calculations. Emmitt (1977) has reasoned that some of his "anomalous" fluxes (i.e., warm/moist downdrafts or cold/dry updrafts) may be caused by this "mechanical turbulence" associated with wave activity. The sounder data would certainly be useful when used in conjunction with data from tethered balloons to identify the dynamical cause of the "fluxes."

In the process of analyzing possible breaking wave activity near the stable layers during wake activity by calculating bulk Richardson numbers, the importance of wind shears through the stable layers was clarified. The preliminary results from tethered balloon data are presented in Table 1. The vertical gradients of wind, $\Delta\overline{u}/\Delta z$, and virtual temperature, $\Delta\overline{\theta}_v/\Delta z$, for the suppressed column are calculated at the top of the mixed layer as delineated by tethered balloon profiles when no stable layer echo appeared on the acoustic facsimile. Although the sample sizes are small and the standard deviations are quite large, tentative conclusions can be drawn. Both columns in Table 1 show slight stability, but the wake region shows stronger wind shear. The mechanical mixing due to this shear is important in maintaining density gradients from which acoustic waves scatter. This result has been assumed for a long time, but only in GATE did the shear mechanism so far outweigh the relatively weak stability mechanism, that the conclusion became clear.

The bulk Richardson number is defined as

$$Ri = \frac{g}{\overline{\theta}_v} \frac{\Delta\overline{\theta}_v}{\Delta z} / \left(\frac{\Delta\overline{u}}{\Delta z}\right)^2 ,$$

where $\overline{\theta}_v$ and $\overline{u}$ are as defined above, and g and z have their usual definitions. Ri calculated using the bulk definition is not as precise as Ri calculated using the flux definition for defining regions of possible shear instability where $Ri < 0.25$. However, three or four subcritical Ri's corresponding to regions of clear breaking wave activity appearing on the sounder records during Phase III of GATE were calculated from tethered balloon data.

An example of shear instability is presented in Fig. 2 showing profiles from a tethered balloon ascent overlaid on an acoustic facsimile record. The ascent occurred between 1959 and 2013, between which times the facsimile indicates a fairly constant level of breaking wave activity within a stable layer shown to be stable from the potential temperature profile measured on the balloon ascent. Bracketed regions A and B represent layers of strong shear in both wind direction and speed. In region A, $Ri = 0.10$, and in region B, $Ri = 0.02$, both easily subcritical. Between these two layers, the windspeed and direction show that the region is fairly uniform with height. The acoustic facsimile record in Fig. 2 indicates that between regions A and B, the breaking wave echoes appear. In fact, the mixed layer, indicated by the region of thermal plume echoes and a neutral to slightly unstable θ profile, seems to suddenly deepen after 1930.

Table 1. Average stabilities ($\overline{\Delta\overline{\theta}_v/\Delta z}$) and wind shears ($\overline{\Delta\overline{u}/\Delta z}$) from tethered balloon data through the stable region in the wakes and at the top of the mixed layer (suppressed) with their standard deviations. The numbers of points in the samples are indicated in parentheses.

	Wake	Standard Deviation	Suppressed	Standard Deviation
$\overline{\frac{\Delta\overline{\theta}_v}{\Delta z}}$	$3.0\text{x}10^{-3}$K m^{-1}(8)	$1.1\text{x}10^{-3}$K m^{-1}	$3.8\text{x}10^{-3}$K m^{-1}(21)	$2.7\text{x}10^{-3}$K m^{-1}
$\overline{\frac{\Delta\overline{u}}{\Delta z}}$	$1.5\text{x}10^{-2}s^{-1}$(8)	$1.2\text{x}10^{-2}s^{-1}$	$1.1\text{x}10^{-2}s^{-1}$(21)	$8.6\text{x}10^{-3}s^{-1}$

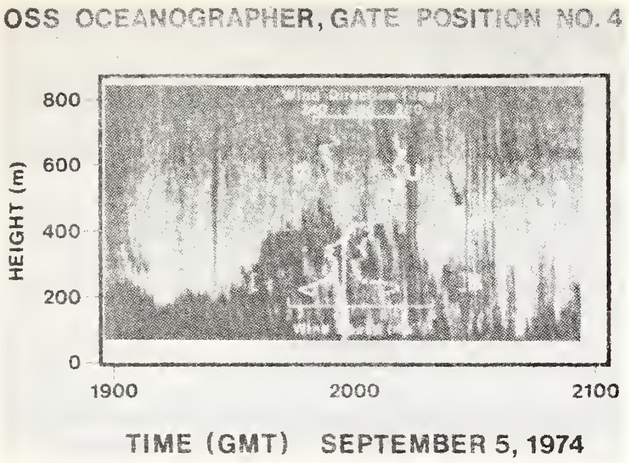

Figure 2. Acoustic facsimile record during a wake occurrence with overlaid profiles of horizontal windspeed U and wind direction ϕ. The bracketed regions A and B indicate levels at which bulk Richardson numbers were calculated.

Soon after 2030 the stable layer echo disappears. The disappearance of the stable layer occurred in other cases of breaking wave activity, also (e.g., after 1930 in Fig. 1).

Although the exact source is not known, Houze (1977) and Zipser (1977) have indicated that the stable layer at relatively low levels in the wake is maintained by mesoscale subsidence below the anvil. As the disturbance moves off, this subsidence must weaken, but neither Houze nor Zipser indicates exactly how this stable layer is broken or dissipated. A hypothesis can be made that, at least occasionally, the dissipating mechanism is non-linear mixing due to shear instabilities.

It is unfortunate that the in-situ data available during GATE are not adequate to study this mechanism in more detail.

3. TEMPORAL STATISTICS OF DISTURBED EVENTS

The temporal and spatial continuity of acoustic sounder data is unsurpassed by that of any other data in GATE. A simple scheme to categorize the GATE boundary layer is to define a disturbed boundary layer as a gust front and a following wake event.

The sounder records (for example, Fig. 1) clearly indicate the arrival of the gust front and the end of the wake (disappearance of the stable layer) associated with precipitating convection during GATE. A disturbed boundary layer is defined here as a signature of a gust front and a wake on the acoustic sounder facsimile records. If only air surface temperature (T_d) or equivalent potential (θ_e) temperature are used as an indicator of a disturbance, it may be misleading. T_d and/or θ_e may return to their ambient values but the stable layer may remain aloft, indicating a region of strong vertical convergence of [illegible] (Gaynor and Mandics, 1978).

Probably the most interesting result of using the above acoustic sounder criterion to study the temporal statistics of the disturbed boundary layer is that, during the three phases of GATE, the boundary layer was found to be disturbed 31% of the time at the locations of the OCEANOGRAPHER. Such a large percentage has obvious repercussions in tropical boundary layer modeling. If the wake is a region of suppressed moist convective activity, how does this large temporal percentage translate into area coverage? Radar can help answer that question, and, indeed, the work of M. Garstang and colleagues at the University of Virginia has shown that the same percentage area is indicated.

The average length of disturbances was 3 h with maximum lengths approaching 17 h on three occasions in Phase III. These events were associated with squall-line activity. We can use the approximate formula for the heating of a layer of depth h from below,

$$H \simeq C_p \rho \frac{\partial T}{\partial t} h = \rho C_p C_H u \Delta T \ , \qquad (1)$$

where C_p is the specific heat at constant pressure, ρ, the air density, and C_H, the bulk aerodynamic coefficient, and the other terms having their standard definitions. The terms to the right in (1) represent the bulk aerodynamic relation. Solving (1) for the approximate recovery time of the mixed layer we get

$$\Delta t = \frac{h}{C_H u} \simeq 17 \text{ h},$$

if h = 400 m, $C_H = 1.3 \times 10^{-3}$ (Pond et al., 1974), and $u = 5 \text{ m s}^{-1}$, indicating that the recovery times shown by the sounder records are reasonable. Of course, (1) ignores advection and mixing from above.

A scheme of categorizing supporting in situ data using acoustic facsimile records was improved upon by C. F. Ropelewski (unpublished manuscript) at the Center for Experiment Design and Data Analysis. The work is reported in the soon-to-be-released Report on the GATE Workshop (July 1977). His categories are as follows:

1) Undisturbed; no perturbations within 2 h of the in situ data.

2) Pre-onset; in situ data averaged between 1.25 h and 0.25 h before the start of the perturbation.

3) Early perturbed; in situ data averaged 1 h or less after the start of the perturbation.

4) Mature perturbed; in situ data averaged between 4 h after the start of the perturbation and its ending.

Table 2. Phase means and means for the three phases of GATE of latent heat flux, LE, sensible heat flux, H, and stress τ for the four boundary layer categories.

	Phase I	Phase II	Phase III	Total
LE(Wm^{-2})				
(1)	67(2787)	107(1016)	127(3157)	100(6960)
(2)	101(278)	84(281)	108(429)	99(988)
(3)	97(640)	99(830)	111(923)	103(2393)
(4)	72(522)	81(328)	93(1177)	86(2027)
H(Wm^{-2})				
(1)	6.7(2788)	9.5(1319)	6.1(3157)	6.9(7264)
(2)	9.6(279)	8.3(281)	8.2(429)	8.6(989)
(3)	16.4(640)	13.6(831)	15.2(923)	15.0(2394)
(4)	12.0(530)	9.1(483)	13.7(1177)	12.3(2190)
τ(Nm^{-2})				
(1)	0.023(3066)	0.048(1373)	0.056(3409)	0.042(7848)
(2)	0.045(303)	0.034(297)	0.045(469)	0.042(1069)
(3)	0.050(708)	0.046(907)	0.052(1034)	0.049(2649)
(4)	0.033(555)	0.026(520)	0.032(1281)	0.031(2356)

The perturbation refers to the gust front/wake identified on the acoustic records. The early perturbed and mature perturbed categories are an attempt to separate gust fronts and wakes that represent different boundary layer dynamic events (Zipser, 1977).

The results of the surface bulk aerodynamic fluxes categorized as above and calculated similarly to those presented in Fig. 1 are listed in Table 2. The results have been separated according to GATE phases and combined. The numbers of 3-min averaged fluxes used in the total averaging are presented in parentheses. Although there is some variation between the phases, the results are in agreement with those Ropelewski obtained from tethered balloon profiles. The mature perturbed (wake) category has the smallest LE and τ of the four categories in the average of all phases because of the light surface winds. Maxima of LE are distributed between categories while maximum H is consistently in the early perturbed stage between the phases. This result is in agreement with Zipser (1977) who showed that although downdraft air is much cooler than the ambient surface air, the mixing to the surface of the somewhat drier air sinking beneath the anvil is not noticeable. The gust front is clearly noticeable as a relatively large τ value only in Phase I. This is probably the result of strong undisturbed surface winds at the ship's stations in Phase II and III and the brief passage of the front which may cause its effects to be lost in the averaging.

4. CONCLUSION

The usefulness of the GATE acoustic sounder has been shown in analyzing boundary layer processes. Used in conjunction with tethered balloon data, the sounder helps identify the dynamic processes that affect the in-situ data. A possible mechanism for the occasionally rapid erosion of the low-level stable layer in a wake region is proposed which may help complete the modeling of the wakes. The results of the categorization of surface flux data by acoustic sounder records agree with existing ideas on wake processes, but show the complexity, in a temporal sense, of the vertical mixing through the stable layer.

5. ACKNOWLEDGMENT

The research reported here was supported by the United States GATE Project Office.

6. REFERENCES

Emmitt, G. D., 1978: Tropical cumulus interaction with and modification of the subcloud region. Accepted for publication by *J. Atmos. Sci.*

Gaynor, J. E., and P. A. Mandics, 1978: Analysis of the tropical marine boundary layer during GATE using acoustic sounder data. To appear in *Mon. Weath. Rev.*

Gaynor, J. E., P. A. Mandics, A. B. Wahr, and F. F. Hall, Jr., 1976: Studies of the tropical marine boundary layer using acoustic backscattering during GATE. Preprints, *17th Conference on Radar Meteorology*, Seattle, Washington, 303-306. (Available through Amer. Meteor. Soc., Boston, Massachusetts).

Hooke, W. H., F. F. Hall, Jr., and E. E. Gossard, 1973: Observed generation of an atmospheric gravity wave by shear instability in the mean flow of the planetary boundary layer. *Boundary-Layer Meteor.*, 5, 29-41.

Houze, R. A., Jr., 1977: Structure and dynamics of a tropical squall-line system observed during GATE. *Mon. Weath. Rev.*, 105, No. 12.

Mandics, P. A., and F. F. Hall, Jr., 1976: Preliminary results from the GATE acoustic echo sounder. *Bull. Amer. Meteor. Soc.*, 57, 1142-1147.

Mandics, P. A., and E. J. Owens, 1975: Observations of the marine atmosphere using a ship-mounted acoustic echo sounder. *J. Appl. Meteor.*, 14, 1110-1117.

Merrill, J. T., 1977: Observational and theoretical study of shear instability in the airflow near the ground. *J. Atmos. Sci.*, 34, 911-921.

Pond, S., D. B. Fissel, and C. A. Paulson, 1974: A note on bulk aerodynamic coefficients for sensible heat and moisture fluxes. *Boundary-Layer Meteor.*, 6, 333-339.

Zipser, E. J., 1977: Mesoscale and convective-scale downdrafts as distinct components of squall line structure. *Mon. Weath. Rev.*, 105, No. 12.

Preprint Volume; Fourth Symposium on Meteorological Observations
and Instrumentation, 410-414, American Meteorological Society, 1978.

ACOUSTIC SOUNDING IN A MOIST TROPICAL MARINE ATMOSPHERIC BOUNDARY LAYER DURING GATE

John E. Gaynor

NOAA/ERL/Wave Propagation Laboratory
Boulder, Colorado 80302

1. INTRODUCTION

A vertically-pointing monostatic atmospheric acoustic sounder was mounted aboard the NOAA Ship OCEANOGRAPHER during the GARP Atlantic Tropical Experiment (GATE) between July and September, 1974. The very moist tropical marine boundary layer with only minor diurnal variations provided a unique and interesting environment for atmospheric acoustic sounding. The instrumentation is described in some detail by Mandics and Owens (1975).

Normally, in a less moist boundary layer over land, acoustic backscatter is predominantly due to refractive index fluctuations caused by temperature variations (Tatarskii, 1971). In fact, in a dry continental boundary layer, humidity fluctuations account for only about 1% of the backscatter.

With humidities consistently between 90% and 100% in the lower boundary layer (the mixed layer) within the GATE region, it is instructive to ask what portion of the acoustic backscatter is caused by humidity fluctuations in this environment. The answer to this question will help interpret the dynamical features outlined on acoustic facsimiles recorded during GATE. Some of these acoustic data have been discussed previously (Mandics and Hall, 1976; Gaynor et al., 1976; Gaynor and Mandics, 1978).

To look into the relative importance of temperature and humidity fluctuations separately and their co-fluctuations requires in situ turbulence data. We make use of the data provided by the NOAA DC-6 aircraft flights during GATE. The theoretical background now exists for acoustic scattering in a moist environment and is outlined in the next section. All that remains is to apply turbulent measurements to the theory. This initial analysis is described in Section 3.

2. THEORETICAL BACKGROUND

The basic theory has been described by Wesely (1976). We follow his approach in combining the effects of temperature and humidity fluctuations on acoustic backscatter.

The effects of humidity are represented in the relation

$$C_n^2 = [C_T^2/4\overline{T}^2]\alpha_a^2, \qquad (1a)$$

$$\alpha_a^2 = 1 + r_{eT}\left(\frac{2DC_e\overline{T}}{C_T\overline{p}}\right) + \left(\frac{DC_e\overline{T}}{C_T\overline{p}}\right), \qquad (1b)$$

where C_n^2 is the acoustic refractive index structure function (to be defined below), C_T^2 is the temperature structure function, $\overline{T}^2$ is the average absolute temperature, $r_{eT} = C_{eT}^2/(C_eC_T)$ is the structural correlation coefficient, C_{eT} is the structure function of temperature and moisture, C_e^2 is the structure function of moisture, $D = 0.307$, $\overline{p}$ is the average ambient air pressure, and α_a^2 is the "correction" factor for moisture. Higher order terms in (1b) have been ignored. The refractive index structure function is expressed as (Tatarskii, 1971)

$$C_n^2 = \overline{(m_1 - m_2)}^2/r^{2/3},$$

where $m \equiv n - \overline{n}$, n is the refractive index and the overbars indicate time averages.

The aircraft data come in the form of spectral densities taken over sections of the flight legs, and these spectra must be converted to structure functions. In the inertial subrange the relation

$$\Phi_T(k_1) = 0.25\, C_T^2\, k_1^{-5/3} \qquad (2)$$

holds reasonably well (Friehe et al., 1975). Φ_T is the one dimensional power spectral density of temperature, and k_1 is the wave number component in the stream-wise direction. Similar relations hold for C_e^2 and C_{eT}^2.

The relations given above provide a very simple procedure (in practice) for calculating the contributions of humidity fluctuations and co-fluctuations of humidity and temperature to acoustic scattering. The next section presents a preliminary look at the data.

3. PRELIMINARY DATA ANALYSIS

One of the motivations behind looking into the problem of the contributions of C_e^2 and C_{eT}^2 to acoustic scattering was to help explain the "hummocky" echoes that occasionally appear on the acoustic facsimile records during GATE. An example of these echoes is given in Fig. 1. The vertically oriented dark regions at the bottom of the record are thermal plumes. Above them is a relatively clear area capped by

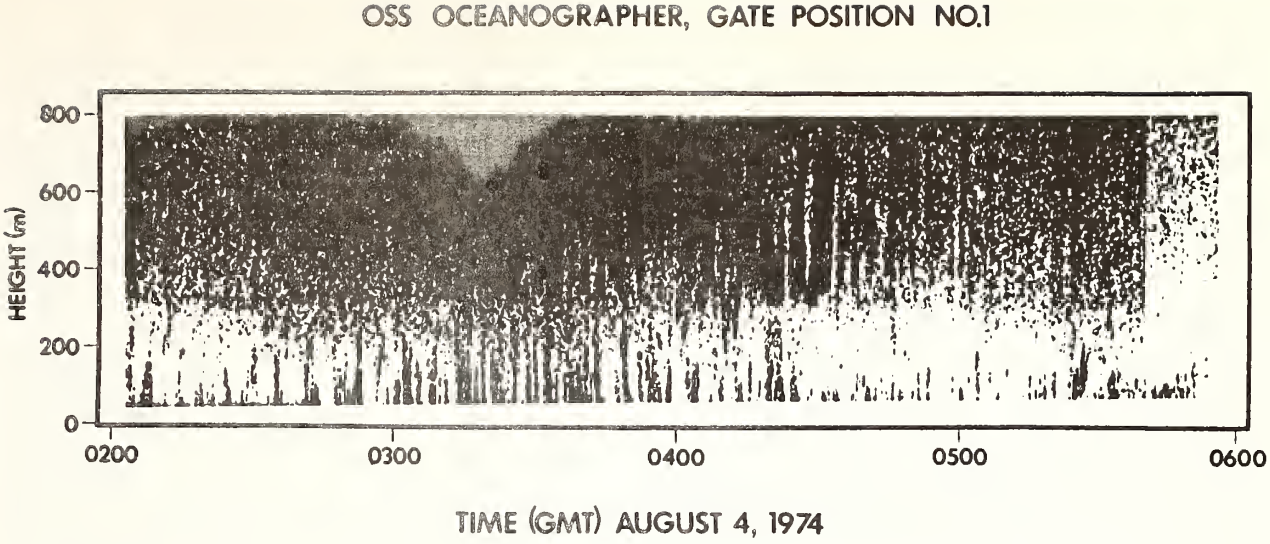

Figure 1. A portion of an acoustic facsimile recorded during GATE showing hummocky echoes.

hummock- or "hat"-shaped echoes. These have been correlated with low-level fair-weather trade cumuli using tethered balloon and photographic data (Gaynor et al., 1976; Gaynor and Mandics, 1978). It is hypothesized that the major portion of the acoustic backscatter within the hummocks is due to C_e^2 or C_{eT}^2. This has not been proved to date, but it is hoped that aircraft data will provide the proof.

The moisture data from the DC-6 refractometer is in the form of water vapor density, ρ_w. To put the structure functions in the form of partial pressure of water vapor, e, the relations

$$C_e^2 = (R_w T)^2 \, C_{\rho_w}^2$$

and

$$C_{eT}^2 = (R_w T) \, C_{\rho_w T}^2$$

are used, where R_w is the gas constant for water vapor. To convert from frequency to wave number for use in (2) we have

$$k_1 = \frac{2\pi f}{\bar{U}}$$

where $\bar{U}$ is the aircraft speed (100 m s^{-1}).

The DC-6 T and ρ_w data from the turbulence probe are well within the accuracy necessary for structure function calculations from spectra (Grossman and Bean, 1973). The filters on the data easily allow calculations from the spectra or cospectra at frequencies up to 2 Hz (Bean et al., 1976). From our experience to date, this frequency is well within the inertial subrange.

Figures 2 through 7 show examples of spectral densities and cospectral densities of T and ρ_w. All the spectra have been smoothed. They constitute two cases, each a 7-min continuous time section of an aircraft leg, each at 153 m above the surface, and each a cross-wind flight. The two flights were on different days of Phase II of GATE. Precipitation occurred

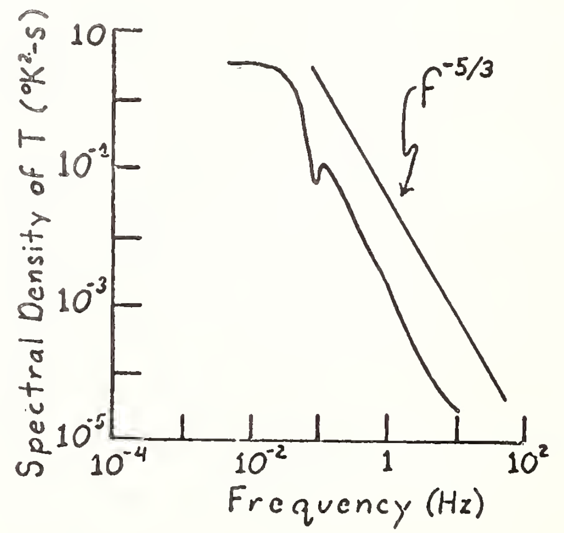

Figure 2. - Temperature spectral density for 13 August.

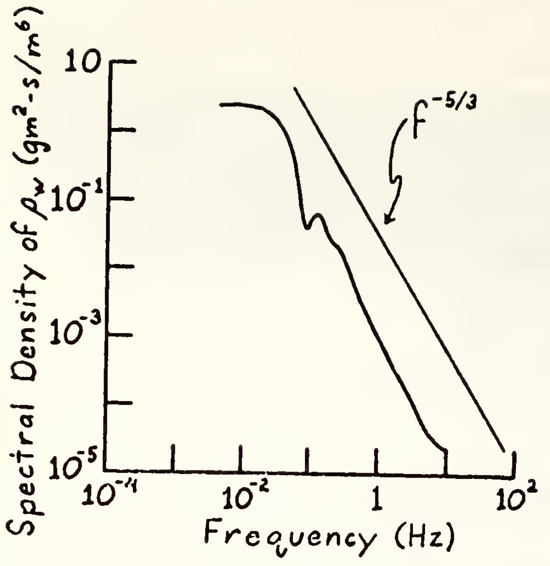

Figure 3. Water vapor spectral density for 13 August.

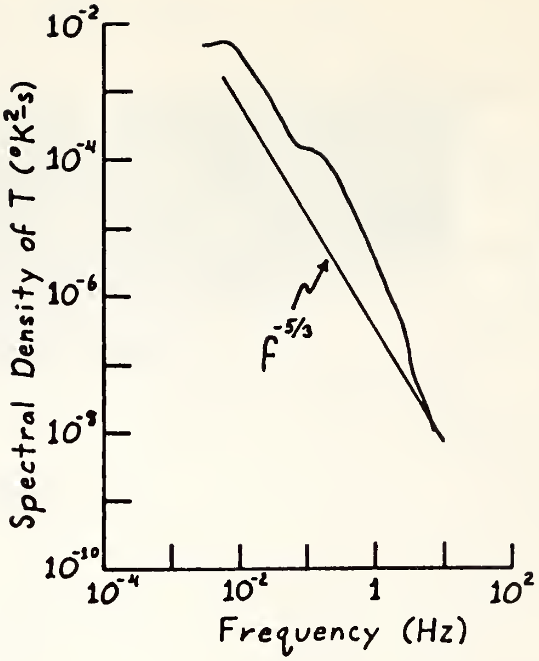

Figure 5. Temperature spectral density for 10 August.

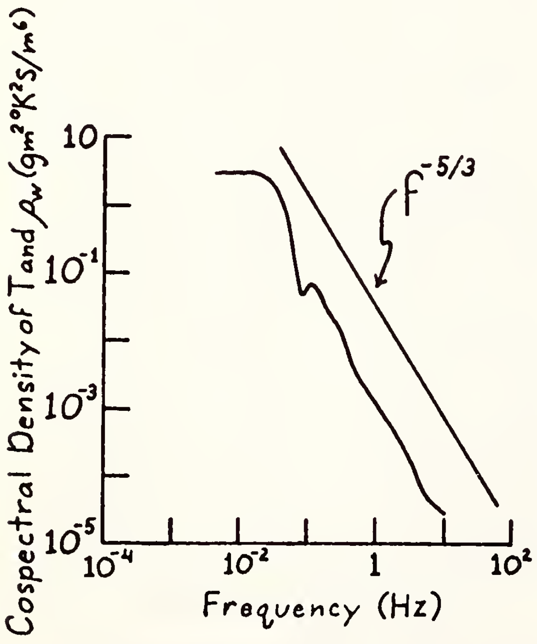

Figure' 4. Cospectral density of temperature and water vapor for 13 August.

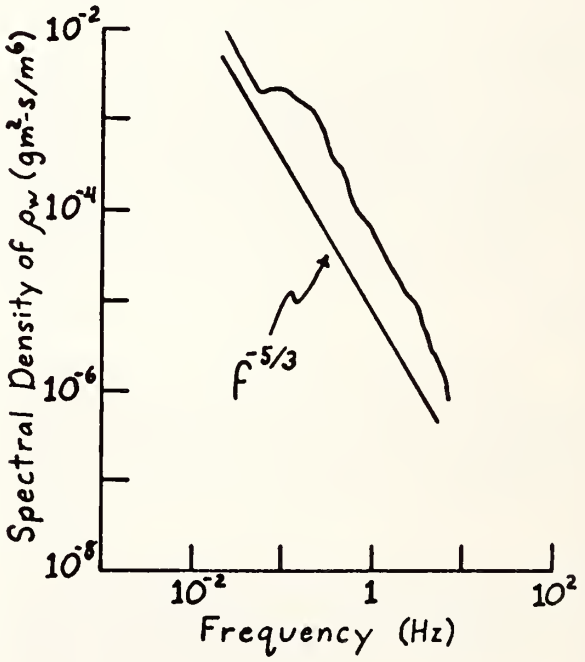

Figure 6. Water vapor spectral density for 10 August.

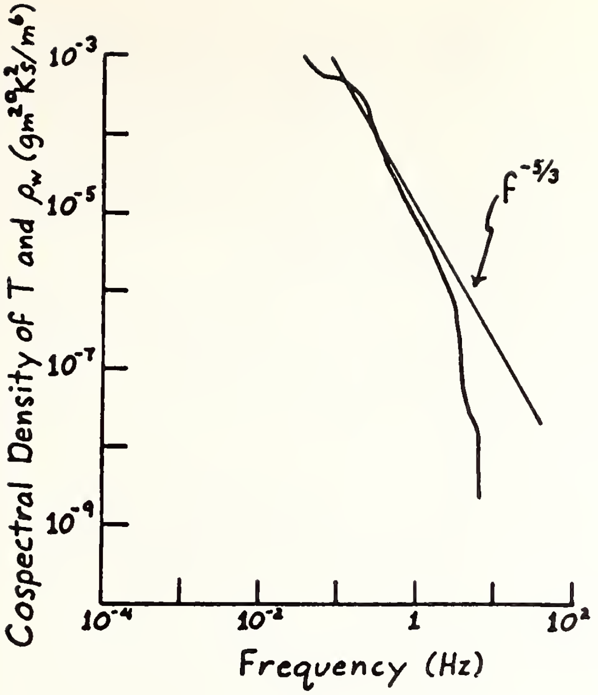

Figure 7. Negative of the cospectral density of temperature and water vapor for 10 August.

during both flights with the latter flight (13 August) exhibiting the deeper convection and more turbulence. The spectra of temperature and cospectra of T and ρ_w for the 10 August case exhibit a slope slightly steeper than -5/3. Because the low-pass filter does not operate at frequencies below 3 or 4 Hz, the cause of this steeper fall-off is unknown. The errors in C_T^2 and C_{eT}^2 could amount to as much as 30% because of this discrepancy.

Figures 2 and 3 show the spectral densities of T and ρ_w, respectively, from part of the DC-6 flight on 13 August. Both show an apparent inertial subrange. Figure 4 shows the $T\rho_w$ cospectral density which is all positive for the bandwidth indicated and also shows an inertial subrange behavior.

In contrast, Figs. 5 through 7 show spectral densities of T and ρ_w, and cospectral density of $T\rho_w$, respectively, for a section of a flight on 10 August. The day was less disturbed with slightly less convective activity. As mentioned above, the inertial subrange in Figs. 6 and 7 is not apparent. The cospectrum in Fig. 7 is negative. Friehe et al. (1975) indicate negative cospectra of temperature and humidity directly over relatively cold water, and negative cospectra of temperature and moisture are becoming well documented near the top of the mixed layer (Wyngaard et al., 1978). However, it is surprising that negative cospectra occur at only 153 m, well below the average height of the mixed layer in GATE which was shown to be between 550 and 600 m during the GATE Workshop (July-August, 1977).

Table 1 shows the results of calculating the terms of Eqs. (1a) and (1b) from the spectral data for the two cases using the relations presented in Section 2 and the beginning of this section. The first column in Table 1 represents the correction due to the co-fluctuations of temperature and moisture. The second column shows the correction for the fluctuations of moisture alone. If the effects of moisture are included in the computations of acoustical C_n^2, the values are 23% and 22% higher for 13 August and 10 August respectively, than those calculated with only the temperature effects included. These corrections are in good agreement with an example given by Fitzjarrald (1978), which also used GATE DC-6 data, but only took into account C_e^2. It is interesting that in the first column in Table 1 is a relatively large negative value for 10 August reflecting the negative $T\rho_w$ co-fluctuations in Fig. 7. Yet, the total correction (α_a^2) is positive and is in close agreement with that on 13 August.

The results presented are only preliminary and work is continuing. The ultimate goal is to generate GATE aircraft-measured profiles of C_T^2, C_e^2 and C_{eT}^2, in the boundary layer categorized according to the intensity of convective activity. From the two examples given here, it appears that the variability in these profiles will make categorization difficult. Not only will these parameters be

Table 1. Terms of Eqs. (1a) and (1b) for the two cases discussed.

	$r_{eT}(2DC_e\bar{T}/C_T\bar{p})$	$(DC_e\bar{T}/C_T\bar{p})^2$	α_a^2
13 August	0.212	0.012	1.23
10 August	-0.83	1.05	1.22

useful for a better understanding of acoustic backscatter in the moist tropical marine atmospheric boundary layer, but applications exists for other remote sensors (e.g., with radio waves, infrared, or optical).

A possible future use of this data would be indirect computations of surface moisture and heat fluxes (Wyngaard and Clifford, 1978). If the effects of temperature and moisture fluctuations on acoustic C_n^2 could ever be separated in a moist environment, the acoustic sounder may provide some opportunity for remote sensor calculations of surface heat and moisture fluxes.

4. CONCLUSION

Although it is difficult to arrive at any firm conclusions from these preliminary calculations it is apparent that the variations in C_T^2, C_e^2 and C_{eT}^2 in the GATE boundary layer are quite large and very dependent on atmospheric conditions. Also apparent are the large contributions made by C_e^2 and C_{eT}^2 in the GATE boundary layer.

The lack of a clear inertial subrange for the temperature spectra and $T\rho_w$ cospectra during one of the two flights is disturbing because the structure functions are defined in terms of inertial subrange behavior. The reason for this ill-defined subrange is unknown. Friehe et al. (1975) also indicated a lack of an inertial subrange of T-spectra over the ocean, but the slope was less steep than -5/3. More GATE data need to be analyzed to make sure that this lack of an inertial subrange is not an artifact of the small data samples.

The GATE aircraft data will provide a complete set of structure function profiles applicable to the tropical marine boundary layer. Much work needs to be done on generating, categorizing and scaling these profiles to make them more universally useful. Also, a description of the importance of C_e^2 and C_{eT}^2 to acoustic backscatter within the hummocky appearing structures needs to be provided.

5. ACKNOWLEDGMENT

The research reported here was supported by the United States GATE Project Office.

6. REFERENCES

Bean, B. R., R. O. Gilmer, R. F. Hartmann, R. E. McGavin, and R. F. Reinking, 1976: Airborne measurement of vertical fluxes of water vapor, sensible heat and momentum during GATE. *GATE Information Bulletin No. 13*, 28-47. (Available from S. Ruttenberg, NCAR.)

Fitzjarrald, D. E., 1978: Horizontal scales of motion in atmospheric free convection observed during the GATE experiment. Submitted to *J. Appl. Meteor.*

Friehe, C. A., J. C. LaRue, F. H. Champagne, C. H. Gibson, and G. F. Dreyer, 1975: Effects of temperature and humidity fluctuations on optical refractive index in the marine boundary layer. *J. Opt. Soc. Amer.*, 65, 1502-1511.

Gaynor, J. E., and P. A. Mandics, 1978: Analysis of the tropical marine boundary layer during GATE using acoustic sounder data. To appear in *Mon. Weath. Rev.*

Gaynor, J. E., P. A. Mandics, A. B. Wahr, and F. F. Hall, Jr., 1976: Studies of the tropical marine boundary layer using acoustic backscattering during GATE. Preprints, *17th Conference on Radar Meteorology*, Seattle, Washington, 303-306. (Available through Amer. Meteor. Soc., Boston, Massachusetts.)

Grossman, R. L., and B. R. Bean, 1973: An aircraft investigation of turbulence in the lower layers of a marine boundary layer. *NOAA Tech. Rpt.* ERL 291-WMPO 4, 166 pp. (Available through the Superintendent of Documents, U.S. Government Printing Office, Washington, D.C. 20402.)

Mandics, P. A., and F. F. Hall, Jr., 1976: Preliminary results from the GATE acoustic echo sounder. *Bull. Amer. Meteor. Soc.*, 57, 1142-1147.

Mandics, P. A., and E. J. Owens, 1975: Observations of the marine atmosphere using a ship-mounted acoustic echo sounder. *J. Appl. Meteor.*, 14, 1110-1117.

Tatarskii, V. I., 1971: *The Effects of the Turbulent Atmosphere on Wave Propagation*, Israel Program for Scientific Translations, N72-18163, 472 pp. (Available from NTIS, Springfield, Virginia.)

Wesely, M. L., 1976: The combined effect of temperature and humidity fluctuations on refractive index. *J. Appl. Meteor.*, 15, 43-49.

Wyngaard, J. C., and S. F. Clifford, 1978: Momentum, heat, and moisture fluxes from structure parameters. Submitted to *J. Atmos. Sci.*

Wyngaard, J. C., W. T. Pennell, D. H. Lenschow, and M. A. LeMone, 1978: The temperature-humidity covariance budget in the convective boundary layer. *J. Atmos. Sci.*, 35, No. 1.

Monthly Weather Review, 106: 223-232, 1978.

Analysis of the Tropical Marine Boundary Layer during GATE Using Acoustic Sounder Data

J. E. Gaynor and P. A. Mandics

Wave Propagation Laboratory, Environmental Research Laboratories, NOAA, Boulder, Colo. 80302

(Manuscript received 16 June 1977, in final form 24 October 1977)

ABSTRACT

An acoustic sounding system placed on the NOAA Ship *Oceanographer* during GATE provided a unique meteorological data set. Examples of three distinct boundary-layer situations are discussed as they appear on the facsimile records of backscattered acoustic intensity: 1) ubiquitous plume echoes associated with undisturbed conditions, 2) cool-air outflows (or wakes) from either squall-line or isolated cumulonimbus activity associated with disturbed conditions and 3) "hat"- or "hummock"-shaped echoes associated with low-level cumulus clouds usually occurring during weakly disturbed conditions. Profiles of potential temperature and mixing ratio from radiosonde flights launched from the *Oceanographer* are compared with the acoustic data. Convective plumes observed during GATE were less vigorous than those seen over land. Bulk aerodynamic fluxes of surface sensible and latent heat varied in time with the passage of thermal plumes. This indicates a minimum averaging time for valid flux estimates of about 30 min. Outflows resulted in order-of-magnitude increases in surface sensible heat flux and large increases in surface stress, but only relatively small increases in latent heat flux. The increased stability following the outflows lasted from a few hours up to 16 h, depending on the intensity of the disturbance. The rate of dissipation of turbulent kinetic energy is calculated in the upper mixed layer for the three cases using an acoustic Doppler-differencing technique. These values are intercompared and compared with those from other studies. Evidence is presented indicating that hummocky echoes were associated with low-level clouds. Plumes underneath the hummocks were characterized by larger moisture content and surface heat fluxes when compared with plumes without hummocks.

1. Introduction

A three-axis acoustic sounder was installed on the NOAA Ship *Oceanographer* and operated during the three experimental phases of GATE in 1974 (Mandics and Hall, 1976). The sounder was a radarlike device in that it emitted short bursts (200 ms) of acoustic energy at regular intervals (typically, once every 5 s). After the pulse transmission, a sensitive receiver was automatically connected to the same antenna to collect signals backscattered by small-scale atmospheric temperature and humidity irregularities. Fig. 1 shows the acoustic antennas mounted in the bow of the ship. The antenna assembly was gyro-mounted to compensate for the ship's pitch and roll motions. An accelerometer provided information on the ship's vertical motions and facilitated the extraction of vertical velocities from the Doppler-shifted acoustic returns. The sounder had to operate at the relatively high acoustic frequency of 2950 Hz most of the time to decrease interference from ambient ship noise. The system configuration and electronic circuitry have been described by Mandics and Owens (1975) and were similar to those of Simmons *et al.* (1971). The purpose of the two forward-tilted antennas (Fig. 1) was to measure the horizontal wind in the lower boundary layer using the Doppler frequency shift of the returned acoustic signals. However, because of contamination by sea scatter and wind noise, quantitative analysis of the data obtained by these two antennas was not possible. The results reported here were obtained from acoustic signals received by the vertically pointed antenna only.

The sounder provided backscattered intensity and Doppler data in the mixed layer and frequently in the lower cloud layer. As described by Mandics and Hall (1976), these data delineated dynamic changes that had profound effects on the tropical mixed layer. This paper describes the changes between disturbed and undisturbed conditions as seen by the sounder as well as the characteristics of the mixed layer and low-level clouds that appeared on occasion as hummocky echoes on the acoustic facsimile records. The acoustic Doppler data provided vertical velocities and estimates of the rate of dissipation of turbulent kinetic energy for various subcloud layer conditions. Supporting meteorological data were obtained from radiosonde flights and the Surface Meteorological Sensing System (SMSS) aboard the *Oceanographer*.

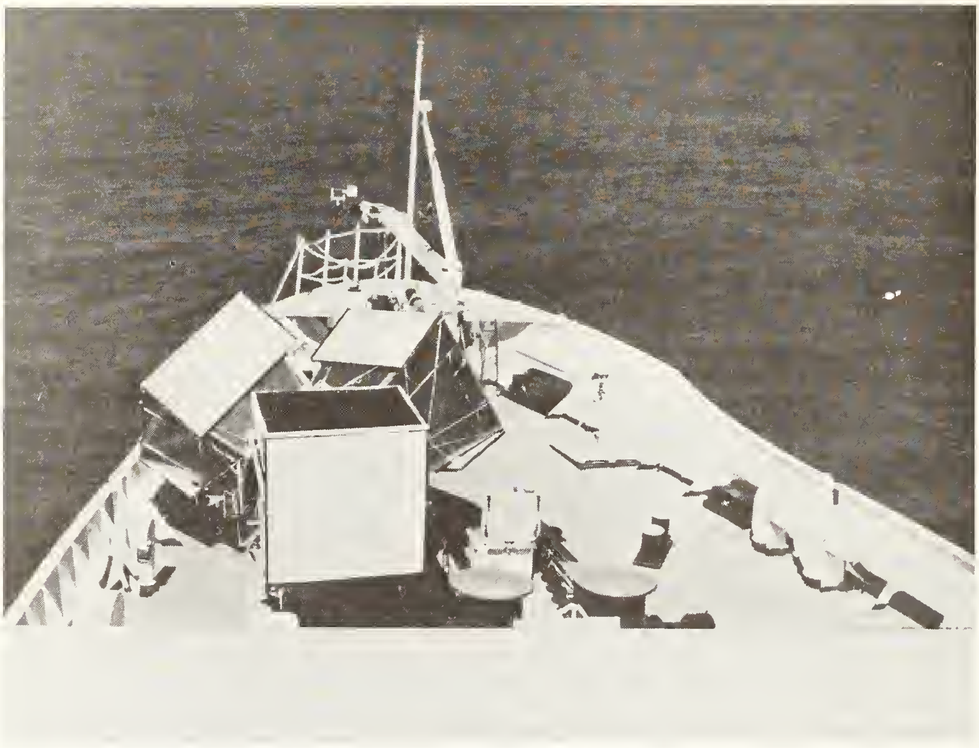

FIG. 1. The three-axis acoustic sounding system mounted in the bow of the NOAA Ship *Oceanographer*.

The radiosondes provided profile information which helped to interpret the acoustic facsimile records. Surface fluxes were calculated from the SMSS data using the bulk aerodynamic method and were compared with structures seen on the facsimiles.

For simplicity, the height region depicted on the facsimiles (from 50 to ~850 m) is referred to as the boundary layer which also includes a portion of the lower cloud layer. As usual, the mixed layer or subcloud layer is the region in which the potential temperature and mixing ratio are nearly constant with height.

2. Interpretation of the acoustic facsimile records

a. The disturbed tropical marine boundary layer

Disturbed weather conditions prevailed at the positions occupied by the *Oceanographer* about 30% of the time in GATE. The acoustic records delineated two basic types of disturbance. One was caused by cold-air outflow from isolated cumulonimbi. The second type was associated with more organized squall-line activity. Air cooled by raindrop evaporation within a cumulonimbus cloud became denser, sank to the surface, and spread out horizontally in the form of a gravity current. During GATE, seven well-developed squall lines passed over the *Oceanographer*, two in Phase I and five in Phase III. Their average temperature drop at 10 m height near the head of the current was 4°C, and the inversion structure on the facsimile lasted for an average of 14 h, slowly weakening and rising with time as plumes developed from below. Smaller, less intense outflows from individual cumulonimbi were much more frequent. These occurred about 130 times during all three phases of GATE, lasted an average of 2 h and produced an average initial temperature drop of about 1°C.

Fig. 2 shows time-height facsimile records of the intensity of backscattered acoustic signals during the passage of an intense, organized squall line in Phase III. Scattering by small-scale (~0.1 m) turbulent temperature (and to a lesser extent humidity) inhomogeneities produced the dark regions seen in the record; white areas correspond to a lack of scatter. Gradual darkening of the record with height resulted from the amplification of ambient noise by the automatic range-compensation circuit in the receiver. Hour marks were provided by turning off the transmitter for one minute at the end of each hour.

Prior to the arrival of the squall line at 1251,[1] vertically oriented structures with their bases at the bottom of the facsimile record depicted convective plumes that were characteristic of suppressed (undisturbed) conditions. For 3 h after 1251, acoustic noise produced by raindrops falling on the antenna

---

[1] All times referred to in this paper are GMT.

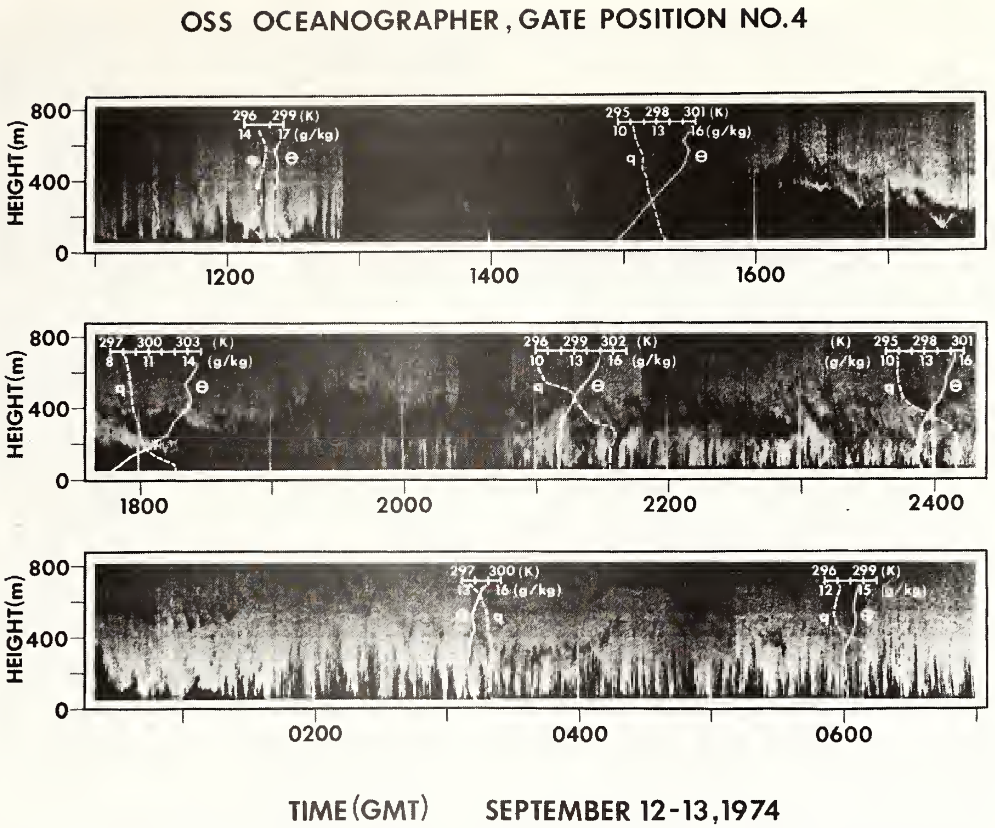

Fig. 2. An acoustic facsimile recorded during the passage of an organized squall line with radiosonde profiles of potential temperature θ and mixing ratio q. The profiles have been placed on the facsimile approximately at the correct flight times.

almost completely obliterated the record. Vertical profiles of potential temperature θ and mixing ratio q, evaluated from high-resolution radiosonde flights are overlaid on the facsimile just preceding, during, and after the cool-air downdraft associated with the squall line passage. There is a significant difference between the radiosonde profiles at 1215 and 1515. They show a cooling of 4 K at the surface and a warming of 3 K at 700 m creating a rather strong temperature inversion during the 3 h period. The two q profiles show a drying of the entire boundary layer with a decrease of 2 g kg^{-1} at the surface and 3 g kg^{-1} near 800 m. Radiosonde-measured wind profiles (not shown) indicate the development of a strong vertical shear in the horizontal wind in the layer between 350 and 500 m at 1515. At 1805, the region above 150 m has dried out and warmed up further, probably because of subsidence after the squall line passage. The moist layer has been squeezed to within 150 m of the surface. The dark region on the acoustic facsimile with its top at about 150 m seems to be associated with acoustic scattering from the layer in which there is a large negative gradient of q and a large positive gradient of θ with height. This is a region of substantial acoustic refractive index changes from which acoustic backscatter originates. The upper dark layer which appears to correspond to a subsiding mass of air is associated with an enhanced positive gradient in θ between 250 and 400 m. The effects of this large outflow on the subcloud layer were similar to those observed by Seguin and Garstang (1976) using aircraft data. The undulations superimposed on the inversion layers between 1600 and 2200 were probably caused by gravity waves and resemble those reported by Hall *et al.* (1976) in density currents over land.

After 1900 (see Fig. 2) thermal plumes have developed, have started rising and have initiated gravity waves within the inversion layers. The mixed layer has been reestablished by 2115. The plumes have moistened the layer up to 300 m (the level at which we see the inversionlike structure on the facsimile), but the region above remains relatively dry. At 0005, the inversion structure became weaker and more diffuse along with weaker gradients in θ and q. The inversion structure at 0315 has risen to around 600 m and is very weak. As indicated by the θ and q profiles, this level corresponds to the top of the mixed layer. The weakness of the scattering is partly due to atmospheric absorption of the acoustic signal at such a high level. The time period from 1600 to 0500 is commonly referred to as the squall-line wake. The profiles at 0600 are representative of typical undis-

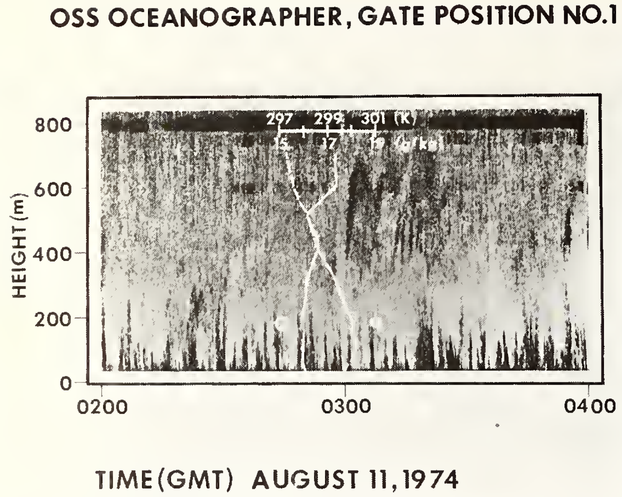

FIG. 3. Acoustic facsimile recorded during a period of hummocky echoes with a radiosonde profile of potential temperature θ and mixing ratio q.

turbed conditions. The potential temperature and mixing ratio were nearly constant up to 400 m where a slight increase in θ and a decrease in q indicated the top of the mixed layer. These profiles agree well with those first presented by Malkus (1956) for suppressed conditions. We see no acoustic backscatter from the top of the mixed layer at 0600 (and during most undisturbed periods) for two reasons: the θ profile does not indicate as strong a stability at the mixed-layer top as previously (cf. with the profile at 0315) and there is little or no vertical shear of the horizontal wind either in direction or speed. The inversionlike structures on the facsimiles (depicted by quasi-horizontal dark layered regions above 100 m) nearly always correspond to a layer of vertical shear (in direction and/or speed) of the horizontal wind. The shear induces mechanical turbulence, which enhances mixing within the vertical gradients of θ and q and increases the likelihood of acoustic backscatter. When the enhanced θ and q gradients associated with outflows are combined with the vertical wind shears, strong acoustic scattering occurs as indicated by the approximately horizontal layering shown between 1500 and 2200 in Fig. 2.

b. Hummocks

About 15% of the time during GATE, "hat"- or "hummock"-shaped echoes appeared above the plumes. An example is shown in Fig. 3. The hummocks appear with bases at 400 m between 0300 and 0320, and a clear, dark hummock is centered at 0355. (The thick horizontal dark line at the top of the facsimile record is caused by direct acoustic reflection from the Boundary Layer Instrument System's (BLIS) balloon and the two intermittent weak echoes below the dark one are reflections from the upper two instrument packages on the tether.) Shaw (1971) observed similar hummocky acoustic returns in Australia and was able to correlate them with low-level cumuli overhead. Hummocky acoustic echoes also have been described by Mandics and Hall (1976). The mixing ratio q profile plotted in Fig. 3 at 0300 shows a moist subcloud layer with not as large a decrease of moisture with height as that observed at 0600 in Fig. 2 when no hummocks were present. In fact, it is very difficult to ascertain the top of the mixed layer from the q profile alone. The θ profile indicates the top of the mixed layer to be around 500 m with a hint of a "transition" layer between 350 and 500 m. The moist subcloud and lower cloud layers in Fig. 3 are to be expected if indeed these hummocks were associated with clouds. Gaynor *et al.* (1976) have shown that mixing ratio time series evaluated from BLIS data at the level of the hummocks correlated well with the presence of hummocky echoes. The mixing ratio reached peak values near saturation within the hummocks and decreased considerably between them.

Visual inspection of all-sky camera photographs taken on the *Oceanographer* allowed us to correlate the appearance of low-level cumuli overhead and the hummocks recorded on the facsimile during daytime. In most cases, when there was a hummock a cloud was observed. However, quite often, low-level clouds had no corresponding hummock. The fact that low clouds were difficult to observe in the all-sky photos, especially when the sun or high cirrus clouds were directly overhead, made the correlation process somewhat uncertain.

Lifting condensation levels (LCL) were computed using *Oceanographer* SMSS data and were compared

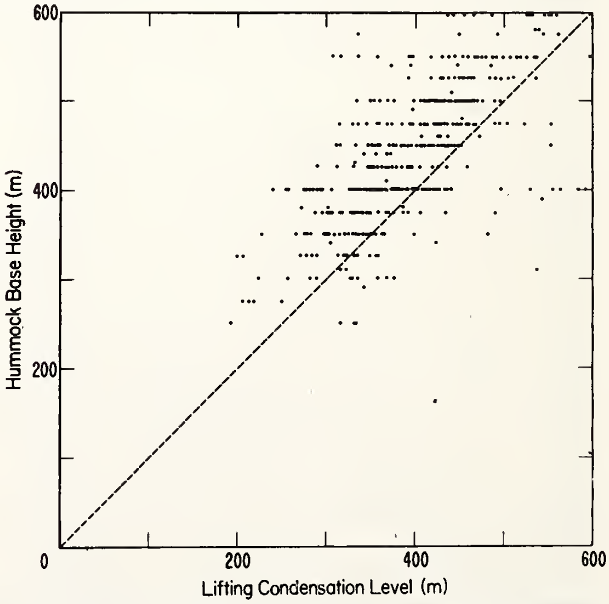

FIG. 4. Scatter diagram of hummock base heights observed on the acoustic facsimile records versus computed lifting condensation levels (LCL) during all three phases of GATE.

with the hummock base heights. The scatter diagram in Fig. 4, containing 500 points of LCL versus hummock base heights for all three phases of GATE, shows that the hummock bases were usually slightly above the LCL. Fig. 4 suggests that the hummocks were caused by acoustic backscatter from within-cloud turbulence or turbulence near the edge of the clouds where strong temperature and moisture mixing with the environment occurred. We conclude, therefore, that the hummocks indicate clouds, but very likely a particular type of cloud.

The acoustic facsimile records reveal that hummocks often appeared after the passage of strong or moderate outflows associated with squall lines or thunderstorms. In some cases, a nearly continuous band of hummocks formed which was associated with low stratiform clouds at an inversion level following squall-line activity. At other times, hummocks were generated by a series of weak outflows that passed over the ship during slightly disturbed conditions. In all cases, the surface streamline analyses from GATE Report No. 17 (International Scientific and Management Group, 1975) indicated synoptic-scale convergence either very close to or directly over the *Oceanographer* when hummocks appeared. We hypothesize that to generate strong enough temperature and moisture turbulence within or at the edge of clouds in the lower cloud layer to produce sufficiently intense acoustic backscattering, a fairly strong temperature and mixing ratio contrast must have existed between the cloud and its environment. In particular, this was true after the passage of a cool-air outflow when moist and cool air underlay drier and potentially warmer air as illustrated by the profiles in Fig. 2. As the convective plumes became more vigorous, they penetrated the top of the mixed layer. Then the increased buoyancy from condensational heating resulted in comparatively strong mixing between the cloud and its environment.

By contrast, the doughnut-shaped echoes seen by 10 cm radar (Hardy and Ottersten, 1969) are caused entirely by clear-air returns and cannot be related to clouds directly. These echoes are two-dimensional (in space) radio-wave manifestations of the thermal plumes that appear as vertical structures in the acoustic time/height facsimile records.

To better understand the mechanism responsible for acoustic scattering in a moist atmosphere, it is necessary to consider the relative importance of temperature and humidity fluctuations. In the boundary layer over relatively dry land, moisture fluctuations are usually negligible and it is assumed that essentially all of the acoustic backscatter is produced by temperature fluctuations at scales of one-half the acoustic wavelength ($\sim$0.1 m) (Tatarskii, 1971). Preliminary analysis of some GATE aircraft temperature and water vapor spectral density data indicates, however, that moisture fluctuations could have contributed up to 25% of the backscattered intensity in the subcloud layer.

The contribution of moisture to scattering may have been even higher within the hummocks. Wesely (1976) showed analytically that the co-fluctuations of temperature and moisture may be an important contributor to acoustic scattering over the ocean. Similarly, Friehe *et al.* (1975) demonstrated experimentally that these co-fluctuations accounted for a large portion of optical scatter 6 m above the ocean's surface. These results can be related directly to acoustic propagation. However, better high-frequency data from collocated temperature and humidity sensors are needed, and more analysis will have to be performed to delineate the relative contribution of moisture and temperature fluctuations to acoustic backscatter in the moist tropical marine environment.

Because the facsimile records present the data on a time-height scale, the spatial proportions of the hummocks (clouds) are considerably distorted. To rectify the situation, we digitized two sections of an acoustic record containing a few hummocks (top half of Fig. 5), and after subtracting the average background noise, we replotted the data using an expanded time scale (bottom half of Fig. 5). Assuming that the hummocks advected with the mean wind at their level, we placed an appropriate length scale on the facsimile. The enlarged hummock sections show patterns that closely correspond to the actual shape of clouds. In Fig. 5 we have overlaid contours of acoustic Doppler-derived vertical velocities w averaged for 15 s on the facsimile record. Vertical velocities obtained from acoustic returns with low signal-to-noise ratio have not been contoured. Note that, although there were upward motions greater than 2 m s^{-1}, substantial downward motions also occurred within the clouds. The downward moving parcels are expected to be in regions of entrainment that would be sufficiently turbulent to produce strong acoustic backscatter. The entrainment characteristics implied here are quite similar to those discussed by Telford and Wagner (1976) for small fair-weather cumuli over land. These cumuli had features that included buoyancy lifting near the front of the cloud as it advects past and entrainment and downward mixing near the top and rear of the cloud.

3. Quantitative analysis

In addition to describing qualitatively the tropical marine boundary layer in hitherto unseen detail, the acoustic data set also allowed the quantitative evaluation of several important parameters. Surface fluxes were compared with facsimile records along with vertical velocities determined from Doppler-shifted acoustic returns. Also, using vertical differencing of

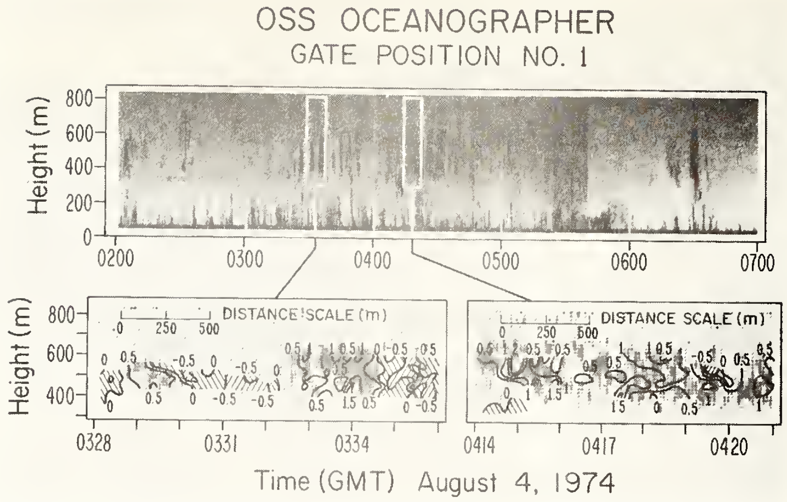

FIG. 5. Facsimile recording of hummocks with two enlarged hummock sections plotted underneath. Contours of 15 s averaged Doppler vertical velocities w with contour intervals of 0.5 m s^{-1} are overlaid on the enlarged sections. The hatched areas indicate downward motion and only the regions of relatively high acoustic signal-to-noise ratio have been contoured.

acoustically determined velocities, we obtained estimates for the rate of dissipation of turbulent kinetic energy.

a. Surface fluxes

The acoustic facsimile in Fig. 6 illustrates an undisturbed situation with plumes extending from near the ocean surface to between 300 and 400 m. The vertical velocity w plotted in Fig. 6, was evaluated from the Doppler-shifted acoustic returns at 177 m and averaged for one minute with a running filter. Variations of w show good correlation with the plumes. The dotted segments within the time series of w indicate regions of low acoustic signal-to-noise ratios in which the Doppler extraction became unreliable. Some of the more intense plumes produced maximum upward velocities near 0.5 m s^{-1}.

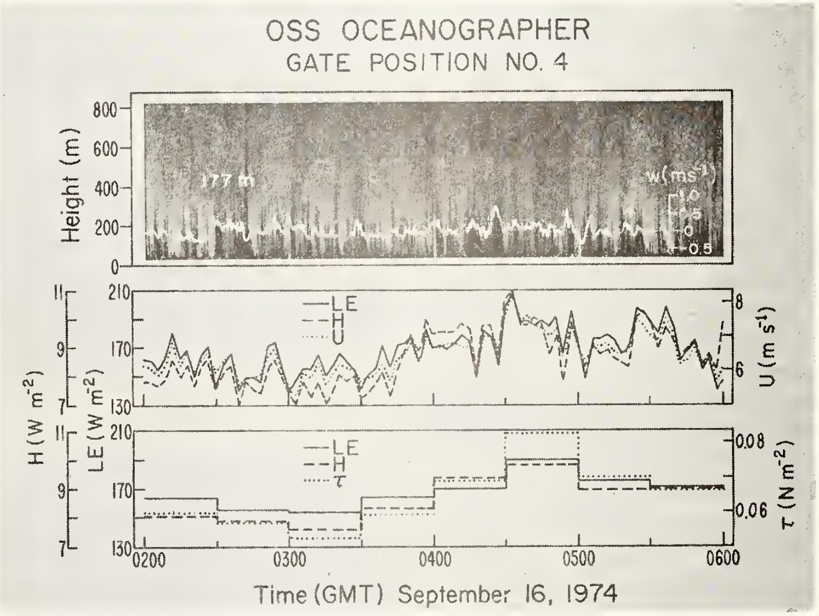

FIG. 6. Acoustic facsimile of an undisturbed boundary layer with time series of Doppler-derived vertical velocity w at 177 m overlaid. Time series of 3 min averaged surface sensible heat flux H surface latent heat flux LE and 10 m horizontal wind U are plotted in the center. In the bottom, 30 min averages of H, LE and surface momentum flux (stress) τ are plotted.

The 3 min averaged surface sensible heat flux H and the latent heat flux LE have been calculated from the *Oceanographer* surface meteorological data using bulk aerodynamic methods (Pond *et al.*, 1974), i.e.,

$$H = 1.54\bar{U}_{10}(\bar{T}_s - \bar{T}_{10}), \tag{1}$$

$$LE = 3.74\times10^3\bar{U}_{10}(\bar{q}_s - \bar{q}_{10}), \tag{2}$$

where $\bar{U}_{10}$ is the averaged horizontal wind at 10 m above the sea surface, $\bar{T}_s$ and $\bar{q}_s$ are the sea surface temperature and mixing ratio (assuming that the air is saturated near the surface), respectively, and $\bar{T}_{10}$ and $\bar{q}_{10}$ are their values at 10 m. In keeping with standard notation, the latent heat flux is denoted by LE, where L is the latent heat of vaporization of water and E is the moisture flux. H and LE are plotted directly below the acoustic facsimile in Fig. 6 along with the 3 min averaged horizontal wind at 10 m which we designate as U. At the base of the plume families (between 0 and 10 m), we find minima in H, LE and U; e.g., the minima at 0418 and 0427 correspond to two rather vigorous plume families advecting past at these times. However, based on physical reasoning we would expect maxima of H and LE at the bases of warm and moist plumes with minima in between. Fig. 6 indicates that because the surface fluxes depend on variations in U and not in the gradients of temperature and mixing ratio, the 3 min averaging time is inadequate. Therefore, the minimum averaging time necessary for the bulk method to provide valid flux estimates is controlled by the period of the plume families. This period depends on the advection speed of the plumes, and for the case in Fig. 6 it is about 10 min. At least two or three periods should be included in the average, consequently a minimum averaging time for the bulk fluxes would be about 30 min. The 30 min averaged fluxes are presented in the bottom of Fig. 6 along with the surface stress τ also calculated by bulk methods using (Pond *et al.*, 1974)

$$\tau = 1.53\times10^{-3}\bar{U}_{10}^2. \tag{3}$$

The three plots at the bottom of Fig. 6 show that the plume-caused variations have been averaged out. Although surface fluxes presented by others were not calculated over the ocean in the same way as those in Fig. 6 and subsequent figures, the agreement between our results and those presented by Leavitt and Paulson (1975) and Paulson *et al.* (1972) from BOMEX data is quite good. Müller-Glewe and Hinzpeter (1975) presented preliminary flux results from GATE, calculated using both direct and bulk or profile methods. These also show good agreement with our results.

BLIS fixed-level data indicate that the plumes were generally slightly warmer and considerably more moist than the environment. There have been cases noted, however, in which the plumes were moist and slightly cooler than the environment while the ocean surface temperature was nearly the same as or slightly less than the air temperature at 10 m. Even when the ocean temperature was more than 0.5°C warmer than the overlying air, plumes were occasionally cooler than the ambient air at the 10 m level. In such situations, the buoyancy is due primarily to the moisture. Within these anomalous plumes, $LE+H>0$ with H slightly less than zero. More data analysis will have to be performed to determine why some plumes remain cooler than the environment when the ocean surface is warmer than the air.

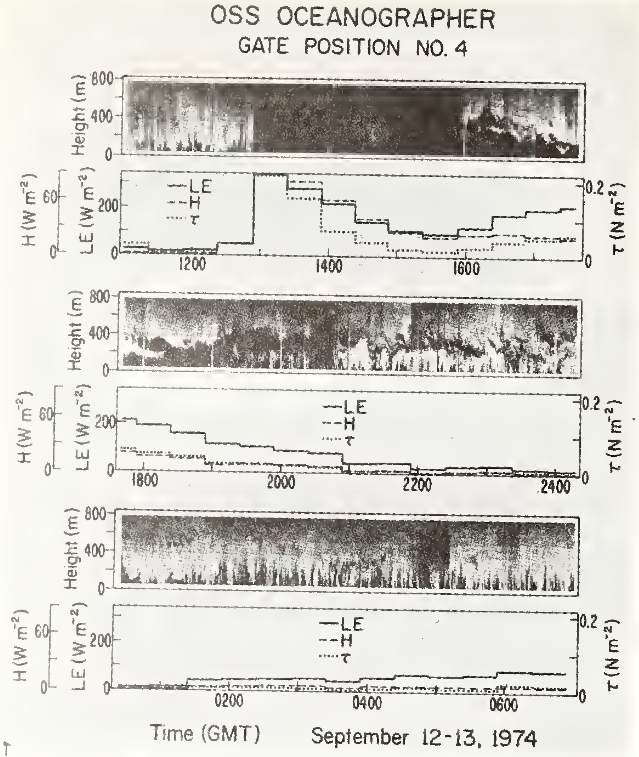

Fig. 7. Acoustic facsimile of the disturbed boundary layer. Time series of 30 min averaged surface sensible heat flux H, surface latent heat flux LE and surface momentum flux (stress) τ are plotted below each facsimile. The averaging periods are adjusted to correspond to the arrival of the squall line.

The squall-line event presented in Fig. 2 is shown again in Fig. 7 with 30 min averaged fluxes plotted beneath the facsimile records. The averaging time was adjusted to coincide with the arrival of the squall-line. The dramatic increases in LE, H and τ immediately following the arrival of the squall line are predominantly caused by the increased surface wind speed. However, because the outflow was considerably cooler and only slightly drier than the ambient air (see Fig. 2), the relative increase in H was larger than that in LE. In fact, H, which is normally close to 20 times smaller than LE (Fig. 6), is only about three times smaller at the head of the outflow. If we could measure "instantaneous" surface fluxes, the changes in these would likely be even more spectacular.

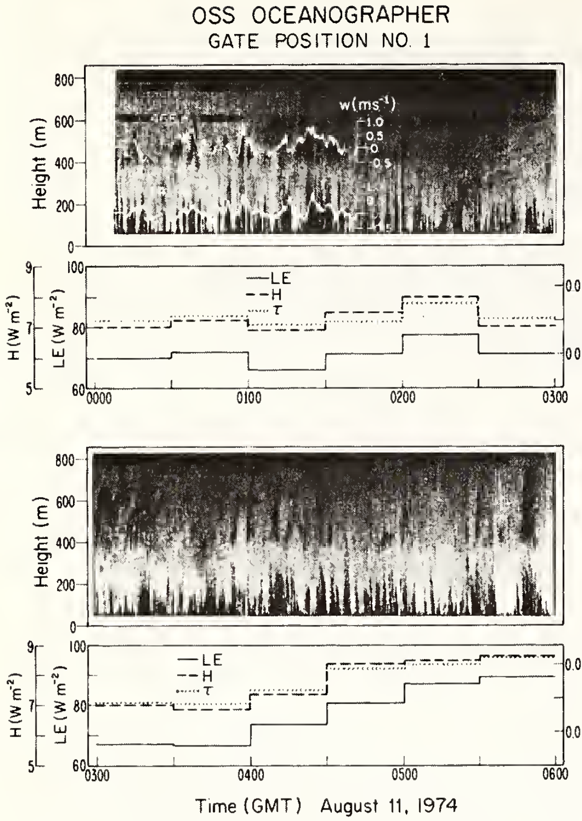

FIG. 8. Acoustic facsimile of a period with hummocky echoes. Time series of Doppler vertical velocity w at 141 and 466 m are overlaid on the upper facsimile. Time series of 30 min averaged surface sensible heat flux H, surface latent heat flux LE and surface momentum flux (stress) τ are plotted below each facsimile.

Note that the elevated surface fluxes (especially LE) continue for nearly 9 h after the squall line arrives. Increases in surface fluxes in the disturbed tropical marine boundary layer have been described by Aspliden (1976), but he was unable to see such detail in the cumulonimbus outflows.

Fig. 2, with the radiosonde profile overlays, clearly shows that the dark, horizontally layered structures undulating between 100 and 400 m on the facsimile correspond to temperature inversions and moisture changes. As Echternacht and Garstang (1976), Zipser (1977) and Houze (1977) have pointed out, the real significance of the resultant stable stratification was that little or none of the surface sensible or latent heat was transferred through the inversion which in this case persisted until about 2400. Because continuous temperature and moisture profiles were not available during GATE, the acoustic sounder facsimile records provided the only reliable indication of the appearance and temporal extent of disturbance-induced low-level inversions.

Fig. 8 shows an example of facsimiles with hummocky echoes. In this figure we have plotted two time series of Doppler-derived vertical velocity, w, at 141 m (plume level) and 466 m (hummock level). These data were processed by a 30 s running low-pass filter. Maximum w within the plumes was close to 0.7 m s^{-1}. Because of the increased buoyancy produced by condensational heating, peak velocities approached 1.0 m s^{-1} within the hummocks. The dotted segments within the w time series in Fig. 8 indicate unreliable data due to low acoustic signal-to-noise ratios. When hummocky echoes appeared at the top of the mixed layer, the surface layer air was slightly cooler and closer to saturation than when no hummocks were present. This conclusion is shown indirectly by comparing the fluxes between Figs. 6 and 8 and referring to the three equations given earlier.

b. The rate of dissipation of turbulent kinetic energy

The rate of turbulent energy dissipation ϵ can be calculated using vertical differencing of acoustically determined vertical velocities, w. Assuming that the fluctuations of interest lie within the inertial subrange, Tatarskii (1971) obtained the following relation for ϵ:

$$\epsilon^{\frac{2}{3}} = \frac{3D(\Delta z)}{8(\Delta z)^{\frac{2}{3}}}. \tag{4}$$

Here Δz is the height increment and $D(\Delta z)$ is the vertical velocity structure function

$$D(\Delta z) = \overline{[\hat{w}(z_1) - \hat{w}(z_1+\Delta z)]^2}, \tag{5}$$

where z_1 is a given height level, and the overbar indicates a time average. The carets on the vertical velocities in Eq. (5) are to remind us that they are volume averages corresponding to the nearly cylindrical-shaped scattering volumes interrogated by the acoustic sounder. The volume dimensions are about 30 m high and 30 m in diameter, increasing in diameter with height. It should be noted that, in order to calculate ϵ from the structure function, $\Delta z/z \ll 1$ must hold. With $\Delta z = 35$ m in our case, this requirement is not satisfied at the lower levels of the calculations; this results in a tendency to severely underestimate the calculated ϵ values below 200 m. Because of this limitation and the decreased signal-to-noise ratios above about 400 m, the ϵ values to be presented are averages between 200 and 400 m where other

TABLE 1. Rate of dissipation of turbulent kinetic energy ϵ stratified according to mixed-layer characteristics and averaged in height between 200 and 400 m and in time for 1 h.

Date	Time (GMT)	Mixed-layer characteristics	ϵ (m^2 s^{-3})
16 September	0300–0400	Plumes only (suppressed)	9.4×10^{-4}
9 September	1630–1730	Isolated cumulonimbus outflow	3.8×10^{-4}
4 August	0400–0500	Hummocks (low-level cumuli)	2.1×10^{-3}

investigators (e.g., Pennell and LeMone, 1974) have found ϵ to be nearly constant.

Table 1 shows hourly averaged ϵ for three cases similar to those discussed previously. The outflow of 9 September was generated by an isolated cumulonimbus and created much less rain noise than that indicated in Figs. 2 and 7 so that reliable acoustic Doppler calculations could be made. The hummocks of August 4 provided stronger and more continuous backscatter than did the case presented in Fig. 8.

An interesting result in Table 1 is the considerably larger value of ϵ below and within the lower portion of the hummocks compared with ϵ in the suppressed case. A likely explanation is that the more vigorous plumes overshot the stable stratification underneath the hummocks and the resultant vertical accelerations within the hummocks caused larger vertical differences in w and therefore larger energy dissipation.

The ϵ values in Table 1 are smaller than those found by Gaynor (1977) who used a similar Doppler-differencing method to compare acoustically determined ϵ with those calculated from nearby meteorological tower wind data over dry prairie land. He found that ϵ averaged 1×10^{-2} m^2 s^{-3} (and was nearly constant with height in agreement with the results of Lenschow, 1974) for a free convective boundary layer. The ϵ values obtained by Pennell and LeMone (1974) for suppressed conditions are in good agreement (within a factor of 2) with the corresponding ϵ value listed in Table 1. However, Merceret's (1976) ϵ values, evaluated during GATE at 150 m height using airborne hot-film anemometers, are only about one-tenth as large as those given in Table 1. There are three likely reasons for this discrepancy. First, the background noise aboard the *Oceanographer* may bias some of the acoustically derived ϵ data to larger values. Second, Merceret's data were recorded in the vicinity of a "dry hole" (a region of dry and probably subsiding air) within which the magnitude of the mechanical turbulence was considerably less than in the examples given here. Third, calculations of ϵ from vertical velocity spectra derived from gust probe measurements aboard the same aircraft and recorded at the same times as Merceret's data indicate larger values (by a factor of 2) than those he obtained from the hot-film anemometer.

4. Conclusions

We have shown that many of the dynamical aspects of the tropical marine boundary layer can be identified and analyzed using the acoustic sounder as a tool. Although acoustic waves backscatter from very small-scale turbulence, this turbulence outlines changes in moisture and temperature associated with much larger scale organized activity. Using Doppler-derived vertical velocities along with *in situ* meteorological data, we have identified some of the detailed characteristics of the structures seen with the sounder.

Surface fluxes and the new dimension of ϵ from Doppler-differencing techniques have been used as tools for analyzing structures shown on the acoustic facsimiles within the mixed and lower cloud layers. Detailed case studies using this information and, if possible, BLIS fluxes, or inferred fluxes at higher levels near the top of the mixed layer and lower cloud layer, must still be completed. The calculated flux profiles will have to be related to synoptic-scale features and generalized for the various cases to be meaningful as a parametric tool.

A question which has been addressed but not answered here must be dealt with: How important are the moisture fluctuations and co-fluctuations of moisture and temperature to acoustic scatter? The answer is important not only to acoustic scattering theory, but also to the understanding of boundary layer turbulence over warm oceans.

Work is continuing on the problems mentioned above using all the in situ data obtained on the *Oceanographer* during GATE and aircraft data for turbulence measurements. We plan to report on the results in the near future.

Acknowledgments. The authors would like to thank J. C. Kaimal and F. F. Hall, Jr., for their helpful comments during manuscript preparation and A. B. Wahr for her computer programming help. A. Zuniga and C. W. King prepared most of the figures and their help is gratefully acknowledged. The research reported here was supported by the United States GATE Project Office.

REFERENCES

Aspliden, C. I., 1976: A classification of the structure of the tropical atmosphere and related energy fluxes. *J. Appl. Meteor.*, **15**, 692–697.

Echternacht, K. L., and M. Garstang, 1976: Changes in the structure of the tropical subcloud layer from the undisturbed to disturbed states. *Mon. Wea. Rev.*, **104**, 407–417.

Friehe, C. A., J. C. La Rue, F. H. Champagne, C. H. Gibson and G. F. Dreyer, 1975: Effects of temperature and humidity fluctuations on the optical refractive index in the marine boundary layer. *J. Opt. Soc. Amer.*, **65**, 1502–1511.

Gaynor, J. E., 1977: Acoustic Doppler measurement of atmospheric boundary layer velocity structure functions and energy dissipation rates. *J. Appl. Meteor.*, **16**, 148–155.

——, P. A. Mandics, A. B. Wahr and F. F. Hall, Jr., 1976: Studies of the tropical marine boundary layer using acoustic backscattering during GATE. *Preprints 17th Conf. Radar Meteorology*, Seattle, Amer. Meteor. Soc., 303–306.

Hall, F. F., Jr., W. D. Neff and T. V. Frazier, 1976: Wind shear observations in thunderstorm density currents. *Nature*, **264**, 408–411.

Hardy, K. R., and H. Ottersten, 1969: Radar investigations of convective patterns in the clear atmosphere. *J. Atmos. Sci.*, **26**, 666–672.

Houze, R. A., Jr., 1977: Structure and dynamics of a tropical squall-line system observed during GATE. *Mon. Wea. Rev.*, **105**, 1540–1567.

International Scientific and Management Group, 1975: Report on the field phase of the GARP Atlantic Tropical Experiment: *Meteorological Atlas.* WMO, ICSU, GATE Rep. No. 17, 179 pp.

Leavitt, E., and C. A. Paulson, 1975: Statistics of surface layer turbulence over the tropical ocean. *J. Phys. Oceanogr.*, **5**, 143–156.

Lenschow, D. H., 1974: Model of the height variation of the turbulence kinetic energy budget in the unstable planetary boundary layer. *J. Atmos. Sci.*, **31**, 465–474.

Malkus, J. S., 1956: On the maintenance of the trade winds. *Tellus*, **8**, 335–350.

Mandics, P. A., and F. F. Hall, Jr., 1976: Preliminary results from the GATE acoustic echo sounder. *Bull. Amer. Meteor. Soc.*, **57**, 1142–1147.

——, and E. J. Owens, 1975: Observations of the marine atmosphere using a ship-mounted acoustic echo sounder. *J. Appl. Meteor.*, **14**, 1110–1117.

Merceret, F. J., 1976: Airborne hot-film measurements of the small-scale structure of atmospheric turbulence during GATE. *J. Atmos. Sci.*, **33**, 1739–1746.

Müller-Glewe, J., and H. Hinzpeter, 1975: Turbulent fluxes in the ITCZ during GATE—Phase III at Station 27. Preliminary scientific results of the GARP Atlantic Tropical Experiment, Vol. 1, WMO, ICSU, GATE Rep. No. 14, 224–232.

Paulson, C. A., E. Leavitt and R. G. Fleagle, 1972: Air-sea transfer of momentum, heat and water determined from profile measurements during BOMEX. *J. Phys. Oceanogr.*, **2**, 487–497.

Pennell, W. T., and M. A. LeMone, 1974: An experimental study of turbulence structure in the fair-weather trade wind boundary layer. *J. Atmos. Sci.*, **31**, 1308–1323.

Pond, S., D. B. Fissel and C. A. Paulson, 1974: A note on bulk aerodynamic coefficients for sensible heat and moisture fluxes. *Bound.-Layer Meteor.*, **6**, 333–339.

Seguin, W. R., and M. Garstang, 1976: Some evidence of the effects of convection on the structure of the tropical subcloud layer. *J. Atmos. Sci.*, **33**, 660–666.

Simmons, W. R., J. W. Wescott and F. F. Hall, Jr., 1971: Acoustic echo sounding as related to air pollution in urban environments. NOAA Tech. Rep. ERL 216-WPL 17, 77 pp.

Shaw, N. A., 1971: Acoustic sounding of the atmosphere. Ph.D. dissertation, Department of Physics, University of Melbourne, 266 pp.

Tatarskii, V. I., 1971: *The Effects of the Turbulent Atmosphere on Wave Propagation.* Israel Program for Scientific Translations, N72-18163, 472 pp. [Available from NTIS].

Telford, J. W., and P. B. Wagner, 1976: The interaction of small cumuli with their environment. *Preprints Int. Cloud Physics Conf.*, Boulder, Amer. Meteor. Soc., 283–287.

Wesely, M. L., 1976: The combined effect of temperature and humidity fluctuations on refractive index. *J. Appl. Meteor.*, **15**, 43–49.

Zipser, E. J., 1977: Mesoscale and convective-scale downdrafts as distinct components of squall line structure. *Mon. Wea. Rev.*, **105**, 1568–1589.

BOUNDARY LAYER CLIMATOLOGIES FROM ACOUSTIC SOUNDER INVESTIGATIONS

Freeman F. Hall, Jr.

NOAA/ERL/Wave Propagation Laboratory
Boulder, Colorado 80302

1. INTRODUCTION

Although the feasibility of quantitative acoustic echo interpretation has been demonstrated, most acoustic sounders record data only on facsimile machines; the darkening of the facsimile record is related qualitatively to the intensity of the scattered sound. The patterns of atmospheric turbulence versus time so displayed can tell the experienced observer much about the state of the atmosphere, and much more can be extracted when additional meteorological observations are made in conjunction with the facsimile.

A paper comparing the typical facsimile record appearance with in situ measurements of temperature, humidity, and wind has been published by Estival and Aubry (1976). They used a tethered balloon for the in situ measurements, and documented the general enhancement of wind shear in elevated layers along with the usually slight temperature stability in elevated shear layers. The usual explanation, that the gradient Richardson number within portions of the layers is small enough to cause the turbulent mixing, is not contradicted by that paper. However, we clearly need to obtain more highly resolved turbulence data in both ground based shear layers and in elevated layers, along with measures of the intermittency of this turbulence, to be absolutely sure that this interpretation is correct.

In a pioneering effort to bring some order out of the chaos of the diversity of facsimile record patterns, Clark and Bendun (1974) proposed a numerical classification scheme. Briefly their pattern types are characterized as follows:

Type 0 - Noisy record or no structure visible.

Types 1-5 Ground based shear layers of increasing depth and showing some horizontal stratification for the types 4 and 5.

Types 6-10 Ground based shear layers with complex, separated elevated bands, descending with time in the types 9 & 10.

Types 11 & 12 Ground-based shear layers with additional elevated layers rising with time.

Type 13 Convective plumes.

In a similar manner, Fukushima et al. (1975) devised a pictorial scheme in which monthly summary charts of facsimile patterns are characterized by alphabetic symbols for wind, precipitation noise, or equipment problems; stratified returns are shown by thick solid lines giving some indication of the structure and appearance in the facsimile charts; and vertical accent symbols are used to characterize convective thermal plumes. In a brief survey paper, Thomson (1975) has provided references to papers treating these various classes of facsimile records.

It seems desirable however, to develop a classification scheme with descriptors that indicate the state of the atmosphere. Enough is now understood about why characteristic facsimile patterns develop to allow this kind of classification.

2. PROPOSED CLASSIFICATIONS

Let us consider first the stably stratified atmosphere. The fundamental echo structure here is the Ground Based Shear Layer (GBSL) shown in Fig. 1. Such layers, measuring from a few tens of meters to several hundred meters thick, show as featureless black bands when the facsimile chart is compressed in time, but they will show distinct, sloping, turbulent wave patterns when the record is stretched out.

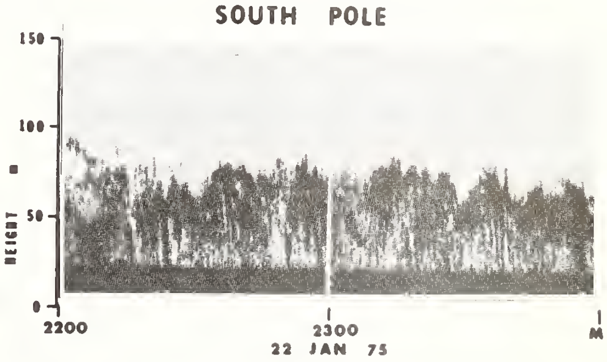

Figure 1. A typical Ground Based Shear Layer (GBSL facsimile).

Such echoes develop when significant wind shear occurs across the ground based stable layer. When this echo appears alone the facsimile can be classified GBSL, followed by the depth of the layer in meters. The classification can be further modified by the adjective "thickening" or "pinching" (T, P) if the layer depth is increasing with time or decreasing with time.

When strong, low-level jets or wind sheets occur within the lower stably stratified region, the GBSL may present a divided appearance.

On stretching out such a facsimile record, the turbulent waves will be found to slope in opposite directions away from the clear, bifurcating region. This pattern represents a modification of the simple shear layer, so it is suggested that the letter B be appended as an adjective to GBSL when the bifurcation appears. Under the strong wind conditions when the GBSL is broken into intermittent bursts, the suffix, I, may be appended to the descriptor.

The GBSL classification may be modified when separated layers aloft occur on the facsimile record. When such layers are clearly not directly associated with the GBSL (as in the bifurcated pattern) it is suggested that EL (elevated layers aloft) be appended to the GBSL designation. In addition, the adjectives "ascending" or "descending" may be appended to the EL modifier since the appearance of these layers may be important in depicting mesoscale subsidence or convergence above the GBSL.

A second general category of the stably stratified atmospheric echoes involves layers separated from the surface, multiple layers, or density currents. When a single elevated shear layer (perhaps quite similar to the GBSL but clearly separated from the surface) is observed it can be classified as an elevated shear layer (ESL) followed by the elevation in meters, or for thick layers, the elevation range. When the layer is known to correspond with a stratus top this designation may be appended to the descriptor.

Under low wind conditions, the appearance of multiple, decoupled layers may occur as shown in Fig. 2. It is suggested that these be simply identified as multiple layers (ML) with the range in elevation appended. Such additional descriptors as undulating (U) may be appended when wave amplitude in the layers significantly exceeds layer thickness. In addition, when complex breaking wave, descending, ascending, or interleafed layers appear it is suggested that the ML pattern be described as complex (C), this being indicative of significant changes occurring in the elevated patterns but probably associated with rather low kinetic energies, for otherwise the patterns would not be separately discerned and decoupled.

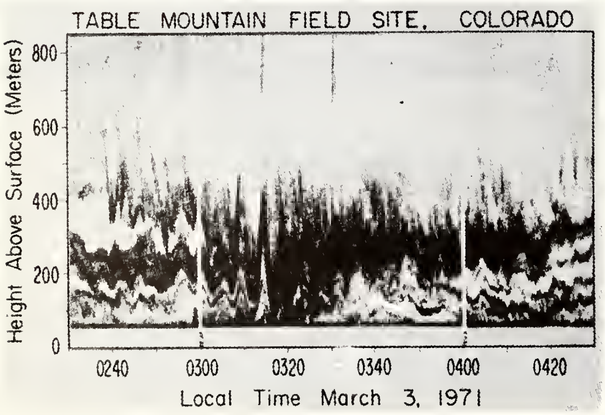

Figure 2. The Multiple Layer (ML) type echo, also Complex (C).

Density currents, be they caused by synoptic or mesoscale fronts, cool outflows from storms, or katabatic winds, may be described as DC. These are transient events, which will probably decay into one or another of the preceding designations after an hour or so. A source descriptor can be appended when the cause of the density current echo is known. When breaking waves appear within the current, as exemplified by Fig. 3, that appearance also seems dynamically significant enough to merit an appending descriptor, BW.

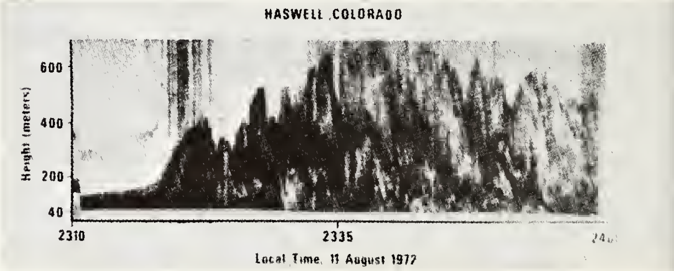

Figure 3. A Density Current (DC) pattern, with Breaking Waves (BW).

When we come to the convectively unstable atmosphere, the convective plume (CP) will be the typical echo. An example is shown in Fig. 4. It may be desirable to append to the CP designation the height to which the plumes can be observed.

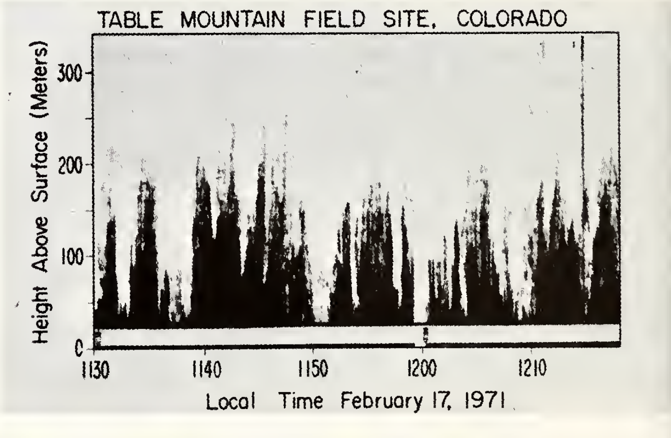

Figure 4. Convective Plume (CP) echoes.

Often combinations of the above descriptors will occur on a single facsimile record. It is suggested that the classifications provided can be used in sequence progressing upward from the surface to describe the features depicted. For example, in Fig. 5 we find convective plumes capped by an elevated shear layer;

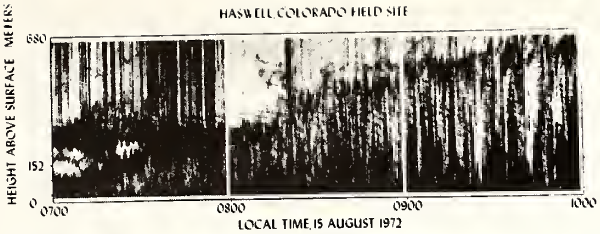

Figure 5. Convective Plumes capped by an Elevated Layer, Ascending (CP, EL, A).

the classification for this record would be CP ESL with the additional qualifier "ascending" applied to the elevated layer.

3. USE OF DESCRIPTORS

It is believed that the descriptors suggested above can be made to fit any facsimile record. When an acoustic sounder is being used to obtain a climatology of the planetary boundary layer, tables of descriptors and appropriate heights for each hour (or possibly somewhat longer) can be assembled, thus providing a semi-quantitative record of what the boundary layer is doing at a particular site. Schubert (1975) gives examples of such climatological record use at two sites in the eastern United States. In any tabular classification of boundary layer structure it is almost essential to have a remarks column for further explanation of unusual events, such as the mesoscale or occluded synoptic scale fronts described by Parry et al. (1975).

It is possible that all of the above classes of echoes can occur within a few hours on a single facsimile record. This is nearly the case in Fig. 6 which begins with a ground-based shear layer that separates on the arrival of colder air (here over the Antarctic ice cap). The convective plumes result from cold air overlying a warmer surface while the multiple layers aloft represent shear interfaces associated with the cold front.

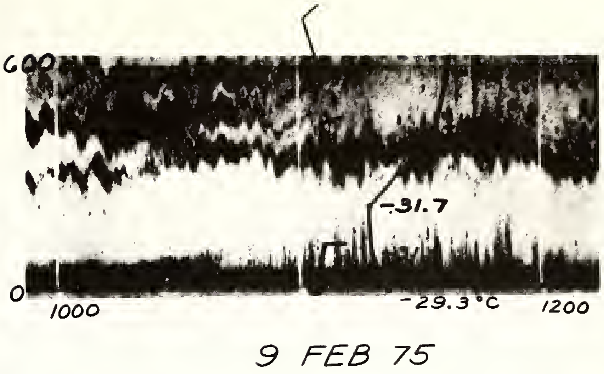

Figure 6. A multiple classification record, (GBSL, 60, ML 300-600, U) changing to (CP, 150, EL 300, U). Here U stands for Undulations.

We have found that all of the descriptors given above can be made to fit onto a single IBM card together with numerical notations of the heights of the layer. By coding the facsimile records in this manner it is possible to assemble much information on the climatology of the planetary boundary layer at the site under investigation. Then such questions can be asked: What is the typical depth of the nocturnal surface-based inversion? How quickly do convective plumes erode the inversion in the morning? How often do density currents modify the cooling rate under nocturnal conditions? When these climatological data are combined with surface observations of temperature and wind, the mesoscale meteorologist can confidently describe boundary layer characteristics to his associates in agricultural meteorology, air pollution monitoring, or airport terminal forecasting disciplines with a high degree of confidence in the correctness of his analyses.

4. REFERENCES

Clark, G. H., and E. O. K. Bendun, 1974. Meteorological research studies at Jervis Bay, Australia. Australian Atomic Energy Comm., Report AAEC/E309, Lucas Heights, Australia, 97 pp.

Estival, A. and M. Aubry, 1976. Interpretation des echos sodar en terme de stratifications atmospheriques, *La Météorologie* 6, No. 5 33-42.

Fukushima, M., K. Akita, and H. Tanaka, 1975. Sodar probing of small-scale temperature structures in the clear atmosphere. *J. Radio Res. Labs. Japan* 22, 23-43.

Parry, H. D., M. J. Sanders, Jr., and H. P. Jensen, 1975. Operational applications of a pure acoustic sounding system. *J. Appl. Meteorol.* 14, 67-77.

Schubert, J. F., 1975. A climatology of the mixed layer using acoustic methods, Preprints Third Symposium Meteorol. Obs. and Instrum., Amer. Meteorol. Soc., Boston, 151-156.

Thomson, D. W., 1975. ACDAR meteorology: The application and interpretation of atmospheric acoustic sounding measurements. Preprints Third Symposium Meteorol. Obs. and Instrum., Amer. Meteorol. Soc., Boston, 144-150.

Journal of Atmospheric Sciences, 35: 18-24, 1978.

Horizontal Velocity Spectra in an Unstable Surface Layer

J. C. Kaimal

NOAA/ERL/Wave Propagation Laboratory, Boulder, Colo. 80302

(Manuscript received 27 May 1977, in final form 20 September 1977)

ABSTRACT

Data from a boundary-layer experiment conducted over a flat, uniform site in Minnesota provide a clue to the behavior of the low-frequency peak in surface-layer horizontal velocity spectra. This portion of the spectra shows systematic behavior only when plotted in dimensionless coordinates appropriate to the mixed layer, whereas the inertial subrange frequencies follow Monin-Obukhov similarity. Based on this observation, interpolation formulas for both the longitudinal and the lateral velocity components are derived. The expressions involve the boundary-layer depth in addition to the usual surface-layer parameters.

1. Introduction

A fairly complete understanding of the spectral and cospectral behavior of turbulence in atmospheric boundary layers has emerged from observational studies[1] conducted by various investigators over the last two decades. The 1968 AFCRL experiment in Kansas (Kaimal *et al.*, 1972) showed that the spectra of wind and temperature, in general, follow Monin-Obukhov similarity within the surface layer.[2] It was observed that spectra from different heights and stabilities, when plotted in dimensionless surface layer coordinates, tend to arrange themselves according to the dimensionless length scale z/L, where z is the height above ground and L the Obukhov length as normally defined. The notable exceptions were the energy-containing regions of the horizontal velocity components u and v in unstable air ($z/L<0$). The low-frequency portion of these spectra followed no particular order as they spread over a wide area on the plots. The w (vertical velocity) spectra, on the other hand, showed an orderly progression of the spectral peak and the low-frequency roll-off with z/L. This behavior implied that some length scale other than z controlled low-frequency spectral behavior in the horizontal components.

Actual evidence of such a length scale was found in spectra obtained from the 1973 AFCRL/MRU[3] boundary-layer experiment in northwestern Minnesota. The data showed the wavelength of the spectral maximum in u and v to be virtually invariant with height but varying with z_i, the depth of the convective boundary layer (Kaimal *et al.*, 1976). The data also showed that velocity spectra (u, v, w) from heights $z>0.1z_i$ can be generalized within the framework of a similarity relationship appropriate to the mixed layer, where z_i is the only length scale, and the surface friction velocity u_*, a critical parameter in the surface layer, has little effect.

The evidence from the Kansas and Minnesota experiments points to a horizontal velocity field that follows different similarity laws in different regions of the spectral range in the surface layer. The objective of this paper is to develop a general framework within which the behavior of u and v over the entire spectral range can be expressed.

2. Broad features of surface-layer spectra

The significant aspects of spectral behavior in the surface layer can be identified in the plots of Fig. 1. The inertial subrange intensity in u falls off rapidly with height and approaches a nearly constant value in the mixed layer ($z_i>z>0.1z_i$). This constant value corresponds to a turbulent dissipation rate ϵ roughly one-half the buoyant production rate at the surface (Q_0g/T) in an undisturbed convective boundary layer (Lenschow, 1974; Pennell and LeMone, 1974; Kaimal *et al.*, 1976). The low-frequency peak at wavelength $\lambda\approx 1.5z_i$ seems unaffected by the variations in the inertial subrange. The v spectrum resembles u in its low-frequency behavior, but tends to maintain an inertial subrange value approximately $\frac{4}{3}$ higher than u, consistent with the requirement for isotropy. The same relationship is maintained in the w spectrum within the inertial subrange (see Fig. 1), but the resemblance between v and w ends here as w reaches its maximum value within a decade of $\lambda = z$ and rolls off at a rapid rate. The v spectrum can therefore be viewed as straddling u and w at either end of the plot, following the u spectrum at wavelengths on the order of z_i and the w spectrum at wavelengths less than z, as shown in Fig. 2.

---

[1] For surveys of these studies see Busch and Panofsky (1968), Busch (1973) and Panofsky (1974).

[2] In this paper, the terms "surface layer" and "mixed layer" are used in reference to the constant flux layer and the layer of near-zero wind and potential gradients above it (Kaimal *et al.*, 1976), respectively.

[3] Meteorological Research Unit, RAF Cardington, U.K.

For convenience, the spectral range will be divided into three regions: region 1, where the spectrum falls off as $n^{-5/3}$ in accordance with the power law predicted for the inertial subrange; region 2, which is a transition between regions 1 and 3; and region 3, where the spectrum shows little if any variation with height. The u and v spectra behave differently in the transition region. While a straight-line approximation is a good one for u, the v spectrum is more complicated with an inflection point at approximately the frequency at which w reaches a maximum. The low-frequency side of the w spectra seems to behave entirely independently of u and v in the surface layer, varying only as a function of z/L (see Fig. 2). In the following sections, the surface layer u and v spectra from the Minnesota experiment will be examined for empirical relationships describing spectral behavior in each of the three regions.

3. Description of data set

The runs selected for this study are the 11 runs used by Kaimal *et al.* (1976) for analysis of mixed-layer spectra. A summary of the mean profiles, variances and fluxes for those periods can be found in the data report by Izumi and Caughey (1976). Readings *et al.* (1974) described the site and the instrumentation used in the experiment. The spectra used here were obtained from three-axis sonic anemometer measurements at 4 and 32 m. Procedures used for computing spectra were described by Kaimal *et al.* (1976). The spectra were subjected to minor smoothing by eye to average out the peaks and valleys near that low-frequency end. A wide range of z/L and z_i/L values are covered in the 22 spectra examined here. Parameters relevant to this study are listed in Table 1. Definitions of the symbols are given in the Appendix.

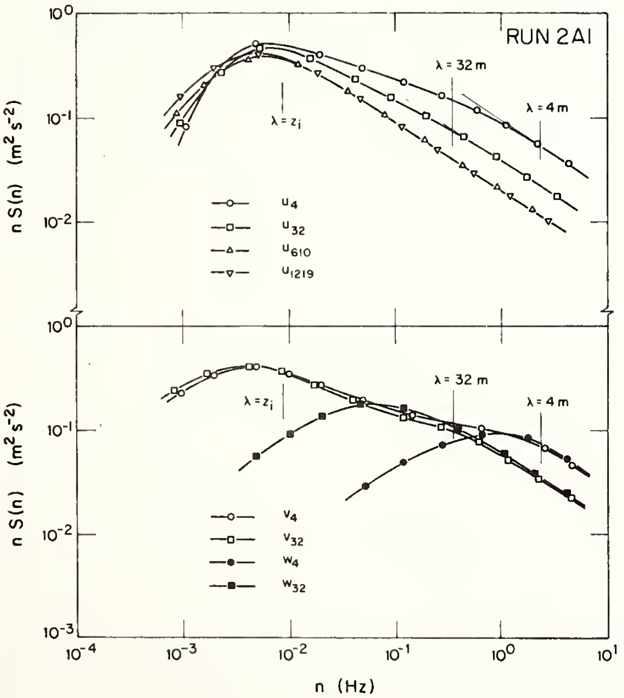

FIG. 1. Typical u, v and w spectra in the boundary layer. Note the decrease in the inertial subrange levels with height and the approach of u to a limiting form above the surface layer.

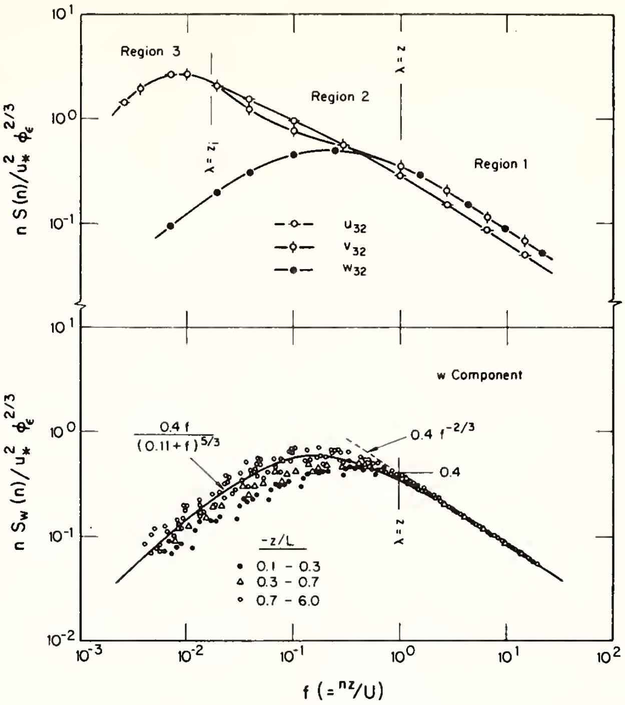

FIG. 2. The spectra of u and v from Run 3A1 (upper plot) showing the frequency range separated into three regions according to scaling laws obeyed in each. Regions 1 and 3 scale with z and z_i, respectively, whereas region 2 provides the transition between the two. The w spectrum shows no such separation. The composite plot of all 4 and 32 m w spectra (lower plot) suggests that a single curve may be used to approximate the shape of w over a wide range of z/L values.

4. Development of empirical forms

Expressions for spectra in regions 1 and 3 are easily derived from the results of earlier studies. The formulations for region 2, however, present some difficulties. The transition from surface-layer to mixed-layer coordinates has to be accomplished while retaining the essential characteristics of the two spectra including the crossover between u and v (see Fig. 2). No simple solution exists, but an approximation to the spectral shapes can be achieved by

TABLE 1. Dimensionless parameters for selected runs.

Run	z(m)	$-z/L$	$\phi_\epsilon^{2/3}$	$-z_i/L$	σ_H^2/u_*^2
2A1	4	0.10	0.87	30.0	9.66
	32	0.77	1.29	30.0	8.93
2A2	4	0.11	0.92	42.5	9.16
	32	0.84	1.29	42.5	8.02
3A1	4	0.17	1.21	96.3	15.47
	32	1.33	1.80	96.3	16.64
3A2	4	0.16	1.25	94.7	14.06
	32	1.32	1.65	94.7	13.76
5A1	4	0.56	1.56	152.8	17.35
	32	4.50	3.13	152.8	16.25
6A1	4	0.70	1.75	367.5	34.75
	32	5.61	3.51	367.5	33.68
6A2	4	0.63	1.73	318.0	34.42
	32	5.00	3.40	318.0	31.35
6B1	4	0.18	1.14	104.0	15.15
	32	1.41	1.90	104.0	16.00
7C1	4	0.46	1.35	115.9	21.77
	32	3.64	2.49	115.9	20.13
7C2	4	0.31	1.15	79.4	16.67
	32	2.44	2.04	79.4	15.33
7D1	4	0.30	1.29	90.7	19.03
	32	2.37	2.37	90.7	19.35

assuming a power law for the spectrum and adjusting the upper and lower limits of region 2.

For region 1 we will use the expressions derived by Kaimal *et al.* (1972) from the Kansas spectra:

$$\frac{nS_u(n)}{u_*^2\phi_\epsilon^{2/3}}=\frac{\alpha_1}{(2\pi k)^{2/3}}f^{-2/3}\approx 0.3f^{-2/3}, \tag{1}$$

$$\frac{nS_v(n)}{u_*^2\phi_\epsilon^{2/3}}=\frac{4nS_u(n)}{3u_*^2\phi_\epsilon^{2/3}}\approx 0.4f^{-2/3}, \tag{2}$$

where ϕ_ϵ is a dimensionless dissipation rate $(=kz\epsilon/u_*^3)$ and f is the dimensionless frequency $(=nz/U)$. The approximation used for the coefficient $\alpha_1(2\pi k)^{2/3}$ fits the range of values generally used[4] for α_1 and k.

According to Monin-Obukhov similarity, ϕ_ϵ should be a function only of z/L. The validity of this prediction is reaffirmed in Fig. 3 where the relationship is approximated by

$$\phi_\epsilon^{2/3}=1+0.75|z/L|^{2/3}. \tag{3}$$

This formula is similar to the derived from the Kansas data, except for the larger coefficient. The Kansas relationship, obtained over a narrower $-z/L$ range (0 to 2.0), was $1+0.5|z/L|^{2/3}$.

The mixed-layer u spectrum is the logical choice for the spectral shape in region 3. The spectrum has a simple functional form and furthermore would serve as the limiting shape for the u spectrum as z extends into the mixed layer. The frequency-weighted spectrum, when normalized by the variance in u to remove run-to-run variations in the spectral level, assumes the form

$$\frac{nS_u(n)}{\sigma_u^2}=\frac{f_i}{1+3.1f_i^{5/3}}, \tag{4}$$

where f_i is the dimensionless frequency $(=nz_i/U)$ appropriate to the mixed layer. The expression on the right satisfies several requirements: it falls off as $f_i^{-2/3}$ at large f_i's, peaks at a wavelength roughly 1.5 times the boundary layer depth as observed by Kaimal *et al.* (1976), and integrates to unity when divided by f_i.

With $nS_u(n)=f_iS_u(f_i)$ we have

$$\int_0^\infty \frac{S_u(f_i)}{\sigma_u^2}df_i\equiv 1=\int_0^\infty \frac{df_i}{1+3.1f_i^{5/3}}.$$

Since $\sigma_u^2\approx\sigma_v^2$, the average of the two, denoted by σ_H^2, will be used in the formulas for region 3, i.e.,

$$\frac{nS_u(n)}{\sigma_H^2}=\frac{nS_v(n)}{\sigma_H^2}=\frac{f_i}{1+3.1f_i^{5/3}}. \tag{5}$$

Normalizing by σ_H^2 permits conversion of (5) to surface-layer coordinates through the empirical relationship (see Fig. 3) suggested by Panofsky *et al.* (1977):

$$\sigma_H/u_*=(12+0.5|z_i/L|)^{1/3}. \tag{6}$$

Figs. 4 and 5 show how (1), (2) and (5) fit the data and where the limits of regions 1 and 3 might be.

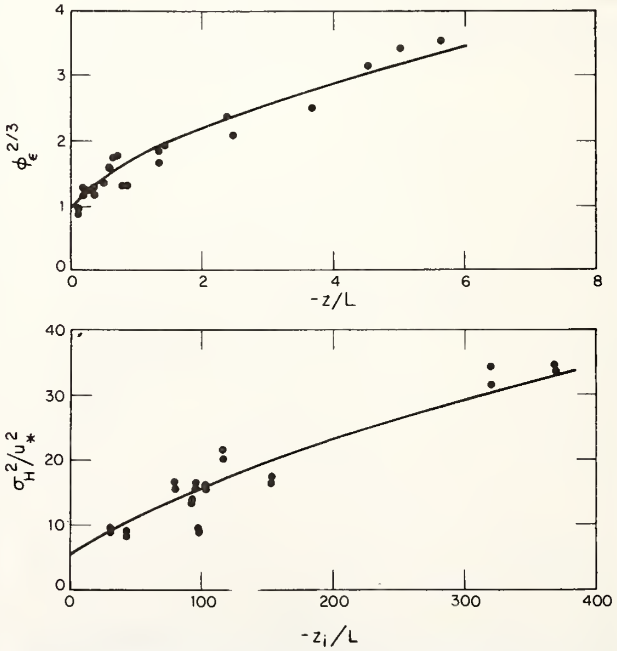

FIG. 3. Dimensionless plots of turbulence dissipation rate and horizontal velocity variance approximated by relationships in (3) and (6), respectively.

---

[4] A combination of $\alpha_1=0.5$ and $k=0.35$ (used with the Kansas data) or $\alpha_1=0.52$ and $k=0.4$ yield the same value for the coefficient. This interrelationship between α_1 and k is merely an accident of the spectral normalization used in (1).

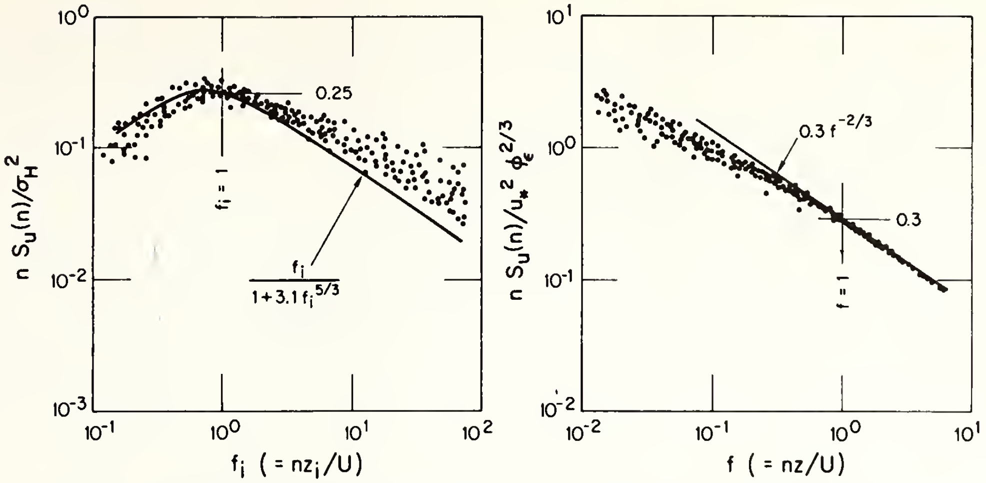

FIG. 4. Composite plots of the upper and lower ends of the *u* spectra showing fit with empirical formulations for regions 1 and 3.

In the absence of independent ϵ measurements, all spectra have been constrained to fall on a single line in the inertial subrange, consistent with (1) and (2). The *u* spectra depart from this line at approximately $f=0.5$, whereas the *v* spectra begin to deviate an octave higher, at around $f=1.0$. On the low-frequency side the data points can be seen following (5) over different ranges on the f_i scale. For *u* and *v* the high-frequency limits are approximately 1.5 and 4.0, respectively.

These limits can now be used to define the upper and lower limits for region 2. The simplest approximation to the spectral shape in this region is a straight line interpolation on the full logarithmic plot, i.e., a power law satisfying the requirement for continuity at the end points. If $-p$ and $-q$ are the slopes for *u* and *v*, they can be defined in terms of the coordinates of the spectra on either side (see Fig. 6).

Eq. (5) can be expressed in surface layer coordinates as

$$\frac{nS_u(n)}{u_*^2\phi_\epsilon^{2/3}}=\frac{nS_v(n)}{u_*^2\phi_\epsilon^{2/3}}\approx\frac{ABf}{1+3.1(Bf)^{5/3}}, \tag{7}$$

where

$$\left.\begin{aligned} A&=\frac{(\sigma_H/u_*)^2}{\phi_\epsilon^{2/3}}\approx\frac{(12+0.5|z_i/L|)^{2/3}}{1+0.75|z/L|^{2/3}}\\ B&=z_i/z \end{aligned}\right\}. \tag{8}$$

With *A* and *B* thus defined, the expressions for *p* and *q* reduce to

$$\left.\begin{aligned} p&=\frac{(\ln 0.44A)}{(\ln 0.33B)}\\ q&=\frac{(\ln 0.30A)}{(\ln 0.25B)} \end{aligned}\right\}. \tag{9}$$

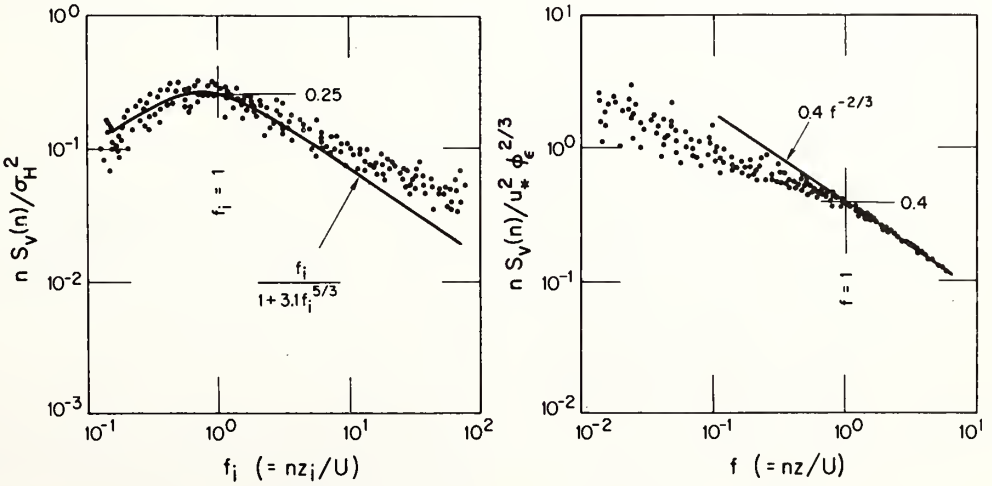

FIG. 5. As in Fig. 4 except for the *v* spectra.

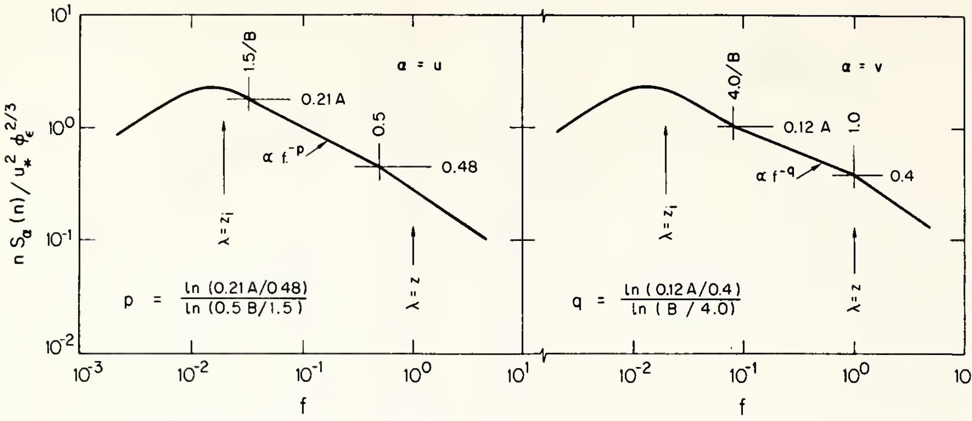

FIG. 6. Schematic of the spectral curves showing the end points of spectra in region 2 and the derivation of spectral slopes in that region. A and B are functions defined in (8).

The equations for the u and v spectra become

$$\frac{nS_u(n)}{u_*^2\phi_\epsilon^{2/3}}=0.48(2f)^{-p}, \tag{10}$$

$$\frac{nS_v(n)}{u_*^2\phi_\epsilon^{2/3}}=0.40f^{-q}. \tag{11}$$

Combining the equations for all three regions we have

$$\frac{nS_u(n)}{u_*^2\phi_\epsilon^{2/3}}=\begin{cases}0.3f^{-2/3}, & \lambda\leqslant 2z\\ 0.48(2f)^{-p}, & 0.67z_i\geqslant\lambda\geqslant 2z\\ ABf/[1+3.1(Bf)^{5/3}], & \lambda\geqslant 0.67z\end{cases} \tag{12}$$

$$\frac{nS_v(n)}{u_*^2\phi_\epsilon^{2/3}}=\begin{cases}0.4f^{-2/3} & \lambda\leqslant z\\ 0.4f^{-p}, & 0.25z_i\geqslant\lambda\geqslant z\\ ABf/[1+3.1(Bf)^{5/3}], & \lambda\geqslant 0.25z_i\end{cases} \tag{13}$$

where A, B, p and q are defined as in (8) and (9).

5. Evolution of the velocity spectra with height

Having developed the spectral forms for u and v in the surface layer it is of interest to see how they evolve into the mixed-layer spectra and how their evolutions compare with that of w. Kaimal *et al.* (1976) have shown that all three components have essentially the same spectral shape in the mixed layer. The contrasts between them become increasingly apparent as one approaches the surface layer.

The composite plot of the w spectrum for all 11 runs used in this study (see Fig. 2) shows a fairly tight grouping of data points in the z/L range from -0.7 to -5.6. The spectra in this range can be approximated by

$$\frac{nS_w(n)}{u_*^2\phi_\epsilon^{2/3}}=\frac{0.4f}{(0.11+f)^{5/3}}. \tag{14}$$

It has its maximum at $f=0.17$, which is in agreement with previous observations (Kaimal *et al.*, 1972, 1976), and falls off as $0.4f^{-2/3}$ at large f's. The only significant departure from the data is its more gradual approach

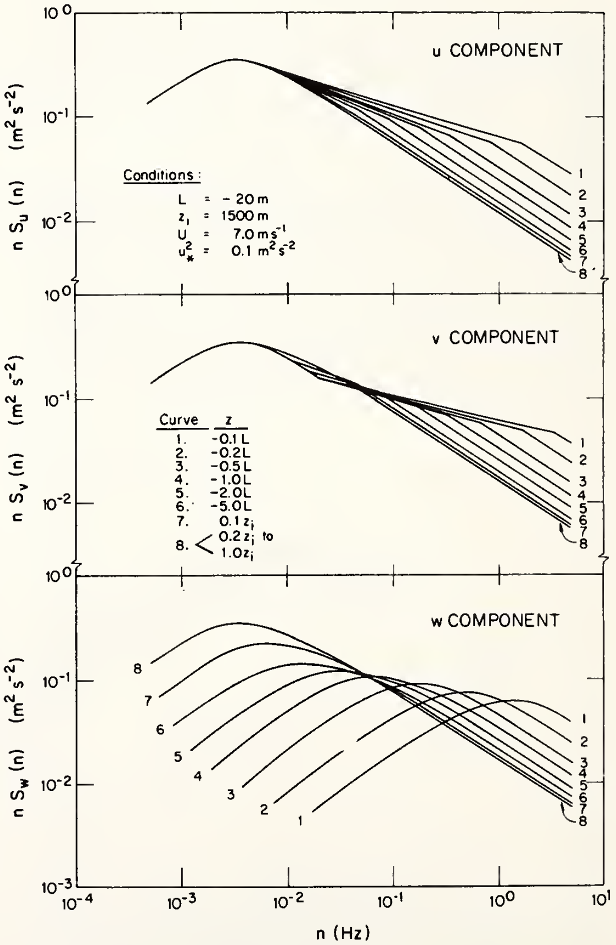

FIG. 7. Evolution of the velocity spectra with height for a hypothetical run.

to the $-\frac{2}{3}$ slope than is justified by the data. Spectra for the less unstable runs, placed somewhat lower in Fig. 2 compared to the empirical curve, peak at a higher frequency and have a shallower slope on the low-frequency side.

The spectral curves for u, v and w for typical values of $L=-20$ m, $z_i=1500$ m, $U=7.0$ m s^{-1} and $u_*^2=0.1$ m^2 s^{-2} are plotted in Fig. 7. The only difference between the mixed-layer u and v spectra is the $\frac{4}{3}$ ratio between their inertial subrange levels. The spectra of w and v have the same form in the mixed layer, but the similarity disappears as z drops below $0.2z_i$. The w spectrum encounters a steady depletion of energy on the low-frequency side as z approaches zero, but no such depletion occurs in u and v. Thus, in the surface layer, the velocity field is essentially two-dimensional at low frequencies (region 3) and becomes truly three-dimensional at wavelengths shorter than the height above ground (region 1).

In plotting the curves in Fig. 7 some adjustments were made to curves 6, 7 and 8 of the v component to smooth the transition between regions 1 and 3. A discontinuity might otherwise exist due to the v spectrum being higher by a factor of $\frac{4}{3}$ compared to u. The sharp corners not withstanding, these and the other curves in Fig. 7 are entirely consistent with spectral behavior observed during the Minnesota experiment.

It should be pointed out that the spectral behavior outlined here is based on observations over a flat, featureless terrain. How the behavior might be over irregular terrain cannot be predicted since the interaction between terrain length scales and spectral scales is not known. Extensive data from carefully designed experiments are needed to establish such relationships. It is also not clear if spectra in the marine atmosphere surface layer would exhibit the same characteristics observed here. Differences in the organization of large-scale convection over oceans and the changing patterns of surface roughness can have significant effects on the spectral shape.

A point not addressed so far in this paper is whether an Eulerian spectrum can provide a reasonably accurate representation of the spatial field when different regions of the spectrum are transported at different velocities. Since the low- and high-frequency ends follow different scaling parameters, it is conceivable that their translation velocities are also different. For example, if the small-scale eddies move at some low velocity associated with u_* as observed by Kaimal (1974), while the large convection cells, which extend through the entire boundary layer, move at a mean wind speed near their center of gravity, the effect would be to narrow the separation between those two scales in spectra constructed from a point measurement. An aircraft flying in the surface layer would find region 2 to be wider than in Eulerian spectra converted to spatial scales through the assumption of Taylor's hypothesis. How serious the discrepancy might be cannot be determined without simultaneous aircraft and tower measurements in the surface layer. The effect of a fluctuating advection velocity on spectra measured in an Eulerian framework has been explored by Wyngaard and Clifford (1977). They find the large-wavenumber properties disturbed by the fluctuations. Under typical conditions in the atmospheric boundary layer the effect is negligible in the inertial subrange, although serious errors can be expected at very high frequencies.

6. Summary

The behavior of unstable surface layer u and v spectra can be generalized if different portions of the spectra are expressed in different similarity coordinates. For this purpose the spectra can be divided into three regions: an inertial subrange region ($\lambda<z$), an energy-containing region ($\lambda>z_i$) and a transition region ($z<\lambda<z_i$). The inertial subrange of both spectra follows Monin-Obukhov similarity, whereas their energy-containing region follows a mixed-layer similarity where z_i is the only controlling length scale. Expressions for the horizontal velocity spectra therefore involve z_i in addition to the usual surface-layer parameters. Empirical forms for the three velocity spectra are derived. The evolution of these spectra with height show how the velocity components approach their mixed-layer forms.

Acknowledgments. The data used in this paper were gathered and processed through the cooperative effort of members of the former Boundary Layer Branch of AFCRL and the Meteorological Research Unit at Cardington. The author is grateful to Drs. H. A. Panofsky and J. C. Wyngaard for helpful discussions and suggestions and to Mrs. Mildred Birchfield for the preparation of the manuscript.

APPENDIX

List of symbols

U	mean wind speed
u, v, w	fluctuating wind components in the longitudinal, lateral and vertical wind directions
T	mean temperature
u_*	surface friction velocity
Q_0	surface kinematic heat flux
g	acceleration due to gravity
k	von Kármán's constant
z	height above ground
z_i	depth of the convective boundary layer
L	Obukhov length $[=-u_*^3/k(g/T)Q_0]$
n	cyclic frequency
λ	wavelength $[\approx U/n]$
f	dimensionless frequency $[=nz/U]$

f_m	dimensionless frequency at the spectral peak
f_i	dimensionless frequency $[=nz_i/U]$
$S(n)$	one-dimensional spectral density
α_1	spectral constant for one-dimensional u spectrum
ϵ	dissipation rate of turbulent kinetic energy
ϕ_ϵ	dimensionless dissipation rate $[=kz\epsilon/u_*^3]$
σ_u, σ_v	standard deviations of u and v
σ_H^2	horizontal velocity variance $[=(\sigma_u^2+\sigma_v^2)/2]$
A	function of z/L and z_i/L
B	dimensionless height $[=z_i/z]$
p	spectral slope for u in region 2.
q	spectral slope for v in region 2.

REFERENCES

Busch, N. E., 1973: The surface boundary layer. *Bound.-Layer Meteor.*, 4, 213–240.

——, and H. A. Panofsky, 1968: Recent spectra of atmospheric turbulence. *Quart. J. Roy. Meteor. Soc.*, **94**, 132–148.

Izumi, Y., and S. J. Caughey, 1976: Minnesota 1973 atmospheric boundary layer experiment data report. AFCRL Res. Pap. No. 547, AFCRL-TR-76-0038, 28 pp.

Kaimal, J. C., 1974: Translation speed of convective plumes in the atmospheric surface layer. *Quart. J. Roy. Meteor. Soc.*, **100**, 46–52.

——, J. C. Wyngaard, Y. Izumi and O. R. Coté, 1972: Spectral characteristics of surface layer turbulence. *Quart. J. Roy. Meteor. Soc.*, **98**, 563–589.

——, ——, D. A. Haugen, O. R. Coté, Y. Izumi, S. J. Caughey and C. J. Readings, 1976: Turbulence structure of the convective boundary layer. *J. Atmos. Sci.*, **33**, 2152–2169.

Lenschow, D. H., 1974: Model of the height variation of the turbulence kinetic energy budget in the unstable planetary boundary layer. *J. Atmos. Sci.*, **31**, 465–474.

Panofsky, H. A., 1974: The atmospheric boundary layer below 150 m. *Advances in Geophysics*, Vol. 18A, Academic Press, 174–177.

——, H. Tennekes, D. H. Lenschow and J. C. Wyngaard, 1977: The characteristics of turbulent velocity components in the surface layer under convective conditions. Submitted to *Bound.-Layer Meteor.*

Pennell, W. T., and M. A. LeMone, 1974: An experimental study of turbulence structure in the fair-weather, trade wind boundary layer. *J. Atmos. Sci.*, **31**, 1308–1323.

Readings, C. J., D. A. Haugen and J. C. Kaimal, 1974: The 1973 Minnesota atmospheric boundary layer experiment. *Weather*, **29**, 309–312.

Wyngaard, J. C., and S. F. Clifford, 1977: Taylor's hypothesis and high-frequency turbulence spectra. *J. Atmos. Sci.*, **34**, 922–929.

Preprint Volume; 18th Conference on Radar Meteorology, 49-54,
American Meteorological Society, 1978.

DOPPLER RADAR MEASUREMENTS OF PLUME DISPERSAL AND DISSIPATION RATES IN THE BOUNDARY LAYER

W. R. Moninger, A. S. Frisch
W. C. Campbell, and R. G. Strauch
NOAA/ERL/Wave Propagation Laboratory
Boulder, CO 80302

1. INTRODUCTION

Measurement of pollutant concentration downwind of elevated point sources has been of considerable interest for some years. Studies have centered on laboratory modelling (e.g. Willis and Deardorff, 1976) and in situ surface measurements (e.g. Islitzer, 1961, Islitzer and Dumbauld, 1963). Studies of three-dimensional pollutant concentrations in plumes in the atmosphere have been rare.

We present two case studies of simulated pollutant plumes from an elevated point source. The plumes consisted of microwave-reflecting chaff released from atop a 150 meter tower. This chaff was released in a continuous stream which lasted for about 15 minutes. We report on the results of two releases at different times during the same day. The plumes were tracked by radar, allowing us to measure relative chaff density as a function of x, y, z and t. In addition, because the radar had Doppler capability, we were able to measure the turbulent kinetic energy dissipation rate within each plume.

2. DESCRIPTION

The 150 m tower is located near Haswell, Colo. The tower stands in the center of a shallow bowl, approximately 75 m deep and 25 km in diameter. The vegetation around the site is buffalo grass about 15 cm high.

The radar was located 7.2 km from the tower, at a bearing of 355°. The wavelength of the radar was 3.2 cm, and the beamwidth was 0.9°. The sample pulse length was about 75 m in depth, and the scanning was such that spacing between radar pulse-volumes was between 100 and 200 m in azimuth, elevation and range.

3. CASE 1, PLUME 6, MARCH 21, 1974

The release of a continuous stream of chaff shown in figure 1 was begun at 0858 local standard time. The ambient temperature at the surface was -3°C, and the wind was out of 200° at 4-5 m/s. Vertical wind shear, as measured by the NCAR boundary layer profiler, was less than .005 s^{-1}. The mixed layer height, as estimated from acoustic sounder records, and from the extent of vertical chaff diffusion, was 350 m.

The plume was scanned for approximately 20 min, until it extended 6.5 km downwind.

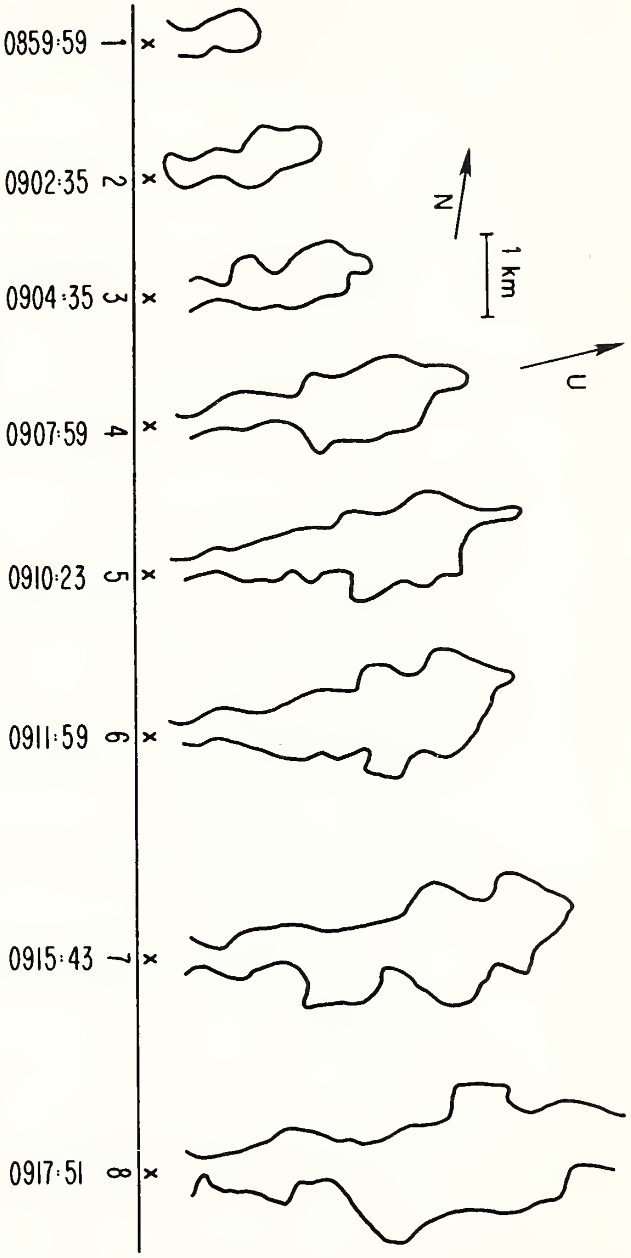

Figure 1. Vertically-integrated chaff concentration for 8 volume scans of Plume 6 (plan view). Scan starting times are indicated. The X's mark the release point.

Figure 1 shows plan views of vertically-integrated chaff concentration at the times indicated. The contour is for a value of relative concentration just slightly above the minimum value detectable by the radar (20 units/km^2). Examination of figure 1 shows considerable variability of crosswind width of the plume. The width can vary quite suddenly, as may be seen particularly well by comparing scan 3 with scan 4, and scan 6 with scan 7. Because these changes in width occur sometime after the chaff has been released from the tower, we conclude that the width variability is not a possible result of clumping of chaff at the release point, but is rather due to meteorological effects. No large-scale bends are seen in the plume, indicating that the wind direction was roughly constant over the area during the 20 min observation time.

Figure 2 shows downwind vertical sections of chaff concentration integrated over the crosswind plume direction. The location of the release point on the tower is indicated by the cross; the wind is blowing toward the right. The contours are drawn at intervals of 56 units/km^2, a value of density somewhat above that of figure 1.

The dashed contour is for twice the chaff concentration of the outer contour. Thus, we see evidence of a rather strong gradient of intensity near the edges of the plume. Maximum concentrations in small volumes within the plume achieve about ten times the value shown by the solid contour.

A cellular structure is evident in figure 2. We attribute this to the effect of large convection cells on the chaff. Such plumes were evident in simultaneous acoustic sounder records, where they showed a spacing of about 1 km if we can assume that the cells are frozen in space and move at the measured speed as shown in a similar situation by Frisch et al. 1975. This is in agreement with the spacing seen in figure 2 between the chaff cells.

The vertical extent of the plume shows that the chaff fills the depth of the boundary layer rather quickly. Chaff has risen to 350 m within 2-3 minutes after it was released.

Finally, in scan 8, evidence of the finite fall velocity of the chaff (~27 cm/sec) can be seen, as the maximum and the average depth of the plume begin to decrease.

4. CASE 2, PLUME 13, MARCH 21, 1974

The plume shown in figure 3 was released from 1745 until 1800 local standard time. The ambient temperature at the surface was +7°C, and the wind was out of 147° at 7 m/s. The mixed layer height, estimated from the vertical extent of the chaff plume was 1500 m. The plume was scanned for approximately 20 minutes, until it had a downwind extent of more than 9 km.

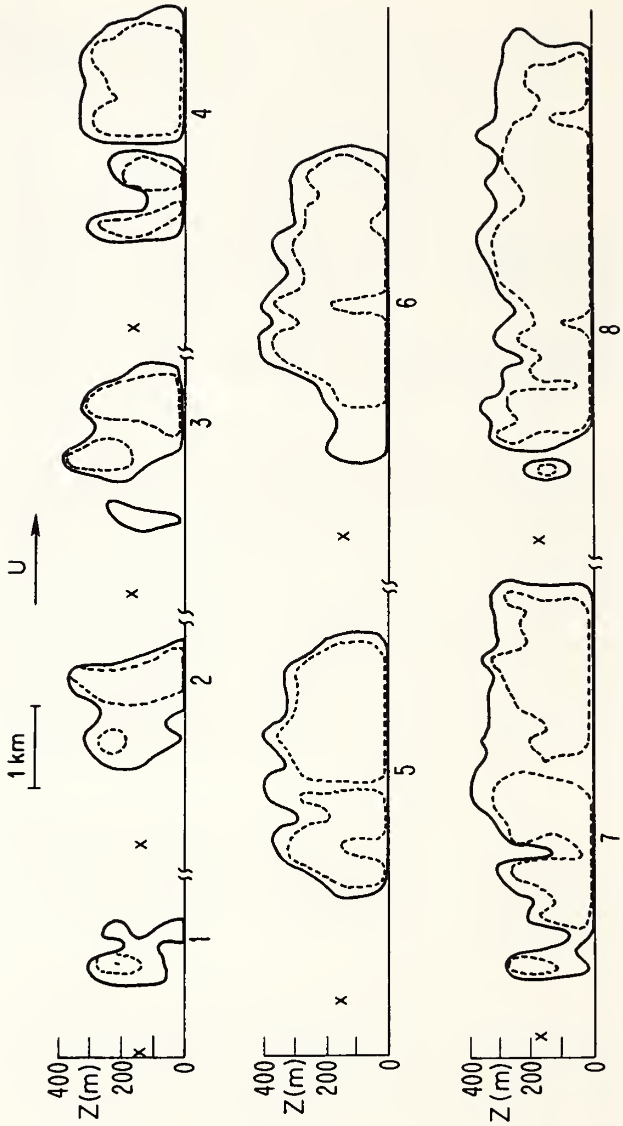

Figure 2. Crosswind-integrated chaff concentration for the 8 volume scans shown in figure 1.

Figure 3 gives a plan view of vertically-integrated chaff concentration between 0 m and 800 m. The contour is drawn at 23 units/km^2. As will be seen, the plume often extended above 800 m, however these high "towers" always occurred above lower parts of the plume, so that 0-800 m integration gives a reasonable representation of the plume's horizontal extent.

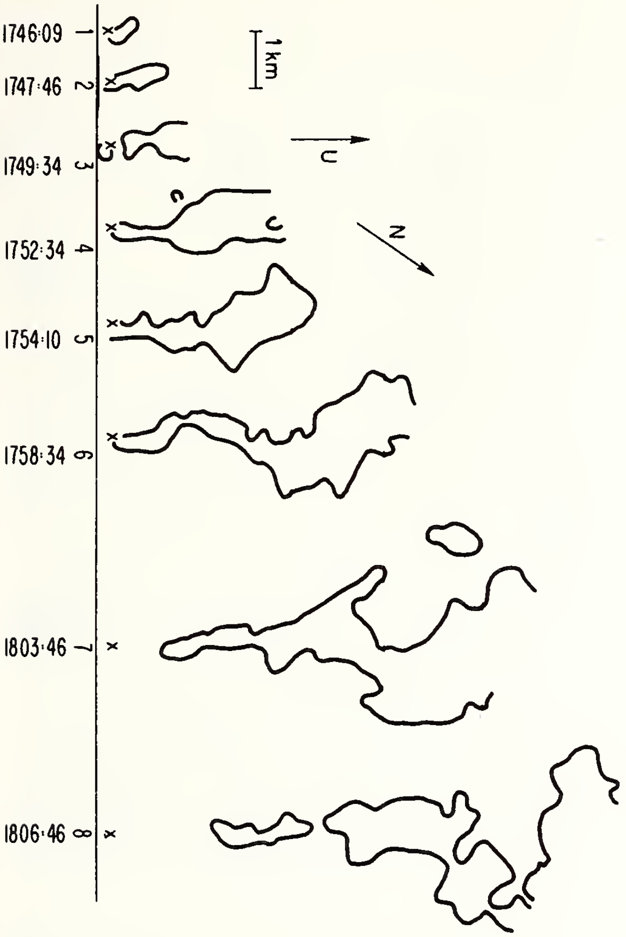

Figure 3. Vertically-integrated (0 to 800 m) chaff concentration for the 8 volume scans of plume 13 (plan view). Scan starting times are indicated. The X's mark the release points.

Figure 4 shows crosswind-integrated chaff concentration for the 8 volume scans of plume 13. The contour is drawn at 53 units/km^2, a higher density than the dashed contour in figure 2. However, we can see the chaff much closer to the release point because of the much greater rate of vertical diffusion for this plume than for plume 6. Here, the cellular structure of the plume is again evident. Particularly in scan 3, we can see a region where there is very low chaff density (probably a downdraft that has blown chaff to the ground) separating two regions of greater density. The cellular structure continues to be evident as the plume advects downwind.

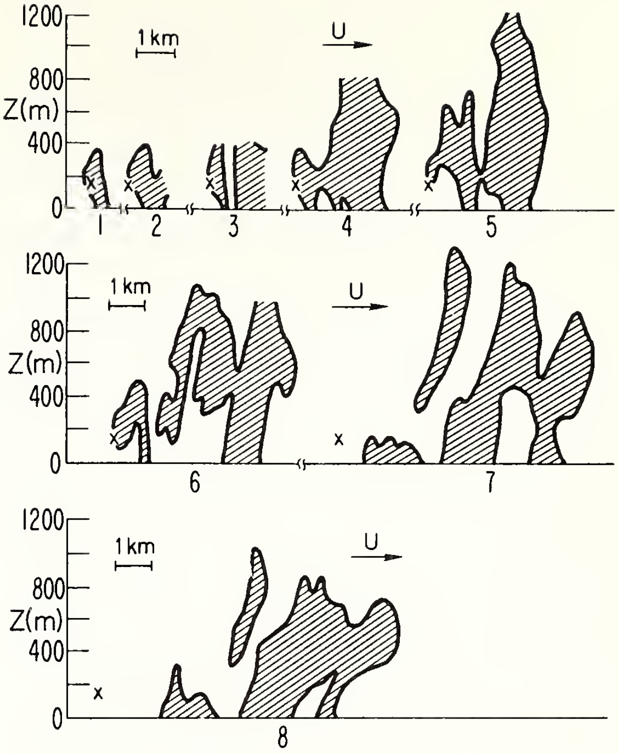

Figure 4. Crosswind-integrated chaff concentration for the 8 volume scans shown in figure 3.

The vertical extent of updrafts is substantial in this late afternoon case; the chaff is carried above 1200 m within 10 minutes.

Between scans 7 and 8 we can see evidence of the fall velocity of the chaff. The upper cloud has fallen from a maximum height of nearly 1300 m to 1100 m, and the whole plume seems to be settling rather uniformly.

5. DISCUSSION

Figure 5 shows the height to the maximum concentration of the plumes, expressed as a fraction of the boundary layer thickness, versus time. The open circles are numerical model results of Deardorff (1972) for a plume from a point source at $Z/Z_i = 0.1$ under convective conditions. (Z_i represents the boundary layer thickness.) The errors represent 50 m, the approximate uncertainty in our estimates of the height of the maximum concentration.

The agreement between the model and plume 13 is quite good, even though the chaff has a fall velocity of 27 cm/sec. The effect of the fall velocity of the chaff is only seen appreciably in the last scan (as noted above).

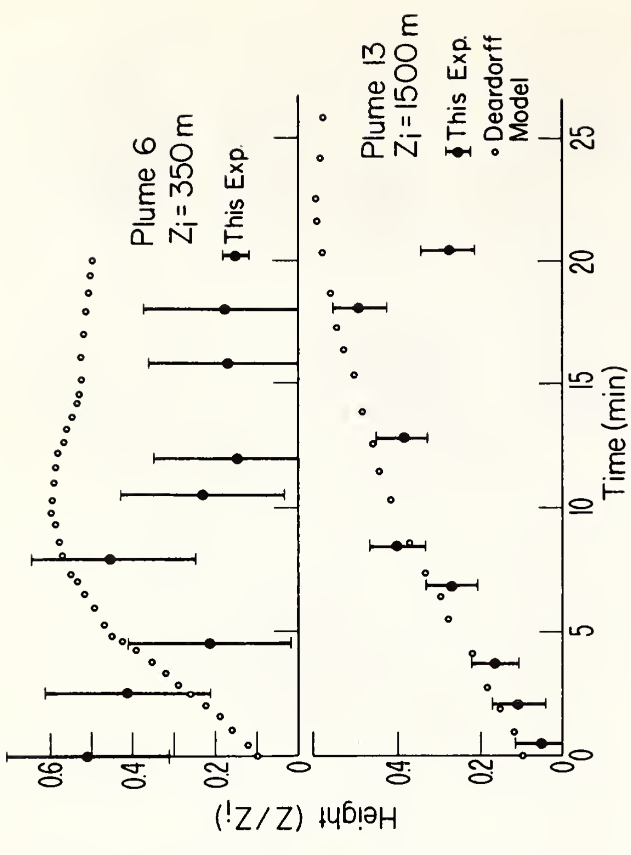

Figure 5. Mean plume height, expressed as a fraction of the boundary layer height. The open circles are from the numerical calculations reported in Deardorff (1972).

Plume 6 was released at $Z/Z_i = 0.43$, not the conditions of Deardorff's model, hence agreement is not to be expected. However, the model does indicate the time scale of the expected diffusion. The model indicates that the mean height should approach $Z/Z_i = .5$ by about 15 min, indicating that the plume should be diffused uniformly throughout the boundary layer by that time. The data show that the maximum concentration approaches $Z/Z_i \simeq 0.18$ after about 12 min. Evidently in the case of plume 6, the vertical mixing was not strong enough to cause the chaff to spread uniformly through the depth of the boundary layer, possibly because of the chaff fall velocity.

Figure 6 shows estimates of σ_y and σ_z (the crosswind and vertical standard deviation) for plume 13, expressed as fractions of the boundary layer depth, Z_i. The σ's were estimated from the data by fitting curves through the horizontal and vertical cross-plume density profile, near the leading edge of the plume. The dashed curve is Deardorff's (1972) model prediction for σ_z. Agreement is seen to be good between the model predictions and the first two data points (t < 10 min). Later the σ_z indicated by radar becomes much smaller than the model result. We believe this may be due to our being unable to account for large regions of low chaff density in our calculations of σ_z. Such regions were often difficult to separate from noise in the radar signal.

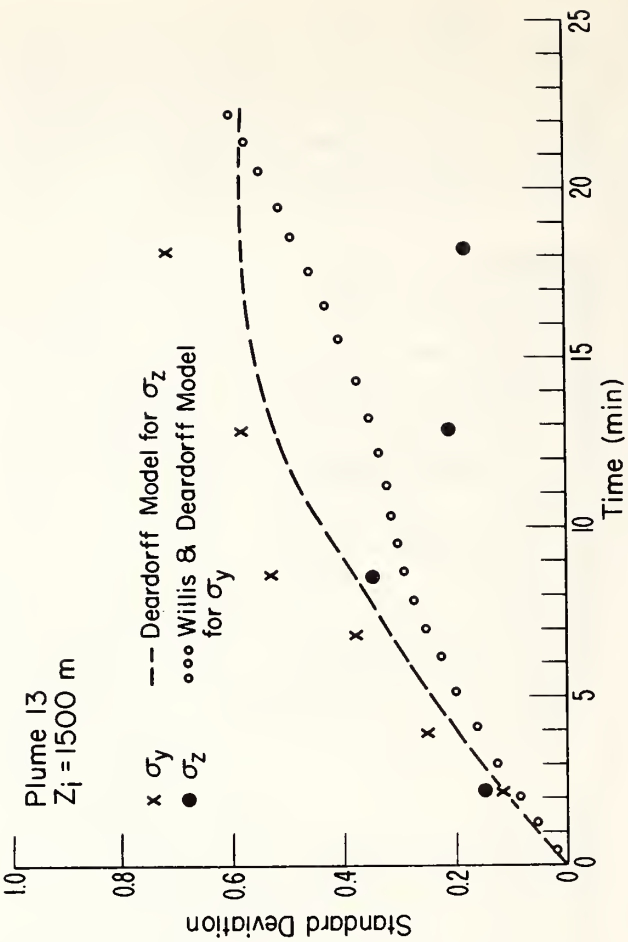

Figure 6. Vertical (σ_z) and crosswind (σ_y) standard deviation of plume 13. The dashed line is from the numerical calculations of Deardorff (1972); the open circles are from the tank model of Willis and Deardorff (1976).

Our data for σ_y appears to be consistent with results from a tank model of Willis and Deardorff (1976) for a point source situated at $Z/Z_i = 0.1$.

Similar data for plume 6 are shown in figure 7. Again, the data appear to be consistent with the models.

7. TURBULENT KINETIC ENERGY DISSIPATION RATES

Since the dissipation rate can give estimates of the turbulent diffusion rates (see Csanady, 1973) and since the radar that we used for the plume studies had Doppler capability, we were able to deduce the dissipation rates at those locations where there was chaff. We used the method of Frisch and Clifford (1974) to derive dissipation rates from second moments of the Doppler spectra. The relevant equations are

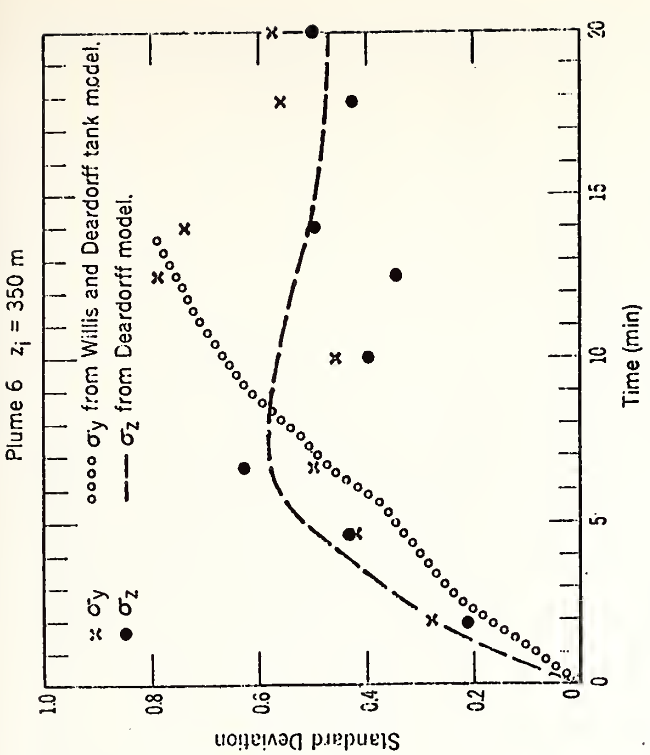

Figure 7. As in figure 6, except that the data is from plume 6.

$$\varepsilon = \frac{1}{\alpha}\left[\frac{\sigma^2}{0.634\left(1 - \frac{\gamma^2}{15}\right)}\right]^{3/2} \quad \text{for } \beta \leq \alpha \qquad (1)$$

$$\varepsilon = \frac{1}{\beta}\left[\frac{\sigma^2}{0.634\left(1 + \frac{\eta^2}{15}\right)}\right]^{3/2} \quad \text{for } \alpha < \beta \qquad (2)$$

where ε is in m^2/sec^3,

$\gamma^2 = 1 - (\beta/\alpha)^2$,

$\eta^2 = 1 - (\alpha/\beta)^2$

and β = 40 m (the range resolution)

α = .0084 x Range (pulse radius)

The second moments of radial velocities were calculated using the radial Doppler velocity spectrum. The threshold of the calculation was done on either side of the peak where the power was 15 dB below its peak value. This was done because there was an inadvertent fluctuating noise level in the radar signal. The method of chosing a threshold 15 dB below the peak yielded the most consistent values of second moments between the data with the relatively high noise level, and the data with the lower noise level. The method does bias the second moments 5 to 7 percent low. However this is negligible when compared to the statistical variations in the second moments, as will be seen below.

The second moments also had to be corrected for the effect of the finite time window over which each pulse volume was observed and for spectral smoothing that was done to avoid spurious peaks. For our pulse repetition period of 512 μs, the combined effect of the time window and the spectral smoothing was to increase the spectral variance by 0.07 m^2/s^2 for spectra from 128 sample points, by 0.017 m^2/s^2 for spectra from 256 sample points, and by a negligible amount for 512 point spectra. These calculated effects were found to be consistent with the apparent width of ground clutter for 128, 256 and 512 point spectra.

For the narrow spectra in the chaff plumes, these corrections were appreciable. For 128 point spectra, the correction lowered the apparent eddy dissipation rate by about 30%.

Figure 8 presents our measurements of the dissipation rates within the plumes. The bars represent statistical uncertainty only. The dissipation rate is seen to be constant throughout the depth of the boundary layer, having a value of 50-60 cm^2/s^3 for both plume 6, the morning case, and plume 13, the late afternoon case.

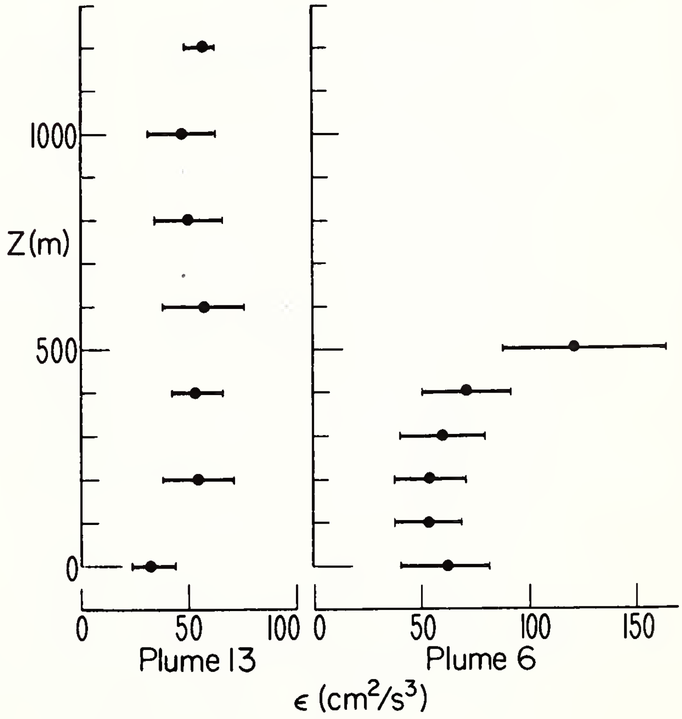

Figure 8. Turbulent kinetic energy dissipation rates for plume 6 and plume 13. Errors are statistical only.

8. CONCLUSIONS

We see that Doppler radar observations of the boundary layer filled with chaff can provide useful information about the plumes from elevated point sources. Individual plumes are modulated quite strongly, at least in the downwind direction, by large scale wind perturbations such as convection cells.

In the two cases we have studied, the rise of the mean chaff plume height, and the vertical spread of the plume seem to be consistent, with the numerical model of Deardorff. The lateral spread of the plume appears to be consistent with what is predicted by the tank model of Willis and Deardorff.

Finally, Doppler radar can provide measurement of the turbulent kinetic energy dissipation rate at all points within the plume at a scale less than 100 m. The large temporal and spatial variations in ε, however, make considerable averaging necessary before meaningful results can be obtained. Thus, many plumes will have to be studied before an understanding is achieved of how variations in ε effect plume dissipation.

9. ACKNOWLEDGMENTS

We gratefully acknowledge the help of Mr. Andrew Johnston and Mr. Nathan Kohn in developing and running the various computer programs used to process this data.

10. REFERENCES

Csanady, G. T., 1973: Turbulent Diffusion in the Environment. Boston, D. Reidel Pub. Co. 248 pp.

Deardorff, J. W., 1972: Numerical investigations of neutral and unstable planetary boundary layers, J. Atmos. Sci., 29, pp 91-115.

Frisch, A. S., R. B. Chadwick, W. R. Moninger, and J. M. Young, 1976: Observations of convective cells in the boundary layer using simultaneous measurements by a dual Doppler radar system, echosonde and microbarograph array. Boundary-Layer Meteor., 10, pp 55-68.

Frisch, A. S. and S. F. Clifford, 1974. A study of convection capped by a stable layer using doppler radar and acoustic echo sounders. J. Atmos. Sci., 31, pp 1622-1628.

Islitzer, N. F., 1961: Short-range atmospheric-dispersion measurements from an elevated source. J. Meteor. (now J. Atmos. Sci.), 18, pp 443-450

Islitzer, N. F. and R. K. Dumbauld, 1963: Atmosperhic diffusion-deposition studies over flat terrain, Inst. J. Air Wat. Poll. (now Air and Wat. Poll.), 7, pp 999-1022.

Willis, G. E. and J. W. Deardorff, 1976: A laboratory model of diffusion into the convective planetary boundary layer. Q. J. Roy. Met. Soc., 102, pp 427-445.

Preprint Volume; Fourth Symposium on Meteorological Observation
and Instrumentation, 357-361, American Meteorological Society, 1978.

ACOUSTIC REMOTE SENSING OF THE PLANETARY BOUNDARY LAYER AT THE SOUTH POLE

W. D. Neff and F. F. Hall, Jr.

NOAA/ERL/Wave Propagation Laboratory
Boulder, Colorado 80302

1. INTRODUCTION

Acoustic sounders (or echosondes) are unique remote sensors of the planetary boundary layer. As long as a turbulent boundary layer exists it can be sensed by a combination of monostatic and bistatic echosondes. This capability is being exploited through a series of experiments at Amundsen-Scott South Pole station which lies at an elevation of 2854 m on the slopes of the Antarctic ice plateau. Early results from these experiments have been described by Neff and Hall (1976a,b) and Neff et al. (1977).

During January and February 1977 we set up a sounding system (Fig. 1) utilizing bistatic geometry and Doppler principles to study the turbulence structure of the statically stable boundary layer which nearly always overlies the ice surface. The homogeneous terrain, the lack of a diurnal insolation cycle, and the weakness of synoptic effects make this an ideal site for such studies. Because waves and dynamical instabilities are an ever present feature of the statically stable boundary layer the experiment site includes a four-element array of microbarographs to track these motions and a temperature structure parameter (C_T^2) measurement (using 13 μm platinum probes spaced 20 cm apart) to identify wave associated bursts near the surface. This latter measurement is useful in identifying intermittency effects that prevail at large bulk Richardson numbers and that appear to be related to the wave-events seen by the echosonde.

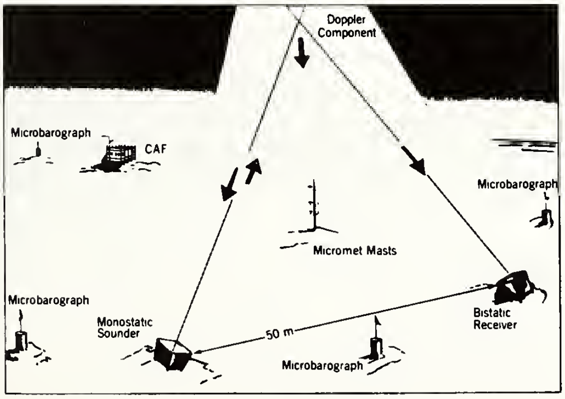

Figure 1. Site plan showing the locations of the acoustic sounders, microbarographs, and micrometeorological mast relative to the new Clean Air Facility (CAF) at South Pole Station. The main station is 200 meters to the left (to the west) of the sounders and the CAF.

At the time of this writing (November 1977), the experiment has operated nearly continuously for ten months with routine data logging (on digital tape) of the monostatic and bistatic intensities, and vertical Doppler at ten heights between 30 m and 150 m and microbarograph and C_T^2 data during each echosonde scan. The pulse repetition period ranged from 1 to 5 seconds depending on the depth of the boundary layer. The monostatic and bistatic echos are displayed on a split-trace, 50 cm wide facsimile recorder. The minimum range was 30 m.

2. THE STRUCTURE OF THE BOUNDARY LAYER

The symmetry of the combined monostatic-bistatic geometry shown schematically in Fig. 1 allows use of the angular dependencies in the expression for the acoustic scattering cross-section at wavenumber k, (Tatarskii, 1971)

$$\sigma_o(\theta) = \frac{\pi}{2} k^4 \cos^2\theta \left[\frac{\phi_T(K)}{T_o^2} + \frac{E(K)\cos^2\theta/2}{\pi C_o^2 K^2} \right] \qquad (1)$$

where $K = 2k \sin\theta/2$, ϕ_T is the isotropic, three-dimensional spectral density of temperature and E is the isotropic three-dimensional turbulent kinetic energy spectral density. The scattering cross-section in equation 1 is thus a function of the scattering angle θ measured from the transmitting beam axis to that of the receiver and of the spectra measured at the Bragg-scale of $K = 2k \sin\theta/2$. For backscatter, only $\phi_T(K)$ contributes. For $\theta = 150°$, as in our experiment, E(K) also contributes. For typical nocturnal boundary layers the contribution from E(K) is one to four times that from ϕ_T using data from Izumi (1971) in the theory presented by Kaimal (1973). The absence of signal at a given height-gate in the bistatic channel thus represents the absence of small-scale velocity turbulence (within the 30 dB dynamic range of the system) at that level. The absence of a monostatic signal in such stable boundary layers indicates the absence of a local potential temperature gradient but not necessarily the absence of velocity turbulence. The absence of signals on both channels suggests a laminar layer which either lacks a source of turbulence or is a region of static stability strong enough to surpress turbulence.

The symmetry of the 15°-inclination of the antennas in Fig. 1 allows the echos to be displayed on the same height-scale as shown in Figs. 2 and 3. Figure 2 was obtained with an 8 m s^{-1} surface wind, a surface air temperature of -30°C, and an inversion strength of about 10°C. The bistatic echo is much more uniform than the monostatic return. This suggests that the vertical distribution of potential temperature is not smoothed effectively by the turbulence. Figure 3 shows numerous elevated turbulent layers to heights over 400 m, separated by "laminar" regions from a "boundary" layer that is less than 40 m deep. As noted by Neff and Hall (1976a) the uppermost of elevated layers (such as those in Fig. 3) marks the top of the temperature inversion as measured by the daily radiosondes. Since a high pressure region was well established over the ice dome at the time that the data in Fig. 3 were taken, these elevated layers may be an artifact of the associated subsidence aloft rather than an effect arising from the radiational cooling of the surface as in typical nocturnal boundary layers.

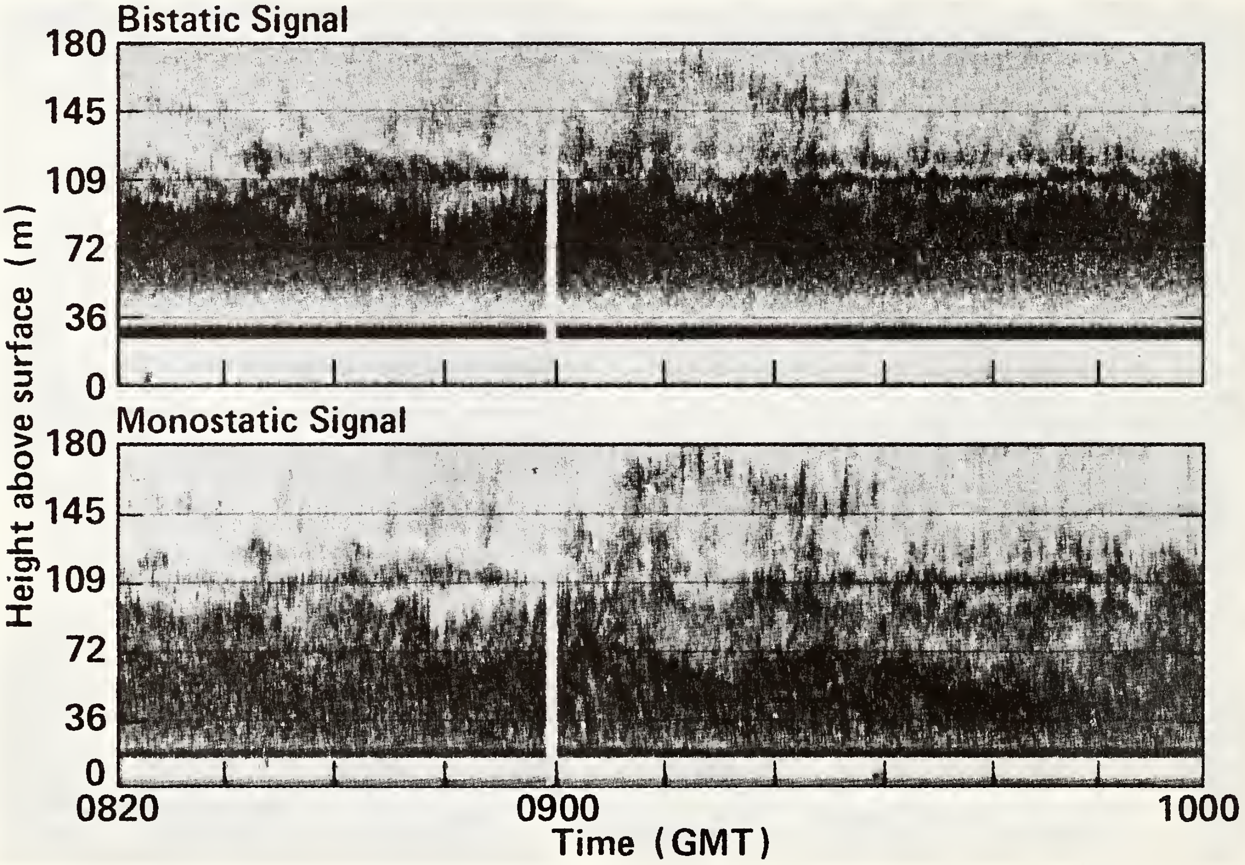

Figure 2. Echosonde recording obtained on 5 February 1977 using the system shown in Fig. 1 under windy (8 m s^{-1}) conditions.

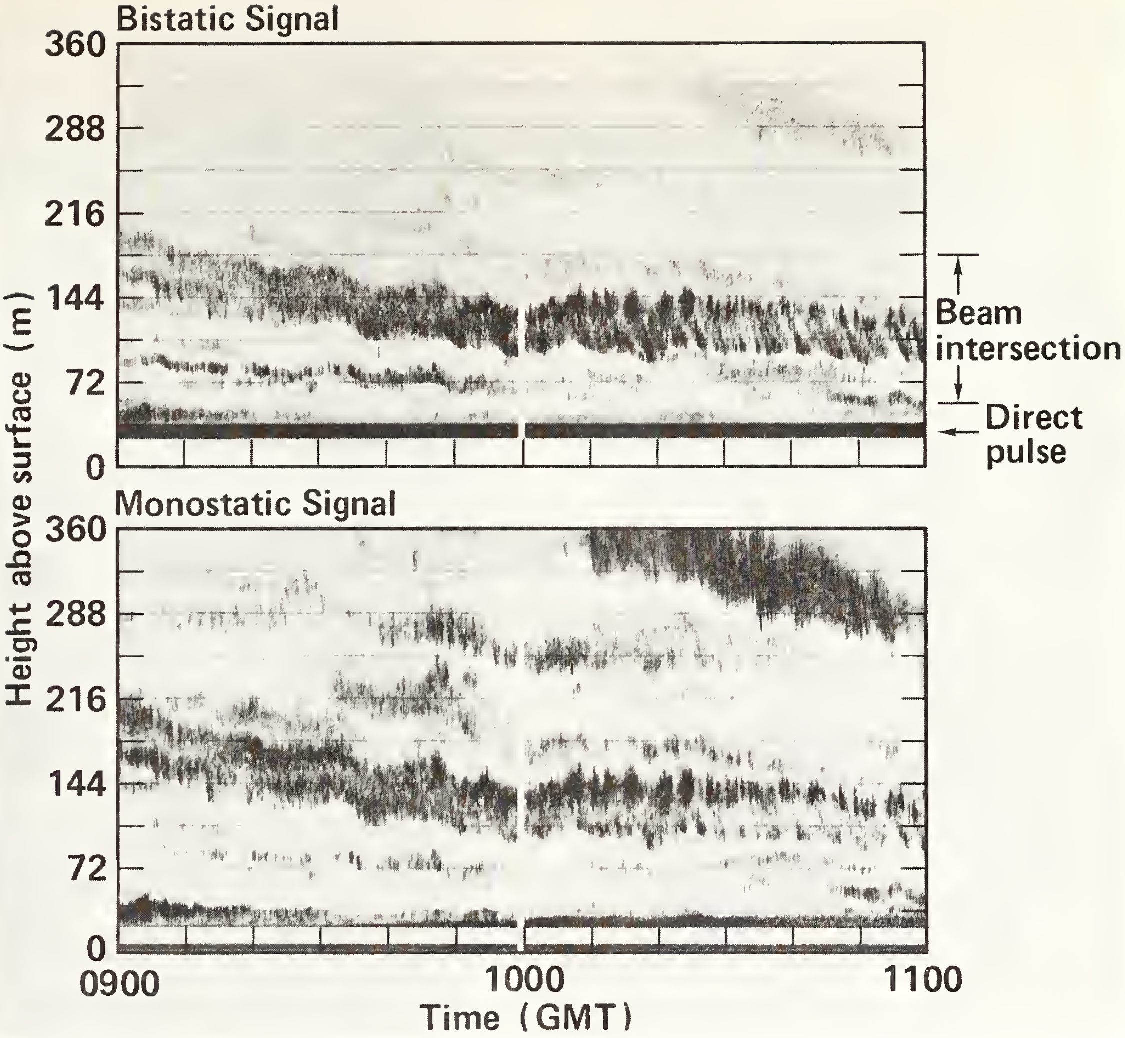

Figure 3. Echosonde recording obtained on 9 February 1977 using the system shown in Fig. 1.

3. DOPPLER DERIVED VERTICAL VELOCITIES

Vertical velocities were derived from an analog frequency-tracking device and recorded at 8 heights through the boundary layer from the bistatic signal. Because the bistatic echo is often much more uniform than the monostatic the time series obtained was much less biased by the occasional absence of signal. This is revealed by spectral analysis of data from the case shown in Fig. 2. Data from a height of 57 m are presented in Fig. 4 where power spectral density times frequency is plotted on a log-log scale versus frequency. No filtering at high frequencies was performed to avoid aliasing because of the filtering already present in the volume averaging of the echosonde. Significant features are the plus-one slope in the region between 0.001 and 0.02 Hz which is in agreement with the sonic anemometer data of Kaimal et al. (1972). The peak near 0.1 Hz is in the same spectral region as the peak in the surface layer results (at z/L = 2) of Kaimal et al., and at higher levels in the nocturnal jet case of Kaimal and Izumi (1965). Comparison of our data with the results of Kaimal et al., suggests that the inertial subrange begins half a decade beyond the highest frequency response of the echosonde (here, the Nyquist frequency of 0.2 Hz.) Spectra were also computed at other heights. The most significant feature was a shifting of the spectral peak to higher frequencies as the top of the surface-based inversion was approached (which is often a region of increased static stability).

4. MICROBAROGRAPH AND SURFACE LAYER C_T^2 DATA

These data reveal surface effects during events such as that shown in Fig. 5 where low level organized patterns are evident. Surface pressure fluctuations, Doppler-derived vertical velocities and the square root of the temperature structure parameter C_T^2 defined by

$$C_T = \sqrt{\overline{(\Delta T)^2}/r^{2/3}}$$

(where r is the separation over which ΔT is measured) are plotted in Fig. 6. The vertical

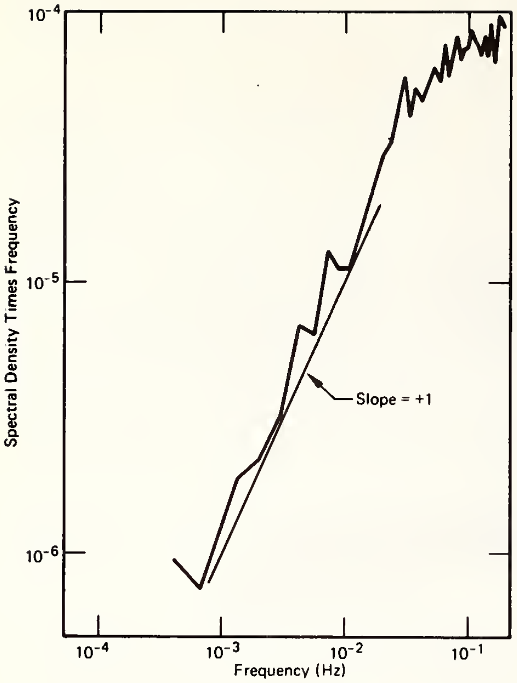

Figure 4. Power spectral density of the echo-sonde-derived vertical velocity at 51 m on a log-log plot, obtained during case shown in Fig. 2.

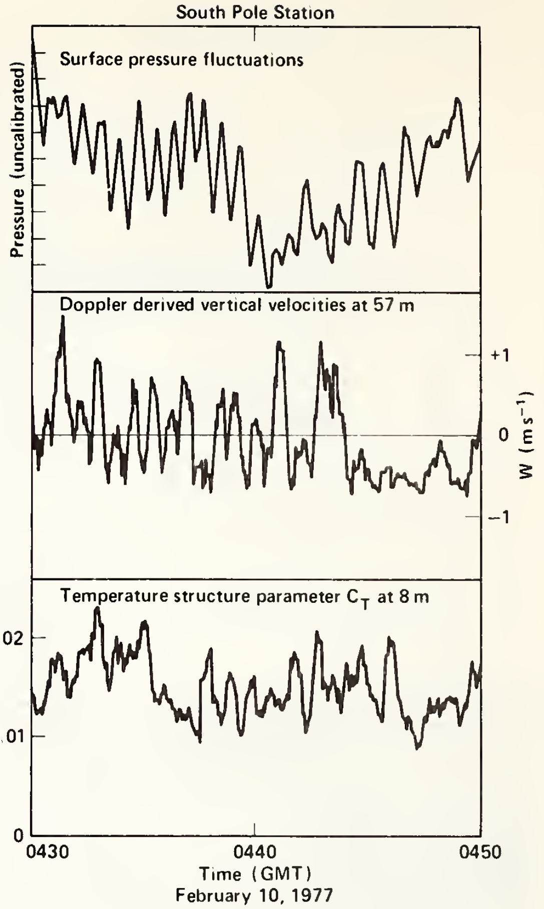

Figure 6. Time series of the temperature structure parameter (which is related to the surface heat flux), the pressure fluctuations from one element of the microbarograph array, and the acoustically-derived vertical velocity. These are for the case shown in Fig. 5.

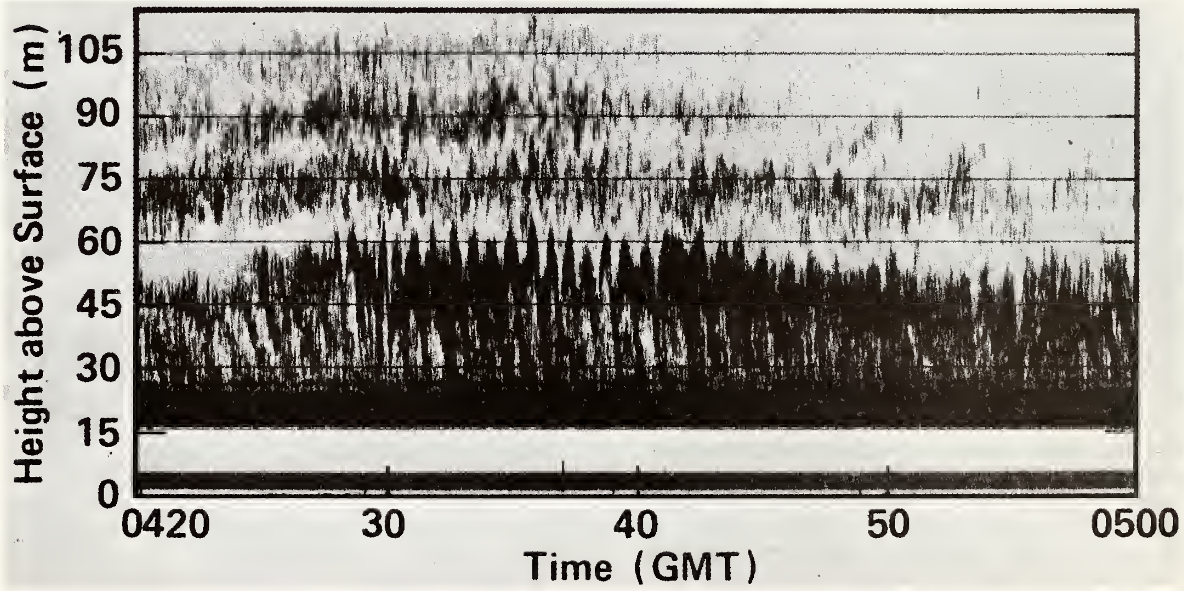

Figure 5. Acoustic sounder facsimile recording obtained on 10 February 1977 at South Pole Station.

velocities were derived from the monostatic signal and are hence biased by the lack of echos between the waves so that the data presented here were interpolated between points where the signal was present. The peak values of 1 m s^{-1} are significant and the large-scale overturning implied by such vigorous motions is reflected by the bursts in C_T measured near the surface. Since C_T reflects the surface heat flux (Wyngaard 1973), these data show that events such as that in Fig. 5 can significantly increase the downward transport of heat.

5. CONCLUSIONS AND PROGNOSIS FOR FUTURE WORK

The quality of the data shown here from early February 1977 suggest that the more than 7000 hours of digitally recorded data to be returned from the South Pole in early 1978 will provide a number of qualitative and quantitative insights into statically stable boundary layer structure. Our analysis will include the use of vertical velocity data and surface measurements to assess the role of waves in maintaining the surface heat budget. During less stable periods (such as during the warm, moist advection periods described by Neff and Hall, 1976a) the inertial subrange may shift to low enough frequencies to be within the bandwidth of the Doppler-echosonde data. This may allow us to extract related turbulence parameters such as dissipation rates. The use of combined monostatic and bistatic data is also expected to provide further insight concerning the formation and evolution of the nocturnal boundary layer.

During January of 1978, we will set up a microprocessor-controlled Doppler echosonde which has been designed to provide wind profiles from 30 m to as high as 400 m in addition to processing the scattering data, and sonic anemometer and microbarograph data. Our spectral analysis suggests that only low-frequency components of the momentum flux will be available from this system.

6. ACKNOWLEDGMENTS

Helpful comments by Chandran Kaimal in applying the spectral analysis presented here are gratefully acknowledged. The experiment was maintained through the 1977 austral winter by Brad Halter and the late Gary Rosenberger of the NOAA-Global Monitoring for Climatic Change Program. This research is supported in part by National Science Foundation grants DPP 74-24415 and DPP 77-04865.

7. REFERENCES

Izumi, Y. (1971), "Kansas 1968 Field Program Data Report", Environmental Research Paper No. 379, Air Force Cambridge Research Laboratories. Available NTIS.

Kaimal, J. C. and Y. Izumi (1965), "Vertical velocity fluctuations in a nocturnal low-level jet", *J. Appl. Met.*, 4, 576-584.

Kaimal, J. C., J. C. Wyngaard, Y. Izumi, and O. R. Coté (1972), "Spectral characteristics of surface layer turbulence", *Quart. J. R. Met. Soc.*, 98, 563-589.

Kaimal, J. C. (1973), "Turbulence spectra, length scales and structure parameters in the stable surface layer," *Boundary Layer Meteorol.* 4, 289-309.

Neff, W. D. and F. F. Hall, (1976a), "Acoustic sounder measurements of the South Pole boundary layer", *Preprint Volume -- 17th Radar Meteorological Conference.* American Meteorological Society, Boston, 297-302.

Neff, W. D. and F. F. Hall (1976b), "Acoustic echo sounding of the atmospheric boundary layer at the South Pole", *Antarctic Journal of the U.S.*, XI(3): 143-144.

Neff, W. D., H. E. Ramm and F. F. Hall Jr., (1977), "Acoustic sounder operations at South Pole Station", *Antarctic Journal of the U.S.*, (to appear Oct. 1977).

Tatarskii, V. I., (1971) *The Effects of the Turbulent Atmosphere on Wave Propagation* (Nauka, Moscow, 1967), transl. Israel Program for Scientific Translations, U.S. Dept. of Commerce, Nat. Tech. Inform. Serv., Springfield, VA., 472 pp.

Wyngaard, J. C. (1973), "On surface-layer turbulence", Chapter 3 in *Workshop on Micrometeorology*, (Haugen, ed.), American Meteorological Society, 392 pp.

Antarctic Journal of the U.S., 13(4): 179-181, 1978.

Boundary layer research at South Pole Station using acoustic remote sensing

W. D. NEFF

Wave Propagation Laboratory
Environmental Research Laboratories
National Oceanic and Atmospheric Administration
Boulder, Colorado 80302

We report here on our analysis of acoustic sounder data obtained during 1977 and on a series of tests planned for a wind-sensing Doppler-acoustic sounder and sonic anemometer installed during January 1978 at wind-sensing Doppler-acoustic sounder and sonic anemometer installed during January 1978 at South Pole Station.

Our 1977 experiment (Neff and Hall, 1978; Neff *et al.*, 1977) focused on the profiling of small-scale turbulent velocity and temperature fluctuations as a means of monitoring the structure and evolution of the atmospheric boundary layer at the South Pole. Through the efforts of Brad Halter and the late Gary Rosenberger of the National Oceanic and Atmospheric Administration's Global Monitoring for Climatic Change Program, we obtained high quality data for the entire year.

Our earlier analysis of 1975 data (Neff and Hall, 1976a,b) documented the ability of acoustic sounding techniques to provide a detailed and continuous picture of the inversion

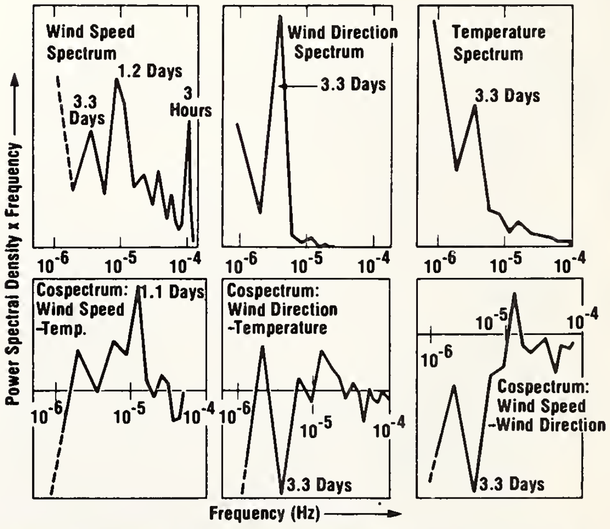

Figure 1. Spectral and cospectral analyses of hourly surface observations obtained during May 1975 at South Pole Station. The negative cospectral peaks at 3.3 days reflect the regular occurrence of cold, gently downslope flows. The nearly diurnal peak in the wind-speed spectrum is related to increases in temperature as shown by its cospectrum with temperature. The temperature spectrum, however, shows that this accounts for only a small part of the variance in temperature.

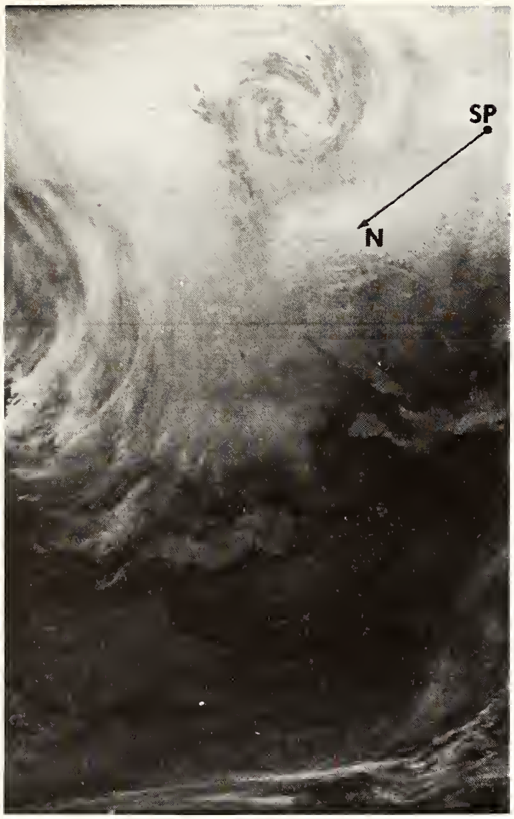

Figure 2. Infrared satellite photograph taken about 2300Z, 7 July 1977, showing cyclonic vortex some 500 kilometers in diameter and located grid northeast of South Pole Station (solid dot).

and revealed a variety of meteorological phenomena unexpected from surface observations alone. On time scales of minutes, "breaking" waves produced short-term increases in the surface heat flux. Longer period oscillations (1/2 to 1 hour) of the inversion depth produced large changes in the surface wind speed but none in the temperature. On synoptic time scales, we found a systematic variation in the surface wind direction and temperature that correlated strongly with distinct changes in our acoustic sounder data. The spectral and cospectral analyses of a month's surface data shown in figure 1 reveal quite clearly the synoptic character of these changes; cold, gentle downslope flows off the dome alternate with strong, warm advection from the Weddell and Atlantic sectors. During such downslope cases, the acoustic sounder data revealed a deepening of the inversion with features similar to those of a surface cold front. In such cases, the boundary layer depth was about 25 percent of the inversion depth, with isolated turbulent patches and layers occupying the remainder of the inversion. Such events occurred typically in conjunction with strong baroclinic upper level winds from the quadrant between 100°E. and 180°. In such cases the geostrophic pressure gradient counters the Archimedian force within the inversion accounting for the light winds and thin boundary layers.

The regular occurrence of such events led us to examine both radiosonde and satellite data in more detail. We found that the direction of the upper level winds had a bimodal distribution with centers at 45°W. and 160°E. The winds from the southeast quadrant were highly baroclinic and in most of the cases associated with the presence of frontal and multilayered echos in the acoustic data. Examination of infrared satellite photographs from July 1977 revealed the case shown in figure 2. The distinctly cyclonic vortex located grid-northeast of the South Pole formed and decayed over a period of 2 days. The acoustic sounder revealed that a surface "front" arrival some 18 hours prior to this photograph. Although moisture is available only rarely as a tracer for such infrared imagery over the antarctic interior, our acoustic-sounder data and spectral analysis of surface data suggest that the propagation and horizontal structure of such systems could be studied easily with an array of remote weather stations.

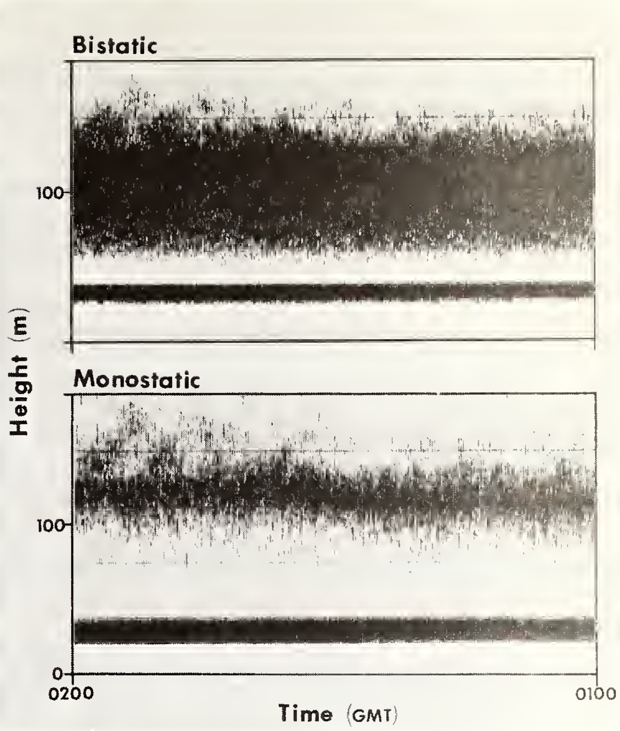

Figure 3. Acoustic sounder backscatter signal (monostatic) compared with scattering at 150° (bistatic). The latter includes a contribution from small-scale velocity fluctuations in addition to one from the temperature fluctuations. The dark band at 30 meters results from the direct pulse between the two antennas. The main beam intersection begins at about 60 meters. The dark band near the bottom of the monostatic trace arises from the ringing of the antenna. The lower record reflects the enhancement of the temperature gradient at the top of the boundary layer, while the upper record shows the uniformity of turbulence within the boundary layer.

Under higher wind conditions the boundary layer typically would grow to heights of as much as 300 meters over periods of 6 to 36 hours. In such cases the increased turbulence often caused a weakening of the temperature gradient within the boundary layer and a corresponding enhancement at the top. These observations confirm the recent model predictions of Brost and Wyngaard (1978), who included both bottom slope and a surface energy budget in a higher order closure model of the statically stable boundary layer. Their model also showed that such boundary layers often require times comparable with the duirnal period to come to equilibrium. Because the South Pole site lacks a diurnal cycle of insulation, data acquired there provide a unique opportunity to test the predictions of these models.

The primary data available from the acoustic backscatter signal are profiles of the temperature spectrum $\partial_T(K)$, at the acoustic wave number K (as in the lower portion of figure 3). A connection with typical model parameters can be made as follows: Wyngaard and Cote (1971) express $\partial_T(K)$ as

$$_T(K) = \beta Q \frac{\partial T}{\partial Z} \epsilon^{-1/3} K^{-5/3} \qquad (1)$$

where β=0.79 ±0.10; Q, the flux of sensible heat; $\frac{\partial T}{\partial Z}$ the background temperature gradient; and ϵ, the rate of destruction of the turbulent kinetic energy. Writing Q in an eddy-diffusivity form as $Q=K_4 \frac{\partial T}{\partial Z}$ we then have

$$\phi_T(K) \approx 0.79\, K_H \left(\frac{\partial T}{\partial Z}\right)^2 \epsilon^{-1/3} K^{-5/3} \qquad (2)$$

The bistatic-sounder echo in figure 3 (see Neff and Hall, 1978, for more discussion of the application of scattering theory to the interpretation of such records) shows a nearly uniform distribution of through the boundary layer. Model predictions of K_H suggest a nearly linear decrease near the top of the inversion. The quadratic behavior of $\left(\frac{\partial T}{\partial Z}\right)^2$ thus will dominate the behavior of $\phi_T(K)$. Changes in the background temperature gradient due to the evolution of the boundary layer or shorter term variations due to internal gravity waves thus should be clearly evident from acoustic data as, indeed, we have found. The strong backscatter echo at the top of the boundary layer shown in figure 3 would correspond to a sharpening of the temperature gradient there as predicted by Brost and Wyngaard and is consistent with (2). The availability of such model results thus provides a basis for the systematic analysis of our digitally recorded sounder data obtained during 1977.

Our 1978 field program has been designed to test a Doppler-acoustic sounder as a means of studying the detailed structure of the boundary-layer wind field. A number of problems with cold sensitivity and power line transients had been solved by midwinter with routine data acquisition begun on 1 July.

Because of the problems of inferring surface stress and heat flux from profile methods at large static stability, we modified, for cold-weather operation, a three-axis sonic anemometer for direct measurement of these fluxes. The sonic electronics were modified so that adjustments could be made in the Clean-Air Facility. This has, however, required additional line drivers and receivers to eliminate crosstalk and noise. These modifications should be completed later in the winter.

Lt. Hans Ramm is the winter scientist during 1978 and participated with me in the 1977 and 1978 summer programs. This research was supported in part by the National Science Foundation under grant DPP 77-04865.

References

Brost, R. A., and J. C. Wyngaard. 1978. A model study of the stably-stratified planetary boundary layer. *Journal of the Atmospheric Sciences* (accepted for publication).

Neff, W. D., and F. F. Hall, Jr. 1976a. Acoustic sounder measurements of the South Pole boundary layer. *Preprint Volume—17th Radar Meteorological Conference.* American Meteorological Society, Boston. pp. 397-402.

Neff, W. D. and F. F. Hall, Jr. 1976b. Acoustic echo sounding of the atmospheric boundary layer at the South Pole. *Antarctic Journal of the U.S.,* 11(3): 143-144.

Neff, W. D., and F. F. Hall, Jr. 1978. Acoustic remote sensing of the planetary boundary layer at the South Pole. *Preprint Volume—Fourth Symposium on Meteorological Observations and Instrumentation.* American Meteorological Society, Boston. pp. 357-361.

Neff, W. D., H. E. Ramm, and F. F. Hall, Jr. 1977. Acoustic sounder operations at South Pole Station. *Antarctic Journal of the U.S.,* 12(4): 167-168.

Wyngaard, J. C., and O. R. Cote. 1971. The budgets of turbulent kinetic energy and temperature variance in the atmospheric surface layer. *Journal of the Atmospheric Sciences,* 28: 190-201.

Errata:

Page 370, paragraph 1: Lines 4, 5 and 6: Delete the phrase "wind sensing Doppler-acoustic sounder and sonic anemometer installed during January 1978 at..."

Page 372, paragraph 2:
Line 2: $\partial_T(K)$ should be $\phi_T(K)$.
Line 5: $\partial_T(K)$ should be $\phi_T(K)$.

Equation 1: The left-hand side of the equation should be $\phi_T(K)$.

Line above equation 2: K_4 should be K_H.

Line 4 of sentence below equation 2: Insert ε so that the sentence ends "uniform distribution of ε through the boundary layer."

Journal of the Atmospheric Sciences, 35: 47-58, 1978.

The Temperature-Humidity Covariance Budget in the Convective Boundary Layer

J. C. Wyngaard

Cooperative Institute for Research in Environmental Sciences, University of Colorado/NOAA, Boulder 80309, and Wave Propagation Laboratory, NOAA, Boulder, Colo. 80302

W. T. Pennell,[2] D. H. Lenschow and M. A. LeMone

National Center for Atmospheric Research,[1] Boulder, Colo. 80307

(Manuscript received 27 May 1977, in final form 30 September 1977)

The behavior of the temperature-humidity covariance ($\overline{\theta q}$) budget in the convectively driven boundary layer is determined through analysis of data from AMTEX and (to a lesser extent) Kansas and Minnesota. In the near-neutral surface layer a balance is found between production and molecular destruction; in the mixed layer, transport is also important. We extend the Corrsin theory for inertial subrange scalar spectral behavior to the temperature-humidity cospectrum, and thus relate the molecular destruction rate of $\overline{\theta q}$ to its inertial range level. Destruction rates inferred from AMTEX cospectra agree with those found from the imbalance of production and transport terms. The budgets within the surface layer and the mixed layer are parameterized separately with appropriate scales.

Both temperature and humidity fluctuations contribute to the small-scale refractive index variations which affect acoustic and electromagnetic wave propagation in the atmosphere. Our results indicate that their joint contribution C_{Tq} to the refractive index structure parameter is directly related to the molecular destruction rate of $\overline{\theta q}$. The results provide a basis for understanding and predicting the behavior of C_{Tq} in the convective boundary layer.

1. Introduction

A convective boundary layer over an evaporating surface has significant fluctuation levels in both temperature and humidity. It has long been observed that these fluctuations can be strongly correlated. The mechanisms through which a turbulent flow maintains strong scalar-scalar correlations are of interest in their own right, and have relevance to a range of disciplines from turbulent chemistry to wave propagation through turbulence.

In the latter application, for example, Gossard (1960) and more recently Friehe *et al.* (1975) and Wesely (1976) have shown how both temperature and humidity fluctuations contribute to refractive index fluctuations. One can write

$$n=-C(\theta+aq), \tag{1}$$

where n, θ and q are fluctuating refractive index, temperature and absolute humidity (units of grams of water vapor per cubic meter), respectively, and C is a conversion constant which we will ignore hereafter. The factor a depends on the wavelength of the acoustic or electromagnetic radiation. In calculating turbulence effects on wave propagation one usually deals with the refractive index structure function (Tatarskii, 1971)

$$\overline{[n(\mathbf{x},t)-n(\mathbf{x}+\mathbf{r},t)]^2}\equiv\overline{(n-n')^2}, \tag{2}$$

where n is measured at $\mathbf{x}$ and n' at $\mathbf{x}+\mathbf{r}$. From Eq. (1) this is

$$\overline{(n-n')^2}=\overline{(\theta-\theta')^2}+2a\overline{(\theta-\theta')(q-q')}+a^2\overline{(q-q')^2}. \tag{3}$$

For separation magnitudes r in the inertial range ($\eta\ll r\ll l$, where η is the Kolmogorov microscale and l the integral scale), locally isotropic, Kolmogorov-Corrsin turbulence is usually assumed. Then structure functions depend on r, not $\mathbf{r}$, so that Eq. (3) can be written

$$\overline{(n-n')^2}=2\overline{\theta^2}\left(1-\frac{\overline{\theta\theta'}}{\overline{\theta^2}}\right)+4a\overline{\theta q}\left(1-\frac{(\overline{\theta q'}+\overline{\theta' q})}{2\overline{\theta q}}\right)+2a^2\overline{q^2}\left(1-\frac{\overline{qq'}}{\overline{q^2}}\right) \tag{4}$$

---

[1] The National Center for Atmospheric Research is sponsored by the National Science Foundation.

[2] Present affiliation: Battelle Pacific Northwest Laboratories, Richland, Wash. 99352.

0022-4928/78/0047-0058$06.00

© 1978 American Meteorological Society

TABLE 1. Values of surface layer scaling parameters, surface virtual temperature flux and mixed layer depth for AMTEX 1975 flights.

Date	z_i (m)	u_* (m s^{-1})	$-T_*$ (K)	$-q_*$ (g m^{-3})	Q_{0V} (m s^{-1} K)	$-L$ (m)
2/15	1200	0.53	0.26	0.28	0.16	76
2/16	1430	0.40	0.28	0.35	0.13	40
2/18	1010	0.35	0.17	0.40	0.08	44
2/22	1900	0.58	0.34	0.52	0.24	67
2/24	1200	0.30	0.25	0.67	0.10	22
2/26	680	0.33	0.12	0.29	0.05	59

and the temperature and humidity structure functions behave as

$$\overline{(\theta-\theta')^2}=2\overline{\theta^2}\left(1-\frac{\overline{\theta\theta'}}{\overline{\theta^2}}\right)=C_T{}^2r^{\frac{2}{3}}, \tag{5}$$

$$\overline{(q-q')^2}=2\overline{q^2}\left(1-\frac{\overline{qq'}}{\overline{q^2}}\right)=C_q{}^2r^{\frac{2}{3}}, \tag{6}$$

where $C_T{}^2$ and $C_q{}^2$ are the temperature and humidity structure parameters. We will show here that the cross term in Eq. (4) also has this r-dependence, so that one can write

$$C_n{}^2=C_T{}^2+2aC_{Tq}+a^2C_q{}^2 \tag{7}$$

as has often been implicity assumed in past literature. We will also show that C_{Tq} is directly related to the molecular destruction term in the $\overline{\theta q}$ budget. Our budget results thus provide a basis for relating C_{Tq} to other turbulence quantities in the convective boundary layer.

2. Measurements

The airplane measurements reported here were made with the NCAR Lockheed Electra over the East China Sea as part of the Air Mass Transformation Experiment (AMTEX) during February 1975. Table 1 is a summary of the surface fluxes and certain boundary layer parameters for the six AMTEX boundary layer flights. Except for those on 24 and 26 February, the measurements were obtained during periods of cold air advection over the Kuroshio, a warm, northward flowing ocean current. Under conditions of strong cold air advection the convectively unstable boundary layer is capped by a well-defined inversion layer at height z_i, usually 1–2 km above the surface, with broken decks of stratocumulus clouds in the upper few hundred meters. On 24 February the mixed layer was also capped by stratocumulus but the inversion was quite weak and surface winds were southwesterly. Conditions on 26 February were like those commonly observed over tropical oceans. Winds were light, the air-sea temperature contrast was small, and the mixed-layer height was about cloud base for the scattered to broken cumulus observed in the area of measurements.

Fig. 1 shows profiles of mean potential temperature and humidity that were typical for the conditions of strong cold air advection. These profiles are made up of both aircraft soundings (i.e., constant heading descents or ascents at about 5 m s^{-1}) and "leg average" values over 60 km long straight and level flight paths. Profiles on 24 and 26 February were similar except that the jumps in Θ and Q were much less pronounced and z_i was more difficult to determine.

The Electra air motion sensing system uses an inertial navigation system (INS) to measure the velocity and angular orientation of the airplane relative to the earth. The longitudinal component of air velocity with respect to the airplane (the aircraft true airspeed) is measured by means of a pitot-static tube, while the lateral and vertical components are measured by means of vanes. These sensors are mounted on a nose boom about 6 m ahead of the aircraft to reduce the error caused by upwash effects on air flow around the fuselage. The air velocity measurements with respect to the airplane are combined with the INS outputs to obtain the three air velocity components relative to the earth, as described by Lenschow (1972).

Temperature is measured with a 25 μm platinum resistance wire thermometer (Rosemount Model No. 102E2AL). The sensor output is corrected for dynamic heating, which is proportional to the square of the aircraft true airspeed. Since the aircraft altitude varies somewhat due to turbulence and pilot control inputs, the temperature measured from the aircraft can be affected by the mean lapse rate. As shown in Fig. 1, the mean potential temperature lapse rate is close to zero. Therefore, potential temperature fluctuations (calculated from temperature and static pressure) are actually used instead of temperature in all the measurements discussed here. In order to convert potential temperature fluctuations to temperature fluctuations, they must be multiplied by the ratio of mean temperature to mean potential temperature. This was not done here since this factor never departed from unity by more than 7%.

Absolute humidity is measured with a cooled-mirror dew-point hygrometer. Both a fixed-path Lyman-alpha hygrometer (LAH) [Buck (1976) describes a variable-path version of this sensor] and a microwave refractometer (McGavin and Vetter, 1965) are used for humidity fluctuation measurements. The LAH was used for all of the humidity fluctuation measurements except for the lowest flight level on 15 February 1975, when the LAH was off-scale, because the refractometer was noisier at high frequencies. The effect of this electronic noise on the data reported here is negligible.

With the exception of the LAH, all of the sensors measuring turbulent fluctuations in the airstream are

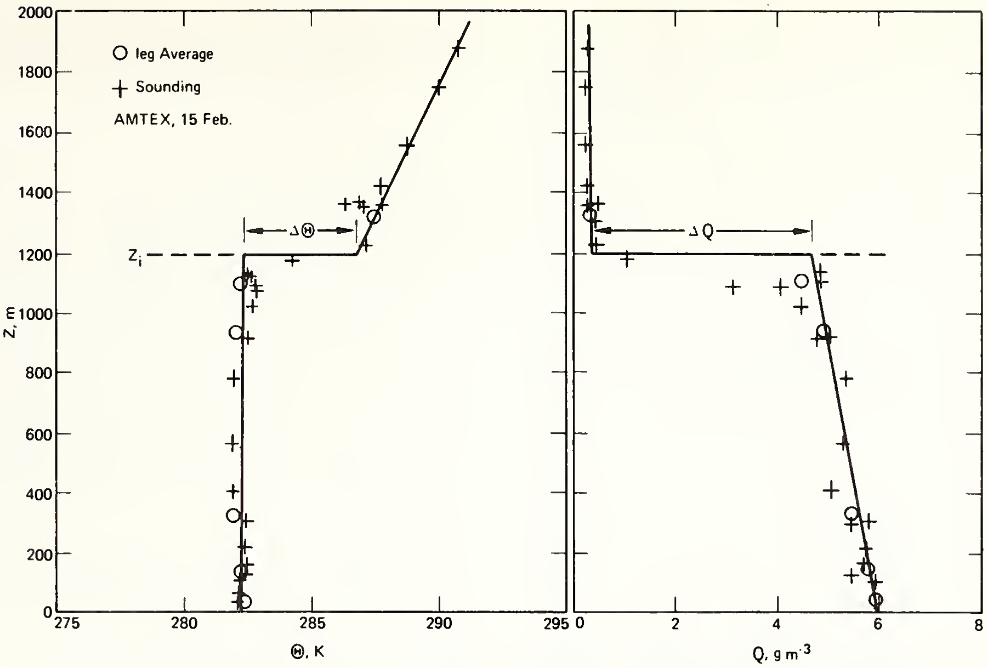

FIG. 1. Typical profiles of mean potential temperature Θ and mean absolute humidity Q during AMTEX. Note the well-defined inversion base at z_i and the jumps $\Delta\Theta$ and ΔQ there.

within a meter of each other on the aircraft nose boom. The LAH is located on the nose boom about 3 m downstream from the other sensors. To compensate for this (which amounts to about 0.03 s delay time) and for the lag introduced by the reduced velocity of the air in the 0.37 m length of tubing upstream from the sensor, the sensor output is advanced by one time interval (0.05 s) with respect to the other variables. The remaining 0.02 s delay is equivalent to a velocity in the hygrometer tubing of 18 m s^{-1}. This seems reasonable in view of the bends in the tubing and the obstruction at the entrance to the tube, which is intended to help keep the sensor free from water by deflecting hydrometeors away from the entrance. The magnitude of this phase advancement was determined by minimizing the phase angle at high frequencies between humidity and vertical velocity w. Vertical velocity, which is used as a reference for phase shift comparisons, is measured with sensors that have negligible phase shift over the bandwidth used for these calculations. Similarly, the LAH response, disregarding the effects of location and ducting, is assumed to have negligible phase shift and attenuation over the bandwidth considered here. The phase angle relationships between humidity, temperature and vertical velocity were found to be independent of the heading of the aircraft with respect to the wind direction to verify that these are instrumental characteristics rather than real physical relationships existing in the atmosphere.

The temperature response, however, has significant phase shift and attenuation. Because of heat conduction between the wire and its housing, the temperature response is not describable by a simple, linear, first-order differential equation with a single time constant characteristic of the resistance wire. McCarthy (1973) attempted to model its response by assuming that its response to ambient air temperature fluctuations can be approximated by the smoothing or filtering function

$$0.7e^{-t/\tau_1}+0.3e^{-t/\tau_2}. \tag{8}$$

The first term represents the response of the sensing element, and the second term is due to heat conduction between the element and its supporting structure which has much greater thermal inertia. McCarthy used the values $\tau_1=0.016$ s and $\tau_2=1.15$ s, which he obtained from the manufacturer. However, measurements from the Electra indicate that a value of $\tau_1=0.03$ s gives better agreement with the observed phase shifts of θ and w, as well as θ and q.

With the exception of the two INS horizontal airplane velocity components, which were recorded at 10 samples per second, the Electra turbulence data were recorded at 50 samples per second. All the variables were low-pass filtered with either analog or digital 4-pole low-pass Butterworth filters with a cutoff frequency of about 10 Hz and then interpolated to a sampling rate of 20 samples per second.

The overland humidity statistics reported here were measured during the 1973 Minnesota experiments, using equipment and techniques described in detail by Champagne *et al.* (1977).

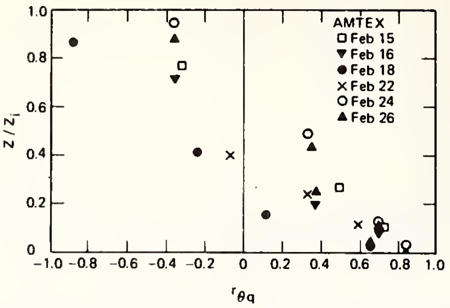

FIG. 2. Vertical profiles of $r_{\theta q}$, the correlation coefficient of temperature and humidity fluctuations, during AMTEX.

3. The $\overline{\theta q}$ budget

It is well-established that $\overline{\theta q}$ is positive above a warm, evaporating surface (Swinbank and Dyer, 1967; Phelps and Pond, 1971; McBean and Miyake, 1972; Friehe *et al.*, 1975; Wesely, 1976). Not as well-documented, but perhaps as physically understandable, are the negative $\overline{\theta q}$ values in the upper portions of the convective ABL. The inversion which typically caps the ABL in these conditions usually has a sharp increase in temperature with height, but a sharp decrease in humidity; thus entrainment leads to large negative $\overline{\theta q}$ values near z_i. Fig. 2, based on data from six days in the AMTEX experiment, shows the vertical profile of the correlation coefficient $r_{\theta q}$, defined by

$$r_{\theta q}=\frac{\overline{\theta q}}{[\overline{\theta^2}\,\overline{q^2}]^{\frac{1}{2}}}. \tag{9}$$

Note from Fig. 2 that $r_{\theta q}$ approaches 1.0 near the surface, changes sign at $z/z_i\approx 0.5$, and can be large and negative near the inversion base.

We can learn much about the maintenance of $\overline{\theta q}$ from its conservation equation, which is derived from those for θ and q. Neglecting radiation and phase change effects (thus restricting our attention to the region below cloud base) the θ equation is (Lumley and Panofsky, 1964)

$$\theta_{,t}+\Theta_{,j}u_j+\theta_{,j}U_j+\theta_{,j}u_j-\overline{\theta_{,j}u_j}=K\theta_{,jj}. \tag{10}$$

Here K is thermal diffusivity, and we denote mean quantities by upper case symbols; a comma denotes differentiation and repeated indices are summed. The q equation is derived by using a mean and turbulent decomposition in the humidity conservation equation. The variable air density introduces many advective terms, but under typical boundary layer conditions most can be neglected. We assume the scale height $h=\rho/(\rho_{,3})\gg l$, where ρ is the mean density and l a characteristic turbulence integral scale. We also assume $(\overline{q^2})^{\frac{1}{2}}/Q\gg(\overline{\theta^2})^{\frac{1}{2}}/T\approx(\overline{\rho'^2})^{\frac{1}{2}}/\rho$, where ρ' is fluctuating density; both are usually excellent approximations. Under these conditions the q equation reduces to

$$q_{,t}+\rho(Q/\rho)_{,j}u_j+q_{,j}U_j+q_{,j}u_j-\overline{q_{,j}u_j}=Dq_{,jj} \tag{11}$$

where D is the diffusivity for q.

Note that the second term in Eq. (10) contains the gradient of mean *potential* temperature, not mean temperature. Thus even though there is a mean vertical gradient of temperature in a neutral ($\Theta_{,3}=0$) atmosphere, vertical velocity fluctuations do not cause temperature fluctuations. Eq. (11) shows an analogous situation exists for humidity. Because ρ decreases with z, a well-mixed layer $[(Q/\rho)_{,3}=0]$ will have a mean vertical gradient of absolute humidity, but vertical velocity fluctuations will not generate q fluctuations.

Multiplying the θ equation by q, the q equation by θ, adding and averaging gives in large Reynolds number turbulence (Tennekes and Lumley, 1972)

$$\overline{(\theta q)}_{,t}=-\Theta_{,j}\overline{u_jq}-\rho(Q/\rho)_{,j}\overline{u_j\theta}-(U_j\overline{\theta q})_{,j}$$
$$-(\overline{u_j\theta q})_{,j}-2(K+D)\overline{\theta_{,j}q_{,j}}. \tag{12}$$

The terms on the right side of Eq. (12) are, in order, production through the mean potential temperature gradient, production through the mean specific humidity gradient, mean advection, turbulent transport and molecular destruction.

In the horizontally homogeneous flows we consider here, the $\overline{\theta q}$ budget simplifies to

$$\overline{(\theta q)}_{,t}=-\Theta_{,3}\overline{wq}-\rho(Q/\rho)_{,3}\overline{w\theta}-(\overline{w\theta q})_{,3}$$
$$-2(K+D)\overline{\theta_{,j}q_{,j}}, \tag{13}$$

where we revert to the notation $u_3=w$. We can now discuss the behavior of the horizontally homogeneous budget (13) in two regions of the convective ABL.

4. The unstable surface layer

We consider both $\overline{wq}$ and $\overline{w\theta}$ to be positive, and both $\Theta_{,3}$ and $(Q/\rho)_{,3}$ negative—the normal situation above a warm evaporating surface. Then both the production terms in Eq. (13) create positive $\overline{\theta q}$. We will now argue that in this situation the transport term is much smaller.

Data on $\overline{w\theta q}$ are scarce, but since under the conditions we are considering θ and q are strongly positively correlated, we expect $\overline{w\theta q}$ to behave much like $\overline{w\theta\theta}$. Fig. 3 is a compilation of $\overline{w\theta^2}$ data from Minnesota (Kaimal *et al.*, 1976) and Kansas (Wyngaard and Coté, 1971), and $\overline{w\theta q}$ data from Minnesota (Champagne *et al.*, 1977) and AMTEX. We non-

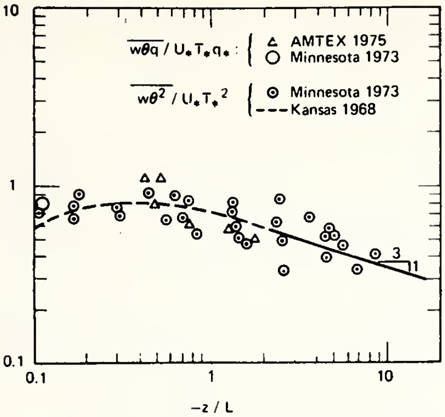

FIG. 3. Data on the vertical fluxes of θ^2 and θq in the surface layer from AMTEX, Minnesota and Kansas.

dimensionalize with the scales

$$\left.\begin{aligned} T_* &= -Q_0/u_* \\ q_* &= -M_0/u_* \\ L &= \frac{-u_*^3 T}{kgQ_{0V}} \end{aligned}\right\}, \tag{14}$$

where Q_0 and M_0 are the surface temperature and moisture fluxes, Q_{0V} is the surface virtual temperature flux $Q_0+(0.61TM_0/\rho)$, and $k=0.35$ (Businger *et al.*, 1971) is the von Kármán constant. The data in Fig. 3, although limited, do support our hypothesis that $\overline{w\theta q}$ and $\overline{w\theta^2}$ behave similarly. Therefore, we will use Fig. 3 to estimate transport of $\overline{\theta q}$ in the unstable surface layer.

Fig. 3 indicates no significant transport in the interval $0.1<-z/L<0.5$. The data for $0.5<-z/L<5$ follow the Kansas local free convection prediction (Wyngaard *et al.*, 1971a)

$$\overline{w\theta^2}=0.75u_*T_*^2(-z/L)^{-\frac{1}{3}}. \tag{15}$$

Assuming this holds for $\overline{w\theta q}$, the transport term in Eq. (13) for $0.5<-z/L<5$ becomes in dimensionless form

$$-(\overline{w\theta q})_{,3}\approx 0.25\frac{u_*T_*q_*}{z}\left(-\frac{z}{L}\right)^{-\frac{1}{3}}. \tag{16}$$

In the surface layer, where $z\ll h$ (where h is the scale height), we have

$$\rho(Q/\rho)_{,3}\approx Q_{,3} \tag{17}$$

and the production terms in Eq. (13) are, in dimensionless form,

$$-\overline{w\theta}\rho(Q/\rho)_{,3}\approx -\overline{w\theta}Q_{,3}=\frac{u_*T_*q_*}{kz}\phi_q \tag{18}$$

$$-\overline{wq}\Theta_{,3}=\frac{u_*T_*q_*}{kz}\phi_h \tag{19}$$

with ϕ_h and ϕ_q the dimensionless mean gradients. We take $\phi_h=\phi_q$ (Businger, 1973) so the two production terms are equal. Businger *et al.* (1971) fit the formula

$$\phi_h=0.74(1-9z/L)^{-\frac{1}{2}} \tag{20}$$

to the Kansas data in the range $0<-z/L<2$, but we will use the expression

$$\phi_h=0.23(-z/L)^{-\frac{1}{3}} \tag{21}$$

which fits the data nearly as well in the range $0.5<-z/L<2$. Then the ratio of transport to production terms for $0.5<-z/L<2$ becomes, from Eqs. (16)–(19) and Eq. (21),

$$\frac{\text{transport}}{\text{production}}\approx 0.2. \tag{22}$$

The ratio is even smaller in the range $0<-z/L<0.5$, assuming the trend in Fig. 3 continues for $-z/L\rightarrow 0$.

Thus within an error of about 20% we can neglect transport in the unstable surface layer, giving for $0<-z/L<2$

$$\overline{(\theta q)}_{,t}\approx -\Theta_{,3}\overline{wq}-Q_{,3}\overline{w\theta}-2(K+D)\overline{\theta_{,j}q_{,j}}. \tag{23}$$

It is easy to show that $\overline{\theta q}$ would have to change significantly over a time scale $\tau\sim z/u_*$ (about 30 s for $z=10$ m and $u_*=0.3$ m s^{-1}) in order for the time term in Eq. (23) to be important. This does not happen, so we can adopt the quasi-steady budget for $0<-z/L<2$

$$\overline{(\theta q)}_{,t}\approx 0\approx -\Theta_{,3}\overline{wq}-Q_{,3}\overline{w\theta}-2(K+D)\overline{\theta_{,j}q_{,j}} \tag{24}$$

which indicates that production is balanced by molecular destruction.

Under more unstable conditions ϕ_h probably decreases faster than indicated by Eq. (21), while Fig. 3 suggests that transport remains a source term. Thus for $-z/L>2$ all three terms—transport, production and molecular destruction—are probably significant.

5. The mixed layer

a. Parameterization of terms

Although strictly speaking the AMTEX boundary layer is horizontally inhomogeneous, the mean advective terms in the turbulent second-moment equations are negligible. Furthermore, a Lagrangian time for air passage through the AMTEX area is much larger than a large eddy turnover time in the boundary layer. Thus we can assume the boundary layer turbulence is locally homogeneous and in equilibrium, and use the AMTEX data to examine the $\overline{\theta q}$ budget [Eq. (13)] in the convectively driven mixed layer.

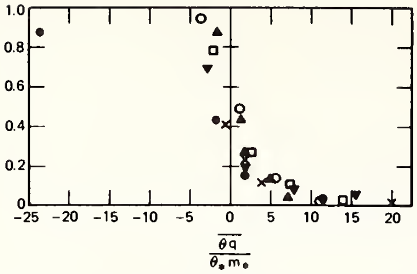

FIG. 4. The $\overline{\theta q}$ profile, made dimensionless with mixed-layer scales, in AMTEX. Symbols as in Fig. 2.

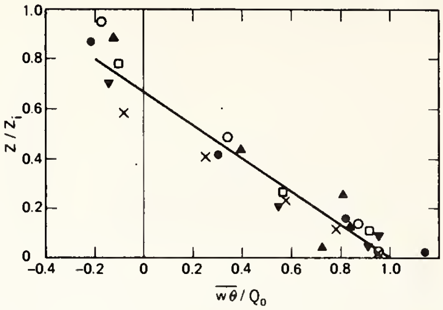

FIG. 6. The sensible heat flux profile, made dimensionless with mixed-layer scales, in AMTEX. The solid line was used in the parameterized $\overline{\theta q}$ budget. Symbols as in Fig. 2.

We will nondimensionalize with mixed-layer scales

$$\left.\begin{aligned} w_* &= [(g/T)Q_{0v}z_i]^{\frac{1}{3}} \\ \theta_* w_* &= Q_0 \\ m_* w_* &= M_0 \end{aligned}\right\}. \tag{25}$$

Fig. 4 shows the vertical profile of nondimensional $\overline{\theta q}$ for six AMTEX days. Our scaling collapses the data over most of the mixed layer. The structure in the entrainment region near z_i depends not only on the scaling parameters in Eq. (25) but also on the inversion layer parameters, such as the jumps $\Delta\Theta$ and ΔQ at z_i and the gradients above. We do not have sufficient data near z_i to examine this critically. Furthermore, stratocumulus clouds existed in the upper few hundred meters of the mixed layer over as much as 80% of the area, and temperature and humidity measurements there are affected by cloud water (Lenschow and Pennell, 1974). In addition, flight levels occasionally penetrated through the top of the mixed layer, giving anomalously large values of $\overline{\theta^2}$, $\overline{q^2}$ and $\overline{\theta q}$. The flight leg on 18 February at $z=0.87\ z_i$ is a good example of this (see Figs. 2 and 4). Hence for profiles of terms in the $\overline{\theta q}$ budget we restrict our attention to the region $0.1<z/z_i<0.8$.

Fig. 5 shows the vertical profile of $\overline{w\theta q}$. Note that near the surface it is consistent with the local free convection expression of Eq. (15), which in mixed-layer variables is

$$\overline{w\theta q}=1.06m_*w_*\theta_*(z/z_i)^{-\frac{1}{3}}. \tag{26}$$

Eq. (26) follows the data up to $z/z_i\approx 0.2$. For the region $0.1<z/z_i<0.8$ the data scatter about the curve (fit by eye)

$$\overline{w\theta q}=2.8m_*w_*\theta_*(1-z/z_i)^2 \tag{27}$$

drawn in Fig. 5. Differentiating Eq. (27) gives an expression for transport in the mixed layer:

$$-(\overline{w\theta q})_{,3}=5.6(m_*w_*\theta_*/z_i)(1-z/z_i). \tag{28}$$

The production terms in the mixed-layer budget [Eq. (13)] involve both fluxes and mean gradients. The AMTEX flux profiles are shown in Figs. 6 and 7. The temperature flux (Fig. 6) is essentially linear in the region $0<z/z_i<0.8$:

$$\overline{w\theta}\approx Q_0(1-1.5z/z_i). \tag{29}$$

The humidity flux (Fig. 7) falls off much less rapidly with height in the mixed layer. We will parameterize

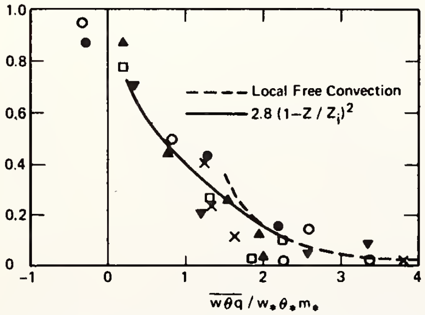

FIG. 5. The $\overline{w\theta q}$ profile, made dimensionless with mixed-layer scales, in AMTEX. The solid curve was used in the parameterized $\overline{\theta q}$ budget. Symbols as in Fig. 2.

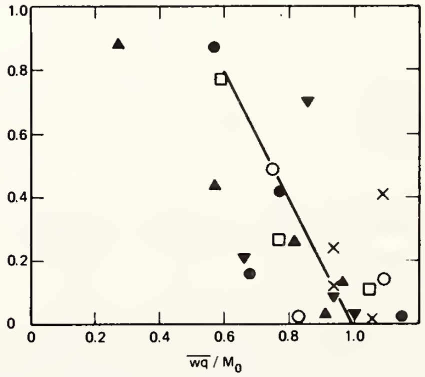

FIG. 7. The humidity flux profile, made dimensionless with mixed-layer scales, in AMTEX. The solid line was used in the parameterized $\overline{\theta q}$ budget. Symbols as in Fig. 2.

the AMTEX profile by

$$\overline{wq}=M_0(1-0.5z/z_i). \tag{30}$$

Our parameterized clear air flux profiles [Eqs. (29) and (30)] are linear interpolations between the surface values and the values induced by entrainment at z_i. The latter are determined by the entrainment velocity w_e and the jumps $\Delta\Theta$ and ΔQ. The value of w_e depends on, among other things, the jump in virtual potential temperature $\Delta\Theta_V$ where Θ_V is defined by

$$\Theta_V=\Theta\left(1+0.61\frac{Q}{\rho}\right). \tag{31}$$

Since Θ_V is always greater above z_i than below ($\Delta\Theta_V$ is positive), entrainment generates negative $\overline{w\theta_V}$ near z_i. This value is typically about -0.2 times the surface value Q_{0V}. Although in principle a clear, inversion-capped mixed layer can have jumps $\Delta\Theta$ and ΔQ of either sign, and hence entrainment-induced values of $\overline{w\theta}$ and $\overline{wq}$ of either sign, in all the AMTEX runs $\Delta\Theta$ was positive and ΔQ negative. Thus the entrainment-induced $\overline{w\theta}$ was negative and $\overline{wq}$ positive. For the AMTEX conditions the profile of $\overline{w\theta_V}$ was determined mainly by $\overline{w\theta}$, so the individual $\overline{wq}$ profiles typically show more variation than $\overline{w\theta}$.

While $(Q/\rho)_{,3}$ in the mixed layer could be fairly accurately estimated, $\Theta_{,3}$ was very small and impossible to determine with any confidence. Instead we used the mixed-layer assumption $\Theta_V=$ constant, which implies to a good approximation for the AMTEX data

$$\Theta_{V,3}=0=\Theta_{,3}+0.61\Theta(Q/\rho)_{,3} \tag{32}$$

$$\Theta_{,3}=-0.61\frac{\Theta}{\rho}\left(Q_{,3}+\frac{Qg}{RT\gamma}\right), \tag{33}$$

where R is the gas constant and $\gamma=1.4$ is the specific heat ratio. For typical values of $Q_{,3}$ this gives a very small, positive $\Theta_{,3}$. On 15 February, for example, $Q_{,3}\approx-1.0\times10^{-3}$ g m^{-4}; from Eq. (33) and the prevailing conditions this gives $\Theta_{,3}\approx0.1$ K km^{-1}. The mixed-layer profiles in Fig. 1 were drawn with these slopes. The Θ and Q profiles for each of the six AMTEX runs analyzed appeared consistent with Eq. (33).

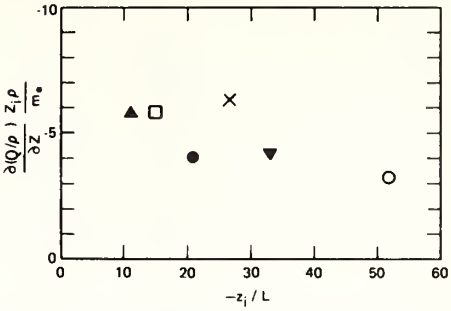

FIG. 8. The mean specific humidity gradient in the AMTEX mixed-layer, made dimensionless with mixed-layer scales, as a function of stability: Symbols as in Fig. 2.

The mean specific humidity gradient in each run was negative. Thus the humidity flux was down the gradient, suggesting the eddy diffusivity parameterization

$$\overline{wq}=-K_q\rho(Q/\rho)_{,3}. \tag{34}$$

We would expect $K_q\approx w_*z_i$ in the mixed layer, and since $\overline{wq}$ scales with M_0 we expect

$$\rho(Q/\rho)_{,3}\approx-\frac{M_0}{w_*z_i}\approx-\frac{m_*}{z_i} \tag{35}$$

in the mixed layer. This is tested in Fig. 8. We will ignore the possible z_i/L dependence suggested by Fig. 8, since the data are limited, and simply average over the runs, finding

$$\rho(Q/\rho)_{,3}=-5\;m_*/z_i. \tag{36}$$

From Eqs. (28), (29), (30), (33) and (36) we can write the $\overline{\theta q}$ budget [Eq. (13)] in the AMTEX mixed layer as

$$\begin{aligned}(K+D)\overline{\theta_{,j}q_{,j}}=(m_*w_*\theta_*/z_i)[&-5A(1-0.5z/z_i)\\&+5(1-1.5z/z_i)+5.6(1-z/z_i)].\end{aligned} \tag{37}$$

Here the parameter $A=(0.61\Theta M_0/\rho Q_0)$ is the ratio of the moisture and sensible temperature contributions to the surface virtual temperature flux. For the AMTEX data A varied between 0.15 and 0.40.

Note that the right side of Eq. (37) changes sign in the mixed layer. The height z_c where this occurs depends only weakly on A, and for the AMTEX conditions one finds from Eq. (37) that $z_c\approx0.8\,z_i$. Thus the molecular destruction term also changes sign at z_c.

Our parameterized AMTEX $\overline{\theta q}$ budget, drawn for $A=0.25$, is shown in Fig. 9. Note that molecular destruction is large over much of the mixed layer.

Whether our parameterizations hold as well for any mixed layer cannot be answered now. It seems necessary to examine in more detail the structure in the entrainment region near z_i and to examine the behavior of the mean profiles in other flows. The recent work by Zeman and Tennekes (1977) should provide a useful framework for analyzing entrainment region structure. Possible starting points for mean profile analysis are the vertical budgets of $\overline{w\theta}$ and $\overline{wq}$. Deardorff (1972) has shown that the $\overline{w\theta}$ budget can ex-

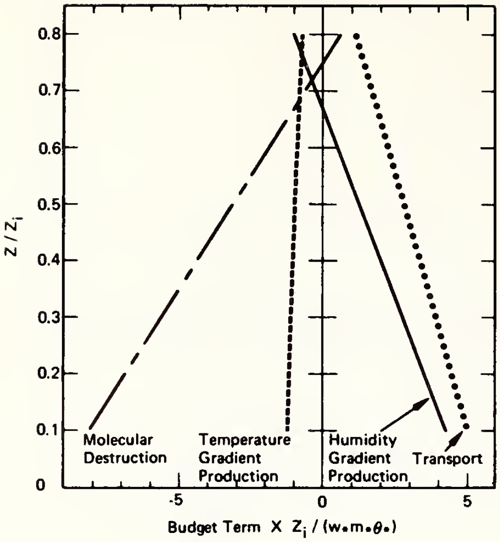

FIG. 9. The parameterized $\overline{\theta q}$ budget in the AMTEX mixed layer for $A=0.25=(0.61\ \Theta\ M_0/\rho Q_0)$.

plain the slightly positive $\Theta_{,3}$ values observed in very unstable, dry mixed layers and possibly the $\overline{wq}$ budget would give similar insight into the behavior of $(Q/\rho)_{,3}$ in the moist case.

b. Relationship to boundary layer growth

We will now show that our parameterized flux profiles [Eqs. (29) and (30)] when combined with jump relations at z_i give reasonable values for the entrainment velocity and the jump in radiative flux at z_i. Following Lilly (1968), Lenschow (1973) and Deardorff (1976) we assume that a linearized version of the equivalent temperature flux

$$\overline{w\theta_e}\equiv\overline{w\theta}+\frac{L}{\rho C_p}\overline{wq} \tag{38}$$

and the total water (water vapor plus liquid and solid water) flux varies linearly with height throughout the mixed layer in both clear and cloudy air except near the top. In the upper hundred meters or so of cloud layers, longwave radiative flux divergence may cause a more rapid decrease in the equivalent temperature flux. Substituting Eqs. (29) and (30) into (38), and using the observed values of Q_0 and M_0, yields

$$\overline{w\theta_e}=Q_{0e}(1-0.73z/z_i). \tag{39}$$

Entrainment of air into the mixed layer results in a nearly discontinuous jump in the fluxes across the turbulent inversion layer capping the mixed layer. According to Lilly (1968), the jump relations for total water (water vapor plus liquid and solid water) and for temperature across the top of the mixed layer are

$$w_e\Delta(Q+L_W)=\overline{-w(q+\mathrm{l}_w)_{z_i}} \tag{40}$$

$$w_{ec}\Delta\Theta_V=\overline{-(w\theta_V)_{z_i}}\qquad\text{(clear air),} \tag{41}$$

$$w_{es}\Delta\Theta_e=\overline{-(w\theta_e)_{z_i}}-\frac{\Theta}{T}\Delta R\qquad\text{(cloudy air),} \tag{42}$$

where w_e, w_{ec} and w_{es} are the total, clear air and cloudy air entrainment velocities, respectively (positive for entrainment of air from aloft into the mixed layer), l_w is the water substance fluctuation, $\Delta(Q+L_W)$ is the jump in total water across the mixed-layer top and ΔR is the jump in radiative flux.

Using the observed average values of $M_0=0.17$ g m^{-2} s^{-1} and $\Delta(Q+L_W)=-2.4$ g m^{-3}, and evaluating Eq. (40) with the aid of Eq. (30), we have $w_e=0.035$ m s^{-1}. Substituting Eqs. (29) and (30) into the virtual potential temperature flux equation and using the observed values of Q_0 and M_0 gives

$$\overline{w\theta_V}=Q_{0V}(1-1.3z/z_i). \tag{43}$$

The observed values of Q_{0V} and $\Delta\Theta_V$ are 0.13 m s^{-1} K and 2.7 K, respectively; therefore, $w_{ec}=0.014$ m s^{-1}. The radiative flux term ΔR in Eq. (42) is the most difficult term to estimate. Therefore, we solve Eq. (42) for ΔR. On the basis of flight observations we estimate the cloud cover at 50%. From the estimates of w_e and w_{ec}, we obtain $w_{es}=0.056$ m s^{-1}. Using the observed values of $Q_{0e}=0.45$ m s^{-1} K and $\Delta\Theta_e=-3.3$ K, we have $\Delta R=0.06$ m s^{-1} K. This value agrees well with values calculated with Sasamori's (1968) radiation model using the observed temperature and humidity profiles.

Lilly (1968) suggested that a solid layer of stratocumulus cannot persist for $\Delta\Theta_e\lesssim 0$, while Deardorff (1976) allowed for negative values of $\Delta\Theta_e$ (but not as large as those observed in AMTEX) due to water substance loading. These results are consistent with the observations of scattered to broken decks of stratocumulus.

Inhomogeneity of cloud cover may also be reflected in inhomogeneous boundary layer structure. In the foregoing discussion we have assumed that the measured fluxes, profiles and boundary layer heights are representative of both cloudy and clear areas. LeMone and Pennell (1976) suggest that wide variations in humidity flux profiles related to variations in cloud cover exist in the trade wind boundary layer.

6. Molecular destruction and the θ-q cospectrum

Our data indicate clearly that the $\overline{\theta q}$ budget is balanced by molecular destruction. Under local isotropy we can write the molecular destruction term as

$$2(K+D)\overline{\theta_{,j}q_{,j}}=6(K+D)\overline{\theta_{,1}q_{,1}}$$

$$=(6K+D)\int_0^\infty \kappa_1{}^2\,\mathrm{Co}_{Tq}(\kappa_1)d\kappa_1. \quad (44)$$

It follows from scaling arguments (Tennekes and Lumley, 1972) that the integral in Eq. (44) must receive its dominant contributions from wavenumbers of the order of η^{-1}. Thus at smaller κ_1, Co_{Tq} cannot fall faster than $\kappa_1{}^{-2}$.

Evidently then the maintenance of $\overline{\theta q}$ occurs in a fashion somewhat analogous to that for $\overline{\theta^2}$ or $\overline{q^2}$. The general features of scalar spectral dynamics are understood: production occurs at large scales, inertial transfer carries the scalar variance to smaller scales, and molecular destruction occurs at the smallest scales. Corrsin (1951) argued that the temperature spectrum Φ_T in the inertial range behaves as

$$\Phi_T=\Phi_T(\epsilon,\kappa,\epsilon_\theta), \quad (45)$$

where ϵ is the dissipation rate of turbulent kinetic energy per unit mass and ϵ_θ the corresponding quantity for $\overline{\theta^2}$. This leads to the well-tested expression for the one-dimensional spectrum

$$\Phi_T=\beta_1\epsilon^{-\frac{1}{3}}\epsilon_\theta\kappa_1^{-5/3}, \quad (46)$$

where $\beta_1\approx0.4$ (Champagne *et al.*, 1977).

We extend Corrsin's argument to the inertial range of the θ-q spectrum:

$$\mathrm{Co}_{Tq}=\mathrm{Co}_{Tq}(\epsilon,\kappa,\epsilon_{\theta q}), \quad (47)$$

where the destruction rate $\epsilon_{\theta q}$ is

$$\epsilon_{\theta q}=2(K+D)\overline{\theta_{,j}q_{,j}}. \quad (48)$$

Thus we predict for the one-dimensional cospectrum

$$\mathrm{Co}_{Tq}=\gamma_1\epsilon^{-\frac{1}{3}}\epsilon_{\theta q}\kappa_1^{-5/3}, \quad (49)$$

where γ_1 is a constant. However, the arguments given by Zeman and Lumley (1976) suggest γ_1 could vary with the molecular diffusivities K and D, if they differ.

We calculated 40 θ-q cospectra from the AMTEX data, each from runs about 18 km long. They are corrected for the inertial-range phase shift mentioned in Section 2 by multiplying by $[|R(f)|\cos\phi]^{-1}$, where $R(f)$ is the (complex) frequency response function obtained from the Fourier transform of Eq. (8) and ϕ is the phase angle of $R(f)$, using values of $\tau_1=0.03$ s and $\tau_2=1.15$ s. This correction assumes the inertial range is locally isotropic and hence that the θ-q quadrature spectrum vanishes there. Fig. 10 is an example of the θ-q cospectum before and after applying this correction. The corrected cospectrum has an extensive inertial range in agreement with Eq. (49) if $\kappa_1=2\pi f/U$ by Taylor's hypothesis.

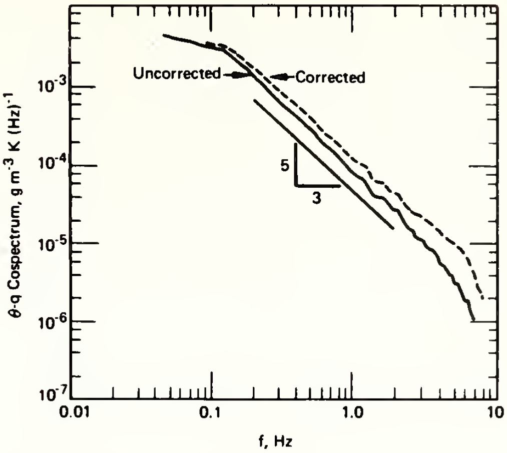

FIG. 10. Frequency cospectrum of humidity (measured with a Lyman-alpha hygrometer and adjusted for the observed time delay) and potential temperature measured on the Electra aircraft. Dashed line has been corrected for both phase shift and attenuation introduced by the thermometer. Both variables are filtered with a 4-pole Butterworth analog filter with a 10 Hz cutoff. The data were obtained from 1344:26 to 1421:45 LT 19 February 1975, at 150 m height over the East China Sea.

Friehe *et al.* (1975) also show a θ-q cospectrum with a $\kappa_1^{-5/3}$ inertial range. Friehe (private communication) has also calculated the θ-q cospectrum for the Minnesota 1973 data reported by Champagne *et al.* (1977). It too has a $\kappa_1^{-5/3}$ inertial range; in addition, we were able to estimate that $\gamma_1\approx0.5$–0.6 by using the surface layer $\overline{\theta q}$ budget [Eq. (24)] to estimate $\epsilon_{\theta q}$.

Our theory indicates that the $\kappa_1^{-5/3}$ range in the θ-q cospectrum should be as extensive as that for the temperature (or humidity) spectrum. Data do not show this, probably because of instrumental attenuation; it is very difficult to make fast-response, closely spaced θ and q measurements.

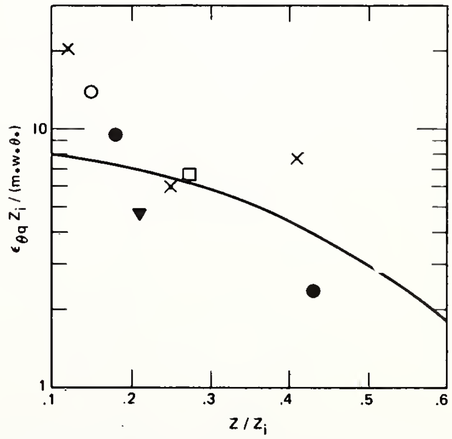

FIG. 11. Molecular destruction rates, made dimensionless with mixed layer scales, from AMTEX. The solid curve is from the parameterized budget (Fig. 9). Symbols as in Fig. 2.

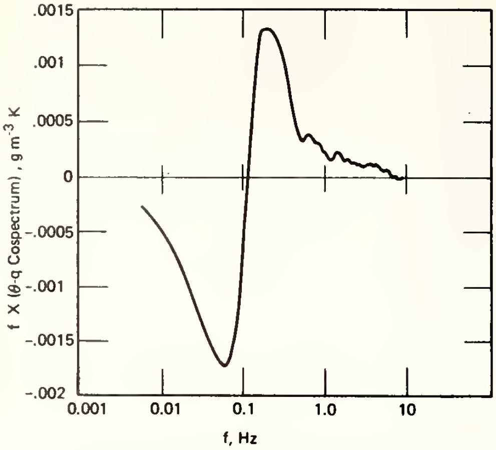

FIG. 12. Cospectrum of θ and q for 24 February 1975 at $z/z_i=0.5$. Cospectral densities are weighted by frequency so that the area between the curve and the x axis is proportional to the covariance.

It was not possible to calculate inertial range θ-q cospectra from all the AMTEX data because of noise problems. However, those available were used for estimates of $\epsilon_{\theta q}$, using Eq. (49) and ϵ values from the inertial range velocity spectra. We used the consensus β_1 value (0.4) for γ_1. The results are shown in Fig. 11, along with the $\epsilon_{\theta q}$ curve from our $\overline{\theta q}$ budget parameterization of Fig. 9. The measured $\epsilon_{\theta q}$ values seem high (compared with the curve) at small z/z_i, perhaps because our parameterization [Eq. (33)] of the mean potential temperature gradient is not accurate there. At z/z_i near 0.1, $\Theta_{,3}$ could still be slightly negative (as in the surface layer), rather than positive (as in the mixed layer). Thus the temperature gradient production term in the budget could be smaller in magnitude or even of the opposite sign near $z\approx 0.1\ z_i$ than indicated in Fig. 9. If so, the parameterized molecular destruction should have larger magnitude there, and hence would agree better with the data of Fig. 11 at small z/z_i. Overall, however, the measured $\epsilon_{\theta q}$ values are consistent with the parameterized curve, giving support to our inertial range cospectral prediction of Eq. (49) with $\gamma_1\approx 0.4$–0.6.

Large eddies complicate the θ-q cospectra (and hence the relationship between $\overline{\theta q}$ and $\epsilon_{\theta q}$), particularly around z_c, the level at which the right-hand side of the parameterized $\overline{\theta q}$ budget in Eq. (37) changes sign. A θ-q cospectrum for $z/z_i=0.5$ appears in Fig. 12. Note that the low-frequency end of the cospectrum is of opposite sign from the higher frequency inertial subrange. This behavior probably reflects the downward transport of warm dry entrained air by kilometer-scale eddies. It also suggests an explanation for the difference between z_c and the height of the $\overline{\theta q}$ zero crossing in Fig. 4. These heights would, of course, be the same if θ and q were correlated in the same sense at all frequencies.

7. Structure parameters

Structure functions are related to spectra through Fourier transforms (Tatarskii, 1971) so the structure parameters are proportional to inertial-range spectral levels. If we consider one-dimensional spectra of temperature and humidity, scaled so that

$$\left.\begin{aligned}\overline{\theta^2}&=\int_0^\infty \Phi_T(\kappa_1)d\kappa_1,\\ \overline{q^2}&=\int_0^\infty \Phi_q(\kappa_1)d\kappa_1,\end{aligned}\right\}\tag{50}$$

then in the inertial range (Wyngaard *et al.*, 1971b)

$$\left.\begin{aligned}\Phi_T&=0.25C_T{}^2\kappa_1{}^{-5/3}\\ \Phi_q&=0.25C_q{}^2\kappa_1{}^{-5/3}\end{aligned}\right\}.\tag{51}$$

Thus Eq. (49) implies that the θ-q cospectrum, scaled so that

$$\overline{\theta q}=\int_0^\infty \mathrm{Co}_{Tq}(\kappa_1)d\kappa_1\tag{52}$$

has an inertial range

$$\mathrm{Co}_{Tq}=0.25\ C_{Tq}\kappa_1{}^{-5/3}.\tag{53}$$

Thus we can relate C_{Tq} to other properties,

$$C_{Tq}=4\gamma_1\epsilon^{-\frac{1}{3}}\epsilon_{\theta q},\tag{54}$$

in analogy to the well-known results for $C_T{}^2$ and $C_q{}^2$:

$$\left.\begin{aligned}C_T{}^2&=4\beta_1\epsilon^{-\frac{1}{3}}\epsilon_\theta\\ C_q{}^2&=4\beta_1\epsilon^{-\frac{1}{3}}\epsilon_q\end{aligned}\right\}.\tag{55}$$

Eq. (54) provides the basis for describing the behavior of C_{Tq} in the boundary layer. Previous research has revealed the behavior of ϵ both in the surface layer and in the mixed layer (Lenschow, 1974; Kaimal *et al.*, 1976). Our $\overline{\theta q}$ budget results here give considerable insight into the behavior of $\epsilon_{\theta q}$ in the same regions.

Acknowledgments. We wish to acknowledge the excellent support of the NCAR Research Aviation Facility in operating the aircraft and data recording system. We also wish to thank Yunn Pann of NCAR, who did much of the programming and data processing on which the computations are based. We are also grateful to Jeanette Trebing of CIRES for her flawless typing of the manuscript, and to Carl A. Friehe for supplying the Minnesota data used here.

APPENDIX

List of Symbols

Roman symbols

A	a parameter in Eq. (43) $[=(0.61\,\Theta M_0/\rho Q_0)]$
C_p	specific heat at constant pressure for air
C_v	specific heat at constant volume for air
C_n^2, C_T^2, C_q^2	structure parameters for refractive index, temperature and water vapor density, respectively
C_{Tq}	joint temperature-humidity structure parameter
Co_{Tq}	one-dimensional cospectrum of temperature and humidity
D	molecular diffusivity for q
f	frequency (Hz)
g	acceleration of gravity (9.8 m s^{-2})
h	scale height
k	von Kármán constant, taken as 0.35
K	molecular diffusivity for θ
l	turbulence integral scale
L	Monin-Obukhov length $[=(-u_*^3T/kgQ_{0V})]$
l_w	fluctuating water substance density (liquid +solid)
L_W	mean water substance density at a given level (liquid and solid)
m_*	mixed-layer scaling parameter for moisture flux [see Eq. (25)]
M_0	surface moisture flux $[=(\overline{wq})_0]$
n	fluctuating refractive index
q	fluctuating absolute humidity (g m^{-3})
q_*	surface layer scaling parameter for humidity flux (see Eq. 14)
Q_0	surface temperature flux $[=(\overline{w\theta})_0]$
Q	at a given level, mean water vapor density (g m^{-3})
$\mathbf{r}$	separation distance between unprimed and primed quantities in Eq. (2)
$r_{\theta q}$	correlation coefficient between θ and q
T	mean temperature
T_*	surface layer temperature scaling parameter [see Eq. (14)]
t	time
u_*	friction velocity [see Eq. (14)]
u_j	fluctuating velocity component in the j direction
U_j	mean velocity component in j direction
w	fluctuating vertical velocity
w_*	mixed-layer velocity scaling parameter [see Eq. (25)]
w_e	entrainment velocity
$\mathbf{x}$	position vector in Eq. (2) for unprimed quantities
$\mathbf{x}+\mathbf{r}$	position vector in Eq. (2) for primed quantities
z	height
z_i	inversion height

Greek symbols

β_1	one-dimensional scalar spectral constant [Eq. (46)]
γ	for air, ratio of C_p/C_v
γ_1	temperature-humidity cospectral constant [Eq. (49)]
Δ	jump in a property across z_i
ϵ	dissipation rate for turbulence kinetic energy
$\epsilon_q, \epsilon_\theta, \epsilon_{\theta q}$	dissipation rates for $\overline{q^2}$, $\overline{\theta^2}$ and $\overline{\theta q}$, respectively
η	Kolmogorov microscale
θ	fluctuating temperature
θ_*	mixed-layer temperature scaling parameter [see Eq. (25)]
Θ	mean potential temperature
ρ	mean air density
τ_1, τ_2	time constants in Eq. (8)
ϕ_h	dimensionless mean temperature gradient
ϕ_q	dimensionless mean moisture gradient, assumed equal to ϕ_h
Φ_T, Φ_q	one-dimensional power spectra

Subscripts and superscripts

$(\ )_s$	saturated
$(\ )_0$	surface value
$(\ )'$	at position $\mathbf{x}+\mathbf{r}$
$(\ )_e$	equivalent
$(\ )_V$	virtual

REFERENCES

Buck, A. L., 1976: The variable path Lyman-alpha hygrometer and its operating characteristics. *Bull. Amer. Meteor. Soc.*, **57**, 1113–1118.

Businger, J. A., J. C. Wyngaard, Y. Izumi and E. F. Bradley, 1971: Flux-profile relationships in the atmospheric surface layer. *J. Atmos. Sci.*, **28**, 181–189.

Businger, J. A., 1973: Turbulent transfer in the atmospheric surface layer. *Workshop on Micrometeorology*, D. A. Haugen, Ed., Amer. Meteor. Soc., 67–100.

Champagne, F. H., C. A. Friehe, J. C. LaRue and J. C. Wyngaard, 1977: Flux measurements, flux estimation techniques, and fine scale turbulence measurements in the unstable surface layer over land. *J. Atmos. Sci.*, **34**, 515–530.

Corrsin, S., 1951: On the spectrum of isotropic temperature fluctuations in an isotropic turbulence. *J. Appl. Phys.*, **22**, 469–475.

Deardorff, J. W., 1972: Theoretical expression for the counter-gradient vertical heat flux. *J. Geophys. Res.*, **77**, 5900–5904.

——, 1976: On the entrainment rate of a stratocumulus-topped mixed layer. *Quart. J. Roy. Meteor. Soc.*, **102**, 563–582.

Friehe, C. A., J. C. LaRue, F. H. Champagne, C. H. Gibson and G. F. Dreyer, 1975: Effects of temperature and humidity fluctuations on the optical refractive index in the marine boundary layer. *J. Opt. Soc. Amer.*, **65**, 1502–1511.

Gossard, E. E., 1960: Power spectra of temperature, humidity, and refractive index from aircraft and tethered balloon measurements. *IEEE Trans. Antennas Propagation*, **AP-3**, 186–201.

Kaimal, J. C., J. C. Wyngaard, D. A. Haugen, O. R. Coté, Y. Izumi, S. J. Caughey and C. J. Readings, 1976: Turbulence structure in the convective boundary layer. *J. Atmos. Sci.*, **33**, 2152–2169.

LeMone, M. A. and W. T. Pennell, 1976: The relationship of trade-wind cumulus distribution to subcloud layer fluxes and structure. *Mon. Wea. Rev.*, **104**, 524–539.

Lenschow, D. H., 1972: The measurement of air velocity and temperature using the NCAR Buffalo aircraft measuring system. NCAR-TN/EDD-74, 39 pp.

——, 1973: Two examples of planetary boundary layer modification over the Great Lakes. *J. Atmos. Sci.*, **30**, 568–581.

——, 1974: Model of the height variation of the turbulence kinetic energy budget in the unstable planetary boundary layer. *J. Atmos. Sci.*, **31**, 465–474.

——, and W. T. Pennell, 1974: On the measurement of in-cloud and wet-bulb temperatures from an aircraft. *Mon. Wea. Rev.*, **102**, 447–454.

Lilly, D. K., 1968: Models of cloud-topped mixed layers under a strong inversion. *Quart. J. Roy. Meteor. Soc.*, **94**, 292–309.

Lumley, J. L., and H. A. Panofsky, 1964: *The Structure of Atmospheric Turbulence.* Interscience-Wiley, 239 pp.

McBean, G. A., and M. Miyake, 1972: Turbulent transfer mechanisms in the atmospheric surface layer. *Quart. J. Roy. Meteor. Soc.*, **98**, 383–398.

McCarthy, J., 1973: A method for correcting airborne temperature data for sensor response time. *J. Appl. Meteor.*, **12**, 211–214.

McGavin, R. E., and M. J. Vetter, 1965: *Humidity and Moisture: Measurement and Control in Science and Industry*, Vol. 2. A. Wexler, Ed. Reinhold, 553–560.

Phelps, G. T., and S. Pond, 1971: Spectra of temperature and humidity fluctuations and of the fluxes of moisture and sensible heat in the marine boundary layer. *J. Atmos. Sci.*, **28**, 918–928.

Sasamori, T., 1968: The radiative cooling calculation for application to general circulation experiments. *J. Appl. Meteor.*, **7**, 721–729.

Swinbank, W. C., and A. J. Dyer, 1967: An experimental study in micrometeorology. *Quart. J. Roy. Meteor. Soc.*, **93**, 494–500.

Tatarskii, V. I., 1971: The effects of the turbulent atmosphere on wave propagation. [NTIS TT 68-50464.]

Tennekes, H., and J. L. Lumley, 1972: *A First Course in Turbulence.* The MIT Press, 300 pp.

Wesely, M. L., 1976: Combined effect of temperature and humidity fluctuations on refractive index. *J. Appl. Meteor.*, **15**, 43–49.

Wyngaard, J. C., and O. R. Coté, 1971: The budgets of turbulent kinetic energy and temperature variance in the atmospheric surface layer. *J. Atmos. Sci.*, **28**, 190–201.

——,—— and Y. Izumi, 1971a: Local free convection, similarity, and the budgets of shear stress and heat flux. *J. Atmos. Sci.*, **28**, 1171–1182.

——, Y. Izumi and S. A. Collins, Jr., 1971b: Behavior of the refractive-index-structure-parameter near the ground. *J. Opt. Soc. Amer.*, **61**, 1646–1650.

Zeman, O., and J. L. Lumley, 1976: Turbulence and diffusion modeling in buoyancy driven mixed layers. *Preprints Third Symp. Atmospheric Turbulence, Diffusion and Air Quality*, Raleigh, Amer. Meteor. Soc., 38–45.

——, and H. Tennekes, 1977: Parameterization of the turbulent energy budget at the top of the daytime atmospheric boundary layer. *J. Atmos. Sci.*, **34**, 111–123.

Proceedings of a Working Conference on Current Measurement,
Tech. Report DEL-SG-3-78, College of Marine Studies,
University of Delaware, 59-65, 1978.

REPRINTED with permission from the author and from Science magazine (198: 138-144, October 1977). The article has been revised, based on further radar system software improvements. The changes are in the results of comparison of the radar measurements with the drifter measurements, and are reflected in Figure 7 and its descriptive text.

Copyright 1977 by the American Association for the Advancement of Science

Ocean Surface Currents Mapped by Radar

Mobile coastal units can map variable surface currents in real time to 70 kilometers, using ocean wave scatter.

D. E. Barrick, M. W. Evans, B. L. Weber

Currents within 1 meter of the ocean surface are highly variable, being driven by geostrophic forces and tides, but are strongly influenced by the local surface wind and wave fields. These currents transport floating matter and thus are of great importance in coastal areas, where considerable damage can be done by surface-borne pollutants and oil. In the case of the large oil spill by the tanker *Argo Merchant* off New England in December 1976, for example, catastrophic environmental damage was averted because strong offshore winds counteracted the normal surface-current drift toward shore. In a positive vein, the upper portion of the sea carries the zooplankton and phytoplankton, which are the dominant components at the bottom of the food chain and are responsible for production of most of the world's oxygen. Many types of fish eggs are borne by surface currents, which are therefore of concern to the fisheries industry. The transport of water with anomalous temperature differences is now believed to be responsible for unusual weather patterns affecting entire continents.

Near-surface current patterns, and how they respond locally to the relevant prevailing forces, are a subject that is largely unknown. Yet the subject is a crucial ingredient for the effective management of operations in coastal waters, and an increasingly important input for global resource monitoring and weather predictions.

Current Measurements

In conventional methods of measuring currents moored meters are used; the most recent types are referred to as vector-averaging current meters and the Aanderaa meter (*1*). These devices must be moored at depths exceeding 10 m, and thus provide little indication of the current at the surface, which is often different. Furthermore, data must be either recorded aboard the buoy (to be picked up later for analysis) or telemetered to shore; the instrumentation for the latter often restricts the operating range from the receiver to tens of kilometers. Surface currents have been measured by tracking floating objects. Qualitative estimates can be obtained by photographing the dispersal of dye packages from an aircraft, or by analyzing satellite infrared and optical imagery of suspended sediment (to a coarser area scale) (*2*). Quantitative measurements are made by photographically recording the positions of time-released floats dropped from the air, as described by Richardson *et al.* (*3*), or by tracking a drifting drogue buoy from a ship (*1*). In the latter case, a high-precision navigation system is required on the ship to accurately establish the drift of the buoy. Operations with aircraft or ships are both expensive and time-consuming for the meager amount of current data obtained (one vector over a period of about 1/2 hour). The velocity accuracy of these float-locating techniques appears to be of the order of 10 to 15 centimeters per second in magnitude and 5° in angle (*2*). The location of such drogues by triangulation, using high-frequency (HF) surface-wave emissions from the buoy, is described in (*3*); although such drogues are inexpensive ($175), the positional accuracy deteriorates with distance from shore, making this an unacceptable alternative near the edge of the continental shelf.

We discuss here a coastally located HF radar system that can measure and map near-surface currents to ranges about 70 kilometers from shore. This instrument deduces current velocity from the echoes scattered continuously from the ocean waves; buoys and drifters are not required. The radar units were built to be transportable and quickly deployable on a beach. A minicomputer controls the radar and processes the signals, permitting a current-vector map to be plotted in the field after 1/2 hour of operation. Two spatially separated radar units are presently employed, simultaneously

---

The authors are scientists with the Sea State Studies Area of the Wave Propagation Laboratories, Environmental Research Laboratories, National Oceanic and Atmospheric Administration, Boulder, Colorado 80302.

but independently, in order to yield the total current vector at each map grid point.

The principles underlying the system have been studied theoretically and experimentally over the past several years. The motion of the waves is seen by the radar as a translation of the frequency of the received echo signal from that of the transmitted signal; this frequency translation is called the echo Doppler shift. The radar can thus resolve and measure the component of scatter velocity along the line between the scatterer and the radar, referred to as the radial velocity. Crombie (*4*) first showed experimentally—and it was later confirmed theoretically (*5*)—that to first order the scatterers at high frequency are ocean wave trains moving toward and away from the radar, having spatial periods precisely one-half the radar wavelength. Thus the scattering mechanism is the diffraction grating or Bragg effect used in holography or in x-ray analysis of crystalline structures. The spectrum of the continuous-wave transmitted signal is a narrow peak at the carrier frequency location, as shown in Fig. 1. In the absence of current, the received first-order sea echo appears as two symmetrically spaced peaks about the carrier, whose Doppler shifts are given by the lowest-order dispersion relation of the scattering gravity waves; that is

$$\pm f_d = 2v_{ph}/\lambda = 2(gL/2\pi)^{1/2}/\lambda = (g/\pi\lambda)^{1/2} \qquad (1)$$

where λ is the radar wavelength, $L = \lambda/2$ is the length of the ocean waves responsible for the first-order Bragg scattering, v_{ph} is the phase velocity of these waves, and g is the gravitational constant.

A current beneath the surface waves represents a transport of the water mass, and can be thought of as a translation of the entire coordinate frame for the waves with respect to the observer at the stationary radar on shore. Hence the two spectral peaks scattered from the waves will be shifted (with respect to the position of the carrier frequency) by a small amount proportional to the radial component of current velocity, as shown at the bottom of Fig. 1. This amount is $\Delta f = 2v_{cr}/\lambda$, where v_{cr} is the mean effective current velocity radial to the radar. In (*6*), radar-deduced radial current observations were compared with drifter measurements of currents at San Clemente Island; the narrow radar beam and short pulse kept the ocean patch size under observation to about 7 by 7 km. The agreement was about ± 10 cm/sec. In these investigations (*6, 7*) the effect of a nonuniform current on the transport of the radar-observed surface waves was also analyzed as a function of depth.

Experiments such as those at San Clemente Island (*6, 7*), resolving the sea echo from narrow azimuthal sectors at high frequency, require long permanent phased-array antenna systems (> 300 m) on the beach to form a narrow beam. When one considers typical current patterns and the various echo-signal Doppler shifts they would produce at different azimuths from the radar, one can conceive of much smaller, simpler antenna systems for determining the direction of arrival of the echo. For example, by comparing the phase between two noninteracting antennas separated by less than one-half wavelength, one can uniquely determine the direction of arrival over 180° of space of a single signal at a given Doppler shift. Crombie (*8*) showed that this simple two-antenna system was adequate to azimuthally resolve sea-echo signals from Florida, looking eastward across the south-to-north Gulf Stream current flow.

Concepts Behind the Present System

Because seawater is nearly a perfect conductor at high frequency (3 to 30 megahertz), the "ground-wave" propagation mode is employed (*9*). In this mode, vertically polarized electric fields are transmitted and received. The propagating fields at these frequencies follow the curvature of the earth and continue well into the shadow region beyond the horizon, even in the absence of atmospheric and ionospheric refractive index anomalies. Mathematical solutions for the ground wave—corrected to include the effects of sea-surface roughness (*9*)—are available. They show that (i) near the radiating source, the field decays with the expected inverse range dependence of free space, and (ii) far into the shadow region, the fields near the surface decay exponentially with range. This exponential range dependence ultimately dictates the maximum distance at which currents can be observed for a particular transmitted power. For the hardware described in the next section, the maximum range for the system—allowing for a 10-decibel signal-to-noise ratio (S/N) at the receiver (*10*)—is about 70 km; this has been verified in our recent experiments, which are discussed below.

Although the system does not employ ionospheric or atmospheric refraction to propagate beyond the horizon, it is incorrect to call it a "line-of-sight" radar (as is a microwave radar). In fact, trying to increase the useful range of the radar by elevating the antennas (in order to increase the distance to the horizon) is counterproductive, because there is a discontinuity in the propagation path in free space between the antennas and the highly conducting seawater. We have established this fact theoretically and also experimentally, by trying to put the antennas on roofs of buildings (but back several hundred meters from the water) to increase the range. We have found that the optimal locations for the antennas are at sea level on the beach, as close to the water as possible; in fact, it

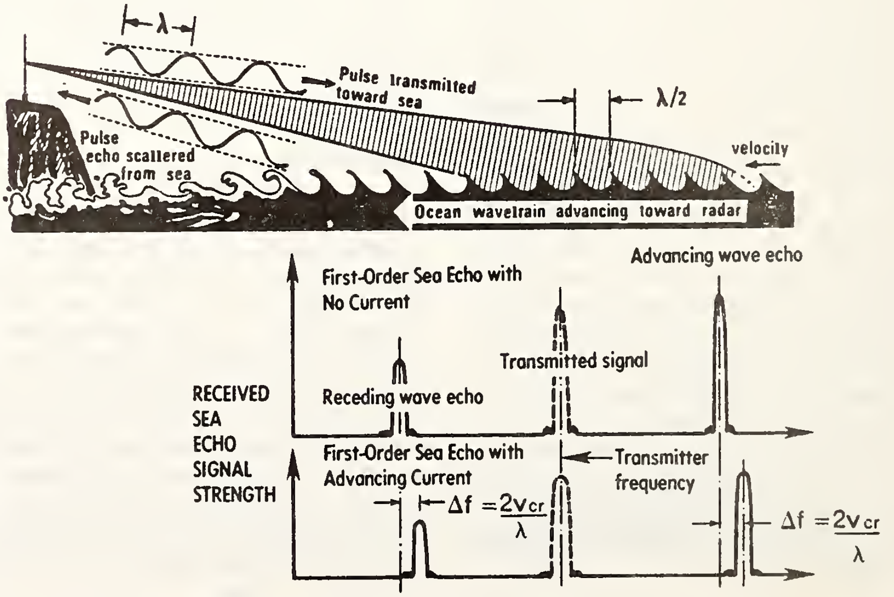
λ
Pulse transmitted toward sea
λ/2
Pulse echo scattered from sea
velocity
Ocean wavetrain advancing toward radar
Advancing wave echo
First-Order Sea Echo with No Current
Transmitted signal
RECEIVED SEA ECHO SIGNAL STRENGTH
Receding wave echo
First-Order Sea Echo with Advancing Current
Transmitter frequency
Δf = 2v_cr/λ
Δf = 2v_cr/λ

Fig. 1. Sketch showing the principles of first-order HF Bragg scatter from the sea, and resulting signal echo spectra without and with an underlying current.

is best if the grounding system beneath the antennas makes electrical contact with the seawater.

A separate antenna is used for transmitting. It produces a slightly directional pattern, peaked out toward the sea, with a half-power beam width of ±90°; its radiation in the backward direction is ~ 10 db lower than that in the forward direction, which minimizes unwanted illumination over land. As with nearly all radars, time gating of the received signal echo referenced to the transmitted pulse time determines the range to the sea echo. Our system transmits a 20-microsecond unmodulated pulse and digitizes the received echo signal every 20 microseconds after transmission. The signal sample from each range (time) gate thus represents the echo from an annulus of the sea surface 3 km in width, concentric with the radar location. A total of 25 consecutive range-gated signals are thus retained for every transmitted pulse, providing a total distance of about 75 km from the radar. The transmitted pulse repetition interval is 1 millisecond.

Since echo-signal Doppler shifts are to be related to current velocities, the time series for each range gate is spectrally processed. This is done digitally at the radar site with a fast Fourier transform (FFT) algorithm. Appropriate digital filtering of the signals is performed before the FFT to prevent spectral aliasing and to maximize S/N. Since the sea surface is a random variable, the sea echo is also a random variable. In fact, each spectral power point output from the FFT is an independent random variable, following a chi-square distribution with two degrees of freedom (*11*).

In the first series of experiments, three colinear independent receiving antennas were employed. The received signal was sampled on each antenna separately and sequentially for each transmission every millisecond, with the other two antennas switched open to minimize mutual interactions. Therefore the FFT outputs from the three antennas (for a given range gate) can be thought of as being measured simultaneously; the only theoretical difference between the signals at the antennas is due to the phase path differences undergone by an echo, at a particular Doppler frequency from a particular direction, arriving at the different positions of the three elements. Three antenna elements, each separated for our first experiments by one-quarter wavelength (3 m at 25 Mhz), aligned parallel to a straight coastline, can unambiguously resolve two sea-echo signals at a particular Doppler frequency from 180° of space. For two signals with complex amplitudes $\dot{A}_1$ and $\dot{A}_2$ from angles α_1 and α_2 (with respect to the perpendicular to the coastline), the three complex received voltages $\dot{V}_A$, $\dot{V}_B$, and $\dot{V}_C$ can be solved in closed form for the desired angles and amplitudes, with the following results (asterisks denote complex conjugates)

$$\alpha_{1,2} = \sin^{-1}\left[\frac{-\tan^{-1}\left(\frac{\mathrm{Im}(x_{1,2})}{\mathrm{Re}(x_{1,2})}\right)}{\pi/2}\right] \quad (2)$$

and

$$\dot{A}_{1,2} = \frac{\dot{V}_A x_{2,1} - \dot{V}_B}{(x_{2,1} - x_{1,2})} \quad (3)$$

where

$$x_{1,2} = \frac{(|\dot{V}_C|^2 - |\dot{V}_A|^2) \pm i(4|\dot{V}_C\dot{V}_B^* - \dot{V}_B\dot{V}_A^*|^2 - (|\dot{V}_C|^2 - |\dot{V}_A|^2)^2)^{1/2}}{2(\dot{V}_C^*\dot{V}_B - \dot{V}_B^*\dot{V}_A)}$$

In reality, since the sea-echo signal amplitudes $\dot{A}_1$ and $\dot{A}_2$ are random variables to which random noise is added, the angles of arrival determined from Eqs. 2 to 4 contain a random error that decreases with increasing S/N. Extensive simulations and special experiments have shown that for 10-db S/N, such angular errors are less than 1° for $|\alpha| < 70°$. We have recently changed to a four-antenna configuration (arranged in a square) to resolve two signals from 360°; this permits us to operate the radar on a peninsula or an island with ocean water subtending more than 180° around the site.

Two sites are required to obtain two radial current-vector components along lines pointing in different directions in order to construct a total current vector at a particular point on the sea. For a straight coastline, the question arises as to how far apart the sites should be. Since a total current vector can be constructed only within the common overlapping areas seen by both sites, it is desirable to maximize this area (by moving the sites closer together). On the other hand, as the sites become close (superposed in the limit), they see most points on the sea in the common area along nearly the same radial direction, which makes construction of the total vector inaccurate. Consequently, we defined the optimization criterion for site separation as the product of the common coverage area times the average of the sine of the angle between the lines to the two sites. This product has a broad maximum, indicating that for a coverage distance from a single site of about 70 km, a site spacing anywhere between 25 and 55 km is adequate.

Various trade-offs were considered in selecting the frequency range 25 to 26 Mhz for our first series of tests (the radar wavelength of 12 m is, to first order, scattered from ocean waves with a 6-m wavelength). At these frequencies atmospheric and external man-made electrical noise are often low, being equal to internal electrical receiver noise, whereas at lower frequencies atmospheric noise seen by the radar increases sharply. In addition, antenna sizes also increase with decreasing frequency, requiring larger structures and more ground area. On the other hand, ground-wave propagation loss decreases with decreasing frequency, offsetting the noise dependence. There are additional reasons for operating at higher frequencies, however. For one thing, above 25 Mhz ionospherically propagated echoes are rarely encountered, whereas at lower frequencies such distant echoes can be folded in with the desired short-range sea return. Two other important reasons for higher frequencies are oceanographic in nature. First, the Bragg-scattering 6-m ocean waves are relatively short and are likely to be present more of the time than longer waves, which require stronger winds to develop them. A wind with a velocity greater than 3 m/sec, blowing longer than 1 hour, will develop 6-m waves to their (equilibrium) root-mean-square height of ~ 10 cm. Inasmuch as the waves are used only as a "tracer" for the underlying currents, it is desirable that they be present as often as possible. Second, the shorter the ocean waves under observation, the more they are influenced by currents very near the surface. A rule of thumb (*6, 7*) is that the depth of the layer whose current will affect a surface wave of length L is $L/2\pi$ (about 1 m for $L = 6$ m). Hence, if one wants to observe currents in the uppermost ocean layers by measuring their effect on the phase speeds of gravity waves, he should use as high a radar frequency as possible. These factors led us to select 25 to 30 Mhz for our initial operations.

Hardware Description

The present two-unit radar system was designed as a prototype of an operational version, with considerably more flexibility than will ultimately be needed, in order to facilitate changes as experience is gained in the field. Yet this system was built to be transported by vehicle (see Fig. 2), easily erected on a beach, and capable of being operated from a portable power supply (a 2.2-kilowatt gaso-

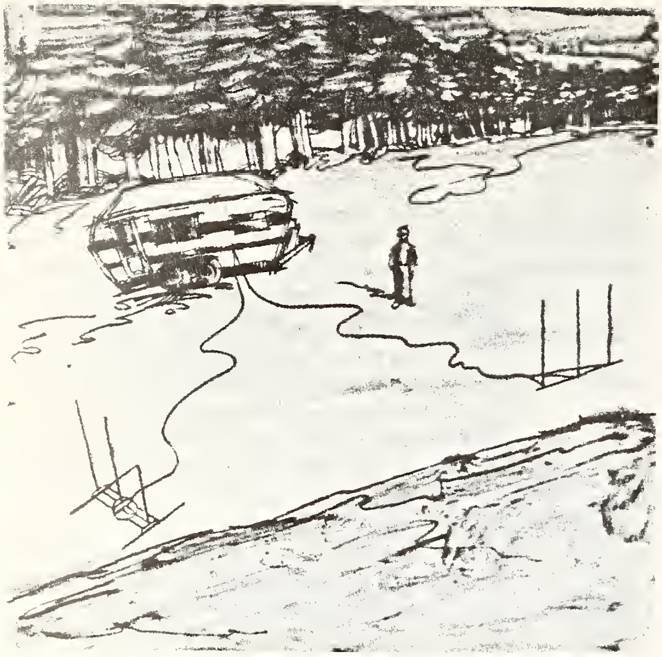

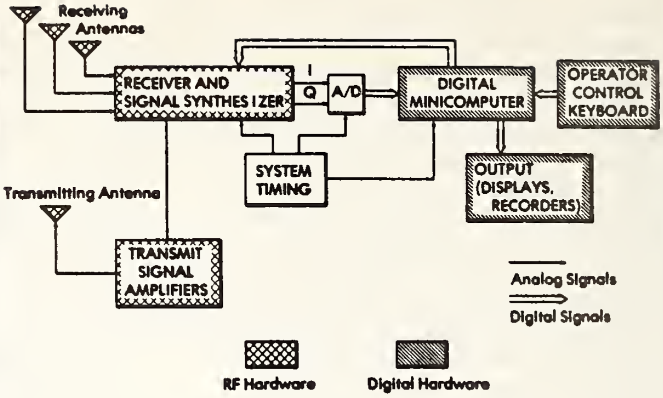

Fig. 2 (left). Sketch of the system as operated on the beach. Transmitting antennas are on the left and receiving antenna on the right. Fig. 3 (right). Block diagram of radar system.

line generator). The entire radar is controlled by a minicomputer, which also does the signal and data processing in the field. The end result is a map—drawn on a pen plotter—of the surface-current vector field.

The system radiates ~ 2.5-kw–peak pulse power, as a stream of 20-μsec pulses every millisecond; thus the average radiated power is only 50 watts. The radar is presently capable of transmitting any operator-selected frequency between 25 and 35 Mhz (in 200-khz increments), but so far we have operated primarily between 25 and 26 Mhz. The transmitting antenna is a log-periodic vertical monopole array of three (or four) elements designed especially for this application at Lawrence Livermore Laboratories (*12*). Both versions were designed to have an input impedance of ~ 50 ohms (real) from 25 to 27 Mhz; the three-element version has a half-power beam width of ± 90°, while the four-element version has ± 43°.

The individual receiving elements are readily available fiberglass-encased citizens-band whips cut to a height of 1.575 m and each fed against a quarter-wavelength, four-element, radial ground screen. The three (and currently four) receiving elements are aligned on the beach with a tape measure and compass. These elements are each connected through one-half wavelength of coaxial cable to a switching network and preamplifier box, which cycles sequentially through each of the antennas at a rate of 1 msec per antenna. From this switch, the signals then pass through a single preamplifier and coaxial line several tens of meters in length to the receiver hardware in the van. From the antenna switch onward, the signals from each antenna pass through the same hardware, eliminating mismatch problems through separate channels. The entire antenna system can be unfurled by two men in about 1/2 hour.

The heart of the radio-frequency system is the receiver (Fig. 3), designed by Barry Research, Inc., especially for this radar. In addition to its obvious function, the receiver also synthesizes the desired carrier frequency and the pulse stream to be transmitted. This stream is amplified in hardware designed and built in-house. Every 20 μsec, the receiver gain is changed under computer control, called a sensitivity time control (STC), in order to compensate for the decrease of echo strength with range. The echo is coherently mixed down to zero-intermediate-frequency in-phase and quadrature (I and Q) signals. These I and Q signals are then digitized with a ten-bit analog-to-digital (A/D) converter every 20 μsec,

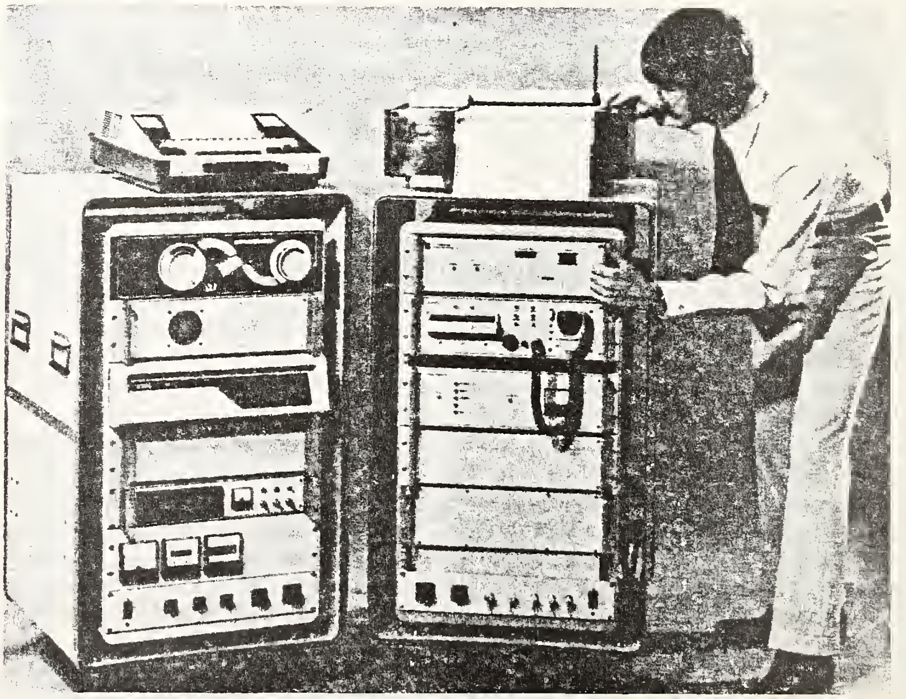

Fig. 4. Photograph of complete radar radio-frequency and digital hardware.

and all subsequent signal processing is done digitally. This includes filtering (called preaveraging, over 1/2 or 1/4 second) to reduce the signal bandwidth to 2 or 4 hertz. The filtered signals for each range gate and each receiving antenna are then collected for 128 or 256 seconds as the input to a 512-point complex FFT; thus, for the 128-second option, for example, the displayed spectrum has a Doppler resolution of 1/128 hertz over a window from − 2 to + 2 hertz. (These parameters can be selected by the operator.) The 1/128-hertz Doppler resolution translates into a radial current velocity resolution of ~ 5 cm/sec.

The heart of the digital system for radar control and data processing is a Digital Equipment Corporation PDP 11/34 minicomputer. The operator communicates with the system through a portable keyboard terminal. Moving-head magnetic disk and nine-track magnetic tape units are available for loading system software into the computer and also for recording and archiving processed radar data. Graphic displays and pen plotters are available to display raw spectra and current-vector plots. Further description of the system hardware is found in (*10*); a photograph of the complete digital and radio-frequency hardware (excluding antennas) for one site is shown in Fig. 4.

Experimental Results and Digital Data Analysis

Initial field operations began with the new radar system in southern Florida during late 1976; there was an additional final week of operations in Florida from 20 to 26 March 1977, during which fairly extensive independent measurements of surface currents were made for comparisons. The Florida area was selected for initial operations and system calibrations because of the fairly regular but strong south-to-north Gulf Stream flow east of Miami. The two sites were located at South Miami Beach (20° 46′00″N,80°07′58″W) and Fort Lauderdale (26°05′01″N,80°06′38″W), approximately 36 km apart. The latitudes and longitudes of the two sites are entered into the computer, along with the azimuthal bearings of the two receiving antenna arrays. The software then calculates the *x*, *y* positions of a rectangular grid (3 by 3 km) of points to the east of the baseline joining the two sites—at which current vectors will be plotted from the radar data—after conversion from the radar-oriented polar coordinates (range and azimuthal bearing from each site). Most of the measurements were made on 25.4 or 25.6 Mhz, with a 128-second coherent integration time (providing a Doppler resolution of 1/128 hertz).

The output of a single FFT is a complex random variable, having Rayleigh amplitude and uniform phase probability densities. The desired first-order portion of the sea echo is random because of the statistical nature of the scattering sea surface. The remaining portion of the FFT output can be thought of as additive random noise with respect to its effect on the desired first-order signal. In reality, there are at least four types of noise, originating from different sources: (i) external atmospheric or man-made noise, (ii) internal receiver noise, (iii) second-order radar sea echo (*13*), and (iv) processor noise due to limited system dynamic range, system nonlinearities, and quantization noise. Finally, the actual current field beneath the waves, instead of being uniform, is more likely to be somewhat turbulent within the spatial resolution scales seen by the radar. Hence, the total signal plus noise is random, and from this we intend to extract (i) an estimate of the azimuth angle of arrival of the signal at each Doppler frequency output from the FFT, (ii) an estimate of the radial current velocity at this range and azimuth, and (iii) the sea-echo signal amplitude.

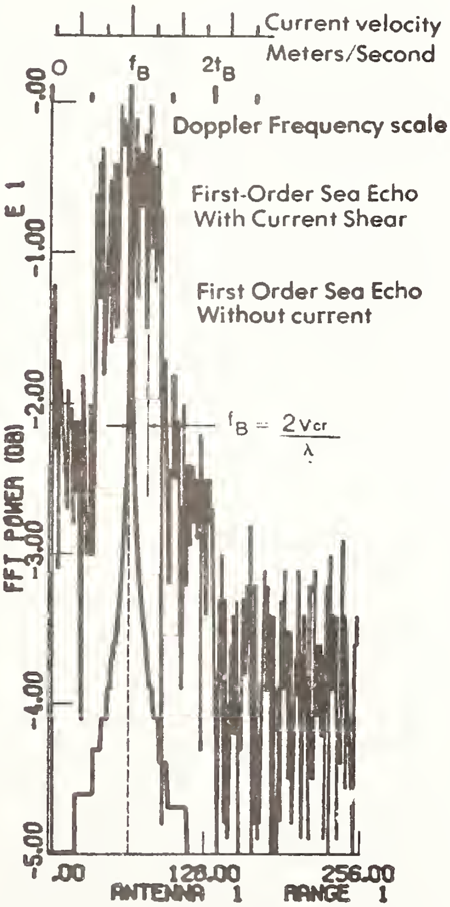

Fig. 5. Plot of FFT spectral power output. The black spectrum is the idealized test sea-echo spectrum in the absence of a current. The gray spectrum is the measured sea echo at 37.5 km from Fort Lauderdale, as modified by Gulf Stream current shear.

Since extraction of the angle of arrival, using the equations given above, requires the use of coherent simultaneous signals from each of three (or four) receiving antennas for a given range cell, we cannot average the individual outputs of the FFT's in order to reduce the effects of random signal fluctuation and noise. Instead, we go through the following process. Figure 5 is an example of the right half of the amplitude-squared output of the FFT processor for the 37.5-km range gate for sea echo measured at Fort Lauderdale. A threshold level is established for the usable portion of the signal (for example, 20 db down from the mean peak level), and the remainder of the FFT output is discarded. The solid curve shows the expected position of the echo in the absence of any current over the semicircular range cell; it occurs at a Doppler shift f_d (Eq. 1). All echo points at Doppler shifts different from f_d are therefore due to currents, and a radial current velocity scale centered on f_d can be given in terms of these Doppler shifts, as shown in Fig. 5. The angle of arrival of the signal at each of these Doppler shifts (or radial current velocities) is then obtained from the complex signals $\dot{V}_A$, $\dot{V}_B$, and $\dot{V}_C$ at each of the three antennas, using Eqs. 2 to 4.

At this point, for a given 128-second run and for each range gate, we have an array of azimuth angles and signal echo amplitudes as a function of radial current velocity. We then interchange the roles of the dependent and independent variables, considering radial velocity as a function of azimuth angle. After accumulating and storing radial velocity data over several consecutive 128-second runs (typically ten), we then average the radial velocities that fall within preset angular "bins."

This averaging is actually done in a manner that gives preference to higher-quality points. First of all, each sample radial velocity point in a particular angular bin is weighted by the ratio of the signal (amplitude squared) to the average noise power level for that same point; higher signal amplitude values give more accurate angle estimates. Second, other quality factors are used to weight the radial velocity samples. For example, in the absence of noise, the amplitudes of $x_{1,2}$ given in Eq. 4 will always be unity. Hence samples whose values of $|x_{1,2}|$ de-

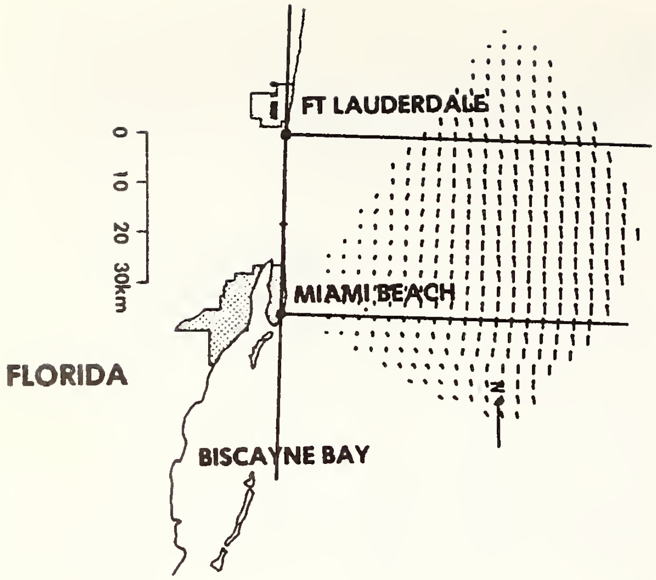

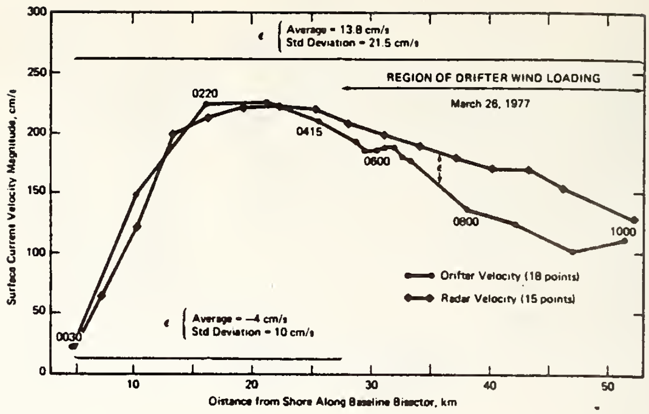

Fig. 6 (left). Computer-generated map of the Gulf Stream current on 20 October 1976 as deduced by radar. Fig. 7 (right). Comparison of radar-deduced surface velocity magnitude with drifter measurements.

part significantly from unity are weighted lower. Finally, the signal-to-noise ratios for all of the samples in a particular angular bin are averaged; this is used in a final thresholding process to decide whether the (weighted) averaged radial velocity for that bin will ultimately be used. If it is not used (because the signals are too low) or if there were no values falling in the bin, then a value for the radial velocity at that angle is calculated by interpolation from the adjacent range-azimuth cells.

In the process of producing a map, the data from both sites are combined (in our case, either by data telemetry between the two sites or by physically transporting the data tapes from one site to the other). Then the arrays of radial current velocities from each radar site together with range and azimuth (in polar coordinates) are entered for each rectangular grid point; also, direction cosines at the grid point are calculated for the radial lines to the sites. This allows the total current vector to be plotted at that grid point. The angular sectors very near the shore are sometimes excluded because the nearly parallel radial velocities seen from each site at these grid points give rise to large vector errors; integration techniques to improve the quality of the maps near shore are being investigated. Figure 6 is an example of a map made in Florida by using these data processing steps. The well-known horizontal shear of the Gulf Stream (outward from the shore) is clearly visible in these maps.

The point to be emphasized is that all of the averaging, weighting, and thresholding procedures described above are done digitally (not arbitrarily or subjectively), according to rules that are being optimized. The mathematical steps involved, beginning with the angle extraction, are nonlinear in nature. Hence it is not possible to obtain mathematical error estimates in closed form. The optimization of the processing algorithms must therefore be based on two methods of quality assessment. First, simulations are employed in which one begins with known current patterns, randomizes the first-order sea-echo spectrum, adds random noise, converts to a time series, and then processes this simulated echo signal to see how well the original current patterns are recovered. We have been using such simulations for nearly 3 years to arrive at our present algorithms. Second, independent measurements of surface currents are obtained during radar operations, using drifters and timed-released floats. Comparisons of these measurements with radar data are the subject of the next section.

Comparison with Drifters

As an ultimate calibration standard, one would like to employ independent measurements of near-surface currents as "ground truth." However, since differences of tens of centimeters per second have been documented in drifter current measurements, there is considerable doubt as to whether disagreements of this order between drifter- and radar-deduced currents are due to radar errors or drifter errors. Furthermore, the two techniques are so dissimilar in nature that there are many reasons why they should respond differently to conditions near the surface. Nonetheless, since drifters are the only established quantitative method of estimating surface currents, we made a series of radar measurements on 23 to 26 March 1977 in Florida in conjunction with ship tracks of drifters in order to establish some initial credibility for this new remote-sensing technique. The Nova University vessel *Youngster III*—supported by a Hi-Fix Navigation system—tracked a drifter at several positions in the radar coverage area over 8- to 12-hour periods on 23 and 25 March. This drifter was drogued with rigid vertical aluminum baffle plates extending 46 cm below the surface float. Each track consisted of a 5- to 8-minute drift whose start and end points were marked navigationally; from this a mean (Lagrangian) drift velocity was calculated. In addition, the National Oceanic and Atmospheric Adminstration vessel *Virginia Key*—supported by a miniranger navigation system—tracked a cork float on 23 and 24 March at other locations in the coverage area. Again, each track lasted about 5 minutes.

The velocities deduced from both radar and drifter measurements, and the differences between them, were relatively similar in all cases. Significantly, the drifter velocities show considerable differences from day to day. For comparison, we show here our longest set of drifter measurements, made eastward from shore (at the midpoint between the two radar sites) to a range of 50 km; these drifter measurements, made with the *Youngster III* and the drogued buoy, required 12 hours to complete. These measurements are shown in Fig. 7 along with radar-deduced current velocities. The total current-vector magnitudes are plotted for each technique.

The agreement is very reasonable, within the range of expected drifter variances.

Both techniques recorded the current shear with distance from shore quite accurately, and observed the current maximum on this particular day at approximately 20 km from shore. Most of the disagreement beyond 27 km was due to the fact that a sudden onset of high winds and breaking waves caused the drifter to tip over, so that it was not measuring surface-current drift properly. Measuring the average error, ε (between straight-line segments joining the two sets of points) and its standard deviation over the path out to 27 km, we obtain 10 cm/s for the standard deviation. If we include the entire path, this standard deviation is 21.5 cm/s.

The 10 cm/s difference may well be the best obtainable agreement between these two techniques because they are intrinsically observing different quantities. The drifter measurement is Lagrangian in nature, averaged over only a short line (400-500 m); the radar measurement is Eulerian, averaged over an area of about 3 by 3 km.

Applications and Future Directions

The HF radar remote-sensing system appears to provide considerably expanded observational capability for coastal physical oceanographic research. Since it is transportable and offers output current maps on site in near real time, the system has a great potential for operational coastal current monitoring and for quick response to offshore accidents. Inasmuch as surface currents are highly variable, elusive, and expensive to measure by existing in situ techniques, this instrument offers an attractive alternative. To duplicate the large areal volume of data vectors obtained with only a 1/2-hour radar operation would require many ships or aircraft tracking drifters simultaneously—an experiment that would cost hundreds of thousands of dollars. Our discussion with commercial manufacturers lead us to believe that streamlined operational versions of our prototype radar could be available for about $50,000 per complete radar pair.

The need to understand and better define the structure of currentlike water movement near the surface becomes more evident as we attempt to further interpret and refine the accuracy of this system. Both theoretical analyses and carefully planned experiments should be undertaken to quantify the effects of current turbulence within the radar cell, wave-wave interactions, and current shear with depth on the radar measurements. Furthermore, the actual linear horizontal drift of particles at the surface (for example, oil) and its relation to mean near-surface current velocity must be determined, especially under conditions of high winds and breaking waves. The similarities and differences between Eulerian areal and Lagrangian linear measurements need to be better understood. The prospect of having continuous surface-current data should provide the impetus to correlate currents with their short-term driving forces (such as winds, waves, and tides). Such a correlation is potentially a means of using the surface-current data to measure, indirectly, those driving forces.

Summary

A high-frequency radar remote-sensing system for measuring and mapping near-surface ocean currents in coastal waters has been analyzed and described. A transportable prototype version of the system was designed, constructed, and tested. With two units operating tens of kilometers apart, the currents were mapped in near real time at a grid of points 3 by 3 km covering areas exceeding 2000 km^2, out to a distance of about 70 km from the shore. Preliminary estimates of the precision of current velocity measurements show it to be about 10 cm/sec.

References

1. P. M. Saunders, *Deep-Sea Res.* **23**, 249 (1976).
2. V. Klemas, G. Davis, J. Lackie, W. Whelan, G. Tornatore, *IEEE Trans. Geosci. Electron* **GE-15**, 97 (1977).
3. W. S. Richardson, H. J. White, Jr., L. Nemeth, *J. Mar. Res.* **30**, 259 (1972).
4. D. D. Crombie, *Nature (London)* **175**, 681 (1955).
5. D. E. Barrick, *IEEE Trans. Antennas Propag.* **AP-20**, 2 (1972).
6. R. H. Stewart and J. W. Joy, *Deep-Sea Res.* **21**, 1039 (1974).
7. D. E. Barrick, J. M. Headrick, R. W. Bogle, D. D. Crombie, *Proc. IEEE* **62**, 673 (1974).
8. D. D. Crombie, in *Proceedings of the IEEE Ocean '72 Conference* (IEEE Publ. 72 CHO 660-1 OCC, Institute of Electrical and Electronics Engineers, New York, 1972), pp. 173–179.
9. D. E. Barrick, *Radio Sci.* **6**, 517 (1971).
10. ______ and M. W. Evans, *NOAA (Natl. Oceanic Atmos. Adm.) Tech. Rep. ERL 373-WPL 47* (1976).
11. D. E. Barrick and J. B. Snider, *IEEE Trans. Antennas Propag.* **AP-25**, 19 (1977).
12. J. L. Willows and R. J. Lytle, *Lawrence Livermore Lab. Rep. UCID-17024* (1976).
13. D. E. Barrick, in *Remote Sensing of the Troposphere*, V. E. Derr, Ed. (Government Printing Office, Washington, D.C., 1972), chap. 12.

Journal of Applied Meteorology, 17: 1014-1022, 1978.

Infrasound Originating Near Mountainous Regions in Colorado

A. J. Bedard, Jr.

Wave Propagation Laboratory, NOAA, Environmental Research Laboratories, Boulder, CO 80302

(Manuscript received 25 September 1975, in final form 13 March 1978)

ABSTRACT

An array of infrasonic microphones, installed near Fraser, CO, operated from February through June 1973. This observatory, in conjunction with a similar, permanent installation at Boulder, triangulated on sources of infrasound in Colorado. We found that the lee of a group of mountains that includes Long's Peak is a preferred source region for infrasound. Heretofore, such triangulations used long propagation paths usually of hundreds of kilometers, which resulted both in poorly defined source regions and signal source characteristics. The generation of local infrasound is probable when the 500 mb winds are high. A comparison with Boulder's historical data shows that most signals occur during the winter months with durations longer than 3 h. One case study presented shows that source motion can occur (20 km over an 8 h period). The identification of a local, accessible infrasonic source region offers wide opportunities for further research (e.g., the study of an active source region using time-lapse photography, dual-Doppler radar, lidar and instrumented aircraft). Comparisons of infrasonic data with measurements of turbulence reported by aircraft suggest a temporal and spatial relation between sources of infrasound and aircraft turbulence encounters.

1. Introduction

Since the early 1950's, the Geoacoustics Research Program Area of NOAA's Wave Propagation Laboratory (formerly the infrasonics group of the National Bureau of Standards) has studied various types of infrasonic signals in the atmosphere. This work, and work by other groups, has demonstrated that low-frequency (1–0.01 Hz passband) acoustic waves are related, for example, to geomagnetic activity (Chrzanowski *et al.*, 1961), earthquakes (Donn and Posmentier, 1964), volcanoes (Goerke *et al.*, 1965), ocean waves (Benioff and Gutenberg, 1939) and severe storms (Bowman and Bedard, 1971; Georges, 1973).

One class of infrasonic signal measured at Washington, DC, for periods of many years during winter months showed a bearing of arrival from the northwest. These signals were called "northwesters" because of their consistent azimuth of arrival. The addition of the Boulder observatory permitted a rough determination of many source locations, which appeared to be mountainous regions in the Pacific Northwest of the United States and Canada.

Data from observatories at Pullman, WA, and Edson, Alberta, supported the belief that mountainous regions were indeed the origin of the signals. Larson *et al.* (1971) showed a relation between these signals and the speed and direction of the 500 mb winds in the generation region. In particular, they detected infrasound on three days when the winds were high and the directions of airflow occurred at right angles to the principle axes of mountain ranges in the source area. They also identified the chief source regions based upon statistical data from these observatories. Infrasonic stations in South America show signals that originate near the Andes during the Southern Hemisphere winter. Green and Howard (1975) completed a statistical study of this class of infrasound on a global scale and found that these mountain-associated sources constitute the most frequent class of infrasound (at frequencies <0.1 Hz). Identification of the source mechanism or mechanisms will permit a fuller interpretation of these global data.

Bearing deviations suffered over long propagation paths through a poorly known atmosphere make the identification of unique terrain features or source mechanisms difficult. Accurate source locations and knowledge of the atmosphere at such locations are not available. Rockway *et al.* (1974) indicated that the secular variation in the numbers of signals of this class could result from the effects of winds upon propagation rather than from a source characteristic. For these reasons, we set up an experiment to determine if there were any sources of infrasound in the vicinity of the Boulder observatory that resulted from airflow over mountains.

2. Description of 1972–73 Boulder-Fraser experiment

a. Fraser, Colorado, observatory

The observatory at Boulder provides bearing information for infrasonic signals; but there is currently no reliable method based on measurements at one observatory alone for distinguishing between local and distant infrasonic signals of this class. Fraser, CO, already the site of instruments for a separate lee-wave study, provided a good east–west baseline with the Boulder site for local sources of infrasound that might occur along the Continental Divide, and its record of low surface winds and hence low background pressure noise was advantageous.

Site 1 of the Fraser array shown in Fig. 1 is the central recording location for sites 2 and 4. Graphic analog-pressure recordings made at site 3 permitted comparison with a colocated acoustic sounder and provided data for a noise study. At site 1, the pressure data were recorded together with time on both analog-magnetic tape and paper-chart recorders. On an after-the-fact basis, we processed the infrasonic data using an analog correlator with a passband having 3 dB points at 1 and 100 s periods. Radio data links brought the signals from sites 2 and 4 to site 1.

b. Additional sources of data

This experiment, initiated as part of a cooperative effort with Dr. D. K. Lilly of the National Center for Atmospheric Research (NCAR), included radiosonde balloon launches and instrumented aircraft from the NCAR Lee Wave program. However, we could not coordinate the observations in real time because of the after-the-fact nature of the infrasound analysis.

In addition to the Fraser and Boulder stations, an array operated at Lowry Air Force Base in Denver, CO, for approximately one month as part of this experiment. Fig. 1 shows the relative position of these observatories. We used surface wind speed data taken 5 mi north of Boulder, data from the National Weather Service Substation at Fraser for the interval, and summarized pilot reports from records at the National Climatic Center at Asheville, NC, and United Air Lines. This study also used Denver radiosonde data in an attempt to relate infrasound observations to airflow over mountains.

c. Infrasonic instrumentation

Details concerning the instrumentation and techniques used in obtaining data are described in papers by Cook and Bedard (1971) and by Georges and Young (1972). Usually each detection system consists of an array of at least four microphones at ground level ~8 km apart. We reduce effects on each microphone caused by local turbulent wind eddies by space filtering. The space filter consists of a line of pipe or hose equipped at intervals with capillary ports to the atmosphere. Daniels (1959), Burridge (1971) and Bedard (1977) described the theory of this noise-reducing line. Without the use of this pipe filter, there would be few intervals when the small amplitude infrasonic signals could be detected.

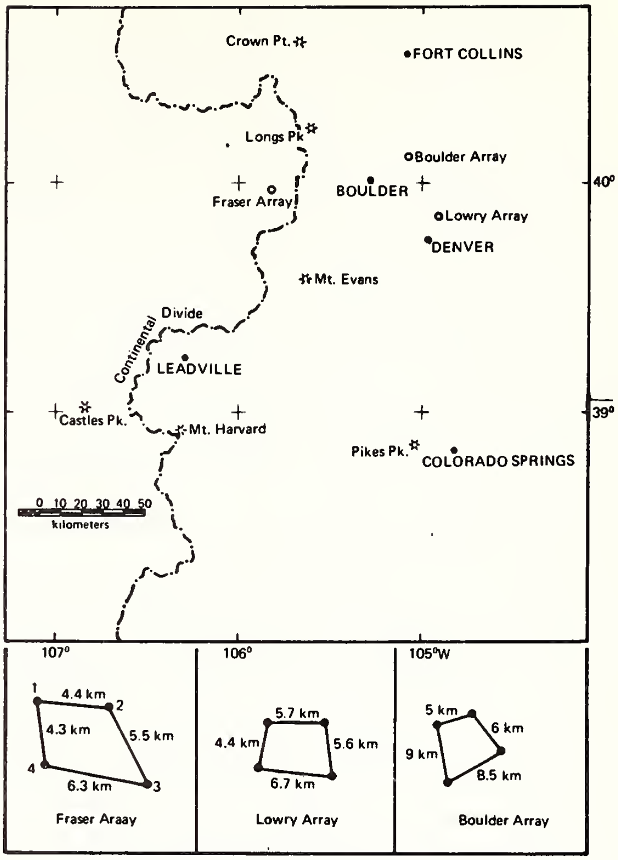

Fig. 1. Array configurations and relative location of observatories.

d. Data reduction

An automatic multichannel analog correlator (Brown, 1963; Bedard and Caldwell, 1970) provided information concerning signal-to-noise ratio, azimuth and horizontal trace velocity for the infrasound. The accuracy of azimuth and velocity determinations usually depend on the quality of the signal and the local noise conditions and for this study were typically ±3° and ± 15 m s^{-1}, respectively. It is also possible that finite source-size effects reduce measurement accuracies (particularly for sources quite close to an observatory).

The background noise-level data were hand digitized and plotted for comparison with digitized local surface wind data. These noise level plots were also used in comparing signal data for the Fraser and Boulder observatories, permitting ready comparison of times of signal and noise for the two locations. Identification of those signals, appearing on both stations during the same time period, permitted discrimination between local and distant signals using triangulation techniques. For our purposes, local shall mean the State of Colorado in the vicinity of the Continental Divide.

3. Case studies of local infrasonic signals

A total of 227 infrasonic signals were identified for the Fraser and Boulder observatories during the period from 7 February to 7 June 1973. A signal is defined as a segment of data resulting from cross correlations between the sites of one observatory, showing a signal-to-noise ratio greater than one-third for a duration usually longer than 20 min at a horizontal trace velocity of $\sim$330 m s^{-1} or higher. A lack of confidence in the measured bearing made it impossible to categorize many signals as to local or distant origin. Many signals observed at one station went undetected at another during the same time period. The lack of data at the second station could usually be explained by an increased local noise level. However, there are 32 cases for which the noise level at the second observatory is low enough for detection, but no signal was found, suggesting that propagation effects or source directional effects may sometimes be important.

Application of the ray tracing program of Georges (1971) to the problem of propagation from a source at 10 km, assuming a Gaussian wind profile centered at 10 km with a maximum of 80 kt and a width of 4 km, predicts a "zone of silence" between about 50 and 275 km downwind. To the extent that the results of ray tracing provide valid insights at these longer wavelengths ($\sim$6 km), one expects large propagation effects controlling the distribution of infrasonic energy at the earth's surface. The low-level winds control the inner limits of the "zone of silence," while temperature structure and winds occurring at high altitudes control the outer limits of the "silent" zone.

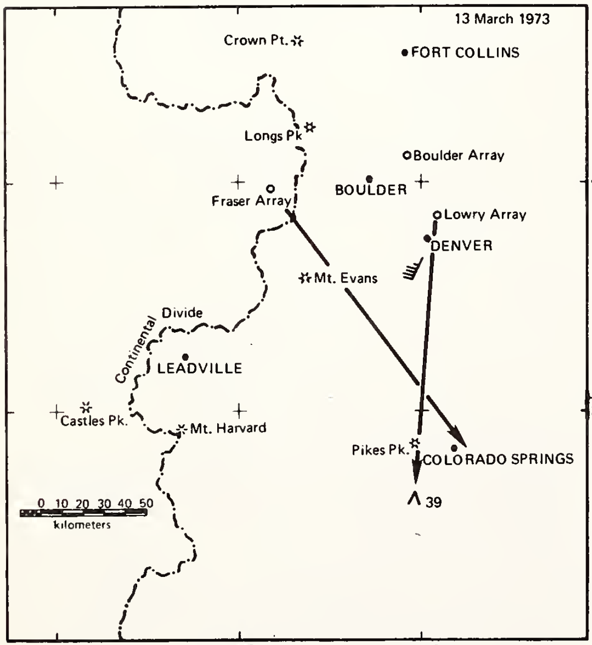

FIG. 2. Infrasound observations of 13 March 1973. The turbulence codes appearing on these figures are defined in the text. Numbers appearing next to these symbols on figures indicate the aircraft height in thousands of feet. The wind vectors show the speed and direction of the 500 mb winds at Denver for the sounding closest to the time of observation of infrasound.

Of 227 signals detected by the three observatories, 29 were local. This section presents the details of representative observations. In Figs. 2–5, the direction of the arrows points from the infrasonic observatory toward the infrasound source location. On several figures, symbols indicate aircraft turbulence encounters. The turbulence codes used by United Airlines and in pilot reports (Pireps) appear below.

Turbulence codes

United Air Lines		Pireps	
Severe	●	Severe	Ѧ
Moderate to severe	◕	Moderate	⋀
Moderate	◑	Light	∧

a. *Infrasound observations of 13 March 1973*

The first case shown is a Fraser-Lowry intersection north of Pike's Peak (Fig. 2). The maximum signal-to-noise ratio for Lowry occurred at 0635 (all times GMT) and for Fraser at 0642. High local noise occurred at the Boulder observatory at this time. Infrasound signal level measured at $\sim$0.5 μbar $p-p$ was detected at Fraser from 0600 to 0800 and from 1800 to 1900. The turbulence report shown on the figure occurred during the interval 1500 to 2100. At 0905 a signal arrived at the Boulder observatory from the direction of this intersection, but is not indicated on the figure.

b. *Infrasound observations of 16 March 1973*

Infrasound detected at Boulder arrived from the northwest between 0300 and 1500. The azimuth of the segment of Boulder signal at 0810 is shown on Fig. 3, together with bearing data for Fraser (0800) and Lowry (0800). During the intervals from 0100 to 1700 for Lowry and from 0750 to 1330 for Fraser, signals continued from these bearings, remaining approximately constant in direction. During these periods, wave clouds existed near Boulder. The aircraft turbulence report in the Denver area occurred during the interval from 2100 GMT 15 March to 0300 GMT 16 March. The aircraft turbulence encounter to the south was for the interval from 0300 to 0900 on 16 March.

c. *Infrasound observations of 9 May 1973*

Fig. 4 shows the signal azimuths observed at the Boulder (0845) and Fraser (0850) observatories. Signal appeared at Boulder from 0445 to 1200 and at Fraser from 0800 to 0910 and from 1400 to 1510. Wave clouds were present in the vicinity during this interval. No aircraft turbulence encounters were reported during the time period. Local atmospheric pressure noise was high

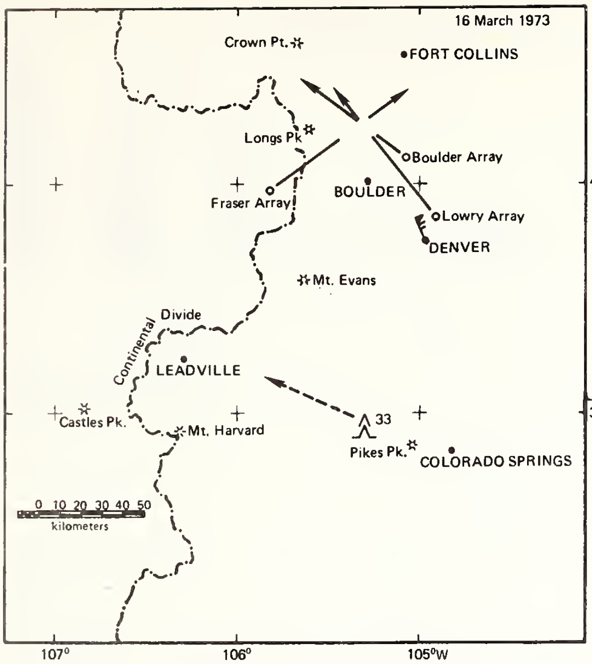

Fig. 3. Infrasound observations of 16 March 1973.

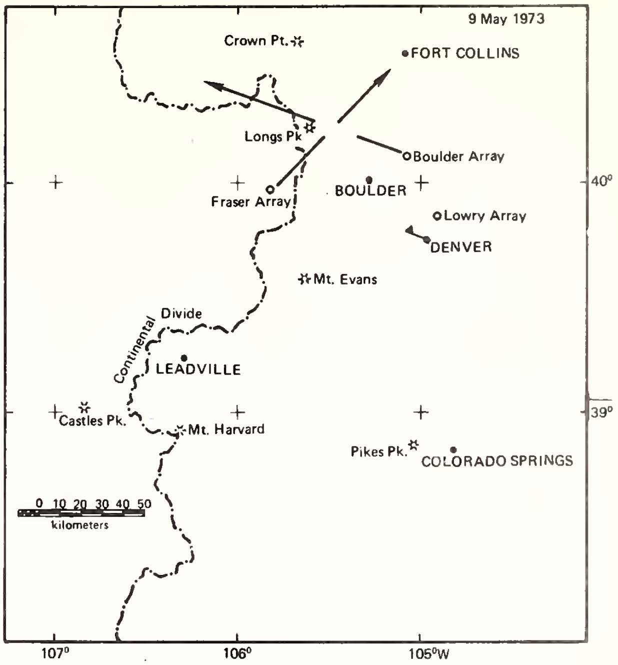

Fig. 4. Infrasound observations of 9 May 1973.

at both observatories prior to signal reception. Noise at Fraser was high enough to cause the gap in signal detection.

d. *Infrasound observations of 10 April 1973*

This case shows apparent source motion. The signal was observed at Boulder from 0300 to 1355 and at Fraser from 0200 to 1300 (see Fig. 5). The source origin moved about 20 km over an 8 h interval. No aircraft turbulence encounters were reported. Two other cases showed similar motions. Spectrum analyses run on this particular signal showed that most of the signal energy occurred at 20 and 40 s periods. We should process many more signals with high signal-to-noise ratios before applying significance to the harmonic relation found between these spectral peaks.

e. *Summary of data*

This set of measurements presents evidence for a preferred region of generation of infrasound and a relation between the 500 mb winds and the generation of this class of infrasound. Fig. 6 shows all local intersections obtained during the test interval. The solid stars identify three-station intersections while the open stars identify two-station intersections. It is obvious from this figure that many of the sources are to the north of Boulder and to the east of the Continental Divide. Fig. 7 is a compilation of the azimuth intersection points for a region to the lee of the group of mountains that includes Long's Peak. On this figure, the point of a wind vector indicates the location of the intersection. The wind vectors correspond to the 500 mb wind velocity measured at Denver for the sounding closest to the time of infrasound observations. Most of the cases involved high-speed winds with a strong component from the west. Nearly half (13) of the local sources identified occurred in this region. When multiple infrasonic signals propagate simultaneously from both local or distant sources, the analysis of low-

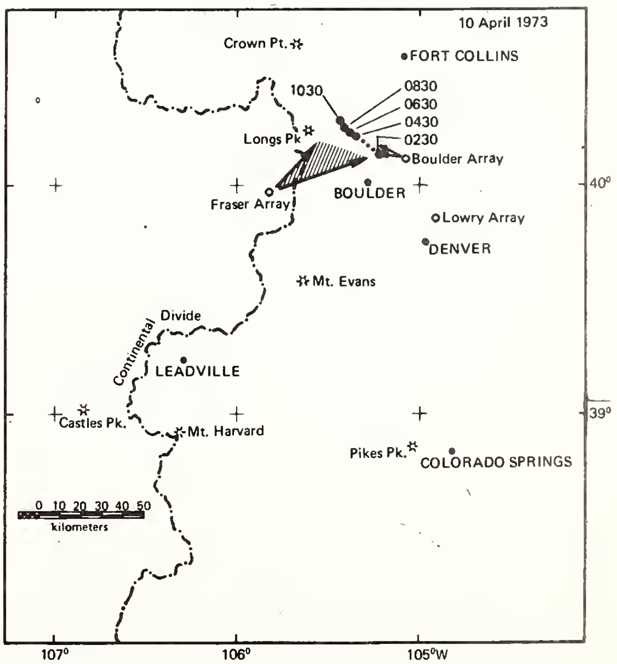

Fig. 5. Infrasound observations of 10 April 1973.

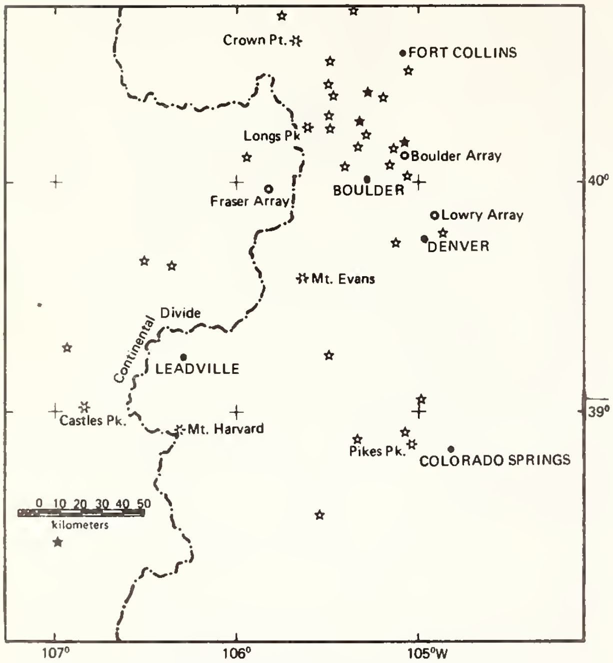

Fig. 6. All local intersections obtained for infrasonic signals during test interval from February through June 1973. The solid stars indicate three-station intersections; the open stars indicate two-station intersections.

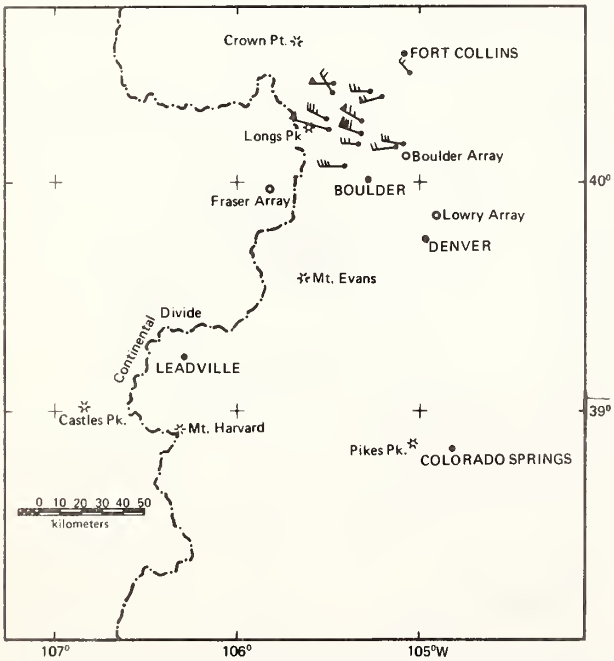

Fig. 7. Compiled azimuth intersections for local source region. The point of each wind vector indicates the location of an intersection, and the wind vectors correspond to the 500 mb winds at Denver for the sounding closest to the time of infrasound observation.

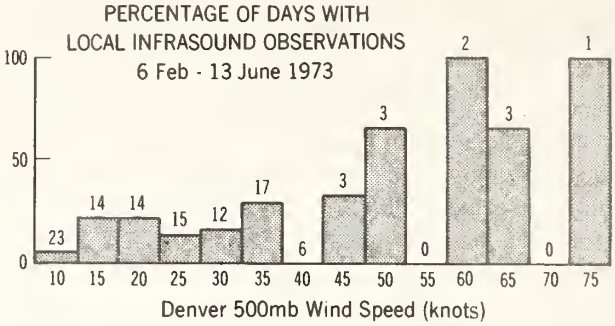

Fig. 8. Relation of local infrasound to Denver 500 mb winds shows the percentage of Denver soundings at various wind speeds accompanied by local infrasound. The number at the top of each bar of the histogram indicates the total number of 500 mb soundings for each speed range.

level signals becomes complex. Also, a combination of propagation effects, local noise conditions and source directional effects could make an array of observatories sense a region preferentially. But the point is not pertinent if one is interested in establishing source characteristics and directing probes in an active source region (omni-directional response for an array of observatories not being required).

High surface winds can prevent an infrasonic observatory from detecting existing infrasound. To compare local infrasound data with the statistics of 500 mb soundings at Denver, we removed time periods of low signal-to-noise ratio at Boulder resulting from high surface winds from the analysis. If the wind speed measured at a site just north of Boulder exceeded 7 kt, that time period was not included in the analysis. Sets of remaining soundings were those for which the reception of low-level infrasound at the Boulder observatory was possible. Fig. 8 is a histogram showing

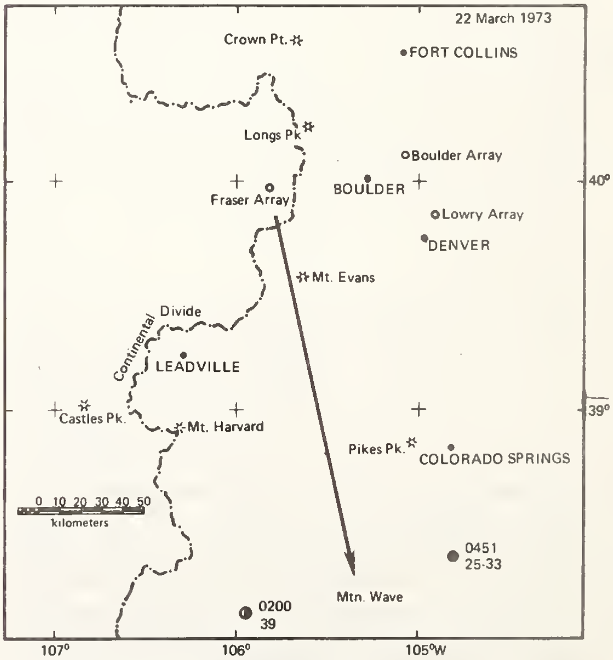

Fig. 9. Turbulence encounter of 22 March 1973.

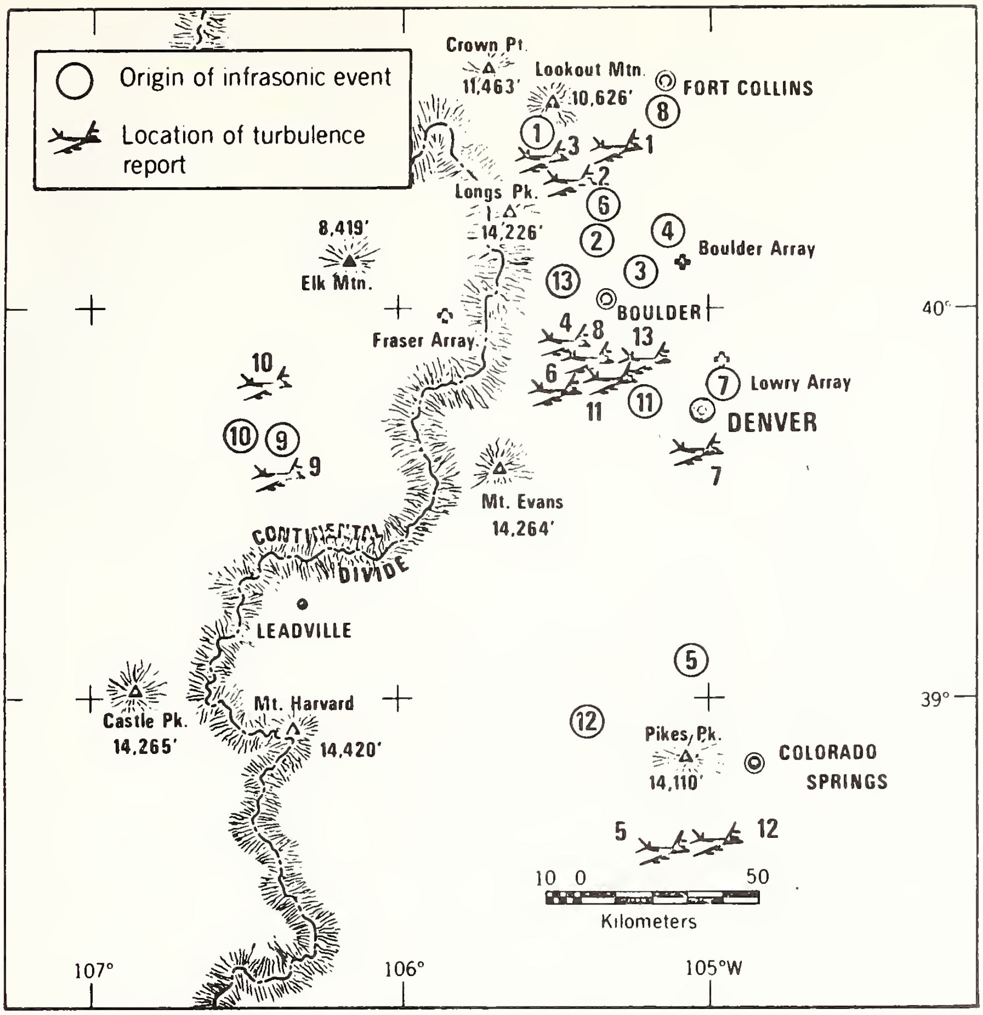

Fig. 10. Comparison of local infrasound origins with aircraft turbulence reports. The numbered circles indicate the location of infrasound source origins, while the correspondingly numbered aircraft indicate the locations of aircraft turbulence reports occurring close to or during the same time intervals as the infrasound generation.

the percentage of soundings at various wind speeds accompanied by infrasound. The number at the top of each bar of the histogram indicates the total number of 500 mb soundings for each speed range. Note that when the wind speed was at ~50 kt or above, we detected infrasound for over 70% of the cases.

4. Possible relationship to aircraft turbulence

Since some possible generation mechanisms for infrasound involve turbulent motions, it seems reasonable to expect that the infrasonic source involves flow fields capable of causing significant aircraft turbulence.

Fig. 9 presents data showing an azimuth of arrival passing near one of the few turbulence encounters characterized as severe during the test interval. Because of local noise, only one infrasonic observatory detected signal from this direction. This case was for 22 March 1973. When the noise decreased at the Fraser observatory, signal appeared at 0540 and continued until 0650 when the noise again increased. Fig. 10 shows a compilation of infrasound intersections together with the location of aircraft-turbulence encounters occurring close to the time of infrasound detections. Numbers on the aircraft, indicating the locations of aircraft turbulence reports, correspond in time to the circled numbers which locate the source region of the infrasound. Note that 13 of the 29 cases of infrasound detected appear on this figure. The pilot reports used represent one of the few available sources of data concerning the state of the upper level atmospheric flow. It is evident that for a number of cases the proximity of the infrasound origin to the location of the reported aircraft turbulence is striking. However, it must be emphasized that convincing evidence of a direct relation is not claimed. Even if a relation exists, it may be an indirect one. These compiled data argue strongly for an experimental and theoretical program to explore the possibility of passively detecting regions causing aircraft turbulence using infrasonic observatories.

Posmentier (1974) described observations of infrasound in the range from 1 to 16 Hz and related these observations to CAT. One problem with this frequency range is that aircraft radiate significant acoustic energy, and it will be necessary to discriminate between such man-made sounds and those originating from atmospheric turbulence. Also, these higher frequencies interact more strongly with the atmosphere, and hence the influence of the propagation path is greater. In spite of these concerns, measurements in this frequency range could be important indices of turbulence. However, the infrasonic data related to airflow across mountains in this paper are below 0.1 Hz and are possibly caused by an entirely different source mechanism.

5. Comparison with historical data for the Boulder Observatory

The data presented thus far are for only a portion of one year. Thus, it is quite a proper objection that these data may not be representative. But evidence for the continued existence of a local preferred source region and insight concerning its characteristics exist in historical data. This section presents historical statistics concerning infrasound observations from the Boulder observatory.

Fig. 11 is a summary of hand-analyzed infrasound observations as a function of azimuth of arrival for the years 1963–68. This figure is from unpublished work of the late Mr. V. Goerke of NOAA who developed a data set of infrasonic signals at the Boulder observatory. In contrast, our more recent work applied the analog correlator described by Brown (1963) which can detect infrasound at signal-to-noise ratios lower than one-third. Since Mr. Georke's results consist of data with signal-to-noise ratios usually >1, the historical data are conservative in terms of signal duration and numbers of signals detected. We know from a global network that most of the signals from around 150° originate from a source near mountainous regions of South America. Most signals arriving from directions between 315° and 340° probably result from distant infrasonic sources located near mountainous regions in the Pacific Northwest (Greene and Howard, 1975). For any given signal, we cannot deduce local or distant origin based upon the data from a single observatory, and we use data from other distant observatories to make these inferences about probable source origin using triangulation.

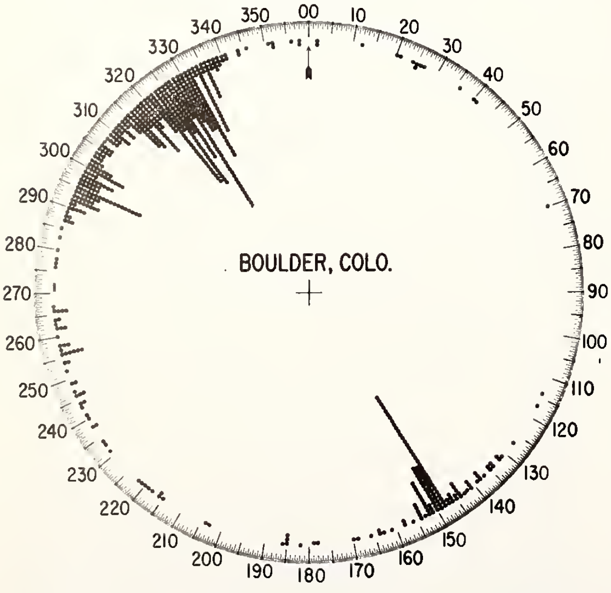

Fig. 11. Azimuthal distribution of historical signals for the Boulder observatory.

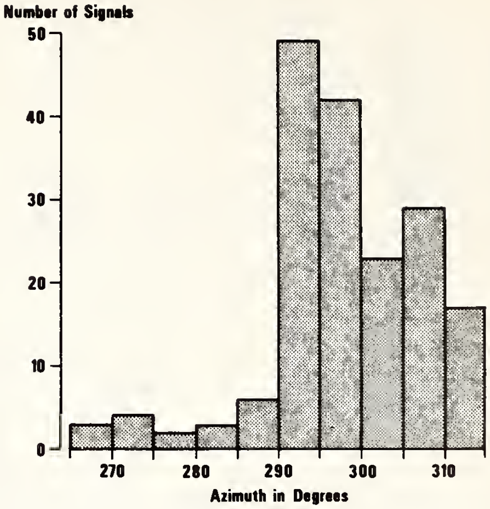

Fig. 12. Number of signals as a function of azimuth.

In Fig. 7, a group of local sources occurred between azimuths of 265° and 315°. Note that Long's Peak is at an azimuth of about 290° from the Boulder observatory. Historically, there has been a group of signals in this range of azimuths. Long's Peak is 14 255 ft high and although the highest mountain in the region, it is only the 15th highest in Colorado. The mountain is unique being knife-like with a great precipice on its east face. Because several other significant peaks including Storm Peak (13 326 ft), Mount Lady Washington (13 281) and Mount Meeker (13 400 ft) are all within 5 mi of Long's Peak, it is far from certain that Long's Peak itself is related to the generation of infrasound.

The next three figures present some of the statistical properties of signals that fall in the range of azimuths bracketing the local source region. Data from more recent years are included with Mr. Georke's data for this analysis. Fig. 12 is a histogram presentng the distribution of signals as a function of azimuth of arrival. Again, note that most signals in this azimuth range pass through the group of local signals shown in Fig. 7.

Fig. 13 shows the number of signals detected in this azimuth range as a function of the month of the year. Note that no signals appeared for June, July or August and that November–March are the months when most signals occurred. Both lee wave and chinook wind occurrences show similar variations with times of year for this part of Colorado.

Fig. 14 is a histogram showing the distribution of signal duration for the historical infrasonic signals in this azimuth range. Note that although many signals are from 2–4 h in duration, considerable numbers are longer than 12 h in duration.

Many signals terminated because increases of local noise obscured the detection. Hence, the data presented in the figure are an estimate of the minimum signal duration. It is certain that the addition of the Fraser observatory, expansion of the Boulder observatory, and application of more sophisticated analysis techniques possible with digital processing would extend the detection time for many signals.

A significant point of this section is that existing historical data can guide future experimental programs. These data indicate that the months of November–March represent the best time to run an experimental program to investigate the source of infrasound. Since Fig. 14 indicates that more than one-half of the signals observed lasted over 3 h, there is frequently ample time for detection of infrasound and real-time guiding of probes, such as dual-Doppler radar or instrumented aircraft for investigations of the source regions.

6. Identification of source mechanism for infrasound

Golitsyn (1961) predicted a peak of infrasonic radiation at a period of 100 s from a consideration of the spectral characteristics of atmospheric motions and predicted properties of acoustic radiation from turbulence. Applying the theory of Lighthill (1962), Meecham (1971), Georges and Young (1972) and Georges (1976) have shown that it is reasonable to expect significant infrasonic radiation from airflow systems. Kimpo (1973) has considered dipole and quadrupole aerodynamic-generation mechanisms and discussed possible methods of discriminating between these. Chimonas (1977) proposed a mechanism based on scattering of energy from very low phase velocity to very high phase velocity domains, involving interactions with terrain irregularities. The identification of the Long's Peak region as a source point should permit experimental definition of conditions in the generation region and produce a well-defined theoretical problem.

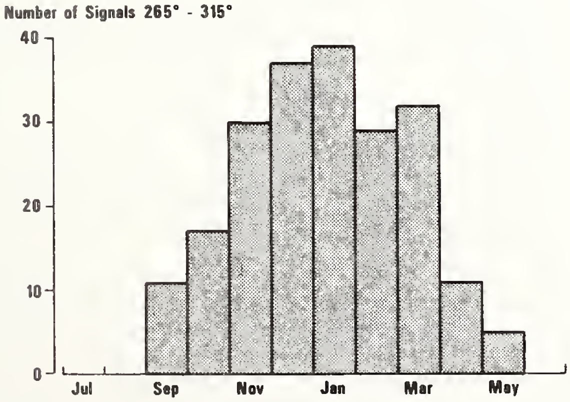

Fig. 13. Number of signals as a function of month of the year.

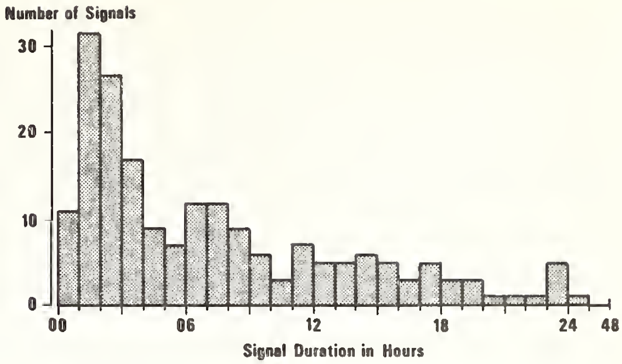

Fig. 14. Number of signals as a function of duration.

Vortex shedding (Suzuki, 1958) is one possible mechanism for infrasound generation. Both numerical and experimental scale-modeling techniques are applicable to the problem of estimating the frequency and intensity of the radiated infrasound. It is possible to compute the spectral distribution of unstable motions in vortex systems and apply these results to lee wave rotors. Lighthill mechanisms, for example, like those causing the radiated sound from jets, are a possible source mechanism. Also a variety of flow/boundary interactions, similar to those active in edge tones and resonators, might radiate significant infrasound. A cyclic release of the latent heat of condensation could either enhance other mechanisms or be directly responsible for the generation of acoustic energy. This last possibility suggests the application of time-lapse photography in the source region. Bedard (1976) presented data suggesting that the source involves monopole, dipole and quadrupole mechanisms.

7. Concluding remarks

The detection of infrasound from such local sources permits identification of basic source properties, whereas distant-source signal waveforms depend greatly on propagation effects. Thus, it is probable that the infrasound detected from wintertime mountainous regions on a global scale reflects source activity, as opposed to seasonal variations caused by propagation changes as cautioned by Rockway *et al.* (1974).

Mountainous regions are a frequent location for clear-air turbulence encounters (Harrison and Sowa, 1966; Dutton and Panofsky, 1970). In a study of three years of aircraft reports covering the western United States, Foltz (1967) showed a possible connection between lee waves and such turbulence. He found maxima of turbulence frequency just to the lee of major mountain ridges. A relation between measurements of CAT and gravity waves produced by mountains is indicated by Lilly (1971) and by Reiter and Foltz (1967). Hence, the choice of the Continental Divide as a location for an experiment is a logical one for studying this important class of CAT. It is probable that both free and standing gravity waves are important contributors to CAT occurrence in the vicinity of mountains. Evidence thus far seems to relate observed infrasound emissions to the turbulent portions of standing wave systems, whereas the traveling waves could produce the slower moving, long-period pressure variations also detected at the earth's surface. Both types of observations could be indices of CAT. Infrasonic observatories can assist instrumented aircraft "prospecting" for CAT, detecting gravity-shear waves and/or infrasound and guiding aircraft to active source regions.

Acknowledgments. The late Mr. Vernon Goerke of the Geoacoustics Research Program Area of NOAA's Wave Propagation Laboratory collected most of the historical data used in this study. His careful work over a large number of years provided a basis of information which made possible a fuller interpretation of the data concerning local signals.

Persons at various sites of the Fraser observatory donated room for the microbarographic equipment. For this help, we are grateful to the Tabernash Airport, the Hurd Creek Ranch and the O'Neil Ranch.

Dr. D. K. Lilly of the National Center for Atmospheric Research made available sounding data for comparisons with the observed infrasound.

REFERENCES

Bedard, A. J., Jr., 1976: Mechanisms for the generation of infrasound by airflow over mountainous regions. *Bull. Amer. Meteor. Soc.*, **57**, 119 (abstract).

——, 1977: The d-c pressure summator: Theoretical operation, experimental tests and possible practical uses. *Fluidics Quart.*, **9**, 26–51.

——, and D. M. Caldwell, 1970: Instructions for the operation of correlator-analyzer N4. ESSA Tech. Man. ERL 2, Boulder, 231 pp.

Benioff, H., and B. Gutenberg, 1939: Waves and currents recorded by electromagnetic barographs. *Bull. Amer. Meteor. Soc.*, **20**, 421–426.

Bowman, H. S., and A. J. Bedard, 1971: Observations of infrasound and subsonic disturbances related to severe weather. *Geophys. J. Roy. Astron. Soc.*, **26**, 215–242.

Brown, R. F., Jr., 1963: An automatic multichannel correlator. *J. Res. NBS*, **67C**, 33–38.

Burridge, R., 1971: The acoustics of pipe arrays. *Geophys. J. Roy. Astron. Soc.*, **26**, 53–69.

Chimonas, G., 1977: A possible source mechanism for mountain-associated infrasound. *J. Atmos. Sci.*, **34**, 806–811.

Chrzanowski, P., G. Greene, K. T. Lemmon, and J. M. Young, 1961: Traveling pressure waves associated with geomagnetic activity. *J. Geophys. Res.*, **66**, 3727–3733.

Cook, R. K., and A. J. Bedard, 1971: On the measurement of infrasound. *Geophys. J. Roy. Astron. Soc.*, **26**, 5–11.

Daniels, F. B., 1959: Noise-reducing line microphone for frequencies below 1 cps. *J. Acoust. Soc. Amer.*, **31**, 529–531.

Donn, W. L., and E. S. Posmentier, 1964: Ground-coupled air waves from the great Alaskan earthquake. *J. Geophys. Res.*, **69**, 5357–5361.

Dutton, J. A., and H. A. Panofsky, 1970: Clear air turbulence: A mystery may be unfolding. *Science*, **167**, 937–944.

Foltz, H. P., 1967: Prediction of clear air turbulence. Dept. Atmos. Sci. Rep. 106, Colorado State University, 145 pp.

Georges, T. M., 1971: A program for calculating three-dimensional acoustic-gravity ray paths in the atmosphere. NOAA Tech. Rep. ERL 212-WPL-16, Boulder, 43 pp.

——, 1973: Infrasound from convective storms: Examining the evidence. *Rev. Geophys. Space Phys.*, **11**, 571–594.

——, 1976: Infrasound from convective storms, Part II: A critique of source candidates. NOAA Tech. Rep. ERL-212-WPL-49, Boulder, 59 pp.

——, and J. M. Young, 1972: Passive sensing of natural acoustic-gravity waves at the earth's surface. *Remote Sensing of the Troposphere*, V. E. Derr, Ed., Chap. 21. [Govt. Print. Office].

Goerke, V. H., J. M. Young and R. K. Cook, 1965: Infrasonic observations of the May 16, 1963, volcanic explosion on the Island of Bali. *J. Geophys. Res.*, **70**, 6017–6022.

Golitsyn, G. S., 1961: The possibility of the heating of the upper atmosphere by long-wave acoustic radiation. *Izv. Geofiz. Ser.*, **7**, 1092–1093.

Greene, G. E. and J. Howard, 1975: Natural Infrasound: A one-year global study. NOAA Tech. Rep. ERL 317-WPL 37, 153 pp.

Harrison, H. T., and D. F. Sowa, 1966: Mountain wave exposure on jet routes of Northwest Airlines and United Air Lines. United Air Lines Meteor. Circ. No. 60, Chicago, 66 pp.

Kimpo, F. L., 1973: Natural aerodynamic sound as source of mountain-associated infrasonic waves. Master's thesis, Washington State University, Pullman, 66 pp.

Larson, R. J., L. B. Craine, J. E. Thomas, and C. R. Wilson, 1971: Correlation of winds and geographic features with production of certain infrasonic signals in the atmosphere. *Geophys. J. Roy. Astron. Soc.*, **26**, 201–214.

Lighthill, M. J., 1962: Sound generated aerodynamically. *Proc. Roy. Soc. London*, **A267**, 147–182.

Lilly, D. K., 1971: Observations of mountain-induced turbulence. *J. Geophys. Res.*, **76**, 6585–6588.

Meecham, W. C., 1971: On aerodynamic infrasound. *J. Atmos. Terr. Phys.*, **33**, 149–155.

Posmentier, E. S., 1974: 1-to-16 Hz infrasound associated with clear air turbulence predictors. *J. Geophys. Res.*, **79**, 1755–1760.

Reiter, E. R., and H. P. Foltz, 1967: The prediction of clear air turbulence over mountainous terrain. *J. Appl. Meteor.*, **6**, 549–556.

Rockway, J. W., G. L. Hower, L. B. Craine and J. E. Thomas, 1974: Applications of ray-tracing to observations of mountain-associated infrasonic waves. *Geophys. J. Roy. Astron. Soc.*, **36**, 259–266.

Suzuki, S., 1958: Aeolian tones in a forest and flowing cloudlets over a hill. *Weather*, **13**, 20–25.

VOL. 83, NO. C2 JOURNAL OF GEOPHYSICAL RESEARCH FEBRUARY 20, 1978

Journal of Geophysical Research, 83: 959-962, February 1978.

Inversion of Second-Order Radar Echoes From the Sea

BELINDA LIPA

Center for Radar Astronomy, Stanford University, Stanford, California 94305

The Doppler spectrum of high-frequency radar echoes from the sea consists of dominant peaks due to first-order Bragg scatter surrounded by a higher-order continuum. Most applications to date have been based on the first-order lines, requiring multiple observations and large or moving antennas. In contrast, inversion of the second-order structure can yield the complete directional ocean wave spectrum from a single radar observation. In this report we describe the first inversion of measured second-order echo spectra from a 21.75-MHz narrow-beam radar looking in a single direction. Estimates of the directional ocean wave spectrum are compared with surface truth provided by tilt buoy and weather station, and fair agreement is found. This initial success is indicative of the potential of this technique for remote sensing of the sea surface.

INTRODUCTION

The Doppler spectrum of a high-frequency radar signal backscattered from the sea surface has been used to give detailed information on the properties of ocean waves (see, for example, *Teague et al.* [1977]). Most applications depend on interpretation of the dominant first-order lines arising from simple Bragg scatter. In this mechanism the radar wave interacts only with ocean waves of one half the radar wavelength moving directly toward or away from the receiver; hence for detailed information on amplitude and directional characteristics one requires observations at several look angles and transmitter frequencies. This is often impractical, owing to limitations on radar design and difficult propagation conditions. A further difficulty is that for the observation of the important lower end of the gravity wave spectrum using the first-order lines the radar frequency must be in the band 50 KHz to 2 MHz, requiring large arrays or moving antennas for the formation of a directional beam. However, the first-order lines are surrounded by a continuum due to higher-order Bragg scatter which involves ocean waves of all angles and wavelengths and therefore can in principle yield the directional ocean wave spectrum from a single Doppler spectrum. Observations of second-order structure show that it is a sensitive function of sea state [*Tyler et al.*, 1972]. *Hasselmann* [1971] first suggested that the second-order Doppler side bands should be proportional to the wave height nondirectional spectrum. He also suggested a convenient normalization in which the side bands are divided by the first-order echo, canceling unknown factors such as path loss and system gains. The relationship between the second-order structure and the directional ocean wave spectrum was derived by *Barrick* [1972] and has the form of a two-dimensional nonlinear integral equation. *Barrick* [1977*a*] derived an approximate closed form technique to obtain the wave height nondirectional spectrum from the second-order structure. Wave height and wave period predicted by using this solution have been found to agree with simultaneous buoy observations [*Barrick*, 1977*b*]. *Lipa* [1977] has derived and discussed a method of integral inversion of the second-order spectrum. This paper describes the first application of this technique to measured data. Derived parameters define the directional distribution of saturated ocean waves and the nondirectional spectrum of unsaturated waves and are found to be in good agreement with surface truth observations provided by a tilt buoy. Inversion of the second-order structure using this method requires radar frequencies in the upper HF band, suitable for sky wave propagation to great distances. The method can therefore be applied to sky wave spectra, if the effects of ionospheric distortion can be eliminated.

INVERSION METHOD

The second-order structure arises from the interaction of the incident ocean wave with two ocean waves to yield four scattered waves which satisfy the second-order Bragg condition. For backscatter of vertically polarized radar of wave number β the radar cross section at a Doppler shift η is given by

$$\sigma(\eta) = 2^6\pi\beta^4 \sum_{m_1,m_2=\pm 1} \iint_{-\infty}^{\infty} |\Gamma|^2 \, \delta[\eta - m_1(g\kappa_1)^{1/2} - m_2(g\kappa_2)^{1/2}] S(m_1\tilde{k}_1) S(m_2\tilde{k}_2) \, dp \, dq \qquad (1)$$

where the scattering ocean wave vectors are given by $\tilde{k}_1 = (p - \beta), q$, $\tilde{k}_2 = -(p + \beta), -q$, the ocean wave numbers are $\kappa_1 = |\tilde{k}_1|$, $\kappa_2 = |\tilde{k}_2|$, and the Bragg condition is imposed by the delta function constraint, where g is the gravitational acceleration, Γ is the transfer coefficient, which is the coherent sum of an electromagnetic and a hydrodynamic term [*Barrick*, 1972], and $S(\tilde{k})$ is the nonsymmetric directional ocean wave spectrum. We seek to determine sufficient parameters to define $S(k)$ by inverting (1). As the number of parameters sought from a given data set is increased, the accuracy is correspondingly decreased. In this first attempt at inversion of a second-order radar spectrum we have assumed that the spectrum is the product of independent factors, an amplitude spectrum dependent only on wave number and a directional factor which is a function of angle relative to the wind:

$$S(\tilde{k}) = F(\kappa)G(\theta) \qquad (2)$$

With this assumption of separability, fewer parameters are required to define the ocean wave spectrum; the parameter set is further reduced by assuming symmetry about an undefined direction, to be determined by the inversion procedure. These approximations apply to short saturated waves when the directional distribution is approximately independent of wavelength, but faster waves may have a narrower spread about the wind direction (see, for example, *Tyler et al.* [1974]). These long waves affect the radar frequency spectrum in the region surrounding the first-order Bragg line, which for high winds and/or radar frequencies is relatively insensitive to the directional distribution of ocean waves as discussed by *Barrick* [1977*a*, *b*]. Results of inversion will then be insensitive to the breakdown of assumption (2) for long waves.

Copyright © 1978 by the American Geophysical Union.

Paper number 7C0995.
0148-0227/78/027C-0995$03.00

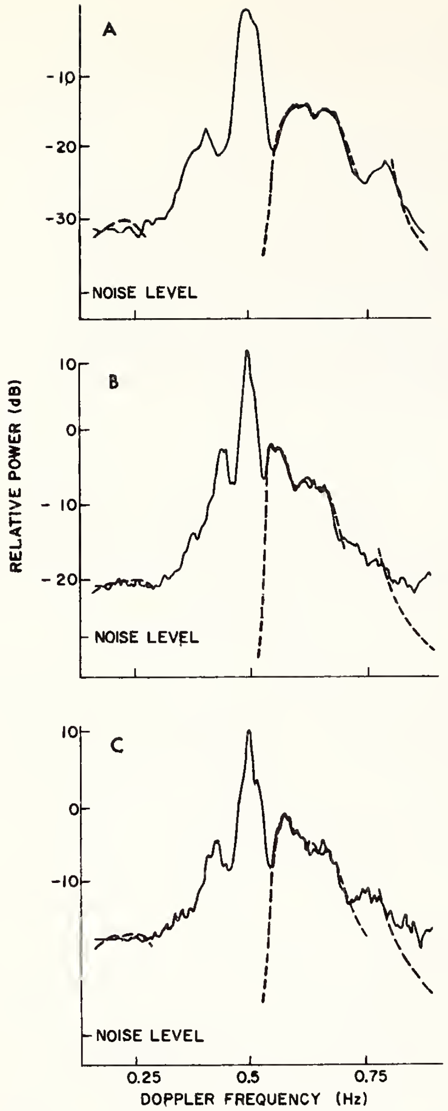

Fig. 1. Radar spectra at positive Doppler shifts. Transmitter frequency is 22 MHz, with frequency resolutions of (*a*) 0,01, (*b*) 0.005, and (*c*) 0.005 Hz. The continuum, assumed to be entirely second order, is normalized by the first-order spectral energy and inverted to give a model of the directional ocean wave spectrum (Figures 2 and 3). The dashed line is the second-order radar spectrum that corresponds exactly to the model wave spectrum in the frequency bands used for inversion. Deviations between the model radar spectrum and the data for Doppler frequency greater than 0.875 Hz may be due to third-order interactions.

When (2) is used, the spectral product in the integral equation becomes a quartic; for example, for m_1, m_2 equal to + 1,

$$S(\tilde{k}_1)S(\tilde{k}_2) \qquad F(\kappa_1)G(\theta_1)F(\kappa_2)G(\theta_2) \tag{3}$$

The solution of the inversion problem is simplified by the fact that the ocean wave number κ_2 is always greater than the radar wave number and for typical radar frequencies corresponds to a saturated wave. We may therefore substitute for $F(\kappa_2)$ the saturated amplitude spectrum [*Phillips*, 1966].

$$F_{\mathrm{sat}}(\kappa) \propto 1/\kappa^4 \tag{4}$$

We then estimate the amplitude spectrum and the directional factor separately using different regions of the spectrum. In the frequency bands separated from the first-order Bragg frequency, both of the contributing ocean waves are saturated with an amplitude spectrum given by (4). The spectral factor

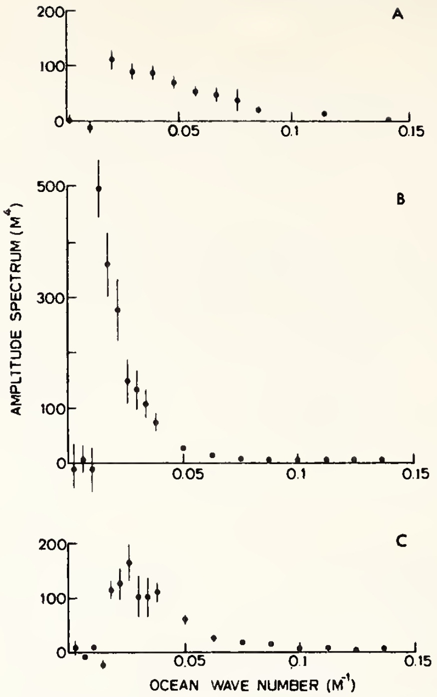

Fig. 2. Amplitude spectra obtained by inversion of radar spectra shown in Figure 1. Error bars represent one standard deviation and are computed from the variance in wave height of the random sea surface.

(3) then reduces to a quadratic function of the directional factor, and the integral equation may be reduced to a set of quadratic equations which are solved by iteration for parameters of $G(\theta)$, including the direction of symmetry.

To derive the amplitude spectrum of the unsaturated waves, we use the spectral points with frequencies slightly greater than the first-order Bragg frequency. In this region the shape of the spectrum is almost independent of ocean wave directional properties. Substituting the derived function $G(\theta)$ and the saturated amplitude spectrum for $F(\kappa_2)$ linearizes the spectral factor (3). It is then straightforward to reduce the integral equation to a set of linear equations which may be solved for parameters of the unsaturated amplitude spectrum.

This inversion method is described in detail by *Lipa* [1977].

DATA AND INVERSION RESULTS

The radar data, provided by the Stanford Center for Radar Astronomy, were measured on the California coast by using a coherent pulse Doppler radar [*Teague et al.*, 1977]. The transmitting antenna was a vertical half rhombic approximately 250 m long and 45 m high at the apex, supported by a helium-filled balloon, and the backscattered signal was received by a wideband loop antenna. The radar beam pointed northwest into the direction of the prevailing winds with a half power beam width of 10° at 22 MHz. Adequate spectra for testing the inversion method were available only in downwind conditions,

TABLE 1. Characteristics of Temporal Spectra

Spectrum	Peak Period, s	rms Wave Amplitude, m
A	8 ± 0.5	0.61 ± 0.09
B	14 ± 1, 12 ± 0.5	0.43 ± 0.04
C	13 ± 1, 11 ± 0.5	0.46 ± 0.04

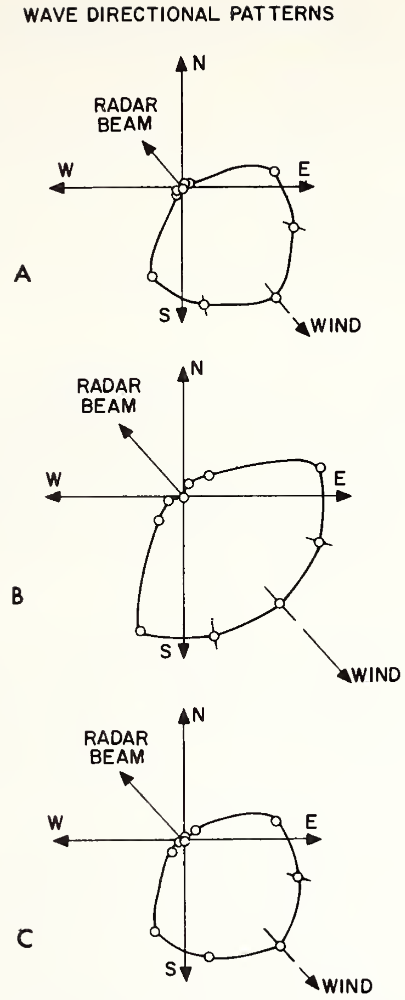

Fig. 3. Directional factors obtained by the inversion of radar spectra shown in Figure 1 for ocean waves of periods of <4.5 s. The model ocean wave spectrum we adopt is the product of the directional factor and the amplitude spectrum.

as high winds in the location normally blow from the northwest, and in addition, the antenna is difficult to control in crosswind conditions. Transmit antenna motion causes a broad spectral hump in the region around zero Doppler shift, which then cannot be used to derive directional information.

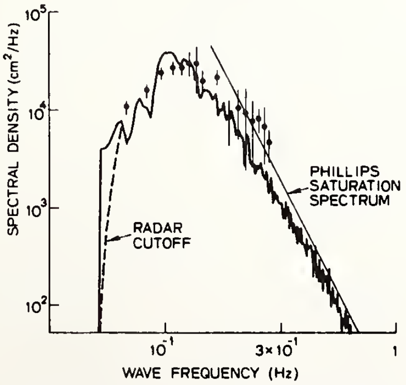

Fig. 4. Comparison of the temporal wave height spectrum obtained by inversion of the radar spectrum shown in Figure 1*a* with that measured by the buoy (continuous line).

TABLE 2. Comparison of Radar and Buoy Observations

	Radar	Buoy
rms wave amplitude, m	0.61 ± 0.1	0.54
Wind direction, deg	312 ± 5	310
N_{10}/N_{00}	−0.56 ± 0.1	−0.59*
N_{01}/N_{00}	0.51 ± 0.09	0.49*
N_{20}/N_{00}	0.51 ± 0.09	0.61*
N_{02}/N_{00}	0.49 ± 0.08	0.58*
N_{11}/N_{00}	−0.12 ± 0.03	−0.19*

*Average for ocean wave period between 1.9 and 4.5 s.

Radar spectra for positive Doppler shifts are shown in Figure 1. Spectra A, B, and C were measured on July 25, October 21, and October 23, 1975, with frequency resolutions of 0.01, 0.005, and 0.005 Hz, respectively. Incoherent averaging was performed over independent spectra measured over a period of 2 hours and four range bins 4 km in extent. Spectra which indicated severe antenna motion were not included in the averaging. Before inversion the spectra were normalized by the first-order energy, obtained by integrating over the first-order region of the spectrum. First-order terms were then subtracted to give the higher-order continuum with a cutoff near the first-order Bragg frequency. The major source of variance in the data is the random surface height of the sea. For each parameter derived by inversion we calculated a corresponding standard error resulting from this source of uncertainty, which decreases with the number N of spectra averaged as $1/(N)^{1/2}$.

The amplitude spectra derived by inverting the radar spectra for frequencies between 0.5 and 0.75 Hz are shown in Figure 2. Spectrum A is characteristic of a moderate well-developed sea, while spectra B and C contain peaks due to long-wavelength low-amplitude swell. The derived peak periods and rms wave amplitudes are given in Table 1.

Derived directional distributions for waves with periods less than 4.5 s are shown in Figure 3. In each case the symmetry direction is calculated to coincide with the radar beam, and most energy propagates within 60° of the wind. It is of interest to note that the popular $\cos^s(\theta/2)$ model for the directional factor provides a poor fit to the derived functions for any value of the spread parameter s. A far better fit is provided by a model defined by

$$G(\theta) = \text{const} \qquad \theta < \theta_c$$
$$G(\theta) = 0 \qquad \theta > \theta_c$$

where θ_c defines a cutoff angle, in our case, 60°.

ESTIMATION OF SUCCESS OF INVERSION

The derived parameters constitute a model of the directional ocean wave spectrum. We consider the inversion of the linearized integral equation to be successful if the following criteria are obeyed:

1. The derived parameters uniquely satisfy the linear equations defined by (1); we find that this criterion is obeyed as the system is overdetermined.
2. The uncertainties in the model due to the variance of the data are reasonably low: the error bars shown in Figures 2 and 3 are considered acceptable for many applications.
3. The model agrees with available surface truth.
4. The model is compatible with the data.

We shall consider the third and fourth points separately.

Comparison with surface truth. For spectrum A in Figure 1, simultaneous tilt buoy observations provided by Scripps Institute of Oceanography are available. We note that the radar provides an areal average over approximately 50 km², while the buoy gives a point measurement, both devices averaging over time. The tilt buoy measures the first six Fourier coefficients of the ocean wave spectrum $S(\kappa, \theta)$, given by

$$N_{pq}(\kappa) = \int_0^{2\pi} \cos^p(\theta) \sin^q(\theta) S(\kappa, \theta)\, d\theta \qquad (5)$$

$$p, q = 0, 1, 2 \qquad |p + q| \leq 2$$

[*Tyler et al.*, 1974]. Of these, five are independent as $N_{00}(\kappa) = N_{02}(\kappa) + N_{20}(\kappa)$. $N_{00}(\kappa)$ is just the spatial spectrum of the ocean waves, which may be compared with that derived by inversion of the radar spectrum. Results are shown in Figure 4, where the spatial spectra have been converted to temporal spectra by using the first-order dispersion relation for gravity waves. We consider agreement between the two observations to be fair, considering that they were obtained by devices which perform different types of averaging.

The next five Fourier coefficients measured by the buoy were normalized by $N_{00}(\kappa)$. The normalized values are approximately constant for wave periods of less than 4.5 s and were averaged to give values for comparison with the radar results, derived by integrating the directional factor shown in Figure 3*a*. Results are given in Table 2, which also contains corresponding rms wave amplitudes and mean wave directions. Errors quoted in Table 2 represent upper bounds on the uncertainties.

For spectra B and C no buoy observations were available. According to the Farallons weather station the wind at the time was from the northwest at 18 and 12 kn (9 and 6 m/s), respectively, with swell of height 5 ft (~1.5 m) and a sea height of 2 ft (~0.6 m) for both B and C. These observations are consistent with our results.

Compatibility with the data. The derived model of the ocean wave spectrum was substituted into the right-hand side of (1), and the corresponding radar spectrum was calculated. A measure of the compatibility of the model wave spectrum with the data is then given by the deviation of the computed radar spectrum from the measured values. For spectrum A the fit is good throughout the whole frequency band. For B and C it is good except for frequencies greater than 0.875 Hz, where model values are considerably less than the data. We draw the conclusion that third-order terms in the perturbation expansion may become significant in this region. This conclusion is supported by model calculations indicating third-order peaks for large Doppler shifts [*Lipa and Barrick*, 1977].

CONCLUSION

We have demonstrated that inversion of the second-order radar spectrum yields detailed information on the directional ocean wave spectrum. The inversion method described derives the amplitude spectrum of long ocean waves (wavelength of >3 m) and the directional factor of shorter saturated waves, together with the direction of maximum symmetry which may be identified with the wind direction. Ocean parameters derived from a measured echo spectrum are found to be in good agreement with concurrent observations made by a tilt buoy. This success lends impetus to the development of methods to derive the complete directional spectrum by inversion of the second-order structure and the assessment of limits of application set by contamination with third-order and viscous terms.

Acknowledgments. I am grateful to W. E. Faulkerson, E. C. Ha, C. C. Teague, and G. L. Tyler of the Stanford Center for Radar Astronomy for the radar data, to R. H. Stewart of Scripps Institute of Oceanography for the buoy observations, and to D. E. Barrick of the NOAA Wave Propagation Laboratory for helpful and continuing discussions on the interpretation of sea scatter. This work was supported by the Office of Naval Research under contract N0014-76-C-0356 and the National Oceanographic and Atmospheric Administration under contract NOAA 03-6-022-35260.

REFERENCES

Barrick, D. E., Remote sensing of sea state by radar, in *Remote Sensing of the Troposphere*, edited by V. E. Derr, U.S. Government Printing Office, Washington, D. C., 1972.

Barrick, D. E., The ocean waveheight nondirectional spectrum from inversion of the HF sea-echo Doppler spectrum, *Remote Sensing Environ.*, *6*, 201–227, 1977*a*.

Barrick, D. E., Extraction of wave parameters from measured HF sea-echo Doppler spectra, *Radio Sci.*, *12*, 415–424, 1977*b*.

Hasselmann, K., Determination of ocean wave spectra from Doppler radio return from the sea surface, *Nature Phys. Sci.*, *229*, 16–17, 1971.

Lipa, B., Derivation of directional ocean-wave spectra by integral inversion of second-order radar echoes, *Radio Sci.*, *12*, 425–434, 1977.

Lipa, B., and D. E. Barrick, The third-order hydrodynamic contribution to the HF radar sea-echo Doppler spectrum, paper presented at meeting of U.S. Nat. Comm./Union Radio Sci. Int., Stanford, Calif., June 1977.

Phillips, O. M., *The Dynamics of the Upper Ocean*, Cambridge University Press, London, 1966.

Teague, C. C., G. L. Tyler, and R. H. Stewart, Studies of the sea using HF radio scatter, *IEEE Trans. Antennas Propagat.*, *AP-25*, 12–19, 1977.

Tyler, G. L., W. E. Faulkerson, A. M. Peterson, and C. C. Teague, Second-order scattering from the sea: Ten-meter observations of the Doppler continuum, *Science*, *177*, 349–351, 1972.

Tyler, G. L., C. C. Teague, R. H. Stewart, A. M. Peterson, W. H. Munk, and J. W. Joy, Wave directional spectra from synthetic aperture observations of radio scatter, *Deep Sea Res.*, *21*, 989–1016, 1974.

(Received July 8, 1977;
revised October 6, 1977;
accepted October 17, 1977.)

Preprint Volume; Conference on Atmospheric Environment of Aerospace Systems and Applied Meteorology, 57-66, American Meteorological Society, November 1978.

THE DULLES INTERNATIONAL AIRPORT WIND-SHEAR DETECTION SYSTEM — STATISTICAL RESULTS

A. J. Bedard, Jr.

NOAA/ERL/Wave Propagation Laboratory
Boulder, Colorado 80302

1. INTRODUCTION

The design and evaluation of wind-shear detection systems require statistical data concerning wind-shear events. The experimental wind-shear measuring system at Dulles International Airport has answered much of this need, recording the strengths and frequencies of various shear events over an 18-month period from November 1976 through March 1978. For this location it is now possible to estimate false alarm and miss-rates for surface arrays of temperature, pressure, or wind sensors or combinations of these. Furthermore, data concerning the magnitude of the shears, their origin, and relationship to the local meteorology provide guidance for wind-shear detection and avoidance.

The Dulles system, comprised of a Doppler acoustic-microwave radar and a dense network of surface sensors described in papers by Hardesty et al. (1977), and Bedard et al. (1977), recorded more than 160 events. This paper reviews the statistics of these events, discussing their implications for the design of systems of surface sensors, particularly for the detection of thunderstorm outflows. Eighty-two percent of 113 significant events occurred in conjunction with thunderstorms, squall-lines, or frontal passages. The chief source of false alarms for anemometers was boundary layer disturbances representing 10% of the total, while gravity shear waves related to the 500-mb winds caused most false alarms for pressure sensors (4% of the total). By using complementary arrays of wind and pressure sensors total system false alarms can be greatly reduced.

These data demonstrate the importance of stable surface layers in determining the representativeness of surface temperature and wind measurements of flow at higher levels (stable surface layers causing underestimates of system severity). Wind vector measurements, providing more information than point temperature measurements, offer operational advantages for detection systems. Conversely, pressure sensors will not reliably detect thin outflows (100-200 m) occurring at a distance from downflows having small dimensions. Again the wind and pressure sensors combine to provide a total system offering high reliability for detection of outflows. The data set offers wide possibilities for further exploitation including case study comparisons with numerical models, case study comparisons with weather radar data, and summaries of shear data and Doppler sounder profiles for computations of aircraft response and design of remote sensing systems.

The observations range from large wind surges, pressure jumps, and temperature drops caused by strong thunderstorm gust fronts to weak wind surges caused by mixing in ground-based inversions. A complete mesoanalysis, as done by Fujita (1978), was not possible for each event. Thus, the categorization of events must remain tentative. Nevertheless the source mechanism for most disturbances was clear and only a small percentage of events seemed difficult to identify. Also, some measurements placed in one category (for example a pre-frontal squall-line) show evidence of other effects as well — a boundary layer break up, gravity waves, and downflows could also accompany the flow discontinuity. Moreover, the definition of an event, with comparisons between the various sensors, was a circular process since each element of the system was itself being evaluated.

One further point of caution is in order before presenting the data. One has to be careful in designing detection systems based upon short-term (~1 year) observations, since it is usually extreme deviations from the norm that cause disasters in terms of lives and property. In spite of these qualifications these data represent great value in terms of being able to relate γ-scale array (~1 km spacings) observations to vertical remote sensor data, permitting documentation of the structure, source, and detectability of a variety of wind-shear events. In fact, we accumulated a great deal of information valuable for the design of detection systems.

2. HISTOGRAMS SHOWING FREQUENCY OF VARIOUS TYPES OF EVENTS AS A FUNCTION OF MONTH-OF-YEAR

2.1 Thunderstorms, Squall-lines and Fronts (Figure 1)

Figure 1 shows that most of these disturbances occur during the summer months. The solid bars indicate the portion of disturbances that were significant (because of the magnitude of the accompanying wind surge or pressure jump). Of the 131 events, 93 we characterize as significant because they could have triggered warning systems based upon surface wind vector changes, upper level flow changes, or pressure jumps. These events related to thunderstorms, squall-lines or fronts accounted for 82% of all of the "significant" events. This breakdown agrees with the percentage obtained (82%) by Bedard and Cairns (1977) for the Chicago O'Hare airport area. The exact agreement is probably accidental.

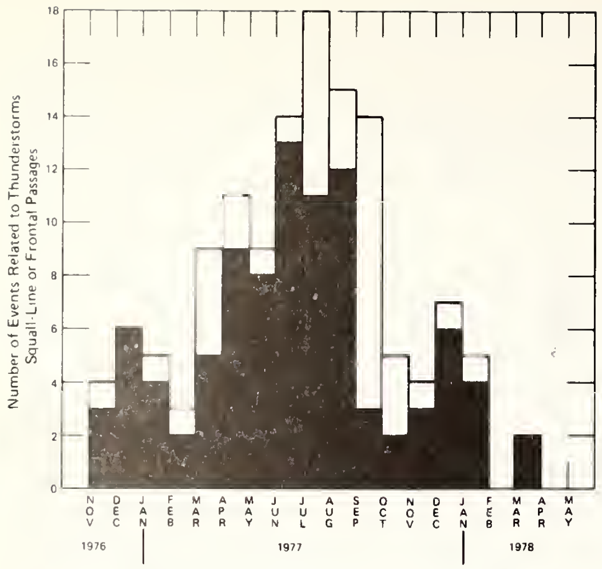

Figure 1. Histogram showing the number of events related to thunderstorms, squall-lines, or frontal passages as a function of month-of-the-year.

2.2 Boundary Layer Effects

The next most frequent class of disturbances is caused by "boundary layer effects". We interpret most of these as resulting from a jet aloft mixing down to the surface through a surface-based inversion. The 18 events in this category accounted for 11 or about 10% of the total number of significant disturbances due to all causes. We shall show that this class of disturbance is a chief source of false alarms for wind detectors. Pressure jumps large enough to trigger dP detectors accompanied three of the surface wind surges. Paradoxically, the existence of a wind surge at the surface can signify the breakup of a surface inversion and the end of a dangerous vertical shear (dU/dZ) situation.

2.3 Gravity-Shear Waves

Whereas boundary layer effects can cause false alarms for wind sensor systems, gravity-shear waves aloft can account for most false alarms on pressure sensor systems. The eight events detected occurred during the fall and winter months accounting for five or about 4%, of the total number of significant events, detected. Only very minor wind speed disturbances occurred at the times of these pressure waves.

2.4 Gravity Waves

Although wind shear may often be a factor in the production and propagation of these waves, the term gravity wave is used to emphasize their frequent relation to ground-based inversions. Such coherent waves can increase the danger of already hazardous wind-shear situations. One of the four waves measured involved both pressure and surface wind changes large enough to cause detection by a system of surface sensors and could have been important to aircraft operations.

2.5 High Winds

High, gusty winds can cause local pressure fluctuations large enough to cause false alarms. Three notable cases occurred during the winter months. Fortunately these fluctuations are of short duration (usually less than 4 seconds) and may be eliminated by requiring significant pressure triggers to have durations longer than 4 seconds or using spatial filters (Bedard, 1977).

3. STATISTICS OF OBSERVATIONS RELATED TO THUNDERSTORMS, SQUALLLINES AND FRONTS

3.1 Surface Wind Observations

Figure 2 is a plot of the surface (standard 7 m height) wind speed change in $m\ s^{-1}$ as a function of the surface wind vector change in $m\ s^{-1}$. Note that while the wind speed change cannot exceed the magnitude of the wind vector change, a significant number of data points indicate that the wind vector change is frequently larger than the wind speed change by a factor of 2 or 3. In fact three points show no wind speed change accompanying wind vector shifts. These data indicate the value in making measurements of wind vector differences.

Figure 3 is a plot of the peak wind speed as a function of vector difference. Although the wind speed surge can be much smaller than the vector change, a wind speed threshold detector (Bedard and Fujita, 1978) with a trigger point at say 20 knots would detect most disturbances having vector shifts in excess of $10\ m\ s^{-1}$. In fact figures 2 and 3 show that the probability of such detection is greater the more severe the vector shift. In these plots where spatial variability occurs with a number of anemometers, the data point represents the average value.

3.2 Surface Pressure Observations

Figure 4 is a plot of the maximum pressure change in mb as a function of the rise time (τ) in seconds for all events for which accurate pressure data were available. Figure 5 is a plot of the maximum pressure change as a function of the rise time τ for events showing a surface wind vector change of at least $7\ m\ s^{-1}$. The straight lines on figures 4 and 5 indicate the approximate threshold of a pressure jump sensor designed for wind-shear detection. The group of points in figure 5, located below the sensor threshold at 900-sec (15 minute) periods represent data from the less accurate station barograph, the only pressure data source for the first 5 months of operation. Thus, this group of data points shown at 900-sec periods represent a maximum rise-time estimate for these events. Note that most of the events having large amplitudes and short rise times (<600 seconds) occur with the larger wind vector surges. As with the anemometer data, where spatial variability occurs with a number of pressure sensors, the data point plotted represents average values of pressure and rise time.

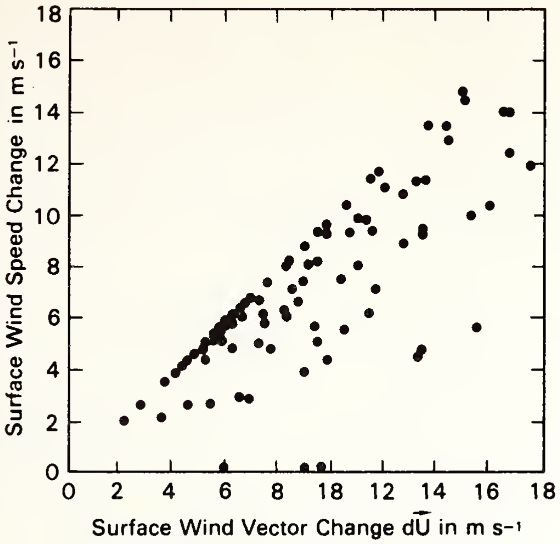

Figure 2. Plot of surface wind speed change as a function of surface wind vector change.

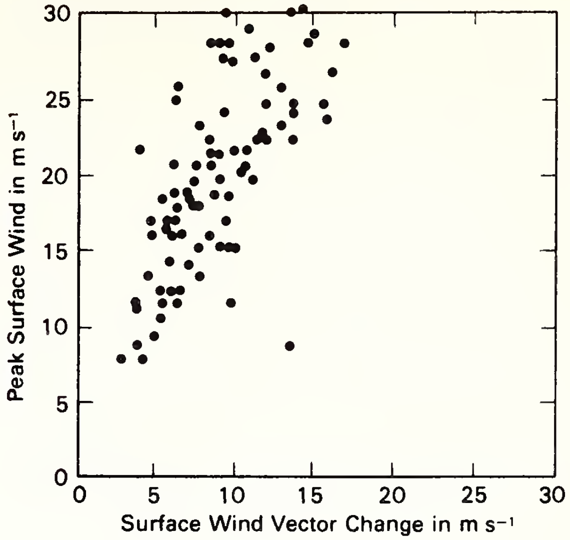

Figure 3. Plot of peak surface wind as a function of surface wind vector change.

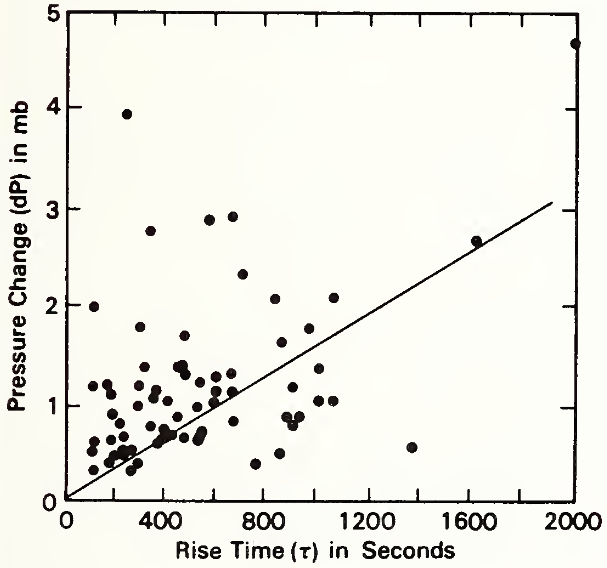

Figure 4. Pressure change (dP) as a function of rise time (τ) for all events.

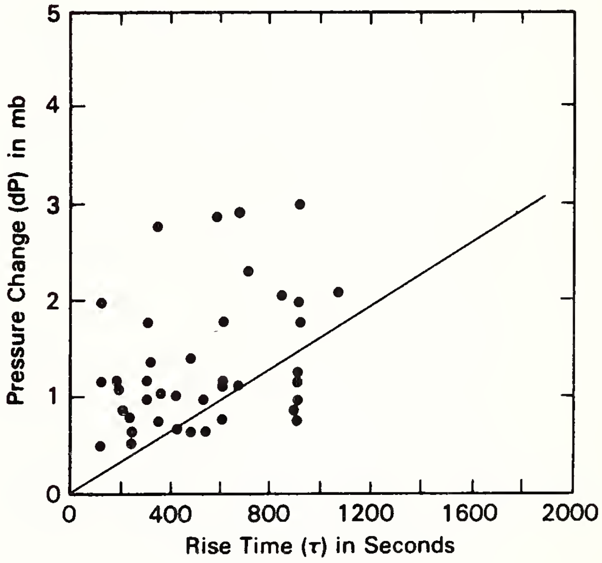

Figure 5. Pressure change (dP) as a function of rise time (τ) for events showing a surface wind vector change exceeding 15 knots.

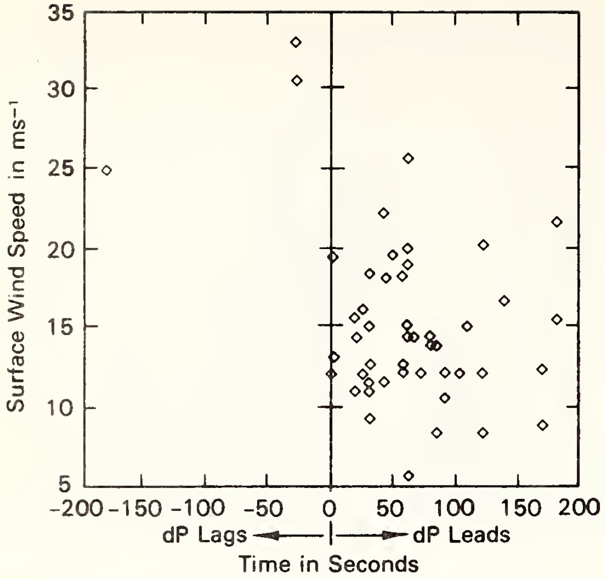

Figure 6. Relative arrival times of pressure and wind disturbances.

Figure 6 is based upon data obtained during 1977 at Chicago's O'Hare International Airport. It shows the arrival times of the start of the pressure jump detector triggers compared with either the time at which the wind vector change for a co-located anemometer exceeded 15 knots or the surge maximum time for low-wind cases. These data obtained at six tower locations near the ends of runways, use the same data recording system eliminating any ambiguity concerning relative arrival times. The plots indicate that a warning of over 1 minute is often provided by dP detectors relative to co-located wind sensors.

3.3 Doppler Acoustic-Microwave Radar Observations

The Doppler acoustic-microwave radar described by Hardesty et al. (1977) provided wind speed and wind direction profiles for comparison with the array of surface sensors. These profiles represent 6 minute exponential averages (with the most recent data weighted most heavily) and are designed to depict the mean flows and not the fine structure. Also, the sounder system did not operate for several key periods. In spite of these limitations profiles obtained permitted the description of 47 events. While there is relatively good agreement between the wind direction estimates obtained by the two methods, there is a considerable amount of scatter in the wind vector comparison. Low-surface wind measurements could result from stable layers near the surface; low sounder estimates could result from failures to detect vertical components or from the averaging time used.

3.4 Surface Temperature Observations

Figure 7 is a plot of the surface wind-vector change in m s^{-1} as a function of the surface temperature change in °C. Although there is considerable scatter, the tendency for the larger temperature decreases to be related to the larger gust surges is evident. However there are also many cases where zero or even positive temperature changes occur. Thus it seems that temperature sensors will not be an effective tool for wind shear warning systems.

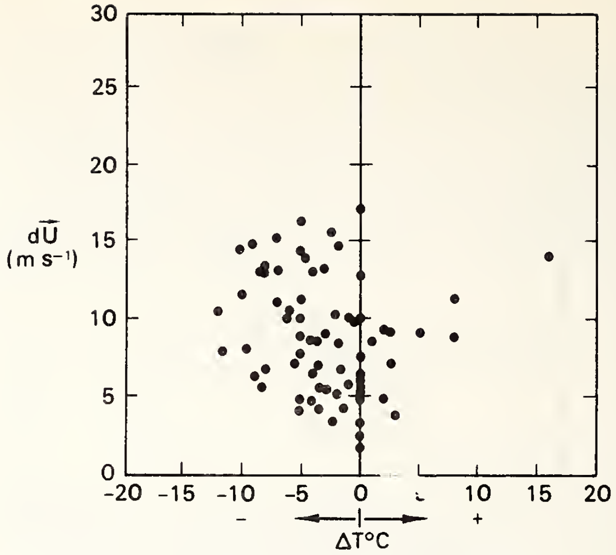

Figure 7. Surface wind vector change as a function of surface temperature change.

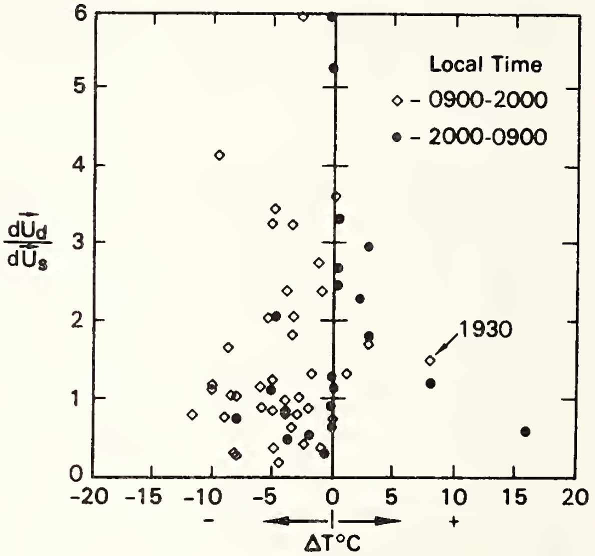

Figure 8. Plot of the ratio of the Doppler sounder wind vector change $\vec{dU}_d$ to the surface wind vector change $\vec{dU}_s$ as a function of the surface temperature change.

Figure 8 is an important figure because it illustrates that both temperature and wind sensors can underestimate the severity of density currents aloft, pointing to stable surface layers as the cause. The ratio $\vec{dU}_d/\vec{dU}_s$ (the Doppler sounder wind vector change to the surface wind vector change) appears as a function of the temperature change in °C. On this plot the open diamonds occur during the hours 0900 to 2000 and the solid circles from 2000 to 0900 local time. This later interval is statistically the time during which stable layers can exist. The choice of these intervals was guided by the results of Geiger (1973). When the ratio $d\vec{U}_d/d\vec{U}_s$ is greater than 1 the wind surge at the surface is less than the discontinuity aloft; the plot shows that in many cases it is significantly less (factors of 2 or more). Of the 19 cases showing zero temperature change or temperature rises 13, or 68%, occurred during intervals of probable stability. Thus we infer that the presence of stable layers can prevent the upper level flow from being represented at lower levels.

Thunderstorm outflows following previous thunderstorms will encounter such stable layers because of the cool air present from the previous storm. We have noted several cases where subsequent outflows demonstrated large spatial variability in the surface wind surges that could be explained by the presence of stable layers.

3.5 Weather Radar Observations

Weather radar observations compared with these surface data indicate a fascinating variety of combinations. Cases range from isolated, small stationary echoes at a distance from the array, well-defined echo lines moving at high speed, and surges developing from bulges in echo lines (as described by Fujita, 1978) to extensions from the ends of echo lines into no-echo regions. We have compared the surface parameters to the echo bearing or propagation direction as well as to the speed of motion of the echo. Events also occurred within broad echo regions, several of these showing evidence of downflow effects. We should perform additional mesoanalyses using selected events from this data base. The valuable analysis of Fujita, 1978, using only data from a single day, is only an example of what could be done with these data.

Figure 9 compares surface wind direction as a function of radar echo direction in degrees, showing quite good agreement. Most systems were located or approached from between azimuths of 250° and 360° from the Dulles array.

In a more complete report to the Federal Aviation Administration (currently in process) we studied the surface wind vector change, pressure disturbance speed, and Doppler radar wind vector change as a function of radar echo speed. There seems to be a tendency for the surface wind vector to be less than the radar echo speed while the speed of the pressure disturbances tends to be greater than the radar echo speed. However, there is a considerable amount of scatter in the data points. It seems that the more rapidly moving echoes are related to the more intense lower level flows and rapidly moving pressure changes. We observed several cases where a slowly moving echo line produced a lobing echo moving from a different direction at over twice the speed of the echo line. Also, we observed one case where the flow surge originated from the rear of an echo that had already passed over the array. Although many line echoes move at approximately uniform speeds we observed cases where it would be quite difficult to infer existing or future surface effects from the conventional weather radar data alone.

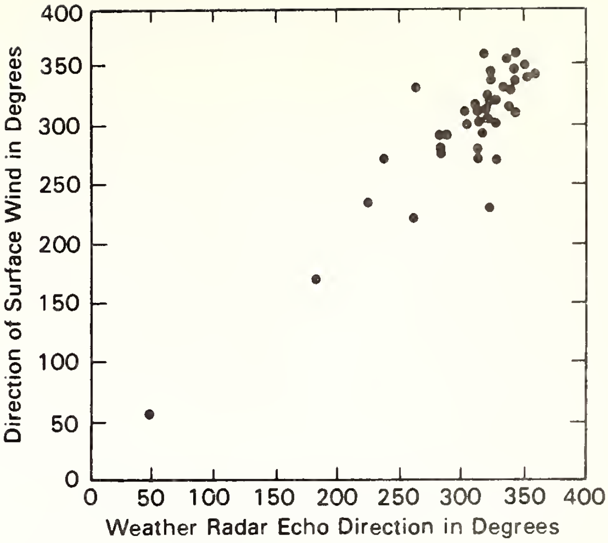

Figure 9. Direction of surface wind as a function of weather radar echo direction in degrees.

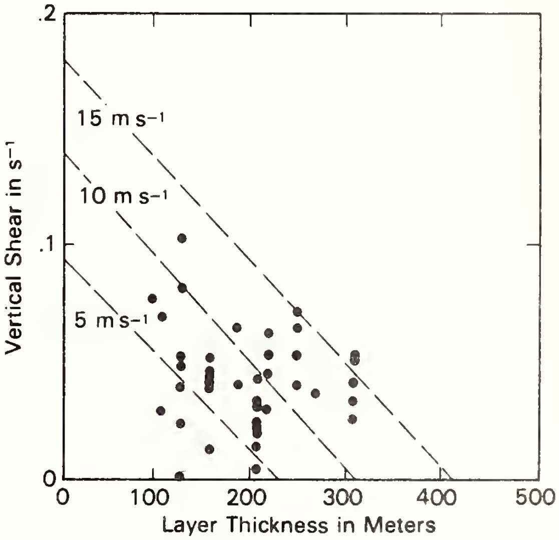

Figure 10. Vertical shear in s^{-1} determined from Doppler acoustic/ microwave radar as a function of layer thickness in meters for thunderstorm squall-line and frontal-related events. The straight lines on this figure indicate lines of constant wind vector change.

3.6 Implications for the Design of Detection Systems

Figures 10 and 11 present several important points concerning vertical wind shear (dU/dZ). Using the Doppler profiles we computed maximum shear values, and these appear as a function of layer thickness in Fig. 10. The lines of equal wind vector change on this figure should also be used as an index of severity. Thus, a shear of .08 occurring over a 50-m layer could be relatively safe compared with the same shear value occurring over a greater thickness and hence representing greater speed changes relative to an air foil. There is a need to define the dangerous situations for a variety of aircraft in terms of both shear magnitude and

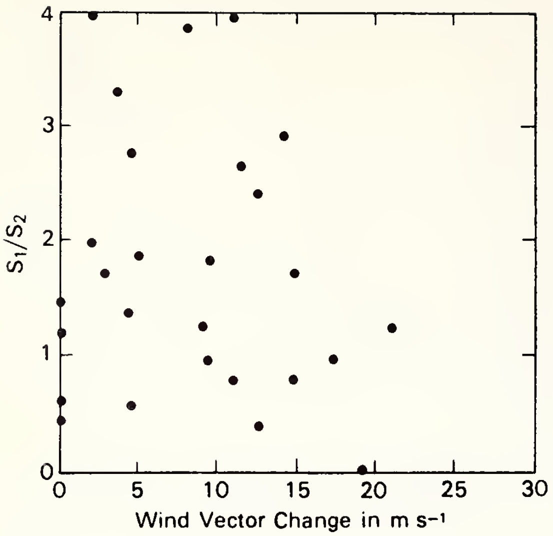

Figure 11. The ratio of vertical shear S_1 associated with discontinuity to the vertical shear S_2 prior to the discontinuity as a function of the horizontal wind vector change.

the layer or length over which the shear occurs. Also the profiles are averaged so that we did not detect the large fluctuating shear components which certainly accompany some average shear conditions. There is a great need to obtain statistics concerning these deviations relative to conditions of mean shear.

Figure 11 is a plot of the vertical shear associated with the flow discontinuity divided by the vertical shear prior to the arrival of the discontinuity as a function of the vector change. When there is no change in the shear magnitude the ratio is 1, values greater than 1 indicating increased shear and less than 1 indicating reduced shear. Surprisingly, for six of the cases the vertical shear decreased behind the flow discontinuity. Perhaps this was caused by the destruction of a stable surface layer. In any event there seems no clear relation between the speed of motion of the discontinuity relative to the medium and the associated vertical wind shear. A summary of wind profiles from these data sets should be made available to those modeling aircraft response.

4. STATISTICS OF OBSERVATIONS RELATED TO BOUNDARY LAYER EFFECTS

4.1 Sample Case Study Illustrating a Boundary Layer Disturbance

Figure 12 shows the surface wind speed disturbance together with vertical profiles at two different times. Also a pressure jump and small temperature disturbance accompanied the wind surge. The large shear that exists at lower levels could have caused a gravity wave disturbance on the basic flow. A sudden penetration of the boundary layer by the upper level flow could explain the wind surge observed. The vertical velocity components could have caused (or have been caused by) the pressure gradient observed.

4.2 Measurement Statistics of Boundary Layer Disturbances

Figure 13 is a plot of the surface wind vector change attributed to boundary layer disturbances as a function of the temperature change in °C. Of the 19 disturbances on the plot all but three occurred with zero or positive temperature changes. Figure 14 is a histogram showing the time-of-day variation of this class. There seems a tendency for these surges to occur during the hours of the day when stable layers occur or during the morning hours when convective activity causes such layers to break up.

4.3 Implications for the Design of Detection Systems

Although most of the surges attributed to boundary layer disturbances tend to be relatively weak (lower than 15 knots), such surges occurred at different times for different anemometers (probably because local terrain effects dominated). The vector differences between some pairs of spatially separated anemometers were significant. Also these boundary layer disturbances tend to occur at times when propagating flow discontinuities show reduced surface interaction. Such effects seem to represent the chief source of false alarms for surface anemometers. Figure 15 is a plot of the vertical shear present during these disturbances. This plot shows strong shears in the lowest 200 meters near the times of these disturbances, suggestive of the existence of stable surface layers. In a number of instances the surface surge coincided with a reduction in the vertical shear. Also, there is evidence (Hill, 1976) that in different geographical locations much larger wind surges could occur.

5. STATISTICS OF OBSERVATIONS RELATED TO GRAVITY-SHEAR WAVES

5.1 Measurement Statistics for Gravity-Shear Wave Disturbances

The horizontal trace speeds of the pressure waves tend to match the 500-mb wind speed above the Dulles location. The speeds are usually higher than pressure disturbance speeds normally measured from thunderstorms or squall-lines (>30 m s^{-1}). The azimuth of the pressure waves often tracks the 500-mb wind direction above the Dulles location. These observations are consistent with past observations, and the percentage (4%) of the total number of significant gravity-shear wave events is consistent with the estimates of Bedard and Cairns (1977) for the Chicago O'Hare airport area.

5.2 Implications for the Design of Detection Systems

Gravity-shear waves related to upper level jet streams represent the most important source of false alarms for pressure sensor systems. The facts that only minor wind speed and direction disturbances accompany these events and that they frequently occur in the absence of adverse weather conditions help to prevent these false alarms from presenting a major problem.

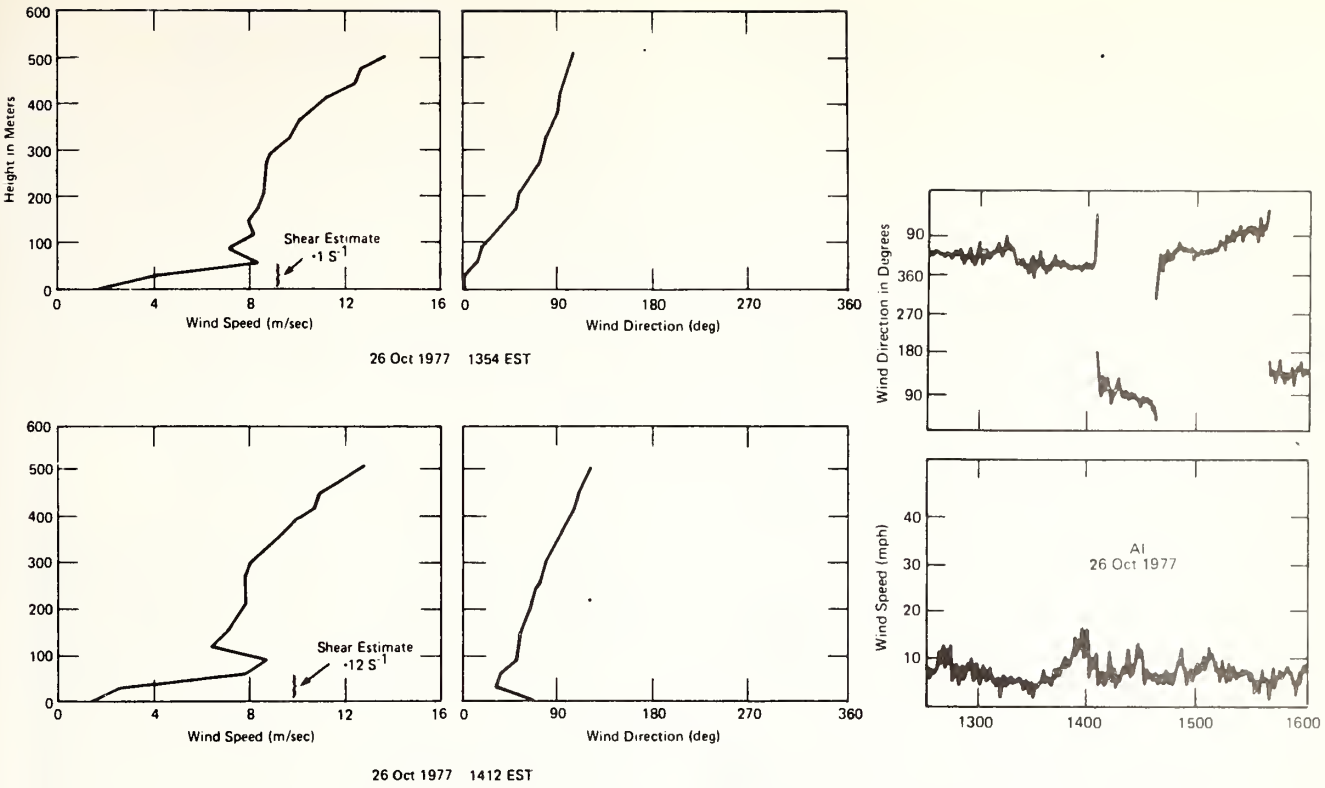

Figure 12. Sample case study illustrating a boundary layer disturbance.

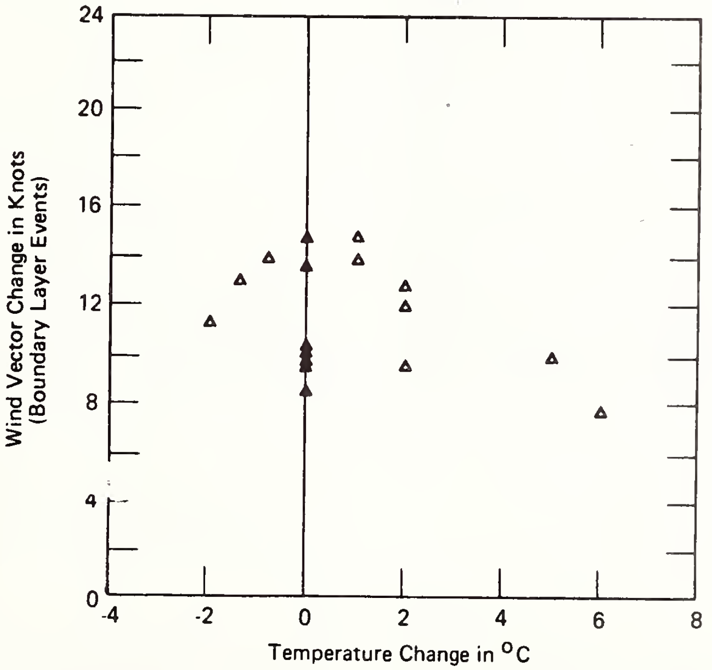

Figure 13. Surface wind vector change in knots as a function of surface temperature change in °C for boundary layer disturbances.

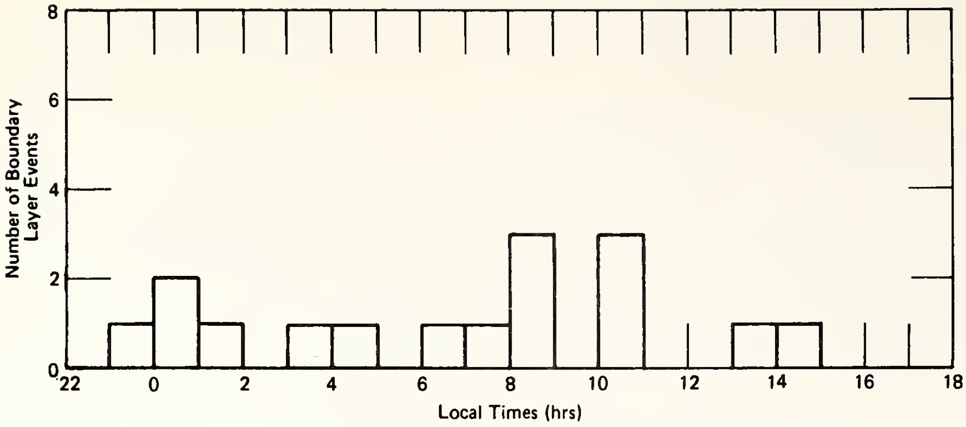

Figure 14. Histogram showing the number of boundary layer disturbances as a function of time of day.

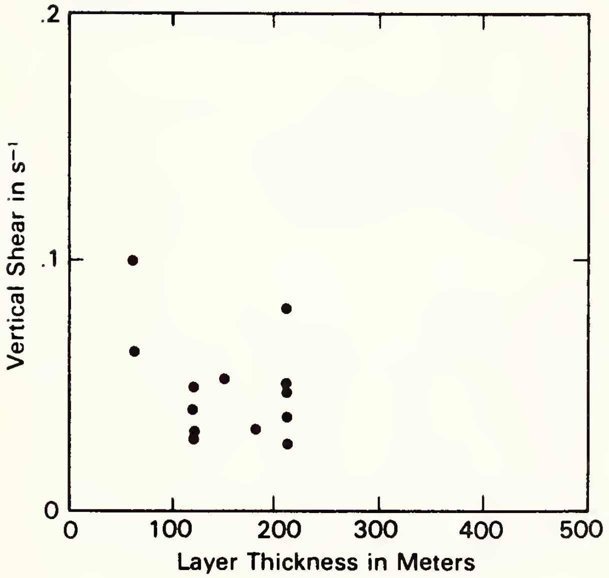

Figure 15. Vertical shear in s^{-1} determined from Doppler acoustic/ microwave radar as a function of layer thickness in meters for events related to boundary-layer disturbances.

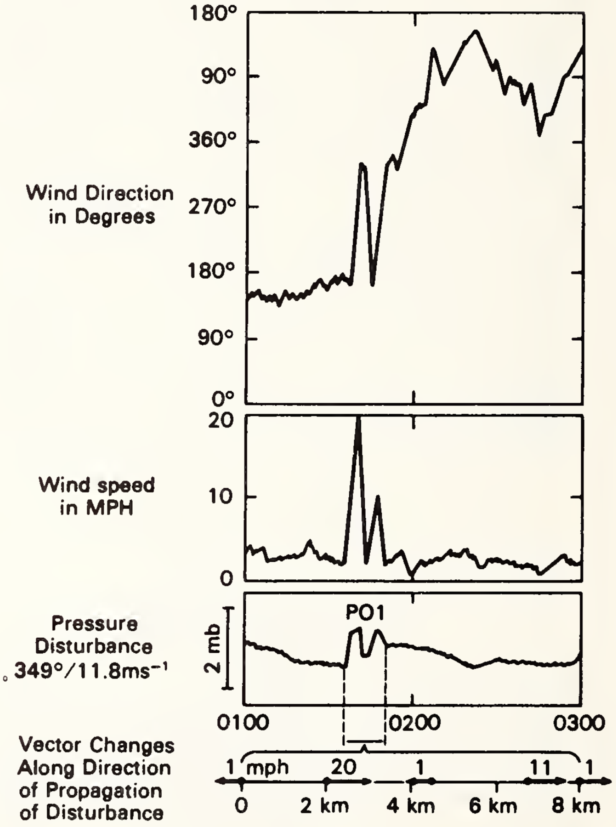

Figure 16. Case study illustrating a gravity wave disturbance on 8 July 1977, occurring between 0100 and 0300 EDT.

6. OBSERVATIONS RELATED TO GRAVITY WAVES

6.1 Case Study Comparing Surface Observations for a Gravity-Wave Event

Coherent wave fields (such as those shown in Figure 16) can increase the hazard for marginally dangerous shear situations. Such gravity wave events producing large enough pressure changes and wind vector shifts to cause wind-shear alerts on wind speed and pressure sensor systems should not be considered false alarms. Figure 16 also shows the large surface wind vector changes that can occur along a flight path coinciding with the direction of propagation of this wave.

6.2 Implications for the Design of Detection Systems

At the Dulles location only one large amplitude gravity wave occurred that was significant in terms of proposed detection systems. Such large waves could constitute a hazard in their own right. Smaller amplitude waves may excite control resonances and hence be important for aircraft operations. In fact, mean shear statistics may not be sufficient for modeling air foil response until the perturbation statistics are also specified (whether their source be waves or incoherent fluctuations). Remote sensing techniques should be applied to obtain these statistics along flight paths under a variety of conditions.

7. CONCLUDING REMARKS

The statistical data presented here support detection concepts requiring combinations of wind and pressure sensors, and suggest two modes of operation for operational use. With no thunderstorm wind-shear threat present (e.g., no weather radar echoes of thunderstorms within 100 km), a system requiring inputs from both pressure sensors and wind sensors, to institute an alert, reduces false alarms caused by both gravity-shear waves and boundary layer breakups. With severe local weather present (e.g., approaching fronts or thunderstorms) requiring detection by only pressure or wind sensors for an alert reduces the possibility of missing events because of stable layers limiting flow near the surface or thin layers from small, distant downflows. Bedard and Hooke (1978) suggest a configuration of pressure sensors, anemometers, and wind speed threshold sensors (Bedard and Fujita (1978)) for thunderstorm wind-shear detection near airports.

Some localities seem susceptible to shears of different origin requiring specifically tailored detection techniques. For example Hill (1976) identifies a chief source of dangerous shear for Reno, Nevada, as downslope winds above a ground-based inversion. A vertically profiling remote sensor (e.g., Hardesty et al., 1977) offers protection in such situations. Although we detected several events which we interpret as downbursts (Fujita and Carecena, 1977) we had no means of independently measuring the magnitude of the vertical speeds involved. We have suggested that closely spaced arrays of pressure and wind threshold sensors (200-m intervals) along runways can detect transient and spatially concentrated downbursts.

As more complete data concerning wind shear become available from different geographical regions, and wind-shear detection systems are developed, care should be taken to keep in mind the multi-faceted nature of the total wind shear problem. There is a great need to increase the cooperative work between those developing wind shear data sets, those estimating and measuring aircraft response, and those developing advanced remote sensors. The production of algorithms defining significant shear for remote sensing systems depends upon definitions of the precise limits of dangerous shear for a variety of aircraft which in turn depend upon the availability of realistic data from case studies of atmospheric shear events, including the fluctuating components.

8. ACKNOWLEDGMENTS

The Systems Research and Development Office of the Federal Aviation Administration supported both the experimental Field Programs and the analysis efforts that led to the development of the valuable data sets described. We are grateful to many individuals in the FAA for their guidance and encouragement; these include Messrs. R. Colao and J. Sowar as well as F. Coons and G. Tinsley. Much of the information presented here will appear as part of a more complete report to the FAA.

9. REFERENCES

Bedard, A. J. Jr., (1977). The d-c pressure summator: Theoretical operation, experimental tests and possible practical uses. Fluidics Quarterly, 9, no. 1, 26-51.

Bedard, A. J. Jr. and M. M. Cairns (1977). Measuring gust fronts using surface sensors. Proc. 10th Conference on Severe Local Storms, Oct. 18-21, Omaha, Nebr., Amer. Meteor. Soc., Boston, Mass., p. 154-159.

Bedard, A. J. Jr. and T. T. Fujita (1978). omnidirectional, tilt insensitive, wind speed threshold detector. Proc. 4th Symposium on Meteorological Observations and Instrumentation, April 10-14, Denver, Colorado. Amer. Meteor. Soc., Boston, Mass., p. 83-86.

Bedard, A. J. Jr., W. H. Hooke and D. W. Beran (1977). The Dulles airport pressure jump detector array for gust front detection. Bull. Amer. Meteor. Soc. 58, no. 9, 920-926.

Bedard, A. J. Jr. and W. H. Hooke (1978). The Dulles airport pressure-sensor array for gust-front detection — system design and preliminary results. Proc. 4th Symposium on Meteorological Observations and Instrumentation, April 10-14, Denver, Colorado. Amer. Meteor. Soc., Boston, Mass., p. 115-124.

Fujita, T. T. (1978). Wind shear at Dulles airport on 18 May 1977. Satellite and Mesometeorology Research Project Research Paper No. 159, Dept. of the Geophysical Sciences, University of Chicago, 19 p.

Fujita, T. T. and F. Carcena (1977). An analysis of three weather-related aircraft accidents. Bull. Amer. Meteor. Soc., 58, no. 11, 1164-1181.

Geiger, R., (1973). The Climate Near the Ground. Harvard University Press, 611 p.

Hardesty, R. M., P. A. Mandics, D. W. Beran and R. G. Strauch (1977). The Dulles airport acoustic/microwave radar wind and wind shear measuring system. Bull. Amer. Meteor. Soc., 58, no. 9, 910-918.

Hill, C. D. (1976). Other kinds of wind shear. NOAA Tech. Memo. NWS WR-108, 17 p.

Proceedings of the Conference on Weather Forecasting and Analysis
and Aviation Meteorology, 347-352, American Meteorological Society, 1978.

THUNDERSTORM-RELATED WIND SHEAR DETECTED AT DULLES INTERNATIONAL AIRPORT USING A DOPPLER ACOUSTIC/MICROWAVE RADAR, A MONOSTATIC SOUNDER AND ARRAYS OF SURFACE SENSORS

A. J. Bedard, Jr.
NOAA/ERL/Wave Propagation Laboratory
Boulder, Colorado 80302

M. J. Sanders, Jr.
NOAA/Systems Development Office
Equipment Development Laboratory
Silver Spring, Maryland 20910

1. INTRODUCTION

We present a case study illustrating how combinations of remote and in-situ sensors can provide much detail concerning atmospheric density currents. The data set combines results from a monostatic acoustic sounder (Parry and Sanders, 1972), a Doppler acoustic/microwave radar (Hardesty et al., 1977) and a dense array of surface sensors (Bedard et al., 1977). Figure 1 shows the locations of the surface pressure array, temperature sensor, and rain gauge in relation to the sounder and radar. The Doppler radar and surface array constituted part of an experimental wind shear detection system and were developed and deployed by the Wave Propagation Laboratory of NOAA, under the sponsorship of the Systems Research and Development Office of the Federal Aviation Administration. The monostatic acoustic radar was operated independently by the Equipment Development Laboratory of NOAA's Weather Service.

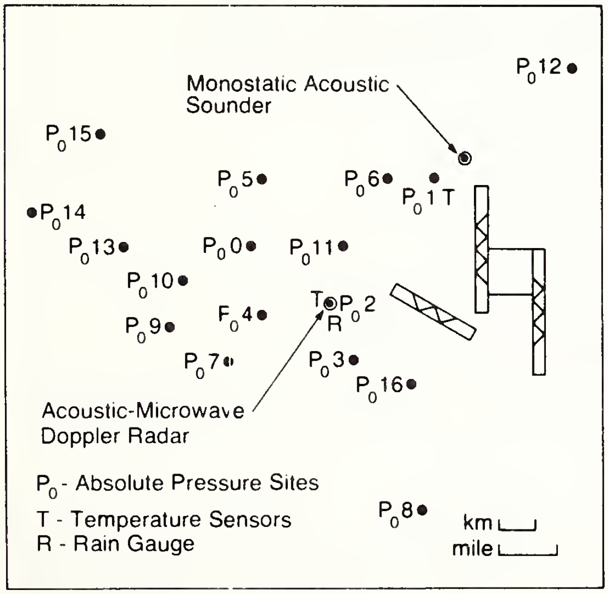

Figure 1. Locations of surface array of absolute pressure sensors, temperature sensor, and rain gauge in relation to the monostatic acoustic sounder and acoustic-microwave radar. The anemometer data are from a sensor at the location of the acoustic-microwave radar.

In addition to providing a vivid illustration of an atmospheric density current inducing mixing in an atmospheric boundary layer, this case study demonstrates how stable layers can limit strong surface-layer/upper-level-flow interactions. Moreover, the "fine structure" shown is illustrative of the realities involved in modeling wind shear-aircraft interactions related to density currents (which appear as complex three-dimensional flow fields, themselves imbedded in complex time-varying flows).

2. THE CASE STUDY OF 27 SEPTEMBER 77

Figure 2 presents the monostatic sounder data together with Doppler sounder vertical wind speed and direction profiles for specific times through the vertical cross section. The top of the solid return at about 300 m probably marks the top of an inversion layer. A rawinsonde observation at 1900 EDT shows the presence of an inversion. At about 2110 EDT, a disturbance with a wave-like structure at the leading edge appears above the inversion layer. We interpret this discontinuity as an atmospheric density current. The Doppler sounder profiles indicate a wind vector change in excess of 10 ms^{-1} at 500 m accompanying the density current. The wind shear between the surface and 300 m also indicates the presence of the stable layer.

Figure 3 shows the monostatic sounder data (the same as in figure 2) together with surface observations of temperature, and rain rate, wind speed, wind direction, and pressure all adjusted to a common time scale. The temperature shows an increase associated with the leading edge of the density current rather than the expected decrease. The increase in rain rate occurring later in the event probably results from a separate source region moving from a different direction. A minor increase in wind speed and a significant rise in pressure accompany the leading edge of the discontinuity. The form of the surface pressure trace is a representation of the form of the density current aloft. This is because an important component of the pressure field results from the integrated density changes in the column of air above the sensor. Data from the pressure sensor (P_{01}) closest to the monostatic sounder show the perturbation at the leading edge.

Figure 4 is a cross-sectional model illustrating a density current flowing on a stable layer and inducing mixing in the boundary layer. This simple model is representative of a situation in the atmosphere, where a cold air outflow (with density ρ2) impinges on or rides over an inversion layer (density ρ1) inducing mixing or eroding the layer. The vectors in the boundary layer depict how the flow can develop, at the same time mixing warmer air down to the

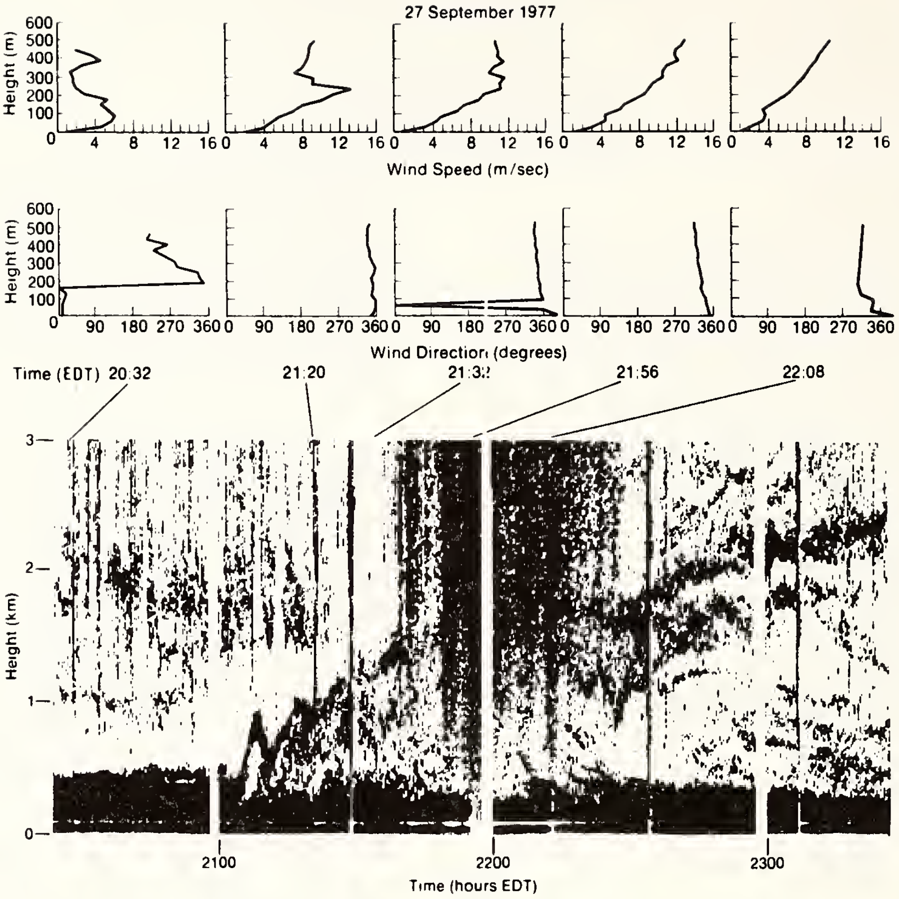

Figure 2. Monostatic sounder record showing an atmospheric density current together with Doppler sounder vertical wind speed and direction profiles.

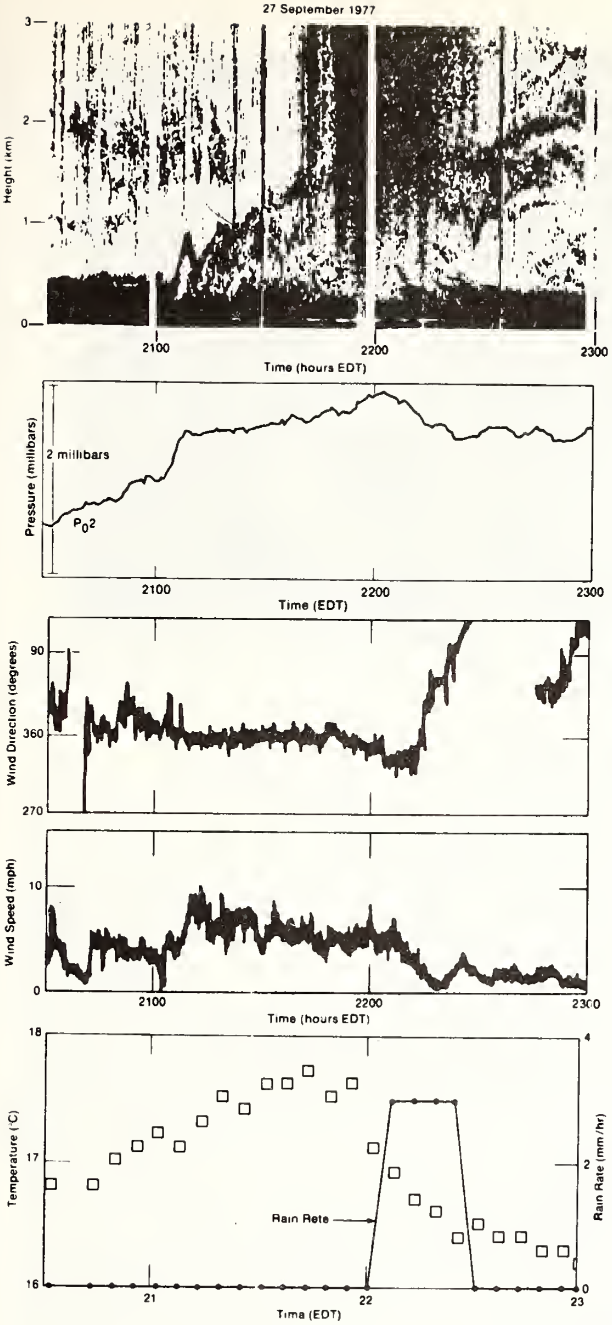

Figure 3. Monostatic sounder data together with surface observations of temperature and rain rate, wind speed, wind direction, and pressure all adjusted to the same time scale.

surface. This simple view can explain the observations shown in figure 3. Greene et al. (1977) present an example showing the erosion of the boundary layer over a 1/2-h time period.

Figure 5 shows weather radar data at 2115 and 2120 EDT. The square on each picture identifies the 10-km site of the Dulles International Airport array. Note that the small stationary echo located just outside the array

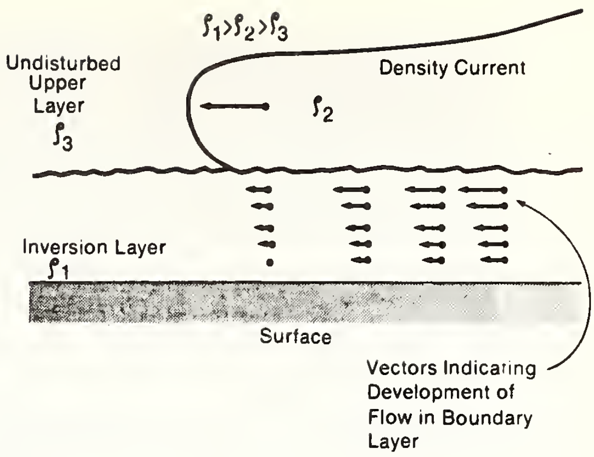

Figure 4. A cross-sectional model of a density current flowing above a stable layer and inducing mixing.

boundary to the NNW is at the approximate bearing of the pressure disturbance. This echo is the probable source of the outflow detailed in this paper.

Figure 6 presents the pressure data for four sites, with asterisks indicating the start of the pressure rise and the pressure maximum for each site. Calculation of azimuth and speed of motion were based upon various three-site combinations. The average rise time and peak pressure change estimates were 352 s and 0.64 mb. The average speed was 12.8 ms^{-1} from an azimuth of 339 degrees.

Comparisons between the various absolute pressure sensors (Fig. 6) indicate that the disturbance following the leading edge of the density current is not evident for P_{03} only 2 km to the west of the propagation path of the disturbance passing through P_{01} (near the monostatic sounder site). We conclude that such density currents can have large perturbations with scale-lengths of the order of kilometers. P_{08}, which is approximately along the P_{01} propagation path, does show a pressure perturbation after the initial jump. Idso (1972) presents data indicating the complex three-dimensional nature these systems can possess. The numerical results of Teske and Lewellen (1977) predict such complex forms for density currents, although thus far they have published results only for the two-dimensional situation.

Using the pressure data nearest the monostatic sounder (P_{01}) together with vertical structure information from the monostatic sounder we estimated the average temperature within the density current. Both the rawinsonde data and monostatic sounder data indicate an inversion height of about 300 m. Taking the peak pressure change of 0.51 mb and estimating a height of 700 m for the current head above the inversion we estimated that the mean temperature in the current was 1.8°C less than the air in front of the current or about 17.7°C. (This calculation ignored dynamic effects.) This value corresponds

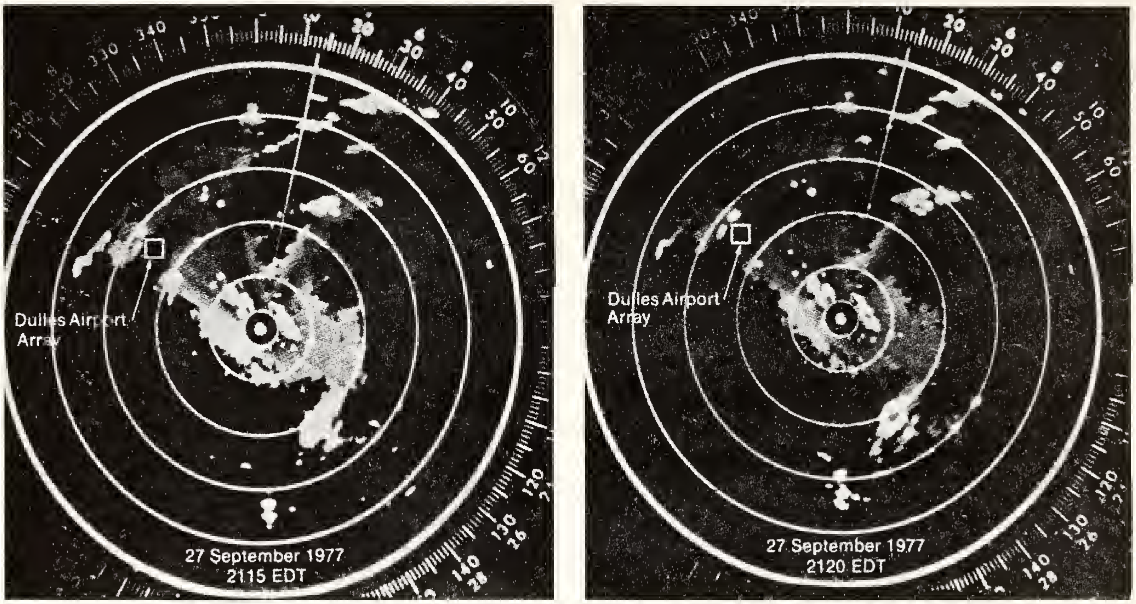

Figure 5. Weather radar data at two times with a square on each picture identifying the 10-km site of the Dulles International Airport array.

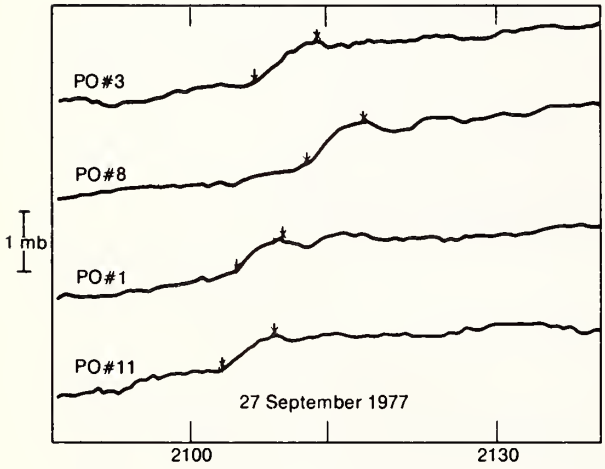

Figure 6. Pressure data for four sites illustrating the progression of a disturbance across the array of pressure sensors.

with the temperature of the air near the surface. Also we computed the amplitudes of the perturbation behind the head from the pressure data alone (again ignoring dynamic effects). We obtained 135 m which is significantly less than the approximately 200 m disturbance noticed on the monostatic sounder. This could result from a failure to account for dynamic effects or from the fact that the pressure sensor and monostatic sounder separation is about 1 km.

The monostatic acoustic sounder provides data on the density-current vertical structure as a function of time from one point on the ground beneath the flow. Since we know the propagation speed of the pressure rise related to the leading edge, we can infer the three-dimensional nature of the flow from both the measured speed and direction of motion as well as from the spatial variability of the pressure disturbance, performing a time-space conversion. Also, data from the Doppler sounder provide wind speed and direction as a function of height through one cross section. Figure 7 shows the inferred three-dimensional structure of the density current from four viewpoints. A rawinsonde observation for 1900 EDT establishes the pre-disturbance temperature profile. Figure 8 combines these data to provide a 3-D view of this outflow air in relation to the undisturbed flow. As the use of combined remote sensing techniques becomes more practical and frequent, such detailed reconstructions will become feasible on a more routine basis.

3. SIGNIFICANCE OF THIS CASE STUDY AND CONCLUDING REMARKS

This case study illustrates the value of using data from multiple sensors (combinations of remote and in-situ sensors) to reconstruct events. Also it shows the complex structures that can exist at the leading edge of density currents. The example indicates how a stable layer can inhibit and slow the interaction of a density current with near-surface layers. Such stable layers can prevent surface anemometers from detecting or adequately estimating the intensity of flow discontinuities at higher levels.

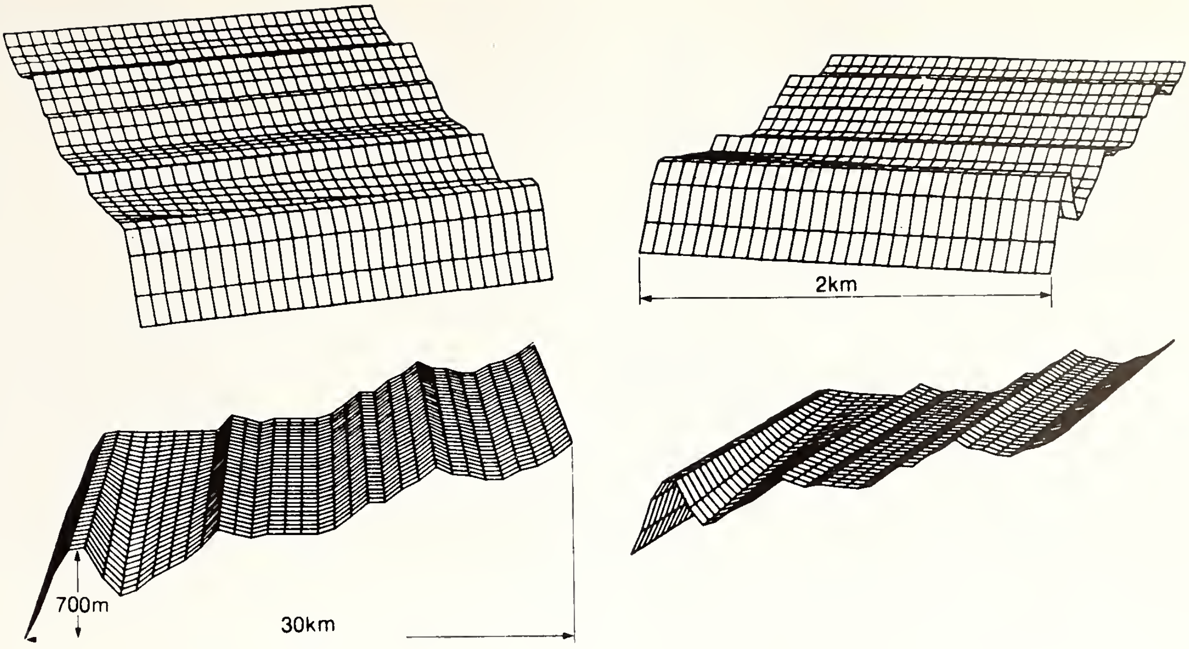

Figure 7. Inferred 3-dimensional structure of the density current from four viewpoints.

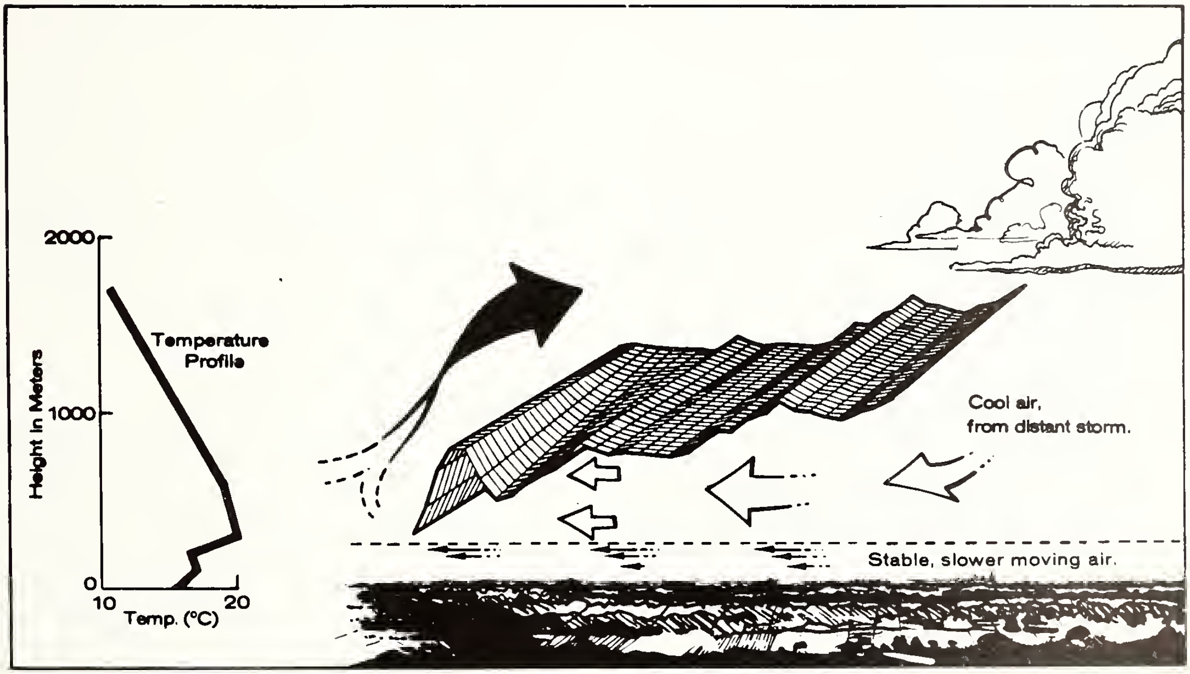

Figure 8. Summary figure illustrating a complex density current flowing from a source region on a stable layer. This figure combines an artist's conception with actual data from the 27 Sept. 1977 case study.

Conversely, this event demonstrates how the form of a density current aloft can be reproduced by surface pressure measurements.

Such situations have practical significance for the design of airport wind-shear detection systems using surface sensors. Although the intensity of the case study presented here is relatively weak, it represents a situation that is frequently present at night or when stable air from previous thunderstorms is present. Further work is needed to define the parameters controlling such density-current/stable-layer interactions for the atmosphere.

4. ACKNOWLEDGMENTS

The Systems Research and Development Office of the Federal Aviation Administration supported both the experimental field programs and the analysis efforts that led to the development of much of this data set.

5. REFERENCES

Bedard, A. J. Jr., W. H. Hooke and D. W. Beran (1977). The Dulles airport pressure jump detector array for gust front detection. *Bull. Amer. Meteor. Soc.*, 58, No. 9, p. 920-926.

Greene, G. E., H. W. Frank, A. J. Bedard Jr., J. A. Korrell, M. M. Cairns and P. A. Mandics (1977). Wind shear characterization. Final Report to the Federal Aviation Administration, prepared by the Wave Propagation Laboratory, NOAA.

Hardesty, R. M., P. A. Mandics, D. W. Beran and R. G. Strauch (1977). The Dulles airport acoustic/microwave radar wind and wind-shear measuring system. *Bull. Amer. Meteorol. Soc.*, 58, No. 9, 910-918.

Idso, S. B., R. S. Ingram and J. M. Pritchard (1972). An American haboob. *Bull. Amer. Meteorol. Soc.*, 53, 930-935.

Parry, H. D. and M. J. Sanders, Jr. (1972). The design and operation of an acoustic radar. IEEE Transactions on Geoscience Electronics GE-10, No. 1, 54-64.

Teske, M. E. and W. S. Lewellen (1977). Turbulent transport model of a thunderstorm gust front. Proc. 10th Conference on Severe Local Storms, Oct. 18-21, Omaha, Nebr., Amer. Meteor. Soc., Boston, Mass, p. 143-150.

Preprint Volume; Conference on Cloud Physics and Atmospheric
Electricity, 528-533, Seattle, Washington, 1978.

GROWTH AND RECIRCULATION OF PRECIPITATION IN AN EVOLVING CONVECTIVE STORM

James E. Dye
National Center for Atmospheric Research*
Boulder, Colorado 80307

L. Jay Miller
NOAA/ERL/Wave Propagation Laboratory
Boulder, Colorado 80302

Brooks E. Martner
University of Wyoming
Laramie, Wyoming 82071

Zev Levin
Tel Aviv University
Ramat Aviv. Israel

1. INTRODUCTION

Knowledge of precipitation particle growth trajectories is fundamental to the prediction and modification of precipitation from convective storms. If the trajectories are complex and variable it is much more difficult to know where seeding should take place in order to attempt to enhance precipitation or suppress hail. The initial precipitation formation case studies being conducted by the Convective Storms Division of NCAR are directed towards determining the origin and growth trajectories of precipitation particles in convective storms in NE Colorado. The approach has been to observe actively growing cumulus clouds simultaneously with penetrating aircraft capable of measuring the microphysical properties of the cloud and with multiple-Doppler radar capable of yielding the three-dimensional air motion inside the cloud.

2. OBSERVATIONAL COMPONENTS AND THE STORM HISTORY

One of the coordinated aircraft/multiple-Doppler radar case studies which is being investigated by the Convective Storms Division of NCAR is the initial precipitation formation case study of 25 July 1976. Two aircraft instrumented for detailed microphysical measurements (the NCAR/NOAA sailplane and the University of Wyoming Queen Air, N10UW); two aircraft instrumented to measure temperature, humidity, vertical air motion and cloud nuclei populations at cloud base (the NCAR Queen Airs, N304D and N306D); three Doppler radars (an NCAR/FOF 5 cm, and two NOAA/WPL 3 cm radars) and the NCAR/FOF 10 cm radar were used simultaneously to investigate the development of precipitation and three-dimensional air motions inside a growing convective storm of moderate intensity in northeast Colorado. The observations span a period of about one hour (1900 to 2000 MDT)[1] starting before the appearance of the first radar echo, through the growing and mature stages of the system, into the dissipating stages of the storm.

Southwestward motion of the complex was associated with nearly continuous propagation in a weakly sheared ($2\times10^{-3}s^{-1}$) environment (Marwitz, 1972). The location and motion of the storm relative to the radars is shown in Fig. 1 for the period 1900 to 1936 MDT. The contours on the left-hand side of the illustration show successive positions of the radar echo at 5 km MSL. The successive positions of the maximum reflectivities at 5 min intervals are indicated by sequential numbers.

During the aircraft investigations of the evolving storm, the sailplane used the updraft to make two ascents in cloud, one from 1900 to 1910 (5 to 7 km, -2 to -15°C), and a second from 1920 to 1932 (5 to 8 km, -2 to -20°C). From 1911 to 1931 N10UW made five horizontal penetrations from southeast to northwest and back directly below the sailplane at about the 5.5 km (-4°C) altitude level, and from 1940 to 1950 made two passes through the cloud base at 4 km (+6°C). The cloud base aircraft N304D and N306D made continuous passes from southwest to northeast and back through both the inflow and the weak outflow of the storm just below the cloud base at 3.7 km (6°C) from 1913 to 1935. The altitudes and times of the sailplane and N10UW cloud penetrations and

---

*This research was performed as part of the National Hail Research Experiment, managed by the National Center for Atmospheric Research and sponsored by the Weather Modification Program, Research Applications Directorate, National Science Foundation.

[1] All times are given in Mountain Daylight time (MDT) and all altitudes are given with reference to Mean Sea Level (MSL).

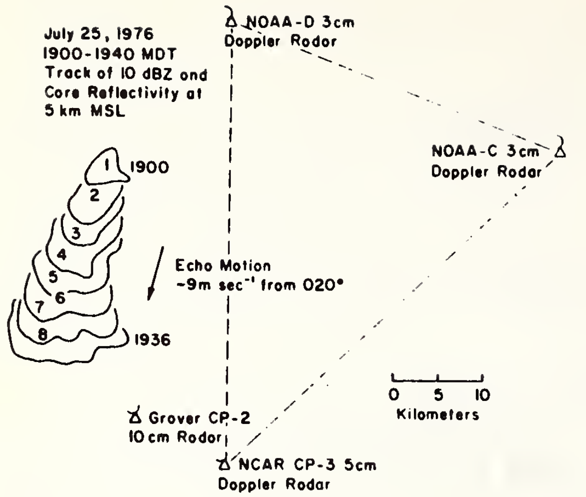

Fig. 1. Tracks of the 10 dBZ reflectivities and core reflectivities for the 25 July 1976 storm shown relative to the radars.

the subcloud aircraft traverses are shown in Fig. 2.

The 10 cm radar reflectivity history of the storm is also shown in Fig. 2 as a time-height profile. Note the successive rise and fall of reflectivity in the upper portion of the cloud. This is a result of the rise and fall of individual turrets as they grow and decay in the evolving storm. The rate of rise of the radar echo top between 1900 and 1920 was about 3 m/sec. Although the rate of rise is relatively constant during this period the overall growth is a result of successive turrets pushing up with speeds of 5-6 m/sec on the southwest side of the storm with each turret rising higher than its predecessor. The maximum reflectivity of the storm also increases with time eventually reaching reflectivities slightly over 60 dBZ. Although reflectivities did briefly exceed 60 dBZ near 1925 and again near 1940, the regions of reflectivity greater than 50 dBZ were small. The aircraft altitudes superimposed on the reflectivity contours do not imply necessarily that the aircraft were flying in the high reflectivities as shown. Though some small hail was encountered by the penetrating aircraft (N10UW), it was unlikely that any hail reached the ground.

3. THREE-DIMENSIONAL MOTION FIELDS

A detailed description of the triple-Doppler radar data analysis scheme was presented by Bohne and Srivastava (1976) and, as used here, was summarized in Miller (1978). Briefly, mean radial velocity estimates in each of the three radar sampling spaces were transformed to a common Cartesian analysis grid under the assumption that these grid point estimates were adequately represented by spatial-weighted averages of neighboring samples. No attempt was made to account for temporal evolution during the time (about 2-3 minutes) necessary to sample the entire storm volume.

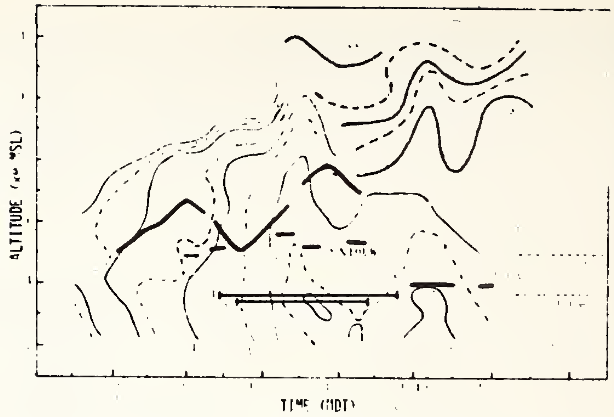

Fig. 2. Time-altitude profile of the reflectivity history of the 25 July 1976 storm as observed by the Grover 10 cm radar. Reflectivities from the NOAA D 3 cm radar were used in the shaded area due to close proximity of the storm to Grover. Times and altitudes of aircraft investigations are shown by heavy lines.

These radial velocities were linearly combined to yield three components of precipitation motion. Large errors in the vertical component precluded using it in deriving vertical air motion. Instead, the horizontal components were used in the integration of the anelastic form of the mass continuity equation to obtain vertical air motion. Because the lowest level divergence estimates applied to a layer centered 400 m above the ground, vertical air motion at this level was approximated by the product of these divergences and this height increment. This gave results at cloud base which were consistent with aircraft observations of vertical air motions of 1 to 3 m/sec. Generally, the Doppler derived horizontal air motion has errors of about 0.5 - 1 m s^{-1} and represents motion at scales larger than 2 km. Uncertainties in the vertical component from the integration are about 1 m/sec. However, the total error depends on unknown errors in the boundary conditions which cannot be accurately assessed.

The triple-Doppler radar measurements show the updraft to be consistently on the western side of the storm, and of the same magnitude as the updrafts observed by the four aircraft at the different levels. Horizontal flow at 5 km MSL relative to the moving storm for the period 1919-1922 MDT is shown superimposed on the radar reflectivity in Fig. 3. The region of updraft derived from the Doppler radars is shaded and regions with vertical velocities 5-10 m sec^{-1} cross hatched. Note the tendency for the updraft core to act as an obstacle to midlevel environmental flow (Newton and Newton, 1959; Fankhauser, 1971). Such flow appears to have caused dynamic entrainment of environmental air on the relative downwind side of the updraft as is discussed in Section 4. This air was evaporatively cooled and sank creating a moderate downdraft. The up- and downdrafts appear as a closed circulation pattern evident in the vertical west-to-east cross section through the core of the storm (at Y = 17.5 km in

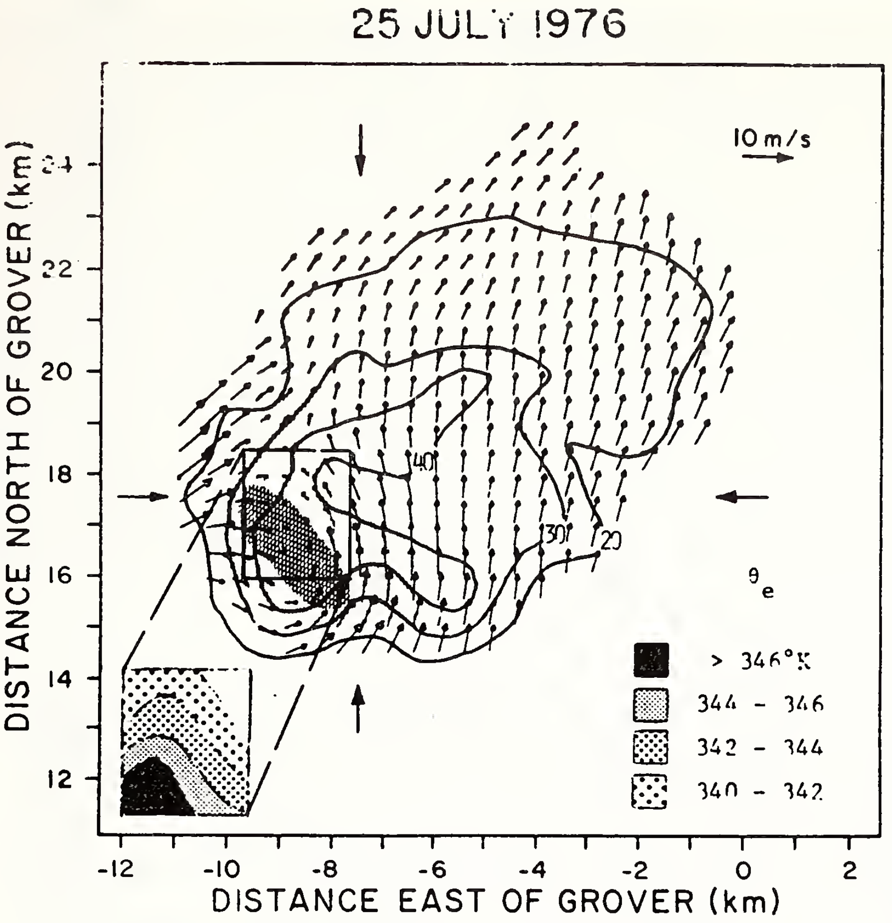

Fig. 3. Horizontal [illegible] motion at 5 km relative to the storm motion derived from the 1916-1922 Doppler radar scans [illegible] shows the updraft region with [illegible] 5-10 [illegible] heavily shaded. The box inset shows θ values [illegible] See text. Arrows [illegible] [illegible] 3 and 4.

[illegible] Y = 17 [illegible] for the [illegible] [illegible] 10, and > [illegible]

[illegible] Fig. [illegible] vertical [illegible] X = [illegible]

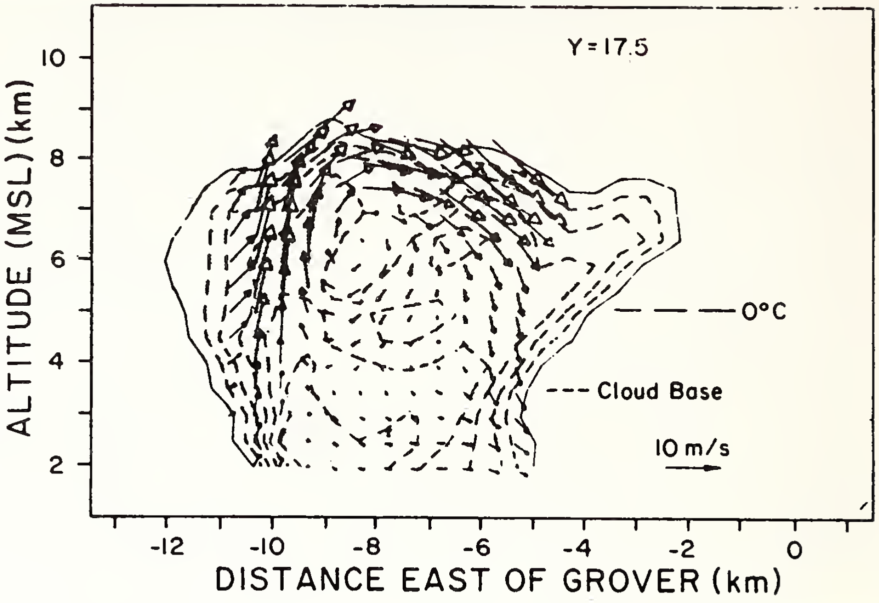

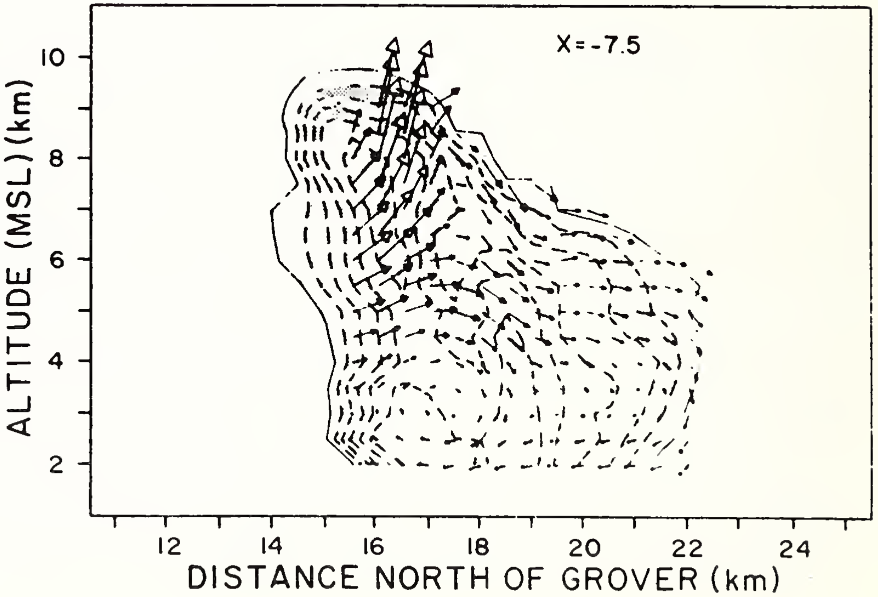

Fig. 3) and shown in Fig. 4. As will be discussed later, this is the same region in which the sailplane and N10UW found water drops and partially melted ice particles. A vertical north-to-south cross section through this same area (at X = -7.5 km in Fig. 3) is presented in Fig. 5. The most intense updraft is in the newer cell (region of > 45 dBZ) on the south side of the storm. Weak downward motion extends to the north in older, less active parts of the storm.

Shortly after this Doppler volume scan 10UW made its third penetration of the storm, skimming past the core of high reflectivity. Figure 6 shows the aircraft track superimposed on the storm echo pattern from the 10 cm radar for the time period 1922 to 1924. Plots of vertical velocity, equivalent potential temperature (θ_e), particle concentrations, and liquid water content are presented in Fig. 7.

Relative to the reflectivity pattern, the location of the updraft region detected by 10UW agrees well with the Doppler updraft location of Fig. 3, even though the aircraft data is from a slightly later time and higher altitude. The magnitude of the updrafts measured by the aircraft are generally larger than those determined by the radar. Since the Doppler observations represent scales only larger than 2 km, small scale variations seen in the aircraft updrafts such as the minima at 1923 near the reflectivity core are not evident in the Doppler data of 1919-1922. This narrow region of weak updraft (only 0.8 km long) was, no doubt, real since it is reflected in corresponding dips in θ_e and liquid water. Such small scale features, are below the resolved scales of the Doppler velocity patterns, but may well be important in terms of precipitation particle trajectories.

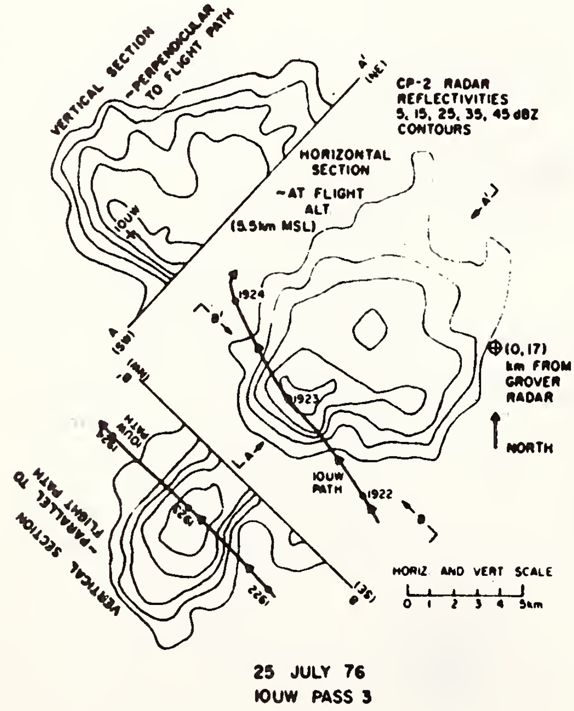
VERTICAL SECTION ~PERPENDICULAR TO FLIGHT PATH
CP-2 RADAR REFLECTIVITIES 5, 15, 25, 35, 45 dBZ CONTOURS
A' (NE)
HORIZONTAL SECTION ~AT FLIGHT ALT (5.5km MSL)
IOUW
1924
1923
1922
B'
A (SW)
B (NW)
IOUW PATH
(0, 17) km FROM GROVER RADAR
NORTH
VERTICAL SECTION ~PARALLEL TO FLIGHT PATH
HORIZ. AND VERT SCALE
0 1 2 3 4 5km
B (SE)
25 JULY 76
IOUW PASS 3

Fig. 6. Flight track of third penetration by Wyoming Queen Air N10UW. Radar reflectivities from the NCAR 10 cm radar at Grover are valid for 1922-1924.

4. THE THERMODYNAMIC STRUCTURE OF THE UPDRAFT--AN ADIABATIC CORE

Sailplane measurements of θ_e are plotted relative to the moving storm for the time period 1921 to 1927 (5.5 to 7.5 km) as an insert in Fig. 3. An unmixed adiabatic region was found near the core of the updraft with increased mixing (decreasing values of θ_e) found as the sailplane moved to the north and east relative to the core. This increased mixing is consistent with a turbulent wake produced by the obstructed flow of environmental air around the updraft as seen in Fig. 3. The θ_e values at 5.5 km from 10UW's pass 3 shown in Fig. 7 reached 345°K in the stronger updrafts, also indicating that this air originated near the surface and rose to the observed level with very little entrainment. Examination of the θ_e measured by a rawinsonde at the ground and by

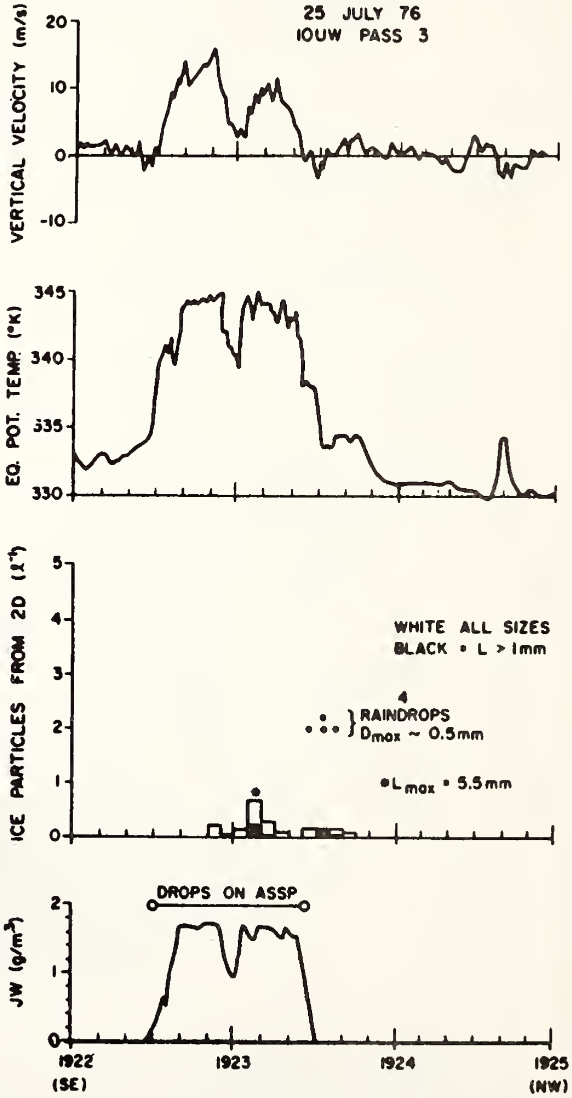

Fig. 7. Vertical velocity, θ_e, particle concentrations (from 2-D probe), and liquid water content versus time from N10UW.

the four research aircraft at different altitudes shows that air from the surface ascended unmixed through the cloud base up to at least 4 km above cloud base (Fig. 8). This cloud is one of several which contained adiabatic cores as reported by Heymsfield *et al.* (1978). The scatter in observed values of θ_e is attributable to the aircraft moving through different regions of the cloud.

THE MICROPHYSICAL STRUCTURE OF THE STORM

During the first ascent of the sailplane, early in the history of the cloud, precipitation particles were observed only near the top of the climb and were almost exclusively ice particles. A few representative photographs of particles from this ascent are shown in Fig. 9a) through d). A 1 mm scale is shown in the upper left-hand photograph. c) is a photograph of the only water drop (~0.5 mm diameter) observed during this ascent. [The dot pair uniquely identifies water drops and is a result of the water drop acting as a lens for each of the two light sources in the camera system (Cannon, 1974)]. The observed time, temperature (T in °C), altitude (Z in km MSL), updraft (W in m/sec), and cloud liquid water content (Q in g/m^3) corresponding to each photograph are as shown. During the second sailplane ascent, particles photographed at relatively low levels in the cloud included water drops, glistening ice particles suggestive of wet growth (g), particles which had dot pairs characteristic of water drops but were distorted and probably in the process of freezing (e), and recently frozen drops (f) and (h).

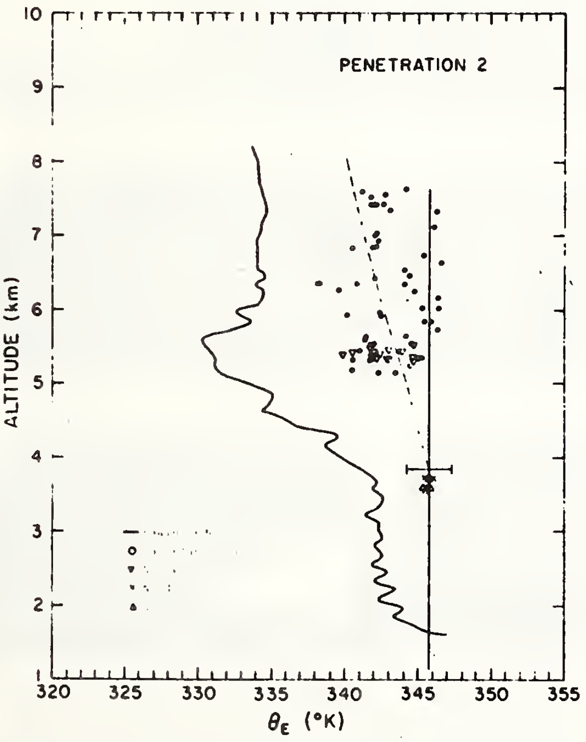

Fig. 8. *Values of equivalent potential temperature measured by the four aircraft and the rawinsonde released at Potter at 1730.*

In the upper regions of the second ascent high concentrations of aggregates with varying degrees of riming (k, l, and o) and graupel (i, m, and n) were observed.

Photograph j shows a 1 millimeter drop at -17°C with a spike protruding from the top. (The spike is difficult to see.) This must have resulted from the recent freezing of a large water drop. Since water drops this large could probably not be formed by coalescence of droplets in this cloud (Dye et al., 1974), it is hypothesized with some confidence that this particle must have been originally an ice particle such as that shown in photographs i, k or l which [illegible] or was carried below the freezing level, melted completely, and was entrained in the updraft and lifted some 3 km to the level where it was observed.

The sizes and concentrations of particles detected by 10UW (Fig. 7) were determined by examination of particle silhouettes from a Particle Measuring Systems 2-D probe (Knollenberg, 1976). Most of the silhouettes were irregular or graupel-like shapes except for the few raindrops which appeared as distinctly smooth circles. On pass 3 the largest sizes and greatest concentrations of ice particles occurred in updraft near the reflectivity core. A few small raindrops (D ~ 0.5 mm, concentration < 0.1 ℓ^{-1}) were detected on this pass farther to the northwest outside the main updraft region. Two subsequent passes at the same altitude detected even larger drops (D ≤ 3.5 mm) which, unlike pass 3, were located in updraft in the reflectivity core region.

Calculations of particle growth rates such as those of Braham (1968) show that neither ice particles nor water drops found in the observed updrafts could have grown to the large size detected by the sailplane or N10UW during the available time from cloud base to the observed altitude. The millimetric precipitation particles must have grown in a higher region of the cloud, been carried down in downdraft, and transferred back to the updraft. The presence of water drops in this cloud, particularly at these low levels, is strikingly different than the absence of water drops which is more typical of the NE Colorado clouds (Dye *et al.*, 1974).

The liquid water content measured by N10UW at 5.5 km (1.5 km above cloud base) was about 1.7 g/m^3 and quite uniform across the updraft. Liquid water contents measured by the sailplane above 6 km were in excess of 3 g/m^3, the saturation limit of the J-W sensor on the sailplane. With liquid water contents of this magnitude particles of >3 mm diameter or larger would have been in the wet growth regime at temperatures warmer than about -5°C (List *et al.*, 1965). The high reflectivities seen near 1925 and 1940 in Fig. 2 may well be a result of the radar detecting these "wet" particles.

6. CONCLUSIONS

The aircraft data clearly show that recirculation was occurring and the closed loop circulation seen in the Doppler radar data of Fig. 4 distinctly show the possibility of transferring particles from the downdraft back into the updraft.

Indeed, preliminary particle trajectory computations using the observed flow field for the 1919 to 1922 Doppler radar scan (assuming steady state motion which ignores the evolving nature of the storm) and simplified microphysics and particle growth calculations show that particles can be fed back into the updraft. In view of the shear which must have existed at the interface between the updrafts and downdrafts it seems likely that turbulent mixing (which the Doppler integration does not resolve) must have also been occurring and probably played a role in transporting particles laterally into the updraft. The trajectories of individual precipitation particles must have been both complex and highly variable from particle to particle. Operationally, it would have been difficult to know where to effectively seed this cloud in order to enhance precipitation (if it was possible at all).

Calculations based on the particle concentrations and sizes observed from N10UW and the sailplane show that at least in some cases the evidently recirculated particles were large enough and numerous enough to produce the observed radar reflectivities in the high reflectivity regions of the storm. This suggests that the recirculation observed in this storm was an important factor in the formation of precipitation in the region of the storm investigated by the aircraft. How important it was in other regions of the storm and in other storms remains to be established.

7. ACKNOWLEDGEMENTS

We wish to thank the many people to numerous to name who participated in the gathering, processing, and analysis of the large data set.

8. REFERENCES

Bohne, A. R. and R. C. Srivastava, 1976: Random errors in wind and precipitation fallspeed measurement by a triple Doppler radar system. *Preprints, 17th Radar Met. Conf.*, Amer. Met. Soc., 7-14.

Braham, R. R., Jr., 1968: Meteorological bases for precipitation development. *Bull. Amer. Meteor. Soc.*, *49*, 343-353.

Cannon, T. W., 1974: A camera for photography of atmospheric particles from aircraft. *Rev. Sci. Instr.*, *45*, 1448-1455.

Dye, J. E., C. A. Knight, V. Toutenhoofd and T. W. Cannon, 1974: The mechanism of precipitation formation in northeastern Colorado cumulus. III: Coordinated microphysical and radar observations and summary. *J. Atmos. Sci.*, *31*, 2152-2159.

Fankhauser, J. C., 1971: Thunderstorm-environment interactions determined from aircraft and radar observation. *Mon. Wea. Rev.*, *99*, 171-192.

Heymsfield, A. J., P. N. Johnson and J. E. Dye, 1978: Observations of moist adiabatic ascent in northeast Colorado cumulus congestus clouds. Submitted to *J. Atmos. Sci.*

Knollenberg, R. G., 1976: Three new instruments for cloud physics measurements. *Proc. Int. Cld. Physics Conf.*, Amer. Meteor. Soc., 554-561.

List, R., P. H. Schuepp and R. G. J. Methot, 1965: Heat exchange ratios of hailstones in a model cloud and their simulation in a laboratory. *J. Atmos. Sci.*, *22*, 710-718.

Marwitz, J. D., 1972: Precipitation efficiency of thunderstorms on the High Plains. *J. Rech. Atmos.*, *6*, 367-370.

Miller, L. J., 1978: Horizontal airflow and precipitation fallspeed in a convective storm from triple Doppler radar measurements. *Preprints, 18th Radar Meteor. Conf.*, Amer. Meteor. Soc., 207-211.

Newton, C. W. and H. R. Newton, 1959: Dynamical interactions between large convective clouds and environment with vertical shear. *J. Meteor.*, *16*, 483-496.

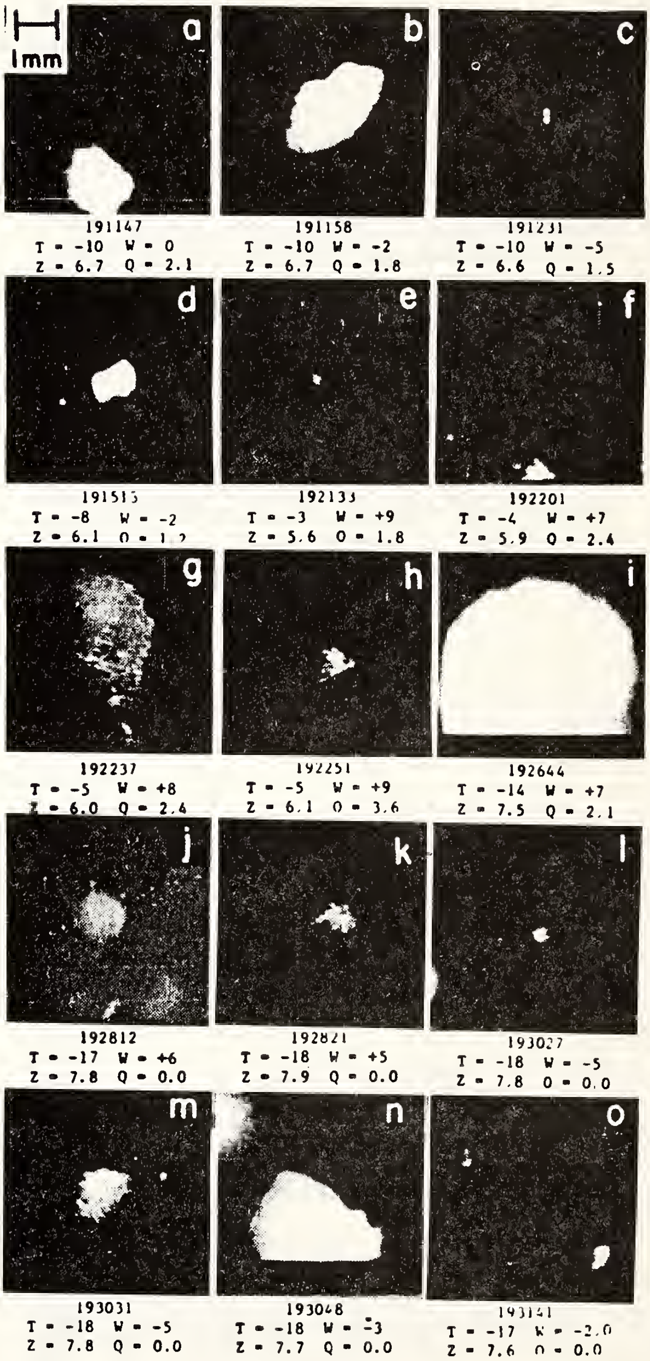

Fig. 9. Precipitation particles photographed during the sailplane flight.

Preprint Volume; 18th Conference on Radar Meteorology, 207-211,
American Meteorological Society, 1978.

HORIZONTAL AIRFLOW AND PRECIPITATION FALLSPEED IN A CONVECTIVE STORM FROM TRIPLE DOPPLER RADAR MEASUREMENTS

L. Jay Miller

NOAA/ERL/Wave Propagation Laboratory
Boulder, Colorado 80302

1. INTRODUCTION

The concept of using multiple Doppler radars to remotely measure atmospheric motions inside convective storms was first introduced by Lhermitte (1968). As shown by Armijo (1969) three radar measurements of non-colinear radial velocities lead to the realization of horizontal wind components and total vertical precipitation motion. The later component which is the sum of vertical air motion and precipitation fall velocity in still air may be separated into its constituents by: 1) applying the mass continuity equation and subtracting this vertical air motion to obtain fall velocity or 2) estimating fall velocity independently and subtracting it from the total to obtain vertical air motion. Bohne and Srivastava (1976) have recently detailed these methods and discussed the random errors involved. Applying such triple Doppler radar techniques, Lhermitte et al. (1977) were successful in obtaining three dimensional precipitation and air motion in a Florida convective storm. They used an empirical fallspeed-reflectivity relation for rain only and estimated air motion by subtracting this fallspeed from the net precipitation vertical motion. Necessarily, this restricted their analysis to heights below the melting level.

This paper discusses preliminary results from a similar analysis of triple radar data obtained during the 1976 summer field program of the National Hail Research Experiment* (NHRE). However, as northeast Colorado precipitation aloft is often composed of graupel and other ice particles (e.g., Knight et al., 1974), we chose to estimate vertical air motion from the continuity equation and then derive a single fallspeed-reflectivity relation which would be applicable at all levels in these storms. These data were taken in a moderate intensity convective storm which developed about 25 km west of the centroid of the three radar triangle and moved south-southwestward.

2. DATA ACQUISITION AND REDUCTION

Four Doppler radars, two NOAA/WPL 3-cm wavelength and two NCAR/FOF 5-cm wavelength were located in the area of northeast Colorado, southeast Wyoming, and southwest panhandle of Nebraska. Data from three of these radars whose relative locations are shown in Fig. 1 were used here. The Field Observing Facility (FOF) radar was equipped with hardware processing of reflectivity and radial velocity information. Both WPL radars digitally recorded the time series return signal for later off-line software processing. All mean radial velocities were determined with the covariance or pulse-pair algorithm (e.g., Rummler, 1968; Miller and Rochwarger, 1972; Berger and Groginsky, 1973). Following Berger and Groginsky (1973), random errors in the radial velocity estimates range from 0.2 to 1.0 m s^{-1} for the signal-to-noise power ratios, numbers of samples, and estimated spectral widths involved. Limited spectral width information generally precludes any attempt to specify point-by-point errors in the radial velocities.

Radial velocity and reflectivity fields in the radar sampling spaces were transformed to a common Cartesian analysis grid under the assumption that each grid point estimate was well represented by a weighted average of its neighboring samples. All samples within a 1 km influence radius were exponentially weighted with a function of the form

$$g(r) = \begin{cases} \exp(-4r^2/R_o^2), & r \le R_o \\ 0, & r > R_o \end{cases} \qquad (1)$$

where r was the distance between sample and analysis grid point. All weights were normalized such that their sum was unity. With an influence radius, R_o, of 1 km scales larger than about 2 km (∿ 3 dB point) were passed by the weighting-filtering operation. Furthermore, this process reduced the errors in grid point estimates of radial velocity to 0.25-0.35 times their original values. From the results of Bohne and Srivastava (1976), the errors in derived horizontal components are 0.1-0.5 m s^{-1} nearly independent of height. Errors in the vertical components are, however, rather sensitive to height obviously becoming infinite in the plane of the radars. For heights above 4 km MSL (2.4 km above radars) the errors in the vertical component are less than 2-3 m s^{-1}.

As indicated by Bohne and Srivastava (1976), there are several ways one can proceed to derive vertical air motion and precipitation fall velocity. When the appropriate boundary conditions can be specified, the mass continuity equation can be integrated upwards from the surface or downwards from the storm top. This vertical air motion estimate can then be subtracted from the total precipitation motion obtained from solving the simultaneous linear equations

$$u\left(\frac{x-x_i}{R_i}\right) + v\left(\frac{y-y_i}{R_i}\right) + W\left(\frac{z-z_i}{R_i}\right) = V_i;\ i = 1,2,3 \qquad (2)$$

---

* The NHRE is sponsored by the National Science Foundation and managed by the National Center for Atmospheric Research.

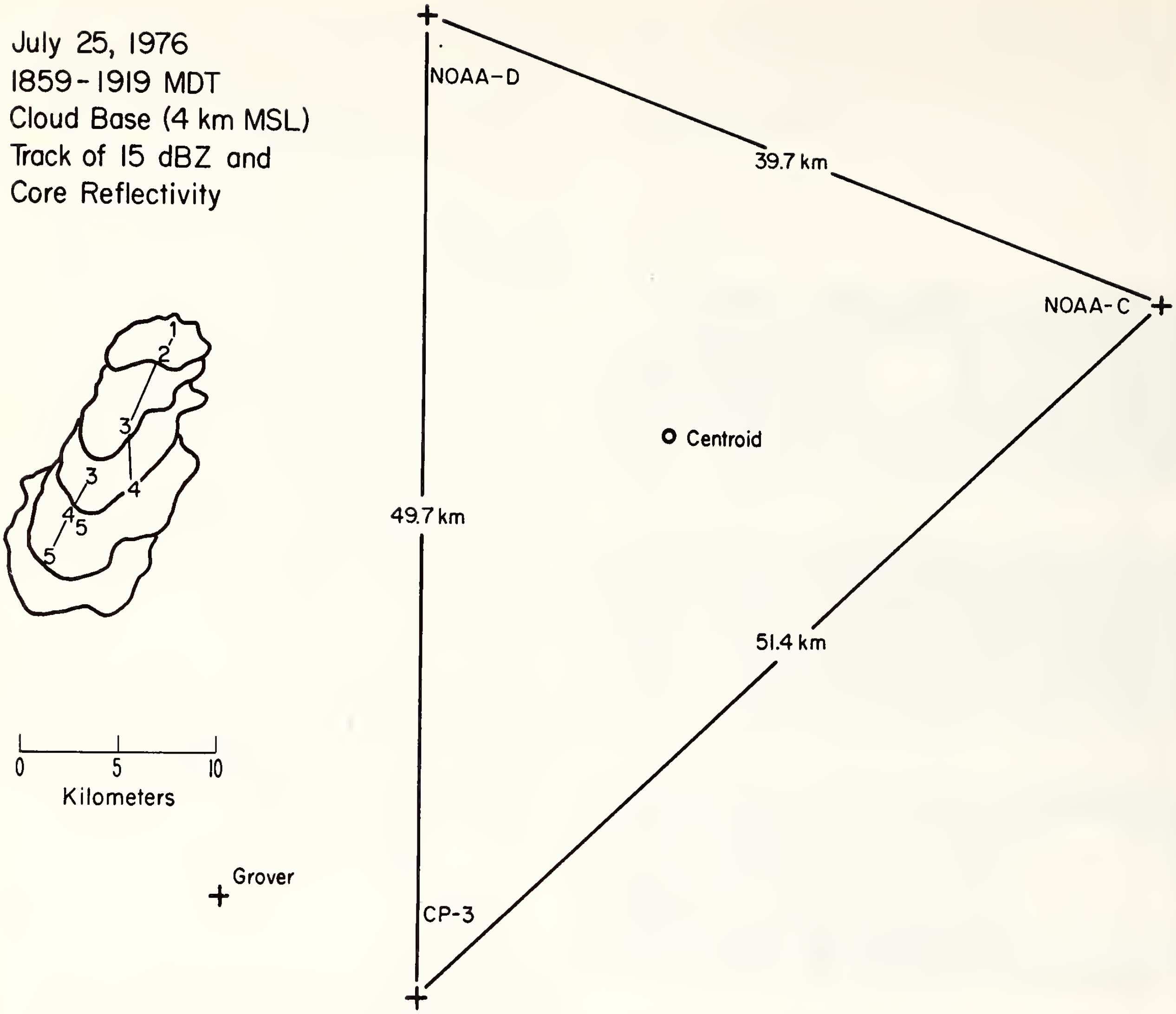

Figure 1. Cloud base track of core and 15 dBZ reflectivity showing relative locations of three Doppler radars and storm

for the components u, v, W (= w + V_T) of motion where V_i is the radial velocity measured by the radar at (x_i, y_i, z_i), and R_i is the slant range between field point (x, y, z) and the radar. Alternatively, one can calculate fall velocity, V_T, from a fall velocity-reflectivity relation and subtract it from W to obtain w, the vertical air motion. Because the component w or V_T which is calculated directly from W will tend to reflect the larger uncertainties in W, this author chose to determine vertical air motion by integrating the continuity equation upwards from the surface. This air motion was then subtracted to obtain fall velocities which could then be compared with the independently measured reflectivity. This scheme was further justified by better agreement between this method and aircraft measurements* of vertical air motion than between any other method (not presented here) and these measurements.

3. ENVIRONMENTAL AND STORM MEAN HORIZONTAL WINDS

Rawinsondes were released from Grover, Colorado and Potter, Nebraska at 1730 MDT. Grover was located about 20 km SSE and ahead of the storm, whereas, Potter was about 70 km ENE of the storm and on the outflow side. These releases were 1 3/4 hour before the radar data. Hodographs are shown in Fig. 2 for both of these wind soundings along with the winds averaged over each level in the storm. As can be seen, there is fair agreement between in-storm and Grover winds below 5 km and agreement between in-storm and Potter winds above this level. Such close agreement between storm and environmental winds requires that air transported vertically must have been acquiring environmental momentum rather quickly. Since the radar data is necessarily biased to only the regions of the storm having echo, this may not have been true of echo-free regions.

---

* Private communication with J. Dye of NCAR.

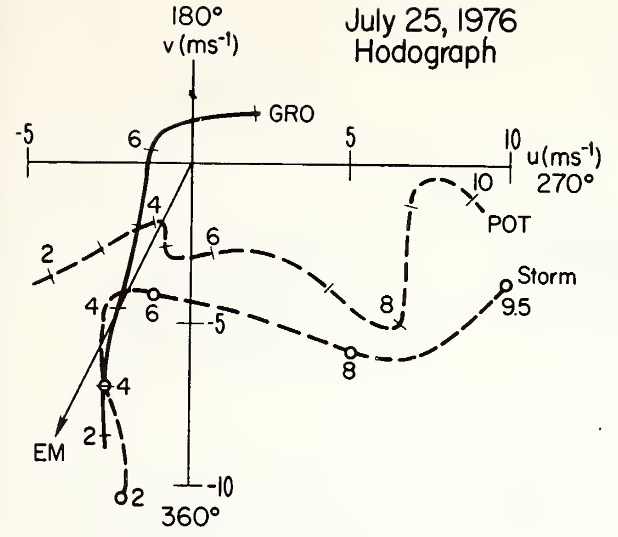

Figure 2. Hodographs of environmental, Grover (GRO) and Potter (POT), and in-storm horizontal winds. Heights are in kilometers above mean sea level. The vector (EM) denotes echo motion from 025°at 9.5 m s^{-1}.

Echo motion determined from reflectivity was from 025° at 9.5 m s^{-1}. This movement was slightly to the right of and at the same speed as the surface winds implying that there were only weak relative motion within the inflow or updraft air in the lowest layers. This will become more evident in the detailed internal flow derived from the analysis of radar data.

4. STORM INTERNAL STRUCTURE

Shown in Fig. 3 are contours of 5 cm reflectivity and vertical air motion on several horizontal planes. Also shown is the relative horizontal vector air motion with isotachs. There was a southeastward tilt to both the reflectivity and updraft structures. Much of this tilt evidently was caused by the vertical shear of the horizontal winds.

At the upper levels there was a general west to east relative flow which carried precipitation downstream. This precipitation must have fallen into potentially cold air intruding on the left front flank near 6 km. From the lack of echo in that area below this level and a downdraft which weakened with decreasing height, it is concluded that saturated descent in the downdraft did not occur. The strong downdraft aloft may have been a result of overshooting of updraft air. However, integration upward to obtain vertical air motion often shows a tendency for the vertical velocity to grow in magnitude, usually due to propagation of errors in divergence, so that this downdraft may or may not have actually existed. The derived updraft did, however, begin to diminish above 8 km lending some credence to this notion.

5. FALLSPEED-REFLECTIVITY RELATION

Vertical air motion determined from integrating the continuity equation was subtracted from the net precipitation motion to obtain the fall velocity. Those velocities aloft at density, ρ, were adjusted to ground level density, ρ_o, by multiplication by the inverse of the correction $(\rho_o/\rho)^{0.4}$ suggested by Foote and duToit (1969). By so doing a single fallspeed-reflectivity relationship, applicable at ground level (1.6 km MSL), could be obtained for comparison with other relations in the literature. The average power law relation thus found was

$$V_T = 0.8\ Z^{.25} \qquad (3)$$

where V_T is in m s^{-1} for reflectivity, Z, in units of mm^6 m^{-3}. Comparing this relation with those listed in Table 1 it is found that a much greater dependence on Z is evident.

Table 1. Some fallspeed-reflectivity relationships of the form $V_T = aZ^b$

Precipitation Type	a	b	Source
Snow	0.817	0.063	Atlas et al. (1973)
Rain	2.6	0.107	Joss and Waldvogel (1970)
Hail (wet)	4.05	0.111	Dyer (1975)

To obtain reliable estimates of a and b in (3) both spatial and temporal averaging was necessary. This implies that averaging over several precipitation types* was most likely happening. Scattergrams of fall velocity versus reflectivity were accumulated at several fixed heights over shorter periods of time to determine if indeed one could obtain reliable estimates of a and b for the various precipitation types. Two such scattergrams, one above and one below the melting level, are shown in Fig. 4. Relationships from Table 1 and Eq. (3) are also shown. The large scatter in V_T for a given Z makes it difficult, if not impossible, to specify reliably any detailed V_T-Z relationship. This scatter is primarily a result of random errors in net precipitation motion.

6. SUMMARY

It has been demonstrated that analysis of triple Doppler radar data leads to reliable estimates of the horizontal motions inside convective storms. Large errors in net vertical

---

* Private communication with J. Dye, NCAR, confirmed that in-situ precipitation samples from a penetrating sailplane consisted of aggregate snow, rain, graupel, and small hail.

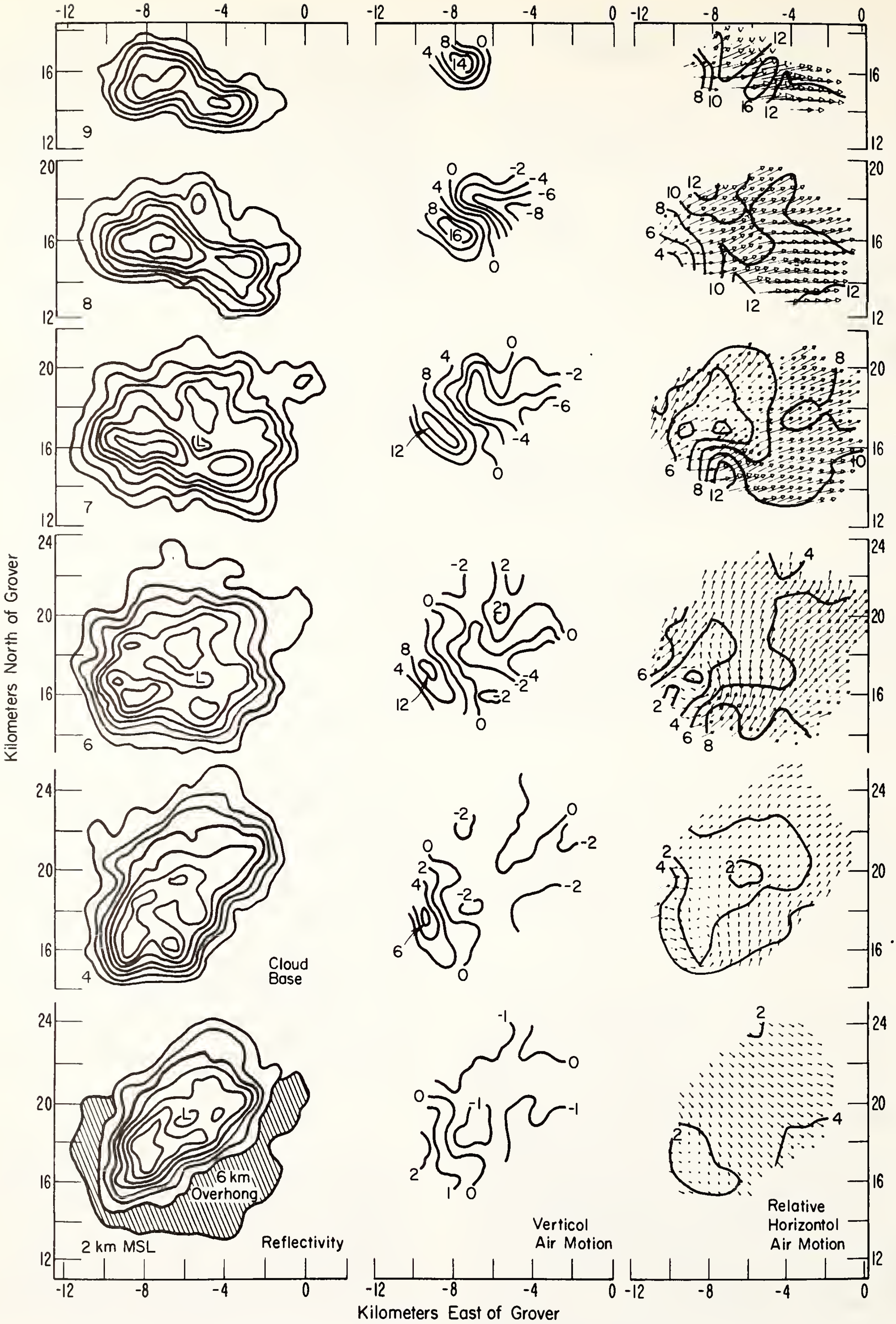

Figure 3. Contours of 5-cm reflectivity starting at 10 dBZ (5 dB increment) and vertical air motion with isotachs in m s^{-1} at six heights (km MSL). Cloud base was at 4 km. Relative motion was determined by subtracting the echo motion (EM, see Fig. 2) from the Doppler derived horizontal winds. These data are for 1919 MDT.

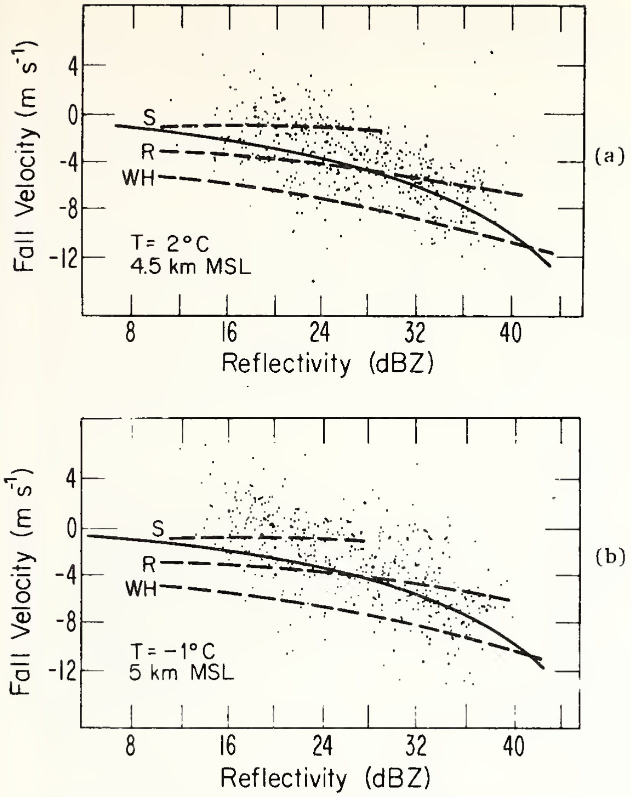

Figure 4. Scattergrams of fall velocity versus reflectivity at two levels for the time period 1859-1922 MDT. Plots were obtained for (a) 4.5 km MSL, T = 2°C and (b) 5 km MSL, T = 1°C. Dashed curves of V_T-Z relations for snow (S), rain (R), and wet hail (WH) are shown (see Table 1). The solid curve is the average V_T relationship for this case.

precipitation motion in this case restricted the derivation of vertical air motion to that obtained by integrating upwards from the surface. This air motion was subtracted from the precipitation motion resulting in fall velocity estimates throughout the storm. Fall velocity was found to be reasonably correlated with reflectivity, but with a greater dependence on reflectivity than is found in the results of others. This was attributed to the necessary averaging process which was over various precipitation types.

7. ACKNOWLEDGMENTS

The author wishes to acknowledge the continued support of the National Center for Atmospheric Research, both with National Science Foundation funds and computing facilities. Technicians and engineers from NCAR's Field Observing Facility did an admirable job in acquiring CP-3 Doppler data. Others from NCAR who were instrumental in data reduction and development of some of the analysis software were I. Harris and C. Mohr. Within NOAA/ERL Wave Propagation Laboratory, N. Kohn and A. Johnston developed a significant portion of the analysis software.

8. REFERENCES

Armijo, L., 1969: A theory for the determination of wind and precipitation velocities with Doppler radars. *J. Atmos. Sci.*, 26, 570-573.

Atlas, D., R. C. Srivastava, and R. S. Sekhon, 1973: Doppler radar characteristics of precipitation at vertical incidence. *Rev. of Geophysics and Space Physics*, 11, 1-35.

Berger, T. and H. L. Groginsky, 1973: Estimates of spectral moments of pulse trains. IEEE International Symposium on Information Theory.

Bohne, A. R. and R. C. Srivastava, 1976: Random errors in wind and precipitation fall-speed measurement by a triple Doppler radar system. AMS 17th Radar Meteor. Conf., 7-14.

Dyer, R. M., 1975: A relation between reflectivity and mean fallspeed in hail. AMS 16th Radar Meteor. Conf., 61-62.

Foote, G. B. and P. S. duToit, 1969: Terminal velocity of raindrops aloft. *J. Appl. Meteor.*, 8, 249-253.

Joss, J. and A. Waldvogel, 1970: Raindrop size distributions and Doppler velocities. AMS 14th Radar Meteor. Conf., 153-156.

Knight, C. A., N. C. Knight, J. E. Dye, and V. Toutenhoofd, 1974: The mechanism of precipitation formation in northeastern Colorado cumulus. I. Observations of the precipitation itself. *J. Atmos. Sci.*, 31, 2142-2147.

Lhermitte, R. M., 1968: New developments in Doppler radar methods. AMS 13th Radar Meteor. Conf., 14-17.

Lhermitte, R. M., K. Sashegyi, and J. Cunning, 1977: Tri-Doppler radar observations of Florida convective storms. AMS 10th Conf. on Severe Local Storms, 90-96.

Miller, K. S. and M. M. Rochwarger, 1972: A covariance approach to spectral moment estimation. *IEEE Trans. on Inf. Theory, IT-18*, 588-596.

Rummler, W. D., 1968: Two-pulse spectral measurements. Tech. Memo. MM-68-4121-15, Bell Telephone Laboratories, Whippany, N.J.

Preprint Volume; Conference on Sierra Nevada Meteorology, 133-134, American Meteorological Society, 1978.

REPORT ON PRELIMINARY DATA FROM A MULTI-DOPPLER RADAR STUDY OF WEATHER SYSTEMS IN AND NEAR THE SIERRA-NEVADA

W. R. Moninger
NOAA/ERL
Wave Propagation Laboratory
Boulder, Colorado 80302

Richard Carbone
National Center for Atmospheric Research*
Boulder, Colorado 80302

During January, February, and March, 1978, a number of cyclonic storm precipitation systems were observed by a triple Doppler radar network located near Sacramento, California. The radar triangle straddled the foothills of the Sierra Nevada mountains and was thus able to observe the effect of the mountain barrier on the storm systems.

The Doppler radars observed portions of widespread pre-frontal precipitation, convective bands associated with frontal passage, and post-frontal convection. We will present preliminary data from the tri-Doppler analysis of these storms.

We have not yet been able to start analysis of the tri-Doppler data, so we present here a general description of the various storm phases deduced from real-time single Doppler displays of velocity and reflectivity factor.

Widespread pre-frontal precipitation was characterized by its horizontal uniformity in reflectivity factor and a well-defined bright band at the melting (0°C) level. Bright band intensity ranged from 30-50 dBZ (typically 40-45 dBZ) at heights ranging from 1.2 to 1.9 km msl. Rain below the bright band ranged from 20 to 35 dBZ which implies rainfall rates from 0.7 to 6.0 mm/hr. Typically, the widespread rain was 25-30 dBZ or about 2 mm/hr. In all cases the bright band was approximately 15 dBZ stronger than the rain below. This suggests the presence of very large aggregate snow in the bright band with drop breakup during the melting process. Echo tops ranged from 6.5 to 8 km msl with little variation within each storm. The small modulations in the reflectivity fields suggest shallow imbedded convection in most cases.

The horizontal wind structure in widespread pre-frontal precipitation was remarkably similar throughout the period of observations. Winds were SSE from the surface to approximately 2 km msl, typically from 155°. The speed increased from 5-15 m sec^{-1} at the surface to 23-36 m sec^{-1} at 0.65 km msl. Speeds decreased above 0.65 km to 15-20 m sec^{-1}. The SSE low-level jet parallel to the Sierra barrier appears to be a feature which is nearly always present along the eastern edge of the Central Valley.

For most of the storms observed there was no orographic component to the winds below about 2 km msl. Above 2 km msl there existed a directional shear which resulted in southerly winds between 2 and 3 km msl and southwesterly winds above the 3 to 4 km msl level. Typical 4 km winds ranged from 190° to 240° with speeds up to 30 m sec^{-1}. A secondary level mid-tropospheric jet usually existed between 4 and 5 km msl with speeds greater than 30 m sec^{-1}. Cyclonic curvature to these mid-tropospheric winds was apparent. The single radar display suggested a cyclonic curvature of about 30° in the flow field approaching the mountains over a horizontal distance of 80 to 100 km. This indicates a convergent zone in the mid-troposphere.

Bands of convection associated with frontal passages were very similar to summer squall lines in the midwest. The bands were oriented roughly north-south with general movement to the east. Individual cells moved from the SW to NE with the horizontal momentum of mid-tropospheric air. Echo tops were generally no higher than those associated with pre-frontal widespread precipitation, usually around 7.0-7.5 km msl. Sometimes the bands were contiguous with widespread rain; at other times they consisted of a line of otherwise isolated cells. Maximum reflectivity factors ranged from 45 to 60 dBZ and were not necessarily associated with the melting (0°C) level. Electrical activity was often observed in these bands.

Wind fields in the convective bands were difficult to interpret in real-time. However, a few qualitative comments may be made. In the storm of February 5, 1978, strong low-level convergence was evidenced by a sharp discontinuity in the wind field. While some directional shear was present across the band, convergence appears to be the primary reason for the discontinuity. Vertical motions are currently estimated to range from 5 to 15 m sec^{-1}. In the case of February 7, 1978, meso-cyclonic circulations were observed in the Doppler triangle. One such circulation has been identified as the remnants of a small tornado which occurred in suburban Sacramento seven minutes prior to the Doppler coverage. Another meso-circulation pattern existed simultaneously and appeared to be anti-cyclonic and located immediately to the north of the tornado meso-cyclone. At the time of observation the velocity differences across the meso-cyclones were only 20-30 m sec^{-1} at about a 5 km diameter. The circulations were present on the western periphery of the squall line and appeared to be in a more general zone of strong directional wind shear associated with the front.

---

* The National Center for Atmospheric Research is funded by the National Science Foundation.

Post-frontal bands were similar to the frontal bands; however, widespread precipitation was usually not associated with them. The intensity of post-frontal precipitation was highly variable — comparable to frontal bands in the strongest cases and to shallow weak instability showers in cases where cold air advection was strong. In the latter situation banded structure was either weak or nonexistent.

It should be emphasized that these are first impressions, based on real-time observations of reflectivity factor and radial wind velocities from a single site. Multi-Doppler processing and analysis will yield full two-dimensional horizontal wind fields and some vertical wind fields, in the foothills and in the Sacramento Valley. These data will allow the accuracy of these first impressions to be assessed.

Preprint Volume; 18th Conference on Radar Meteorology, 432-436,
American Meteorological Society, 1978.

RADAR MEASUREMENT OF WIND SHEAR AND WIND PROFILES FOR AIR SAFETY

R. G. Strauch and W. R. Moninger

NOAA/ERL/Wave Propagation Laboratory
Boulder, Colorado 80302

1. INTRODUCTION

In recent years wind shear has been recognized as the probable cause of a number of costly aircraft accidents that have occurred during landing or takeoff. Changes in air speed caused by shear induced changes in headwind are dangerous for large aircraft at low altitudes because of the relatively long time between pilot input and aircraft response. Headwind shear can be caused by vertical gradients (speed or direction) of the horizontal wind or horizontal gradients of the horizontal wind. In addition, vertical air motions, particularly those associated with thunderstorms, can cause unexpected rate-of-climb or descent changes that are believed to have contributed to accidents (Fujita and Caracena, 1977). The Federal Aviation Administration has supported research and development of remote sensing techniques to find a ground-based device that can give warnings of dangerous wind shears and also give information that will enable the pilot to compensate for wind changes that will be encountered by the aircraft at low altitudes. Early efforts were directed toward development of an acoustic sounder system that could measure wind profiles in the lowest few hundred meters of the atmosphere. These efforts have resulted in the installation of a wind shear test facility at Dulles Airport in 1976 (Hardesty et al., 1977). Other ground-based remote sensing instruments that have been considered for airport use include CO_2 lidar and microwave radar. In-situ networks of wind, pressure, and temperature sensors are also being tested.

An ideal ground-based wind measurement system would be capable of measuring the wind profile along the approach and departure paths and should be capable of advance warning of abrupt changes that may propagate into these paths. It must be able to operate in all weather regimes. The Dulles Airport test facility uses a combination of in-situ and remote sensors including a microwave Doppler radar to provide a wind shear warning system. Recent experiments have shown that microwave Doppler radars, both FM-CW (Chadwick et al., 1976) and pulsed (Hennington et al., 1976) can measure winds in the lower atmosphere in optically clear air. Radar therefore has the potential of providing wind shear warning for all weather. This paper discusses the utility and limitations of the radar system at Dulles Airport and the application of microwave radar to the wind shear problem.

2. THE MICROWAVE RADAR AT DULLES AIRPORT

The wind shear test facility at Dulles Airport uses a low power 3-cm pulse Doppler radar to measure wind profiles during precipitation. An acoustic sounder obtains wind profiles in the optically clear air, but in moderate or heavy precipitation it is not able to operate because of the increased noise of raindrops at the transducer. The microwave radar is computer controlled and is programmed to obtain wind profiles that complement or replace the acoustic data during precipitation. Vertical profiles of the horizontal wind are obtained at the test site which is displaced from the runways by several km. The radar measures wind speed and direction from radial velocity measurements along 4 orthogonal azimuths. If the signal-to-noise ratio of the received signal is below 10 dB for any range location and azimuth, that radial velocity is not used. The antenna elevation angle, θ_e, is fixed at 11.5 deg so a 1-μs sampling interval (range gate spacing) provides wind estimates at 30-m height intervals. Vertical resolution is limited by the 2.2 deg beamwidth for ranges exceeding 800 m. The maximum height of interest is 600 m so the maximum range of interest is 3 km. Minimum radar range is about 450-m.

The radar operates at a wavelength of 3.22 cm with 5 kW peak power. Pulse duration is 0.5 μs. A pair of pulses, separated by 256 μs, is transmitted every 1024 μs (Campbell and Strauch, 1976). Radial velocity estimates are obtained from the phase angle of the autocovariance for 640 pairs of pulses. The antenna is stationary during the dwell time. A vertical profile of the horizontal wind is obtained every minute. The standard error of estimate of mean radial velocity will be less than 0.1 m/s for nearly all meteorological conditions.

The maximum unambiguous velocity is ± 31.4 m/s. Range aliasing cannot occur since the height of a second trip echo would have to be about 30 km in order to be observed. However, the video return from the second pulse of a pair can be contaminated with second trip echo from the first pulse. This occurs when echoes with tops of 7.5 km or greater are at a range of about 40 km from the radar. This contamination can degrade the velocity estimate, but unless the reflectivity of the distant echo exceeds the near-range (< 3 km) reflectivity by 20 dB the degradation would be negligible. The radar has operated for 15 months with no down time and no evidence of velocity aliasing. It operates unattended and is normally activated by a signal from a rain gauge. Figure 1 compares measurements by the acoustic sounder and the radar in light precipitation.

Two major assumptions are made in computing the horizontal velocity profile: a) The vertical motion of the precipitation particles at

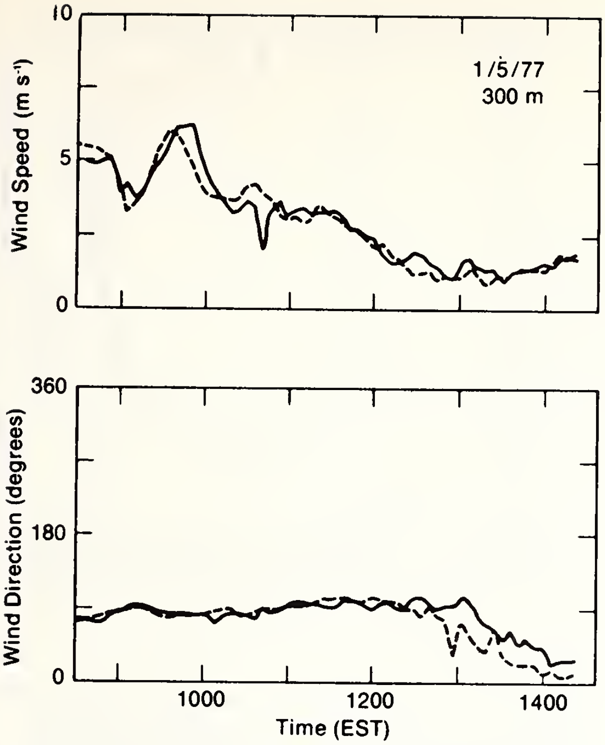

Figure 1. Comparison of acoustic (solid line) and microwave radar (dashed line) measured winds at 300 m altitude. (From Hardesty et al., 1977).

a fixed height is the same for all 4 azimuths observed. b) The components of the horizontal velocity at the radar site can be described by the average of two values measured at the same height but 180 deg apart in azimuth and separated by 2R cos θ_e where θ_e = 11.5 deg and R < 3 km. Horizontal velocity profiles are relatively insensitive to differences in vertical motion between measurement points because vertical velocity terms are weighted by $\frac{\sin \theta_e}{2}$.

Measured horizontal velocity profiles may not represent the actual profile encountered by the aircraft because of the displacement of the radar from the runway. However, alternate antenna scanning schemes could be used to overcome this deficiency. One method is shown in Fig. 2. The antenna elevation angle is about 3 degrees (the glide slope angle) so vertical motion of the particles can be neglected. Horizontal winds are assumed to be the same at the two measurement points near the aircraft track. The wind component toward the radar is the average of the two radial velocity measurements, and the cross-wind component is the difference of the measurements divided by 2 sin(Δθ/2) where Δθ is the azimuth difference of the measurement points. If the standard error of estimate for the radial measurement is 0.1 m/s, then the crosswind error will be 1 m/s for an azimuth difference of 8 degrees if horizontal gradients are negligible. Vertical particle motion (V_z) would cause an error of V_z sin θ_e in the radial wind but would not affect crosswind measurements.

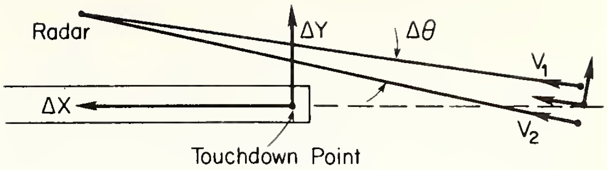

Figure 2. Measurement of 2 dimensional wind profiles with a two-point scan.

Another potential use of the radar at Dulles Airport is for monitoring storm location and storm motion in the vicinity of the airport. Doppler measurements of radial velocity fields and spectral width may also be useful for identifying parts of the storm where hazardous winds are located.

3. WIND MEASUREMENTS IN THE OPTICALLY CLEAR AIR

Sensitive microwave radars can detect refractive index fluctuations in the optically clear air (Hardy and Katz, 1969), and recently a number of experiments with VHF and microwave radars have demonstrated that wind profiles can be measured from the Doppler shift of the received signals. A recent extended operation of the FM-CW radar (Chadwick et al., 1978) indicates that wind profiles can always be obtained in the boundary layer for a variety of meteorological conditions. Doviak and Jobson (1977) reported wind fields measured in clear air with dual Doppler radars with ranges that exceed 40 km. Radar returns are confined to the boundary layer at these ranges. While very high power or large aperture radars are required to measure winds at higher altitudes (Balsley et al., 1977), radars used for air traffic control at airports should have sufficient sensitivity to measure winds to heights required for air safety. Typical boundary layer radar reflectivity for refractive index fluctuations is 10^{-14} m^{-1} (Kropfli et al., 1968) which corresponds to -25 dBZ for scattering from hydrometeors. Longer dwell times are needed to obtain accurate velocity estimates for signals obtained from the clear air than for signals obtained in precipitation; however, rapid scanning should not be required for clear air wind profile measurements.

The FM-CW Doppler radar has demonstrated that it can measure wind profiles in the boundary layer using the velocity-azimuth display (VAD) technique at high elevation angles. Minimum range for this radar is about 20 m and resolution of 20 m can be achieved. A pulsed radar with a 1-μs pulse width and a 1.5-deg beamwidth could not obtain this resolution or minimum altitude. At high elevation angles the vertical resolution would be limited by the pulse width while at low elevation angles it would be limited by the vertical dimension of the antenna illumination. The FM-CW radar is at a disadvantage compared with pulsed radars for measuring at low elevation angles (along the glide slope) because it uses two antennas. For a fixed total aperture the vertical beamwidth will be twice that of a pulsed radar, and at low elevation angles it is the antenna beamwidth which limits vertical resolution. Both types of radars face the difficult problem of measuring weak signals in the presence of strong ground clutter for short range measurements at low elevation angles. Clutter is a much less serious a problem for precipitation targets because measurements can be made at greatly reduced transmitter power. The meteorological signal can be extracted if the clutter does not cause saturation of the rf portion of the receiver. Any single clutter target will be more likely to cause saturation for a pulsed radar, but data would be lost only at the range of the clutter target. The FM-CW radar, while less likely to be saturated by a single target, observes all clutter targets simultaneously and will be unable to obtain data at any range if its receiver is saturated. The total clutter power must be below rf saturation for the FM-CW radar. Radar siting will be crucial for making clear air measurements at short range. The FAA and NOAA are working to equip an air traffic control radar (ASR-8) with a 15-foot diameter parabolic antenna to investigate the potential of this radar for measuring wind in all weather regimes. The potential for identifying hazardous areas in thunderstorms using reflectivity, radial velocity and Doppler spectral width is also being investigated. Since this radar has a standby transmitter and receiver channel, there would be important economic benefits if the standby channel could be used as a Doppler weather radar.

4. SIMULATION OF RADAR-MEASURED DOPPLER VELOCITY PROFILES

The mean Doppler velocity measured by a radar depends on the radial velocity distribution of the scatterers in the radar resolution cell, so that the radar-measured velocity profile is a filtered version of the actual radial velocity component along the axis of the radar beam. Velocity gradients that exist over distances less than the radar beamwidth will cause a broadening of the Doppler spectrum but will not be revealed by the radar-measured mean velocity. Velocity gradients that exist over distances comparable with the beamwidth will be smoothed so that peak values will not be measured. Further, if the radar is offset from the runway so that the radial direction is parallel to but not along the flight path, then the radar measures the actual velocity component along the flight path only if the wind field does not have significant horizontal gradients. Computer simulation of the effects of finite beamwidth and radar displacement from the runway on radar-measured radial velocity profiles were made for a number of wind shear models.

Sample results are shown in Figs. 3-5 for a pulsed radar with a 1.5-deg beamwidth, a 1 μs pulse length, and a minimum radar range of 450 m. Uniform reflectivity is assumed. The radar antenna is pointed parallel to the runway with a 3-deg elevation angle. The solid lines show the actual velocity component (headwind)

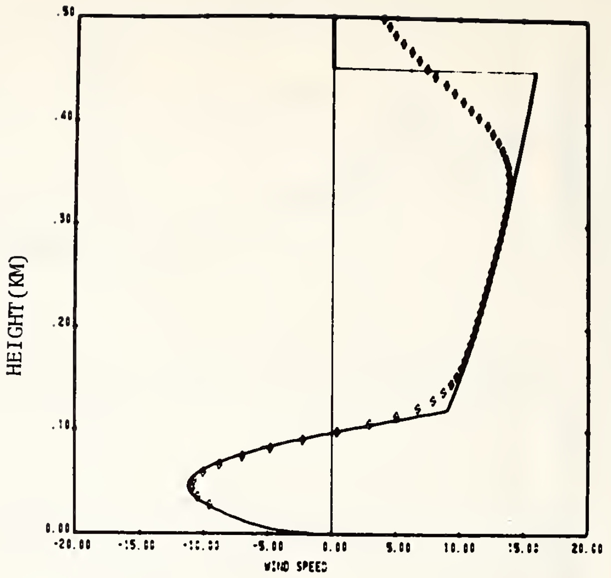

Figure 3. Expected value of radar-measured radial velocity (diamond points) and actual radial velocity (solid line) for a low-level wind shear model. See part 4 for details.

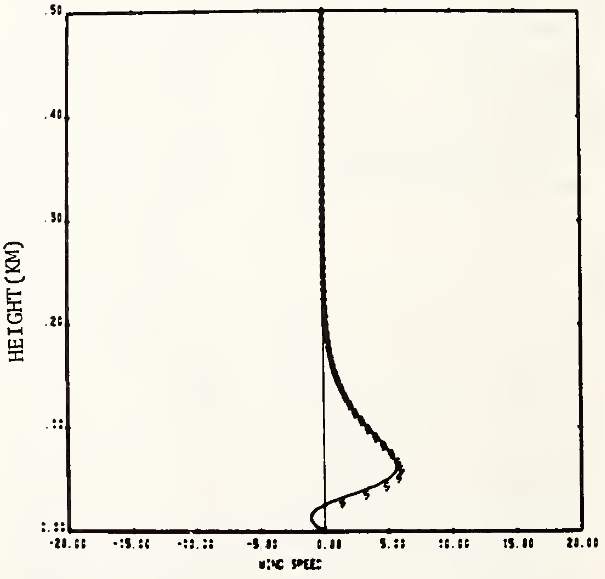

Figure 4. Expected value of radar-measured radial velocity (diamond points) and actual radial velocity (solid line) for a thunderstorm outflow model. Radar displacement (see Fig. 2) is Δx = Δy = 0.1 km. Storm location is Δx = Δy = -0.5 km.

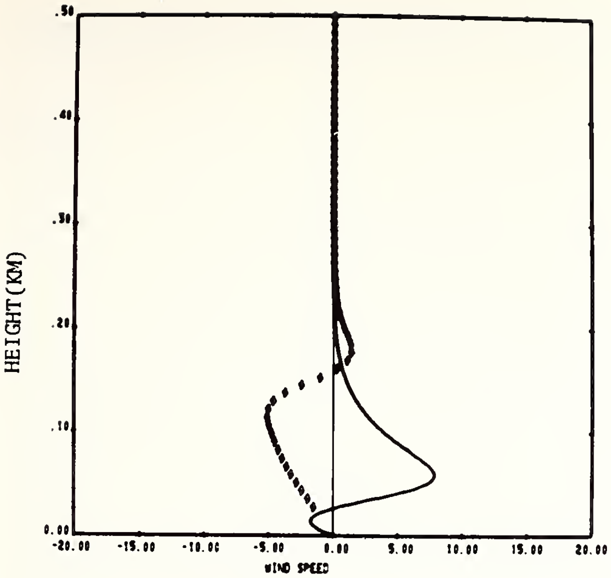

Figure 5. Expected value of radar-measured radial velocity (diamond points) and actual radial velocity (solid line) for a thunderstorm outflow model. Radar displacement (see Fig. 2) is $\Delta x = 2.5$ km, $\Delta y = 0.1$ km. Storm location is $\Delta x = \Delta y = -0.5$ km.

that would be encountered by a landing aircraft on a 3-deg glide slope, and the diamond points are the expected values of the mean radar-measured radial velocity. For Fig. 3, the input wind profile is

$$v(z) = 5(z/20)^{0.43} \text{ m/s} \qquad 0 \le z \le 1500 \text{ feet}$$
$$\theta = \theta_o \qquad 0 \le z \le 100 \text{ feet}$$
$$\theta = 0.4(z-100)+\theta_o \qquad 100 \le z \le 400 \text{ feet}$$
$$\theta = 120 + \theta_o \qquad 400 \le z \le 1500 \text{ feet}$$

where θ is the wind direction, and the surface wind direction (θ_o) is parallel to the runway. There are no horizontal gradients so the location of the radar relative to the runway is not important. The wind profile was set to zero abruptly at 1500 feet. Figure 3 illustrates the effects of finite beamwidth in smoothing velocity gradients. The gradient at low level is represented reasonably well by the radar but the discontinuity at 1500 feet is not. The discontinuity at 1500 feet altitude is smoothed by the 235 m vertical extent of the radar beam (range = 9 km) while at low altitude the smoothing is less because the beamwidth is only about 70 m. Effects of pulse length are negligible because a 1-μs pulse length covers only an 8 m altitude change.

Figures 4 and 5 show the results for an input model that represents the "downburst" from a thunderstorm. This model was derived to represent the wind fields depicted by Fujita and Caracena (1977). The direction of the horizontal wind is radially outward from the downburst center and the magnitude is given by

$$V_H \text{ (m/s)} = 150\, z\, e^{-(10z)^2} \frac{1}{R} (1-e^{(-2R)^2})$$

where z is the altitude (km) and R is the distance (km) from the downburst center. Maximum horizontal winds occur 560 m from the downburst center. Vertical wind satisfies the continuity equation and is given by

$$W \text{ (m/s)} = -6(1-e^{-(10z)^2})\, e^{-(2R)^2} .$$

Figure 4 shows the radial velocity profiles when the radar is offset from the end of the runway ($\Delta y = \Delta x = 100$ m, see Fig. 2) while the downburst is centered at $\Delta y = \Delta x = -500$ m. When the radar is not offset the profiles are well represented by the radar measurements, which indicates that the radar resolution is sufficient to depict the gradients. The offset location of the radar introduces a small error (Fig. 4) in the measured profile. However, when the offset is increased to more realistic values ($\Delta x = 2.5$ km, $\Delta y = 100$ m, Fig. 5) the resulting radar-measured profile is obviously not a useful representation of the velocity along the flight path for this model.

Simulation results show that a 1.5 deg beamwidth should be sufficient to measure wind shears at altitudes that cause problems for aircraft during landing and takeoff. When the wind field contains horizontal gradients measurements must be made near the actual flight path, so an antenna scan must be used if the radar is offset from the end of the runway. If the wind profile is measured with a fixed antenna the presence of significant horizontal gradients can be detected by measuring the profile at two elevation angles or by temporal changes in the profile.

5. CONCLUSION

Microwave Doppler radar offers a potential solution to the problems posed by low level wind shear for aircraft during landing and takeoff. It should be possible to measure wind profiles to several hundred meters altitude in all types of weather if ground clutter does not prevent measurements at ranges as short as 1 km. Wind measurements in the optically clear air would be made with slow antenna scans, whereas rapid scanning would be possible when the signal-to-noise ratio is high as with precipitation targets. Wind profiles could be measured using VAD scanning when the wind profile above the radar site is representative of the wind profile encountered by the aircraft. In cases where horizontal gradients of the horizontal wind are significant, measurements made adjacent to the aircraft track should yield two dimensional wind profiles with sufficient accuracy for aircraft safety. In addition to providing short range wind shear data a microwave Doppler radar could provide surveillance of thunderstorms in the vicinity of the airport. The combination of reflectivity and first and second moments of the Doppler spectrum would allow identification of hazardous areas of storms and advance warning of when these areas will cross landing or takeoff paths.

6. ACKNOWLEDGMENTS

Development of microwave radar for wind shear warning is supported by the Federal Aviation Administration under the direction of Messrs. K. Coonley and I. Goldman. Mr. B. Sweezy of WPL developed the simulation programs. Some of the wind shear models were developed by Messrs. Camp and Fichtl of NASA's Marshall Space Flight Center.

7. REFERENCES

Balsley, B. B., N. Cianos, D. T. Farley, and M. J. Baron, 1977: Winds derived from radar measurements in the Arctic troposphere. *J. Appl. Meteor.* 16(11).

Campbell, W. C., and R. G. Strauch, 1976: Meteorological Doppler radar with double pulse transmission. Preprints, 17th Radar Meteor. Conf., Am. Meteor. Soc., Boston, 42-44.

Chadwick, R. B., K. P. Moran, R. G. Strauch, G. E. Morrison, and W. C. Campbell, 1976: Microwave radar wind measurements in the clear air. *Radio Sci.* 11, 795-802.

Chadwick, R. B., K. P. Moran, and G. E. Morrison, 1978: Measurements toward C_n^2 climatology in the boundary layer. Preprints, 18th Radar Meteor. Conf., Am. Meteor. Soc., Boston.

Doviak, R. J., and C. T. Jobson, 1977: Mapping clear air winds with dual Doppler radars. Proceedings, URSI Open Symposium, LaBaule, France, 505-510.

Fujita, T. T., and F. Caracena, 1977: An analysis of three weather-related aircraft accidents. *Bull. Amer. Meteor. Soc.* 58(11).

Hardesty, R. M., P. A. Mandics, D. W. Beran, and R. G. Strauch, 1977: The Dulles airport acoustic-microwave radar wind and wind shear measuring system. *Bull. Am. Meteor. Soc.* 58, 910-918.

Hardy, K. R., and I. Katz, 1969: Probing the clear atmosphere with high power, high resolution radars. *Proc. IEEE,* 57, 468-480.

Hennington, L., R. J. Doviak, D. Sirmans, D. Zrnic, and R. G. Strauch, 1976: Measurement of winds in the optically clear air with microwave pulse-Doppler radar. Preprints, 17th Radar Meteor. Conf., Am. Meteor. Soc., Boston, 342-348.

Kropfli, R. A., I. Katz, T. G. Konrad, and E. B. Dobson, 1968: Simultaneous radar reflectivity measurements and refractive index spectra in the clear atmosphere. *Radio Sci.* 3, 991-994.

Proceedings of the Cloud Physics and Atmospheric Electricity Conference, 341-346, Seattle, Washington, 2 August 1978.

10.3

PHASE DETECTION OF CONVECTIVE CLOUD HYDROMETEORS USING LIDAR

Kelvin S. Danielson
Department of Atmospheric Science
Colorado State University
Fort Collins, Colorado

and

Vernon E. Derr
National Oceanic and Atmospheric Administration
Boulder, Colorado

1. INTRODUCTION

A significant portion of convective cloud growth takes place prior to the formation of radar echoes. It is likely that the microphysics, dynamics and general morphology of convective clouds during the pre-radar-echo phase plays an important role in subsequent cloud development and organization. The 1977 South Park Area Cumulus Experiment (SPACE) had as one of its goals the definition and description of these pre-radar-echo clouds. The SPACE experiment is well suited to such a study because the mountains directly to the west of the experimental region act as an elevated heat source which initiates the development of convective activity in virtually the same location on a daily basis. Thus, fixed location instruments can be placed in advantageous locations for the frequent collection of data.

The SPACE program utilized the NOAA lidar provided by NOAA Wave Propagation Laboratory (WPL) and two instrumented powered aircraft loaned to SPACE by the Bureau of Reclamation HIPLEX program to study clouds during early stages of development. This paper presents data taken August 1, 1977 in the South Park region with the Wyoming Queenaire (10 UW), the MRI cloud physics aircraft (1 MR) and the NOAA lidar. These data serve two basic purposes. One is to describe fair weather convective clouds. The second is to compare and contrast the data taken with the various instruments. Such intercomparisons help to define instrument capabilities when the instruments are operated independently. Initial analyses of lidar data taken during early stages of more intense convective activity are also presented.

On August 1, 1977 convective activity in South Park was characterized by fair weather cumulus. The synoptic analysis on August 1 indicated a 500 mb long wave ridge extended from Alaska to southern Utah while the long wave trough was located in east-central United States. The entire Rocky Mountain West including South Park was under generally northwesterly flow aloft and large scale subsidence. The center of the surface high pressure zone was over northeastern Colorado at 0600Z. By 1800Z the surface high pressure zone was centered over extreme eastern Kansas. In South Park the morning winds were northwesterly aloft but easterly on the surface. This easterly flow at the surface had provided a good low level moisture supply. The surface moisture was capped by a 4.7C inversion from the surface (723 mb: 2950 m) to 684 mb. The surface layer moisture appeared to be mixed vertically after the inversion was broken by surface heating. All three soundings taken in South Park on August 1 indicated a generally stable environment with only moderate moisture contents above the surface layer. These factors resulted in a day with scattered fair weather cumulus forming over the mountains by late morning. Cloud bases were generally at the CCL of approximately 480 mb (~5791 meters, 19,000 feet).

2. INSTRUMENTS

Powered aircraft and lidar were utilized in describing the fair weather cumulus clouds on August 1, 1977. Both aircraft were used to penetrate the clouds. The MRI cloud physics aircraft measured state parameters and cloud drop size distributions plus a number of other variables. The distributions are obtained from three different Particle Measurement Systems (PMS) probes. The ASSP probe measures the distribution from 2 to 30 μm in approximately 2 μm steps. A PMS one-dimensional probe measures the distribution from 20 μm to 300 μm in 20 μm steps while a second PMS one-dimensional probe measures the distribution between .3 mm and 4.5 mm in .3 mm steps. Liquid water contents in clouds are computed by calculating the volume of water in the distributions measured by the respective PMS probes. The Wyoming cloud physics Queenaire was also used to investigate the fair weather cumulus on August 1, 1977. State parameters, liquid water content and droplet distribution data were obtained from the aircraft in addition to a number of other variables. PMS probes are at the heart of the Wyoming Queenaire drop distribution detection system. A PMS ASSP probe is used for the small drops (2-30 μm) while a two-dimensional PMS probe is used for the larger drops. The two-dimensional PMS probe can measure drops from 25 μm to 800 μm. The major advantage of the two-dimensional PMS probe is that it is possible to record the shape of the particles. The shape of the image recorded provides clues as to whether the particles are composed of ice or water. Cloud water contents are obtained in two ways on the Wyoming Queenaire. One is by integrating over the droplet distribution. The other is through the use of a Johnson-Williams liquid water device.

Ground based lidar systems provide an alternative mode of studying clouds with too small or too few particles for a radar echo. The study of nascent clouds in the pre-first-echo (radar) stage is only possible, remotely, by the use of powerful lidar devices at shorter wavelengths. Small droplets or ice particles have very small radar cross sections for even three centimeter radar. Calculations for a cloud distributed as described in Deirmendjian (1976) (Cloud C.1) show that the radar cross section is larger for .7 μm lidar signals than for 3 cm radar by a factor of 10^{11}. Cloud C.1 has a density of 6.2 X 10^{-2} gm/m^3 at droplet density of 10^8 per m^3. The radii range from .03 to 12.3 μm. On the other hand, the extinction coefficient for lidar wavelengths is 10^5 greater than for radar wavelengths. Greater interaction cross sections must result in greater attenuation. Two conclusions may be drawn. The lidar is indispensible for the remote sensing of thin and/or less dense clouds; the radar is required to penetrate denser clouds. Present day lidars and short wave radars overlap in sensitivity and penetration, so that a carefully chosen combination can be used to study clouds from birth to dissipation.

The lidar used in SPACE 1977 is the NOAA lidar system depicted in Fig. 1.

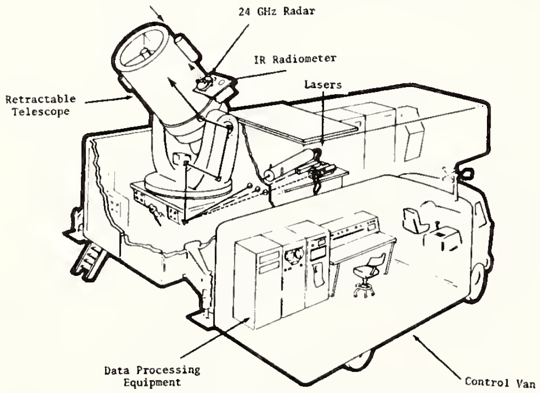

Fig. 1. Cut-away view of remote sensing facility.

This combined remote sensing system consists of a ruby lidar, a 24 GHz radar, and an infrared (8-12 μm) radiometer paraxially placed on an altitude-azimuth quick-traverse mount. The lidar signal is plane polarized. The receiver detects depolarization by measuring the signal in two perpendicular polarizations, one of which is parallel to the transmitted polarization. The pulse width of the lidar signal is 10 ns, but resolution is normally limited to 20 m by a receiver integration time of 60 ns. The peak pulse power transmitted by the lidar is approximately 150 mw. The maximum pulse repetition frequency is 1.0 s^{-1}. The receiver consists of a 70 cm diameter mirror, Newtonian mount. The detector system has two channels for polarization measurements, employing photomultipliers.

The radar system has a peak power of 40 kw, a pulse repetition frequency of 2000 s^{-1}, and a range resolution of 22.5 km.

The radiometer is a Barnes PRT-5 with a temperature resolution of 0.1°C.

Auxilary systems available include acoustic sounders and solar photometers. The spectral extinction coefficient of clouds and aerosols are measured as a function of wavelength by a series of filters repetitively inserted into the optical path of the solar photometers. Standard RG-8, OG-1, OG-2 Schott filters are employed as well as an "open" position subject to detector response. An IT-3 radiometer has been converted to look directly at the sun and obtain the extinction coefficient in the range 8-12 μm.

This system of lidar-radar photometry and radiometry permits simultaneous measurements of the backscatter, extinction and emission coefficients.

3. PROCEDURE

The acquisition of combined aircraft and lidar data for the August 1 experiment was coordinated primarily by visual observations. Aircraft personnel would choose a cloud located in the proximity of the lidar site. Lidar personnel on the ground would visually observe the location of the aircraft and direct the lidar at the appropriate cloud.

For the analyses, aircraft position was determined using VOR-DME navigational data. VOR-DME data are not accurate enough to specify exact locations within the clouds being studied. Therefore, no attempt is made to compare in-cloud spatial variations of liquid water and ice as detected by the aircraft with spatial variations as detected by the lidar. The navigational data is used to compute the general location of the aircraft so that it can be compared with the general location of the cloud being studied by the lidar. This assures that the visual field coordination was accurate and that the same cloud is being investigated.

For the purpose of this analysis, average data on in-cloud drop distributiosn and liquid water contents will be used. The ASSP on both aircraft was used to determine the existence of a cloud for the analysis algorithm. Liquid water contents for both aircraft are calculated using ASSP data. Intercomparisons between ASSP derived liquid water contents and Johnson-Williams (JW) liquid water content values indicate that the ratio of liquid water from ASSP to liquid water from the JW varies from about 1:1 to 1:5. Preliminary investigations indicate that a part of the problem may be ASSP coincidence errors at high concentrations. Since quite low concentrations existed in the clouds on August 1, ASSP values may be quite good.

The MRI cloud physics aircraft one-dimensional PMS probes appear to have a minor noise problem in the small drop size increments. In order to correct for this, an average clear air noise distribution is computed and is then subtracted from the in-cloud distributions. Liquid water contents from these probes are calculated using the adjusted distributions.

The ASSP probe distributions from the Wyoming Queenaire and the MRI aircraft were also compared. The distributions derived from the ASSP probe data of the two aircraft have very similar shapes. The ASSP on the Wyoming aircraft measures consistently higher droplet concentrations than the MRI ASSP. No attempt is made to normalize the data from these two ASSP probes for this analysis. All drops smaller than 30 μ are assumed to be water. This means that anything measured by ASSP probes is considered to be liquid.

The University of Wyoming two-dimensional PMS probe is used in this study to determine if larger hydrometeors (25 μ to 800 μ) are in an ice or water phase. This is done by actually looking at a representation of the image. Visual keys developed at the University of Wyoming were used to make the distinction.

Two cloud variables are measured remotely by the lidar. One value is the approximate water content of the cloud. Water content is derived from the backscatter cross-section (β) which the lidar measures. The parameter β is strongly water content and drop size distribution dependent. If the drop size distribution can be specified, water content can be calculated. The drop size distributions used for these calculations were measured by Diem (1948). Different distributions are used for fair weather cumulus and cumulus conjestus. These distributions are quite similar to the actual distributions measured in South Park. The backscatter cross-section (β) is also slightly hydrometeor phase dependent. Thus, the water content calculation will vary depending on the phase of the cloud hydrometeors as well as the distribution. The ratio of density (ρ) to the backscatter cross-section (β) is displayed in Table 1 for both ice and water. Multiplying the backscatter cross-section by the appropriate value will give the water content.

Table 1

ρ/β^*

	Water	Ice
Fair weather Cumulus	123.2 gm sr/m^2	96.8 gm sr/m^2
Cumulus Conjestus	261.4 gm sr/m^2	213.6 gm sr/m^2

$^*\beta$ is in units of $(^{-1}sr^{-1}$; ρ is in units of (gm m^{-3})

The second measurement obtained from the lidar is the ratio of ice to water. This is done by measuring the depolarization of the returned signal. Sassen (1976) describes the process in detail. In general, a depolarization between .2 and .4 is approximately 50% ice while a depolarization greater than .4 is probably all ice.

4. RESULTS

Figures 2 and 3 represent averages of the lidar backscatter cross-section (Beta) and the depolarization, respectively, for August 1, 1977. The data are plotted to indicate the geometrical position of the data with respect to the lidar position. The legend on Fig. 2 gives the conversion from the symbol displayed to the range of β which it represents. A similar legend is displayed on Fig. 3 for depolarization. The time period associated with a given set of lidar data is displayed next to an azimuth angle which specifies the region where the data were collected.

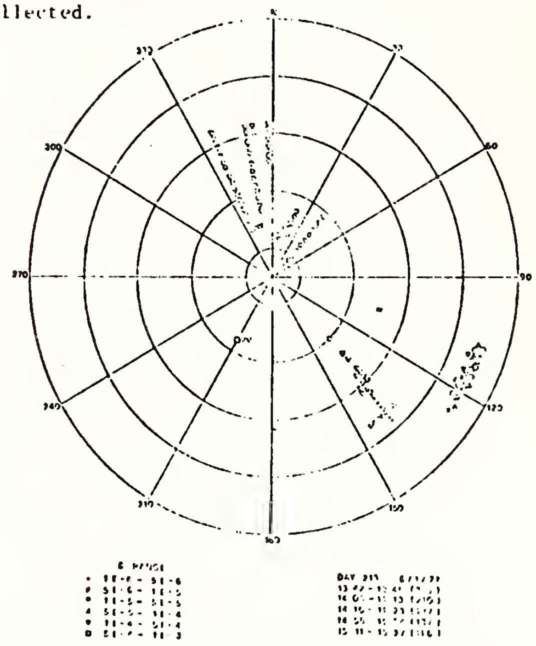

Fig. 2. Beta from lidar.

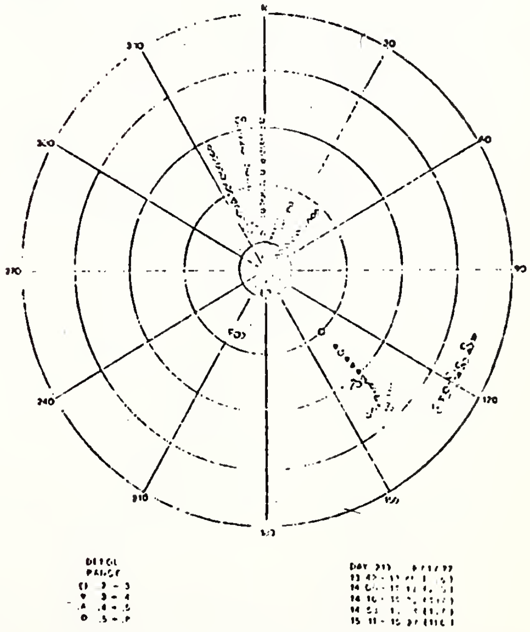

Fig. 3. Depolarization from lidar.

For time period 14:06-14:13 and 14:16-14:23 simultaneous aircraft data are available from the MRI aircraft. The average distribution from this time period is very narrow as is indicated by Fig. 4. The one-dimensional probes for larger drop sizes had few events. In the case of the probe measuring from 20-300 μ the in-cloud data could not be distinguished from clear air instrument noise. Figure 5 displays the data from the .3-4.5 mm one-dimensional PMS probe. On both Figs. 4 and 5 the number displayed represents the total number of drops in the increment represented by that portion of the histogram. Also note that the volume in which the concentration is specified is a cm^3 in Fig. 4 and m^3 in Fig. 5. The aircraft data were collected at a relatively constant level ranging from approximately 470-480 mb. The temperature measured by the aircraft at this level ranged from -11C to -13C. Cloud diameter at this time was approximately 1.25 km. The cloud vertical extent was less than a kilometer. All drops measured by the PMS ASSP probe (2-30 μ) are assumed to be in a liquid state. This assumption is based both on temperature and size considerations.

The liquid water contents (LWC) computed from the MRI ASSP data for this time period were variable. Values of LWC were at .01 g/m^3 or less. By comparison the lidar backscatter values on this cloud would indicate that the LWC was approximately .02 to .03 g/m^3, which is at least a factor of 3 larger than the average ASSP derived LWC for all these clouds. A number of reasons for this difference can be given. First, the ASSP on the MRI aircraft had lower values than the Wyoming ASSP suggesting that the distribution estimate from MRI might be too low. Second, the PMS one-dimensional probes on the MRI aircraft can not distinguish low concentrations of drops because of noise problems. Even a slight increase in the contribution by drops of a larger size could make up the difference. Third, the distribution used to calculate the ρ/β for the lidar is broader than the observed distribution. Thus, if the narrower observed distribution was used to calculate ρ/β the values might coincide more closely.

The lidar also gives an estimate of ice to water in the cloud. The Wyoming Queenaire which made several penetrations later in the day collected the images of larger particles. A careful review of these images indicated that virtually all the larger particles are ice. The small drops (2-30μ), as pointed out earlier, are all considered to be in liquid form. Thus, since no significant number of large drops were measured in the cloud, the aircraft data would indicate mainly water. The lidar data indicates that for this time period the depolarization is between .2 and .4 which is indicative of a mixture of liquid and ice phase particles. This discrepancy could again be attributed to an inability of aircraft to detect small numbers of larger particles owing to instrument noise.

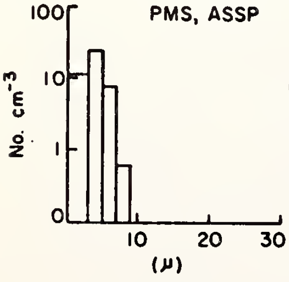

Fig. 4

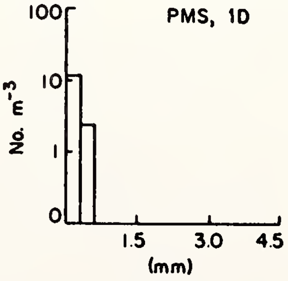

Fig.5

Average drop size distributions, 14:06-14:23 MDT.

Simultaneous aircraft and lidar data are also available for the time period 15:11-15:27. The symbolic plot of measured backscatter cross-sections on Fig. 2 indicates a much greater variation of backscatter cross-section for this cloud. The range of liquid water contents calculated for this cloud is from .0002 to .03 g/m^3.

Water contents computed from the aircraft measured drop size distributions also vary considerably more in this cloud than the earlier cloud. Values as great as .8 g/m^3 were measured in one very small area of this cloud. An average value of water content for the cloud over the specified time period was approximately .01 g/m^3 if the one small region of very high water content is eliminated from the calculation.

As is indicated by Figs. 6, 7 and 8 a higher concentration of large hydrometeors existed in this cloud than in the first one discussed. It should be noted that both the 20-300 μ and the .3 to 4.5 mm distributions are dominated by data collected in the cloud region which contained high water contents. However, even if these data are removed, the distributions are broader for this cloud than for the first cloud studied. Since all the larger hydrometeors appear from PMS two-dimensional data to be ice, one would expect a higher depolarization than in the first cloud. This is the case as can be seen in

Fig. 6

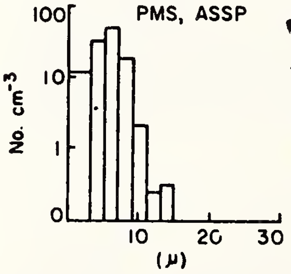

Fig. 7

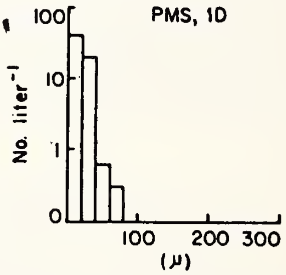

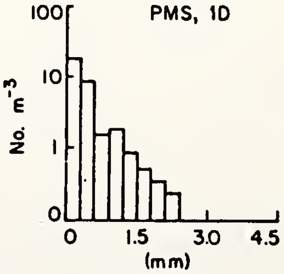

Fig. 8

Average drop size distributions, 15:11-15:27 MDT.

Fig. 3. Large variability of depolarization is again obvious, but considerably more ice seems to be present in this cloud.

Figures 9 and 10 show cross-section (β) and depolarization data from lidar scans of a cumulus conjestus cloud which occurred on July 19, 1977. No drop distribution spectra are available for this cloud making interpretation of water content from β difficult. Rough calculations of LWC for the 13.1° elevation scan which is near the cloud top of the growing convective cloud indicates that the LWC is close to 1 g/m^3. The depolarization data for this 13.1° elevation scan clearly shows the existence of a large percentage of liquid water. This is consistent with data collected by Sax et al. (1976) for growing convective clouds in Florida.

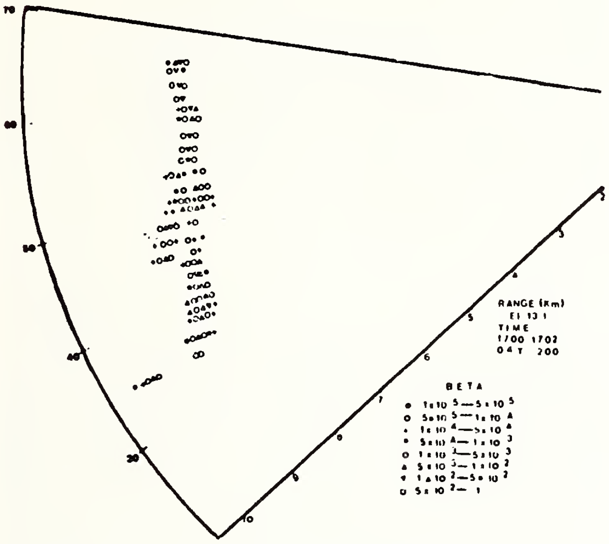

Fig. 9. Lidar measured backscatter cross-section (.) for the top of an actively growing cumulus cloud on July 19, 1978.

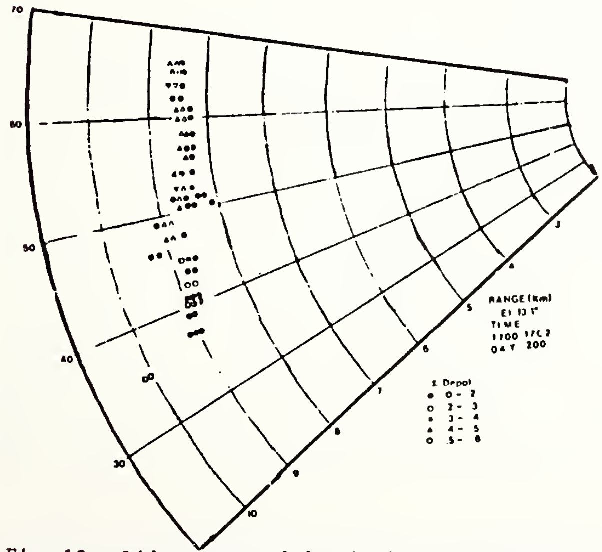

Fig. 10. Lidar measured depolarization for the top of an actively growing cumulus on July 19, 1978

Figures 11 and 12 show a scan of lidar data from another cloud on July 19. In contrast to the cloud in Figs. 9 and 10 this portion of the cloud is composed mainly of ice and has LWC on the order of .3 g/m or less.

These two examples of data from July 19 demonstrate that lidar can be used to assist in the evaluation of actively growing cumuli. The lidar has greatest utility in portions of clouds with relatively low LWC or those portions of the cloud which are not very thick. Investigation of cloud top with lidar as shown in Figs. 9 and 10 suggest that lidar might be useful in evaluating microphysical changes of cloud top due to seeding. Figures 10 and 11 suggest a means of investigating the region of the cloud which does not contain precipitation sized particles.

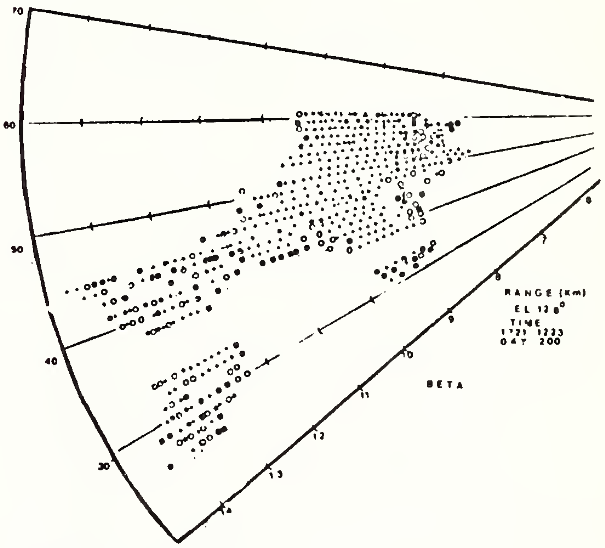

Fig 11. Lidar measured backscatter cross-section (β) from a cloud region which had no radar echo.

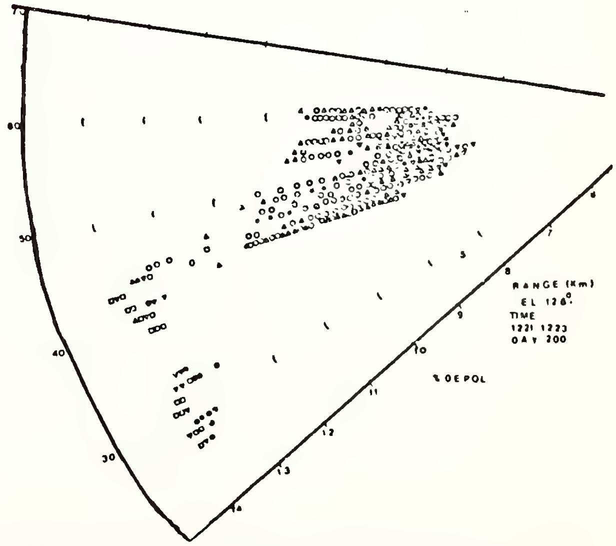

Fig. 12. Lidar measured depolarization from a cloud region which had no radar echo.

5. CONCLUSIONS

(1) The data indicates that high altitude fair weather continental cumulus clouds have water contents which are typically very small (less than .01 g/m^3). (2) Large particles in these clouds exist in the form of ice. (3) Cloud tops of actively growing cumulus contain mainly liquid water. (4) Lidar can be used to remotely investigate these clouds. (5) More data on both aircraft sensors and lidar are needed to clarify interpretations.

6. ACKNOWLEDGEMENTS

The National Oceanic and Atmospheric Administration provided the lidar; personnel for data collection, data reduction and analyses. The Bureau of Reclamation supported the aircraft studies directly plus providing additional support under Contract No. 7-08-83-V3006. NSF helped fund the experiment under Grant No. ATM77-09770. The NCAR FOF and RAF both contributed equipment and personnel to SPACE.

7. REFERENCES

Deirmendjian, D., 1969: Electromagnetic Scattering of Spherical Polydispersion. The Rand Corp., Santa Monica, California, American Elsrvier Publishing Co., Inc., New York, 290 pp.

Diem, M., 1948: Messungen der Grosse von Wolkenelementen. II. Rdsch. I, 261.

Sassen, K., 1976: An Evaluation of Polarization Diversity Lidar for Cloud Physics Research. Ph.D. Dissertation, University of Wyoming, Laramie, Wyoming.

Sax, R.I., J.C. Eden and P.T. Willis, 1976: Single-Level Microphysical Structure of Florida Cumuli: Selected Case Studies. Preprints of International Conference on Cloud Physics, AMS, Boulder, Colorado, p. 332-337.

Monthly Weather Review, : 1488-1494, October 1978.

Internal Structure and Development Processes of C-Scale Aggregates of Cumulus Clouds

Raúl E. López[1]

National Hurricane and Experimental Meteorology Laboratory, NOAA, Coral Gables, FL 33124

(Manuscript received 17 March 1978, in final form 28 June 1978)

ABSTRACT

Large echoes (C-scale in GATE terminology; approximately 100 to 10 000 km²) seem to produce most of the precipitation that occurs in tropical systems. These large echoes are seen to last several hours and comprise many smaller and short-lived cells that grow and die within their bounds or are merged with them. In this paper, quantitative GATE radar data are used to statistically characterize these composite echoes as a whole, and to study their internal structure, formation and development processes. In addition, statistics of the individual cells making up the composite echoes are presented. These are compared to similar data for cells that develop individually away from the aggregates. In this way, some information is obtained about the duration, rain-producing ability and the size of those cells that merge to form larger groups compared to those clouds that form, develop and die relatively independently of one another.

1. Introduction

Ample evidence has been produced in the last few years to indicate that size, height and duration distributions of convective radar echoes follow, in general, a log-normal probability law (Biondini, 1976; López, 1976, 1977; Houze and Cheng, 1977; Nasim, 1977). Fig. 1 presents, as an example, the echo size distribution for one disturbance observed in GATE from 7–9 August 1974. The principal characteristic of this distribution is that the vast majority of the echoes are small and that there are few very large ones. Thus, Fig. 1 shows that about 90% of the echoes cover areas which are less than about 50 km², while the other 10% cover areas that range from about 50 to 2500 km².

To ascertain the relative importance of each echo size, a graph of the percentage of total observed rainfall produced by different percentiles of the largest echoes has been computed from digital data for all of the echoes on the radarscope of the NOAA ship *Oceanographer* at 3 h intervals from 9–14 August and 1–6 September 1974 in GATE. This distribution is shown in Fig. 2. It can be seen that, although there are few, the largest echoes are responsible for most of the precipitation observed. For example, the largest 10% of the echoes account for 90% of the precipitation. Similar results have also been verified in other places (e.g., Woodley *et al.*, 1971; López, 1976). In view of the importance of these echoes, they should be statistically characterized and their formation processes investigated. In this paper, quantitative GATE radar data are used to statistically characterize these echoes and to study their internal structure, formation and development processes.

Before the results of the analyzes are presented it is convenient to explain the data-processing philosophy employed. In this paper large numbers of echoes are identified, measured and tracked during their lifetimes. Because the main interest is in statistically characterizing populations of echoes it is important that as much meaningful information is used as it is present in the data. In order to eliminate noise and spurious values a threshold level of about 15 dBZ has been used throughout the analyzes. This is equivalent to the minimum detectable signal (−95 dBm) at around 75 km. Actually, the effective sensitivities of radars decrease with range; so that echo parameters such as area would tend to be on the average smaller with range if the threshold used is not that of the minimum detectable signal at the maximum range considered. However, a high threshold level would have the effect of reducing the areas of echoes closer in and even ignoring completely the weaker echoes. Rather than biasing the populations in this way, a smaller threshold was used. The range bias, on the other hand, is smoothed out somewhat on account of the following considerations:

1) The unit employed in the definition of area classes was selected in such a way that the magnitude of the bias due to reduced sensitivity with

---

[1] Most of the work reported in this paper was done while the author was with the Wave Propagation Laboratory, ERL, NOAA, Boulder, CO.

0027-0644/78/0000-0000$00.00

© 1978 American Meteorological Society

range falls within the basic class interval. A sample of about 750 echoes from the population used in Fig. 1 was stratified by range. The maximum difference in mean echo area between ranges of 50 and 200 km were around 10 km^2. This was the unit employed. No apparent bias in echo duration with range was noticed in the sample.

2) The echo populations are mostly described by means of frequency distributions in cumulative form. This has the effect of smoothing out the range bias as an echo or cell that is erroneously assigned to a lower size class will appear in the accumulation for the correct (larger) class and all subsequent (larger) classes.

3) Large samples were usually selected over fairly long time periods. In this way the chances of observing echoes and cells of a given size class at many different ranges are increased, reducing the bias error for that echo size class.

4) The principal results stressed in the paper have to do with differences between large samples, where a similar bias in the two samples has a good probability of being cancelled.

In studying the internal structure of the larger echoes it has been found that their areas can be divided into several distinct regions. These regions can be tracked back and forth and can be seen to form, reach a maximum reflectivity, decay and eventually dissipate relatively independent of each other. They also retain their relative positions among themselves and their general configurations from one time period to the next. In general, a core of higher reflectivity is present in the region. These entities making up the total echo are called *cells*. They seem to be the basic building blocks forming larger echoes. Since not much is known about these entities it is difficult and probably incorrect to attempt at this time to make an objective definition of these cells in terms of a specific reflectivity contour or a gradient of reflectivity from the core of the cell outward.

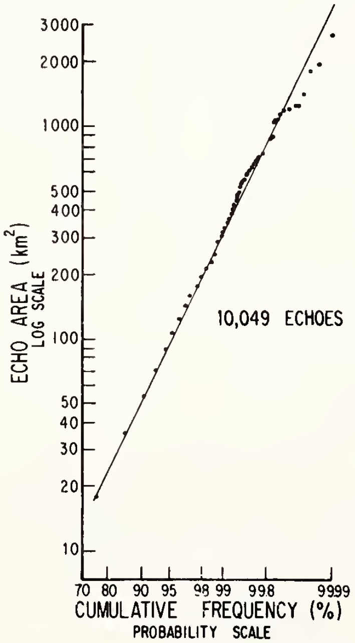

Fig. 1. Cumulative frequency distributions of the maximum area attained by radar echoes in log-probability coordinates. Data were obtained by the NOAA ship *Oceanographer* during GATE for the period 7–9 August 1974.

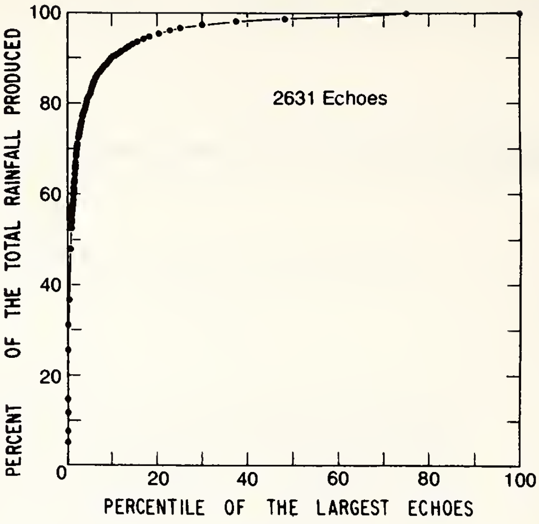

Fig. 2. Percentage of the total observed rainfall produced by different percentiles of the largest echoes. Data were obtained by the NOAA ship *Oceanographer* at 3 h intervals during the period 9–14 August and 1–6 September 1974 in GATE.

These cells are continuously changing during their lifetimes so that a fixed intensity threshold or gradient would only delineate part of the cell and apply for only part of its life cycle or maybe even result in the rejection of some cells completely. For these reasons a subjective determination was employed in the paper where all sources of information are considered, e.g., cell configuration, relative position within the echo, growth history, etc. Although subjective, this method is physically oriented and uses more information than automatic, mechanical selection schemes. Those echoes that do not show evidences of being made up of these distinct regions or cells are termed *individual* or isolated echoes. When isolated cells (or groups of cells) do merge they can usually be still identified as distinct entities within the larger conglomerate until they dissipate. In this way cells and isolated echoes have been tracked as entities through their entire lifetimes even if mergers or splits are involved. When echoes came into or moved out of the maximum range considered they were not used for the statistics presented.

On some occasions rainfall values are given for echoes and cells. The Z–R relationship used was

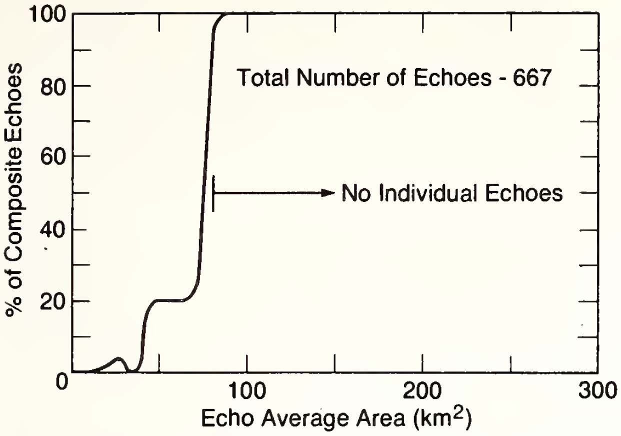

FIG. 3. Percentage of composite echoes observed as a function of average echo area. Data are a subset of the data used for Fig. 2.

$Z = 350R^{1.25}$. This formula was given by Hudlow (1975) in the documentation for the GATE *Oceanographer* radar set. At the GATE workshop in Boulder, Austin (1977) presented a new relationship ($Z = 230R^{1.25}$) and tables of corrections to the recorded reflectivity values due to system bias and attenuation. Since most of the analyses presented in this paper had been completed at that time it was decided to present the old values and just make reference to the original $Z - R$ relationship used. After all, the main emphasis of this paper is not on rainfall values as such but on the structure and development of echoes. Furthermore, the rainfall values are almost exclusively used in a relative way (comparison of grouped vs isolated echoes). If the rainfall values are multiplied by 2.3, rainfall values can be obtained which correspond to the new $Z - R$ relationship and are corrected for system bias. No correction for the attenuation of the radar signal has been made.

A description of the data used can be found in Hudlow (1975). In general the data consist of average values of returned power for a volume of 2 km in range by 2° azimuth by 2° elevation. The time between recorded PPI scans at base tilt (0.5° elevation) is 15 min.

2. Characteristics of composite echoes

A representative sample of 667 echoes was selected from all echoes observed by the *Oceanographer* from 9–14 August and 1–6 September 1974. These echoes were tracked throughout their lifetimes. Again, digitized data were employed for the analyses. Only echoes that had average areas over their lifetimes under 500 km^2 were selected (the maximum areas were as large as 10 000 km^2 in a few cases). Analysis of the sample indicates that there are many *individual* echoes which never merge, never split, and appear to contain only one cell or reflectivity maximum. On the other hand, there are several *composite* echoes which were seen to either form as the result of cell growth in close proximity (and/or merger), split into several echoes, or contain several connected reflectivity maxima or cells at least at the minimum detectable signal.

Fig. 3 shows the percentage of composite echoes in each average area class. It can be seen that, in general, echoes having average areas >80 km^2 are composite echoes. It seems that single-celled echoes can grow up to that area and no more, and that larger echoes are formed by several cells growing next to each other.

The typical composite echo reaches a maximum area of 377.5 km^2 and has an average area over its lifetime of 201.4 km^2. The average echo rainfall rate, as computed from the relationship $Z = 350\ R^{1.25}$ given by Hudlow (1975) is 1.4 mm h^{-1} while the maximum rate is 2.0 m h^{-1}. The typical echo produces 1232 mm km^2 of rain during a lifetime of 2.6 h. In the mean, these echoes consist of five cells, although the maximum number of cells is eight. Typically, during the lifetime of the echo, around 15 cells appear, grow and dissipate in close proximity.

In general, at the start of a composite echo, a few cells are observed to occur together. With time, new cells form next to the old ones. The old ones may decay while the newer ones grow and develop. During the lifetime of the composite echo, many cells can go through their cycles of growth and decay. Although there is some variation in cell size and duration, usually the particular area covered by a composite echo depends on the *average number* of cells present during the lifetime of the echo. Similarly, the duration depends on the *total number* of cells appearing next to the other cells during the life span of the echo. As the average radar reflectivity of the echoes does not vary much with cell area, the rain-producing ability of composite echoes depends largely upon the number of cells making up the echo both in space and time.

The data show a wide variety of echo formation and growth modes. For example, an echo can exist which, on the average, is made up of three cells next to one another. During the lifetime of the echo, 12 cells might go through their individual life cycles. A similar-sized echo (containing three cells on the average) may go through only six cells during a much shorter lifetime. As a result, there are no unique area-duration relationships; echoes having the same average or maximum area can have widely different lifetimes and vice versa. Fig. 4 shows an attempt to derive such a relationship for the data of Fig. 1. The mean duration for each maximum area class is indicated, together with its standard deviation. No clear area-versus-lifetime relationship emerges. The vari-

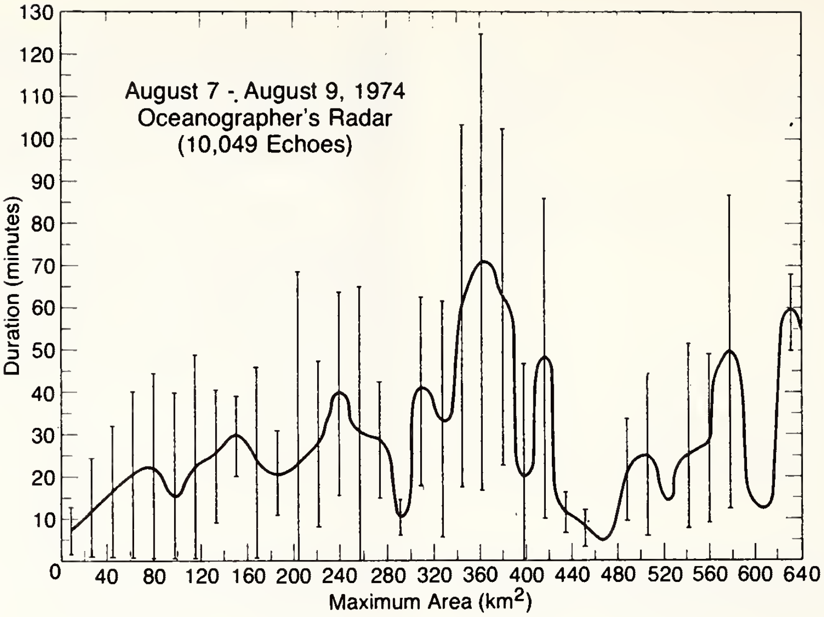

Fig. 4. Average echo duration as a function of maximum echo area. Data source as in Fig. 1.

ation of lifetime within each area class is certainly very large. A very general trend for longer duration with larger area can be detected for the echoes having maximum areas below 250 km². However the scatter of individual values is so large (as indicated by the one sigma bars) that the relationship is not too meaningful. Actually there is more of an upper bound than a direct relationship, so that echoes that last very long are usually the largest, but not necessarily the other way around. Most of the smaller echoes are composed of only one or just a few cells. On the other hand, it is surprising to see that large echoes can have very short durations. In these cases it seems that several cells were formed together (explaining the large echo area) within a short period of time but that further cell formation was halted (probably because of the high competition for the available low-level moisture supply). In this way the lifetime of the whole echo approximates the lifetime of the individual cells which originated very close in time in the initial formation of the group. Actually, long-lasting echoes (~2 h) do not have too many cells at any one time (but many cells are part of the echo with time) and thus have medium size echo areas (~300–400 km²). When the same data of Fig. 4 are stratified by area or duration alone, log-normal distributions are observed (Nasim, 1977). (Fig. 1 shows the corresponding log-probability plot for the area distribution.) Therefore, a bivariate log-normal distribution is suggested. Such a distribution is shown in Fig. 5.

This joint log-normality both in size and duration, together with the fact that size and duration are basically determined by the number of cells growing together during the lifetime of the echo, indicates that composite echoes form by a stochastic process of cell growth. In this process, the number of new cells forming next to the old ones is directly proportional to both the size of the existing echo and a random factor. [The process obeys the law of proportionate effects, which is the generation principle of the log-normal distribution (López, 1977).].

3. Characteristics of individual cells

At this point, the question should be raised as to the origin and identity of the cells making up composite echoes. Visual cloud observations (e.g., Zipser,

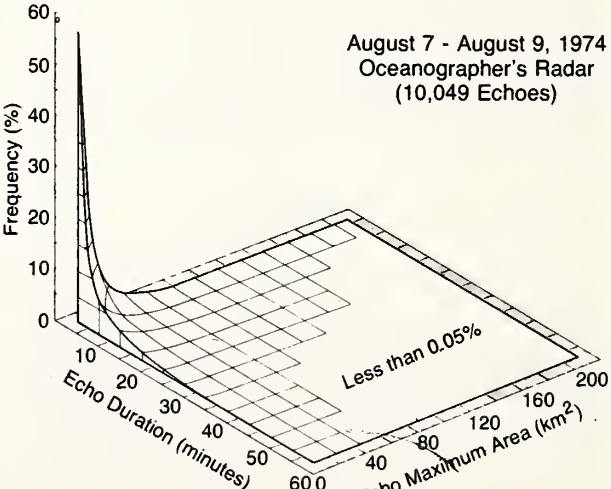

Fig. 5. Combined frequency distribution of echo duration and echo maximum area. Data source as in Fig. 1.

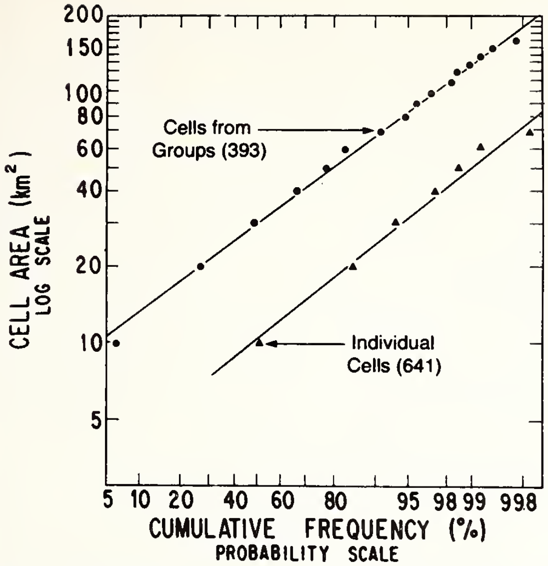

FIG. 6. Cumulative frequency distribution of maximum area in log-probability coordinates for the cells of composite (groups) and for single-cell (individual) echoes.

1969; Woodley and Powell, 1970) indicate that tropical cumulus clouds can grow in clusters where, as one cloud dissipates, others form on its side. Such a cloud system could last much longer than typical isolated cumuli. The echo signature of such a system would appear as a conglomerate of distinct reflectivity areas (corresponding to the different raining clouds) at various stages of growth and dissipation. This is just what is observed from the radar data as described above.

On the other hand, the radar cells described in this paper, which appear as new, distinct portions of an echo mass, must be correlated with active convective cloud elements. Actually these cells have areas and durations of the same order of magnitude as their neighboring single-cell echoes, which are clearly the results of individual clouds. In view of these arguments and of the behavior of the cells as described, it is reasonable to conclude that the radar cells are the results of individual cloud entities which are growing next to each other.

It is generally believed that clouds growing close together are more vigorous than clouds which are separated from one another. This is predicated on the idea that clouds in proximity are mutually better protected from the dilution resulting from entrainment of dry environmental air. If this is true, it would be expected that the cells constituting the composite echoes would be bigger, have a longer lifetime, and be more intense than isolated, single-celled echoes.

In order to test this inference, around 400 cells making up larger composite echoes were identified and tracked throughout their life cycles. These cells can generally be tracked for 45 min to an hour (others can last as long as 4 h). They usually retain their relative positions within the composite echo during their lifetimes. The tracking was done manually from PPI displays of the digital radar data. The time interval between PPI's was 15 min. The area of the larger composite echoes was divided among the different cells. The determination of the boundaries of the cells was subjective with reference to the cell configuration, relative position within the echo and its growth history. For comparison, 641 single-cell, isolated echoes were also tracked and analyzed. These echoes existed in the same general region and during the same time period as the composite echoes, but never merged or

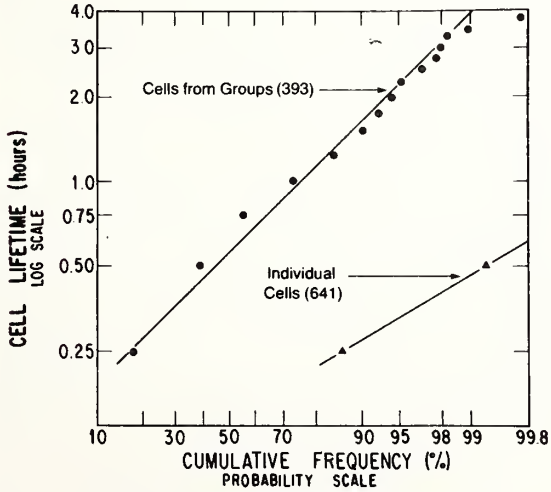

FIG. 7. As in Fig. 6 except for lifetime.

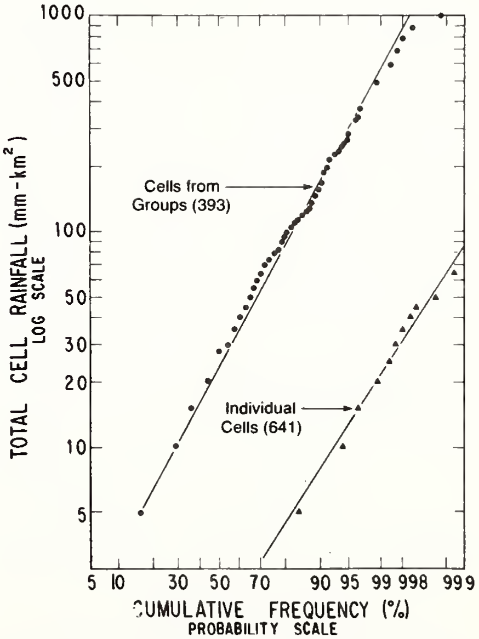

FIG. 8. As in Fig. 6 except for total rainfall.

showed signs of containing more than one radar reflectivity maximum.

Fig. 6 shows the log-probability plot of the frequency distribution of maximum area attained both by the cells making up composite echoes and by isolated individual echoes. The composite echoes have cells which are, in the mean, larger than the individual, isolated echoes. A similar plot of echo duration in Fig. 7 shows that, on the average, cells existing in groups last longer than isolated, single-cell echoes. Note that 99% of the single-cell echoes lasted less than 30 min. It is reasonable to expect from these characteristics that cells growing in groups should produce more rain than the isolated echoes. This is shown to be the case in Fig. 8.

At this point two interpretations could be advanced to explain the fact that the cells making up the composite echoes are larger, last longer and rain more than isolated single-cell echoes:

1) The larger, longer-lasting clouds have a higher probability of merging together into composite echoes but otherwise have the same properties as comparable individual echoes.

2) The clustering of clouds enhances their dynamics (maybe because of protection from entrainment) and in consequence clustered clouds are more vigorous than isolated ones.

If the first explanation is true, cells and isolated echoes of similar size should have the same mean duration, mean radar reflectivity, and should produce the same total amount of rain. Fig. 9 shows such a comparison for duration. All of the individual echoes lasted around 15 min, while the composite echo cells of comparable area lasted up to 90 min. Fig. 10 similarly shows that in general cells from groups have a greater rainfall rate than the individual echoes. Finally, Fig. 11 shows the comparison for total rain volume produced. As expected the cells produce more rain than their isolated counterparts.

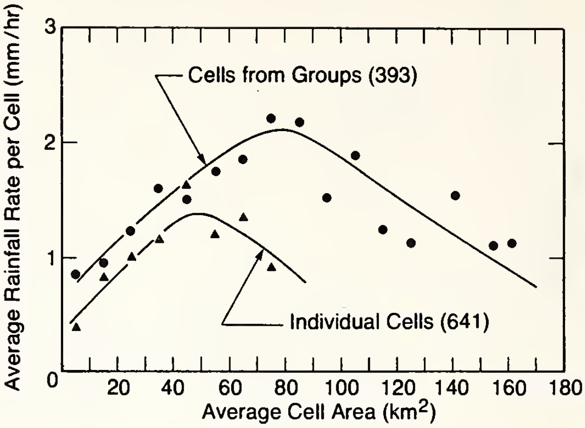

Fig. 10. As in Fig. 9 except for average rainfall.

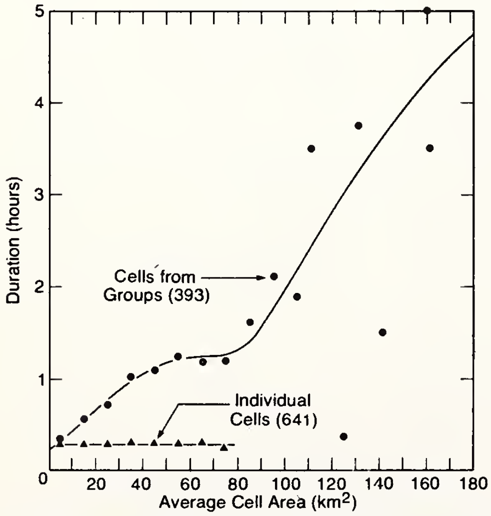

Fig. 9. Duration as a function of average area for the cells of composite (groups) and for single-cell (individual) echoes.

The evidence thus indicates that the second alternative might be correct: that clustering of convective cloud elements enhances their dynamics and produces echoes which are larger, last longer and are more intense, and as a result produce more rain than similar-sized convective elements developing in isolation from others. It is possible, however, that a larger cloud size increases the probability of merging with other, but the data points to a discernible enhancement of clustered convective elements.

4. Conclusions and further questions

The results presented in this paper for the intensive observational period of GATE indicate that, although they are in the minority, the largest 10%

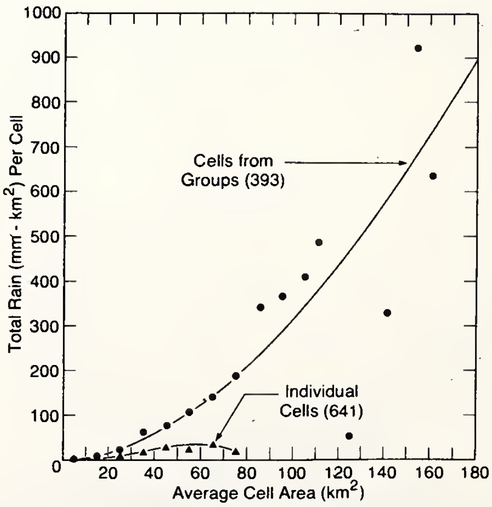

Fig. 11. As in Fig. 9 except for total rain.

of the echoes account for about 90% of the observed rainfall. These largest echoes can be classified as C (~100 to 10 000 km^2) and C–B (~10 000 to 50 000 km^2) scale. The C–B scale echoes usually correspond to squall lines, wide bands or widespread precipitation. In this investigation, the C–B scale echoes have not been considered; there are so few that their structure can be better analyzed from the case-study viewpoint (Houze, 1977). The present study has concentrated on the C-scale echoes which have average areas over their lifetime under 500 km^2.

The principal difference between the C-scale and the smaller, much more numerous D–scale echoes ($\lesssim$100 km^2) is the cellularity of the former. The C-scale echoes contain several maxima of radar reflectivity, while the smaller D-scale echoes never show signs of being composed of more than one. In the case of the C-scale echoes, several clustered cells go through their life cycles, with new ones forming to their side and older ones dissipating. The average size and duration of the composite echoes depend upon how many cells are found in the cluster at the same time and the total number appearing and dying during the lifetime of the composite echo. Since the size and duration distributions of the echoes are both log-normal, it is suggested that the composite echoes grow by a process that depends upon the size of the echo and on random factors.

The cells making up the composite echoes are related to individual convective elements which would probably be seen visually as cloud elements developing in a mass of growing and decaying cloud entities. It is possible that the convective cloud elements profit from their aggregation in that partial protection from entrainment of dry environmental air is achieved. This might be the reason for the fact that the cells making up the composite echoes are generally bigger, last longer and rain more than the single-celled echoes that correspond to relatively isolated clouds.

Two questions naturally arise:

- What is the mechanism by which new clouds form in close proximity to older ones?
- What conditions determine whether a single-celled or a composite echo forms?

In regard to the first question, it is usually argued that the evaporative downdrafts from raining clouds can induce the formation of new clouds. Actually, comparison of rainfall-versus-time with number-of-cells-versus-time curves for some of the composite echoes showed that, while the patterns are very similar, they can have a time lag of 30–45 min. Thus, pulses in rainfall along the lifetime of the echo were antecedent to the appearance of similar pulses in the number of cells. Unfortunately, however, most of the digital data in GATE were recorded every 15 min and it is difficult to get accurate growth curves for the composite echoes with that time resolution.

Some insight into the answer to the second question could probably be gained by the analysis of the initial conditions under which groups of cells start forming versus corresponding conditions for individual echoes. It could be that the initial arrangement, size, spacing, etc., of the first echoes are determining factors in the future development of composite echoes.

Answers to these questions could provide valuable information about the mechanisms of growth and formation of C-scale convective systems which could be useful both for the understanding of the role of cumulus clouds in the energetics of larger scale systems and for the modification and artificial stimulation of cloud conglomerate growth.

Acknowledgments. This work was supported by a grant from the U.S. GATE Project Office. Most of the data reduction was ably done by Miss Linda Crownover.

REFERENCES

Austin, P., 1977: Radar data quality. Report of the U.S. GATE Program Workshop, NSF/NOAA, 723 pp.

Biondini, R., 1976: Cloud motion and rainfall statistics. *J. Appl. Meteor.*, **15**, 1100–1111.

Houze, R. A., Jr., 1977: Structure and dynamics of a tropical squall-line system. *Mon. Wea. Rev.*, **105**, 1540–1567.

——, and C.-P. Cheng, 1977: Radar characteristics of tropical convection observed during GATE: mean properties and trends over the summer season. *Mon. Wea. Rev.*, **105**, 964–980.

Hudlow, M. D., 1975: Documentation for GATE *Oceanographer* radar raw digital data subset. Available from World Data Center, National Climatic Center, Asheville, NC, 50 pp.

López, R. E., 1976: Radar characteristics of the cloud populations of tropical disturbances in the northwest Atlantic. *Mon. Wea. Rev.*, **104**, 268–283.

——, 1977: The lognormal distribution and cumulus cloud populations. *Mon. Wea. Rev.*, **105**, 865–872.

Nasim, A. S., 1977: Study of the radar echo population of an eastern Atlantic tropical disturbance. M.S. thesis, Dept. of Physics, University of Puerto Rico, 67 pp.

Woodley, W. L., and R. N. Powell, 1970: Documentation and implications of the behavior of seeded cloud 17, May 30, 1968. ESSA Tech. Memo. ERL TM-AOML 6, 29 pp.

——, J. Simpson, A. H. Miller, J. J. Fernández-Partagás, and W. Riebasme, 1971: Florida cumulus seeding experiment for drought mitigation, April–May 1971. NOAA Tech. Memo. ERL OD 9, 160 pp.

Zipser, E. J., 1969: The role of organized unsaturated convective downdrafts in the structure and rapid decay of an equatorial disturbance. *J. Appl. Meteor.*, **8**, 799–814.

Journal of Applied Meteorology, 17: 1220-1224, August 1978.

Some Microphysical Properties of an Ice Cloud from Lidar Observation of Horizontally Oriented Crystals

C. M. R. PLATT[1]

Cooperative Institute for Research in Environmental Sciences, University of Colorado/NOAA, Boulder 80309

N. L. ABSHIRE AND G. T. MCNICE

Wave Propagation Laboratory, NOAA, Boulder 80302

(Manuscript received 28 November 1977, in final form 7 April 1978)

ABSTRACT

Lidar observations of a winter ice cloud in the zenith gave a very high reflection but a very small depolarization. When the lidar was tilted more than 0.5° away from the zenith, the reflection amplitude fell to 3% of it's zenith value, but the depolarization increased. The above properties proved unambiguously that reflection was occurring from the specular surfaces of horizontal crystals. These properties were used to estimate some cloud microphysical properties. At a selected time, the estimates gave a mean "diameter" of 74 μm for the horizontal faces, a crystal number density of $0.78\ \ell^{-1}$, and a maximum departure of the crystal axis from the horizontal of 0.5°. The fraction of the total crystal cross section which was specularly reflecting was estimated as unity.

1. Introduction

The depolarization ratio obtained from a linear polarized lidar pulse when reflected from a population of cloud particles has been shown to give a measure of cloud glaciation (Schotland *et al.*, 1971; Sassen, 1974) and possibly some information on cloud crystal habit (Sassen, 1977). Recently, Platt (1977) reported some very high-amplitude lidar reflections from a middle-level cloud when observed in the vertical, and an attendant low depolarization. Subsequently, these results were interpreted in terms of reflections from horizontally aligned hexagonal plate crystals (Platt, 1978; hereafter referred to as PI). In PI the backscatter properties of large, horizontally aligned plate crystals were analyzed. It was shown that information on the crystal number density, size and the quality of the crystals could be estimated provided that the change in the magnitude of the backscatter coefficient with angle near the zenith and the depolarization ratio were measured. In previous measurements (Platt, 1977), the lidar was not scanned away from the vertical, but the backscatter coefficients and depolarization ratios for vertical viewing were consistent with the above interpretation. It was apparent that reflections were occurring specularly from a few crystals in each pulse volume which happened to be correctly aligned. This would explain, quite simply, the low depolarization (Liou and Lahore, 1974; Chýlek, 1977) and high backscatter.

Subsequent to the work in PI, lidar observations were made on a winter ice cloud near Boulder, CO. When the lidar was scanned away from the vertical a dramatic decrease in lidar backscatter occurred. For a zenith angle of only 0.5° the backscatter decreased to about 3% of the zenith value. This fact, together with the high backscatter coefficients and low depolarization ratios observed in the zenith were strong evidence that the lidar was observing specular reflections from ice crystal plates with their long axes aligned in the horizontal. For if the lidar scan was at a zenith angle which was greater than the maximum angle of departure of the crystal long axes from the horizontal (the flutter angle) then all specularly reflected light would be directed away from the lidar receiver, and the receiver signal would indeed drop dramatically. For greater zenith angles the signal would be composed of light which had undergone multiple internal reflections within the crystals.

In this note the observations made near Boulder are described, together with estimates of the maximum angle of flutter of the crystals and their number densities and sizes.

2. Lidar and aircraft measurements

The lidar measurements were made with the WPL/ERL/NOAA monostatic lidar (Derr *et al.*, 1976), at a site about 8 mi north of Boulder. The lidar was pointed in the vertical and then scanned away from the vertical in small-angle increments. Calibrated values of the backscatter coefficient and the depolariza-

---

[1] On leave from CSIRO, Division of Atmospheric Physics, Aspendale, Victoria, 3195, Australia.

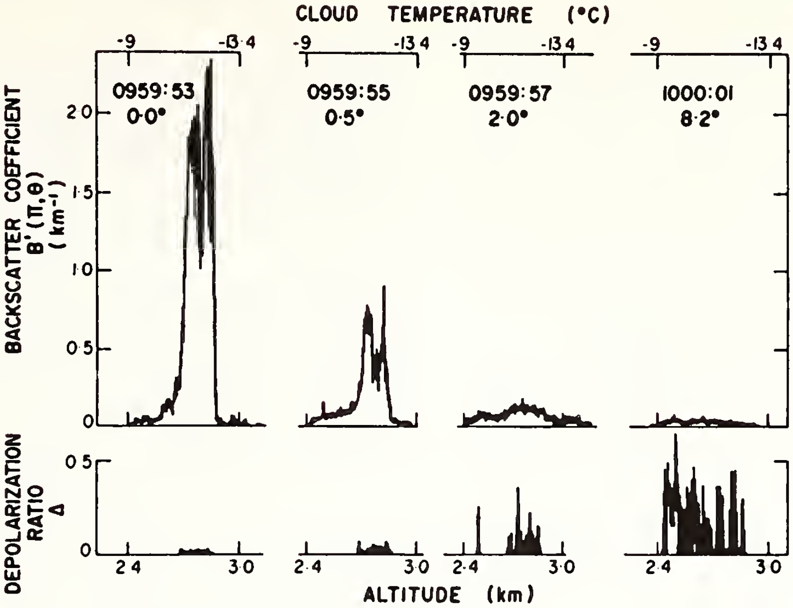

FIG. 1. Cloud backscatter coefficients $B'(\pi,\theta)$ and depolarization ratios for zenith angles of (a) 0.0°, (b) 0.5°, (c) 2.0° and (d) 8.2° at the times shown.

tion ratio and their variations with range were recorded for each angle. The scans were repeated at regular intervals.

An instrumented aircraft obtained simultaneous measurements of temperature versus altitude. Visual pilot observations indicated an ice cloud. A strong subsun was observed below the aircraft when flying in, or above, the cloud, which gave independent evidence of the presence of oriented crystals.

The cloud was observed on 24 January 1977. It was rather tenuous in nature and the ground was visible to the pilot through the cloud for most of the time.

A series of lidar returns are shown in Fig. 1. It is obvious, immediately, that the cloud returns have the characteristic features predicted for horizontal ice crystals. The reduction in backscatter for 0.5° zenith angle is quite large. For $\theta=2.0°$ the backscatter is an order of magnitude smaller. The depolarization ratio is seen to vary from about 0.01 at $\theta=0.0°$ to values in the region of 0.3 at $\theta=8.2°$. Two further cloud profiles taken in the vertical are shown in Figs. 2 and 3. The backscatter coefficient $B(\pi)$ is very high and the depolarization ratio is almost vanishingly small. These profiles were among the strongest recorded and are discussed later.

3. Discussion

Several lidar scans away from the vertical were made during the observation period, with the lidar being fired at small-angle increments. A convenient method of obtaining the relative intensity of backscatter at each zenith angle θ is to calculate $\gamma'(\pi,\theta)$, the integrated backscatter through the cloud,

$$\gamma'(\pi,\theta)=\int_{z_b}^{z_T} B'(\pi,\theta)dz, \qquad (1)$$

where it is understood that $B'(\pi,\theta)$ is the measured isotropic backscatter coefficient at angle θ and z_b and z_T are the cloud base and top, respectively. Attenuation of the pulse in the cloud causes $B'(\pi,\theta)$ to be less than its actual value $B(\pi,\theta)$. However, in this cloud there was evidence that attenuation was very low. First, pilot reports indicated a tenuous cloud, with the ground usually visible through the cloud. Second, the very high backscatter in Fig. 3 shows very little apparent attenuation toward cloud top, and the attenuation would be even smaller for the other cases with lower backscatter. The intensity $\gamma'(\pi,0)$ can be compared with $\gamma'(\pi,\theta)$ at zenith angle θ to estimate the maximum angle of crystal flutter $\delta\xi$. The ratio of $\gamma'(\pi,\theta)$ to $\gamma'(\pi,0)$ for angles near and at the zenith and for four separate lidar scans between 0930 and 1030 LT are shown in Fig. 4. A line of best fit was drawn by eye through unity ratio at zero zenith angle and the four other points. The horizontal broken line shows the typical value of $\gamma'(\pi,\theta)/\gamma'(\pi,0)$ found for angles $\geqslant 0.6°$. The value of θ at the intersection of the lines is defined here as the maximum angle of flutter $\delta\xi$. This definition gives $\delta\xi=0.56°$. However, 0.06° must be subtracted for the transmitter beamwidth, so that $\delta\xi\approx 0.5°$.

The number of crystals in the lidar pulse volume which are correctly aligned for specular reflection to the receiver is very sensitive to the maximum angle of crystal flutter, $\delta\xi$, assuming that the crystals' axes have two degrees of freedom of rotation about the horizontal. Signal "spikes" which are probably due

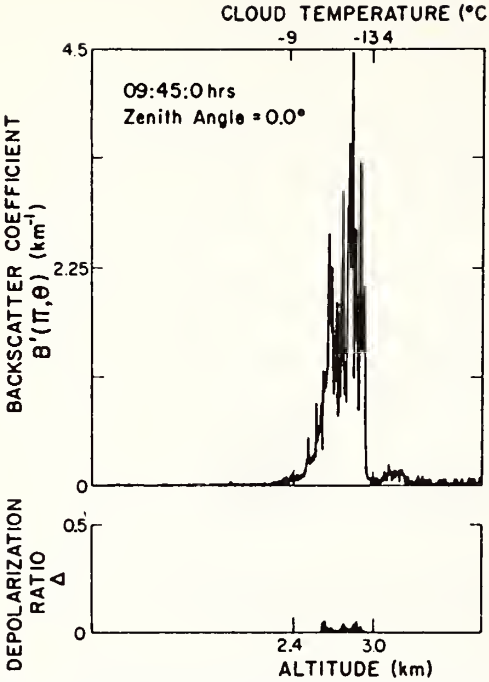

FIG. 2. Cloud backscatter coefficients and depolarization ratio profiles when the cloud was fairly homogeneous and showing single crystal "spikes."

to reflections from a single crystal are evident in the profiles of Figs. 1 (0.5°) and 2, near the cloud base. For a given lidar geometry, the backscatter coefficient of one "spike" will give a measure of the area of specular reflection from an individual crystal.

Toward the cloud centers, the large and fluctuating signal indicates that more than one reflection is being obtained in each pulse volume. An estimation of the average number in each volume can be made, leading to a cloud number density. Finally, for the cases of many reflections from each pulse volume, the average signal together with the estimated crystal diameters and angle of flutter, will give an estimate of the *fraction* of the total crystal cross-section which is specularly reflecting. The above aspects are considered separately below to give a tentative picture of the cloud microphysics at one time (Fig. 2).

The power returned to the receiver from a single crystal is given in PI as

$$P_R = P_0(2RA/z^2\delta\phi)[\exp(-2\tau_{\mathrm{atm}})], \qquad (2)$$

where P_0 is the transmitter power, A the crystal reflecting cross-section, z the range, $\delta\phi$ the solid angle of the transmitter beam, R the normal reflectivity of the crystal surface, and τ_{atm} the atmospheric optical depth at the laser wavelength between the cloud and the ground.

In terms of the backscatter coefficient $B(\pi)$, the return power is given by the standard lidar equation

$$P_R = P_0[c\Delta t A_1 B(\pi)/8\pi z^2] \exp(-2\tau_{\mathrm{atm}}), \qquad (3)$$

where c is the velocity of light, Δt the pulse duration and A_1 the receiver aperture. Combining Eqs. (2) and (3) will give the individual crystal area for a given measured maximum backscatter coefficient of the "spike" signal

$$A = (c\Delta t A_1 \delta\phi / 16\pi R) B(\pi). \qquad (4)$$

Values of A_1 and Δt for the NOAA lidar are shown in Table 1. Using these figures and $R = 0.02$ (PI) we obtain a value for A of 1.08×10^{-8} m^2 per unity backscatter coefficient (in km^{-1}). For simple hexagonal crystals we assume that the cross section is circular and thus a crystal radius can be defined. This radius is given for the NOAA lidar by

$$r = 59\sqrt{B(\pi)}\ \mu\mathrm{m}, \qquad (5)$$

where $B(\pi)$ is now in units per kilometer. In many cases, the spike signals in the pulse volume overlap. However, if we assume that the number of spike signals arising from a pulse volume is given by a statistical distribution about a mean value and we also ignore the small contribution to the signal by non-aligned crystals, then the mean backscatter coefficient will give a measure of the product of the number n of crystals and their backscatter coefficients $B(\pi)$. Further, the "noise" fluctuation level through the cloud (assuming a homogeneous cloud) compared to the mean signal will be related to n. Thus, assuming Poisson statistics, $n = (SN)^2$, where SN is the mean signal-to-noise ratio. It is apparent from many of the returns, i.e., Fig. 1 (0.5°) and Fig. 3 that the cloud is not homogeneous with altitude.

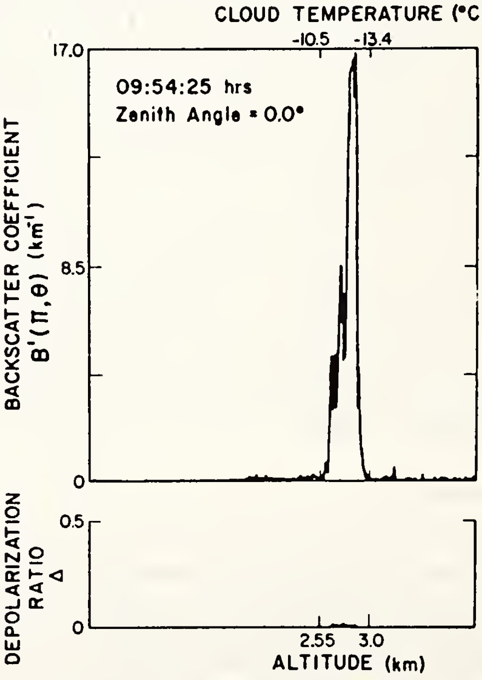

FIG. 3. Very high cloud backscatter coefficients and very low depolarization ratios. The angle of flutter may have decreased.

Also, the noise on the very weak signals at $\theta=2°$ and 8.2° in Fig. 1 is photon and instrumental noise rather than noise from signal spikes. However, Fig. 2 shows more uniform "noise" and at a level which is much greater than photon noise. The mean backscatter coefficient, defined here as $\gamma'(\pi)/h$, where h is the cloud depth, is ~ 2 km^{-1}. The rms "spike" noise is estimated by eye to be 0.9 km^{-1}. Thus, $\mathrm{SN}\approx 2.2$, from which $n\approx 4.8$. This indicates that each spike signal has a backscatter coefficient of 0.4 km^{-1}, on average. From Eq. (4), the radius of the crystal is 37 μm. The small spikes near the cloud base have a $B(\pi)$ of about 0.25 km^{-1}, yielding a crystal radius of 29 μm.

The number of crystals n_a optimally aligned in a lidar pulse volume is given in PI as

$$n_a=\pi n_0 l D^2(\delta\theta/8\delta\xi)^2, \tag{6}$$

where $\delta\theta$ is the transmitter beam angle ($<\delta\xi$), n_0 the crystal number density, l the pulse length and D the receiver diameter. The fundamental assumption in the derivation of this equation is that the main crystal axis is equally likely to take up any angle between horizontal and the angle $\delta\xi$ from the horizontal. Having obtained n_a, we can solve for n_0. For the lidar parameters of Table 1 and using $\delta\xi=0.5°$, $n_a=4.8$, (Fig. 2) we obtain $n_0\approx 0.8$ crystals l^{-1}.

Expressions for mean values of $B(\pi)_{\parallel}$ and $B(\pi)_{\perp}$ for the case where there are many overlapping spike signals in each pulse volume were also derived in PI. $B(\pi)_{\parallel}$ and $B(\pi)_{\perp}$ are backscatter coefficients for radiation returned in the same polarization plane as the transmitter beam and in the orthogonal plane respectively. [Also, $B(\pi)=B(\pi)_{\parallel}+B(\pi)_{\perp}$.] The model assumes a mixture of anisotropic imperfect crystals for which $B(\pi)_{\parallel}=B(\pi)_{\perp}$ and perfectly reflecting crystals for which $B(\pi)_{\perp}=0$:

$$\left.\begin{aligned} B(\pi)_{\parallel}&=(n_0\pi d^2)[0.01f/(\delta\xi(1+2R))+0.25(1-f)] \\ B(\pi)_{\perp}&=(n_0\pi d^2/4)(0.25(1-f)) \end{aligned}\right\}, \tag{7}$$

where d is the crystal diameter and f the fraction of the total number of crystals which are specularly reflecting. Using $B(\pi)=2$ km^{-1}, $n_0=0.8^{-1}$, $d=74$ μm, we obtain $f\approx 1.0$. That the value of f equals unity is completely fortuitous. However, it might indicate that the crystals in the cloud were mostly well-formed hexagonal crystals. The temperature range in the cloud was from about -9 to -13°C, a range in which hexagonal crystals form, but without dendritic growth. Thus, it could be expected that many of the crystals would be perfectly formed. Finally, we consider Fig. 3. The mean backscatter coefficient is 7 km^{-1} and for the top part of the cloud it increases to 16 km^{-1}. The mean value is 3.5 times that in Fig. 2. If this increase was due to a growth in crystal *size* then *both* signal and noise would increase by 3.5, and the SN would still be 2.2. In fact just the opposite appears to have occurred and $\mathrm{SN}\approx 7$, so that $n_a\approx 49$. However, it is also possible that the maximum angle of flutter was less at 0954 than it had been at 0945. This would have the apparent effect of increasing both n_a and SN. The flutter angle was not measured at the time that Fig. 4 was obtained.

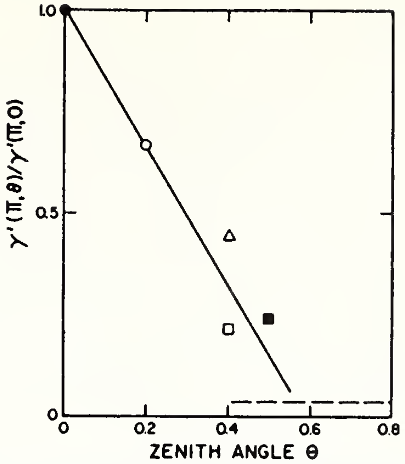

Fig. 4. The dependence of the integrated backscatter on the zenith angle, normalized to unity at $\theta=0.0$.

Table 1. WPL/ERL/NOAA lidar characteristics.

Transmitter	
Type	Pulsed ruby laser
Energy	2 J
Pulse length	30 ns
Beam divergence	1 mrad
Receiver	
Type	Newtonian
Area	1.54 m²
Field of view	3 mrad
Polarizer	Polaroid
Electronic time-gate	60 ns

In summary, we can estimate the cloud properties of Fig. 2 as follows:

Cloud-base altitude $=2.4$ km
Cloud-top altitude $=3.0$ km
Temperature range $=-9$ to -13°C
Number density $=0.8$ l^{-1}
Mean crystal diameter $=74$ μm
Average backscatter coefficient $=2$ km^{-1}
Maximum angle of departure of long axis of crystal from horizontal $=0.5°$
Fraction of total crystal cross section which is specularly reflecting ~ 1

The cloud at the time of Fig. 3 (9 min later) would be expected to have the same properties, except that n_0 has increased to ~ 8 l^{-1}.

4. Conclusion

The angular properties of the lidar backscatter from the observed cloud prove rather conclusively that ice crystals with their large axes oriented in the horizontal were being observed. These properties are similar to those predicted in PI. Although the calculations presented here are necessarily very tentative, they indicate the type of information on the cloud microstructure which might be obtained. By tailoring the lidar geometry (e.g., using a very narrow transmitting beam), single crystal reflections from a pulse volume could be observed, and their radii could be deduced.

Signal "spikes" were first noted by Schotland *et al.* (1971) in a laboratory experiment. They concluded also that the signals originated from reflections off crystal planar surfaces. Sassen (1977) subsequently demonstrated that the crystal diameters calculated from spike signals compared favorably with the diameters measured directly. Sassen used a continuous laser which measured the spike amplitudes and numbers as the crystals traveled through the laser beam. The lidar pulse method selects a volume of cloud and measures the number of spikes and their amplitudes at one single time.

The large backscatter coefficients of Figs. 1–3 are further evidence that specular reflections are being observed. The calculated value of $\gamma'(\pi)$ in Fig. 3 was 2.78, which is much greater than that measured for cirrus clouds (Platt, 1973) and compares with the value of 7.6 obtained by Platt (1977a) from an altostratus cloud layer. For that cloud it was also suspected that the layer might be composed of horizontally oriented crystals as the depolarization was also low but no scans away from the vertical were made.

The presence of preferred orientation in ice crystal clouds has, of course, been known for many years from the large variety of optical effects obtained when the clouds are illuminated by the sun. However, it is apparent that lidar measurements can give more definitive information on crystal orientation and on the cloud microstructure.

Acknowledgments. One of the authors (C. M. R. Platt) is indebted to CIRES for a Visiting Fellowship, to Dr. V. E. Derr and his atmospheric spectroscopy group for the use of data taken with the NOAA lidar, for the excellent data reduction facilities and for much help and encouragement.

REFERENCES

Chýlek, P., 1977: Depolarization of electromagnetic radiation scattered by non-spherical particles. *J. Opt. Soc. Amer.*, 67, 175–178.

Derr, V. E., N. L. Abshire, R. E. Cupp and G. T. McNice, 1976: Depolarization of lidar reforms from virga and source cloud. *J. Appl. Meteor.*, 15, 1200–1203.

Liou, Kuo-Nan, and H. Lahore, 1974: Laser sensing of cloud composition: A backscattered depolarization technique. *J. Appl. Meteor.*, 13, 257–263.

Platt, C. M. R., 1973: Lidar and radiometer observations of cirrus clouds. *J. Atmos. Sci.*, 30, 1191–1204.

——, 1977: Lidar observation of a mixed-phase altostratus cloud. *J. Appl. Meteor.*, 16, 339–345.

——, 1978: Lidar backscatter from horizontal ice crystal plates. *J. Appl. Meteor.*, 17, 482–488.

Sassen, K., 1974: Depolarization of laser light backscattered by artificial clouds. *J. Appl. Meteor.*, 13, 923–933.

——, 1977: Ice Crystal habit discrimination with the optical backscatter depolarization technique. *J. Appl. Meteor.*, 16, 425–431.

Schotland, R. M., K. Sassen and R. Stone, 1971: Observations by lidar of linear depolarization ratios for hydrometers. *J. Appl. Meteor.*, 10, 1011-1017.

Journal of Applied Meteorology, 17: 482-488, April 1978.

Lidar Backscatter from Horizontal Ice Crystal Plates

C. M. R. PLATT[1]

Cooperative Institute for Research in Environmental Sciences, University of Colorado/NOAA, Boulder, Colo. 80309

(Manuscript received 7 November 1977, in final form 4 January 1978)

ABSTRACT

Some unusual lidar returns from an altostratus cloud are interpreted in terms of reflections from hexagonal ice plates falling with their long axes aligned in the horizontal. Such an explanation is consistent with the observed high backscatter coefficients and low depolarization ratios and also with the temperature range (−12 to −20°C) of the cloud layers, as well as the known fall characteristics of naturally occurring ice platelets. Backscatter efficiencies are calculated for "perfect" ice platelets when illuminated at or near an axis orthogonal to the crystal long axis. It is shown that very high backscatter coefficients can potentially be measured from a cloud of ice plates, depending on the fraction of crystals which are "perfect," the degree to which the plates' long axes stay horizontal, and the angle of the lidar to the vertical.

It is further shown that reflection from a single crystal gives an appreciable signal-to-noise ratio at the receiver and that only a few crystals will be correctly aligned in the horizontal in a typical laser pulse volume, and for realistic particle number densities.

1. Introduction

Lidar observations made on an altostratus cloud on 9 August 1975 revealed a layered structure possessing variable optical properties (Platt, 1977). The topmost layer was characterized by very high backscatter coefficients and an apparent large backscatter to extinction ratio. At the same time, the measured depolarization ratio was generally in the range from 0.03 to 0.05, except near the bottom of the layer. Because of these characteristics, the cloud layer was interpreted as composed of small droplets; however, it was pointed out then that an alternative explanation could be that the strong backscatter and low depolarization could occur from horizontally oriented hexagonal ice plates. If such an explanation were true, then the backscatter characteristics would give a means of identifying the cloud as an ice cloud in a certain phase of development, and could be used for such identification. Previous work (Schotland *et al.*, 1971; Sassen, 1974; Derr *et al.*, 1976) has revealed quite a wide range of depolarization ratios from ice clouds, with a characteristic value of about 0.4 for hexagonal ice columns and bullets, and high values, often greater than unity, from virga at the base of storm clouds. It thus seems that depolarization measurements on mixed phase clouds may give information not only on the particle phase (Sassen, 1974), but also on the *type* of ice crystal and its evolution. The suggestion that ice plates can give a unique lidar signature is explored further in this note.

2. Growth and fall characteristics of hexagonal ice plates

The temperature range from −8 to −25°C is one in which ice crystals grow as hexagonal plates. In the range from −12 to −15°C where the greatest growth rate occurs, dendritic plate crystals may also form (Mason, 1968), although these require a water-saturated environment. Initially, a plate grows in three dimensions, until its short axis is about 50 μm. At this point, the long axis is about 1200 μm and any further growth occurs mainly along this axis (Ono, 1969). When the crystal obtains sufficient fall velocity, the ventilation around the crystal will favor water supersaturation near the edges of the plates, which will cause dendritic growth. According to Ono, the rate of dendritic growth accelerates rapidly as the crystal diameter increases from 200 to 400 μm. If plate crystals are present in a cloud of mixed phase, then attachment of small frozen drops (riming) will occur when the crystal diameter is greater than about 400 μm. In Ono's measurements in natural clouds, the size distribution of plates had a rather sharp peak in the 200-400 μm diameter region. Crystals with diameters less than 100 μm and greater than 400 μm were rare.

The fallspeed of plates increases with increasing diameter, but for diameters >100 μm, the fall velocity is independent of diameter and is about 35 cm s^{-1} (Fletcher, 1962). Jayaweera and Mason (1965) studied the behavior of freely falling discs and columns in a viscous fluid. For Reynolds numbers ($\mathrm{Re}=vd/\nu$, where v is fall velocity, d crystal diameter and ν kinetic viscosity) less than 0.01 (very small crystals), the discs

---

[1] On leave from CSIRO, Division of Atmospheric Physics, Aspendale, Australia.

0021-8952/78/0482-0488$05.00
© 1978 American Meteorological Society

had no preferred orientation. For 0.01 Re<0.1 the discs oriented themselves to offer maximum resistance to motion, i.e., the long axis horizontal. They remained oriented and fell with a steady motion until $\mathrm{Re}\geqslant 50$. At this point, a persistent fluttering occurred. At a temperature of −20°C and pressure of ~330 mb, Re varies between 0.07 for a 10 μm diameter crystal to 14 for a 2000 μm crystal. Thus most plate crystals in the atmosphere should fall with their long axes horizontal. Strong evidence for this fall characteristic of plates in the real atmosphere is provided by Ono's observations of the riming pattern of plate crystals (Ono, 1969). For dendrites, however, some oscillation or flutter apparently occurred.

3. Backscatter characteristics of ice plates

Generally, the crystal dimension for the long axis is much greater than the laser wavelength (0.69 μm for ruby laser). In that case, light is backscattered either as a specular reflection from the front and back surfaces of the crystal or as a skew reflection and refraction involving the front, side and back surfaces. If a plate is falling with its long axis horizontal, it will cause only a specular reflection to a vertically pointing lidar. If the lidar is pointing *away* from the vertical, only skew rays backscattered through internal reflections will be observed.

Consider a parallel-sided plate illuminated as illustrated in Fig. 1. As ice is nearly transparent at visible wavelengths, then light will be reflected from the front and back surfaces in nearly equal amounts. As the reflectance of ice is small, contributions from further internal reflections will be negligible. Suppose that an amplitude of light a is reflected from each crystal surface. If the surfaces are plane parallel and the ice is homogeneous, then interference between the beams from the two surfaces can occur. Thus the reflected amplitude will be $2a\cos(\delta/2)$ where $\delta=2\pi t\sec\theta/\lambda$ and t is the crystal thickness, θ the angle of incidence and λ the wavelength. The normal reflected intensity I will be

$$I=4a^2\cos^2\delta/2. \tag{1}$$

Thus the reflected intensity will go through maxima and zero as t or θ change.

It is not clear from past work as to whether ice crystal plates in the atmosphere have sufficiently plane parallel surfaces or are sufficiently homogeneous to give interference effects. The work of Sassen (1977) indicates that interference probably does not occur. In that case the reflected intensities would add incoherently from the two surfaces to give a total intensity of $2a^2$. In the analysis that follows, this latter case is assumed.

The volume sampled by a lidar pulse typically contains many thousands of cloud particles. However, in a natural cloud, it can be anticipated that horizontal-falling ice plates will possess some degree of "flutter" about the horizontal, caused by small-scale turbulence, larger scale eddies, wind shear, or riming and dendritic growth (Jayaweera and Mason, 1966). In this case, only those crystals correctly oriented in the horizontal will give specular reflection to a lidar receiver, and it is not obvious that there will be many such crystals. However, we consider first the hypothetical case where the transmitter pulse volume does contain sufficient correctly aligned crystals to enable us to define an average backscatter efficiency per crystal, and to average out interference effects if they are indeed occurring. We shall subsequently calculate the probable number of correctly aligned crystals in a typical lidar pulse volume and the signal from each such crystal.

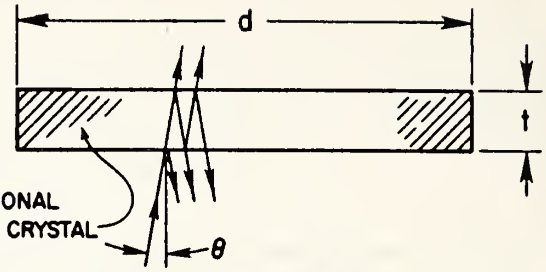

Fig. 1. Multiple reflections from a plate crystal.

The lidar backscatter intensity at the receiver will depend on the number of crystals in the pulse volume, the crystal diameters, and the angles of departure of the crystal long axes from the horizontal. For an ensemble of crystals which are taking up every possible angle between the horizontal and some maximum angle of displacement $\delta\xi$, only those crystals which are normal to the incident laser beam will reflect radiation specularly back to the receiver. More accurately, those crystals displaced through an angle $<\delta\psi$ from the horizontal will reflect back to the receiver, where $\delta\psi$ is half the angle subtended by the receiver aperture. Now, as $\delta\xi$ increases, the probability of a crystal being favorably oriented diminishes. Without an exact knowledge of the motion of the crystal long axes as they "flutter" about a horizontal plane, the probability of favorable orientation cannot be predicted accurately. However, if the angles of flutter are very small, the crystals would not experience any great rotational accelerations, so that to a good approximation it can be argued that all angles of the crystal long axis between horizontal and maximum angle of flutter are equally likely. Further, it is assumed that the planes of rotation of the crystals are randomly oriented in the horizontal.

Now the angle through which the long axis rotates during one complete flutter is $2\delta\xi$, so that radiation is reflected away from the vertical within an angle of $4\delta\xi$. If the solid angle around the angle $4\delta\xi$ is $\delta\Omega$, then for a large ensemble of crystals within the transmitter pulse volume the average backscatter cross section J_b per unit steradian is given by

$$J_b=2RA/\delta\Omega, \tag{2}$$

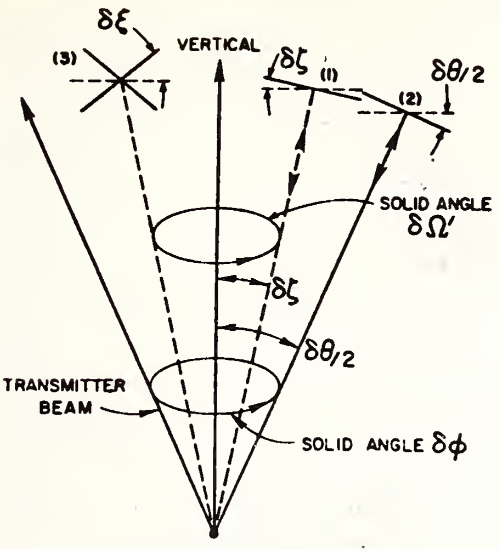

FIG. 2. Schematic of transmitter beam. Crystal (1): maximum angle of flutter $\delta\xi=\delta\zeta$, $\delta\zeta<\delta\theta/2$; reflection to receiver only within cone, solid angle $\delta\Omega'$. Crystal (2): maximum angle of flutter $\delta\xi=\frac{1}{2}\delta\theta$; reflection to receiver anywhere in cone $\delta\phi$. Crystal (3): maximum angle of flutter $\delta\xi>\frac{1}{2}\delta\theta$; reflection to receiver anywhere in cone.

where A is the cross-section area of the crystal presented to the lidar radiation and R the normal reflectance of the crystal surfaces. As it is assumed that radiation is reflected incoherently from the back and front surfaces, the total reflection is $2R$. The refractive index of ice at about 0.7 μm is 1.31 so that R is 0.02.

Referring to Fig. 2 we distinguish between two cases, depending on whether the angle of flutter $\delta\xi$ is greater or less than $\delta\theta/2$, where $\delta\theta$ is the angle defining the transmitter beam. First, let $\delta\xi\leqslant\delta\theta/2$. We assume that the lidar transmitter and receiver axes are coaxial and aligned together exactly in the vertical. (Typically, $\delta\theta$ is from 0.5 to 2 mrad and the receiver angle $\delta\psi$ is set larger than $\delta\theta$.) Only those crystals in the transmitter beam which lie within a cone of angle $\delta\xi$ ($=\delta\zeta$, say) to the vertical will be capable of reflection to the receiver. We therefore define an *effective* cross section

$$J_b(e)=[2RA/\delta\Omega][\delta\Omega'/\delta\phi],$$

where $\delta\Omega'$ is the solid angle containing the angle $\delta\zeta$, and $\delta\phi$ the solid angle of the transmitter beam. Now as $\delta\xi=\delta\zeta$, then $\delta\Omega'=\pi\delta\xi^2$ (for small angle $\delta\xi$). But $\delta\Omega=4\pi\delta\xi^2=4\delta\Omega'$ so that

$$J_b(e)=2RA/4\delta\phi. \tag{3}$$

Also since $\delta\phi=\pi\delta\theta^2/4$ ($\delta\theta\ll1$),

$$J_b(e)=2RA/\pi\delta\theta^2. \tag{4}$$

The backscatter efficiency $q(\pi)$ can be defined as the backscatter cross section per steradian divided by the geometrical cross section. Thus

$$q(\pi)=2R/\pi\delta\theta^2[\text{sr}^{-1}]. \tag{5}$$

The extinction efficiency q_e is defined in a similar manner. The extinction cross section J_e of the crystals is composed of $2RA$ for reflection (entirely in the back direction) and $\sim A$ for diffraction, so that $J_e=A(1+2R)$ and $q_e=1+2R$. The backscatter-to-extinction ratio k is then defined as $4\pi q(\pi)/q_e$, so that

$$k=8R/\delta\theta^2(1+2R). \tag{6}$$

The values of $q(\pi)$ and k are seen to be independent of the angle of flutter $\delta\xi$.

The second case occurs if $\delta\xi>\delta\theta/2$. As the solid angle $\delta\Omega$ in Eq. (2) is equal to $4\pi\delta\xi^2$, then

$$k=2R/\delta\xi^2(1+2R). \tag{7}$$

To summarize, if the flutter $\delta\xi$ is less than $\delta\theta/2$, then k is constant, but if $\delta\xi$ becomes greater than $\delta\theta/2$, k decreases as $\delta\xi^2$. This dependence on $\delta\xi$ is shown in Fig. 3, which shows that k is very large for small $\delta\xi$. For comparison, the value of k is 0.65 for a model water cloud (Deirmendjian, 1964) and about 0.3 for a cirrus ice cloud (Platt, 1973). Clearly, the backscatter enhancement from near-horizontally aligned plates is potentially very large.

The above treatment predicts the average backscatter characteristics for a large number of randomly oriented crystals. It is obviously important to determine how many of such crystals are favorably aligned for reflection to the receiver in a typical transmitter volume and in a cloud containing a realistic number of plate crystals. The number will depend on the transmitter beam angle $\delta\theta$ and the depth of cloud l which is illuminated. The illuminated volume V is given by

$$V=\pi z^2\delta\theta^2 l/4, \tag{8}$$

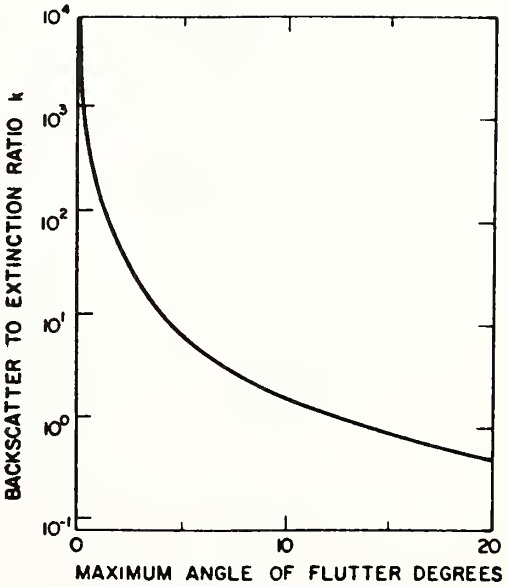

FIG. 3. Dependence of average backscatter to extinction ratio k per crystal on angle of flutter $\delta\xi$ for a laser pulse volume containing many aligned crystals.

where z is the range (altitude). When $\delta\xi < \delta\theta/2$ then the probability $P(\delta\xi)$ of correct alignment is given by

$$P(\delta\xi) = D^2/4z^2\delta\theta^2, \tag{9}$$

where D is the receiver diameter. The number of aligned crystals n_a in the volume V is thus given by

$$n_a = n_0 V P(\delta\xi) = \pi n_0 l D^2/16, \tag{10}$$

where n_0 is the number of crystals per unit volume.

If $\delta\xi > \delta\theta/2$, then

$$n_a = n_0 l D^2 (\delta\theta/8\delta\xi)^2. \tag{11}$$

The number of ice crystals in clouds in the temperature range from −12 to −20°C ranges from about 1 to 100 l^{-1} (Mossop, 1968; Heymsfield, 1977). The predicted number n_a of aligned crystals from Eq. (11) is shown in Table 1 for different values of $\delta\xi$ and $n_0 = 10\, l^{-1}$, $D = 0.3$ m, $l = 3$ m (pulse length of 20 ns), $\delta\theta = 0.002$ rad. The factor f gives the proportion of crystals in the cloud which have "perfect" surfaces (see Section 5). It is apparent that for any angle of flutter greater than about 1°, the probable number of crystals which are aligned correctly becomes less than unity.

Thus, for cases of low number density and where only small height increments in a cloud are being examined, the former treatment of obtaining an average backscatter efficiency may not be valid. Even for a homogeneous cloud, the backscatter could fluctuate considerably from one pulse volume to the next. It is thus pertinent to ask whether the reflection from a single "perfect" crystal in the pulse volume would give sufficient photons at the receiver to be detected with a good signal-to-noise ratio.

If P_0 is the laser power, then the power P_i incident on a crystal of area A at range z is given by

$$P_i = P_0 A / z^2 \delta\phi, \tag{12}$$

where $\delta\phi$ is the solid angle of the transmitter beam. As the angle subtended by a crystal surface at a given range from the transmitter is much less than the angle subtended by the receiver aperture at the same range, all the radiation which is reflected back by a favorably aligned planar crystal will enter the receiver. Thus the power P_R returned at the receiver will be simply equal to $2RP_i$ or

$$P_R = 0.04 P_0 A / z^2 \delta\phi, \tag{13}$$

where the reflectance at the crystal is $2R$.

TABLE 1. Number of crystals n_a oriented to give a reflection at the lidar receiver. Lidar pulse length = 20 ns, $\delta\xi$ = angle of flutter, f = fraction of "perfect" crystals.

$\delta\xi$ (deg)	f 0.2	0.4	0.6	0.8	1.0
0.1	34.81	69.61	104.42	139.23	174.04
0.5	1.39	2.78	4.18	5.57	6.96
1	0.35	0.70	1.04	1.39	1.74
2	0.087	0.17	0.26	0.35	0.43
4	0.022	0.044	0.065	0.087	0.11
6	0.0097	0.019	0.029	0.039	0.048
8	0.0054	0.011	0.016	0.022	0.072
10	0.0035	0.0070	0.010	0.014	0.017

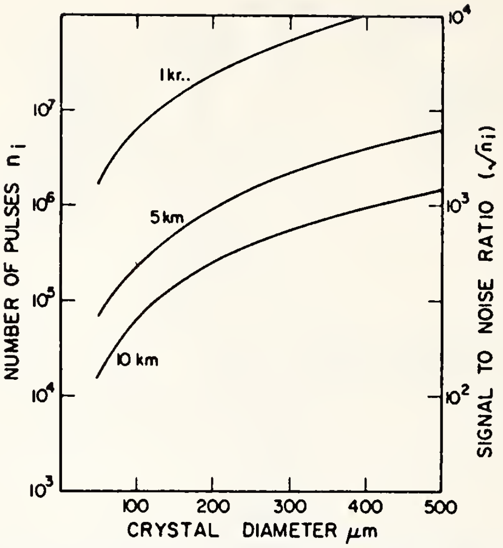

FIG. 4. Number of photons received from a single crystal reflection for various ranges versus crystal diameter.

The number of photons n_R returned within the pulse time τ is

$$n_R = G P_R \tau, \tag{14}$$

where G is the ratio of photon number n_R to energy at the lidar wavelength. The number of electron pulses counted at the output of the receiver photomultiplier is

$$n_i = q \epsilon n_R, \tag{15}$$

where q is the photomultiplier quantum efficiency and ϵ the optical efficiency.

Fig. 4 shows n_i for different ranges and crystal diameters. Clearly, the signal recorded from a single crystal is quite large. The signal to noise ratio for each pulse is equal to $n_i^{\frac{1}{2}}$. The signal from a cloud of some depth, containing many lidar pulse lengths, will thus tend to fluctuate with range, the individual crystal pulses being dependent on the crystal size. If the interference effect given by (1) does occur it introduces an additional variable into the single crystal reflection amplitude.

4. Depolarization characteristics of ice plates

Liou and Lahore (1974) have studied theoretically the depolarization from hexagonal platelets. For normal reflection on the surface parallel to the long axis, the depolarization is predicted to be zero. As radiation returns to the receiver only *via* a normal reflection, the depolarization ratio for horizontal, or near horizontal,

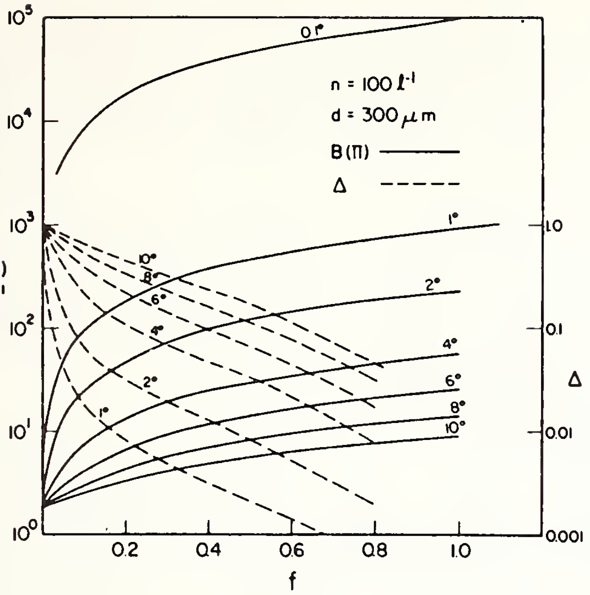

FIG. 5. Dependence of $B(\pi)_{\parallel}$ and Δ on angle of flutter $\delta\xi$ and factor f (see text).

platelets will be zero. Only if fluttering causes large departures of the crystal surfaces from the horizontal will reflections from skew rays start to give appreciable depolarization (and backscatter).

5. Model of lidar backscatter from natural clouds containing ice plates

Even if optimum conditions exist for hexagonal plate growth, there is unlikely to be a complete population of perfect plates in a natural cloud. Dendritic growth, riming and shattering can cause the scattering in the back direction to be partly non-specular. Thus lidar backscatter will be determined by both the quality of the crystals and their orientations. On the other hand, for small departures from the horizontal, the depolarization will be affected by the crystal quality only.

To illustrate these effects, we consider a simple model. This assumes that 1) a fraction $(1-f)$ of the crystals are "imperfect," i.e., they exhibit isotropic scattering and a depolarization ratio of unity (the value of k in each polarization is then 0.25); and 2) a fraction f of the crystals have perfect crystal faces, giving a depolarization ratio of zero. The crystals are assumed to have a circular cross section of diameter d. We consider the case when $B(\pi)_{\parallel}$ is integrated sufficiently in height to smooth any fluctuations to give a mean $B(\pi)_{\parallel}$. The backscatter coefficients for the two polarizations are then given by

$$B(\pi)_{\parallel}=(n_0q_e\pi d^2/4)[2fR/\delta\xi^2(1+2R)+0.25(1-f)], \quad (16)$$

$$B(\pi)_{\perp}=(n_0q_e\pi d^2/4)[0.25(1-f)], \quad (17)$$

where q_e is the extinction efficiency $(=1.04\approx 1)$. Also,

$$\Delta=B(\pi)_{\perp}/(B\pi)_{\parallel}. \quad (18)$$

The dependence of $B(\pi)_{\parallel}$ and Δ on f and $\delta\xi$ for one value of n_0 and d is shown in Fig. 5. As f increases, more crystals are available for reflection and $B(\pi)_{\parallel}$ increases. At the same time, the depolarized component decreases. The model forces the depolarization ratio to zero when $f=1$, which may not be exactly correct for real hexagonal crystals. It implies that Δ will be extremely small if $\delta\xi\approx 0.1°$, even if f is small. At the other extreme, Δ is forced to unity when $f=0$. Again, this may not be correct in clouds of "imperfect" crystals, where Δ may be less than unity, as in the case for cirrus clouds. However, the model does illustrate that Δ could rapidly become small with the appearance of horizontal plate crystals, even if they comprise only a small fraction of the total crystal population. The model also gives a "sensible" value of $B(\pi)_{\parallel}$ ($\sim$2 km^{-1}) for the case when $f=0$, although of course $B(\pi)_{\parallel}$ is dependent on both n_0 and the crystal diameter.

6. Comparison with observations

Several laboratory studies have been made which are relevant to the present topic. In these studies, depolarization in backscattering from ice crystals formed in a cold chamber was measured with continuous He–Ne lasers. Schotland *et al.* (1971) observed intensity spikes in the amplitude of the backscatter, which repeated over short periods of time. These spikes were observed mainly in the parallel polarization return; the spikes were interpreted as being specular reflections from the faces of the crystals and, qualitatively, they exhibited low depolarization. A further investigation by Sassen (1974) confirmed these results and he established that most backscatter from platelets was due to specular reflections from the crystal surfaces, and depolarization in the spike events was no more than a few percent. Liou and Lahore performed a similar experiment. Although spiking events were not so obvious, they were observing crystals in the horizontal plane, so that spiking would be mainly absent for horizontally aligned crystals.

A vertical lidar return from the altostratus cloud observed by Platt (1977) is shown in Fig. 6. The value of depolarization ratio Δ from 4.2 to 4.6 km altitude was $\sim$0.4, which is the figure often observed in cirrus clouds of columnar crystals. The maximum observed backscatter coefficient of 1 km^{-1} is also rather typical of cirrus. Above 4.6 km, there is an increase of about a factor of 5–10 in backscatter coefficient, whereas the depolarization ratio falls gradually to about 0.04. The backscatter figures are affected by attenuation of the laser pulse by the lower ice layer, predicted to be at least 0.5 (Platt, 1977). Thus the maximum values of $B(\pi)_{\parallel}$ are at least 12 km^{-1} and the integrated backscatter is about 6 which is much higher than the typical

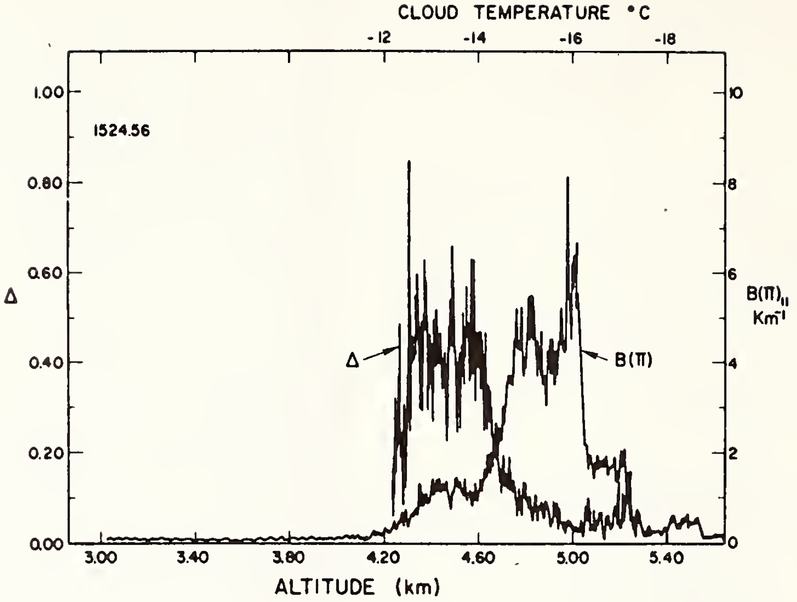

Fig. 6. Profile of $B(\pi)_{\parallel}$ and Δ obtained from an altostratus cloud with a vertical pointing calibrated lidar on 9 August 1975 (Platt, 1977).

value of ~ 0.4 measured in cirrus. The above characteristics are consistent with the backscatter from this layer being caused, at least partially, by reflections from ice crystal plates. The air temperatures in the layer are also optimum for growth of ice plates. The behavior of $B(\pi)_{\parallel}$ and Δ at the bottom of the layer is consistent, at least qualitatively, with the decrease of available plate surfaces and a growth of irregular crystals. From Fig. 5, a change in Δ from 0.04 to 0.4 corresponds, for $\delta\xi = 2$ for instance, to a change in $B(\pi)_{\parallel}$ from 40 to about 6 km^{-1}. By postulating that the crystal density is 25 l^{-1}, then $B(\pi)_{\parallel}$ changes from 10 to 1.5 km^{-1}, which is in rough agreement with Fig. 5 when attenuation by the lower layer is included. The corresponding number of aligned crystals in each pulse volume for $B(\pi)_{\parallel} = 10$ km^{-1} ($f = 0.16$, $\delta\xi = 2.0$, $\eta_0 = 25$ l^{-1}) is about 0.22. However, in the lidar experiment the height intervals were integrated over 100 ns, so that the average number n in ~ 15 m is predicted to be 1.1. The signal-to-noise ratio of fluctuations in the cloud profile would be $\sim n^{\frac{1}{2}} \approx 1$. Fluctuations with range do occur in the values of $B(\pi)_{\parallel}$ in Fig. 6 and these are also evident in earlier profiles (Platt, 1977), but they would indicate a signal-to-noise ratio of about 3, or 9 crystals per 15 meters. An unknown in the calculation of n is whether the crystal population is composed of fully "perfect" and "imperfect" crystals as implied in Table 1, or whether each crystal is "perfect" with a proportion $(1-f)$ of imperfect area. In the latter case, f is effectively unity in Table 1, and for the above example, the number of particles in each volume will be ~ 5 per 15 meters.

The above discussion shows qualitative agreement between Fig. 6 and theory, but the angle $\delta\xi$ was not known so it is hard to carry the comparison any further. This angle could be measured by scanning the lidar away from the vertical and noting any dramatic decrease in backscatter.

7. Conclusions

The calculations in this article have shown that large backscatter is possible from horizontally oriented ice crystals using a vertical pointing lidar. They also give the important result that the depolarization ratio from an *ice* cloud may be only a few percent. Thus low depolarization ratios from middle level clouds must be treated with caution.

Values of $B(\pi)_{\parallel}$ and Δ measured in an altostratus cloud layer agree qualitatively with a simple model in which the crystal population is composed of a fraction f of perfect crystal faces and a fraction $(1-f)$ of imperfect faces. It has also been shown that only a few crystals in each laser pulse volume are needed to give a large signal at a receiver. Calculations using realistic crystal numbers measured in actual clouds indicate that the signal could fluctuate considerably from one pulse volume to the next, even for a homogeneous cloud. Such fluctuations were observed in the altostratus cloud.

Given a reasonably horizontal homogeneous cloud layer, information on the nature of the crystal population, the presence of horizontal ice crystals and their maximum flutter could be obtained by scanning a lidar away from the vertical. Information could then be obtained on crystal numbers and even size, although the latter would be complicated by the predicted interference effect. Also, determination of the crystal number would require direct sampling of crystals to determine the degree of riming, dendritic growth and shattering. Finally, it should be pointed out that if crystals are falling with their long axes very close to the horizontal then a lidar must be aligned very accurately in the vertical before reflections from crystal surfaces will be observed.

Acknowledgments. This work was done while the author was a Visiting Fellow at the Cooperative Institute for Research in Environmental Sciences (CIRES), University of Colorado/NOAA, Boulder, Colorado.

REFERENCES

Deirmendjian, D., 1964: Scattering and polarization properties of water clouds and hazes in the visible and infrared. *Appl. Opt.*, **3**, 187–196.

Derr, V. E., N. L. Abshire, R. E. Cupp and G. T. McNice, 1976: Depolarization of lidar returns from virga and source cloud. *J. Appl. Meteor.*, **15**, 1200–1203.

Fletcher, N. H., 1962: *The Physics of Rain Clouds.* Cambridge University Press, 86 pp.

Heymsfield, A. J., 1977: Precipitation development in stratiform ice clouds: a microphysical and dynamical study. *J. Atmos. Sci.*, **34**, 367–381.

Jayaweera, K.O.L.F., and B. J. Mason, 1965: The behavior of freely falling cylinders and cones in a viscous fluid. *J. Fluid Mech.*, **22**, 709–720.

—— and ——, 1966: The falling motions of loaded cylinders and discs simulating snow crystals. *Quart. J. Roy. Meteor. Soc.*, **92**, 151–156.

Liou, Kuo-nan, and H. Lahore, 1974: Laser sensing of cloud composition. A backscattered depolarization technique. *J. Appl. Meteor.*, **13**, 257–263.

Mason, B. J., 1971: *The Physics of Clouds.* Clarendon Press, 671 pp.

Mossop, S. C., 1968: Comparisons between concentrations of ice crystals in clouds and the concentrations of ice nuclei. *J. Rech. Atmos.*, **3**, 119–124.

Ono, A., 1969: The shape and riming properties of ice crystals in natural clouds. *J. Atmos. Sci.*, **26**, 138–147.

Platt, C. M. R., 1973: Lidar and radiometric observations of cirrus clouds. *J. Atmos. Sci.*, **30**, 1191–1204.

——, 1977: Lidar observations of a mixed-phase altostratus cloud. *J. Appl. Meteor.*, **16**, 339–345.

Sassen, K., 1974: Depolarization of laser light backscattered by artificial ice clouds. *J. Appl. Meteor.*, **13**, 923–933.

——, 1977: Ice crystal habit discrimination with the optical backscatter depolarization technique. *J. Appl. Meteor.*, **16**, 425–431.

Schotland, R. M., K. Sassen and R. Stone, 1971: Observations by lidar of linear depolarization ratios for hydrometeors. *J. Appl. Meteor.*, **10**, 1011–1017.

NOAA Technical Memorandum ERL WPL-33, 1978

AEROSOL CHARACTERIZATION AT COLSTRIP, MONTANA SPRING AND FALL, 1975

N. L. Abshire, V. E. Derr, G. M. Lerfald, G. T. McNice,
R. F. Pueschel and C. C. Van Valin

Aerosols in the Colstrip, Montana, atmosphere have been monitored prior to operation of a large coal-fired power plant to establish a baseline for future studies. This project is a part of EPA's Montana Coal-Fired Power Program. Observations showed total particle counts corresponding to a clean rural atmosphere, with typical Aitken nuclei counts of 1500 cm^{-3} near the surface and decreasing to less than 500 cm^{-3} a few hundred meters above the surface, but occasionally rising to more than 5000 cm^{-3}. The ice nuclei count was twice as high as expected for this type of environment, and was apparently correlated with the rather high incidence of heavy metals found in aerosols collected on membrane filters. Calculations of the optical properties from these samples predict a slight cooling effect at the surface except when the ground is snow covered, when a slight warming can be expected. Airborne measurements of blackbody temperature under stable nighttime conditions showed no variation with altitude, indicating the aerosols are presently generating little if any effect on surface temperatures.

Acoustic sounder records show numerous occasions of temperature inversions higher than the 150 meter stacks, with some extending as high as 1000 meters and persisting all day.

Optical turbidity measured in the Fall was consistent with values obtained in other rural environments in the high plains, averaging about .07.

Preliminary results from the dual polarization lidar indicates that this will be a useful method for discriminating between dust and power plant effluent.

Journal of Applied Meteorology, 17: 669-676, 1978.

Persistent Horizontal Rolls in the Urban Mixed Layer as Revealed by Dual-Doppler Radar

R. A. Kropfli and N. M. Kohn

Environmental Research Laboratories, NOAA, Wave Propagation Laboratory, Boulder, Colo. 80302

(Manuscript received 11 July 1977, in final form 17 November 1977)

ABSTRACT

The Wave Propagation Laboratory (WPL) dual-Doppler radar system has been used in METROMEX to study the effect of a large urban area (St. Louis) on air motions within the planetary mixing layer during clear conditions. It was demonstrated that aircraft-dispensed chaff could be used to trace the air motion over a several hundred square kilometer area and through the entire depth of the developed mixing layer. Data from two days having similar temperature and wind profiles have been selected for discussion. Both data sets suggest the presence of horizontal roll vortices existing throughout the duration of the observations (20–70 min) and beyond the extent of the chaff cloud (8–12 km). A comparison with the temperature field reveals that a line of convergence ($\sim 10^{-3}$ s^{-1}) 300 m above the surface was found to coincide with a thermal ridge of about 0.2°C measured by instruments on the University of Wyoming aircraft. Differences in the apparent roll structures on these two days may be explained in terms of the cross-roll shear and buoyancy resulting from the elongated urban heat island. Also, a persistent localized region of relatively high convergence was observed on the convergence line several kilometers downwind from an area of concentrated industrial activity at Granite City.

1. Introduction

The general objective of the Wave Propagation Laboratory (WPL) in METROMEX (Metropolitan Meteorological Experiment) is to study the nature of the perturbation wind field within the urban convective mixing layer during clear conditions. The observational effort was concentrated during the mid-afternoon hours since it was found that convective motions were necessary for the echo-producing chaff to be dispersed throughout the mixing layer from the surface to several kilometers in height. Specific questions that may eventually be resolved by these measurements are the following: 1) How is the perturbation wind field related to profiles of mean wind and temperature? 2) How significant is the heat island or increased surface roughness on the urban wind field? 3) Are there frequently occurring, persistent wind patterns over a large metropolitan area? 4) Can such patterns explain the downwind precipitation anomaly that has been documented by other METROMEX participants (Semonin and Changnon, 1974)? Answers to such questions will impact on strategies to improve air quality in large metropolitan areas and may shed light on the extent to which large cities inadvertently modify the local climate.

2. Method of data collection and analysis

The two X-band Doppler radars used in these clear air observations have been used in a similar fashion to observe air motions in severe storms (Kropfli and Miller, 1976). Details of the coplane method of generating wind fields from radial velocities measured by two Doppler radars were first discussed by Lhermitte and Miller (1970) and a comprehensive error analysis has been performed by Miller and Strauch (1974). Only the essentials will be mentioned here. The two radars are set to scan synchronously through a common tilted plane passing through the echo and the radar baseline. After completion of a scan, the tilt angle is incremented and a similar scan is performed. The process is repeated until the entire echo volume is observed. The duration of such a volume scan in this experiment was about 1 min, which is small compared with time scales important in kilometer-deep convection.

Processing of these data to generate the three-dimensional wind fields involved the following steps: 1) computation of mean radial velocity estimates for each radar by a pulse-pair method (Rumler, 1968), 2) editing of these pulse-pair velocities to eliminate noise-contaminated estimates, 3) interpolation to a common grid so that the radial velocities could be vectorially combined to yield two-dimensional velocity and divergence fields within each tilted plane, 4) integration of the anelastic continuity equation in cylindrical coordinates to yield the velocity component normal to each plane, and 5) transformation to a Cartesian coordinate system so that the final wind field could be displayed and interpreted. The integration is performed with the usual boundary condition $w=0$ at the surface.

0021-8952/78/0669-0676$06.00

© 1978 American Meteorological Society

Since the X-band radars used in these observations are not sensitive to echoes from the clear atmosphere (with the exception of occasional echoes from insects at close range), it was necessary to fill the volume of interest with X-band chaff. This was routinely accomplished by continuously releasing chaff from a small aircraft flying repeated 15 km across-wind runs at 500 m above ground level (AGL). (All heights will be given as AGL.) The duration of such releases was typically 1 h. Convective motions usually distributed the chaff throughout the boundary layer within 30 min. The radar observations were usually begun at this time and were continued until the echoes became too weak to observe. Chaff densities achieved by this method were about 10^4 km^{-3} or about one chaff needle per 50 m cube. Echoes from such chaff clouds usually resulted in signal-to-noise ratios of 0 to 10 dB at ranges of 15 to 40 km. Although it is desirable to have even stronger signals, these echoes were adequate to yield accurate estimates of velocity. The pulse repetition period used in these measurements varied from 350 to 500 μs corresponding to Nyquist velocities from 23 to 16 m s^{-1}.

To increase the accuracy to the fullest possible extent and also to display the persistent wind field patterns, the three-dimensional velocity estimates at each grid point were averaged over many volume scans. All data presented below have been averaged in this way and represent the wind field average over 20–60 min. Small-scale nonpersistent features are therefore removed by this process. This averaging procedure also allowed a direct computation of the uncertainty in the average wind field from the variance of the velocity estimates at each point. The resulting uncertainties (standard deviations) in the horizontal and vertical velocities in the averaged flow patterns that follow were found to be 15 and 10 cm s^{-1}, respectively. These numbers, of course, include measurement uncertainties as well as actual short-term wind fluctuations. Although it is not possible to separate these two contributions to the standard deviation with accuracy, one can estimate the expected variance of the mean velocity estimate as given by Zrnic (1977). The difference between the measured variance and the computed variance must be attributed to kilometer-scale wind fluctuations during the averaging time.

If one uses a 500 μs pulse period as we did, an estimated Doppler spectral width of 0.5 m s^{-1}, and a 0 dB signal-to-noise ratio, Zrnic's results suggest a standard deviation of the mean radial velocity estimate of 0.31 m s^{-1}. Since the 400 m radar sampling resolution allowed 10 radar pulse volumes to be effectively averaged in the coplane processing, this standard deviation was reduced by $10^{\frac{1}{2}}$ so that the individual volume scans contained radial velocities with standard deviations of about 0.1 m s^{-1}. This value for the standard deviations of the radial velocity estimate along with the contours of normalized variance for coplane particle velocity components (Fig. 6 of Miller and Strauch, 1974) yields errors in the orthogonal horizontal velocity components of about 0.08 m s^{-1}. Since this value is four or five times smaller than that computed from the 15 or 17 volume scans used in obtaining the averaged results, we conclude that most of the measured variance is due to kilometer-scale wind fluctuations over the duration of the measurements.

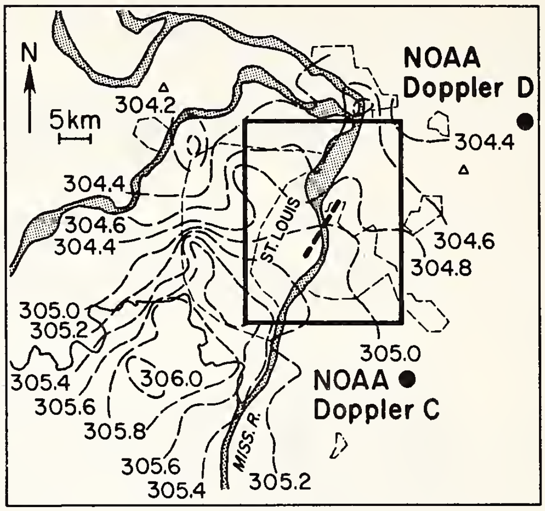

FIG. 1. St. Louis metropolitan area with superimposed θ countours (K) at 300 m AGL derived from University of Wyoming aircraft data at ~1430 CDT 28 July 1975. Solid square indicates region within which chaff drops were made and is the region displayed in Figs. 3 and 5.

3. Analysis of 28 July 1775 wind field

The St. Louis metropolitan area and the region extensively probed by the Doppler radars are shown in Fig. 1. Superimposed on this map is the field of potential temperature at 300 m for 28 July 1975. These temperature measurements were obtained by the University of Wyoming aircraft and they will be related to the boundary layer wind field.[1] Note that the solid block in this figure is the area displayed in Figs. 3 and 6. The upstream temperature profile, also from the Wyoming aircraft, is shown in Fig. 2 and indicates that the base of the capping inversion was at 1.6 km AGL.

The total wind field near the mid-point of the convectively mixed layer on 28 July is shown in Fig. 3a. This wind field represents an average of 17 volume scans taken during a 70 min period. Except for Fig. 4, all other wind fields presented for this date also represent such long-term averages. It is apparent that the mean wind is from 20° at 4 m s^{-1}. The chaff-dispensing aircraft had been flying a pattern across the northeastern edge of the wind field from a point on the

---

[1] These data were taken from the University of Wyoming M. S. thesis by K. K. Wong entitled "Urban perturbations on the mixing layer airflow in St. Louis."

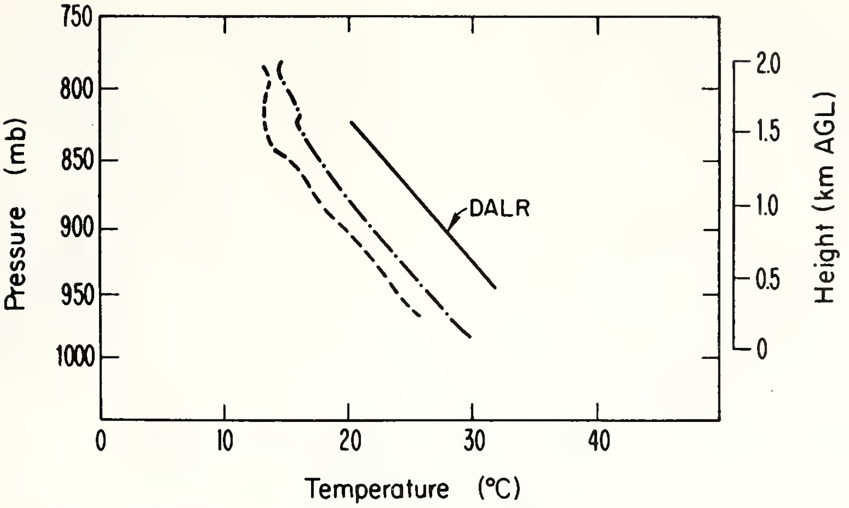

Fig. 2. Upstream temperature profile at 1615 CDT 28 July 1975 (dot-dashed) and at 1615 CDT 4 August 1975 (dashed). Capping inversions are at 1.55 and 1.30 km, respectively.

northern tip of St. Louis to just northeast of East St. Louis on this day. Note that an area of ~250 km² was filled with chaff to the extent that reliable wind measurements were possible.

The mean velocity of the entire chaff cloud was removed from the data and the resulting perturbation wind field is shown in Figs. 3b, 3c and 3d at elevations of 0.3, 0.8 and 1.3 km, respectively. Immediately apparent in Fig. 3b is a 12 km line of convergence at 300 m extending about 10° to the right of the mean wind direction at this level. Adjacent to this line of convergence is a line of divergence 3–4 km to the northwest and a less obvious region of divergence to the southwest. There is also a localized area of enhanced convergence which did not move with the mean wind on the northeastern end of the convergence line. This 1.5 km diameter region had a convergence of 1.4×10^{-3} s^{-1} in contrast to values of about half this amount farther downstream along the convergence line.

It appears that this convergence pattern is the result of heat sources within the heavily industrialized area around Granite City and the central business district to the southwest. There is reasonable consistency between the convergence line, shown as a heavy dashed

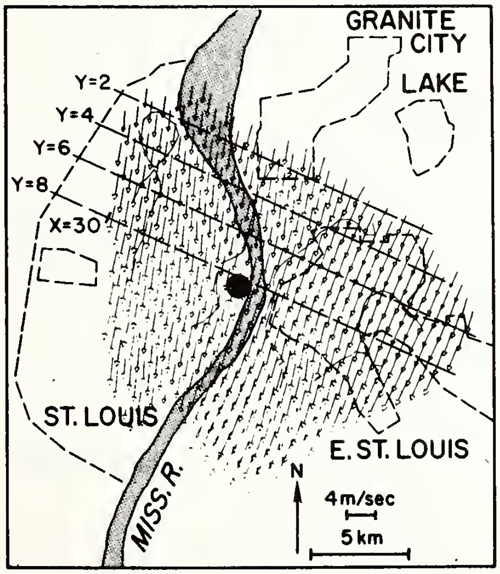

Fig. 3a. Total wind field at 0.8 km AGL on 28 July 1975. Winds are obtained from an average of 17 volume scans taken during a 70 min period ending at 1557 CDT. The Gateway Arch is indicated by the dot just to the west of the Mississippi River at the location $X=22.6$, $Y=8.5$.

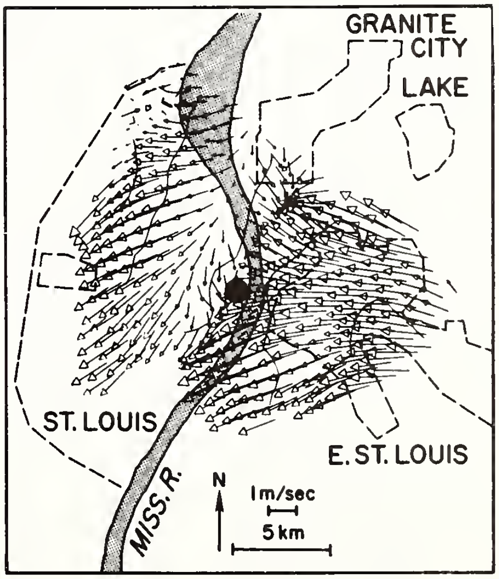

Fig. 3b. Eddy wind field at 0.3 km AGL. Winds are obtained from an average of 17 volume scans taken during a 70 min period ending at 1557 CDT. The mean wind over the entire chaff cloud has been subtracted from these data.

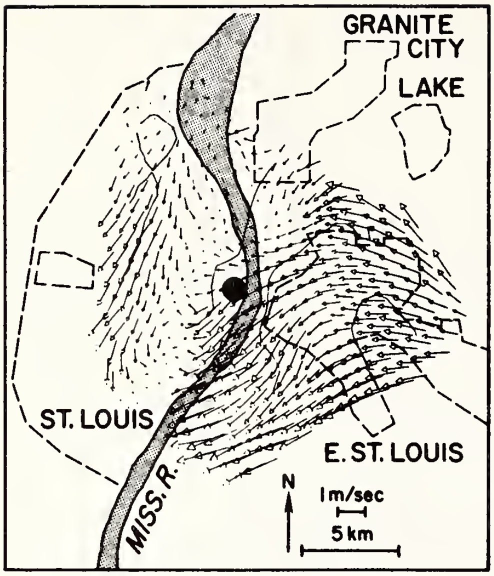

Fig. 3c. As in Fig. 3b except at 0.8 km AGL.

line in Fig. 1, and the thermal ridge also shown in the figure. The thermal pattern at 300 m indicates a 0.2° contrast between the region of convergence and neighboring regions of divergence to either side.

Near the mixing layer mid-point at 800 m, the perturbation wind field appears as shown in Fig. 3c. Although other cases we have analyzed indicate the eddy pattern is usually not as well organized at this level, it is seen that the convergence line is still visible, though somewhat weaker and not as localized.

The eddy pattern near the top of the mixing layer at 1300 m is shown in Fig. 3d. Note the eddy flow reversal from lower levels over East St. Louis. Divergence observed just south of Granite City and to a lesser extent to the southwest is necessary if the vertical velocity component is to be reduced to zero near the top of the mixing layer. The upstream temperature profile obtained from the University of Wyoming aircraft indicated that a capping inversion existed at 1.6 km, just 300 m above this level. Chaff was observed to be carried to near the 2 km level over East St. Louis, which indicates a strong distortion of the capping inversion by the presence of the city.

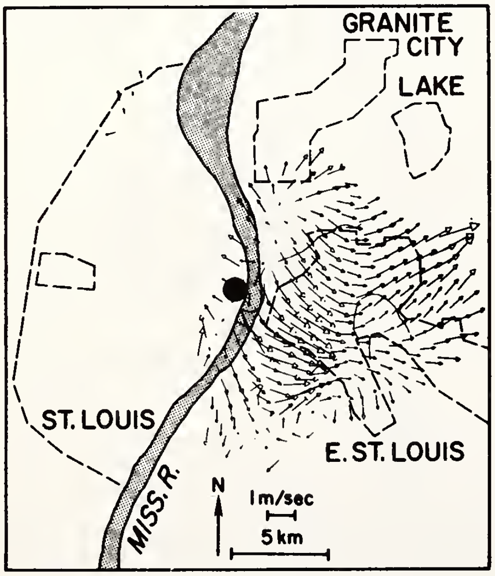

Fig. 3d. As in Fig. 3b except at 1.3 km AGL.

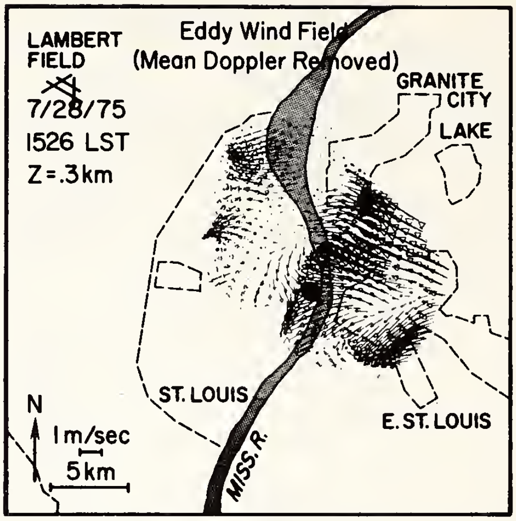

Fig. 4. Eddy wind at 0.3 km AGL. Winds are obtained for an average of 2 volume scans taken during a 2 min period centered at 1526 CDT.

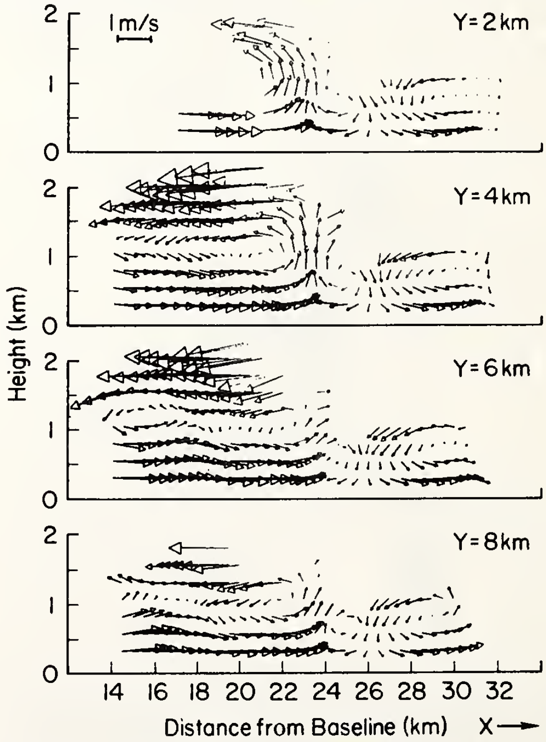

Fig. 5. Vertical cross-sections of eddy wind field through lines indicated in Fig. 3a. This is from the same data set used in Fig. 3.

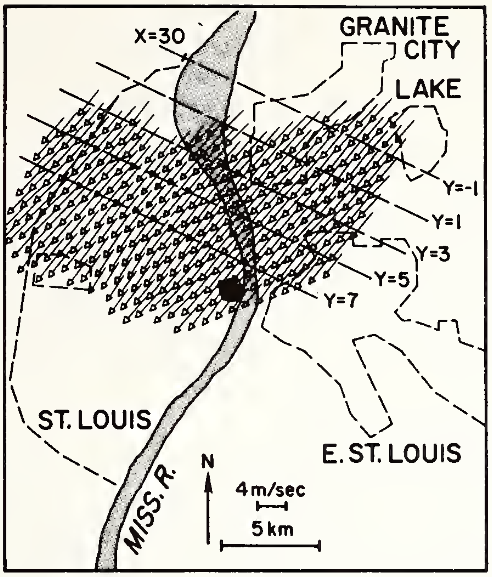

Fig. 6a. As in Fig. 3a except this figure represents an average of 15 volume scans over a 20 min period ending at 1445 CDT on 4 August 1975. Height is 0.8 km AGL.

The horizontal plane at 300 m for the 2 min data set at 1526 is shown in Fig. 4. This illustrates that the low-level convergence is easily apparent even when smaller, less-persistent features are present. Although these data near the mid-point of the 1 h observation time represent a much shorter time interval than the data shown in Fig. 3, they nevertheless have a great deal of similarity with the 70 min averaged data set in Fig. 3b.

Most illustrative of the character of the perturbation field is the series of vertical cross sections shown in Fig. 5. These cross-sections are taken at a spacing of 2 km along the lines indicated in Fig. 3a. From the similarity of the velocity patterns on different vertical cross sections it is apparent that the mode of convection favored on this day was the horizontal roll oriented nearly along the mean wind. Three such rolls can be seen, especially at $Y=4$. The largest roll, located over East St. Louis, has a counterclockwise circulation when observed from the northeast and has the urban heat island as its source. An intermediate-sized roll of the same sense is located to the west (right). Less well-defined and much smaller is a clockwise roll between the two larger rolls. The dominant updraft at $X=23$ km had a magnitude of up to 1 m s^{-1} for the 1 h period;

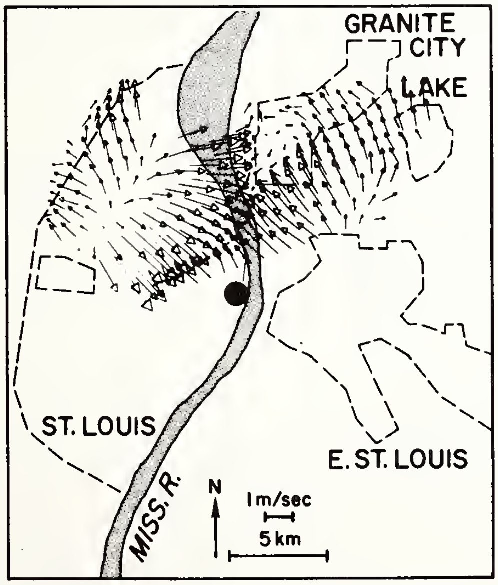

Fig. 6b. As in Fig. 3b except this figure represents an average of 15 volume scans over a 20 min period ending at 1445 CDT on 4 August 1975. Height is 0.3 km AGL.

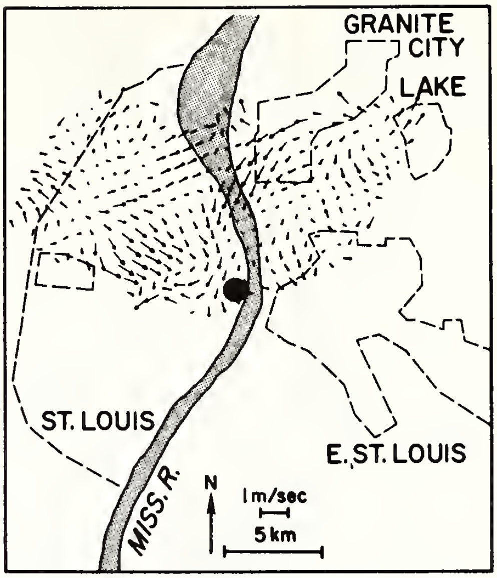

Fig. 6c. As in Fig. 5b except at 0.8 km AGL.

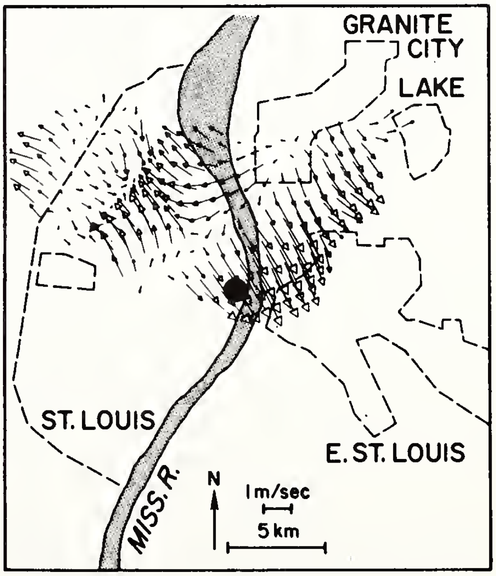

Fig. 6d. As in Fig. 5b except at 1.3 km AGL.

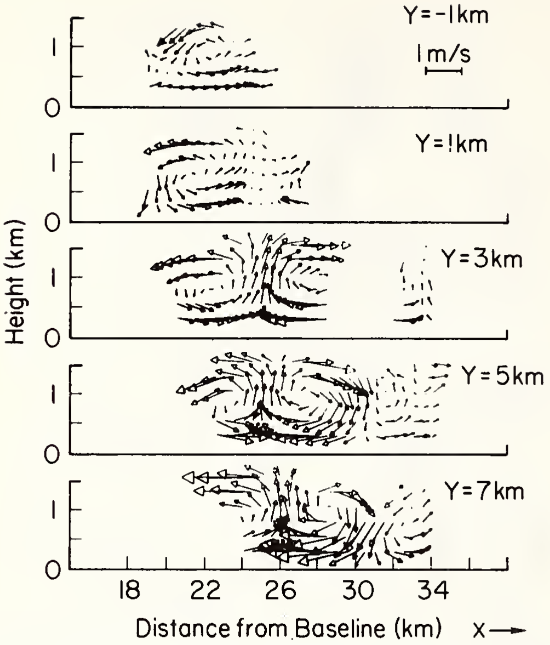

FIG. 7. Vertical cross sections of eddy wind field through line indicated in Fig. 5a. This is from the same data set used in Fig. 5.

single-volume scans indicated that the updraft may have been as high as 2 m s^{-1} over a short time period. An explanation for the size differences in these rolls is to be offered after the discussion of the 4 August data.

4. Analysis of 4 August 1975 wind field

Fig. 6a shows that the total mid-level wind field on 4 August was very similar to that on 28 July (see Fig. 3a). The mean wind in the lower half of the mixing layer differed by less than 1.5 m s^{-1}. As will be discussed later, the notable difference between the total wind profiles on these two days was the reduced shear on 4 August. The upstream temperature profile in Fig. 2 was similar to that on 28 July except that the base of the capping inversion was at 1300 m AGL. The profile below the inversion was nearly dry adiabatic from near the surface to the inversion.

The eddy pattern on 4 August at the 300 m level in Fig. 6b shows a convergence-divergence pattern similar to that on 28 July 1975. Similar to the data shown for 28 July, these data represent an average of 15 volume scans taken during a 20 min period. Although the area of coverage is not as extensive as on 28 July, there exists a similar convergence line extending southwest from Granite City to St. Louis. To either side of this are regions of divergence. The mid-level eddy field in Fig. 6c is not well organized, similar to other cases that are not presented here. Fig. 6d near the top of the boundary layer indicates that the convergence-divergence pattern is reversed from the pattern at 300 m.

As one would expect, the vertical component is small near the top of the boundary layer as shown in the vertical cross sections of Fig. 7. These cross sections are taken through the lines indicated on Fig. 6a. Fig. 7 shows that the convective structure was again in the form of horizontal rolls, although of equal size on this occasion.

It should be emphasized that the features described above were long-lasting on both days and were apparent in the data regardless of how the averages were taken (see Fig. 4). The roll structure was indicated even when single volume scans were considered. In such "instantaneous" samples, however, there were smaller less persistent features that were smoothed out in the longer term averages.

5. Conclusions

The hodograph in Fig. 8 indicates the mean radar-derived wind at each level for the two cases considered here. Although the mean wind in the lower half of the boundary layer was not very much different, it is evident that there was in fact a significant difference in the shear on the two days. The cross-roll component of shear on 28 July was 1.5×10^{-3} s^{-1} and nearly zero on 4 August. It is suggested that this difference may account for the difference in roll size on these two days. Rolls of opposite sense were the same size on 4 August (the no-shear case) but were very different in size when the cross-roll shear existed on 28 July. It is suggested that the cross-roll linear wind shear enhanced the rolls having counterclockwise (CCW) rotation in Fig. 5 but acted to suppress the clockwise (CW) roll. The reason for the CCW roll on the left of this figure being larger than the CCW roll on the right is presumably that the heat island forced this roll, while there was no equivalent forcing for the CCW roll on the right. Since there was no shear in the boundary layer on 4 August, there was

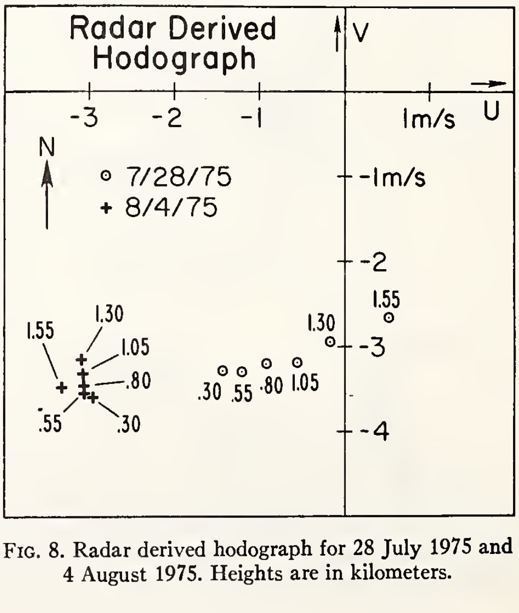

FIG. 8. Radar derived hodograph for 28 July 1975 and 4 August 1975. Heights are in kilometers.

no such enhancing-suppressing mechanism, and the rolls are the same size in Fig. 7.

These observations suggest that the structure observed on 28 July, the sheared case, might be simulated in two dimensions by the superposition of linear shear and a field of counter-rotating rolls of equal magnitude. Such a simulation was performed by adding the streamfunctions for linear cross-roll shear and for equal-size counter-rotating rolls. The appropriate spatial derivative of the streamfunction resulted in the two-dimensional wind field shown in Fig. 9. Dimensions were chosen to be roughly equivalent to the observed fields on 28 July. The simulated wind field contains the essential features of the wind field observed on 28 July. The addition of cross-roll shear significantly reduces the CW roll. Without this shear these rolls, centered at $X=3$ km and $X=7$ km, would have been of equal size. Although this kinematic analysis is by no means proof that such superposition is generally valid, it suggests that heat-island induced rolls that would be equal in size when the shear is weak can be greatly changed when larger scale cross-roll shear is present.

These observations indicate that under certain conditions, the horizontal roll mode of convection exists over an urban area, and it is locked to thermal features generated by the city, although topography should not be totally ruled out at this time. Boundary layer shear does not seem to be a necessary condition for the existence of these rolls as we have seen from the 4 August case. Although horizontal rolls have been predicted by theory (Brown, 1972) for an inflection point instability in a stratified Ekman boundary layer, and their existence has been deduced from tower and aircraft measurements (LeMone, 1973), such rolls have not, to the authors' knowledge, been observed in connection with strong forcing from an urban heat island.

This is not to suggest that urban forcing is the only cause of roll convection, but rather that an urban heat island may increase the frequency of occurrence of rolls. Only two cases are described here but five others have been analyzed at this time and are described by Kropfli (1977). Of these five cases one strongly indicates the presence of rolls, another is indeterminate and three other cases do not show rolls at all. From this admittedly limited sample it appears that rolls occur over St. Louis about half the time during clear afternoon conditions in the summer.

Although convective cells, both aligned and unaligned, were observed with the sensitive Wallops Island radars (Konrad, 1968, 1970), rolls were never observed there.[2] On only four days during June and July 1970 were rolls observed by LeMone (1973). It is tempting to conclude that rolls may occur much less frequently when strong thermal forcing from a heat island is absent. Even when the heat island is present, the complete data set that includes all seven days indicates that PBL winds in excess of about 3.2 m s^{-1} are necessary for the development of rolls at St. Louis (Kropfli, 1977). Only one of the seven cases analyzed was not consistent with this. This conclusion is in agreement with Le Mone (1973) whose observations indicated that "rolls consistently occurred in moderately strong winds . . . ."

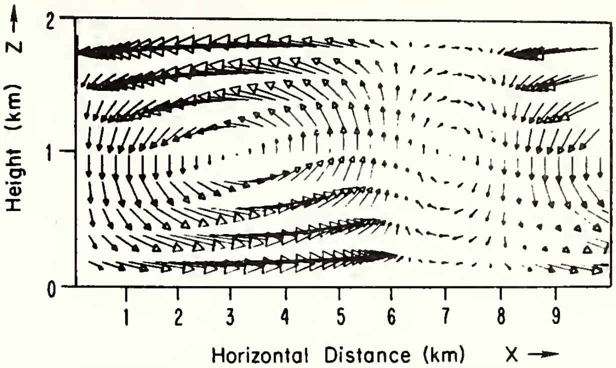

FIG. 9. Simulated wind field from superposition of uniform counter-rotating horizontal rolls and linear cross-roll shear.

The orientation and relative sizes of these persistent rolls can be understood in terms of urban thermal effects, mean wind direction and wind shear. Other cases with different boundary layer wind profiles that have not been shown here also reveal persistent features in the wind patterns. In these cases, however, the horizontal roll structure is not observed. These cases are also being investigated and will be reported at a later time.

These two cases and data from another day not discussed here seemed to suggest that about 1 m s^{-1} updraft perists over the southwest corner of Granite City, a region of heavy industrial activity. There were no data to suggest that this is not the case. The clearest evidence of the strong Granite City updraft was the 28 July case in which divergence values in excess of -1×10^{-3} s^{-1} persisted over this area at the 300 m level for the duration of the observations. The low-level convergence within a 1.5 km diameter area was nearly twice the convergence values observed anywhere else in the scanning area.

The elongated low-level convergence line observed here is not too dissimilar from a result of the three-dimensional primitive equation model of the St. Louis heat island by Vukovich *et al.* (1976). Their northeasterly wind case study with strong geostrophic flow produced a low-level convergence line nearly coincident with the 28 July convergence line. To either side were regions of weak downdraft. Although the wind direction in their case was similar to our observations, their wind speed and temperature profiles differed greatly from ours. Their temperature profile was stable throughout and the geostrophic wind was 10 m s^{-1}.

Of all the cases considered by Vukovich *et al.* (1976)

---

[2] I. Katz, private communication.

this strong northeast wind case produced the largest updraft which they attribute to the heat island effect being intensified by topographically induced convergence. It would be of much interest to compare radar measurements of the three-dimensional boundary layer wind field with results of such numerical models that use the observed wind and temperature profiles as initial conditions. It is hoped that the results presented here and other cases not discussed here can be used in such comparisons.

These experiments have shown that hundreds of square kilometers of the clear boundary layer wind field can be monitored over extended periods of time by dual-Doppler radar. The data reduction and analysis problem, while still a formidable task, is becoming manageable.

Acknowledgments. The encouragement and support from Dr. Earl Gossard throughout the course of this work has been greatly appreciated. We are also grateful to K. K. Wong of the University of Wyoming for the temperature soundings and the potential temperature map in Fig. 1. This work was sponsored in part by the National Science Foundation under Grant AEW75-19217.

REFERENCES

Brown, R. A., 1972: On the inflection point instability of a stratified Ekman boundary layer. *J. Atmos. Sci.*, **29**, 850–859.

Konrad, T. G., 1968: The alignment of clear air convective cells. *Proc. Int. Conf. Cloud Physics*, Toronto, 539–543.

——, 1970: The dynamics of the convective process in clear air as seen by radar. *J. Atmos. Sci.*, **27**, 1138–1147.

Kropfli, R. A., 1977: A dual Doppler radar study of the urban boundary layer: A summary of METROMEX results. NOAA Tech. Memo. ERL-WPL-26, 22 pp.

——, and L. J. Miller, 1976: Kinematic structure and flux quantities in a convective storm from dual-Doppler radar observations. *J. Atmos. Sci.*, **33**, 520–529.

LeMone, M. A., 1973: The structure and dynamics of horizontal roll vortices in the planetary boundary layer. *J. Atmos. Sci.*, **30**, 1077–1091.

Lhermitte, R. M., and L. J. Miller, 1970: Doppler radar methodology for the observation of convective storms. *Preprints 4th Radar Meteor. Conf.*, Tucson, Amer. Meteor. Soc., 133–138.

Miller, L. J., and R. G. Strauch, 1974: A dual Doppler radar method for the determination of wind velocities within precipitating weather systems. *Remote Sensing Environ.*, **3**, 217–233.

Rumler, W. O., 1968: Two-pulse spectral measurements. Tech. Memo. MM-68-4121-15, Bell Telephone Laboratories, Whippany, N. J.

Semonin, Richard G., and S. A. Changnon, Jr., 1974: METROMEX: Summary of 1971–1972 results. *Bull. Amer. Meteor. Soc.*, **55**, 95–100.

Vukovich, Fred M., J. W. Dunn, III and Bobby W. Crissman, 1976: A theoretical study of the St. Louis heat island: The wind and temperature distribution. *J. Appl. Meteor.*, **15**, 417–44.

Zrnic, D. S., 1977: Spectral moment estimates from correlated pulse pairs. *IEEE Trans. Aerospace Elect. Sys.*, **13**, 344–354.

Preprint Volume; Fourth Symposium on Meteorological Observation and Instrumentation, 275-277, American Meteorological Society, 1978.

QUANTITATIVE ACOUSTIC MEASUREMENTS OF ATMOSPHERIC TURBULENCE

Edmund H. Brown

NOAA/ERL/Wave Propagation Laboratory
Boulder, Colorado 80302

1. INTRODUCTION

The boundary layer includes the part of the earth's atmosphere influenced by conditions at the ground, in particular by fluxes of momentum and heat. The boundary layer can either have an "open" structure, acting as a pathway for fluxes to affect higher levels and perturb mesoscale processes, or it can have a "closed" structure, acting as an impenetrable container disconnected from large-scale events. In the first case, information on the structure should have considerable impact on future, more sophisticated, weather prediction methods. In the second, boundary layer studies should have immediate value for predicting the strength and duration of air pollution events.

The fluxes of momentum and heat in the boundary layer depend on the dynamic structure, that is, on wind shear, buoyant thermal plumes, and internal waves. In turn, wind shear, thermal plumes, and breaking internal waves produce small-scale turbulence. Thus, the boundary layer always represents a turbulence-containing region of the atmosphere. But, for atmospheric remote sensing, sound waves produce the strongest interaction with turbulence (Little, 1969). For this reason, the echosonde, which employs acoustic scattering, has the potential for becoming a powerful instrument for boundary layer studies. Realization of the potential, however, depends on obtaining sufficient accuracy in quantitative acoustic measurements (Brown, 1977).

2. MEASUREMENTS

Qualitative aspects of echosonde returns displayed on facsimile recorders have come into increasing use during the last decade. Such displays clearly show thermal plumes in unstable conditions, layers and internal waves in stable conditions, and the passage of fronts (McAllister *et al.*, 1969). Linking the echosonde to the microcomputer may shortly provide continuous data on geometric parameters associated with the qualitative features, such as the boundary layer height h (Owens, 1977), the height and thickness of elevated layers, the width profile of thermal plumes, or the wavelength and amplitude of internal waves.

The recent development of the bistatic Doppler echosonde has solved the problem of remote measurement of the 3-dimensional mean wind field, that is, at least to accuracies of a few tenths of a meter per second (Beran *et al.*, 1974). In particular, the echosonde can give the mean horizontal wind profile U(z) as a function of altitude z. Also, Gaynor (1977) has used Doppler differencing on the returns w(z) of a monostatic Doppler echosonde to measure profiles of the turbulent velocity structure parameter C_V^2. Although the Doppler differencing technique probably will yield better results than methods based on monostatic-bistatic intensities, the accuracy of the technique needs evaluation by comparison with *in situ* sensors.

The acoustic intensities of monostatic echosonde returns depend only on the intensities of the temperature fluctuations, that is, on the turbulent temperature structure parameter C_T^2. Neff (1975) began the study of the accuracy of echosonde measurements of C_T^2. The accuracy is affected both by the "excess attenuation" studied by Brown and Clifford (1976), and by refractive effects of mean winds. Haugen and Kaimal (1978) have recently compared acoustic measurements with tower measurements. Neff (1978) has made similar comparisons and, in addition, estimated the relative contributions of refraction and excess attenuation to the measurement errors. The development of methods of correction for both sources of error, resulting in meteorologically useful profiles of C_T^2, now appears quite plausible.

3. APPLICATIONS

The usefulness of quantitative echosonde measurements in boundary layer studies was suggested by the author at the 3rd Atmospheric Acoustics Workshop in Toronto, and in a meeting of the Acoustical Society of America (Brown, 1975). An alternative scheme was given by Kerman (1976). Briefly, the former method obtains data for the surface layer parameters, the friction velocity u_* (a normalized shear stress or momentum flux), the normalized convective heat flux $-u_*T_*$ or the equivalent reduced temperature T_*, and the Monin-Obukhov length $L_* = u_*^2T/(gT_*)$. (The non-conventional addition of the subscript * on L_* is almost forced on researchers of wave propagation through turbulence by the prior conventional uses of L for pathlength, as well as L_o for the outer scale.) The above surface layer parameters are obtained from echosonde measurements of $C_T^2(z)$, $C_V^2(z)$, and the mean wind shear $U_z(z) = \partial U/\partial z$ derived from U(z). The connection between the two sets of data depends on empirical functions obtained from similarity theory for the surface layer — roughly the lowest few tens of meters of the boundary layer. In turn, use of values of C_T^2 and C_V^2 appropriate to the surface layer depends on extrapolation from echosonde measurements at higher altitudes by means of the equations $C_T^2 = az^{-4/3}$ and $C_V^2 = b + cz^{-2/3}$.

If flux divergences are neglected, the rate of dissipation of turbulent kinetic energy ε satisfies the equation

$$\varepsilon = u_*^2 U_z (1 - Rf), \qquad (1)$$

where Rf is the flux Richardson number, $Rf = -(g/T)u_* T_*/(u_*^2 U_z) = -u_*/(L_* U_z)$. But, ε also satisfies the equation

$$2\varepsilon^{2/3} = C_V^2 . \qquad (2)$$

The third parameter Rf depends on C_T^2, but in an indirect way. Wyngaard et al. (1971) give a table of the empirical function $f_3(Ri)$, where Ri is the gradient Richardson number. Thus, the equation

$$Ri^2 f_3(Ri) = (g/T)^2 \, C_T^2/(z^{4/3} U_z^4) \qquad (3)$$

provides solutions for Ri from data on C_T^2 and U_z. Similarly, Businger et al. (1971) give a table of the empirical function $g_2(z/L_*) = Ri$, so that L_* may be obtained from $Ri = Ri(C_T^2, U_z)$. Substituting the resulting values of $L_* = L_*(C_T^2, U_z)$ in the definition of Rf immediately transforms (1) into an equation for the single unknown u_*,

$$u_*^2 U_z + u_*^3 L_*^{-1}(C_T^2, U_z) = 2^{-3/2} C_V^3 . \qquad (4)$$

(The exponent -1 in the second term of (4) implies here the inverse of the values of L_*, not the inverse function.) The final parameter follows from the equation (the definition of L_*)

$$T_* = (T/g) u_*^2 / L_* . \qquad (5)$$

4. EXTENSIONS

Clearly, extension of the above scheme to the entire boundary layer requires further analysis. More importantly, the list of echosonde measurements given above does not exhaust the set of all that are possible and useful. We illustrate the point by a particular example, one that raises a number of questions worth both analytical and experimental study. We suppose an unstable boundary layer capped by an elevated inversion — a structure frequently associated with severe air pollution events. Echosonde measurements of the boundary layer height h, together with a knowledge of the strength of local pollution sources, provide a measure of the severity of the event. In addition, the strength of the capping inversion, $\Theta_z = \partial\Theta/\partial z$, derived from the mean potential temperature Θ, plays an important role in the duration of such an event (unfortunately, other factors, such as subsidence, complicate the problem). Thus, simultaneous echosonde measurements of h and Θ_z would have considerable impact on air pollution predictions.

If we examine the average daytime behavior of C_T^2 we find that, at some point below h, the decrease of C_T^2 with altitude is reversed: C_T^2 now increases with z to a value at h much larger than at the minimum, then rapidly decreases again above h. Similarly, C_V^2, which is approximately constant over the upper, well-mixed part of the boundary layer, has a smaller increase near h that forms a small bump on the profile. Such behavior is clearly seen in the typical curves of C_T^2 and C_V^2 given by Brown and Clifford (1976). The departure from the -4/3 and -2/3 power laws near h is caused by entrainment of warmer air in the capping inversion by rising turbulence in the thermal plumes. Since the inversion tends to strongly suppress turbulence, the region of mixing of warmer air by entrainment is restricted to a layer of some average thickness ℓ. Facsimile records frequently show such a band of higher acoustic intensity due to higher C_T^2 with a roughly constant thickness at the top of the boundary layer. Because of the mixing, the potential temperature is approximately constant over the entrainment layer but, at the top, makes a jump ΔΘ to the value appropriate to the inversion. The Figure shows the approximate behavior in such an entrainment layer, with ℓ equal to an average of the measured values for which C_T^2 is above some appropriately chosen minimum, $C_{T\,max}^2$, the average of the greatest values of C_T^2, Θ_z the average potential temperature gradient in the capping inversion, and ΔΘ an effective value of the temperature jump.

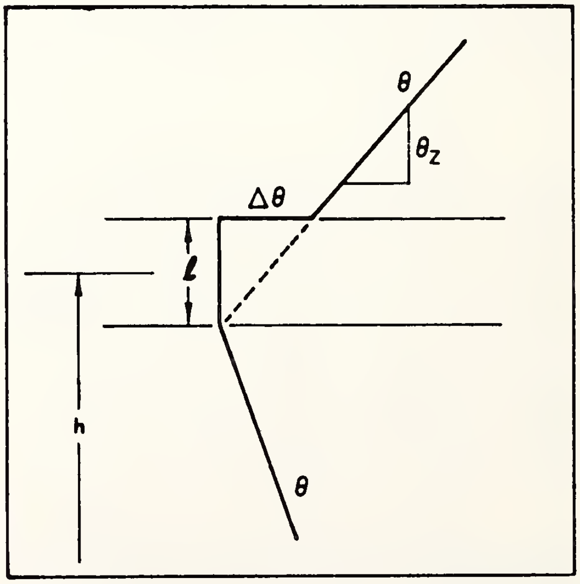

FIGURE

If we now make some approximations, namely, that we can use the Kolmogorov law, and that the largest eddies that can contribute to the jump $\Delta\Theta$ are the size of the entrainment layer thickness, then we can write

$$\Delta\Theta^2 \text{ eff} = C_{T\,\max}^{2} \cdot \ell^{2/3} . \qquad (6)$$

But, if the behavior shown in the Figure at least roughly corresponds to the average effective changes in potential temperature, we have also $\Theta_z \approx \Delta\Theta/\ell$. Introducing this approximation in (6) gives

$$\Theta_z^{\;2} \approx C_{T\,\max}^{2} \cdot \ell^{-4/3}. \qquad (7)$$

Thus, echosonde measurements of the average maximum C_T^2 at the top of the boundary layer, and of the average thickness of the entrainment layer will immediately give some effective measure of the strength of the capping inversion. Of course, such measurements assume we can obtain high enough signal-to-noise ratio at the range h. A more sophisticated analysis also could include measurements of C_v^2, since the entrainment layer parameters depend, not only on the strength of the inversion, but also on the intensity of the turbulence.

5. ACKNOWLEDGMENTS

Thanks are due W. D. Neff and Dr. J. C. Wyngaard for helpful conversations on the problem of entrainment.

6. REFERENCES

Beran, D. W., B. C. Willmarth, F. C. Carsey, and F. F. Hall Jr. (1974), "An acoustic Doppler wind measuring system," *J. Acoust. Soc. Amer.*, 55, 334-338.

Brown, E. H. (1975), "Some applications of atmospheric acoustics," *J. Acoust. Soc. Amer.*, 58, Suppl. 1, 108.

Brown, E. H. (1977), "Quantitative acoustic measurements of atmospheric turbulence," *Proc. 9th Internat. Congress on Acoust.*, 2, 712 (Published by the Spanish Acoustical Society, Madrid).

Brown, E. H. and S. F. Clifford (1976), "On the attenuation of sound by turbulence," *J. Acoust. Soc. Amer.*, 60, 788-794.

Businger, J. A., J. C. Wyngaard, Y. Izumi, and E. F. Bradley (1971), "Flux profile relationships in the atmospheric surface layer," *J. Atmos. Sci.*, 28, 181-189.

Gaynor, J. E. (1977), "Acoustic Doppler measurements of atmospheric boundary layer velocity structure functions and energy dissipation rates," *J. Appl. Meteor.*, 16, 148-155.

Haugen, D. A. and J. C. Kaimal (1978), "Measuring temperature structure parameter profiles with an acoustic sounder," *J. Appl. Meteor.* (to appear).

Kerman, B. R. (1976), "A note on the interpretation of acoustic sounder returns," *Boundary-Layer Meteor.*, 10, 303-310.

Little, C. G. (1969), "Acoustic methods for the remote probing of the lower atmosphere," *Proc. IEEE*, 57, 571-578.

McAllister, L. G., J. R. Pollard, A. R. Mahoney, and P. J. R. Shaw (1969), "Acoustic sounding-a new approach to the study of atmospheric structure," *Proc. IEEE*, 57, 579-587.

Neff, W. D. (1975), "Quantitative evaluation of acoustic echoes from the planetary boundary layer," NOAA Tech. Rept. ERL 322-WPL-38, 34 pp (Available from U.S. Government Printing Office, Washington, D.C.)

Neff, W. D. (1978), "Beam-width effects on acoustic backscatter in the planetary boundary layer," *J. Appl. Meteor.* (to appear).

Owens, E. J. (1977), "Microcomputer-controlled acoustic echo sounder," NOAA Tech. Memo. ERL WPL-21, 76 pp, Boulder, Colorado.

Wyngaard, J. C., Y. Izumi, and S. A. Collins Jr. (1971), "Behavior of the refractive-index structure-parameter near the ground," *J. Opt. Soc. Amer.*, 61, 1646-1650.

Journal of Atmospheric Sciences, 35: 382-396, 1978.

Packet-Scale Motions Forced by Nonlinearities in a Wave System

G. Chimonas

*Cooperative Institute for Research in the Environmental Sciences, University of Colorado/NOAA, Boulder 80309
and Wave Propagation Laboratory, NOAA, Boulder, Colo. 80302*

(Manuscript received 13 June 1977, in final form 1 November 1977)

ABSTRACT

Second-order theory is formulated for a wave packet propagating in a stratified fluid, and the packet-scale flows in the system are examined. These large-scale flows originate from interactions between first-order field components with wavenumbers k and $k+\Delta$, which force second-order motions with wavenumber Δ (large scale) as well as the more familiar harmonics. The perturbation method used produces second-order field equations in which by-products of the linearized wave packet fields appear as source terms. The large-scale part of this forced flow is extracted through a k space projection operation. This flow field is then obtained, first formally for a rather general system and then explicitly for a packet propagating in a simple model of the surface layer inversion. Flow within the body of the packet takes the form of a quasi-horizontal velocity field with a marked vertical shear structure. This flow is examined for consistency with steady-state assumptions and for stability with respect to local Kelvin–Helmholtz wave formation. It appears that such flows can be unstable at physically realizable amplitudes, and this is suggested as a possible source of the turbulent laminae observed in atmospheric inversions.

1. Introduction

The linearized theory of wave propagation in a fluid provides an excellent basis for interpreting most wave events observed in geophysics. Nevertheless, it is recognized (e.g., Tolstoy, 1973) that many important consequences of such wave activity derive from nonlinear effects. For instance, the vertical transfer of horizontal momentum by gravity waves and its subsequent deposition in a localized part of the atmosphere is believed to be one cause of clear air turbulence (Bretherton, 1969a). Such stress transfers have received considerable attention (Bretherton, 1969b; Bretherton and Garrett, 1968; Jones, 1973), and are now formulated in rather abstract but general terms.

A rather different class of nonlinear effects deals with the breakdown of the flow and its radical departure from the linear perturbation state. This is one of the more significant (and recalcitrant) problems in atmospheric dynamics, since it includes all those situations in which laminar flow is an inadequate description of the state. Transports of matter, momentum and energy in directions other than that of the mean wind require an understanding of these complex flows. This is the province of turbulence theory. At the present time there is no operable theory that seeks to solve this problem using the exact equations of motion at all scales (at least for the high Reynolds number flows encountered in the atmosphere). The task is approached rather from its two extremes. On the one hand, the smaller scale stochastic motions are studied without too much regard for the dynamics that generate the larger scales and connect them with the smaller. On the other hand, when the initial breakdown of the laminar flow is examined, it is rarely pursued beyond the first stage of an assumed cascade toward the stochastic scales.

This paper is work of the latter kind. It identifies one of the many atmospheric situations that could lead to breakdown of the laminar flow and obtains, at least within its own limits of consistency, a quantitative estimate of when the breakdown starts. The system examined is rather simple. It consists of a wave packet propagating horizontally in a stably stratified fluid bounded below by a rigid plane surface. The forced nonlinear flows with horizontal scales on the order of the wave packet length are then calculated and examined.

At some critical amplitude the Richardson number in these large-scale flows falls in certain regions below the magic number of $\frac{1}{4}$, which is now commonly accepted as one criterion for the onset of turbulence. The primary aim of this paper is to investigate whether such amplitudes may be realistically achieved. There are many competing processes that may prevent their realization. Most obviously there are nonlinear interactions at the small scales in which cascading proceeds from the wave that forms the packet into its higher harmonics (e.g., Maslowe, 1973; Kelly and Maslowe, 1970; Stuart, 1971; Einaudi, 1970; Drazin, 1970). Even if these short-scale interactions do not prevent the process examined here, there are competing processes at the large scales. One such displays itself automatically in the analysis, and takes the form of a continued convergence of fluid within the packet profile.

This is inconsistent with the basic assumption of a steady state, and its threshold condition (that the flow velocity should exceed the packet velocity) also violates the ordering of the perturbation expansion. Accordingly, if this state is reached before the Richardson number is depressed below $\frac{1}{4}$ we may be reasonably certain that the process of primary interest here cannot occur. This will be used so as to eliminate the possibility of the Richardson-number-type breakdown occurring, although the converse assumption (which is really needed here) cannot be made.

A far more ambitious and general formulation of interaction within a wave packet has been given by Grimshaw (1977). This paper concentrates on, and gives numerical results for, just one of the components covered in Grimshaw's work. A basic study of processes in shortwave-longwave interactions has been given by Benney (1977) an alternative mechanism for breakdown of the flows is advanced by Landahl and Criminale (1977), while much of the current interest in packet-scale motions is attributable to the earlier work of Bretherton and his coworkers, referenced above, and more recently to McIntyre (1973).

The source mechanisms for waves in the stably stratified planetary boundary are themselves a topic of current research. We do not wish to increase the complexity of the work presented here by introducing such considerations. Instead, a simple atmospheric model that allows a spectrum of neutral wave modes is adopted, and the nonlinear analysis is applied to a packet constructed from them. It is anticipated that the qualitative effects obtained will characterize comparable wave systems whatever their origin. However, a wave packet produced by shear instability, one of the most obvious sources for the waves, contains a special region about the critical level whose effects have not been included in this analysis. Recent work by Lalas and Einaudi (1976) has produced alogrithms that yield these eigenmodes for a very wide class of atmospheric conditions. It remains to be seen if the approach used here can be generalized to include wave packets of these modes, and whether, at least well away from the critical levels, there is any great change in the nonlinear behavior.

2. Formulation procedure

The flow dynamics will be formulated through the equations of motion for an incompressible dissipationless fluid. These equations will be solved in a perturbation scheme based on a zero-order state that is horizontally homogeneous, but inhomogeneous in the vertical direction, where density gradients and the gravitational acceleration provide a stable stratification. The fluid is bounded below by a rigid horizontal surface.

The zero-order state is chosen so that the linearized approximation for perturbations around it (the first-order perturbation theory) allows the existence of a set of vertically confined horizontally propagating sinusoidal wave modes. A suitable linear superposition of these modes is then made to provide a two-dimensional wave packet of finite length in the direction of its propagation.

The second-order perturbation theory for the system is then examined and solved for the large-scale flow associated with the packet. The term "large scale" is used here to denote a flow field that changes significantly only in a horizontal distance comparable with the length of the wave packet. Small scale will be used to describe variations over a distance of the order (or less) of the wavelengths of the modes that are used to construct the packet. It is necessary that the two scales can be clearly distinguished, which implies that the packet is constructed from a narrow spectral band of the modes.

The large-scale part of the second-order flow will be obtained in a stationary approximation, and then examined for self-consistency. The interest here is to find the amplitude of the packet at which either the stationary approximation breaks down or secondary Kelvin–Helmholtz instabilities can be expected.

3. The equations of motion and the perturbation approach

The fluid is governed by the equations of motion

$$\left.\begin{aligned} &\rho\frac{D\mathbf{V}}{Dt}+\nabla p-\rho\mathbf{g}=0\\ &\frac{D\rho}{Dt}=0\\ &\nabla\cdot\mathbf{V}=0\\ &\frac{D}{Dt}=\frac{\partial}{\partial t}+\mathbf{V}\cdot\nabla \end{aligned}\right\}, \tag{1}$$

where **V** is the fluid velocity, ρ the density, p the pressure and **g** the gravitational acceleration. A Cartesian coordinate system will be used with z in the negative direction to **g**.

The perturbation approach used here assumes that the fields can be expressed as sequential sums, i.e.,

$$\left.\begin{aligned} \mathbf{V}&=\mathbf{V}_0+\mathbf{V}_1+\mathbf{V}_2+\cdots+\mathbf{V}_n+\cdots\\ p&=p_0+p_1+p_2+\quad+p_n+\cdots\\ \rho&=\rho_0+\rho_1+\rho_2+\quad+\rho_n+\cdots \end{aligned}\right\}, \tag{2}$$

for which terms with subscript 0 provide an exact solution of the set (1) (the background or zero-order state of the fluid), while the terms with subscript 1 satisfy the set (1) to first order in any departure from the background state (i.e., they are solutions of the linearized equations). Higher values of the subscript represent iterative corrections to the linearized approximation: a subscript n denotes a correction of magnitude $(p_1/p_0)^n$. Boundary conditions are imposed on the fields at each order, which introduces sets of homogeneous constraints. The procedure will be carried to the second order in this work.

The set of fields (2) is substituted into the set of equations (1) and terms of the same order extracted as separate sets of equations. At the zero order any flow

$$\left.\begin{aligned} &\mathbf{V}_0=\hat{x}U_0(z)+\hat{y}V_0(z)\\ &\rho_0=\rho_0(z)\\ &p_0=\text{constant}-\int_0^z g\rho_0(z)dz \end{aligned}\right\} \tag{3}$$

satisfies the equations. The specific choice of $\rho_0(z)$, $U_0(z)$ and $V_0(z)$ can be delayed until later, but they must be regarded as given quantities in the higher order equations.

The first-order equations yield

$$\left.\begin{aligned} \rho_0\left(\frac{\partial}{\partial t}+\mathbf{V}_0\cdot\nabla\right)\mathbf{V}_1+\rho_0\mathbf{V}_1\cdot\nabla\mathbf{V}_0+\nabla p_1-\rho_1\mathbf{g}=0\\ \left(\frac{\partial}{\partial t}+\mathbf{V}_0\cdot\nabla\right)\rho_1+\mathbf{V}_1\cdot\nabla\rho_0=0\\ \nabla\cdot\mathbf{V}_1=0 \end{aligned}\right\}. \tag{4}$$

These equations and their boundary conditions must allow a set of modes from which a wave packet can be constructed.

The second-order fields are governed by

$$\left.\begin{aligned} &\rho_0\left(\frac{\partial}{\partial t}+\mathbf{V}_0\cdot\nabla\right)\mathbf{V}_2+\rho_0\mathbf{V}_2\cdot\nabla\mathbf{V}_0+\nabla p_2-\rho_2\mathbf{g}\\ &=-\rho_1\left(\frac{\partial}{\partial t}+\mathbf{V}_0\cdot\nabla\right)\mathbf{V}_1-\rho_1\mathbf{V}_1\cdot\nabla\mathbf{V}_0-\rho_0\mathbf{V}_1\cdot\nabla\mathbf{V}_1\\ &\left(\frac{\partial}{\partial t}+\mathbf{V}_0\cdot\nabla\right)\rho_2+\mathbf{V}_2\cdot\nabla\rho_0=-\mathbf{V}_1\cdot\nabla\rho_1\\ &\nabla\cdot\mathbf{V}_2=0 \end{aligned}\right\}, \tag{5}$$

where the inhomogeneous terms on the right are completely specified by the chosen form of the wave packet. The second-order flow of interest is the forced solution of this set of equations. That is, the second-order fields must obey the boundary conditions and the requirement that they vanish when the amplitude of the wave packet is set equal to zero.

4. Formal solutions of the equations

The sets (3), (4) and (5) will now be recast in forms that allow them to be solved, first formally and later numerically. Since we are imposing homogeneity in the y direction on the solutions at all levels, it is convenient to set the zero-order flow component $\hat{y}V_0(z)$ identically zero. Subsequent manipulations are more direct if the scale length H associated with the stratification

$$H(z)=-\rho_0\left(\frac{d\rho_0}{dz}\right)^{-1} \tag{6}$$

is much greater than the vertical scale associated with the first-order perturbations. Wherever it is convenient (and consistent), the great difference between these two scales will be used to introduce simplifying approximations.

The first-order set of equations (1) is most simply treated in the Fourier transformed spaces of t and x. The convention we adopt for these transformations of any function $F(x,z,t)$ is

$$\left.\begin{aligned} F(x,z,t)&=\int_{-\infty}^{\infty}dk\int_{-\infty}^{\infty}d\omega F(k,z,\omega)e^{+i(\omega t-kx)}\\ F(k,z,\omega)&=\frac{1}{(2\pi)^2}\int_{-\infty}^{\infty}dx\int_{-\infty}^{\infty}dtF(x,z,t)e^{-i(\omega t-kx)} \end{aligned}\right\}. \tag{7}$$

Defining

$$\mathbf{V}_1(x,z,t)=\hat{\mathbf{x}}u(x,z,t)+\hat{\mathbf{z}}w(x,z,t)$$

and applying the double transformation to the set (4) gives a system that can be reduced to a single second-order differential equation for w (say) plus subsidiary relationships:

$$\left.\begin{aligned} &\frac{d^2w(k,z,\omega)}{dz^2}+\frac{1}{\rho_0}\frac{d\rho_0}{dz}\frac{dw(k,z,\omega)}{dz}+\left[\frac{N^2k^2}{(\omega-kU_0)^2}\right.\\ &\qquad\left.-\frac{1}{\rho_0(\omega-kU_0)}\frac{d}{dz}\left(\rho_0\frac{dU_0}{dz}\right)-k^2\right]w(k,z,\omega)=0\\ &u(k,z,\omega)=-\frac{i}{k}\frac{dw(k,z,\omega)}{dz}\\ &\rho_1(k,z,\omega)=\frac{i}{\Omega}w(k,z,\omega)\frac{d\rho_0}{dz}\\ &p_1(k,z,\omega)=-\frac{i\Omega}{k^2}\rho_0\frac{dw(k,z,\omega)}{dz}\\ &\Omega=\omega-kU_0\\ &N^2(z)=-g\frac{d\rho_0}{dz}\rho_0^{-1} \end{aligned}\right\}. \tag{8}$$

The differential equation in (8) is reduced to canonical form with the transformation

$$w(k,z,\omega)=\rho_0^{-\frac{1}{2}}(z)\phi(k,z,\omega). \qquad (9)$$

This introduces several terms with factors ρ_0^{-1} $(d\rho_0/dz)$. As has been suggested above, this term proves too small to be significant in the calculations, and we adopt the Boussinesq approximation of dropping all such terms unless they also include a factor g. Then the set (8) becomes

$$\left.\begin{aligned} &\frac{d^2\phi}{dz^2}+\left[\frac{N^2k^2}{(\omega-kU_0)^2}-\frac{1}{(\omega-kU_0)}\frac{d^2U_0}{dz^2}-k^2\right]\phi=0 \\ &u=-\frac{i}{k}\rho_0^{-\frac{1}{2}}\frac{d\phi}{dz} \\ &\rho_1=-\frac{i}{\Omega}\frac{d\rho_0}{dz}\rho_0^{-\frac{1}{2}}\phi \\ &p_1=-\frac{i\Omega}{k^2}\rho_0^{+\frac{1}{2}}\frac{d\phi}{dz} \end{aligned}\right\}. \qquad (10)$$

The boundary conditions required of ϕ are (setting the bounding plane surface at $z=0$)

$$\left.\begin{aligned} \phi(\omega,0,k)=0 \\ \operatorname{Lim}_{z\to\infty}\phi(\omega,z,k)=0 \end{aligned}\right\}. \qquad (11)$$

It is assumed that $N^2(z)$ and $U_0(z)$ allow a continuum of eigensolutions $\phi_w(k,z,\omega)$ satisfying the differential equation in (10) and the boundary conditions (11). Such eigensolutions will be obtained in some arbitrarily chosen convention of normalization, since the equations are homogeneous, and to establish ϕ (or w) we must choose an amplitude function $A(\omega,k)$, where

$$w(k,z,\omega)=\rho_0^{-\frac{1}{2}}(z)A(\omega,k)\phi_w(k,z,\omega).$$

Inverting the transforms gives the spatial function

$$w(x,z,t)=\rho_0^{-\frac{1}{2}}(z) \times\int_{-\infty}^{\infty}dk\int_{\infty}^{\infty}d\omega A(\omega,k)\phi_w(k,z,\omega)e^{-i(\omega t-kx)}, \qquad (12)$$

with analogous expressions for u, ρ_1 and p_1 derived from the polarization conditions of (10).

The nonlinear formulas will involve many of these expressions. It is convenient to introduce a shorthand notation for the representation of a function as this inverse transformation on the $A(\omega,k)$ weighted eigenfunctions:

$$f(x,z,t)=\int_{-\infty}^{\infty}dk\int_{-\infty}^{\infty}d\omega A(\omega,k)f_w(k,z,\omega)e^{-i(\omega t-kx)} =[f_w(k,z,\omega)]^t, \qquad (13)$$

where f_w is any function we might seek to express using $\phi_w(k,z,\omega)$ and its derivatives.

The zero- and first-order problems present no difficulties in themselves. Even without the Boussinesq approximation, the eigenfunctions of the second-order differential equation in (8) can be found using known numerical techniques for very general forms of N^2 and U_0 (see, e.g., Lalas and Einaudi, 1976). However, the next step in the calculation, namely, the evaluation of the large-scale nonlinear flow without the use of numerical modeling, requires certain restrictions on the weighting function $A(\omega,k)$. The approach used here requires that the first-order wave system conforms closely in behavior to a simple wave packet. Thus $A(\omega,k)$ must be sharply localized about some central values of the parameters, say ω_c and k_c, and its width in ω,k space must be restricted to reduce dispersion to an acceptable level.

We now consider the second-order field equations (5). A linear inhomogeneous problem allows that the inhomogeneous terms be separated into as many parts as is convenient, the system solved for each part separately, and the sum of these part solutions added together to provide the total solution. We wish to divide the inhomogeneous terms into a large-scale and a small-scale part. Only the large-scale flow field is of interest here, so no attempt will be made to solve for the remaining terms.

Suppose that an operation, denoted symbolically by angle braces, extracts the large-scale part of the inhomogeneous terms. (The operator is developed in the Appendix.) Then this operator can be applied to the terms on the right-hand side of (5), and the set reduces to the equations for the large-scale components of the second-order fields $\mathbf{V}_2p_2$, ρ_2 only, say, $\bar{\mathbf{V}}$, $\bar{p}$, $\bar{\rho}$:

$$\left.\begin{aligned} &\rho_0\left(\frac{\partial}{\partial t}+\mathbf{V}_0\cdot\nabla\right)\bar{\mathbf{V}}+\rho_0\cdot\bar{\mathbf{V}}\nabla\mathbf{V}_0+\nabla\bar{p}-\bar{\rho}g \\ &=\left\langle-\rho_1\left(\frac{\partial}{\partial t}+\mathbf{V}_0\cdot\nabla\right)\mathbf{V}_1 \right. \\ &\qquad\left. -\rho_1\mathbf{V}_1\cdot\nabla\mathbf{V}_0-\rho_0\mathbf{V}_1\cdot\nabla\mathbf{V}_1\right\rangle \\ &\left(\frac{\partial}{\partial t}+\mathbf{V}_0\cdot\nabla\right)\bar{\rho}+\bar{\mathbf{V}}\cdot\nabla\rho_0=\langle-\mathbf{V}_1\cdot\nabla\rho_1\rangle \\ &\nabla\cdot\bar{\mathbf{V}}=0 \end{aligned}\right\}. \qquad (14)$$

These large-scale flows travel with the group velocity $\hat{\mathbf{x}}V_G$ of the first-order wave packet (Appendix), so the operator $\partial/\partial t$ may be replaced with $-V_G(\partial/\partial x)$ when it acts on these scales.

Defining

$$\bar{\mathbf{V}}=\hat{\mathbf{x}}\bar{u}+\hat{\mathbf{z}}\bar{w} \qquad (15)$$

and using the restricted form

$$\mathbf{V}_0=\hat{\mathbf{x}}U_0(z),$$

the set (14) may be recast as

$$\rho_0(U_0-V_G)\frac{\partial}{\partial x}\bar{u}+\rho_0\bar{w}\frac{\partial}{\partial z}U_0+\frac{\partial\bar{p}}{\partial x}$$
$$=\left\langle-\rho_1\left(\frac{\partial}{\partial t}+U_0\frac{\partial}{\partial x}\right)u-\rho_1\mathbf{V}_1\cdot\nabla U_0-\rho_0\mathbf{V}_1\cdot\nabla u\right\rangle$$
$$=F_x(x-V_Gt,\, z),\quad(16)$$

$$\rho_0(U_0-V_G)\frac{\partial}{\partial x}\bar{w}+\frac{\partial\bar{p}}{\partial z}+\bar{\rho}g$$
$$=\left\langle-\rho_1\left(\frac{\partial}{\partial t}+U_0\frac{\partial}{\partial x}\right)w-\rho_0\mathbf{V}_1\cdot\nabla w\right\rangle$$
$$=F_z(x-V_Gt,\, z),\quad(17)$$

$$(U_0-V_G)\frac{\partial\bar{\rho}}{\partial x}+\bar{w}\frac{\partial}{\partial z}\rho_0$$
$$=\langle-\mathbf{V}_1\cdot\nabla\rho_1\rangle=Q(x-V_Gt,\, z),\quad(18)$$

$$\frac{\partial\bar{w}}{\partial z}+\frac{\partial\bar{u}}{\partial x}=0.\quad(19)$$

The time-dependence of these equations may be suppressed as it is clear that the system can be solved for time $t=0$, and the forms at all other times recovered by the transformation $x\rightarrow x-V_Gt$. (Equivalently, we could work in the frame of reference for which the packet is stationary.)

Eqs. (16)–(19) reduce to an equation in $\bar{w}$ when we subtract the x derivative of (17) from the z derivative of (16) and use the (18) and (19) to eliminate terms in $\partial\bar{u}/\partial x$ and $\partial\bar{\rho}/\partial x$. This results in

$$\frac{\partial^2\bar{w}}{\partial z^2}+\frac{\partial^2\bar{w}}{\partial x^2}+\frac{1}{\rho_0}\frac{d\rho_0}{\partial z}\frac{\partial\bar{w}}{\partial z}$$
$$+\left[\frac{N^2}{(U_0-V_G^2)}-\frac{1}{\rho_0(U_0-V_G)}\frac{d}{dz}\frac{\rho_0dU_0}{dz}\right]\bar{w}$$
$$=\frac{1}{\rho_0(U_0-V_G)}\left[\frac{\partial F_z}{\partial x}-\frac{\partial F_x}{\partial z}-\frac{gQ}{(U_0-V_G)}\right]$$
$$=\rho_0^{\frac{1}{2}}S(x,z).\quad(20)$$

As with (8) and (9) the first derivative on z can be removed with the substitution

$$\bar{w}(x,z)=\rho_0^{-\frac{1}{2}}\Phi(x,z),\quad(21)$$

giving

$$\frac{\partial^2\Phi}{\partial z^2}+\frac{\partial^2\Phi}{\partial x^2}+Q(z)\Phi=S(x,z),\quad(22)$$

where

$$Q(z)=\frac{N^2(z)}{(U_0-V_G)^2}-\frac{1}{\rho_0(U_0-V_G)}\frac{d}{dz}\left(\frac{\rho_0dU_0}{dz}\right)$$
$$-\frac{1}{2\rho_0}\frac{d^2\rho_0}{dz^2}+\left(\frac{1}{2\rho_0}\frac{d\rho_0}{dz}\right)^2.\quad(23)$$

The formal solution of (22) follows immediately from the application of Fourier and Green's function theory. Let $G(z,z',K)$ be the solution of the equation

$$\frac{d^2}{dz^2}G(z,z',K)+[Q(z)-K^2]G(z,z',K)=\delta(z'-z),\quad(24)$$

where $\delta(z'-z)$ is the Dirac delta function with the appropriate boundary conditions.

Then

$$\bar{w}(x,z)=\rho_0^{-\frac{1}{2}}\int_{-\infty}^{\infty}dKe^{-iKx}\int_0^{\infty}dz'G(z,z',K)S(K,z')$$
$$\equiv\rho_0^{-\frac{1}{2}}(z)\int_{-\infty}^{\infty}dKe^{-iKx}\int_0^{\infty}dz'G(z,z',K)$$
$$\times\frac{1}{2\pi}\int dx'e^{iKx'}S(x',z').\quad(25)$$

In its general form $G(z,z',K)$ couples the integrations over the two spaces z' and K. However, for large-scale flows generated by the type of wave packet envisioned in this paper, it will almost always be possible to separate G into two factors, one involving only (z,z'), the other only K. This makes the evaluation of (25) much easier. The separation follows from an examination of (24) for the Green's function. The function K occurs only through the term $[Q(z)-K^2]$. For any stratification $N^2(z)$ which has at most at a finite number of isolated zeros in the z domain, it will always be possible to choose a sufficiently narrow spectral function $A(\omega,k)$ to ensure that the factor K^2 can be dropped from Eq. (24). That is, $|Q(z)|\gg K^2$ except over a negligibly small part of the z domain. We now consider a model flow for which explicit evaluation of the expression (25) is rather simple. This model allows the separation of G, and moreover provides all terms involving z and z' as simple trigonometric functions. Thus the integration on z' becomes trivial.

5. A model calculation

The large-scale flow field will be obtained for a wave packet traveling in a two-layer stably stratified fluid. This model can be regarded as a greatly simplified representation of inversion conditions in the atmospheric boundary layer. Let the zero-order state consist of a static layer of fluid of depth D and constant Brunt-

Väisälä frequency N_L above which there is a second static layer of smaller constant stratification $N_u(<N_L)$ extending to infinity on z.

It is worth recognizing at the outset several consequences of such a model. Since there is no upper reflecting boundary and N_L^2 is positive, the very long wavelength, low-phase velocity waves that will be forced by the chosen packet are all propagating, rather than evanescent, at large z. This means that a stationary solution will only be applicable to second order in the perturbation theory (which is the order pursued here). A fourth-order calculation would have to include the radiation damping of the packet. A related aspect of the dynamics is that since these very longwaves are nonmodal, there will be no resonance excitations in this scheme. Modes could be found for a broader (in k space) packet and/or a smaller value of N_L in the upper layer. Finally, since the model is windless, the breakdown mechanism we wish to examine is operating under very unfavorable conditions. A background wind shear, and hence an associated finite zero-order Richardson number, would require lower packet amplitudes to provide subcritical perturbed Richardson numbers.

The eigenmodes $\phi_w(k,z,\omega)$, the Green's function $G(z,z',K)$, the source function $S(x,z)$ and the flow $\bar{u}(x,z)$ in this system are presented below.

a. The modes

From (10) and (11) the eigenmodes of the system must be solutions of

$$\frac{d^2\phi_w}{dz^2}+\left[\frac{N^2k^2}{\omega^2}-k^2\right]\phi_w=0, \tag{26}$$

with

$$N^2=\begin{cases}N_u^2(<N_L^2), & z>D\\ N_L^2, & z<D\end{cases} \tag{27}$$

and the boundary conditions

$$\phi_w=0 \quad \text{at} \quad z=0 \quad \text{and} \quad z=\infty. \tag{28}$$

Both ϕ_w and $d\phi_w/dz$ must be continuous across D, and the standard theory shows that eigenmodes will only exist for

$$N_u^2<\omega^2<N_L^2. \tag{29}$$

From (26), the boundary conditions and matching of ϕ_w, the function is

$$\phi_w(k,z,\omega)=\begin{cases}\sin[kz(N_L^2/\omega^2-1)^{\frac12}], & z<D\\ \sin[kD(N_L^2/\omega^2-1)^{\frac12}] & \\ \quad\times\exp[-|k|(z-D)(1-N_u^2/\omega^2)^{\frac12}], & z>D.\end{cases} \tag{30}$$

The final condition, matching $d\phi/dz$ across $z=D$, gives the dispersion equation for the modes

$$\tan[kD(N_L^2/\omega^2-1)^{\frac12}]=-(N_L^2-\omega^2)^{\frac12}(\omega^2-N_u^2)^{-\frac12}. \tag{31}$$

In the alternative form

$$k=D^{-1}(N_L^2/\omega^2-1)^{-\frac12}\times[n\pi-\tan^{-1}\{(N_L^2-\omega^2)^{\frac12}(\omega^2-N_u^2)^{-\frac12}\}, \tag{32}$$

we readily obtain k as a function of ω for any branch n (integer).

We shall seek to construct a wave packet traveling toward $x=+\infty$, so the acceptable branches are those for which ω/k is positive in the adopted convention of (7).

Differentiating (32) with respect to ω gives the group velocity on a modal branch as

$$V_G=\frac{d\omega}{dk}=\frac{\omega D(N_L^2-\omega^2)(\omega^2-N_u^2)^{\frac12}}{kDN_L^2(\omega^2-N_u^2)^{\frac12}+\omega^3}. \tag{33}$$

A little numerical work with (32) and (33) provides everything we need to know about the modes.

b. The Green's function

In the Boussinesq approximation to this model, Eq. (24) simplifies to

$$\frac{d^2}{dz^2}G(z,z',K)+\left[\frac{N^2}{V_G^2}-K^2\right]G(z,z',K)=\delta(z'-z). \tag{34}$$

It is easily shown or checked *a posteriori* that for the wave packets examined here

$$K^2\ll\frac{N_u^2}{V_G^2}\left(<\frac{N_L^2}{V_G^2}\right) \tag{35}$$

for the large-scale component of the flow. Thus an excellent approximation to (34) is provided by

$$\frac{d^2G(z,z',K)}{dz^2}+\frac{N^2}{V_G^2}G(z,z',K)=\delta(z'-z). \tag{36}$$

No functional dependence on K^2 remains in Eq. (36), but the sign of K plays a role in determining the Green's function. For z greater than both z' and D the Green's function corresponds to the spatial part of a plane gravity wave whose source of generation is at lesser z. The time-dependence of this wave is

$$\exp(i\omega t)=\exp(iV_GKt),$$

where V_G is a positive constant, so the wave will correspond to an upward propagation of energy if we adopt the solution

$$\operatorname{Lim}_{z\to\infty}G(z,z',K)=\text{constant } x \exp[\pm i(N_u^2/V_G^2)^{\frac12}z],$$

where the positive root is taken if K is positive, the negative root otherwise. We will write this as

$$\operatorname{Lim}_{z\to\infty}G(z,z',K)=\text{constant } xe^{imz}, \tag{37}$$

with

$$m=\operatorname{sgn}(K)(N_u^2/V_G^2)^{\frac12}. \tag{38}$$

The lower boundary condition is

$$G(0,z',K)=0, \tag{39}$$

and the standard theory of Green's functions then yields

$$G(z,z',K)=\begin{cases} -n^{-1}[\alpha\sin(nz)+\cos(nz)]\sin(nz'), & z>z',\quad z<D \\ -n^{-1}[\alpha\sin(nz')+\cos(nz')]\sin(nz), & z<z',\quad z'<D \\ -n^{-1}[\alpha\sin(nD)+\cos(nD)]\sin(nz)e^{im(z'-D)}, & z<D,\quad z'>D \end{cases} \tag{40}$$

where

$$n=(N_L^2/V_G^2)^{\frac{1}{2}}, \tag{41}$$

$$\alpha=\frac{imn+(n^2-m^2)\cos(nD)\sin(nD)}{m^2\sin^2(nD)+n^2\cos^2(nD)}. \tag{42}$$

Only the Green's function for field points $z<D$ is displayed, as the calculation will be restricted to the forced flow in this lower region.

We now seek to separate the K and (z,z') dependence of the Green's function. For the first two regions of Eq. (40) this is trivial, but the third region contains the term

$$e^{im(z'-L)}=\exp[i(N_u^2/V_G^2)^{\frac{1}{2}}(z'-D)\operatorname{sgn}(K)], \tag{43}$$

which by itself would prevent the functional separation. However, the Green's function always occurs in a product with the source function. In this third region $(z'>D)$ this source function has the evanescent form $e^{-2\sigma z'}$, where $e^{-\sigma z'}$ is the characteristic decay rate of the modes in the upper region. As 2σ is certainly very much greater than $(N_u^2/V_G^2)^{\frac{1}{2}}$, the source function is effectively zero before $\exp[N_u(z'-D)/V_G]$ departs significantly from the value unity. Thus bearing in mind the context in which it is to be used, the Green's function in this region may be taken as

$$G(z,z',K)=-n^{-1}[\alpha\sin(nD)+\cos(nD)]\sin(nz),\quad z<D,\quad z'>D. \tag{44}$$

Now it is possible to write the separated form

$$G(z,z',K)=G_1(z,z')+i\operatorname{sgn}(K)G_2(z,z'), \tag{45}$$

where G_1 and G_2 are completely independent of K. Explicitly

$$G_1(z,z')=\begin{cases} -n^{-1}[\beta\sin(nz)+\cos(nz)]\sin(nz'), & z>z',\quad z<D \\ -n^{-1}[\beta\sin(nz')+\cos(nz')]\sin(nz), & z<z',\quad z'<D \\ -n^{-1}[\beta\sin(nD)+\cos(nD)]\sin(nz), & z<D,\quad z'>D \end{cases} \tag{46}$$

$$G_2(z,z')=\begin{cases} -n^{-1}\gamma\sin(nz)\sin(nz'), & z<D,\ z'<D \\ -n^{-1}\gamma\sin(nD)\sin(nz), & z<D,\ z'>D \end{cases} \tag{47}$$

$$\beta=\frac{(n^2-m^2)\cos(nD)\sin(nD)}{m^2\sin^2(nD)+n^2\cos^2(nD)}, \tag{48}$$

$$\gamma=\frac{nN_uV_G^{-1}}{m^2\sin^2(nD)+n^2\cos^2(nD)}. \tag{49}$$

c. The source function

Collecting results from Eqs. (16)–(20), the source function for the model appears as

$$S(x,z)=\frac{\rho_0^{-\frac{1}{2}}}{V_G}\left[\frac{\partial}{\partial x}\left\langle\rho_1\left(\frac{\partial w}{\partial t}+\rho_0\mathbf{V}_1\cdot\nabla w\right)\right\rangle+\frac{\partial}{\partial z}\left\langle-\rho_0\mathbf{V}_1\cdot\nabla u-\rho_1\frac{\partial}{\partial t}u\right\rangle+\frac{g}{V_G}\langle\mathbf{V}_1\cdot\nabla\rho_1\rangle\right]. \tag{50}$$

Arguments that lead to the Boussinesq approximation in linearized wave theory apply equally well in comparing the magnitudes of the various terms on the right side of (50). So unless there is some dramatic cancellation among the leading terms, those in ρ_1 (but not $g\rho_1$) can be dropped, and factors of ρ_0 can be commuted at will with the operator $\partial/\partial z$:

$$S(x,z)\approx\frac{\rho_0^{\frac{1}{2}}}{V_G}\left[+\frac{\partial}{\partial x}\langle\mathbf{V}_1\cdot\nabla w\rangle-\frac{\partial}{\partial z}\langle\mathbf{V}_1\cdot\nabla u\rangle+\frac{g}{V_G\rho_0}\langle\mathbf{V}_1\cdot\nabla\rho_1\rangle\right] \tag{51}$$

$$=\frac{\rho_0^{\frac{1}{2}}}{V_G}\left[\frac{1}{2}\frac{\partial^2}{\partial x\partial z}\langle w^2-u^2\rangle-\frac{\partial}{\partial z}\left\langle w\frac{\partial u}{\partial z}\right\rangle+\frac{\partial}{\partial x}\left\langle u\frac{\partial w}{\partial x}\right\rangle+\frac{g}{V_G\rho_0}\frac{\partial}{\partial x}\langle u\rho_1\rangle+\frac{g}{V_G\rho_0}\frac{\partial}{\partial z}\langle w\rho_1\rangle\right]. \tag{52}$$

In the wave-packet representation (13) the polarization relations of (10) allow all the first-order fields to be expressed in terms of ϕ_w and its derivatives. On this basis the source function can be rewritten

$$\begin{aligned}S(x,z)=\frac{\rho_0^{-\frac{1}{2}}}{V_G}\frac{1}{2}\frac{\partial\phi}{\partial x\partial z}&\left\langle-\left[-\frac{i}{k}\frac{d\phi_w}{dz}\right]^t\left[-\frac{i}{k}\frac{d\phi_w}{dz}\right]^t+[\phi_w]^t[\phi_w]^t\right\rangle-\frac{\partial}{\partial z}\left\langle[\phi_w]^t\left[ik\left(\frac{N^2}{\omega^2}-1\right)\phi_w\right]^t\right\rangle\\&+\frac{\partial}{\partial x}\left\langle\left[-\frac{i}{k}\frac{d\phi_w}{dz}\right]^t[-ik\phi_w]^t\right\rangle-\frac{N^2}{V_G}\frac{\partial}{\partial x}\left\langle\left[-\frac{i}{k}\frac{d\phi_w}{dz}\right]^t\times\left[\frac{i}{\omega}\phi_w\right]^t\right\rangle-\frac{N^2}{V_G}\frac{\partial}{\partial z}\left\langle[\phi_w]^t\left[\frac{i}{\omega}\phi_w\right]^t\right\rangle.\end{aligned} \tag{53}$$

In the Appendix we have developed the properties of the angle brace operation and derived approximate expressions that are relevant to these calculations. Specifically, (A12) and (A14) reduce this source function to the form

$$S(x,z)=\frac{\rho_0^{-\frac{1}{2}}}{2V_G}\frac{\partial^2}{\partial x\partial z}\left\{-\left(\frac{1}{k}\frac{d\phi_w}{dz}\right)^2+\left[1+\frac{N^2}{\omega^3 kV_G}(\omega^2-2(kV_G)^2)\right]\phi_w{}^2\right\}_{k=k_c}\times \mathrm{O}(x-V_Gt), \tag{54}$$

$$=\frac{\rho_0^{-\frac{1}{2}}}{2V_G}\frac{\partial^2}{\partial x\partial z}S(k_c,z)\mathrm{O}(x-V_Gt). \tag{55}$$

This is known once the (real) eigensolution ϕ_w is obtained for wavenumber $k=k_c$. In (54) the operator $\partial/\partial z$ does not apply to the function N^2.

The two have been commuted on the understanding that (54) be separated into the regions $z>D$ and $z<D$, with N^2 a constant in each.

d. Formulas for the flow fields

The results of the previous three sections allow a presentation of the flow fields in a form suitable for numerical evaluation.

Substituting the model Green's function of (45) and the model source function of (55) into the general expression (25) produces

$$\bar{w}(x,z)=\rho_0^{-\frac{1}{2}}(z)\int_{-\infty}^{\infty}dKe^{-iKx}\int_0^{\infty}dz'[G_1(z,z')+i\,\mathrm{sgn}(K)G_2(z,z')]\frac{1}{2\pi}\int dx'e^{iKx'}\frac{\rho_0^{-\frac{1}{2}}(z')}{2V_G}\times\frac{\partial^2}{\partial x'\partial z'}S(k_c,z')\mathrm{O}(x'-V_Gt), \tag{56}$$

$$=\frac{1}{2V_G\rho_0}\frac{\partial}{\partial x}\mathrm{O}(x-V_Gt)\int_0^{\infty}dz'G_1(z,z')\frac{d}{dz'}S(k_cz')+\frac{1}{2V_G\rho_0}\frac{\partial}{\partial x}\left\{\int_0^{\infty}dz'G_2(z,z')\frac{d}{dz'}S(k_cz')\right\}\times\left\{\int_{-\infty}^{\infty}dKe^{-iKx}i\,\mathrm{sgn}(K)\times\frac{1}{2\pi}\int dx'e^{iKx'}\mathrm{O}(x'-V_Gt)\right\}. \tag{57}$$

Between (57) and (56) all distinction between $\rho_0(z)$ and ρ_0 as measured at some typical level in the fluid has been suppressed.

The continuity equation

$$\frac{\partial\bar{w}}{\partial z}=\frac{\partial\bar{u}}{\partial x}=0$$

allows the horizontal component of flow to be derived from (57):

$$\bar{u}(x,z)=\frac{1}{2V_G\rho_0}\mathrm{O}(x-V_Gt)\int_0^{\infty}dz'\frac{d}{dz}G_1(z,z')\frac{d}{dz'}S(k_c,z')-\frac{1}{2V_G\rho_0}\left\{\int_0^{\infty}dz'\frac{d}{dz}G_2(z,z')\frac{d}{dz'}S(k_c,z')\right\}\times\left\{\int_{-\infty}^{\infty}dKe^{-iKx}i\,\mathrm{sgn}(K)\times\frac{1}{2\pi}\int_{-\infty}^{\infty}dx'e^{iKx'}\mathrm{O}(x'-V_Gt)\right\}. \tag{58}$$

The integrations on z' are elementary in this model, and the modified reinversion of $\mathrm{O}(x')$ is available in standard texts for the more orthodox choices of O. So spatial plots of $\bar{u}$ and $\bar{w}$ are obtained from a very simple computational routine.

For the numerical examples given below a Gaussian wave packet is used. In this case the amplitude function [(A12) and Appendix] is

$$A(\omega,k)\equiv A(k)=a\{\exp[-(k-k_c)^2/\Delta^2]+\exp[-(k+k_c)^2/\Delta^2]\}. \tag{59}$$

From this, the function $\mathrm{O}(x)$ appearing in (58) is obtained from (A14) as

$$\mathrm{O}(x)=\pi^{\frac{1}{2}}2\Delta e^{-\Delta^2x^2}|a|^2\int_{-\infty}^{\infty}dL\exp[-D^2/4\Delta^2]=C\exp(-\Delta^2x^2), \tag{60}$$

while the modified inversion

$$\int_{-\infty}^{\infty}dKe^{-iKx}i\,\mathrm{sgn}(K)\frac{1}{2\pi}\int_{-\infty}^{\infty}dx'e^{iKx'}\mathrm{O}(x)=2C\pi^{-\frac{1}{2}}e^{-\Delta^2x^2}\int_0^{\Delta x}dse^{s^2}. \tag{61}$$

The normalization constant C will be referred to the ground level mean-square-velocity fluctuations at the packet maximum, i.e.,

$$\langle u^2(z=0)\rangle|_{x=0}=a^2\pi^{\frac{1}{2}}\left(\frac{N_L{}^2}{\omega^2(k_c)}-1\right)2\Delta\int_{-\infty}^{\infty}dL\times\exp[-(D^2/4\Delta^2)]\exp(-x^2\Delta^2)=\left(\frac{N_L{}^2}{\omega^2(k_c)}-1\right)C\exp(-x^2\Delta^2),$$

or

$$C=\left(\frac{N_L{}^2}{\omega^2(k_c)}-1\right)^{-1}\langle u^2(z=0)\rangle|_{x=0}. \tag{62}$$

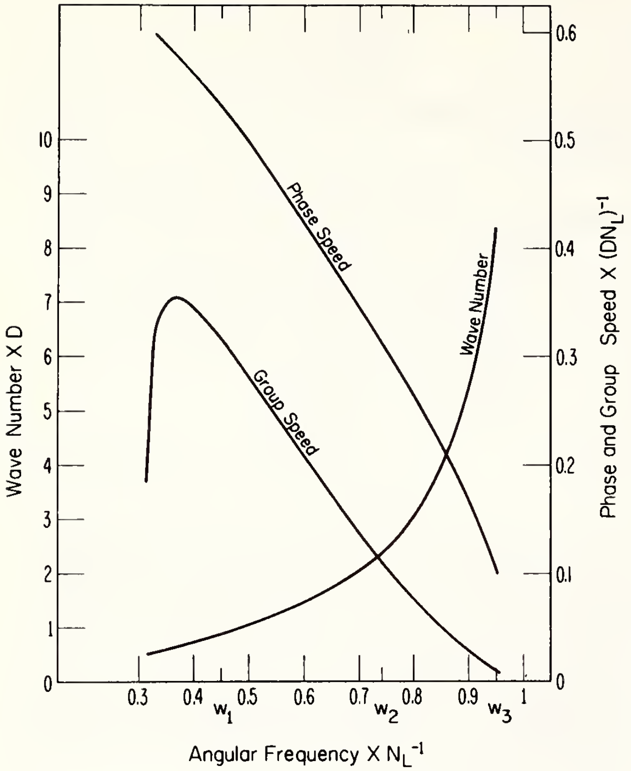

FIG. 1. The characteristics of the gravest wave mode as a function of frequency.

6. Results

All the numerical results given below are for a ratio $N_u^2/N_L^2=0.1$ between the stratifications in the upper and lower layers. Fig. 1 shows the properties of the gravest modes [$n=1$ in (32)] for this model. It is seen that the group velocity of the packet can be much less than the phase velocity of the waves from which it is formed. This appears to be the main reason that the large-scale nonlinear flows may be at least as important as the small scales.

Three wave packets are considered, one constructed at the high frequency end, one at the low, and one at the center of the allowed range. Their central frequencies are shown by ω_1, ω_2 and ω_c in Fig. 1.

Figs. 2–4 give the horizontal flow speed $\bar{u}$ within these systems. The vertical scale covers the region between ground level and the interface between the two layers (at $z=D$). Each curve corresponds to a vertical cross section through the packet at the specified value of x/L, where the packet envelope $O(x)$ [(60)] has the Gaussian form $\exp(-x^2/L^2)$.

The vertical structure of the flows comes from the interplay of two scales, one introduced by the source function, the other by the Green's function. The source function has a vertical wavelength λ_S of one-half that of the waves within the packet, while the Green's function has a characteristic length λ_G found from (40) and (41) to be $2\pi V_G/N_L$. These two scales are shown in Figs. 2–4 giving the flow structure. It appears that the flow structure is largely dominated by whichever is the smaller of the two.

The vertical component of the flow velocity is obtained by integrating the continuity equation. However, if the length L of the packet is much greater than its height D, the flow is essentially horizontal.

The amplitude of the nonlinear flow is given with reference to the group velocity of the packet and the mean square of the horizontal velocity fluctuations of the waves at ground level in the packet center, i.e., the abscissa is $\bar{u}V_G/\langle u_1^2\rangle|_{x=0,z=0}$. On this scaling the ampli-

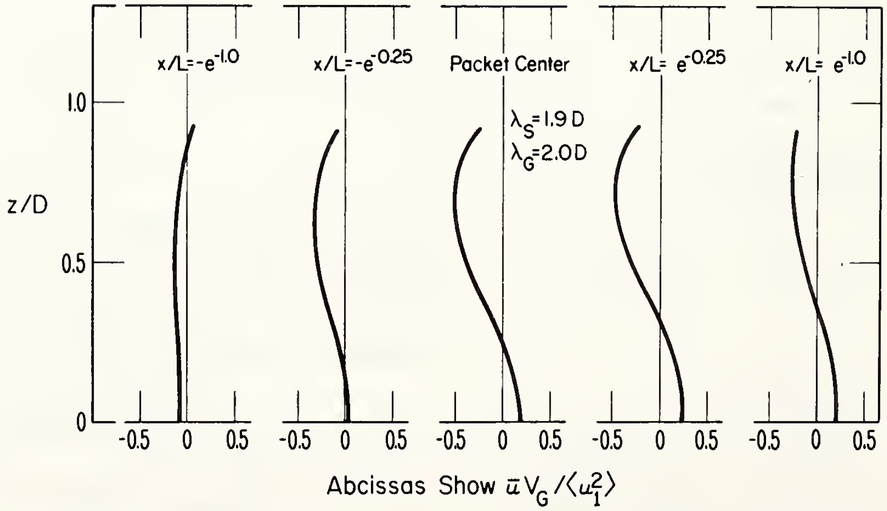

FIG. 2. The large-scale horizontal flow through the packet. The vertical coordinate is normalized to the depth of the lower layer. The flow velocity is shown at five vertical sections through the packet—at the packet center, and at the front and rear where the packet amplitude has fallen to $e^{-\frac{1}{4}}$ and e^{-1} of its central values. This packet is constructed from modes around $\omega=0.447\ N_L$.

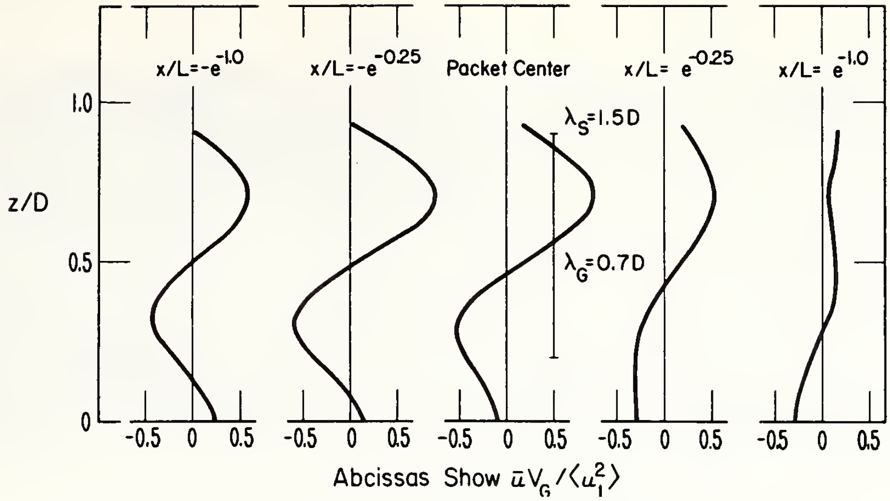

FIG. 3. As in Fig. 2 but for a packet constructed from modes about $\omega=0.742\ N_L$.

tudes in the three packets are remarkably similar. Moreover in absolute terms the differences are not remarkable. Thus compare the packets corresponding to Figs. 2 and 4. In the former the group velocity is 30 times as great as in the latter. However, the waves comprising the first packet have almost horizontal flow fields—the ratio of maximum horizontal to maximum vertical speed is about 3:1, while for the other packet the flow field of these primary waves is more nearly vertical, with the above ratio near 1:3. Thus if we were to normalize to unit kinetic energy density in each packet and express $\bar{u}$ in absolute terms, the flow field in the latter packet would appear to be about three times as great as in the former. But this similarity does not hold at all in comparisons of the flow breakdown. As will be seen, the packet corresponding to Fig. 4 is far more likely to depart from laminar flow than is that of Fig. 2.

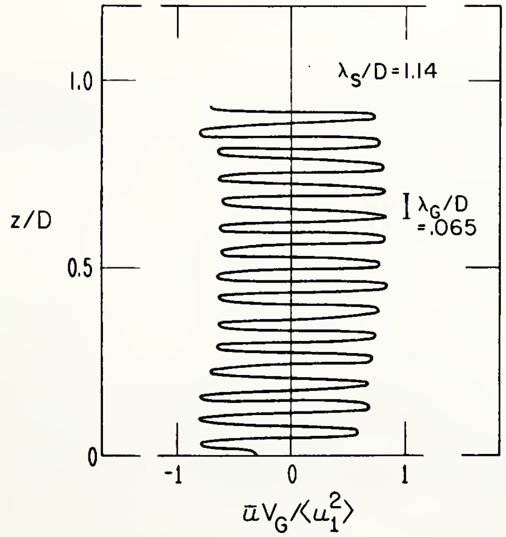

FIG. 4. As in Fig. 2 but showing only the vertical cross section at the center of the packet constructed from modes about $\omega=0.949N_L$.

To see what effect the large-scale nonlinear flow has on the system as a whole, we consider streamlines in the frame of reference of the packet. In this frame the flow should be in a steady state.

Fig. 5 shows streamline configurations that result when $|\bar{u}|<|V_G|$; confluence of the streamlines occurs where $\bar{u}$ speeds the flow from front to back of the packet ($\bar{u}$ negative in Figs. 2–4), diffluence occurs for the opposite sense of $\bar{u}$. This distortion of the flow changes the local stratification of the system, lowering the Brunt-Väisälä frequency where the flow broadens, increasing it where the streamlines are pinched together.

Fig. 6 indicates that if $\bar{u}>V_G$ over some range of x, there is no stationary state; C is a focus of (maximum) continued inflow of fluid, while D is a corresponding point of outflow. Clearly, the flow cannot be described by the steady streamline picture. Moreover, the perturbation expansion scheme has broken down, in that second-order quantities are now as large as some zero orders.

However, stationary flows of Fig. 5 and the catastrophic system of Fig. 6 are not necessarily achievable

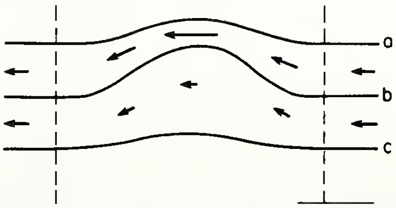

FIG. 5. Schematic of streamlines for the packet system. The vertical dashed lines indicate the horizontal limits of the packet, outside of which the fluid velocity is the packet group velocity. Flow velocity is indicated by the arrows. Between streamlines a and b the nonlinear flow speeds the stream back through the packet, while between b and c it opposes the particle motion.

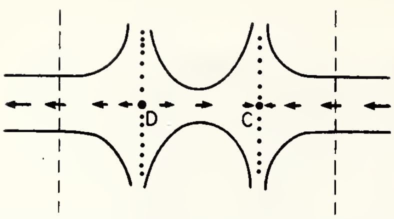

FIG. 6. As in Fig. 5, but now the nonlinear component of the flow opposing the stream exceeds the inflow rate causing a breakdown of the steady streamline hypothesis.

for a given packet. In the first place the lifetime of the packet is limited, and this restricts the degree to which the system can approach its hypothetical final state. In the second place there is a hierarchy of possible instabilities and cascades, at both the short and long scales, which may alter the entire character of the flow.

Suppose the flows $\bar{u}$ could be instantaneously switched on at some initial instant. The streamlines would begin to distort from parallel straight lines at a rate determined by the convergence/divergence of fluid along them. For an infinitely long packet ($w \rightarrow \infty$) there will be no distortion of the lines at any finite later time.

Approximately, if the instantaneous separation of two streamlines is η the development of η is given by

$$\frac{\partial \eta}{\partial t} - \eta \frac{\partial \bar{u}}{\partial x} = 0$$

(which is exact only at the initial instant) or

$$\eta(t) = \eta(0) \exp\left(\frac{\partial \bar{u}}{\partial x} t\right)$$

$$\approx \eta(0) \exp(\bar{u}_{\max} t / L).$$

The final value $\eta(\infty)$ of η, if it exists, is approximately

$$\eta(\infty) = \frac{V_G}{V_G - \bar{u}} \eta(0),$$

whence the time required to reach this state is

$$t_\infty \approx \frac{L}{\bar{u}} \ln\left(\frac{V_G}{V_G - \bar{u}}\right).$$

Even if L is relatively small, the "final state" indicated by the stationary solution will not be reached, since dispersion of the packet both weakens the flow $\bar{u}$ and increases the effective value of L. If $\bar{u}$ is large, then either the streamline breakdown of Fig. 6 or secondary instabilities discussed below become important. Thus it appears that the flows shown in Figs. 2–4 rarely (if ever) lead to a stationary distortion of the form shown in Fig. 5. For weak flows the streamlines will remain nearly plane parallel, while for strong flows they will be destroyed.

If the energy density in the wave packet is large, two sets of possibly competing nonlinear processes must be considered. At the short scales there can be a cascade of energy from the basic waves into the sequence of higher harmonics, while at the large scale the shears in the flow can lead to Kelvin–Helmholtz type instabilities and subsequently turbulence. A qualitative estimate of the relative importance of the two can be made.

Kelvin–Helmholtz instabilities are likely to set in if the Richardson number Ri falls below 0.25 anywhere in the flow. The cascade will commence when the amplitudes of the wave velocity perturbations approach the wave phase speed.

For the packet in Fig. 2 the minimum Richardson number in the flow $\bar{u}$ occurs around $x=0$, $z=0.45D$. Using these values

$$\mathrm{Ri} = \frac{N_L^2}{\left(\dfrac{d\bar{u}}{dz}\right)^2} = \frac{N_L^2}{\left(1.6\dfrac{\langle u_1^2\rangle}{DV_G}\right)^2}$$

$$= \left[1.6\left(\frac{V_P}{V_G}\right)^2\left(\frac{V_G}{N_L D}\right)\frac{\langle u_1^2\rangle}{V_P^2}\right]^{-2}$$

or

$$\mathrm{Ri} = \left[1.42\frac{\langle u_1^2\rangle}{V_P^2}\right]^{-2}.$$

Thus the Richardson number will reach the critical value of $\frac{1}{4}$ only for flows in which $\langle u_1^2\rangle / V_P^2 > 1$, so the cascade process sets in first.

The situation is very different for the packet in Fig. 4. Now the analysis gives

$$(\mathrm{Ri})_{\min} = \left[110\frac{\langle u_1^2\rangle}{V_P^2}\right]^{-2}$$

so the shear instabilities will occur for wave packets that are two orders of magnitude too weak for cascading.

The packet in Fig. 3. is between these clear cut extremes yielding

$$(\mathrm{Ri})_{\min} = \left(4.8\frac{\langle u_1^2\rangle}{V_P^2}\right)^{-2}$$

which by itself is insufficient to determine whether one process will dominate.

Cascading at the smaller scales and shear instabilities on the large-scale flow have been presented here as though they were competing processes. More realistically the cascading will modify the large-scale flow profile, but this does not necessarily imply a weakening of the shears within it. If cascading occurs to any significant extent, the wave spectrum within the packet becomes multipeaked. The analysis of the Appendix must

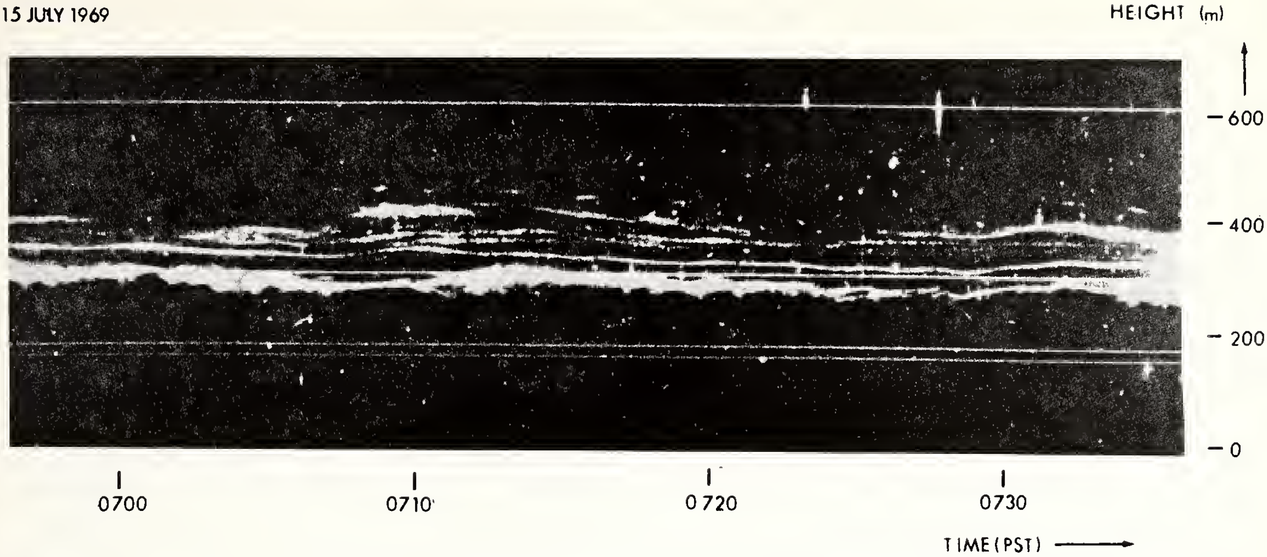

FIG. 7. An FM/CW radar record showing a stack of quasi-horizontal layers of turbulence in a tropospheric inversion. The light areas correspond to radar returns from small-scale turbulence. Undulations in the layers suggest wave activity throughout the region.

then be modified to extract the large-scale flow contributions from each of these localized maxima in the weighting function $A(k)$. The result will be a superposition of flows, one from each of the harmonics. The amplitude of the flows shown in Figs. 2–4 is proportional to the energy density within the packet. If this energy is shared without loss through a sequence of "packets," the amplitude of the total large-scale flow will be relatively unaffected. The additional vertical structure, arising from the smaller values of λ_S introduced with each harmonic, may in fact lead to more intense shears at some altitudes. Consequently, Kelvin–Helmholtz breakdown of the large-scale flow in a wave packet appears to be a very real possibility.

7. Comparison with observations

The stably stratified boundary layer displays a great wealth of wave activity and is the obvious place to seek examples of the flows discussed above. Figs. 7 and 8 are examples of radar and acoustic sounder records showing rather regularly spaced horizontal layers of turbulence. Similar records can be found in Gossard and Richter (1970), Gossard *et al.* (1971), Metcalf and Atlas (1973) and Gossard (1974).

It is tempting to interpret these laminae in terms of a flow field of the form in Fig. 4, with shear instabilities and turbulence about the altitudes of maximum vertical shear.

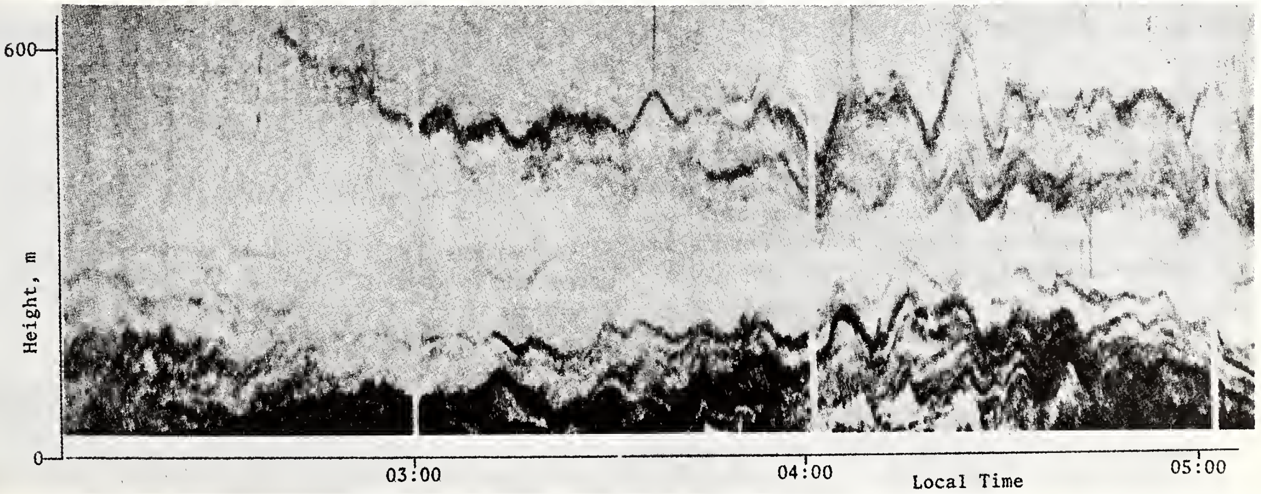

FIG. 8. An acoustic sounder record showing layers of turbulence in the nocturnal inversion. The dark areas correspond to radar returns from small-scale turbulence. The layers are highly distorted, suggesting much wave activity within the region.

We know of no such records for which detailed spectra of the wave activity in the region are also available. We hope that a suitable data set will become available in the future, allowing a quantitative test of the theory to be made. Clearly the theory will have to be modified to take account of the actual stability and wind profiles that exist through the observed region. This implies a considerable amount of numerical work to evaluate the source function, Green's function, and the spatial integrals which in this paper were obtained analytically. However, this task is well within the capabilities of presently available computers. The real difficulty lies in obtaining a detailed data set.

8. Plans for future work

We intend to generalize the formulation and generate the numerical codes that will be needed in the analysis of the type of data set that would provide a quantitative test of the large-scale nonlinear flow effects. But there is another area in which these concepts may be applied. It is known (Einaudi and Lalas, 1974) that shear instabilities in a stratified flow occur in two forms, a short-wavelength type that may properly be called Kelvin–Helmholtz waves, and a long-wavelength form which has the properties of internal gravity waves. The Kelvin–Helmholtz waves have relatively large growth rates in flows with physically acceptable shears, and are often observed in the atmosphere. But the internal gravity waves have such small growth rates that it is difficult to see how they could ever reach observable amplitudes through the shear mechanism. Nevertheless, observation above the jet stream (Hooke and Hardy, 1975) reveals waves which have just those properties expected of the shear modes at internal gravity wave scales (Mastrantonio *et al.*, 1976). A possible explanation is that the packets of fast growing Kelvin–Helmholtz waves force the modal response at the larger scales through a near-resonance form of the nonlinear mechanism described in this paper. This idea is currently under investigation.

Acknowledgments. I am indebted to Drs. E. E. Gossard and F. F. Hall of WPL/NOAA for permission to use the FM/CW radar and acoustic sounder records (Figs. 7 and 8), and for their valuable suggestions during the development of this paper. The work was supported in part by the National Science Foundation under Grant GA-32604.

APPENDIX

Interactions Across the Wave Packet

1. Extraction of the large-scale portion of the source function

In the mathematical development of this paper [(14) *et seq.*] an operation denoted symbolically by angle braces was used to extract the large scale parts of a function. This operation will now be defined and relevant properties displayed.

The symbol $\langle\ \ \rangle$ is often used to indicate an average, and in many papers dealing with wave trains of finite length local (nonlinear) properties of the packet are "extracted" by suggesting an average over one local wavelength. In such a procedure a function like $\langle(\partial/\partial x)V_1^2\rangle$ is strictly zero, while $(\partial/\partial x)\langle V_1^2\rangle$ gives a nonzero result displaying the spatial growth and decay of the packet. It is often difficult, if not impossible, to unambiguously define a local spatial average that will suppress unwanted small scales while leaving intact all terms that contribute to the dynamics of the packet scale motions.

On the other hand if, as is done here, the angle brace operation is defined as a projection in wavenumber space, there is no difficulty in eliminating the small spatial scales (large wavenumber) while retaining all contributions to the larger scales. The procedure is unambiguous and has the distinct advantage that it commutes with derivative operators.

Moreover, when applied to inhomogeneous systems such as the set (14), it provides the large-scale solution without compromising the smaller scales. The latter could be obtained by applying the complement $I-\langle\ \ \rangle$.

Development of the operator $\langle\ \rangle$ will be tailored to the particular needs of this paper, although it is clear that it could be generalized.

The operator $\langle\ \rangle$ is applied to by-products of linearized fields [(14)] that can be expressed as packets of modes [(12) and (13)].

The form given to the packets in (12) and (13) can be shortened. We assume that the modes are accompanied by a dispersion relation that provides a unique relationship between ω and k over the packet. Then treating ω as a given function of k the packet representation reduces to

$$f(x,z,t)=[f_w(k,z,\omega(k)]^t \tag{A1}$$

$$=\int_{-\infty}^{\infty} dk A(\omega(k),k) f_w(k,z,\omega(k)) \times\exp[i(\omega(k)t-kx)]. \tag{A2}$$

All functions $[f_w]^t$ that occur in the formulation correspond to physical variables, requiring the reality conditions

$$\left.\begin{aligned} A(-k)&=A^*(k)\\ \omega(-k)&=-\omega(k)\\ f_w(z,-k)&=f_w^*(z,k)\end{aligned}\right\}, \tag{A3}$$

where the asterisk represents complex conjugation.

The general form of the function on which the angle braces act can be written as

$$F(x,z,t)=[f_1]^t[f_2]^t$$

$$=\int_{-\infty}^{\infty}dk_1\int_{-\infty}^{\infty}dk_2A(k_1)A(k_2)f_1(z,k_1)f_2(z,k_2)$$

$$\times\exp[i(\omega(k_1)t+\omega(k_2)t-k_1x-k_2x)].\quad\text{(A4)}$$

We assume that $A(k)$ peaks about some value $|k|=k_c$ and is effectively zero outside of a narrow band

$$k_c-\Delta\leqslant|k|\leqslant k_c+\Delta.\quad\text{(A5)}$$

This is the usual condition for a well-behaved wave packet, and it provides a clear way of separating the scales. Consider the double k space integration in (A4). If k_1 and k_2 have the same sign, the integrand contributions have wavenumber of order $\pm2k_c$; when they have opposite signs, contributions arise from wavenumbers of order $\pm2\Delta$. Thus the large scale part of $F(x,z,t)$ is obtained by limiting the two k space integrations to opposite halves of their domains:

$$\langle F(x,z,t)\rangle=\left\{\int_{(k_c-\Delta)}^{(k_c+\Delta)}dk_1\int_{-(k_c+\Delta)}^{-(k_c-\Delta)}dk_2\right.$$

$$\left.+\int_{-(k_c+\Delta)}^{-(k_c-\Delta)}dk_1\int_{(k_c-\Delta)}^{(k_c+\Delta)}dk_2\right\}f_1(z,k_1)f_2(z,k_2)A(k_1)A(k_2)$$

$$\times\exp[i(\omega(k_1)t+\omega(k_2)t-(k_1+k_2)x)],\quad\text{(A6)}$$

which is recast using the reality conditions (A3) into the form

$$\langle F(x,z,t)\rangle$$

$$=\int_{(k_c-\Delta)}^{(k_c+\Delta)}dk_1\int_{(k_c-\Delta)}^{(k_c+\Delta)}dk_2f_1(z,k_1)f_2^*(z,k_2)A(k_1)A^*(k_2)$$

$$\times\exp[i(\omega(k_1)t-\omega(k_2)t-(k_1-k_2)x)]+\text{cc},\quad\text{(A7)}$$

where cc is the complex conjugate of the function preceding it. This completes the definition of the operator $\langle\ \rangle$, but it is expedient to obtain approximations to (A7) based on expansions in the small parameter Δ/k_c. To do this let

$$\left.\begin{aligned}k_1&=k_c+\zeta_1\\k_2&=k_c+\zeta_2\end{aligned}\right\}\quad\text{(A8)}$$

and expand functions of k to first order about $k=k_c$:

$$f(k,z)=f(k_c+z)+\zeta\left.\frac{\partial f}{\partial k}\right|_{k=k_c}+\ldots$$

$$=f(k_c+z)+\zeta f'(k_c)+\ldots,\quad\text{(A9)}$$

$$\omega(k)=\omega(k_c)+\zeta\left.\frac{\partial\omega}{\partial k}\right|_{k=k_c}+\ldots$$

$$=\omega(k_c)+\zeta V_G+\cdots.\quad\text{(A10)}$$

Inserting these expressions into (47) yields

$$\langle F(x,z,t)\rangle$$

$$=\int_{-\Delta}^{\Delta}d\zeta_1\int_{-\Delta}^{\Delta}d\zeta_2\{[f_1(k_c,z)f_2^*(k_c,z)+\zeta_1f_1'(k_c)f_2^*(k_c)$$

$$+\zeta_2f_1(k_c,z)f_2'^*(k_c)]A(k_c+\zeta_1)A^*(k_c+\zeta_2)$$

$$\times\exp[i(\zeta_1-\zeta_2)(V_Gt-x)]+\text{cc}\}+O\left(\frac{\Delta}{k_c}\right)^2,\quad\text{(A11)}$$

$$=2\ \text{Re}[f_1(k_c,z)f_2^*(k_c,z)]O(x-V_Gt)$$

$$-\text{Im}[f_1'(k_c)f_2^*(k_c,z)-f_1(k_c,z)f_2'^*(k_c)]\frac{\partial O(x-V_Gt)}{\partial x}$$

$$-2\ \text{Re}[f_1'(k_c)f_2^*(k_c,z)+f_1(k_c,z)f_2'^*(k_c)]$$

$$\times\text{Im}\left[B^*(x-V_Gt)\frac{\partial B(x-V_Gt)}{\partial x}\right]+O\left(\frac{\Delta}{k_c}\right)^2,\quad\text{(A12)}$$

where

$$B(x-V_Gt)=\int_{-\Delta}^{\Delta}d\zeta A(k_c+\zeta)\exp[i\zeta(V_Gt-x)]\quad\text{(A13)}$$

$$O(x-V_Gt)=|B(x-V_Gt)|^2.\quad\text{(A14)}$$

If B is real within a constant phase factor, the third term in (A12) will be identically zero. Many simple forms of the wave packet A, for instance a Gaussian shape peaking at k_c, lead to this property in B.

The numerical work in this paper used such a packet shape.

2. *Comparison with the real-space wave packet representation*

Many authors (see e.g. Grimshaw, 1977) chose to use a wave packet represented *a priori* in x space, rather than in k space as has been done here. Since there is always a one to one correspondence between the two representations, identical results must be obtained by either route when the same order of approximation is maintained. To demonstrate this we briefly establish the correspondence between the two approaches in evaluating one particular term of (52), namely $\langle w\rho_1\rangle$. Equation numbers prefixed G refer to equations in the paper by Grimshaw (1977).

In the wavenumber representation

$$w=\int_{-\infty}^{\infty}dkA(\omega,k)\phi_w(z)e^{i(\omega t-kx)},\quad\text{(A15)}$$

$$\rho_1=\int_{-\infty}^{\infty}dk(i/\omega)\rho_0'A(\omega,k)\phi_w(z)e^{i(\omega t-kx)}.\quad\text{(A16)}$$

Hence using $f_1=\phi_w$ and $f_2=(i/\omega)\rho_0'\phi_w$ in (A12) gives

$$\langle w\rho_1\rangle=\rho_0'\frac{V_G}{\omega_c^2}|\phi_w|^2\frac{\partial O(x-V_Gt)}{\partial x}+O\left(\frac{\Delta}{k_c}\right)^2. \quad \text{(A17)}$$

The other approach is to start from

$$w=B(x,t)\phi_w e^{i(\omega t-kx)}+\text{cc} \\ +\text{higher corrections [cf. G(2.13)]}, \quad \text{(A18)}$$

where the space and time variations of B are assumed to be much longer scale than the variations contained in the exponential. Manipulating the linearized equatioys of motion provides

$$\left.\begin{aligned} w_+ &= \left[B(x,t)\phi_w+\frac{\partial B}{\partial x}\phi_w'\right]\exp(i\omega t-k_cx) \\ &\qquad\qquad\qquad\qquad\text{[cf. G(2.26)]} \\ w &= w_+ + \overset{*}{w}_+ \end{aligned}\right\}, \quad \text{(A19)}$$

$$\rho_1=\frac{i\rho_0'w_+}{\omega}-\frac{\rho_0'}{\sigma^2}\frac{\partial w_+}{\partial t^*}+\text{cc} \quad \text{[c.f. G(3.5)]}, \quad \text{(A20)}$$

where $\partial/\partial t^*$ acts only on the envelope function; as a result averaging over the phase of the exponential and taking

$$\frac{\partial}{\partial t^*}=-V_G\frac{\partial}{\partial x} \quad \text{[see ¶ following G(4.6)]} \quad \text{(A21)}$$

gives the result (A17) again.

It is not clear that one approach offers any significant advantage over the other at this degree of complexity. Note that in both approaches it is necessary to carry "higher order" terms to obtain the first non-zero contribution to the source function.

REFERENCES

Benney, D. J., 1977: A general theory for interactions between short and long waves. *Stud. Appl. Math.*, **56**, 81–94.

Bretherton, F. P., and C. J. R. Garrett, 1968: Wave trains in inhomogeneous moving media. *Proc. Roy. Soc. London*, **A302**, 529–554.

Bretherton, F. P., 1969a: Waves and turbulence in stably stratified fluids. *Radio Sci.*, **4**, 1279–1287.

——, 1969b: Momentum transport by gravity waves. *Quart. J. Roy. Meteor. Soc.*, **95**, 213–243.

Drazin, P. G., 1970: Kelvin-Helmholtz instability of finite amplitude. *J. Fluid Mech.*, **43**, 321–335.

Einaudi, F., 1970: Shock formation in acoustic gravity waves. *J. Geophys. Res.*, **75**, 193–200.

——, and D. P. Lalas, 1974: Some new properties of Kelvin-Helmholtz waves in an atmosphere with and without condensation effects. *J. Atmos. Sci.*, **31**, 1995–2007.

Gossard, E. E., 1974: Dynamic stability of an isentropic shear layer in a statically stable medium. *J. Atmos. Sci.*, **31**,483–492.

——, and J. H. Richter, 1970: Internal waves in the atmosphere from high-resolution radar measurements. *J. Geophys. Res.*, **75**, 3523–3536.

——, D. R. Jensen and J. H. Richter, 1971: An analytical study of tropospheric structure as seen by high-resolution radar. *J. Atmos. Sci.*, **28**, 794–806.

Grimshaw, R. H. J., 1977: The modulation of an internal gravity-wave packet, and the resonance with the mean motion. *Stud. Appl. Math.*, **56**, 241–266.

Hooke, W. H., and K. R. Hardy, 1975: Further study of the atmospheric gravity waves over the Eastern Seaboard on 18 March 1969. *J. Appl. Meteor.*, **14**, 31–38.

Jones, W. L., 1973: Asymmetric wave-stress tensors and waves spin. *J. Fluid Mech.*, **58**, 737–747.

Kelly, R. E., and S. A. Maslowe, 1970: The non-linear critical layer in a slightly stratified shear flow. *Stud. Appl. Math.*, **49**, 301–326.

Lalas, D. P., and F. Einaudi, 1976: On the characteristics of gravity waves generated by atmospheric shear layers. *J. Atmos. Sci.*, **33**, 1248–1259.

Landahl, M. T., and W. Criminale, 1977: Wave breakdown in stratified shear flows. *J. Fluid Mech.*, **79**, 481–497.

Maslowe, S. A., 1973: Finite amplitude Kelvin-Helmholtz billows. *Bound.-Layer Meteor.*, **5**, 43–52.

Mastrantonio, G., F. Einaudi, D. Fua and D. P. Lalas, 1976: Generation of gravity waves by jet streams in the atmosphere. *J. Atmcs. Sci.*, **33**, 1730–1738.

McIntyre, Michael E., 1973: Mean motions and impulse of a guided internal gravity wave packet. *J. Fluid Mech.*, **60**, 801–811.

Metcalf, J. I., and D. Atlas, 1973: Microscale ordered motions and atmospheric structure associated with thin echo layers in stably stratified zones. *Bound. Layer Meteor.*, **4**, 7–35.

Stuart, J. T., 1971: Non-linear stability theory. *Annual Reviews of Fluid Mechanics*, Vol. 3, Annual Reviews, 347–370.

Tolstoy, I., 1973: *Wave Propagation*. McGraw-Hill, 393–414.

IEEE Transactions on Antennas and Propagation, AP-26: 699-705, 1978.

Remote Sensing of Sea State by Analysis of Backscattered Microwave Phase Fluctuations

S. F. CLIFFORD AND D. E. BARRICK, MEMBER, IEEE

Abstract—The relative phase of a normally incident microwave signal scattered off the sea surface is a random function of space and time. The statistics of these random phase fluctuations contain information about the wave-height statistics. This study demonstrates that the wave-height spectra can be deduced directly in terms of the spectra of the phase fluctuations without recourse to inversion techniques even when surface roughness exceeds many wavelengths of the incident signal. In the particular case of a nadir-directed satellite-mounted microwave source operating in the backscatter mode, the wave-height and phase spatial spectra are proportional with a constant proportionality of $(2k_0)^2$, where k_0 is the wavenumber of the scattered signal.

Manuscript received March 19, 1977; revised February 15, 1978. This work was supported in part by a grant from NASA/Wallops Island, order number P-67,583 (G).

The authors are with the Wave Propagation Laboratory, Environmental Research Laboratories, National Oceanic and Atmospheric Administration, Boulder, CO 80302.

I. INTRODUCTION

MANY techniques have been suggested for deriving knowledge of the sea state from both passive and active electromagnetic observations. These include various high-frequency (HF) scatter techniques [1], [2], the laser profilometer [3], the short pulse microwave altimeter [4], and the microwave scatterometer [5]. We propose a new technique that obtains direct information about sea state parameters from analysis of the phase fluctuation spectrum of a microwave signal reflected off the sea surface. The technique requires an airplane-borne or satellite-mounted microwave source that illuminates the sea surface at normal incidence and detects the backscattered return. By applying the theoretical model of scattering that found such useful application to the problem of optical and microwave propagation in random media, we are able to derive

U.S. Government work not protected by U.S. copyright.

the wave-height spectrum directly in terms of the spectrum of backscattered phase fluctuations.

II. ANALYSIS

From existing theoretical formulations based on physical optics [6], [7] we can derive the following equation for the magnetic field backscattered from a perfectly conducting ocean surface for a normally incident spherical wave

$$H(\rho') = \frac{-ik_0 \mathbf{C}_0}{2\pi} \int_A d^2\rho' \, \frac{e^{i2k_0 r} \sec\theta}{r^2}, \tag{1}$$

where k_0 is the wavenumber of the incident radiation, $\mathbf{C}_0$ is the incident polarization vector of the magnetic field, and r is the distance from the scattering point P to the point of observation P' (see Fig. 1). The origin of coordinates is at $(\rho', 0) = (x', y', 0)$; $r = \sqrt{\rho_1{}^2 + [z' - \xi(\rho_1 + \rho')]^2}$; ξ is the wave height at P, θ is the angle from the nadir to the scattering point P; A is the illuminated area, and z' is the height of the transmitter-receiver above the mean sea surface. To a close approximation z', the height of the transmitter, can replace $z' - \xi$ in $\sec\theta/r^2$; however, in the phase we must retain ξ because we assume that the wave-height variations are much greater than a wavelength of the microwave signal. These approximations give

$$\mathbf{H}(\rho') = \frac{-ik_0 \mathbf{C}_0}{2\pi z'} \int_A d^2\rho_1 \, \frac{e^{i2k_0\sqrt{r_0{}^2 - 2z'\xi + \xi^2}}}{r_0}, \tag{2}$$

where $r_0 = \sqrt{\rho_1{}^2 + z'^2}$.

We now introduce the angle θ_1, which is the angle from the nadir to the mean sea surface plane beneath the point P, and expand the argument of the exponential in terms of θ_1,

$$\begin{aligned} 2k_0\sqrt{r_0{}^2 - 2z'\xi + \xi^2} &= 2k_0[(r_0 - \xi)^2 \\ &\quad + 2(1 - \cos\theta_1)\xi r_0]^{1/2} \\ &\approx 2k_0(r_0 - \xi)\left[1 + \frac{\theta_1{}^2 \xi r_0}{2(r_0 - \xi)^2} \right. \\ &\quad \left. - \cdots \right], \end{aligned} \tag{3}$$

where we have approximated $(1 - \cos\theta_1) \sim 1 - \theta_1{}^2/2$ which is valid if $\theta_1 \ll 1$. Since $\theta_1 \leqslant \theta_0$ where θ_0 is the half beamwidth, assumed to be less than a few degrees, this approximation is reasonable. The second term in (3) may be ignored if

$$\frac{k_0 \theta_1{}^2 \xi r_0}{(r_0 - \xi)} \sim k_0 \theta_0{}^2 \xi_{\mathrm{rms}} \ll 1. \tag{4}$$

For a typical microwave signal ($\lambda = 3$ cm) $k_0 \sim 200\ \mathrm{m}^{-1}$ and for a rough sea surface $\xi_{\mathrm{rms}} \sim 1$ m, the approximation is valid if $\theta_0 < 4°$. With this approximation applied to (3) we obtain the final working equation

$$\mathbf{H}(\rho') = \frac{-ik_0 \mathbf{C}_0}{2\pi z'} \int_A d^2\rho_1 \, \frac{e^{i2k_0[r_0 - \xi(\rho_1 + \rho')]}}{r_0}. \tag{5}$$

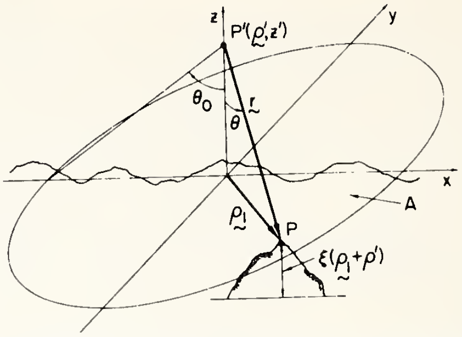

Fig. 1. Geometry of seascatter. Satellite source with beamwidth θ_0 at P' illuminates surface area A. Signal is returned from wave-height perturbation ξ at point P.

Because polarization fluctuations are ignored in the formulation, (C_0 is a constant), we can drop the vector character of the scattered field and deal with the scalar H instead of $\mathbf{H}$. The first steps are to normalize H to H_0, the field that would be received if the sea were perfectly calm, and define $\gamma(\rho') = H(\rho')/H_0$. The dependence of γ on the amplitude and phase fluctuations of the backscattered field can be explicitly shown by writing H and H_0 in phasor notation, $H = Ae^{i\phi}$ and $H_0 = A_0 e^{i\phi_0}$. The total field H is a random variable whose amplitude and phase have both mean A_0 and ϕ_0 and fluctuating parts A_1 and ϕ_1; consequently,

$$\gamma = (A/A_0)e^{i(\phi - \phi_0)} = (1 + A_1/A_0)e^{i\phi_1}. \tag{6}$$

If we ignore the normalized amplitude fluctuations with respect to the enormously larger phase fluctuations, which is a reasonable approximation in the case of scattering from the sea surface (see Appendix), the fluctuations in γ can be entirely attributed to phase fluctuations, i.e.,

$$\gamma(\rho') \cong e^{i\phi_1(\rho')}. \tag{7}$$

The problem remaining is to relate the statistics of γ to the wave-height statistics by analysis of (5).

Consider the equation for γ,

$$\gamma(\rho') = \frac{-ik_0 C_0}{2\pi z' H_0} \int_A d^2\rho_1 \, \frac{e^{i2k_0[r_0 - \xi(\rho_1 + \rho')]}}{r_0}. \tag{8}$$

Both γ and $\exp[-i2k_0\xi]$ may be written in terms of their two-dimensional Fourier-Stieltjes amplitudes (a generalization of the Fourier transform for random functions; see Yaglom [8]) as

$$\gamma(\rho') = \int d\gamma(\mathbf{K}) e^{i\mathbf{K}\cdot\rho'}, \tag{9}$$

and

$$e^{-i2k_0\xi(\rho_1 + \rho')} = \int dB(\mathbf{K}) e^{i\mathbf{K}\cdot(\rho_1 + \rho')}. \tag{10}$$

Substituting (9) and (10) into (8), we obtain the relationship between the random amplitudes $d\gamma$ and dB in the form

$$d\gamma(\mathbf{K}) = \frac{-ik_0C_0}{2\pi z' H_0} \int_A d^2\rho_1 \frac{e^{i2k_0r_0+i\mathbf{K}\cdot\boldsymbol{\rho}_1}}{r_0} \, dB(\mathbf{K}). \tag{11}$$

Equation (11) demonstrates that $d\gamma$, which can be related to the phase fluctuations by means of (7), is simply the random spectral amplitude dB (K), which depends upon the wave-height variations times a weighting function $I(\mathbf{K})$, that is,

$$d\gamma(\mathbf{K}) = I(\mathbf{K}) \, dB(\mathbf{K}), \tag{12}$$

where

$$I(\mathbf{K}) = \frac{-ik_0C_0}{(2\pi z')H_0} \int_A d^2\rho_1 \frac{e^{i2k_0\sqrt{\rho_1^2+z'^2}+i\mathbf{K}\cdot\boldsymbol{\rho}_1}}{\sqrt{\rho_1^2+z'^2}}. \tag{13}$$

For a circular illumination pattern of diameter D, substitute $\mathbf{K} = (K, \theta)$ and integrate over angles

$$I(K) = \frac{-ik_0C_0}{z'H_0} \int_0^{D/2} d\rho_1\rho_1 \frac{e^{i2k_0\sqrt{\rho_1^2+z'^2}}}{\sqrt{\rho_1^2+z'^2}} J_0(K\rho_1), \tag{14}$$

where $I(\mathbf{K})$ is now a function of only the magnitude of the two-dimensional wavenumber K.

From (12) and (14) we can calculate the power spectral density of $d\gamma$ in terms of the power spectral density of dB and ultimately relate the phase statistics to wave-height statistics. First, we multiply (12) by its complex conjugate

$$\langle d\gamma(\mathbf{K}_1)d\gamma^*(\mathbf{K}_2)\rangle = I(\mathbf{K}_1)I^*(\mathbf{K}_2)\langle dB(\mathbf{K}_1)\, dB^*(\mathbf{K}_2)\rangle, \tag{15}$$

and from the definition (10), calculate the expression in the angle brackets on the right side of (15), that is

$$\langle e^{-i2k_0[\xi(\rho_1)-\xi(\rho_2)]}\rangle = \int e^{i\mathbf{K}_1\cdot\boldsymbol{\rho}_1} \int e^{-i\mathbf{K}_2\cdot\boldsymbol{\rho}_2} \langle dB(\mathbf{K}_1)\, dB^*(\mathbf{K}_2)\rangle. \tag{16}$$

If ξ is assumed to be a zero-mean statistically homogeneous Gaussian random variable, which is a reasonable assumption for the wave-height fluctuations [2], it is not difficult to show that [9]

$$\langle e^{-i2k_0[\xi(\rho_1)-\xi(\rho_2)]}\rangle = e^{-2k_0^2D_\xi(\rho_1-\rho_2)}, \tag{17}$$

where D_ξ is the so-called structure function of the wave-height variations defined by

$$\begin{aligned} D_\xi(\rho_1-\rho_2) &= \langle[\xi(\rho_1)-\xi(\rho_2)]^2\rangle \\ &= 2\sigma_\xi^2[1-R_\xi(\rho_1-\rho_2)], \end{aligned} \tag{18}$$

and σ_ξ^2 and R_ξ are, respectively, the variance and the spatial correlation function of the wave height. Substituting this result into (16), we obtain

$$e^{-2k_0^2D_\xi(\rho_1-\rho_2)} = \int e^{i\mathbf{K}_1\cdot\boldsymbol{\rho}_1} \int e^{-i\mathbf{K}_1\cdot\boldsymbol{\rho}_2} \langle dB(\mathbf{K}_1)\, dB^*(\mathbf{K}_2)\rangle. \tag{19}$$

On the left side of (19) we have a function of $(\rho_1 - \rho_2)$ alone (a consequence of the statistical homogeneity assumption). In order to have a similar dependence on the right side, the quantity in the angle brackets must have the form

$$\langle dB(\mathbf{K}_1)\, dB^*(\mathbf{K}_2)\rangle = F(\mathbf{K}_1)\delta(\mathbf{K}_1-\mathbf{K}_2)d^2\mathbf{K}_1d^2\mathbf{K}_2. \tag{20}$$

Substituting this result into (19), we find that F satisfies the relation

$$e^{-2k_0^2D_\xi(\rho_1-\rho_2)} = \int d^2\mathbf{K}_2F(\mathbf{K}_2)e^{i\mathbf{K}_2\cdot(\boldsymbol{\rho}_1-\boldsymbol{\rho}_2)} \tag{21}$$

and of course, by the Fourier inversion theorem

$$F(\mathbf{K}) = \frac{1}{(2\pi)^2} \int d^2\rho e^{-2k_0^2D_\xi(\rho)}e^{-i\mathbf{K}\cdot\boldsymbol{\rho}}. \tag{22}$$

Equation (22) has the same form as the classic integral for the average received power that appears in nearly all treatments of plane-wave scatter from rough Gaussian surfaces since Isakovich's [10] pioneering work in 1952. The principal contribution of the subsequent analysis is (1) to show how this result can be extended to spherical-wave scatter via simple transfer-function concepts, and (2) to employ these concepts to derive the statistics of the received signal phase, rather than its average intensity.

By an analogous procedure we can determine the form of the left side of (15). From (9) and (7),

$$\begin{aligned} \langle\gamma(\rho_1)\gamma^*(\rho_2)\rangle &= \langle e^{i[\phi_1(\rho_1)-\phi_1(\rho_2)]}\rangle \\ &= \int e^{i\mathbf{K}_1\cdot\boldsymbol{\rho}_1} \int e^{-i\mathbf{K}_2\cdot\boldsymbol{\rho}_2} \\ &\quad \times \langle d\gamma(\mathbf{K}_1)d\gamma^*(\mathbf{K}_2)\rangle. \end{aligned} \tag{23}$$

Again, if it is assumed that the phase fluctuations ϕ_1 are normally distributed, we can take recourse to the theorem for Gaussian random variables as in the steps leading to (17); then,

$$\begin{aligned} \langle e^{i[\phi_1(\rho_1)-\phi_1(\rho_2)]}\rangle = e^{-\frac{1}{2}D_\phi(\rho_1-\rho_2)} &= \int e^{i\mathbf{K}_1\cdot\boldsymbol{\rho}_1} \\ &\cdot \int e^{-i\mathbf{K}_2\cdot\boldsymbol{\rho}_2} \langle d\gamma(\mathbf{K}_1)d\gamma^*(\mathbf{K}_2)\rangle, \end{aligned} \tag{24}$$

where D_ϕ is the structure function of the phase fluctuations. In order to have the $\rho_1 - \rho_2$ dependence on the right side of (24),

$$\langle d\gamma(\mathbf{K}_1)d\gamma^*(\mathbf{K}_2)\rangle = G(\mathbf{K}_1)\delta(\mathbf{K}_1-\mathbf{K}_2)d^2\mathbf{K}_1d^2\mathbf{K}_2, \tag{25}$$

G must satisfy

$$e^{-\frac{1}{2}D_\phi(\rho)} = \int d^2\mathbf{K}G(\mathbf{K})e^{i\mathbf{K}\cdot\rho} \tag{26}$$

and the inverse relation

$$G(\mathbf{K}_1) = \frac{1}{(2\pi)^2}\int d^2\rho e^{-\frac{1}{2}D_\phi(\rho)}e^{-i\mathbf{K}_1\cdot\rho}. \tag{27}$$

We now can substitute (25) and (20) into (15) and obtain

$$G(\mathbf{K}_1) = |I(K_1)|^2F(\mathbf{K}_1). \tag{28}$$

The result of the steps leading to (28) is to transform the scattering problem to the spatial frequency domain. The conventional approach to sea scatter calculations is to take a form of the physical optics integral (5) and to determine the desired statistics of H by approximating the integral, e.g., assuming plane wave incidence, applying stationary phase, etc., using information about typical surface roughness parameters, and averaging. Equation (28) demonstrates that the statistics of H may be determined exactly by transforming the scattering problem into the spatial frequency domain. Here the linear system aspect of the problem is emphasized, and the spectral statistics of the received field $G(\mathbf{K})$ factor conveniently into two terms, separating the spectral quantity that depends on the wave-height statistics for plane-wave incidence $F(\mathbf{K})$ from a quantity $|I|^2$ that depends solely on the propagation geometry. Equation (28) is the equation of a linear system in the spatial frequency domain that describes how the input spectrum (the angular spectrum of scattered plane waves leaving the sea surface F), is multiplied by a transfer function $|I|^2$ so that the resultant $G = |I|^2F$ is the angular spectrum of scattered waves at the receiver. Examination of (13), which is the definition of I, reveals that it is also the diffraction integral for the field backscattered from a sinusoidal surface irregularity of wavenumber K whose amplitude is small in terms of the radio wavelength, observed at a distance z' from the surface. Therefore, the physical interpretation of $|I|^2$ is that it describes the angular distribution of power scattered by a single Fourier surface component in the "slightly rough" or Rayleigh limit [2], [11], [12]. This result could have been anticipated, since from linear system theory, $|I|^2$ is the transfer function or the frequency response of the medium.

Equation (28) can be solved formally to give the wave-height statistics by using the Fourier transform. By inserting the definition of F from (22) into (28), we obtain

$$e^{-2k_0{}^2D_\xi(\rho)} = (2\pi)^2\int d^2\mathrm{K}_1e^{i\mathrm{K}_1\cdot\rho}\,|I(K_1)|^{-2}G(\mathrm{K}_1), \tag{29}$$

or, by substituting the definition of G,

$$D_\xi(\rho) = -\frac{1}{2k_0{}^2}\ln\left\{\int d^2\mathrm{K}_1e^{i\mathrm{K}_1\cdot\rho}\,|I|^{-2}\cdot\int d^2\rho_1e^{-i\mathrm{K}_1\cdot\rho_1-\frac{1}{2}D_\phi(\rho_1)}\right\}. \tag{30}$$

Without any further approximation we can find the wave-height structure function, a quantity directly related to the power spectral density, by measuring the structure function of the phase fluctuations of the backscattered signal, computing the Fourier transform of $\exp[-\frac{1}{2}D_\phi]$, multiplying by $|I|^{-2}$ [found from (14)], Fourier transforming the result and, finally, computing the logarithm. In a practical case, we would use the satellite or airplane velocity v times the time lag τ as the vector ρ_1. In this instance, the D_ϕ would be computed from the recorded time series of the phase fluctuations, where

$$D_\phi(\tau) = \langle[\phi_1(t) - \phi_1(t+\tau)]^2\rangle, \tag{31}$$

and the transforms in (30) would reduce to their one-dimensional analogs.

III. APPROXIMATIONS

In this section, we will show that, for certain propagation parameters, (28) and (30) reduce to an especially simple form. The quantity $I(K)$ is defined by

$$I(K) = \frac{-ik_0C_0}{z'H_0}\int_0^{D/2} d\rho_1\rho_1\frac{e^{i2k_0\sqrt{\rho_1{}^2+z'^2}}}{\sqrt{\rho_1{}^2+z'^2}}J_0(K\rho_1), \tag{32}$$

where, from geometrical optics, $H_0 = C_0\exp[i2k_0z']/(2z')$ is the field observed at the receiver in the absence of surface roughness.[1] If we change variables to $y = \sqrt{\rho^2+z'^2}$ and note from Fig. 1 that $D/2 = z'\tan\theta_0$, (32) reduces to

$$I(K) = -i2k_0e^{-i2k_0z'}\int_{z'}^{z'\tan\theta_0} dye^{i2k_0y}J_0(K\sqrt{y^2-z'^2}). \tag{33}$$

After considerable manipulation, this integral can be evaluated in terms of Lommel's functions of two variables

$$I(K) = e^{i2k_0z'(\sec\theta_0-1)}\left[e^{i2k_0z'(1-\sec\theta_0)-i(K^2z'/4k_0)} - J_0(Kz'\tan\theta_0) + iU_1\left(\frac{K^2z'}{2k_0}, Kz'\tan\theta_0\right) + U_2\left(\frac{K^2z'}{2k_0}, Kz'\tan\theta_0\right)\right], \tag{34}$$

where the Lommel function is defined by

$$U_\nu(\omega, z) = \sum_{m=0}^{\infty}(-1)^m\left(\frac{\omega}{z}\right)^{\nu+2m}J_{\nu+2m}(z). \tag{35}$$

A plot of $|I|^2$ from (34) is shown in Fig. (2). There are three important features of this curve. First, from (34), $|I(0)|^2 =$

---

[1] The spherical nature of the reflecting earth can be accounted for, if necessary, by replacing z' in the denominator by $z' + a$, where a is the radius of the earth.

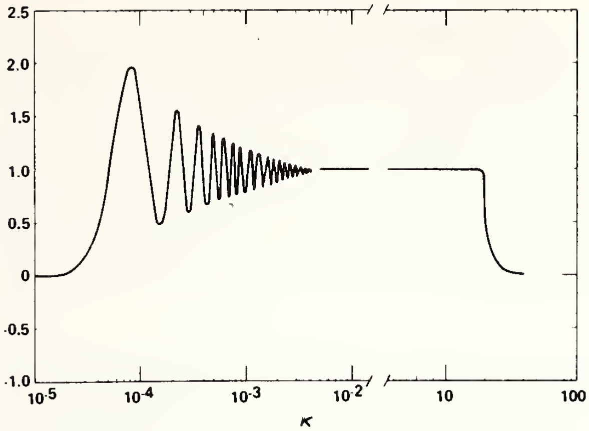

Fig. 2. Plot of transfer function $|I|^2$ versus K. For $K/2k_0 = \sin\theta$, $|I|^2$ is also angular spectrum of plane waves scattered from truncated Fourier component of surface roughness of wavenumber K.

$4\sin^2[k_0z'(1-\sec\theta_0)]$, the scattering cross section of a circular plate of diameter $2z'\tan\theta_0$. Second, the curve asymptotically approaches its final value of unity beginning at $K \approx 2(z'\tan\theta_0)^{-1}$, indicating the irregularities in the surface roughness that are larger than, or of the same order as, the beam diameter are severely affected by the truncated illumination of the beam pattern; whereas, higher spatial frequencies are not. Third, the cutoff of $|I|^2$ occurs at a spatial wavenumber $K = 2k_0\tan\theta_0$. These three characteristics have simple physical interpretations. The quantity $|I|^2$ describes the first-order Bragg scattering properties of different Fourier components of the surface roughness that are truncated by the finite illumination pattern of the transmitter. For very low spatial frequencies ($K \to 0$) the irregular surface resembles a flat, circular plate so that the power at $K = 0$ should be proportional to the scattering cross section of that particular geometry. As observed, the scattering properties of short-wavelength Fourier components of surface roughness (much less than the beam diameter $2z'\tan\theta_0$) are essentially unaffected by the truncated illumination pattern, whereas larger spatial wavelengths will have their scattering lobes considerably broadened. Finally, from the Bragg theory, surface irregularities of spatial wavenumber K will backscatter energy at an angle $\theta = \sin^{-1}[K/2k_0]$. Clearly, when $K/2k_0 > \tan\theta_0$ most of the energy will be scattered out of the receiving cone. This accounts for the precipitous decrease of $|I|^2$ beyond the point $K = 2k_0\tan\theta_0$.

A useful engineering approximation for $|I|^2$ can be obtained from (34):

$$|I(K)|^2 = \begin{cases} 1 + J_0^2(Kz'\tan\theta_0) \\ \quad - 2\cos[2k_0z'(1-\sec\theta_0)]J_0(Kz'\tan\theta_0), \\ \qquad \text{for } K \leqslant 2k_0\tan\theta_0 \\ 0, \qquad \text{for } K > 2k_0\tan\theta_0. \end{cases} \tag{36}$$

From Fig. (2), we see that $|I|^2 \approx 1$ in the region $(z'\tan\theta_0)^{-1} \ll K \leqslant 2k_0\tan\theta_0$. For typical satellite parameters $\theta_0 \sim 0.05$, $k_0 \cong 200\ \text{m}^{-1}$, and $z' \sim 10^6$ m, we have $2 \times 10^{-5}\ \text{m}^{-1} \ll K \lesssim 20\ \text{m}^{-1}$. Over this broad spectral range the angular spectrum of plane waves arriving at the receiver $G(K)$ is identical to the angular spectrum of scattered waves just above the ocean surface $F(K)$.

Because there is negligible area under $|I|^2$ in the region $0 \leqslant K \leqslant 10(z'\tan\theta_0)^{-1}$ compared with the region $10(z'\tan\theta_0)^{-1} \leqslant K \leqslant 2k_0\tan\theta_0$ for a typical satellite geometry, we make a negligible error by assuming that $|I|^2$ is roughly constant throughout the entire region $0 \leqslant K \leqslant 2k_0\tan\theta_0$. From (28) we see that $G(\mathbf{K}) = F(\mathbf{K})|I|^2$. If $F(K)$ has no significant power beyond $K = 2k_0\tan\theta_0$, then $G(\mathbf{K}) = F(\mathbf{K})$, and from their respective definitions, [(22) and (27)] $D_\phi(\rho) = 4k_0^2D_\xi(\rho)$. Hence, the wave-height statistics are proportional to the phase statistics.

To estimate the bandwidth of $F(K)$, note that $F(K)$ is the power spectral density of $\exp[i2k_0\xi]$ with ξ a random variable. A reasonable estimate of the bandwidth of a phase modulated signal is the maximum instantaneous spatial frequency. For a phase modulated wave $\exp[i\phi(x)]$ the bandwidth $\delta \leqslant (\partial\phi/\partial x)_{\max}$. In the case of phase modulation due to ocean waves $\delta \sim 2k_0s$ where s is the rms wave slope. Again, to minimize spectral distortion, the bandwidth of $F(K)$ must be less than the spectral width of $|I|^2$, i.e.,

$$\tan\theta_0 > s. \tag{37}$$

For $s \cong 0.04$ a half-beamwidth of approximately three degrees will satisfy (36). Under this approximation, the phase statistics and wave height statistics are proportional, that is

$$D_\phi(\rho) = 4k_0^2D_\xi(\rho). \tag{38}$$

IV. CONCLUSIONS

We have shown that, for reasonable microwave propagation parameters ($f_0 \sim 10$ GHz, $k_0 \sim 200\ \text{m}^{-1}$, $\theta_0 \sim 0.05$ rad antenna half-beamwidth), the phase structure function[2] can be written directly in terms of the wave-height structure function giving

$$D_\phi(\rho) = 4k_0^2D_\xi(\rho). \tag{39}$$

This also implies the following relationship between the signal phase spatial spectrum $S_\phi(\mathbf{K})$ and the two-dimensional wave-height spatial spectrum $S(\mathbf{K})$:

$$S_\phi(\mathbf{K}) = 4k_0^2S(\mathbf{K}). \tag{40}$$

A satellite traversing a line can measure the above quantities only along a single direction, i.e., $\mathbf{K} = K\cos\alpha\hat{x} + K\sin\alpha\hat{y}$, where α is the nadir-pointing track angle with respect to an arbitrary x-y coordinate geometry at the earth's surface. This unidirectional wave spectral measurement is identical to that obtained from an airborne laser profilometer, where the received signal phase (or time of flight) varies in direct proportion to the height of the sea as the instrument "profiles" the ocean waves. The important conclusion to be drawn here is that the final spectral results (40) are identical for the laser profilometer and the microwave nadir-pointing phase-measuring radar, even though the scattering mechanisms are entirely different. In the former case, the reflection occurs from an infinitesimally small moving spot on the surface, whereas in the latter the scatter originates from a continuous, rough sea patch tens of kilometers in diameter.

---

[2] Assumed in this discussion is the continuous measurement of phase beyond a single 0–360° interval.

A final, obvious result, is implied by (39) and (40), relating the rms sea wave height k to the rms signal phase σ_ϕ:

$$\sigma_\phi = 2k_0 h. \tag{41}$$

APPENDIX I

In the derivation of (7), we ignore the contributions of the amplitude fluctuations. If these fluctuations are retained (7) would have read

$$\gamma(\rho') = e^{x(\rho') + i\phi_1(\rho')}, \tag{A1}$$

where $x = \ln(A/A_0)$ is the logarithm of the relative amplitude of the received signal. The contribution of x in the final result (38) can be estimated by computing $\langle\gamma\gamma^*\rangle$. If we assume that fluctuations in x and ϕ_1 are uncorrelated, then

$$\langle\gamma(\rho')\gamma^*(\rho' + \rho)\rangle = \langle e^{x(\rho') + x(\rho' + \rho)}\rangle\langle e^{i[\phi_1(\rho') - \phi_1(\rho' + \rho)]}\rangle. \tag{A2}$$

From (24) the second factor of (A2) can be written in terms of the phase structure function, and we obtain

$$\langle\gamma(\rho')\gamma^*(\rho' + \rho)\rangle = \langle e^{x(\rho') + x(\rho' + \rho)}\rangle e^{-\frac{1}{2}D_\phi(\rho)}. \tag{A3}$$

To estimate the error in ignoring the first factor we compute the indicated expected value in two cases, when the x's are completely correlated and then, when they are completely uncorrelated. If the amplitude fluctuations are Rayleigh distributed, that is,

$$P(A) = \frac{A}{\sigma^2} e^{-A^2/(2\sigma^2)}, \tag{A4}$$

then it is easy to prove that

$$P(x) = 2e^{2x} e^{-e^{2x}}. \tag{A5}$$

From (A5), we calculate the expected value for the case of perfect correlation,

$$\langle e^{2x}\rangle = 1, \tag{A6}$$

and for the case of uncorrelated random variables,

$$\langle e^x\rangle\langle e^x\rangle = \pi/4. \tag{A7}$$

Therefore, throughout the whole range of displacements ρ,

$$\pi/4 \leqslant \langle e^{x(\rho') + x(\rho' + \rho)}\rangle \leqslant 1. \tag{A8}$$

Equation (A4) is the error attributed to ignoring amplitude fluctuations. To compute the ultimate error in the estimate of the phase fluctuations, we note that (A4) enters into the final calculation (38) in the form

$$D_\phi(\rho) = 4k_0^2 D_\xi(\rho) + 2\ln\left[\langle e^{x(\rho') + x(\rho' + \rho)}\rangle\right]. \tag{A9}$$

The second term ranges between zero and $2\ln(\pi/4) = -0.48$ as ρ increases. In the same range of ρ, the first term goes from zero to $4k_0^2\sigma_\xi^2$, where σ_ξ^2 is the waveheight variance. For a rough sea surface $\sigma_\xi \sim 1$ and $4k_0^2\sigma_\xi^2 \sim 1.6 \times 10^5$. Clearly, the error introduced by ignoring amplitude fluctuations is insignificant.

APPENDIX II

As pointed out by the reviewers, there is an additional more fundamental interpretation of (28) in terms of the coherence function of the wave field upon reception. Actually, the coherence history is recorded in (28). Initially, the wave emitted by the antenna of aperture size d_0 illuminates the sea surface with a wave that is coherent over its illuminated spot diameter $D \sim 2z'/(k_0 d_0)$. Immediately upon reflection the wave phase front has the same corrugations as the sea surface itself; therefore, the coherence properties just above the sea surface are determined by the properties of the rough surface. The coherence function of the wave back at the receiver will be a convolution of the surface statistics and purely geometrical propagation factors such as λ, z', and d_0.

To illustrate these points, we return to the Fourier transformed version of (28)

$$M(\rho) \equiv \frac{\langle H(\rho')H^*(\rho' + \rho)\rangle}{|H_0|^2} = \int d^2\mathbf{K}_1 e^{i\mathbf{K}_1\cdot\rho}\,|I(K_1)|^2 \cdot \int d^2\rho_1 \frac{e^{-2k_0^2 D_\xi(\rho_1) - iK_1\cdot\rho_1}}{(2\pi)^2}, \tag{A10}$$

where M is the mutual coherence function (MCF) of the received field. (Note $e^{-2k_0^2 D_\xi(\rho_1)}$ is the MCF of the scattered field at the sea surface immediately after scattering). For illustrative purposes only, we assume that $|I|^2$ is a Gaussian function of the form

$$|I|^2 \sim e^{-K^2/(2k_0 \tan\theta_0)^2}, \tag{A11}$$

in line with the behavior of $|I|^2$ exhibited in its approximate version (36). We now approximate $D_\xi(\rho_1) = 2\sigma_\xi^2[1 - R_\xi(\rho_1)]$ by a quadratic function of ρ_1, that is, $D_\xi(\rho_1) \approx 2\sigma_\xi^2\rho_1^2/\rho_s^2$ where from the definition of $R_\xi(\rho_1)$, ρ_s is the correlation length of the irregular sea surface that has a wave-height variance σ_ξ^2. It is not difficult to show that this assumption reduces the coherence function of the wave just as it leaves the sea surface to a form consistent with Barrick's [6], [13] stationary phase solution in terms of rms wave slope, that is,

$$e^{-2k_0^2 D_\xi(\rho_1)} = e^{-4k_0^2\sigma_\xi^2[1 - R_\xi(\rho_1)]} = e^{-4k_0^2\sigma_\xi^2(\rho_1^2/\rho_s^2)}. \tag{A12}$$

To proceed further, we note that $\rho_s = 2\sigma_\xi s^{-1}$, where s is the rms surface slope, and therefore

$$e^{-2k_0^2 D_\xi(\rho_1)} \equiv e^{-(\rho_1/\rho_{0s})^2} = e^{-k_0^2 s^2 \rho_1^2} \tag{A13}$$

where from our development ρ_{0s} is interpreted as the coherence length of the wave just as it leaves the sea surface. The form of (A13) is now identical to that of Barrick's solution. If we insert (A13) and (A11) into (A10) we obtain the result

$$M(\rho) \propto \exp \frac{-\rho^2}{4}\left[\frac{1}{k_0^2 \tan^2 \theta_0} + \frac{1}{k_0^2 s^2}\right]^{-1}, \qquad \text{(A14)}$$

so the coherence length of the received field, defined roughly by $M(\rho_0) = e^{-1}$, becomes

$$\rho_0 = 2\left[\frac{1}{k_0^2 \tan^2 \theta_0} + \frac{1}{(k_0 s)^2}\right]^{1/2}. \qquad \text{(A15)}$$

To put the result in final form, note that $\tan \theta_0 \sim 2/(k_0 d_0)$, so that

$$\rho_0 = \left[d_0^2 + \frac{4}{(k_0 s)^2}\right]^{1/2}. \qquad \text{(A16)}$$

Note that as the coherence length of the field at the surface $\rho_{0s} = (k_0 s)^{-1} \to 0$, that is, the scattering is completely incoherent, we obtain the result attributable to the Van Cittert-Zernike theorem; namely, you obtain independent samples of the scattered *field* each time the receiver aperture moves its diameter. The result (A16), the modified Van Cittert-Zernicke theorem, shows that in partially coherent scattering, which is the case applicable to the sea scatter problem, there is an additional surface-dependent term that contributes to the coherence length of the received field. In the general case $d_0 \sim 4(k_0 s)^{-1}$ so that a more complicated inversion procedure than that suggested by (38) will be necessary (see comments about (30)).

Finally, as a caution, (38) demonstrates that the phase correlation length is the same as the wave-height correlation length. This should not be confused with the *coherence* length of the field which is given by (A16) and is considerably smaller. The field decorrelates in a distance much shorter than the distance over which the phase decorrelates.

REFERENCES

[1] D. E. Barrick, "First-order theory and analysis of MF/HF/VHF scatter from the sea," *IEEE Trans. Antennas Propagat.*, vol. AP-20, pp. 2-10, Jan. 1972.

[2] D. E. Barrick, "Remote sensing of sea state by radar," in *Remote Sensing of the Troposphere*, V. E. Derr, Ed. Washington, DC: U.S. Government Printing Office, 1972, pp. 12.1-12.24.

[3] P. Wadhams, "Airborne laser profiling of swell in an open ice field," *J. Geophysical Res.*, vol. 80, pp. 4520-4528, 1975.

[4] J. T. McGoogan, "Satellite altimetry applications," *IEEE Trans. Microwave Theory Tech.*, vol. MTT-23, pp. 970-978, 1975.

[5] C. T. Swift, and W. L. Jones, Jr., "Satellite radar scatterometry," *1974 IEEE INTERCON*, Technical Papers, Paper No. 34/4, 1974.

[6] D. E. Barrick, "Relationship between slope probability density and the physical optics integral in rough surface scattering," in *Proc. IEEE*, vol. 56, pp. 1728-1729, 1968.

[7] G. T. Ruck, D. E. Barrick, W. D. Stuart, and C. K. Krichbaum, *Radar Cross Section Handbook, Vols. I and II.* New York: Plenum, 1970, pp. 50-63 and 719-727.

[8] A. M. Yaglom, *Introduction to the Theory of Stationary Random Functions.* Englewood Cliffs, NJ: Prentice-Hall, 1962, 223.

[9] V. I. Tatarskii, *The Effects of the Turbulent Atmosphere on Wave Propagation.* Springfield, VA: National Technical Information Service, 1971, 472.

[10] M. Isakovich, "The scattering of waves from a statistically rough surface," *Zhurnal Eksperimentalnoi Teoreticheskoi Fiziki (USSR)*, vol. 23, pp. 305-314, 1952. English translation by M. Friedman.

[11] Lord Rayleigh, *Theory of Sound, Vol. II.* London: Macmillan, 1929, pp. 89-96.

[12] S. O. Rice, "Reflection of electromagnetic waves from slightly rough surfaces," in *Theory of Electromagnetic Waves*, M. Kline, Ed. New York: Interscience, 1951, pp. 351-378.

[13] D. E. Barrick, "Rough surfaces," Chapter 9 of *Radar Cross Section Handbook, Vol. II*, G. Ruck, Ed. New York: Plenum, 1970, pp. 671-772.

Radio Science, 13: 985-989, 1978.

Spot size of the radar return from a radar-acoustic sounding system (RASS) due to atmospheric refractive turbulence

S. F. Clifford, Ting-i Wang, and J. T. Priestley

Wave Propagation Laboratory, Environmental Research Laboratories, National Oceanic and Atmospheric Administration, US Department of Commerce, Boulder, Colorado 80302

(Received March 1, 1978.)

We have calculated the intensity profile on the receiving plane of a radar-acoustic sounding system (RASS) in the presence of varying amounts of atmospheric refractive turbulence. The results indicate that the refractive turbulence produces corrugations in the initially spherical acoustic wavefronts and these corrugations scatter electromagnetic energy over a large solid angle in the backward hemisphere. The net effect is to leave the scattered beamshape nearly unchanged from its form in the case of a homogeneous atmosphere. Of course the on-axis intensity is reduced considerably but the energy is scattered into such a large solid angle that this produces only an increased background level or tails in the electromagnetic intensity profile.

INTRODUCTION

The radar-acoustic sounding system (RASS) is potentially an effective tool for remotely sensing temperature profiles in the lower atmosphere. RASS measures temperature by launching an acoustic pulse vertically and then measuring its speed by tracking it with a Doppler radar, the absolute temperature being proportional to the square of the speed of sound. The reflected electromagnetic wave would be undetectably weak if it were not for the possiblity of taking advantage of two effects. The first is the constructive interference that occurs for the backscattered wave—Bragg scattering when the electromagnetic wavelength is made twice the acoustic wavelength. The second is the focusing effect of the electromagnetic wave off the almost-spherical acoustic wavefronts, which causes the returning electromagnetic energy to be concentrated into a small spot perhaps not much larger than the transmitting antenna. Each of the above phenomena is capable of increasing the intensity of the returning signal by several orders of magnitude and both are needed.

The second phenomenon, however, contains the seeds of a major problem: the fact that the returning signal is concentrated into a small spot makes it difficult to "catch." The problem arises because wind can advect the pulse horizontally causing the spot to miss the receiving antenna.

Irrespective of what method is used to catch the spot—a field of receiving antennas, a movable antenna, or some other method—a major design consideration is the spot size on the ground or, more specifically, its intensity profile on the ground. In an earlier paper [*Clifford and Wang*, 1977] the intensity at the center of the spot was computed under realistic turbulence conditions. In the present paper, we extend our previous work to the entire intensity profile. This process of specular reflection from the advected acoustic pulse was hypothesized by *North* [1974] and *Bhatnagar et al.* [1977] and experimentally verified by *Frankel et al.* [1977].

We should note that *Bhatnagar* [1977] and *Bhatnagar et al.* [1977] predicted that the coherence of vertically propagating acoustic waves was not affected by turbulence for frequencies below a few kilohertz. This is in substantial disagreement with our findings. However, Bhatnagar *et al.* used the model of altitude dependence of C_n^2 proposed by *Brown and Keeler* [1975]. Unfortunately, this model ignored the effects on C_n^2 of velocity fluctuations and hence underestimates C_n^2 dramatically for altitudes above several tens of meters [see *Brown and Clifford*, 1976]. If we assume a more realistic model in which C_n^2 is a constant (i.e., $m_a = 0$ for Bhatnagar *et al.*) and if we let $C_n^2 = 3.5 \times 10^{-7}\ \mathrm{m}^{-2/3}$ (the lower limit of Eq. (18) of Brown and Clifford), we obtain a coherence length (in the notation of Bhatnagar *et al.*) X_c that is about 800 m at $f_a =$

This article not subject to U.S. copyright. Published 1978 by the American Geophysical Union.

0048-6604/78/1112-0985$01.00

1 kHz. A further source of difficulty is the key role that the outer scale of refractive turbulence plays in the formulation of Bhatnagar *et al.* For the particular functional form they assume, that is, increasing as the square root of height, there is a range at which the outer scale is less than the beamwidth. This distorts the beamwidth dependence which would occur in the real atmosphere because the outer scale in the horizontal dimension is of the order of the largest-scale intermittency in the refractive turbulence. This can be, and is observed to be, of the order of at least one kilometer in the horizontal direction at heights above a few hundred meters, much larger than the beamwidth at these heights.

In a recent paper, *Frankel et al.* [1977] performed an experiment to test the coherency of the acoustic wave front. They fixed the range to 300 m, and then varied the pulse length (N cycles) of the acoustic wave. The results indicate that the received power is linearly proportional to N^2. Hence they concluded that the coherency of the acoustic wave front is maintained. However, we should point out that this experiment can only test the longitudinal coherence of the wave and tests nothing of the transverse wave front coherence which we believe is one of the principal mechanisms of the degradation of RASS.

ANALYSIS

To calculate focal spot size, we start from the expression for the electric field (Eq. (4) of *Clifford and Wang* [1977]),

$$E_s(\boldsymbol{\rho}) = \frac{k_e^2 \xi_0 A_0}{2\pi} \int_{V(R)} d^3\mathbf{r}_1 r_1^{-2} \frac{\exp(ik_e|\boldsymbol{\rho} - \mathbf{r}_1|)}{|\boldsymbol{\rho} - \mathbf{r}_1|} \cdot \exp[ik_e r_1 + \chi(\mathbf{r}_1)] \cos[k_a r_1 + S_1(\mathbf{r}_1)] \tag{1}$$

The quantity E_s is the electric field of wavenumber k_e, scattered from an acoustic pulse of wavenumber k_a, observed at the point $\boldsymbol{\rho}$. The acoustic pulse has been distorted by the refractive turbulence intervening between the source and scattering volume $V(R)$ such that, at the range R, it produces a refractive index variation N_1 of the form

$$N_1(\mathbf{r}_1) = \begin{cases} \xi_0 \mathrm{Re}\{\exp[ik_a r_1 + \psi(\mathbf{r}_1)]/r_1\}; \\ \quad R - N\lambda_a/2 < r_1 < R + N\lambda_a/2 \\ 0; \quad \text{otherwise,} \end{cases} \tag{2}$$

N is the number of cycles in the acoustic pulse, $\psi = \chi + iS_1$, χ and S_1 are the log-amplitude and relative phase perturbations imposed by the refractive turbulence. The electric field incident upon the distorted acoustic pulse has an amplitude A_0 and because of the phase and amplitude distortions suffered by the acoustic wave, the focal spot will be smeared out from the sharp focus expected in the case of a smooth spherical reflector, by an amount that depends on the severity of the acoustic refractive turbulence and the range to the scattering volume.

To calculate the profile of the beam in the receiving plane we multiply (1) by its complex conjugate, that is,

$$\langle I(\boldsymbol{\rho})\rangle = \langle|E_s(\boldsymbol{\rho})|^2\rangle = \frac{k_e^4 \xi_0^2 A_0^2}{(2\pi)^2} \int_{V(R)} d^3\mathbf{r}_1 \frac{\exp(ik_e|\boldsymbol{\rho} - \mathbf{r}_1|)}{r_1^2|\boldsymbol{\rho} - \mathbf{r}_1|} \cdot \int_{V(R)} d^3\mathbf{r}_2 \frac{\exp[-ik_e|\boldsymbol{\rho} - \mathbf{r}_2| + ik_e(r_1 - r_2)]}{r_2^2|\boldsymbol{\rho} - \mathbf{r}_2|} \cdot \langle\exp[\chi(\mathbf{r}_1) + \chi(\mathbf{r}_2)] \cos[k_a r_1 + S_1(\mathbf{r}_1)] \cdot \cos[k_a r_2 + S_1(\mathbf{r}_2)]\rangle \tag{3}$$

For reasonable propagation parameters, such as the range assumed to be much greater than the acoustic pulse length, $R \gg N\lambda_a$, there are many simplifying assumptions that can be made. In the denominator of the integral of (3), we make an approximation with negligible error by setting $r_1 \sim r_2 \sim R$ and because $R \gg N\lambda_a$ and $R \gg \rho$, by assumption, then $|\boldsymbol{\rho} - \mathbf{r}_1| \sim |\boldsymbol{\rho} - \mathbf{r}_2| \sim R$. The quantity inside the angle brackets, that imply an ensemble average, was evaluated in Appendix I of *Clifford and Wang* [1977] and found to be

$$\langle\exp[\chi(\mathbf{r}_1) + \chi(\mathbf{r}_2)] \cos[k_a r_1 + S_1(\mathbf{r}_1)] \cdot \cos[k_a r_2 + S_1(\mathbf{r}_2)]\rangle = (1/2)\exp[-(1/2)D_w(\mathbf{r}_1,\mathbf{r}_2)] \cdot \cos[k_a(r_1 - r_2)] \tag{4}$$

where D_w is the wave structure function defined by

$$D_w(\mathbf{r}_1,\mathbf{r}_2) = \langle[\psi(\mathbf{r}_1) - \psi(\mathbf{r}_2)]^2\rangle = D_\chi(\mathbf{r}_1,\mathbf{r}_2) + D_s(\mathbf{r}_1,\mathbf{r}_2) \tag{5}$$

where

$$D_\chi(\mathbf{r}_1,\mathbf{r}_2) = \langle[\chi(\mathbf{r}_1) - \chi(\mathbf{r}_2)]^2\rangle \tag{6}$$

and similarly

$$D_s(\mathbf{r}_1, \mathbf{r}_2) = \langle [S_1(\mathbf{r}_1) - S_1(\mathbf{r}_2)]^2 \rangle \tag{7}$$

Taking advantage of all these simplifications in (3), we obtain

$$\langle I(\rho) \rangle = \frac{k_e^4 \xi_0^2 A_0^2}{8\pi^2 R^6} \int_V d^3\mathbf{r}_1 \int_V d^3\mathbf{r}_2 \exp\{ik_e [|\rho - \mathbf{r}_1| - |\rho - \mathbf{r}_2|] + ik_e(r_1 - r_2)\} \cos [k_a(r_1 - r_2)] \cdot \exp[-(1/2) D_w(\mathbf{r}_1, \mathbf{r}_2)] \tag{8}$$

The wave structure function has the approximate functional form $D_w(\mathbf{r}_1, \mathbf{r}_2) \sim D_w[Rg, R]$, where $g = [\sin^2\theta_1 + \sin^2\theta_2 - 2 \sin\theta_1 \sin\theta_2 \cos(\phi_1 - \phi_2)]^{1/2}$. [In an earlier paper, an erroneous form of the angular dependence of D_w was assumed (equation (8) of *Clifford and Wang* [1977]). The correct dependence is as stated here. To correct the results, (21) of that paper should read $I = H^{-6/5}$. Figures 1 and 2 of the paper can easily be modified to the correct form by replacing H by $4.24H^2$ in the abscissa of Figure 1, and changing the 10 db range limitation ordinate of Figure 2 to the 27 db range limitation. The range dependence mentioned in the abstract will be changed to $R^{-26/5}$ in the case of strong turbulence.] Substituting D_w into (8) and changing to spherical coordinates, we obtain

$$\langle I(\rho) \rangle = \frac{k_e^4 \xi_0^2 A_0^2}{8\pi^2 R^6} \int_0^{2\pi} d\phi_1 \int_0^{2\pi} d\phi_2 \int_0^{\gamma} d\theta_1 \sin\theta_1 \cdot \int_0^{\gamma} d\theta_2 \sin\theta_2 \int_{R-N\lambda_a/2}^{R+N\lambda_a/2} dr_1 r_1^2 \int_{R-N\lambda_a/2}^{R+N\lambda_a/2} dr_2 r_2^2 \cdot \exp\{ik_e [|\rho - \mathbf{r}_1| - |\rho - \mathbf{r}_2| + \mathbf{r}_1 - \mathbf{r}_2] - (1/2)\mathrm{D}_w [Rg, R]\} \cos [k_a(r_1 - r_2)] \tag{9}$$

where γ is the smaller of the acoustic or electromagnetic half beamwidths; γ_a and γ_e respectively. If we note that $\gamma \ll 1$, $r_1^2 \sim r_2^2 \sim R^2$ and without loss of generality $|\rho - \mathbf{r}_{1,2}| \sim [\rho^2 + r_{1,2}^2 - 2\rho r_{1,2} \sin\theta_{1,2} \cos\phi_{1,2}]^{1/2}$ then (9) becomes

$$\langle I(\rho) \rangle = \frac{k_e^4 \xi_0^2 A_0^2}{8\pi^2 R^6} \int_{R-N\lambda_a/2}^{R+N\lambda_a/2} dr_1 \int_{R-N\lambda_a/2}^{R+N\lambda_a/2} dr_2 \int_0^{\gamma} d\theta_1 \sin\theta_1 \cdot \int_0^{\gamma} d\theta_2 \sin\theta_2 \int_0^{2\pi} d\phi_1 \int_0^{2\pi} d\phi_2 \exp[ik_e(r_1 - r_2)] \cdot \cos [k_a(r_1 - r_2)] \exp \{ik_e [(r_1^2 + \rho^2 - 2\rho \mathrm{r}_1 \sin\theta_1 \cos\phi_1)^{1/2} - (\mathrm{r}_2^2 + \rho^2 - 2\rho \mathrm{r}_2 \sin\theta_2 \cdot \cos\phi_2)^{1/2}]\} \exp \{-(1/2) D_w [Rg, R]\} \tag{10}$$

After expanding the square roots we can drop all but the two largest terms if $k_e \rho^2/R \lesssim 1$, that is, if $\rho_{\max} \leq (\lambda_e R)^{1/2}$. Assuming the validity of this approximation for a RASS system (with $\lambda_e \sim 0.2$ m and $R \sim 1000$ m, then $\rho_{\max} \leq 14$ m), we can write

$$\langle I(\rho) \rangle = \frac{k_e^4 \xi_0^2 A_0^2}{8\pi^2 R^2} \int_{R-N\lambda_a/2}^{R+N\lambda_a/2} dr_1 \int_{R-N\lambda_a/2}^{R+N\lambda_a/2} dr_2 \cdot \exp[i2k_e(r_1 - r_2)] \cos [k_a(r_1 - r_2)] \int_0^{\gamma} d\theta_1 \theta_1 \cdot \int_0^{\gamma} d\theta_2 \theta_2 \int_0^{2\pi} d\phi_1 \int_0^{2\pi} d\phi_2 \exp \{-(1/2) D_w [Rg, R]\} \cdot \exp \{ik_e \rho [\theta_1 \cos\phi_1 - \theta_2 \cos\phi_2]\} \tag{11}$$

To obtain (11), we have made the small-angle approximations $\sin\theta_1 = \theta_1$ and $\sin\theta_2 = \theta_2$. In (11), the r_1, r_2 integrals are now straightforward, so that

$$\langle I(\rho) \rangle = \frac{k_e^4 \xi_0^2 A_0^2}{16\pi^2 R^2} (N\lambda_a)^2 \left\{ \frac{\sin [(k_a - 2k_e) N\lambda_a/2]}{(k_a - 2k_e)(N\lambda_a/2)} \right\}^2 \cdot f(\rho) \tag{12}$$

where

$$f(\rho) = \int_0^{\gamma} d\theta_1 \theta_1 \int_0^{\gamma} d\theta_2 \theta_2 \int_0^{2\pi} d\phi_1 \int_0^{2\pi} d\phi_2 \cdot \exp \{-(1/2) D_w [Rg, R]\} \exp \{ik_e \rho [\theta_1 \cos\phi_1 - \theta_2 \cos\phi_2]\} \tag{13}$$

The function $f(\rho)$ now determines the shape of the RASS focal spot. The result of (13), found by the integration procedure shown in (13)–(20) of *Clifford and Wang* [1977], is plotted in Figure 1, where

$$H = 1.46\, k_a^2 R^{8/3} \gamma^{5/3} \int_0^1 du\, C_n^2(Ru) u^{5/3} \tag{14}$$

Apparently, spot size doesn't change substantially even for a relatively strong turbulence case ($H \geq 100$). This can be explained physically by noting that the acoustic wave front can be decomposed into two parts, the unperturbed spherical wavefront and the random wavefront perturbed by atmospheric turbulence. The EM wave scattered by the random part will radiate to a very large angle (probably the whole lower hemisphere). This will produce a small background scatter level over a large solid angle on the receiving plane. In the

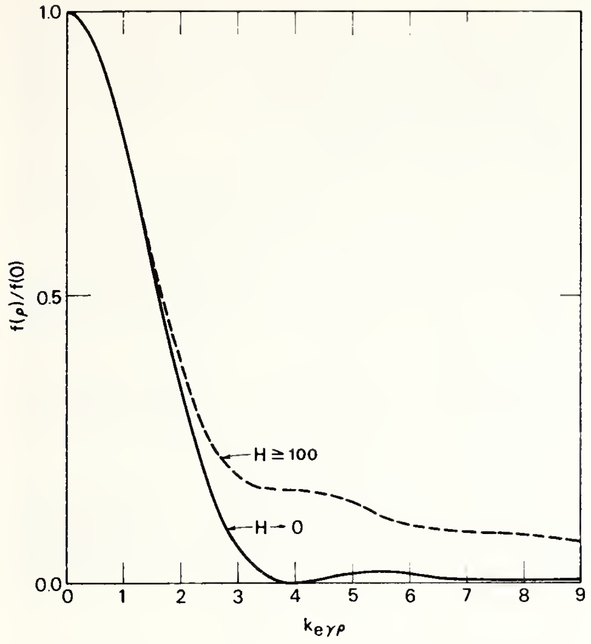

Fig. 1. The normalized receiving intensity profile $f(\rho)/f(0)$ of RASS with the presence of turbulence. Here the turbulence parameter $H = 1.46\, k_a^2 R^{8/3}\gamma^{5/3}\int_0^1 du\, C_n^2(Ru)u^{5/3}$; k_a and k_e are the acoustic and EM wave number respectively; R is the range, γ is the smaller of the acoustic or EM beamwidth; ρ is the distance from the center of the beam; and C_n^2 is the atmospheric turbulence structure constant.

presence of turbulence, the original, unperturbed, spherical pulse will scatter a greatly reduced amount of energy but into such a narrow solid angle that this will still predominate in the determination of the received spot size and, as a result, the spot size becomes quite insensitive to the amount of refractive turbulence.

DISCUSSION

We would now like to examine these results from a practical or engineering point of view. We want to know how the results affect the design and the performance of a RASS system.

At first glance the factor k_e in the abscissa of Figure 1 makes it appear that the spot size is dependent upon the frequency of the RASS. Actually the spot radius ρ is determined by $k_e\gamma$. If we assume that the antenna producing the smaller beam is of fixed size, the factor $k_e\gamma$ is constant. Therefore the spot size can be regarded as being determined by the size of the "controlling" antenna and independent of frequency.

From Figure 1 let us take γ as the half-angle of the controlling beam (smaller of the two beams) at the 3 dB point. (The calculation upon which Figure 1 is based actually assumes that the beam is uniform within the cone of half-angle γ and zero outside that cone but for present purposes this is a small point.) If we assume that the controlling beam is being emitted from a uniformly "illuminated" circular antenna of radius a, its relative beam intensity as a function of angle θ will be

$$I(\theta) = [2\,J_1(ka\sin\theta)/ka\sin\theta]^2$$

or for small angles,

$$I(\theta) = [2\,J_1(ka\theta)/ka\,\theta]^2 \tag{15}$$

At the 3 dB point this becomes

$$I(\gamma) = .5 = [2\,J_1(ka\gamma)/ka\,\gamma]^2 \tag{16}$$

or $k\gamma = 1.6/a$. Thus, if the electromagnetic beam is smaller we obtain $k_e\gamma = 1.6/a_e$, and if the acoustic beam is smaller it becomes $k_a\gamma = 1.6/a_a$. Since the electromagnetic and acoustic wave numbers need to be Bragg-matched (i.e., $k_a = 2\ k_e$), we obtain $k_e\gamma = 0.8(a_a)^{-1}$. Therefore the factor $k_e\gamma$ in the abscissa of Figure 1 may be replaced by $1.6/a_e$ or $.8/a_a$ depending upon which beam is smaller.

If we measure the spot size by its 3 dB point then reading off the graph we have $\rho = 1.6(k_e\gamma)^{-1} = a_e$ when the electromagnetic beam is smaller and $\rho = 2a_a$ when the acoustic beam is smaller.

We, therefore, conclude that if the ratio of antenna radii a_e/a_a is significantly greater than 2.0 then the spot diameter will be the same as that of the radar antenna. Similarly, if a_e/a_a is significantly less than 2.0 then the spot diameter will be twice that of the acoustic antenna. If the ratio a_e/a_a is in the intermediate range near 2.0 then we would expect the spot size would be determined by the convolution of two disks, one the size of the radar antenna and the other twice the size of the acoustic antenna.

One practical result of all this is that if one attempts to build a portable RASS by going to a higher frequency and thereby being able to reduce the antenna sizes, as suggested by *Frankel et al.* [1977], the spot size is going to be reduced accordingly, making it harder to catch.

CONCLUSION

We have calculated the received intensity profile of RASS as perturbed by atmospheric turbulence. Using a realistic turbulence model, the results indicate that the received intensity profile (spot size) remains unchanged for weak and strong turbulence. We have also pointed out that the limiting range obtained by *Bhatnagar et al.* [1977] would be smaller if a realistic turbulence model were used in their theory.

Acknowledgments. We are indebted to N. Bhatnagar for pointing out the erroneous assumption of our previous paper.

REFERENCES

Bhatnagar, N. (1977), Interaction of electromagnetic and acoustic waves in a stochastic atmosphere, Ph.D. dissertation, Stanford University, Stanford, CA.

Bhatnagar, N., M. S. Frankel, and A. M. Peterson (1977), Interaction of electromagnetic and acoustic waves in a stochastic atmosphere, Proc. Symp. EM Wave Propagation and Non-ionized Media, La Baule, France, pp. 928–934, available from P. Misme, CNFRS, 3 Ave. de la République, 92131 Issy-les-Moulineaux, France.

Brown, E. H., and S. F. Clifford (1976), On the attenuation of sound by turbulence, *J. Acoust. Soc. Amer., 60*, 788–794.

Brown, E. H., and R. J. Keeler (1975), Applications of propagation parameters to atmospheric echosondes, paper presented at 16th Radar Meteorology Conference, Houston, Texas.

Clifford, S. F., and T. Wang (1977), The range limitation on radar-acoustic sounding systems (RASS) due to atmospheric refractive turbulence, *IEEE Trans. Antennas Propagat., AP-25*, 319–326.

Frankel, M. S., N. J. F. Chang, and M. J. Sanders, Jr. (1977), A high-frequency radio acoustic sounder for remote measurement of atmospheric winds and temperature, *Bull. Amer. Meteorol. Soc.*, *58*, 928–934.

North, E. M., Jr. (1974), A radio acoustic sounding system for remote measurement of atmospheric temperature, *Fin. rep. SU-SEL-73-021*, Stanford Electronics Laboratories, Stanford, CA.

Laser Beam Propagation in The Atmosphere, 9-43, Springer-Verlag, 1978.

2. The Classical Theory of Wave Propagation in a Turbulent Medium

S. F. Clifford

With 9 Figures

An important consideration in any description of laser propagation in the atmosphere is the geometry of the optical path. The influence of various kinds of optical scatterers is often quite sensitive to the transmitter-receiver configuration. For example, the type of atmospheric refractive index irregularities that we consider important in this work, where forward scatter dominates, has a negligible effect when we calculate their contribution to backscatter. We restrict our attention in this book to the problem most commonly known as line-of-sight optical propagation. The receiver is in full view of the transmitter such that, in the absence of the atmosphere, the irradiance would be constant in time, with a value determined by the transmitter geometry plus vacuum diffraction effects. The introduction of the atmosphere between source and receiver produces spatial and temporal fluctuations in the received irradiance and other wave parameters such as phase, angle of arrival, and frequency that are due to random variations in atmospheric refractive index along the optical path.

This problem should be differentiated from wave scattering where the scattering volume is remote from both the transmitter and receiver and, in the absence of refractivity fluctuations to deflect some of the incident wave energy, there would be no received signal. In the line-of-sight case, the transmitter or receiver, or both, are usually imbedded in the turbulent medium, and the intervening refractive index fluctuations merely perturb the vacuum parameters of the wave.

There are two areas where analysis of this model has direct practical relevance. In communications, the motivation for studying the problem arises from the desire to take advantage of the potentially wide bandwidth of an optical system. In this context, the atmospherically induced noise degrades system performance and is something to be overcome. In contrast, this model is also being studied for its potential for remotely sensing atmospheric turbulence parameters, in which context the random fluctuations imposed by the atmosphere are the signal to be studied and the information is contained in them.

In this chapter, we are concerned with the effect on an optical wave of refractive index fluctuations caused by turbulent effects in the atmosphere. As we shall see, these refractive index fluctuations are primarily the result of small temperature fluctuations transported by the turbulent motion of the atmosphere. Changes in the optical signal due to absorption or scattering by molecules or aerosols are not discussed. The changes in refractive index caused by temperature fluctuations are usually smooth random functions of both space and time. As an aid in understanding the effects of the refractive index fluctuations, a region of high or low refractive index is often thought of as an eddy, which may behave very much as a lens. In this model the atmosphere may be thought of as a large number of random lenses, having different shapes and scale sizes, that move randomly through space. It should be kept in mind, however, that the refractive index is varying within an eddy, and no discontinuities in the refractive index are present.

In the earth's atmosphere, the interaction of an electromagnetic wave with a single refractive index fluctuation or eddy is extremely weak. To first order, there is no amplitude change at the position of the eddy, but merely a phase change caused by the change in velocity of the small segment of the wave that traverses the eddy. Because induced phase fluctuations are not the same at different points perpendicular to the direction of propagation, they may cause focusing or defocusing effects, local deviations in the direction of wave propagation, and eventually, through interference, irradiance fluctuations at the receiver. Because these eddies do not have sharp edges, we may ignore reflections. Similarily, the bounding surfaces of the fluctuating region are assumed not to have any sharp discontinuities. The process we consider here is merely diffraction of the wave by random inhomogeneities. As we shall see in Chapter 3, although the effect of an individual eddy on the wave is quite weak, the cumulative effect of many eddies can be extremely strong.

2.1 Description of the Atmosphere

2.1.1 Atmospheric Refractive Index

The refractive index of air at optical frequencies is given approximately by

$$n-1=77.6(1+7.52\times10^{-3}\lambda^{-2})(P/T)10^{-6}, \tag{2.1}$$

where P is the atmospheric pressure in millibars, T is the temperature in Kelvin, and λ is the wavelength of light in μm. Therefore, $n_1=n-1$ is a measure of the deviation of the refractive index from its free space value, and at sea level it has a typical value of 3×10^{-4}. In writing (2.1), we have neglected a term that depends on the water vapor pressure. Over land, this humidity-dependent term contributes significantly less than 1%. (For a more extensive analysis of optical refractive index with formulas valid to one part in 10^7, see *Owens* [2.1].) *Wesely* and *Alcaraz* [2.2] and *Friehe* et al. [2.3] indicated that a third contribution to (2.1) arises from the product of the temperature and humidity and that this term could significantly affect the refractive index on over-water paths. We shall be content here to use (2.1) and to ignore the refinements in the model described in [2.2].

2.1.2 The Role of Atmospheric Turbulence

The refractive index fluctuations that we are considering are those that result from the naturally occurring random fluctuations in wind velocity called turbulence. The description and phenomenology of turbulence constitute a vast field, perhaps best described in [2.4–7]. The following arguments will merely sketch the derivation outlined in these texts.

Because turbulence is a random process, it must be described in terms of statistical quantities. It is hopeless to attempt to predict the velocity of a given parcel of air as it is buffeted about in the open atmosphere. In fact, it is nearly impossible to do a complete statistical analysis; therefore, we settle for a more meager description. *Kolmogorov* [2.8], when considering the time variation of the difference of two velocities at two points in space separated by a displacement vector $\boldsymbol{r}$, found that the mean-square velocity difference could be described by a universal form over a rather broad range of spatial scale sizes of motion. His so-called structure tensor is defined in general by

$$D_{ij}(\boldsymbol{r})=\langle[v_i(\boldsymbol{r}_1+\boldsymbol{r})-v_i(\boldsymbol{r}_1)][v_j(\boldsymbol{r}_1+\boldsymbol{r})-v_j(\boldsymbol{r}_1)]\rangle, \tag{2.2}$$

where v_i and v_j refer to the different components of the velocity, and the angle brackets indicate an ensemble average. Two further assumptions greatly simplify (2.2). The first is the assumption of local homogeneity, which implies that the velocity difference statistics depend only on the displacement vector $\boldsymbol{r}$. The second is the assumption of local isotropy, which implies that only the magnitude of $\boldsymbol{r}$ is important. The adjective "local" applies because we are considering differences between the velocities at two points and hence only scale sizes of the order of the separation are important (velocity components with scale sizes larger than the separation will tend to be filtered out by the subtraction process).

The impact of these two assumptions on (2.2) allows D_{ij} to be written in the form

$$D_{ij}(r)=[D_{rr}(r)-D_{tt}(r)]n_in_j+D_{tt}(r)\delta_{ij}, \tag{2.3}$$

where $\delta_{ij}=1$ for $i=j$, $\delta_{ij}=0$ for $i\neq j$, and the n_i are components of the unit vector directed along $\boldsymbol{r}$. The quantities D_{rr} and D_{tt} are, respectively, the structure functions of the wind velocity component parallel and transverse to the displacement $\boldsymbol{r}$. By making one further assumption of incompressible turbulence, that is, $\boldsymbol{\nabla}\cdot\boldsymbol{v}=0$ (*Batchelor* [2.4]), we can write D_{tt} in terms of D_{rr}, that is,

$$D_{tt}=\frac{1}{2r}\frac{d}{dr}(r^2D_{rr}). \tag{2.4}$$

The important result of the analysis leading to (2.3) and (2.4) is that the statistical structure of turbulence can now be described by the single structure function D_{rr} where

$$D_{rr}=\langle[v_r(r_1+r)-v_r(r_1)]^2\rangle\,. \tag{2.5}$$

Kolmogorov [2.8] found that as long as the separation r lay in the so-called inertial subrange of turbulence, D_{rr} has a universal form

$$D_{rr}=C_v^2 r^{2/3}\,, \tag{2.6}$$

where C_v^2 is the velocity structure constant, a measure of the total amount of energy in the turbulence. This form should persist for values of r between the microscale of turbulence l_0 up to the outer scale of turbulence L_0. The microscale corresponds to the eddy size below which dissipation of energy in the eddy through viscous effects becomes important. The outer scale corresponds to the largest scale size for which the eddies may be considered to be isotropic. (Near the ground l_0 is of the order of millimeters and L_0 of the order of meters. Both quantities appear to increase with height above ground.) If this result is true, and indeed the amount of supporting experimental evidence is amazing (*Myrup* [2.9] and *Kaimal* et al. [2.10]), then (2.6) is all we need to know about turbulence to model most optical propagation through the atmosphere.

2.1.3 The Turbulence Model of Refractivity Fluctuations

We have yet to relate our turbulence model to the refractivity formula (2.1). A critical intermediate step involves the concept of a conservative passive additive (*Tatarskii* [2.11, 12]). Conservative quantities have the property that, if we can identify an air parcel with a certain characteristic number, it will then retain that number no matter how that parcel moves about in space. Strictly speaking, temperature is not a conservative quantity. Any vertical displacement of an air parcel will produce a temperature change because, at any given height, the parcel will tend to equalize its pressure with that of the background. This pressure change produces adiabatic temperature changes; consequently, if we define a new quantity, that is the difference between the absolute temperature T and the changes in temperature with height caused by an adiabatic lapse rate, we shall obtain a conservative quantity. For this reason we shall analyze the fluctuations in the potential temperature $\Theta=T-\gamma_a z$, where $\gamma_a=9.8$ C/km, and relate the statistics of Θ to the velocity fluctuation statistics. Passive additives do not affect the turbulence dynamics; that is, when they are inserted into the turbulent medium they do not affect its statistics, so that the two-thirds law described in (2.6) still applies for the velocity fluctuations. It was first shown by *Corrsin* [2.13] that conservative passive additives also obey the two-thirds law;

thus, there is a well-defined universal structure function for the potential temperature variations, and it has the form

$$D_\Theta(r) = C_\Theta^2 r^{2/3} \tag{2.7}$$

in its inertial subrange. (The inertial subrange of the temperature fluctuations is defined by slightly different scale sizes (*Tatarskii* [2.11, 12]) than the velocity fluctuations. This is unimportant for our discussion.) All that remains in order to construct our statistical model of the refractivity variations, that is, to find its two-thirds law, is to relate the refractive index n to one or more conservative passive additives.

Equation (2.1) defines n in terms of the temperature T and pressure P. To calculate a structure function for n, we must know how to relate changes in refractive index to changes in pressure and temperature. We accomplish this by finding the differential of (2.1)

$$\delta n = \frac{79P}{T}\left(\frac{\delta P}{P} - \frac{\delta T}{T}\right) \times 10^{-6}. \tag{2.8}$$

[In calculating (2.8), we have assumed a value for λ in (2.1) corresponding to red light, $\lambda \approx 0.6 \times 10^{-6}$ m.] If the pressure fluctuations are measured at a point fixed with respect to the ground, they are relatively small and rapidly dispersed. Consequently, the observed refractive index variations will be produced almost exclusively by temperature fluctuations, and we can neglect the $\delta P/P$ term. From the definition of potential temperature Θ, we can see that refractivity variations δn at a fixed height will be a function of $\delta\Theta$ alone, so that

$$\delta n = -79P\frac{\delta\Theta}{T^2} \times 10^{-6}. \tag{2.9}$$

Finally, because $\delta\Theta$ is a conservative passive additive, δn is also, and we may write a two-thirds law for the refractivity fluctuations

$$D_n(r) = C_n^2 r^{2/3}. \tag{2.10}$$

To complete the calculation, from (2.9) we can write the refractive index structure constant C_n^2 directly in terms of C_Θ^2 as

$$C_n^2 = \left(\frac{79P}{T^2} \times 10^{-6}\right)^2 C_\Theta^2. \tag{2.11}$$

We have now shown that the refractive index fluctuations have the same statistical properties, that is, obey the same structure function law as velocity turbulence, and that variations in optical refractive index are caused by variations in temperature. Equation (2.11) relates the refractivity and temperature structure parameters with a coefficient that depends only upon the mean atmospheric pressure and temperature. Hereafter in the text, we shall follow the usual convention and write C_T^2 in place of C_Θ^2; however, it is important to remember in the following sections that the significant physical quantity is the structure constant of potential temperature.

Finally it should be noted that the structure constant is not really a constant, but a function of both time and space. It is really a coefficient that describes the strength of the refractive index turbulence. In practice, care must be taken with problems concerned with appropriate averaging times when determining this constant. Workers in optical propagation tend to use quite different averaging times when determining C_T^2 or C_n^2.

2.1.4 Stationary Random Functions

The frequency content of a time-varying, physically realizable, deterministic signal such as a pulse is easily determined by taking its Fourier transform. If the pulse is $p(t)$, then its transform $W(\omega)$ is defined by

$$W(\omega)=\frac{1}{2\pi}\int_{-\infty}^{\infty} dt p(t) \mathrm{e}^{-\mathrm{i}\omega t}, \tag{2.12}$$

where $\omega=2\pi f$ and f is the frequency in Hertz. If we wish to reconstruct $p(t)$ exactly, we merely invert the relation (2.12) in the conventional way,

$$p(t)=\int_{-\infty}^{\infty} d\omega W(\omega) \mathrm{e}^{\mathrm{i}\omega t}, \tag{2.13}$$

and obtain an exact point-for-point reconstruction of the time signal from knowledge of $W(\omega)$. We are able to reconstruct $p(t)$ exactly because $W(\omega)$ is, in general, a complex quantity that tells not only the relative amplitudes of the different frequencies (power) but also how they must be shifted relative to each other (phase) to make up the final time-domain function.

In a completely analogous way, we can write a stationary random function in terms of a Fourier-Stieltjes transform (*Yaglom* [2.14])

$$p(t)=\int_{-\infty}^{\infty} dH(\omega) \mathrm{e}^{\mathrm{i}\omega t}. \tag{2.14}$$

Equation (2.14) expresses the relation between a given realization of a random process and its spectrum in the same sense that (2.13) does for a deterministic function; however, in this case, $p(t)$ and $dH(\omega)$ are both random variables and therefore are not the same for each realization of the random process. The function $dH(\omega)$ plays the same role as $W(\omega)d\omega$ in (2.13). In fact, if $H(\omega)$ were differentiable, we could write $dH(\omega)=H'(\omega)d\omega$ and have an exact analog to (2.13). The particular form $dH(\omega)$ allows us to use (2.14) even in the case in which the spectrum of our random process is not differentiable; for example, (2.14) is a useful generalization for random processes consisting of a finite number of random harmonic generators.

The notion of stationarity is the time-domain analogy of spatial homogeneity discussed in Section 2.1.2. Stationarity implies that statistical quantities, such as the mean and variance, do not vary with time. For example, if we find the mean value of a process at t_0, it should be identical with the value found at t_0+t. The mean referred to is the ensemble mean or expected value, that is indicated by angle brackets, and we average over different realizations of the random process. Unfortunately, we do not have at our disposal an ensemble of identical atmospheres which we may observe. Usually, we have a single function of time, say, of atmospheric temperature fluctuations, and we must invoke the assumption of ergodicity to obtain estimates of ensemble averages. An ergodic random process is one whose infinite time average is equal to its ensemble average; and, if we can make this assumption, then we can substitute time averages wherever we have ensemble averages. This leads to another problem. We cannot average forever as required in the ergodic hypothesis. Our only hope is that the process is sufficiently band limited so that a reasonable averaging time will give a stable number. How long to average and what filtering effects the averaging time, record length, and sampling rate have on the observations are the subject of an entire area of research, time series analysis. For further details of this extremely interesting and rich field, consult [2.15–17], and, for application to atmospheric processes, [2.18]. These considerations have a bearing on how well you can measure the relevant statistical quantities discussed in the following chapters. It is interesting that the structure function, already introduced in Section 2.1.2, was created in response to these problems. The structure function behaves as a high pass filter because, as we shall see later, the subtraction process removes the slowly varying large-scale fluctuations that affect both points of the measurement and provides a much more stable number than the related correlation function.

Equation (2.14) has associated with it a host of mathematical problems, some outlined in the above paragraph. A further related difficulty is that (2.14) and its inverse violate at least two conditions usually required for the existence of a Fourier transform: absolute integrability (finite area), and $dH(\omega)$ and $p(t)$ may have an infinite number of maxima and minima. Consequently, the interpretation of (2.14) for random functions is much more cloudy than the precise relatives (2.12, 13) for physically realizable deterministic functions. These mathematical difficulties are overcome when we consider ensemble-averaged properties of the random process. An example is the correlation function, defined by

$$B(t,t+\tau)=\langle p(t)p^*(t+\tau)\rangle\,, \qquad (2.15)$$

where the asterisk indicates a complex conjugate. After substituting (2.14, 15) takes the form

$$B(t,t+\tau)=\int_{-\infty}^{\infty}\int_{-\infty}^{\infty} e^{i\omega_1 t-i\omega_2(t+\tau)}\langle dH(\omega_1)dH^*(\omega_2)\rangle\,, \tag{2.16}$$

where we have assumed the ability to interchange integration and averaging. From our discussion of stationarity, we know that if $p(t)$ is a stationary random function, then the correlation function cannot depend on the time t when the average is taken. The only mathematical way $B(t,t+\tau)$ can be independent of t for all possible t's is if $\langle dH(\omega_1)dH^*(\omega_2)\rangle$ takes the form,

$$\langle dH(\omega_1)dH^*(\omega_2)\rangle=\delta(\omega_1-\omega_2)P(\omega_1)d\omega_1 d\omega_2\,, \tag{2.17}$$

where $\delta(\omega_1-\omega_2)$ is the Dirac delta function. Then (2.16) reduces to

$$B(t,t+\tau)=B(\tau)=\int_{-\infty}^{\infty} d\omega_1\, e^{-i\omega_1\tau}P(\omega_1)\,. \tag{2.18}$$

The function $P(\omega_1)$ is called the power spectral density of the function $p(t)$. Note the important result in (2.18) that, by assuming that only equal frequencies $\omega_1=\omega_2$ are correlated, all the phase information about the function $p(t)$ is lost. We cannot reconstruct the details of $p(t)$ from knowledge of $P(\omega)$. The information contained in $P(\omega)$ is the amount of power that exists in a given process per unit frequency interval. To see this, we note that because $[p(t)p^*(t)]$ is the instantaneous power, then from (2.15), $B(t,t)$ is its average value, that is,

$$B(t,t)=\langle p(t)p^*(t)\rangle\,, \tag{2.19}$$

and

$$\langle p(t)p^*(t)\rangle=\int_{-\infty}^{\infty} P(\omega)d\omega\,. \tag{2.20}$$

Since the left side is the average power, $P(\omega)d\omega$ must be the power in a frequency band from ω to $\omega+d\omega$.

In summary, the only meaningful spectral measure of a stationary random process is its power spectral density. Unlike the case of realizable deterministic variables where complete reconstruction of the time function is possible from knowledge of its Fourier transform, knowledge of the power spectral density does not permit exact reconstruction of the random process because phase information has been lost.

2.1.5 The Power Spectral Density of the Refractive Index Fluctuations

In Section 2.1.3 we considered briefly the spatial structure of the random refractive index fluctuations. In Section 2.1.4 the temporal characteristics of a general random variable were considered, with a brief discussion of time series analysis problems. To connect these two points of view in our physical model of the atmosphere, we make the assumption of "frozen turbulence", which implies that temporal variations of meteorological variables at a point are produced by advection of these quantities by the mean flow and not by changes in the variables themselves ([2.11, 12]). This point of view forces a one-to-one correspondence between spatial and temporal fluctuations. For example, if we place a point temperature sensor in the atmosphere, record its fluctuating readings in time, and find its temporal power spectral density $P(\omega)$, then, because of the frozen turbulence assumption and with the knowledge of the mean windspeed v_0, we can directly convert to a one-dimensional spectral density in terms of the spatial wave number K. The spatial wave number for a given temporal frequency ω will be $K=\omega v_0$. In this chapter, we shall consider the spatial statistics as more fundamental and the temporal statistics as derivable from them using the mean windspeed. (A more detailed description of the assumption of "frozen turbulence" and its limitations is given by *Tatarskii* [2.12].)

We can write the refractive index as the sum of a mean plus a fluctuating part

$$n(\boldsymbol{r})=\langle n(\boldsymbol{r})\rangle+n_1(\boldsymbol{r}), \tag{2.21}$$

where $\langle n_1(\boldsymbol{r})\rangle=0$ by definition. (Note that this definition of n_1 is slightly different than the n_1 defined in Section 2.1.1.) The variable $n_1(\boldsymbol{r})$ can be decomposed in terms of a three-dimensional Fourier-Stieltjes integral

$$n_1(\boldsymbol{r})=\int dN(\boldsymbol{K})\mathrm{e}^{\mathrm{i}\boldsymbol{K}\cdot\boldsymbol{r}}, \tag{2.22}$$

where $\boldsymbol{K}=(K_x, K_y, K_z)$ is the three-dimensional spatial wave number and dN is the random spectral amplitude [respectively, the analogs of ω and dH in (2.14)]. Following the analysis in Section 2.1.4, we consider the covariance function of the refractive index field at two positions separated by $\boldsymbol{r}$,

$$B_n(\boldsymbol{r}_1+\boldsymbol{r},\boldsymbol{r}_1)=\langle n_1(\boldsymbol{r}+\boldsymbol{r}_1)n_1(\boldsymbol{r}_1)\rangle\,. \tag{2.23}$$

If we substitute (2.22) into (2.23), then we obtain the spatial analog of (2.16),

$$B_n(\boldsymbol{r}_1+\boldsymbol{r},\boldsymbol{r}_1)=\iint \mathrm{e}^{\mathrm{i}\boldsymbol{K}\cdot(\boldsymbol{r}_1+\boldsymbol{r})-\mathrm{i}\boldsymbol{K}'\cdot\boldsymbol{r}_1}\langle dN(\boldsymbol{K})dN^*(\boldsymbol{K}')\rangle\,. \tag{2.24}$$

From our earlier discussion of homogeneity, we know that a statistically homogeneous random field cannot have its average properties depend upon the location in the field at which the average is computed, that is, the same result should obtain if we translate our sensors to any other position in the field and perform the same operation. The impact of this assumption on (2.23) is to make $B_n(\boldsymbol{r}_1+\boldsymbol{r},\boldsymbol{r}_1)=B_n(\boldsymbol{r})$. For the double integral in (2.24) to depend only upon $\boldsymbol{r}$ as required by the homogeneity assumption, the quantity in the angle brackets must satisfy the relation

$$\langle dN(\boldsymbol{K})dN^*(\boldsymbol{K}')\rangle = \delta(\boldsymbol{K}-\boldsymbol{K}')\Phi_n(\boldsymbol{K})d^3\boldsymbol{K}d^3\boldsymbol{K}', \tag{2.25}$$

where now δ is the three-dimensional Dirac delta function and $\Phi_n(\boldsymbol{K})$ is the three-dimensional spectral density of the refractive index fluctuations. Substituting (2.25) into (2.24) and performing the $\boldsymbol{K}'$ integration, we obtain the well-known Fourier transform relation between the spectral density and the covariance function,

$$B_n(\boldsymbol{r}) = \int d^3\boldsymbol{K}\, e^{i\boldsymbol{K}\cdot\boldsymbol{r}}\Phi_n(\boldsymbol{K}). \tag{2.26}$$

To invert (2.26), we Fourier transform both sides of the equation to obtain

$$\Phi_n(\boldsymbol{K}) = \frac{1}{(2\pi)^3}\int d^3\boldsymbol{r} B_n(\boldsymbol{r})\, e^{-i\boldsymbol{K}\cdot\boldsymbol{r}}. \tag{2.27}$$

We are at complete liberty to construct these same relations in one or two spatial dimensions ([2.11, 12]). The procedure is identical to that resulting in either (2.18) or (2.26). We shall make extensive use of the two-dimensional transform relations in later sections.

A further assumption we wish to impose upon the turbulent refractivity fluctuations is that they be isotropic, that is, that statistical quantities such as the covariance function depend merely on the distance between sensors and not on the orientation of the line joining them. Mathematically, this implies that $B_n(\boldsymbol{r}) = B_n(r)$ and, from the inverse transform of (2.26), that $\Phi_n(\boldsymbol{K}) = \Phi_n(K)$. If we substitute this latter result into (2.26), and change to spherical coordinates $\boldsymbol{K} = (K, \theta, \phi)$ and $d^3\boldsymbol{K} = K^2 \sin\theta d\theta d\phi dK$, the angular integrations may be performed to yield

$$B_n(r) = \frac{4\pi}{r}\int_0^\infty dK K\Phi_n(K)\sin(Kr). \tag{2.28}$$

Similarly, we can integrate (2.27) over the angle coordinates to obtain

$$\Phi_n(K) = \frac{1}{2\pi^2 K}\int_0^\infty dr r B_n(r)\sin(Kr). \tag{2.29}$$

Once we have assumed a homogeneous and isotropic turbulence model, we can generate expressions for $B_n(r)$ and $\Phi_n(K)$ from Kolmogorov's structure function law $D_n(r)$. First, we expand the definition of the isotropic form of the structure function

$$D_n(r) = \langle[n_1(\boldsymbol{r}_1+\boldsymbol{r}) - n_1(\boldsymbol{r}_1)]^2\rangle \tag{2.30}$$

into three terms and note that the assumption of homogeneity requires $\langle n_1^2(r_1+r)\rangle = \langle n_1^2(r)\rangle = \langle n_1^2\rangle = B_n(0)$ and by definition $\langle n_1(r+r_1)n_1(r_1)\rangle = B_n(r)$; consequently,

$$B_n(0) - B_n(r) = \tfrac{1}{2}D_n(r). \tag{2.31}$$

Computing the relation between $\Phi_n(K)$ and $D_n(r)$ is more complicated. From (2.28), after taking the limit as $r \to 0$ and substituting into (2.31) for $B_n(0)$, we obtain the structure function in terms of the spectral density Φ_n in the form

$$D_n(r) = 8\pi \int_0^\infty dK K^2 \Phi_n(K)\left[1 - \frac{\sin(Kr)}{(Kr)}\right]. \tag{2.32}$$

[It is clear from (2.32), as mentioned above, that $D_n(r)$ removes the influence of large-scale refractive index fluctuations. The $[1-(Kr)^{-1}\sin(Kr)]$ term in (2.32) severely attenuates spatial frequencies in the range $K < r^{-1}$, that is, those spatial frequencies with periods larger than the spacing between measurement points. Note that there is no such high pass filtering in the definition of $B_n(r)$ in (2.28).] We now must invert (2.32) to obtain Φ_n in terms of D_n, which is not quite as straightforward as inverting a simple Fourier transform relation; however, it can be accomplished without too much difficulty in terms of derivatives of $D_n(r)$ (*Strohbehn* [2.19] and *Tatarskii* [2.12]),

$$\Phi_n(K) = \frac{1}{4\pi^2 K^2} \int_0^\infty \frac{\sin(Kr)}{(Kr)} \frac{d}{dr}\left[r^2 \frac{d}{dr} D_n(r)\right] dr. \tag{2.33}$$

Now we can find the spectral density function Φ_n in terms of Kolmogorov's inertial subrange model,

$$D_n(r) = C_n^2 r^{2/3}; \quad l_0 \ll r \ll L_0. \tag{2.34}$$

By substituting (2.34) into (2.33) and performing the indicated operations, we get the integral

$$\Phi_n(K) = \frac{5}{18\pi} C_n^2 K^{-3} \int_{l_0}^{L_0} dr \sin(Kr) r^{-1/3}. \tag{2.35}$$

If we let the limits go to 0 and ∞, this integral reduces to

$$\Phi_n(K) = 0.033 C_n^2 K^{-11/3}, \tag{2.36}$$

where we assume (2.36) is only valid for $2\pi L_0^{-1} \ll K \ll 2\pi l_0^{-1}$. Both (2.34) and (2.36) are equally valid and equivalent descriptions of the turbulent refractive index fields.

There are other common forms of Φ_n that were derived to effect a smooth transition at the limits of the inertial subrange instead of a sharp truncation as in (2.36). For eddy sizes less than the microscale of turbulence, l_0, the energy in the turbulence is dissipated due to viscosity effects. While the exact form of the spectrum in this region is still under investigation, it is clear that the spectrum must fall off more rapidly than $K^{-11/3}$. A different model that accomplishes this was described by *Tatarskii* [2.12], that is,

$$\Phi_n(K)=0.033C_n^2K^{-11/3}\exp(-K^2/K_m^2), \tag{2.37}$$

where $K_m=5.92/l_0$. Similarly, for eddy sizes greater than L_0, the energy in the eddies must be less than that predicted by the Kolmogorov model. This effect can be approximated to some degree by the Von Kármán spectrum (*Tatarskii* [2.11])

$$\Phi_n(K)=\frac{\Gamma(11/6)}{\Gamma(1/3)}\,\frac{\pi^{-9/2}}{8}\langle\delta_n^2\rangle L_0^3(1+K^2/K_0^2)^{-11/6}, \tag{2.38}$$

where $K_0=2\pi/L_0$, and $\langle\delta_n^2\rangle$ is the variance of the refractivity fluctuations and is related to C_n^2 by $C_n^2\approx 1.9\langle\delta_n^2\rangle K_0^{2/3}$. These spectra have the correct behavior only in the inertial subrange, that is, $\Phi_n(K)=K^{-11/3}$ for $2\pi L_0^{-1}\ll K\ll 2\pi l_0^{-1}$. Outside of this range, particularly for small values of K, there is no physical basis for their behavior; consequently, they should be used only as an indication of the effects of l_0 and L_0 on the propagation statistics that we shall calculate in later sections. Another way to state this difficulty is that if the propagation statistics strongly depend on the microscale l_0, or particularly the outer scale L_0, then the propagation problem probably requires more accurate information on the atmospheric effects than is presently available.

2.1.6 Behavior of C_n^2 in the Open Atmosphere

The central role of the refractive index structure constant C_n^2 will become evident in the next subsection when we calculate the statistics of the fluctuating parameters of an optical wave propagating through atmospheric turbulence. In this subsection, we describe some of the most recent information about the behavior of C_n^2 as a function of altitude and time of day.

Figure 2.1 illustrates a typical example of the behavior of C_n over a 24-h period at a height of 2 m above the ground. The data were taken on a flat mesa in the lee of the Rocky Mountains near Boulder, Colorado, where the vegetation and irregularities in the ground surface were less than 0.3 m. The refractive index structure constant was derived from C_T^2 using (2.11). We computed C_T^2 from measurements of the mean-square temperature difference of two fine-wire thermometers (*Lawrence* et al. [2.20]) by dividing this quantity by the thermometer separation to the two-thirds power in accordance with (2.7).

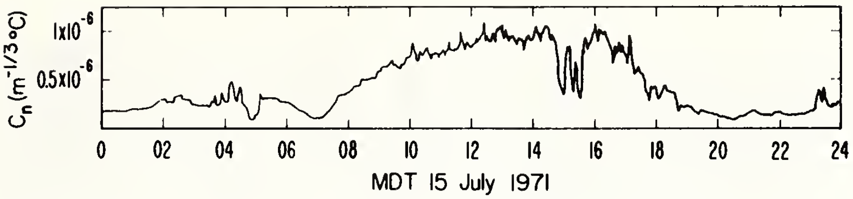

Fig. 2.1. Plot of the behavior of the refractive index structure parameter for a 24 h period on a clear sunny day

The diurnal cycle of C_n, evident in Fig. 2.1, is typical of its behavior in the surface layer of the earth (approximately the lowest 30–100 m). The intensity of the temperature fluctuations (hence C_n) is quite small at night and in the early morning hours until solar heating of the ground becomes significant enough to initiate convective instability (*Hess* [2.21]). This instability generates temperature fluctuations at a given height in the following manner. The sun-heated surface materials warm a thin layer of the air above. If air parcels from the layer become displaced upward, they find themselves warmer, and hence less dense and more buoyant, than the ambient air; therefore, they continue to accelerate upward. It is the mixing of these hot rising air parcels with cool descending air parcels that produces the observed temperature irregularities. This process continues, causing C_n to increase, until late afternoon when solar heating subsides, producing a consequent drop in C_n. A typical range of measurable C_n^2 values for a sunny day at 2 m above the ground is $10^{-17}\,\mathrm{m}^{-2/3} < C_n^2 < 10^{-12}\,m^{-2/3}$. In Fig. 2.1, the sharp dips in C_n values, occurring between 1400 and 1600, are due to intermittent cloud cover. The sun heats only the top layer of the ground; when clouds temporarily obscure the sun, the ground rapidly cools, the temperature structure of the air above rapidly becomes more uniform, and C_n decreases precipitously.

There have been many measurements that have attempted to define the spatial variation of C_n^2. Investigators have obtained *in situ* data from temperature sensors that were tower mounted [2.22], aircraft mounted [2.20, 23, 24], and balloon borne [2.25]. Remote sensing of C_n^2 probably began with the measurement of stellar scintillations to infer high altitude C_n^2 values (see *Hufnagel* and *Stanley* [2.26]) and has progressed to the present-day use of acoustic sounders as remote sensors of C_T^2 and hence optical C_n^2 [2.22, 27]. Aircraft mounted and balloon-borne sensors gave the first indication of the complex behavior of C_n^2 with altitude. In fact, these measurements have been the primary force in changing the exponential C_n^2 profile [2.26] to a more realistic statistical model [2.28].

Acoustic sounder records provide the most complete picture of the spatial structure of C_n^2 in the planetary boundary layer (roughly the lower 1 km of the atmosphere). Although most of the early echo sounder results have been qualitative in nature, recently there has been progress in quantifying the sounder returns by comparing the sounder-derived C_T^2 values with those

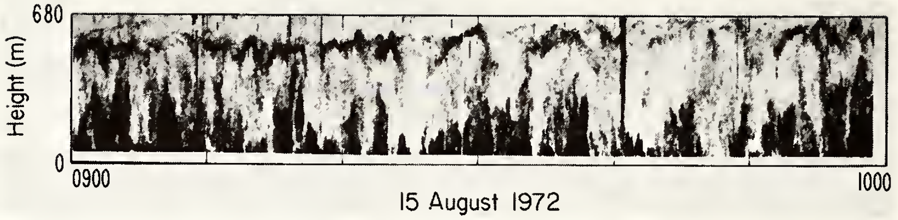

Fig. 2.2. Height-time plot of the strength of acoustic echo sounder returns

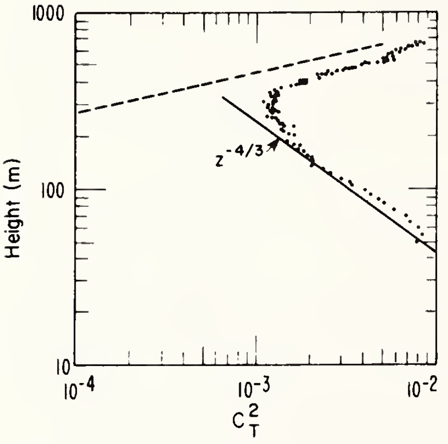

Fig. 2.3. Acoustic echo sounder derived values of C_T^2 versus height in the planetary boundary layer

measured by temperature sensors mounted on a nearby tower (*Neff* [2.22]). Figure 2.2 is a height-time plot of the strength of acoustic echo returns. The atmosphere was interrogated by a 20 ms acoustic pulse emitted from a vertically pointing antenna that also detected the echo return with an approximate vertical spatial resolution of 3–4 m. Height-time intervals of strong echo return (dark regions) indicate the presence of intense temperature fluctuations, whereas height-time intervals of weak echo return (light regions) indicate relatively weak temperature fluctuations. (The first 34 m are blank because of the time required to wait for the sounder to stop ringing from transmission and prepare to receive.) It is readily apparent from this record that, even in the space of the 60-min time pictured, the spatial structure of C_T^2 (hence C_n^2) is extremely varied. The dark vertical structures originating at the bottom of the record are associated with thermal plumes which are regions of warm rising air containing large thermal contrast. The light areas between plumes are thermally homogeneous regions of cool descending air.

Figure 2.3 contains a more quantitative estimate of the C_T^2 values. Each dot was obtained by inverting the formula for the acoustic scattering cross section and then obtaining C_T^2 from the measured cross-section value. (From the theory [2.11, 12], the backscattering cross-section is proportional to C_T^2. For a further discussion of the measurement technique and the assumptions involved in

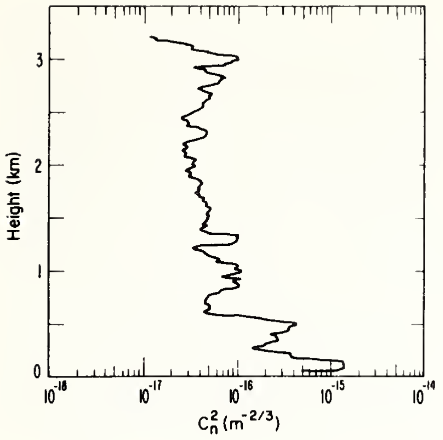

Fig. 2.4. Airplane-borne temperature sensor determinations of C_n^2 versus height

deriving Fig. 2.3, see *Neff* [2.22].) These data are averages over the period from 0900 to 0950. The facsimile record for the same period is shown in Fig. 2.2. From the data in Fig. 2.3, we see that $10^{-3}\,\mathrm{m}^{-2/3}\,{}^{\circ}\mathrm{C}^2 < C_T^2 < 10^{-2}\,\mathrm{m}^{-2/3}\,{}^{\circ}\mathrm{C}^2$, corresponding to approximate refractive index structure constant values of $10^{-15}\,\mathrm{m}^{-2/3} < C_n^2 < 10^{-14}\,\mathrm{m}^{-2/3}$. (The acoustic sounder data were also compared with tower-measured C_T^2 at a height of 92 m, and the measurements agreed to within 50%.) The solid line represents a decrease of C_T^2 with height as $z^{-4/3}$, which is the theoretical prediction for the behavior of C_T^2 in the daytime surface layer (*Tsvang* [2.23] and *Wyngaard* et al. [2.29]). The extension of the "minus four-thirds" region above the first 100 m was noted earlier by *Tsvang* and confirmed by these data. There is, as of yet, no theoretical justification for the extension of the surface layer C_T^2 behavior to higher altitudes, although *Frisch* and *Ochs* [2.30] have shown that the $-4/3$ law should describe the C_T^2 behavior up to 20% of the convective layer depth. The convective layer depth increases during the morning and reaches a value of 1–2 km in the afternoon when fully developed. For the data of Fig. 2.3, it was about 700 m thick. In the nighttime surface layer, the only behavior predicted theoretically (*Wyngaard* et al. [2.29]) is that C_T^2 will decrease with height more slowly than $z^{-2/3}$.

Above the first few hundred meters there is no theoretical prediction of C_n^2 behavior. Figure 2.4 illustrates the complicated behavior of the C_n^2 profile up to a height of 3.2 km. This curve is the average of data from three consecutive days, each day's data consisting of one profile taken during daylight hours (*Ochs* and *Lawrence* [2.24]). The three measured profiles were averaged together and then a 100 m running average applied to the resultant curve. (Each data point represents a 1 minute average.) Even after averaging, the curve illustrates an extensively varying C_n^2 structure which, except for the overall tendency to decrease with height, appears to be random in nature. Other data using balloon-borne sensors (*Bufton* et al. [2.25]) show the same random behavior of C_n^2 with a decreasing mean up to heights of 15 km. In the unsmoothed data of both *Ochs* and *Lawrence* and *Bufton* et al., a typical variation in C_n^2 in a 100–200 m altitude range is more than an order of magnitude. This indicates an extensively layered structure of turbulence with typical thicknesses of 100–200 m, instead of a smoothly varying profile as early models hypothesized. *Bufton* et al. found what appeared to be orographic effects (turbulence associated with mountain lee waves) present in the 3–7 km region, a decrease to a region of minimum values in the 7–9 km range, and, in the 9–15 km range, a region of sharp peaks superimposed on a relatively constant C_n^2 background value. They again attributed this increased spiking in the profile to the highly layered structure in this region, and cite this as confirmation of the theories of increased C_n^2 near the tropopause. *Bufton* et al. found general agreement with the earlier model of *Hufnagel* and *Stanley* [2.26] with the exception of the intense layering, especially near the tropopause.

Recently, in response to the data of [2.24, 25] and the optical measurements of [2.31–33], *Hufnagel* [2.28] derived a new model with several features not found in his earlier work. Based on these experimental observations, he suggests the following C_n^2 model,

$$C_n^2 = \{[(2.2 \times 10^{-53}) h^{10} (W/27)^2] \mathrm{e}^{-h/1000} + 10^{-16} \mathrm{e}^{-h/1500}\} \exp[r(h,t)] , \tag{2.39}$$

where h is the height in meters above sea level. The model is valid for $3\,\mathrm{km} < h < 24\,\mathrm{km}$. The variable r is a zero-mean, homogeneous, Gaussian random variable with a covariance function given by

$$\langle r(h+h_1, t+\tau) r(h,t) \rangle = A(h_1/100) \mathrm{e}^{-\tau/5} + A(h_1/2000) \mathrm{e}^{-\tau/80} , \tag{2.40}$$

where

$$A(h/L) = \begin{pmatrix} 1 - |h/L| , & |h| < L \\ 0 \quad , & \text{otherwise} \end{pmatrix} . \tag{2.41}$$

(The interval τ is measured in minutes.) From (2.40), it follows that $\langle r^2 \rangle = 2$ and $\langle \exp(r) \rangle = \mathrm{e} \approx 2.7$. These numbers may be substituted into (2.39), after finding the expected value $\langle C_n^2 \rangle$, to determine the behavior of the mean profile. Finally, the function W in (2.39) is a correlating factor defined by

$$W = [(1/15\,\mathrm{km}) \int_{5\,\mathrm{km}}^{20\,\mathrm{km}} v^2(h) dh]^{1/2} , \tag{2.42}$$

where v is the wind speed at height h. The parameter W, the rms wind speed in the height range from 5–20 km, turns out to account for 60% of the variance of the stellar scintillation data of *Mikesell*. [Data for $v(h)$ are readily obtained from the daily radiosonde profiles determined by the National Weather Service.] Note that W is a random function of time, and *Hufnagel* has found from Maryland data that W is normally distributed with a mean of 27 m/s and a standard deviation of 9 m/s. To extend this model down to local ground level, we should add the surface layer C_T^2 dependence, for example, $z^{-4/3}$ for daytime, and account for orographic effects and any sharp inversion layers that may influence local values of C_T^2. (For further discussion, see *Hufnagel* [2.28].)

It should be noted that this new model is an empirical one based on a limited amount of data, but is probably the best model available at this time. In a certain sense, the model is also inconsistent, and hence it is important to understand the assumptions made in its development. First, when C_n^2 was first derived in (2.10), it was assumed that it represented an average quantity, but in (2.39) C_n^2 is a random variable. The distinction here is that in optical propagation experiments we are usually interested in reasonably short time scales, for example, seconds or minutes. Therefore optical workers usually consider C_n^2 values averaged over these time scales. In (2.39), r and W are parameters that represent slowly varying quantities, with time scales on the order of hours or days. With this interpretation, the model in (2.39) is consistent and highly useful in practical situations. An ultimate model for C_n^2 might also include parameters that account for seasonal, diurnal, and geographical effects.

Finally, we consider the statistics of the C_n^2 fluctuations as measured by three different techniques. From data taken on a 12 m tower, *Kallistratova* and *Timanovskiy* [2.34] determined C_n^2 from the mean profiles of wind speed and temperature, using a relation derived by *Obukov* [2.35]. During the daytime (1115–1515 LT), they observed that 84% of the values of C_n^2 were in the range $5.4 \times 10^{-14}\,\mathrm{m}^{-2/3} < C_n^2 < 5.4 \times 10^{-13}\,\mathrm{m}^{-2/3}$; whereas at night, 59% of the values were in the range $5.4 \times 10^{-15}\,\mathrm{m}^{-2/3} < C_n^2 < 5.4 \times 10^{-14}\,\mathrm{m}^{-2/3}$. Their observations also indicated a much larger spread of C_n^2 data in the nighttime than in the daylight hours. *Neff* [2.22] observed both tower-measured and sounder-derived values of C_n^2 and found a tendency for both sets of data to be log normally distributed in the early morning (0510–1000 LT) with a mean $\langle C_n^2 \rangle \sim 7 \times 10^{-16}\,\mathrm{m}^{-2/3}$ and a standard deviation of $1.5 \times 10^{-15}\,\mathrm{m}^{-2/3}$. In the afternoon, the data deviated from log normality and had a mean $\langle C_n^2 \rangle \sim 3.0 \times 10^{-15}\,\mathrm{m}^{-2/3}$ and a standard deviation of $2.0 \times 10^{-14}\,\mathrm{m}^{-2/3}$. *Neff* did not analyze any nighttime data so that comparison with the data of *Kallistratova* and *Timanovskiy* during that time is not possible; however, if we use the 4/3 rule to scale Neff's daytime data at 92 m down to the 12 m measurement height of *Kallistratova* and *Timanovskiy*, these data fall into the range of most probable C_n^2 values found by the Soviet workers. This agreement is quite remarkable, considering the completely different measurement techniques used in the two experiments. Both studies give C_n^2 data for the summer months, and there appears to be no equivalent study available for the other seasons of the year.

In this subsection we have sketched some of the most recent observations and attempts to model the behavior of the refractive index structure constant in the open atmosphere. Knowledge of this behavior is exceedingly important, as will become obvious in the next section where we define the central role of the refractive index fluctuations in atmospheric optical propagation.

2.2 The "Classical" Theory of Optical Propagation

There is an extensive literature on the subject of the theory of line-of-sight propagation through the atmosphere and other random media. The early work by *Chernov* [2.36] and by *Tatarskii* [2.11] solved the wave equation directly using perturbation techniques. More recently, *Lee* and *Harp* [2.37], using a highly physical approach employing a weak phase screen model, rederived the classical results, usually with much more ease than with the *Chernov* and *Tatarskii* approach. *Fante* [2.38] described the power of transport theory in connection with the propagation of beams through turbulent plasmas. This technique can also be applied to the atmospheric optical propagation problem and appears to have some advantages for beam wave propagation.

Because this chapter is somewhat historical, we shall develop the theoretical results directly from Maxwell's equation, using a perturbation technique that is perhaps best described in the early works of *Tatarskii* [2.11, 12]. To maintain simplicity in the derivation and consistency with Tatarskii's original work, we shall assume that a plane wave is incident upon the random medium and consider the resultant fluctuations of amplitude and phase only. Other important quantities, such as phase difference and angle-of-arrival fluctuations, were considered in *Lee* and *Harp* [2.37]. *Lawrence* and *Strohbehn* [2.39] and *Fante* [2.40] reviewed most of the significant work in this area and provided a good source of references. Chapter 5 gives a full mathematical treatment of the more general beam wave case.

2.2.1 The Wave Equation for Optical Propagation

We assume that the atmosphere has zero conductivity and unit magnetic permeability and that the electromagnetic field has a sinusoidal time dependence, given by $e^{-i\omega t}$. [The following results are directly applicable to the pulse propagation problem for pulses longer than about 100 ps (*Fante* [2.40]).] We can derive the amplitude and phase statistics for short pulses by Fourier decomposition of the waveform into a spectrum of plane waves. (Some relevant references are [2.41–47].) Under these circumstances, Maxwell's equations take the following form:

$$\nabla \cdot \boldsymbol{H} = 0 \tag{2.43}$$

$$\nabla \times \boldsymbol{E} = \mathrm{i}k\boldsymbol{H} \tag{2.44}$$

$$\nabla \times \boldsymbol{H} = -\mathrm{i}kn^2\boldsymbol{E} \tag{2.45}$$

$$\nabla \cdot (n^2\boldsymbol{E}) = 0, \tag{2.46}$$

where $\mathrm{i} = \sqrt{-1}$, $k = \omega/c$ is the wave number of the radiation, ω is its radian frequency, and c is the speed of light in free space. The ∇ operator is the well-known vector derivative $(\partial/\partial x, \partial/\partial y, \partial/\partial z)$. The quantities $\boldsymbol{E}$ and $\boldsymbol{H}$ are the vector amplitudes of the electric and magnetic fields and are a function of position alone; the assumed sinusoidal time dependence is contained in the wave number k. The atmospheric refractive index $n(\boldsymbol{r})$ is a random function of position with the statistical properties described in Section 2.1.

To generate the more familiar wave equation for the electric field, we take the curl of (2.44) and, after substituting (2.45), obtain

$$-\nabla^2\boldsymbol{E}+\nabla(\nabla\cdot\boldsymbol{E})=k^2n^2\boldsymbol{E}\,. \tag{2.47}$$

Equation (2.46) is expanded and solved for $\nabla\cdot\boldsymbol{E}$, and the result inserted into (2.47) and we obtain the final form of the vector wave equation

$$\nabla^2\boldsymbol{E}+k^2n^2\boldsymbol{E}+2\nabla(\boldsymbol{E}\cdot\nabla\log n)=0\,. \tag{2.48}$$

In (2.48) we have substituted the gradient of the natural logarithm for $\nabla n/n$.

The last term on the left-hand side is related to the change in polarization of the wave as it propagates. Various authors [2.19, 48–52] considered the effects of this term in great detail and deemed it negligible for $\lambda \ll l_0$. *Clifford* [2.52] also showed that the depolarization effects of the atmosphere are negligible even when the wavelength λ is greater than the inner scale l_0. These results permit us to drop the last term, and (2.48) then simplifies to

$$\nabla^2\boldsymbol{E}+k^2n^2\boldsymbol{E}=0\,. \tag{2.49}$$

Two final points about (2.49) will be considered before launching into its solution. First, from (2.44), we see that $\boldsymbol{H}$ is a function of $\boldsymbol{E}$ and that any results derived from (2.49) directly apply to $\boldsymbol{H}$. Second, because (2.49) is easily decomposed into three scalar equations, one for each component of the electric field, we may solve one scalar equation and ignore the vector character of the wave until the final solution; therefore we need only analyze

$$\nabla^2E+k^2n^2E=0\,, \tag{2.50}$$

where E is either the magnitude of the electric field, if it is linearly polarized, or any of the vector components of an arbitrarily polarized field.

2.2.2 Solution by the Method of Small Perturbations

The method of small perturbations involves the expansion of E into a series of ever-decreasing terms that may or may not converge, that is,

$$E=E_0+E_1+\dots\,. \tag{2.51}$$

Each term E_m is assumed to be of the order of smallness $(n_1)^m$. Now, if the magnitude of successive terms is sufficiently small compared to the next lower order term $|E_{m+1}| \ll |E_m|$, the series converges and a finite number of terms will accurately describe the propagation problem. Unfortunately, this does not occur for all situations in our problem and the series may be divergent. The physical significance of this fact is related to the interpretation of higher order terms as multiple scatter. The zero-order term represents the unscattered wave, the first order represents single scattering, the second order double scattering, and so forth. It turns out that multiple scattering (higher order terms) becomes increasingly important as the strength of the refractive index fluctuations increases, either by n_1 becoming larger or by the thickness of the medium increasing so that the total integrated refractive index change becomes large. We shall ignore these problems and solve for the single scatter solution in this chapter, leaving the full discussion of the higher order terms for Chapter 3. However, we should remember that the single scatter results are valid in a wide range of practical problems.

The procedure that follows is to substitute $E = E_0 + E_1$ into (2.50) and to equate to zero each group of terms of the same order in n_1. This results in two equations,

$$\nabla^2 E_0 + k^2 E_0 = 0 \tag{2.52}$$

$$\nabla^2 E_1 + k^2 E_1 + 2k^2 n_1 E_0 = 0 . \tag{2.53}$$

In (2.53), we have ignored terms like $n_1 E_1$ because, as stated above, E_1 is of order n_1 and therefore the product $n_1 E_1$ is of order n_1^2. Following *Tatarskii* [2.11, 12], we assume that the incident or unperturbed field is a unit amplitude plane wave propagating in the z direction, $E_0 = \exp[ikz]$, and, after noting that it satisfies (2.52), we substitute it into (2.53) where it becomes part of the source term. The resulting equation is

$$\nabla^2 E_1 + k^2 E_1 = -2k^2 n_1 \mathrm{e}^{ikz} . \tag{2.54}$$

The major advantage of the perturbation procedure is that we have transformed (2.50), which is a homogeneous partial differential equation with random, space-dependent coefficients, to the nonhomogeneous partial differential equation with constant coefficients given in (2.54). Although we have sacrificed considerable generality in this process, (2.50) may not be solved without specifying the particular form of n_1 (not merely its statistics), whereas (2.54) may be solved as it stands. Its solution is simply the convolution of the source term on the right-hand side with the Green's function of the equation, i.e.,

$$E_1(\boldsymbol{r}) = (4\pi)^{-1} \int_V d^3 r' \frac{\mathrm{e}^{ik|\boldsymbol{r}-\boldsymbol{r}'|}}{|\boldsymbol{r}-\boldsymbol{r}'|} [2k^2 n_1(\boldsymbol{r}') \mathrm{e}^{ikz'}] . \qquad (2.55$$

Equation (2.55) states that the scattered field observed at $\mathbf{r}$ is that due to a spherical wave emitted at $\mathbf{r}'$, that is $|\mathbf{r}-\mathbf{r}'|^{-1}\exp(ik|\mathbf{r}-\mathbf{r}'|)$, whose amplitude is proportional to the product of the local refractive index fluctuation $n_1(\mathbf{r}')$ and the strength of the incident radiation, and whose phase is determined by the total number of wavelengths along the path from source to scatterer to receiver. We then integrate these contributions from all points $\mathbf{r}'$ over the entire scattering volume V.

There are several simplifications of (2.55) allowed by the particular characteristics of laser propagation. Monochromatic light, scattered by weak, large-scale refractivity fluctuations, is contained in a narrow cone about the forward scatter $(+z)$ direction. From the laws of diffraction, the angle of scattering will be a maximum for the smallest eddies of interest, whose scale size is the microscale of turbulence l_0. The scattering angle in this case is of the order λ/l_0, and for typical values ($\lambda=0.6\times10^{-6}$ m and $l_0=2\times10^{-3}$ m) is 3×10^{-4} radians. Hence, the maximum extent of the atmosphere perpendicular to the z direction, from which scattered radiation is incident on a receiver, is typically much less than the longitudinal distance from scatterer to receiver. Mathematically, if $z-z'$ is the longitudinal distance from scatterer to receiver and if $|\varrho-\varrho'|$ is the transverse displacement from the z axis, then we would expect that $|z-z'|\gg|\varrho-\varrho'|$ would be a good approximation and we may directly replace $|\mathbf{r}-\mathbf{r}'|$ by $z-z'$ in the denominator of (2.55).

For the argument of the exponential we must be more careful because what is important there is not just the relative size of the transverse and longitudinal displacements of the scatterers, but how many wavelengths are contained in these distances. We must retain terms that are large enough to make the argument go through more than 2π radians. Expanding $k|\mathbf{r}-\mathbf{r}'|$ in a binomial series, we have

$$k|\mathbf{r}-\mathbf{r}'|=k(z-z')\left[1+\frac{(\varrho-\varrho')^2}{2(z-z')^2}-\frac{(\varrho-\varrho')^4}{8(z-z')^4}+\dots\right]. \tag{2.56}$$

By assuming that the maximum transverse extent is approximately $\lambda L/l_0$ and $z-z'\sim L$, where L is the total path length, the second term in (2.56) is of the order $\pi\lambda L/l_0^2$. Therefore, if $l_0\ll\sqrt{\lambda L}$, the second term is large and we must retain it. For $\lambda=0.6\times10^{-6}$ m and for a typical path of 1 km, the Fresnel length $\sqrt{\lambda L}$ is ~2.5 cm; with $l_0=0.2$ cm, the condition for the second term being large is satisfied. (The third and successive terms are negligible by the same argument; for example, the third term is of the order λ^3L/l_0^4 which is extremely small for the above parameters.) In summary, we need retain only $z-z'$ in the denominator of (2.55) and the first two terms of (2.56) in the exponential, and this results in the expression

$$E_1(\mathbf{r})=\frac{k^2e^{ikz}}{2\pi}\int_V d^3\mathbf{r}'\exp\left\{\frac{ik[(\varrho-\varrho')^2]}{2(z-z')}\right\}\frac{n_1(\mathbf{r}')}{(z-z')}. \tag{2.57}$$

The Fresnel approximation (2.56) transforms the Green's function scattering integral (2.55) to the so-called Fresnel diffraction formula (2.57). This formula (2.57) is the exact solution to the diffusion equation with a source term $-2k^2n_1$ (*Tatarskii* [2.11]). One further interesting point about (2.57) is that the exponential term is the equation for the location of the interference fringes produced in the receiving plane at z by the interference of the incident plane wave with the scattered spherical wave (Huygen's wavelet) emitted from the point (ϱ', z'). It is these fringes that produce the amplitude and phase fluctuations that we observe in atmospheric optical propagation.

Questions of interest in this problem are: What are the amplitude or intensity fluctuations relative to the free space values, that is, how much will the received amplitude fluctuate due to its interaction with the atmosphere? and what are the phase fluctuations relative to the phase of the unperturbed wave? Following *Tatarskii* [2.11, 12], we use a technique that takes advantage of the simplifications implicit in the weak scattering assumption to obtain expressions for the amplitude and phase fluctuations in terms of E_1. The field $E=E_0+E_1$ by assumption; therefore, in terms of amplitude and phase, we have

$$\frac{E}{E_0}=1+\frac{E_1}{E_0}=\frac{A}{A_0}\exp[\mathrm{i}(s-s_0)], \tag{2.58}$$

where we have written $E=A\exp(\mathrm{i}s)$ and $E_0=A_0\exp(\mathrm{i}s_0)$. Taking the natural logarithm of (2.58), we obtain

$$\log\left(1+\frac{E_1}{E_0}\right)=\log\left(1+\frac{A_1}{A_0}\right)+\mathrm{i}(s-s_0), \tag{2.59}$$

where A_1 is the amplitude of E_1. Because $|E_1/E_0|\ll 1$ and $A_1/A_0\ll 1$, we may expand the logarithm in a power series and retain only the first term so that (2.59) becomes

$$\frac{E_1}{E_0}\cong\frac{A_1}{A_0}+\mathrm{i}(s-s_0). \tag{2.60}$$

This implies that we may obtain the amplitude ratio from the real part of (2.57) and the relative phase fluctuations from the imaginary part, provided that we normalize this equation by the initial wave E_0. Consequently, we may write

$$A_1/A_0=\frac{k^2}{2\pi}\int_V d^3r'\cos\left[\frac{k(\varrho-\varrho')^2}{2(z-z')}\right]\frac{n_1(r')}{(z-z')} \tag{2.61}$$

and

$$(s-s_0)=\frac{k^2}{2\pi}\int_V d^3r'\sin\left[\frac{k(\varrho-\varrho')^2}{2(z-z')}\right]\frac{n_1(r')}{(z-z')}. \tag{2.62}$$

[In (2.61) and (2.62), we have used the fact that $n_1(\boldsymbol{r}')$ is real, that is, there is no attenuation of the wave as it propagates.] By convention, we define $\chi = \ln(A/A_0) \cong A_1/A_0$ and $s - s_0 = s_1$. Hereafter, we shall be considering the log amplitude χ because that is often what is measured experimentally, but recall that, for the weak scatter point of view, it is identical to the normalized amplitude fluctuation A_1/A_0.

We still have not taken advantage of the path geometry to simplify our equations. In particular, because we are considering a plane wave, we expect statistical homogeneity of both the amplitude and phase fluctuations in the plane $z = \text{constant}$. Of course, this is not true along the z axis because we expect the fluctuations of χ and s to increase with increasing z as the wave propagates through progressively more refractive turbulence. Consequently, it is useful to expand the refractive index field $n_1(\boldsymbol{r}')$ as a two-dimensional Fourier-Stieltjes transform of the form

$$n_1(\boldsymbol{r}') = \int d\nu(\boldsymbol{K}, z')\, \mathrm{e}^{\mathrm{i}\boldsymbol{K}\cdot\boldsymbol{\varrho}'}\,, \tag{2.63}$$

where we have transformed the variation of the refractive index field only in the plane perpendicular to the propagation direction and allowed the random amplitude $d\nu$ to be a function of z'. Equation (1.63) is the same, in principle, as those discussed in Section 2.1.5; specifically, it is analogous to the three-dimensional transform in (2.22). If we substitute this expression for n_1 into (2.61) and (2.62) and interchange the integration over $d\nu$ with that over $d^3\boldsymbol{r}'$, then

$$\begin{bmatrix} \chi(\boldsymbol{r}) \\ s_1(\boldsymbol{r}) \end{bmatrix} = \frac{k^2}{2\pi} \int \int_0^z dz' \frac{d\nu(\boldsymbol{K}, z')}{(z-z')} \int d^2\varrho'\, \mathrm{e}^{\mathrm{i}\boldsymbol{K}\cdot\boldsymbol{\varrho}'} \left\{ \begin{matrix} \cos \\ \sin \end{matrix} \left[\frac{k(\boldsymbol{\varrho} - \boldsymbol{\varrho}')^2}{2(z-z')} \right] \right\}, \tag{2.64}$$

where we have used the fact that $d^3\boldsymbol{r}' = d^2\varrho' dz'$.

The integral over $\boldsymbol{\varrho}'$ is readily performed after substituting $\boldsymbol{\varrho}'' = \boldsymbol{\varrho}' - \boldsymbol{\varrho}$. Because the cosine and sine terms are functions of the magnitude of $\boldsymbol{\varrho}''$ alone, we can use polar coordinates $\boldsymbol{\varrho}'' = (\varrho'', \theta)$ and integrate directly over θ. If we denote the inner integrals of (2.64) as $I_{1,2}$, we have

$$I_{1,2} = \mathrm{e}^{\mathrm{i}\boldsymbol{K}\cdot\boldsymbol{\varrho}} \int_0^\infty d\varrho''\varrho'' \left\{ \begin{matrix} \cos \\ \sin \end{matrix} \left[\frac{k\varrho''^2}{2(z-z')} \right] \right\} \int_0^{2\pi} d\theta\, \mathrm{e}^{\mathrm{i}K\varrho''\cos(\theta-\psi)}\,, \tag{2.65}$$

where we let $\boldsymbol{K} = (K, \psi)$ in the last term. The result of the inner integration is the Bessel function $2\pi \mathrm{J}_0(K\varrho'')$ (*Gradshteyn* and *Ryzhik* [2.53]) which, when substituted into (2.65), leaves the integral

$$I_{1,2} = 2\pi\, \mathrm{e}^{\mathrm{i}\boldsymbol{K}\cdot\boldsymbol{\varrho}} \int_0^\infty d\varrho''\varrho''\mathrm{J}_0(K\varrho'') \left\{ \begin{matrix} \cos \\ \sin \end{matrix} \left[\frac{k\varrho''^2}{2(z-z')} \right] \right\}. \tag{2.66}$$

The integral in (2.66) is the Hankel transform of the cosine or sine term (*Erdélyi* [2.54] and *Gradshteyn* and *Ryzhik* [2.53]). After performing this integration, (2.66) becomes

$$I_{1,2}=\frac{2\pi(z-z')}{k}\mathrm{e}^{\mathrm{i}\boldsymbol{K}\cdot\boldsymbol{\varrho}}\left\{\begin{matrix}\sin\\ \cos\end{matrix}\left[\frac{K^2(z-z')}{2k}\right]\right\}, \tag{2.67}$$

and (2.67) substituted into (2.64) gives the final result

$$\begin{bmatrix}\chi(\boldsymbol{r})\\ s_1(\boldsymbol{r})\end{bmatrix}=\int \mathrm{e}^{\mathrm{i}\boldsymbol{K}\cdot\boldsymbol{\varrho}}\left(k\int\limits_0^z dz'dv(\boldsymbol{K},z')\left\{\begin{matrix}\sin\\ \cos\end{matrix}\left[\frac{K^2(z-z')}{2k}\right]\right\}\right). \tag{2.68}$$

This expression can be interpreted in terms of a two-dimensional Fourier expansion similar to (2.63), that is, the term in brackets in (2.68) plays the same role as $dv(\boldsymbol{K},z')$ in (2.63). Therefore, we can interpret the quantity in brackets in (2.68) as the random spectral amplitudes of the amplitude and phase fluctuations.

As in any description of a random process, we must settle for averaged properties of the outcome of experiments. Consequently, we consider the two-dimensional covariance functions $B_\chi(\boldsymbol{\varrho})$ and $B_s(\boldsymbol{\varrho})$. (The first moments of χ and s_1, that is, $\langle\chi\rangle$ and $\langle s_1\rangle$, are both zero because, by definition, $\langle n_1\rangle=0$. This result is due to retaining only the first-order perturbation term E_1 in the initial expansion of the field. If we retained second-order or higher terms, $\langle\chi\rangle$ and $\langle s_1\rangle$ would be nonzero, but small.) We use the two-dimensional covariance functions for the reasons alluded to earlier, namely, the statistical homogeneity of the amplitude and phase fluctuations in the plane $z=\text{constant}$. Normally, $B_\chi(\boldsymbol{\varrho})$ and $B_s(\boldsymbol{\varrho})$ are computed in the receiving plane, which we shall later assume is located at the position $z=L$, that is,

$$B_\chi(\boldsymbol{\varrho},z)=\langle\chi(\boldsymbol{\varrho}_1+\boldsymbol{\varrho},z)\chi^*(\boldsymbol{\varrho}_1,z)\rangle\,, \tag{2.69}$$

with a similar definition for $B_s(\boldsymbol{\varrho},z)$. If we insert (2.68) into (2.69), we obtain the fourfold integral

$$\begin{bmatrix}B_\chi(\boldsymbol{\varrho})\\ B_s(\boldsymbol{\varrho})\end{bmatrix}=k^2\iint \mathrm{e}^{\mathrm{i}\boldsymbol{K}\cdot(\boldsymbol{\varrho}_1+\boldsymbol{\varrho})-\mathrm{i}\boldsymbol{K}'\cdot\boldsymbol{\varrho}_1}\int\limits_0^z dz'\int\limits_0^z dz''\left\{\begin{matrix}\sin\\ \cos\end{matrix}\left[\frac{K^2(z-z')}{2k}\right]\begin{matrix}\sin\\ \cos\end{matrix}\left[\frac{K'^2(z-z'')}{2k}\right]\right\}$$
$$\cdot\langle dv(\boldsymbol{K},z')dv^*(\boldsymbol{K}',z'')\rangle\,. \tag{2.70}$$

We already know how to handle the quantity in the angle brackets from the discussion in Section 2.1.5. For the particular case of two-dimensional random amplitudes, such as dv, the equation

$$\langle dv(\boldsymbol{K},z')dv^*(\boldsymbol{K}',z'')\rangle=\delta(\boldsymbol{K}-\boldsymbol{K}')F_n(\boldsymbol{K}',z'-z'')d^2Kd^2K' \tag{2.71}$$

pertains. The function $F_n(\boldsymbol{K}', z'-z'')$ is the two-dimensional spectral density of the refractive index fluctuations defined by

$$F_n(\boldsymbol{K}', z'-z'') = \int_{-\infty}^{\infty} dK_z \Phi_n(\boldsymbol{K}', K_z) \cos[K_z(z'-z'')] , \tag{2.72}$$

where Φ_n is the three-dimensional refractivity spectrum. After inserting (2.71) into (2.70) and performing the $\boldsymbol{K}'$ integration, (2.70) reduces to

$$\begin{bmatrix} B_\chi(\varrho) \\ B_s(\varrho) \end{bmatrix} = \int d^2\boldsymbol{K} \exp^{i\boldsymbol{K}\cdot\varrho}$$

$$\cdot \left(k^2 \int_0^z dz' \int_0^z dz'' \left\{ \begin{matrix} \sin \\ \cos \end{matrix} \left[\frac{K^2(z-z')}{2k} \right] \begin{matrix} \sin \\ \cos \end{matrix} \left[\frac{K^2(z-z'')}{2k} \right] \right\} F_n(\boldsymbol{K}, z'-z'') \right) . \tag{2.73}$$

Because the Fourier transform of the quantities in the brackets equals their respective covariance functions, these quantities must be the two-dimensional spectral densities of χ and s. To be consistent with the notation in (2.72), we shall denote these spectra as $F_\chi(\boldsymbol{K}, 0)$ and $F_s(\boldsymbol{K}, 0)$.

Equation (2.73) can be simplified greatly by considering some of the properties of F_n as well as the geometric characteristics of the optical propagation problem. (The remaining part of the analysis closely parallels [2.11, 12] where it is done in considerably more detail.) First, it is apparent from (2.72) that $F_n(\boldsymbol{K}, z'-z'')$ is an even function of $z'-z''$, that is,

$$F_n(\boldsymbol{K}, z'-z'') = F_n(\boldsymbol{K}, z''-z') . \tag{2.74}$$

Second, F_n expresses the correlation of n_1 on adjacent planes along the z axis, and clearly only those refractive index homogeneities whose size $2\pi K^{-1}$ is as large as or greater than the separation of the two planes $z'-z''$ will contribute significantly to that correlation. Smaller eddies will not intersect the two planes and will not contribute much to the correlation. From this argument and the assumption of isotropic turbulence $F_n(\boldsymbol{K}, z'-z'') = F_n(K, z'-z'')$, we expect that F_n will decay rapidly for $K|z'-z''| > 1$. To take optimum advantage of these facts, we make the transformation of variables $\xi = z'-z''$, $2\eta = z'+z''$. After noting that the Jacobian of this transformation is unity and with F_n now even in ξ, we can write the amplitude and phase spectra in the following form:

$$\begin{bmatrix} F_\chi(K,0) \\ F_s(K,0) \end{bmatrix} = k^2 \int_0^L d\xi F_n(K,\xi) \int_{\frac{\xi}{2}}^{L-\frac{\xi}{2}} d\eta \left[\cos\left(\frac{K^2\xi}{2k}\right) \mp \cos\left(\frac{K^2(L-\eta)}{k}\right) \right] . \tag{2.75}$$

In (2.75), we have dropped the vector notation because of the assumption of an isotropic spectrum for F_n. We also have replaced the position variable z by L, the total path length through the medium. To simplify (2.75) even further, we note, as above, that $F_n \to 0$ for $\xi > K^{-1}$, or equivalently, the important region of integration is for $\xi \leqq K^{-1}$. This implies that the argument of the first cosine satisfies $K^2\xi/(2k) \leqq K/2k$. Now $K_{\max} \sim 2\pi l_0^{-1}$ where l_0 is the microscale of turbulence; therefore, $K/2k$ is of the order λ/l_0 which, from our earlier assumption, is much less than unity. Consequently, $\cos[K^2\xi/(2k)]$ is approximately unity for the entire range of integration over ξ. Further, if we make the assumption $\xi \ll L$, we can ignore its presence in the η integration limits. This is obviously true because in the important region of integration $\xi \leqq K^{-1}$ and for the Kolmogorov spectrum, K^{-1} has a maximum value of $L_0/(2\pi)$; consequently, $\xi \leqq L_0$. Therefore, if $L_0 \ll L$ then we can drop the ξ dependence inside the η integral altogether. Physically, this requires that our path length be much longer than the outer scale length. Because $L_0 \sim 1$ m near the ground, this is easily satisfied for reasonable optical paths. The final result of all these assumptions is that the two integrals in (2.75) become independent. The ξ integration is easily performed in the case $L_0 \ll L$ because, for $\xi \leqq L_0$, the upper limit may be replaced by infinity with negligible error. The final integration follows from the definition (2.72), that is,

$$\int_0^\infty d\xi F_n(K,\xi) = \pi \Phi_n(0,K), \tag{2.76}$$

and for isotropic turbulence $\Phi_n(0,K) = \Phi_n(K)$. The η integration is readily performed, and the final result for the amplitude and phase spectra becomes

$$\begin{bmatrix} F_\chi(K,0) \\ F_s(K,0) \end{bmatrix} = \pi k^2 L \left[1 \mp \left(\frac{k}{K^2 L}\right) \sin\left(\frac{K^2 L}{k}\right)\right] \Phi_n(K). \tag{2.77}$$

2.2.3 Covariance and Structure Functions for Kolmogorov Turbulence

In (2.77), we found the power spectral density of the amplitude and phase fluctuations of a plane optical wave propagating through a random refractive index field whose power spectrum is $\Phi_n(K)$. The first factor in (2.77) is the optical transfer function for the atmosphere. When the minus sign applies (log-amplitude spectrum), this function approaches zero as $K \to 0$, or equivalently, it suppresses the influence of the large-scale refractive index irregularities on the log-amplitude fluctuations. On the other hand, when the plus sign applies (phase spectrum), as $K \to 0$, this function approaches a constant and does not suppress the large-scale inhomogeneities.

If we insert the Kolmogorov spectrum (2.36) in (2.77), the log-amplitude spectrum would be band limited with a peak at a spatial frequency $K \sim 2\pi(\lambda L)^{-1/2}$, whereas, the phase spectrum would depend quite strongly on the largest scales and, consequently, would have a maximum at $K \sim 2\pi L_0^{-1}$. This implies that the log-amplitude fluctuations are produced largely by

Fresnel zone size eddies with scale size of the order $\sqrt{\lambda L}$ and the phase fluctuations are produced by the largest scale eddies in the medium. This latter fact makes the measurement of the phase structure function preferable to the phase covariance function because, as discussed before, the structure function acts as a spatial filter to remove the influence of large-scale eddies. The difficulty in measuring the phase covariance function directly is that large spatial scales imply long measurement times to get adequate, stable statistics, and, if you wait too long, the nonstationarity of the atmosphere will contaminate the data.

From (2.77), we can compute more easily measured quantities such as the covariance of the log-amplitude and the structure function of the phase fluctuations. The relation between $F_\chi(K,0)$ and the covariance function $B_\chi(\varrho)$ is given by the two-dimensional Fourier transform (2.73). Because we have assumed that F_χ is isotropic in $\boldsymbol{K}$, this relation can be simplified by changing variables in (2.73) from $\boldsymbol{K}=(K_x,K_y)$ to circular coordinates K and θ. Then we may perform the integral over the angular coordinate as we did in (2.28) and (2.29) to yield the isotropic transform

$$B_{\chi,S}(\varrho)=2\pi\int_0^\infty dK\,K\,\mathrm{J}_0(K\varrho)F_{\chi,S}(K,0)\,, \tag{2.78}$$

where $\mathrm{J}_0(K\varrho)$ is the zero-order Bessel function of the first kind, defined by the relation

$$\mathrm{J}_0(K\varrho)=\frac{1}{2\pi}\int_0^{2\pi}\mathrm{e}^{iK\varrho\cos\theta}d\theta\,. \tag{2.79}$$

When (2.77) is substituted into (2.78), we obtain

$$B_{\chi,S}(\varrho)=2\pi^2k^2L\int_0^\infty dK\,K\,\mathrm{J}_0(K\varrho)\left[1\mp\left(\frac{k}{K^2L}\right)\sin\left(\frac{K^2L}{k}\right)\right]\Phi_n(K)\,. \tag{2.80}$$

Since it is nearly impossible to measure $B_S(\varrho)$ because of its sensitivity to large spatial and temporal scales, the physically useful quantity is the phase structure function, defined in analogy to (2.31) as

$$D_S(\varrho)=2[B_S(0)-B_S(\varrho)]\,. \tag{2.81}$$

Substituting (2.80) into (2.81) gives

$$D_S(\varrho)=4\pi^2k^2L\int_0^\infty dK\,K\left[1+\left(\frac{k}{K^2L}\right)\sin\left(\frac{K^2L}{k}\right)\right][1-\mathrm{J}_0(K\varrho)]\,\Phi_n(K)\,. \tag{2.82}$$

We are finally ready to calculate the exact form of $B_\chi(\varrho)$ and $D_S(\varrho)$ by inserting the Kolmogorov spectrum for Φ_n and integrating. Using (2.80), we

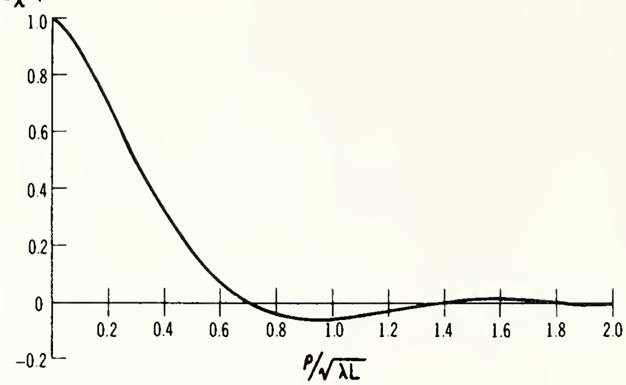

Fig. 2.5. Plot of the normalized covariance function of the log-amplitude fluctuations as a function of spacing in Fresnel zones

first calculate the variance of the log-amplitude σ_χ^2 from $B_\chi(0)$. After performing the integration (*Tatarskii* [2.11, 12]) and using the assumption $l_0 \ll \sqrt{\lambda L}$, we obtain

$$\sigma_\chi^2 = 0.31 k^{7/6} L^{11/6} C_n^2 . \tag{2.83}$$

As we shall see in later chapters, it is the breakdown of the validity of this formula for long paths and strong turbulence that caused a reexamination of the validity of the perturbation approach.

Figure 2.5 illustrates the behavior of the normalized covariance function $b_\chi(\varrho) = B_\chi(\varrho)/\sigma_\chi^2$ in the receiving plane $z = L$. Note again the preeminent role of the Fresnel length $\sqrt{\lambda L}$ and the negative tail indicative of the band limited nature of the spatial spectrum. The negative tail implies that for any two points in the receiving plane separated by approximately one Fresnel length, on the average, one point will be in a region that is brighter than the average irradiance and the other will be in a region that is darker. (The rather complicated expressions for B_χ/σ_χ^2, involving hypergeometric functions, are available in *Lawrence* and *Strohbehn* [2.39].)

Finally, inserting the Kolmogorov spectrum into (2.82), we can calculate directly the power law of the phase structure function. For the case where the separation ϱ satisfies the condition $l_0 \ll \varrho \ll \sqrt{\lambda L}$, we have ([2.11, 12])

$$D_s(\varrho) = 1.46 C_n^2 k^2 L \varrho^{5/3} \tag{2.84}$$

and, for $\sqrt{\lambda L} \ll \varrho \ll L_0$,

$$D_s(\varrho) = 2.92 C_n^2 k^2 L \varrho^{5/3} . \tag{2.85}$$

The behavior of $D_s(\varrho)$ for $\varrho \gg L_0$ is unknown because we have only specified the spectrum Φ_n in the inertial subrange. The detailed behavior of D_s for large ϱ

depends on the particular form of Φ_n in the low spatial frequency region, which is probably not a universal function.

The above formulas for the amplitude and phase statistics were derived using the Born approximation (2.55). The range of validity of this approximation is determined by the smallness of the scattered field with respect to the unperturbed field, i.e., $|E_1| \ll |E_0|$. In his earlier work accomplished in the 1950s, *Tatarskii* [2.11], using a technique first described by *Rytov* [2.55], derived these same results under apparently less restrictive conditions requiring only the smallness of the gradient of the complex phase of the scattered wave compared with the unperturbed phase gradient. Initially, many workers believed that this gave the amplitude and phase results a much greater range of validity in terms of C_n^2 and path length than the Born approximation derivation. Russian workers such as *Pisareva* [2.56], *Feinberg* [2.57], *Tatarskii* [2.58], and later American workers *Hufnagel* and *Stanley* [2.26] and *Brown* [2.59] challenged the claim for the extended range of validity of the Rytov method. It is now well established that the optimistic estimates of the range of validity of the Rytov approximations were unfounded and the results obtained by this method are valid only when $\sigma_\chi^2 \leqq 0.3$. This failure is due to the fact that the Rytov technique fails to account for multiple scattering effects in a consistent manner.

It appears from some experimental work (*Gurvich* et al. [2.60]), where measurements have been made in strong integrated turbulence, that the phase results (2.84) and (2.85) and other related quantities such as angle-of-arrival fluctuations (*Strohbehn* and *Clifford* [2.48]) have a greater range of validity than the log-amplitude statistics (*Fante* [2.40]). It may then be true that measurements of the phase fluctuation statistics in the late afternoon on long paths where we expect $\sigma_\chi^2 > 0.3$ will agree with the first-order theory results even though the amplitude statistics will not.

2.2.4 A Qualitative Interpretation of the First-Order Scattering Theory

Figure 2.6 illustrates schematically the interaction of a plane optical wave with the turbulent atmosphere. The wave, initially having a uniform phase front at A, encounters refractive index irregularities between A and B. At location B, the wave has experienced phase changes which are due only to the speeding up and slowing down of different segments of the wave front. The bumpy nature of the wave front at B produces a deviation of the local wave normals so that rays, emanating from different portions of the wavefront, will eventually interfere and produce irradiance fluctuations (scintillations) at C. It is this process that produces the observed log-amplitude variance (2.83) and the spatial structure described statistically by the covariance function in Fig. 2.5.

There are several important characteristics of the scintillation-producing process that can be gleaned from a simple geometric analysis of the propagation problem. In Fig. 2.7, a refractive index irregularity of radius l, located at z, is illuminated by a plane optical wave. A detector at path position L

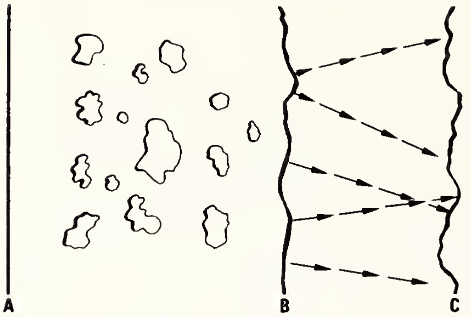

Fig. 2.6. Schematic of the interaction of a plane optical wave with atmospheric refractive index fluctuations

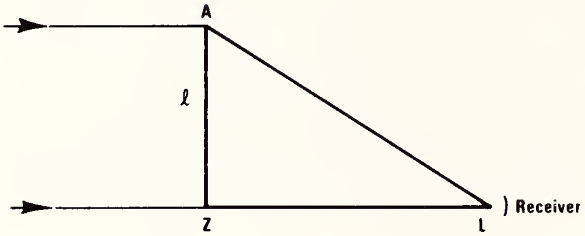

Fig. 2.7. Diagram of the geometry for determining the size l of the most effective eddy located at path position z on a total optical path of length L

observes the scintillation pattern that the irregularity produces. The criterion that determines the effectiveness of this eddy in producing irradiance fluctuations at L is the amount of excess phase path between AL and ZL, that is, for this eddy to be completely effective in producing scintillation, the ray paths AL and ZL should differ by at least one-half wavelength of the incoming plane wave; this produces strong interference of the signal at L. From the geometry of Fig. 2.7, this criterion requires that $l = \sqrt{\lambda(L-z)}$. This minimum size irregularity also turns out to be the most effective size for producing scintillation; smaller eddies at z contribute less because of the weaker refractivity fluctuations associated with them in the Kolmogorov spectrum, and hence, because the amplitude of the field scattered by the eddy is proportional to its refractivity fluctuation, proportionally less scattered energy. Larger eddies at z will not produce strong scintillation because they do not diffract light through a large enough angle to reach the observer at $z = L$. Since an eddy of size l diffracts light through an angle λ/l, in order to be observed at $z = L$ the eddy must diffract energy through an angle $l/(L-z)$. However, by assumption, the eddy is larger than a Fresnel zone and, as a consequence, the inequality $\lambda/l < l/(L-z)$ pertains and no energy reaches the observer. Therefore, as predicted by the theoretical results (2.77) and confirmed by our geometric argument, the most effective eddy for producing scintillations at the receiver is the eddy whose size is equal to that of a Fresnel zone for the rest of the optical path.

Because the refractive index irregularities are illuminated by a plane wave, the disturbance they produce at the receiver will have the same scale size, and hence, the predominant size of the spatial structure in the scintillation pattern also will be the size of a Fresnel zone for the whole path. This explains why the

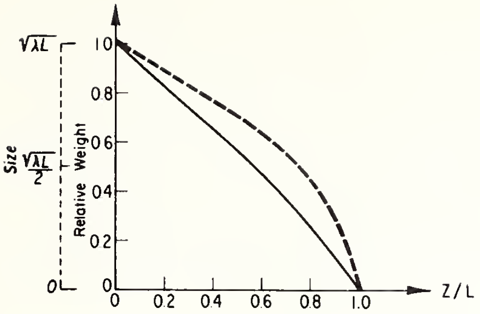

Fig. 2.8. The dashed curve is the size (in Fresnel zones $\sqrt{\lambda L}$) of the most effective eddy for producing scintillation on an optical path of length L in the z direction; the solid curve is the relative importance of refractive turbulence in producing scintillation as a function of position

covariance function (Fig. 2.5) depends only on the Fresnel length and not on the entire refractive index spectrum.

Finally, the dashed curve in Fig. 2.8 shows the behavior of the radius of the most effective irregularity as a function of path position. Note that the largest (smallest) scale structure in the scintillation pattern originates from the transmitter (receiver) end of the path. One further piece of information readily available from the diagram is the relative effectiveness of different portions of the path for producing scintillation. Because we are performing a one-dimensional calculation, we assume the Kolmogorov spectrum in its one-dimensional form, that is, $K^{-5/3}$, and we insert the most effective eddy size $l=\sqrt{\lambda(L-z)}$ into this form of the spectrum. Then we obtain the optical scintillation-weighting function for the path $W \sim [(L-z)]^{5/6}$. This function describes the relative effectiveness of each portion of the propagation path for producing optical scintillation. The solid curve in Fig. 2.8 shows this function; note that the beginning of the path is most effective in contributing to the scintillation and that the end near the receiver has a very small influence. The dominance of the Fresnel zone sized eddies occurs because of the geometry of the propagation problem and not because of any predominant size of refractive index eddies in the atmosphere.

2.3 The Early Experimental Work

Perhaps the first experiments in line-of-sight optical propagation along near-ground paths were carried out by *Tatarskii* et al. [2.61] and *Gurvich* et al. [2.62]. There have also been many experiments with stellar scintillations that predated this work, for example [2.63–67], but their relevance in direct comparison with the theory is limited. The advantage of the near-ground, horizontal-path measurements is the ability to control the experimental path length, and more importantly to measure C_n^2 directly with temperature probes.

Tatarskii et al. [2.61] and *Gurvich* et al. [2.62] found quite good agreement between the theoretical results for the variance (2.83) and covariance (Fig. 2.5) of the fluctuations in the log-amplitude. In their experiments, they also found

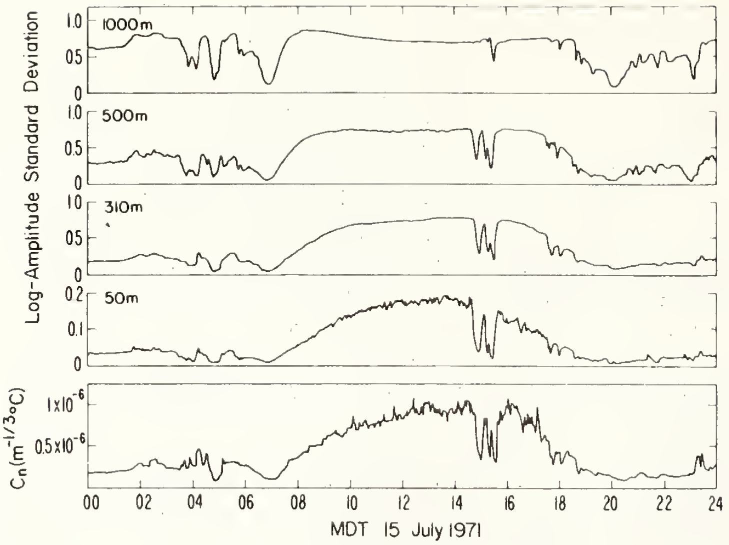

Fig. 2.9. Variance of the log-amplitude standard deviation σ_χ at each of four path lengths compared to the refractive index structure parameter C_n

that the irradiance fluctuations were log normally distributed, that is, the logarithm of the irradiance was normally or Gaussian distributed. Their actual technique was to measure the log irradiance fluctuations $\sigma^2 = (\log I/I_0)^2$ and use the relation $\sigma^2 = 4\sigma_\chi^2$ to check the theory. It is perhaps expected that they would obtain good agreement with the first-order theory because the maximum observed scintillation of their incandescent source was $\sigma_\chi^2 \sim 0.1$, which is sufficiently weak to prevent the effects of multiple scattering from dominating. Most recent experiments show the multiple-scattering regime sets in at about $\sigma_\chi^2 \gtrsim 0.3$.

Following the initial success of the theory, Soviet scientists *Gracheva* and *Gurvich* [2.68] were the first to observe the so-called saturation phenomenon. Initially, the log-amplitude variance would increase as predicted by (2.83) with increasing path length or C_n^2, only to stop increasing and saturate when $k^{7/6}L^{11/6}C_n^2 > 1$. Further observations of this phenomenon were made in the Soviet Union [2.69, 70] and later in the United States [2.71, 72]. Some authors [2.73, 74] even noted a decrease in σ_χ^2 with further increases in integrated turbulence when $k^{7/6}L^{11/6}C_n^2 \gg 1$.

Figure 2.9 illustrates some recent data on the saturation phenomenon (*Clifford* et al. [2.75]). Here we have simultaneous measurements of σ_χ for 24 h over four different optical paths—50, 310, 500, and 1000 m. Also shown for the same period is a direct point measurement of C_n derived from fine-wire thermometer measurements of C_T. The theory (2.83) indicates that σ_χ is proportional to C_n. This is clearly evident on the 50 m path where there appears to be detailed correlation between C_n and σ_χ. On the longer paths, the increase in refractive turbulence does not produce a corresponding increase in σ_χ. In fact, on the 1000 m path as C_n increases between 800 and 1400 MDT, σ_χ actually decreases. The path length dependence in (2.83) also appears to be inadequate to explain the data, that is, $\sigma_\chi \sim L^{11/12}$. Again, the log-amplitude standard deviation, instead of being roughly proportional to path, tends at times to level off and even decrease.

Interestingly, almost all experimenters noted that the probability distribution remained log normal even when the weak scattering theory failed. This remains especially surprising today because it is well demonstrated experimentally that the structure of the two-dimensional scintillation pattern, as indicated by the covariance function, is drastically altered in strong turbulence from the prediction (Fig. 2.5). This was the state of the theory in the late 1960s. Severe doubt had been cast on the validity of the weak scattering theory, especially with regard to the Rytov assumption (*Strohbehn* [2.19]). This stimulated a prodigious amount of theoretical attempts, both purely mathematical, using techniques from quantum electrodynamics to solve the scattering equation (2.50) and new physical models of propagation to bring the theoretical predictions closer in line with experimental reality. These results will be discussed in more detail in Chapters 3 and 4.

References

2.1 J.C.Owens: Appl. Opt. **6**, 51 (1967)

2.2 M.L.Wesely, E.C.Alcaraz: J. Geophys. Res. **78**, 6224 (1973)

2.3 C.A.Friehe, J.C.LaRue, F.H.Champagne, C.H.Gibson, C.F.Dreyer: J. Opt. Soc. Am. **65**, 1502 (1975)

2.4 G.K.Batchelor: *The Theory of Homogeneous Turbulence* (Cambridge University Press, London 1953)

2.5 J.L.Lumley, H.A.Panofsky: *The Structure of Atmospheric Turbulence* (Interscience, New York 1964)

2.6 A.S.Monin, A.M.Yaglom: *Statistical Fluid Mechanics: Mechanics of Turbulence*, Vol. 1 (MIT Press, Cambridge, Mass. 1971)

2.7 H.Tennekes, J.L.Lumley: *A First Course in Turbulence* (MIT Press, Cambridge, Mass. 1972)

2.8 A.Kolmogorov: In *Turbulence, Classic Papers on Statistical Theory*, ed. by S.K.Friedlander and L.Topper (Interscience, New York 1961) p. 151

2.9 L.O.Myrup: Tellus **21**, 341 (1969)

2.10 J.C.Kaimal, J.C.Wyngaard, Y.Izumi, O.R.Coté: Quart. J. Roy. Meteorol. Soc. **98**, 563 (1972)

2.11 V.I.Tatarskii: *Wave Propagation in a Turbulent Medium*, translated by R.A.Silverman (McGraw-Hill, New York 1961)

2.12 V.I.Tatarskii: *The Effects of the Turbulent Atmosphere on Wave Propagation* (Translated by Israel Program for Scientific Translations; originally published in 1967) U.S. Dept. of Commerce, National Technical Information Service, Springfield, Va. 1971)

2.13 S.Corrsin: J. Appl. Phys. **22**, 469 (1951)

2.14 A.M.Yaglom: *An Introduction to the Theory of Stationary Random Functions*, translated by R.A.Silverman (Prentice Hall, Englewood Cliffs, New York 1962)

2.15 N.Wiener: *Extrapolation, Interpolation, and Smoothing of Stationary Time Series, with Engineering Applications* (Wiley and Sons, New York 1949)

2.16 R.B.Blackman, J.W.Tukey: *The Measurement of Power Spectra, from the Point of View of Communications Engineering* (Dover Publ., New York 1958)
2.17 G.M.Jenkins, D.G.Watts: *Spectral Analysis and Its Applications* (Holden-Day, San Francisco 1968)
2.18 F.Pasquill: *Atmospheric Diffusion; The Dispersion of Windborne Material from Industrial and Other Sources* (Van Nostrand, New York 1962)
2.19 J.W.Strohbehn: Proc. IEEE **56**, 1301 (1968)
2.20 R.S.Lawrence, G.R.Ochs, S.F.Clifford: J. Opt. Soc. Am. **60**, 826 (1970)
2.21 S.L.Hess: *Introduction to Theoretical Meteorology* (Holt, New York 1959)
2.22 W.D.Neff: NOAA Tech. Rept. ERL 322-WPL **38** (1975)
2.23 L.R.Tsvang: Radio Sci. **4**, 1175 (1969)
2.24 G.R.Ochs, R.S.Lawrence: NOAA Tech. Rept. ERL **251**-WPL **22** (1972)
2.25 J.L.Bufton, P.O.Minott, M.W.Fitzmaurice, P.J.Titterton: J. Opt. Soc. Am. **62**, 1068 (1972)
2.26 R.E.Hufnagel, N.R.Stanley: J. Opt. Soc. Am. **54**, 52 (1964)
2.27 D.W.Beran, W.H.Hooke, S.F.Clifford: Boundary-Layer Meteorol. **4**, 133 (1973)
2.28 R.E.Hufnagel: "Proc. Topical Meeting on Optical Propagation Through Turbulence" (Boulder, Colo. 1974)
2.29 J.C.Wyngaard, Y.Izumi, S.A.Collins,Jr.: J. Opt. Soc. Am. **61**, 1646 (1971)
2.30 A.S.Frisch, G.R.Ochs: J. Appl. Meteorol. **14**, 415 (1974)
2.31 A.H.Mikesell: Publ. U.S. Naval Obs., 2nd Series **17** (4), 137 (1955)
2.32 A.N.Demidova: Izv. Glav. Astronom. Obs. **21** (6), 2 (1960)
2.33 J.L.Bufton: NASA Tech. Rept., TR-R-**369** (1971)
2.34 M.A.Kallistratova, D.F.Timanovskiy: Izv. Akad. Nauk. SSSR, Atmos. Ocean. Phys. **7**, 46; Russ.: **1**, 73 (1971)
2.35 A.M.Obukov: Izv. Akad. Nauk. SSSR **13**, 96 (1949)
2.36 L.A.Chernov: *Wave Propagation in a Random Medium*, translated by R.A.Silverman (McGraw-Hill, New York 1960) p. 168
2.37 R.W.Lee, J.C.Harp: Proc. IEEE **57**, 375 (1969)
2.38 R.L.Fante: IEEE Trans. AP-**21**, 750 (1973)
2.39 R.S.Lawrence, J.W.Strohbehn: Proc. IEEE **58**, 1523 (1970)
2.40 R.L.Fante: Proc. IEEE **63**, 1669 (1975)
2.41 H.Su, M.Plonus: J. Opt. Soc. Amer. **61**, 256 (1971)
2.42 A.Ishimaru: IEEE Trans. AP-**20**, 10 (1972)
2.43 L.W.Pickering, R.E.McIntosh: IEEE Trans. AP-**20**, 528 (1972)
2.44 M.Plonus, H.Su, C.Gardner: IEEE Trans. AP-**20**, 801 (1972)
2.45 C.Gardner, M. Plonus: J. Opt. Soc. Am. **64**, 68 (1974)
2.46 I.Sreenivasiah, A.Ishimaru: EE Dep. Univ. Wash: AFCRL-TR-74-02045 (1974)
2.47 C.Liu, A.Wernik, K.Yeh: IEEE Trans. AP-**22**, 624 (1974)
2.48 J.W.Strohbehn, S.F.Clifford: IEEE Trans. AP-**15**, 416 (1967)
2.49 A.A.M.Saleh: IEEE J. QE-**3**, 540 (1967)
2.50 V.I.Tatarskii: Izv. VUZ, Radiofiz. **10**, 1762 (1967); [English transl.: Radiophys. Quant. Electron **10**, 987 (1967)]
2.51 Y.A.Kravtsov: Izv. VUZ, Radiofiz. **13**, 281 (1970); [English transl.: Radiophys. Quant. Electron **13**, 217 (1970)]
2.52 S.F.Clifford: PhD Thesis, Dartmouth Coll., Hanover, N.H. (1969)
2.53 I.S.Gradshteyn, I.M.Ryzhik: *Table of Integrals, Series, and Products*, translated by Scripta Technica, Inc. (Academic Press, New York 1965)
2.54 A.Erdélyi: *Tables of Integral Transforms*, Vol. 2, ed. by A.Erdélyi (McGraw-Hill, New York 1954)
2.55 S.M.Rytov: Izv. Akad. Nauk SSSR (Ser. Fiz.) **2**, 223 (1937)
2.56 V.V.Pisareva: Soviet Phys.-Acoust. **6**, 87 (1960)
2.57 Y.L.Feinberg: Moscow: Academy of Sciences USSR (1961)
2.58 V.I.Tatarskii: Izv. VUZ, Radiofiz. **5**, 490 (1962)
2.59 W.P.Brown,Jr.: J. Opt. Soc. Am. **56**, 1045 (1966)

2.60 A.S.Gurvich, M.Kallistratova, N.Time: Radiophys. Quant. Electron. **11**, 771 (1968)

2.61 V.I.Tatarskii, A.S.Gurvich, M.A.Kallistratova, L.V.Terenteva: Astronom. Zh. **35**, 623 (1958)

2.62 A.S.Gurvich, V.I.Tatarskii, L.R.Tsvang: Dokl. Akad. Nauk. SSSR **123**, 655 (1958)

2.63 E.Gaviola: Astron. J. **54**, 155 (1949)

2.64 A.H.Mikesell, A.A.Hoag, J.S.Hall: J. Opt. Soc. Am. **41**, 689 (1951)

2.65 M.A.Ellison, H.Seddon: Monthly Notices Roy. Astron. Soc. **112**, 73 (1952)

2.66 I.G.Kolchinski: Astronom. Zh. **34**, 638 (1957)

2.67 V.A.Krasilnikov: Dokl. Akad. Nauk. SSSR **65**, 291 (1949)

2.68 M.E.Gracheva, A.S.Gurvich: Izv. VUZ, Radiofiz. **8**, 717 (1965); [English transl.: Radiophys. Quant. Electron **8**, 511 (1965)]

2.69 M.E.Gracheva: Izv. VUZ, Radiofiz. **10**, 775 (1967); [English transl.: Radiophys. Quant. Electron **10**, 424 (1967)]

2.70 A.S.Gurvich, M.A.Kallistratova, N.S.Time: Izv. VUZ, Radiofiz. **11**, 1360 (1968); [English transl.: Radiophys. Quant. Electron **11**, 771 (1968)]

2.71 P.H.Deitz, N.J.Wright: Ballistic Res. Labs., Aberdeen Proving Ground, Md. BAL-Memo Rept.-**1941**-Rev. (1968)

2.72 G.E.Mevers, D.L.Fried, M.P.Keister,Jr.: J. Opt. Soc. Am. **55**, 1575 (1965), Abstract

2.73 G.R.Ochs, R.S.Lawrence: J. Opt. Soc. Am. **59**, 226 (1969)

2.74 M.E.Gracheva, A.S.Gurvich, M.A.Kallistratova: Izv. VUZ, Radiofiz. **13**, 56 (1970); [English transl.: Radiophys. Quant. Electron **13**, 40 (1970)]

2.75 S.F.Clifford, G.R.Ochs, R.S.Lawrence: J. Opt. Soc. Am. **64**, 148 (1974)

NOAA Technical Report ERL 397-WPL 52, March 1978

A BASIC COMPARISON OF LIDAR AND RADAR FOR REMOTE SENSING OF CLOUDS

V. E. Derr

Both radar and lidar have proved valuable in studying cloud microphysics and dynamics. Because of the large difference in wave-length, the two techniques have differing penetration capabilities and detection sensitivities. A "system-free" comparison of radar and lidar for several missions and many cloud types is presented to permit the optimum choice of technique for field studies of cloud formation, development, and precipitation.

Society of Petroleum Industry Biologists, Energy/Environment
'78, Symposium on Energy Development Impacts, 259-264, 1978.

NOAA SURFACE MAPPING RADAR: THEORY AND APPLICATION

Michael Evans
National Oceanic and Atmospheric Administration
Wave Propagation Laboratory - R45x5
325 S. Broadway
Boulder, CO 80302

Abstract

The National Oceanic and Atmospheric Administration has developed a remote sensing instrument for the measurement of surface currents over large areas of oceans. This system utilizes the backscatter of a surface current induced Doppler shifted signal from 6 m ocean waves. A single map, containing 800 surface current vectors and covering 2000 square kilometers of ocean, can be produced in less than eight minutes. The CODAR (Coastal Ocean Dynamics Radar) system has been successfully tested in Florida, Alaska, California, Georgia, and Washington over the previous two years.

Introduction

The NOAA surface-current mapping radar is a recent development in the field of remote sensing with direct applications in physical oceanography. We have given this system the name CODAR for Coastal Ocean Dynamics Radar. The CODAR system is capable of producing a "map" of surface currents covering an area of several thousand square kilometers in less than eight minutes. For the first time simultaneous measurements of thousands of points over a large area of ocean are possible. Areas of potential use for this system include: real time oil spill trajectory monitoring, environmental impact studies, worst-case production platform designs, fish-egg transport studies, beach-erosion studies, coastal-zone management, and nuclear power plant thermal plume trajectory analysis. We present a brief technical description of the radar principles, followed by examples of measurements made to date using this system.

Theory of Operation

The CODAR system utilizes backscatter of high frequency (HF) surface waves from the ocean surface. Previous work (3) has shown that such a signal scatters from ocean waves 1/2 the transmitted wave length (e.g., ≈ 6 m long ocean waves at 25.6 MHz) as illustrated in Fig. 1. Such waves are nearly always present and are essentially fully developed at ≈ 5 cm height. A 6 m wave will travel in deep water (> 2 m) at a known velocity of 3 m/s. This velocity produces a Doppler shift of ± .516 Hz on the backscattered 25.6 MHz pulse whose sign depends on the wave direction relative to the radar (radially toward or away from). If a surface current is present a further Doppler shift is superimposed on that produced by the wave motion. By analyzing the spectrum of the echo from the ocean surface, we are thus able to determine the surface current.

SURFACE MAPPING RADAR

Ordinarily, a very large antenna array would be required to obtain the angular resolution required for these measurements. However, it has been possible to use the properties of the Doppler spectrum to separate signals arriving from different directions by measuring the phase differences between echoes arriving at four whip antennas. A detailed discussion of the entire process is given elsewhere (1,2). Figure 2 illustrates a block diagram of the complete system.

A single system is capable of resolving only the radial component of the surface currents. Therefore, we use two radars separated by 20 km to 50 km and combine the radial currents in the common overlap area to produce a total surface current map. The individual sites may be shore-based or located on platforms and are capable of obtaining data in a 360° arc. While we believe ship operation is possible, we presently require a stable platform.

The maximum range of the CODAR system is approximately 60 km. For two shore based sites (with ≈ 30 km separations) the total coverage area is approximately 2000 km^2 providing a display of approximately 800 current vectors arranged on a rectangular grid. Each vector represents the average surface current in a 2.4 km x 2.4 km square. The size of the square is a function of the transmitter pulse length and is variable. As a 6 m ocean wave is only influenced by currents to a depth of about one meter, we are truly measuring surface currents in this square.

Hardware

All the electronics for a single CODAR site are contained in a shock mounted 35" enclosure. Depending on specific requirements a micro-processor version is feasible with a further size reduction of 40%. One of the key features of this system is its portability; we often deploy radar stations in helicopter cargo slings and use small diesel generators to supply power. The transmitting antenna is a simple collapsible Yagi, and four CB whips are used for receiving (Fig. 3,4). Typical hardware deployment time for a complete site is 2 hours (not including housing).

At the present time, all hardware items are available from commercial vendors, with the exception of the HF receiver. The estimated cost of duplicating the two site CODAR system varies from 50 K to 125 K depending on specific requirements.

A single CODAR site consists of the following items:

1. DEC PDP 11/34A computer
2. 9 track digital tape recorder
3. Video terminal
4. Transmitter
5. Receiver

6. Graphic device
7. VHF communications and telemetry
8. Receiving and transmitting antennas.

Figure 5 illustrates the CODAR system in a typical configuration. Surface current maps are routinely produced in the field in real time, and no further processing is necessarily required; magnetic tape is used only for data archiving. The system requires no calibrations. Our present software allows automatic programming of data acquisition and processing at predetermined intervals.

Field Operations

Considerable effort has been devoted to comparing CODAR data with conventional surface drifters. Typical point intercomparisons yield differences of 10% to 15%. This is the same magnitude error we observe between initially colocated drifters. While the absolute accuracy of the CODAR system is difficult to measure, we feel that it is superior to any known conventional technique because of its internal consistency. The hardware is capable of resolving 1 mm/s while our present analysis software resolves 1 cm/s. We have observed during field operations consistent well behaved current flows of several cm/s. The ultimate accuracy is dependent on signal to noise ratios and second order effects in the scattering mechanism. Extensive ground truth experiments have been conducted over the past two years in Miami, Florida; Savannah, Georgia; and Cook Inlet, Alaska. One main fact became quite obvious during these tests: the poor performance of conventional surface drifters under conditions of high seas and wind. With the CODAR system only the personnel not the data suffered during a Gulf of Alaska storm.

We have operated the CODAR system in six major experiments over the previous two years. The locations, dates, and main purposes are:

1.	Ft. Lauderdale-Miami, Fla.	July-Sept.	1976	Test
		October	1976	Test
		December	1976	Test
		March	1977	Data
2.	Seldovia-Anchor Pt. Alaska	June-July	1977	Data
3.	Pescadero, Calif.	January	1978	Test
4.	Hilton Head Is. S. Carolina Wassaw Is. Georgia	May	1978	Data
5.	Augustine Is.-Cape Douglas Alaska	June-July	1978	Data
6.	Dungeness Spit-Whidbey Is. Wash.	August	1978	Data

We will briefly describe the purpose and general results of each set of these experiments.

Florida was chosen for the initial field testing due to the consistent and well known characteristics of the Gulf Stream. The majority of the time in Florida was used to finalize the design of the hardware and software systems.

SURFACE MAPPING RADAR

The Gulf Stream itself provided the initial ground truth. The cooperation of NOVA University in Ft. Lauderdale was a key element in the success of our early efforts. During March of 1977 a week long series of ground truth experiments were conducted using ships from both NOVA University and NOAA's AOML Laboratory. Figure 6 illustrates a typical intercomparison between surface drifters and the CODAR system during this period. General observations on the behavior of the Gulf Stream include:

1. A weak, intermittent counter current near shore.
2. Movement of the Gulf Stream's peak in an East-West direction on almost a daily basis.
3. Variations in the magnitude of the Gulf Stream on a daily basis.

As the system was experimental throughout this period, little useful oceanographic data was actually collected.

In June of 1977 we conducted our first extensive field measurement, supported by BLM, Dept. of Interior. Data was collected over a several week period with systems at Anchor Pt. and Seldovia, Alaska (Fig. 7). Our most interesting data set was obtained over a 24 hour period covering the entire day of July 13, 1977. Maps were produced at 1/2 hour intervals and later converted to 16 mm film. The result is a movie showing two complete tidal cycles. Initial analysis of this data shows that the flow in and around Kachemak Bay is predominently driven by the 12 and 24 hour tidal variations as expected. Both the magnitude and direction of the surface current were found to be strongly dependent on geographic location. This data clearly demonstrated one of the major advantages of the CODAR system over conventional techniques: The ability to separate spatial and temporal features in the circulation pattern. Drifters tend to mix the two together. Also, this experiment pointed up another important fact. At least for tidal driven flows, the radar indirectly measures currents all the way from the surface to the bottom because tidal currents are nearly independent of depth.

The Pescadero, California operation was a joint venture with Scripps Institute and Stanford University. Radial currents, from single sites, were obtained using both the NOAA and Stanford radars simultaneously. During this time, surface drifters and the Scripp's tilt buoy were deployed. The data was obtained for experimental purposes involving minimum current resolution and wave height directional spectrum capabilities, and is presently under investigation.

The Savannah experiment was a demonstration project for the Department of Energy. Maps were produced at 1 hour intervals over a 72 hour period beginning on May 9, 1978. Skidaway Institute of Oceanography measured the temperature, salinity, and current velocity at 1 meter depth intervals using two vessels at fixed locations. These measurements were both preceded and followed by hydrographic sections. The

Coast Guard provided extensive surface drifter measurements using both ships and helicopters. A time sequence of surface current maps, from this experiment, is shown in Figure 8. Initial analysis shows a well defined offshore pattern. Turbulence behind the many marsh islands is evident in more detailed maps. We plan to analyze this data in detail at a later date.

The Augustine Is.-Cape Douglas experiment in June of 1978 was the most severe operational test of CODAR to date. Both sites were deployed by helicopter from the NOAA ship SURVEYOR. The site separation was the maximum attempted to date: 56 km. Fifteen days of data were obtained during this period. During the last eight days the system was operated continuously twenty four hours a day. Initial analysis shows the expected strong tidal flow along the coast, with a somewhat complicated circulation pattern in Kamishak Bay. Considerable variability in the circulation pattern is visible on a daily basis. We were fortunate to have a major storm develop over Cook Inlet part way through the measurement period. We have just started analysis of this data and expect to obtain unique insight into the interactions of a storm with the general circulation system.

We are presently deploying the CODAR system in the Puget Sound area. In cooperation with NOAA's PMEL laboratory, intensive data will be collected on a continuous basis from August 21 through August 23, 1978. Various measurement systems including surface drifters and current meters will be deployed during this period. This work is being sponsored by the Environmental Protection Agency via NOAA's MESA program office.

Program Areas

We are now developing two different enhancements to the basic CODAR system. The first of these involves using integration techniques and the equation of continuity to increase the overall coverage area of the system by typically 100%. Initial results using these techniques are very promising. The second enhancement is the development of a deep drogued disposible drifter. This system will allow measurement of the drifter's position to within ± 500 m at potential ranges of several hundred kilometers. The drifter velocity will be measured, independent of the position track, with accuracies of ± 2 cm/s. We are designing this system to be used with either a stand alone shore based interrogation package or with an existing CODAR system. In either case, up to 64 different drifters may be interrogated sequentially. A typical measurement of position and instantaneous velocity will require about four minutes. Using the CODAR system for surface currents and the drifters simultaneously for sub-surface currents will provide detailed information on not only the general circulation pattern but the total water column as well. Other areas of research within the Sea State Studies program area include:

SURFACE MAPPING RADAR

1. Development of a wave height directional spectrum measuring capability for the CODAR system.
2. Utilizing the Sea-Sat satellite radar altimeter for obtaining ocean waveheights.
3. Development, in conjunction with Stanford Research Institute, of an over-the-horizon (OTH) HF radar wave height measuring capability.
4. Development of an ocean-floor based, disposible vertical current profiler.

Conclusions

In terms of cost-benefit factor alone the CODAR system provides a 2000 to 1 improvement over conventional systems and techniques. As with many technological advances, the ultimate capability of the CODAR system will be determined by the users, not the designers of the system. We are frequently confronted by oceanographers who are incapable of comprehending the vast quantities of previously unobtainable information which the CODAR system can provide. We have collected over the past two years in excess of 900 magnetic tapes. This translates to 18,000 surface current maps or 1.5×10^7 current vectors! We are now attempting to initiate cooperative ventures with several oceanographic organizations with the purpose of analyzing and publishing results of our past experiments.

We have received in excess of one hundred inquiries, including several from foreign countries, regarding the CODAR system with numerous requests for hardware purchases and field operations. Based on our own experimental results and the interest of the scientific community it would appear that HF remote sensing is now finally capable of significantly impacting physical oceanography.

References

1. Barrick, D. E. and Evans, M. W. (1976) Implementation of coastal current mapping HF radar system. Progress Report No. 1, NOAA Tech. Report ERL 373-WPL 47 July 1976.

2. Barrick, D. E., Evans, M. W., and Weber, B. L. (1977) Ocean surface currents mapped by radar. Science, Vol. 198, No. 4313 Oct. 14, 1977, pp. 138-144.

3. Crombie, D. D. (1955) Doppler spectrum of sea echo at 13.56 mc/s. Nature 175, pp. 681-682.

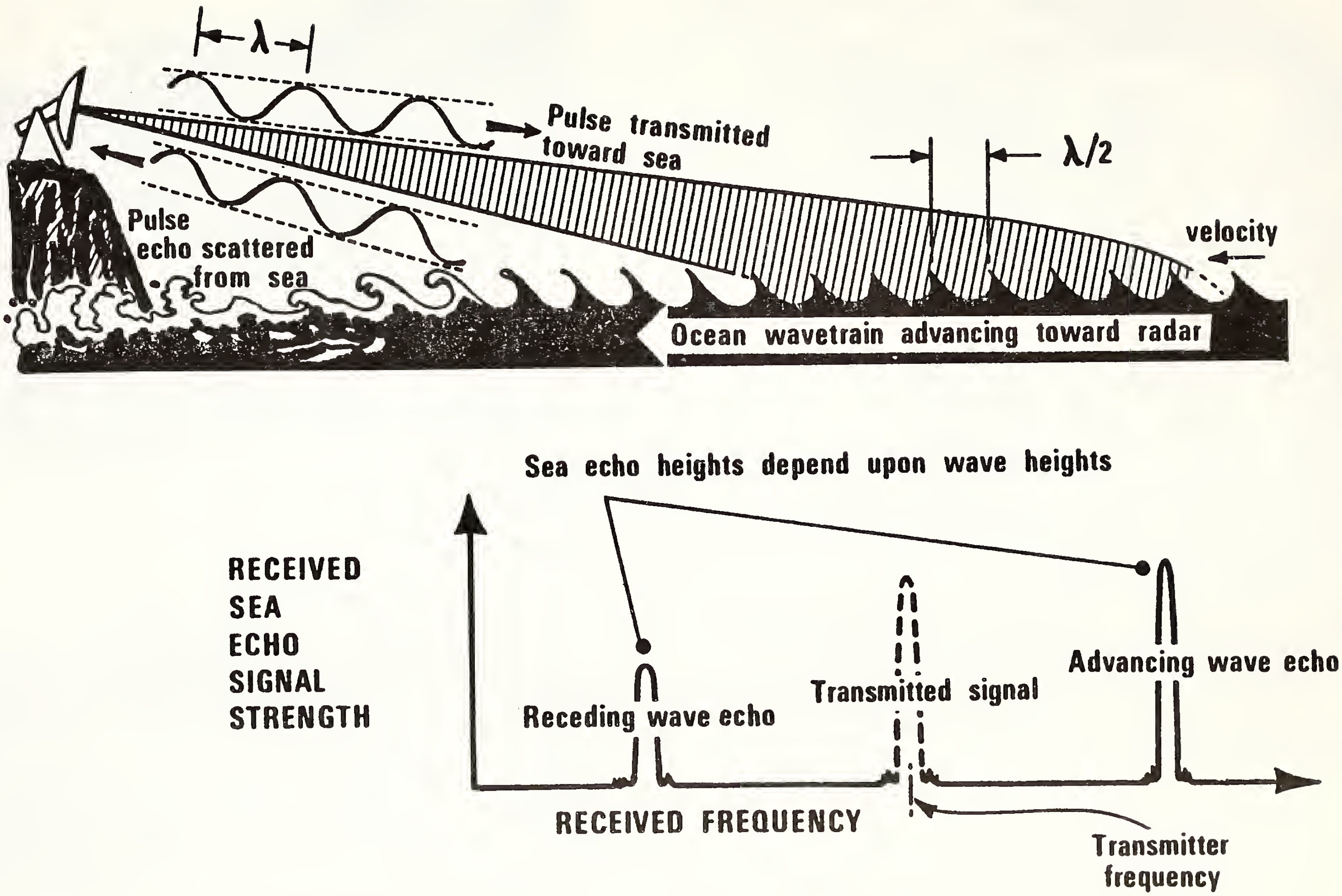
λ
Pulse transmitted toward sea
λ/2
Pulse echo scattered from sea
velocity
Ocean wavetrain advancing toward radar
Sea echo heights depend upon wave heights
RECEIVED SEA ECHO SIGNAL STRENGTH
Receding wave echo
Transmitted signal
Advancing wave echo
RECEIVED FREQUENCY
Transmitter frequency

Figure 1. Principle of CODAR operation showing H.F. backscatter.

[illegible]-74-556

CODAR SYSTEM BLOCK DIAGRAM

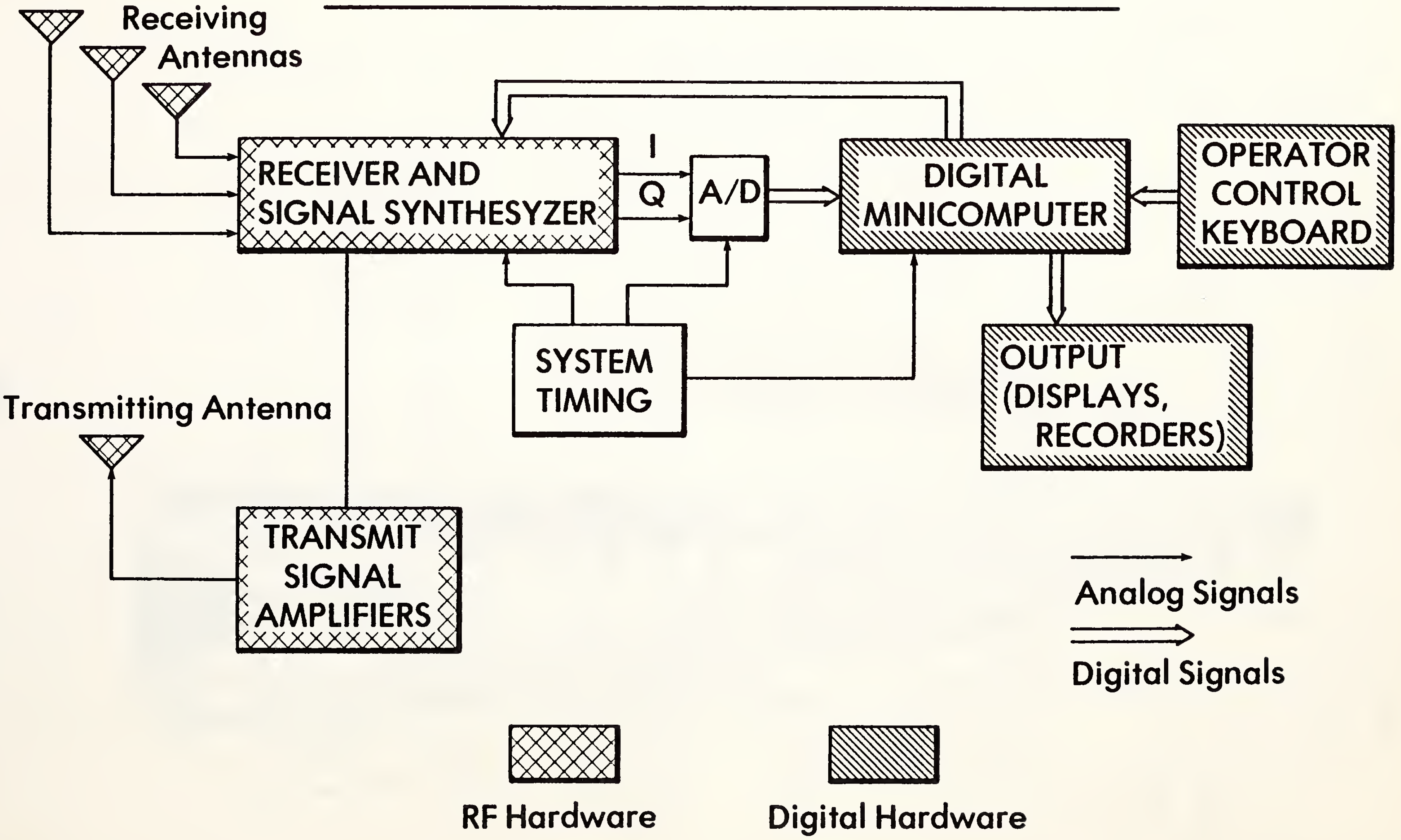

Figure 2.

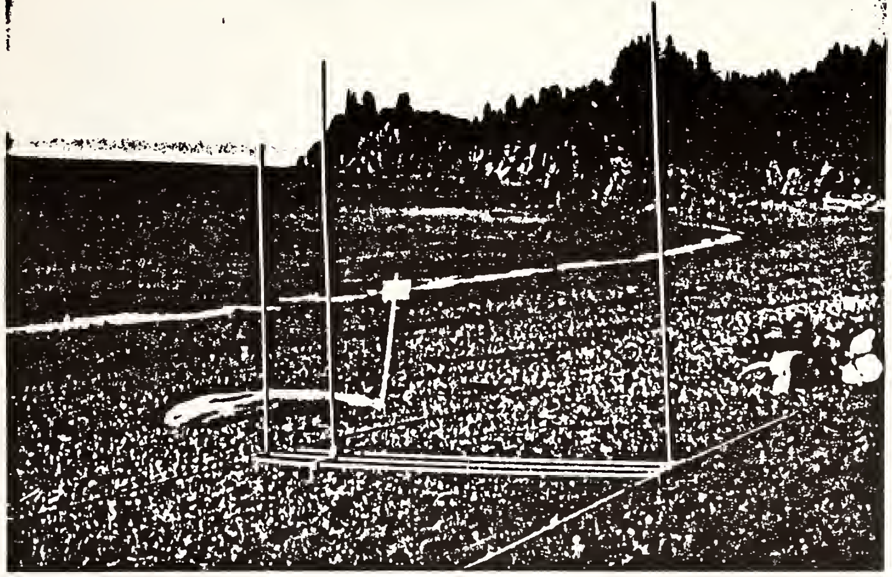

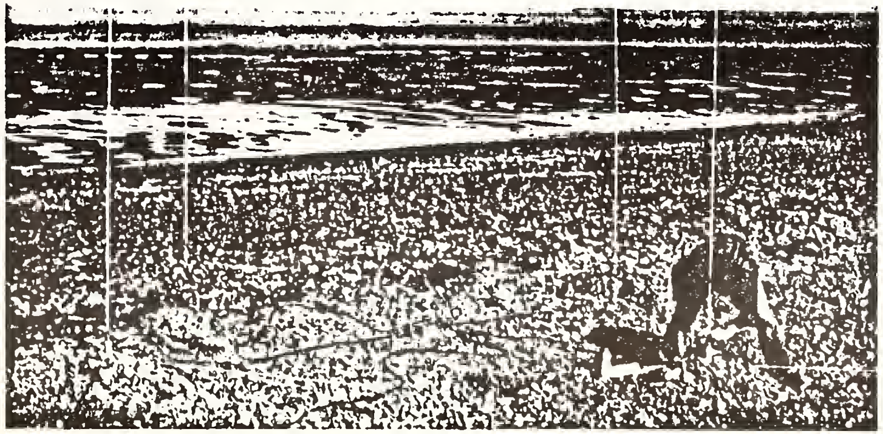

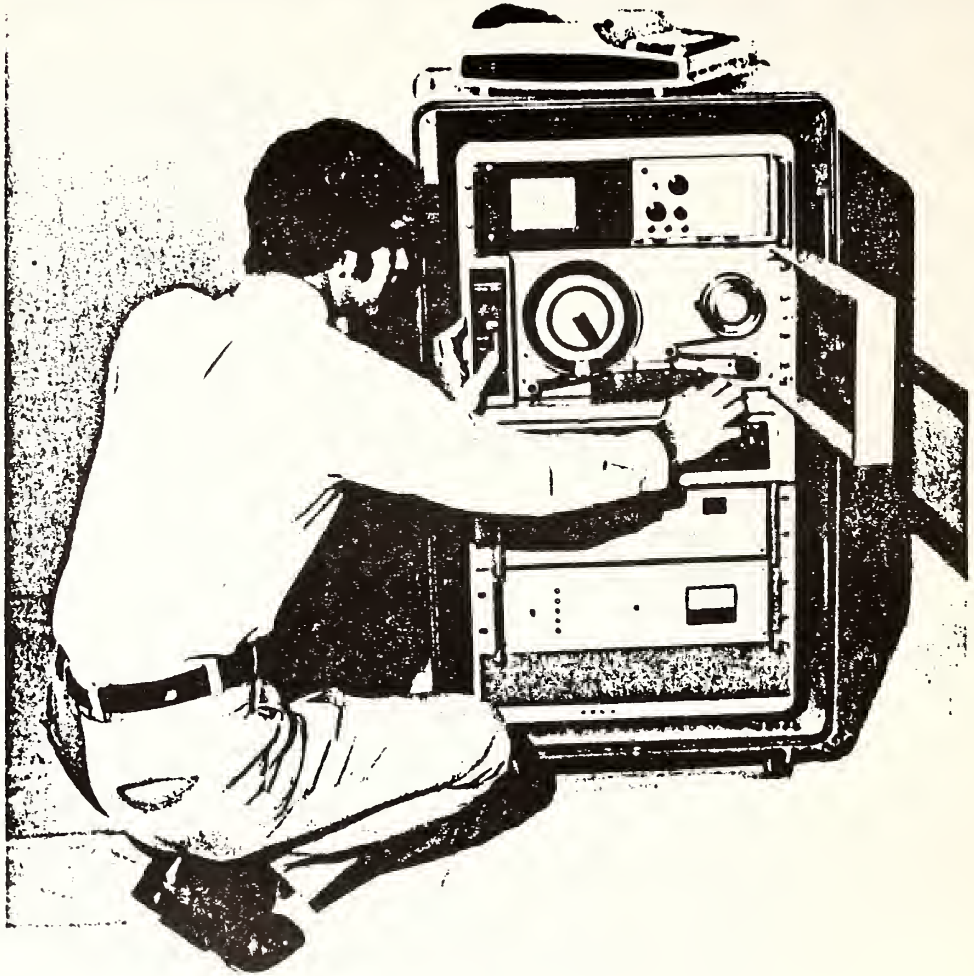

Figure 3. (Upper Left) Transmitting Antenna

Figure 4. (Lower Left) Receiving Antenna

Figure 5. (Above) CODAR System

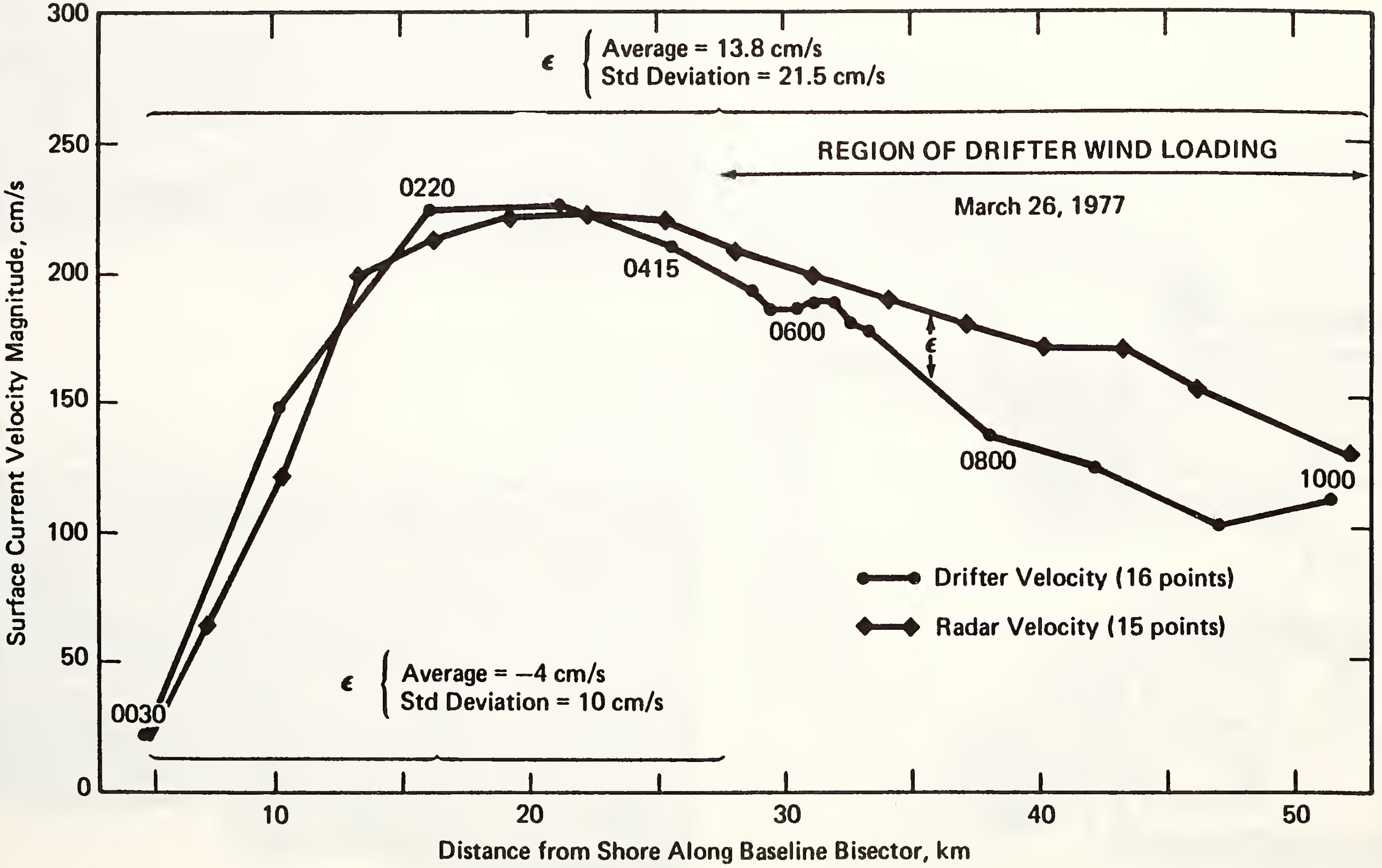

Figure 6. CODAR system vs surface drifter, Miami/Ft. Lauderdale, Florida.

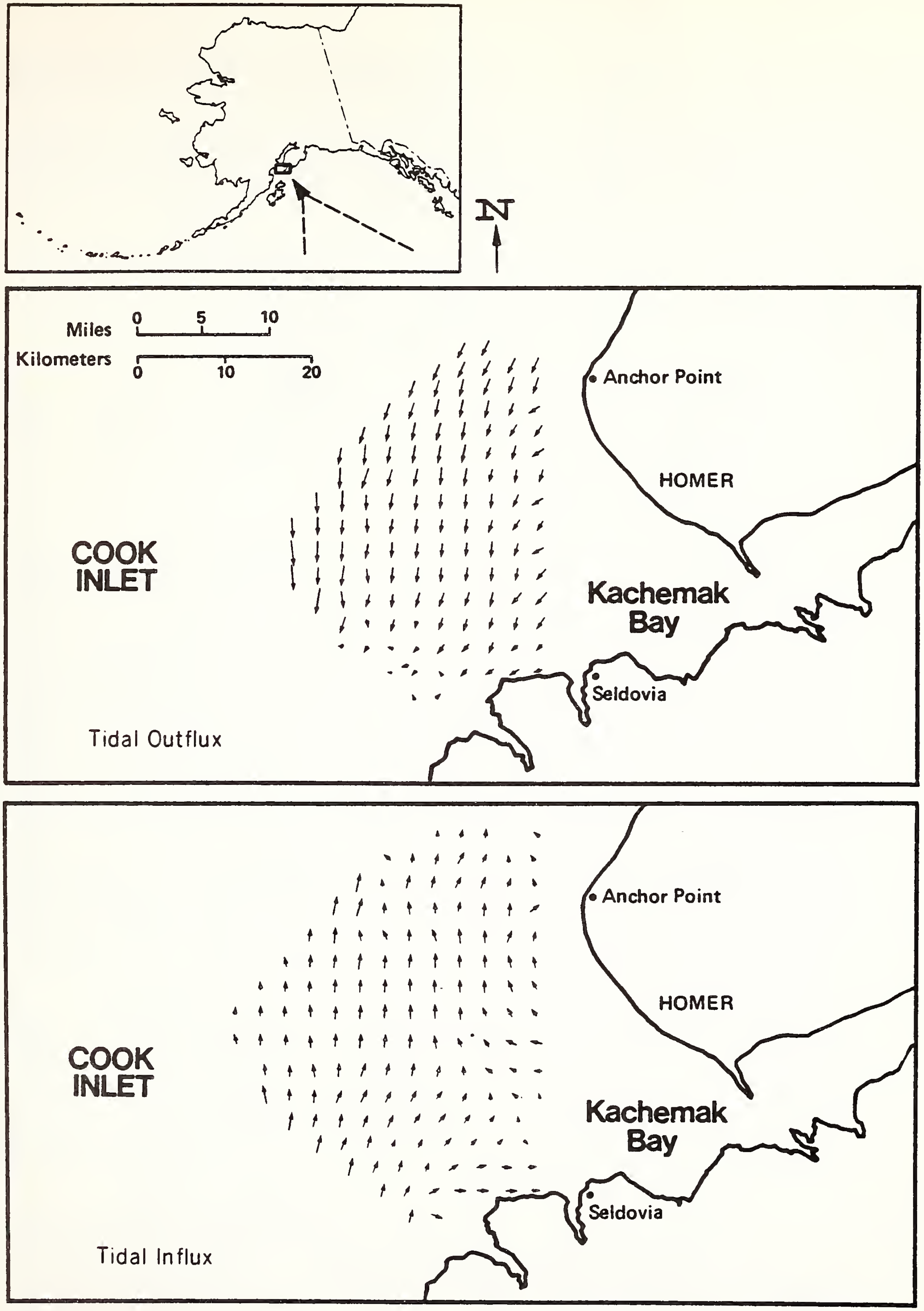

Figure 7. Surface current patterns on July 1, 1977. Bottom at 1120 hours Top at 1920 hours.

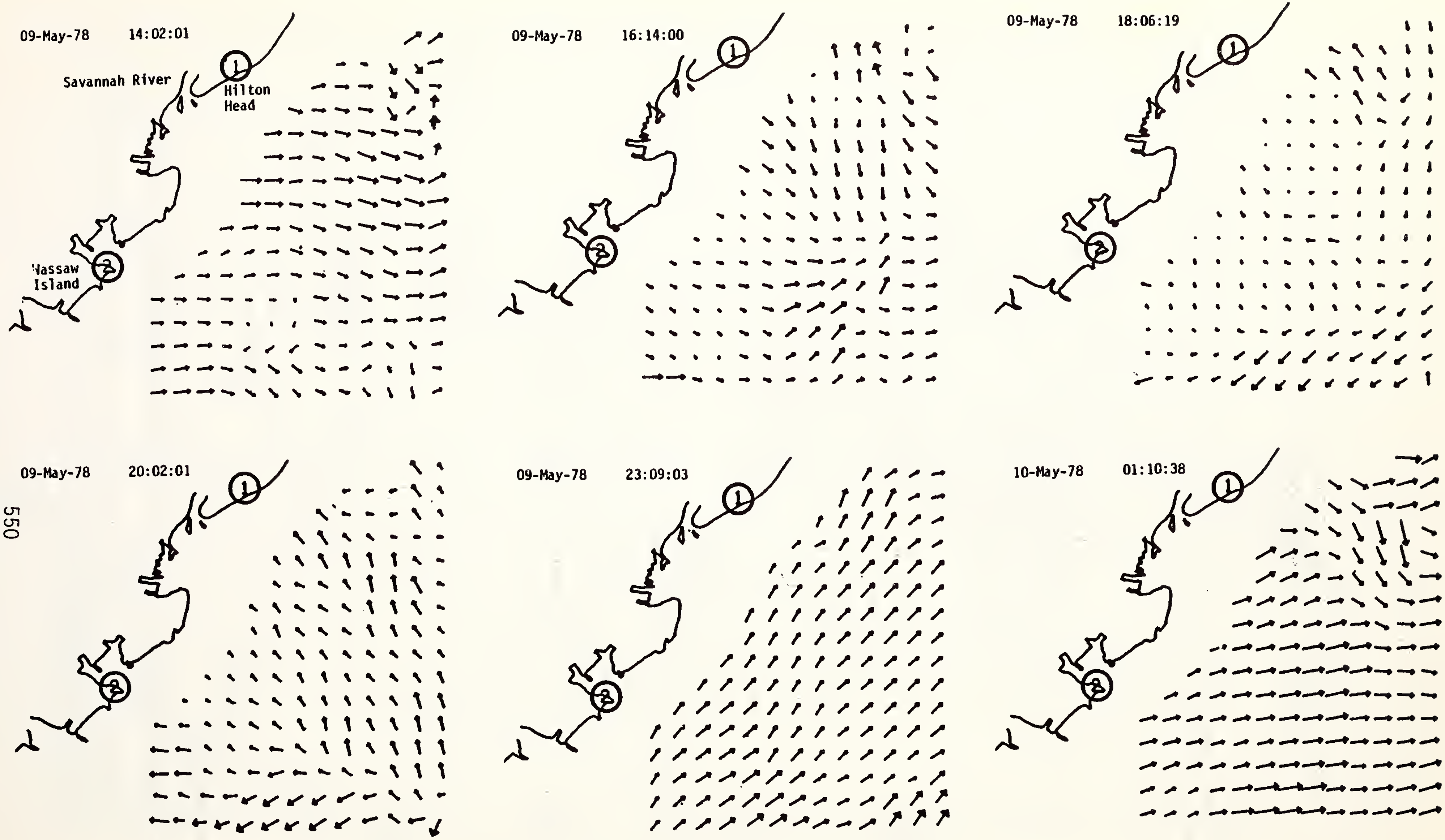

Figure 8. Sequence of six surface current maps from Savannah, Georgia test 9-10 May 1978. The total map coverage area is not shown. Site separation is 30 km. Maximum surface current velocity is 36 cm/s.

Radio Science, 13: 255-259, 1978.

The distribution of radio refractive index structure parameter in boundary layers undergoing spatial or temporal transition

E. E. Gossard

Wave Propagation Laboratory, Environmental Research Laboratories, National Oceanic and Atmospheric Administration, US Department of Commerce, Boulder, Colorado 80302

(Received June 29, 1977; revised September 8, 1977.)

The height distribution of C_ϕ (the structure parameter of potential refractive index) in a steady, horizontally uniform boundary layer are calculated assuming power laws for meteorological quantities. The results are then compared with those of more rigorous models examined by Wyngaard *et al.* It is shown that the results are in very satisfactory agreement when the power is properly chosen. Finally, power-law profiles are used to calculate horizontal and temporal variations in vertical profiles of C_ϕ and to calculate radio-duct thickness for several boundary transitional conditions.

1. INTRODUCTION

With the widespread realization of the capabilities of new clear-air Doppler radars, there is renewed interest in the spatial distribution of radio refractive index and its statistics. Of particular interest is the refractive index structure parameter C_ϕ^2, which is the turbulence-related quantity of primary concern for the prediction of clear-air backscatter. The Wave Propagation Laboratory of NOAA has developed a frequency-modulated, continuous-wave (FM-CW) radar with Doppler capability whose principal value is that it can monitor wind and wind shear in the planetary boundary layer. Therefore, it is urgent to determine how changes and modifications in the boundary layer affect C_ϕ^2 and the performance of the radar. This paper presents methods for calculating the height distribution of C_ϕ^2 in boundary layers undergoing spatial or temporal transition.

2. FORMULATION OF THE PROBLEM

The refractive index parameter to be used is the potential refractive index ϕ, which is defined as the refractive index of a parcel of air brought adiabatically and without change in absolute humidity to a pressure level of 1000 mb. In terms of meteorological quantities

$$\phi = (77.6/\theta)(P - 4810\, e_p/\theta) \qquad (1)$$

where θ is potential temperature and e_p is the potential vapor pressure [see, e.g., *Bean and Dutton,* 1966]. So defined, the quantity ϕ can be considered to diffuse much as θ, e_p, or any passive additive undergoing turbulent mixing. The approach that will be followed in this paper is to solve the diffusion equation for $\phi(z,x,t)$ and $C_\phi(z,x,t)$, where x, y, z, and t are the three space coordinates and time, respectively, with z being the vertical direction. The quantity of primary interest is C_ϕ, where [*Corrsin,* 1951; *Ottersten,* 1969]:

$$C_\phi^2 \approx 3.2\, \varepsilon^{-1/3} \varepsilon_\phi \qquad (2)$$

ε is the turbulent-dissipation rate and ε_ϕ is the rate of destruction of the half variance of ϕ. For a steady-state regime of turbulence, the kinetic energy balance equation under conditions of forced convection can be represented, according to *Lumley and Panofsky* [1964], by

$$\varepsilon \approx -\overline{u'w'}\, (\partial u/\partial z)(1 - R_f) \qquad (3)$$

where R_f is related to the more common Richardson number, $Ri = (g/\theta)(d\theta/dz)/(du/dz)^2$, by the ratio of the eddy coefficients of heat to momentum. Under neutral or stable conditions that ratio is near unity. Symbols with a prime refer to turbulent perturbations. Furthermore, assuming that the destruction of the half variance of ϕ is balanced by shear production,

$$\varepsilon_\phi \approx -\overline{\phi' w'}\, \partial\phi/\partial z \qquad (4)$$

Both (3) and (4) neglect potentially important terms such as radiative flux divergence and divergence of energy and pressure forces. This has been cus-

Copyright © 1978 by the American Geophysical Union.

0048-6604/78/0304-0255$03.00

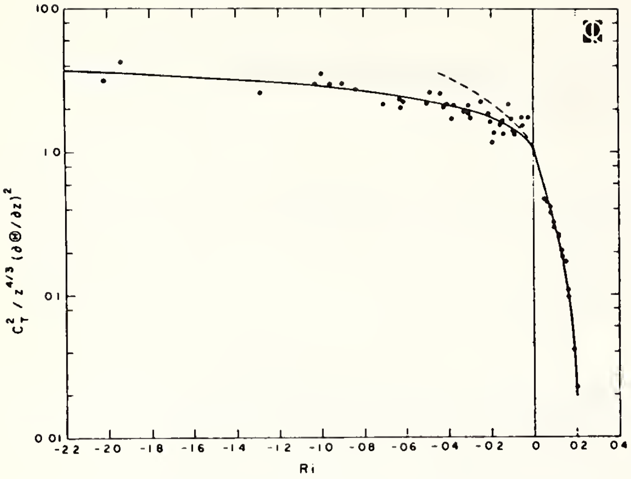

Fig. 1. Measured data reported by *Wyngaard et al.* [1971] compared with (5) (dashed curve) and best-fit curve (solid curve). For $Ri > 0$ solid and dashed curves are indistinguishable.

tomary in studies of this type, because of difficulties in evaluating the neglected terms experimentally. Nevertheless, this approximation must ultimately be justified by experiment.

Defining the eddy coefficient K for ϕ by $\overline{\phi' w'} = -K(\partial\phi/\partial z)$ and defining the friction velocity u_* such that $u_*^2 = -\overline{u' w'}$, (3) and (4) can be substituted into (2), yielding

$$\frac{C_\phi^2}{z^{4/3}(d\phi/dz)^2} = 3.2\, k_0^{4/3}(1 - \alpha Ri)^{4/3}(1 - Ri)^{-1/3} \tag{5}$$

where a log-linear velocity profile has been assumed so that $K/u_* = k_0 z(1 - \alpha Ri)$. The universal constant α is estimated by *Businger et al.* [1971] to be 4.7.

The result (5) may be compared with measured data reported by *Wyngaard et al.* [1971] and is shown in Figure 1. The right-hand side of (5) is plotted as a dashed curve. Throughout the stable range it nearly coincides with the solid curve that fits the data but fails seriously in the range of negative *Ri*. From this we can conclude that the assumptions and the balance equations we have used are an adequate representation of conditions in the steady-state, uniform surface layer of the atmosphere under neutral or stable conditions.

Under unstable conditions, Wyngaard *et al.* suggest that

$$C_\phi^2 = k_0^2 \phi_*^2 z^{-2/3} g(z/L) \tag{6}$$

is a good fit to their data, where

$$g(z/L) = 4.9\ [1 - 7(z/L)]^{-2/3}$$

L is the Monin-Obukov length representing static stability, and

$$z/L = Ri/(1 - \alpha Ri) \tag{7}$$

Plots of C_ϕ vs. height from (5) and (6) are shown in the lower frame of Figure 2 for several stabilities represented by L. Thse curves represent the probable best estimate of the height distribution of C_ϕ in the idealized boundary layer. However, the model used cannot be applied to the diffusion equation to obtain useful solutions except by numerical methods and high-speed computers. On the other hand, if power-law profiles had been used instead of log-linear profiles, then

$$u = bz^m,\ \theta - \theta_s = b_1 e^m,\ \phi - \phi_s = b_2 z^m$$

where ϕ_s and θ_s are surface values and b, b_1, and b_2 are constants. Then

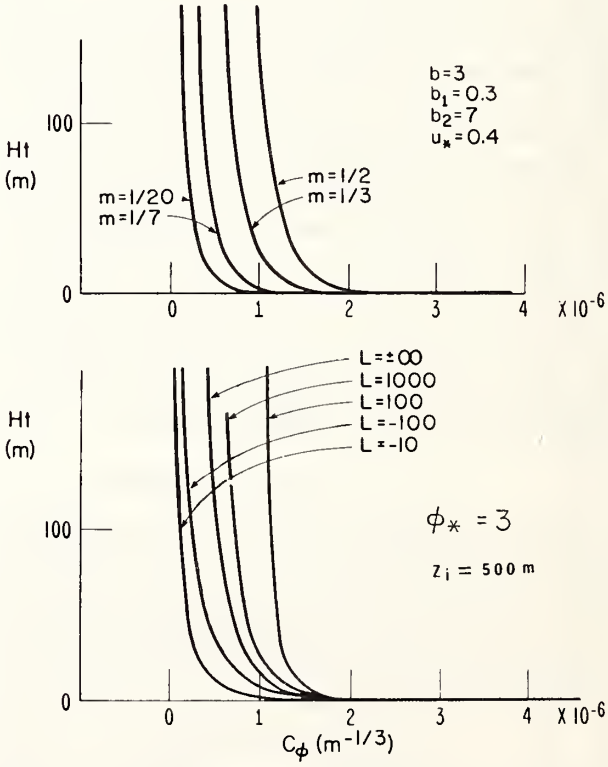

Fig. 2. Height distributions of C_ϕ assuming log-linear height distribution of ϕ (bottom frame) and power law (top frame) from (5), (6), and (8), for various values of stability (*m* and *L*).

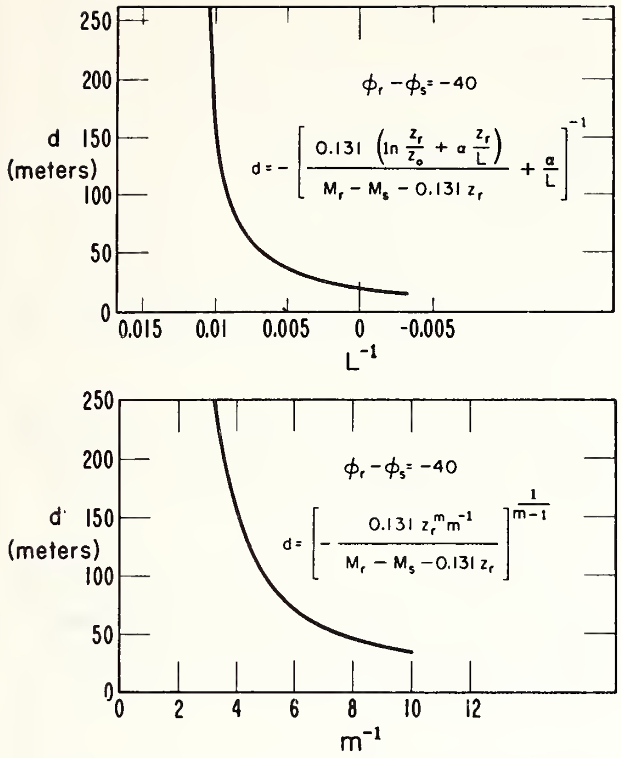

Fig. 3. Comparison of surface duct thickness d vs. stability assuming log-linear height distribution of ϕ (top frame) and power law (bottom frame). A ray launched horizontally at the height d will exactly follow the curvature of the earth by definition. The modified refractive index M is a modification of ϕ such that the curvatures of all rays have added to them the curvature of the earth i.e., they are bent upward.

$$C_\phi^2 = 3.2\left(\frac{u_*}{bm}\right)^{4/3} z^{4(1-m)/3}(1 - Ri)^{-1/3}\left(\frac{\partial\phi}{\partial z}\right)^2 \tag{8}$$

The term that includes Ri stays very near unity for reasonable values of Ri because of the small negative power to which the expression is raised. The effect of stability is almost completely reflected in m. The resulting distribution of C_ϕ vs. height is shown in the top frame of Figure 2 for several values of m.

To further test the adequacy of the power law, it is revealing to compare the prediction of surface duct thickness for the two models. The thickness of the duct in meters is the height at which $d\phi/dz = 0.131$ (m^{-1}). The results for the two models are shown in Figure 3, where the modified refractive index $M = \phi + 0.131z$ and z is in meters.

It is evident that the power-law profiles, with properly chosen values of m, can give a very adequate representation of the more rigorous model. They have the important advantage that classical solutions to the diffusion equations can then be applied.

3. BOUNDARY LAYERS UNDERGOING MODIFICATION

Written in general form, the diffusion equation for ϕ is

$$\underbrace{\partial\phi/\partial t}_{\text{temporal term}} + \underbrace{u\,\partial\phi/\partial x + \mathrm{v}\,\partial\phi/\partial y + w\,\partial\phi/\partial z}_{\text{advective terms}}$$

$$= \underbrace{\frac{\partial}{\partial x}\left(K_x\frac{\partial\phi}{\partial x}\right) + \frac{\partial}{\partial y}\left(K_y\frac{\partial\phi}{\partial y}\right) + \frac{\partial}{\partial z}\left(K_z\frac{\partial\phi}{\partial z}\right)}_{\text{diffusion terms}} \tag{9}$$

where the quantities K_x, K_y, K_z are the eddy diffusion coefficients of ϕ in the x, y, and z directions, and u, v, and w are the corresponding velocity components. Thus formulated, the eddy coefficients can be considered functions of position. This use of the eddy coefficients in diffusion problems is classical. However, it lacks any fundamental physical basis and depends on a tenuous analogy

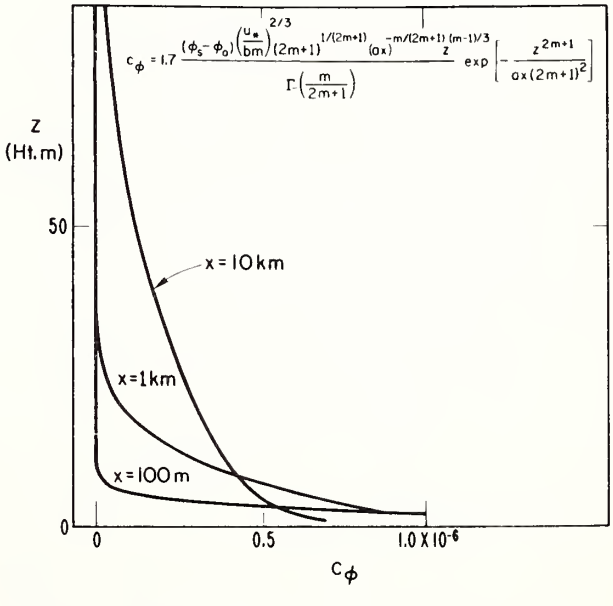

Fig. 4. Height distribution of C_ϕ at various distances downwind of an abrupt surface discontinuity in ϕ, e.g., downwind of a shoreline. Subscript "o" indicates unmodified value and "s" indicates the (water) surface value; $\phi_s - \phi_o = 10$ and $m = 1/3$.

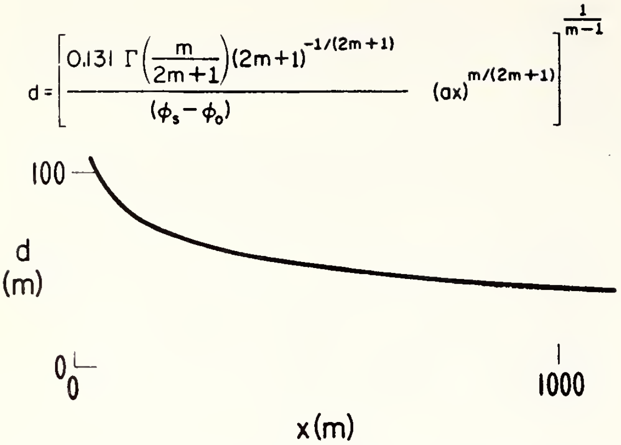

Fig. 5. Radio duct thickness vs. distance offshore with the same assumptions as in Figure 4.

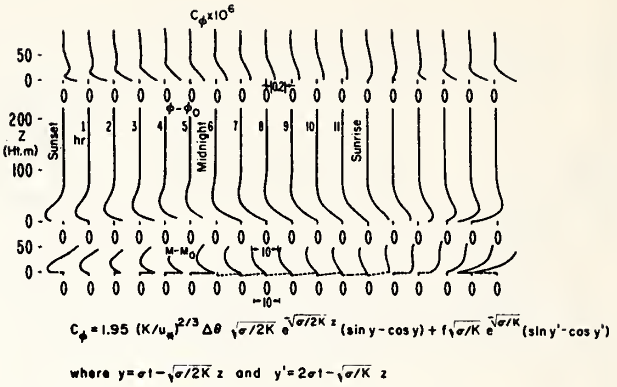

Fig. 6. Calculated structure parameter (top frame), height distribution of potential refractive index (middle frame), and height distribution of M (bottom frame). The minima of the M curves indicate height of the surface duct.

with molecular diffusion for its justification. With the use of modern computers one can numerically solve a more rigorous formulation. However, it is the intent in this paper to go as far as possible without relying on large computers and also to provide useful functional relationships for predict-

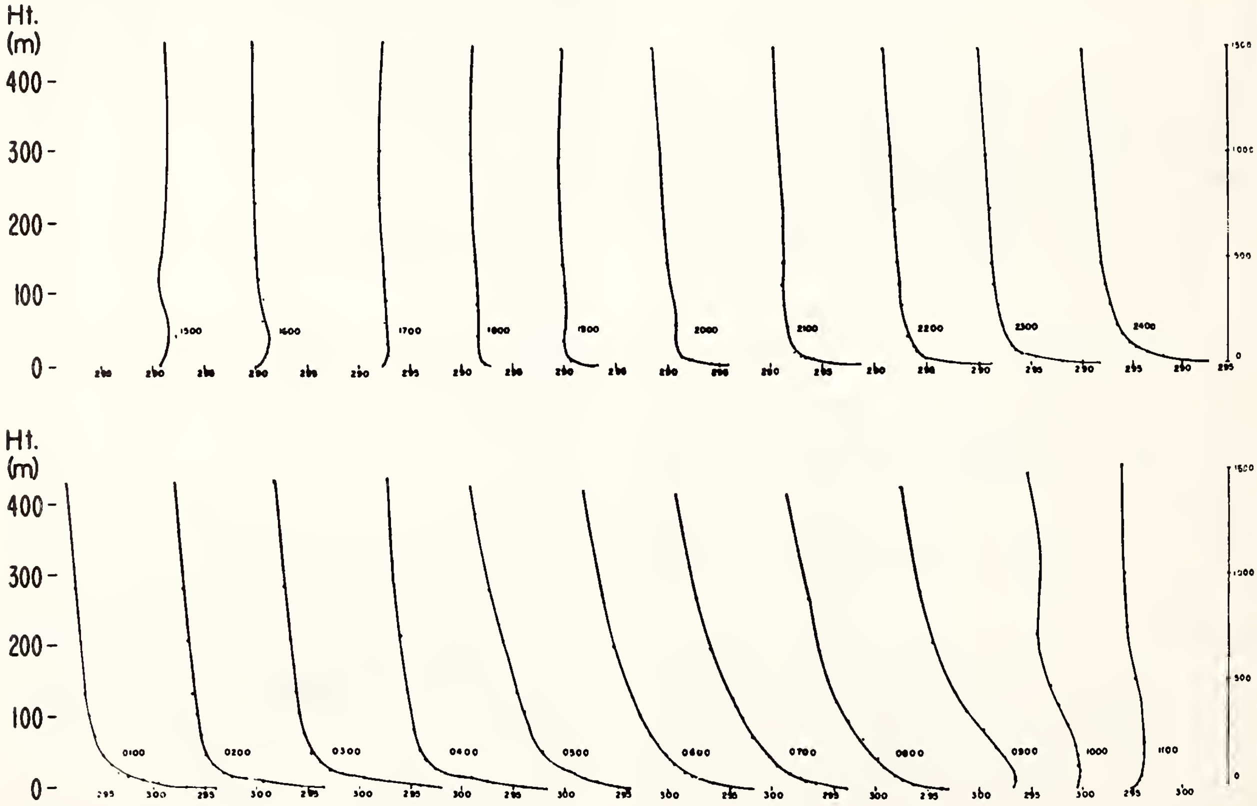

Fig. 7. Height distributions of potential refractive index measured near Sentinel, Arizona, using tower and captive balloon [adapted from *Rocco and Smyth,* 1949]. Sunset occurred at about 1900 LT. Should be compared with middle frame of Figure 6.

ing system performance. In the past, analytic solutions of (9) have provided numerical results in close agreement with observations except under conditions of relatively extreme stability.

When the boundary layer is temporally stationary ($\partial\phi/\partial t = 0$) and horizontally uniform with $w = 0$ (i.e., the advective terms are zero) the left-hand side of (9) is zero, and $K_z\ \partial\phi/\partial z$ is constant. This is the constant flux approximation that is usually valid near the ground. For a transition taking place in the x direction $\partial\phi/\partial x$ is no longer zero, although the x divergence of flux in the x direction $(\partial/\partial x)(K_x\partial\phi/\partial x)$ can still be considered negligible. Then

$$u\ \partial\phi/\partial x = (\partial/\partial z)[K(z)\ \partial\phi/\partial z] \qquad (10)$$

Using power-law distributions we find $K = (u_*^2/bm)z^{1-m}$. *Frost* [1946] dealt with the corresponding problem in moisture flux (evaporation) and found that the variable transformation to $\zeta = z^{2m+1}/ax(2m + 1)^2$ permitted straightforward solution of (10). The corresponding solution for $\partial\phi/\partial z$ may be used in (8) to obtain C_ϕ. The results are shown in Figure 4 for three offshore distances, and Figure 5 shows the corresponding duct thickness.

For a horizontally uniform boundary layer that is not in steady state, (9) reduces to

$$\partial\phi/\partial t = (\partial/\partial z)\ [K(z)\ \partial\phi/\partial z] \qquad (11)$$

There are simple solutions to this equation if K is assumed constant. Although this assumption is unrealistic, the resulting solution may be expected to reveal some of the qualitative features to be observed during diurnal cycles or other quasi-sinusoidal variations in temperature or humidity at Earth's surface. Data recorded at O'Neill, Nebraska, and Manor, Texas, were used to fit a trochoidal function to the temperature at $z \approx 0$ and at a few meters above the ground. A best average value of K was determined from the amplitude difference and phase lag at the two heights. The resulting distributions of ϕ, C_ϕ, and $M \approx \phi + 0.131z$ are shown in Figure 6. Although the model is crude, it shows features (such as the small C_ϕ values before sunrise) that are observed with acoustic and radar sounders. Height distribution of ϕ should be compared with observed distribution shown in Figure 7.

REFERENCES

Bean, B. R., and E. J. Dutton (1966), *Radio Meteorology*, sect. 6.3.3, *NBS Monogr. 92*, US Government Printing Office, Washington, DC.

Businger, J. A., J. C. Wyngaard, Y. Izumi, and E. F. Bradley (1971), Fluxprofile relationships in the atmospheric surface layer, *J. Atmos. Sci.*, *28*, 181–189.

Corrsin, S. (1951), On the spectrum of isotropic temperature fluctuations in an isotropic turbulence, *J. Appl. Phys.*, *22*, 417–423.

Frost, R. (1946), Turbulence and diffusion in the lower atmosphere, *Proc. Roy. Soc. London Ser. A.*, *186*, 20–35.

Lumley, J. A., and H. A. Panofsky (1964), *The Structure of Atmospheric Turbulence*, 239 pp., John Wiley, New York.

Ottersten, H. (1969), Atmospheric structure and radar backscattering in clear air, *Radio Sci.*, *4*, 1179–1193.

Rocco, M. D., and J. B. Smyth (1949), Diffraction of high-frequency radio waves around the earth, *Proc. IRE*, *37*, 1195–1203.

Wyngaard, J. C., Y. Izumi, and S. A. Collins, Jr. (1971), Behavior of the refractive-index-structure parameter near the ground, *J. Optical Soc. Amer.*, *61*, 1646–1650.

Radio Science, 13: 489-500, 1978.

The height distribution of refractive index structure parameter in an atmosphere being modified by spatial transition at its lower boundary

Earl E. Gossard

Wave Propagation Laboratory, Environmental Research Laboratories, National Oceanic and Atmospheric Administration, US Department of Commerce, Boulder, Colorado 80302

(Received June 13, 1977.)

An approximate method for solution of problems in turbulent diffusion is described and applied to radio wave propagation in the lower atmosphere for some boundary value problems not previously examined in the literature. The results of the approximate method are compared with results of a special case for which the diffusion equation can be solved exactly. The height distribution of the refractive index structure parameter and the thickness of the radio duct are calculated for air moving over a lower surface that (a) changes refractive index abruptly (e.g., a shoreline), (b) changes refractive index continuously, or (c) suddenly increases or decreases surface roughness.

INTRODUCTION

Recently, interest in radio refractive index distribution in the boundary layer has been renewed because of the development of radars capable of measuring clear-air backscatter from turbulent fluctuations in refractive index. Some types of radar, such as the frequency-modulated continuous wave radars, can observe atmospheric structure as close as 20 m from the antennas, with a spatial resolution of 1–2 m. More recently the addition of Doppler capability to these clear-air sounders [*Strauch et al.*, 1976; *Chadwick et al.*, 1976] has made them very useful new tools in the study of boundary layer processes. Both the scattering and the refractive properties of the boundary layer are related to the gradient with height of the refractive index, so this is the boundary-layer property with which this paper is mainly concerned. Specifically, it will focus on the way a mass of air is modified as it moves over an underlying surface whose properties undergo spatial transition (in temperature, moisture, or roughness). This paper uses an approximation which gives results similar to those of the diffusion equation in order to examine some changes in lower boundary not previously studied. The classical diffusion equation is, of course, itself an approximation. It neglects diffusion due to gradients of properties in horizontal planes compared with vertical diffusion and it employs the concept of an eddy coefficient which may or may not be a function of height. If sufficient money and time on high speed computers are available, one can solve this type of problem more rigorously. For example, various assumptions about relationships between higher-order terms in the kinetic and thermal energy balance equations can be made which lead to closure and numerical solution. These techniques have usually been applied to the development of the daytime convective boundary layer. For a few examples, see *Deardorff* [1974*a, b*], *Wyngaard and Coté* [1974], *Mellor and Yamada* [1974], *Zeman and Lumley* [1976], *Burk* [1977]. This approach has the advantage of minimal approximations in the solution and is valuable for research in atmospheric dynamics and kinematics, but it is costly in time delays and computer time. Depending on the model chosen from the hierarchy of closure models available, the computer time can be many tens of hours for each hour of real time studied, whereas solution of the classical diffusion equation gives quick and adequate results for many practical applications at little cost [*Slade*, 1968]. Furthermore, solutions of the diffusion equation can provide guidance in minimizing the cost of studies that use numerical methods by providing foreknowledge of the behavior to be expected. It is the purpose of this paper to point out and evaluate an approximate method for the solution in elementary functions of some diffusion problems not hitherto attacked in this way. It will then be used to deduce the change in the height distribution of the refractive

This article not subject to U.S. copyright. Published 1978 by the American Geophysical Union.

index structure parameter and the change in surface duct thickness as a mass of air undergoes modification by a spatially changing lower boundary.

Attention will be directed mainly toward boundary-layer effects on the propagation of radio waves, but the results are entirely applicable to optical systems as far as clear-air refraction and scintillation are concerned. The refractivity N is related to the true refractive index n such that $N = (n - 1) \times 10^6$. For radio waves,

$$N = (77.6/T)(p + 4810e/T) \tag{1}$$

and for optical waves

$$N \simeq 79\, p/T \tag{2}$$

where p is pressure in millibars, e is vapor pressure in millibars, and T is temperature in K [*Bean and Dutton,* 1966]. Thus the optical refractive index depends on temperature and pressure (and very weakly on humidity), whereas humidity is of primary importance in the radio refractive index.

In what follows, a quantity called potential refractive index is used whose symbol is ϕ [*Kerr,* 1951]. It is obtained from (1) or (2) by replacing temperature by potential temperature θ, vapor pressure by potential vapor pressure e_p, and pressure by 1000 millibars, where

$$\theta = T(1000/p)^{0.286} \tag{3}$$

and

$$e_p \simeq e(1000/p) \tag{4}$$

If profiles of θ and e_p have the same functional form, it can be shown [e.g., *Gossard and Anderson,* 1952] that ϕ must also have the same form to a very good order of approximation.

HORIZONTALLY UNIFORM BOUNDARY LAYER

It will be necessary to compare the approximate method with an exact solution of the diffusion equation for some hypothetical model in order to evaluate the validity of the approximation. Such exact solutions do not exist for logarithmic or log-linear profiles of properties, so it is convenient to adopt power-law profiles of wind and potential refractive index for this purpose. Therefore, it will first be demonstrated that the power-law profiles can provide a very adequate representation of real data and of the more theoretically acceptable results obtained using log-linear profiles. To do this a horizontally uniform boundary layer will first be analyzed, comparing expressions for C_ϕ^2 and duct thickness obtained using power-law profiles with experimental and theoretical results based on log-linear forms.

We first consider only temperature, because temperature data collected at Liberal, Kansas, have been analyzed for C_θ^2 by *Wyngaard et al.* [1971]. From dimensional considerations they concluded that

$$C_\theta^2 = k_0^2\, \theta_*^2\, z^{-2/3}\, g(z/L) \tag{5}$$

where z is height, $k_0\theta_* = z\,d\theta/dz$, k_0 is von Karman's constant, and L is the Monin-Obukov length that appears in the theory leading to log-linear boundary-layer profiles. From analysis of their data Wyngaard *et al.* find

$$g = 4.9\ [1 - 7(z/L)]^{-2/3},$$

unstable conditions $(z/L \leq 0)$

$$g = 4.9\ [1 + 2.75(z/L)],$$

stable conditions $(z/L \geq 0)$

The solid curves in the lower frame of Figure 1 are plots of C_θ vs. height from these relations.

In the presence of a capping inversion, *Frisch and Ochs* [1975] suggest that (5) be modified by a factor G which is a function only of the dimensionless quantity z/z_i where z_i is the height of the capping inversion. Using data collected by light aircraft off the coast of southern California, they find that

$$G(z/z_i) = 1.0 + 0.84\, z/z_i + 4.13\,(z/z_i)^2$$

$$\text{for} \quad 0 \leq z/z_i < 0.8 \tag{6}$$

The dashed curves in the lower frame of Figure 1 are the modified profiles using (6) assuming $z_i = 500$ m. We wish to compare these results with the predictions of a model that assumes power-law profiles. To do this a functional relationship between C_θ and the profile gradients must be found.

In the inertial subrange the spectrum of potential temperature is [*Corrsin,* 1951]:

$$E_\theta = a\varepsilon^{-1/3}\, \varepsilon_\theta\, k^{-5/3} \tag{7}$$

where ε is turbulent dissipation rate, ε_θ is one half the rate of destruction of temperature variance, k is wavenumber, and a is a constant. Alternatively

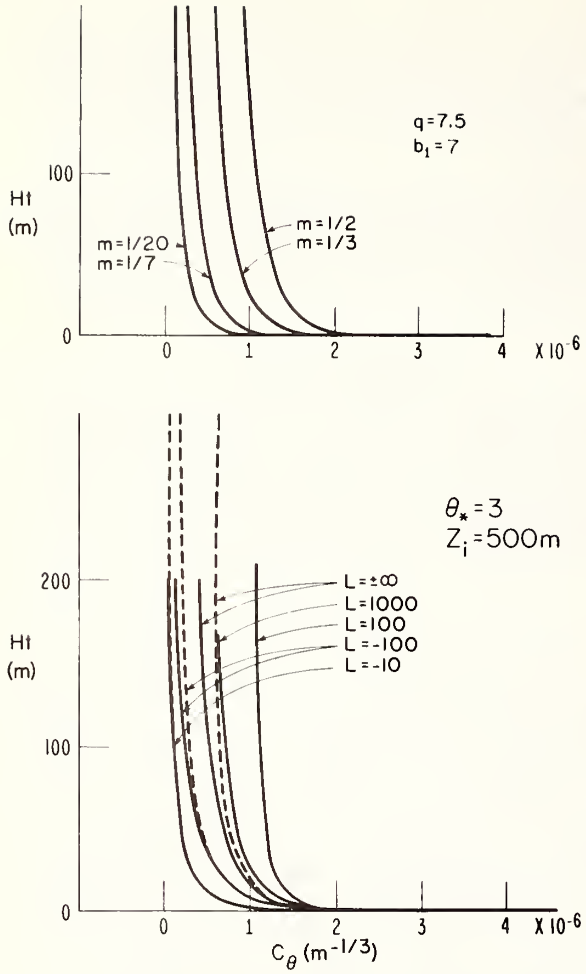

Fig. 1. Height profiles of temperature structure parameter in horizontally homogeneous atmosphere for various stabilities. Demonstrates that a power m can be chosen such that power-law profiles of parameters can provide a realistic representation of actual observations. Bottom: from measurements reported by *Wyngaard et al.* [1971] (solid curves), and modification of profiles suggested by *Frisch and Ochs* [1975] in the presence of a capping inversion (dashed curves). Top: structure parameter profiles calculated assuming power-law profiles of properties.

the turbulence can be described in terms of a structure function

$$D(l) = C_\theta^2 l^{2/3}$$

where l is air parcel separation and the structure parameter C_θ was given by *Ottersten* [1969] as

$$C_\theta^2 = 2.8\, \varepsilon^{-1/3} \varepsilon_\theta \qquad (8)$$

Wyngaard et al. [1971] found the constant "a" appearing in (7) to be 0.8 for the one-dimensional case; the constant in (8) is about four times this, which would imply a value of 3.2 instead of 2.8. In this paper a value of 3.2 will be used.

Assuming the turbulent regime to be in steady state, the kinetic energy balance equation in the regime of forced convection is approximately [*Lumley and Panofsky,* 1964]:

$$\varepsilon \simeq -\overline{u'w'}\,(\partial u/\partial z)(1 - R_f) \qquad (9)$$

where R_f is the flux Richardson number related to the gradient Richardson number Ri as follows:

$$(K_m/K_h)\, R_f = Ri = (g/\theta)(d\theta/dz)/(du/dz)^2$$

Primes denote deviations from the ambient (unprimed) quantity, overbars denote means, u and w are horizontal and vertical velocities, K_h and K_m are the eddy diffusion coefficients of heat and momentum respectively. Their ratio is usually thought to be near unity under neutral and stable conditions, and it will be so chosen in this paper. Use of the balance equations (9) and (10) is only valid for stable and near-neutral conditions and when the turbulence is both homogeneous and in steady state. These equations also neglect transport divergence of energy, higher-order fluxes, and pressure terms generally presumed to be small.

The corresponding balance equation for rate of destruction of temperature variance (actually $\overline{\theta'^2}/2$) is

$$\varepsilon_\theta \simeq -\overline{\theta' w'}\,\partial\theta/\partial z \qquad (10)$$

The vertical flux of horizontal momentum $\overline{u'w'}$ is given by

$$u_*^2 = -\overline{u'w'} = K_m\,\partial u/\partial z \qquad (11)$$

thus defining the so-called friction velocity u_*. The vertical heat flux is

$$-\overline{\theta' w'} = K_h\,\partial\theta/\partial z \qquad (12)$$

Substituting (9), (10), (11), and (12) into (8) (using the constant 3.2 instead of 2.8), it is found that

$$C_\theta = \sqrt{3.2}\,(K/u_*)^{2/3}(1 - Ri)^{-1/6}\,|\partial\theta/\partial z| \qquad (13)$$

Power-law profiles are now assumed for wind and potential temperature, that is,

$$u = \frac{u_r}{z_r^m} z^m \equiv u_* q z^m, \quad \theta - \theta_s = \frac{\theta_r - \theta_s}{z_r^m} z^m = b_1 z^m \qquad (14)$$

where the subscript r applies to some reference level at which measurements are made, s applies to the surface, and q is an arbitrary constant of proportionality. It follows that

$$du/dz = mu_{*}qz^{m-1}, \quad d\theta/dz = mb_1 z^{m-1}$$

and from (9) that

$$K/u_{*} = (1/qm)z^{1-m} \tag{15}$$

so

$$C_\theta = \sqrt{3.2}\, m^{1/3}\, b_1(q^{-2/3})(1 - Ri)^{-1/6}\, z^{(m-1)/3} \tag{16}$$

where $Ri = (g/\theta)(b_1/(u_*^2 q^2 m)\, z^{1-m}$. Equation (16) is used to plot the curves in the top frame of Figure 1, and it is seen that values of m can be found which agree very well with the results of Wyngaard *et al.* over a wide range of atmospheric stabilities. This is merely pointed out as a useful fact and is not intended to imply any fundamental physical merit to the power-law profile.

It is also revealing to compare the ducting properties of the power-law profile with those of the log-linear. In both the radio and the optical cases a ray launched horizontally will remain parallel with the earth's surface in a "standard" atmosphere if

$$d\phi/dz \simeq -0.131\ (m^{-1}) \tag{17}$$

so this can be considered one criterion for ducting.

If $\phi(z)$ is chosen to be log-linear, e.g.,

$$\phi - \phi_s = \phi_{*}\ [\ln(z/z_0) + \beta\, z/L] \tag{18}$$

it follows that the duct thickness

$$d = -[0.131/\phi_{*} + \beta/L]^{-1} \tag{19}$$

where $\phi_{*} = (\phi_r - \phi_s)[\ln(z_r/z_0) + \beta\, z_r/L]^{-1}$ and $\beta \simeq 4.7$ under near-neutral and stable conditions [*Businger et al.*, 1971].

If $\phi(z)$ is chosen to obey a power law, say

$$\phi - \phi_s = b\, z^m, \tag{20}$$

it follows that the duct thickness

$$d = -(0.131/mb)^{1/(m-1)} \tag{21}$$

where $b = (\phi_r - \phi_s)z_r^{-m}$. Equations (19) and (21) have been used to plot duct thickness against L and m in Figure 2. Again, it is readily seen that a value of m can be found that provides a remarkably good representation of the log-linear result for a chosen atmospheric stability. This statement is not intended to have fundamental physical implications, but it does imply that power-law models will provide a good representation of reality in the mathematically more complicated solutions of the diffusion equation which are the interest in this paper.

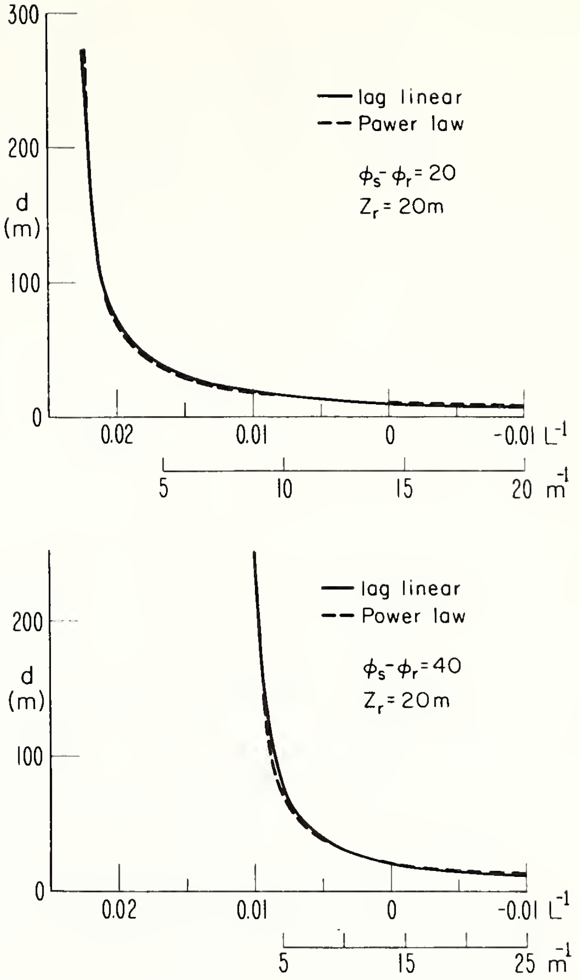

Fig. 2. Radio or optical duct thickness vs. atmospheric stability for two values of $\phi_s - \phi_r$. Shows that the power-law profile results are virtually exact duplicates of the log-linear results for linearly related m and l. A roughness $z_0 = 0.001$ cm was chosen.

PROPAGATION IN AN ATMOSPHERE UNDERGOING MODIFICATION

Diffusion equation method. The classical equation for two-dimensional, steady-state diffusion of a passive property away from (or toward) a plane lower boundary is

$$u\, \partial\phi/\partial x = (\partial/\partial z)[K(z)\, \partial\phi/\partial z] \tag{22}$$

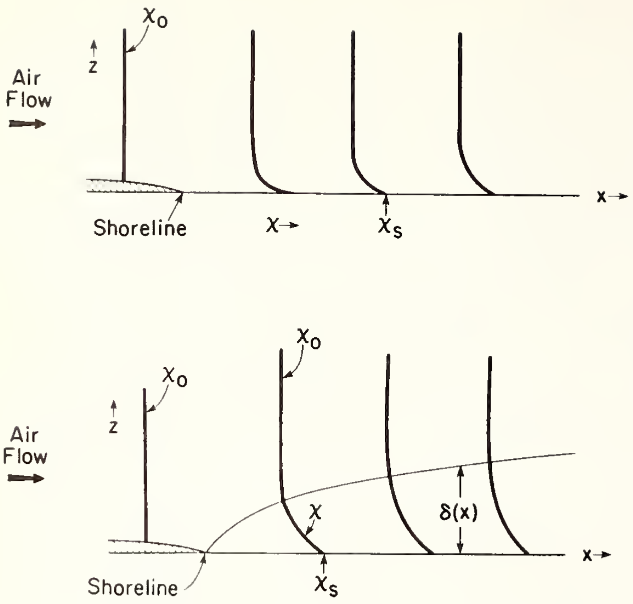

Fig. 3. Schematic picture of the change in the height distribution of some property χ as it is advected over a lower boundary whose properties differ from those prior to transition. Illustrates the case when $\chi_s \neq \chi_0$, where χ_0 is the profile of the property prior to transition; in this case χ_0 is constant.

where x is the horizontal direction of mean air flow and z is vertical. In its derivation horizontal variation of the gradient of ϕ in x is neglected compared with the vertical variation of the gradient in z. Furthermore, it depends on the fictitious concept of an "eddy" viscosity replacing the Reynolds stress terms in the basic equations. However, equations of this kind have provided a very adequate representation of diffusion in many practical applications without resort to numerical methods and high-speed computers, and it is our intention to use it as a basis for evaluating an approximate method for the prediction of propagation of radio and optical waves in transitional masses of air.

Suppose it is desired to compute the height distribution of refractive index structure parameter and radio duct thickness downwind of a transition in the lower boundary beyond which heat and/or moisture are flowing from the boundary into the air mass. The situation is illustrated schematically for any passive property χ in the top frame of Figure 3 where the flow is from land to water. Examples of this kind of modification have been published by *Craig* [1946] and are shown in Figure 4. The air trajectories are shown along with the profiles of potential temperature, vapor pressure, and refractive index.

For the moment the value of the properties at the sea surface will be assumed to be constant, independent of x after the transition (i.e., $\phi = \phi_s$), and a constant $\phi = \phi_0$ prior to transition ($x < 0$). Using (14) and (15), (22) gives

$$\partial\phi/\partial x = az^{-m}(\partial/\partial z)[x^{1-m}\,\partial\phi/\partial z] \tag{23}$$

where $a = (m\,q^2)^{-1}$.

Analyzing the flux of moisture from a water surface (evaporation), *Frost* [1946] found the solution of (23) to be

$$\chi - \chi_0 = \frac{\chi_s - \chi_0}{\Gamma[m/(2m+1)]}\int_{\zeta_0}^{\infty} \zeta^{-(m+1)/(2m+1)} \exp(-\zeta)\,d\zeta \tag{24}$$

where $\zeta = z^{2m+1}/ax(2m+1)^2$. For our purposes χ may be interpreted as ϕ. The integral is essentially the incomplete gamma function which is tabulated, but for duct thickness and refractive index structure parameter, it is the gradient of ϕ that matters. From (24) we find that

$$\frac{\partial\phi}{\partial z} = (\phi_0 - \phi_s)\frac{(2m+1)^{1/(2m+1)}}{\Gamma[m/(2m+1)]}\,\frac{z^{m+1}}{(ax)^{m/(2m+1)}} \cdot \exp[-z^{2m+1}(ax)^{-1}(2m+1)^2] \tag{25}$$

If d is duct thickness, d^{2m+1}/ax is small for appreciably large x and the exponential tends to unity, so

$$d \simeq \left[\frac{0.131\Gamma[m/(1+m)](2m+1)^{-1/(2m+1)}}{(\phi_s - \phi_0)} \cdot (ax)^{m/(2m+1)}\right]^{1/(m-1)} \tag{26}$$

Noting that the factor containing *Ri* is near unity for a reasonable range of *Ri* ($-0.5 < Ri < 0.2$) because of the small negative power ($-1/6$) to which it is raised, (13) gives

$$C_\phi \simeq \sqrt{3.2}\,\{(\phi_s - \phi_0)(m\,q)^{-2/3}(2m+1)^{1/(2m+1)} \cdot (ax)^{-m/(2m+1)} z^{(m-1)/3}/\Gamma[m/(2m+1)]\}\exp[-z^{2m+1} \div ax(2m+1)^2] \tag{27}$$

These results will now be compared with the results from an approximate method to evaluate its validity.

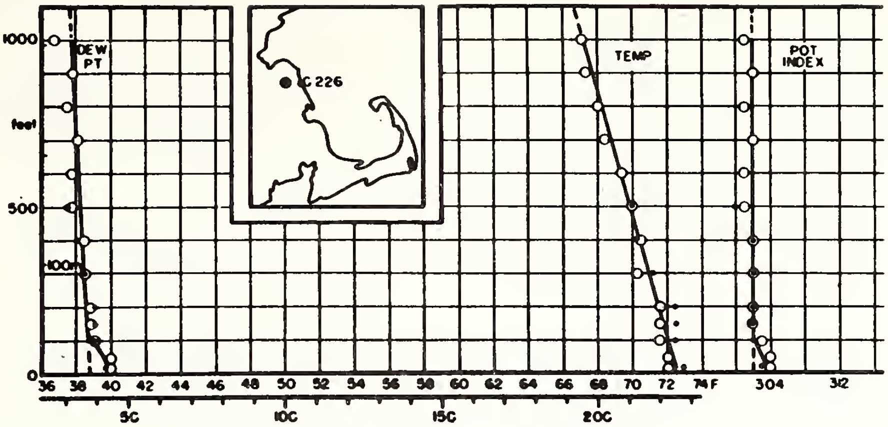

70°50'W, 42°10'N (over land); 18 October 1944; o ascent 14^h35^m 14^h47^m, • ascent 14^h49^m 14^h54^m; wind 230° 18 mph at 1000 ft, SW 10 mph at surface.

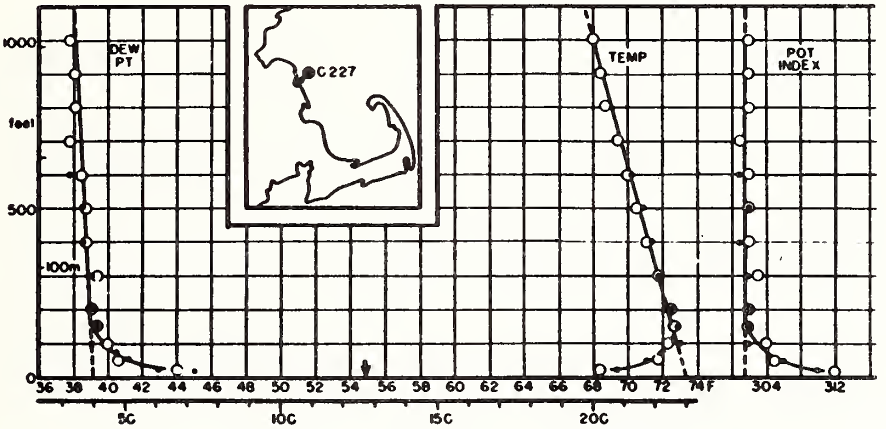

70°40'W, 42°13'N; 18 October 1944; o ascent 15^h05^m–15^h15^m, • ascent 15^h20^m 15^h26^m; (direction not observed) at surface (WSW 10 mph at South Weymouth); 1000-ft trajectory wind 230° 18 mph at 1000 ft, 4 mi, ¼ hr, from Scituate.

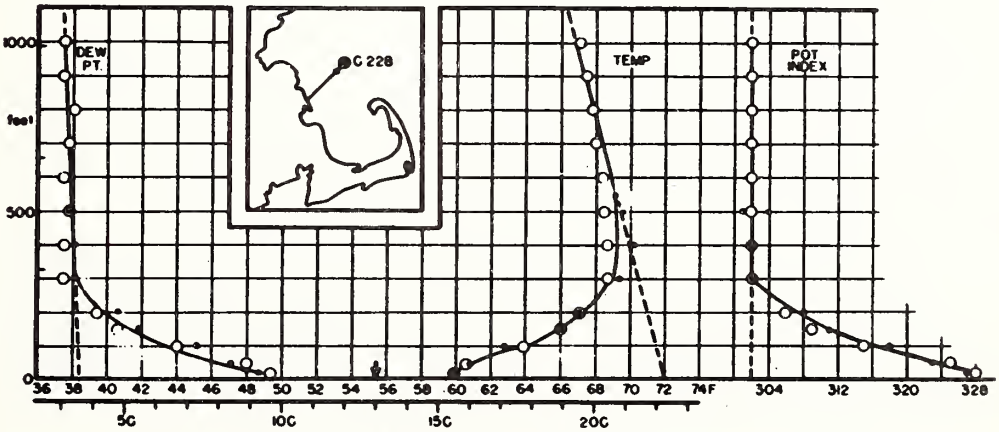

70°25'W, 42°17'N; 18 October 1944; o ascent 15^h53^m 16^h03^m, • ascent 16^h05^m 16^h10^m; wind 230° 20 mph at 1000 ft, S 3B at surface; 1000-ft trajectory 19 mi, 1 hr, from Marshfield.

Fig. 4. Observed modification of potential refractive index height distribution (right-hand curve) as a homogeneous air mass moves offshore of Buzzard's Bay, Massachusetts [*Craig*, 1946].

Flux integral method. This method is valuable because it allows great flexibility in the class of physical problems that can be solved. It was first used by von Karman to obtain the velocity distribution in unstratified flow downwind of the leading edge of a flat plate in a wind tunnel. Although well known in aerodynamics, it has received little attention in geophysics and no use in radio propagation problems.

von Karman constructed the so-called momentum integral

$$D(x) = \rho \int_0^{\delta(x)} u\,(u_\delta - u)\,\mathrm{d}z$$

where $D(x)$ is the total drag on the plate per unit width, δ is the depth of the boundary layer above the flat plate and u_δ is the velocity of the flow outside the boundary layer (assumed to be constant both for $x < 0$ and $z > \delta$). The derivative of D with downwind distance x was then equated to the momentum flux per unit area toward the plate, assuming the flux to be independent of height for $z < \delta$ and zero above δ.

The approach can be generalized for any passive quantity, i.e.,

$$M(x) = \int_0^{\delta(x)} u\,(\chi - \chi_0)\,\mathrm{d}z \tag{28}$$

where χ may be momentum density (ρu), water vapor density (ρs where s is specific humidity), heat energy density ($\rho\, c_p\, \theta$ where c_p is specific heat at constant pressure), or $\rho\phi$ where $\rho\phi$ is without physical interpretation. $M(x)$ is the total flux from a strip of unit width, so d $M(x) = F(x)$ dx where F is the vertical flux per unit area of momentum, water vapor, or heat respectively. For ϕ there is no comparable interpretation, but F then has dimensions of mass flux.

Analogous to (12),

$$F = -K(z)\,\partial\phi/\partial z \tag{29}$$

where the sign has been chosen so that flux is upward when ϕ decreases with height. If power laws are assumed, (11) and (29) give

$$F = -(u_*/qm)\, z^{1-m}\, \partial\phi/\partial z \tag{30}$$

The height distribution of ϕ can be written in the form

$$\phi - \phi_s = (\phi_0 - \phi_s)(z/\delta)^m \tag{31}$$

because $\phi = \phi_\delta = \phi_0$ for $x < 0$ or $z > \delta$; therefore

$$F(x) = (u_*/q)(\phi_s - \phi_0)\,\delta(x)^{-m} \tag{32}$$

Case when ϕ_s and ϕ_0 are constant—Model A. Then (28) gives

$$F(x) = \partial M(x)/\partial x = u_*\, q(\partial/\partial x)(\phi_s - \phi_0) \int_0^{\delta(x)} z^m \left[1 - \left(\frac{z}{\delta}\right)^m\right] \mathrm{d}z \tag{33}$$

$$= (u_*/q)(\phi_s - \phi_0)\,\delta^{-m}$$

and it is readily found that

$$\delta = [(q^2 m)^{-1}\,(2m + 1)^2 x]^{1/(2m+1)} \tag{34}$$

Substituting δ into (31),

$$\frac{\partial\phi}{\partial z} = (\phi_0 - \phi_s)(2m + 1)^{-2m/(2m+1)} \frac{mz^{m-1}}{(ax)^{m/(2m+1)}} \tag{35}$$

where $a = (q^2 m)^{-1}$. Ignoring the exponential factor in (25) (which is essentially unity for appreciable x) it is seen that (35) is identical to (25) except that the factor $(2m + 1)/\Gamma[m/(2m + 1)]$ has been replaced by m. The two factors are compared in Table 1 over the probable range of m. It is apparent that the approximation involved in the use of (28) and (29) is satisfactory.

From (35) and (17) the duct thickness is readily found to be

$$d = \left[\frac{0.131}{\phi_s - \phi_0} \frac{(2m + 1)^{2m/(2m+1)}}{m} (ax)^{m/(2m+1)}\right]^{1/(m-1)} \tag{36}$$

and from (13) (assuming $(1 - Ri)^{-1/6} \simeq 1$ as before),

$$C_\phi \simeq \sqrt{3.2}\,(\phi_s - \phi_0)(mq)^{-2/3}(2m + 1)^{-2m/(2m+1)} \cdot m(ax)^{-m/(2m+1)}\, z^{(m-1)/3} \tag{37}$$

Equations (36) and (37) differ from (26) and (27) only in that the factor $(2m + 1)/\Gamma[m/(2m + 1)]$ has been replaced by m. A plot of the boundary layer thickness $\delta(x)$ is shown as curve A in Figure 5, and a plot of duct thickness is shown as curve

TABLE 1. Comparison of $(2m + 1)/\Gamma[m/(2m + 1)]$ with m.

m	$(2m + 1)/\Gamma[m/(2m + 1)]$	m
1/7	0.15	0.147
1/5	0.20	0.200
1/2	0.55	0.500

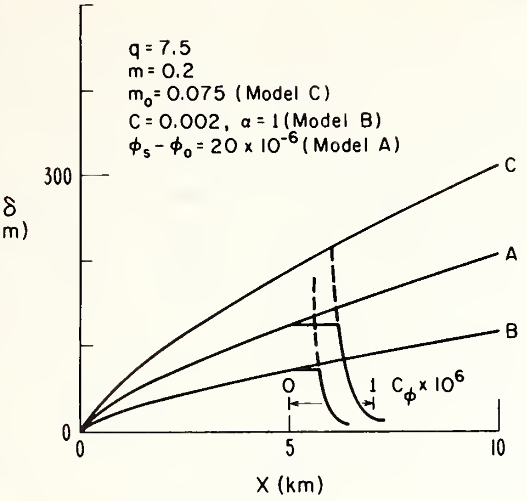

Fig. 5. Increase in depth of boundary layer δ with distance x from transition for Models A, B, and C and the conditions indicated in legend. Profiles of C_ϕ at a distance of 5 km downwind of transition are also shown. C_ϕ artificially drops to zero above δ because of the assumption in this approximation that $F = 0$ above δ, i.e., $\partial\phi/\partial z = 0$ for $z > \delta$. Actually it continues to decrease as $z^{(m-1)/3}$ in accord with (37) shown by the dashed curves.

A in Figure 6. The profile of C_ϕ 5 km from transition is also shown in Figure 5. The value of C_ϕ artificially drops to zero at the height δ because in this approximation $\partial\phi/\partial z = 0$ for $z > \delta$. Of course it actually continues to decrease as $z^{(m-1)/3}$ in accord with (37). We now proceed to use the approximate method to solve some problems that are otherwise intractable.

Case in which ϕ_s depends on x—Model B. Imagine a mass of air moving out of its source region over a surface that becomes progressively warmer (or colder) and/or moister (or dryer). For convenience assume that

$$\phi_s - \phi_0 = cx^\alpha \tag{38}$$

where $\phi_s = \phi_0$ at $x = 0$ in the source region. Returning to (33), it is no longer possible to take $\phi_s - \phi_0$ outside the differentiation sign, and we find

$$(m+1)\delta^{2m}\frac{\partial\delta}{\partial x} + \alpha x^{-1}\delta^{2m+1} - \frac{(m+1)(2m+1)}{m}q^{-2} = 0 \tag{39}$$

The variables x and δ are no longer separable, but $\delta^{2m+1} = Bx$ is again a solution where B is a constant of proportionality to be determined. Substituting into (39) we find

$$\frac{m+1}{2m+1}\delta^{2m+1} + B\alpha x - \frac{(m+1)(2m+1)}{m}q^{-2}x = 0$$

whence it follows that

$$B = \frac{(m+1)(2m+1)^2 q^{-2}}{m\,[m+1+\alpha(2m+1)]} \equiv \frac{a(2m+1)^2(m+1)}{\alpha(1+2m)+1+m} \tag{40}$$

where $a = (q^2 m)^{-1}$. Substituting for $\phi_0 - \phi_s$ in (31) using (38) and for δ using $\delta = (Bx)^{1/(2m+1)}$, we find

$$\phi - \phi_s = -cx^\alpha (Bx)^{-m/(2m+1)} z^m \tag{41}$$

When $\alpha = 0$, the problem is that solved previously, i.e., $c = \phi_s - \phi_0 =$ constant, and $B = a(2m + 1)^2$ yielding (34) and (35).

Obtaining $\partial\phi/\partial z$ from (41), the radio duct thickness is found to be

$$d = [0.131\,(mc)^{-1} B^{m/(2m+1)} x^{-\alpha+m/(2m+1)}]^{1/(m-1)} \tag{42}$$

and the structure parameter

$$C_\phi = \sqrt{3.2}\,(mq)^{-2/3}(cmx^\alpha)(Bx)^{-m/(2m+1)} z^{(m-1)/3} \tag{43}$$

A plot of $\delta(x)$ from (38) is shown as curve B in Figure 5 and a plot of duct thickness is shown as curve B in Figure 6 for the assumptions indicated in the caption. Plots of C_ϕ vs. height are shown in Figure 5.

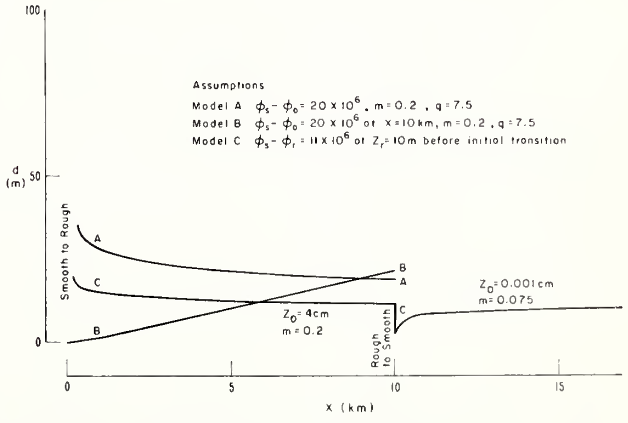

Fig. 6. Change in radio or optical duct thickness with distance x from transition for Models A, B, and C for conditions indicated in legend. The transitions in surface roughness apply to Model C only.

Case when there is a transition in surface roughness—Model C. In the power-law representation, m is influenced by surface roughness as well as atmospheric stability. If a power-law profile is fitted to a log-linear at appropriate heights for the physical problem of interest (e.g., 20 and 2 meters), m and q can be readily calculated by a variety of methods, and realistic profiles before and after transition in surface roughness can be easily deduced (see appendix A).

Now suppose the profiles of wind and potential refractive index u_0, ϕ_0 before transition and u, ϕ after transition are given by

$$\begin{aligned} u_0 &= u_{*_0} q_0 z^{m_0}, & \phi_0 - \phi_s &= b_0 z^{m_0}, \\ u &= u_* q z^m, & \phi - \phi_s &= b z^m \end{aligned} \tag{44}$$

Thus u_*, u and ϕ, ϕ_* depend on x. Noting that $u = u_0$ and $\phi = \phi_0$ at $z = \delta$, (29) gives

$$F = u_* b/q = (b_0 u_{*_0} q_0/q^2)\delta^{2(m_0-m)} \tag{45}$$

and from (28),

$$F = \frac{dM(x)}{dx} = b_0 u_{*_0} q_0 \left(\frac{1}{2m+1} - \frac{1}{m+m_0+1}\right) \cdot (d/dx)(\delta^{2m_0+1})$$

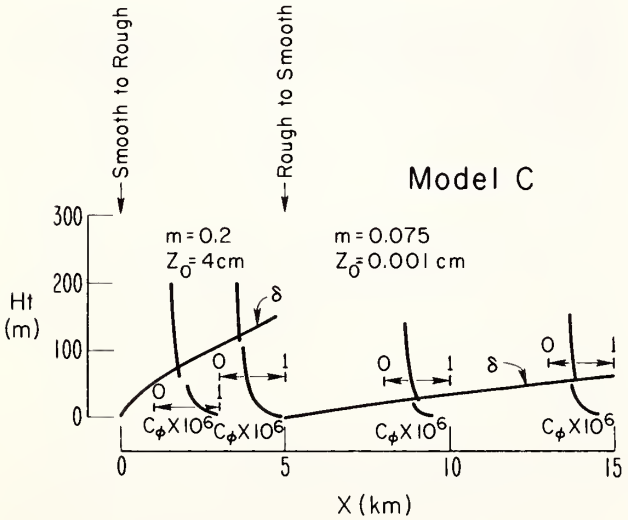

Fig. 7. Increase in depth of boundary layer δ with distance x downwind of transitions in surface roughness z_0. Profiles of C_ϕ are plotted at x = 1, 3, 8, 13 km. The discontinuities in C_ϕ at the height δ are artificial, resulting from the discontinuity in flux which is assumed to occur at δ in this approximation. Actually, the discontinuity would of course be smoothed.

whence

$$\delta = (Bx)^{1/(2m+1)} \tag{46}$$

where

$$B = q^{-2}(2m+1)^2(m+m_0+1)/(m_0-m)(2m_0+1)$$

When the transition is from a relatively rough to a relatively smooth surface, appendix A shows that $m_0 > m$. When it is from smooth to rough, $m > m_0$.

Using (17), (44), and (46), the duct thickness is found to be

$$d \simeq [-0.131(b_0 m)^{-1}(Bx)^{(m-m_0)/(2m+1)}]^{1/(m-1)} \tag{47}$$

and from (13), (44), and (46),

$$C_\phi \simeq -\sqrt{3.2}\,(qm)^{-2/3} b_0 m (Bx)^{(m_0-m)/(2m+1)} z^{(m-1)} \tag{48}$$

where $b_0 = (\phi_{0r} - \phi_s) z_r^{-m_0}$ and z_r is some reference height. The factor $(1 - Ri)^{-1/6} \simeq 1$ for reasonably small Ri ($-0.5 < Ri < 0.2$). Plots of boundary layer thickness $\delta(x)$ for transition from a smooth to a rough surface are shown in Figure 7 and the corresponding duct thickness is shown as curve C in Figure 6. The height distribution of C_ϕ is shown in Figure 7, superimposed on the boundary layer depth, for transitions from smooth to rough and rough to smooth boundaries. Only roughness is presumed to change; surface refractive index is continuous.

In the derivation of (47) and (48) it was assumed that the initial profile of ϕ was only altered by the change in roughness of the lower boundary; whereas in the derivation of (36) and (37) surface roughness was assumed to remain unchanged at a transition of ϕ_s. In that case duct thickness *decreased* with distance after transition. However, for a change in roughness, (47) shows that duct thickness may either increase or decrease with x, depending on whether the transition is from rough to smooth ($m_0 > m$) or from smooth to rough ($m_0 < m$). Thus intuition is not a reliable guide in this kind of problem.

We note in passing that the relative evaporation between rough and "slick" portions of a banded water surface can be examined by substituting (46) into (45) and letting $b_0 = (e_{pr} - e_{p0}) z_r^{-m}$.

Case when profiles are assumed to be logarithmic. This is the case for which (28) has found considerable application in aerodynamics. The fluid is then assumed to be neutral, and the distribution of momentum downwind of the leading edge of a flat plate or airfoil is typically examined. Here we use the method to examine the distribution of refractive index when the profiles of wind and refractive index are logarithmic rather than power-law.

We choose ϕ_0 constant and assume ϕ to be of the form

$$\phi - \phi_s = (\phi_\delta - \phi_s)[\ln(z/z_0)]/[\ln(\delta/z_0)] \qquad (49)$$

where z_0 is a small length characterizing the roughness of the surface. We further assume that

$$u = (u./k_0)\ln(z/z_0)$$

where $k_0 \simeq 0.4$ is von Karman's constant. Then

$$K = u.^2/(\partial u/\partial z) = k_0 u.\, z \qquad (50)$$

From (29),

$$F = -K\,\partial\phi/\partial z = -k_0 u.\,(\phi_\delta - \phi_s)/\ln(\delta/z_0) \qquad (51)$$

Returning now to (28) and noting that $\phi_\delta = \phi_0$ = constant, we find

$$F = \partial M(x)/\partial x = (u.\, z_0/k_0)(\phi_\delta - \phi_s)$$
$$\cdot \frac{\partial}{\partial x}\int_1^{\delta/z_0} \ln(z/z_0)\left(1 - \frac{\ln(z/z_0)}{\ln(\delta/z_0)}\right) d(z/z_0)$$
$$= -k_0 u.\,(\phi_\delta - \phi_s)/\ln(\delta/z_0)$$

Integration leads to the equality

$$(u.\, z_0/k_0)(\phi_s - \phi_\delta)(\partial/\partial x)[\delta/z_0 + 1 - (2\delta/z_0)/\ln(\delta/z_0)$$
$$+ 2/\ln(\delta/z_0)] = k_0 u.\,(\phi_s - \phi_\delta)/\ln(\delta/z_0)$$

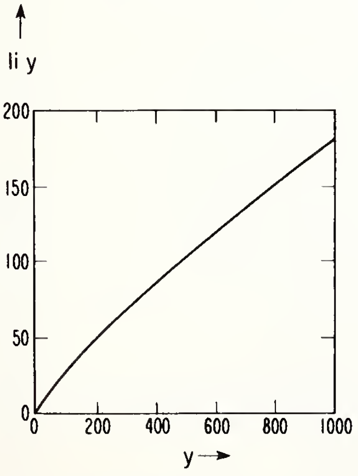

Fig. 8. Plot of logarithmic integral, li y.

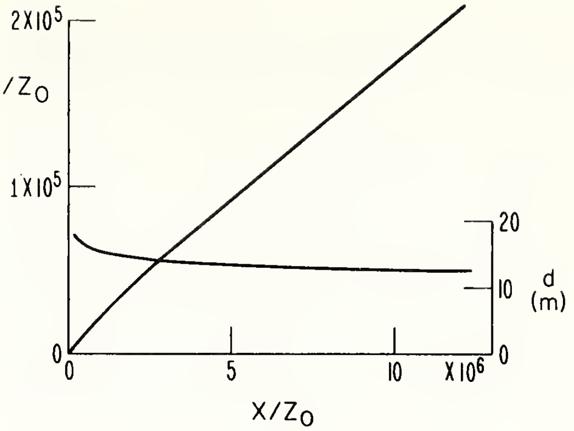

Fig. 9. Change in depth of boundary layer δ and duct thickness d with distance x downwind of a transition in surface value of ϕ, assuming logarithmic profiles of properties.

and differentiation with x gives the equality

$$\int \ln(\delta/z_0)\, d(\delta/z_0) - 2\int d(\delta/z_0) + 2\int d(\delta/z_0)/\ln(\delta/z_0)$$
$$- 2\int d(\delta/z_0)/(\delta/z_0)\ln(\delta/z_0) = (k_0^2/z_0)x$$

which integrates to

$$k_0^2\frac{x}{z_0} = \frac{\delta}{z_0}\ln\frac{\delta}{z_0} - 3\frac{\delta}{z_0} + 3 + 2\ln\frac{\delta}{z_0}$$
$$+ 2\frac{\ln(\delta/z_0)}{2.2!} + 2\frac{\ln(\delta/z_0)}{3.3!}\ldots \qquad (52)$$

so

$$k_0^2\frac{x}{z_0} = \frac{\delta}{z_0}\ln\frac{\delta}{z_0} - 3\frac{\delta}{z_0} + 3 + 2\,\mathrm{li}\frac{\delta}{z_0}$$
$$- 2\gamma - 2\ln[\ln(\delta/z_0)] \qquad (53)$$

where $\gamma = 0.5772$ is Euler's constant and li is the logarithmic integral shown in Figure 8. In writing the above equality, the identity

$$\int\frac{dy}{\ln y} = \ln(\ln y) + \ln y + \frac{\ln y}{2\cdot 2!} + \frac{\ln y}{3\cdot 3!}\ldots = \mathrm{li}\,y - \gamma$$

has been used.

As before, to obtain the duct height, d, we take the height derivative of (49) and solve for the height at which $d\phi/dz = -0.131$, we find

$$d = (1/0.131)(\phi_s - \phi_0)/\ln(\delta/z_0) \qquad (54)$$

where δ/z_0 can be found from (53) for a given

x. Of course (53) cannot be solved explicitly for δ as in the earlier models, but it is explicit in x and can easily be plotted. It is shown in Figure 9.

Similarly, from (13) and (49),

$$C_\phi \simeq \sqrt{3.2}\, k_0^{2/3} (\phi_s - \phi_0) [\ln(\delta / z_0)]^{-1} z^{-1/3} \tag{55}$$

where δ / z_0 is again found from (53). In this approximation $(1 - Ri)^{1/6} \simeq 1.0$ for reasonably small values of Ri. The plot of duct thickness vs. distance off shore is shown as curve D in Figure 9 assuming $z_0 = 0.001$ cm—a typical value for water surfaces. Comparing Figure 9 and Figures 5 and 6 it is readily seen that the behavior of boundary layer thickness and duct thickness is very similar for logarithmic profiles and power-law profiles if a power of 1/10 is chosen as the power-law index under neutral stability conditions. This is in agreement with the comparisons of duct thickness for power-law and log-linear profiles shown in Figure 2.

CONCLUSIONS

The cases studied in this paper demonstrate the value of the proposed approximate method for investigating boundary transitions and boundary-layer wind profiles hitherto considered to be analytically intractable.

APPENDIX A

If some kind of log-linear profile is assumed to be most representative of real boundary layers, it is desirable to fit power-law profiles to it in some objective manner because changes in both atmospheric stability and surface roughness are reflected in the power m. In much of this paper, values of $m = 0.2$ and $q = 7.5$ were chosen for illustration as being generally representative of real atmospheric stability and surface roughness conditions. However, when discussing transitions in surface roughness it becomes necessary to define a specific method for deducing profile parameters (see (14)).

The following procedure is suggested. If two suitable heights z_1 and z_2 are chosen at which the profiles are to match,

$$\frac{\ln(z_1/z_0) + \beta\, z/L}{\ln(z_2/z_0) + \beta\, z/L} = \left(\frac{z_1}{z_2}\right)^m \tag{A1}$$

where z_0 is a small length representative of surface roughness, β is a universal constant $\simeq 4.7$ under stable conditions, $\simeq 3$ under neutral and slightly unstable conditions [*Businger et al.*, 1971], and L is the Monin-Obukov length representative of atmospheric stability—positive under stable conditions and negative under unstable conditions. First select L to represent the stability conditions of interest and z_0 to represent the appropriate roughness (see Table 2). The profile index m is then readily found.

Next note that for some height at which the profiles are to match,

$$u_1 = \frac{u_*}{k_0}\left(\ln \frac{z_2}{z_0} + \beta \frac{z_2}{L}\right) = u_*\, q\, z_2^m$$

where $k_0 \simeq 0.4$ is von Karman's constant. In general, u_* will depend on x, but it can be cancelled from both sides of the equation so

$$q = \frac{1}{k_0}\left(\ln \frac{z_2}{z_0} + \beta \frac{z_2}{L}\right) z_2^{-m} \tag{A2}$$

at one of the heights previously chosen.

For the plot in Figure 7, neutral conditions were chosen so $L = \infty$. A transition between grassland and water was assumed, so values of $z_0 = 4$ and 0.001 cm respectively were chosen. For profiles fitting at heights of 2 and 20 meters this leads to profile indices of 0.2 and 0.075 respectively. Equation (A2) then yields corresponding values of $q = 8.5$ and 29 respectively if z_2 is chosen to be 20 meters. The values of m and q are both reversed

TABLE 2. Roughness parameter for various typical surfaces.

Surface	z_0 (cm)
Sea surface	0.001
Mud flats, smooth ice	0.001
Sun-baked sandy alluvium (level desert, India)	0.03
Sand	0.04–0.06
Lawn (1 cm grass length)	0.10
Lawn (1.5 cm grass length)	0.20
Natural snow surface	0.20–0.50
Lawn (3 cm grass length)	0.60–0.80
Lawn (5 cm grass length)	1.0–2.0
Downland (winter)	1.0–2.0
Fallow land	2.0–3.0
Russian steppe	2.0–3.0
Downland (summer)	2.0–4.0
Open grass land	3.0–4.0
Long grass (60–70 cm length)	4.0–9.0
Wheat field	4.5
Turnip field	6.5
Fully grown root crops	14.0

if the flow is from smooth-to-rough instead of rough-to-smooth.

Other methods of fitting the power-law profiles to the log-linear also suggest themselves. One method especially appropriate to ducting problems would be to solve for the "best fit" of curves of m^{-1} vs. height to curves of L^{-1} vs. height, as shown in Figure 2 to obtain m for a given atmospheric stability and roughness (L and z_0).

REFERENCES

Bean, B. R., and E. J. Dutton (1966), *Radio Meteorology, Nat. Bur. Stand. Monogr. 92*, 423 pp., US Government Printing Office, Washington, DC.

Burk, S. D. (1977), The moist boundary layer with a higher-order turbulence closure model, *J. Atmos. Sci., 34*, 629–638.

Businger, J. A., J. C. Wyngaard, Y. Izumi, and E. F. Bradley (1971), Flux-profile relationships in the atmospheric surface layer, *J. Atmos. Sci.*, *28*, 181–189.

Chadwick, R. B., K. P. Moran, R. G. Strauch, G. E. Morrison, and W. C. Campbell (1976), Microwave radar wind measurements in the clear air, *Radio Sci.*, *11*, 795–802.

Corrsin, S. (1951), On the spectrum of isotropic temperature fluctuations in an isotropic turbulence, *J. Appl. Phys.*, *22*, 417–423.

Craig, R. A. (1946), Measurements of temperature and humidity in the lowest 1000 feet of the atmosphere over Massachusetts Bay, *Papers in Physical Oceanography and Meteorology*, Vol. 10, No. 1, Massachusetts Institute of Technology and Woods Hole Oceanographic Institution, Cambridge, Massachusetts.

Deardorff, J. W. (1974*a*), Three-dimensional numerical study of the height and mean structure of a heated planetary boundary layer, *Bound-layer Meteorol.*, *7*, 81–106.

Deardorff, J. W. (1974*b*), Three-dimensional numerical study of turbulence in an entraining mixed layer, *Bound-layer Meteorol.*, *7*, 199–226.

Frisch, A. S., and G. R. Ochs (1975), A note on the behavior of the temperature structure parameter in a convective layer capped by a marine inversion, *J. Appl. Meteorol.*, *14*, 415–419.

Frost, R. (1946), Turbulence and diffusion in the lower atmosphere, *Proc. Roy. Soc. London*, *186*, 20–35.

Gossard, E. E., and L. J. Anderson (1952), The oceanic duct and its effect on microwave propagation, *Rep. 305*, Navy Electronics Laboratory, San Diego, California.

Kerr, D. E. (Ed.) (1951), *Propagation of Short Radio Waves*, 706 pp., Dover, New York.

Lumley, J. L., and Hans A. Panofsky (1964), *The Structure of Atmospheric Turbulence*, Vol. XII, 222 pp., Interscience, New York.

Mellor, G. L., and T. Yamada (1974), A hierarchy of turbulence closure models for planetary boundary layers, *J. Atmos. Sci.*, *31*, 1791–1806.

Ottersten, H. (1969), Atmospheric structure and radar backscattering in clear air, *Radio Sci.*, *4*, 1179–1193.

Slade, D. H. (Ed.) (1968), *Meteorology and Atomic Energy*, US Atomic Energy Commission, Office of Information Services, Washington, DC.

Strauch, R. G., W. C. Campbell, R. B. Chadwick, and K. P. Moran (1976), Microwave FM-CW Doppler radar for boundary-layer probing, *Geophys. Rev. Lett.*, *3*, 193–196.

Wyngaard, J. C., and O. R. Coté (1974), The evolution of the convective planetary boundary layer—A higher-order closure model study, *Bound-layer Meteorol.*, *7*, 289–308.

Wyngaard, J. C., Y. Izumi, and S. A. Collins, Jr. (1971), Behavior of the refractive-index-structure parameter near the ground, *J. Opt. Soc. Amer.*, *61*, 1646–1650.

Zeman, O., and J. L. Lumley (1976), Modeling buoyancy driven mixed layers, *J. Atmos. Sci.*, *33*, 1974–1988.

Radio Science, 13: 953-961, 1978.

Spectra of fluctuations in refractivity, temperature, humidity, and the temperature-humidity cospectrum in the inertial and dissipation ranges

R J. Hill

Wave Propagation Laboratory, Environmental Research Laboratories, National Oceanic and Atmospheric Administration,
Boulder, Colorado 80302

(Received October 26, 1977.)

Recent theoretical and experimental advances have produced a model of the power spectrum of quantities mixed by turbulence. This model is applicable for arbitrary diffusivity and is thereby capable of predicting the high wavenumber shape of the spectra of refractivity, temperature, humidity, and the temperature-humidity cospectrum. Equations for the mean refractivity and the refractivity variance are formed from temperature, pressure, and humidity fluctuations; the accuracy of neglecting the higher-order terms in the fluctuations is determined. In order to apply the model power spectrum for temperature and humidity fluctuations in the atmosphere, it is first determined under what conditions temperature and humidity satisfy a simple continuity equation that balances temporal changes, advection, and diffusion. Experiments have shown that the temperature spectrum in air has a "bump" at high wave numbers. This feature is understood in terms of the theoretical model, and the bump is predicted to appear in the refractivity and humidity spectra and in the temperature-humidity cospectrum as well as in the temperature spectrum. The bump in the humidity spectrum is smaller than that in the temperature-humidity cospectrum, which is in turn smaller than the bump in the temperature spectrum; this effect is caused by the fact that the diffusivity of water vapor in air is slightly greater than that of heat in air. The shape of the refractivity spectrum depends on the relative contributions of the temperature spectrum, humidity spectrum, and temperature-humidity cospectrum. The refractivity spectrum can have an enhanced bump if the contribution of the temperature-humidity cospectrum is negative and nearly cancels the contributions of the temperature and humidity spectra. The impact of these developments on radio wave propagation is discussed.

1. INTRODUCTION

Knowledge of the spatial power spectrum of refractivity fluctuations is necessary for understanding the scattering and propagation of electromagnetic waves in turbulent media. The spectrum of temperature fluctuations in the atmospheric surface layer has been accurately measured at inertial range and larger wave numbers by *Champagne et al.* [1977] and by *Williams and Paulson* [1977]. Their measurements reveal that there is a "bump" in the temperature spectrum at high wavenumbers. The theoretical models of scalar spectra developed by *Hill* [1978] give the interpretation that this bump is a tendency to a viscous-convective range at wavenumbers lower than those wavenumbers at which the diffusion of heat causes the spectrum to decrease rapidly. These models of the scalar spectrum are applicable for arbitrary diffusivity and therefore provide a means of predicting the shape of the humidity spectrum and the temperature-humidity cospectrum. The ability to predict theoretically the humidity spectrum and temperature-humidity cospectrum is particularly important at high wavenumbers because frequency response limitations make it impossible to measure these spectra at high wavenumbers by present techniques. Since the refractivity fluctuation is caused by temperature and humidity fluctuations, the predicted temperature spectrum, humidity spectrum, and temperature-humidity cospectrum are used to obtain the spectrum of refractivity fluctuations.

The analysis presented here consists of three parts. In section 2 the refractivity is expressed as a function of the fluctuations of pressure, temperature, and humidity. A determination is made of the accuracy of retaining only the lowest order in fluctuations in the mean refractivity and refractivity variance. For this purpose the values of averaged quantities are taken to be those typical of the

Copyright © 1978 by the American Geophysical Union.

0048-6604/78/1112-0953$01.00

atmospheric surface layer. In section 3 one finds an investigation of the approximations that are required so that the temperature and humidity are described by (6), which balances temporal changes and advection against diffusion. When temperature and humidity satisfy such an equation the model of the scalar spectrum may be used to predict the temperature spectrum, humidity spectrum, and temperature-humidity cospectrum; this is done in section 4, along with a presentation of the resulting refractivity spectrum.

2. MEAN AND FLUCTUATING REFRACTIVITY

The refractivity of air may be approximated by [*Gossard,* 1960]:

$$N = A\frac{P}{T} - BQ + C\frac{Q}{T}$$

where T is absolute temperature, P is total atmospheric pressure, and Q is the absolute humidity. The coefficients A, B, and C are functions of the wavelength. At optical frequencies the last term is usually neglected. Pressure, temperature, and humidity are expressed in terms of their mean values $\langle P\rangle$, $\langle T\rangle$, and $\langle Q\rangle$ and their fluctuations P', T', and Q' as

$$P = \langle P\rangle + P', \quad T = \langle T\rangle + T', \quad Q = \langle Q\rangle + Q'$$

The fluctuations have zero mean values. The refractivity may then be written as

$$\begin{aligned} N = {} & (A\langle P\rangle/\langle T\rangle)(1 + P'/\langle P\rangle)(1 + T'/\langle T\rangle)^{-1} \\ & - B\langle Q\rangle(1 + Q'/\langle Q\rangle) + (C\langle Q\rangle/\langle T\rangle)(1 + Q' \\ & \div\langle Q\rangle)(1 + T'/\langle T\rangle)^{-1} \end{aligned} \tag{1}$$

The mean refractivity is found by averaging (1). Use is made of the identity

$$(1 + T'/\langle T\rangle)^{-1} = \sum_{i=0}^{\infty} (-1)^i (T'/\langle T\rangle)^i$$

Then,

$$\begin{aligned} \langle N\rangle = {} & \frac{A\langle P\rangle}{\langle T\rangle}\left[1 + \sum_{i=2}^{\infty}(-1/\langle T\rangle)^i\langle(T')^i\rangle\right] - B\langle Q\rangle \\ & + \frac{C\langle Q\rangle}{\langle T\rangle}\left[1 + \frac{1}{\langle Q\rangle}\sum_{i=1}^{\infty}(-1/\langle T\rangle)^i\langle Q'(T')^i\rangle\right] \end{aligned}$$

where the pressure fluctuations have been neglected in accordance with the estimates given in appendix A. In the first term, the leading term of the summation is $\langle T'^2\rangle/\langle T\rangle^2$ which, from the estimate (A2) of appendix A, is about 10^{-5} to 10^{-7}. Therefore, the entire sum in the first term is neglected. In the last term, the leading term within the summation is $-\langle Q'T'\rangle/(\langle Q\rangle\langle T\rangle)$. The temperature-humidity covariance has been measured over water by *Friehe et al.* [1975]. Values of $-\langle Q'T'\rangle/(\langle Q\rangle\langle T\rangle)$ obtained from their data are -3×10^{-6} over the ocean and 4×10^{-5} over the Salton Sea. Therefore, the entire sum in the last term is neglected relative to unity. Thus an expression for the mean refractivity which is accurate to about one part in 10^5 is

$$\langle N\rangle \simeq A\langle P\rangle/\langle T\rangle - B\langle Q\rangle + C\langle Q\rangle/\langle T\rangle$$

The fluctuation in the refractivity N' is $N - \langle N\rangle$. When pressure fluctuations are ignored it becomes

$$\begin{aligned} N' = {} & G\left[-\frac{T'}{\langle T\rangle} + \sum_{i=2}^{\infty}(-1/\langle T\rangle)^i(T'^i - \langle T'^i\rangle)\right] - BQ' \\ & + \frac{C}{\langle T\rangle}\left[Q' + \sum_{i=1}^{\infty}(-1/\langle T\rangle)^i(T'^iQ' - \langle T'^iQ'\rangle)\right] \end{aligned} \tag{2}$$

where $G \equiv A\langle P\rangle/\langle T\rangle + C\langle Q\rangle/\langle T\rangle$. This expression for N' has a mean value that is identically zero.

The refractivity variance, $\langle N'^2\rangle$, formed from (2) contains infinite sums containing second-order and higher-order averaged quantities. The values of the third-order terms are estimated in appendix A for the atmospheric surface layer; it is shown that an approximation to the refractivity variance, accurate to a few tenths of one percent, is

$$\langle N'^2\rangle = a^2\langle T'^2\rangle + b^2\langle Q'^2\rangle + 2ab\langle T'Q'\rangle \tag{3}$$

where

$$a = (A\langle P\rangle + C\langle Q\rangle)/\langle T\rangle^2 \tag{4}$$

$$b = B - C/\langle T\rangle \tag{5}$$

Equation (3) is identical to the refractivity variance obtained by assuming that the fluctuations may be treated as differential quantities and therefore that

$$N' = \frac{\partial N}{\partial T} T' + \frac{\partial N}{\partial Q} Q' + \frac{\partial N}{\partial P} P'$$

$$= \left(-\frac{AP}{T^2} - \frac{CQ}{T^2} \right) T' + \left(-B + \frac{C}{T} \right) Q' + \frac{A}{T} P'$$

When pressure fluctuations and terms that are second order in the fluctuations are neglected,

$$N' = -\frac{A\langle P \rangle + C\langle Q \rangle}{\langle T \rangle^2} T' + \left(-B + \frac{C}{\langle T \rangle} \right) Q'$$

This is just (2) to first order in the fluctuations and it leads to (3).

3. CONTINUITY EQUATIONS FOR TEMPERATURE AND HUMIDITY

The simplest case of an advected and diffusing scalar quantity, S, is one in which S satisfies

$$\partial S/\partial t + \mathbf{V} \cdot \nabla S = D_s \nabla^2 S \qquad (6)$$

where D_s is the diffusivity of the scalar. The theory of the spatial power spectrum of scalar fluctuations in turbulent flow uses (6) as its starting point [*Hill*, 1978]. In compressible fluids, such as the atmosphere, neither the temperature T nor the humidity Q satisfies (6); it will be shown under what conditions T and Q approximately satisfy (6).

From the equation for the conservation of entropy [*Lumley and Panofsky*, 1964], the potential temperature $\theta = T(P_o/P)^{.286}$ (P_o is a reference pressure and $.286 = 1 - \gamma^{-1}$, where γ is the ratio of specific heats) satisfies

$$\partial\theta/\partial t + \mathbf{V} \cdot \nabla\theta = D_T(\theta/T)\nabla^2 T \simeq D_T \nabla^2 \theta$$

where D_T is the thermal diffusivity. The approximation $(\theta/T)\nabla^2 T \simeq \nabla^2\theta$ neglects the contribution of pressure fluctuations to $\nabla^2\theta$. With this approximation the potential temperature satisfies (6). From the estimates (A1) and (A2), the fluctuations in θ are caused by fluctuations in T, and the contribution of pressure fluctuations is small. Considering two points having some vertical separation, the mean pressure gradient causes a difference in the potential temperature between these points; this difference is small provided that the vertical separation is small. For instance, if the fluctuating temperature causes a 0.1 K temperature difference between points spaced 1 m apart vertically, then the mean pressure gradient contributes only about 10% to the difference in potential temperature between these points. Therefore, at small length scales the distinction between θ and T is unimportant and T may be taken as satisfying (6).

The humidity Q satisfies

$$\partial Q/\partial t + \nabla \cdot (\mathbf{V}Q) = D_Q \nabla^2 Q \qquad (7)$$

where D_Q is the diffusivity of water vapor in air. Thus Q does not satisfy (6). The number density of molecules of humid air, ρ, satisfies

$$\partial\rho/\partial t + \nabla \cdot (\mathbf{V}\rho) = 0 \qquad (8)$$

From (7) and (8) it then follows that

$$\partial(Q/\rho)/\partial t + \mathbf{V} \cdot \nabla(Q/\rho) = (1/\rho) D_Q \nabla^2 Q \qquad (9)$$

The left-hand side of (9) is the same as (6) with $S = Q/\rho$, but the diffusion term is different from that of (6).

There is a subtle reason for using the total number density of humid air, ρ, instead of the number density of dry air or the mass density of humid air or the mass density of dry air. The reason is that, unlike ρ, the latter three quantities do not satisfy (8); in fact, their equivalent of (8) has a diffusion term on the right-hand side. This fact can be made obvious for the number density of dry air; the case of the mass densities then follows from the differences in the molecular masses of water molecules and dry air constituents. Suppose a small parcel of air contains more water molecules than the surrounding air. The mutual diffusion of the water molecules and dry air constituents causes the number density of water molecules in the parcel to decrease. At constant temperature and pressure the water molecules that leave the parcel are replaced on a one-to-one basis by dry air molecules. Therefore, the number density of dry air changes in response to the diffusion of water molecules. Using (7) and (8) it may be shown that the number density of dry air satisfies (8) with the right-hand side replaced by $-D_Q \nabla^2 Q$. In obtaining (9), the use of an air density other than ρ will simply lead to a more complicated diffusion term on the right-hand side. For instance, the specific humidity (mass of water vapor per unit volume divided by the mass of humid air per unit volume) satisfies an equation similar to (9) but with a more complicated diffusion term.

The humidity, Q, satisfies (6) approximately if the atmosphere can be considered approximately incompressible, $\nabla \cdot \mathbf{V} = 0$; the several requirements for this incompressibility approximation are now given. The assumption of incompressibility requires that vertical displacements be sufficiently small so that the mean gradient of the pressure may be sufficiently small so that the mean gradient of the pressure may be neglected. A further requirement is that the humidity fluctuation caused by the fluctuation in the density of air is much smaller than the total humidity fluctuation. In order to treat the fluctuation of temperature and humidity at length scales so small that the diffusion of heat is important, it is necessary to consider the fluctuations in the air density as being an example of compressible flow. The reason is that the diffusion of heat out of or into small-scale temperature fluctuations causes the air to expand or contract, and thermal expansion or contraction is an example of compressible flow. At constant pressure (thus neglecting pressure fluctuations) and constant Q/ρ and to first order in fluctuations the perfect gas law gives the humidity fluctuation caused by the fluctuation in the air density as $Q'_{\mathrm{comp}} = -\langle Q\rangle T'/\langle T\rangle$. This relationship says that the humidity fluctuation caused by density variations follows the temperature fluctuation. For the total humidity fluctuation, Q', to be much greater than the humidity fluctuation caused by temperature fluctuations, Q'_{comp}, it is required that

$$\langle Q'^2\rangle^{1/2}/\langle Q\rangle \gg \langle T'^2\rangle^{1/2}/\langle T\rangle \tag{10}$$

The estimates (A2) and (A3) indicate that (10) is usually satisfied; of course there may be geophysical situations in which (10) is not satisfied. In obtaining (10) it was assumed that Q/ρ was constant following a fluid particle; this assumption is not strictly applicable at very small length scales where diffusion is important because of the diffusion of water vapor. However, water vapor and heat have nearly the same diffusivity; thus (10) is sufficient to insure that the air density fluctuations contribute only slightly to small-length-scale humidity fluctuations.

4. REFRACTIVITY SPECTRUM

The power spectrum of the refractivity fluctuation is now expressed in terms of the power spectra of temperature and humidity and the temperature-humidity cospectrum. In this section the temperature and humidity are assumed to satisfy (6); the requirements for this to be valid are given in section 3. Isotropic turbulence is assumed. The transfer spectrum $T_{S_1S_2}(k)$ and the scalar spectrum $\Gamma_{S_1S_2}(k)$ are the averages over a sphere in wave vector space of the Fourier transforms, over the separation vector **r**, of the quantities

$$-\langle S_1'(\mathrm{x}+r)\mathbf{V}'(\mathrm{x})\cdot\nabla S_2'(\mathrm{x}) + S_2'(\mathrm{x}+\mathbf{r})\mathbf{V}'(\mathrm{x})\cdot\nabla S_1'(\mathrm{x})\rangle$$

$$\text{and}\quad \langle S_1'(\mathrm{x}+r)S_2'(\mathrm{x})\rangle$$

respectively; $\mathbf{V}'$ is the velocity fluctuation; S_1 and S_2 are to be replaced by T, Q, or N. Then the spatial power spectrum of temperature fluctuations $\Phi_T(k)$ is related to $\Gamma_{TT}(k)$ by

$$\Gamma_{TT}(k) = 4\pi k^2\Phi_T(k)$$

with the analogous relationship holding for N and Q. The spectrum $\Gamma_{TQ}(k)$ is just the temperature-humidity cospectrum. The variances are given by

$$\langle T'^2\rangle = \int_0^\infty \Gamma_{TT}(k)\,\mathrm{d}k$$

$$\langle T'Q'\rangle = \int_0^\infty \Gamma_{TQ}(k)\,\mathrm{d}k$$

and so forth.

From (6) the scalar spectra satisfy

$$\partial\Gamma_{TT}/\partial t = T_{TT} - 2k^2D_T\Gamma_{TT} \tag{11}$$

$$\partial\Gamma_{QQ}/\partial t = T_{QQ} - 2k^2D_Q\Gamma_{QQ} \tag{12}$$

$$\partial\Gamma_{TQ}/\partial t = T_{TQ} - k^2(D_T + D_Q)\Gamma_{TQ} \tag{13}$$

Using equations (4) and (5) and to lowest order in T' and Q', the refractivity fluctuation is

$$N' = -aT' - bQ'$$

so

$$\Gamma_{NN} = a^2\Gamma_{TT} + b^2\Gamma_{QQ} + 2ab\Gamma_{TQ} \tag{14}$$

$$T_{NN} = a^2T_{TT} + b^2T_{QQ} + 2abT_{TQ}$$

Then, from (11)–(13), Γ_{NN} satisfies

$$\begin{aligned}\partial\Gamma_{NN}/\partial t = T_{NN} - 2k^2\,[a^2D_T\Gamma_{TT} + b^2D_Q\Gamma_{QQ}\\ + ab(D_T + D_Q)\Gamma_{TQ}]\end{aligned} \tag{15}$$

If D_T and D_Q were equal, then (15) would have the same form as (11)–(13); unfortunately $D_T \neq D_Q$.

In the inertial-convective range of wave numbers, *Corrsin* [1951] used dimensional analysis to obtain the wave number dependence of the temperature spectrum. The rates of diffusive dissipation of temperature and humidity variance are denoted χ_T and χ_Q, respectively, and ε is the rate of dissipation of turbulent kinetic energy. Then Corrsin's analysis gives

$$\Gamma_{TT}(k) = \beta\chi_T\varepsilon^{-1/3}k^{-5/3} \tag{16}$$

$$\Gamma_{QQ}(k) = \beta\chi_Q\varepsilon^{-1/3}k^{-5/3} \tag{17}$$

The analogous dimensional analysis for the temperature-humidity cospectrum is given by *Wyngaard et al.* [1978], they find

$$\Gamma_{TQ}(k) = \beta'\chi_{TQ}\varepsilon^{-1/3}k^{-5/3} \tag{18}$$

It is assumed here that $\beta' = \beta$. Experimental determinations of β_1, where $\beta = 5\beta_1/3$, are reviewed by *Hill* [1978]; $\beta_1 \simeq 0.43$ so $\beta \simeq 0.72$.

Equation (18) may also be obtained from (16) and (17) by noting that at inertial-convective wave numbers the effects of diffusion are negligible and therefore the spectrum of $T + Q$ (and for that matter the spectrum of N) satisfies an equation of the form (11) with the diffusion term neglected. Then, by the methods that give (16) and (17), $\Gamma_{(T+Q)(T+Q)} \propto k^{-5/3}$. Now $\Gamma_{(T+Q)(T+Q)} = \Gamma_{TT} + \Gamma_{QQ} + 2\Gamma_{TQ}$; since the left-most spectra are proportional to $k^{-5/3}$ it follows that $\Gamma_{TQ} \propto k^{-5/3}$. Furthermore, for inertial-convective range wave numbers the diffusion terms in (15) are neglected and (15) then has the form of (11). The dimensional result of *Corrsin* [1951] then applies to the spectrum of refractivity fluctuations so

$$\Gamma_{NN}(k) = \beta\chi_N\varepsilon^{-1/3}k^{-5/3} \tag{19}$$

The relationship between the dissipation rates and the structure parameters is

$$4\pi(.033)C_T^2 = \beta\chi_T\varepsilon^{-1/3}$$

and similarly for C_Q^2, C_{TQ}, and C_N^2. Equations (16)–(19) and (14) give

$$\chi_N = a^2\chi_T + b^2\chi_Q + 2ab\chi_{TQ}$$

Equivalently,

$$C_N^2 = a^2C_T^2 + b^2C_Q^2 + 2abC_{TQ}$$

A dimensionless temperature spectrum, $\tilde{\Gamma}_{TT}$, is given by

$$\tilde{\Gamma}_{TT}(k) = \eta^{-3}\nu\Gamma_{TT}(k)/\chi_T$$

with $\tilde{\Gamma}_{NN}$, $\tilde{\Gamma}_{QQ}$, and $\tilde{\Gamma}_{TQ}$ defined in the same manner; ν is the kinematic viscosity and $\eta = (\nu^3/\varepsilon)^{1/4}$ is the Kolmogorov microscale. In the inertial-convective range all of the dimensionless spectra are $\beta(k\eta)^{-5/3}$. In terms of the dimensionless spectra (14) is

$$\tilde{\Gamma}_{NN} = a^2\frac{C_T^2}{C_N^2}\tilde{\Gamma}_{TT} + b^2\frac{C_Q^2}{C_N^2}\tilde{\Gamma}_{QQ} + 2ab\frac{C_{TQ}}{C_N^2}\tilde{\Gamma}_{TQ} \tag{20}$$

The dimensionless spectrum $\tilde{\Gamma}_{TQ}$ is positive at high wave numbers; however, the quantities Γ_{TQ}, χ_{TQ}, C_{TQ}, or $\langle T'Q'\rangle$ may be either positive or negative. The dimensionless spectrum $\tilde{\Gamma}_{TQ}$ may or may not be negative at wave numbers lower than the inertial-convective range; the experimental observations of *Wyngaard et al.* [1978] give an example of a temperature-humidity cospectrum that changes sign at low wave numbers. From (5) the coefficient b is negative at radio wave frequencies (since the polarizability of water vapor dominates) but positive at optical frequencies. Consequently, the last term in (20) may either increase or decrease $\tilde{\Gamma}_{NN}$. This latter effect has been demonstrated experimentally by *Gossard* [1960] and *Friehe et al.* [1975].

A model of the transfer spectrum has been developed by *Hill* [1978]; this model is

$$T_{s_1s_2}(k) = (\partial/\partial k)D_S(k)(\partial/\partial k)k^{-2}\Gamma_{s_1s_2}(k)$$

where

$$D_S(k) = (3/11)\beta^{-1}\varepsilon^{1/3}k^{14/3}\,[(k/k^\dagger)^{2\delta} + 1]^{-1/(3\delta)}$$

and, by comparison with experiment, the parameters δ and $k^\dagger$ are assigned the values

$$\delta = 1.9, \quad \eta k^\dagger = 0.072$$

In the steady state, (11)–(13) then become linear, homogeneous, second-order differential equations. Solution of (11) in the steady state by *Hill* [1978] has yielded excellent agreement with the temperature spectra measured by *Champagne et al.* [1977] and *Williams and Paulson* [1977]. Since this model of the transfer spectrum is applicable for arbitrary diffusivity it can predict the shape of Γ_{QQ} at high wave numbers where Γ_{QQ} is unmeasurable by present techniques. Furthermore, it is assumed that the model transfer spectrum also applies to $T_{TQ}(k)$ so that $\Gamma_{TQ}(k)$ is also predicted by the model. Then, through (14) the shape of $\Gamma_{NN}(k)$ may be obtained.

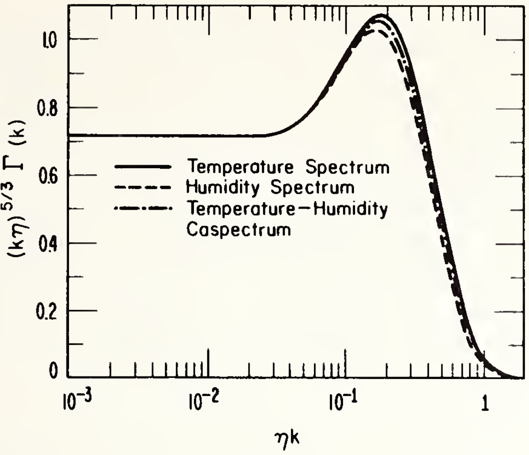

Fig. 1. Calculated temperature and humidity spectra and temperature-humidity cospectrum.

The model predictions for $\bar{\Gamma}_{TT}$, $\bar{\Gamma}_{QQ}$, and $\bar{\Gamma}_{TQ}$ are illustrated in Figures 1 and 2. The differences in the three spectra are caused by the difference between the diffusivities D_T, D_Q, and $(D_T + D_Q)/2$. For atmospheric temperatures of about 300 K, the Prandtl number of air, ν/D_T, is 0.72 whereas the Schmidt number of water vapor in air, ν/D_Q, is 0.63, where D_Q is obtained from expressions given by *Mason and Marrero* [1970]. Thus D_Q is about 14% larger than D_T.

In Figure 1 the curves tend to the constant β at low wave numbers; this flat portion of the curves is the inertial-convective range. The pronounced bump at higher wave numbers is shown by *Hill* [1978] to be caused by the onset of the viscous-convective range at wave numbers lower than those at which the spectra decrease because of diffusion. This bump is evident in the temperature spectra measured by *Champagne et al.* [1977] and by *Williams and Paulson* [1977]. The parameter $k^\dagger$ is a wave number that parameterizes the location of the transition between the inertial-convective range and the viscous-convective range. The importance of $k^\dagger$ to the shape of the spectra in Figure 1 is seen by locating $k^\dagger\eta = 0.072$ in Figure 1. Figure 2 contains the dimensionless dissipation spectra. The area under the curves in Figure 2 is $\nu/(2D_T)$, $\nu/(2D_Q)$, and $\nu/(D_T + D_Q)$ for the dissipation spectra of temperature, humidity, and temperature-humidity, respectively.

In the Salton Sea experiment by *Friehe et al.* [1975], Γ_{TQ} was negative and tended to cancel the contributions to the refractivity spectrum made by Γ_{TT} and Γ_{QQ}. An extreme case of such cancellation is presented in Figure 3. For this case, called case 1, Γ_{NN} is determined from (20) with the coefficients satisfying

$$[a^2 C_T^2] / [b^2 C_Q^2] / [2abC_{TQ}^2] = 2/1/(-2.9)$$

Then the Γ_{TQ} contribution to Γ_{NN} closely cancels that of Γ_{TT} and Γ_{QQ} in the inertial-convective range, but the cancellation is less close at higher wave numbers. Consequently the bump in Γ_{NN} is larger than the bump in any of Γ_{TT}, Γ_{QQ}, or Γ_{TQ}. A less extreme case, case 2, is also shown in Figure 3;

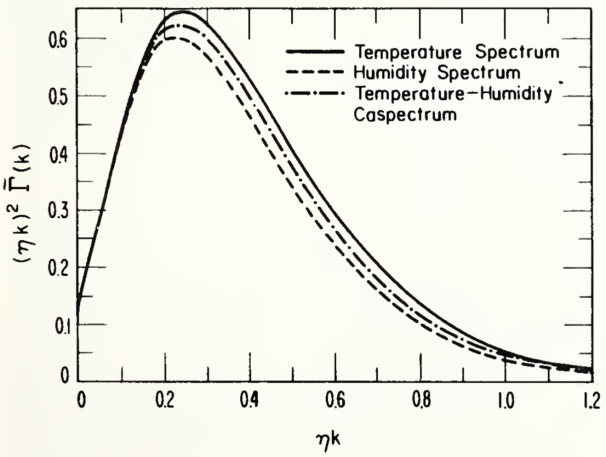

Fig. 2. Calculated dissipation spectra.

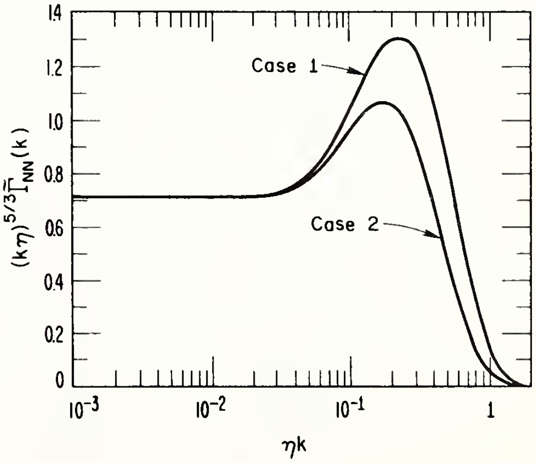

Fig. 3. The refractivity spectrum for cases 1 and 2 described in the text.

for case 2,

$$[a^2 C_T^2] / [b^2 C_Q^2] / [2abC_{TQ}^2] = 5/0.1/1$$

In this case the shape of Γ_{NN} is nearly the same as that of Γ_{TT}.

5. SUMMARY AND DISCUSSION

In section 2 and appendix A the importance to $\langle N \rangle$ and $\langle N'^2 \rangle$ of terms containing higher orders in the fluctuations T' and Q' is investigated. For conditions typical of the atmospheric surface layer it is found that good accuracy is obtained when only the lowest order in the fluctuation is retained.

The potential temperature, θ, satisfies (6). With the neglect of pressure fluctuations and a restriction to small vertical displacements it is shown in section 3 that the temperature, T, also satisfies (6) approximately. Neither the humidity, Q, nor Q/ρ satisfies (6). However, with the neglect of pressure fluctuations, with a restriction to small vertical displacements, and if $\langle Q'^2 \rangle^{1/2} / \langle Q \rangle \gg \langle T'^2 \rangle^{1/2} / \langle T \rangle$, then the humidity, Q, does satisfy (6) approximately.

With T and Q assumed to satisfy (6), the scalar spectral model developed by *Hill* [1978] is used to predict the spectral shapes of Γ_{TT}, Γ_{QQ}, and Γ_{TQ}. The bump in the temperature spectrum observed by *Champagne et al.* [1977] and *Williams and Paulson* [1977] makes its appearance in all three of these spectra. The bump in Γ_{QQ} is smaller than that in Γ_{TQ} which is in turn smaller than the bump in Γ_{TT}; this effect is due to the fact that $D_Q > D_T$.

The refractivity spectrum Γ_{NN} is determined from the model predictions for Γ_{TT}, Γ_{QQ}, and Γ_{TQ}. At wave numbers higher than those of the inertial-convective range the shape of Γ_{NN} is not unique; rather Γ_{NN} depends on the relative contributions of Γ_{TT}, Γ_{QQ}, and Γ_{TQ}. For the case in which the contribution from Γ_{TQ} nearly cancels those of Γ_{TT} and Γ_{QQ}, then Γ_{NN} has a more pronounced bump than does Γ_{TT} or Γ_{QQ} or Γ_{TQ}. The cospectrum is expected to be negative whenever warm, dry air lies above cold, moist air. This occurs near the ground at night and over water that is colder than the air, the latter case being observed by *Friehe et al.* [1975]. This also occurs at the top of the convective boundary layer as observed by *Wyngaard et al.* [1978].

The spectral shapes at high wave numbers are important for optical propagation in the turbulent atmosphere. The bump in the temperature spectrum is shown by *Hill and Clifford* [1978] to produce a corresponding bump in the variance of log-intensity. Furthermore, they show that the covariance of log-amplitude, the structure function of phase, and the lateral coherence length differ from those predicted using the Tatarskii model of the temperature spectrum. In the absence of experimental support, *Tatarskii* [1971] assumed that the temperature spectrum has a gaussian cutoff at diffusive range wave numbers. With the advent of observational support and theoretical modeling, the study of optical propagation can use realistic refractivity spectra.

The presence of the bump can also be important for radio wave scattering. For instance, the Chatanika radar is capable of observing backscatter from turbulence in the stratosphere [*Balsley and Farley*, 1976; *Balsley et al.*, 1977]. From HICAT data, *Chen* [1974] shows that the energy dissipation rate ε of stratospheric clear air turbulence is typically 10 to 10^3 cm^2 sec^{-3}. For $\varepsilon = 10$ cm^2 sec^{-3} the Kolmogorov microscale, η, increases from 0.26 cm at 10 km altitude to 1.3 cm at 24 km altitude. The wavelength, λ, of the Chatanika radar is 23 cm, so for backscatter the radar senses irregularities at the wave number $K = 2(2\pi/\lambda) \simeq 0.5$ radians cm^{-1}. Then, for altitudes from 10 to 24 km, $K\eta$ varies from 0.13 to 0.6. Examination of Figure 1 shows that $K\eta$ is near the peak of the bump for 10 km altitude and $K\eta$ is well within the dissipation range at 20 km. Use of $\varepsilon = 10^3$ cm^2 sec^{-1} would shift these estimates of $K\eta$ toward the left on Figure 1 by roughly a factor of 3. The structure constant C_T^2 is a property of the inertial-convective range. A determination of C_T^2 from stratospheric echoes observed by the Chatanika radar requires, in principle, the use of Figure 1 and an independent measure of ε because $K\eta$ does not lie in the inertial-convective range.

APPENDIX A

An investigation is made of the accuracy of neglecting terms in the refractivity variance that are of order higher than $\langle T'^2 \rangle$, $\langle Q'^2 \rangle$ and $\langle T'Q' \rangle$. The first terms within the summations in (2) are retained; these terms then give higher-order terms in $\langle N'^2 \rangle$. The values of these terms are investigated for conditions that are typical of the atmospheric surface layer. For this purpose typical values of rms fluctuating pressure, temperature, and humidity, as well as the temperature skewness, are taken from surface-layer experiments.

Pressure fluctuations arise from the dynamics of the turbulence. In the near-neutral surface layer, *Elliott* [1972] found that the root-mean-square pressure fluctuation was -2.6 times the kinematic surface stress. Whether or not Elliott's result applies to the unstable surface layer is unknown. When one uses the stress values $\langle uw \rangle$ measured over land by *Champagne et al.* [1977] and *Haugen et al.* [1971], the rms pressure fluctuations given by Elliott's result are typically 10^{-2} to 10^{-3} millibars. For the same experiments the rms temperature fluctuation is typically between 1.0 and 0.1 K. The rms temperature fluctuation depends strongly on height. The rms humidity fluctuations measured by *Champagne et al.* [1977] are about 0.5 g/m^3 which is comparable to the rms humidity fluctuations over water [*Friehe et al.*, 1975]. The mean pressure is taken to be 10^3 mb, the mean temperature to be 300 K, and the mean humidity is taken from *Champagne et al.* [1977] to be about 10 g/m^3; then

$$\langle P'^2 \rangle^{1/2} / \langle P \rangle \simeq 10^{-5} \text{ to } 10^{-6} \tag{A1}$$

$$\langle T'^2 \rangle^{1/2} / \langle T \rangle \simeq 3 \times 10^{-3} \text{ to } 3 \times 10^{-4} \tag{A2}$$

$$\langle Q'^2 \rangle^{1/2} / \langle Q \rangle \simeq 5 \times 10^{-2} \tag{A3}$$

Values of temperature, humidity, and pressure variance reported by *Gossard* [1960] are comparable to those implied by (A1), (A2), and (A3). Data reported by *Friehe et al.* [1975] give values of $\langle Q'^2 \rangle^{1/2} / \langle Q \rangle$ equal to 1.4×10^{-2} for the open ocean data and 9×10^{-2}, for the Salton Sea data. The direct effect of pressure fluctuations is in the first term of (1). From the estimates (A1) and (A2) it is seen that the pressure fluctuations may be neglected relative to the effects of temperature fluctuations in the first term of (1) to an accuracy of not less than 3%. There is also an indirect effect of pressure fluctuations, namely that adiabatic pressure fluctuations cause both temperature and density fluctuations and therefore humidity fluctuations as well. When the perfect gas law, the adiabatic law, and the estimates (A1), (A2), and (A3) for the fluctuation levels are used, then it is found that this indirect effect of pressure fluctuations may be neglected as well. Of course, one can imagine a laboratory flow in which the pressure fluctuations are large and the temperature and humidity fluctuations are kept small; then both of the effects of pressure fluctuations may not be negligible. However, the effects of pressure fluctuations are neglected in this study.

The refractivity variance is formed from (2) and only averages containing up to three fluctuating quantities are retained; the refractivity variance with the summations truncated is

$$\begin{aligned}\langle N'^2 \rangle &= G^2\sigma_T^2(1 - 2\sigma_T^2 S) - 2GB(\langle T'Q' \rangle / T) \\ &\quad \cdot (-1 + U\sigma_T) + 2GC(\langle T'Q' \rangle / \langle T^2 \rangle)[-1 \\ &\quad + (1 + 2U)\sigma_T] + B^2\langle Q'^2 \rangle - (2BC/\langle T \rangle)\langle Q'^2 \rangle \\ &\quad \cdot (1 - V\sigma_T) + (C^2/T^2)\langle Q'^2 \rangle(1 - 2V\sigma_T + R^2\sigma_T^2)\end{aligned} \tag{A4}$$

where

$$\sigma_T \equiv \langle T'^2 \rangle^{1/2} / \langle T \rangle$$

$$S \equiv \langle T'^3 \rangle / \langle T'^2 \rangle^{3/2}$$

$$V \equiv \langle T'Q'^2 \rangle / (\langle T'^2 \rangle^{1/2} \langle Q'^2 \rangle)$$

$$R \equiv \langle T'Q' \rangle / (\langle T'^2 \rangle \langle Q'^2 \rangle)^{1/2}$$

$$U \equiv \langle T'^2 Q' \rangle / (\langle T'Q' \rangle \langle T'^2 \rangle^{1/2})$$

Values of S given by *Tillman* [1972] from atmospheric surface layer data lie between 0.1 and 1.2 depending on stability. Values of the temperature-humidity correlation coefficient R are given by *Wyngaard et al.* [1978] for the boundary layer over water, and R may be deduced from the data reported by *Friehe et al.* [1975]. These values of R are found to extend from -1.0 to 1.0. Since temperature and humidity are often well correlated, the statistic V is expected to have an absolute magnitude close to that of the temperature skewness S, or smaller. Unfortunately, neither V nor U has been deduced from data. It is speculated that the absolute magnitude of U is of order unity. However, U may tend to infinity if $\langle T'Q' \rangle$ tends to zero but $\langle T'^2 Q' \rangle$ does not; it is assumed that this would be a rare occurrence and is neglected. Therefore, it is assumed that S, V, R, and U have absolute magnitudes of order unity or smaller. In this case the first and last terms in (A4) contain higher-order terms which are of order σ_T^2. From the estimate (A2), σ_T^2 is 10^{-5} to 10^{-7}; thus these higher-order terms are negligible. The second, third, fifth, and sixth terms in (A4) contain higher-order terms that are of the order of σ_T. From the estimate (A2) these higher-order terms may be neglected to within an accuracy of a few tenths of one percent.

Acknowledgments. The author thanks E. E. Gossard and J. C. Wyngaard for their helpful comments. This research was supported by the national Research Council through the Resident Research Associateship Program.

REFERENCES

Balsley, B. B., and D. T. Farley (1976), Auroral zone winds detected near the tropopause with the Chatanika UHF Doppler radar, *Geophys. Res. Lett.*, *3*, 525–528.

Balsley, B. B., N. Cianos, D. T. Farley, and M. J. Baron (1977), Winds derived from radar measurements in the arctic troposphere and stratosphere, *J. Appl. Meteorol.*, *16*, 1235–1239.

Champagne, F. H., C. A. Friehe, J. C. LaRue, and J. C. Wyngaard (1977), Flux measurements, flux estimation techniques, and fine-scale turbulence measurements in the unstable surface layer over land, *J. Atmos. Sci.*, *34*, 515–530.

Chen, W. Y. (1974), Energy dissipation rates of free atmospheric turbulence, *J. Atmos. Sci.*, *31*, 2222–2225.

Corrsin, S. (1951), On the spectrum of isotropic temperature fluctuations in isotropic turbulence, *J. Appl. Phys.*, *22*, 469–473.

Elliott, J. A. (1972), Microscale pressure fluctuations measured within the lower atmospheric boundary layer, *J. Fluid Mech.*, *53*, 351–383.

Friehe, C. A., J. C. LaRue, F. H. Champagne, C. H. Gibson, and G. F. Dreyer (1975), Effects of temperature and humidity fluctuations on the optical refractive index in the marine boundary layer, *J. Opt. Soc. Amer.*, *65*, 1502–1511.

Gossard, E. E. (1960), Power spectra of temperature, humidity, and refractive index from aircraft and tethered balloon measurements, *IRE Trans. Antennas Propagat.*, *AP-8*, 186–201.

Haugen, D. A., J. C. Kaimal, and E. F. Bradley (1971), An experimental study of Reynolds stress and heat flux in the atmospheric surface layer, *Quart. J. Roy. Meteorol. Soc.*, *97*, 168–180.

Hill, R. J. (1978), Models of the scalar spectrum for turbulent advection, *J. Fluid Mech.*, *88*, 541–562.

Hill, R. J., and S. F. Clifford (1978), Modified spectrum of atmospheric temperature fluctuations and its application to optical propagation, *J. Opt. Soc. Amer.*, *68*, 892–899.

Lumley, J. L., and H. A. Panofsky (1964), *The Structure of Atmospheric Turbulence*, p. 59, John Wiley, New York.

Mason, E. A., and T. R. Marrero (1970), The diffusion of atoms and molecules, *Advan. At. Mol. Phys.*, *6*, 155–232.

Tatarskii, V. I. (1971), *The Effects of the Turbulent Atmosphere on Wave Propagation*, p. 76, Keter Press, Jerusalem.

Tillman, J. E. (1972), The indirect determination of stability, heat, and momentum fluxes in the atmospheric boundary layer from simple scalar variables during dry unstable conditions, *J. Appl. Meteorol.*, *11*, 783–792.

Williams, R. M., Jr., and C. A. Paulson (1977), Microscale temperature and velocity spectra in the atmospheric boundary layer, *J. Fluid Mech.*, *83*, 547–567.

Wyngaard, J. C., W. T. Pennell, D. H. Lenschow, and M. A. LeMone (1978), The temperature-humidity covariance budget in the convective boundary layer, *J. Atmos. Sci.*, *35*, 47–58.

Journal of Fluid Mechanics, 88, part 3: 541-562, 1978.

Models of the scalar spectrum for turbulent advection

By R. J. HILL

Wave Propagation Laboratory, Environmental Research Laboratories, National
Oceanic and Atmospheric Administration, Boulder, Colorado 80302

(Received 9 August 1977 and in revised form 22 February 1978)

Several models are developed for the high-wavenumber portion of the spectral transfer function of scalar quantities advected by high-Reynolds-number, locally isotropic turbulent flow. These models are applicable for arbitrary Prandtl or Schmidt number, ν/D, and the resultant scalar spectra are compared with several experiments having different ν/D. The 'bump' in the temperature spectrum of air observed over land is shown to be due to a tendency toward a viscous–convective range and the presence of this bump is consistent with experiments for large ν/D. The wavenumbers defining the transition between the inertial–convective range and viscous–convective range for asymptotically large ν/D (denoted k^* and k_1^* for the three- and one-dimensional spectra) are determined by comparison of the models with experiments. A measurement of the transitional wavenumber k_1^* [denoted $(k_1^*)_{\text{meas}}$] is found to depend on ν/D and on any filter cut-off. On the basis of the k^* values it is shown that measurements of β_1 from temperature spectra in moderate Reynolds number turbulence in air ($\nu/D = 0{\cdot}72$) may be over-estimates and that the inertial–diffusive range of temperature fluctuations in mercury ($\nu/D \simeq 0{\cdot}02$) is of very limited extent.

1. Introduction

Knowledge of the spatial power spectra of temperature and humidity fluctuations in turbulent flow is needed in treating the propagation and scattering of sound, optical, and radio frequency waves. The importance of such scalar fluctuations lies in their influence on the refractive index fluctuations in turbulent media. Four models of the scalar spectrum are developed for arbitrary Prandtl or Schmidt numbers; these models are applicable to high Reynolds number flows. The models give a unified treatment of scalar spectra for arbitrary Prandtl or Schmidt numbers; therefore, fitting the models to existing data allows one to predict the shape of scalar spectra that have not been measured, an example being the humidity spectrum at wavenumbers higher than can be observed by present techniques. The models are presented in §4 after reviewing the observational data and previous models of the scalar spectrum.

The three-dimensional scalar spectrum $\Gamma(k,t)$ and its one-dimensional counterpart $\Psi(k_1,t)$ are herein normalized so that they are the spectral budgets of the mean-squared scalar fluctuation:

$$\langle n^2\rangle = \int_0^\infty \Gamma(k,t)\,dk = \int_0^\infty \Psi(k_1,t)\,dk_1,$$

where n is the fluctuation in the concentration or temperature. Assuming isotropy, the diffusive dissipation rate χ of the mean-squared fluctuations is then given by

$$\chi = 2D\int_0^\infty k^2\,\Gamma(k,t)\,dk = 6D\int_0^\infty k_1^2\,\Psi(k_1,t)\,dk_1, \tag{1}$$

where D is the diffusivity. The relationship between $\Gamma(k,t)$ and $\Psi(k_1,t)$ is given by

$$\Psi(k_1,t) = \int_{k_1}^\infty \frac{\Gamma(k,t)}{k}\,dk. \tag{2}$$

There are several possible wavenumber ranges for the scalar spectrum depending on the ratio ν/D (ν being the kinematic viscosity) which is the Prandtl number Pr for temperature, or the Schmidt number Sc for molecular species. The terminology for these wavenumber ranges depends first on whether the wavenumber lies in the inertial or viscous range of the energy spectrum and second on whether the wavenumber lies in the convective or diffusive range of the scalar spectrum. For $\nu \gg D$ there may exist an inertial–convective range, a viscous–convective range, and a viscous–diffusive range. For $\nu \ll D$ the important wavenumber ranges are the inertial–convective and inertial–diffusive ranges.

For the scalar field the set of similarity parameters is χ, ϵ, ν, D, and the wavenumber k (Gibson 1968), where ϵ is the rate of viscous dissipation of turbulent kinetic energy per unit mass of fluid. Three useful scaling wavenumbers may be constructed from this set of parameters:

$$k_d \equiv (\epsilon/\nu^3)^{\frac{1}{4}}, \quad k_b \equiv (\epsilon/\nu D^2)^{\frac{1}{4}}, \quad k_c \equiv (\epsilon/D^3)^{\frac{1}{4}};$$

these are the Kolmogorov, Batchelor, and Corrsin wavenumbers, respectively. It was Batchelor (1959) who clarified the fact that k_b and k_c parameterize the rapid decrease in the scalar spectrum due to diffusion for the cases $\nu \gg D$ and $\nu \ll D$, respectively. It is useful to denote by k_L a wavenumber that is characteristic of the wavenumbers at which the turbulence contains most of its energy and at which the scalar field contains most of its mean-squared fluctuation. The similarity parameters may be rearranged by forming two non-dimensional parameters, ν/D and k/k_d, to give the set $\chi, \epsilon, \nu, \nu/D$, and k/k_d. Dimensional analysis then gives (Boston & Burling 1972; Gibson 1968)

$$\Gamma(k) = \chi\epsilon^{-\frac{3}{4}}\nu^{\frac{5}{4}}\,H(\nu/D, k/k_d), \quad k \gg k_L, \tag{3}$$

where H is a non-dimensional function. The use of ν rather than D as a scaling parameter, or the use of k_d to scale the wavenumber rather than k_b or k_c, is arbitrary owing to the existence of the non-dimensional parameter ν/D.

The dimensional analysis for the inertial–convective range does not include the parameters ν or D as dissipation is not an important process for this range. The results of Oboukhov (1949) and Corrsin (1951) for the inertial–convective scalar spectrum show that

$$\Gamma(k) = \beta\chi\epsilon^{-\frac{1}{3}}k^{-\frac{5}{3}} \quad \text{for} \quad k_L \ll k \ll \text{smaller of } k_d \text{ and } k_c, \tag{4}$$

where β is a non-dimensional constant which we call the Oboukhov–Corrsin constant. The requirement that k be much smaller than either k_d or k_c merely limits the inertial–convective range to wavenumbers below those at which viscosity or diffusion is important.

A unified treatment of the viscous–convective and viscous–diffusive ranges is given by Batchelor (1959). His theory assumes that, at viscous-range length scales, the velocity field has spatial variation that is smooth relative to the spatial variation of a scalar having $D \ll \nu$. Batchelor shows that the local gradients of the scalar become aligned with the local axis of the least principal rate of strain and that the local gradients increase because of the straining while the amplitude of the fluctuation is decreased by diffusion. The typical time for a change in magnitude of the local rate of strain or for a rotation of the local principal axes of the rate-of-strain tensor relative to the fluid is assumed to be long compared with the lifetime of a given scalar fluctuation. Thus the velocity field is considered as a temporally persistent and spatially uniform straining describable by a single effective least principal rate of strain γ. The deduction for the scalar spectrum in the viscous–convective and viscous–diffusive ranges is

$$\Gamma(k) = -\chi\gamma^{-1}k^{-1}\exp(Dk^2/\gamma) \quad \text{for} \quad k \geqslant k_d. \tag{5}$$

Batchelor estimates the parameter γ as $-0{\cdot}5(\epsilon/\nu)^{\frac{1}{2}}$ in which case the argument of the exponent in (5) is $-2(k/k_b)^2$. If $k \ll k_b$ then the exponential in (5) is nearly unity and the viscous–convective spectrum becomes

$$\Gamma(k) = -\chi\gamma^{-1}k^{-1} \quad \text{for} \quad k_d \leqslant k \ll k_b. \tag{6}$$

Equation (6) may be obtained by dimensional analysis with parameters χ, γ, and k.

Kraichnan (1968) has estimated the effect of allowing γ to have large but infrequent local deviations from its usual value. The result of such spatial fluctuations in γ is that the k^{-1} viscous–convective power law is unchanged but the viscous–diffusive range decreases more gently than the Gaussian decrease predicted by Batchelor. Kraichnan found that the viscous–diffusive range was dominated by the infrequent occurrences of the very large values of γ, but the viscous–convective range was dominated by the typical occurrence of the moderate values of γ.

For the inertial–diffusive range Batchelor, Howells & Townsend (1959) hypothesize that the dominant contributions to $\Gamma(k)$ at wavenumber k are due to motions of the fluid with a scale size of k^{-1} acting on gradients in the scalar concentration that are nearly spatially uniform owing to the action of diffusion. Since most of the diffusive dissipation of the scalar spectrum occurs in the lowest wavenumber region of the inertial–diffusive range, Batchelor *et al.* (1959) set these gradients equal to the root-mean-square gradient of the scalar fluctuations. Their prediction is given by:

$$\Gamma(k) = \tfrac{1}{3}\alpha\chi\epsilon^{\frac{2}{3}}D^{-3}k^{-\frac{17}{3}} \quad \text{for} \quad k_c \ll k \ll k_d, \tag{7}$$

where α is the Kolmogorov constant. An alternative theory for the inertial–diffusive range by Gibson (1968) gives $\Gamma(k) \propto k^{-3}$.

2. Observations of the scalar spectrum

The $k^{-\frac{5}{3}}$ power law in the inertial–convective range is observed in a number of experiments: sodium chloride and temperature fluctuations in water by Gibson & Schwarz (1963); temperature fluctuations in water by Grant *et al.* (1968); ammonium acetate solute in water by Gibson, Lyon & Hirshsohn (1970*a*); temperature fluctuations in the atmospheric boundary layer by Pond *et al.* (1966), Gibson, Stegen & Williams (1970*b*), Boston & Burling (1972), Williams & Paulson (1977), and Champagne *et al.* (1977).

The k^{-1} power law in the viscous–convective range is strikingly verified by Grant *et al.* (1968) from temperature fluctuations in the ocean and by Gibson *et al.* (1970*a*) from ammonium acetate fluctuations ($Sc \gg 1$). The k^{-1} behaviour is also observed in the temperature ($Pr \simeq 7$) and sodium chloride ($Sc \simeq 700$) fluctuations in water as measured by Gibson & Schwarz (1963), and in the measurements of dye fluctuations in water ($Sc \simeq 2 \times 10^4$) by Nye & Brodkey (1967) and by McKelvey *et al.* (1975). No inertial–convective range was expected or observed in these latter two experiments.

There are very few measurements of scalar spectra for which the Prandtl or Schmidt number is small compared with unity. Measurement of the temperature spectrum in mercury ($Pr \simeq 0{\cdot}02$) was undertaken by Clay (1973) and by Rust & Sesonske (1966). Experiments have been performed on turbulent flow in weakly ionized argon gas ($Sc \simeq 0{\cdot}07$) passing through a discharge tube (Granatstein, Levine & Subramanian 1971; Garosi, Bekefi & Schulz 1970; Kuyel & Gruber 1973). Unfortunately these flows are at low Reynolds numbers; there are strong fluctuations in the neutral-gas temperature, and the velocity and ionization distributions are strongly inhomogeneous with thrashing of the plasma column observed. Thus, interpretation of the experiments in terms of local similarity theory appears impossible. Nevertheless, Bugnolo (1972) uses a Heisenberg model to describe the ionization-concentration spectrum. The effects that Bugnolo (1972) identifies as inertial–diffusive behaviour are shown by Kuyel & Gruber (1973) to be due to strong fluctuations in the density of the neutral gas.

In conclusion, the $k^{-\frac{5}{3}}$ inertial–convective law and the k^{-1} viscous–convective law appear well supported. Moreover, the scaling expressed by (3) appears adequate in those cases in which it has been tested. Unfortunately the diffusive ranges have not been adequately resolved except in the case of temperature fluctuations in air ($Pr \simeq 0{\cdot}72$) and in mercury ($Pr \simeq 0{\cdot}02$).

The value of the Oboukhov–Corrsin constant β, which appears in (4), may be obtained from one-dimensional temperature spectra when an inertial–convective range is in evidence, and by indirect estimates, which are summarized by Paquin & Pond (1971). In an inertial–convective range the one-dimensional temperature spectrum has the same form as the three-dimensional temperature spectrum in (4) with β replaced by a different constant β_1; isotropy implies $\beta = \frac{5}{3}\beta_1$. The indirect estimates of β_1 reviewed by Paquin & Pond (1971) indicate a value of about 0·38. The values of β_1 determined from observation of an inertial–convective range are as follows: Gibson & Schwarz (1963), 0·35; Grant *et al.* (1968), $0{\cdot}31 \pm 0{\cdot}06$; Lin & Lin (1973), $0{\cdot}6 \pm 0{\cdot}06$; Williams & Paulson (1977) data, $0{\cdot}50 \pm 0{\cdot}02$; Champagne *et al.* (1977), 0·41; Boston & Burling (1972), $0{\cdot}76 \pm 0{\cdot}02$;† Gibson *et al.* (1970*b*), 1·16 and Clay (1973) obtained

$$\beta_1 = 0{\cdot}55 \pm 0{\cdot}05, \quad 0{\cdot}56 \pm 0{\cdot}02 \quad \text{and} \quad 0{\cdot}52 \pm 0{\cdot}13$$

from temperature spectra in water, air, and mercury. The data of Gibson *et al.* (1970*b*) and Boston & Burling (1972) were obtained in the boundary layer over the ocean and a tidal flat, respectively. Recently, it has been shown by Schmitt, Friehe & Gibson (1978) that contamination of the fluctuating temperature signal can occur by salt spray depositing on resistance wire sensors. The contaminated sensors then respond to humidity as well as temperature fluctuations. This contamination is present in the

† We obtain $\beta_1 = 0{\cdot}76$ by rescaling the Boston & Burling (1972) data so that the area under the scaled dissipation spectrum is $\frac{1}{6}Pr$ where $Pr = 0{\cdot}72$.

Gibson *et al.* (1970*b*) data (C. A. Friehe, private communication), and may therefore explain their large β_1 value (Schmitt *et al.* 1978).

The β_1 determinations by Boston & Burling (1972), Williams & Paulson (1977), and Champagne *et al.* (1977) used a scalar dissipation rate determined by integrating the dissipation spectrum. The temperature spectral shapes found by Williams & Paulson and by Champagne *et al.* are in good agreement with each other and show a 'bump' at high wavenumbers. This bump also appears in the high-Reynolds-number air-jet data obtained by McConnell (1976). Such a bump is not evident in the Boston & Burling data, and the reasons for the discrepancy between their measurements and those of Williams & Paulson and of Champagne *et al.* are not clear. If the data of Gibson *et al.* (1970*b*) and Boston & Burling (1972) are excluded because of the salt-spray contamination problem, then the bump in the temperature spectrum in air appears to be a consistently observed feature for high-Reynolds-number turbulence.

The existence of the bump implies that β_1 should be determined from spectral values at wavenumbers such that $k/k_d \lesssim 0{\cdot}03$. A determination of β_1 from temperature spectra in air obtained at moderate Reynolds numbers may have a substantial contribution from the bump if portions of the spectrum at $k/k_d > 0{\cdot}03$ are used; such a determination of β_1 is a misinterpretation of the data. Thus the β_1 value of $0{\cdot}6 \pm 0{\cdot}06$ determined from moderate Reynolds number turbulence by Lin & Lin (1973) is in better agreement with the β_1 values found by Champagne *et al.* (1977) and Williams & Paulson (1977) than is at first apparent. The existing data now seem sufficiently consistent that we should recommend that β_1 be considered to lie between 0·41 and 0·50, which is based mainly on the determinations by Champagne *et al.* (1977) and by Williams & Paulson (1977).

3. Previous models of scalar spectral transfer

The simplest case of an advected scalar is the conserved passive scalar that has the following continuity equation:

$$\frac{\partial N}{\partial t} + \mathbf{V}.\nabla N = D\nabla^2 N.$$

The equation for the scalar spectrum that follows from this continuity equation is

$$\frac{\partial \Gamma(k,t)}{\partial t} - T(k,t) = -2Dk^2\,\Gamma(k,t),$$

where $T(k,t)$ is the scalar spectral transfer function. The fact that one equation in two unknowns results is the closure problem due to the coupling of the continuity equation to the nonlinear Navier–Stokes equations. To avoid the closure problem a model for $T(k,t)$ is used.

In this section we consider models of the scalar spectral transfer function $T(k)$, in particular, those developed by Corrsin (1964), Pao (1964, 1965), Leith (1968), and Kraichnan (1968). It is useful to introduce the scalar spectral flux function $F(k)$, which is defined by

$$T(k) \equiv -\frac{\partial F(k)}{\partial k}.$$

Thus, in the steady-state case the scalar spectrum satisfies

$$\frac{\partial F(k)}{\partial k} = -2Dk^2\,\Gamma(k). \tag{8}$$

In the steady state $F(k) = \chi$ if k lies in a convective range.

Corrsin (1964, 1961) generalized an energy cascading concept, which was originated by Onsager (1949), to the case of turbulently advected scalars. The model consists of writing the spectral flux function in the form

$$F(k) = s(k)\,\Gamma(k). \tag{9}$$

Corrsin (1964) took $s(k)$ as $k/\tau(k)$, where $\tau(k)$ is a time scale obtained by dimensional analysis using the parameters k and $E(k)$; he then used Kolmogorov's inertial range form for $E(k)$. Corrsin (1964) has also shown that if $\tau(k) = -\gamma^{-1}$, where γ is an effective rate of strain, then one obtains (5) and (6) for the viscous–convective and viscous–diffusive ranges of Batchelor (1959).

Pao (1964, 1965) proposed that the scalar flux $F(k)$ is due to a continuous cascading in wavenumber space rather than as a geometrical progression as proposed by Onsager. Pao obtained $s(k)$ in the inertial–convective and inertial–diffusive ranges by dimensional analysis using the parameters ϵ and k, and in the viscous–convective and viscous–diffusive ranges using the parameters γ and k, where γ is an effective rate of strain. Pao (1964) showed that the dimensional result in the viscous range, namely $s(k) = -\gamma k$, is identical with the theory by Batchelor (1959). However, Pao (1965) has assumed that the inertial-range form of $s(k)$ is valid even for $k > k_d$ when $\nu \gg D$; this assumption contradicts the results of Batchelor (1959) for the viscous–convective and viscous–diffusive ranges, and is also inconsistent with the experimental evidence of Grant *et al.* (1968).

Using the Pao (1964) model for the flux function (8) becomes

$$\frac{\partial s(k)\,\Gamma(k)}{\partial k} = -2Dk^2\,\Gamma(k), \tag{10a}$$

where

$$s(k) = \beta^{-1}\epsilon^{\frac{1}{3}}k^{\frac{5}{3}} \quad \text{for} \quad k \ll k_d, \tag{10b}$$

$$s(k) = l\gamma k \qquad \text{for} \quad k \gg k_d, \tag{10c}$$

and l is a non-dimensional negative constant.

The solutions to (10a) are

$$\Gamma(k) = \chi\beta\epsilon^{-\frac{1}{3}}k^{-\frac{5}{3}}\exp\left[-(3\beta/2)(k/k_c)^{\frac{4}{3}}\right], \quad k \ll k_d, \tag{11}$$

and

$$\Gamma(k) \propto k^{-1}\exp\left[-(D/l\gamma)\,k^2\right], \qquad k \gg k_d, \tag{12}$$

where (4) is the boundary condition used to determine the proportionality constant in (11). In the inertial–convective range $k \ll k_c$ and (11) gives the $k^{-\frac{5}{3}}$ power law. For $D \gg \nu$ the exponential in (11) causes the scalar spectrum to decrease rapidly for $k > k_c$. Thus the decrease of the scalar spectrum in the inertial–diffusive range is given as an exponential of the four-thirds power of the wavenumber, which is more rapidly decreasing than the $k^{-\frac{17}{3}}$ variation predicted by Batchelor *et al.* (1959) for the inertial–diffusive range. For $D \ll \nu$ it follows that $k_c \gg k_d$, and therefore the exponential in (11) is close to unity over the entire inertial–convective range. With $l = -1$ (12) is identical with Batchelor's theory as expressed in (5). Unfortunately there is no connexion between the inertial-range and viscous-range forms for $s(k)$ in the Corrsin–Pao model.

A model called the diffusion approximation has been developed by Leith (1968) for a scalar field advected by turbulence. This model consists of a spectral flux function of the form

$$F = -D_s \frac{\partial Q_s}{\partial k}. \tag{13}$$

The product $D_s Q_s$ is obtained by dimensional analysis with the parameters $\Gamma(k)$, $E(k)$ and k.

Leith invokes the equilibrium solution of Lee (1952) in order to obtain D_s and Q_s from their product. The Lee equilibrium solution applies to non-dissipative systems that have a truncation in wave vector space so that there is a maximum wavenumber allowed. With no dissipation and no spectral transfer beyond the maximum wavenumber, the spectrum increases as k^2 in order that the spectral transfer from lower to higher wavenumbers shall be balanced by transfer from high to low wavenumbers. The relevance of truncating wave vector space in the absence of dissipation is obscure. Thus the relevance of the requirement that $\Gamma(k)$ should be proportional to k^2 in the absence of diffusive dissipation in unclear. With the assertion that $\Gamma(k) \propto k^2$ if $D = 0$, the analysis by Leith yields

$$D_s \propto k^{\frac{11}{2}} E(k)^{\frac{1}{2}},$$

$$Q_s = k^{-2}\, \Gamma(k).$$

In the inertial range Leith adopts the inertial-range form of the energy spectrum. The resulting steady-state solutions for the diffusion approximation are found by Leith to be modified Bessel functions. These solutions behave as $k^{-\frac{5}{3}}$ in the inertial–convective range and decrease more slowly in the inertial–diffusive range than does the Corrsin–Pao model. However, for sufficiently large k in the inertial–diffusive range the solutions of the diffusion approximation decrease faster than any negative power of the wavenumber. In particular the solutions of the diffusion approximation decrease faster, at sufficiently large k, than the $k^{-\frac{17}{3}}$ variation predicted by Batchelor *et al.* (1959).

Unfortunately, the diffusion approximation does not represent $\Gamma(k)$ well in the viscous ranges. It may be shown that the diffusion approximation is inconsistent with a power law variation of $\Gamma(k)$ if $E(k)$ is decreasing faster than a power of k. For increasing k, the decrease in $E(k)$ in the viscous range causes a decrease in the diffusion approximation for scalar flux $F(k)$; consequently $\Gamma(k)$, as predicted by the diffusion approximation, increases markedly in the viscous–convective range for large *Pr* or *Sc*. It is concluded that the usefulness of the diffusion approximation is restricted to *Pr* or *Sc* less than unity.

A model of the scalar spectral transfer function for the viscous–convective and viscous–diffusive ranges of a scalar satisfying *Pr* or $Sc \gg 1$ is given by Kraichnan (1968). The spectral flux function for Kraichnan's model is given by

$$F(k) = \frac{\Lambda}{15} k^4 \frac{\partial}{\partial k} [k^{-2}\, \Gamma(k)], \tag{14}$$

where Λ is independent of wavenumber.

For Kraichnan's model the solution in the steady state is given by Mjolsness (1975) as

$$\Gamma(k) = 5(\chi/\Lambda)\,k^{-1}(1+\rho)\exp(-\rho), \tag{15}$$

where $$\rho \equiv (30D/\Lambda)^{\frac{1}{2}}\,k.$$

If $\rho \ll 1$, then (15) gives $\Gamma(k) \propto k^{-1}$, which is the viscous–convective dependence predicted by Batchelor (1959). In the viscous–diffusive range we have $\rho \gg 1$ and (15) gives $\Gamma(k) \propto \exp(-\rho)$; this exponential decrease of the scalar spectrum in the viscous–diffusive range is much more gradual than that in (5).

4. Models of the scalar spectrum for arbitrary ν/D

In this section we describe four models of the scalar spectral transfer function $F(k)$. We seek simple models that are capable of quantitatively describing the entire high-wavenumber portion of the scalar spectrum for arbitrary ν/D. Recognizing that such models are basically speculative, we desire to keep the models as simple as possible. In particular, the scalar spectral transfer function $T(k)$ shall not contain the energy spectrum $E(k)$ because the shape of the energy spectrum is not known in detail in the viscous range. Furthermore, we require that the models have empirical support; that is, their predictions must adequately agree with available experiments. All of the models described have the $k^{-\frac{5}{3}}$ inertial–convective and k^{-1} viscous–convective behaviours; the models differ mainly in their predictions for the diffusive ranges and for the transition between the inertial–convective and viscous–convective ranges. These models are generalizations of the Corrsin–Pao model and of the models of Leith and Kraichnan, which are reviewed in the previous section.

For large Prandtl or Schmidt number the scalar spectrum makes a transition from a $-\frac{5}{3}$ power law in the inertial–convective range to a -1 power law in the viscous–convective range; the average of these exponents is $-\frac{4}{3}$. We locate the transition between these two ranges by the transitional wavenumber k^*. Specifically, we define k^* as the wavenumber between the inertial–convective and viscous–convective ranges at which

$$\left.\frac{\partial \ln \Gamma(k)}{\partial \ln k}\right|_{k=k^*} = -\tfrac{4}{3} \quad \text{for} \quad D \ll \nu. \tag{16}$$

Although k^* is defined in (16) only for $D \ll \nu$, the models that follow give k^* significance even for $D \gg \nu$. In the model spectra for $D \gg \nu$, k^* is a wavenumber at which a transition occurs between an inertial–diffusive range at wavenumbers lower than k^* and a viscous–diffusive range at higher wavenumbers. The one-dimensional scalar spectrum $\Psi(k_1)$ also makes a transition between the inertial–convective and viscous–convective range for $D \ll \nu$; we define this second transitional wavenumber k_1^* by

$$\left.\frac{\partial \ln \Psi(k_1)}{\partial \ln k_1}\right|_{k_1=k_1^*} = -\tfrac{4}{3} \quad \text{for} \quad D \ll \nu. \tag{17}$$

We anticipate that k^* and k_1^* are not equal and that $k_1^* < k^*$. If a simple model having $\Gamma(k) \propto k^{-\frac{5}{3}}$ for $k < k^*$ and $\Gamma(k) \propto k^{-1}$ for $k > k^*$ is substituted into (2) and (17) then k^* is found to be roughly twice as large as k_1^*. The ratio k^*/k_1^* is found on the basis of a model in § 5.3. Moreover, if k^*/k_d is a constant then k_1^*/k_d is expected to be a function of ν/D.

The results of the following analysis are expressed using Kolmogorov scaling for $\Gamma(k)$ and $\Psi(k)$, that is, the following non-dimensional scalar spectra are used:

$$\tilde{\Gamma}(k) \equiv \frac{k_d^3 \nu}{\chi} \Gamma(k).$$

$$\tilde{\Psi}(k) \equiv \frac{k_d^3 \nu}{\chi} \Psi(k).$$

4.1. *Model* 1

The first model is an extension to the case of scalar advection of the model for energy transfer developed by Lin (1972). Two time scales are defined as follows:

$$\tau_1 = \epsilon^{-\frac{1}{3}} k^{-\frac{2}{3}}, \quad \tau_2 = Q(\nu/\epsilon)^{\frac{1}{2}}. \tag{18}$$

The time scale τ_1 exceeds τ_2 in the inertial range whereas the opposite is true in the viscous range. The non-dimensional constant Q is a free parameter to be determined by comparison with experiment.

The Corrsin–Pao model is used by taking the function $s(k)$ in (9) to be

$$s(k) = \frac{\beta^{-1} k}{\tau_1 + \tau_2}.$$

This form satisfies the requirement that $s(k)\,\Gamma(k) \to \chi$ in the inertial–convective range when (4) is used for $\Gamma(k)$. A non-dimensional wavenumber y is defined as $y \equiv Q^{\frac{3}{2}} k/k_d$. From (10*a*) the equation for the scalar spectrum is

$$A^{-1} \frac{d}{dy}\left[\frac{y^{\frac{5}{3}}\,\Gamma(y)}{1+y^{\frac{2}{3}}}\right] = -2y^2 \Gamma(y),$$

where $A \equiv \beta Q^{-2} Pr^{-1}$.

This equation is solved subject to (1) and yields the following Kolmogorov-scaled spectrum:

$$\tilde{\Gamma}(y) = \beta Q^{\frac{5}{2}} y^{-\frac{5}{3}} (1+y^{\frac{2}{3}}) \exp\left[-A\left(\tfrac{3}{2} y^{\frac{4}{3}} + y^{2}\right)\right].$$

In the inertial–convective range this solution reduces to (4). In the limit $A \ll 1$ and $y \gg 1$ the solution reduces to (5) which is the viscous–convective and viscous–diffusive form predicted by Batchelor (1959) with the least principal rate-of-strain parameter given by $\gamma = -(Q\beta)^{-1} (\epsilon/\nu)^{\frac{1}{2}}$. The inertial–diffusive range is characterized by $Ay^{\frac{4}{3}} \gg 1$ and $y \ll 1$ in which case the above solution reduces to (11), which is the prediction of the Corrsin–Pao model for the inertial–diffusive range.

4.2. *Model* 2

This model is an extension of the Corrsin–Pao model in which it is required that $s(k)$ and $d \ln s(k)/d \ln k$ make a smooth transition between their inertial–convective and viscous–convective forms. The transition is located at the transitional wavenumber k^*, as defined in (16). The hyperbolic tangent is used to give the smooth transition in the above derivative of $s(k)$ and a parameter a is introduced which governs the width of the transition. It is assumed that

$$\frac{d \ln s(k)}{dz^*} = \tfrac{5}{3} - \tfrac{1}{3}[1 + \tanh(az^*)],$$

where $z^* \equiv \ln(k/k^*)$. Integrating this equation and requiring that $s(k)\,\Gamma(k) = \chi$ in the inertial–convective range yields

$$s(k) = \beta^{-1}\epsilon^{\frac{1}{3}}k^{\frac{5}{3}}[(k/k^*)^{2a}+1]^{-1/(3a)}.$$

This $s(k)$ has the form of (10*b*, *c*) for $k \ll k^*$ and $k \gg k^*$, respectively. Model 1 is just a special case of this model with $a = \frac{1}{3}$.

The scalar spectrum is the solution of (10*a*) using the above $s(k)$. The solution is given in terms of the Kolmogorov-scaled spectrum $\tilde{\Gamma}$ as

$$\ln[\beta^{-1}(k^*/k_d)^{\frac{5}{3}}\,\tilde{\Gamma}(k)] = -\tfrac{4}{3}z^* + \frac{1}{3a}\ln[2\cosh(az^*)]$$
$$-2\beta(k^*/k_d)^{\frac{4}{3}}\,Pr^{-1}\int_{-\infty}^{z^*}\exp(5w/3)\,[2\cosh(aw)]^{1/(3a)}\,dw. \quad (19)$$

The above scalar spectrum has two free parameters to be determined by comparison with experiment: k^*/k_d locates the transition between inertial–convective and viscous–convective ranges, and a determines the width of the transition. This model will be successful in predicting scalar spectra for arbitrary ν/D only if the same values of (k^*/k_d) and a apply for all ν/D. For $z^* \lesssim -1$ the integral above may be approximated by $\frac{3}{4}\exp(\frac{4}{3}z^*)$. The appearance of the Prandtl number in the last term shows that this term describes the decrease of the spectrum in the diffusive ranges. For $k \ll k^*$, (19) reduces to (11), the exponential in (11) being significant only for $D \gg \nu$. Thus (19) yields the inertial–convective and inertial–diffusive predictions of the Corrsin–Pao model. For $k \gg k^*$, (19) becomes proportional to the spectrum in (5); for $D \ll \nu$ the proportionality becomes an equality with

$$\gamma = -\beta^{-1}(k^*/k_d)^{\frac{2}{3}}(\epsilon/\nu)^{\frac{1}{2}}.$$

Thus the viscous–convective and viscous–diffusive ranges predicted by Batchelor (1959) result from this model.

4.3. *Model* 3

The third model is different from the first two in that it is a diffusion model based on a spectral flux function having the form of (13) with $Q_s(k) = k^{-2}\,\Gamma(k)$. This model derives from the inertial-range form of Leith's diffusion approximation and from the viscous-range form of Kraichnan's flux function. The procedure introduced by Lin (1972) is now used to assert that the form of $D_s(k)$ at all high wavenumbers is obtained by dimensional analysis using the wavenumber and $(\tau_1+\tau_2)$ from (18). The parametric wavenumber $k^s = k_d Q^{-\frac{3}{2}}$ is introduced and the flux function in (13) is required to satisfy $F(k) = \chi$ for wavenumbers in the inertial–convective range; the resulting $D_s(k)$ is

$$D_s(k) = \tfrac{3}{11}\beta^{-1}\epsilon^{\frac{1}{3}}\frac{k^{\frac{14}{3}}}{1+(k/k^s)^{\frac{2}{3}}}.$$

The wavenumber k^s should not be confused with the transitional wavenumber k^* which is defined by (16). In terms of the non-dimensional wavenumber $y = k/k^s$ the equation for the scalar spectrum is

$$\frac{d}{dy}\left\{\frac{y^{\frac{14}{3}}}{1+y^{\frac{2}{3}}}\frac{d}{dy}[y^{-2}\,\Gamma(y)]\right\} = \tfrac{22}{3}\beta\,Pr^{-1}(k^s/k_d)^{\frac{4}{3}}\,y^2\,\Gamma(y).$$

This equation has one free parameter, namely $k^{\S}/k_d$, which is to be chosen by comparison with experiment.

For $k \ll k^{\S}$, $D_s(k) \propto \epsilon^{\frac{1}{3}} k^{\frac{14}{3}}$, which is the inertial-range form of $D_s(k)$ given by Leith (1968), and this model gives (4) for the inertial–convective range; if, in addition, $D \gg \nu$ then the inertial–diffusive range form for $\Gamma(k)$ given by Leith (1968) results. For $k \gg k^{\S}$, $D_s(k) \propto Q^{-1}(\epsilon/\nu)^{\frac{1}{2}} k^4$, which is similar to Kraichnan's (1968) model, and the solutions of this model are proportional to the scalar spectrum in (15) with the non-dimensional wavenumber $\rho = (22\beta/3)^{\frac{1}{2}} (k^{\S}/k_d)^{-\frac{1}{3}} (k/k_b)$; if, in addition, $D \ll \nu$ then the proportionality becomes an equality with

$$\Lambda = (\tfrac{45}{11}) \beta^{-1} (\epsilon/\nu)^{\frac{1}{2}} (k^{\S}/k_d)^{\frac{2}{3}}. \tag{20}$$

4.4. *Model* 4

The final model is also a diffusion model. In analogy with the second model, it is required that $D_s(k)$ and $d \ln D_s(k)/d \ln k$ make smooth transitions between their inertial-range and viscous-range formulae. As in the second model, the hyperbolic tangent is used to give the smooth transition to the above derivative of $D_s(k)$. Two parameters are introduced: the wavenumber $k^{\dagger}$ and a non-dimensional constant b which governs the width of the transition. The wavenumber $k^{\dagger}$ should not be confused with the transitional wavenumber k^* as defined by (16). It is assumed that

$$\frac{d \ln D_s}{dz^{\dagger}} = \tfrac{14}{3} - \tfrac{1}{3}[1 + \tanh(bz^{\dagger})],$$

with $z^{\dagger} \equiv \ln(k/k^{\dagger})$. Subject to the condition $F(k) = \chi$ in the inertial–convective range, we have

$$D_s(k) = \tfrac{3}{11} \beta^{-1} \epsilon^{\frac{1}{3}} k^{\frac{14}{3}} [(k/k^{\dagger})^{2b} + 1]^{-1/(3b)}.$$

In terms of the non-dimensional wavenumber $x \equiv k/k^{\dagger}$ the equation for the scalar spectrum is

$$\frac{d}{dx}\left\{x^{\frac{14}{3}}(x^{2b}+1)^{-1/(3b)} \frac{d}{dx}[x^{-2}\Gamma(x)]\right\} = \tfrac{22}{3} \beta \, Pr^{-1} (k^{\dagger}/k_d)^{\frac{4}{3}} x^2 \, \Gamma(x).$$

This equation contains two free parameters to be determined by comparison with experiment, namely $(k^{\dagger}/k_d)$ and b. The asymptotic solutions of this equation are the same as those of model 3 with $k^{\S}$ replaced by $k^{\dagger}$. Model 3 is a special case of model 4 with $b = \frac{1}{3}$.

5. Comparison of the models with experiment

All four of the models described in the previous section yield scalar spectra with the $k^{-\frac{5}{3}}$ inertial–convective range form and the k^{-1} power law for the viscous–convective range. The differences between the models are illustrated in figure 1 for several Prandtl numbers; the values of the model parameters used for figure 1 are those obtained in the following by comparison with the data of Champagne *et al.* (1977).

All four model spectra are the solutions of linear, homogeneous differential equations; any such solution multiplied by a constant is also a solution. Therefore, the models are not capable of predicting a value of β, and β is used as an adjustable parameter when fitting data.

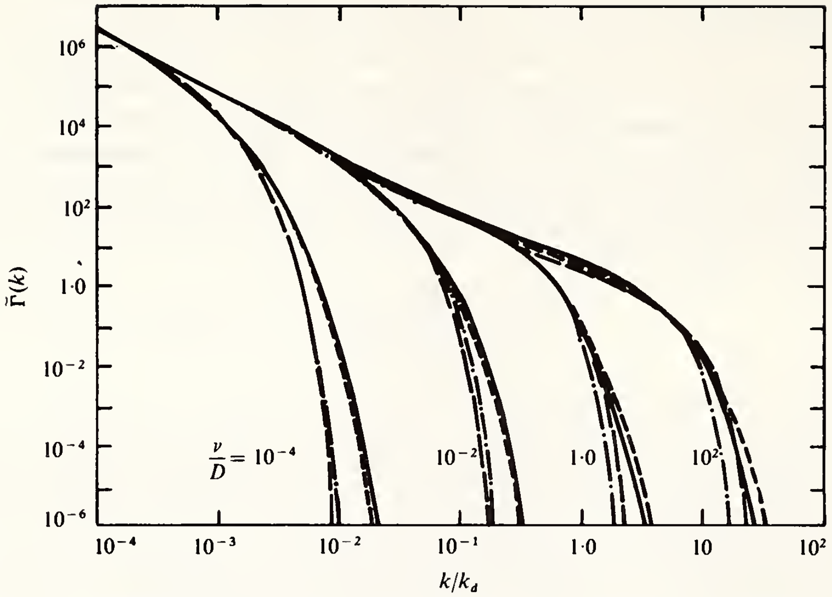

Figure 1. The model spectra for four values of ν/D. – – –, model 1; —·—, model 2; - - - -, model 3; ——, model 4.

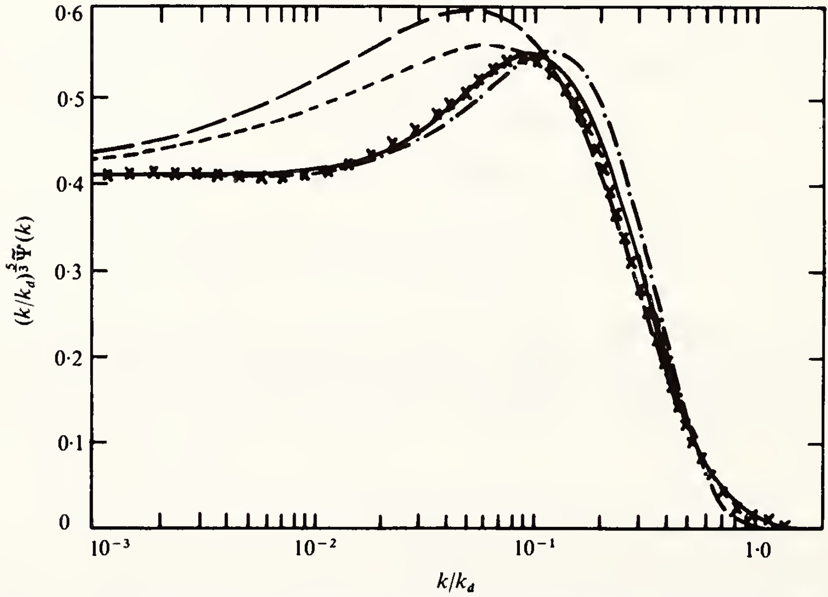

Figure 2. Comparison of the models with the data obtained by Champagne *et al.* (1977). ×, data. The symbols for the models are the same as in figure 1.

5.1. *Temperature fluctuations in the atmospheric surface layer*

We now compare the models with temperature spectra measured in the atmospheric surface layer by Champagne *et al.* (1977) and by Williams & Paulson (1977). No noise correction was found necessary by Champagne *et al.*, but a noise correction was used by Williams & Paulson. Both data sets were corrected for the aliasing due to the fluctuating

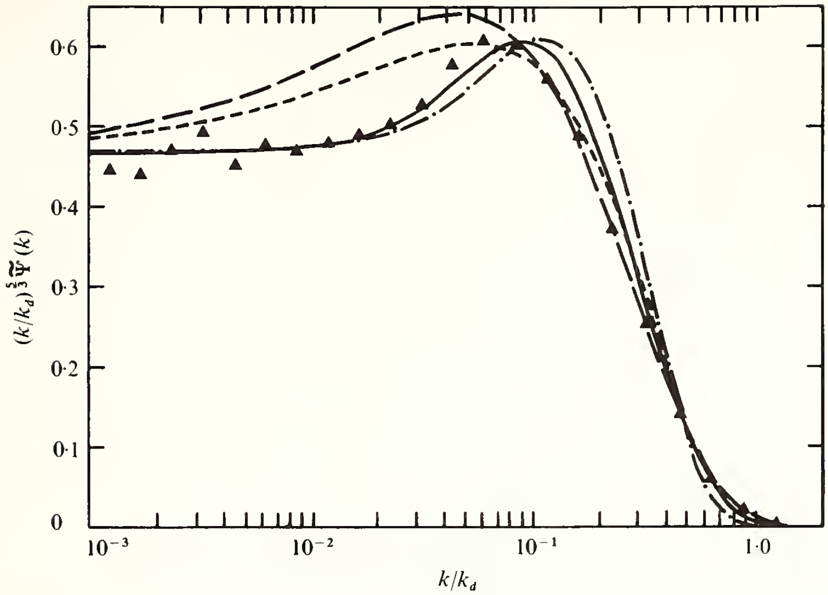

FIGURE 3. Comparison of the models with the data obtained by Williams & Paulson (1977). ▲, data. The symbols for the models are the same as in figure 1.

Data set	Model 1 Q	Model 2 $k^*/k_d, a$	Model 3 $k^§/k_d$	Model 4 $k^†/k_d, b$
Champagne *et al.*	2·5	0·074, 1·4	0·174	0·072, 1·9
Williams & Paulson	2·2	0·073, 1·7	0·22	0·071, 2·0

TABLE 1. Values of the model parameters.

convection velocity (Wyngaard & Clifford 1977). The one-dimensional spectra are computed for the models and are compared with the data in figures 2–7. The Prandtl number is taken to be 0·72, and the β_1 values used are 0·41 and 0·46 for the Champagne *et al.* data and Williams & Paulson 9-run-average, respectively. The values of the model parameters used for the figures are given in table 1.

Figures 2 and 3 present the function $(k/k_d)^{\frac{5}{3}}\tilde{\Psi}(k)$; this function is the constant β_1 in the inertial–convective range. Both data sets show a pronounced 'bump' at high wavenumbers; this bump is reflected in all four of the models. The 'bump' is the appearance of a tendency toward a viscous–convective range at wavenumbers lower than those at which diffusive dissipation sharply reduces the spectrum It is evident from figures 2 and 3 that models 1 and 3 have a much too gradual transition between the inertial–convective and viscous–convective ranges. In fact, the curves for models 1 and 3 closely approach the constant β_1 only for wavenumbers smaller than those shown in the figures. Consequently the parameters for these two models are chosen by matching the peak values of the model's dissipation spectra with those of the data. Models 2 and 4, on the other hand, reproduce the bump in the data quite well. The parameters for models 2 and 4 are then chosen to obtain a bump with about the same height and width as the data, without regard to the position of the bump maximum.

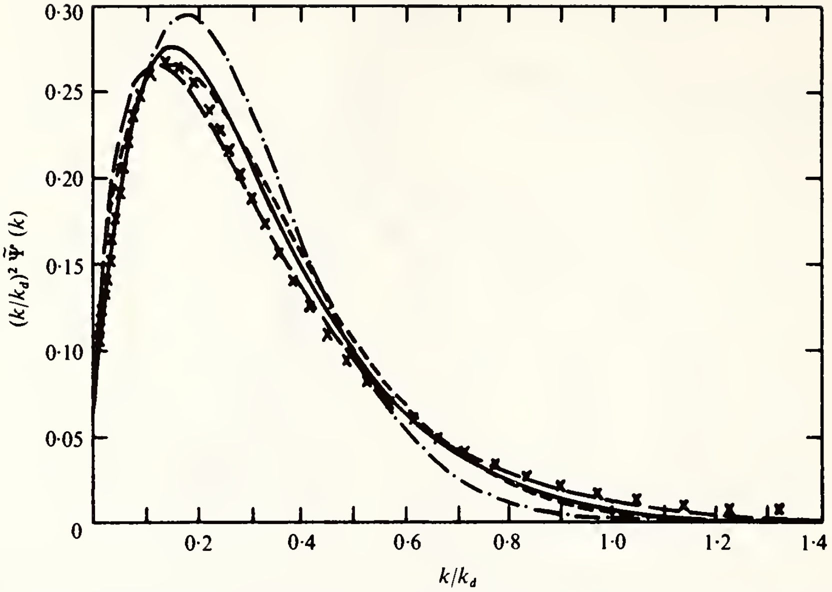

Figure 4. Comparison of the model one-dimensional dissipation spectra with the data obtained by Champagne *et al.* (1977). ×, data. The symbols for the models are the same as in figure 1.

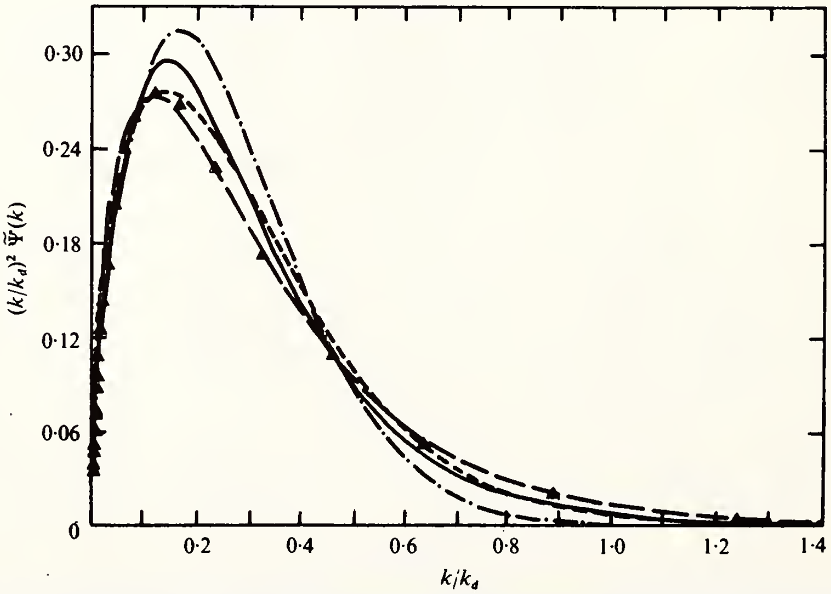

Figure 5. Comparison of the model one-dimensional dissipation spectra with the data obtained by Williams & Paulson (1977). ▲, data. The symbols for the models are the same as in figure 1.

The crosses (×) in figures 2, 4 and 6 are the result of applying the fluctuating-convection-velocity correction to a polynomial fit to the uncorrected data; the calculations were done by the experimenters. This polynomial fit is excellent for the dissipation spectrum and for the function $k^4\Psi(k)$. However, this polynomial fit slightly underestimates the height of the bump. It is seen in figure 2 that models 2 and 4 have a

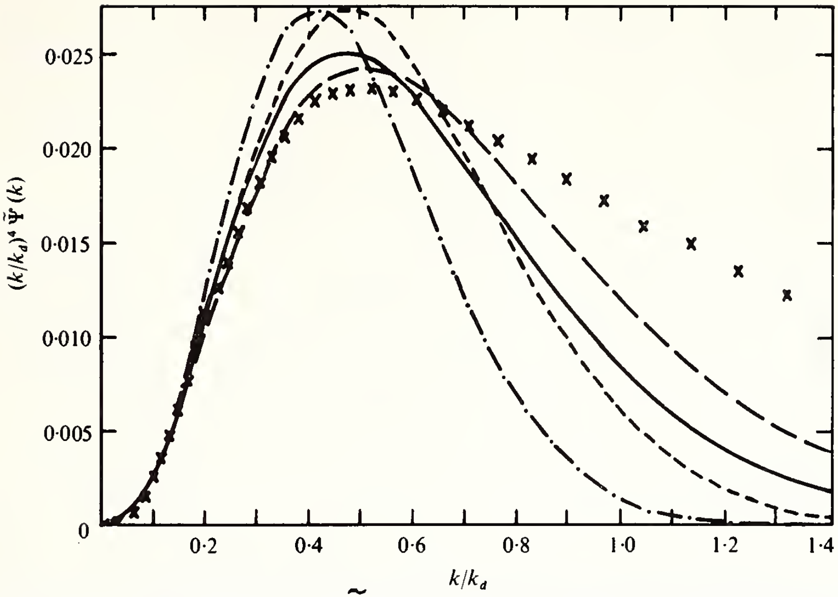

FIGURE 6. Comparison of $(k/k_d)^4 \tilde{\Psi}(k)$ with the data obtained by Champagne *et al.* (1977). $\times$, data. The symbols for the models are the same as in figure 1.

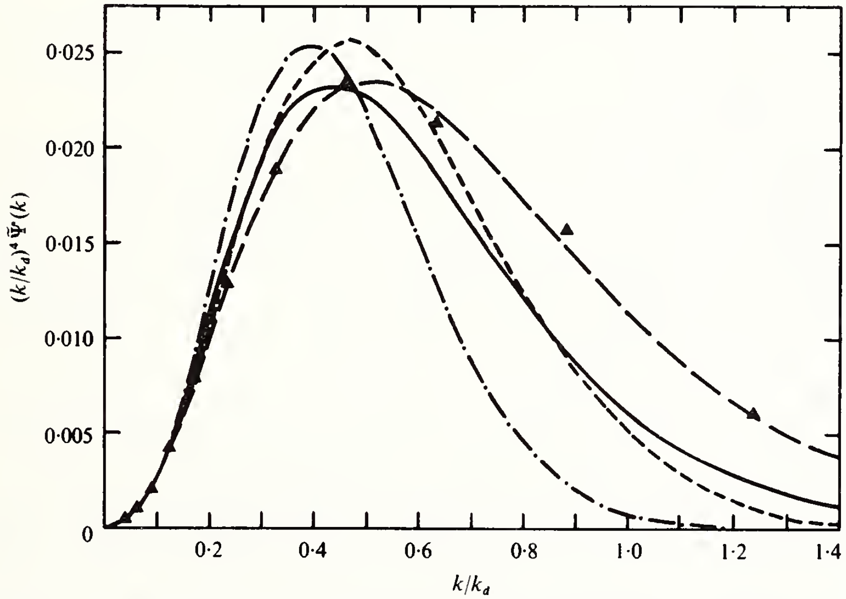

FIGURE 7. Comparison of $(k/k_d)^4 \tilde{\Psi}(k)$ with the data obtained by Williams & Paulson (1977). ▲, data. The symbols for the models are the same as in figure 1.

slightly higher bump than the data; this is intentional in order to compensate for the bias in the polynomial fit to the data.

The scaled dissipation spectra are compared with the data in figures 4 and 5. By (1), the area under all of the curves must be the same, namely $\frac{1}{6}Pr$. A dissipation spectrum that falls more rapidly at high wavenumbers must then have a higher peak value at the

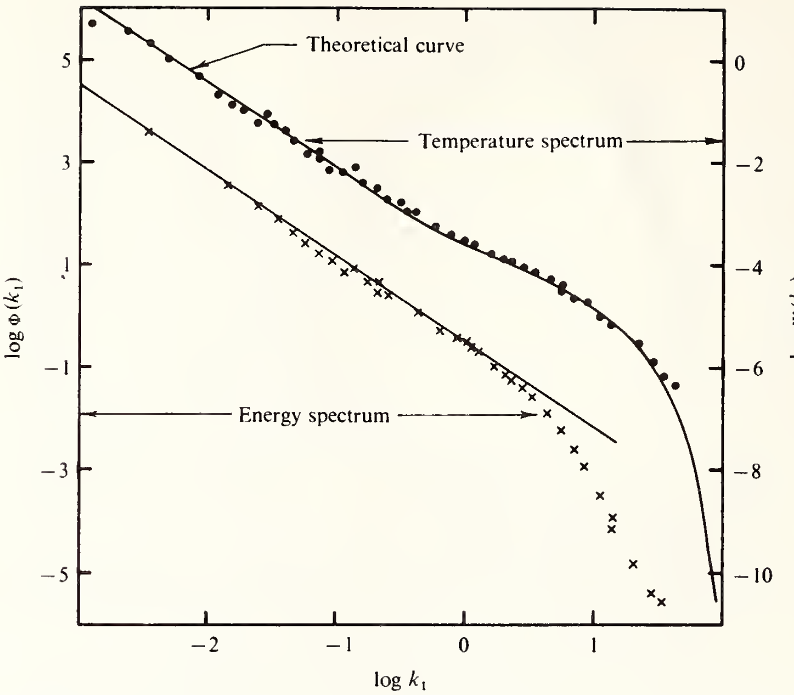

FIGURE 8. Comparison of model 2 with the one-dimensional temperature spectrum for run 2 of Grant *et al.* (1968). Also shown is the one-dimensional energy spectrum for their run 2.

lower wavenumbers. Comparing the position of the peak in the dissipation spectrum with the position of the bump maximum in figures 2 and 3 shows that a higher peak in the dissipation spectrum tends to move the bump maximum to higher wavenumbers. Model 2 has a relatively rapidly falling tail in the dissipation spectrum and consequently a higher peak in the dissipation spectrum; therefore the bump maximum is at a slightly higher wavenumber than the data. The above remarks are the motivation for ignoring the position of the bump maximum in fitting models 2 and 4 to the data.

Figures 6 and 7 present the fourth wavenumber moment of the scaled one-dimensional spectrum. In interpreting these figures, and also figures 4 and 5, it should be kept in mind that the accuracy of the data is questionable at $(k/k_d) \gtrsim 0{\cdot}8$. For instance, in figure 6 there is noise evident in the data for $k/k_d \gtrsim 0{\cdot}8$; the signal-to-noise ratio was unity at $k/k_d \simeq 1{\cdot}0$ (Champagne *et al.* 1977). If one could remove this noise then the data points would be lower at the higher wavenumbers, in better agreement with the model spectra. In figure 4 the area under the data and model curves must be $\frac{1}{6}Pr$, with $Pr = 0{\cdot}72$. If the tail of the data in figure 4 were reduced by a noise subtraction then the values near the peak would be increased, resulting in even better agreement with model 4.

5.2. *Temperature fluctuations in the ocean*

We compare the spectrum from model 2 with the one-dimensional temperature spectrum from the sea water measurements by Grant *et al.* (1968). The comparison with their run 2 is presented in figure 8 along with their one-dimensional energy spectrum for that run. The thermal diffusivity used is the same as used by Grant *et al.* (1968), namely $1{\cdot}44 \times 10^{-3}\,\mathrm{cm}^2\,\mathrm{s}^{-1}$. As is appropriate to the water temperature of their run 2 we take $Pr = 9{\cdot}2$. The value of k^*/k_d is taken to be 0·044. We use $\beta_1 = 0{\cdot}31$ as given by Grant *et al.* (1968) for their run 2. The values of β_1, k^*/k_d, and Pr are sufficient to determine $\tilde{\Gamma}(k)$. For run 2 Grant *et al.* (1968) give

$$\epsilon = 0{\cdot}52\,\mathrm{cm}^2\,\mathrm{s}^{-3} \quad \text{and} \quad \chi = 4{\cdot}2 \times 10^{-3}\,{}^\circ\mathrm{K}^2\,\mathrm{s}^{-1};$$

this is then sufficient information to determine the unscaled spectrum $\Psi(k_1)$, which is presented in figure 8. Owing to difficulties in comparing with data in graphical form, only model 2 is presented; however, comparison with figure 1 illustrates the differences between the models in the viscous–convective and viscous–diffusive ranges. However, model 4 and $Pr = 9{\cdot}2$ was used to obtain k^*/k_d based on the estimate by Grant *et al.* (1968) that $k_1^*/k_d = 0{\cdot}024 \pm 0{\cdot}008$; this resulted in $k^*/k_d = 0{\cdot}041 \pm 0{\cdot}013$, in good agreement with $k^*/k_d = 0{\cdot}044$ used in model 2 to produce figure 8.

In a stratified medium, such as the ocean, it is possible that 'fossil turbulence' contributes to measured temperature spectra. Grant *et al.* (1968) present temperature and energy spectra measured in both Discovery Passage and the open ocean. Their energy spectra from the open ocean have anomalous shapes with little or no inertial range, and it can be speculated that the corresponding temperature spectra may be contaminated by fossil turbulence. Their energy spectra from Discovery Passage, run 2 being an example, have two to three decades of inertial range, which implies active, high-Reynolds-number turbulence. Thus it is assumed that the temperature spectra from Discovery Passage are not affected by fossil turbulence.

5.3. *Comparison with ammonium acetate fluctuations*

Gibson *et al.* (1970*a*) have measured the spectrum of ammonium acetate fluctuations in a sphere wake at downstream positions of 2·17 and 7·5 diameters, which we refer to as runs 1 and 2 respectively. The data were low-pass filtered; the resultant filtered one-dimensional spectra have a transition from an inertial–convective to a viscous–convective range at the wavenumbers $0{\cdot}04k_d$ and $0{\cdot}03k_d$ for runs 1 and 2 respectively. We denote the measured transitional wavenumber by $(k_1^*)_{\mathrm{meas}}$ and investigate the relationship between $(k_1^*)_{\mathrm{meas}}$ and the transitional wavenumbers k_1^* and k^* as defined in (16) and (17). For this purpose, model 4 is used with $b = 1{\cdot}9$ and a Schmidt number of 700, although the results are insensitive to variation of the Schmidt number. In order to simulate the low-pass filter we truncate the integration in (2) at an upper limit of $0{\cdot}8k_d$ and $2{\cdot}0k_d$ (corresponding to experimental conditions) for runs 1 and 2 respectively; the resulting theoretical, filtered, one-dimensional spectra represent the data well and have the transition from inertial–convective to viscous–convective range at $0{\cdot}04k_d$ and $0{\cdot}03k_d$ if $k^\dagger/k_d$ is taken to be 0·09 and 0·075 for runs 1 and 2 respectively. The transitional wavenumber k_1^* of the unfiltered one-dimensional spectrum is then $0{\cdot}034k_d$ and $0{\cdot}029k_d$ for runs 1 and 2 respectively, whereas k^* is $0{\cdot}068k_d$ and $0{\cdot}057k_d$.

Several facts are evident from the above results. First, $k^\dagger$, a parameter of model 4, is not k^*; $k^\dagger/k^* \simeq 1{\cdot}32$. Second, the transitional wavenumbers in the filtered spectra, $(k_1^*)_{\mathrm{meas}} = 0{\cdot}04k_d$ and $0{\cdot}03k_d$, are different from the values of k_1^* from the unfiltered spectra, $k_1^* = 0{\cdot}034k_d$ and $0{\cdot}029k_d$; the percentage discrepancy between the transitional wavenumber in the data ($0{\cdot}04k_d$ and $0{\cdot}03k_d$) is greater than the percentage

Data set	ν/D	k^*/k_d	q
Grant *et al.* (1968)	9·2	0·041 ± 0·013	6·2 ± 1·4
Champagne *et al.* (1977) and Williams & Paulson (1977)	0·72	0·054 ± 0·001	5·1 ± 0·06
Gibson *et al.* (1970*a*)	700	0·062 ± 0·006	4·7 ± 0·2

TABLE 2. Values of k^*/k_d and q determined by comparing model 4 with experiments.

discrepancy between the k_1^* values ($0{\cdot}034k_d$ and $0{\cdot}029k_d$) that result from the model fit to the data. Thus the filtering increases the value of the transitional wavenumber by an amount that depends on the value of the cut-off wavenumber relative to k^*. Third, the transitional wavenumbers k^* and k_1^* are unequal; for large ν/D we have $k^*/k_1^* \simeq 1{\cdot}98$. Fourth, in order to interpret low-pass filtered data, such as those of Gibson *et al.* (1970*a*), in terms of the universal constant k^*/k_d the use of a model of the scalar spectrum is needed.

The values of k^*/k_d determined by comparing model 4 with the experiments performed by Grant *et al.* (1968), the two runs by Gibson *et al.* (1970*a*), and by Champagne *et al.* (1977) and Williams & Paulson (1977) are brought together in table 2. These values of k^*/k_d are all consistent within experimental uncertainties. This lends strong support to the assertion that the bump observed in the temperature spectrum in air ($\nu/D = 0{\cdot}72$) is the beginning of a viscous–convective range. From top to bottom in table 2 the experiments are listed from highest Reynolds number to lowest; while the k^*/k_d values increase from top to bottom. This suggests, but does not prove, that k^*/k_d might decrease with increasing Reynolds number.

Model 4 can be used to determine Batchelor's constant q, which is defined by $\gamma = -q^{-1}(\epsilon/\nu)^{\frac{1}{2}}$. For the viscous–convective range, comparison of (6) and (15) gives $\gamma = -\frac{1}{5}\Lambda$. Then (20), with $k^{\S}$ replaced by $k^{\dagger}$, gives

$$q = \tfrac{11}{9}\beta(k^{\dagger}/k_d)^{-\frac{2}{3}} = 1{\cdot}016\beta(k^*/k_d)^{-\frac{2}{3}}. \tag{21}$$

Equation (21) is very nearly the same as is obtained by equating (4) and (6) at $k = k^*$. Batchelor's constant, as determined from the k^*/k_d values, is also given in table 2; β is assumed to be 0·72 for this purpose. The values of q in table 2 tend to increase with increasing Reynolds number.

5.4. *Comparison with temperature fluctuations in mercury*

Clay (1973) has measured temperature fluctuations in mercury ($Pr \simeq 0{\cdot}018$) in order to observe an inertial–diffusive range. Two power laws were observed over very limited ranges of wavenumber. A k^{-3} power law was found for $0{\cdot}025 < k/k_d < 0{\cdot}039$. At the highest observable wavenumbers the spectrum steepened to a $k^{-\frac{17}{3}}$ power law between $k/k_d = 0{\cdot}12$ and 0·23. The observed values of β_1 increase with increasing Reynolds number from roughly 0·3 to 0·75. The β_1 values did not level off with increasing Reynolds number even though an inertial–convective range was observable at the highest Reynolds numbers attained.

Both the three-dimensional and the one-dimensional spectra are computed for $Pr = 0{\cdot}018$ using model 4 with the parameters obtained from the comparison with the data of Champagne *et al* (1977). The dissipation spectra are presented in figure 9 along

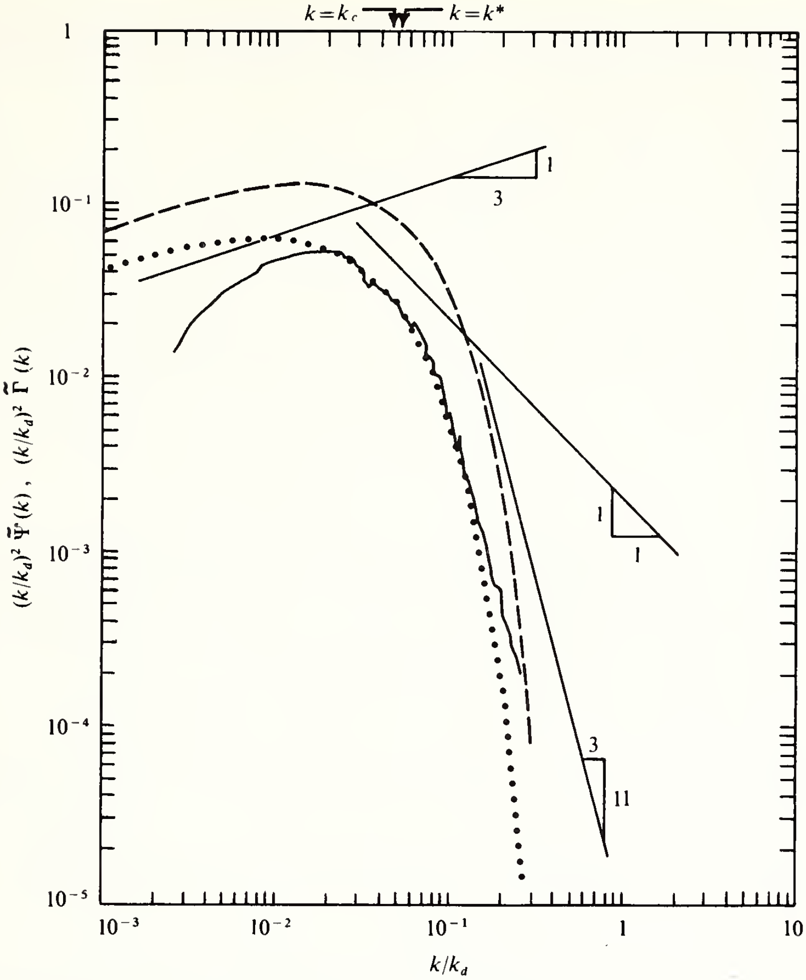

FIGURE 9. Comparison of model 4 with the temperature spectrum in mercury measured by Clay (1973). The dashed and dotted curves are the model three-dimensional and one-dimensional spectra, respectively. The solid curve is the measured one-dimensional spectrum.

with the measured temperature spectrum in mercury that appears in figure 19 of Clay (1973). The straight lines having slopes $\frac{1}{3}$, -1, and $-\frac{11}{3}$ correspond to spectral power laws $k^{-\frac{5}{3}}$, k^{-3}, and $k^{-\frac{17}{3}}$, respectively. The model spectrum was determined using $\beta_1 = 0{\cdot}43$. The scaling in figure 19 of Clay (1973) is apparently in error; the spectral values must be multiplied by 0·54 in order that the area under the scaled dissipation spectrum equals $\frac{1}{6}Pr$ as it should. In view of this scaling error and the variation of the measured values of β_1 with Reynolds number, the measured spectrum in figure 9 was displaced vertically to obtain a best fit to the model. Because of this displacement, it cannot be said that the model compares favourably with the data. However, it is seen that the shape of the model spectrum follows that of Clay's data for wavenumbers between $k/k_d = 0{\cdot}02$ and 0·2. Of course, none of the models developed here have a power-law inertial–diffusive range. In addition, the model spectrum was used to estimate the effect of the fluctuating-convection-velocity aliasing for Clay's experiment; this effect was found to be negligible.

The inertial–convective range power law of the model appears for k/k_d smaller than about 0·003. Such low wavenumbers lie within the variance-containing range of the data. Thus the model interprets the data as having no true inertial–convective range because the Péclet number is too small.

In previous sections it was found that $k^*/k_d \simeq 0{\cdot}05$. Therefore, for $Pr \ll 1$ the model predicts that there is a transition from an inertial–diffusive range to a viscous–diffusive range at wavenumbers near $k^* \simeq 0{\cdot}05k_d$. This suggests the conjecture that the steepening of the measured spectrum from k^{-3} to $k^{-\frac{17}{3}}$ near $k = 0{\cdot}05k_d$ is due to a transition from an inertial–diffusive range to a viscous–diffusive range. Since the transitional wavenumber k^* is rather small, e.g. $k^*/k_d \simeq 0{\cdot}05$, it is evident that the inertial–diffusive range for $Pr = 0{\cdot}018$ might be of very limited extent. A convincing measurement of an inertial–diffusive range would require $\nu/D \simeq 10^{-3}$ and a high Reynolds number flow.

6. Conclusion

Four models of the scalar spectral transfer function are developed and the resulting scalar spectra are compared with experiment. These models are applicable for arbitrary ν/D for high Reynolds number flow and all have the expected $k^{-\frac{5}{3}}$ variation in the inertial–convective range and the k^{-1} variation in the viscous–convective range. Models 1 and 3 give a good fit to the dissipation spectra found by Champagne *et al.* (1977) and Williams & Paulson (1977); however, these models do not represent the data well in the inertial–convective range. Models 2 and 4 are in good agreement with the data gathered by Champagne *et al.* and by Williams & Paulson. An outstanding feature of the temperature spectra observed by these experimenters is the 'bump' at high wavenumbers. The models show that this bump is a tendency to a viscous–convective range at wavenumbers lower than the wavenumbers at which diffusion rapidly decreases the temperature spectrum.

Values of the transitional wavenumber k^* are determined from measurements and are given in table 2. These values appear to increase slightly with decreasing Reynolds number; whether or not this effect is real remains a matter for further experimentation and theoretical insight. Using the values of k^*/k_d from the large ν/D experiments of Grant *et al.* (1968) and Gibson *et al.* (1970*a*), the models then predict a bump in the temperature spectrum in air, $Pr = 0{\cdot}72$. Thus a consistent picture emerges for the spectrum of scalar fluctuations for arbitrary ν/D.

For constant k^*/k_d, the ratio of k^* to the transitional wavenumber observed in a one-dimensional scalar spectrum is a function of ν/D and also of the location of a low-pass filter cut-off, if any. The transitional wavenumber k_1^* is defined in (17) only for asymptotically large ν/D; model 4 gives $k^*/k_1^* = 1{\cdot}98$.

The values found for k^*/k_d, namely about 0·05, have the following implications. First, values of β_1 determined from the level of the temperature spectrum in air measured in moderate Reynolds number flows may be too large owing to the presence of the bump. An accurate determination of β_1 requires the observation of an inertial–convective range in the temperature spectrum in air at wavenumbers less than about $0{\cdot}03k_d$. Second, the inertial–diffusive range for temperature fluctuations in mercury is of very limited extent; a convincing observation of the inertial–diffusive range would require $\nu/D \simeq 10^{-3}$ and a high Reynolds number flow.

Model 4 gives the best fit to the data obtained by Champagne *et al.* (1977) and by Williams & Paulson (1977). This model can then predict the shape of such spectra as the humidity spectrum, which has not been measured at high wavenumbers because of limited frequency response of the sensors. The predicted humidity spectrum and temperature–humidity co-spectrum given by Hill (1978) have a bump corresponding to that observed in temperature spectra in air. Model 4 is recommended for use in computing quantities relevant to optical and radio wave propagation in turbulent media. Such an application to optical propagation is made by Hill & Clifford (1978). An application to VHF radio wave scattering from turbulence-induced fluctuations in the *D* region ionization is made by Hill (1976).

The author thanks S. A. Bowhill, P. K. Rastogi, J. C. Wyngaard, C. A. Friehe, C. H. Gibson and J. P. Clay for their helpful discussions, and F. H. Champagne, C. A. Friehe, J. C. LaRue, R. M. Williams, C. A. Paulson, and J. P. Clay for allowing the use of their data. The author is indebted to R. M. Jones for his help with the computations. Figure 8 is taken, in part, from page 435 of the paper by Grant *et al.* (1968) and is reproduced here by permission of the Cambridge University Press. The research described was supported by NSF grant ATM-73-06485 and by the National Research Council through the Resident Research Accociateship program.

REFERENCES

Batchelor, G. K. 1959 Small-scale variation of convected quantities like temperature in turbulent fluid. Part 1. General discussion and the case of small conductivity. *J. Fluid Mech.* **5**, 113–133.

Batchelor, G. K., Howells, I. D. & Townsend, A. A. 1959 Small-scale variation of convected quantities like temperature in turbulent fluid. Part 2. The case of large conductivity. *J. Fluid Mech.* **5**, 134–139.

Boston, N. E. & Burling, R. W. 1972 An investigation of high wavenumber temperature and velocity spectra in air. *J. Fluid Mech.* **55**, 473–492.

Bugnolo, D. S. 1972 Turbulence in weakly ionized plasma. *J. Plasma Phys.* **8**, 143–158.

Champagne, F. H., Friehe, C. A., LaRue, J. C. & Wyngaard, J. C. 1977 Flux measurements, flux-estimation techniques, and fine-scale turbulence measurements in the unstable surface layer over land. *J. Atmos. Sci.* **34**, 515–530.

Clay, J. P. 1973 Turbulent mixing of temperature in water, air and mercury. Ph.D. thesis, University of California at San Diego.

Corrsin, S. 1951 On the spectrum of isotropic temperature fluctuations in isotropic turbulence. *J. Appl. Phys.* **22**, 469–473.

Corrsin, S. 1961 The reactant concentration spectrum in turbulent mixing with a first-order reaction. *J. Fluid Mech.* **11**, 407–416.

Corrsin, S. 1964 Further generalization of Onsager's cascade model for turbulent spectra. *Phys. Fluids* **7**, 1156–1159.

Garosi, G. A., Bekefi, G. & Schulz, M. 1970 Response of a weakly ionized plasma to turbulent gas flow. *Phys. Fluids* **13**, 2795–2809.

Gibson, C. H. 1968 Fine structure of scalar fields mixed by turbulence. II. Spectral theory. *Phys. Fluids* **11**, 2316–2327.

Gibson, C. H., Lyon, R. R. & Hirschsohn, I. 1970*a* Reaction product fluctuations in a sphere wake. *A.I.A.A. J.* **8**, 1859–1863.

Gibson, C. H. & Schwarz, W. H. 1963 The universal equilibrium spectra of turbulent velocity and scalar fields. *J. Fluid Mech.* **16**, 365–386.

Gibson, C. H., **Stegen**, G. R. & **Williams**, R. B. 1970*b* Statistics of the fine structure of turbulent velocity and temperature fields measured at high Reynolds number. *J. Fluid Mech.* **41**, 153–167.

Granatstein, V. L., **Levine**, A. M. & **Subramanian**, M. 1971 Laser probing of a weakly ionized turbulent gas: comparison of neutral and plasma fluctuations. *Phys. Fluids* **14**, 2581–2587.

Grant, H. L., **Hughes**, B. A., **Vogel**, W. M. & **Moilliet**, A. 1968 The spectrum of temperature fluctuations in turbulent flow. *J. Fluid Mech.* **34**, 423–492.

Hill, R. J. 1976 Small-scale fluctuations in D-region ionization due to hydrodynamic turbulence. *Aeron. Rep.* 75, Dep. Elec. Eng., University of Illinois, Urbana, IL 61801.

Hill, R. J. 1978 Spectra of fluctuations in refractivity, temperature, humidity, and the temperature-humidity cospectrum in the inertial and dissipation ranges. *Radio Science* (to be published).

Hill, R. J. & **Clifford**, S. F. 1978 The modified spectrum of atmospheric temperature fluctuations and its application to optical propagation. *J. Opt. Soc. Am.* (to be published).

Kraichnan, R. H. 1968 Small-scale structure of a scalar field convected by turbulence. *Phys. Fluids* **11**, 945–953.

Kuyel, B. & **Gruber**, S. 1973 Experimental turbulence spectra in neutral and ion components of a weakly ionized gas. *Phys. Fluids* **16**, 1842–1847.

Lee, T. D. 1952 On some statistical properties of hydrodynamical and magneto-hydrodynamical fields. *Quart. Appl. Math.* **10**, 69–74.

Leith, C. E. 1968 Diffusion approximation for turbulent scalar fields. *Phys. Fluids* **11**, 1612–1617.

Lin, S. C. & **Lin**, S. C. 1973 Study of strong temperature mixing in subsonic grid turbulence. *Phys. Fluids* **16**, 1587–1598.

Lin, J. T. 1972 Velocity spectrum of locally isotropic turbulence in the inertial and dissipation ranges. *Phys. Fluids* **15**, 205–207.

McConnell, S. 1976 The fine structure of velocity and temperature measured in the laboratory and atmospheric marine boundary layer. Ph.D. thesis, University of California, San Diego.

McKelvey, K. N., **Yieh**, H. N., **Zakanycz**, S. & **Brodkey**, R. S. 1975 Turbulent motion, mixing, and kinetics in a chemical reactor configuration. *A.I.Ch.E. J.* **21**, 1165–1176.

Mjolsness, R. C. 1975 Diffusion of a passive scalar at large Prandtl number according to the abridged Lagrangian interaction theory. *Phys. Fluids* **18**, 1393–1394.

Nye, J. O. & **Brodkey**, R. S. 1967 The scalar spectrum in the viscous-convective subrange. *J. Fluid Mech.* **29**, 151–163.

Oboukhov, A. M. 1949 Structure of the temperature field in turbulent flow. *Izv. Akad. Nauk SSSR, Ser. Geogr. i Geofiz.* **13**, 58–69.

Onsager, L. 1949 Statistical hydrodynamics. *Nuovo Cimento*, Suppl. 6, pp. 279–287.

Pao, Y. H. 1964 Statistical behavior of a turbulent multicomponent mixture with first-order reactions. *A.I.A.A. J.* **2**, 1550–1559.

Pao, Y. H. 1965 Structure of turbulent velocity and scalar fields at large wavenumbers. *Phys. Fluids* **8**, 1063–1075.

Paquin, J. E. & **Pond**, S. 1971 The determination of the Kolmogoroff constants for velocity, temperature and humidity fluctuations from second- and third-order structure functions. *J. Fluid Mech.* **50**, 257–269.

Pond, S., **Smith**, S. D., **Hamblin**, P. F. & **Burling**, R. W. 1966 Spectra of velocity and temperature fluctuations in the atmospheric boundary layer over the sea. *J. Atmos. Sci.* **23**, 376–386.

Rust, J. H. & **Sesonske**, A. 1966 Turbulent temperature fluctuations in mercury and ethylene glycol in pipe flow. *Int. J. Heat Mass Transfer* **9**, 215–227.

Schmitt, K. F., **Friehe**, C. A. & **Gibson**, C. H. 1978 Humidity sensitivity of atmospheric temperature sensors by salt contamination. *J. Phys. Ocean.* **8**, 151–161.

Williams, R. M. & **Paulson**, C. A. 1977 Microscale temperature and velocity spectra in the atmospheric boundary layer. *J. Fluid Mech.* **83**, 547–567.

Wyngaard, J. C. & **Clifford**, S. F. 1977 Taylor's hypothesis and high-frequency turbulence spectra. *J. Atmos. Sci.* **34**, 922–929.

Journal of The Optical Society of America, 68: 1067-1072, 1978.

Optical propagation in turbulent water

R. J. Hill

Wave Propagation Laboratory, Environmental Research Laboratories, National Oceanic and Atmospheric Administration, Boulder, Colorado 80302

(Received 16 December 1977)

The spectrum of optical refractive-index fluctuations caused by temperature or salinity fluctuations in turbulent water is much different from the refractive-index spectrum of temperature or humidity fluctuations in air. This occurs because the ratio of kinematic viscosity to diffusivity is much greater for temperature and salinity fluctuations in water than for temperature and humidity fluctuations in air. In turbulent water the temperature and salinity spectra have viscous-convective ranges that extend roughly one and two decades in wave number, respectively. The consequences of these viscous-convective ranges for optical propagation in water are examined. It is found that the variance of log intensity, as a function of Fresnel-zone size, rises far above its large Fresnel-zone-size asymptotic form, and the covariance function of log-amplitude is relatively narrow when the viscous-convective range dominates its shape. If the viscous-convective range dominates the shape of the structure function of phase, then the structure function is proportional to the spacing and is less sensitive to outer scale effects than for propagation in air. Likewise, the lateral coherence length has a new asymptotic form arising from a viscous-convective range and is also less sensitive to outer scale effects than for propagation in air.

I. INTRODUCTION

It was shown by Batchelor[1] on theoretical grounds that if the diffusivity D of a quantity in a fluid is much smaller than the kinematic viscosity ν of the fluid in which the quantity is being advected by turbulence, then the spatial power spectrum $\Phi(\kappa)$ of the fluctuations of that quantity should have a viscous-convective range such that $\Phi(\kappa) \propto \kappa^{-3}$. At yet higher wave numbers $\Phi(\kappa)$ has a viscous-diffusive range where it falls rapidly because of diffusion of the quantity. At wave numbers smaller than those in the viscous-convective range, $\Phi(\kappa)$ has an inertial-convective range (for high-Reynolds-number turbulence) wherein $\Phi(\kappa) \propto \kappa^{-11/3}$, as predicted by Corrsin.[2] The spectrum $\Phi(\kappa)$ decreases less rapidly in the viscous-convective range than in the inertial-convective range. For $\nu/D \gg 1$, a length scale at which diffusion of the quantity is important is Batchelor's scale $l_B = (\nu D^2/\epsilon)^{1/4}$, where ϵ is the rate of dissipation of turbulent kinetic energy per unit mass of fluid. The relationship between the Kolmogorov microscale $\eta = (\nu^3/\epsilon)^{1/4}$ and Batchelor's scale is simply $\eta = l_B(\nu/D)^{1/2}$. Therefore, $\nu/D \gg 1$ implies that $\eta \gg l_B$.

II. SPECTRA OF TEMPERATURE AND SALINITY FLUCTUATIONS IN WATER

Temperature and salinity (sodium chloride) in water have $\nu/D \simeq 7.0$ and 700, respectively. Thus the temperature and salinity spectra in water both have well-developed viscous-convective ranges. On the other hand, temperature and humidity in air have $\nu/D \simeq 0.72$ and 0.63, respectively; these spectra have only the very beginnings of a viscous-convective range.[3] In water, the viscous-convective range has been observed experimentally for temperature fluctuations by Grant *et al.*[4] and for ammonium acetate fluctuations by Gibson *et al.*[5] Other observations of the viscous-convective range are reviewed by Hill.[6]

An accurate model of $\Phi(\kappa)$ for turbulently advected quantities of arbitrary ν/D has been developed by Hill[6] (namely, his model 4). This model gives excellent agreement with the temperature spectra measured in air by Champagne *et al.*[7] and Williams and Paulson.[8] This model is used here to predict $\Phi(\kappa)$ for temperature and salinity fluctuations in water, and the spectra are presented in Figs. 1 and 2. These figures

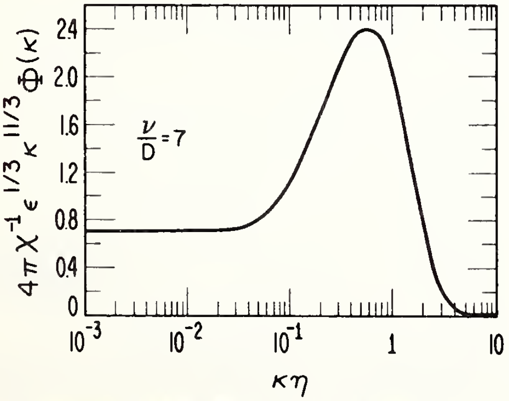

FIG. 1. Spectrum of temperature fluctuations in turbulent water.

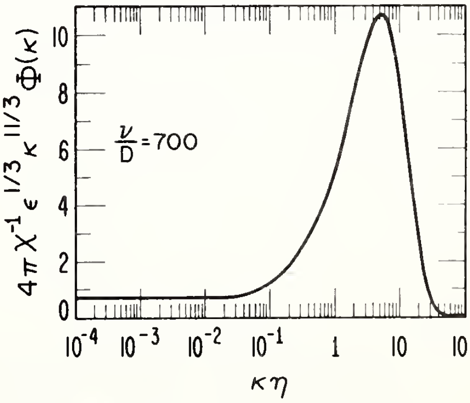

FIG. 2. Spectrum of salinity fluctuations in turbulent water.

© 1978 Optical Society of America

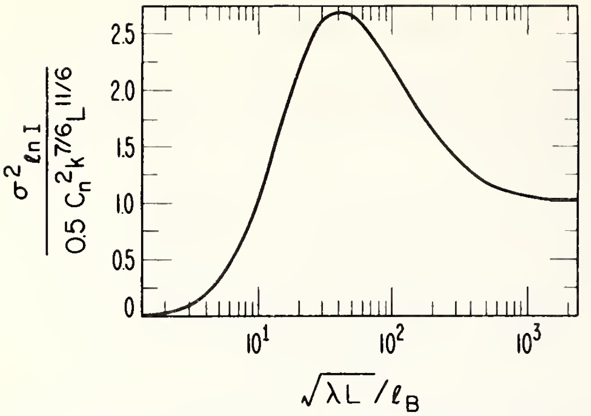

FIG. 3. Variance of log-intensity caused by temperature fluctuations in turbulent water.

show the function $F(\kappa) = 4\pi\chi^{-1}\epsilon^{1/3}\kappa^{11/3}\Phi(\kappa)$ versus scaled wave number $\kappa\eta$, χ is the rate of dissipation of mean-squared temperature fluctuations. The function $F(\kappa)$ tends to the Obukhov-Corrsin constant β in the inertial-convective range; measurements of β reviewed by Hill[6] suggest $\beta \simeq 0.72$. Thus the inertial-convective range where $\Phi(\kappa) \propto \kappa^{-11/3}$ is the flat part of the curves in Figs. 1 and 2. In the viscous-convective range where $\Phi(\kappa) \propto \kappa^{-3}$, the function $F(\kappa)$ increases as $\kappa^{2/3}$. The rising portion of the curves is the viscous-convective range. At higher wave numbers in the viscous-diffusive range the spectra fall toward zero.

III. VARIANCE OF LOG-INTENSITY AND THE COVARIANCE FUNCTION FOR OPTICAL PROPAGATION IN TURBULENT WATER

The variance of log-intensity $\sigma^2_{\ln I}$, is calculated for a spherical wave propagating through homogeneous turbulence by using Eq. (T8) of Lawrence and Strohbehn.[9] Weak refractive turbulence (i.e., unsaturated scintillation) is assumed. For sufficiently large Fresnel-zone size, $(\lambda L)^{1/2}$, the variance of log-intensity tends to satisfy

$$\sigma^2_{\ln I} \simeq 0.5\, C_n^2 k^{7/6} L^{11/6}, \qquad (1)$$

where k is the optical wave number, L is path length, λ is optical wave length, and C_n^2 is the refractive-index structure parameter.

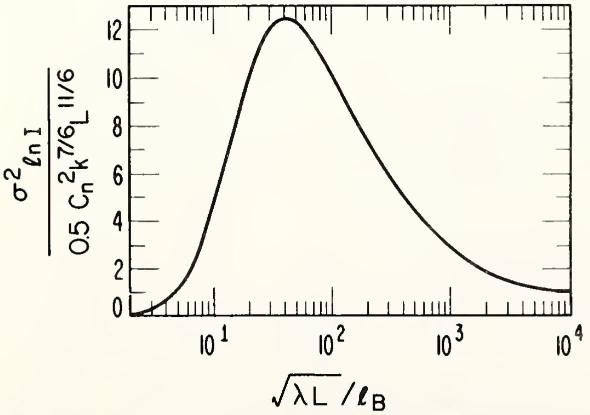

FIG. 4. Variance of log-intensity caused by salinity fluctuations in turbulent water.

The variance of log-intensity normalized by its asymptotic form [Eq. (1)] is presented as a function of $(\lambda L)^{1/2}/l_B$ in Figs. 3 and 4. Figure 3 contains the variance of log-intensity generated by temperature fluctuations in water ($\nu/D = 7.0$) as determined from the $\Phi(\kappa)$ in Fig. 1. Figure 4 presents $\sigma^2_{\ln I}$ from salinity fluctuations in water ($\nu/D = 700$) as determined from the $\Phi(\kappa)$ in Fig. 2. For large $(\lambda L)^{1/2}/l_B$, the inertial-convective range of $\Phi(\kappa)$ determines the variance of log-intensity, and the curves in Figs. 3 and 4 must tend to unity. For small $(\lambda L)^{1/2}/l_B$, the viscous-diffusive range gives the dominant contribution to $\sigma^2_{\ln I}$, and the curves in Figs. 3 and 4 must tend to zero. For the intermediate values of $(\lambda L)^{1/2}/l_B$, the variance of log-intensity is principally determined by the viscous-convective range where $\Phi(\kappa) \propto \kappa^{-3}$, and a pronounced bump in $\sigma^2_{\ln I}$ is evident in the figures. The normalized variance in Fig. 3 rises to a maximum value of about 2.7; in Fig. 4 the maximum value, about 12.5, is larger because the viscous-convective range is more extensive for salinity fluctuations than for the temperature fluctuations. For temperature fluctuations in air ($\nu/D = 0.72$) the graph analogous to Figs. 3 and 4 is given by Hill and Clifford.[10] They show that there is a bump in the variance of log-intensity for optical propagation in air; the maximum value of that bump is only about 1.3, which is much less than the case of salinity fluctuations.

Batchelor's[1] prediction for the spectrum in the viscous-convective range can be used to yield

$$\Phi_n(\kappa) = 0.033\, C_n^2 q \beta^{-1} \eta^{2/3} \kappa^{-3}. \qquad (2)$$

Batchelor's constant q arises from his definition of an effective least principal rate-of-strain parameter γ by $\gamma = -q^{-1}(\epsilon/\nu)^{1/2}$. The model spectrum used to generate Figs. 1 and 2 gives $\beta/q = 0.142$. For $\nu/D \gg 1$ and a given value of $(\lambda L)^{1/2}/l_B$ such that the variance of log-intensity is dominated by the viscous-convective range, then substituting Eq. (2) into Eq. (T8) of Lawrence and Strohbehn[9] gives

$$\sigma^2_{\ln I} = C_n^2 (kL)^{3/2}\, q \beta^{-1} \eta^{2/3} A$$

with

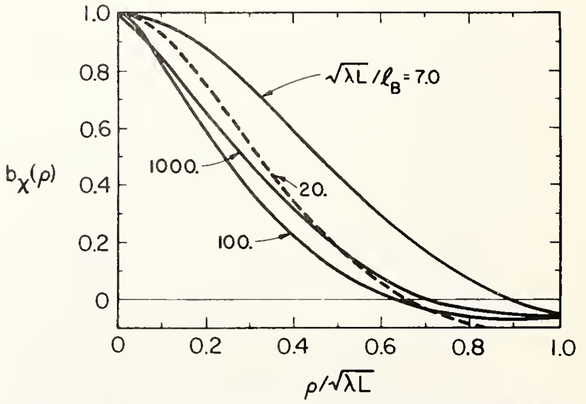

FIG. 5. Covariance function of log-amplitude from temperature fluctuations in water.

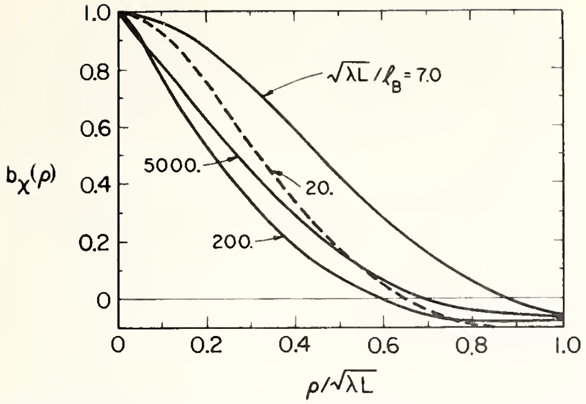

FIG. 6. Covariance function of log-amplitude from salinity fluctuations in water.

$$A = 0.066(2\pi)^{3/2} \int_0^\infty \{1 - x^{-1} [\cos(\pi x^2/2)C(x) + \sin(\pi x^2/2)S(x)]\}x^{-2}\, dx,$$

where $C(x)$ and $S(x)$ are the Fresnel integrals. Assuming that k, L, β, and A are known, then a measurement of $\sigma^2_{\ln I}$, C_n^2, and η for salinity fluctuations can give an experimental measurement of q.

The covariance functions of log-amplitude for plane waves propagating through homogeneous temperature and salinity fluctuations in water are now discussed. Weak refractive turbulence is assumed. A rapidly decreasing refractive-index spectrum gives a wider covariance function than does a slowly decreasing spectrum. Therefore, when $(\lambda L)^{1/2}/l_B$ and the spacing ρ are such that the covariance function is dominated by contributions from the viscous-convective range of the spectrum, then one expects the covariance function to be narrower than when the dominant contributions come from an inertial-convective range. For those values of $(\lambda L)^{1/2}/l_B$ and ρ such that the rapidly falling diffusive range dominates the covariance, then one expects the widest covariance functions of all.

The covariance functions of log-amplitude for plane waves are determined from the spectra in Figs. 1 and 2 and are presented in Figs. 5 and 6. In Fig. 5, the values of $(\lambda L)^{1/2}/l_B$ = 7.0, 20, 100, and 1000 correspond, respectively, to those values of $(\lambda L)^{1/2}/l_B$ for which the variance of log-intensity is dominated by the viscous-diffusive range, has a value near the peak of the bump, is dominated by the viscous-convective range, and is nearly equal to its large Fresnel-zone asymptotic form. The values of $(\lambda L)^{1/2}/l_B$ used in Fig. 6 have the same import. As expected, the covariance functions are widest for the smallest values of $(\lambda L)^{1/2}/l_B$ so that the diffusive range dominates, narrowest for the intermediate $(\lambda L)^{1/2}/l_B$ such that the viscous-convective range dominates, and are of intermediate width for the largest $(\lambda L)^{1/2}/l_B$ when the inertial-convective range dominates. When the viscous-convective range dominates, the covariance function in Fig. 5 $[(\lambda L)^{1/2}/l_B = 100]$ is slightly wider than in Fig. 6 $[(\lambda L)^{1/2} = 200]$. This is because the viscous-convective range is shorter for temperature fluctuations in water ($\nu/D = 7.0$) than for salinity fluctuations in water ($\nu/D = 700$). Even so, the narrowest covariance functions in Figs. 5 and 6 are only slightly narrower than the large-Fresnel-zone covariance functions for propagation in air.

IV. STRUCTURE FUNCTION OF PHASE FOR PLANE WAVES

The structure function of phase $D_S(\rho)$, for a plane wave propagating in homogeneous turbulence, is related to $\Phi_n(\kappa)$ by[9]

$$D_S(\rho) = 4\pi^2 k^2 L \int_0^\infty [1 - J_0(\kappa\rho)] \times [1 + (k/\kappa^2 L)\sin(\kappa^2 L/k)]\Phi_n(\kappa)\, \kappa\, d\kappa. \quad (3)$$

A normalized form of the structure function is defined by

$$\tilde{D}_S(\rho) \equiv D_S(\rho)/2.92\, C_n^2 k^2 L[(\lambda L)^{1/2}]^{5/3}.$$

For asymptotically large ρ such that $(\lambda L)^{1/2} \ll \rho$, the structure function of phase derives its form from the inertial-convective range where $\Phi_n(\kappa) \propto \kappa^{-11/3}$. In this case $\tilde{D}_S(\rho) \simeq [\rho/(\lambda L)^{1/2}]^{5/3}$, provided that outer scale effects are negligable. For ρ values such that the $\kappa^{-11/3}$ law dominates the form of $D_S(\rho)$, the outer scale effects on $D_S(\rho)$ are not negligible even for Reynolds numbers as large as those found in the atmospheric surface layer.[10,11] Consequently the $\rho^{5/3}$ power law is not expected to be observable. For sufficiently small ρ the form of $D_S(\rho)$ derives from the dissipation range of $\Phi_n(\kappa)$, in which case $D_S(\rho) \propto \rho^2$.

If $\nu/D \gg 1$ and if ρ lies between the asymptotic limits where $D_S(\rho) \propto \rho^2$ and $\rho^{5/3}$, then the form of $D_S(\rho)$ can be dominated by the viscous-convective range where $\Phi_n(\kappa) \propto \kappa^{-3}$. In this case a new power law is predicted by substituting Eq. (2) into Eq. (3), giving

$$D_S(\rho) \propto (q/\beta)C_n^2 k^2 L \eta^{2/3} \rho. \quad (4)$$

Thus, if $\nu/D \gg 1$, then $D_S(\rho) \propto \rho^2$ for small values of ρ; $D_S(\rho) \propto \rho$ for intermediate values of ρ; finally, for asymptotically large Reynolds numbers, $D_S(\rho) \propto \rho^{5/3}$ for large values of ρ.

The function $\tilde{D}_S(\rho)[\rho/(\lambda L)^{1/2}]^{-5/3}$ is given for various values of $(\lambda L)^{1/2}/l_B$ in Figs. 7 and 8 as determined from the spectra of Figs. 1 and 2. The region at large ρ where the function

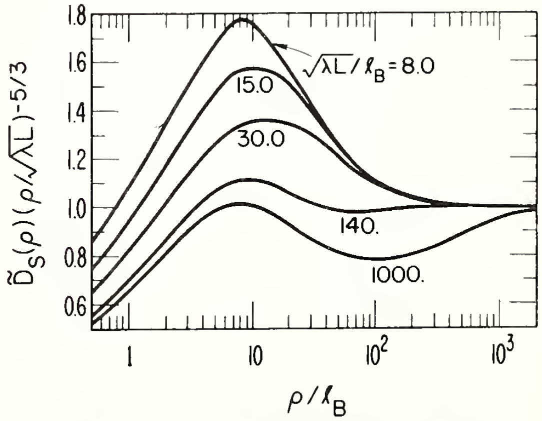

FIG. 7. Structure function of phase normalized by its large-ρ asymptotic form. Curves are computed from the spectrum of temperature fluctuations in water.

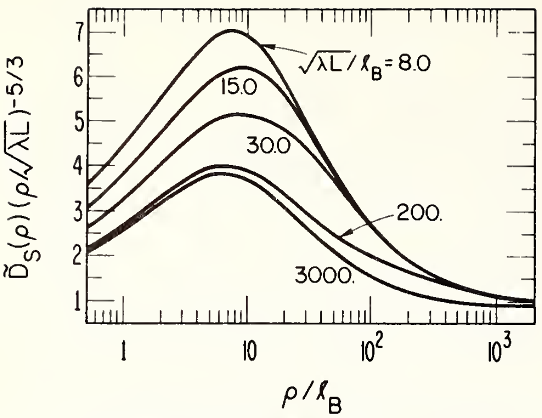

FIG. 8. Structure function of phase normalized by its large-ρ asymptotic form. Curves are computed from the spectrum of salinity fluctuations in water.

tends to unity is the $D_S(\rho) \propto \rho^{5/3}$ power law region. The $D_S(\rho) \propto \rho^2$ law is accurate for $\rho/l_B < 2.0$. The pronounced bump in the structure function of phase is, of course, caused by the viscous-convective range in the spectra. The bump is much larger in these figures, corresponding to $\nu/D = 7.0$ and 700, than the bump predicted for temperature fluctuations in air,[10] corresponding to $\nu/D = 0.72$.

In Figs. 9 and 10 the structure function, normalized by the asymptotic form in Eq. (4), is given as determined from the temperature and salinity spectra of Figs. 1 and 2, respectively. If these curves are flat at intermediate values of ρ then the power law in Eq. (4) holds. Figure 9 shows that $\nu/D = 7.0$ is not large enough for Eq. (4) to be valid. Figure 10 shows a somewhat flat portion for $\nu/D = 700$ and $20 < \rho/l_B < 200$; however, one needs $\nu/D \gg 700$ for Eq. (4) to be accurate. For small values of $(\lambda L)^{1/2}/l_B$, namely, $(\lambda L)^{1/2}/l_B = 8.0$, 15.0, and 30.0. Figure 10 shows that the constant of proportionality for Eq. (4) is approximately unity. On the other hand for large values of $(\lambda L)^{1/2}/l_B$, namely, $(\lambda L)^{1/2}/l_B = 3000$, this proportionality constant is seen to be about ½. This change in the proportionality constant by a factor of 2.0 is caused by the fact that for κ within the viscous-convective range the factor $[1 + (k/\kappa^2 L)\sin(\kappa^2 L/k)]$ in Eq. (3) changes from a value of 2.0 for small $(\lambda L)^{1/2}/l_B$ to a value oscillating about 1.0 for large $(\lambda L)^{1/2}/l_B$. For intermediate $(\lambda L)^{1/2}/l_B$, specifically $(\lambda L)^{1/2}/l_B = 200$ in Fig. 10, this factor changes from 2.0 to nearly 1.0 within the viscous-convective range.

As noted previously, the structure function of phase is sensitive to outer scale effects for optical propagation in turbulent air, $\nu/D = 0.72$. This sensitivity is greatest at large ρ, but it extends even to small values of ρ where $D_S(\rho) \propto \rho^2$.[10] The reason for this sensitivity is that for $\Phi_n(\kappa) \propto \kappa^{-11/3}$ the integrand in Eq. (3) increases as $\kappa^{-2/3}$ for small κ. If, on the other hand, $\nu/D \gg 1$ and the integrand in Eq. (3) is dominated by a viscous-convective or viscous-diffusive range then the spectrum $\Phi_n(\kappa) \propto \kappa^{-3}$ gives a much better rejection of outer scale effects than does the $\kappa^{-11/3}$ spectrum. Consequently, for $\nu/D \gg 1$ and $\rho \lesssim 10\eta$ the structure function of phase is insensitive to outer scale effects. Of course, if ρ is so large that one would have $D_S(\rho) \propto \rho^{5/3}$ for asymptotically large Reynolds numbers, then the structure function is sensitive to outer scale effects if $\nu/D \gg 1$ because the spectrum $\Phi_n(\kappa) \propto \kappa^{-11/3}$ dominates the structure function.

V. COHERENCE LENGTH FOR PLANE WAVES

The coherence length ρ_0 is the length transverse to the propagation direction over which the phase is coherent. For plane waves, ρ_0 is obtained from

$$1 = 4\pi^2 k^2 L \int_0^\infty [1 - J_0(\kappa\rho_0)]\Phi_n(\kappa)\,\kappa\,d\kappa. \qquad (5)$$

The coherence length depends on the parameter $Y_B \equiv k^2 L C_n^2 l_B^{5/3}$ as well as on the parameters that govern the shape of $\Phi_n(\kappa)$, e.g., ν/D and the outer scale. If Y_B is small then $\Phi_n(\kappa)$ may be approximated as being proportional to $\kappa^{-11/3}$ providing the outer scale is very large; in this case, Yura[12] shows that ρ_0 is proportional to $\rho_1 \equiv (k^2 C_n^2 L)^{-3/5}$. If Y_B is so large that the dissipation range of $\Phi_n(\kappa)$ dominates in Eq. (5) then ρ_0 is proportional to[12] $\rho_2 \equiv [k^2 L C_n^2 l_B^{-1/3}]^{-1/2}$. If Y_B has an intermediate value and if $\nu/D \gg 1$, then $\Phi_n(\kappa)$ may be approximated by its viscous-convective range formula in Eq. (2).

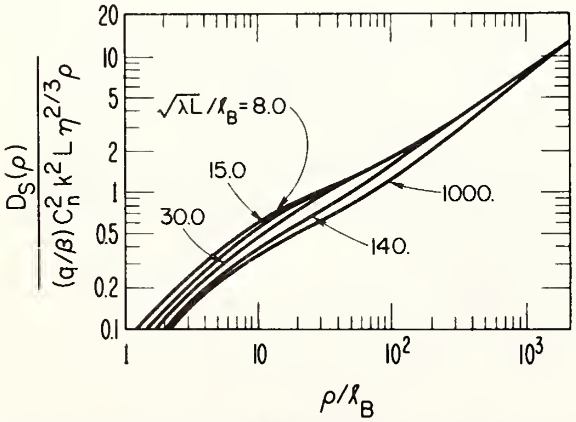

FIG. 9. Structure function of phase normalized by the asymptotic expression in Eq. (4). Curves are computed from the spectrum of temperature fluctuations in water.

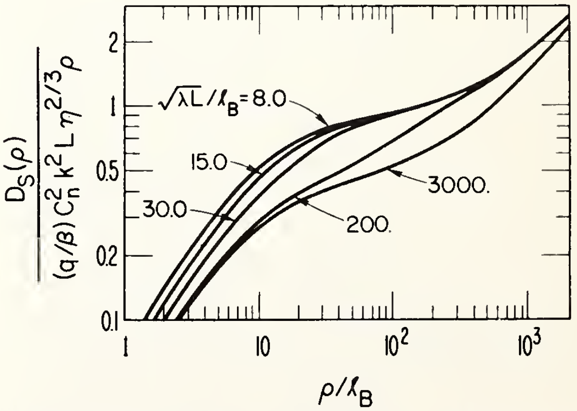

FIG. 10. Structure function of phase normalized by the asymptotic expression in Eq. (4). Curves are computed from the spectrum of salinity fluctuations in water.

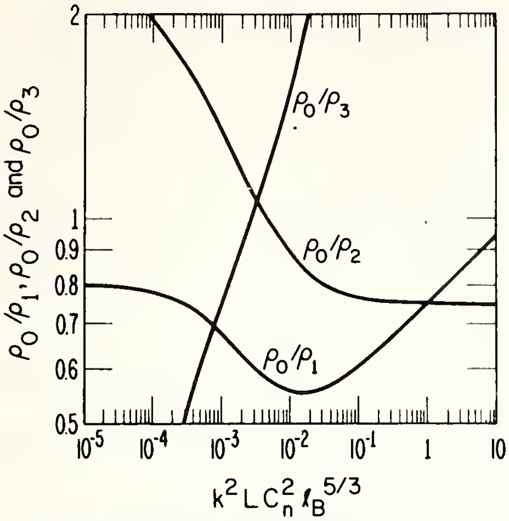

FIG. 11. Coherence length ρ_0 scaled by the asymptotic forms ρ_1, ρ_2, and ρ_3 for plane waves propagating in temperature fluctuations in water.

Substitution of Eq. (2) into Eq. (5) gives a new asymptotic form for the coherence length, namely

$$\rho_3 \equiv 0.77\, \beta q^{-1}[k^2LC_n^2\eta^{2/3}]^{-1}.$$

The coherence length scaled by the three asymptotic forms ρ_1, ρ_2, and ρ_3 is presented in Figs. 11 and 12 as determined from the temperature fluctuation spectrum in Fig. 1 and from the salinity fluctuation spectrum in Fig. 2. The regions in Figs. 11 and 12 where the curves are flat gives the values of Y_B for which the asymptotic forms are valid. It is seen that the ρ_0/ρ_1 curves are flat for small Y_B, and the ρ_0/ρ_2 curves are flat for large Y_B. For temperature fluctuations in water (ν/D = 7.0), Fig. 11 shows that ρ_0/ρ_3 is not constant for any Y_B. For salinity fluctuations in water (ν/D = 700), Fig. 12 has a ρ_0/ρ_3 curve that bends toward becoming constant. Therefore, in order to have a range of Y_B in which $\rho_0 \propto \rho_3$ one needs ν/D much larger than 700 so that the viscous-convective range in $\Phi_n(\kappa)$ is much more extensive than for salinity fluctuations.

For the coherence length, the viscous-convective range, where $\Phi_n(\kappa) \propto \kappa^{-3}$, gives a better rejection of outer scale effects than does the inertial-convective range where $\Phi_n(\kappa) \propto \kappa^{-11/3}$. This same effect was noted for the structure function of phase in the previous section. In the case of temperature fluctuations in air (ν/D = 0.72), $\Phi_n(\kappa)$ has no viscous-convective range; the spectrum only just begins to enter a viscous-convective range before diffusion causes the spectrum to decrease. For the case of air, Hill and Clifford[10] show that the coherence length is affected by the outer scale even for large $k^2LC_n^2l_0^{5/3}$, where l_0 the inner scale for temperature fluctuations in air. On the other hand, for $\nu/D \gg 1$ and for large Y_B where $\rho_0 \propto \rho_2$, the coherence length is insensitive to the outer scale because of the existence of an extensive viscous-convective range.

The propagation distance Z_B at which $\rho_0 = l_B$ is now determined. Now $\rho_0 = l_B$ implies $\rho_0/\rho_2 = (k^2Z_BC_n^2l_B^{5/3})^{1/2}$, and the ρ_0/ρ_2 curves on Figs. 11 and 12 may be read to give

$$Z_B = 0.57(k^2C_n^2l_B^{5/3})^{-1}$$

for ν/D = 7.0, and

$$Z_B = 0.135(k^2C_n^2l_B^{5/3})^{-1}$$

for ν/D = 700.

VI. CONCLUSIONS

The spectrum of refractive-index fluctuations is different in different fluids. The spectrum is also different if different quantities (e.g., temperature versus salinity) are responsible for refractive index fluctuations within the same fluid (e.g., water). The implications for optical propagation through temperature and salinity fluctuations in water are discussed in this paper. However, the same type of propagation effects can occur in other fluids. For instance, $\nu/D \simeq 5 \times 10^3$ for temperature fluctuations in glycerine; consequently the variance of log-intensity and structure function of phase would have even larger bumps from temperature fluctuations in glycerine than for salinity fluctuations in water (ν/D = 700). On the other hand, $\nu/D \simeq 18$ for temperature fluctuations in ethanol. Consequently, the corresponding curves for variance of log-intensity, covariance function of log-amplitude, structure function of phase, and coherence length would lie between the curves depicted here for temperature (ν/D = 7.0) and salinity (ν/D = 700) fluctuations in water. Because of the variability of the spectrum of refractive-index fluctuations for different fluids and different advected quantities, optical propagation through different fluids and advected quantities can be used as a testing ground for the theory of optical propagation in turbulent media as well as for the theory of turbulent advection. In fact, it is suggested that measurement of the variance of log-intensity can be used to determine Batchelor's constant if $\nu/D \gg 1$.

The spectrum of refractive-index fluctuations can have an even more unusual behavior than that portrayed in Figs. 1 and 2 if more than one quantity is involved in determining the

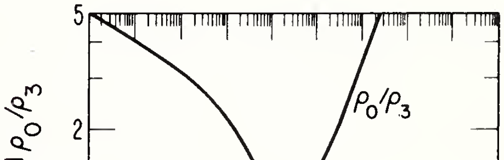

FIG. 12. Coherence length ρ_0 scaled by the asymptotic forms ρ_1, ρ_2, and ρ_3 for plane waves propagating in salinity fluctuations in water.

refractive-index fluctuations. Consider, for instance, turbulent water containing both temperature and salinity fluctuations. Suppose that $C_T^2 \gg C_S^2$, where C_S^2 is the structure parameter of salinity fluctuations. Then the refractive-index spectrum can be dominated by the temperature spectrum for $\kappa\eta \lesssim 2.0$ but be dominated by the salinity spectrum for $\kappa\eta \gtrsim 2.0$. In this event the refractive-index spectrum, when graphed as in Figs. 1 and 2, can have a double-bump appearance, and the variance of log-intensity, when plotted as in Figs. 3 and 4, can also have a double-bump appearance. Clearly, the interpretation of optical propagation experiments in turbulent water and other fluids requires the ability to predict the shape of the spectra of advected quantities.

ACKNOWLEDGMENT

This research was supported by the National Research Council through the Resident Research Associateship Program.

[1] G. K. Batchelor, "Small-scale variation of convected quantities like temperature in turbulent fluid, Part I, General discussion and the case of small conductivity," J. Fluid Mech. **5**, 113–133 (1959).

[2] S. Corrsin, "On the spectrum of isotropic temperature fluctuations in isotropic turbulence," J. Appl. Phys. **22**, 469–473 (1951).

[3] R. J. Hill, "Spectra of fluctuations in refractivity, temperature, humidity, and the temperature-humidity cospectrum in the inertial and dissipation ranges," Radio Sci. (to be published).

[4] H. L. Grant, B. A. Hughes, W. M. Vogel, and A. Moilliet, "The spectrum of temperature fluctuations in turbulent flow," J. Fluid Mech. **34**, 423–492 (1968).

[5] C. H. Gibson, R. R. Lyon, and I. Hirschsohn, "Reaction product fluctuations in a sphere wake," AIAA J. **8**, 1859–1863 (1970).

[6] R. J. Hill, "Models of the scalar spectrum for turbulent advection," J. Fluid Mech. (to be published).

[7] F. H. Champagne, C. A. Friehe, J. C. LaRue, and J. C. Wyngaard, "Flux measurements, flux-estimation techniques, and fine-scale turbulence measurements in the unstable surface layer over land," J. Atmos. Sci. **34**, 515–530 (1977).

[8] R. M. Williams, Jr. and C. A. Paulson, "Microscale temperature and velocity spectra in the atmospheric boundary layer," J. Fluid Mech. **83**, 547–567 (1977).

[9] R. S. Lawrence and J. W. Strohbehn, "A survey of clear-air propagation effects relevant to optical communications," Proc. IEEE **58**, 1523–1545 (1970).

[10] R. J. Hill and S. F. Clifford, "The modified spectrum at atmospheric temperature fluctuations and its application to optical propagation," J. Opt. Soc. Am. **68**, 892–899 (1978).

[11] A. Consortini, L. Ronchi, and E. Moroder, "Role of the outer scale of turbulence in atmospheric degradation of optical images," J. Opt. Soc. Am. **63**, 1246–1248 (1973).

[12] H. T. Yura, "Optical beam spread in a turbulent medium: effect of the outer scale of turbulence," J. Opt. Soc. Am. **63**, 107–109 (1973).

Journal of The Optical Society of America, 68: 892-899, 1978.

Modified spectrum of atmospheric temperature fluctuations and its application to optical propagation

R. J. Hill and S. F. Clifford

Wave Propagation Laboratory, Environmental Research Laboratories, National Oceanic and Atmospheric Administration, Boulder, Colorado 80302

(Received 8 December 1977)

Recent experiments reveal the high-wave-number form of the power spectrum of temperature fluctuations in turbulent flow. It is precisely this high-wave-number portion of the temperature spectrum that strongly affects optical propagation in the atmosphere. An accurate model of the spectra of advected quantities, such as temperature, has been developed and is applied here to optical propagation. An outstanding feature of the model and the observed temperature spectrum is a "bump" at high wave numbers. The accurate model of the temperature spectrum is used to compute the temperature structure function, the variance of log intensity as a function of Fresnel-zone size, the covariance function of log amplitude, the structure function of phase, as well as the phase coherence length. These results are compared with the predictions of Tatarskii's spectrum. The bump in the temperature spectrum produces a corresponding bump in the temperature structure function, the variance of log intensity, and the structure function of phase. The accurate model is also used to determine the shape of the structure function of aerosol concentration fluctuations; it is found that this structure function varies as the logarithm of the separation distance for small separations.

I. INTRODUCTION

Accurate measurements of the spatial power spectrum of temperature fluctuations in the atmospheric surface layer have been performed by Champagne *et al.*[1] and by Williams and Paulson.[2] These measurements reveal that at high wave numbers the temperature spectrum decreases less rapidly than predicted by the $\kappa^{-11/3}$ law of Oboukhov[3] and Corrsin[4]; of course, at yet higher wave numbers the temperature spectrum decreases rapidly due to the diffusion of heat. Several theoretical models of the scalar transfer spectrum for quantities advected by turbulent flow have been developed by Hill.[5] When applied to temperature fluctuations in air, one of these models is in excellent agreement with the data of Champagne *et al.*[1] and of Williams and Paulson.[2] There now exists an accurate model of the temperature spectrum for use in calculating quantities relevant to optical propagation through turbulence. Moreover, the scalar spectral model is capable of predicting the form of such spectra as the humidity spectrum and the temperature-humidity cospectrum. Hill[6] uses the predicted forms of the temperature spectrum, humidity spectrum, and the temperature-humidity cospectrum to predict the form of the spectrum of refractive index fluctuations.

Our knowledge of temperature fluctuations in turbulent flow has undergone recent advances from both the experimental and theoretical standpoints. The purpose of this paper is to present the implications of these recent advances to optical propagation through the turbulent atmosphere. It is assumed that the refractive index fluctuations are due entirely to temperature fluctuations.

The notation we use is as follows: $B_\chi(\rho)$, covariance func-

0030-3941/78/6807-0892$00.50

© 1978 Optical Society of America

tion of log amplitude; C_n^2, refractive-index structure parameter; C_T^2, temperature structure parameter; $D_s(r)$, structure function of an advected scalar having arbitrary ν/D; $D_T(r)$, temperature structure function; $D_S(\rho)$, structure function of phase; $\tilde{D}_S(\rho)$, normalized structure function of phase defined by Eq. (11); D, diffusivity, in particular that of heat in air; $k = 2\pi/\lambda$, optical wave number; L, path length; l_0, inner scale for temperature fluctuations in air, defined by Eq. (4); $\mathrm{Pr} \equiv \nu/D$, Prandtl number, $\mathrm{Pr} = 0.72$ for air; r, spatial separation; Z_i, propagation distance at which $\rho_0 = l_0$; $\beta \simeq 0.72$, Obukhov-Corrsin constant for the inertial-convective range; ε, rate of dissipation of turbulent kinetic energy; $\eta \equiv (\nu^3/\varepsilon)^{1/4}$, Kolmogorov microscale; κ, spatial wave number; $\kappa_m \equiv 5.92/l_0$; $\tilde{\kappa} \equiv \kappa l_0$, dimensionless spatial wave number; λ, optical wavelength; ν, kinematic viscosity; ρ, spatial separation parallel to the wave front; ρ_0, lateral coherence length; $\rho_1 \equiv (k^2 C_n^2 L)^{-3/5}$; $\rho_2 \equiv [kL^{1/2}(C_n^2)^{1/2} l_0^{-1/6}]^{-1}$; $\sigma_{\ln I}^2$, variance of log intensity; $\tilde{\sigma}_{\ln I}^2$, variance of log intensity normalized by its large-Fresnel-zone asymptotic formula; $\Phi_n(\kappa)$, three-dimensional spatial power spectrum of refractive index fluctuations; $\Phi_s(\kappa)$, three-dimensional spatial power spectrum for a scalar having arbitrary ν/D; $\Phi_T(\kappa)$, three-dimensional spatial power spectrum of temperature fluctuations; $\tilde{\Phi}_T(\kappa) \equiv 4\pi\chi^{-1}\varepsilon^{1/3}\eta^{-11/3}\Phi_T(\kappa)$, dimensionless form of $\Phi_T(\kappa)$; χ, rate of dissipation of temperature variance.

II. SPECTRUM OF TEMPERATURE FLUCTUATIONS

In the inertial-convective range the three-dimensional spatial power spectrum of temperature fluctuations is

$$\Phi_T(\kappa) = (4\pi)^{-1}\beta\chi\varepsilon^{-1/3}\kappa^{-11/3}, \tag{1}$$

where χ is the rate of dissipation of mean-squared temperature fluctuations and ε is the rate of viscous dissipation of turbulent kinetic energy per unit mass of fluid. The measurements of the Obukhov-Corrsin constant β are reviewed by Hill,[5] and the value $\beta = 0.72$ is recommended. In the absence of observational support, Tatarskii[7] assumed that the temperature spectrum in the inertial-convective and dissipation ranges could be represented by

$$\Phi_T(\kappa) = (4\pi)^{-1}\beta\chi\varepsilon^{-1/3}\kappa^{-11/3}\exp(-\kappa^2/\kappa_m^2), \tag{2}$$

which is simply Eq. (1) with a Gaussian cutoff at high wave numbers.

The inertial-convective range [Eq. (1)] is just one of four high-wave-number ranges that are possible for scalar quantities (e.g., temperature, humidity, salinity) advected by high-Reynolds-number turbulence. If the diffusivity D is much smaller than the kinematic viscosity ν, then there is a range of wave numbers where viscosity is important to the energy spectrum but convection, not diffusion, is important to the scalar spectrum; this range is called the viscous-convective range. At yet higher wave numbers diffusion causes the scalar spectrum to decrease rapidly; this is the viscous-diffusive range. On the other hand, if $D \gg \nu$ then diffusion reduces the scalar spectrum at wave numbers within the inertial range of the energy spectrum; this is termed the inertial-diffusive range.

Batchelor[8] predicted that the spatial power spectrum has a κ^{-3} power law in the viscous-convective range, which is less rapidly decreasing than the $\kappa^{-11/3}$ power law for the inertial-convective range [Eq. (1)]. Batchelor's prediction has been verified experimentally by Grant *et al.*[9] and Gibson *et al.*[10] A review of the theory and experiment on scalar advection is given by Hill.[5]

Experiments have consistently shown[5] that the transition from the inertial-convective to viscous-convective range occurs at a relatively low wave number of about $0.054/\eta$, where $\eta = (\nu^3/\varepsilon)^{1/4}$ is the Kolmogorov microscale. This implies that even for temperature fluctuations in air, where ν/D is only 0.72, the spectrum $\Phi_T(\kappa)$ will just begin to enter a viscous-convective range before it is cut down by diffusion at yet higher wave numbers. It will be shown that this effect gives rise to a bump in the spectrum of temperature fluctuations in air.

Several models of the scalar spectrum have been developed by Hill[5] These models are applicable for arbitrary ν/D and are well behaved in all four of the high-wave-number ranges (i.e., the inertial-convective, inertial-diffusive, viscous-convective, and viscous-diffusive ranges). In particular these models have the $\kappa^{-11/3}$ power law in the inertial-convective range and the κ^{-3} power law in the viscous-convective range. An accurate model of the spectrum of fluctuations of advected quantities in high-Reynolds-number turbulence is generated by solving the following second-order, linear, homogeneous differential equation (model 4 of Hill[5]):

$$\frac{d}{d\kappa} H(\kappa) \frac{d}{d\kappa} \Phi_T(\kappa) = 2D\kappa^4\Phi_T(\kappa), \tag{3a}$$

$$H(\kappa) = (3/11)\beta^{-1}\varepsilon^{1/3}\kappa^{14/3}[(\kappa/\kappa^\dagger)^{2b} + 1]^{-1/(3b)}, \tag{3b}$$

$$\kappa^\dagger = 0.072/\eta, \quad b = 1.9. \tag{3c}$$

This model is called a diffusion model and reduces to Leith's diffusion approximation[11] in the inertial-convective and inertial-diffusive ranges and it reduces to Kraichnan's model[12] in the viscous-convective and viscous-diffusive ranges. When applied to temperature fluctuations in air, Eqs. (3a), (3b), and (3c) produce a temperature spectrum that is in excellent agreement[5] with the measured temperature spectrum of Champagne *et al.*[1] The choice of the parameters $\kappa^\dagger$ and b in Eq. (3c) arises from comparing the model with the data of Champagne *et al.*[1]; $\kappa^\dagger$ parameterizes the position and b parameterizes the width of the transition between the inertial-convective and viscous-convective ranges for $\nu \gg D$.

In Fig. 1 we plot $4\pi\chi^{-1}\varepsilon^{1/3}\kappa^{11/3}\Phi_T(\kappa)$ as a function of the scaled wave number $(\kappa\eta)$. The solid curve is the accurate model spectrum from Eq. (3a) whereas the dashed curve is the Tatarskii model from Eq. (2). The outstanding feature illustrated in Fig. 1 is the pronounced bump in the temperature spectrum which is not represented by the Tatarskii spectrum. This spectral bump is present in the data obtained by Champagne *et al.*[1] and by Williams and Paulson.[2] The bump is interpreted by Hill[5] as being the beginning of a viscous-convective range at lower wave numbers than the wave numbers at which diffusion strongly decreases the temperature spectrum. Reference to Eq. (1) shows that the curves in Fig. 1 must tend to the constant β for wave numbers in the inertial-convective range. The curves in Fig. 1 are universal in the sense that they do not change with changes in χ or ε (i.e., with changes in C_T^2). The immediate implication of the bump in the temperature spectrum is that there is enhanced optical

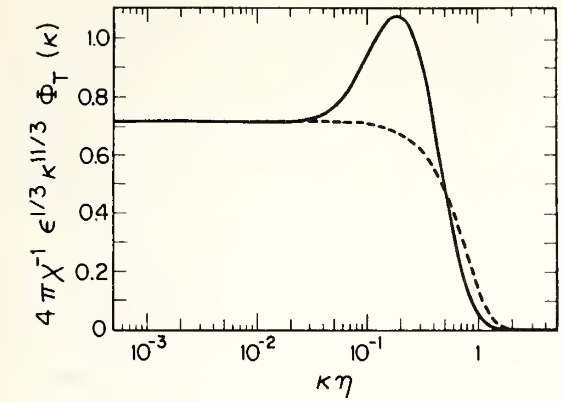

FIG. 1. Spatial power spectrum Φ_T of temperature fluctuations in air ($\nu/D = 0.72$). The solid curve is the accurate model; the dashed curve is the Tatarskii model.

scintillation when the Fresnel zone size lies at a length scale corresponding to the bump.

Hill[6] uses the model in Eqs. (3a), (3b), and (3c) to show that the spectrum of humidity fluctuations and the temperature-humidity cospectrum also have a bump. Hill[6] uses the model temperature and humidity spectra and the temperature-humidity cospectrum to predict the high-wave-number shape of the refractivity spectrum. The refractivity spectrum then also has a bump. In the following it is assumed that temperature fluctuations dominate the refractivity fluctuations for optical wavelengths and the contribution of humidity fluctuations is neglected.

III. TEMPERATURE STRUCTURE FUNCTION, THE INNER SCALE AND MICROSCALE

The inner scale l_0 is defined as the spacing r at which the large-r and small-r asymptotic forms of the temperature structure function are equal, thus

$$C_T^2 l_0^{2/3} \equiv (\chi/6D) l_0^2. \tag{4}$$

The relationship between the structure function $D_T(r)$ and the spectrum $\Phi_T(\kappa)$ is

$$D_T(r) = 8\pi \int_0^\infty \left(1 - \frac{\sin(\kappa r)}{\kappa r}\right) \Phi_T(\kappa)\kappa^2\, d\kappa. \tag{5}$$

Substitution of the inertial-convective range form for Φ_T gives the relationship between C_T^2 and the dissipation rates

$$C_T^2 = (9/10)\Gamma(1/3)\beta\chi\epsilon^{-1/3}, \tag{6}$$

where Γ is the gamma function. Then Eqs. (4) and (6) give the ratio

$$\begin{aligned} l_0/\eta &= [27\beta\Gamma(1/3)/5\ \mathrm{Pr}]^{3/4} \qquad (7)\\ &= 7.4 \quad \text{for air.} \end{aligned}$$

An expression equivalent to Eq. (7) is given by Tatarskii.[13] The Kolmogorov microscale η can be measured by a determination of ϵ; then Eq. (7) gives l_0.

The purpose of defining l_0 by Eq. (4) is that l_0 is a measure of the spacing at which $D_T(r)$ begins to decrease because of the diffusion of heat. Batchelor[8] showed that for $\nu/D \ll 1$ the length scale at which diffusion is important is Corrsin's scale $l_C = (D^3/\epsilon)^{1/4}$. Equation (7) gives l_0 proportional to l_C

$$l_0 = [27\beta\Gamma(1/3)/5]^{3/4} l_C = 5.4 l_C.$$

For $\nu/D \gg 1$, Batchelor[8] showed that the appropriate diffusion length scale is Batchelor's scale $l_B = (D^2\nu/\epsilon)^{1/4}$. If $\nu/D \gg 1$, then $l_0 \ll l_B$. Thus l_0 is not an appropriate diffusion length scale if $\nu/D \gg 1$, two cases being temperature fluctuations in water $\nu/D \simeq 8$ and salt fluctuations in water $\nu/D \simeq 700$. The reason that l_0 is not appropriate for $\nu/D \gg 1$ is that the viscous-convective range lies at length scales intermediate to those where the structure function varies as $r^{2/3}$ and r^2; in this case Eq. (4) is not an appropriate definition of a diffusion length scale.

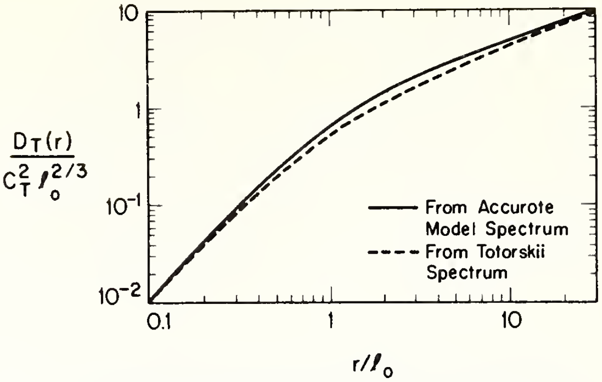

FIG. 2. Temperature structure function from both the accurate model spectrum and the Tatarskii spectrum.

Equation (5) can be used to compute the structure function from the model spectra Φ_T. Figure 2 presents the structure functions for temperature fluctuations in air determined from both the accurate model spectrum and from Tatarskii's model. The bump in the temperature spectrum produces correspondingly larger values of D_T for r near $2l_0$, than D_T calculated from Tatarskii's spectrum. Figure 2 shows that the inertial-convective range where $D_T(r) \propto r^{2/3}$ lies at $r \gtrsim 20l_0$.

For laboratory experiments of typically modest Reynolds number the outer scale effects are important at spacings of roughly $20l_0$. In this case, one does not expect to see a range where $D_T(r) \propto r^{2/3}$. In order to simulate outer scale effects for a modest Reynolds number experiment, the structure

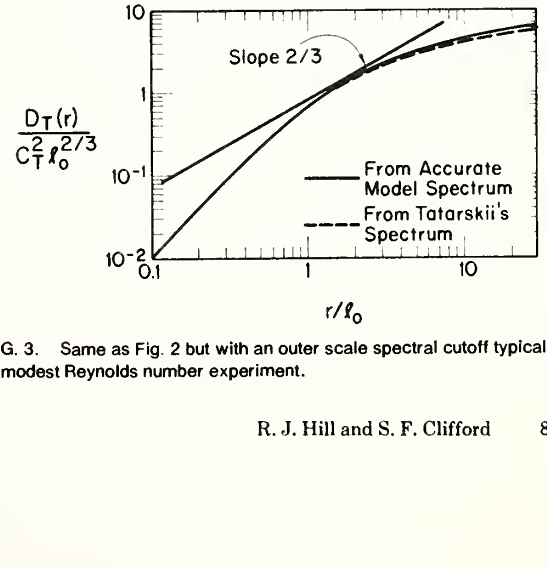

FIG. 3. Same as Fig. 2 but with an outer scale spectral cutoff typical of a modest Reynolds number experiment.

function is calculated by multiplying the spectra in Fig. 1 by an *ad hoc* outer scale cutoff given by $\exp[-(10^{-2}/\kappa\eta)^2]$. The resulting D_T is presented in Fig. 3. At modest Reynolds numbers D_T approaches a constant for $r \gtrsim 20 l_0$ and becomes tangent to the $r^{2/3}$ law near $r = 2l_0$. Given some scatter in the data, if the data are plotted on a notoriously insensitive log-log plot with a straight line of slope 2/3 superimposed, then the data appear to have an $r^{2/3}$ behavior. However, this is just an illusion since the structure function is merely passing tangent to the 2/3 slope. High-Reynolds-number turbulence is needed to observe a true inertial-convective range.

IV. STRUCTURE FUNCTION OF AEROSOL CONCENTRATION FLUCTUATIONS

In the viscous-convective range the scalar spectrum has the κ^{-3} power law, but the corresponding viscous-convective range in the structure function is surprisingly not a power law in r. If the κ^{-3} power law is substituted into Eq. (5) then the structure function is seen to be independent of r, (i.e., it is a constant); however, the remaining integral is logarithmically divergent at large wave numbers. Therefore, the form of the structure function in the viscous-convective range depends on the form of the spectrum in both the viscous-convective and viscous-diffusive ranges. Thus the structure function is not independent of r in the viscous-convective range; its dependence on r depends on the dissipation range of the spectrum.

The model spectrum from Eqs. (3a), (3b), and (3c) can be used to generate a structure function of a scalar quantity $D_s(r)$ for arbitrary ν/D. The limiting form of the structure function in the viscous-convective and viscous-diffusive ranges can be obtained from the asymptotic solutions of Eqs. (3a), (3b), and (3c). For a viscous-convective and viscous-diffusive range we need $\kappa \gg \kappa^\dagger$ and $\nu \gg D$ in which case the solution of Eqs. (3a), (3b), and (3c) reduces to

$$\Phi_s(\kappa) = (5\chi/4\pi\Lambda)\kappa^{-3}(1 + \kappa l_s)\exp(-\kappa l_s),$$

where

$$\Lambda \equiv (45/11\beta)(\kappa^\dagger\eta)^{2/3}(\epsilon/\nu)^{1/2} = 1.0\,(\epsilon/\nu)^{1/2}$$

and

$$l_s \equiv (22\beta/3)^{1/2}(\kappa^\dagger\eta)^{-1/3}l_B = 5.5 l_B.$$

The length scales l_s and l_B are length scales at which diffusion is important. From Eq. (5) the viscous-convective and viscous-diffusive ranges in the structure function are given by

$$D_s(r) = \frac{10\chi}{\Lambda}\int_0^\infty \left(1 - \frac{\sin(ur/l_s)}{ur/l_s}\right)(1+u)u^{-1}e^{-u}\,du$$
$$= (5\chi/\Lambda)\ln[1 + (r/l_s)^2].$$

For r in the viscous-diffusive range, i.e., $r \ll l_s$, then power series expansion of the logarithm gives $D_s(r) \propto r^2$, as is expected from Eq. (5) when the sine function is expanded in power series. In the viscous-convective range $l_s \ll r \ll (\kappa^\dagger)^{-1}$, so $(r/l_s)^2 \gg 1$ and $D_s(r) \propto \ln(r/l_s)$. Thus the structure function for $\nu/D \gg 1$ varies as $r^{2/3}$ in the inertial-convective range $[r \gg (\kappa^\dagger)^{-1}]$, changes to logarithmically decreasing in the viscous-convective range ($l_s \ll r \ll (\kappa^\dagger)^{-1}$), and changes once again to the r^2 power law in the viscous-diffusive range ($r \ll l_s$).

Fluctuations in the concentration of aerosol particles are responsible, in part, for variations in the scattered intensity of light propagating in turbulent media. The structure function of aerosol concentration fluctuations has been measured by Post and Lerfald[14] using optical methods. The structure function of aerosol concentration fluctuations is not the only quantity needed to describe the variations in scattered power since spatial fluctuations in the size distribution and particle concentration also effect the scattered power.

Aerosols are an example of a very slowly diffusing quantity (i.e., $D \ll \nu$). Therefore, aerosol concentration fluctuations will exhibit a viscous-convective range at small length scales. We estimate that $\nu/D \simeq 10^7$ for a particle having a radius of 1 μm; this estimate is based on the elastic spheres approximation for collisions of the particles with air molecules. Then the length scale l_s is roughly $2 \times 10^{-4} l_0$. If $l_0 \simeq 1$ cm then l_s is roughly the particle diameter, namely 2 μm. Of course, this diffusion length scale is meaningless since the interparticle spacing is much larger, and the aerosols cannot be treated as a continuum on length scales smaller or on the order of the interparticle spacing. For 10^3 particles per cubic centimeter the interparticle spacing is 0.1 cm.

It is now simple to predict the shape of the structure function of aerosol concentration fluctuations. For $r > 10^2 l_0$, the aerosol structure function varies as $r^{2/3}$; whereas for $r < 10 l_0$, but greater than the interparticle spacing, the aerosol structure function behaves as $\ln(r)$. For r less than the interparticle spacing the aerosol structure function is undefined. For $10 l_0 < r < 10^2 l_0$ the aerosol structure function makes a transition between the $r^{2/3}$ and $\ln(r)$ forms. The spacings $10 l_0$ and $10^2 l_0$, which mark the limits of validity of the asymptotic forms $r^{2/3}$ and $\ln(r)$, were found by calculations of the structure function for $\nu/D \gg 1$ using the model in Eqs. (3a), (3b), and (3c).

V. VARIANCE OF LOG INTENSITY

For a spherical wave propagating through homogeneous turbulence the variance of log intensity is given by Eq. (T8) of Lawrence and Strohbehn[15]

$$\sigma^2_{\ln I} = 8\pi^2 k^2 L \int_0^\infty F(x)\Phi_n(\kappa)\kappa\,d\kappa,$$

where

$$F(x) = 1 - x^{-1}\,[\cos(\pi x^2/2)C(x) + \sin(\pi x^2/2)S(x)]$$

and

$$x = (\kappa^2 L/2\pi k)^{1/2},$$

where L is the path length, $k = 2\pi/\lambda$, λ is the optical wavelength, and $C(x)$ and $S(x)$ are the Fresnel integrals. These expressions assume point apertures and weak refractive turbulence, i.e., unsaturated scintillation.

For asymptotically large Fresnel zone size, $\sqrt{\lambda L}/l_0 \gg 1$, the variance of log intensity becomes

$$\sigma^2_{\ln I} = A C_n^2 k^{7/6} L^{11/6}, \qquad (8)$$

where $A = 0.50$ for spherical waves and $A = 0.123$ for plane waves. A convenient normalized variance is $\tilde{\sigma}^2_{\ln I}$ given by

$$\tilde{\sigma}^2_{\ln I} = \sigma^2_{\ln I}/[A C_n^2 k^{7/6} L^{11/6}].$$

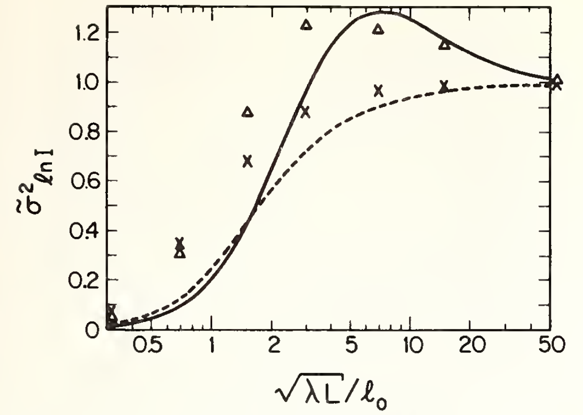

FIG. 4. Variance of log intensity for negligible saturation. Solid curve: spherical waves, accurate model; dashed curve: spherical waves, Tatarskii model; Δ: plane waves, accurate model; X: plane waves, Tatarskii model.

The normalized variance is given in Fig. 4 as a function of $\sqrt{\lambda L}/l_0$ for both spherical and plane waves. For plane waves the formula for the variance of log intensity is four times Eq. (9) (see Sec. VI) evaluated at $\rho = 0$. The normalized variance tends to unity for $\sqrt{\lambda L} \gg l_0$. For small $\sqrt{\lambda L}/l_0$ the variance is dominated by the dissipation range of Φ_T and the variance is consequently small. For increasing $\sqrt{\lambda L}/l_0$ the variance obtains contributions from progressively lower wave numbers where Φ_T is larger. The bump in the temperature spectrum produces a corresponding bump in the variance of log intensity. This bump in the variance is, of course, absent when the Tatarskii spectrum is used to predict the variance. The peak of the bump in the variance lies at slightly smaller $\sqrt{\lambda L}/l_0$ for plane waves than for spherical waves.

Consider the case of red light propagating along a path a few meters above the ground. For a 50 m path $\sqrt{\lambda L}/l_0$ may be as small as 0.7. For a 500 m path, $\sqrt{\lambda L}/l_0$ may be as large as 6. Consequently, lasers used on short paths in the surface layer are typically operating on the steep portion of the solid curve in Fig. 4. There are three requirements for Eq. (8) to apply. First, the turbulence should be homogeneous. Second, saturation should be negligible. Third, from Fig. 4, $\sqrt{\lambda L}/l_0$ should be greater than about 30. For red light, a $\sqrt{\lambda L}/l_0$ value of 30 would require a path length of roughly 150 km, in which case saturation and inhomogeneity would be important. For infrared light having $\lambda \simeq 10.6\ \mu$m, $\sqrt{\lambda L}/l_0 = 30$ requires a path length of roughly 9 km. Therefore the interpretation of the variance of log intensity in terms of C_n^2 is never exactly governed by the limiting formula in Eq. (8).

VI. COVARIANCE FUNCTION OF LOG AMPLITUDE

For a plane wave propagating through homogeneous turbulence the covariance function of log amplitude is given by Eq. (T19) of Lawrence and Strohbehn[15]

$$B_\chi(\rho) = 2\pi^2 k^2 L \int_0^\infty \left(1 - \frac{k}{\kappa^2 L}\sin\frac{\kappa^2 L}{k}\right) \times J_0(\kappa\rho)\Phi_n(\kappa)\kappa\, d\kappa. \quad (9)$$

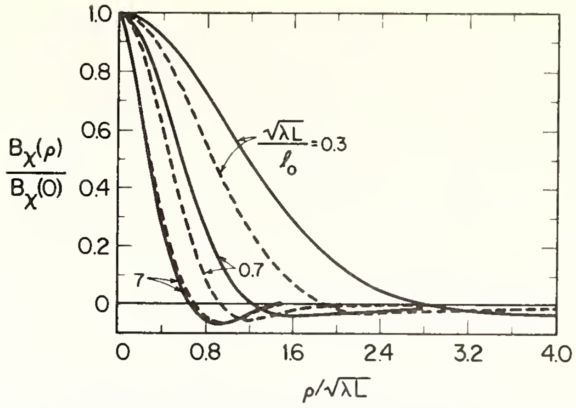

FIG. 5. Covariance function of log amplitude for plane waves. Solid curves: accurate model; dashed curves: Tatarskii model.

The covariance function is determined from both the accurate model spectrum as well as the Tatarskii spectrum and is presented in Figs. 5 and 6. Figure 5 contains the covariance function for $\sqrt{\lambda L}/l_0 = 0.3, 0.7, 7.0$ whereas Fig. 6 emphasizes the small ρ behavior for $\sqrt{\lambda L}/l_0 = 0.3, 0.7, 1.5$, and 7.0. For the smaller values of $\sqrt{\lambda L}/l_0$ the covariance function is wider when determined from the accurate model spectrum than when determined from the Tatarskii spectrum. For $\sqrt{\lambda L}/l_0 = 7$ the accurate model spectrum gives a narrower covariance function than does the Tatarskii spectrum. For $\sqrt{\lambda L}/l_0$ as large as 50 there is essentially no difference between the covariance functions determined from the two model spectra. The Tatarskii model gives a covariance function that becomes narrower as $\sqrt{\lambda L}/l_0$ goes from small values to large values. The accurate model spectrum gives a covariance function which becomes narrower as $\sqrt{\lambda L}/l_0$ goes from small values to a value at which the variance of log intensity (Fig. 4) is near its maximum; for yet larger $\sqrt{\lambda L}/l_0$ the covariance function becomes wider and approaches a limiting width.

VII. STRUCTURE FUNCTION OF PHASE

For a plane wave propagating in homogeneous turbulence the structure function of phase $D_S(\rho)$ is given by Eq. (T32) of

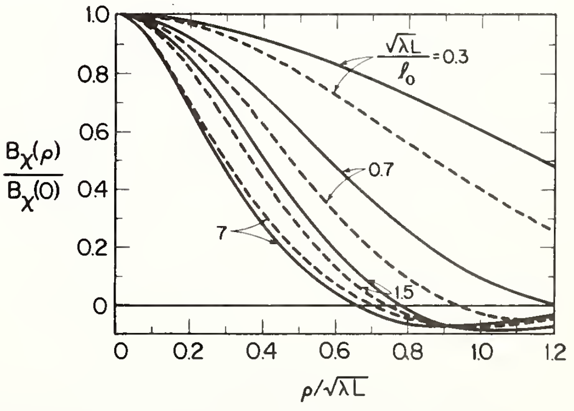

FIG. 6. Covariance function of log amplitude for plane waves. Solid curves: accurate model; dashed curves: Tatarskii model.

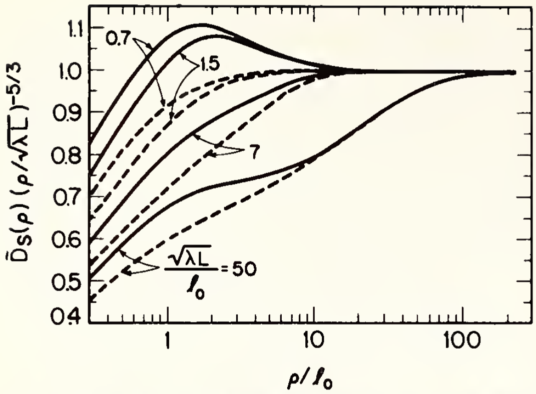

FIG. 7. Structure function of phase for plane waves and no outer scale. Solid curves: accurate model; dashed curves: Tatarskii model.

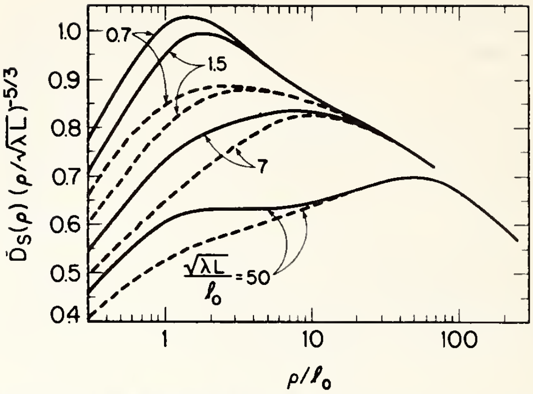

FIG. 9. Structure function of phase for plane waves and an outer scale cutoff. Solid curves: accurate model; dashed curves: Tatarskii model.

Lawrence and Strohbehn[15]

$$D_S(\rho) = 4\pi^2 k^2 L \int_0^\infty [1 - J_0(\kappa\rho)] \times \left[1 + \frac{k}{\kappa^2 L} \sin\left(\frac{\kappa^2 L}{k}\right)\right] \Phi_n(\kappa)\kappa\, d\kappa. \quad (10)$$

A convenient normalized structure function of phase is

$$\tilde{D}_S(\rho) = D_S(\rho)/2.92\, C_n^2 k^2 L \sqrt{\lambda L}^{5/3}. \quad (11)$$

For $l_0 \ll \sqrt{\lambda L} \ll \rho$, $\tilde{D}_S(\rho) \simeq (\rho/\sqrt{\lambda L})^{5/3}$.

The structure function of phase is computed from Eq. (10) using both the accurate model spectrum and Tatarskii's spectrum; these spectra behave like $\kappa^{-11/3}$ to arbitrarily low wave numbers. Figure 7 presents $\tilde{D}_S(\rho)(\rho/\sqrt{\lambda L})^{-5/3}$ for several values of $\sqrt{\lambda L}/l_0$. These curves must all tend to unity for large ρ; the flat portions of the curves at large ρ are where $D_S(\rho) \propto \rho^{5/3}$ holds. The bump in the temperature spectrum, Φ_T, produces a corresponding bump in $D_S(\rho)$ which lies near $\rho \simeq 2l_0$. Moreover, $D_S(\rho)$, determined from the accurate model spectrum, is larger at small ρ than $D_S(\rho)$ predicted by the Tatarskii spectrum.

Figure 8 gives $\tilde{D}_S(\rho)(\rho/\sqrt{\lambda L})^{-2}$ for two values of $\sqrt{\lambda L}/l_0$. These curves are flat at small ρ where $D_S(\rho) \propto \rho^2$. The Tatarskii spectrum predicts too small a value for $D_S(\rho)$ at asymptotically small ρ.

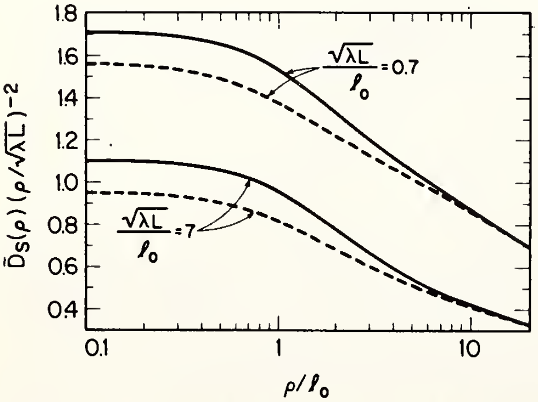

FIG. 8. Structure function of phase (plane waves, no outer scale) showing the ρ^2 dependence at small ρ. Solid curves: accurate model; dashed curves: Tatarskii model.

It is well known that the structure function of phase is sensitive to the form of Φ_n at low wave numbers. The spectra used to obtain Fig. 7 have no outer scale. To investigate the effects of an outer scale we use an *ad hoc* assumption for an outer scale form of Φ_T. We introduce the factor $\exp[-(10^{-4}/\kappa\eta)^2]$ into Φ_T; this low-wave-number cutoff is roughly appropriate for a height of several meters in the atmospheric surface layer. The resulting structure function of phase is illustrated in Fig. 9. The only difference between Figs. 7 and 9 is the outer scale cutoff used for Fig. 9.

The $\rho^{5/3}$ power law at large ρ is absent in Fig. 9. When an outer scale cutoff is used, $D_S(\rho)$ increases more slowly than $\rho^{5/3}$ at large ρ; this behavior is in agreement with experiment (Clifford *et al.*[16] and Pollaine *et al.*[17]) and was pointed out theoretically by Consortini and Ronchi[18] and by Consortini *et al.*[19] In Fig. 9 an inflection through a $\rho^{5/3}$ power law appears near $\rho = 5l_0$ for $\sqrt{\lambda L}/l_0 = 50$. This apparent power law is a manifestation of the combination of the spectral bump and the outer scale cutoff; it is not an asymptotic $\rho^{5/3}$ range.

Comparison of Figs. 7 and 9 shows that $D_S(\rho)$ is smaller when the outer scale cutoff is used than when the cutoff is not used. This is true even at small separations. Consequently $D_S(\rho)$ is sensitive to the inhomogeneous and anisotropic nature of turbulence at large length scales.

VIII. COHERENCE LENGTH FOR PLANE WAVES

For plane waves the coherence length ρ_0 (the distance transverse to the propagation axis over which the wave is coherent) is obtained by solving the following equation:

$$1 = 4\pi^2 k^2 L \int_0^\infty [1 - J_0(\kappa\rho_0)]\Phi_n(\kappa)\kappa\, d\kappa.$$

In terms of the dimensionless wave number $\tilde{\kappa} = \kappa l_0$ and the dimensionless temperature spectrum $\tilde{\Phi}_T(\tilde{\kappa})$ this equation becomes

$$(k^2 L C_n^2 l_0^{5/3})^{-1} = 4\pi^2(0.033/\beta)(l_0/\eta)^{-11/3} \times \int_0^\infty [1 - J_0(\tilde{\kappa}\rho_0/l_0)]\tilde{\Phi}_T(\tilde{\kappa})\tilde{\kappa}\, d\tilde{\kappa}. \quad (12)$$

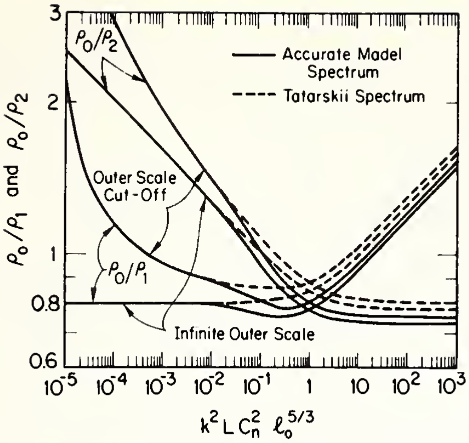

FIG. 10. Phase coherence length scaled by both ρ_1 and ρ_2 for both an infinite and a finite outer scale. Solid curves: accurate model; dashed curves: Tatarskii model.

This result shows that ρ_0/l_0 is a function only of $k^2LC_n^2l_0^{5/3}$.

Yura[20] shows that for small $k^2LC_n^2l_0^{5/3}$ the coherence length ρ_0 is proportional to $\rho_1 \equiv (k^2C_n^2L)^{-3/5}$ in the absence of outer scale effects; whereas for large $k^2LC_n^2l_0^{5/3}$ the coherence length is proportional to $\rho_2 \equiv [kL^{1/2}(C_n^2)^{1/2}l_0^{-1/6}]^{-1}$. Yura[21] shows that when the outer scale effects are taken into account ρ_0 tends to infinity as $k^2LC_n^2l_0^{5/3}$ tends to zero.

The coherence length determined from Eq. (12) is presented in Fig. 10. This figure gives both ρ_0/ρ_1 and ρ_0/ρ_2 as functions of $k^2LC_n^2l_0^{5/3}$; the solid curves are calculated using the accurate model spectrum whereas the dashed curves are calculated using the Tatarskii spectrum. Furthermore, Fig. 10 presents the coherence length calculated both with an infinite outer scale as well as with the outer scale cutoff discussed in Sec. VII. For $k^2LC_n^2l_0^{5/3} > 10$ the ρ_0/ρ_2 curves tend to be flat, verifying the asymptotic relationship $\rho_0 \propto \rho_2$ predicted by Yura.[20] For $k^2LC_n^2l_0^{5/3} < 0.01$ the ρ_0/ρ_1 curve is flat if the outer scale is infinite; this verifies the asymptotic relationship $\rho_0 \propto \rho_1$ predicted by Yura. However, when the outer scale cutoff is used there is no region where $\rho_0 \propto \rho_1$. The ρ_0/ρ_1 curve that includes the outer scale effects shows that ρ_0 increases dramatically for small $k^2LC_n^2l_0^{5/3}$ as predicted by Yura. Figure 10 shows that the presence of an outer scale affects the coherence length even for $k^2LC_n^2l_0^{5/3} \gg 10$. Consequently, the phase coherence length is affected by the inhomogeneous and anisotropic nature of temperature fluctuations at the large length scales.

The propagation distance Z_i, at which the lateral coherence length is equal to the inner scale, satisfies[21]

$$Z_i \propto (k^2C_n^2l_0^{5/3})^{-1}.$$

Since $\rho_0 = l_0$ implies $\rho_0/\rho_2 = (k^2LC_n^2l_0^{5/3})^{1/2}$, it follows from Fig. 10 that, for plane waves and infinite outer scale,

$$Z_i = 0.72(k^2C_n^2l_0^{5/3})^{-1}, \quad (13)$$

whereas from the ρ_0/ρ_2 curve that includes the outer scale cutoff effect we have

$$Z_i = 0.67(k^2C_n^2l_0^{5/3})^{-1}. \quad (14)$$

For $\lambda = 0.63\ \mu$m, $l_0 = 0.8$ cm, and $C_n^2 = 10^{-13}\ \mathrm{m}^{-2/3}$ we have Z_i = 226 m and 210 m from Eqs. (13) and (14), respectively. Whereas, if $\lambda = 10.6\ \mu$m, then $Z_i = 6.4 \times 10^4$ m and 5.9×10^4 m from Eqs. (13) and (14), respectively. The abscissa of Fig. 10 may now be expressed in terms of the ratio of the propagation distance L to Z_i. For an infinite outer scale

$$k^2LC_n^2l_0^{5/3} = 0.72L/Z_i,$$

whereas the outer scale cutoff gives

$$k^2LC_n^2l_0^{5/3} = 0.67L/Z_i.$$

IX. CONCLUSION

Recent theoretical and experimental advances have produced an accurate model of the spectra of fluctuations of advected quantities in turbulent flow. These advances make it possible to predict the high-wave-number form of the temperature spectrum, humidity spectrum and the temperature-humidity cospectrum, and therefore the spectrum of refractive-index fluctuations as well. The accurate model has been used to predict the spectra of temperature and salinity fluctuations in turbulent water. These latter two spectra have extensive viscous-convective ranges, and the implications for optical propagation in turbulent water is given by Hill.[22]

An outstanding feature of the experimentally measured and the theoretically predicted temperature spectrum is the bump at high wave numbers. By comparison, the Tatarskii spectrum does not well represent the temperature spectrum at high wave numbers. The temperature structure function is determined from both spectral models. It is found that the temperature structure function has a bump for r near the inner scale; the structure function from the Tartarskii spectrum does not have such a bump. The aerosol-concentration structure function has a form that is different from that of the temperature structure function for small r. The former is slowly varying at those spacings where the latter varies as r^2.

The presence of the bump in the temperature spectrum has important implications for optical propagation. It is shown that there is a corresponding bump in the variance of log intensity. It is concluded that the large-Fresnel-zone asymptotic form of the variance of log intensity is rarely applicable to a geophysical situation because Fig. 4 shows that $\sqrt{\lambda L}/l_0 \gtrsim 30$ is required for Eq. (8) to be valid.

The covariance function of log amplitude is determined from both spectral models. It is found that for small $\sqrt{\lambda L}/l_0$ the covariance function is wider than predicted by the Tatarskii spectrum; but for larger $\sqrt{\lambda L}/l_0$ the accurate model spectrum gives a narrower covariance function than does the Tatarskii spectrum.

The bump in the temperature spectrum produces a corresponding bump in the structure function of phase for spatial separations near the inner scale. The accurate model spectrum predicts that the structure function of phase is larger at small separations than when the Tatarskii spectrum is used. We investigate the effect on the structure function of phase of an outer scale cutoff typical of the atmospheric surface layer. It is found that no extensive $5/3$ power law region is expected for optical propagation in the atmosphere. The structure function of phase is sensitive to outer scale effects, even at small ρ. Therefore, understanding phase fluctuations requires a model of the inhomogeneity and anisotropy of the refractive index fluctuations at large length scales.

The phase coherence length ρ_0 for plane waves is determined for both an infinite and a finite outer length scale, and the asymptotic formulae $\rho_0 \propto \rho_1$ and $\rho_0 \propto \rho_2$ are illustrated. For an outer scale cutoff that is appropriate to a height of several meters in the atmosphere surface layer, the asymptotic formula $\rho_0 \propto \rho_1$ is not accurate for any values of $k^2LC_n^2l_0^{5/3}$. For $k^2LC_n^2l_0^{5/3}$ of the order of unity, the bump in the temperature spectrum causes ρ_0 to be smaller than when ρ_0 is determined from the Tatarskii spectrum. Just as in the case of the structure function of phase, the phase coherence length is sensitive to outer scale effects, particularly for small $k^2LC_n^2l_0^{5/3}$.

It is common practice to use the $\kappa^{-11/3}$ power law in Eq. (1) to deduce quantities relevant to optical propagation through turbulence. The results of using Eq. (1) with no diffusive cutoff is obvious from the figures. In Fig. 1, Eq. (1) would give a straight line extending the flat portion of the curves across the breadth of the graph. In Fig. 2, Eq. (1) results in a straight line of slope ⅔ that tends to be parallel to the curves at large r. The $\kappa^{-11/3}$ power law would result in a straight, flat line extending across Figs. 4 and 7, intersecting the ordinant at 1.0. In Figs. 5 and 6, Eq. (1) gives a covariance function that lies between the solid and dashed curves corresponding to $\sqrt{\lambda L}/l_0 = 7.0$. The $\kappa^{-11/3}$ power law, with no outer scale cutoff, results in the ρ_0/ρ_1 curve becoming a straight, flat line across Fig. 10, intersecting the ordinate at 8.0. For many applications, it is a crude assumption to assert that Eq. (1) applies to optical propagation.

ACKNOWLEDGMENTS

We thank J. C. Wyngaard for helpful discussions. The first author was supported by the National Research Council through the Resident Research Associateship Program.

[1] F. H. Champagne, C. A. Friehe, J. C. LaRue, and J. C. Wyngaard, "Flux measurements, flux-estimation techniques, and fine-scale turbulence measurements in the unstable surface layer over land," J. Atmos. Sci. 34, 515–530 (1977).

[2] R. M. Williams, Jr. and C. A. Paulson, "Microscale temperature and velocity spectra in the atmospheric boundary layer," J. Fluid Mech. 83, 547–567 (1977).

[3] A. M. Oboukhov, "Structure of the temperature field in turbulent flow," Izv. Akad. Nauk. SSSR, Ser. Geogr. i Geofiz. **13**, 58–69 (1949).

[4] S. Corrsin, "On the spectrum of isotropic temperature fluctuations in isotropic turbulence," J. Appl. Phys. **22**, 469–473 (1951).

[5] R. J. Hill, "Models of the scalar spectrum for turbulent advection" J. Fluid Mech. (to be published).

[6] R. J. Hill, "Spectra of fluctuations in refractivity, temperature, humidity, and the temperature-humidity cospectrum in the inertial and dissipation ranges" Radio Sci. (to be published).

[7] V. I. Tatarskii, *The Effects of the Turbulent Atmosphere on Wave Propagation* (Keter, Jerusalem, 1971), p. 65.

[8] G. K. Batchelor, "Small-scale variation of convected quantities like temperature in turbulent fluid, Part I, General discussion and the case of small conductivity," J. Fluid Mech. **5**, 113–133 (1959).

[9] H. L. Grant, B. A. Hughes, W. M. Vogel, and A. Moilliet, "The spectrum of temperature fluctuations in turbulent flow," J. Fluid Mech. **34**, 423–492 (1968).

[10] C. H. Gibson, R. R. Lyon, and I. Hirschsohn, "Reaction product fluctuations in a sphere wake," AIAA J. **8**, 1859–1863 (1970).

[11] C. E. Leith, "Diffusion approximation for turbulent scalar fields," Phys. Fluids **11**, 1612–1617 (1968).

[12] R. H. Kraichnan, "Small-scale structure of a scalar field convected by turbulence," Phys. Fluids **11**, 945–953 (1968).

[13] V. I. Tatarskii, *Wave Propagation in a Turbulent Medium* (McGraw-Hill, New York, 1961), pp. 46–48.

[14] M. J. Post and G. M. Lerfald, "Experimental measurements of atmospheric aerosol inhomogeneities," Technical Digest of the Topical Meeting on Optical Propagation Through Turbulence, Rain, and Fog; August 9–11, 1977, Boulder, Colorado. Available from: Optical Society of America, 2100 Pennsylvania Ave., N.W., Washington, D.C. 20037.

[15] R. S. Lawrence and J. W. Strohbehn, "A survey of clear-air propagation effects relevant to optical communications," Proc. IEEE **58**, 1523–1545 (1970).

[16] S. F. Clifford, G. M. B. Bouricius, G. R. Ochs, and Margot H. Ackley, "Phase variations in atmospheric optical propagation," J. Opt. Soc. Am. **61**, 1279–1284 (1971).

[17] S. Pollaine, A. Buffington, F. S. Crawford, and R. A. Muller, "A measurement of the phase structure function," Technical Digest of the Topical Meeting on Optical Propagation Through Turbulence, Rain, and Fog; August 9–11, 1977, Boulder, Colorado. Available from: Optical Society of America, 2100 Pennsylvania Ave., N.W., Washington, D.C. 20037.

[18] A. Consortini, and L. Ronchi, "Some comments on the theory of E.M. propagation in a turbulent atmosphere," Nuovo Cimento Lett. **2**, 683–688 (1969).

[19] A. Consortini, L. Ronchi, and E. Moroder, "Role of the outer scale of turbulence in atmospheric degradation of optical images," J. Opt. Soc. Am. **63**, 1246–1248 (1973).

[20] H. T. Yura, "Atmospheric turbulence induced laser beam spread," Appl. Opt. **10**, 2771–2772 (1971).

[21] H. T. Yura, "Optical beam spread in a turbulent medium: effect of the outer scale of turbulence," J. Opt. Soc. Am. **63**, 107–109 (1973).

[22] R. J. Hill, "Optical propagation in turbulent water" J. Opt. Soc. Am. (to be published).

Applied Optics, 17: 3608-3612, 1978.

Fine calibration of large-aperture optical scintillometers and an optical estimate of inner scale of turbulence

R. J. Hill and G. R. Ochs

Large-aperture optical scintillometers [Ting-i Wang *et al.*, J. Opt. Soc. Am. **68**, 334 (1978)] lose their calibration if they are sensitive to portions of the spatial spectrum of temperature fluctuations where $\kappa^{-11/3}$ fails to hold. The model temperature spectrum having the bump [R. J. Hill, J. Fluid Mech. **88**, 541 (1978); R. J. Hill and S. F. Clifford, J. Opt. Soc. Am. **68**, 892 (1978)] is used to find conditions under which the scintillometers maintain their calibration. We find that the aperture size D should be at least twenty times the inner scale l_0 if the contribution of the spectral bump is to be ignored. For application in the surface layer, one needs the height above ground of the optical path to be much greater than three times the aperture size if outer-scale effects are to be negligible. It is shown that the inner scale dependence of a scintillometer having $D/l_0 \simeq 2.0$ and the lack of such dependence for a scintillometer having $D/l_0 \simeq 20.0$ can be used to estimate both l_0 and C_n^2 if the two systems are used simultaneously on the same path. A preliminary experiment was performed in the atmospheric surface layer with scintillometers having aperture sizes of 2.0 cm, 5.0 cm, and 15.0 cm; the results are consistent with the existence of the spectral bump. The inner scale is estimated by comparing data from the 2.0-cm and 15.0-cm systems. Using this inner scale, the C_n^2 values from the 5.0-cm and 15.0-cm scintillometers are corrected for the spectral bump; the corrected values are in agreement. Other turbulence parameters are not deduced from the l_0 and C_n^2 estimates because the l_0 values have been found to be insufficiently accurate.

I. Introduction

Wang *et al.*[1] describe a saturation-resistant optical technique for measuring the refractive-index structure parameter C_n^2. This technique uses a large-aperture incoherent transmitter and a large-aperture receiver. They show that if the transmitter and receiver aperture diameters, D_t and D_r, are sufficiently large compared with the Fresnel-zone size $(\lambda L)^{1/2}$, the first-order scattering theory is adequate, i.e., the saturation of scintillation may be ignored. The criterion for this to be true is[1]

$$\frac{D_r + D_t}{(\lambda L)^{1/2}} > 2(\sigma_\chi^2)^{5/3}, \qquad (1)$$

where σ_χ^2 is the variance of log-amplitude. Throughout the following we assume that the first-order scattering theory applies.

Wang *et al.*[1] describe both a single-receiving-aperture scintillometer as well as a scintillometer having two receiving apertures of equal diameter that are tangent to each other. Hereafter we assume that $D_t = D_r = D$. Consider the limit that $D \gg (\lambda L)^{1/2}$ and assume that the spatial power spectrum of refractive-index fluctuations $\Phi_n(\kappa)$ is proportional to $\kappa^{-11/3}$; then, for the scintillometer with a single circular receiving aperture, the variance of log-intensity $\sigma_{\ln I}^2$ is given by[1]

$$\sigma_{\ln I}^2 \simeq 0.9 C_n^2 L^3 D^{-7/3}, \qquad (2)$$

where L is the pathlength. For the scintillometer having tangent circular apertures, the difference of the intensities in the apertures satisfies[1]

$$\frac{\overline{(I_A - I_B)^2}}{\bar{I}^2} \simeq 1.44 C_n^2 L^3 D^{-7/3}, \qquad (3)$$

where I_A and I_B are the intensities in the two receivers, and $\bar{I}$ is the mean intensity. Taking the difference of intensities observed by tangent apertures has several advantages over the single aperture technique. It renders the measurement less sensitive to fluctuating background light and support vibrations, and it gives better rejection of larger-size refractive-index fluctuations.[1]

Recent experimental evidence[2,3] and theoretical analysis[4] show that the spatial power spectrum of temperature fluctuations has a bump at wavenumbers

---

R. J. Hill is with Cooperative Institute for Research in Environmental Sciences, University of Colorado/NOAA, Boulder, Colorado 80309, and G. R. Ochs is with NOAA Environmental Research Laboratories, Wave Propagation Laboratory, Boulder, Colorado 80302.

Received 25 May 1978.
0003-6935/78/1115-3608$0.50/0.

© 1978 Optical Society of America.

between $0.05\eta^{-1}$ and $0.4\eta^{-1}$, where η is the Kolmogorov microscale. The spectrum of humidity fluctuations and the temperature–humidity cospectrum are also predicted to have a bump.[5] Some effects of the spectral bump on optical propagation in the turbulent atmosphere are described by Hill and Clifford.[6]

Equations (2) and (3) depend, of course, on the assumption that $\Phi_n(\kappa) \propto \kappa^{-11/3}$. Wang *et al.*[1] determine the effects of the inner scale l_0 on large-aperture scintillometers by using the Tatarskii model for the temperature spectrum. The Tatarskii spectrum is proportional to $\kappa^{-11/3}$ multiplied by a Gaussian cutoff at high wavenumbers. We determine the effects of both the spectral bump and the inner scale by using the accurate temperature spectrum introduced by Hill[4] and applied to optical propagation by Hill and Clifford.[6] The presence of the spectral bump requires a minimum ratio of aperture size to inner scale such that Eqs. (2) and (3) are approximately valid, i.e., that the scintillometer measurement of C_n^2 is independent of the inner scale. If the ratio D/l_0 is sufficiently small, the measured scintillation depends on l_0 as well as on C_n^2. We exploit this effect in order to obtain an optical estimate of inner scale.

II. Bump in the Variance for Wide Apertures

For single circular transmitting and receiving apertures, both having diameter D, the variance of log-intensity is

$$\sigma_{\ln I}^2 = 16\pi^2k^2L\int_0^1 du\int_0^\infty d\kappa\kappa\Phi_n(\kappa) \times \sin^2\left[\frac{\kappa^2Lu(1-u)}{2k}\right]\left[\frac{2J_1(x_1)}{x_1}\frac{2J_1(x_2)}{x_2}\right]^2, \qquad (4)$$

where $u = z/L$,

$x_1 = \kappa Du/2$ and

$x_2 = \kappa D(1-u)/2$.

The pathlength is denoted by L, position on the path by z, and optical wavenumber by $k = 2\pi/\lambda$. The first-order scattering approximation is used to obtain Eq. (4).

For the case of tangent receiving apertures, we denote the normalized mean-squared difference of the intensities by $\sigma_{\Delta I}^2$, that is,

$$\sigma_{\Delta I}^2 = \frac{\overline{(I_A - I_B)^2}}{\bar{I}^2} \qquad (5)$$

If the two receiving apertures and the transmitting aperture all have diameter D, and to lowest order in the ratio of fluctuating intensity to mean intensity, $\sigma_{\Delta I}^2$ is given by Eq. (4) with the factor $2[1 - J_0(\kappa Du)]$ introduced into the integrand. In the limit that $D \gg (\lambda L)^{1/2}$ and $D \gg l_0$, $\sigma_{\ln I}^2$ and $\sigma_{\Delta I}^2$ tend to the formulas in Eqs. (2) and (3), respectively.

The variances $\sigma_{\ln I}^2$ and $\sigma_{\Delta I}^2$ are calculated using the temperature spectrum $\Phi_T(\kappa)$, introduced by Hill and Clifford.[6] Homogeneous turbulence along the optical path is assumed. These variances, normalized by their large-D asymptotic forms [Eqs. (2) and (3)], are presented in Fig. 1 as functions of D/l_0. For large D/l_0 the curves should tend to unity. The curves for $D/(\lambda L)^{1/2}$ = 2.1, 5.3, and 16.0 are given in Fig. 1. For $D/(\lambda L)^{1/2}$ = 5.3 and 16.0 the curves are indistinguishable, whereas the curve for $D/(\lambda L)^{1/2}$ = 2.1 falls slightly below the other two. This verifies that when $D/(\lambda L)^{1/2}$ is large enough the variances become independent of wavelength λ, or, equivalently, the normalized variances become independent of the Fresnel-zone size $(\lambda L)^{1/2}$. Even $D/(\lambda L)^{1/2}$ as small as 2.1 is sufficient to give a variance that is approximately independent of λ.

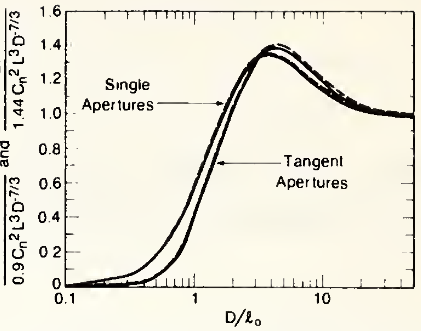

Fig. 1. The normalized variances as functions of D/l_0 for both single and tangent aperture scintillometers. Dashed curves for $D/(\lambda L)^{1/2}$ = 5.3 and 16.0; full curves for $D/(\lambda L)^{1/2}$ = 2.1.

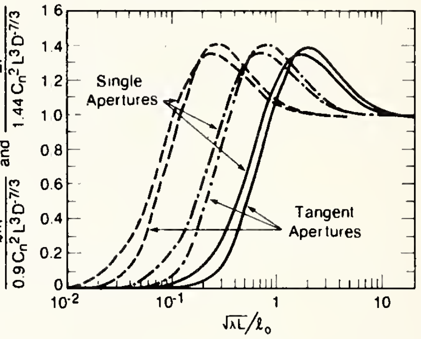

Fig. 2. The normalized variances as functions of $(\lambda L)^{1/2}/l_0$ for both single and tangent aperture scintillometers. $D/(\lambda L)^{1/2}$ = 16.0, 5.3, and 2.1 for the dashed, dash–dot, and full curves, respectively.

The bump in the spatial spectrum of temperature fluctuations produces a corresponding bump in the variances presented in Fig. 1. For a single receiving aperture the spectral bump would cause a 35% overestimate of C_n^2 if $D/l_0 \simeq 4$ and if Eq. (1) was used to deduce C_n^2 from $\sigma_{\ln I}^2$. For the tangent-aperture scintillometer the spectral bump would cause a 40% overestimate of C_n^2 if $D/l_0 \simeq 5$ and if Eq. (2) was used to deduce C_n^2 from $\sigma_{\Delta I}^2$. From Fig. 1, we need $D/l_0 \gtrsim 20.0$ in order that C_n^2 may be obtained from Eqs. (1) or (2).

The normalized variances are presented in Fig. 2 as functions of $(\lambda L)^{1/2}/l_0$ for $D/(\lambda L)^{1/2}$ = 2.1, 5.3, and 16.0. Since the normalized variances are approximately independent of $(\lambda L)^{1/2}$, the curves in Fig. 2 present the dependence of the normalized variances as functions of $1/l_0$, where $1/l_0$ is measured in units of $(\lambda L)^{1/2}$. For point receiver and transmitter apertures the curve analogous to those in Fig. 2 is given by Hill and Clifford.[6]

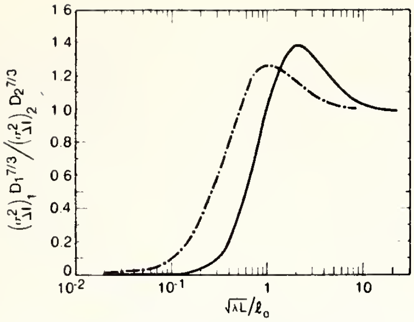

Fig. 3. The ratio in Eq. (7) for $D_1/D_2 = 2.1/16.0$ (full curve) and $D_1/D_2 = 5.3/16.0$ (dash–dot curve).

For Eqs. (1) and (2) to apply we have shown that one needs $D/(\lambda L)^{1/2} \gtrsim 2.1$ and $D/l_0 \gtrsim 20.0$. Besides these restrictions, it is required that the scintillometer be insensitive to refractive-index fluctuations on length scales comparable with the outer scale. Wang *et al.*[1] show that the tangent-aperture scintillometer is sensitive to refractive-index fluctuations having spatial sizes as large as two to three times the aperture size, and the single-aperture scintillometer is sensitive to much larger spatial sizes. Consequently, the outer scale should be very much larger than $3.0D$ for the tangent-aperture scintillometer, with a more severe restriction for the single-aperture scintillometer. For application to the atmospheric surface layer one may use the height above ground h as a rough estimate of the outer scale. For the tangent-aperture case, one then needs $h \gg 3.0D$.

III. Optical Method for Estimating Inner Scale

The shape of the curves in Fig. 2 can be exploited to estimate l_0. Suppose that an optical path is set up such that $(\lambda L)^{1/2}/l_0 \simeq 1.0$, and that two large-aperture scintillometers measure $\sigma^2_{\ln I}$ or $\sigma^2_{\Delta I}$, one of the scintillometers having $D/(\lambda L)^{1/2} = 16.0$ and the other having $D/(\lambda L)^{1/2} = 2.1$. In this case, the scintillometer having $D/(\lambda L)^{1/2} = 16.0$ can measure C_n^2 nearly independent of l_0. By noting the shape of the solid curve $[D/(\lambda L)^{1/2} = 2.1]$ on Fig. 2 it is seen that for $(\lambda L)^{1/2}/l_0 \simeq 1.0$ a measurement of $\sigma^2_{\ln I}$ or $\sigma^2_{\Delta I}$ is sensitive to changes in l_0. Therefore, knowing C_n^2 from the larger-aperture scintillometer, the scintillometer having $D/(\lambda L)^{1/2} = 2.1$ can be used to estimate l_0. If $(\lambda L)^{1/2}/l_0 \simeq 2.0$, rather than 1.0, Fig. 4 of Hill and Clifford[6] shows that a measurement of $\sigma^2_{\ln I}$ using point transmitting and receiving apertures will give an estimate of l_0 if C_n^2 is known from a larger-aperture scintillometer that is insensitive to l_0.

When two large-aperture scintillometers are used to estimate l_0, the effect of l_0 on the larger-aperture scintillometer can be accounted for by considering the ratios

$$[(\sigma^2_{\ln I})_1 D_1^{7/3}]/[(\sigma^2_{\ln I})_2 D_2^{7/3}] \tag{6}$$

or

$$[(\sigma^2_{\Delta I})_1 D_1^{7/3}]/[(\sigma^2_{\Delta I})_2 D_2^{7/3}], \tag{7}$$

where the subscript 1 denotes the smaller-aperture size, and the subscript 2 denotes the larger. The ratios (6) and (7) are independent of C_n^2 but do depend on l_0. For $D_1/(\lambda L)^{1/2} \geq 2$ the ratios (6) and (7) are also approximately independent of λ, and L, and therefore of $(\lambda L)^{1/2}$ as well. The ratios (6) and (7) may be obtained by taking the ratio of values from Fig. 2 for a given $(\lambda L)^{1/2}/l_0$. For the case of tangent apertures, we present in Fig. 3 the ratio (7) as a function of $(\lambda L)^{1/2}/l_0$ for $D_1/D_2 = 2.1/16.0$ and $D_1/D_2 = 5.3/16.0$. By measuring a value of the ratio (7), Fig. 3 gives a value of $(\lambda L)^{1/2}/l_0$ and thereby gives an estimate of the inner scale l_0.

IV. Experiment

In order to measure the bump in the variance for wide apertures, an experiment was performed over flat terrain at the Table Mountain field station near Boulder, Colorado. Measurements were made using transmitter and receiver apertures of equal diameter; the diameters of 15.0 cm, 5.0 cm, and 2.0 cm were used. The optical path was 160 m long and 1.5 m above the ground. The transmitters produced incoherent light from frosted quartz–iodine incandescent bulbs. As noted previously, Fig. 1 shows that $\sigma^2_{\ln I}$ and $\sigma^2_{\Delta I}$ are nearly independent of wavelength λ. Therefore, an average over the wavelengths of white light makes very little difference to the theoretical discussion in the previous sections. Using a wavelength $\lambda = 0.55\ \mu$m, the Fresnel-zone-size $(\lambda L)^{1/2}$ is 0.938 cm. Then the values of $D/(\lambda L)^{1/2}$ used in the experiment are 16.0, 5.3, and 2.1; therefore, the theoretical curves in Figs. 1, 2, and 3 apply to the experiment. The nominal value $(\lambda L)^{1/2} = 0.938$ cm may be considered a scaling length and is used throughout the following.

Data were obtained for both single and tangent receiving apertures. We consider only data for the tangent apertures because of their better rejection of outer scale effects and because of the close proximity to the ground. The three transmitters were spaced roughly 1 m apart, and the three receivers were spaced likewise. The optical paths crossed near midpath, and data were obtained by all three receivers simultaneously. Consequently, the three aperture sizes were measuring the same refractive-index field at the same time. A value of the quantity

$$\Xi \equiv \sigma^2_{\Delta I}/(1.44 L^3 D^{-7/3}) \tag{8}$$

was obtained for each of the three aperture sizes; Ξ is just the normalized variance shown in Fig. 1 multiplied by C_n^2. If $D/l_0 \geq 20.0$, then $\Xi \simeq C_n^2$. However, the D/l_0 dependence illustrated in Fig. 1 is not negligible in our experiment, so the asymptotic form in Eq. (3) is not accurate, and therefore $\Xi \not\simeq C_n^2$.

We denote the values of Ξ obtained from each of the three aperture sizes by Ξ(2 cm), Ξ(5 cm), and Ξ(15 cm). Given l_0, one can obtain the value of C_n^2 by dividing Ξ(2 cm), Ξ(5 cm), or Ξ(15 cm) by values taken from Figs. 1 or 2. The values of Ξ(2 cm), Ξ(5 cm), and Ξ(15 cm) are shown in Fig. 4; these values are 1-min averages plotted as functions of time during an 80-min run. The value of Ξ(15 cm) is usually greater than Ξ(2 cm) but less than Ξ(5 cm); examination of Fig. 2 shows that this requires $0.55 \lesssim (\lambda L)^{1/2}/l_0 \lesssim 1.0$. The data in Fig. 4 show random variations of as much as a factor of 3 over the 80-min

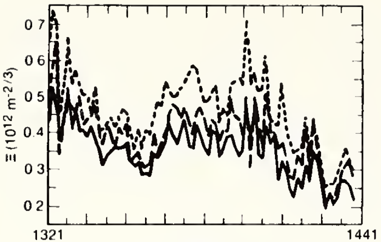

Fig. 4. One-minute average values of Ξ for an 80-min run. Ξ(2 cm), solid curve; Ξ(5 cm), short dashed curve; Ξ(15 cm), long dashed curve.

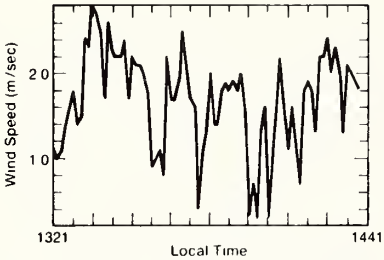

Fig. 5. Wind speed during the 80-min run.

run; thus conditions were not stationary, which is far from ideal. The wind speed measured by a single-propeller anemometer at a height of 1.5 m is given in Fig. 5; the wind speed also illustrates the lack of stationarity.

The ratio $\Xi(D_1)/\Xi(D_2)$ is the same as the ratio in (7). The ratios Ξ(5 cm)/Ξ(15 cm) and Ξ(2 cm)/Ξ(15 cm) are calculated from the data and are given in Fig. 6; these ratios are independent of C_n^2, and their predicted dependence on l_0 is given in Fig. 3. Figure 3 indicates that Ξ(5 cm)/Ξ(15 cm) should not exceed about 1.27. However, the data in Fig. 6 show Ξ(5 cm)/Ξ(15 cm) exceeding 1.27 at times. In fact, with $(\lambda L)^{1/2}/l_0 \simeq 1.0$, Fig. 3 indicates that the observed minute-by-minute variation of Ξ(5 cm)/Ξ(15 cm) is inconsistent with the expected variation of l_0. Consequently, the variability of the ratios in Fig. 6 should be associated either with random errors or insufficient averaging time.

The model temperature spectrum introduced by Hill and Clifford[6] (which is the basis for Figs. 1, 2, and 3) applies to a very large ensemble average with each sample in the ensemble having the same C_n^2 and l_0. For an insufficient averaging time or for nonstationary conditions, the actual path-averaged temperature spectrum will only approximate the model because C_n^2 and l_0 do change with time, and Figs. 1, 2, and 3 will not apply in detail. Because of the nonstationary nature of the wind speed in Fig. 5, an averaging time longer than 1 min would not necessarily be more representative of homogeneous and stationary turbulence.

The values of Ξ(2 cm)/Ξ(15 cm) $\simeq$ 0.9 shown in Fig. 6 are sensitive to the inner scale; this is evident by locating 0.9 on the ordinate of Fig. 3 and noting the slope of the solid curve. Figure 3 is used in conjunction with the measured Ξ(2 cm)/Ξ(15 cm) in Fig. 6 to estimate the inner scale l_0, which is presented in Fig. 7. The typical value of l_0 is estimated to be 1.0 cm, which is larger than expected for a height of 1.5 m under cloudy conditions with a wind speed of roughly 2.0 m sec^{-1}. This estimate of l_0 depends on accurately knowing the rapidly falling portion of the curves in Fig. 3, which, in turn, depends on accurately predicting the shape of the temperature spectrum in the dissipation range. Under nonstationary conditions our knowledge of the dissipation range of the temperature spectrum is particularly uncertain; therefore, the estimated values of l_0 must be viewed with skepticism. The variability of l_0 with time shown in Fig. 7 is believed to be largely caused by random error in the Ξ(2 cm)/Ξ(15 cm) values and is not thought to represent the actual changes in l_0 during the experiment.

An accurate optical measurement of l_0 and C_n^2 can, in principle, determine several other turbulence parameters. For instance, the rate of viscous dissipation of turbulent kinetic energy ϵ is given in terms of l_0 by $l_0 = 7.4(\nu^3/\epsilon)^{1/4}$, where ν is the kinematic viscosity. Unfortunately, the 1/4 power renders an ϵ determination sensitive to errors in l_0. The velocity structure parameter C_v^2 is then given in terms of ϵ by $C_v^2 = 2\epsilon^{2/3}$. Of course, C_T^2 may be determined from C_n^2. Finally, for application to a horizontally homogeneous surface layer, Wyngaard and Clifford[7] show that C_T^2 and C_v^2 may be used to provide estimates of kinematic momentum flux, heat flux, and the Monin-Obukhov length. Unfortunately, the determination of ϵ, C_v^2, momentum and heat flux, and Monin-Obukov length is sensitive to errors in the estimate of l_0, and the present data could not produce sufficiently accurate estimates.

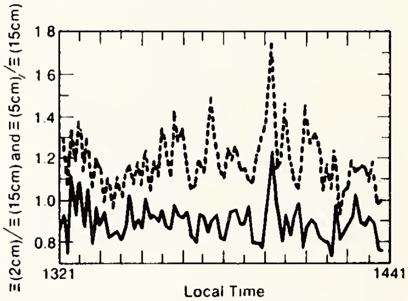

Fig. 6. The ratios Ξ(5 cm)/Ξ(15 cm) (dashed curve) and Ξ(2 cm)/Ξ(15 cm) (full curve) for the 80-min run.

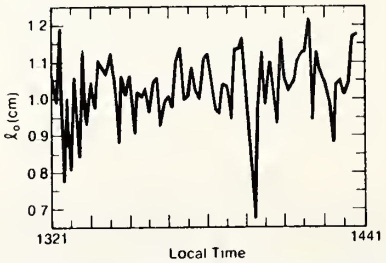

Fig. 7. The estimated inner scale during the 80-min run.

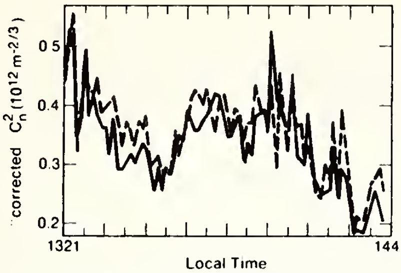

Fig. 8. The corrected C_n^2 from the 5-cm (full curve) and 15-cm (dashed curve) scintillometers.

For $l_0 \simeq 1.0$ cm, Figs. 1 and 2 show that Ξ(5 cm) and Ξ(15 cm) are weak functions of l_0. Consequently, the approximate l_0 values in Fig. 7 can be used to obtain C_n^2 from the Ξ(5 cm) and Ξ(15 cm) values in Fig. 4. The true or corrected values of C_n^2 determined from the 5-cm and 15-cm systems are given in Fig. 8. These corrected values are seen to be in much closer agreement than the uncorrected values Ξ(5 cm) and Ξ(15 cm) in Fig. 4.

V. Conclusion

The model temperature spectrum introduced to optical propagation by Hill and Clifford[6] is used to predict the dependence upon the inner scale of C_n^2 values measured by large-aperture scintillometers. The bump in the temperature spectrum implies that one needs $D/l_0 \gtrsim 20.0$ in order that Eqs. (2) and (3) are valid approximations. For $D/l_0 \simeq 4.0$, the optical scintillometer can cause as much as a 40% overestimate of C_n^2 if Eqs. (2) or (3) are used. Wang *et al.*[1] show that the restrictions $D/(\lambda L)^{1/2} \gtrsim 2.0$ and Eq. (1) must also prevail in order that Eqs. (2) or (3) shall be valid. A further restriction is that a scintillometer should be sensitive only to refractive-index fluctuations of sufficiently small scale that they are locally isotropic; for tangent-aperture scintillometers used in the surface layer, one desires $h \gg 3.0D$, whereas the single-aperture scintillometers are more sensitive to large-scale fluctuations.

It is shown in Sec. III that using two scintillometers of different aperture size can result in a measurement of both C_n^2 and l_0. This technique uses the fact that a scintillometer is relatively insensitive to l_0 if the aperture size is large enough and that another scintillometer is sensitive to both C_n^2 and l_0 if its aperture size is roughly twice the inner scale. However, the analysis of the data given here provides only a crude estimate of l_0. There may be better optical systems for measuring inner scale.

The data presented in Sec. IV are consistent with the bump in the variances presented in Figs. 1 and 2 and, therefore, with the bump in the model temperature spectrum. The inner scale, estimated from the observed value of Ξ(2 cm)/Ξ(15 cm), is about 1.0 cm. The discrepancy between the values shown in Fig. 4 for the 5-cm and 15-cm apertures is seen to be greatly reduced in Fig. 8, where a correction is made for the bump in the variances of Figs. 1 and 2. Although this evidence is consistent with the bump in the variances, it cannot be considered conclusive because of the unknown outer-scale effects on the 15-cm aperture scintillometer and because of the nonstationary conditions. Alternative explanations can be found for the behavior exhibited in Fig. 4. For instance, Ξ(15 cm) < Ξ(5 cm) could be attributed to the reduction in $\Phi_n(\kappa)$ for κ near the reciprocal of the outer scale, while Ξ(2 cm) < Ξ(5 cm) can be attributed to the decrease in $\Phi_n(\kappa)$ for κ near the reciprocal of l_0.

The authors thank Ting-i Wang, R. S. Lawrence, S. F. Clifford, and J. C. Wyngaard for their assistance and advice.

References

1. Ting-i Wang, G. R. Ochs, and S. F. Clifford, J. Opt. Soc. Am. 68, 334 (1978).
2. F. H. Champagne, C. A. Friehe, J. C. LaRue, and J. C. Wyngaard, J. Atmos. Sci. 34, 515 (1977).
3. R. M. Williams, Jr., and C. A. Paulson, J. Fluid Mech. 83, 547 (1977).
4. R. J. Hill, J. Fluid Mech. 88, 541 (1978).
5. R. J. Hill, Radio Sci. 13, to appear Nov.–Dec. issue (1978).
6. R. J. Hill and S. F. Clifford, J. Opt. Soc. Am. 68, 892 (1978).
7. J. C. Wyngaard and S. F. Clifford, J. Atmos. Sci. 35, 1204 (1978).

U. S. Department of Transportation Report FAA-RD-78-46, February 1978

SIMULATION OF RADAR-MEASURED DOPPLER VELOCITY PROFILES IN LOW-LEVEL WIND SHEAR (PHASE I)

W. B. Sweezy, W. R. Moninger, R. G. Strauch

A computer simulation of radar-measured radial velocity profiles was made to evaluate the effects of finite antenna beamwidth and the location of the radar on the measurement of low-level wind shear. The inputs to the computer simulation program are the radar characteristics and the existing wind field - the outputs are the wind component along any line (usually the glide path) and the radar-measured radial velocity profile for a given antenna location and antenna pointing. The results show that a radar beamwidth of 1.5 deg. provides sufficient spatial resolution to measure low-level wind profiles. However, when the wind fields contain horizontal gradients, headwinds and tailwinds encountered by an aircraft on the glide path cannot be measured by a fixed-beam radar that is offset from the end of the runway. A steerable antenna is needed to adequately measure the wind profile for these cases.

NOAA Technical Memorandum ERL WPL-40, November 1978

GRAVITY WAVE PROPAGATION IN THE PRESENCE OF A CURRENT WITH AN ARBITRARY VERTICAL PROFILE

Bob Weber

This paper determines analytically the effect of current shears upon the phase velocity of gravity waves on the oceans surface and the resulting consequences for an HF sea echo radar which measures surface currents. Past treatments of this subject have restricted the current profile in order to avoid singularities in the Rayleigh equation or they have required the use of numerical methods which do not readily allow generalizations to be drawn. It is found that the phase velocities of these waves depend upon the current at all depths but with more weight given to the current near the surface. For weak shears and deep water, the weighting approaches the exponential weighting derived by Stewart and Joy (1974). Therefore, an HF sea echo radar does not measure the current just at the surface with the result that its estimate of the surface current will be in some error due to a shear. However, large errors (amounting to more than 10% of the phase velocity of the gravity wave causing the sea echo) should be detectable by measuring the excess separation of the advancing and receding Bragg lines in the sea echo Doppler spectrum.

Journal of Atmospheric Science, 35: 1204-1211, 1978.

Estimating Momentum, Heat and Moisture Fluxes from Structure Parameters

J. C. Wyngaard

Cooperative Institute for Research in Environmental Sciences, University of Colorado/NOAA, Boulder 80309 and Wave Propagation Laboratory, NOAA, Boulder, CO 80302

S. F. Clifford

Wave Propagation Laboratory, NOAA, Boulder, CO 80302

(Manuscript received 26 September 1977, in final form 22 March 1978)

ABSTRACT

A theory is developed for obtaining the vertical fluxes of momentum, heat and moisture in a quasi-steady, locally-homogeneous surface layer from measurements of the structure parameters of velocity, temperature and humidity. The momentum flux is shown to be generally more sensitive to measurement errors in the structure parameters and to uncertainties in certain turbulence parameters than are the heat and moisture fluxes. The structure parameters can, in principle, be obtained from path-averaged wave propagation measurements; for example, the temperature structure parameter C_T^2 is readily obtained from optical scintillations. It is estimated that in the case of C_T^2 a path-averaged optical measurement requires about 1% of the averaging time of a conventional measurement of C_T^2 under typical conditions.

1. Introduction

The vertical fluxes of momentum, heat and moisture near the earth's surface are important both for boundary layer structure and dynamics and for larger scale atmospheric flow as well. Unfortunately, they are very difficult and expensive to measure directly, as discussed by Kaimal (1975). In addition, direct flux measurements require long averaging times (Wyngaard, 1973) and are apt to be unrepresentative over even mildly inhomogeneous terrain.

Indirect techniques, by which one infers fluxes from measurements of other flow properties, can be simpler and less expensive than direct measurements. Champagne *et al.* (1977) recently surveyed several of these indirect techniques, and showed that direct and indirect momentum, heat and moisture flux measurements compare well in the unstable surface layer over land.

Most of these indirect flux measurement techniques, when used with tower-based instrumentation, involve only point measurements. Such indirect techniques give little if any relief from the problems of long averaging times and spatial nonrepresentativeness. An optimum indirect approach would involve some spatial averaging, and would require only short time-averaging periods to give statistically reliable measurements.

With this in mind we recast the indirect flux measurement approach of Champagne *et al.* (1977) in terms of structure parameters, rather than dissipation rates, and extend it to the stably stratified case. This gives a theory, recently anticipated by Wesely (1976), for inferring surface-layer fluxes from structure parameters. For the case of the temperature structure parameter, we find that a significant reduction in averaging time is gained by dropping the conventional, point-measurement approach in favor of the measurement of path-averaged optical scintillations.

2. The indirect method

a. Theory

The vertical fluxes of horizontal momentum, temperature and water vapor are nearly independent of height in the lowest few tens of meters for typical conditions over uniform surfaces. We denote the surface values of these fluxes by τ_0, Q_0 and M_0, respectively. They define a scaling velocity u_*, a scaling temperature T_* and a scaling humidity q_* (Busch, 1973):

$$u_* = (\tau_0/\rho)^{\frac{1}{2}} \quad \text{[friction velocity (m s}^{-1}\text{)]}, \tag{1}$$

$$T_* = -Q_0/u_* \quad \text{[scaling temperature (K)]}, \tag{2}$$

$$q_* = -M_0/u_* \quad \text{[scaling humidity (g m}^{-3}\text{)]}, \tag{3}$$

where ρ is air density.

We denote the dissipation rates of turbulent kinetic energy, temperature variance and humidity variance by ϵ, χ_θ and χ_q. We define dimensionless dissipation rates by

$$\epsilon=\frac{u_*^3}{kz}\phi_\epsilon, \tag{4}$$

$$\chi_\theta=\frac{u_*T_*^2}{kz}X_\theta, \tag{5}$$

$$\chi_q=\frac{u_*q_*^2}{kz}X_q. \tag{6}$$

Here k is the von Kármán constant and z is height above the surface. Champagne *et al.* (1977) based their indirect flux measurement scheme on these dissipation rates, but we will now show that their scheme can be reworked to use structure parameters as inputs.

We consider structure functions for separation distances $r=|\mathbf{r}|$ in the inertial range of scales and we further assume these scales to be locally isotropic (Tennekes and Lumley, 1972). For temperature and humidity, these are related to the structure parameters C_T^2 and C_q^2 such that

$$D_T(\mathbf{r})=\overline{[T(\mathbf{x})-T(\mathbf{x}+\mathbf{r})]^2}=C_T^2r^{\frac{2}{3}}, \tag{7}$$

$$D_q(\mathbf{r})=\overline{[q(\mathbf{x})-q(\mathbf{x}+\mathbf{r})]^2}=C_q^2r^{\frac{2}{3}}. \tag{8}$$

The velocity structure function is a second-rank tensor, and as such the direction of the separation vector is important (Tatarskii, 1971). However, one can use the geometry of isotropic tensor functions to relate the various components (Batchelor, 1960). For simplicity we will use only one component, that for streamwise velocity and streamwise separation. In the inertial range this is

$$\overline{[u_1(\mathbf{x})-u_1(\mathbf{x}+\mathbf{r})]^2}=C_V^2r^{\frac{2}{3}},\quad \mathbf{r}=(r,0,0), \tag{9}$$

where C_V^2 is the velocity structure parameter.

The structure functions are related to one-dimensional spectra through Fourier transforms (Tatarskii, 1971). In the inertial range these spectra are

$$F_u=0.25C_V^2\kappa_1^{-5/3}=\alpha_1\epsilon^{\frac{2}{3}}\kappa_1^{-5/3}, \tag{10}$$

$$F_\theta=0.25C_T^2\kappa_1^{-5/3}=\beta_{1\theta}\chi_\theta\epsilon^{-\frac{1}{3}}\kappa_1^{-5/3}, \tag{11}$$

$$F_q=0.25C_q^2\kappa_1^{-5/3}=\beta_{1q}\chi_q\epsilon^{-\frac{1}{3}}\kappa_1^{-5/3}, \tag{12}$$

where the spectra are scaled such that the integral over the half-line is the variance, e.g.,

$$\int_0^\infty F_u(\kappa_1)d\kappa_1=\overline{u_1^2}. \tag{13}$$

We can rewrite (10)–(12) as

$$\epsilon=0.125(C_V^2)^{\frac{3}{2}}\alpha_1^{-\frac{3}{2}}, \tag{14}$$

$$\chi_\theta=0.125C_T^2(C_V^2)^{\frac{1}{2}}\alpha_1^{-\frac{1}{2}}\beta_{1\theta}^{-1}, \tag{15}$$

$$\chi_q=0.125C_q^2(C_V^2)^{\frac{1}{2}}\alpha_1^{-\frac{1}{2}}\beta_{1q}^{-1}. \tag{16}$$

We now solve (4)–(6) for u_*, T_* and q_*, use (14)–(16) to express the dissipation rates, and arrive at the following equations for fluxes:

$$\tau_0/\rho=0.25k^{\frac{2}{3}}\alpha_1^{-1}z^{\frac{2}{3}}C_V^2\phi_\epsilon^{-\frac{2}{3}}, \tag{17}$$

$$Q_0=0.25k^{\frac{2}{3}}\alpha_1^{-\frac{1}{2}}\beta_{1\theta}^{-\frac{1}{2}}z^{\frac{2}{3}}(C_V^2)^{\frac{1}{2}}(C_T^2)^{\frac{1}{2}}X_\theta^{-\frac{1}{2}}\phi_\epsilon^{-\frac{1}{6}}, \tag{18}$$

$$M_0=0.25k^{\frac{2}{3}}\alpha_1^{-\frac{1}{2}}\beta_{1q}^{-\frac{1}{2}}z^{\frac{2}{3}}(C_V^2)^{\frac{1}{2}}(C_q^2)^{\frac{1}{2}}X_q^{-\frac{1}{2}}\phi_\epsilon^{-\frac{1}{6}}. \tag{19}$$

Note if Q_0 (or M_0) is negative, we must take the negative square root of C_T^2 (or C_q^2) in (18) [or (19)].

The expressions (17)–(19) for fluxes contain the dimensionless dissipation rates ϕ_ϵ, X_q and X_θ. In order to deal with these, we assume we have a quasi-steady, locally homogeneous surface layer whose structure follows Monin-Obukhov similarity. Thus ϕ_ϵ, X_θ and X_q depend only on z/L, where L is the Monin-Obukhov length

$$L=\frac{-u_*^3T}{kgQ_{0V}} \tag{20}$$

and $Q_{0V}=Q_0+0.61TM_0/\rho$. This use of the virtual temperature flux Q_{0V} accounts for the effects of humidity fluctuations on buoyancy (Lumley and Panofsky, 1964).

We now rewrite the right-side of the L definition (20) by using (17)–(19) to express u_*^3 and Q_{0V}. We also make a second assumption: that the scalar spectral constants, and the dimensionless scalar dissipation rates, are equal ($\beta_{1\theta}=\beta_{1q}=\beta_1$; $X_\theta=X_q=X$). Then (20) becomes

$$\begin{aligned}&[(C_T^2)^{\frac{1}{2}}+(0.61T/\rho)(C_q^2)^{\frac{1}{2}}](g/T)z^{\frac{2}{3}}(C_V^2)^{-1}\\&\qquad=-0.5k^{-\frac{2}{3}}\beta_1^{\frac{1}{2}}\alpha_1^{-1}zX^{\frac{1}{2}}\phi_\epsilon^{-5/6}L^{-1}.\end{aligned} \tag{21}$$

The right side of (21) varies only with z/L, since k, β_1 and α_1 are constants. We define this to be $S(z/L)$:

$$S(z/L)\equiv-0.5k^{-\frac{2}{3}}\beta_1^{\frac{1}{2}}\alpha_1^{-1}zX^{\frac{1}{2}}\phi_\epsilon^{-5/6}L^{-1}. \tag{22}$$

We note from (21) that S can be calculated from measurements of structure parameters:

$$S(z/L)=[(C_T^2)^{\frac{1}{2}}+(0.61T/\rho)(C_q^2)^{\frac{1}{2}}](g/T)z^{\frac{2}{3}}(C_V^2)^{-1}. \tag{23}$$

Eqs. (22) and (23), in conjunction with (17)–(19), allow us to estimate fluxes from structure parameters. To do this, we calculate S from (23), using measured structure parameters. As explained in the next section, the right side of (22) has been determined experimentally; thus one knows $S(z/L)$, and having S one can infer z/L. Then having z/L, one knows X and ϕ_ϵ in (17)–(19), which with the structure parameters and the constants give the fluxes.

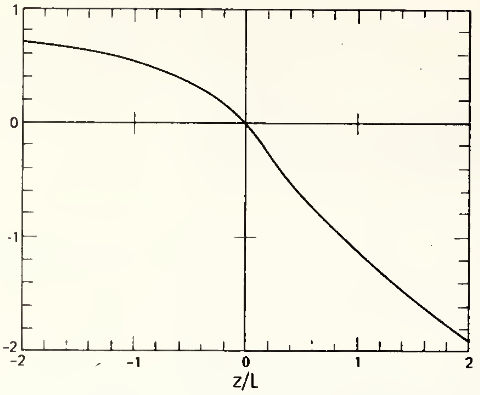

FIG. 1. The stability function S [defined in (22)] as a function of z/L, calculated from (24)–(27) with $k=0.35$, $\alpha_1=0.5$, $\beta_1=0.4$.

b. Examples

We will explore further this flux estimation technique by introducing some surface layer data. We take $k=0.35$ (Businger *et al.*, 1971) and $\alpha_1=0.5$, $\beta_1=0.4$ (Champagne *et al.*, 1977). For unstable conditions we will use (as did Champagne *et al.*, 1977)

$$\phi_\epsilon=[1+0.5(-z/L)^{\frac{2}{3}}]^{\frac{3}{2}}, \tag{24}$$

$$X=\frac{1.48}{[1-9(z/L)]^{\frac{1}{2}}}, \tag{25}$$

which are based on the 1968 Kansas experiments, and should be good approximations in the range $0\leqslant -z/L<2$. For stable conditions, the Kansas data indicate that the turbulent transport terms in the budgets of turbulent kinetic energy and temperature variance are negligible (Wyngaard and Coté, 1971). This implies that molecular destruction balances production caused by the mean wind and temperature gradients. Using the Kansas forms for these gradients (Businger *et al.*, 1971) gives for stable conditions in the range $0\leqslant z/L\leqslant 1$

$$\phi_\epsilon=1+3.7z/L, \tag{26}$$

$$X=2[0.74+4.7(z/L)]. \tag{27}$$

Fig. 1 shows a plot of $S(z/L)$ calculated from (22) using $k=0.35$, $\alpha_1=0.5$, $\beta_1=0.4$ and the expressions (24)–(27) for ϕ_ϵ and X. Note that S is well-behaved in the sense that one can infer a z/L value from the value for S. Note also that one must know *a priori* the signs of Q_0 and M_0.

In this example we used ϕ and X expressions approximating surface-layer behavior over a limited range, roughly $-2<z/L<1$. More stable conditions at $z=5$ m, say, would typically have very low turbulence levels and negligible fluxes, and we will not consider these. More unstable conditions can be found under very light winds and strong insolation, when the heat and moisture fluxes could be large. Thus it is useful to consider briefly the extension of the technique to very unstable conditions.

From the definition of z/L,

$$\frac{z}{L}=\frac{(g/T)Q_{0V}}{u_*^3/kz}. \tag{28}$$

We can interpret large negative z/L values as meaning $(g/T)Q_{0V}\gg u_*^3/kz$, or that the rate of turbulent energy production by bouyancy effects is large compared with that by shear. Thus at large $-z/L$ we expect large velocity variances relative to u_*^2; in the convective limit ($L\to 0$), u_*^2 vanishes but the velocity variances and C_V^2 are finite. Thus indirect stress measurements of the type discussed here are inherently limited to stabilities not far from neutral.

We can extend our indirect technique for Q_0 and M_0 to very unstable conditions, however. Rather than use asymptotic forms in the expressions (18) and (19) for Q_0 and M_0, it is simpler to start from the Kansas results for C_T^2 under unstable conditions (Wyngaard *et al.*, 1971):

$$C_T^2=\frac{4.9Q_0^2u_*^{-2}z^{-\frac{2}{3}}}{(1-7z/L)^{\frac{2}{3}}}. \tag{29}$$

This can be written, using (20), as

$$C_T^2\doteq 2.7Q_0^2z^{-\frac{4}{3}}(g/T)^{-\frac{2}{3}}Q_{0V}^{-\frac{2}{3}}\left(\frac{-7z/L}{1-7z/L}\right)^{\frac{2}{3}}. \tag{30}$$

Although the extension to C_q^2 has not been experimentally verified, according to the Monin-Obukhov similarity hypothesis (Busch, 1973) the analogous expression should hold:

$$C_q^2=2.7M_0^2z^{-\frac{4}{3}}(g/T)^{-\frac{2}{3}}Q_{0V}^{-\frac{2}{3}}\left(\frac{-7z/L}{1-7z/L}\right)^{\frac{2}{3}}. \tag{31}$$

At $-z/L=1$ the stability term in (30) and (31) is within 10% of its asymptotic value of 1.0. Hence measurements of C_T^2 and C_q^2 in the very unstable surface layer ($-z/L>1$) would in principle give both Q_0 and M_0 through solution of

$$C_T^2=2.7Q_0^2z^{-\frac{4}{3}}(g/T)^{-\frac{2}{3}}[Q_0+0.61T(M_0/\rho)]^{-\frac{2}{3}}, \tag{32}$$

$$C_q^2=2.7M_0^2z^{-\frac{4}{3}}(g/T)^{-\frac{2}{3}}[Q_0+0.61T(M_0/\rho)]^{-\frac{2}{3}}. \tag{33}$$

Under dry ($0.61TM_0\ll\rho Q_0$), very unstable conditions we find, from (32)

$$Q_0\approx 0.5(C_T^2)^{\frac{3}{4}}z(g/T)^{\frac{1}{2}}. \tag{34}$$

Measurements at Table Mountain, near Boulder, using C_T^2 inferred from optical scintillations over a 300 m path at $z=4$ m, support (34) (Wyngaard *et al.*, 1978a).

3. Error analysis

Fluxes estimated through our indirect technique are subject to errors from a number of sources. We will consider here in detail the flux errors from two such sources: the specification of universal constants and stability functions, and the measurement of the structure parameters.

We examine first the effect of errors in constants and stability functions. Assume for the moment that the structure parameters are known exactly, so one calculates S from (23) without error. However, (22) shows that a z/L value inferred from S will be in error if k, β_1, α_1, X or ϕ_ϵ is in error. We see from the flux expressions (17)–(19) that the fluxes will also be in error, both directly through the errors in k, β_1, α_1, X and ϕ_ϵ and indirectly through the changes in X and ϕ_ϵ caused by errors in their argument z/L.

In spite of intensive micrometeorological research in the past few decades, significant uncertainties remain in both the values of the universal constants k, α_1 and β_1, and the functions X and ϕ_ϵ. Currently used values of the von Kármán constant k range from the 0.35 found in Kansas (Businger *et al.*, 1971) to the traditional value of 0.40 or even slightly larger (Pruitt *et al.*, 1973; Frenzen, 1973, 1977). The spread in currently used values for the one-dimensional Kolmogorov velocity spectral constant α_1 is about as large, in percentage terms, at about 0.45–0.55. The temperature spectral constant β_1 has undergone larger excursions, partly because of recently discovered measurement problems. Hill's (1978) recent survey gives a range of 0.40–0.50 for β_1. The functions X and ϕ_ϵ are more difficult to measure accurately than are k, α_1 and β_1, so that their uncertainties are even larger. Yaglom (1977), in his review of flux-profile relationships, has discussed these and related uncertainties in detail. We stress, therefore, that our choices for k, α_1, β_1, X and ϕ_ϵ in the previous section are undoubtedly somewhat in error, and we turn now to an analysis of the effects of such errors on the flux estimates.

We consider separately the effects of errors in k, α_1, β_1, X and ϕ_ϵ, and allow no other errors. We assume the error level is sufficiently small that we can use a linearized analysis. It is convenient to do this by differential calculus, as we can illustrate by an example involving an error in β_1. We write the stability index S as, from (22),

$$S=S(k,\beta_1,\alpha_1,z/L,X,\phi_\epsilon). \tag{35}$$

We assume S is calculated exactly from structure parameters, using (23); thus $dS=0$, so that

$$0=\frac{\partial S}{\partial \beta_1}d\beta_1+\frac{\partial S}{\partial (z/L)}d(z/L). \tag{36}$$

Thus the error in z/L, $d(z/L)$, caused by the error in β_1, $d\beta_1$ is

$$d(z/L)=-\frac{\partial S}{\partial \beta_1}\left[\frac{\partial S}{\partial (z/L)}\right]^{-1}d\beta_1. \tag{37}$$

Now let F be any one of the fluxes. From (17)–(19), we have in general

$$F=F(k,\alpha_1,\beta_1,X,\phi_\epsilon). \tag{38}$$

The flux error is

$$dF=\frac{\partial F}{\partial \beta_1}d\beta_1+\frac{\partial F}{\partial X}dX+\frac{\partial F}{\partial \phi_\epsilon}d\phi_\epsilon, \tag{39}$$

which, on using

$$dX=\frac{dX}{d(z/L)}d(z/L), \tag{40}$$

$$d\phi_\epsilon=\frac{d\phi_\epsilon}{d(z/L)}d(z/L), \tag{41}$$

and (37), finally yields

$$dF=\left\{\frac{\partial F}{\partial \beta_1}-\left[\frac{\partial F}{\partial X}\frac{dX}{d(z/L)}+\frac{\partial F}{\partial \phi_\epsilon}\frac{d\phi_\epsilon}{d(z/L)}\right]\frac{\partial S}{\partial \beta_1}\left[\frac{\partial S}{\partial (z/L)}\right]^{-1}\right\}d\beta_1. \tag{42}$$

The calculation of the flux errors induced by errors in k, α_1, X and ϕ_ϵ proceeds similarly. The results of this error analysis appear in Fig. 2. The upper panel shows that momentum flux is relatively sensitive to errors in α_1, for example; the sign of the flux error is opposite that of the error in α_1, has the same percentage magnitude at $z/L=0$, and increases for stable or unstable stratification. The momentum flux is less sensitive to errors in ϕ_ϵ, and relatively insensitive to errors in k, β_1 and X. The lower panel indicates that the errors induced in the scalar fluxes (Q_0 and M_0) are, on the average, smaller than stress errors.

From our earlier discussion, the expected errors in k, α_1 and β_1 are of the order of 15% or less. Thus Fig. 2 suggests these should not cause serious flux uncertainties. The situation for X and ϕ_ϵ is less clear; the uncertainty in these is probably greater, perhaps of the order of 20–30%. In view of this, and the results in Fig. 2, it seems that under unstable conditions one can expect some difficulties in estimating momentum flux accurately (say to within 20%); accurate scalar flux estimates should be easier. While the individual curves are different on the stable side, the overall situation there should be about the same.

The second source of flux error that we will analyze lies in the measurement of the structure parameters. We denote the measured structure parameters with

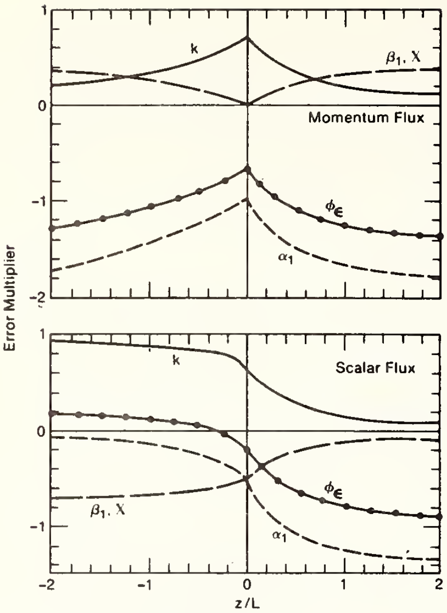

FIG. 2. Flux error multipliers (fractional flux error/fractional input parameter errors), with input parameters varied separately: (——) k varied; (- - - -) α_1 varied; (— —) β_1 or X varied; (—) ϕ_ϵ varied. Top panel, effect on momentum flux; bottom panel, effect on scalar fluxes.

a subscript m:

$$(C_T^2)_m = C_T^2(1+e_T), \quad (43)$$

$$(C_q^2)_m = C_q^2(1+e_q), \quad (44)$$

$$(C_V^2)_m = C_V^2(1+e_V). \quad (45)$$

Here e_T, e_q and e_V are the fractional errors incurred in the measurement of the structure parameters. We assume now that k, α_1, β_1, X and ϕ_ϵ are known exactly, and that there are no other errors. We consider a large ensemble of experiments and take e_T, e_q and e_V to be statistically independent and have zero mean; the root-mean-square (rms) fractional errors are assumed equal and denoted by e.

We calculated the rms, fractional errors in the fluxes by again assuming small input errors ($e<0.3$, say) and performing a linearized analysis. The results are presented in Fig. 3. The results shown are for the dry-land (large Bowen ratio) case, where

$$\frac{0.61TM_0}{\rho Q_0} \ll 1. \quad (46)$$

Results for typical over-sea conditions ($0.61TM_0 \approx \rho Q_0$) differ only slightly from those of Fig. 3. The results of Fig. 3 indicate that the momentum flux is most sensitive to structure parameter errors. This sensitivity is largest under unstable conditions, where the rms, fractional momentum flux error is about twice that in the structure parameters. The scalar fluxes are less sensitive, particularly under unstable conditions.

Finally, we made several key assumptions in our development of our indirect technique, and these are also a potential source of errors. We assumed $\beta_{1\theta} = \beta_{1q}$, which is plausible but not firmly verified. We also assumed $X_\theta = X_q$; Warhaft's (1976) arguments suggest they might differ slightly, but here again there appear to be no data suitable for a critical examination of this question. There is also the question of the extent to which the locally homogeneous, stationary surface layer follows M-O similarity. Businger (1973) has examined some of the effects on surface-layer structure caused by the large, convective-driven eddies which fill the unstable planetary boundary layer. Panofsky *et al.* (1977) used recent data to show that horizontal wind variances in the unstable surface layer are not M-O similar but are tied to these large eddies. It seems possible that they could also cause deviations from M-O similarity in the turbulent kinetic energy budget, and hence also in X and ϕ_ϵ, in the unstable surface layer. Further research on deviations from M-O similarity would be particularly useful.

4. Averaging times

While the statistical properties we are discussing, such as fluxes and structure parameters, are in principle determined from ensemble averages, in practice we must use time averages. It is known (Haugen *et al.*, 1971; Wyngaard, 1973) that very long averaging times are required in order that direct, single-point heat and momentum flux estimates in the unstable surface layer approach their true ensemble means. Indications are that several hours are required for accurate flux estimates in the mid-regions of a convective boundary layer. Higher moments require even longer averaging times, and this is a serious limitation of fixed-point boundary layer turbulence measurements.

Our indirect flux measurement method requires time-averaged structure parameters. These can be found in two ways—from paired, point measurements, using their definitions in (7)–(9), or, in prin-

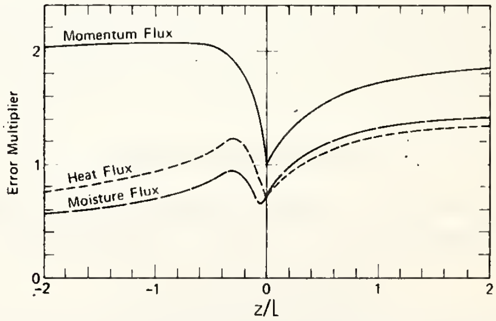

FIG. 3. Flux error multipliers (rms fractional flux error divided by rms fractional structure parameter errors). For simultaneous, statistically independent, equal-amplitude structure parameter errors, and $0.61TM_0 \ll \rho Q_0$ (dry land).

ciple, from path-averaged optical, acoustic or radio wave measurements (Tatarskii, 1971).

As an example of the second, C_T^2 can be determined from optical scintillations. Under normal conditions over dry land ($0.61TM_0 \ll \rho Q_0$) optical refractive index fluctuations are caused almost entirely by temperature fluctuations (Friehe *et al.*, 1975), and the refractive index structure parameter C_n^2 is proportional to C_T^2. The log-intensity variance of a point detector receiving a spherical wave of wavenumber κ over a horizontal, uniform path of length R is (Lawrence and Strohbehn, 1970)

$$\sigma_{\ln I}^2 = 0.50 C_n^2 \kappa^{7/6} R^{11/6} \tag{47}$$

in the linear theory. Thus C_T^2 can be found from log-intensity variance measurements or from spaced temperature sensors.

The structure parameters C_V^2 and C_q^2 can also (in principle) be determined from other wave propagation measurements. Humidity contributes to both the optical and radio refractive index, so intensity and phase fluctuations at the detector also contain information on C_q^2. The time changes in intensity and phase are affected not only by the mean wind across the optical and radio path, but also by the velocity fluctuations along the path; thus the received beam also contains information on C_V^2. In a more direct way, acoustic intensity fluctuations are caused by C_V^2. Techniques for inferring C_q^2 and C_V^2 from wave propagation measurements are yet to be demonstrated, however, and we will confine ourselves here to C_T^2.

Each of the two ways of determining C_T^2—from spaced, point temperature measurements or from optical scintillations—requires time averaging of a random signal. Our question is: how do the required averaging times compare?

We base our analysis on the discussion by Lumley and Panofsky (1964). They show that the averaging time T required to determine within a fractional error e the average f_T, defined by

$$f_T = \frac{1}{T} \int_t^{t+T} f(t')dt', \tag{48}$$

is

$$T = \frac{2\overline{f'^2}\tau}{\bar{f}^2 e^2}, \tag{49}$$

where τ is the integral scale of $f(t)$ and $\overline{f'^2}$ is the ensemble average variance of f about its ensemble mean $\bar{f}$. In each case here f is a squared signal:

$$f_{\text{direct}} = [T(\mathbf{x},t) - T(\mathbf{x}+\mathbf{r},t)]^2 = \Delta T^2, \tag{50}$$

$$f_{\text{optical}} = (\ln I)^2. \tag{51}$$

Thus

$$\left.\frac{\overline{f'^2}}{\bar{f}^2}\right|_{\text{direct}} = \frac{\overline{(\Delta T^2 - \overline{\Delta T^2})^2}}{(\overline{\Delta T^2})^2} = K_{\Delta T} - 1, \tag{52}$$

$$\left.\frac{\overline{f'^2}}{\bar{f}^2}\right|_{\text{optical}} = \frac{\overline{[(\ln I)^2 - (\overline{\ln I)^2}]^2}}{[(\overline{\ln I)^2}]^2} = K_{\text{optical}} - 1, \tag{53}$$

where K is the kurtosis of the signal, i.e.,

$$K_x = \frac{\overline{x^4}}{(\overline{x^2})^2}. \tag{54}$$

If we fix the accuracy requirements, the ratio of required averaging times becomes

$$\frac{T_{\text{direct}}}{T_{\text{optical}}} = \frac{[\tau(K-1)]_{\text{direct}}}{[\tau(K-1)]_{\text{optical}}}. \tag{55}$$

We will now estimate K and τ for the two processes. Taking the direct measurement first, we assume that the separation vector $\mathbf{r}$ of the temperature sensors is perpendicular to the mean horizontal wind $\bar{\mathbf{V}}$. The integral scale of the time signal $\Delta T^2(t) \equiv [T(\mathbf{x},t) - T(\mathbf{x}+\mathbf{r},t)]^2$ is defined in terms of its correlation function $R_{\Delta T^2}(\tau)$, i.e.,

$$\tau_{\Delta T^2} = \int_0^\infty R_{\Delta T^2}(\tau)d\tau \Big/ R_{\Delta T^2}(0), \tag{56}$$

where $R_{\Delta T^2}(\tau)$ is

$$R_{\Delta T^2}(\tau) = \overline{[\Delta T^2(0) - \overline{\Delta T^2}(0)][\Delta T^2(\tau) - \overline{\Delta T^2}(\tau)]}. \tag{57}$$

In order to make this tractable we will assume, for estimation purposes, that $\Delta T^2(t)$ is a Gaussian process. When (57) is expanded the fourth moments can be expressed as products of second moments, and we find

$$R_{\Delta T^2}(\tau) = 2R_{\Delta T}^2(\tau), \tag{58}$$

where $R_{\Delta T}(\tau)$ is the correlation function of ΔT, i.e.,

$$R_{\Delta T}(\tau) = \overline{[T(\mathbf{x},0) - T(\mathbf{x}+\mathbf{r},0)][T(\mathbf{x},\tau) - T(\mathbf{x}+\mathbf{r},\tau)]}. \tag{59}$$

Expanding (59), assuming Taylor's hypothesis in order to relate temporal and streamwise spatial correlations, and assuming local isotropy gives

$$R_{\Delta T}(\tau) = D_T(\mathbf{r} - \bar{\mathbf{V}}\tau) - D_T(\bar{\mathbf{V}}\tau). \tag{60}$$

In this range of separation we have

$$D_T(\mathbf{r}) = D_T(r) = C_T^2 r^{\frac{2}{3}}, \tag{61}$$

$$R_{\Delta T}(\tau) = C_T^2 |\mathbf{r} - \bar{\mathbf{V}}\tau|^{\frac{2}{3}} - C_T^2 |\bar{\mathbf{V}}\tau|^{\frac{2}{3}}. \tag{62}$$

Combining (56), (58) and (62) and integrating gives finally

$$\tau_{\Delta T^2} \approx r/3U, \tag{63}$$

where $U = |\bar{\mathbf{V}}|$.

We also need the kurtosis of ΔT. Park (1976) has measured structure functions of velocity and temperature at 3.8 and 4.8 m above the ocean, and finds that for streamwise separations in the range 1 cm$<r$ $<$100 cm,

$$K_{\Delta T} \approx 100\,(r/\eta)^{-0.4}, \tag{64}$$

where $\eta = (\nu^3/\epsilon)^{\frac{1}{4}}$ is the Kolmogorov microscale and ν the kinematic viscosity. Measurements at 1.4 m over a wheat canopy by Antonia and Van Atta (1978) suggest a constant in (64) closer to 80 and an exponent $-\frac{1}{3}$, but the difference for our purposes is negligible and we will use (64).

The expression for the averaging time for direct measurement of C_T^2 becomes, from (49), (51), (63) and (64),

$$T_{\text{direct}} \propto (30/U) r^{0.6} \eta^{0.4}. \tag{65}$$

This estimate should be useful throughout the boundary layer, although we will use it only in the surface layer. Note that the $\eta^{0.4}$ term is essentially constant there ($\eta^{0.4} \approx \epsilon^{-0.1}$) so the dominant influences on T_{direct} are r and U. We should not expect (65) to hold as we approach free convection ($U \rightarrow 0$) under unstable conditions. There the large eddies give short term mean horizontal wind speeds of the order of $w_* = [(g/T_0)Q_0 z_i]^{\frac{1}{3}}$ in the surface layer, and thus T_{direct} does not grow without bound in this case as $U \rightarrow 0$, as implied by (65).

We turn now to the optical scintillations. Log-intensity fluctuations are closely Gaussian (Lawrence and Strohbehn, 1970) so $K_{\text{optical}} = 3$, and

$$R_{(\ln I)^2}(\tau) = 2R^2_{\ln I}(\tau). \tag{66}$$

The correlation function $R_{\ln I}$ has been calculated (Clifford *et al.*, 1974). For a point detector and spherical waves, we find by numerical integration

$$\tau_{\text{optical}} \approx \frac{0.27(\lambda R)^{\frac{1}{2}}}{U_n}, \tag{67}$$

where λ is the optical wavelength, R the optical path length, and U_n the mean wind transverse to the path. Combining these results for K and τ for the optical process gives

$$T_{\text{optical}} \propto \frac{0.5(\lambda R)^{\frac{1}{2}}}{U_n}. \tag{68}$$

Note that U_n here plays the role of U in the expression (65) for T_{direct}, and we should not expect that $T_{\text{optical}} \rightarrow \infty$ as $U_n \rightarrow 0$ under very unstable conditions. Note also that T_{optical} is predicted to increase as the path length R increases. This is because optical technique essentially measures the intensity of eddies of size near $(\lambda R)^{\frac{1}{2}}$, and the averaging time to determine this intensity increases linearly with the eddy size. The increased averaging time indicated for longer paths should be offset by the increased representativeness of the longer path estimate. The path weighting function for the optical scintillation technique is closely parabolic, varying as $[(x/R)(1-x/R)]^{5/6}$, where x is the position along the optical path.

Combining (65) and (68) gives

$$\frac{T_{\text{direct}}}{T_{\text{optical}}} \approx \frac{60 r^{0.6} \eta^{0.4} U_n}{(\lambda R)^{\frac{1}{2}} U}. \tag{69}$$

For a typical case $r = 20$ cm, $\eta = 0.1$ cm, $U_n = U$, $\lambda = 0.6 \times 10^{-6}$ m, $R = 300$ m, giving

$$\frac{T_{\text{direct}}}{T_{\text{optical}}} \approx 100. \tag{70}$$

This indicates that the optical technique for determining C_T^2 under these conditions will require only 1% the averaging time of the direct measurement, for the same accuracy. Our experience indicates that at $z = 5$ m under typical conditions this means 10–20 s as opposed to 15–30 min. This estimate should hold throughout the surface layer.

5. Discussion

Other parameters which can in principle be determined from propagation measurements, such as the mean vertical gradients of wind, temperature and humidity, can also be used to infer fluxes indirectly. In fact this is the traditional approach to indirect flux measurements, as discussed by Champagne *et al.* (1977). We cast our theory in terms of structure parameters because they enter directly into the theory of wave propagation through turbulence; thus one can (in principle) infer structure parameters by observing turbulence effects on propagated waves.

Up to this point we have made no mention of the joint temperature-humidity structure parameter C_{Tq} which arises through the correlation between temperature and humidity fluctuations. C_{Tq} also affects electromagnetic and acoustic wave propagation (Gossard, 1960; Friehe *et al.*, 1975), since the refractive index fluctuation n can be expressed in general as

$$n = -C(\theta + aq), \tag{71}$$

where C is a conversion constant and the factor a depends on the wavelength of the radiation. Eq. (71) implies that the structure parameters are related by (Wyngaard *et al.*, 1978b)

$$C_n^2 \propto C_T^2 + 2aC_{Tq} + a^2 C_q^2. \tag{72}$$

Wyngaard *et al.* (1978b) discuss the surface layer behavior of C_{Tq}, showing that it is maintained by processes analogous to those which maintain C_T^2 and C_q^2. Our theory here could have been posed in terms of C_{Tq} rather than C_q^2, but we chose not to do this since at present there is no demonstrated technique for determining either one from propagation measurements. As propagation effects become better explored, however, the structure parameter C_{Tq} might well be a useful key to surface layer fluxes.

Acknowledgments. We are grateful to Dr. Joel Park for supplying his thesis data, to Jeanette Trebing for her flawless typing of the manuscript, and to R. J. Hill and the referees for helpful suggestions.

REFERENCES

Antonia, R. A., and C. W. Van Atta, 1978: Structure functions of temperature fluctuations in turbulent shear flows. *J. Fluid Mech.*, **84**, 561–580.

Batchelor, G. K., 1960: *The Theory of Homogeneous Turbulence.* Cambridge University Press, 197 pp.

Busch, N. E., 1973: On the mechanics of atmospheric turbulence. *Workshop on Micrometeorology*, Amer. Meteor. Soc., 1–65.

Businger, J. A., 1973: A note on free convection. *Bound.-Layer Meteor.*, **4**, 323–326.

——, J. C. Wyngaard, Y. Izumi and E. F. Bradley, 1971: Flux-profile relationships in the atmospheric surface layer. *J. Atmos. Sci.*, **28**, 181–189.

Champagne, F. H., C. A. Friehe, J. C. LaRue and J. C. Wyngaard, 1977: Flux measurements, flux-estimation techniques, and fine-scale turbulence measurements in the unstable surface layer over land. *J. Atmos. Sci.*, **34**, 515–530.

Clifford, S. F., G. R. Ochs and R. S. Lawrence, 1974: Saturation of optical scintillation by strong turbulence. *J. Opt. Soc. Amer.*, **64**, 148–159.

Frenzen, P., 1973: The observed relation between the Kolmogorov and von Kármán constants in the surface boundary layer. *Bound. Layer Meteor.*, **3**, 348–358.

Frenzen, P., 1977: A generalization of the Kolmogorov-von Kármán relationship and some further implications on the values of the constants. *Bound.-Layer Meteor.*, **11**, 375–380.

Friehe, C. A., J. C. LaRue, F. H. Champagne, C. H. Gibson and G. F. Dreyer, 1975: Effects of temperature and humidity fluctuations on the optical refractive index in the marine boundary layer. *J. Opt. Soc. Amer.*, **65**, 1502–1511.

Gossard, E. E., 1960: Power spectra of temperature, humidity, and refractive index from aircraft and tethered balloon measurements. *IEEE Trans. Antennas Propagation*, **AP-3**, 186–201.

Haugen, D. A., J. C. Kaimal and E. F. Bradley, 1971: An experimental study of Reynolds stress and heat flux in the atmospheric surface layer. *Quart. J. Roy. Meteor. Soc.*, **97**, 168–180.

Hill, R. J., 1978: Models of the scalar spectrum for turbulent advection. To appear in *J. Fluid Mech.*

Kaimal, J. C., 1975: Sensors and techniques for direct measurement of turbulent fluxes and profiles in the atmospheric surface layer. *Atmos. Tech.*, **7**, 7–14 [Available from NCAR].

Lawrence, R. A., and J. W. Strohbehn, 1970: A survey of clear-air propagation effects relevant to optical communications. *Proc. IEEE*, **58**, 1523–1545.

Lumley, J. L., and H. A. Panofsky, 1964: *The Structure of Atmospheric Turbulence.* Interscience-Wiley, 239 pp.

Panofsky, H. A., H. Tennekes, D. H. Lenschow and J. C. Wyngaard, 1977: The characteristics of turbulent velocity components in the surface layer under convective conditions. *Bound.-Layer Meteor.*, **11**, 355–361.

Park, J. T., 1976: Inertial subrange turbulence measurements in the marine boundary layer. Ph.D. thesis, University of California, San Diego.

Pruitt, W. O., D. L. Morgan, and F. J. Lourence, 1973: Momentum and mass transfers in the surface boundary layer. *Quart. J. Roy. Meteor. Soc.*, **99**, 370–386.

Tatarskii, V. I., 1971: *The Effects of the Turbulent Atmosphere on Wave Propagation.* [NTIS No. TT-68-50464].

Tennekes, H., and J. L. Lumley, 1972: *A First Course in Turbulence.* The MIT Press, 300 pp.

Warhaft, Z., 1976: Heat and moisture flux in the stratified boundary layer. *Quart. J. Roy. Meteor. Soc.*, **102**, 703–707.

Wesely, M. L., 1976: A comparison of two optical methods for measuring line averages of thermal exchanges above warm water surfaces. *J. Appl. Meteor.*, **15**, 1177–1188.

Wyngaard, J. C., 1973: On surface-layer turbulence. *Workshop on Micrometeorology*, Amer. Meteor. Soc., 101–149.

——, and O. R. Coté, 1971: The budgets of turbulent kinetic energy and temperature variance in the atmospheric surface layer. *J. Atmos. Sci.*, **28**, 190–201.

——, Y. Izumi, and S. A. Collins, Jr., 1971: Behavior of the refractive index structure parameter near the ground. *J. Opt. Soc. Amer.*, **61**, 1646–1650.

——, J. C. Kaimal, G. R. Ochs, R. J. Hill and D. C. Sorensen, 1978a: An optical heat flux experiment. *Preprints 4th Symp. Meteorological Observations and Instrumentation*, Denver, Amer. Meteor. Soc., 47–50.

——, W. T. Pennell, D. H. Lenschow and M. A. LeMone, 1978b: The temperature-humidity covariance budget in the convective boundary layer. *J. Atmos. Sci.*, **35**, 47–58.

Yaglom, A. M., 1977: Comments on wind and temperature flux-profile relationships. *Bound.-Layer Meteor.*, **11**, 89–102.

Preprint Volume; Fourth Symposium on Meteorological Observations
and Instrumentation, 15-18, American Meteorological Society, 1978.

EFFECTS OF SAMPLING RATES AND AVERAGING PERIODS ON METEOROLOGICAL MEASUREMENTS

Duane A. Haugen

NOAA/ERL/Wave Propagation Laboratory
Boulder, Colorado 80302

1. INTRODUCTION

The range of space and time scales of atmospheric motions is nearly infinite. However, studies of atmospheric motions are almost always limited to a relatively narrow range of scales. This invariably raises questions of the sampling rates and averaging periods that should be chosen to assure a proper understanding of the particular scales of motion being studied. In this paper, I will discuss sampling rates and averaging periods related to turbulent motions in the atmospheric boundary layer.

The first part of the paper is based on work by Lumley and Panofsky (1964), Wyngaard (1973), and Wyngaard et al. (1974). The objective is to illustrate sampling and averaging problems inherent in in situ measurements of turbulence quantities such as means, variances, covariances, and higher order moments. Sampling problems related to computation of turbulence spectra are *not* discussed.

The second part of the paper deals with the problem of comparing in-situ sensors and remote probes in the measurement of wind speed means, variances, and covariances. The discussion is restricted to the comparison of conventional anemometry with devices that derive wind data from measured Doppler frequency shifts of backscattered energy.

2. MEASUREMENT OF TURBULENCE PROPERTIES

The statistical theories of turbulence employ a concept defined as the ensemble average. In principle, an ensemble average of a property can be obtained by observing a random process an infinite number of times while holding fixed all the controlling conditions for the process. For example, suppose that the air speed at a fixed point in a wind tunnel is a random process controlled by the physical properties of the tunnel, the density of the air, and the pressure head driving the mean flow. An ensemble of air speeds can be obtained by repeatedly measuring the speed while holding the controlling conditions constant. One can then imagine computing moments (mean, variances, third moments, etc.) or any other turbulence property desired from this ensemble. The result, by definition, would be a perfect description of the turbulence property computed. We define any *finite* set of air speed values as a *realization of turbulence* for the same constant controlling conditions. Any turbulence property we compute from this realization will probably differ from its ensemble value. There are various statistical techniques we can use to estimate the error or difference between a value based on a realization and its ensemble value. But the basic point to appreciate is that our knowledge of a turbulence property will always be imperfect based as it is on finite realizations of the turbulence. Statistical theories, however, predict that the size of error decreases in direct proportion to the number of realizations and to the length of the observation period of a given realization.

Let us now consider these same concepts in the context of the atmospheric boundary layer. The first complication we note is that we can rarely define with confidence the controlling conditions for any random process. This has profound effect on our knowledge of turbulence for it means that, contrary to the wind tunnel example, we have great difficulty in defining a realization of turbulence. As a direct consequence, we frequently resort to measuring a time series of a process at a fixed point in space. The resulting time averages are then the only estimates we have of the corresponding ensemble averages. The literature is rich with evidence, however, that these estimates are very reliable for carefully chosen conditions of horizontally homogeneous flat terrain and near stationary turbulence. Experiment and theory are well-linked in this case and have established a firm basis for a large number of similarity analyses. But even for this idealized situation, there are serious sampling and averaging problems to consider which depend strongly on the particular turbulent process. Lumley and Panofsky (1964, pp. 35-38) show that the averaging period, T, required to measure a random process, f, to a given level of accuracy, a, is given by

$$T \cong \frac{2\tau \overline{f'^2}}{\overline{f}^2 a^2} \qquad (1)$$

where τ is the integral time scale of f and $\overline{f'^2}$ is the ensemble average variance of f about its ensemble mean, $\overline{f}$. Using this expression, they estimate that it takes roughly five times as long to determine a fourth moment to the same accuracy as a second moment. This same expression is used by Wyngaard (1973) and Wyngaard et al. (1974) to estimate averaging times for Reynolds stress, $\overline{uw}$, and heat flux, $\overline{w\theta}$. Within the framework of a mathematical model of boundary layer flow, they show that it takes roughly twice as long for the heat flux and ten to two hundred times as long for Reynolds stress to attain the same accuracies as for the variance.

Translation of these estimates into specific recommendations for averaging times is not possible with our present knowledge of boundary layer turbulence. Both τ and $\overline{f'^2}/\overline{f}^2$ are functions of the process f itself, of height, and of stability. However, for purposes of illustration, let us assume that τ equals one second for all processes (admittedly a crude assumption).

Then, as suggested by Wyngaard in the cited references, the guidelines presented in Table 1 can be computed.

Table 1. Percentage error of estimates for selected random processes and averaging periods, T.

Process	T = 15 min	T = 60 min
Mean wind speed	1%	0.5%
Wind speed variance	7%	3.5%
Heat flux	10%	5%
Reynolds stress	20 to 100%	10 to 50%

On the basis of these computations, it seems reasonable to assume that third moment terms such as $\overline{uvw}$, uw^2 and $\overline{uw\theta}$ which appear in various turbulent energy budget equations will have uncertainties equal to or greater than the Reynolds stress uncertainties.

If the averaging period could be increased indefinitely, then obviously the error in estimating all processes could be reduced to a negligible amount. However, a 60-min average is about as long as practical for the atmospheric boundary layer. Longer averaging periods are adversely affected by the diurnal cycle in surface heat flux and height of the mixed layer. Indeed, to minimize non-stationarity effects, one should always choose averaging periods 3 to 4 hours away from the transition periods near dawn and dusk. An example of observational periods selected with this in mind may be seen in a recent study by Kaimal et al. (1976).

Let us now briefly discuss the effects of sampling rate on estimates of turbulent processes. In light of the preceding discussion, this is a trivial problem for stationary turbulence where one can extend the averaging period indefinitely. Provided we have a sensor that introduces no errors due to response characteristics and we completely sample all scales of motion, we could sample, say, once an hour for 1000 hours or once a second for 1000 seconds and expect each realization to be an equally good estimate of the ensemble value. (It should be noted that this is true for computing processes such as moments. It can cause serious error in computing spectra. That is, a statistically stable estimate of the variance can be obtained with a very slow sampling rate, but the variance spectra would be seriously distorted by aliasing effects.) However, we have already noted that averaging periods should not exceed 1 hour for most boundary layer studies. Once the length of the averaging period is fixed, it becomes important to choose sampling rates optimized for the processes one wishes to study. In an attempt to obtain an empirical judgment of the magnitude of this problem, data were selected from a series of boundary layer experiments conducted in Minnesota (Izumi and Caughey, 1976). Four periods, each 150 min long, were analyzed for the convective boundary layer.

The basic data were recorded at a sample rate of 10 per second. Three additional sample rates were chosen for study: 1 per second, 1 per 10 seconds, 1 per 100 seconds. For each of the four sample rates, variances of the wind and temperature data, heat flux, and Reynolds stress were computed for averaging periods of 15, 30, 75, and 150 minutes. Percentage differences were then noted between a process' value based on a 10/sec sample rate and its value at each of the other three sample rates. The maximum range observed of these differences for two selected heights is presented in Figs. 1 through 3 as a function of sample size. The differences decrease from over 100% for very small sample sizes ($N \leq 90$) to only a few percent for large sample sizes ($N \geq 900$). It is also seen that the relative errors between the different processes is consistent with the guidelines suggested in Table 1 for choosing averaging periods, i.e., the differences observed for Reynolds stress values appear asymptotically greater than for heat flux or variance.

It is interesting to note that the differences are comparable with those given in Table 1 for 60 minute averaging periods when the sample size, N, is equal to or greater than 450 (equivalent to an averaging period of 75 minutes and a sample rate of once per 10 seconds). We have implied by this study that the values based on sample rates of 10 per second are our best possible estimates of the ensemble values, but this may be entirely unwarranted; estimates based on slower sampling rates may be equally accurate

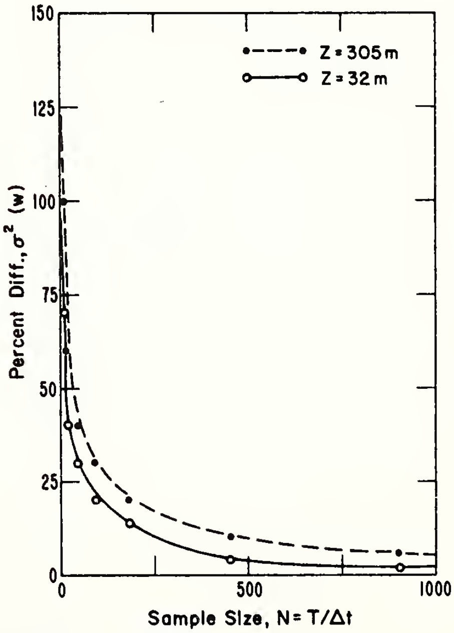

Figure 1. Percent difference, $\sigma^2(w)$, vs sample size.

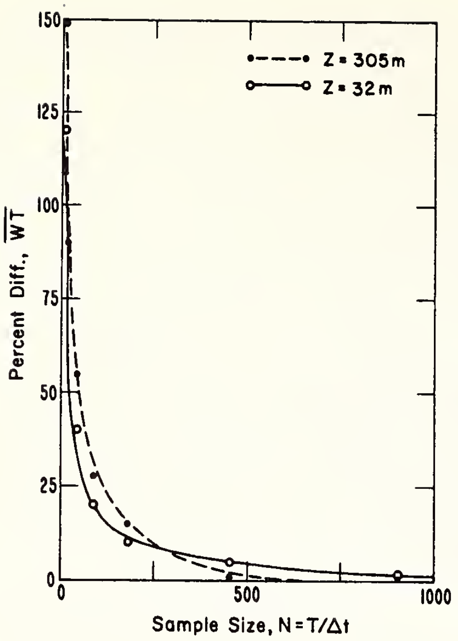

Figure 2. Percent difference, $\overline{wT}$, vs sample size.

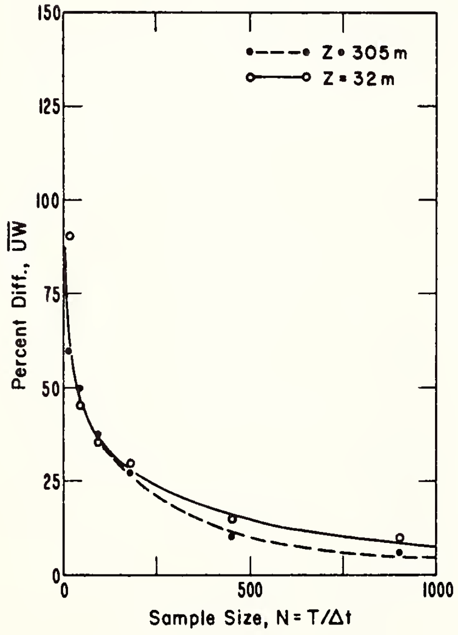

Figure 3. Percent difference, $\overline{uw}$, vs sample size.

estimates of the ensemble values. However, it must be noted that this cannot be confidently determined on the basis of the analysis summarized here. In effect, the results simply describe the accuracy with which the realizations based on the slower sampling rates approximate the realization based on a rate of 10 per second. Therefore, until such time as extensive similarity analyses are performed with differing sample rates, it seems prudent to achieve the most reliable realization possible. This means that sample rates should generally be governed by the scale sizes that contribute to the process of interest.

It must be noted that sampling problems introduced by horizontal inhomogeneities in terrain cover or topography or by non-stationarities such as frontal passages, fast-moving large-scale pressure system, meso-scale disturbances such as rain cells, or diurnal variations in the boundary layer have been ignored in all of the above. The possible effect of complex terrain on momentum flux profiles may alone be sufficient to warrant relatively high sample rates.

It is risky to do so, but on the basis of the material presented here, I will suggest some general guidelines for gathering turbulence data in the boundary layer. Record data at a rate of 1 to 5 times a second for convective situations, 5 to 20 times a second for stable situations. Plan to use averaging periods of 15 to 60 minutes. Averaging for longer than 60 minutes can be undesirable in many instances. Modify these guidelines as necessary to accommodate any spectral analyses planned. Expect to be plagued with considerable scatter in any analyses involving Reynolds stress or any of the higher-order moments regardless of (any reasonable) sample rate and averaging period chosen.

3. COMPARISON OF REMOTE PROBING AND IN SITU SENSORS

Let us consider remote probe devices that measure the wind by detecting the Doppler frequency shift of a backscattered signal. The transmitted energy that irradiates the atmosphere is always of some finite beamwidth which leads to a Doppler *spectrum* in each backscatter return. Ideally, the Doppler spectrum is unimodal and the wind speed sample will be derived from the frequency shift for the Doppler spectral peak. The width of the Doppler spectrum is interpreted as Doppler shifts caused by turbulent eddies roughly equal to and smaller than the size of the volume. Given these broad characteristics, it is possible to outline some simple guidelines to follow for comparing devices of this type with conventional anemometry. Three different turbulent processes are discussed for illustration purposes: mean wind speeds, wind component variances, Reynolds stresses. Two classes of experiments are considered. One is characterized by the sampling volume of the remote probe device being focused to within a very few meters of the anemometer; the other by being focused, say, 100 to 300 meters from the anemometer. It is assumed that conditions of horizontal homogeneity and stationarity prevail.

Let us examine sampling and averaging problems for mean wind speed first. If the sampling volume is small and focused close to the anemometer, then the remote probe device and the anemometer can be assumed to sample the same random process. In this case, the averaging period can be as short as a minute, say, and will provide a suitable set of mean wind speed comparison data. In the large separation case, one should assume that the random processes being sampled are spatially separated by one or more integral scales of turbulence. They should then be treated as independent realizations of the same turbulent process. In keeping with the estimates given in Table 1, this means the set of mean wind speed comparison data should be based on roughly 15-min averages to minimize differences arising solely from sample departures from the ensemble mean.

Similar reasoning can be applied to the problem of comparing variances and Reynolds stresses. Again, in keeping with Table 1, one should use averaging periods of, say, 3 to 5 minutes for comparison data obtained practically in the same volume, 60 minutes for sampling volumes well separated in space. In the latter case, particularly, one should expect substantially more scatter in the data points than in the comparison of mean wind speeds. (As a practical matter, it should be noted that the scatter is reduced significantly if comparison data for the large separation case are obtained only when the wind is blowing from the remote probe device to the in-situ anemometer. An application of this elementary rule of thumb may be seen in Haugen et al., 1975.)

There is a sampling problem to consider in determining variances with the remote probe devices. Turbulent wind fluctuations of scale size roughly equal to or less than the size of the sampling volume will not enter the variance computations. That is, the finite sampling volume acts as a filtering device which suppresses the high frequency wind fluctuations. This means that an underestimation of the variance will always be superimposed on the natural scatter obtained in a set of comparison data. It might well be possible to reduce this underestimation to a negligible level by using a measure derived from the time history of the widths of the Doppler spectra or the areas under the Doppler spectra. The mechanics for an optimum method to do this would most likely depend on the underlying operating characteristics of the particular Doppler device.

It does not follow that the spatial filtering is equally serious for observations of Reynolds stress. If the sampling volume is sufficiently small, the only eddy sizes filtered out will be those which do not contribute to the covariance. To my knowledge, there has been no systematic evaluation of any remote probe device for the measurement of either variances or covariances. We hope to conduct studies of this type at the Boulder Atmospheric Observatory in the near future.

4. ACKNOWLEDGMENTS

The preparation of this paper has been considerably eased as a result of many fruitful discussions with my colleagues at the Wave Propagation Laboratory. I am particularly grateful to Drs. D. W. Beran, F. F. Hall, Jr., W. H. Hooke, J. C. Kaimal, R. L. Schwiesow, and J. C. Wyngaard for their time and interest.

5. REFERENCES

Haugen, D. A., J. C. Kaimal, C. J. Readings, and R. Rayment, 1975: A comparison of balloon-borne and tower-mounted instrumentation for probing the atmospheric boundary layer, *J. Appl. Meteor.*, 14, 540-545.

Izumi, Y., and S. J. Caughey, 1976: Minnesota 1973 atmospheric boundary layer experiment data report, AFCRL-TR-76-0038, AF Geophys. Labs., Bedford, Mass., 28 pp.

Kaimal, J. C., J. C. Wyngaard, D. A. Haugen, O. R. Coté, Y. Izumi, S. J. Caughey, and C. J. Readings, 1976: Turbulent structure in the convection boundary layer, *J. Atmos. Sci.*, 33, 2152-2169.

Lumley, J. L., and H. A. Panofsky, 1964: *The Structure of Atmospheric Turbulence*, Interscience Pub., New York, 239 pp.

Wyngaard, J. C., 1973: On surface layer turbulence, *Workshop in Micrometerology*, D. A. Haugen, Ed., Amer. Meteor. Soc., Boston, 101-149.

Wyngaard, J. C., S. P. S. Arya, and O. R. Coté, 1974: Some aspects of the structure of convective planetary boundary layers, *J. Atmos. Sci.*, 31, 747-754.

Proceedings of the International Conference on Acoustics, Speech, and Signal Processing, 91-95, Tulsa, Oklahoma, 10-17 April 1978.

NON-OPTIMAL CONVERGENCE OF ADAPTIVE LMS WITH UNCORRELATED DATA

R. Jeffrey Keeler

NOAA/ERL/WPL, R45x2
Boulder, Colorado 80302

Abstract

Convergence analysis of the adaptive least mean square (LMS) algorithm is based on the fundamental assumption that the data vector is uncorrelated with the weight vector at each iteration. This assumption has been taken to mean that successive data vectors are uncorrelated. However, when adaptation of the algorithm is performed at intervals less than the filter length plus the prediction delay and the input is a sinusoid in white noise, it is shown that the convergent weight vector no longer satisfies the minimum mean squared error optimality criterion. Furthermore, it is shown that the adaptation proceeds with a time constant determined by the input noise power. Results of a computer experiment verify the analytic description of the non-optimal convergence.

Introduction

The adaptive least mean square (LMS) algorithm has been applied to many signal processing applications, e.g., adaptive linear prediction filtering for frequency estimation [1,2], adaptive noise cancelling [3], and adaptive line enhancement [4]. A complete development of the algorithm, summarized below, is available in all of the above references. The basic filter structure is shown in Figure 1.

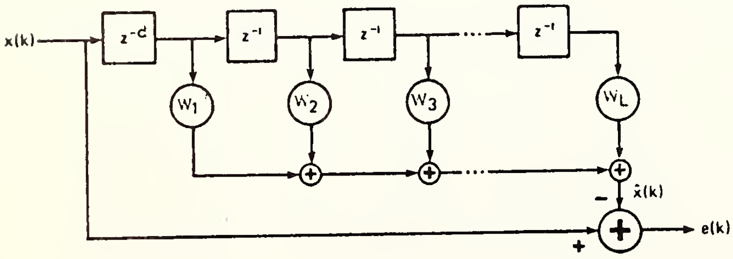

Figure 1. Basic adaptive linear prediction filter.

The prediction distance is d units, and the data interval on which the prediction is based is L data samples. The LMS algorithm that updates the weights of the prediction filter is

$$W_{k+1} = W_k + \mu e_k X_k \tag{1}$$

with e_k the error between the actual input data sample x_k and the predicted sample $\hat{x}_k$, and X_k the L dimension data vector at time k. Vectors and matrices shall be denoted by capital letters, and scalars, by lower case letter. A convergence analysis shows that when the weight vector W_k is uncorrelated with the data vector X_k, the LMS algorithm drives the mean weight vector $E\{W_k\}$ to a steady state which is identical to the optimal minimum mean squared error (mse) filter. Thus, the mean steady state weight vector is

$$W^* = R^{-1}P \tag{2}$$

with R the data autocorrelation matrix $E\{X_k X_k\}^T$ and P a data correlation vector $E\{x_k X_k\}$. For a sinusoid at frequency ω_0 in white noise, having a signal-to-noise ratio SNR and subject to certain non-restrictive conditions [5], the optimal weight vector is approximated by

$$W^* = \left(\frac{L}{2} + \frac{1}{SNR}\right)^{-1} [\cos\omega_0 d \quad \cos\omega_0(d+1) .. \cos\omega_0(d+L-1)]^T . \tag{3}$$

Furthermore, for this case the filter gain at ω_0 is easily shown to be

$$a^* = \frac{L}{2} / \left(\frac{L}{2} + \frac{1}{SNR} \right) \tag{4}$$

The convergence analysis of the LMS algorithm invokes the "fundamental assumption" that the weight vector W_k is uncorrelated with the data vector X_k for all k. However, when weight vector updates are performed every sample, this assumption is clearly erroneous because, as the data samples propagate down the prediction filter, successive data vectors are correlated exactly at a lag of 1.

It will be shown that this erroneous assumption may lead to a steady state weight vector that is not optimal in producing a minimum mean squared error. Consequently, the predicted data sequence $\{\hat{x}_k\}$ will have a noise component additional to that which standard theory predicts. Furthermore, frequency estimates based on the filter coefficients or the $\hat{x}_k$ data may be adversely affected.

When the adaptation updates are performed every $h=$ L+d-1 input samples, successive data vectors, i.e., X_k, X_{k-h}, X_{k-2h} etc., are uncorrelated. However, W_k is still correlated with X_k because

CH1285-6/78/0000-0091$00.75©1978IEEE

the input sample at time $k-h$, x_{k-h} (which is used to form the error e_{k-h} that in turn is used to calculate W_k) has propagated only $L+d-1$ steps and is the last element of the data vector X_k. Therefore, for the LMS algorithm, W_k is in fact correlated with X_k except when the update interval is greater than or equal to $L+d$. The convergence analysis presented in most references assumes no correlation between W_k and X_k for separating $E\{X_k X_k^T W_k\}$ into $R\,E\{W_k\}$ to obtain the mean weight vector convergence result. This assumption is clearly unjustified.

Calculation of steady state W_∞

Pursuing the above observation analytically is not easy. However, analyzing a simplified case will demonstrate the consequences of falsely assuming uncorrelated W_k and X_k. The input vector X_k can be separated into a deterministic signal vector S_k and a random noise vector N_k, i.e., $X_k=S_k+N_k$, with $X_k=[x_{k-1}x_{k-2}\cdot\cdot\cdot x_{k-L}]^T$, $S_k=[s_{k-1}s_{k-2}\cdot\cdot\cdot s_{k-L}]^T$, $N_k=[n_{k-1}n_{k-2}\cdot\cdot\cdot n_{k-L}]^T$. Let h represent the update interval. We have observed that h must be greater than or equal to $L+d$ for the fundamental assumption to be valid, however the algorithm is generally updated every sample. Denote the subscript on the weight vector in terms of h so that successively indexed weight vectors are calculated every h input samples. The LMS algorithm is then

$$W_{\frac{k+h}{h}} = W_{k/h} + \mu e_k X_k$$

$$= W_{k/h} + \mu(x_k X_k - X_k X_k^T W_{k/h}) \,. \qquad (5)$$

For the preceding adaptation (h samples earlier)

$$W_{k/h} = W_{\frac{k-h}{h}} + \mu e_{k-h} X_{k-h}$$

$$= W_{\frac{k-h}{h}} + \mu(x_{k-h} X_{k-h} - X_{k-h} X_{k-h}^T W_{\frac{k-h}{h}}). \qquad (6)$$

We observe that for $h<L+d$, x_{k-h} is used to calculate $W_{k/h}$ in (6) and also that x_{k-h} is one of the elements of X_k in (5). Consequently $W_{k/h}$ and X_k are correlated. We desire to calculate the steady state weight vector

$$W_\infty = E\{W_{k/h}\} = E\{W_{\frac{k+h}{h}}\}, \qquad (7)$$

but the correlation in the $\mu X_k X_k^T W_{k/h}$ term prevents calculating a simple expectation in (5). By separating X_k into a deterministic signal and a random noise term, and by calculating the expectation on (1), we get (after removing several null terms)

$$E\{W_{\frac{k+h}{h}}\} = E\{W_{k/h}\} + [s_k S_k - S_k S_k^T E\{W_{k/h}\} - S_k E\{N_k^T W_{k/h}\}$$

$$- E\{N_k S_k^T W_{k/h}\} - E\{N_k N_k^T W_{k/h}\}] \,. \qquad (8)$$

Eq. (6) must be repeatedly substituted into (8) for all previous weight vectors until the expectation operation yields only zero terms. This "telescoping" operation must be performed L times for $h=1$ but only once (as above) when $h=L$. We shall investigate the $h=L$ case in detail.

Rewriting (8) for $h=L$

$$E\{W_{\frac{k+L}{L}}\} = [I-\mu S_k S_k^T]\,E\{W_{k/L}\} + \mu s_k S_k \qquad \text{term } 0$$

$$-\mu S_k\, E\{N_k^T W_{k/L}\} \qquad \text{term 1}$$

$$-\mu E\{N_k S_k^T W_{k/L}\} \qquad \text{term 2}$$

$$-\mu E\{N_k N_k^T W_{k/L}\} \,. \qquad \text{term 3} \quad (9)$$

Term 0 is the "signal portion" of the LMS algorithm. Terms 1 and 2 are additional terms that arise when W_k and X_k are correlated. Term 3 is the "noise portion" of the LMS when N_k and $W_{k/L}$ are uncorrelated, but when N_k and $W_{k/L}$ are correlated, term 3 can be separated into this "noise portion" component plus two additional terms, that cause the non-optimal convergence. The effect of terms 1, 2 and 3 are calculated separately and then combined. The μ dependence is temporarily suppressed.

Term 1

By substituting (6) with $h=L$ into (9) and removing the null term $E\{N_k^T W_{\frac{k-L}{L}}\}$,

$$S_k\, E\{N_k^T W_{k/L}\} = S_k\, E\{N_k^T \mu [(s_{k-L}+n_{k-L})^T$$

$$-(S_{k-L}+N_{k-L})^T W_{\frac{k-L}{L}}]\,[S_{k-L}+N_{k-L}]\}$$

$$= \mu S_k\, E\{n_{k-L} N_k^T\} S_{k-L}$$

$$= \mu\, \sigma_n^2\, s_{k-2L}\, S_k \,. \qquad (10)$$

Term 1 has a form similar to the driving term $\mu s_k S_k$ in term 0. Note that many of the terms in (10) are zero because the consecutive data vectors are uncorrelated for $h=L$, i.e., $E\{N_k^T N_{k-L}\}=0$ and $E\{N_k N_{k-L}^T\}=0$. This simplification is the principle reason that an analytic solution to this $h=L$ problem is possible.

Term 2

Performing the same substitution and removal of null terms as above,

$$E\{N_k S_k^T W_{k/L}\} = \mu S_k^T S_{k-L} E\{n_{k-L} N_k\}$$

$$= \mu \sigma_n^2 S_k^T S_{k-L} [0 \ . \ . \ . \ 0 \ 1]^T . \qquad (11)$$

Term 2 is of a form that drives only the last element of W_k. This is the key term when W_k and X_k are correlated.

Term 3

Again substituting and removing null terms,

$$E\{N_k N_k^T W_{k/L}\} = E\{N_k N_k^T W_{\frac{k-L}{L}}\} + \mu E\{N_k N_k^T\} s_k S_{k-L}$$

$$-\mu E\{N_k N_k^T S_{k-L}^T W_{\frac{k-L}{L}}\} S_{k-L}$$

$$-\mu E\{N_k N_k^T N_{k-L}^T W_{\frac{k-L}{L}} N_{k-L}\} . \qquad (12)$$

This expression is considerably simplified if we assume that for all k the weight vector predicts the signal portion of the input s_k accurately except for gain, i.e.,

$$S_k^T W_{k/L} = S_k^T W^* = a^* s_k , \text{ for all } k \qquad (13)$$

with a^* the filter gain. Using this assumption (which will be verified subsequently), and noting that N_k is uncorrelated with $W_{\frac{k-L}{L}}$ and N_{k-L}, (12) simplifies to

$$E\{N_k N_k^T W_{k/L}\} = \sigma_n^2 E\{W_{\frac{k-L}{L}}\} + \mu \sigma_n^2 (1-a^*) s_k S_{k-L}$$

$$-\mu \sigma_n^4 E\{W_{\frac{k-2L}{L}}\} . \qquad (14)$$

For nearly all cases of interest (i.e., $\alpha/L \ll 1$), the term in σ_n^4 may be ignored, and the third term in (9) is approximated by

$$E\{N_k N_k^T W_{k/L}\} = \sigma_n^2 E\{W_{\frac{k-L}{L}}\} + \mu \sigma_n^2 (1-a^*) s_k S_{k-L} . \qquad (15)$$

Combining these three expressions, the recursion for the expected value of the weight vector during convergence to a steady state with $h=L$ (i.e., (5) can be rewritten as

$$E\{W_{\frac{k+L}{L}}\} = [I - \mu S_k S_k^T] E\{W_{k/L}\} + \mu s_k S_k$$

$$-\mu^2 \sigma_n^2 s_{k-2L} S_k$$

$$-\mu^2 \sigma_n^2 S_k^T S_{k-L} [0 \ . \ . \ . \ 0 \ 1]^T$$

$$-\mu \sigma_n^2 E\{W_{\frac{k-L}{L}}\} - \mu^2 \sigma_n^2 (1-a^*) s_k S_{k-L} . \qquad (16)$$

For steady state $E\{W_{\frac{k-L}{L}}\} = E\{W_{k/L}\}$. The autocorrelation matrix of the input is $R = S_k S_k^T + \sigma_n^2 I$ and the recursion driving vector is $P = s_k S_k$. The mean weight vector recursion from (9) can now be written as

$$E\{W_{\frac{k+L}{L}}\} = [I - \mu R] E\{W_{k/L}\} + \mu P$$

$$-\mu^2 \sigma_n^2 [s_{k-2L} S_k + (1-a^*) s_k S_{k-L}]$$

$$-\mu^2 \sigma_n^2 S_k^T S_{k-L} [0 \ . \ . \ . \ 0 \ 1]^T . \qquad (17)$$

The correlation between W_k and X_k (actually only N_k) introduces the two additional terms. These terms modify the driving term, μP, in two different ways. The first driver modifying term, $\mu^2 \sigma_n^2 [s_{k-2L} S_k + (1-a^*) s_k S_{k-L}]$, has the same form as P. This term changes, at most, only the magnitude and phase of μP. In fact, if an integral number of input sinusoidal periods fit into the filter length L, this term modifies only the magnitude of the driving term. In most cases of practical interest $\mu^2 \sigma_n^2 \ll \mu$, (or equivalently in the case of a single sinusoid in white noise input, $\alpha/L \ll 1$), so we can ignore this first modifying term. However, the second driver modifying term $\mu \sigma_n^2 S_k^T s_{k-L} [0 \ . \ . \ . \ 0 \ 1]^T$, cannot be ignored. It is nominally L times larger than the first extra term and it has a different form than μP. This second modifying term affects only the L^{th} element of W_k. Depending on the $S_k^T S_{k-L}$ inner product, the element w_L may be larger or smaller than the other elements of W_k.

The preceding analysis holds only for the LMS algorithm update interval exactly equal to the filter length, i.e., $h=L$. When $h<L$, consecutive data vectors X_k, X_{k+h}, etc., are no longer uncorrelated, and more terms must be included in the expansion of the last three terms in (9). Many of these additional terms, which "telescope" back through at most L adaptations, are multiplied by μ each time and become less significant with each iteration.

The mean weight vector recursion can be summarized as follows: For an input consisting of a deterministic signal s_k in white noise n_k of variance σ_n^2 and $\alpha/L \ll 1$, the mean weight vector recursion for the LMS algorithm is

$$E\{W_{\frac{k+L}{L}}\} = [I - \mu R] E\{W_{k/L}\} + \mu P - \sigma_n^2 S_k^T S_{k-L} [0 \ldots 0 \ 1]^T . \qquad (18)$$

The last term in this recursion changes the μP driving term and causes the mean steady state weight vector to converge to a weight vector that does *not* produce a minimum mse output error sequence!

Example

As an example of how to calculate the non-optimal steady state weight vector, consider an input consisting of a DC level as a signal in white noise, i.e., $x_k = A+n_k$. For $\alpha/L<<1$ we may use (2) and (18) to calculate $W_\infty=\lim_{k\to\infty} E\{W_k\}$.

$$W_\infty = R^{-1} A^2 \{\underline{1} - L \mu \sigma_n^2 \quad [0 \ . \ . \ . \ 0 \ 1]^T\} \tag{19}$$

with $\underline{1} = [1 \ 1 \ 1 \ . \ . \ . \ 1]^T$. Because $R=A^2\underline{1}\,\underline{1}^T+\sigma_n^2 I$, R^{-1} may be calculated using Woodbury's Identity [6],

$$R^{-1} = \frac{1}{\sigma_n^2} I - \frac{A^2}{\sigma_n^2(\sigma_n^2 + LA^2)} \underline{1}\,\underline{1}^T$$

$$= \frac{1}{\sigma_n^2(\sigma_n^2 + LA^2)} \begin{bmatrix} (L-1)A^2+\sigma_n^2 & -A^2 \ . \ . \ . & -A^2 \\ -A^2 & . & . \\ . & \quad . & . \\ . & \quad\quad . & . \\ . & \quad\quad\quad . & -A^2 \\ -A^2 \ . \ . \ . & -A^2 & (L-1)A^2+\sigma_n^2 \end{bmatrix} \tag{20}$$

At high SNR (i.e., SNR>>1/L), (20) can be substituted into (15) to obtain the non-optimal steady state weight vector

$$W_\infty = W^* + \frac{\alpha}{L} [1 \ 1 \ . \ . \ . \ 1 \ (1-L)]^T \tag{21}$$

with $W^* = \frac{1}{L}\underline{1}$. For $L=8$ and $\alpha=0.2$,

$$W_\infty=[.15 \ .15 \ .15 \ .15 \ .15 \ .15 \ .15 \ -.05]^T \ . \tag{22}$$

Note that the modification of the driving term in (18) has "forced" the L^{th} element of W_∞ to be different from the first L-1 elements. The non-optimal weights still predict the signal exactly as assumed in (13).

For the filter parameters given above, and with adaptations every L=8 input samples, (h=8), a simulation must be run for approximately 10^5 input samples in order for the convergence described in (18) to be complete. Performing this simulation yields a mean steady state weight vector given by

$$W_\infty =[.150 \ .165 \ .147 \ .160 \ .130 \ .145 \ .133 \ -.035]^T . \tag{23}$$

The theoretical and simulated results are shown in Figure 2. This experiment shows that non-optimal convergence does indeed occur for a stationary input sequence.

Although the analytic description of steady state convergence, when the update interval is less then L+d-1, is extremely complicated, the simulation is easy to perform. When the weight vector is updated at every input sample, (h=1), and the prediction delay is unity (d=1), the steady state weight vector for a DC input signal closely approximates a ramp,

$$W_\infty =[.001 \ .032 \ .059 \ .082 \ .154 \ .183 \ .218 \ .262]. \tag{24}$$

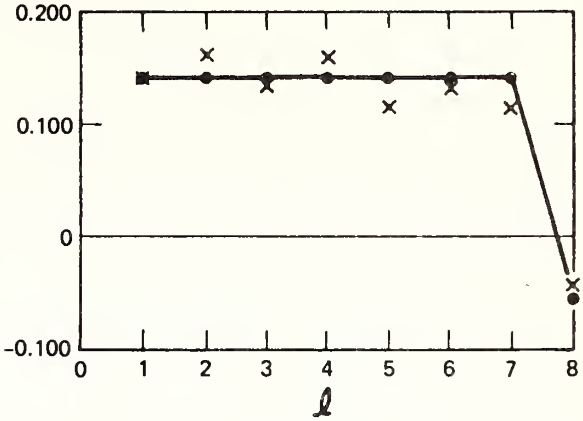

Figure 2. Comparison of theoretical (dots) steady state weight vector with experimental (x's) steady state weight vector.

This experimental result is shown in Figure 3A.

Update intervals $1<h<L+d$ generate a steady state weight vector for a DC input that has pronounced "dips" in the weight vector at elements corresponding to $\ell=jh-d+1$ for $j=1,2,\ldots$. For example, [d=1, h=2] generates

$$W_\infty =[.182 \ -.045 \ .193 \ .038 \ .225 \ .032 \ .244 \ .110]^T \tag{25}$$

and [d=2, h=5] generates

$$W_\infty =[.175 \ .159 \ .147 \ .021 \ .171 \ .156 \ .199 \ .184]^T. \tag{26}$$

These curves are shown in Figures 3B and 3C.

Evidently, these dips are generated because of correlations between certain elements of W_k and the input noise sample n_k that is included in the succession of data vectors X_k, X_{k+h}, etc. When the input noise sample that is used to generate the update for W_k has propagated entirely through the prediction filter, the correlation, of course, ceases. It seems reasonable that the correlation between W_k and X_{k+h} will be smaller than the correlation between W_k and X_k and so on down the filter. This decrease in correlation apparently explains the decrease in the size of the dips in the weight vector for elements farther down the filter. If we assume that the convergence of the difference W_∞-W^* is independent of the convergence of W^* alone, then the steady state ramp may be explained. The W^* component of W_∞ maintains a constant filter gain at the input frequency regardless of α. Therefore, the predicted signal component of $\hat{x}_k$ is identical to that in the optimal convergence case. For DC or sinusoidal inputs, any combination of weights that predicts

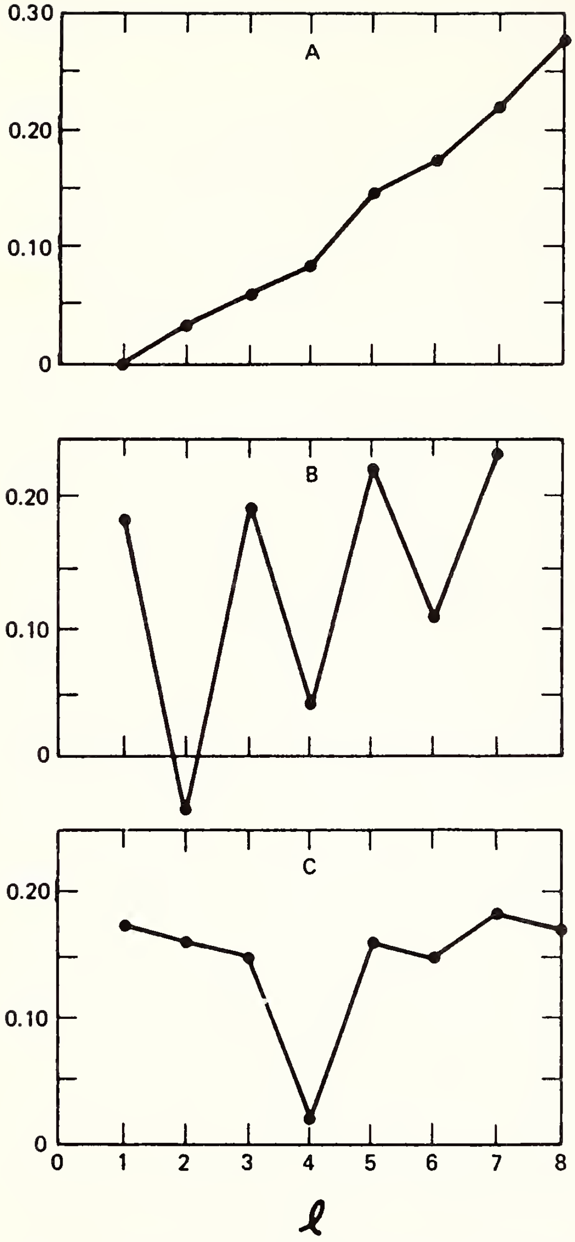

Figure 3. Steady state weight vectors for L=8.
A. d=1, h=1
B. d=1, h=2
C. d=2, h=5

the same signal component of $\hat{x}_k$ minimizes the contribution to mse due to uncancelled signals. Therefore, the optimal convergence of the optimal component W* together with the convergence of the difference component $V_\infty = W_\infty - W^*$, which is generated by decreasing correlations of W_k with $X_{k+\ell}$, (h=1), explains the trapezoidal envelope of the non-optimal steady state weight vector that frequently has been observed but not understood.

The transfer function of the non-optimal prediction filter W_∞ may be calculated by superposition. By modelling the envelope of the steady state weight vector for the h=1 case as a trapezoid, the W* component is real and even about $\ell = L/2$, and V_∞ is real and odd about $\ell = L/2$. The W* component has a transform that is real and even about ω_0, and the V_∞ component has a transform that is imaginary and odd about ω_0. We conclude that the magnitude of the non-optimal transfer function remains symmetric, and thus unbiased spectrum estimates involving the non-optimal prediction filter remain unbiased. The only adverse effect is the modification of the transfer function at frequencies away from ω_0 and the subsequent passage of more input noise. This excess mse due to V_∞ is easily shown to have a power of $V_\infty^T R V_\infty$.

References

1. Keeler, R. J. and L. J. Griffiths, "Acoustic Doppler Extraction by Adaptive Linear Prediction Filtering", *J. Acoust. Soc. Am.*, vol. 61, May 1977, p.1218-1227.

2. Griffiths, L. J., "Rapid Measurement of Digital Instantaneous Frequency", *IEEE Trans. on Acoust., Speech, and Sig. Proc.*, vol. ASSP-23, April 1975, p. 207-222.

3. Widrow, B. et al., "Adaptive Noise Cancelling: Principles and Applications", *IEEE Proceedings*, vol. 63, December 1975, p. 1692-1716.

4. Zeidler, J. R., E. H. Sartorius, D. M. Chabries, and H. T. Wexler, "Adaptive Enhancement of Multiple Sinusoids in Uncorrelated Noise", accepted for publication in *IEEE Trans. in Acoust., Speech, and Sig. Proc.*, 1977.

5. Keeler, R. J., "Adaptive Frequency Estimation Using Linear Prediction Filtering", Ph.D. Thesis, Univ. of Colo., 1978.

6. Zielke, G., "Inversion of Modified Symmetric Matrices", *J. of Assoc. of Comp. Mach.*, vol. 15, July 1968, p.402-408.

IEEE Transactions on Acoustics, Speech, and Signal Processing, ASSP-26: 469-471, October 1978.

Uncertainties in Adaptive Maximum Entropy Frequency Estimators

R. JEFFREY KEELER

Abstract—For a real sinusoid in white noise, the weight vector noise associated with an adaptive maximum entropy (AME) frequency estimator causes the spectrum peak to shift away from the input frequency. For a long adaptive filter, approximate expressions for this estimator's peak value and frequency variance are derived. For low SNR, the probability of obtaining a spurious peak is evaluated.

I. ADAPTIVE MAXIMUM ENTROPY (AME) FREQUENCY ESTIMATION

One step adaptive linear prediction filters have been effectively used to estimate the input frequency of sinusoids in white noise [1], [2]. Because the adaptive weights are random variables, the resultant adaptive maximum entropy (AME) frequency estimate is a random variable. In this correspondence some stochastic properties of the AME estimator are discussed.

For a unit power real sinusoid of constant frequency ω_0 in white noise of variance σ_n^2, i.e., $x_k = \sqrt{2} \cos \omega_0 k + n_k$, the autocorrelation matrix R and autocorrelation vector P can be expressed as

$$R = C_0 C_0^T + S_0 S_0^T + \sigma_n^2 I \tag{1}$$

$$P = C_0 \tag{2}$$

where $C_0 = (\cdots, \cos l\omega_0, \cdots)^T$, $S_0 = (\cdots, \sin l\omega_0, \cdots)^T$, $l = 1, 2, \cdots, L$. Applying the matrix inversion lemma we can calculate the steady state weight vector W^*,

$$W^* = R^{-1}P = \Delta^{-1} [(S_0^T S_0 + 1/\mathrm{SNR})C_0 - (C_0^T S_0)S_0] \tag{3a}$$

with

$$\Delta = C_0^T C_0 S_0^T S_0 (C_0^T S_0)^2 + L/\mathrm{SNR} + 1/\mathrm{SNR}^2 \tag{3b}$$

where SNR is defined as $1/\sigma_n^2$. For large L and central ω_0, i.e., $2\pi/L < \omega_0 < \pi - 2\pi/L$,

$$W^* \cong KC_0, \tag{4a}$$

with

$$K = (L/2 + 1/\mathrm{SNR})^{-1}. \tag{4b}$$

Because of noise at the input, the weight vector has a time-varying, L dimensional error vector V_k associated with it,

$$V_k = W_k - W^*. \tag{5}$$

An approximation to the covariance of V_k for an adaptive LMS processor is [3]

$$\mathrm{Cov}\ \{V_k\} \cong \frac{\mu}{2} \epsilon_{\min} I, \tag{6}$$

where I is the identity matrix. $\epsilon_{\min}$ is the minimum mean-squared prediction error

$$\epsilon_{\min} = 1 + \sigma_n^2 - P^T W^* \simeq \sigma_n^2. \tag{7}$$

The factor of 2 difference from Widrow's expression arises because the adaptive LMS algorithm used in this paper is

$$W_{k+1} = W_k + \mu \epsilon_k X_k, \tag{8a}$$

with

$$\mu = \alpha / L(1 + \sigma_n^2). \tag{8b}$$

Convergence of the algorithm is guaranteed if $0 < \alpha < 2$ [1].

From (6) the magnitudes of components of the weight vector noise are independent and identically distributed. If the input noise is Gaussian, then the weight vector error on each component is zero mean, Gaussian with variance σ_v^2. When (7) and (9) are substituted into (6),

$$\sigma_v^2 = \frac{\mu}{2} \epsilon_{\min} \simeq \frac{\alpha}{2L(1 + \mathrm{SNR})}. \tag{9}$$

Griffiths [1] has defined a modified maximum entropy spectrum estimate

$$Q(\omega) = |1 - \Gamma^T(\omega) W|^{-2} \tag{10}$$

where $\Gamma(\omega) = (\cdots, e^{-j\omega l}, \cdots)^T$ and the k dependence is suppressed on W_k. For large L and central ω we may use (4) to verify that the peak value of the spectrum estimator occurs at ω_0 and is

$$Q(\omega_0) = \left(\frac{\mathrm{SNR} \cdot L}{2} + 1 \right)^2 \tag{11}$$

Note that large values of this frequency estimator can be obtained for any SNR simply by making the filter length L sufficiently large. For SNR's greater than −20 dB, filter lengths of at least $L = 16$ yield an actual $Q_{\max}$ which agrees very closely with the value predicted from (11).

II. ESTIMATOR BIAS AND VARIANCE AT HIGH SNR

To study the error in the AME frequency estimate due to weight vector fluctuations, i.e., "peak shift," we first note that only the behavior of $Q(\omega)$ near ω_0 is of interest. The weight error vector V_k may be decomposed into two components in the C_0 and S_0 directions and a component $V_{p,k}$ that is orthogonal to both C_0 and S_0.

Therefore, the total weight vector is

Manuscript received August 1, 1977; revised May 26, 1978.

The author is with NOAA/ERL/Wave Propagation Laboratory, Boulder, CO 80302.

0096-3518/78/1000-0469$00.75 © 1978 IEEE

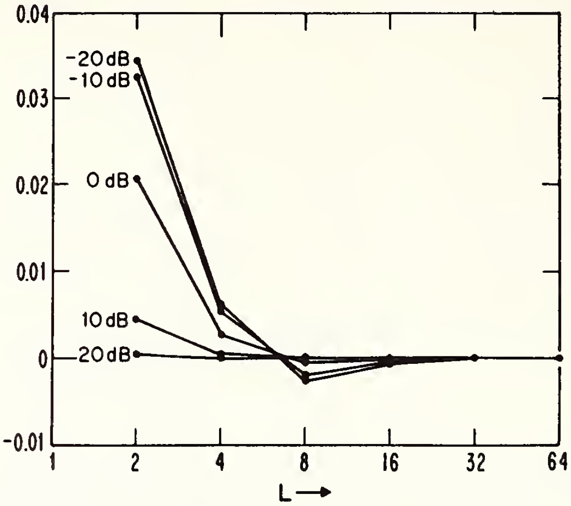

Fig. 1. Bias in maximum entropy frequency estimator versus filter length as a function of SNR. $f = 0.200$.

$$W_k = W^* + a_k C_0 + b_k S_0 + V_{p,k}, \tag{12}$$

where a_k and b_k are zero mean, random variables. Only the first three terms contribute to $Q(\omega)$ at frequencies near ω_0; therefore, the $V_{p,k}$ component may be neglected.

When (12) is substituted into (10), a general expression for $Q(\omega)$ at some time k (dependence suppressed) is

$$Q(\omega) = \left(1 + \frac{(K+a)^2 + b^2}{4} Y^2(\omega) - \left[(K+a)\cos(\omega - \omega_0)\frac{L+1}{2} - b\sin(\omega - \omega_0)\frac{L+1}{2}\right] Y(\omega)\right)^{-1} \tag{13a}$$

$$Y(\omega) = \frac{\sin(\omega - \omega_0)L/2}{\sin(\omega - \omega_0)/2}. \tag{13b}$$

For $b = 0$, (13) is an even function about its maximum at ω_0. Therefore, the peak of $Q(\omega)$ is an unbiased frequency estimator regardless of the value of a. If L is not large, the frequency estimate is biased. The bias is due to the interaction of the positive and negative components of the real signal. Fig. 1 shows the bias at a normalized frequency $f = 0.200$ for filter lengths of $L = 2$ to $L = 64$ and SNR's from -20 dB to +20 dB. The frequency estimator is essentially unbiased at this frequency for $L \geqslant 8$.

For $|\omega - \omega_0| << 2\pi/L$ the trigonometric functions in (13) can be approximated by a few terms of the Taylor series. Setting $\partial Q(\omega)/\partial\omega = 0$, we find the error in $Q(\omega)$ to be

$$\omega_{pk} - \omega_0 = -2b/(K+a)(L+1). \tag{14}$$

For SNR $>> 2/L$ that $K \simeq 2/L$ and for α sufficiently small that $|aL/2| << 1$ (a is proportional to $\sqrt{\alpha}$, from (9)), the error is

$$\omega_{pk} - \omega_0 = -b. \tag{15}$$

Under these conditions the variance of the AME frequency estimator is just the variance of b,

$$\acute{E}\{(\omega_{pk} - \omega_0)^2\} = \acute{E}\{b^2\} \simeq \frac{\alpha}{2L(\text{SNR} + 1)}. \tag{16}$$

III. Spectrum Ambiguity at Low SNR

At low SNR's for which $Q(\omega_0) < 10$ the problem with the AME frequency estimator is not peak shift so much as it is choosing a false peak for the estimate of the input frequency. We could say that the AME spectrum is "ambiguous." Let the SNR be low enough (SNR $\lesssim 2/L$) so that $Q(\omega_0)$ is not significantly greater than false spectral peaks which are caused by random fluctuation of the V_p components. Then the sidelobes of the true peak at ω_0 can be considered sufficiently small that the contribution to false peaks away from ω_0 is due entirely to weight vector noise. Each component of V_p is zero mean Gaussian with variance $\sigma_v^2 = \alpha/2L$.

Let p represent the probability that the false peak at frequency ω_i, $Q(\omega_i)$, is above some threshold Q_{th}. Then

$$p = \Pr\{Q(\omega_i) > Q_{\text{th}}\}. \tag{17}$$

It is possible to show that the false peaks behave independently and that $Q(\omega_i)$ is caused solely by v_i, the component of V_p along C_i, that is, $v_i = V_p^T C_i/|C_i|$. We know $|C_i| = \sqrt{L/2}$ for large L. From (10)

$$Q(\omega_i) = (1 - v_i\sqrt{L/2})^{-2}. \tag{18}$$

With $Q_{\text{th}} = Q$ for notational simplicity,

$$p = \Pr\{(1 - v_i\sqrt{L/2})^{-2} > Q\}$$
$$= \Pr\{\sqrt{2/L}(1 - 1/\sqrt{Q}) < v_i < \sqrt{2/L}(1 + 1/\sqrt{Q})\}. \tag{19}$$

Because v_i is zero mean Gaussian with variance $\alpha/2L$, this probability can be approximated by

$$p \simeq \frac{2}{\sqrt{Q}} \frac{1}{\sqrt{2\pi}} e^{-2/\alpha} \tag{20}$$

for values of $Q > 2$. Therefore, $1 - p$ is the probability that this particular false peak is below threshold and $(1-p)^{L/2-1}$ is the probability that all $L/2 - 1$ false peaks are below the threshold. Therefore, $1 - (1-p)^{L/2-1}$ is the probability that *any* false peak is above threshold, or the probability of an ambiguous spectrum arising,

$$P_A \cong 1 - (1-p)^{L/2-1}. \tag{21}$$

If we let Q_{th} be a fraction of $Q(\omega_0)$, i.e., $Q_{\text{th}} = rQ(\omega_0)$ then

$$P_A \cong 1 - \left(1 - \frac{0.8}{\sqrt{r}\left(\frac{\text{SNR} \cdot L}{2} + 1\right)} e^{-2/\alpha}\right)^{L/2-1} \tag{22}$$

Notice the extreme sensitivity to α in this expression. Decreasing α by a factor of 2 can considerably decrease P_A at the penalty of doubling the convergence time. As an example, if $r = 0.24$, $L = 1000$, SNR = -30 dB, $\alpha = 0.25$, then $P_A \cong 0.16$. For $\alpha = 0.125$, $P_A \simeq 6 \times 10^{-5}$

REFERENCES

[1] L. J. Griffiths, "Rapid measurement of digital instantaneous frequency," *IEEE Trans. Acoust., Speech, Signal Processing*, vol. ASSP-23, pp. 207-222, Apr. 1975.

[2] R. J. Keeler and L. J. Griffiths, "Acoustic Doppler extraction by adaptive linear prediction filtering," *J. Acoust. Soc. Amer.*, vol. 61, no. 5, pp. 1218-1227, May 1977.

[3] B. Widrow *et al.*, "Adaptive noise cancelling: Principles and applications," *Proc. IEEE*, vol. 63, pp. 1692-1716, Dec. 1975.

Proceedings of the International Conference on Acoustics, Speech, and Signal Processing, 365-368, Tulsa, Oklahoma, 10-17 April 1978.

COMPLEX COVARIANCE/MAXIMUM ENTROPY DOPPLER ESTIMATES FOR PULSED CO_2 LIDAR

R. Jeffrey Keeler

NOAA/ERL/WPL, R45x2
Boulder, Colorado 80302

and

Robert W. Lee

Lassen Research
Manton, California 96059

Abstract

A complex covariance spectral moment estimator for Doppler processing is presented as a means of reducing data acquired by a ground-based optical radar (lidar) before estimating a volumetric wind field. This estimator is equated to the first-order complex maximum entropy mean frequency estimator. It is also shown that the first-order estimator is the only order for which the complex maximum entropy frequency estimator is unbiased.

Introduction

Presently, accurate aviation terminal area weather monitoring and forecasting is hindered by the inability to remotely observe meteorological data in the vicinity of the aircraft operations area. For example, detecting hazardous wind shear conditions is vitally important for safely landing large aircraft, however no data collection device that can remotely sense the existing wind field is currently operational. Preliminary studies have shown that a ground-based pulsed coherent CO_2 lidar is able to measure these wind profiles [1]. After a brief summary of the proposed lidar wind measurement system, we will compare the recently developed class of maximum entropy frequency estimators [2,3] to the complex covariance (pulse pair) frequency estimator that is widely used in meteorological radar systems [4,5]. We show the equivalence of the first order complex maximum entropy estimator and the complex covariance estimator and furthermore show that higher order maximum entropy estimators are biased in general.

Lidar System Description

A pulsed CO_2 coherent lidar system for measuring atmospheric wind velocities was developed by NASA during 1968-1970 [6]. This system achieves range resolution by controlling the pulse length, and it utilizes a laser amplifier to generate the necessary power. The propagating pulse volume can be optically focussed at the desired range to achieve an enhanced echo from aerosol scattering at the point of interest. Both water droplets and dust particles, suspended in the atmosphere and moving with it, scatter the incident optical radiation. Receiving optics collect the backscattered and Doppler-shifted radiation and direct it onto an infrared detector, where it is mixed with a local oscillator laser or a small portion of the master oscillator. The detector generates an electrical signal at a frequency equal to the difference of the two incident optical beams; this signal can then be processed by standard frequency estimation techniques to estimate the Doppler shift (or equivalently, the radial velocity component) at the given range gate. Figure 1 is a schematic diagram for a typical lidar system using a filter bank for the Doppler shift estimator.

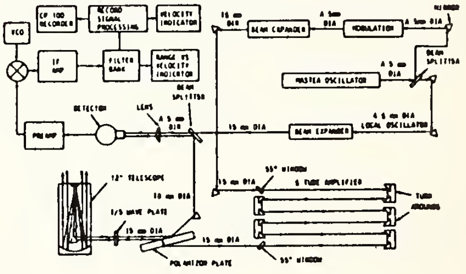

Figure 1. Lidar System Block Diagram.

The radar (or lidar) equation may be used to estimate the expected signal-to-noise ratio (SNR) of a pulsed coherent lidar system. The power density SNR is defined as the ratio of the signal power spectral density at the frequency of interest to the noise power spectral density, and may be approximated by

$$SNR = \frac{\eta\ J\ \beta(R)\ c\ \tau}{32\ h\nu}\ \frac{D^2}{R^2}\ e^{-2\int \mu(R)dR} , \qquad (1)$$

where typical system parameters for a ground-based lidar are

CH1285-6/78/0000-0365$00.75©1978IEEE

η = total system efficiency = 0.10
J = transmitted energy = 5 joules
R = range
$\beta(R)$ = backscatter cross section vs range
D = optics diameter = 0.5 m
$e^{-2\int\mu(R)dR}$ = round trip extinction loss
$h\nu$ = energy of single photon = 1.9×10^{-20} joules
C = velocity of light = 3×10^{8} m/sec
τ = pulse length = 3 μsec.

This SNR equation neglects any loss due to atmospheric turbulence and assumes that the telescope is focussed at the range of interest. For a tropical atmosphere, the water vapor concentration causes a larger extinction loss than for any other model atmosphere. Using these $\mu(R)$ and $\beta(R)$ profiles, at some zenith angle, gives a conservative estimate of the SNR. Figure 2 shows for three different zenith angles, the SNR vs range for a CO_2(λ=10.6 μm) lidar having the above system parameters. Reasonably high SNR's can be expected for ranges up to 20 km.

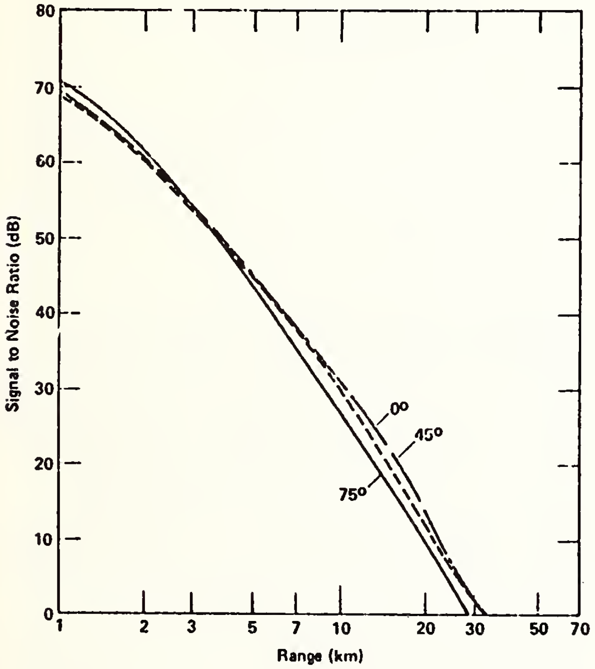

Figure 2. SNR vs range of ground-based coherent lidar for 3 zenith angles and tropical propagation conditions.

Because a given lidar shot will provide radial velocity estimates at the various tropospheric range gates (heights up to 20 km), a scan pattern should provide as dense a 3-dimensional field of these velocity estimates as is practical. Ideally, the estimates would be equally spaced in the troposphere so that an appropriate 2- or 3-dimensional velocity field (2-D if we ignore vertical velocities) could be fitted to the tropospheric velocity estimates in some least squares sense.

Doppler Extraction

The requirement for a coherent lidar Doppler processor might be satisfied conceptually by one of several frequency estimation devices or algorithms. The optical data might be processed directly by an optical spectrum analyzer such as a Bragg cell device. Alternatively, surface acoustic wave (SAW) devices, based on the chirp Z-transform approach, could be utilized by frequency conversion to approximately 10-20 MHz. However, subsequent calculation of the spectral moments would be required on both these device-oriented approaches. On the other hand, digital signal processing algorithms include the FFT and maximum entropy spectral estimators (both deterministic and adaptive), as well as several techniques that estimate the spectral moments directly. This, of course, is the only information required of a wind velocity estimation system.

The best known and most widely implemented of the direct moment estimation algorithms is the class of complex covariance frequency estimators [4] commonly called "pulse pair" estimators in meteorological (microwave) radar literature. The complex covariance technique uses the argument of a lagged complex autocorrelation estimate to evaluate the first moment of the received Doppler spectrum. Because coherent microwave radars can measure only the relative phase of the echo from a specified range gate, many pulses are required to yield a frequency estimate. Since the complex covariance at a lag equal to the pulse spacing may be calculated using successive pairs of pulses, this first moment spectrum estimator has been called the pulse pair estimator. Since only the complex covariance value is necessary to make the frequency estimate, one may calculate this correlation from a single acoustic radar pulse or a single optical radar (lidar) pulse. The slower propagation speed or shorter wavelengths, respectively, allow many data values from a single pulse to be used in calculating the complex covariance. This complex covariance frequency estimator is given as

$$\hat{f}_{cc} = \frac{1}{2\pi\,\tau}\,\text{Arg}\,[r(\tau)] \qquad (2)$$

where τ is the complex covariance lag value. For example, a unit power complex sinusoid centered at frequency ω_0 in white noise having variance σ_n^2 has a complex covariance given by

$$r(\tau) = \begin{cases} 1+\sigma_n^2 & \tau=0 \\ e^{j\omega_0\tau} & \tau\geq 1 \end{cases} \qquad (3)$$

Choosing any appropriate lag value τ, with $\tau\neq0$, the complex covariance frequency estimate is

$$\hat{f}_{cc} = \omega_0/2\pi = f_0 \qquad (4)$$

Thus $\hat{f}_{cc}$ is unbiased by a white noise input. The total received power is given by $r(0)$ and the spectral width (second moment) is a function of the covariance function evaluated at both 0 and τ lags. As explained in [5] this second moment estimator is biased by the SNR.

The class of maximum entropy frequency estimators is well documented in [2] and [3]. Results of experiments using these estimators have been acclaimed superior to the FFT-derived spectrum estimates, especially with respect to resolution of sinusoids and sharpness of spectrum peaks. Recent results show that although maximum entropy techniques yield biased frequency estimators, these estimators are asymptotically unbiased with increasing order of the estimator [7,8].

Following [9], let us define the maximum entropy frequency estimator as $\hat{f}_Q$, corresponding to the peak value of the modified maximum entropy spectrum estimate $Q(\omega)$,

$$Q(\omega) = \left|1-\sum_{\ell=1}^{N} a_\ell \, e^{-j\omega\ell}\right|^{-2} \tag{5}$$

where a_ℓ are the N^{th} order linear prediction filter coefficients that correspond to the maximum entropy power spectrum. (See Figure 3 for a basic linear prediction filter that can be used to generate a maximum entropy power spectrum.)

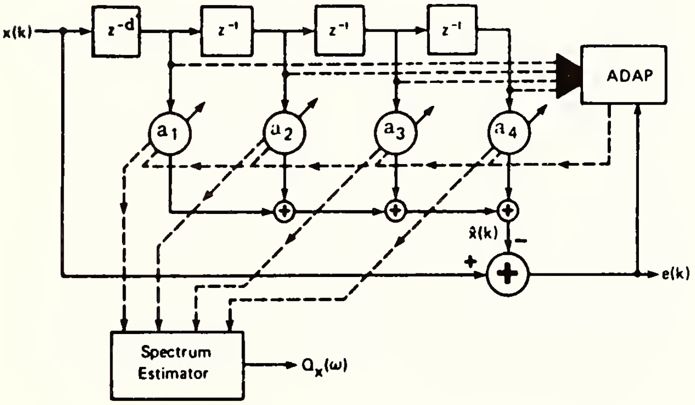

Figure 3. Basic adaptive linear prediction spectrum estimator. (N=4).

Several methods exist for obtaining this set of filter coefficients $\{a_\ell\}_{\ell=1}^{N}$. The classical technique (the autocorrelation method) utilizes a set of so-called "normal equations" to calculate $\{a_\ell\}_{\ell=1}^{N}$ from a set of estimated covariance values $\{r(\ell)\}_{\ell=1}^{N}$. These filter coefficients also define a set of polynomial coefficients as defined in (5). The resulting maximum entropy spectrum estimate is equivalently defined as the inverse squared magnitude of the Z-transform of the impulse response of the minimum mean squared error (mmse) filter $\{1,-a_1,\ -a_2,\ .\ .\ .\ -a_N\}$, evaluated on the unit circle. Therefore, for a complex first order maximum entropy spectrum estimator (i.e., only a single zero filter is used to form the linear prediction error sequence), the peak of the spectrum estimate is identical to the angle of the single zero in the Z plane. The complex normal equation for $N=1$ is then

$$r(0)\ a = r(1) \tag{6}$$

where the complex variable a is the single complex filter coefficient. That is,

$$a = r(1)/r(0) \tag{7}$$

Substituting (7) into (5) gives the maximum entropy spectrum estimator

$$Q(\omega) = \left|1 - a\, e^{-j\omega}\right|^{-2}, \tag{8}$$

which is the inverse squared magnitude of the Z-transform of the single zero mmse filter with impulse response $\{1,-a\}$. The peak of this "single pole power spectrum" is precisely the angle to the zero of the $\{1,-a\}$ minimum mse filter. The complex first order maximum entropy frequency estimate is

$$\begin{aligned} \hat{f}_Q &= \frac{1}{2\pi}\,\mathrm{Arg}\,[a] \\ &= \frac{1}{2\pi}\,\mathrm{Arg}\,[a] \\ &= \omega_0/2\pi \\ &= f_0 \end{aligned} \tag{9}$$

Thus $\hat{f}_Q=\hat{f}_{cc}$ for any SNR and any ω_0. The first order complex maximum entropy and the complex covariance frequency estimators are identical.

It is easy to show that only the first order complex maximum entropy frequency estimator is unbiased for all SNR's. For a noiseless sinusoidal input, any order linear prediction filter gives perfect prediction, and, consequently, the maximum-entropy spectrum estimate is unbiased. In order for the complex maximum-entropy frequency estimator to be unbiased as the SNR is decreased, the "dominant" complex zero (the one closest to the unit circle that generates the peak of $Q(\omega)$) must trace out at a locus that is a radial at angle ω_0. This zero is a root of the denominator polynomial $P(z)$, which is evaluated on the unit circle to give $Q(\omega)$. In the case of a first order estimator, it is the only zero of the denominator polynomial.

The complex maximum entropy spectrum estimate is derived from knowledge of the optimum (i.e., minimum mse) complex weight vector. This weight vector is known to be [8]

$$A^* = \beta\Gamma(\omega_0) \tag{10a}$$

with

$$\beta = \frac{1}{N+\sigma_n^2} \tag{10b}$$

and

$$\Gamma(\omega_0) = [e^{j\omega_0}\ e^{j\omega_0(2)} \ldots e^{j\omega_0(L)}]^T \qquad (10c)$$

The denominator polynomial P(z) is

$$P(z) = 1-a_1z^{-1}-a_2z^{-2}\ldots-a_Nz^{-N}$$

$$= z^{-N} \prod_{n=1}^{N} (z-\lambda_n) \qquad (11)$$

where the λ_n are the N roots of P(z). In order that these roots have loci of radials in the Z plane as the SNR is changed, the roots must change only in magnitude, i.e.,

$$P_\alpha(z) = z^{-N} \prod_{n=1}^{N} (z-\alpha\lambda_n) \qquad (12)$$

where $0 \leq \alpha \leq 1$ is an SNR dependent constant. Rewritten, this becomes

$$P_\alpha(z) = (z/\alpha)^{-N}\ \pi(z/\alpha-\lambda_n)$$

$$= P(z/\alpha)$$

$$= [1-a\ (z/\alpha)^{-1}-a_2(z/\alpha)^{-2}\ldots a_N(z/\alpha)^{-N}]$$

$$= 1-\alpha\, a_1z^{-1}-\alpha^2\, a_2z^{-2}\ldots-\alpha^N a_N\ z^{-N} \qquad (13)$$

Thus, if the roots of P(z) lie on radial loci as the SNR, or α, is varied, then the n^{th} coefficient of P(z) varies as the n^{th} power of α. Substituting the coefficients given by (10) into (11), we find P(z) for the general complex case to be

$$P(z)=1-\beta\ e^{j\omega_0}\ z^{-1}-\beta\ e^{j2\omega_0}z^{-2}-\ldots-\beta\ e^{jN\omega_0}z^{-N}, \qquad (14)$$

which is not the same form given in (13) except for the N=1 case. Thus, *only* the first order complex maximum entropy frequency estimator, i.e., $\hat{f}_{Q_1}$, corresponding to the peak of

$$Q_1(\omega) = \left|1 - \frac{1}{1+\sigma_n^2}\, e^{-j(\omega_0-\omega)}\right|^{-2}, \qquad (15)$$

is unbiased at all SNR's (all values of σ_n^2). That is,

$$\hat{f}_{Q_1} = \omega_0/2\pi = f_0 \qquad (16)$$

for all SNR's.

Conclusions

We have described a lidar wind estimation system and identified the requirement for a Doppler processor. The desirability of directly extracting the first three moments of the received power spectra for each range gate (without having to calculate the spectrum itself) makes the complex-covariance frequency estimator appear extremely attractive. We have shown the equivalence of this complex covariance estimator with the first-order complex maximum-entropy frequency estimator, thereby removing any "mysticism" associated with one estimator by those familiar with the other. Having compared the maximum-entropy and complex-covariance estimators, we may easily describe an adaptive complex-covariance frequency estimator as the first order complex adaptive linear-prediction (or adaptive maximum-entropy) frequency estimators described in [9] and [10]. In many cases, a higher order maximum-entropy estimator is required (e.g., when multiple sinusoids are expected), and the complex-covariance approach may be discarded immediately. Higher order maximum-entropy frequency estimators are biased, but we have indicated that they are asymptotically unbiased as the order is increased. References [7] and [8] extend this maximum-entropy order selection specification in more detail.

References

1. Staff of Wave Propagation Lab, "Ground-based and Airborne CO_2 Pulsed Coherent Lidar for Remote Wind Measurement", NOAA Tech. Report, in preparation, 1977.

2. Burg, J. P., "Maximum Entropy Spectral Analysis", Ph.D Thesis, Stanford Univ., Stanford, Calif., May 1975.

3. Ulrych, T. J. and T. N. Bishop, "Maximum Entropy Spectral Analysis and Autoregressive Decomposition", *Rev. Geophys. and Space Phys.* vol. 13, no. 1, 1974, p.183-200.

4. Sirmans, D. and B. Bumgarner, "Numerical Comparison of 5 Mean Frequency Estimators", *J. Appl. Meteorol.*, vol. 14, 1975, p.991-1003.

5. Miller, K. S. and M. M. Rochwager, "A Covariance Approach to Spectral Moment Estimation", *IEEE Trans. on Info. Th.*, vol. IT-18, 1972, p.588-596.

6. Huffaker, R. M., "Laser Doppler Detection Systems for Gas Velocity Measurement", *App.. Opt.*, vol. 9, 1970, p.1026.

7. Zielder, J. R., E. H. Sartorius, D. M. Chabries, and H. T. Wexler, "Adaptive Enhancement of Multiple Sinusoids in Uncorrelated Noise", accepted for publication in *IEEE Trans. on Acoust., Speech, and Sig. Proc.*, 1977.

8. Keeler, R. J., "Adaptive Frequency Estimation using Linear Prediction Filtering", Ph.D Thesis, Univ. of Colorado, Boulder, Colo., 1978.

9. Griffiths, L. J., "Rapid Measurement of Digital Instantaneous Frequency", *IEEE Trans. on Acoust. Speech, and Sig. Proc.*, vol. ASSP-23, April 1975, p.2 07-222.

10. Keeler, R. J. and L. J. Griffiths, "Acoustic Doppler Extraction by Adaptive Linear Prediction Filtering", *J. Acoust. Soc. Am.*, vol. 61, May 1977, p.1218-1227.

NOAA Technical Memorandum ERL WPL-35, 1978

MUDRAS
MULTIPLE DOPPLER RADAR ANALYSIS SYSTEM

Nathan M. Kohn
Andrew L. Johnston
Carl Mohr

MUDRAS, Multiple Doppler Radar Analysis System is a software package consisting of four data formats and nine computer programs which provide analysts a flexible tool for processing and interpreting meteorological data. The data formats are called MUDRAS time series, MUDRAS pulse pair, MUDRAS archive, and MUDRAS cartesian tapes; these are described under Tape Organization. These programs are implemented on the CDC 6600 at NOAA (National Oceanic and Atmospheric Administration) and the CDC 7600 at NCAR (National Center for Atmospheric Research) and are written principally in FORTRAN.

Included in this package are a tape library system and a set of procedures for initiating and monitoring production runs. This package has been utilized for processing data obtained from numerous experiments including NHRE (National Hail Research Experiment, 1973-1976), METROMEX (Metropolitan Meteorological Experiment, 1975), SPACE (South Park Area Cumulus Experiment, 1977).

Preprint Volume; 18th Conference on Radar Meteorology, 94-99,
American Meteorological Society, 1978.

TEMPERATURE RETRIEVAL FROM DUAL-DOPPLER RADAR WIND FIELD DATA

James A. Leise

NOAA/ERL/Wave Propagation Laboratory
Boulder, Colorado 80302

1. INTRODUCTION

Wind field data obtained from Doppler radars have proved invaluable to mesoscale meteorology. These radar methods give detailed three-dimensional descriptions about the dynamics and kinematics of atmospheric wind fields. Sometimes the effects of other meteorological variables such as density, pressure, and temperature are clearly visible in the data. For example, dry convection over St. Louis has been studied in this way (Kropfli and Kohn, 1977). It is therefore a natural step to try to deduce the effects of density, pressure and temperature in a more direct fashion. This requires a model together with a sizeable amount of computation.

The quantity on which we will focus attention is buoyancy. It has the advantage of being relatively straightforward to obtain and seems to provide the key to getting density, pressure, and temperature.

In order to make the theory applicable to dual-Doppler radar data, it is important that the model used to compute buoyancy be compatible with the dual-Doppler data acquisition methods. This amounts to a suitable use of the continuity equation (Lhermitte, 1970; Miller and Strauch, 1974; Ray et al., 1975; Doviak et al., 1976).

The most serious obstacles in obtaining buoyancy appear to be numerical. This is because a large number of numerical derivatives and products together with a division are needed to compute this quantity. These operations are all sensitive to noise in the data.

In order to cope with these difficulties new editing and filtering methods have been developed. Because these methods are somewhat complicated they will not be discussed at length here. However, we will illustrate how they work and how they make the computation of buoyancy a viable procedure.

Finally all numerical methods are checked against a synthetic data model of analytic functions. This model is not intended to be physically interesting. Rather, it provides a data set for which the derivatives and consequently the buoyancy can be computed exactly.

2. GENERAL THEORY

The model that we use for this feasibility study is of the simplest kind. It is that of a non-turbulent, dry, convective atmosphere. It is worth emphasizing, however, that the methods given below are adaptable to more complicated models.

The momentum equations are

$$\rho \frac{du}{dt} = - \frac{\partial p}{\partial x} \tag{2.1}$$

$$\rho \frac{dv}{dt} = - \frac{\partial p}{\partial y} \tag{2.2}$$

$$\rho \frac{dw}{dt} = - \frac{\partial p}{\partial z} - \rho g \tag{2.3}$$

where

$$\frac{d}{dt} = \frac{\partial}{\partial t} + u \frac{\partial}{\partial x} + v \frac{\partial}{\partial y} + w \frac{\partial}{\partial z} \tag{2.4}$$

denotes the material derivative and where ρ, p and $\overline{v} = (u,v,w)$ denote the density, pressure, and velocity. The continuity equation is

$$\frac{1}{\rho} \frac{d\rho}{dt} = - \nabla \cdot \overline{v} \tag{2.5}$$

The pressure in (2.1) and (2.2) can be removed by cross differentiation with (2.3) in a manner similar to that of obtaining the vorticity equation. These equations together with the anelastic form of the continuity equation result in the following system

$$H R_x - F R_z = \frac{\partial F}{\partial z} - \frac{\partial H}{\partial x} \tag{2.6}$$

$$H R_y - G R_z = \frac{\partial G}{\partial z} - \frac{\partial H}{\partial y} \tag{2.7}$$

$$u R_x + v R_y + w R_z = - \nabla \cdot \overline{v} \tag{2.8}$$

where

$$F = \frac{du}{dt}, \quad G = \frac{dv}{dt}, \quad H = \frac{dw}{dt} + g$$

$$R = \log(\rho)$$

and subscripts denote partial derivatives. These equations are easily recognized as a system of three equations in the three unknowns R_x, R_y, and R_z. We define buoyancy as

$$B = g \frac{1}{\rho} \frac{\partial \rho}{\partial z} = g R_z \tag{2.9}$$

and we see that B is computable from the above system. Moreover, because Doppler radars provide the velocity data, all other quantities in this system can be computed from data. In other words, this system provides a way of computing the buoyancy from three-dimensional wind field data.

Buoyancy, in itself, may or may not be interesting insofar as it is used to interpret data or gain insight into the physics. The importance of this quantity lies in the observation that if density is known *only at the ground* then the buoyancy field may be integrated to obtain the density wherever velocity data are available. If, in addition, pressure is known at the ground then the third momentum equation (2.3) may be integrated to obtain pressure. Finally given density, pressure, and an equation of state, temperature may be deduced. It is in this sense that we say that buoyancy is the key to density, pressure, and temperature.

3. DUAL-DOPPLER METHODOLOGY

It should be noted that the above theory was presented in rectangular coordinates whereas dual-Doppler data acquisition is often done in cylindrical coordinates. However, for theoretical purposes any coordinate system will do and rectangular coordinates are desirable for purposes of exposition. With this in mind, dual-Doppler data acquisition can be described as measuring two velocity components u and v. The third component w is computed from the continuity equation. This is done by modeling a background density as

$$\rho_o(z) = ce^{\kappa z} \tag{3.1}$$

for suitable constants c and κ. The important features of this approximation are that the atmosphere is allowed to be compressible and that the density must be horizontally homogeneous.

With this assumption the continuity equation (2.5) becomes

$$\frac{\partial w}{\partial z} + \frac{1}{\rho_o}\frac{\partial \rho_o}{\partial z} w = -\frac{\partial u}{\partial x} - \frac{\partial v}{\partial y} \tag{3.2}$$

which is a first order differential equation for the third velocity component w. This equation is easily integrated starting with a known boundary condition at the ground.

The point of all this is that data sets obtained from dual-Doppler processing are somewhat model dependent and reflect the assumptions of the model. Consequently, any attempt to extract other kinds of information from such data sets must be done in a compatible manner.

4. THE PERTURBATION BUOYANCY

We here implement a perturbation method of the most elementary kind. First, consider the density ρ_o used to compute the third velocity component w as a background quantity to which is added a smaller incompressible quantity ρ' which depends on x,y, and z. Thus

$$\rho(x,y,z) = \rho_o(z) + \rho'(x,y,z). \tag{4.1}$$

Substituting (4.1) into (2.6)-(2.8) results in the following system:

$$HR'_x - FR'_z = \frac{\partial F}{\partial z} - \frac{\partial H}{\partial x} + FR_o \tag{4.2}$$

$$HR'_y - GR'_z = \frac{\partial G}{\partial z} - \frac{\partial H}{\partial y} + GR_o \tag{4.3}$$

$$uR'_x + vR'_y + wR'_z = 0 \tag{4.4}$$

where $R_o = \frac{1}{\rho}\frac{\partial \rho_o}{\partial z}$

$$R'_x = \frac{1}{\rho}\frac{\partial \rho'}{\partial x}, \quad R'_y = \frac{1}{\rho}\frac{\partial \rho'}{\partial y}, \quad R'_z = \frac{1}{\rho}\frac{\partial \rho'}{\partial z}.$$

This is a system of three equations in the three unknowns R'_x, R'_y, and R'_z. The perturbation buoyancy B' is then computed as

$$B' = g\frac{1}{\rho}\frac{\partial \rho'}{\partial z} = gR'_z. \tag{4.5}$$

This is a curious quantity. For example, at the null point of a horizontal convergence zone where u and v vanish, the perturbed continuity equation (4.4) states that B' must be zero. Also the third component w will usually be a maximum at such a convergence point. This means that buoyancy, as defined, cannot line up with updrafts or downdrafts. This is purely a consequence of continuity and has nothing to do with the formulation of the momentum equations.

To compute B', first multiply (4.2), (4.3), and (4.4) by u, v and H respectively. Subtracting the first two equations from the third gives

$$B' = -N/D \tag{4.6}$$

where

$$N = u\left(\frac{\partial F}{\partial z} - \frac{\partial H}{\partial x}\right) + v\left(\frac{\partial G}{\partial z} - \frac{\partial H}{\partial y}\right) + (uF + vG)R_o$$

$$D = (wH + uF + vG)/g.$$

It is interesting to note that the only visible dependence of B' on the background density is in the numerator N. It should, however, be remembered that there is also an invisible contribution in w via dual-Doppler processing.

5. THE SYNTHETIC DATA MODEL

The first step in the computation of B' from data is the calculation of F, G and H. Each of the quantities requires three numerical derivatives and three multiplications of data dependent quantities. Therefore, the computation of B' requires 13 numerical derivatives and 16 multiplications of data dependent quantities. With real data this is a serious undertaking. A check of the numerical methods used and the quality of the resulting answers is therefore very important. If such a check were done by comparison with a numerical model, all one would succeed in doing is comparing one set of numerical methods against another.

In order to circumvent this kind of circular reasoning, we use a model of analytic functions for which all derivatives can be computed exactly. While such a model need not be physically interesting, it is desirable that it at least be plausible insofar as scale sizes and magnitudes are concerned.

To begin, stability theoretic standing waves have the general form

$$u(x,y,z) = u_o(z) + f(z) \sin(kx) \cos(\ell y) \quad (5.1)$$

$$v(x,y,z) = g(z) \cos(kx) \sin(\ell y) \quad (5.2)$$

$$w(x,y,z) = h(z) \cos(kx) \cos(\ell y). \quad (5.3)$$

If we assume that density depends only on height then the continuity equation becomes

$$kf(z) + \ell g(z) + \frac{dh(z)}{dz} = - h(z)R_o \quad (5.4)$$

where $R_o = \frac{1}{\rho_o} \frac{\partial \rho_o}{\partial z}$.

The game is then to model R_o and choose u_o, f, g, and h so as to satisfy (5.4) and the boundary conditions

$$u_o(o) = f(o) = g(o) = h(o) = 0 \quad (5.5)$$

$$f(\infty) = g(\infty) = h(\infty) = 0. \quad (5.6)$$

This is most easily done by first choosing u_o, f, and h and then computing g from (5.4). It should be noted that the continuity equation (5.4) is the important feature of the simulation. The boundary conditions are only niceties.

For purposes of completeness we finally list the functions and parameters used

$$u_o = 0 \text{ (no shear)}$$

$$f(z) = c_1 \sin(\gamma z)e^{-\alpha(z-z_o)}$$

$$h(z) = c_2 z \sin(\beta z)e^{-\alpha(z-z_o)}$$

and

$$k = \ell = 19.635 \text{ km}^{-1}, \quad gR_o = .001 \text{ sec}^{-2}$$

$$\alpha = 1 \text{ km}^{-1}, \quad \beta = 1.5 \text{ km}^{-1}, \quad \gamma = 3 \text{ km}^{-1}$$

$$z_o = 1 \text{ km}, \quad c_1 = -2. \quad , \quad c_2 = .0085 .$$

6. SIMULATION RESULTS

The quantity that seems to govern the quality of digitally computed answers is the number of sample points per cycle of the data. The number of points per cycle is a measure of resolution. For example, numerical derivatives degrade in accuracy as the number of points per cycle is decreased. It is well known that at high frequencies derivatives are powerful amplifiers of noise.

Computing products of data dependent quantities presents its own set of problems. The product of two periodic functions results in sum and difference frequencies. If we require that no computed quantity should exceed half the folding frequency or 4 points/cycle, then frequencies higher than 16 points/cycle in the velocity data should not be used. For real data, this requires filtering out higher frequencies.

The most threatening problem is the division by D in (4.6) needed to compute the perturbation buoyancy B'. This is because D is approximately equal to the vertical velocity w which can vanish. Unless the numerator N also vanishes, B' will be infinite. Simulations indicate that both the numerator and denominator do indeed vanish at the same time. The reason for this is not known. However, with the introduction of noise, B' will often have unreasonably large values. We have found that it is possible to simply edit such points out and replace them with interpolated values.

With this background we now turn to a specific simulation. For this study 10 horizontal planes, each containing a grid of 30 x 30 points, was used. The horizontal scales were set at 30 points/cycle with about 16 points/cycle in the vertical. The first plane was positioned 75 m above the ground with successive planes spaced 150 m apart. The grid points in the horizontal planes are spaced about 100 m apart. All figures shown are for the third plane above the ground. The axes are scaled in km.

Figure 1 is a horizontal vector plot of the u and v components of the wind field. The parameters were chosen so that u and v are almost balanced in this plane with peak values of about 3 m/sec. The center of this vector plot is a strong convergence region. Figure 2 shows contours of the vertical velocity w. The numbers on the contours represent units above or below the mean. Thus, in this plane w also peaks at about 3 m/sec. Furthermore w increases in amplitude with height until at the 7th plane it reaches about 10 m/sec. Figure 3 shows the effect of adding random noise to w as follows:

$$w + 6. * (\mathrm{RANF} - .5)\ ,\ 0 \le \mathrm{RANF} \le 1\ .$$

Figure 4 shows the result of applying a new three-dimensional low pass filter to the noisy vertical velocities. This filter yields quality smoothing right up to the edge of the data set. Using conventional methods only the middle square would be left. This filter is the essential ingredient in making the buoyancy computation work. Figure 5 shows the exact buoyancy B' computed with exact derivatives. It should be noted that there is at least a doubling of frequencies over the input velocity fields. Figure 6 shows how the computation is degraded with the use of 5-point numerical derivatives. Figure 7 shows the result of attempting the computation of B' from the noisy velocity field without the benefit of noise reduction methods. Finally, Figure 8 shows how the filtering and editing methods retrieve the desired signal. Although the contours are a bit deranged, the peaks and valleys are for the most part positioned correctly. Finally the magnitudes are fairly good and are about an order of magnitude smaller than the background quantities.

It is our judgment that if these numerical methods can hold up to this kind of punishment, then they are indeed suitable for use on data. More importantly, these are general purpose methods which can be used on a variety of problems.

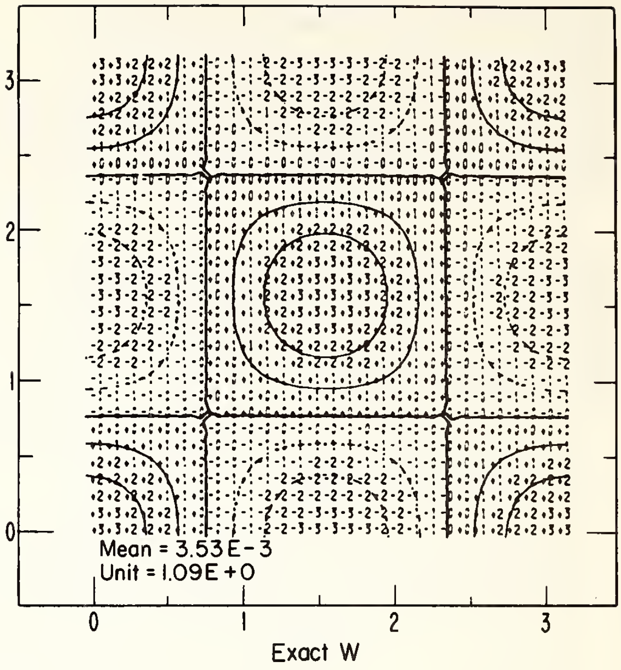

Figure 2. Contours of the simulated vertical velocity field. The numbers represent units above or below the mean. The physical units are m/sec.

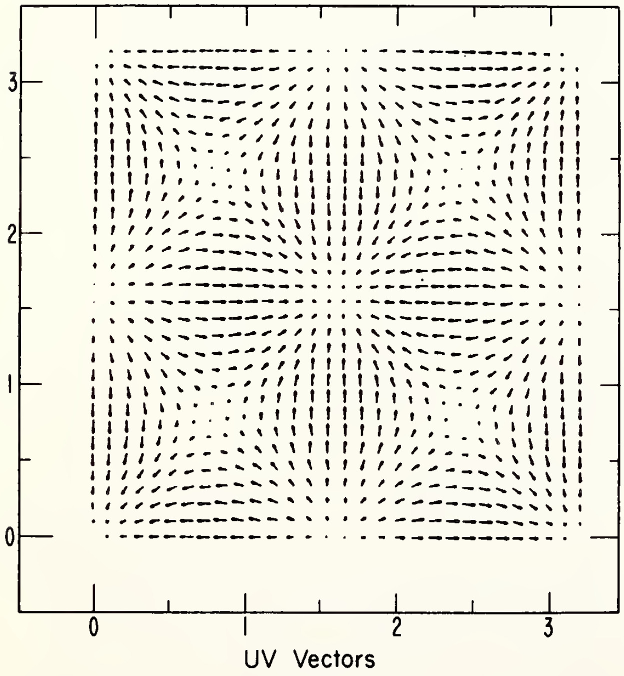

Figure 1. The simulated horizontal vector field for the third plane (375 m) above the ground. The x and y axes are scaled in km.

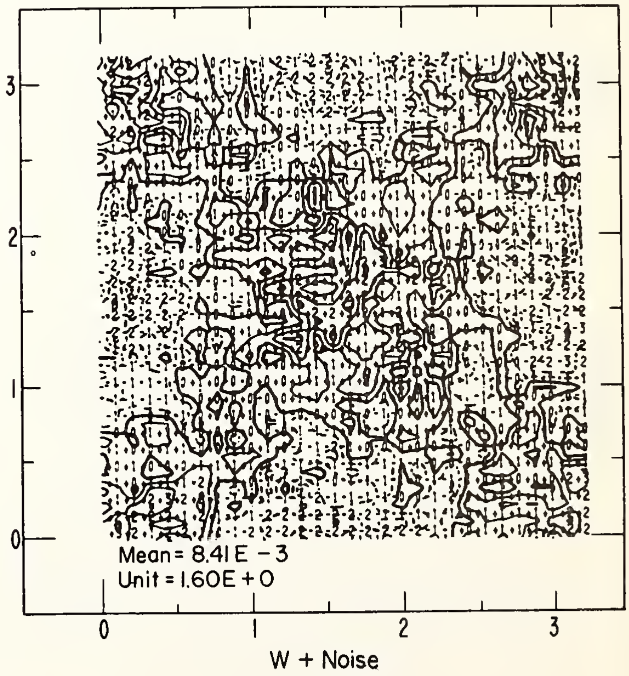

Figure 3. The simulated vertical velocity field plus random (white) noise.

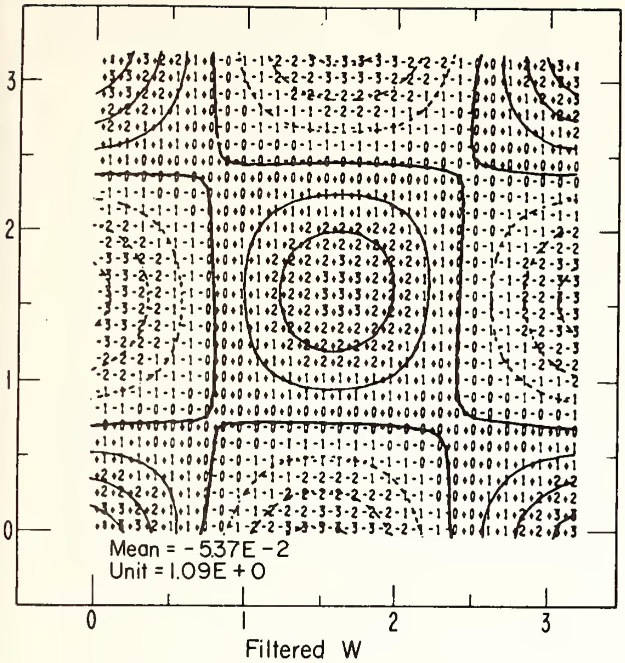

Figure 4. The velocity field resulting after the noisy velocity field of Figure 3 is lowpass filtered.

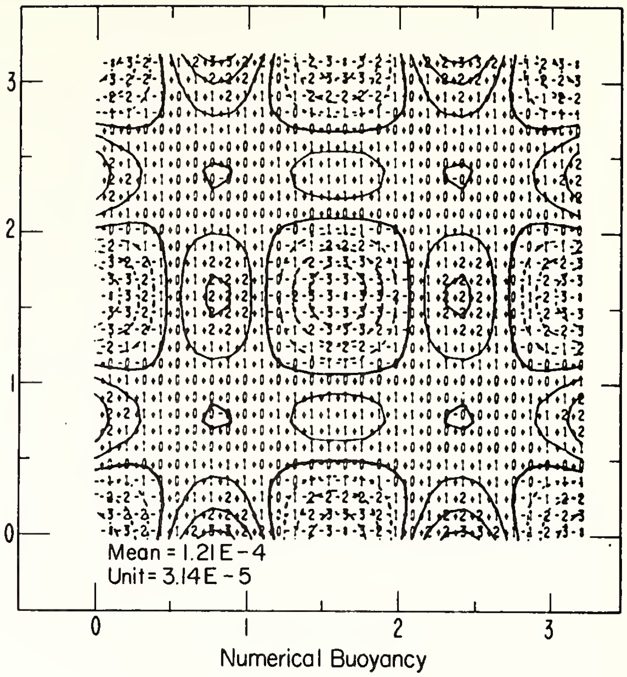

Figure 6. The buoyancy computed using 5-point numerical derivatives.

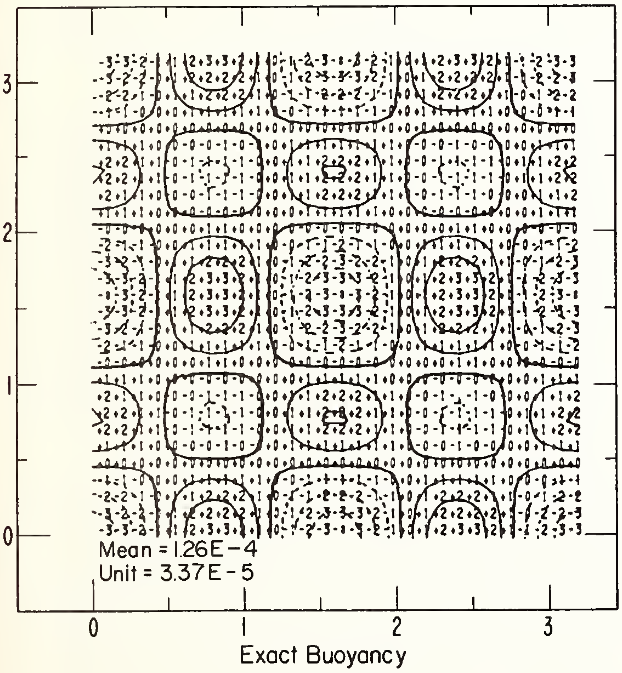

Figure 5. The exact buoyancy computed using exact derivatives. The physical units are sec^{-2}.

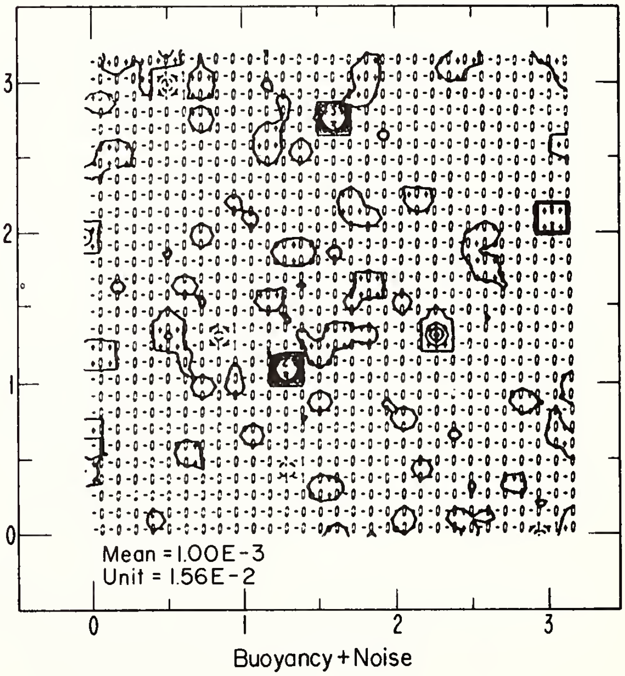

Figure 7. An attempt to compute buoyancy from the noisy velocity field of Figure 3.

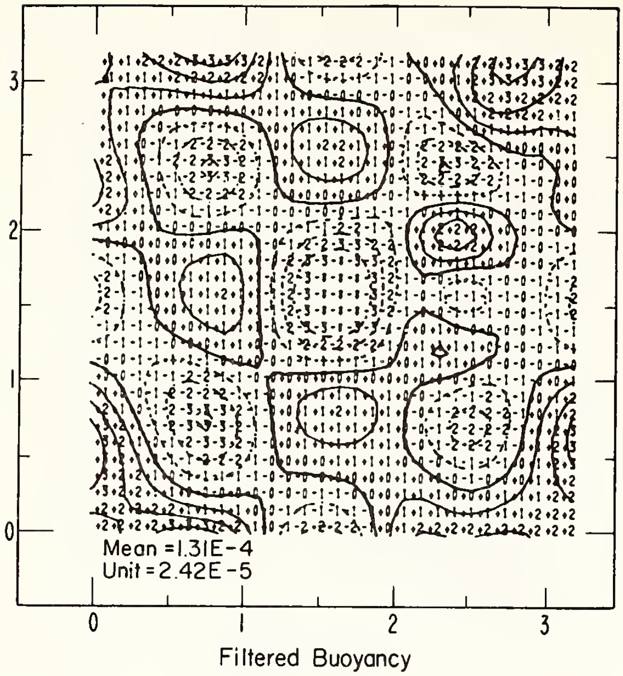

Figure 8. The buoyancy computed from the noisy velocity field using 5-point derivatives and noise reduction methods.

7. REFERENCES

Doviak, R. J., P. S. Ray, R. G. Strauch and L. J. Miller, 1976: Error estimation in wind fields derived from dual-Doppler radar measurement. *J. Appl. Meteorol.*, 15, 868-878.

Kropfli, R. A. and N. M. Kohn, 1977: Dual-Doppler radar observations of the convective mixing layer at St. Louis. *Preprints 17th Radar Meteorology Conf.*, Seattle, Amer. Meteor. Soc., 321-325.

Lhermitte, R. M., 1970: Dual-Doppler radar observations of convective storm circulation. *Preprints 14th Radar Meteorology Conf.*, Tucson, Amer. Meteor. Soc., 139-144.

Miller, L. J. and R. G. Strauch, 1974: A dual-Doppler radar method for the determination of wind velocities within precipitating weather systems. *Remote Sensing Environ.*, 3, 217-233.

Ray, P. S., R. J. Doviak, C. B. Walker, D. Sirmans, J. Carter and B. Bumgarner, 1975: Dual-Doppler observations of a tornadic storm. *J. Appl. Meteor.*, 14, 1521-1530.

Preprint Volume; 18th Conference on Radar Meteorology, 155-158, American Meteorological Society, 1978.

THE DETERMINATION OF CONVECTIVE SHOWER POPULATIONS FROM RADAR DATA

Raúl E. López

National Hurricane and Experimental Meteorology Laboratory
Coral Gables, Florida 33124

1. INTRODUCTION

In the last few years evidence has been presented that indicates that convective echo populations follow a lognormal probability law in their size, height and duration distributions. López (1976) showed this to be the case for tropical systems in the Western Atlantic. Simultaneously and independently, Biondini (1976) found a similar distribution for south Florida showers. Recently López (1977a) presented size and duration distributions for convective echoes in many different parts of the world which also follow a lognormal law. Clear air convective plumes follow the same law as well as the incipient fair weather cumuli that form in association with them (López, 1977b). As soon as the GATE radar data was available, Houze and Cheng (1977) took an overall view at the convective echo populations present at midday during the 3 phases of the experiment. They also obtained lognormal distributions. At the same time Nasim (1977) analyzed all of the echoes of one GATE disturbance appearing on the *Oceanographer's* radarscope during the lifetime of the system (11,000 echoes) and he also found lognormal distributions for maximum echo area and duration.

Most of the work on echo populations mentioned was done from microfilm records and by tracking echoes during their entire lifetimes. A maximum height, area or diameter were assigned to characterize the echo, and frequency distributions were constructed. This method can be called the lifetime approach, since it seeks to characterize the echoes according to their lifetime properties. On the other hand, some investigators spurred by the availability and quality of the GATE digital radar data, have derived echo populations by analyzing the echoes present on the radar scope at specific times: the instantaneous approach.

Obviously, this last method does not provide an accurate characterization of the echo population, since echoes might be observed in their growing or dying stages and thus might be assigned to smaller area or height classes than they actually belong to. In addition, the instantaneous approach underestimates the contribution of the small, short-lived echoes to the total population present during a period of time. On the other hand, the instantaneous approach is much faster and yields itself more easily to computerized techniques. However, a correction must be applied if it is to be used to characterize accurately a convective system as to the relative number of echoes of a given type that would exist in it during a given period of time. Accordingly, the objective of this paper is to explore the problems and the data needs involved in such a correction and to lay the mathematical foundation for such a scheme.

2. ECHO GROWTH CHARACTERISTICS

Generally the echo population from convective systems can be divided into a variety of area classes; the echoes in each class attaining a different maximum area. During its life cycle each echo grows to its maximum size and then dissipates until it disappears. At a particular sampling time an echo can be detected theoretically at any point during its growth and decay process. The probability of detecting an echo belonging to maximum-area class s at a time during its lifetime when it has an area a ($a \leq s$) is clearly dependent on the frequency of occurrence of echoes in that size class and the details of the growth curve of an echo of that class. On the other hand, an echo belonging to a different maximum-area class can be observed in the same sample at a point in its different life cycle when it has the same area as the previous echo. Again, the probability of this event is dependent on the frequency of occurrence of echoes in the new class and the corresponding growth curve. The sum of these probabilities over all classes gives the probable frequency of occurrence of echoes of an area a in the instantaneous-view sample. From these relationships it seems theoretically possible to obtain the lifetime-view frequency distribution from the instantaneous-view distribution, provided that the growth curves for each of the maximum-area classes are known.

In order to explore the growth characteristics of radar echoes, 10,000 echoes of a disturbance observed in GATE from 7-9 August 1974 were tracked during their entire life cycles. In Figure 1, the mean and standard deviation of the duration for each maximum-area class is indicated. No clear area vs. lifetime relationship emerges. The variation of lifetime within each area class is certainly very large. This means that an echo attaining a certain maximum size can have several modes of growth.

The reason for this lies in the fact that all echoes having maximum areas above 80 km^2 are composed of several cells (López, 1978). A cell can be defined as an area having a maximum in radar reflectivity within a larger echo that maintains its identity for a period of around 15 minutes. The cells comprising such a composite echo go through their individual life cycles of growth and decay with various degrees of time overlap, some dissipating while new ones appear in close connection to the remaining cells. In the mean the composite echoes consist of 5 cells, although the mean maximum number of cells is 8. Typically, during

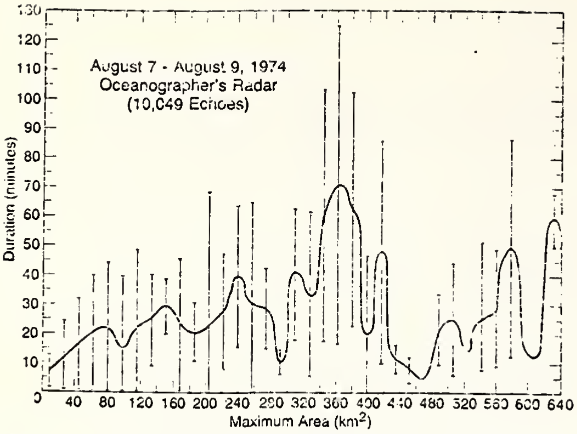

Figure 1. Average echo duration as a function of maximum echo area. Vertical bars indicate the standard deviation for each mean value. Data obtained by the NOAA ship *Oceanographer* during GATE for the period 7-9 August 1974.

the lifetime of the echo around 15 cells appear, grow, and dissipate in close proximity one to the other. Although there is some variation in cell size and duration, in general the particular area and duration of a composite echo depend respectively on the average number of cells present and on the total number appearing during its lifetime. This is the reason for the variety of echo formation and growth modes. For example, an echo can exist which in the average is made up of 3 cells in close connection to each other. During the lifetime of the echo a total of 12 cells might go through their individual life cycles. A similar sized echo (containing 3 cells in the average) may go through only 6 cells during a much shorter lifetime. As a result, there are no unique area-duration relationships. Echoes having the same average or maximum area can have widely different lifetimes and vice versa.

Figure 2 illustrates these echo growth characteristics. There the data of Figure 1 has been stratified by maximum area and lifetime class and a bivariate frequency distribution computed. A bivariate lognormal distribution results. Thus, not only are the maximum-area classes lognormally distributed, but within each area class the echoes are lognormally distributed by duration also. As an example, an echo can attain a maximum area of 50 km^2 while its duration can be 5, 10, 60, 100 minutes, etc. depending on the growth and formation mode. The majority of the echoes, however, would tend to have small durations. With reference to the genesis law of the lognormal distribution this figure indicates that the composite echoes grow by a process which is dependent both on the size of the echo and on random factors.

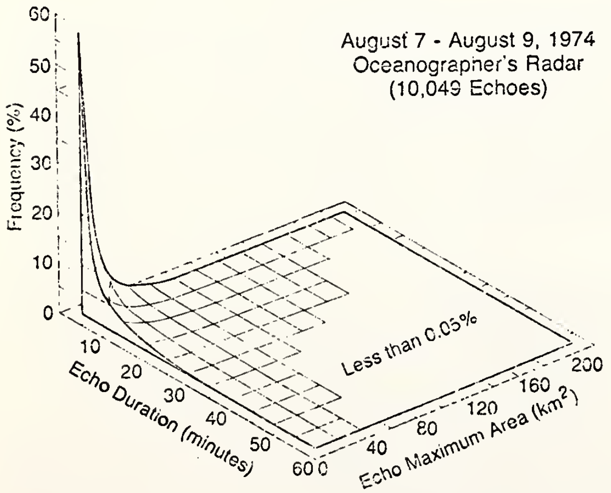

Figure 2. Combined frequency distribution of echo duration and maximum area. Data source as in Figure 1.

At this stage it can be seen that in order to obtain lifetime-view from instantaneous-view frequency distributions, the growth curve for each maximum area and echo duration class combination must be specified. This task is not completely hopeless since the cellularity of the echoes makes the echo formation and growth processes amenable to simple physical modeling.

3. MATHEMATICAL FOUNDATION FOR THE SAMPLING PROBLEM

The mathematical treatment presented in this section is similar in its approach to the statistical interpretation of plume and cloud measurements developed by Vul'fson (1964). In his situation he wanted to derive diameter distributions from plume and cloud transect measurements obtained from an aircraft. In the present case we want to derive echo maximum area distributions from instantaneous measurements of echo area. In his method Vul'fson assumed a cylindrival or spherical shape for the convective elements, while in the present case information about growth curves must be obtained or assumed.

The basic approach used in this section is to express the instantaneous sampling process in terms of the probability distribution function of observing an echo which at some time during its lifetime obtains a certain maximum area (the lifetime view distribution), and the probability of observing that echo at a time during its life cycle when it has a given area (related to the growth curve of the echo). The resulting expression is a set of integral equations which could be solved by inversion techniques to yield the lifetime-view frequency distribution.

Let $F(s,\tau)$ be the distribution function of the probability of an echo attaining a maximum area s and lasting a time period τ within an area A (radar scope) and in a large time interval $T(T>>\tau)$. This is the lifetime view distribution being sought. This function has the following property:

$$\int_0^\infty \int_0^\infty F(s,\tau)\,ds\,d\tau = 1 \qquad (1)$$

Furthermore define N as the total number of echoes per unit area and unit time defined likewise over A and T.

The number of echoes detected at a particular time t and over area A that attain at some time during their lives a maximum area within s and $s+ds$ can be now expressed as

$$\int_0^\infty \tau(s)[N\ F(s,\tau)ds]d\tau\ , \qquad (2)$$

where $\tau(s)$ are the lifetimes of echoes attaining a maximum area s. The factor $\tau(s)$ has the effect of including those echoes which, although not attaining maximum area at t, are nevertheless detected at this time. The integration over lifetime includes echoes having different durations but belonging to the same area class. The total number of echoes detected at time t and over area A would in turn be

$$\int_0^\infty\int_0^\infty \tau(s)N\ F(s,\tau)dsd\tau = N\bar{\tau}\ , \qquad (3)$$

where $\bar{\tau}$ is the average lifetime.

On the other hand, the number of echoes attaining at some time a maximum area within s and s+ds and detected at time t (2) can also be expressed as

$$\int_0^\infty N\bar{\tau}u(s,\tau)dsd\tau\ , \qquad (4)$$

where $u(s,\tau)$ is the distribution function of the probability of an echo present at time t and attaining a maximum area s during its lifetime τ. From (2) and (4) the relationship between the distribution of maximum echo areas occurring during the time interval T and the distribution of maximum echo areas present at time t can be obtained:

$$\bar{\tau}\int_0^\infty u(s,\tau)d\tau = \int_0^\infty \tau(s)F(s,\tau)d\tau\ . \qquad (5)$$

Now, at time t the echoes do not necessarily show their maximum area s but most probably an area a less than s. The probability W(a)da of detecting an echo with an area between a and a+da (the observed instantaneous frequency distribution) is equal to the product of the probability $u(s,\tau)ds$ of detecting an echo at time t which has a lifetime between τ and $\tau+d\tau$ and attains a maximum area between s and s+ds during its lifetime, and the sum of the conditional probabilities $v(x_i|s,\tau)dx_i$ of detecting that echo at times during its lifetime between x_i and x_i+dx_i when it had an area between a and a+da, summed over all possible values of maximum area s and lifetime τ:

$$W(a)da = \int_0^\infty d\tau\int_0^\infty u(s,\tau)ds\sum_{i=1}^{n} v(x_i|s,\tau)dx_i\ . \qquad (6)$$

Since there is an equal probability of detecting an echo at any time x_i during its lifetime $\tau(s)$,

$$v(x_i|s,\tau) = 1/\tau(s)\ . \qquad (7)$$

The number of times n that the echo of maximum area s and lifetime τ has an area a will be dependent on the shape of its growth curve.

Substituting (7) and (5) into (6) one obtains

$$W(a)da = \frac{1}{\bar{\tau}}\int_0^\infty\int_0^\infty F(s,\tau)dsd\tau\sum_{i=1}^{n} dx_i\ . \qquad (8)$$

This is the basic equation relating the instantaneous-view, W(a)da, to the lifetime-view, $F(s,\tau)dsd\tau$, frequency distributions. The term involving the sum represents the time interval during the lifetime τ of an echo when the echo (belonging to maximum-area class s) has an area a. This is a function of the growth curve of the echo and is the crucial item of information necessary to complete the procedure. It is expected that more research into the growth modes of cumulus clouds and their radar echoes will provide the necessary information. As it was mentioned before, the lognormality of both area and duration distributions and the cellularity of echoes greater than 80 km^2 in area promise some interesting avenues of investigation. Before more information is acquired on growth curves it is not advisable to look further into inversion techniques that could retrieve $F(s,\tau)$ in terms of W(a).

4. ADDITIONAL SAMPLING PROBLEMS

As was mentioned before most frequency distributions of echo area, duration and height have been found to be lognormal over a wide variety of convective situations. Occasionally, however echo frequency distributions depart from normality in the range of the largest or longest 2% of echoes. López (1977b) has indicated that this might be a reflection of a natural limit to cloud growth. The lognormal, as well as any other long tailed frequency distribution, calls for echoes of ever increasing height, area, or duration, while the atmosphere limits the areal, vertical and temporal extent of clouds and their echoes.

As an illustration consider the theoretical lognormal distribution of Figure 3. The log probability plot of this curve is the straight line in Figure 4. If the original distribution, however, is truncated at points A or B the resulting log probability plots in Figure 4 will show a departure toward higher frequencies for the largest size or duration classes. On the other hand, a sampling process which is biased against small

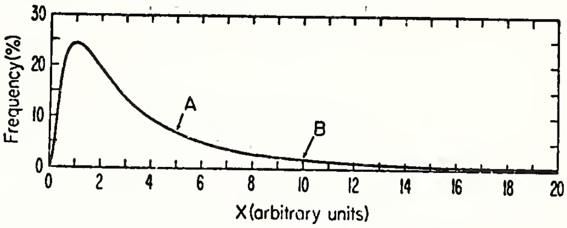

Figure 3. A tneoretical lognormal frequency distribution with geometric mean and standard deviation equal to 1 in arbitrary units of x.

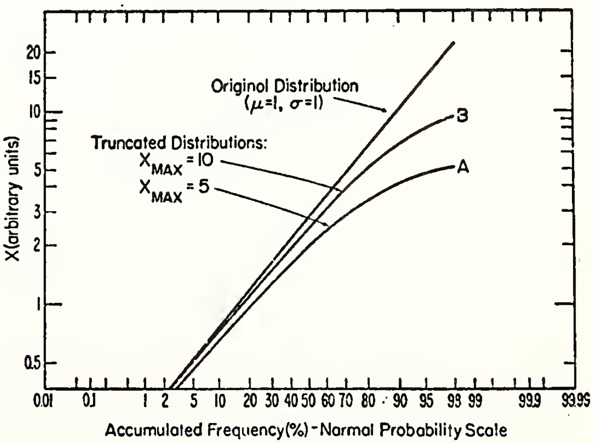

Figure 4. The accumulated frequency distributions of a theoretical lognormal distribution (straight line) and the same for the theoretical distribution truncated at the upper end (curves A and B).

echoes would produce a frequency distribution which departs towards lower frequencies for the smallest size or duration classes. As an example, consider the theoretical distribution of Figure 3 truncated at x=1 and at x=2, i.e., smaller values of x ignored. The resulting frequency distributions are shown in Figure 5 plotted in log probability coordinates. This type of biasing against small echoes would be expected in the case of radars suffering from moderate to severe attenuation in the presence of heavy intervening rainfall, and of radars with a large beam width. Figure 6 shows an example for GATE that shows both the upper and lower end truncation effects. The measurements were made from digital radar data obtained from the NOAA ship *Oceanographer* at 3-hourly intervals for the period 9-14 August and 1-6 September 1974.

5. SUMMARY

Some of the problems encountered in deriving echo population distributions have been discussed. In order to characterize accurately the populations, echoes should be tracked throughout their entire life cycles and their maximum development characteristics noted. This procedure is time consuming and some attempts have been made to obtain instantaneous (no tracking) echo statistics. The conversion of one type of distribution to the other has been discussed in this paper, and the mathermatical groundwork for a conversion scheme was developed. The major problem at this time is the need for information on the growth processes of clouds and their resulting echoes. Apart from the smallest sizes, echoes seem to grow by units or cells which appear and dissipate close to each other. The size and duration of an echo depend on the number of cells present simultaneously and the total number of cells growing and dying during the echo lifetime.

6. REFERENCES

Biondini, R., 1976: Cloud motion and rainfall statistics. J. Appl. Meteor., 15, 1100-1111.

Houze, R.A., Jr. and C.-P. Cheng, 1977: Radar characteristics of tropical convection observed during GATE: mean properties and trends over the summer season. Mon. Wea. Rev., 105, 964-980.

López, R.E., 1976: Radar characteristics of the cloud populations of tropical disturbances in the northwest Atlantic. Mon. Wea. Rev., 104, 268-283.

_______, 1977: The lognormal distribution and cumulus cloud populations. Mon. Wea. Rev., 105, 865-872.

_______, 1977b: Some properties of convective plume and fair-weather cumulus fields as measured by acoustic and lidar sounders. J. Appl. Meteor., 16, 861-865.

_______, 1978: Internal structure and development process of C-scale aggregates of cumulus clouds. Proc. 11th Tech. Conf. on Hurricanes and Tropical Met., 13-16 Dec. 1977, Miami, Florida.

Nasim, A.S., 1977: Study of the radar echo population of an eastern Atlantic tropical disturbance. M.S. Thesis, Dept. of Physics, University of Puerto Rico, June 1977, 67 pp.

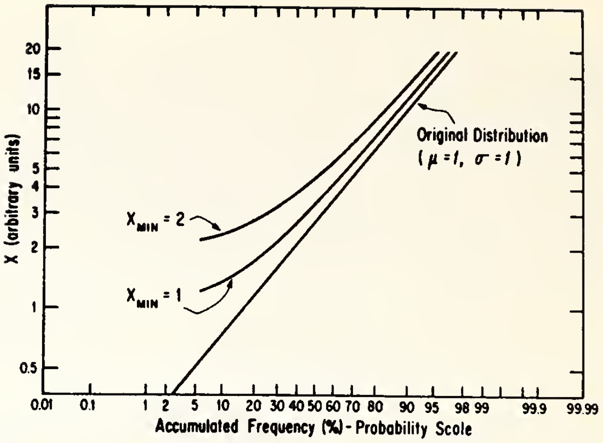

Figure 5. Same as Figure 4 except for truncation at the lower end.

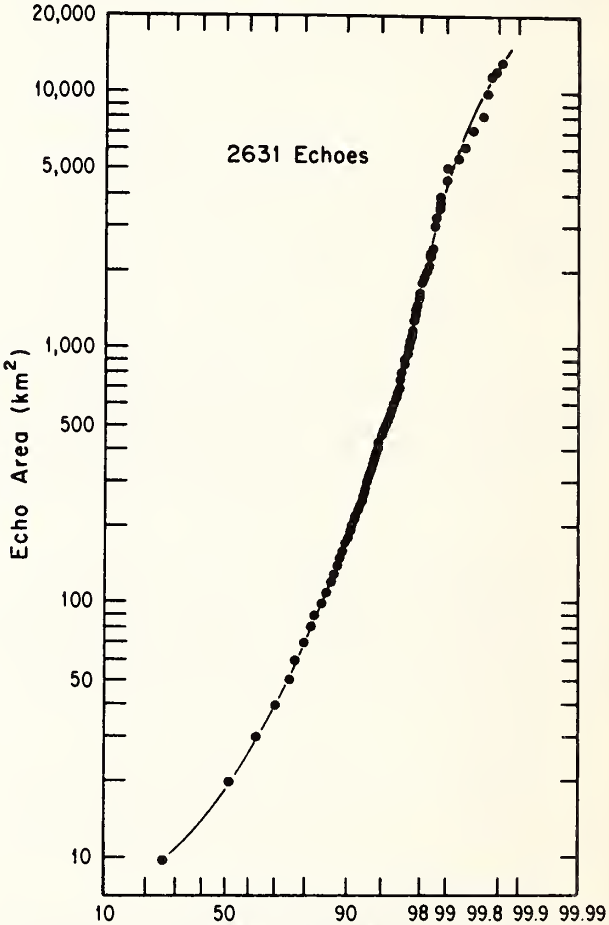

Figure 6. Frequency distribution of echo area in log probability coordinates. Data from the radar of the NOAA ship *Oceanographer* at 3-hour intervals during the period 9-14 August and 1-6 September 1974 in GATE.

American Society for Testing and Materials, ASTM-653:
159-182, 1978.

R. J. Serafin[1] *and R. Strauch*[2]

Meteorological Radar Signal Processing

REFERENCE: Serafin, R. J. and Strauch, R., "**Meteorological Radar Signal Processing,**" *Air Quality Meteorology and Atmospheric Ozone, ASTM STP 653,* A. L. Morris and R. C. Barras, Eds., American Society for Testing and Materials, 1978, pp. 159-182.

ABSTRACT: Modern meteorological Doppler radar has applications related to measurements of precipitation intensities and kinematics in convective storms, widespread stratiform precipitating systems, winter frontal and cyclonic storm systems, and other cloud systems. In addition, air velocities may be measured in the optically clear atmosphere from backscatter due to refractive index perturbations or from dispersed chaff tracers.

In order to derive the maximum scientific benefit from Doppler radar it is necessary to process vast quantities of data in real time at rates in excess of 1 MHz. Fortunately, current integrated circuit technology permits such processing. However, this ability to process data rapidly also produces data rapidly and results in large data sets which must be stored and processed further for outputs of maximum meteorological significance to be derived. Even when data compression ratios of 100:1 are achieved in real time, modern meteorological Doppler radar can produce 9-track, 732-m (2400-ft) tapes at the rate of two per hour.

This paper describes the chain of processing from real-time processing and acquisition, to displaying processed single and multiple Doppler radar data. The paper also describes briefly the meteorological significance of the work.

KEY WORDS: radar, radar meteorology, Doppler radar, FM-CW radar, multiple Doppler radars, coherent signal processing, ozone

Meteorological radar has proved to be among the most powerful tools available for observing remotely many atmospheric phenomena. The National Weather Service uses an extensive national network of weather radars for storm detection, tracking, and warning in its forecasting services to the public. Aircraft of all types are equipped with storm-avoidance radars, and atmospheric researchers rely heavily on radar for studies of convective storms, winter frontal and cyclonic storms, hurricanes, and other cloud systems. Sensitive radars can sometimes obtain useful measurements from the optically clear air when the refractive index variability, because of temperature and humidity gradients, is sufficiently great. Alternatively, reflecting chaff may be dispersed to increase the radar cross section in clear air.

---

[1] Manager, Field Observing Facility, National Center for Atmospheric Research, Boulder, Colo. 80302. The National Center for Atmospheric Research is sponsored by the National Science Foundation.

[2] Research electronic engineer, National Oceanic and Atmospheric Administration/Environmental Research Laboratories/Wave Propagation Laboratory, Boulder, Colo. 80302.

The advent of low-cost, high-speed digital integrated circuits has resulted in substantial advances in the field of radar meteorology. Special-purpose real-time digital processors and new processing algorithms have greatly improved quantitative measurements of radar observables. However, while offering the promise of unprecedented data quality, as well as high spatial and temporal resolution, these new processing methods have presented meteorologists with the formidable problems of storing and analyzing vast quantities of data.

Using a typical beam width of 1 deg and a pulse width of 1 μs (150 m), and assuming a maximum range of 150 km, the total number of resolution cells in a typical plan-position indicator (PPI) scan is 360 000. Modern meteorological radar will assign as many as three variables to each of these cells. Consequently, there are of the order of 10^6 8-bit words per scan which must be stored. A typical scan rate for research applications is 10 deg/s so that a PPI is completed in 36 s. It follows that the rate at which data are acquired is about 30 000 words per second, which will fill a 732-m (2400-ft) reel of 9-track, 1600-characters per inch tape in about 20 min.

Because of the great value of such observations in contributing to the understanding of the atmosphere in case studies, for the process of initializing numerical models, and for the comparison of conceptual models, many research groups throughout the world have undertaken the challenge of processing radar meteorological data. In this paper we will review some of the fundamentals of radar meteorology related to signal processing, discuss methods for processing signals in real time and after the fact, and present some examples of results obtained with single and multiple arrays of Doppler radars.

Signal Characteristics

Before proceeding with a discussion of real-time processing methods, it will be useful to describe the nature of the radar signals received from meteorological targets. In doing so we will treat the general situation, in which both the amplitude and the phase of received signals are measured. As we shall see, it is the time rate of change of phase which is related to the Doppler velocity. Thus Doppler radars are often referred to as coherent or phase-coherent radars. Incoherent radars measure only the intensity of the received signals and thus may be viewed as restricted versions of the more general Doppler radar.

Distributed Targets

The problem facing the radar meteorologist is that of determining the important parameters of the backscattered energy from the targets that are distributed within the volume sampled by the radar. This sample volume, approximately cylindrical in shape, is defined by the antenna beam widths in elevation and azimuth and by the pulse width; typically these are of the order of 1 deg and 1 μs. The corresponding spatial resolution orthogonal to the beam axis is given by $r\theta$ where θ is the beam width and r is the target range. Along the beam axis the resolution is $c\tau_0/2$ where c is the velocity of light and τ_0 is the pulse width.

Meteorological targets (ice crystals, snow flakes, raindrops, or hailstones) will generally fill the sample volume. This volume is interrogated by a transmitted signal at frequency ω_0, of the form

$$s(t) = A \cos \omega_0 t$$

Each of the hydrometeors in the sample volume scatters back a signal of the form

$$s_i(t) = a_i \cos (\omega_0 t - \phi_i)$$

where a_i is the amplitude and ϕ_i the phase. In general ϕ_i is given by

$$\phi_i = \frac{4\pi r_i}{\lambda_0}$$

where r_i is the range to the ith hydrometeor and λ_0 is the wavelength. The composite signal, s_r, from all targets within the sample volume is thus given by a summation over the sample volume

$$s_r(t) = \sum_V a_i \cos (\omega_0 t - \phi_i)$$

It is convenient to represent the signal in its analytic form

$$x_r(t) = e^{j\omega_0 t} \sum_V a_i e^{-j\phi_i}$$

Ignoring the carrier frequency term, the complex modulation can be graphically illustrated in the complex plane. The terms contributing to x_r will have varying amplitudes, a_i, dependent upon their sizes and varying phases, ϕ_i, because of their positions. Furthermore, because the dimensions of the sample volume are much greater than λ_0, we can expect all values of ϕ_i to be on the interval $(0,2\pi)$. Figure 1 illustrates a number of vectors with random amplitudes and phases adding up to the resultant vector with amplitude A_r and phase ϕ_r. This situation may be viewed as a two-dimensional random-walk problem. Since the number of component vectors is very large, the central limit theorem may be applied to establish that the statistics of ϕ_r will be uniform on the interval $(0,2\pi)$ and A_r will be governed by the Rayleigh probability density function. It follows that the functions $A_r \cos \phi_r$ or $A_r \sin \phi_r$ exhibit first-order Gaussian statistics [*1*].[3] The product $A_r e^{j\phi_r}$ is referred to as the complex envelope of the signal.

The Doppler Spectrum

If the particles within the sampled volume were stationary in relation to the radar, there would be no fluctuation of the complex envelope. However, these particles are in motion in relation to the radar and in relation to one another. Factors contributing to their motion include the mean wind, small-scale turbulence,[4] wind shear, and the varying fall speeds of the particles. The Doppler frequency shift caused by each particle is simply the time derivative of the instantaneous phase, that is, ω_i; the instantaneous Doppler frequency of the signal received from the ith scatter is

$$\omega_i \equiv -\dot{\phi}_i = \frac{-4\pi \dot{r}_i}{\lambda_0} = \left(-2\pi \frac{2v_i}{\lambda_0}\right)$$

where v_i is the projection of the particle's vector velocity along the beam axis (the radial velocity component).

Because the number of contributing particles within the sample volume is quite large (on the order of 10^6 or greater), the distribution of velocities within the volume is essentially continuous and is dictated by the parameters mentioned earlier. Thus the received signal is not monochromatic but exhibits a distribution of received power with frequency, namely, a unique power spectral density determined by the kinematics of the processes within the sample volume.

The received signal, x_r, is

$$x_r(t) = A_r(t)e^{j\phi_r(t)}$$

$x_r(t)$ is a complex random function of time which can only be described

---

[3] The italic numbers in brackets refer to the list of references appended to this paper.

[4] Small-scale turbulence refers to turbulence with scales on the order of the dimensions of the sample volume and smaller. A detailed discussion of pulse volume filtering is given by Srivastava and Atlas [*2*].

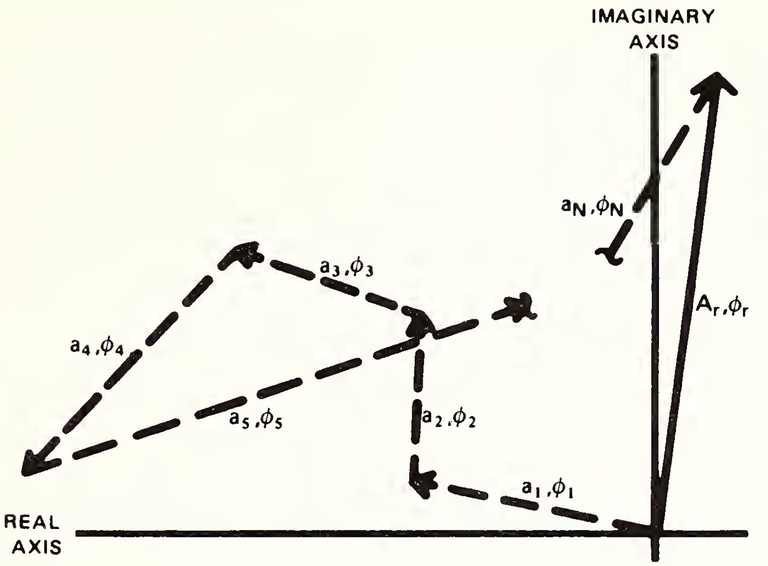

FIG. 1—*Received signal representation in the complex plane. See text for explanation.*

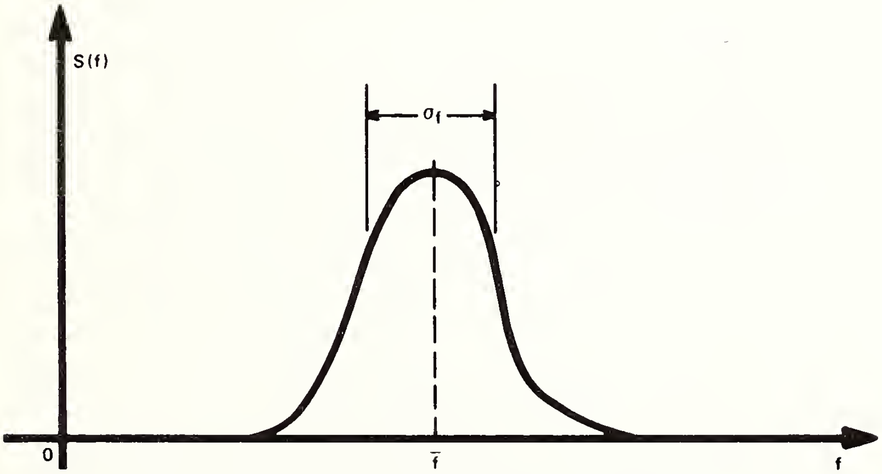

FIG. 2—*The Doppler spectrum. See text for explanation.*

statistically. Its important parameters are the average intensity, the power spectral density and its moments, and the autocorrelation function, all of which are related.

The average signal intensity is given by

$$P_r = \overline{|x_r^2|} = \overline{A_r^2}$$

where the overbar represents a time average. If the process is statistically stationary during the measurement interval, then the time averages can be replaced by statistical averages, and, indeed, analyses of the characteristics of radar meteorological signals usually assume that they are stationary.

The complex autocorrelation function, $R(\tau)$, is given by

$$R(\tau) \equiv \overline{x_r(t)\, x_r^*(t + \tau)}$$

where * denotes the complex conjugate. The power spectral density is simply the Fourier transform of the autocorrelation function and is given by

$$S(f) = \int_{-\infty}^{+\infty} R(\tau) e^{j2\pi f\tau}\, d\tau$$

It can readily be shown that

$$P_r = \int_{-\infty}^{+\infty} S(f)\, df = R(0)$$

Moments of the Doppler Spectrum

It should be clear that if either $S(f)$ or $R(\tau)$ is known, all of the relevant signal parameters can be determined. The mean frequency and variance of the spectrum are defined by

$$\bar{f} \equiv \frac{\int f S(f)\, df}{\int S(f)\, df}$$

$$\sigma_f^2 \equiv \frac{\int (f - \bar{f})^2 S(f)\, df}{\int S(f)\, df}$$

Figure 2 is a diagram of the Doppler spectrum and its first and second moments. The mean frequency is interpreted as the average velocity of the particles along the beam, and σ_f, the spread of the spectrum, is a measure of the spread of the velocities of the particles observed. Clearly, these expressions show that the normalized version of $S(f)$ is interpreted as a probability density function for the distribution of frequencies (or velocities) within the sample volume.

Interpretation of Radar Data

Before proceeding further with a discussion of how these parameters are obtained from the raw radar data, we must comment briefly on their significance.

It can be shown [*3*] that the energy scattered back from spherical hydrometeors is proportional to the sixth power of the particle diameter, provided that the radar wavelength, λ_0, is larger than about ten particle diameters. In this case the received power is proportional to Z, the reflectivity factor, which is defined as

$$Z \equiv \frac{1}{V} \sum_{V} D^6$$

$$dBZ = 10 \log_{10} Z$$

where Z conventionally has units of mm^6/m^3. Operational weather radars routinely convert Z values to rain rates for hydrological studies and for flood forecasting.

In the preceding discussion, we have described the Doppler spectrum and its moments in terms of the Doppler frequency shift. However, since the target velocity, v, and the Doppler frequency, f, are related by the linear expression

$$f = \frac{2v}{\lambda_0}$$

it is a simple matter to convert from one to the other. Doppler radars measure only that component of particle velocity which is along the radar beam, that is, the projection of the three-dimensional particle velocity onto the radar beam vector. Lhermitte and Atlas [*4*] first showed how a single Doppler radar could be used to measure the mean winds aloft in stratiform precipitation. Later work, as illustrated well by Browning and Wexler [*5*], has demonstrated how single Doppler radars may be used to measure convergence and deformation of the wind field as well. In the vertically pointing mode, Doppler radars have been used successfully to measure the particle size distribution [*6, 7*]. With the development of improved Doppler processing and display techniques, Donaldson [*8*] illustrated the potential for locating the tornado-spawning mesocyclonic rotations in severe storms.

Finally, among the most exciting Doppler radar applications has been the extension of the technique to include multiple Doppler arrays for measurements of three-dimensional air motion. Lhermitte [*9*] and Lhermitte and Miller [*10*] pioneered this work, showing how two Doppler radars may be used to obtain the vector motion fields. In 1975, the first triple Doppler radar experiment took place, thus promising the least ambiguous measurements of air motion in thunderstorms made up to that time [*11*].

Real-Time Processing, Recording, and Display

Phase Detection

Coherent phase detection enables us to obtain two orthogonal signals which are identical to the real and imaginary parts of the complex modulation. This is done by demodulating the received signal in two phase detectors whose references are separated by $\pi/2$ rad. The phase detector outputs are referred to as the in-phase and quadrature (real and imaginary) components, which yield the received signal,

$$\begin{aligned} x_r(t) &= A_r(t)\,[\cos \phi_r(t) + j \sin \phi_r(t)] \\ &= A_r(t) e^{j\phi_r(t)} \end{aligned}$$

Thus, the complex modulation discussed earlier is not just a convenient method for analysis but an exact representation of the signals with which we deal. As a practical matter, the complex representation is necessary if we are to differentiate between positive and negative Doppler velocities.

Sampling and the Demultiplexing Problem

With the conventional pulsed Doppler radar, the transmitted signal is in the form of a train of coherent pulses, each with a duration on the order of 1 μs, that are repeated at a pulse repetition frequency (PRF) on the order of 1000/s. For each microsecond within the millisecond PRF interval, T_0, we may receive information from an independent region in space. If we wish to obtain information about each of these sample volumes they must be treated independently. This requires that the received signal samples be demultiplexed. Consider the diagram shown in Fig. 3. At time zero, a pulse is transmitted, and immediately we begin to receive a signal, which is sampled once every microsecond. The first sample is x_{00}, the next x_{01}, and so forth until we have received energy from the farthest unambiguous range, Mμs removed from the radar.

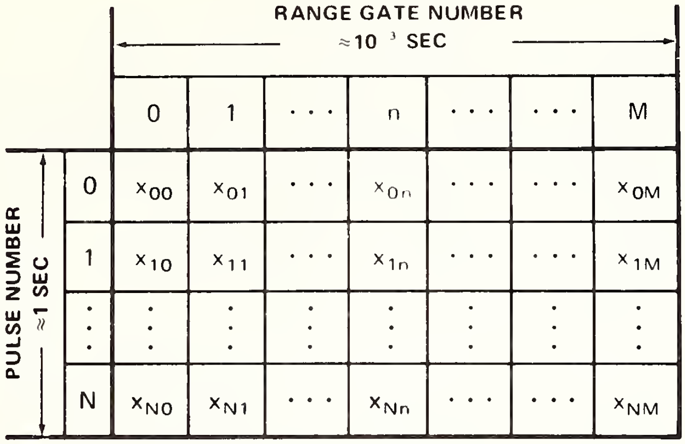

	0	1	· · ·	n	· · ·	· · ·	M
0	x_{00}	x_{01}	· · ·	x_{0n}	· · ·	· · ·	x_{0M}
1	x_{10}	x_{11}	· · ·	x_{1n}	· · ·	· · ·	x_{1M}
⋮	⋮	⋮	⋮	⋮	⋮	⋮	⋮
N	x_{N0}	x_{N1}	· · ·	x_{Nn}	· · ·	· · ·	x_{NM}

FIG. 3—*Acquisition of multiplexed signal samples. See text for explanation.*

At this point a second pulse is transmitted, and so forth. Thus the data matrix is filled by filling rows in sequence from the zeroth row down through the Nth row. However, if we want to determine the characteristics of targets at a given range, say in the nth range gate, we must process the signals in the nth column: that is, the signals are collected by rows but must be processed by columns. If we simply choose to store the entire matrix in a digital memory, then $N \times M$ complex storage locations must be provided. This quantity may be as large as 10^6 memory locations, since averaging times on the order of 0.5 to 1 s are desired in many applications.

A second important consideration is that of sampling. Clearly, with the pulsed radar we do not receive a continuous signal, $x(t)$, from a given range but, instead, receive samples, x_{kn}, of the complex signal separated by the PRF interval. The Nyquist frequency is then PRF/2, and, because we have both the real and imaginary parts of the received signal, the unambiguous Doppler frequency range of the radar is found to be on the interval $-\text{PRF}/2 < f_d < +\text{PRF}/2$ where f_d is the Doppler frequency.

Real-Time Signal Intensity Estimation

The signal intensity, P_n, is proportional to the target reflectivity factor, Z, which in turn is related to the number and sizes of precipitation particles within the sample volume. Sirmans and Doviak [*12*] provide a comprehensive treatment of the subject, discussing and comparing a number of algorithms for estimating P_n. We will confine ourselves to simple block averaging of the intensity variables; that is, we form the sum

$$\hat{P}_n \equiv \frac{1}{N} \sum_{k=0}^{N-1} |x_{kn}|^2$$

where the circumflex represents an estimate of P_n. It is important to note that for any finite number of samples, N, or, equivalently in an integration time, $T = N/\mathrm{PRF} = NT_0$, it will not be possible to determine P_n exactly, but by extending T we can reduce the variance of $\hat{P}_n$. It is well known that the average value and variance of $\hat{P}_n$ are given by

$$E(\hat{P}_n) = P_n$$

$$\mathrm{var}\,(\hat{P}_n) = E[(\hat{P}_n - P_n)]^2 \simeq \frac{P_n^2}{\sigma_n T}$$

where E ( ) is the expected value and var ( ) is the variance. The variance of one of the $|x_{kn}|^2$ is P_n^2; thus we note that the variance of the sample mean, $\hat{P}_n$, is reduced inversely by the number of degrees of freedom, $\sigma_n T$, of the signal being observed.

Because the estimate, $\hat{P}_n$, is simply the sum of N quantities, the total sequence, $x_{kn}(0 < k < N - 1)$, needs to be stored only as a series of partial sums. We may, if the digital arithmetic is fast enough, simply add each of the $|x_{kn}|^2$ in an accumulator and provide an accumulator for each range gate. The storage requirement has thus been reduced from $N \times M$ to simply M, and, since N may be on the order of 10^3, savings on that order are realized in size, cost, and complexity of equipment. The common method for performing the arithmetic is shown in Fig. 4. The signal intensity, $|x_{i+1}(t)|^2$, from the $i + 1$th pulse is applied to an analog-to-digital (A/D) converter. A synchronous clock triggered from the $i + 1$th transmitted pulse generates a pulse for each range gate, n, and the converter then generates the digital word proportional to $|x_{i+1,n}|^2$, that is, the $i + 1$th sample from the nth range gate. The partial sums are stored in a recirculating shift register which is M locations long. The shift register is clocked synchronously and makes one complete recirculation during each interpulse period, T_0. The previous partial sum and the current sample are added and stored until all N samples have been accumulated. The estimates may then be displayed and stored on digital tape. The A/D converter must operate at the rate $1/MT_0$, which is of the order of 10^6/s, but the rate will increase as the radar resolution increases. Similarly, the adder and shift register must be capable of operation at these speeds. We feel that it is now possible to process the intensity data at rates of 5×10^6/s, thus obtaining 30-m resolution along the beam, provided that the radar is capable of transmitting a 0.2-μs pulse.

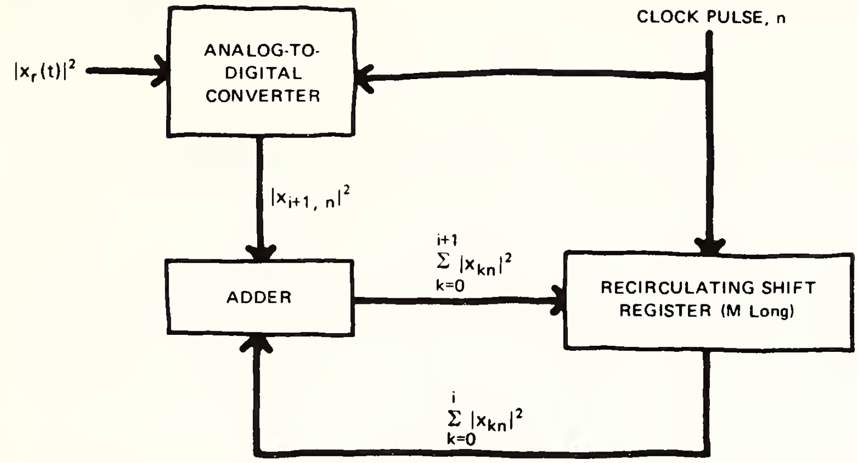
CLOCK PULSE, n
$|x_r(t)|^2$
ANALOG-TO-DIGITAL CONVERTER
$|x_{i+1,n}|^2$
$\sum_{k=0}^{i+1} |x_{kn}|^2$
ADDER
RECIRCULATING SHIFT REGISTER (M Long)
$\sum_{k=0}^{i} |x_{kn}|^2$

FIG. 4—*Digital integrator for signal intensity estimation. See text for explanation.*

In practice, it is difficult to build receivers with a sufficiently wide dynamic range to handle adequately the range of magnitudes of P_n that one might expect from atmospheric targets. Even with range-squared normalization, P_n may vary over a range of 70 dB (10^7), and such a range is likely to saturate a sensitive linear receiver. Thus we usually use receivers with logarithmic characteristics for intensity measurements, and we average log ($|x_{kn}|^2$). When this is done, the estimates are biased and the statistics change [*12*], but the effects are known, and the advantage of wide dynamic range justifies the use of the log receiver.

Real-Time Mean Velocity Estimation

Earlier in this discussion we have described the Doppler parameters in terms of the Doppler spectrum. It is clear then, that one method of obtaining the first and second moments of the spectrum is to Fourier analyze the complex time series in each of the 1000 or so range gates and to compute the moments in a straightforward fashion. However, this method requires very large digital storage capacity and generally high cost. Instead, the most commonly employed technique is to work with the complex autocorrelation function as first described by Rummler [*13*]. Lhermitte [*14*] was the first to implement this technique for meteorological use.

Successive pairs of the complex signal samples are used to estimate the complex autocorrelation function, $R_n(T_0)$, through the simple algorithm

$$\hat{R}_n(T_0) = \frac{1}{N} \sum_{k=0}^{N-1} x_{k+1,n} x^*_{kn}$$

The expected value of $\hat{R}_n(T_0)$ is $R_n(T_0)$, which, when the spectrum is symmetrical, is of the form

$$R_n(T_0) = P_n \rho(T_0)$$

where $\rho(T_0)$ is the correlation coefficient.

Thus the mean frequency is determined from the expression

$$\bar{f}_n = \frac{1}{j2\pi T_0} \operatorname{Arg}\,[R_n(T_0)]$$

When the spectra are asymmetrical the estimator is biased, but the bias is generally small and can be tolerated. Because the method operates on successive pulse pairs of the received signal, it has been commonly referred to as the pulse-pair processing technique.

Note that the storage requirements are approximately $1/N$ of what is required to store the time series, because, again, we are storing partial sums. Moreover, the number of complex multiplications per range gate is N, while with a Fast Fourier Transform algorithm, $N \log_2 N$ would be required.

Recording

In estimating both the intensity and the mean velocity, each N complex samples result in just two derived variables. Thus the data rate has been reduced by a factor of $N/2$. With $N = 128$ and an input bandwidth of 1 MHz, the output data rate is 18 kHz, which can be easily recorded on nine-track magnetic tape. A third variable would increase the recording rate to 27 kHz, which is still easily recorded.

In many *post facto* analyses, complete examination of the Doppler spectrum is mandatory. This is true when bimodal spectra exist, due, for example, to strong wind shear. The complete Doppler spectrum is also of interest in studies of turbulence, and, when pointing vertically, the complete spectrum permits one to deduce the particle size distributions and to separate hail from rain. In these cases, there are essentially two practical alternatives. The first is to digitize and record the raw coherent data in a number of range gates limited by the recording rates of the recorder available. The use of a nine-track, 1600 characters per inch, 45 in./s recorder will limit the recording to about 5 percent of the raw video data rate.

When the complete signal must be recorded, video tape presents a reasonable solution [*15*]. The coherent video signals can be recorded on a video tape recorder and later digitized in the laboratory and analyzed with a general purpose computer. While this method is time consuming, and the data suffer somewhat in quality because of the video tape recorder, a recording of the complete raw data set is achieved, thus ensuring that all possible characteristics of the meteorological event can be eventually examined.

Displays

Because of the very large quantities of data involved, any effective real-time examination of radar meteorological data requires that they be displayed pictorially. The earliest types of radar displays simply used analog data to modulate the brightness of a cathode ray tube. The data were normally shown in plan view (the plan-position indicator (PPI)) or as vertical cross sections (the range-height indicator (RHI)). Even with the addition of grey-scale encoding or with contours provided, displays of reflectivity data were only marginally acceptable because of their semi-quantitative nature. Displays of Doppler velocity data that use grey-scale coding are difficult to interpret.

These problems have been solved through the use of real-time color displays [*16*]. Through the use of a digital memory and a color television monitor, it has been possible to produce high-resolution images of radar data in a television format, and, by adding the dimension of color, such displays have demonstrated that 16 or more levels of coding can be easily distinguished in real time. Thus it has been possible for meteorologists to measure accurately the intensity of high-reflectivity cores in thunderstorms and to locate regions of vorticity and turbulence. In stratiform rain, it is a simple matter to measure wind profiles, identify precipitation maxima, and accurately locate the melting level. Such data are extremely important in research applications where the scientist must decide how many of his resources, for example, aircraft, rawinsondes, and people, should be devoted to observing a particular storm system and where within that system their energies should be focused.

Ultra-Sensitive High-Resolution Radar

Up to this point we have confined the discussion to pulsed radar, wherein high-range resolution is obtained by virtue of a short transmitted pulse or, equivalently, a large transmitted bandwidth. Another method for achieving a wide bandwidth is to transmit a frequency modulated wave. Such frequency-modulated-continuous-wave (FM-CW) radars have proven to be extremely valuable tools for probing the clear boundary layer with a range resolution on the order of a few meters [*17*].

The FM-CW radar transmits (continuously from one antenna) a linearly swept frequency signal as shown by the solid line in Fig. 5. The back-scattered power is received with a second antenna, and the received signal from a single-point target is illustrated by the dashed line. The frequency

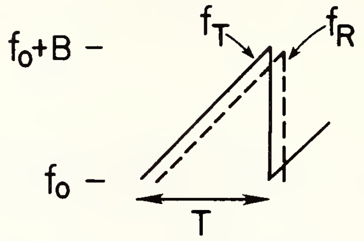

FIG. 5—*Linear frequency modulation for an FM-CW radar.* f_T *is the transmitted frequency,* f_R *is the received frequency, and* B *is the transmitted bandwidth.* f_o *is the transmitted frequency at the start of the sweep and* T *is the duration of the sweep.*

at the detector output is the difference between the transmitting frequency and the frequency that was transmitted some time earlier and which has been scattered back to the receiving antenna.

The bandwidth of the transmitted rf signal can be as high as 200 MHz, while the signals that appear at the mixer output are in the audio range. The large rf bandwidth is required for good range resolution, and the low frequency of the mixer output allows real-time spectral processing. The signal processing scheme that is used depends on whether range information alone is desired or whether both range and velocity are needed.

Signal Processing for Range Information

In contrast to a pulsed radar which determines target range by the time delay between the transmitted pulse and the received signal, the FM-CW radar determines target range by the frequency of the signal at the mixer output. The signal frequency is $f_s = |f_T - f_R|$, and appears at the mixer output for $(T - \tau)$s during each sweep (see Fig. 5) where τ is the round trip propagation time to the target.

The signal frequency for a single-point target depends on the target range and the target velocity. The significant terms in the expression for signal frequency are [*18*].

$$f_s \doteq \frac{2B}{cT} R + f_d$$

where B is the transmitted bandwidth, T is the duration of the sweep, and R is the range. The Doppler shift, f_d, can be neglected except for very short-range targets, and the signal frequency can be taken as a measure of range. Thus, signal processing for range information involves measurement of the power spectrum of the signal obtained during *each* frequency sweep and averaging of the power spectra from successive sweeps. Spectral index points are labeled as range (or height).

The FM-CW radar usually operates in a zenith-pointing mode, and its output is a time-height picture of the reflectivity structure over the radar. The important point in the data processing, when only range information is desired, is that the power spectrum be computed after *each* sweep. It is not possible to separate range and velocity contributions to the signal frequency if the signal is analyzed for each sweep.

Signal Processing for Range and Velocity Information

The technique used to measure both range and velocity with an FM-CW Doppler radar involves spectral analysis of the signal obtained during a large number of consecutive sweeps rather than from a single sweep as for the conventional FM-CW radar. The entire Doppler velocity spectrum can be measured. The frequency of the signal during each sweep depends on both range and velocity, but the phase of the signal changes from sweep to sweep only if the target is moving. It is this phase change that enables the Doppler spectrum to be measured, just as occurs with the coherent pulse Doppler radar described earlier. A complete description of the theory is given by Strauch [*18*], but a simple explanation is available from a consideration of the voltage waveform of the signal at the output of the mixer.

If the FM-CW radar observes a stationary target, the output of the mixer is identical for every sweep. Whereas the signal from a single-point target yields a $[(\sin x/x)]^2$ power spectrum if only one sweep is analyzed, elementary Fourier series analysis shows that the power spectrum of the signal from repetitive sweeps must be discrete, with power only at frequencies that are harmonics of $1/T$. If the target is moving, the phase of the signal changes from sweep to sweep, and the rate of phase change is the Doppler frequency. The power spectrum of the moving target is therefore the same as that of a stationary target but translated by the Doppler shift. The power spectral density plot is therefore a range and velocity map, with ground clutter appearing at harmonics of $1/T$ and moving targets at other frequencies, as illustrated in Fig. 6.

Range resolution (ΔR), velocity resolution (ΔV), unambiguous range (R_m), and unambiguous velocity (V_m) are the same as those of a pulse Doppler radar whose pulse width is the reciprocal of the FM-CW radar bandwidth and whose pulse repetition interval is the same as the sweep repetition interval of the FM-CW radar. These are

$$\Delta R = c/2B$$

$$\Delta V = \lambda/2NT$$

$$R_m = cT/2$$
$$V_m = \pm\lambda/4T$$

where N is the total number of sweeps (or pulses) used in the data processing.

Post Processing

Processing on a General Purpose Computer

After the data are collected and recorded in the field, the meteorologist is faced with the challenging tasks of editing, selecting situations of specific meteorological interest, and analyzing the data. In order to facilitate these tasks, it is often necessary to add housekeeping data to the data collected in the field and to provide an archive data tape suitable for automatic processing on a general purpose computer. It is also useful to generate a printed archive catalog that summarizes the data collected. Such a catalog will list dates, time of day, type of antenna scan, elevation angle during a PPI scan, azimuth angle during an RHI scan, and the times associated with the beginning and end of a scan and assign sequential numbers to scans, etc.

The next problem relates to analysis. How are the data to be examined? Again, pictures of observed variables or derived variables are of paramount importance. Figure 7 is an example of a contoured PPI display generated on a general purpose computer. While it is a relatively simple matter to make displays from the data as they have been scanned (for example, a PPI display from data acquired in the PPI scan mode), a much more formidable problem, which might be referred to as spatial demultiplexing, exists. Radar data are normally recorded on tape in sequential fashion as they are collected, range gate by range gate and then beam width by beam width. Consequently, they are most readily available in the same sequence. The coordinate system in which they are acquired is spherical (range, azimuth, elevation), resulting in scanned surfaces with undesirable shapes. For example, the conventional PPI display actually represents the projection, onto a flat surface, of data collected from a conical surface. Sequences of such conical scans separated by selected elevation angles are used to make volume scans. While the PPI is an extremely useful tool for real-time use or for taking a quick look at radar data, optimum analysis requires that data be examined on a variety of surfaces, principally horizontal and vertical planes, in order to determine best the three-dimensional structure of the meteorological event. Thus there is a need for three-dimensional coordinate conversion of the data. While, in principle, this can be easily accomplished, the task requires large computers if it is to

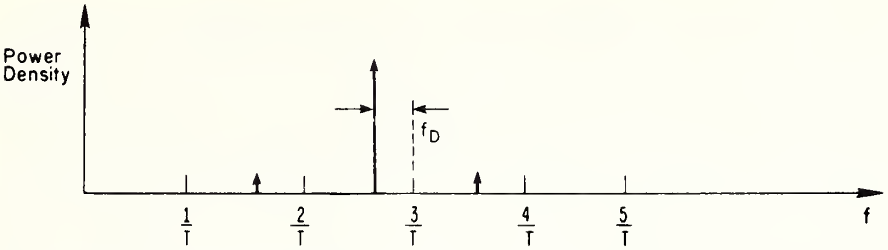

FIG. 6—*Power spectrum of the output signal of an FM-CW Doppler radar.* T *is the duration of the sweep.* f_d *is the Doppler shift, and* f *is frequency.*

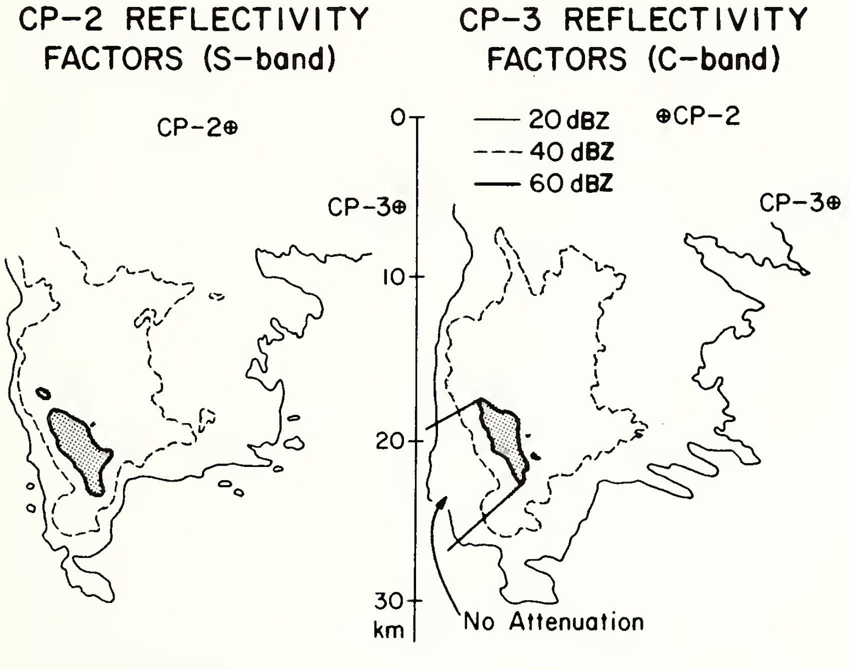
CP-2 REFLECTIVITY FACTORS (S-band)
CP-3 REFLECTIVITY FACTORS (C-band)
CP-2⊕
CP-3⊕
0
10
20
30
km
20 dBZ
40 dBZ
60 dBZ
⊕CP-2
CP-3⊕
No Attenuation

FIG. 7—*Contoured reflectivity factors in PPI mode. The contours represent* Z *values measured in a severe hailstorm in northeast Colorado where the hail fell from the high reflectivity (60 dBZ) core. This storm was scanned by two National Center for Atmospheric Research radars, the CP-2, and S-band (10-cm wavelength), and the CP-3, a C-band (5-cm wavelength) system. The two radars are located as shown. The data have been provided through the courtesy of the National Hail Research Experiment, Convective Storms Division, National Center for Atmospheric Research, Boulder, Colorado.*

be done efficiently. Again, the principal problem is that of memory and access.

Consider a typical volume of a convective storm composed of perhaps 20 conical sector scans. If we assume that each conical scan contains 10^5

data words, we see that storage of the data will require two million locations with high-speed access. Let us further assume that this storm occupies a region some 30 km by 30 km in areal cross section and is 15 km high and we wish to transform the data onto a three-dimensional rectangular grid with grid spacing of 500 m. The total number of grid points is thus 108 000. The problem has now been reduced to one of assigning to each grid point a value obtained from an objective analysis of the original stored data set. Such volume scans are typically completed in 3 min in real time, and it may be necessary to analyze between 10 and 50 such scans for each storm. The problems associated with processing single radar data are magnified when multiple Doppler radars are involved. With three Doppler radars, the data from each of the radars must be spatially interpolated (filtered) to one of the rectilinear grid points. The three measured Doppler velocities are then transformed, using a matrix inversion, into three orthogonal velocity components, v_x, v_y, and v_z. It is at this point that effective analysis of the data can begin.

It is fair to say that the post-processing of single radar data on the surfaces scanned is well in hand. However, the problems related to coordinate conversions, three-dimensional objective interpolation, and multiple Doppler radar vector winds have taxed the capabilities of the largest computers. Much remains to be done in this field, both in objective treatment of the data sets and in analysis of the final products.

Interactive Systems

An alternative to the general purpose computer lies in smaller, more specialized systems which permit a great deal of scientist interaction. Such a system could consist of a minicomputer for control, large disk storage, a large random access memory, various peripheral arithmetic hardware, displays, and video and film recording. To date, such a system has not been fully developed for radar use, although both the University of Miami and the National Center for Atmospheric Research are working on prototypes at this time. We feel that such systems may ultimately relieve large computers from much of the data processing burden associated with meteorological radar. More importantly, however, because of the interactive feature, scientists should be able to alter data sets to meet their specific needs, which would thus result in efficiency and improved understanding of the meteorological processes under study.

Radar Probing of the Cloud-Free Atmosphere

Radar observations in the optically clear air have applications to measurements of boundary layer turbulence, diffusion, and transport processes, which are extremely important in air pollution studies. Hardy

[*19*] reviews the clear-air radar observations made with incoherent radars. High-resolution FM-CW radars show that the clear-air radar scattering is usually from layers, as shown in Fig. 8.

Recently there have been a number of Doppler radar observations of clear-air radar signals. The primary motivation for this work has been the measurement of wind profiles and turbulence and the study of the clear-air scattering layers. Three types of radars have been used: (*a*) microwave high-power coherent pulsed Doppler radars, (*b*) very high frequency (VHF) pulsed Doppler radars, and (*c*) FM-CW Doppler radar.

Pulse Doppler radar measurements of clear air turbulence were reported by Starr and Browning [*20*]. Hennington et al [*21*] measured clear air wind profiles with a 10-cm pulsed Doppler radar. The wind profiles were measured by measuring the mean radial velocity for a number of adjacent range intervals at several azimuth angles. The radar-measured winds showed excellent agreement with rawinsonde data.

Green et al [*22*] report measurements of winds in the troposphere using VHF (7.41-m wavelength) pulsed Doppler radar at a Colorado mountain site. This radar uses a large coaxial-cable phased antenna array that can be pointed off-zenith to measure horizontal winds. Layered reflectivity structure is not evident in their data, but they used long pulse lengths (1-km range resolution) so that it would be difficult to determine whether the radar returns were from thin layers. They report wind profile measurements to 10-km altitude, and comparisons with rawinsonde data showed good agreement.

FM-CW Doppler radar measurements of boundary layer winds are reported by Chadwick et al [*23*]. The FM-CW Doppler radar, because it is able to detect weak moving echoes in the presence of strong ground clutter, can measure the wind at all altitudes in the boundary layer. The typical height resolution of wind profiles is 25 m.

Doppler Radar Measurements Using Artificial Radar Targets

The wind field in the boundary layer has been studied, using artificial radar targets (chaff) to provide the radar echo. The chaff can be dispensed from aircraft as point or line sources that are diffused by atmospheric turbulence. A point source of chaff needles can diffuse to fill 1 km^3 in about 15 min in the convective boundary layer. However, in the still atmosphere, the chaff will rapidly settle to the ground with little diffusion. The chaff needles fall with random orientation and can be observed with radar that is horizontally or vertically polarized.

Frisch and Clifford [*24*] used chaff targets to measure the eddy dissipation rate, the rate at which turbulent kinetic energy is dissipated in the atmosphere through molecular viscosity. They measured the width of the velocity spectrum to obtain a measurement of the turbulent motions in

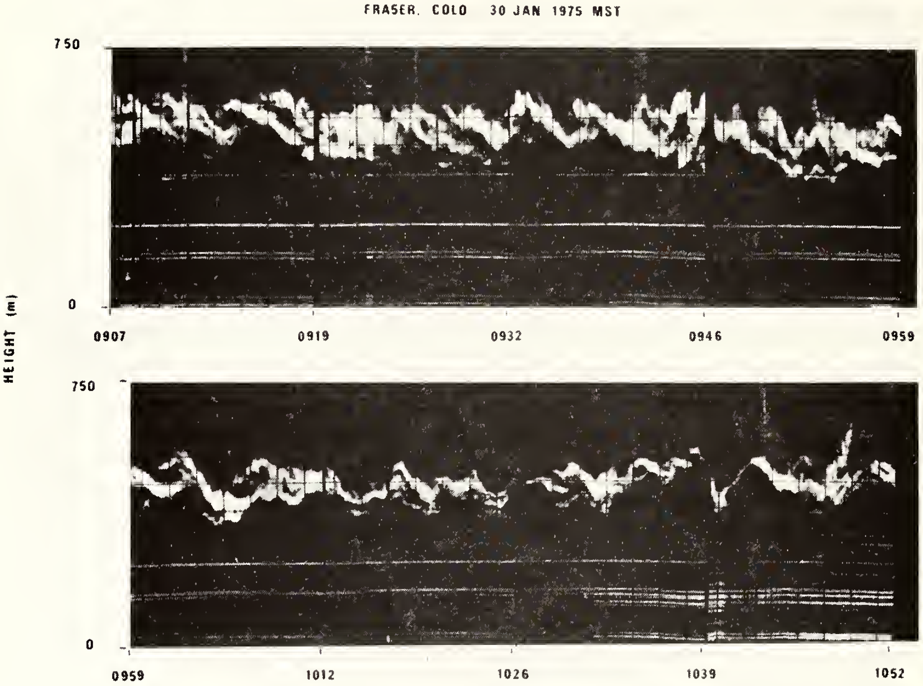

FIG. 8—*Radar signals from the optically clear air, as observed with an FM-CW radar. MST is Mountain Standard Time.*

the atmosphere on scale sizes less than the pulse volume. Then, assuming isotropic turbulence, they related the measured Doppler spectral width to the eddy dissipation rate. Comparisons made with *in situ* instruments on a nearby tower showed excellent agreement with their radar results.

Kropfli and Kohn [*25,26*] used chaff dispensers on a small aircraft to fill the depth of the boundary layer over an area of about 300 km^2 near St. Louis during the 1975 METROMEX project. They observed the chaff motion throughout the boundary layer with dual-Doppler radars, and the data were analyzed to obtain three-dimensional wind fields. By averaging the measured wind fields obtained from several radar scans of the entire volume, they were able to separate those features of the flow field that persisted at fixed locations from those features that moved with the mean wind. Figure 9 shows the wind field at 300-m altitude, after removing the mean wind. A 12-km-long line of convergence is evident. About 3 km northwest of this line is a line of divergence. At the top of the boundary layer the eddy flow is reversed; the line of low-level convergence is a line of divergence at a 1300-m altitude, and the line of low-level divergence becomes an area of convergence at the top of the boundary layer. Kropfli

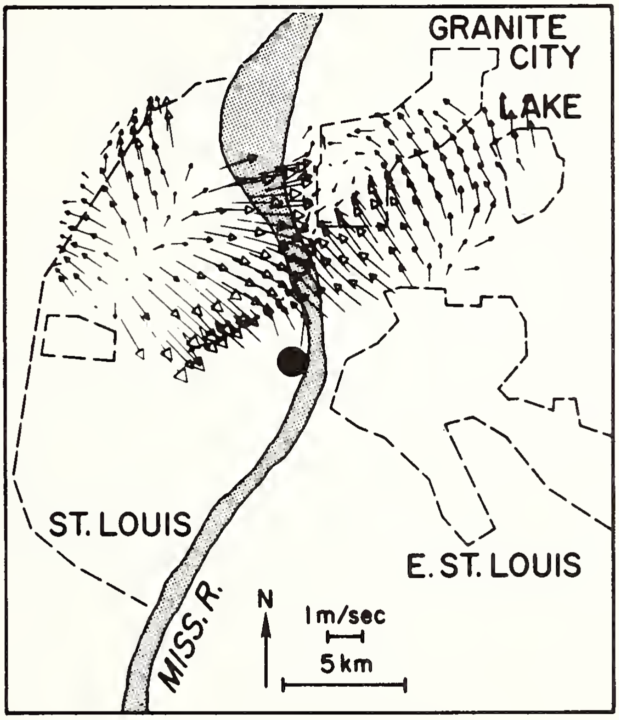

FIG. 9—*Horizontal wind field over St. Louis at 0.3 km altitude as revealed by dual-Doppler radar, measured during the 1975 METROMEX project. The mean wind has been removed.*

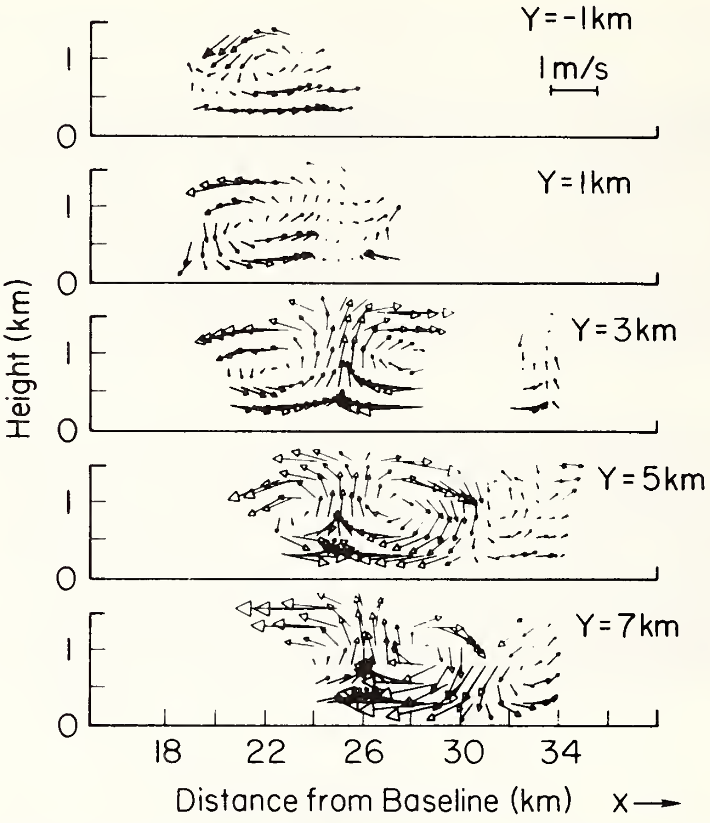

FIG. 10—*Vertical cross sections of the eddy wind field over St. Louis measured during the 1975 METROMEX project. The planes shown are parallel to the mean flow.*

and Kohn show that a thermal ridge of 0.2°C in the temperature field coincided with the low-level convergence. Figure 10 shows the wind field in the vertical planes parallel to the mean flow. The persistent circulation over the city is clearly shown by the radars.

Although clear-air radar work has thus far been confined to research, the potential capability for operational applications has been demonstrated. Whether or not operational use is made of this radar capability will depend in part on whether other parameters (water vapor and temperature), now measured by radiosondes, can also be measured remotely.

References

[*1*] Davenport, W. B. and Root, W. L., *An Introduction to the Theory of Random Signals and Noise*, McGraw-Hill, New York, 1958.

[*2*] Srivastava, R. C. and Atlas, D., "The Effects of a Finite Radar Pulse Volume on Turbulence Measurements," *Preprints, 15th Radar Meteorology Conference*, American Meteorological Society, Boston, Mass., 1972, pp. 297-302.

[*3*] Atlas, D. in *Advances in Geophysics*, Vol. 10, Academic Press, New York, 1964, pp. 317-478.

[*4*] Lhermitte, R. M. and Atlas, D., *Proceedings of the 9th Weather Radar Conference*, American Meteorological Society, Boston, Mass., 1961, pp. 218-223.

[*5*] Browning, K. A. and Wexler, R., *Journal of Applied Meteorology*, Vol. 7, 1968, pp. 105-113.

[*6*] Joss, J. and Waldvogel, A., "Raindrop Size Distributions and Doppler Velocities," *Preprints, 14th Radar Meteorology Conference*, American Meteorological society, Boston, Mass., 1970, pp. 153-156.

[*7*] Pasqualucci, F., "Measurements of Drop Size Distributions Using a 35 GHz Doppler Radar," *Preprints, 15th Radar Meteorology Conference*, American Meteorological Society, Boston, Mass., 1972, pp. 173-178.

[*8*] Donaldson, R. J., Jr., *Journal of Applied Meteorology*, Vol. 9, 1970, pp. 661-670.

[*9*] Lhermitte, R. M., "Dual Doppler Radar Observation of Convective Storm Circulation," *Preprints, 14th Radar Meteorology Conference*, American Meteorological Society, Boston, Mass., 1970, pp. 139-144.

[*10*] Lhermitte, R. M. and Miller, L. J., "Doppler Radar Methodology for the Observation of Convective Storms," *Preprints, 14th Radar Meteorology Conference*, American Meteorological Society, Boston, Mass., 1970, pp. 133-138.

[*11*] Lhermitte, R. M. and Gilet, M., "Acquisition and Processing of Tri-Doppler Radar Data," *Preprints, 17th Radar Meteorology Conference*, American Meteorological Society, Boston, Mass., 1976, pp. 1-14.

[*12*] Sirmans, D. and Doviak, R., "Meteorological Radar Signal Intensity Estimation," National Oceanic and Atmospheric Administration Technical Memo ERL/NSSL-64, National Severe Storms Laboratory, U.S. Department of Commerce, Norman, Okla., 1973.

[*13*] Rummler, W. D., "Introduction of a New Estimator for Velocity Spectral Parameters," Technical Memo MM-68-4121-5. Bell Telephone Laboratories, Whippany, N.J., 1968.

[*14*] Lhermitte, R. M., "Real-Time Processing of Meteorological Doppler Radar Signals," *Preprints, 15th Radar Meteorology Conference*, American Meteorological Society, Boston, Mass., 1972, pp. 364-367.

[*15*] Haag, K. W., "Video Tape Recording of Weather Radar Signals," *Preprints, 17th Radar Meteorology Conference*, American Meteorological Society, Boston, Mass., 1976, pp. 33-35.

[*16*] Gray, G. R., Serafin, R. J., Atlas, D., Rinehart, R. E., and Boyajian, J. J., *Bulletin of the American Meteorological Society*, Vol. 56, 1975, pp. 580-588.

[*17*] Richter, J. H., *Radio Science*, Vol. 4, 1969, pp. 1261-1268.

[*18*] Strauch, R. G., "Theory and Application of the FM-CW Doppler Radar," Ph.D. Thesis, University of Colorado, Boulder, Colorado, 1976.

[*19*] Hardy, K. in *Remote Sensing of the Troposphere*, V. E. Derr, Ed., U.S. Department of Commerce, Washington, D.C., 1972, Chapter 14.

[*20*] Starr, J. R. and Browning, K. A., "Doppler Radar Measurements of Clear Air Turbulence," *Preprints, 15th Radar Meteorology Conference*, American Meteorological Society, Champaign-Urbana, 1972, pp. 248-251.

[*21*] Hennington, L., Doviak, R. J., Sirmans, D., Zrnic, D., and Strauch, R. G., "Measurement of Winds in the Optically Clear Air with Microwave Pulse-Doppler Radar," *Preprints, 17th Radar Meteorological Conference*, American Meteorological Society, Boston, Mass., 1976, pp. 342-348.

[*22*] Green, J. L., Warnock, J. M., Winkler, R. H., and Van Zandt, T. E., *Geophysical Research Letter*, Vol. 2, 1975, pp. 19-21.

[*23*] Chadwick, R. B., Moran, K. P., Strauch, R. G., Morrison, G. E., and Campbell, W. C., *Radio Science*, Vol. 11, 1976, pp. 795-802.

[*24*] Frisch, A. S. and Clifford, S. F., *Journal of Atmospheric Science*, Vol. 31, 1974, pp. 1622-1628.

[*25*] Kropfli, R. A. and Kohn, N. M., "Duel-Doppler Radar Observations of the Convective

Mixing Layer at St. Louis," *Preprints, 17th Radar Meteorological Conference*, American Meteorological Society, Boston, Mass., 1976, pp. 321-325.

[*26*] Kropfli, R. A. and Kohn, N. M., "Persistent Horizontal Rolls in the Urban Mixing Layer as Revealed by Dual-Doppler Radar," presented at the 6th American Meteorological Society Conference on Inadvertent and Planned Weather Modification, Champaign Urbana, Oct. 1977.

Preprint Volume; 18th Conference on Radar Meteorology, 376-380,
American Meteorological Society, 1978.

IMPROVED DOPPLER VELOCITY ESTIMATES BY THE POLY-PULSE-PAIR METHOD

R. G. Strauch, R. A. Kropfli, W. B. Sweezy, W. R. Moninger
NOAA/ERL/Wave Propagation Laboratory
Boulder, Colorado 80302

and

R. W. Lee

Lassen Research
Manton, California 96059

1. INTRODUCTION

During the past several years most meteorological microwave Doppler radars have obtained estimates of mean Doppler velocity from the phase angle of the complex covariance of the received signal from successive transmitted pulses. This estimation technique, generally called pulse-pair processing, can be implemented in real time for a large number of range locations, and it has given the radar meteorologist access to greatly expanded Doppler data sets whose accuracy is comparable with, or in some cases better than, estimates obtained with spectral processing.

Pulse-pair processing has been proposed for pulse Doppler lidar (Strauch, 1976) where the estimate of mean velocity must be made from the signal received for one laser pulse. The lidar signal can be processed with the pulse-pair method by sampling the signal at any desired sampling rate and calculating the phase angle of the complex covariance for a time delay equal to the sampling period. Miller and Rochwarger (1972) showed that the quality of the estimates obtained with pulse-pair processing depends on the sample spacing. Lee (1977) recognized that not only could improved estimates be obtained for lags other than the first but also that the error in the estimates caused by noise is uncorrelated for the various lags. Hence improved estimates can be obtained by averaging the estimates obtained with various lags in a "poly-pulse-pair" processing scheme. Lee also noted the applicability of poly-pulse-pair processing for microwave Doppler radar where lag times are restricted to multiples of the radar pulse repetition period. In this paper we examine further the applicability of poly-pulse-pair processing for microwave Doppler radar and apply it to actual data that is ideally suited for this technique, i.e., data with low signal-to-noise ratio and with Doppler spectral widths that are much less than the Nyquist velocity interval. This is frequently the case with radar observations of chaff dispersed within the planetary boundary layer, of refractive index fluctuations in the optically clear air, and of some precipitation regimes such as snow. It probably cannot be used in severe storm applications. Note that the Nyquist velocity interval is $\frac{\lambda}{2nT}$ where λ is the radar wavelength, n is the lag number, and T is the pulse period. Thus estimates made with higher order lags may have to rely on those made with lag 1 to resolve ambiguities.

2. PULSE PAIR ESTIMATES FOR VARIOUS LAGS

The accuracy of the pulse-pair estimation technique has been examined by Miller and Rochwarger (1972), Berger and Groginsky (1973), and Zrnic (1976). It has been tested on simulated and actual data by Sirmans and Bumgarner (1975). Figure 1 illustrates Zrnic's results for the standard deviation of the estimate of normalized mean frequency ($\hat{f}T$) as a function of normalized spectral width (wT), signal-to-noise ratio, and the number of contiguous pulse pairs (M). These results apply to single lag processing with the lag time equal to the pulse repetition period (T).

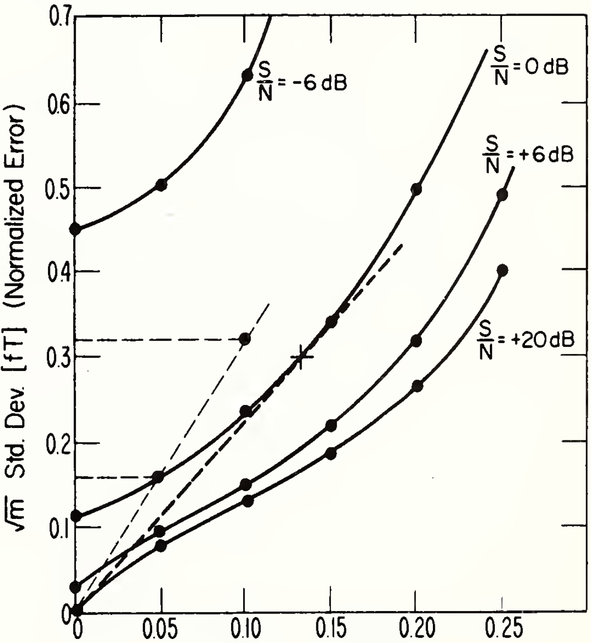

Figure 1. Theoretical standard deviation of the estimate of the normalized mean Doppler frequency by single pulse pair processing.

It can be readily be seen from Fig. 1 that if the mean velocity is calculated by pulse-pair-processing with a lag time of 2T, 3T, etc. then the standard error of estimate of mean velocity will be less for these lags than for single lag when the normalized widths of the Doppler spectra are small. For example, if the signal-to-noise ratio is 0 dB and the normalized width is 0.05, then, from Fig. 1, the normalized frequency error is 0.16. If the second lag is used, the normalized width is 0.10 and the normalized frequency error increases to 0.24. To scale these normalized frequency errors to the actual velocity error one must multiply the normalized error by $[\frac{2nT}{\lambda} \sqrt{M}]^{-1}$. Therefore, using the second lag as opposed to the first, we must halve the scaling factor. (M can be considered constant.) But as we have seen above the normalized error is not doubled for the second lag. (See dashed line in Fig. 1.) Hence the actual velocity error is less for the second lag. From Fig. 1 (dotted line) we see that the standard error of estimate of mean velocity is less for longer lags until the normalized width (nTw) becomes greater than about 0.13 for a S/N of 0 dB and somewhat larger for larger S/N.

The predicted performance of the pulse-pair estimator for various lags is given in Figs. 2a and 2b for a radar wavelength of 3.2 cm, a pulse repetition period of 350 microsec, and a signal dwell time of 45 millisec (128 radar samples). The standard deviation of mean velocity is improved for all lags and signal-to-noise ratios when the width of the spectrum is less than 1 m/s. However, when the width of the spectrum is 4 m/s, the standard error of mean velocity estimate increases rapidly for n > 2. For spectral widths of 2 m/s or less, the second and third lags will always give better estimates than the first.

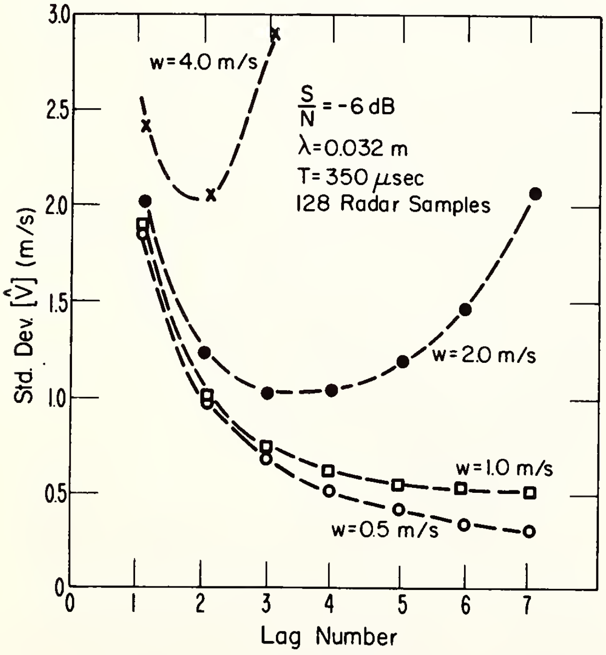

Figure 2a. Theoretical standard deviation of the mean Doppler velocity estimate by single pulse pair processing as a function of lag number for S/N = -6 dB.

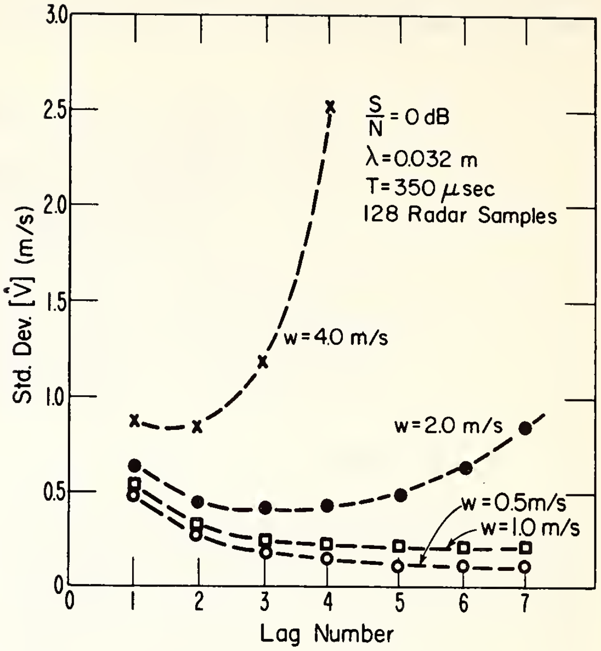

Figure 2b. Theoretical standard deviation of the mean Doppler velocity estimate by single pulse pair processing as a function of lag number for S/N = 0 dB.

3. PULSE-PAIR ESTIMATES WITH LINEAR COMBINATIONS OF ESTIMATES FROM SEVERAL LAGS

As we have seen, the error in the pulse-pair estimate for any given lag depends on the width of the Doppler spectrum and the signal-to-noise ratio. From Fig. 1 we see that when the signal-to-noise ratio is low (< 0 dB) and the normalized spectral width is small (< 0.1), then the major portion of the error in the estimate is caused by noise and not the spectral width. For example even for a spectral width of zero there is a substantial normalized error of .45 when S/N = - 6 dB. Since errors caused by noise are uncorrelated for the various lags (Lee, 1977), significant improvement in the quality of the estimate can be obtained by averaging various lags. On the other hand, if the signal to noise ratio is high then the estimates obtained with different lags will be highly correlated (for narrow spectra) and averaging will not improve the estimates.

We restrict attention to narrow spectra because the estimated error increases rapidly with spectral width. Figures 3a and 3b show the improvement expected in the estimate of mean velocity when estimates obtained with various lags are averaged with uniform weight. As pointed out by Lee (1977), the optimum averaging scheme would weight the estimate for each lag inversely proportional to the variance of the velocity estimate for that lag. However, this requires a priori knowledge of both the signal-to-noise ratio and the spectral width, and, for data where poly-pulse-pair processing is of most value (low signal-to-noise ratio and narrow

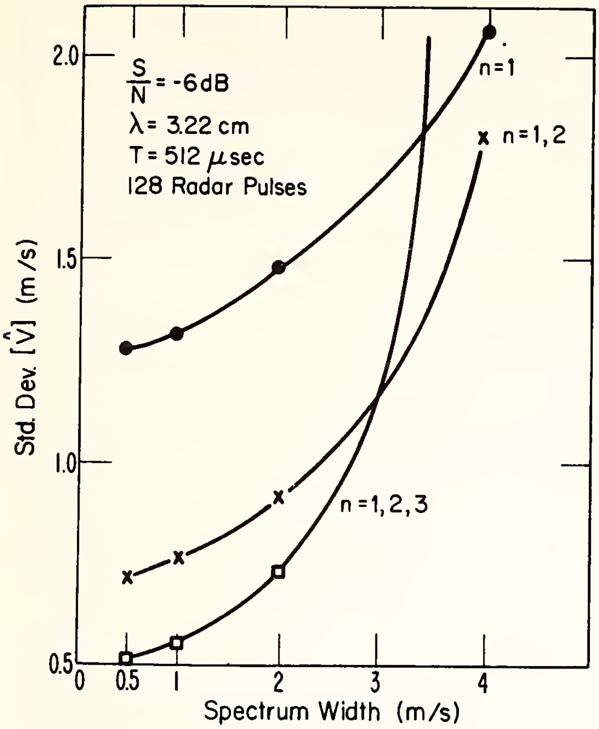

Figure 3a. Theoretical standard deviation of the estimate of the mean Doppler velocity by single pulse pair processing as a function of spectral width when estimates with various lags are averaged with uniform weights. S/N = -6 dB.

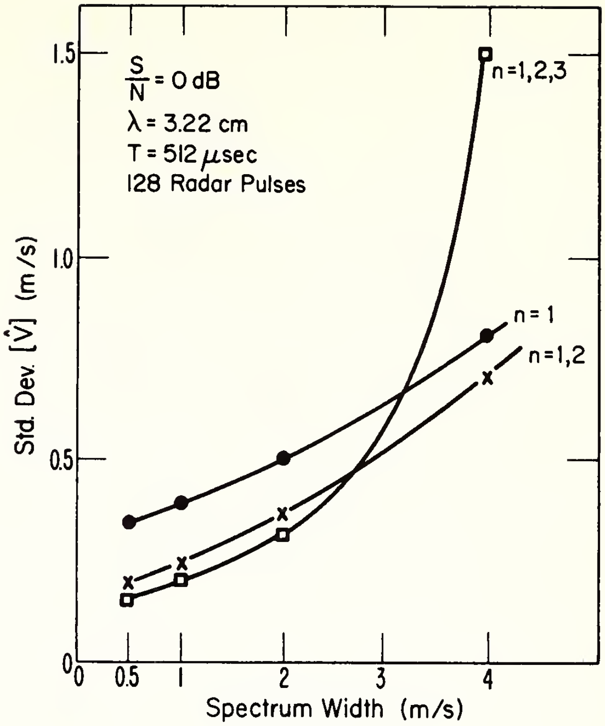

Figure 3b. Theoretical standard deviation of the estimate of the mean Doppler velocity by single pulse pair processing as a function of spectral width when estimates with various lags are averaged with uniform weights. S/N = 0 dB.

spectra) we do not have a satisfactory estimate of either. Therefore we have chosen to use equal weights recognizing that some additional improvement could be obtained if the first lag were weighted less.

From Figs. 3a and 3b we see that significant improvement over the first lag by itself can be obtained by averaging the estimates of the first two lags for spectral widths as high as 4 m/s, and if we restrict the technique to data with spectral widths less than 2 m/s, then we can further improve the estimates by averaging the results for the first 3 lags. When the signal-to-noise ratio is + 6 dB or more there is little to be gained by averaging because the estimates for the various lags are highly correlated. The data in Figs. 3a and 3b are for a 3.2 cm wavelength radar with a 512 microsec repetition period and a 65 millisec dwell time. The correlation coefficient for the portion of the estimate error that is not caused by noise is taken as 1. This is a valid approximation for narrow spectral widths.

4. TESTS WITH EXPERIMENTAL DATA

These concepts were applied to a real data set to which samples of receiver noise were added to bring all data above a specified intensity level to a known, fixed signal-to-noise ratio. Pulse pair estimates with various lags and poly-pulse-pair estimates for the average of several lags were then compared to the pulse pair estimates before the noise was added. Since the signal-to-noise ratio before the addition of noise samples was greater than + 5.8 dB, the pulse pair estimates for these data were very accurate and were considered as "truth" to which the noise-degraded estimates could be compared. RMS errors between the noise-degraded estimates and the undegraded estimates were then computed for various signal-to-noise ratios. The results are given in Fig. 4.

The data that were used in this test were obtained from chaff measurements in the boundary layer during METROMEX (Kropfli and Kohn, 1976). The observed narrow Doppler widths of about 1 m/s and radial velocities less than 5 m/s were typical for afternoon boundary layer observations and are ideally suited for poly-pulse-pair processing.

Figure 4 indicates a significant improvement in the second lagged estimate over the first at weak signal to noise ratios. For example, the RMS error reduction is greater than a factor of 2 for S/N less than -3 dB. A significant improvement is achieved even at 0 dB. Furthermore, the third lagged estimate shows a slight improvement over the second. A total of 396 velocity estimates were used to compute each RMS error at a particular S/N and lag number. Because of the inherent difficulty in computing second moments of Doppler spectra, no attempt was made to stratify the errors by Doppler width as well as S/N. A variety of

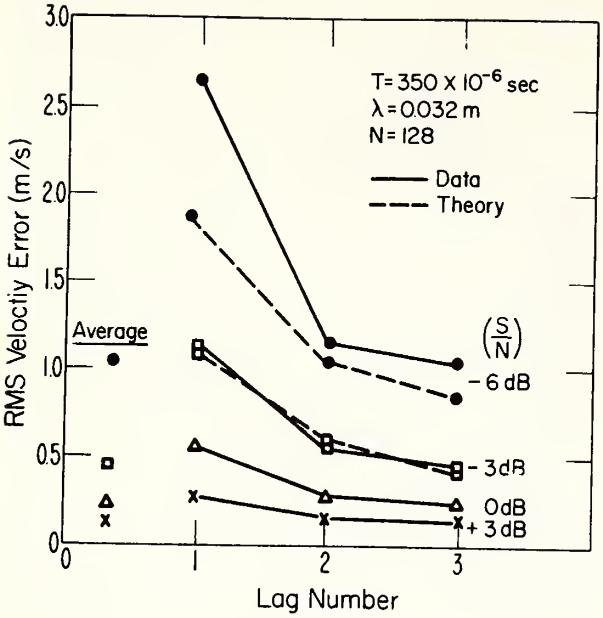

Figure 4. RMS velocity error of various lagged estimates as a function of S/N and lag number for experimental data (solid) and theory (dashed).

widths are therefore included in the 396 estimates.

Points listed under "average" on the left hand side of Fig. 4 indicate the measured RMS error of estimates formed from the average of the first 3 lagged estimates at each signal to noise ratio. It can be seen that the additional improvement over the second or third lag is very slight. Since two or three times the amount of calculation is required, the average estimate would be chosen over a single lagged estimate only when extreme accuracy is required and computational cost is not important.

Also shown in Fig. 4 are theoretical RMS errors computed from the results of Zrnic (1977). It is seen that there is excellent agreement between the experimental data and Zrnic's result for $S/N \geq -3$ dB, although theory tends to underestimate the RMS errors by 15 to 30% at $S/N = -6$ dB. (Data points and theoretical values are the same for signal-to-noise ratios greater than 0 dB.) A nominal Doppler width of 1 m/s was assumed in the theoretically derived errors.

5. TESTS WITH SIMULATED SIGNAL PLUS NOISE

We have also performed simulations similar to those described by Sirmans and Bumgarner (1975) and we find excellent agreement with theory for S/N ratios greater than -3 dB as is shown in Fig. 5. However, for S/N ratios of -6 dB we find the same discrepancy between theory and simulations as we find between theory and data in Fig. 4. This suggests that assumptions required in deriving the theoretical expressions for the standard error of the estimate may be invalid at $S/N < -3$ dB.

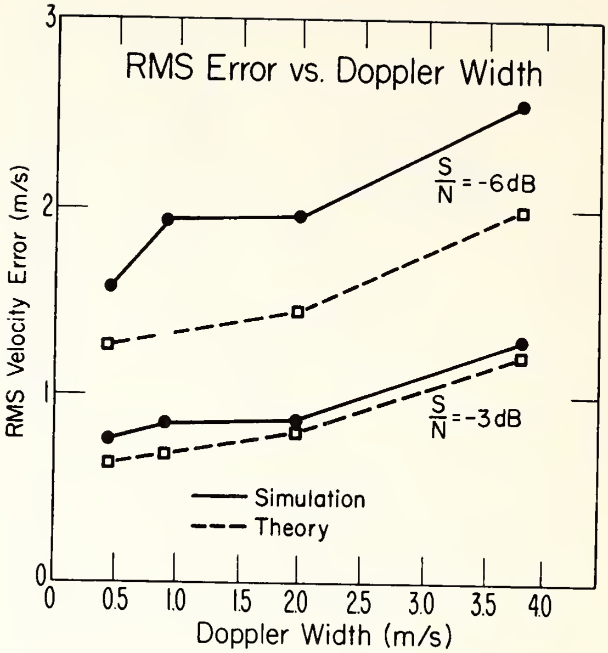

Figure 5. RMS errors vs Doppler width for simulated data and theory. Each simulated RMS estimate was derived from 512 velocity estimates with each velocity estimate the result of 128 radar samples spaced by $T = 512$ μs. $\lambda = .032$ m was assumed.

6. CONCLUSIONS

Poly-pulse pair processing can improve the quality of mean velocity estimates for weak signal-to-noise ratio data if the spectral widths are small compared to the Nyquist interval. These improved estimates can be obtained only at a significant increase in computational cost. Often, however, estimates obtained with a pulse-pair-processing algorithm that uses a single lag of 2 or 3 times the pulse repetition period will be significantly better than that obtained for lag 1. When poly-pulse-pair processing or processing that uses a single lag greater than the first is used, potential velocity ambiguities can be resolved by means of the estimate made with the first lag.

At very weak signal-to-noise ratios (< - 3 dB) the expected error of single lagged estimates is larger than that predicted by theory. This was found to be true for both real data and simulated data.

Poly-pulse-pair processing has application to microwave radar only for special data sets because of the requirement of narrow spectra and because the sampling interval is restricted to multiples of the pulse-repetition period. The types of observations most suitable for these techniques are in the convective boundary layer, snow, and light stratiform rain. These restrictions are lessened somewhat for the processing of laser radar data because the sampling rate can be made continuously variable.

7. REFERENCES

Kropfli, R. A. and N. M. Kohn, 1976: Dual Doppler radar observations of the convective mixing layer at St. Louis, Proc. of the 17th Conference on Radar Meteorology, AMS., Seattle, Washington, 321-325.

Lee, R. W., 1977: Poly-pulse-pair Doppler estimation, Submitted for Publication.

Miller, K. S., and M. M. Rochwarger, 1972: A covariance approach to spectral moment estimation, *IEEE Trans. Inform. Theory,* IT-18, 588-596.

Sirmans, D., and W. B. Bumgarner, 1975: Numerical comparison of five mean frequency estimators, *J. Appl. Meteor.,* 14, 991-1003.

Strauch, R. G., 1977: Design study of a ground-based and airborne CO_2 pulsed coherent lidar for remote wind measurements, Chap. 14, NOAA Tech. Report, In Press.

Zrnic, D. S., 1977: Spectral moment estimates from correlated pulse pairs. *IEEE Trans. on Aerospace and Electronic Systems,* Vol. 13, no. 4, 344-354.

Preprint Volume; 18th Radar Meteorological Conference, 401-404,
American Meteorological Society, 1978.

COMPARISON OF MAXIMUM ENTROPY METHOD ESTIMATION OF DOPPLER VELOCITY MOMENTS WITH CONVENTIONAL TECHNIQUES

W. B. Sweezy

NOAA/ERL/Wave Propagation Laboratory
Boulder, Colorado 80302

1. INTRODUCTION

The most common ways of estimating the moments (mean and variance) of velocity spectra measured by Doppler radar are the fast Fourier transform (FFT) and the pulse-pair-processing (PPP) covariance method. The FFT and PPP were among the methods for estimating the first moment that were compared by Sirmans and Bumgarner (1975). Our study (motivated, in part, by the need to obtain better second moment estimates) compares FFT and PPP estimates with those obtained from the maximum entropy method (MEM) for estimating power spectra. The moments are calculated by each of the three methods using computer simulated data. The simulation generates a complex time series having a velocity spectrum composed of a Gaussian signal spectrum with specified moments, and a noise spectrum for a specified signal-to-noise ratio. Since the greatest need for improved moment estimates is in cases of low signal-to-noise ratio and relatively broad spectrum, particular attention is given to these cases. Various techniques for reducing the noise bias in the moment estimates are applied to the spectral methods (FFT and MEM). The relative merits of each method are evaluated by examining the error statistics and the worst case errors.

2. THE MAXIMUM ENTROPY METHOD

It is not possible to give a detailed description of MEM spectral analysis in this discussion, but since it is a relatively new method a brief outline is included. The MEM was introduced by Burg (1967), but it was not published in the open literature until a few years later. Lacoss (1971) and Markel (1972) were among the first to publish complete detailed explanations of the method. In recent years the MEM has been refined and expanded by several investigators including Burg (1975), Ulrych and Bishop (1975), Haykin and Kesler (1976), and Strand (1977).

The MEM approximates the frequency spectrum by an all-pole model, namely,

$$S(f) = \frac{E_n}{|1 + \sum_{k=1}^{n} a_{kn} W^k|^2} ,$$

where $W = e^{-2\pi i f \Delta t}$. The a_{kn} are coefficients of a "whitening" filter of length n, such that for a given complex time series, z(t), with zero mean, the output of the filter, given by

$$\varepsilon_n(t) = z(t) + a_{1n} z(t+\Delta t) + \ldots + a_{nn} z(t+n\Delta t),$$

resembles "white" noise. E_n is the (average) power spectral density of $\varepsilon_n(t)$. The filter coefficients are determined by a recursion relationship with the autocovariance function of z(t), that is the coefficients for a filter of length n are determined from the coefficients of a filter of length (n-1) and n terms of the autocovariance function.

Computation techniques and computer programs are described by Strand, Young, and Chadwick (1977). The paper by Makhoul (1975), in addition to those cited above, is suggested for a complete description of the MEM and other linear prediction techniques. In contrast to windowing methods which taper and truncate the autocovariance function, the MEM provides a non-zero extension of the autocovariance function. In Fig. 1 an MEM spectrum is compared with a FFT spectrum with a Hanning window.

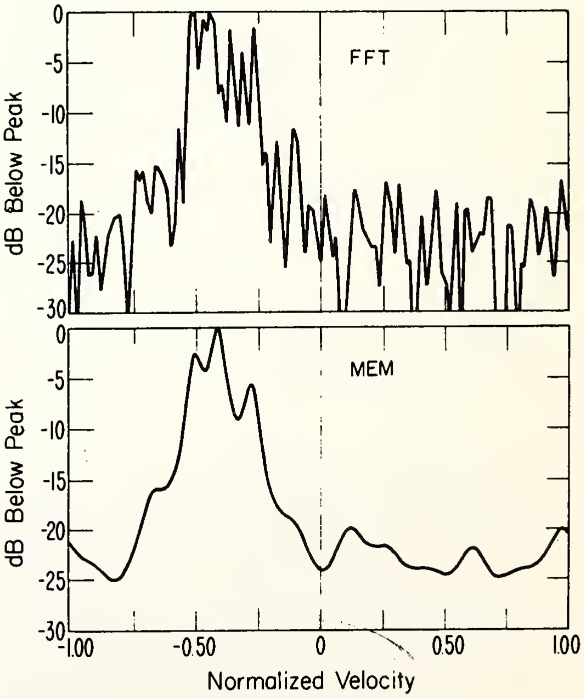

Figure 1. Comparison of FFT and MEM estimates of spectra derived from a simulated time series of 128 samples with signal-to-noise ratio 10 dB, true normalized mean velocity -0.39 and true normalized spectrum width 0.095.

3. REDUCTION OF NOISE BIAS

Whenever any estimate of the velocity spectrum that contains noise as well as signal power is used, the moment calculations are biased by the noise. The effect for the first moment is illustrated in Fig. 2. The reduction in slope is due to noise and the sharp drop near the Nyquist velocity is due to aliasing. The noise bias can be reduced and the effect of aliasing can be eliminated by balancing the spectrum with respect to the mode, i.e., by shifting the spectrum cyclically within the Nyquist interval until the mode is in the center of the interval. The estimate of the mean is given by the sum of the mode and the calculated mean. Since balancing the spectrum does not reduce the noise bias in the second moment, the methods of noise subtraction and signal isolation, as well as a combination of both, are used. For noise subtraction the noise is assumed to be "white" so that the noise power spectral density is independent of frequency. For the MEM, E_n is the desired estimate of the noise spectrum. For the FFT, the noise spectrum is estimated as the average below a threshold. The threshold is adjusted until the spectrum below it approximates the statistical properties of "white" noise (Hildebrand and Sekhon, 1973). In signal isolation only that portion of the spectrum which contains the mode and extends above the noise is used to estimate the moments.

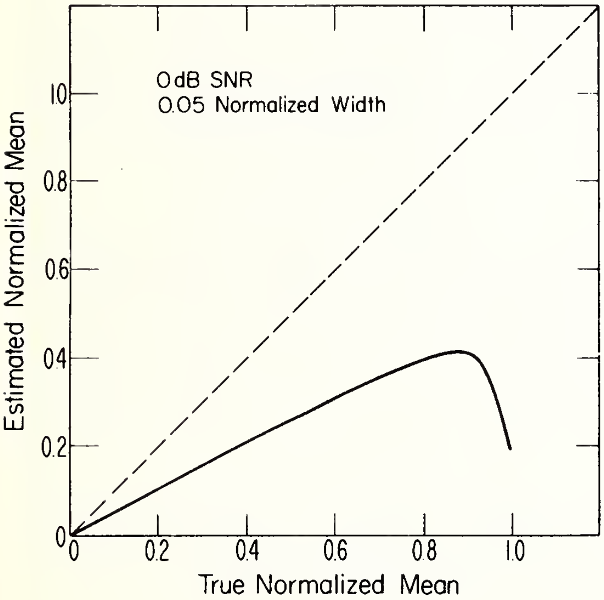

Figure 2. An illustration of the effects of noise and aliasing on the estimation of the first moment using spectral methods.

4. RESULTS

Time-series of 1024 points were simulated and quantized to 8 bits. For comparisons using various sample lengths the shorter samples were extracted from independent 1024 point samples. Fifty realizations for each sample size and signal-to-noise ratio, with the true normalized mean velocity uniformly distributed in the Nyquist interval and the true normalized spectrum width uniformly distributed between 0.05 and 0.2, were used to determine the error statistics. The MEM spectra were estimated with twelve filter coefficients. In Fig. 3 the expected errors in the first moment are illustrated for the three methods, for fixed sample length as a function of signal-to-noise ratio. The results for the spectral methods (FFT and MEM) are with noise subtraction. The addition of signal isolation provided only slight improvement in the MEM and in some cases degraded the FFT results because of the failure of the algorithm to properly isolate the signal. In Fig. 4 the same results are shown as a function of sample length for fixed signal-to-noise ratio. Figures 5 and 6 illustrate the same results for the second moment. However, for second moments, the combination of noise subtraction and signal isolation show significant improvement over noise subtraction alone in the MEM results.

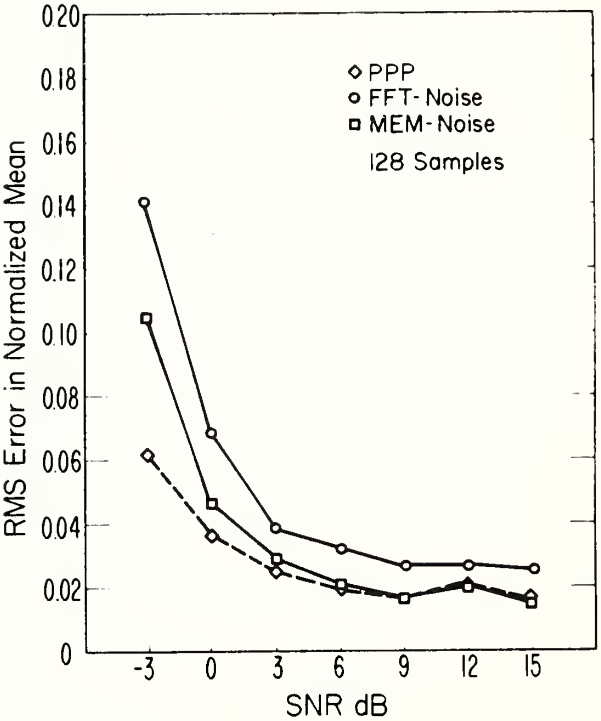

Figure 3. Comparison of the rms errors in the PPD first moment estimates with those in the MEM and FFT estimations with noise subtraction illustrates the superiority of the PPP first moment estimator, particularly at very low signal-to-noise ratios.

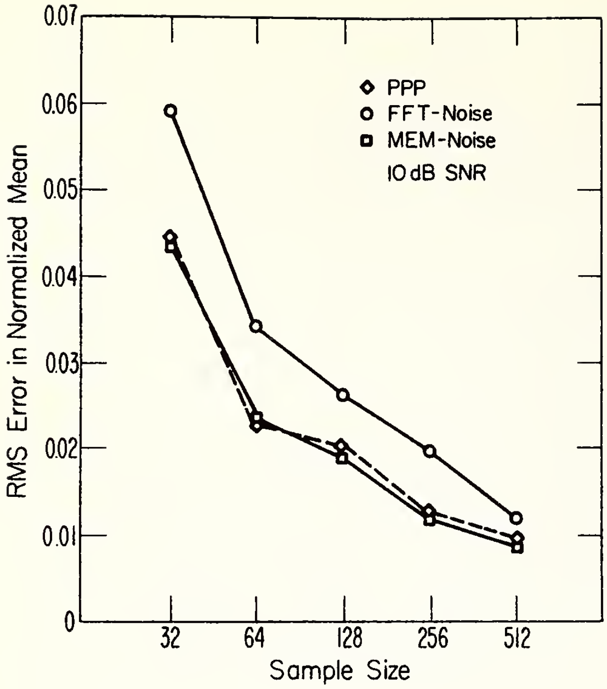

Figure 4. Comparison of the rms errors in the first moment estimators illustrates the finite data window effects.

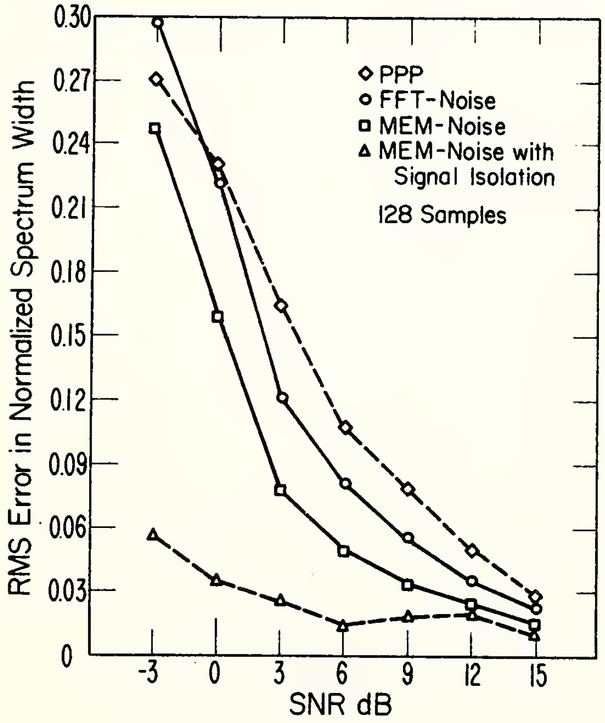

Figure 5. Comparison of the rms errors in the second moment estimators, PPP, FFT and MEM with noise subtraction, and MEM with both noise subtraction and signal isolation, shows that the MEM is a very good second moment estimator.

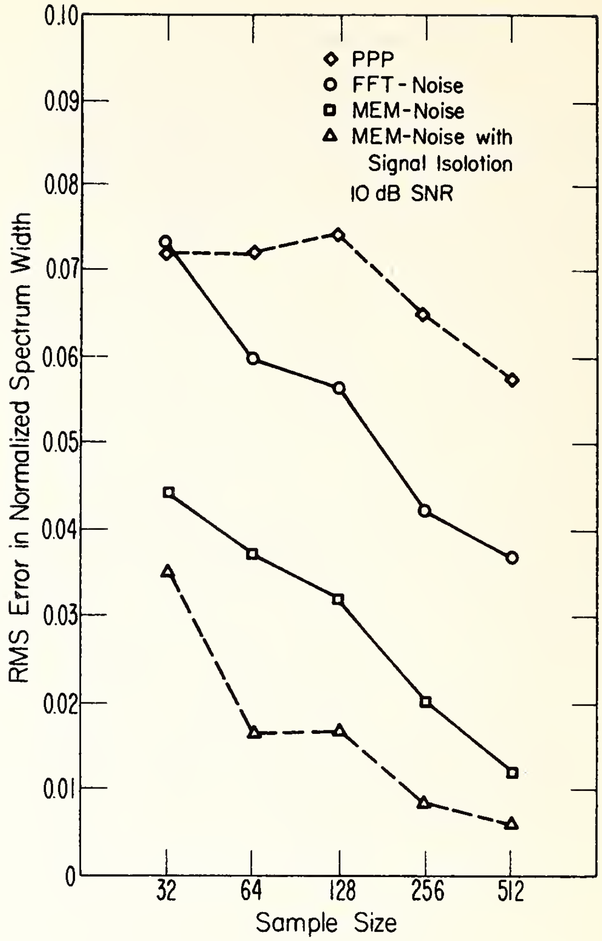

Figure 6. Comparison of the rms errors in the second moment estimator demonstrates the effects of window "broadening" in the spectral methods, but again illustrates value of the MEM as a second moment estimator.

5. CONCLUSIONS

The PPP appears to be "best" estimator of mean velocities, both from the standpoint of accuracy and computing efficiency. This agrees with the results of Sirmans and Bumgarner (1975). However, in real data with ground return or image spectrum, the use of spectral methods with signal isolation may be necessary. In these cases, results indicate that the MEM is superior to the FFT.

The MEM (with signal isolation) appears to be by far the most accurate estimator of the second moment. The MEM in its present form sacrifices some computing efficiency. With optimization, however, it could be comparable to the FFT for large sample sizes with few filter coefficients.

7. REFERENCES

Burg, J. P., 1967: Maximum entropy spectral analysis, *37th Annual Intl. SEG Meeting*, Oklahoma City, OK.

Burg, J. P., 1975: Maximum entropy spectral analysis, *Ph.D. Dissertation, Dept: of Geophysics,* Stanford University.

Haykin, S., and S. Kesler, 1976: The complex form of the maximum entropy method for spectra estimation, *Proc. IEEE,* 64, 822-823.

Hildebrand, P. H. and R. S. Sekhon, 1973: Objective determination of the noise level in Doppler spectra, *Tech. Report no. 32, Lab. Atmospheric Probing, Dept. Geophys. Sci.,* University of Chicago.

Lacoss, R. T., 1971: Data adaptive spectral analysis methods, *Geophysics,* 36, 661-675.

Makhoul, J., 1975: Linear prediction: a tutorial review, *Proc. IEEE,* 63, 561-580.

Markel, J. D., 1972: Digital inverse filtering — a new tool for format trajectory estimation, *IEEE Trans. on Audio and Electroacoustics, AU-20,* 113-119.

Sirmans, D., and B. Bumgarner, 1975: Numerical comparison of five mean frequency estimators, *J. Appl. Meteor.,* 14, 991-1003.

Strand, O. N., 1977: Multichannel complex maximum entropy (autoregressive) spectral analysis, *IEEE Trans. on Automatic Control, AC-22.*

______, J. M. Young and R. B. Chadwick, 1977: Computer programs for maximum entropy spectral analysis of real and complex single-channel time series, *NOAA Tech. Memo.* ERL WPL-19.

Ulrych, T. J. and T. N. Bishop, 1975: Maximum entropy spectral analysis and autoregressive decomposition, *Rev. Geophys. and Space Phys.,* 13, 185-200.

Author Index*

NAME	PAGE NUMBER IN REPRINT VOLUME
Abshire, N.L.	452, 464
Alpers, W.R.	268
Barrick, D.E.	1, 258, 385, 491
Bedard, A.J.	166, 176, 392, 405, 415
Beran, D.W.	23, 116
Brost, R.A.	315
Brown, E.H.	29, 180, 473
Burton, E.B.	93
Campbell, W.C.	129, 263, 359
Carbone, R.	432
Chadwick, R.B.	125, 129, 263
Chappel, C.F.	93
Chimonas, G.	476
Clifford, S.F.	215, 245, 491, 498, 503, 605, 620
Cohen, R.	130
Cupp, R.E.	307
Danielson, K.S.	439
Decker, M.T.	137, 250
Derr, V.E.	139, 201, 216, 226, 303, 439, 464, 538
Dye, J.E.	421
Earnshaw, K.B.	209, 231, 234
Evans, M.W.	385, 539
Fedor, L.S.	258

---

*Underlined page number indicates first-authorship.

Frisch, A.S. 359

Fujita, T.T. 176

Gaynor, J.E. 329, 334, 339

Golden, J.H. 93

Gossard, E.E. 102, 263, 551, 556

Greunke, R.G. 209

Guiraud, F.O. 117, 137, 250

Hall, F.F. 29, 349, 365

Haugen, D.A. 140, 145 155, 307, 628

Hill, R.J. 162, 568, 577, 599, 605, 613

Hogg, D.C. 103

Hooke, W.H. 107, 130, 166, 285

Huffaker, R.M. 115

Johnston, A.L. 644

Kaimal, G.R. 140, 145, 162, 186, 297, 352

Keeler, R.J. 632, 637, 640

Kohn, N.M. 465, 644

Kropfli, R.A. 465, 679

Lawrence, R.S. 209, 215, 231, 234

Lee, R.W. 640, 679

Leise, J.A. 645

Le Mone, M.A. 373

Lenschow, D.H. 373

Lerfald, G.M. 139, 216, 303, 464

Levin, Z. 421

Lipa, B. 401

Little, C.G. 23, 93, 116, 180

Lopez, R.E. 445, 651
Mandics, P.A. 339
Martner, B.E. 421
McNice, G.T. 452, 464
Miller, L.J. 421, 427
Mohr, C. 644
Moninger, W.R. 359, 432, 434, 618, 679
Moran, K. P. 125, 129, 263
Morrison, G.E. 125, 129, 263
Murphy, A.H. 93
Neff, W.D. 148, 155, 365, 370
Newman, J.T. 307
Ochs, G.R. 162, 215, 221, 241, 245, 613
Pearl, E.W. 93
Pennell, W.T. 373
Platt, C.M.R. 452, 457
Post, M.J. 139, 159, 226, 307
Priestley, T. 498
Pueschel, R.F. 464
Rufenach, C.L. 268
Sanders, M.J., Jr. 415
Schiesow, R.L. 226, 307
Serafin, R.J. 655
Sorensen, D.C. 162
Strauch, R.G. 263, 359, 434, 618, 655, 679
Sweezy, W.E. 618, 679, 684

Van Valin, C.C.	464
Wang, T.T.	209, 221, 230, 231, 234, 241, 245, 498
Weber, B.L.	385, 619
Westwater, E.R.	117, 137, 250, 276, 310
Wright, W.M.	180
Wyngaard, J.C.	120, 162, 315, 373, 620

☆ U. S. GOVERNMENT PRINTING OFFICE 1980 - 677-096/1239 Reg. 8

PENN STATE UNIVERSITY LIBRARIES
A000072832790